Transactions of the ASME

EDITORIAL STAFF
Editor, J. J. JAKLITSCH, JR.
Production Editor, STELLA ROBINSON
Editorial Production Asst. BETH DARCHI
Associate Editors
Air Pollution Control H. E. HESKETH
Diesel and Gas Engine Power F. PEKAR
Gas Turbine A. J. WENNERSTROM
Power D. T. BERUBE
Solar Energy F. KREITH
Energetics M. L. SAVITZ
Fuels C. R. PELLEY
Nuclear Engineering P. W. IANNI
POLICY BOARD, COMMUNICATIONS
Chairman and Vice-President I. BERMAN
Members-at-Large J. E. ORTLOFF, J. W. LOCKE, M. J. RABINS, W. J. WARREN
Policy Board Representatives
Basic Engineering, F. LANDIS
General Engineering, A. A. SEIREG
Industry, R. K. HAMPTON
Power, R. E. REDER
Research, G. P. COOPER
Codes and Stds., L. L. ELDER
Computer Technology Com., A. A. SEIREG
Nom. Com. Rep., S. ROGACKI
Business Staff
345 E. 47th St.
New York, N. Y. 10017
(212) 644-7789
Mng. Dir., Publ., C. O. SANDERSON
OFFICERS OF THE ASME
President, DONALD N. ZWIEP
Exec. Dir. & Sec'y, ROGERS B. FINCH
Treasurer, ROBERT A. BENNETT

Journal of Engineering for Power (ISSN 0022-0825) is edited and published quarterly at the offices of The American Society of Mechanical Engineers, United Engineering Center, 345 E. 47th St., New York, N. Y. 10017. ASME-TWX No. 710-581-5267, New York. Second Class postage paid at New York, N.Y., and at additional mailing offices.

CHANGES OF ADDRESS must be received at Society headquarters seven weeks before they are to be effective. Please send old label and new address.

PRICES: To members, $25.00, annually; to nonmembers, $50.00. Single copies, $15.00 each. Add $1.50 for postage to countries outside the United States and Canada.

STATEMENT from By-Laws. The Society shall not be responsible for statements or opinions advanced in papers or . . . printed in its publications (B 13, Par. 4).

COPYRIGHT © 1980 by the American Society of Mechanical Engineers. Reprints from this publication may be made on condition that full credit be given the TRANSACTIONS OF THE ASME—JOURNAL OF ENGINEERING FOR POWER, and the author, and date of publication be stated.

INDEXED by the Engineering Index, Inc.

Journal of Engineering for Power

Published Quarterly by The American Society of Mechanical Engineers
VOLUME 102 • NUMBER 2 • APRIL 1980

225 Utilization of the Cold by LNG Vaporization with Closed-Cycle Gas Turbine (79-GT-84)
G. Krey

231 Starting Torque Characteristics of Small Aircraft Gas Turbines and APU's (79-GT-95)
C. Rodgers

239 Application of All-Ceramic Nozzel to Radial Flow Turbine (79-GT-96)
J. C. Napier

244 Fractography of Reaction-Sintered Si_3N_4 (79-GT-97)
M. G. Mendiratta, P. L. Land, R. Ruh, R. W. Rice, and D. C. Larsen

249 Recent Developments on Gas Turbine Control Systems (79-GT-98)
P. D. Greenhalf

257 An Experimental Study of Endwall and Airfoil Surface Heat Transfer in a Large Scale Turbine Blade Cascade (79-GT-99)
R. A. Graziani, M. F. Blair, J. R. Taylor, and R. E. Mayle

268 Evaluation of Laminated Porous Wall Materials for Combustor Liner Cooling (79-GT-100)
D. A. Nealy and S. B. Reider

277 Mechanical Reliability Considerations in the Modern High Temperature Industrial Gas Turbine (79-GT-101)
J. J. Korta

283 The Influence of the Blading Surface Roughness on the Aerodynamic Behavior and Characteristic of an Axial Compressor (79-GT-102)
K. Bammert and G. U. Woelk

288 The Relationship of Power and Heat Production with Closed Cycle Gas Turbines (79-GT-103)
H. U. Frutschi

292 Development Progress on the Atmospheric Fluidized Bed Coal Combustor for Cogeneration Gas Turbine System for Industrial Cogeneration (79-GT-104)
R. S. Holcomb

297 Industrial Type Gas Turbines for Offshore Applications (79-GT-105)
G. Elmhed, S. Ferm, and S. O. Svensson

303 The Role of the Ceramic Heat Exchanger in Energy and Resource Conservation (79-GT-106)
C. F. McDonald

316 Measurements of the Four-Quadrant Characteristics on a Multistage Turbine (79-GT-107)
K. Bammert and P. Zehner

322 Forced Vibrations of a Single Stage Axial Compressor Rotor (79-GT-108)
J. A. Fabunmi

329 Friction Damping of Resonant Stresses in Gas Turbine Engine Airfoils (79-GT-109)
J. H. Griffin

334 The Time-Variant Aerodynamic Responses to a Stator Row Including the Effects of Airfoil Camber (79-GT-110)
S. Fleeter, W. A. Bennett, and R. L. Jay

344 Aerodynamic and Aeroelastic Characteristics of Oscillating Loaded Cascades at Low Mach Number—Part I: Pressure Distribution, Forces, and Moments (79-GT-111)
H. Atassi and T. J. Akai

352 Aerodynamic and Aeroelastic Characteristics of Oscillating Loaded Cascades at Low Mach Number—Part II: Stability and Flutter Boundaries (79-GT-112)
T. J. Akai and H. Atassi

357 Modal Analysis of Gas Turbine Buckets Using a Digital Test System (79-GT-124)
H. A. Nied

369 Optimization for Rotor Blades of Tandem Design for Axial Flow Compressors (79-GT-125)
K. Bammert and R. Staude

376 An Analysis of Aeroengine Fan Flutter Using Twin Orthogonal Vibration Modes (79-GT-126)
R. A. J. Ford and C. A. Foord

(*Continued on page 368*)

Downloaded 03 Jun 2010 to 171.66.16.159. Redistribution subject to ASME license or copyright; see http://www.asme.org/terms/Terms_Use.cfm

382 The Development of Wake Flow in a Centrifugal Impeller (79-GT-152)
M. W. Johnson and J. Moore

391 Effect of Interblade Phase Angle and Incidence Angle on Cascade Pitching Stability (79-FT-153)
F. O. Carta and A. O. St. Hilaire

397 Removal of Gaseous Alkali Metal Compounds from Hot Flue Gas by Particulate Sorbents (79-GT-154)
S. H. D. Lee and I. Johnson

403 Dependence of Soot Production on Fuel Blend Characteristics and Combustion Conditions (79-GT-155)
W. S. Blazowski

409 Improvements in the Utilization of Gas Turbine Compression Plant (79-GT-156)
B. M. Huggett and D. R. Ingham

416 Weak Extinction Limits of Turbulent Heterogeneous Fuel/Air Mixtures (79-GT-157)
D. R. Ballal and A. H. Lefebvre

422 The Experimental Behavior of Premixed Flames in Tubes: The Effects of Diluent Gases (79-GT-168)
J. Odgers, I. White, and D. Kretschmer

427 A Partial Oxidation Staging Concept for Gas Turbines Using Broadened Specification Fuels (79-GT-169)
R. M. Clayton

434 Improving Turbine Component Efficiency (79-GT-176)
K. D. Mach

437 A Design Review of Ceramic Components for Turbine Engines (79-GT-183)
P. J. Coty, A. D. Lane, J. B. Lee, and L. J. Meyer

448 The Prediction of Steady, Circumferential Pressure and Temperature Distortions in Multistage Axial Flow Compressors (79-GT-184)
H. Mokelke

459 The Effects of LBG Composition and Combustor Characteristics on Fuel NO_x Formation (79-GT 185)
B. A. Folsom, C. W. Courtney, and M. P. Heap

468 Assessment of Hot Gas Clean-Up Systems and Turbine Erosion/Corrosion Problems in Pfbc Combined Cycle Systems (79-GT-195)
J. Stringer, S. Ehrlich, W. W. Slaughter, and A. C. Dolbec

476 Low Frequency Gas Turbine Noises (79-GT-196)
J. R. Newman and K. I. McEwan

482 Steam Turbines for Cogeneration Power Plants (78-JPGC/Pwr-16)
I. Oliker

486 Design and Testing of a Cavity-Type, Steam-Generating, Central Receiver for a Solar Thermal Power Plant
R. J. Zoschak, S. F. Wu, and D. N. Gorman

495 Do Photovoltaics Have a Future? (79-Sol-7)
B. F. Williams

498 Double-Row Discrete-Hole Cooling: an Experimental and Numerical Study
G. Bergeles, A. D. Gosman, and B. E. Launder

504 The Effect of Material Properties on the Thermal Efficiency of the Minto Solar Wheel
S. Lin and R. Bharwaj

TECHNICAL BRIEF

508 Simulation of Whirl Interaction in Pinion-Gear Systems Supported on Oil by Film Bearings
B. Hamad and A. Seireg

DISCUSSION

510 Discussion of a previously published paper by
J. R. Mondt

511 Discussion of a previously published paper by
J. H. Wagner, T. H. Okiishi, and G. J. Holbrook

512 Discussion of a previously published paper by
D. Japikse and R. Pampreen

Downloaded 03 Jun 2010 to 171.66.16.159. Redistribution subject to ASME license or copyright; see http://www.asme.org/terms/Terms_Use.cfm

G. Krey
Head of Gas Turbine Department.
Gutehoffnungshütte Sterkrade AG,
Oberhausen,
W. Germany

Utilization of the Cold by LNG Vaporization with Closed-Cycle Gas Turbine[1]

In the course of the world-wide efforts to save energy, the utilization of cold in connection with the regasification of liquefied natural gas gains more and more importance. The aim is the partial recovery of the energy consumed in liquefaction. There are particular advantages when using the closed-cycle gas turbine, in which the exergy of the liquefied natural gas is transformed to electrical energy with a very high efficiency. The paper deals with the optimization, design, and operational behavior of such a plant.

Introduction

For the regasification of liquefied natural gas (LNG), two processes are mainly used today: sea water and submerged vaporization. Both require energy. For sea water vaporization the consumption is approximately 0.008 kWh/kg_{LNG}, for driving the sea water circulating pumps, and for submerged vaporization it is approx. 0.2 kWh/kg_{LNG}, for heating the water bath as the intermediate heat carrier for LNG vaporization. With an annual average ratio of application of the sea water and submerged vaporization processes of 70 to 30 percent (e.g., at LNG terminals on the North Sea) a mean consumption of approximately 0.08 kWh/kg_{LNG} results when the energy required for the sea water pumps is converted to the thermal energy equivalent by applying an assumed electrical efficiency of 35 percent. This consumption figure represents about 0.6 percent of the calorific value of the natural gas, which is about 48,000 kJ/kg. The exergy of the LNG cold (the LNG temperature after liquefaction is about −160°C) is not utilized at all.

In the endeavor to use energy more economically, increasing efforts are being made today to find LNG vaporization processes which allow part of the energy required for liquefaction to be recovered by utilization of the LNG cold. One process which meets this requirement and which is outstanding in many respects, is the application of the closed-cycle gas turbine. This turbine, which is successfully used in heat-and-power stations for the combined generation of electrical power and heat [1] is, in fact, predestined to be used in LNG vaporization with the utilization of cold. Its advantages are:

- simple design,
- high efficiency also at part-load operation [2, 3],
- high flexibility in adaptation to variations in natural gas and electricity consumption,
- possibility of using optimum working gas,
- high reliability in operation thanks to many years' experience with plants in service [4, 5], and
- low operating costs [6].

Process Diagram

The process diagram of the plant is shown in Fig. 1. The closed-cycle gas turbine installation consists of the following components:

- machine set with turbine, turbo compressor and generator on one common shaft,
- vaporizer,
- heater, and
- recuperator.

The T, s diagram in Fig. 2 shows how the cycle works. It can be seen that in the vaporizer the temperature of the working medium is reduced far below the ambient temperature by transfer of the low-

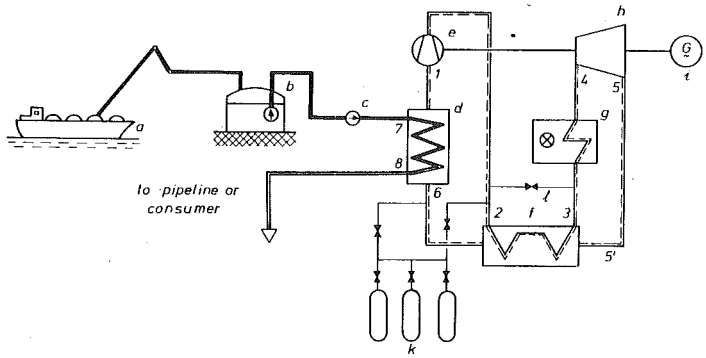


Fig. 1 Process diagram: — liquefied natural gas, ═ vaporized natural gas, ┅ working gas, a = LNG tanker, b = LNG tank with primary pump, c = secondary pump, d = vaporizer, e = compressor, f = recuperator, g = heater, h = turbine, i = generator, k = multi-chamber storage system, l = heat bypass

[1] The work which this paper is based on was furthered with funds contributed by the Ministry for Research and Technology of the Federal Republic of Germany (BMFT) and the Commission of the European Community.

Contributed by the Gas Turbine Division and presented at the Gas Turbine Conference and Exhibit and Solar Energy Conference, San Diego, California, March 12–15, 1979 of THE AMERICAN SOCIETY OF MECHANICAL ENGINEERS. Manuscript received at ASME Headquarters December 18, 1978. Paper No. 79-GT-84.

Copyright © 1980 by ASME
Downloaded 01 Jun 2010 to 171.66.16.58. Redistribution subject to ASME license or copyright; see http://www.asme.org/terms/Terms_Use.cfm

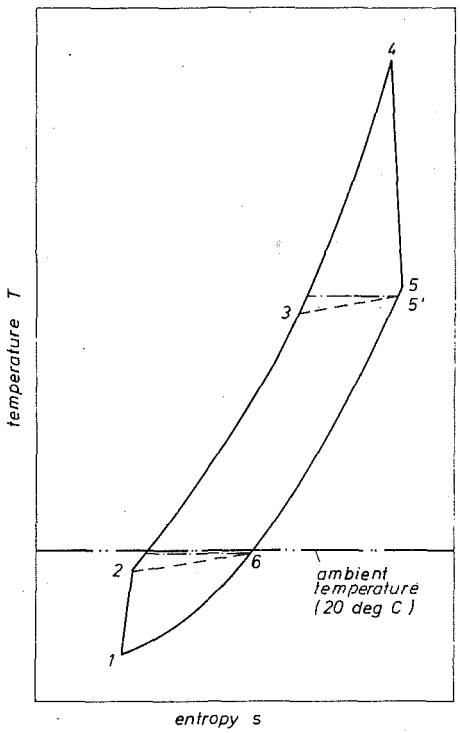


Fig. 2 *T, s* **diagram of the closed-cycle gas turbine (For points 1 to 6 see Fig. 1)**

temperature waste heat of the cycle to the cold LNG applying the cross counter-flow principle. The cold is utilized in that owing to the low compressor inlet temperature the power consumption of the compressor is considerably lower than in a plant where the lower cycle temperature is 20°C. Since the useful power increases by the amount of energy thus saved, the efficiency of the plant increases correspondingly (from 30 to over 50 percent). Furthermore, since there are no cooling tower losses as in the case of conventional heat-and-power stations, the overall rate of fuel utilization is considerably increased (from 70 to approximately 90 percent). The achievable electrical energy with this process, referred to the LNG quantity to be vaporized, is about 0.3 kWh/kg_{LNG}. About 4 percent of the vaporized LNG quantity is required for firing the heater of the plant.

Working Medium

A suitable working medium is nitrogen, with which there is no danger of fire, as with air, in the event of a leak in a vaporizer tube and natural gas entering the circuit. To prevent embrittlement of the high-temperature materials as a result of nitration, approximately 0.5 percent (by volume) oxygen is added to the nitrogen. Since nitration is prevented already at an oxygen content of 0.2 percent and the ignition limit is only at 8 percent, there are no problems in controlling the oxygen concentration thanks to the wide range available. As compared with other inert gases, such as helium, nitrogen offers the additional advantage of the real gas behavior in the lower temperature range, whereby the power input required for the compressor work is further reduced. In addition, when using nitrogen instead of helium the number of compressor and turbine stages decreases thanks to the about seven times smaller gas constant. This advantage is of particular importance here since for achieving optimum efficiencies it is necessary to have relatively high pressure ratios—as will be shown later. Finally, nitrogen is cheap; its present price is only about 0.1 dollar/kg.

Cycle Layout

In the layout of the cycle the "cold end" has to be adapted to the particular thermodynamic conditions of the natural gas. There are differences not only in composition (depending on the origin of the liquefied gas) but also in the pressures and temperatures upstream the vaporizer. The required temperature of the natural gas after vaporization is generally at least + 2°C. In order to meet the requirement for optimum layout of the vaporizer duly respecting the conditions given on the gas side, the most favorable combination of the following parameters has to be determined:

- expansion ratio of the turbine, π_T
- temperature difference in the recuperator, ΔT_R
- minimum temperature difference in the vaporizer $\Delta T_{V,\,min}$
- ratio of temperature spans in the vaporizer ξ

These parameters are defined as follows:

- The expansion ratio of the turbine is the quotient of the total pressures upstream and downstream the turbine

$$\pi_T = \frac{p_4}{p_5}. \tag{1}$$

(The indices are the same as in Fig. 1.)

- The temperature difference in the recuperator is the difference measured at the "hot end" of the heat exchanger

$$\Delta T_R = T_{5'} - T_3. \tag{2}$$

- The minimum temperature difference in the vaporizer is the smallest difference between the temperatures of the working medium and the natural gas. It can arise at the gas inlet or outlet of the vaporizer or inside the vaporizer as can be seen from the Q, T diagram in Fig. 3 for a supercritical state of the natural gas.
- The ratio of the temperature spans in the vaporizer is the quotient of heating of the natural gas and cooling of the medium

$$\xi = \frac{T_8 - T_7}{T_6 - T_1} = \frac{\dot{m}_M \cdot c_{pm,M}}{\dot{m}_{NG} \cdot c_{pm,NG}}. \tag{3}$$

In this equation $\dot{m}$ is the mass flow rate, c_{pm} the mean specific heat and the indices M and NG, the working medium and natural gas.

With given data of the natural gas (composition, pressure and temperature upstream and downstream the vaporizer), the thermodynamic conditions in the vaporizer are clearly and technically correctly defined by the parameters $\Delta T_{V,min}$, ξ and p_6. The cycle parameter which is left to be freely chosen is the expansion ratio π_T or

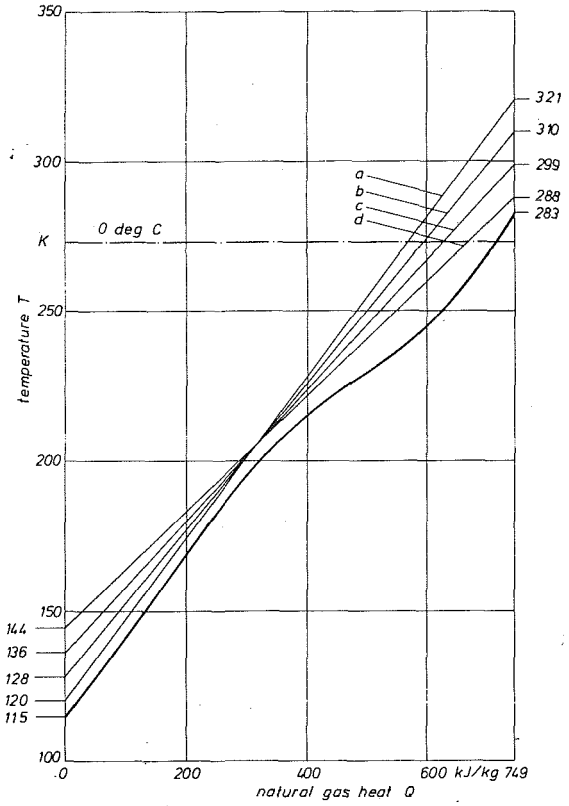


Fig. 3 *Q, T* **diagram: — natural gas (p_{NG} = 80 bar; supercritical), — working gas, $\Delta T_{V,min}$ = 5 K, aξ = 0.84, bξ = 0.92, cξ = 1.03, dξ = 1.17**

Downloaded 01 Jun 2010 to 171.66.16.58. Redistribution subject to ASME license or copyright; see http://www.asme.org/terms/Terms_Use.cfm

Table 1

Quantity	Unit	Value
Composition of natural gas:		
nitrogen N_2	mol-%	1.03
methane CH_4	"	85.92
ethane C_2H_6	"	8.60
propane C_3H_8	"	3.04
butane C_4H_{10}	"	1.21
pentane C_5H_{12}	"	0.20
Density in normal state (at 0°C ; 1.013 bar)	kg/m^3	0.843
Calorific value H_u	kJ/kg	48,364
Pressure downstream vaporizer		
Case 1: supercritical	bar	80
Case 2: subcritical	bar	15
Temperature upstream vaporizer	K	115
Temperature downstream vaporizer	K	283

Table 2

Quantity	Unit	Value
Turbine inlet temperature	K	993
Turbine inlet pressure *	bar	38.5
Sum of relative pressure losses	%	13
Turbine efficiency	%	90
Compressor efficiency	%	86
Heater efficiency	%	92
Generator efficiency	%	98
Medium:		
nitrogen N_2	% by vol.	99.5
oxygen O_2	% by vol.	0.5

* base value for cycle optimization

the temperature difference in the recuperator ΔT_R, if at first given values are assumed for the efficiencies of the turbo machines, which however are not fully independent of π_T. Let us consider the efficiency at terminals, η_{Kl}, as the criterion for optimization of the cycle layout, which is defined by the equation

$$\eta_{Kl} = \frac{P_{Kl}}{Q_{zu}} \tag{4}$$

where P_{Kl} is the power at the generator terminals and Q_{zu} the fuel heat added in the heater. While primarily a thermodynamic measure, the efficiency at terminals is also suitable for finding technically and economically optimum solutions.

Tables 1 and 2 show the base data chosen for the example of a calculation. The assumed composition of the natural gas corresponds to the quality H. The supercritical pressure of 80 bar chosen for Case 1 is typical in feeding vaporized natural gas into a pipeline. If the natural gas after vaporization is used for firing, e.g., in a power plant near the LNG terminal, lower pressures are applied. Therefore an alternative pressure of 15 bar is given for Case 2, at which the state of the natural gas is subcritical. The cycle data in Table 2 are based on the many years of experience of GHH STERKRADE in the construction and operation of closed-cycle gas turbines [4, 5].

Supercritical State of Natural Gas. In Fig. 4 the efficiency at terminals is shown as a function of the turbine expansion ratio for various ξ values (see Fig. 3) at a constant temperature difference in the vaporizer of 5 K for the supercritical state of the natural gas (Case 1). As can be seen, the efficiency at terminals rises with increasing expansion ratio (broken lines). The relevant recuperator temperature differences decrease at the same time. Theoretically the curves end where the temperature difference is zero. By connecting the points of equal temperature difference one arrives at the unbroken lines, which are best suited for optimization of the cycle layout. It can be seen that these efficiency curves have slight peaks which with decreasing recuperator temperature difference increase by approximately 0.7 percentage points per 10 K and move to smaller expansion ratios. However the expansion ratio is of minor importance. The temperature difference in the recuperator is of primary influence on

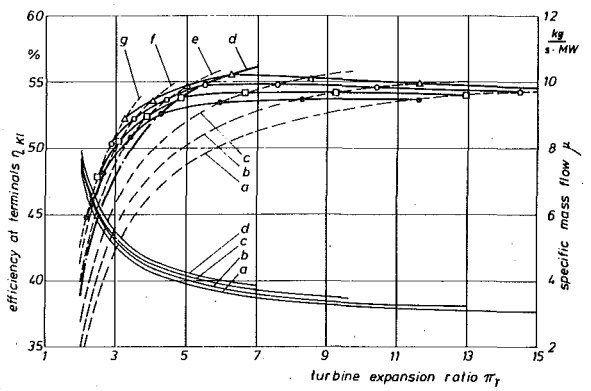


Fig. 4 Efficiency at terminals and specific mass flow: — η_{Kl} at ΔT_R = const., - - - η_{Kl} at ξ = const., — μ at ξ = const. (for a to g see legend for Figs. 3 and 5), $\Delta T_{V,min}$ = 5 K, △ ΔT_R = 20 K, ○ ΔT_R = 30 K, □ ΔT_R = 40 K, ● ΔT_R = 50 K

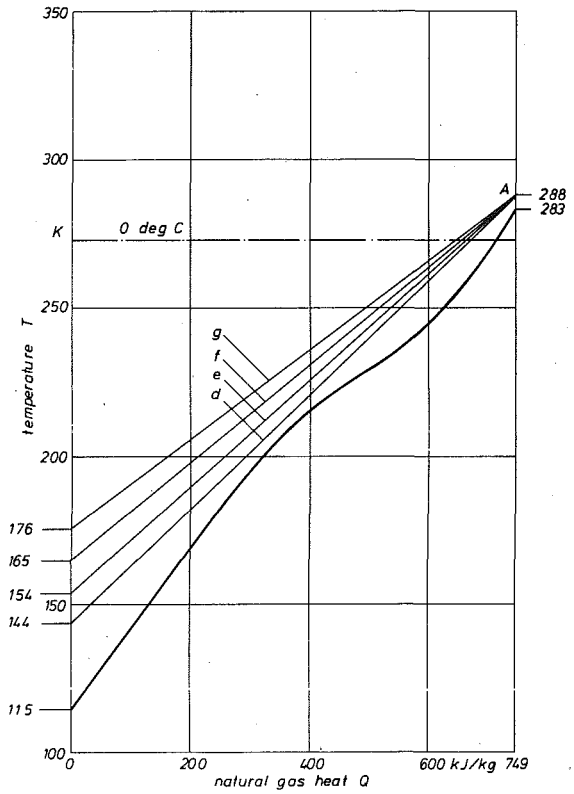


Fig. 5 Q, T diagram: — natural gas (p_{NG} = 80 bar; supercritical), — working gas, $\Delta T_{V,min}$ = 5 K, dξ = 1.17, eξ = 1.25, fξ = 1.37, gξ = 1.50

Downloaded 01 Jun 2010 to 171.66.16.58. Redistribution subject to ASME license or copyright; see http://www.asme.org/terms/Terms_Use.cfm

the efficiency. With temperature differences below approximately 30 K the points of optimum efficiency are on the limit curve for ξ = 1.17, which results in the event of the given minimum temperature difference in the vaporizer arising in the vaporizer itself and at the natural-gas outlet of the vaporizer (Fig. 3, curve d). If the ξ value of 1.17 is exceeded—the cooling curve of the working medium then turns round the point A fixed in the Q, T diagram (Fig. 5)—the efficiencies at terminals decrease considerably. From this results the following layout criterion: *The minimum temperature difference should always arise in the vaporizer itself and in borderline cases also at the natural-gas outlet of the vaporizer.*

The ξ limit curve also shows the minimum expansion ratio which is required for achieving a high or optimum efficiency as a function of the recuperator temperature difference. With a temperature difference of 50 K the minimum expansion ratio is 4.3 and the efficiency at terminals is 52.6 percent. At the top the limit curve ends in a combination of values which is just within the limits of technical acceptability: recuperator temperature difference 20 K, expansion ratio 6.3, efficiency at terminals 55.6 percent. Hence the required expansion ratios are relatively high as compared with the value of about 3 for the optimum point with closed-cycle air turbines.

A remarkable result to be seen from Fig. 4 is that each point of optimum efficiency corresponds to a certain compressor inlet temperature. Any decrease beyond this optimum compressor inlet temperature causes a reduction in efficiency.

In Fig. 4 also the specific mass flow μ is entered, which is defined as the ratio of turbine mass flow to power at terminals,

$$\mu = \frac{\dot{m}_T}{P_{Kl}}. \tag{5}$$

This figure decreases with rising expansion ratio and decreasing ξ value. The μ values are within the range from 3 to 4 kg/s MW.

As compared with a closed-cycle air turbine, where the specific mass flow is about 10 kg/s MW thanks to the higher value of approximately 20°C of the lower cycle temperature, the μ values with LNG vaporization are very small. In order to still achieve sufficiently high volume flow rates particularly in the compressor so as to create favorable aerodynamic conditions, a correspondingly low pressure level in the cycle has to be chosen.

The influence of the minimum temperature difference in the vaporizer is shown in Fig. 6 for the two ξ values 1.17 and 1.04. If this temperature difference is increased by 5 K the efficiency at terminals decreases by approximately 0.7 percentage points at constant recuperator temperature difference. If the temperature difference of the recuperator is reduced at the same time by 10 K the efficiency remains almost constant. However, in that case the lowest expansion ratio determined by the limit curve for ξ = 1.17 increases.

Subcritical State of Natural Gas. Fig. 7 shows the Q, T diagram for the subcritical state of the natural gas (Case 2) with a minimum temperature difference in the vaporizer of 5 K. The ξ limit value is 1.08 in this case. For raising the temperature of the natural gas from 115 K to 283 K, a heat of approximately 850 kJ/kg is required, while in Case 1 of the supercritical state this value is only approximately 750 kJ/kg. The efficiency at terminals and specific mass flow rate are shown in Fig. 8.

The main deviations from the results for the supercritical state are:

- the achievable efficiencies are higher,
- the optimum efficiencies are on the ξ limit curve even with higher recuperator temperature differences,

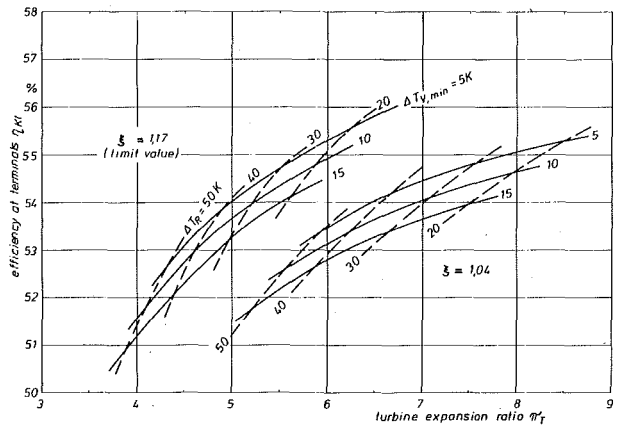


Fig. 6 Influence of the minimum temperature difference in the vaporizer

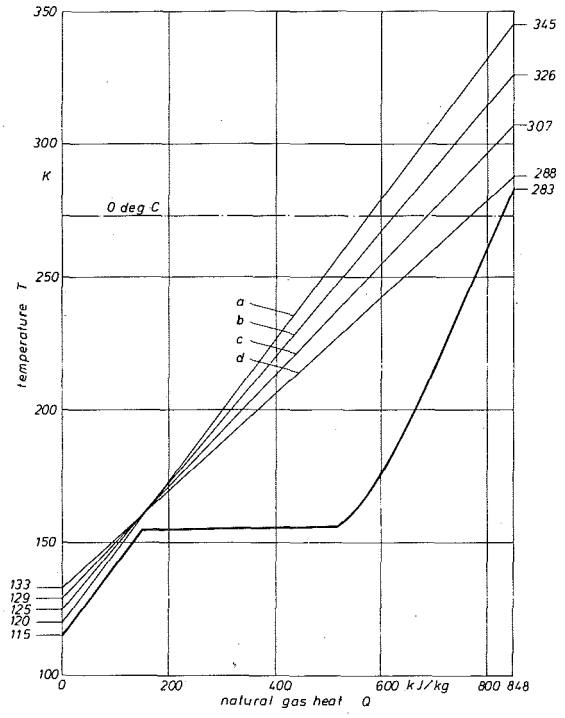


Fig. 7 Q, T diagram: — natural gas (p_{NG} = 15 bar; subcritical), — working gas, $\Delta T_{V,min}$ = 5 K, aξ = 0.75, bξ = 0.84, cξ = 0.94, dξ = 1.08

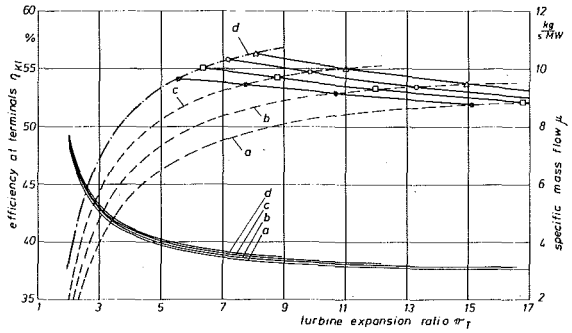


Fig. 8 Efficiency at terminals and specific mass flow (for legend see Fig. 4, for a to d see Fig. 7)

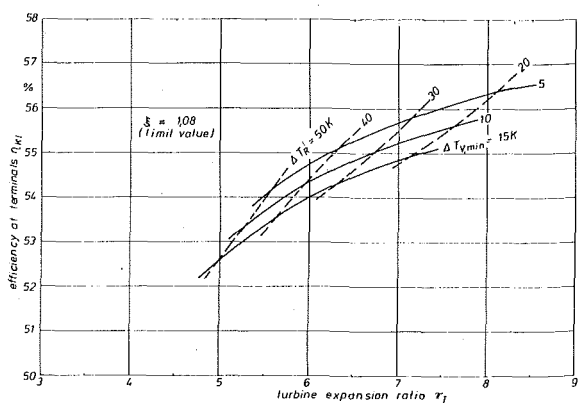


Fig. 9 Influence of the minimum temperature difference in the vaporizer

Downloaded 01 Jun 2010 to 171.66.16.58. Redistribution subject to ASME license or copyright; see http://www.asme.org/terms/Terms_Use.cfm

- the higher efficiencies correspond to higher expansion ratios,
- the specific mass flow rates are lower.

The influence of the minimum temperature difference in the vaporizer is similar to that in the case of the supercritical state of the natural gas (Fig. 9).

Plant Arrangement

Figure 10 shows the circuit diagram of a closed-cycle gas turbine used at an LNG terminal with optimized cycle data for the supercritical state of the natural gas as per Case 1 (Table 1). Further design data of the plant are shown in Table 3. The quantity of natural gas flowing through the vaporizer is approximately 565,000 kg/h, the power at terminals is 180 MW.

Figure 11 shows the general arrangement of the gas turbine plant conceived by GHH STERKRADE for this duty class with two blocks of 90 MW. Each turbo set consists of a seven-stage axial turbine and a 15-stage axial compressor. The speed is 3000 rpm. The recuperator is of the cross counter-flow type with straight tubes. Each block has two LNG vaporizers with coiled tubes handling the natural gas. The heater, which is located outdoors, consists of an uncooled combustion chamber with ceramic brick lining followed by a convection channel. Flue gas recirculation ensures that the temperature of the combustion gases at the outlet of the combustion chamber does not exceed 1500°C so that the maximum tube wall temperature in the protective bundle and high-temperature portion is limited to 800°C.

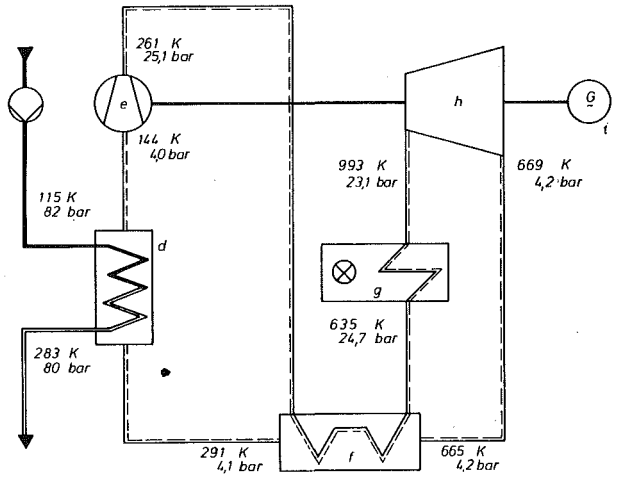


Fig. 10 Circuit diagram of an optimized plant. For legend see Fig. 1

Table 3

Quantity	Symbol	Unit	Value
Turbine inlet temperature	T_4	K	993
Compressor inlet temperature	T_1	K	144
Turbine expansion ratio	π_T	-	5.5
Compressor inlet pressure	p_1	bar	4.0
Ratio of temperature spans in the vaporizer	ξ	-	1.15
Min. temperature difference in vaporizer	$\Delta T_{V,min}$	K	6
Recuperator temperature difference	ΔT_R	K	30
Sum of relative pressure losses	$\Sigma\varepsilon$	%	13
Power at terminals	P_{Kl}	MW	90
Gas turbine mass flow	$\dot{m}_M$	kg/s	375
LNG mass flow	$\dot{m}_{LNG}$	kg/s	78.5
Efficiency at terminals	η_{Kl}	%	54.4
Overall efficiency	η_{ges}	%	89.9
Specific mass flow	μ	kg/s.MW	4.16
Specific power yield	-	kWh/kg_{LNG}	0.32

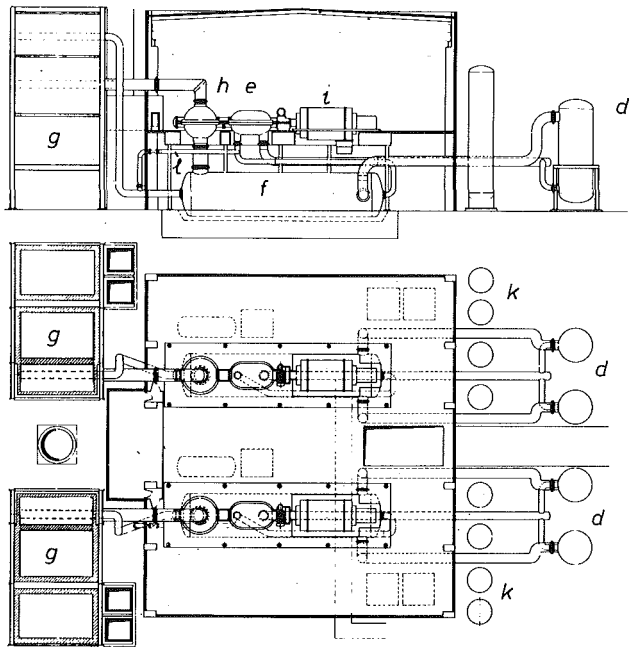


Fig. 11 General arrangement of a 180-MW plant. For legend see Fig. 1

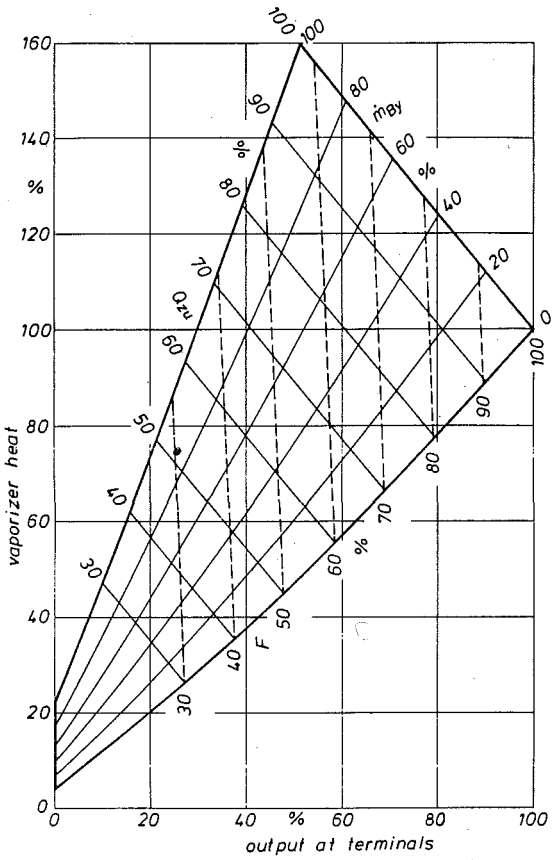


Fig. 12 Performance diagram

Downloaded 01 Jun 2010 to 171.66.16.58. Redistribution subject to ASME license or copyright; see http://www.asme.org/terms/Terms_Use.cfm

Control

Output control is achieved by varying the pressure level, at which the efficiency remains practically constant down to an output of 40 percent. For storage of the working medium extracted from the circuit for part-load operation, a multi-chamber storage system (Fig. 1) is used whose basic design is described in [7]. On reduction of the circuit inventory the electrical output and the heat transferred in the vaporizer decrease at the same rate. If both outputs are to be varied at different rates, pressure control is combined with a by-pass control by opening a by-pass line past the recuperator (heat by-pass *l* in Fig. 1). Fig. 12 shows the performance diagram in which the vaporizer heat is plotted against the electrical output. The parameters are the fuel heat input Q_{zu}, the circuit inventory F and the mass flow through the heat by-pass $\dot{m}_{By}$ referred to the total mass flow through the by-pass and the recuperator. With a by-pass flow of 100 percent the full high-pressure side mass flow would be sent past the heat exchanger. The diagram shows that the vaporizer heat and the output at terminals can be controlled within a wide range independently of each other. Thanks to this flexibility the closed-cycle gas turbine can be used with optimum results for LNG vaporization with utilization of cold even where the consumption of natural gas and electrical energy varies to a very great extent.

Summary

The closed-cycle gas turbine is particularly suitable for LNG vaporization using the LNG cold. The fact that vaporization can be coupled with the generation of electrical energy at an electrical efficiency which is above average, allows part of the energy consumed in the liquefaction of natural gas to be recovered.

In the cycle layout the "cold end" of the gas turbine cycle has to be adapted to the given data of the natural gas. From the cycle optimization there result certain rules for the layout of the vaporizer. The efficiency is mainly influenced by the temperature differences in the recuperator and the vaporizer. An increase in the minimum temperature difference in the vaporizer of 5 K can be compensated by reducing the temperature difference in the recuperator of 10 K to maintain the efficiency. A point of optimum efficiency corresponds to a particular optimum compressor inlet temperature. A temperature below this value will cause the efficiency to decrease. As compared with a closed-cycle air turbine with a lower cycle temperature of 20°C, the LNG vaporization plant requires a higher expansion ratio and consequently more turbine and compressor stages. The lower specific mass flow ratio allows a lower pressure level to be chosen. The combination of pressure level and heat by-pass control results in high flexibility with regard to variations in consumption of natural gas and electrical energy.

References

1 Bammert, K., "Heizkraftwerke mit Heißluftturbinen," Fifth World Energy Conference, Vienna, 1956, Report 188 G 1/23. Austrian National Committee 9, 1957, pp. 2795–2815.

2 Griepentrog, H., "LNG-Verdampfung mit einer Gasturbine im Geschlossenen Kreislauf," Das Gas- und Wasserfach, Vol. 8, 1977.

3 Weber, D., "Generation of Electricity and Vaporization of LNG with Closed-Cycle Gas Turbines," presented at the Energy Systems Show, Hanover Fair, 1978.

4 Bammert, K., Rurik, J., Griepentrog, H., "Highlights and Future Development of Closed-Cycle Gas Turbines," *Trans. ASME,* Vol. 96, 1974, pp. 342–348.

5 Bammert, K., Groschup, G., "Status Report on Closed-Cycle Power Plants in the Federal Republic of Germany," The 21st Annual International Gas Turbine Conference. ASME-Paper 76-GT-66, March 1976.

6 Weber, D., "Die 'kalte' Energie," *Gasturbinen im geschlossenen Prozeß für die LNG-Verdampfung,* Energie 30, 1978, No. 7, pp. 238–241.

7 Bammert, K., Krey, G., Krapp, R., "Die 50-MW-Heliumturbine Oberhausen, Aufbau und Regelung," *Schweizerische Bauzeitung,* Vol. 92, 1974, No. 1, pp. 235–240.

Downloaded 01 Jun 2010 to 171.66.16.58. Redistribution subject to ASME license or copyright; see http://www.asme.org/terms/Terms_Use.cfm

C. Rodgers

Technical Consultant.
Solar Turbines International
2200 Pacific Highway
San Diego, CA 92138
Mem. ASME

Starting Torque Characteristics of Small Aircraft Gas Turbines and APU's

Starting torque characteristics of small self-sufficient gas turbine engines often present a belated problem to the development engineer, particularly when proceeding into final engine qualification testing over the required range of operational environments. A common procedure is therefore to conservatively over-design the start system with consequent penalties in weight, cost, and size. The various aspects of engine starting are discussed and it is shown that the dominant factor controlling start characteristics at sub-zero ambient temperatures is lubricant viscous shear effects. The magnitude of this effect is such that stored energy start system weights for rapid starting of small aircraft auxiliary power units may weigh as much as the power unit itself. The same auxiliary power units, if used as starters for larger main propulsion gas turbines, are burdened with the incompatibility of torque output dependent upon air density, yet main engine cranking torque is dependent basically upon lubricant viscosity. It is concluded that start system over-design philosophy will tend to persist pending the application of external starting torque directly to the high speed shaft itself with uncoupling of all but necessary viscous parastic shear sources, or until such time as detailed research and development is devoted in applied tribology to further reduce viscous shear effects in high speed turbo-machinery.

Small Gas Turbines

The majority of small gas turbines with airflows of less than 5.0 lb/s (2.25 kg/s) manufactured today find major utilization in airborne application for light aircraft and helicopters propulsion, as well as for auxiliary power units (APU's). A smaller fraction are used in electrical ground power generation, emergency generator sets, pilotless drone aircraft, and vehicular applications. In general, small gas turbines are of relatively simple design with a minimum number of rotating components for cost reasons. In this respect, a popular feature is the utilization of a single (or two) stage centrifugal compressor often accompanied by a single-stage radial inflow turbine.

Two basic types are manufactured, the single-shaft (normally constant speed) version, and the two-shaft variable speed version with a mechanically separate power turbine. Single-shaft versions are usually found in APU's and electrical generator sets, whereas two-shaft versions are generally used in helicopter engines, and vehicular engines, since their output torque characteristic provides a better match to the load requirements. Typical maximum output power characteristics of single-shaft engines as a function of ambient temperatures and altitude are shown on Fig. 1 for a constant turbine inlet temperature. Two-shaft engines have similar power versus ambient temperature lapse rates, modified slightly as dependent upon speed limitations.

For a given rotating assembly inertia, the single-shaft gas turbine has better starting characteristics since the all excess horsepower above that required to drive the compressor is available for acceleration. The gas producer rotating assembly inertia of the fixed geometry, two-shaft gas turbine can, however, be somewhat lower than that of the single-shaft, thus a relative comparison of starting characteristics is not readily apparent.

Another fundamental starting difference between the single and two-shaft gas turbine is that the single-shaft engine is normally accelerated from zero to 100 percent rated design speed, whereas the

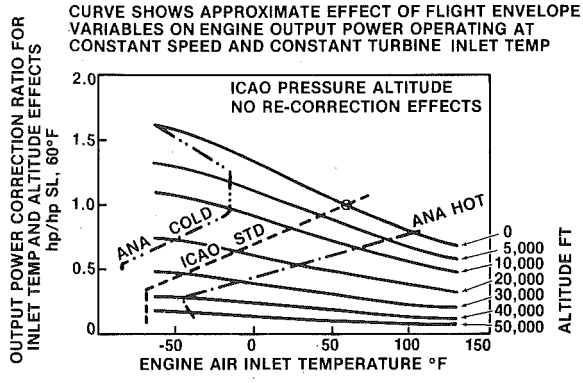


Fig. 1 Typical effect of ambient conditions on gas turbine output power

Contributed by the Gas Turbine Division and presented at the Gas Turbine Conference and Exhibit and Solar Energy Conference, San Diego, California, March 12–15, 1979 of THE AMERICAN SOCIETY OF MECHANICAL ENGINEERS. Manuscript received at ASME Headquarters December 18, 1978. Paper No. 79-GT-95.

Copyright © 1980 by ASME

Downloaded 01 Jun 2010 to 171.66.16.58. Redistribution subject to ASME license or copyright; see http://www.asme.org/terms/Terms_Use.cfm

two-shaft engine is accelerated from zero-idle speed, normally in the range of 55–70 percent design speed.

Typical "aerodynamic" starting torque characteristics of single and two-shaft versions of a convertible, common gas turbine type as shown in Fig. 2 at sea level standard conditions, where torque is expressed as a percent of the engine design torque at SLS conditions. A convertible gas turbine is defined in this instance as a machine which uses the same gas producer and differs only in that the power turbine is either mechanically coupled to, or separated from the gas producer rotating assembly. The aerodynamic torque is that torque solely due to compressor and turbine rotation either in negative (deceleration) or positive (acceleration) output torque modes.

Fig. 2 shows that the output torque of the single-shaft engine is considerably larger than that of the two-shaft engine using the same acceleration fuel control schedule, i.e., turbine inlet temperature versus speed variation. As previously mentioned, this is a consequence of the power turbine torque not being available for acceleration of the gas producer. The cranking or resisting torque is conventionally shown on the positive ordinate[1] and increases until ignition is achieved after which the external power assist (starter) can be dropped out and the engine commences to accelerate by itself. Acceleration is continued as determined by the selected acceleration fuel schedule, the ambient temperature, and engine conditions, the effect of which will be discussed later.

The two-shaft idle speed is shown to be 60 percent design speed where the throttle control can be held, subsequent activation producing acceleration to rated speed.

Not all two-shaft gas turbines are compromised for convertibility into single-shaft versions, thus the relative torque levels depicted in Fig. 2 may not be strictly comparative. Two-shaft engines may have lower gas producer inertias, variable power turbine nozzles, or hotter acceleration fuel schedules to compensate for acceleration torque.

The impact of the many engine transient operating variables on the starting of small gas turbines is complex, thus accurate prediction is virtually impossible. Some of the many factors influencing engine starting are discussed below.

Engine Starting

It is difficult to estimate with any reasonable accuracy the starting characteristics of small gas turbines because of the synergistic nature of the problem. Engine starting characteristics are influenced (among other intangibles) by:

- initial engine design selection
- engine performance
- engine fuel control scheduling
- mechanical features
- magnitude of applied torque
- starter selection

Due to the complex interrelation of these factors, engine starting characteristics are only realistically obtained by actual test under controlled conditions with a specific start system. Although extrapolation of the characteristics thereby obtained to other operating conditions and start systems without actual test is not recommended, however, it is often necessary. A purpose of this paper is to indicate the general trend of other start conditions and systems on individual engine starting characteristics, to possibly avoid the pitfalls so often encountered by graphical extrapolation.

Initial Engine Design Selection. During the initial start phase approximately below 30 percent design speed, the aerodynamic and viscous drags at normal ambient temperatures may be relatively small in relation to the basic starter applied torque. In such cases, the starter applied torque is approximately equal to the basic flywheel acceleration torque as determined from the rotating assembly inertia and acceleration, i.e., $Ip\dot{\omega}$.

Under these conditions, examination of several small gas turbines with different start systems have shown that the starting difficulty (or amount of starting energy required) can be correlated with the product of the rotating assembly polar moment of inertia and the square of the rotational speed, IpN^2.

Since the start system weight is a function of the stored starting energy, general trends have been established for start system weight as a function of IpN^2 as shown in Fig. 3. These trends are useful in early engine design to indicate the potential effect of compressor and turbine geometry and design speed upon start system weight for normally equal start times at normal ambient conditions.

At −65°F ambient conditions, hydraulic start system weight for small APU's may approach that of the APU powerplant itself, thus it behooves the APU designer to scrutinize all possible sources of reducing rotor inertias. Such a scrutiny is common practice in turbocharger design, for example, where fast accelerations are required for response and smoke abatement. Rotor blade number and disk configurations are whittled to that only necessary for structural integrity at design or design overspeed condition. The trade-off on APU engine turbine blade number is extremely weight effective, and turbine efficiencies of up to three percent points may be sacrificed to this extent for non-continuous duty operation.

The IpN^2 relationship can be expanded to show that for similar

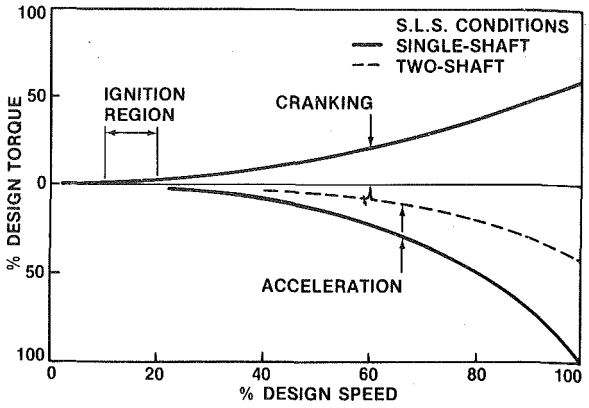


Fig. 2 Typical aerodynamic starting torques

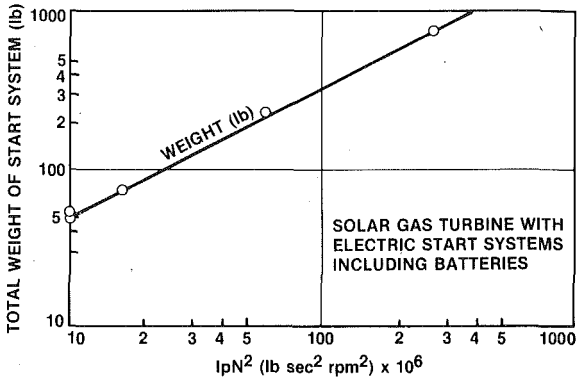


Fig. 3 Correlation of starting difficulty

[1] A confusing practice stemming from piston engines, since the cranking torque with no ignition is negative, and the accelerating torque with combustion taking place is positive.

Nomenclature

hp = horsepower
Ip = polar moment of inertia
N = rotational speed, rpm
p = pressure
SL = sea level
SLS = sea level standard day (60°F) conditions
T = temperature
$\dot{\omega}$ = acceleration
η = efficiency
μ = viscosity
Δ = difference

Subscripts

c = compressor
1 = compressor inlet
2 = compressor exit
3 = turbine inlet
t = turbine

Downloaded 01 Jun 2010 to 171.66.16.58. Redistribution subject to ASME license or copyright; see http://www.asme.org/terms/Terms_Use.cfm

engine and start system design configurations the start system weight can be expressed by:

$$\text{Start System Weight} \propto \frac{\text{Constant}}{\text{Engine Specific Power (hp/pps)}} \quad (1)$$

This expression indicates that in applications where the start weight is an important consideration, i.e., intermittent duty airborne APU's and JFS's (Jet Fuel Starters), it is beneficial to design for maximum specific power. This is not always conducive towards minimum fuel economy as the optimum pressure ratios for minimum specific fuel consumption and maximum specific power are not equal, furthermore, high specific power can also be obtained with high specific speed turbomachinery designed beyond the optimum specific speed conditions. In applications where continuous duty airborne APU's are required, there is a trade-off between engine designs for maximum specific power and minimum specific fuel consumption, and engine wet weight (engine + start system + fuel) becomes the yardstick. Studies by the author have shown that for small airborne gas turbines APU's designed for rapid starts under sub-zero ambient conditions, a maximum specific power design is preferred providing operating time does not exceed approximately one to two hours.

Start system design and weight is most often, however a secondary consideration in the preliminary design phase of small gas turbines particularly for commercial ground power applications. It is the feasibility of even starting gas turbines at −65°F ambient conditions without external heating aids, rapid starting for emergency power generator sets, and the desirability to start aircraft gas turbines over a wide operating envelope, that has prompted more attention towards unaided starting than has previously been afforded to internal combustion engines types. The degree of attention, however, is still minor as witnessed by the limited amount of published literature on gas turbine starting.

Engine mechanical design aspects such as selection of bearing types and number, accessory gearbox configuration, and starter type may compromise the aerodynamic design to some degree, and do directly influence the engine starting characteristics. These aspects are examined later.

Engine Performance. The engine performance behavior during and immediately following accelerations or decelerations is predicted in the early engine development phase using steady-state compressor, combustor, and turbine component characteristics, yet it is well known that the transient and steady-state component performances may be different. For example, the first start of a gas turbine requires a longer time than subsequent starts. Re-acceleration compressor stall is an engine transient characteristic which has continually plagued engine development.

Quasi-transient performance estimates using steady state component characteristics are useful in the preliminary design phase to determine the aerodynamic cranking (no light) torque and to establish a first-cut acceleration fuel schedule dependent upon the fuel metering technique. These estimates can be quite detailed dependent upon the sophistication of the analytical model selected [1], or may be simply scaled up or down from existing data within similarity restraints. An approximate analysis of aerodynamic cranking torque levels for single-shaft small gas turbines can be conducted assuming:

$$\begin{aligned} &\bullet\ T_3 = T_2 \quad \Delta T_c = \text{Constant at design speed} \\ &\bullet\ \frac{P_2/P_1 \text{ Design}}{P_2/P_1 \text{ Crank}} \propto \left(\frac{T_3/T_1 \text{ design}}{1 + \Delta Tc/T_1}\right)^{0.5} \quad (2) \\ &\bullet\ \eta_t \text{ Design} = 80 \text{ percent} \quad \eta_t \text{ Crank} = 80 \text{ percent} \end{aligned}$$

Under these conditions, the aerodynamic cranking (negative) specific horsepower can be calculated as a function of design pressure ratio and turbine inlet temperature ratio, and typical results are shown plotted in Fig. 4. Also shown in Fig. 4 is the ratio of negative cranking to positive design specific horsepower indicating that higher turbine inlet temperatures and low pressure ratios are desired for minimum cranking requirements.

Cranking powers at speeds below design can be calculated according

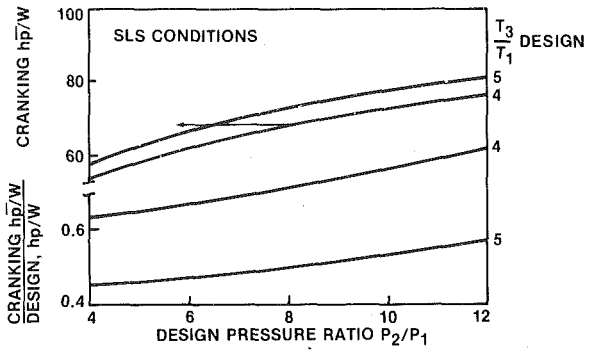


Fig. 4 Typical aerodynamic cranking specific horsepower

to a cubic relationship with speed, or square relationship with torque, i.e.,

$$\text{Aerodynamic Cranking Power} = \text{Cranking hp design} \times \left(\frac{N}{N \text{ Design}}\right)^3 \quad (3)$$

These data are known to provide reasonable agreement with small gas turbine engines built at the author's company. Cranking power at other ambient temperatures and altitudes can be estimated assuming constant compressor volume flow and temperature rise for a given speed (in the range 0–40 percent design), thus aerodynamic cranking power becomes proportional to density.

Determination of the positive acceleration power is best accomplished by complete analysis of the component characteristics and fuel control scheduling, the latter of which will be discussed shortly. The approximate magnitude of the positive acceleration power for a single shaft engine is:

$$\text{Acceleration Power} \propto \text{Design Power} \left(\frac{N}{N \text{ Design}}\right)^n \quad (4)$$

The exponent n is a function of the fuel schedule and typically varies from 3.0 to 4.0 for fixed geometry engines with no surge bleed bypass requirements, and from 4.0 to 5.0 if bleed is used to prevent surge encroachment. Acceleration power levels for two-shaft engines may be up to 70 percent lower than single-shaft units, which is dependent upon the fuel margin available for acceleration between the steady state fuel and surge fuel limitations.

From the previous dissertation, we may generate a typical aerodynamic starting torque characteristic as shown in Fig. 2, essentially useful for preliminary design purposes at normal ambient conditions. It will be seen later that these simplified characteristics are altered considerably as dependent upon the actual transient nature of starting and the many synergistic effects involved. Some of the many reasons for differences between the steady-state and transient performance characteristics of gas turbines are:

- heat transfer effects resulting in nonadiabatic compression and expansion, plus loss of heat input to the cold components,
- tip and axial clearance variation effects on the compressor, turbine, and seal components,
- quenching of the combustor influencing response and burning characteristics,
- instantaneous behavior of the components as constant volume rather than continuous flow machinery.

Heat transfer effects have been previously examined [2], particularly with regard to its effect on compressor surge margin. Substantial increases have been observed in transient fuel flow demands for small gas turbines at the author's company, directly relating to heat losses to the "cold" casings and flame quenching effects on combustion efficiency. Heat exchanged engines are notorious in this respect as the large mass of the heat exchanger acts as thermal reservoir absorbing heat during start, and dissipating heat (with possible bearing soak-back problems) on shutdown.

Small gas turbines are particularly sensitive to tip clearances effects [3], since clearance gap to blade height ratios tend to be larger than those of bigger gas turbines. In most instances, the minimum engine

Downloaded 01 Jun 2010 to 171.66.16.58. Redistribution subject to ASME license or copyright; see http://www.asme.org/terms/Terms_Use.cfm

operating clearances are established by transient engine tests to determine limiting rub clearances gaps. Some tuning can be accomplished by matching thermal responses of the rotors and stationary shrouds and by appropriate material selection. Computation of engine transient performance using steady-state component performance characteristics does entail small errors due to the effect of transient clearance effects on both component efficiency and pressure flow characteristics. These effects are relatively small when compared with the transient behavior of the combustor. Fig. 5 shows extraordinary transient combustor efficiencies for a small short annular combustor with an inner diameter of six in. with an annulus height of approximately one in. tested in a gas turbine. It is apparent that starting performance with fuel flow metered as a function of speed would be quite inconsistent with such dramatic variations in combustor efficiency and thus turbine inlet temperature.

Engine Acceleration Fuel Schedule. The simplest form of fuel control conventionally used for small gas turbines is that in which fuel is metered across a valve whose metering area, hence fuel flow, is controlled by compressor discharge pressure. Biasing parameters on more complex versions of such a control system might be ambient temperature, altitude, speed, or even turbine temperature topping. Without some form of biasing, the simple discharge pressure control is subject to surge line encroachment as ambient temperature decreases. Thus sufficient surge margin must be set at high ambient temperature operation to avoid surge at sub-zero ambient temperature operation.

Small gas turbines require extreme accuracy in manufacture of the fuel control systems components to ensure consistent fuel scheduling rates. Even though the assembled controls are normally flow-calibrated prior to installation, some flow tolerance band must be permitted if fuel controls are to be produced economically.

Engine surge fuel margin is basically governed by the flow/pressure characteristics of the compressor and turbine, and, to a lesser degree, by the efficiency levels of the compressor and turbine. Variations in compressor and turbine airflow capacities of ±2 percent are typical for small gas turbines in high quantity production, thus a nominal surge margin of at least four percent must be initially considered to avoid the possibility of surge with a compressor passing the high flow limit and turbine swallowing the low flow limit. Differences in component efficiency performance levels due to tolerance variations, surface finish, clearances, contamination, erosion, etc., will necessitate a further margin of safety in initial selection of the engine operating point in relation to the compressor surge line.

The difficulty in estimating start system performance normally entails optimization of an engine acceleration fuel schedule to suit a wide operating envelope by conducting actual engine developmental testing. Prior to such testing an initial fuel schedule may be selected based upon component performance matching studies, fuel control metering mode, starter input torque, and fuel atomization requirements. This fuel schedule is subsequently tried on the prototype engine to determine if a successful start can be accomplished, and what modifications are required to improve start characteristics. Extensive testing may include mapping fuel requirements at part-speed, surge fuel limitations, (acceleration characteristics), and effects of ambient conditions. During such testing, part-speed engine transient performance can be checked with quasi-transient performance estimates to refine the analytical model, and reassess start performance predictions at environmental conditions not readily capable of simulation. Extension of the tests described to qualify altitude operation, different fuel types, and different starter types are customary. Thus optimization of engine acceleration fuel requirements can be prolonged.

Fig. 6 shows the starting performance of a two-shaft gas turbine with an open-loop fuel schedule and different levels of applied starter torque in order to demonstrate the synergistic nature of the starting process. With a fixed fuel flow schedule, Fig. 6 shows that measured power turbine inlet temperature varies considerably in the early start phase as a function of acceleration time. Increasing the starter torque is observed to reflect in increased resisting torque (this effect will be discussed in more detail later) and in changes in the overall engine

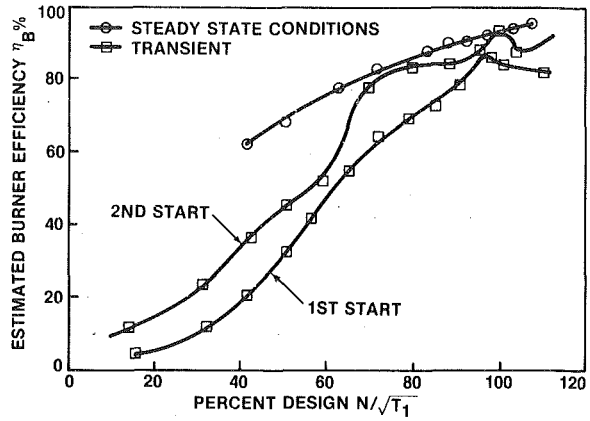


Fig. 5 Transient burner efficiency variations

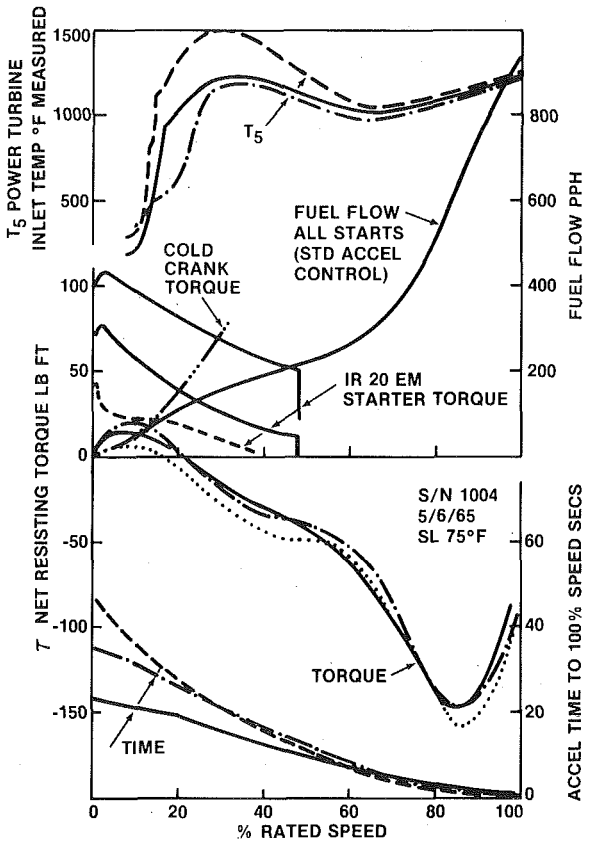


Fig. 6 Saturn gas turbine starting performance

starting torque characteristics.

Advanced electronic control systems modulate engine acceleration fuel requirements with hot-end limitations through the use of fast response temperature sensors and computerized techniques to minimize the variation effects of transient combustor efficiency.

Such closed loop turbine temperature control, however, must have a response equal to that of the most sensitive turbine component, and be rugged enough for reliable operation. Consequently, their use in the past has been associated with larger gas turbines. Whatever fuel metering system or control mode is adapted, the finally evolved acceleration fuel schedule will determine the positive engine torque available for acceleration to idle and rated speed. It is desirable to provide positive acceleration at the lowest speed attainable in order to either accelerate the engine faster or minimize starter system weight. Ignition and self-sustaining speeds as low as ten percent and 25 percent respectively have been recorded on small APU gas turbines.

Mechanical Features. The mechanical features of the engine starter drive train and support bearings are possibly the most dominant single factor controlling starting at sub-zero ambient tempera-

Downloaded 01 Jun 2010 to 171.66.16.58. Redistribution subject to ASME license or copyright; see http://www.asme.org/terms/Terms_Use.cfm

tures. Inadequate clearances and dissimilar metal contraction rates have been known for example to cause interference binding preventing starting. High oil viscosity throughout the train and bearings increases drag torque by an order of magnitude. Parasitic losses in the oil and fuel pumps increase also with the change in viscosity.

At normal ambient temperatures, the mechanical losses in the drive train, bearings, and accessories are on the order of 1 to 4 percent of the design power rating dependent upon train reduction ratio and type and number of bearings and accessories. Miniature gas turbines (less than 20 hp) tend to exhibit higher mechanical losses on the order of nine percent of rated power, since it is not cost effective to scale accessories, especially when ultra high rotational speeds are employed.

During preliminary engine design, a mechanical design configuration is selected after many design iterations to best compromise all the design criteria and constraints. The creative designer will generate an efficient design in which mechanical losses are minimized to avoid impacting such factors as cost, performance, and oil cooler requirements. Although these mechanical losses at normal ambient temperatures and design speed may be small (2–5 percent) and seemingly negligible relative to the aerodynamic drag, oil viscous shearing at start initiation results in larger mechanical than aerodynamic drag.

The effect of ambient temperature on cold cranking torque of a small gas turbine at ten percent speed is shown in Fig. 7. The cranking torque shown is that composing mechanical drag from the starter drive train via the main planetary reduction gear (ratio 7.1:1) bearings, accessories, and aerodynamic drag. Total mechanical losses at design speed for this engine were approximately four percent of the total engine output. Light aircraft type oils, MIL-7808 and MIL-0-6081, were used but nevertheless cranking torque increased by a factor of 4.0 to 5.3 at −65°F with higher oil viscosity. Examination of the apparent oil viscosity variation (based on ambient temperature) and the increase in cranking torque indicated a relationship similar to that presented in [4] and [5] based upon cold starting of diesel and automative engines where:

$$\frac{\text{Cranking Torque}}{\text{Cranking Torque reference}} \propto \left(\frac{\mu}{\mu}\,\text{ref}\right)1/3 \qquad (5)$$

The reference conditions define the cranking torque and apparent oil viscosity at design ambient. This relationship may be applied to project mechanical drag at sub-zero ambient conditions providing:

- mechanical drag at the reference condition is known to be reasonably accurate by estimation or direct measurement.
- Aerodynamic torque is assumed negligible in the range of 0 to 15 percent speed.

Direct measurement of the mechanical torque at the reference condition is recommended, as estimation of the reference condition imposes considerable uncertainty. A conservative estimation of the mechanical losses can be made on the hypothesis that the torque required for gears, bearings, and accessories remains constant, i.e., mechanical power is proportional to speed.[2] This is supported to some degree (at normal ambient temperatures) by individual engine system and gearbox tests, thus if the design mechanical power loss is defined, the low speed mechanical torque can be approximated. Fig. 8 shows low speed starting torque trends derived by using the previous arguments.

The data of Figs. 4, 7 and 8 lead to a crude method of arriving at the complete starting torque characteristics of a typical single-shaft gas turbine at SLS and SL −65°F conditions as shown in Fig. 9. Maximum engine starting torque at −65°F is assumed to follow the trend of Fig. 1 for constant turbine inlet temperature, which will depend upon the actual fuel schedule selected. Transition from ignition to engine assist follows observed results, but is conjectural.

The method is highly empirical and of questionable accuracy, but is presented to analytically substantiate the reasons for large cranking

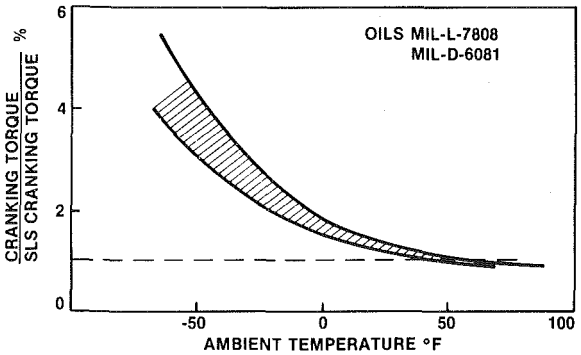


Fig. 7 Effect of ambient temperature on cold cranking torque

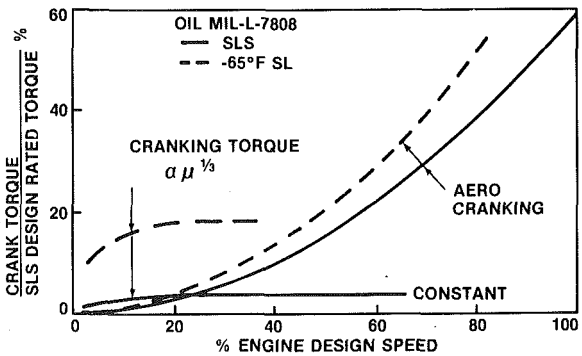


Fig. 8 −65°FSL cranking torque estimation

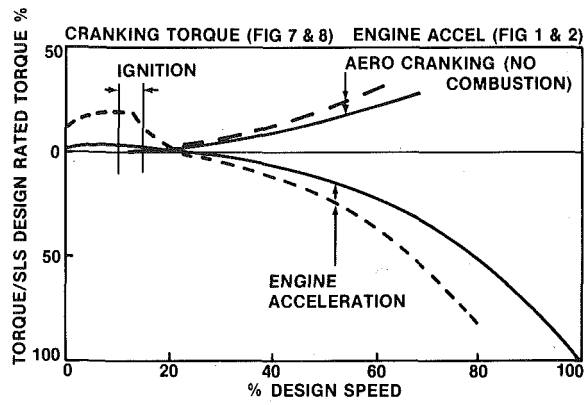


Fig. 9 Typical single-shaft gas turbine starting characteristic

torque requirements when operating small gas turbines at sub-zero ambient temperatures. Obviously, such a crude empirical method is a finite improvement over the presumption that aerodynamic torque alone is the dominant resistance at sub-zero conditions, and serves as a handy resource when no previous data base is available. Additional quantitative data concerning the starting torque characteristics of small APU's at sea level −40°F can be found in [7].

The magnitude of viscous shear losses has resulted in stored energy start system weights for rapid starting of small APU's that exceed the dry APU weight itself. Fig. 10 shows a hydraulic start breadboard system consisting of a 250 cu in accumulator and a back-up 125 cu in accumulator for starting of a small TITAN gas turbine at SL −65°F conditions. The same APU's when employed as starters for larger prime propulsion gas turbines are burdened with the incompatibility of starter torque output dependent upon air density, yet prime engine cranking torque is basically dependent upon lubricant viscosity. Fortunately, a main engine restart at altitude occurs with the lubricant already heated to some degree. Altitude and sub-zero starting conditions, however, will continue to require excessively heavy start systems until viscous shear losses can be reduced by either:

- Application of external starting torque direct to the high speed shaft itself with uncoupling of all but necessary viscous parastic shear sources.
- Advancement in applied tribology to reduce viscous shear effects

[2] Steady-state torque requirements on two small gas turbines with light oil at normal ambient temperatures support the relationship:

- Mechanical drag torque αN

Under transient conditions, however, viscous mechanical losses are a function of both speed and load, as will be discussed later.

Downloaded 01 Jun 2010 to 171.66.16.58. Redistribution subject to ASME license or copyright; see http://www.asme.org/terms/Terms_Use.cfm

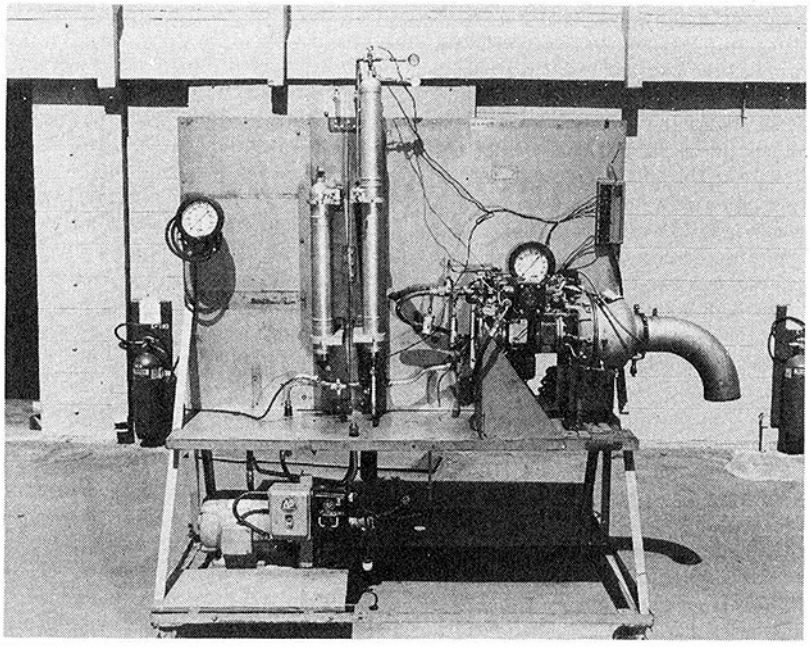


Fig. 10 Hydraulic start breadboard system

in the accessory and mainshaft components of gas turbines [6].

Magnitude of Applied Torque. A start problem that has been encountered in some gas turbines is that the cranking torque at a given ambient temperature increases with the magnitude of the applied external torque. Fig. 11 shows such an example and was experimentally attained by conducting engine cold cranking tests at various levels of applied starter torque. With a starter torque of five percent engine design rated torque the effect of starter torque magnitude on cranking torque is small, but doubling the applied starter torque nearly doubles the cranking torque in the vicinity of ten percent speed. This effect could prevent a meaningful start system optimization, but fortunately a "point of no return" where increasing the applied starter energy has not decreased start time, has yet to be observed.

For rapid (5–10 s) APU start requirements, it is not uncommon to employ starters providing up to 20 percent of the design rated engine output torque.

A similar effect was discussed in [8] relating to the increase of viscosity in lubricants with pressure and the importance of this pressure effect in actual machine elements. Tests were undertaken to show differences in friction and operating temperature when heavily loaded partial journal bearings were operated with two different oils in the same viscosity range but of widely different viscosity index and viscosity pressure characteristics.

If the bearing is lightly loaded, this effect is practically non-existent. However, as the load is increased the phenomenon becomes increasingly evident until, at loads on the order of several thousand pounds per square inch of bearing area, a twofold increase in friction and higher operating temperatures became quite evident. Since viscosity increase results in higher friction, its presence is partially masked by a rise in operating temperature which tends to decrease viscosity. However, higher friction causes higher temperature and when equilibrium conditions are established under comparable conditions, it will be found that both friction and temperature are higher with the lubricant more sensitive to the viscosity-pressure effect. Pressure/viscosity effects are presumably present in the cranking torque trends of Fig. 7, but are impossible to diagnose without identification of the viscous loss division and local instantaneous oil film viscosities.

Detailed analysis of this viscosity pressure dependence during an engine start is essentially impractical, although one may conceive of a complex analytical model combining all engineering sciences including tribology to simulate the complete engine transient behavior. However, before conceiving such a model, more basic experimental and analytical investigation of viscous shear effects in gas turbine

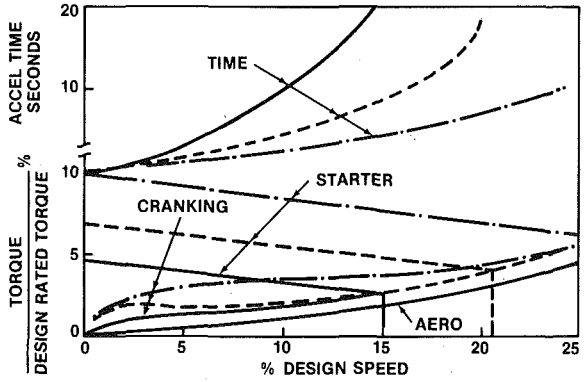


Fig. 11 Effect of starter torque level on cold cranking torque

mechanical components is mandatory, supported by actual engine tests with carefully controlled oil conditions and accurate torque sensing devices. Attempts to conduct the same were made at the author's company several years ago, however, became sidetracked by the discovery of torsional oscillation effects in the starter drive shafting with an amplified time scale. Without digressing again, it is entirely plausible that torsional oscillation effects are manifest in most high energy start systems. Of paramount importance in any evaluation of acceleration torque is the accurate measurement of speed versus time, particularly in the start initiation phase. It is further advisable to use at least two independent techniques of speed measurement for cross reference purposes. The phenomena of increasing applied and resisting torques is not always observed and less apparent when the external torque is applied directly or closer to the main rotating assembly. Some high energy direct impingement start systems capable of making complete engine starts to 100 percent rated speed in less than 5 seconds have not exhibited the effect. This would lead to the conclusion that the phenomena is only significant when overall viscous losses are relatively high.

Starter Selection. Some of the many types of starters that may be selected for self-sufficient starting of small gas turbines are investigated in [9] where it was concluded that the best overall engine/airframe starter choice was a miniature gas turbine starter or air turbine starter. In installations where development cost of a miniature gas turbine starter or APU for an air turbine starter was prohibitive, a battery/electric or accumulator/hydraulic motor start system was recommended. Integral impingement starters of the low pressure, hot and cold air variety, as well as high pressure stored air variety were

Downloaded 01 Jun 2010 to 171.66.16.58. Redistribution subject to ASME license or copyright; see http://www.asme.org/terms/Terms_Use.cfm

investigated but were discarded in favor of the more conventional start systems. An inherent advantage of the integral or direct coupled high speed electric or hydraulic starter is that lubricant viscous drag losses may be reduced, especially if the accessory drive can be driven by externally stored energy. It would seem that a more detailed study of integral starters is warranted where starter torque requirements at the sub-zero ambient conditions are more clearly identified.

A conventional method of sizing starters for aircraft propulsion gas turbines is to stipulate a 30 s start time to idle (or no load) at SLS conditions, and in addition to provide a torque greater than engine cold cranking requirements. It is general knowledge, however, that successful engine starts can be made from a hung-start condition where the starter applied torque intersects the cold cranking torque, especially with engines using sophisticated acceleration temperature modulating control systems. Even with simplified open loop control systems, it is possible to hang a start, decelerate, and achieve ignition on deceleration. With engine assistance then available, a successful start is attainable.

The advantages of a hesitated or hung-start are:

- Starter system weight, cost, and size can be reduced.
- The hesitation period allows lubricant warmup with corresponding reduction in viscosity.

Hung-starts have been considered undesirable in the past due to the following reasons:

- Without temperature topping, overtemperature shutdown may occur with consequent risk of hot section thermal damage.
- Prolonged operation at speeds other than the normal operating zones endanger additional high cycle fatigue modes.
- Delay of a "scramble" flight status.

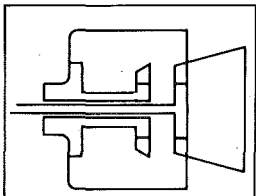
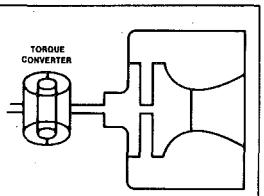
Advocation of a hung-start as a normal operating mode is not recommended, however, offers a potential solution to the problems of sub-zero ambient temperature starting.

A current controversial issue regarding Jet Fuel Starter (JFS) type selection for large main propulsion engines are the alternate configurations of:

- Two-shaft JFS with hot or cold-end mechanical drive to accessory gearbox.
- Single-shaft JFS drawing through hydraulic torque converter and clutch.

Fundamentally, both JFS configurations provide essentially the same output torque characteristics, since both the hydraulic torque converter and power turbine behave as similar fluid dynamic machines but with different working fluids. The pros and cons of both systems are listed in Table 1, but often other noncomparative criteria, such as development risk, availability, etc., finally dictate configuration selection.

Table 1 Comparison of single and two-shaft jet fuel starters (JFS) (fixed geometry components)

	 TWO-SHAFT JFS	 SINGLE SHAFT JFS
Advantages	• Reduced number of torque conversion components • Higher torque converter (P. T.) efficiency • Higher torque output at altitude	• Elimination of power turbine rotor, nozzle and shaft • Shafting only on cold side with simplified bearing system • Symmetrical engine flow path • Lower powerhead cost • Adapatability of powerhead to other integral hp/bleed markets
Disadvantages	• Torque conversion done in hot section • Power turbine over speed danger • *Hot bearing soak back* condition • Concentric shafting • Increased number of high speed hot components with reduced reliability	• Lower converter efficiency • Fixed power converter at constant input speed creates altitude matching compromises • *Fill and drain requirement* • Increased oil and pump capacity • Higher number of total components (powerhead plus torque connector) • Higher net weight

A most attractive gas turbine APU configuration from the standpoint of its own starting capability is that of the completely pneumatic link type.

Such a configuration is shown in Fig. 12, where starting is accomplished via an in-line high speed hydraulic starter declutched at starter drop out. The only driven accessory is a 3KVA and ignition generator. The APU power link is completely pneumatic to an accessory gearbox mounting engine driven accessories and a variable nozzle air turbine starter motor. The APU powerhead may be mounted remotely if necessary, and may function in a dual start mode with ground power units. Integration of the APU and accessory drive system is shown in Fig. 13.

The major compromise of the conventional fixed geometry bleed APU in compressor match point selection and acceleration surge margin is avoided by use of a variable geometry compressor diffuser.

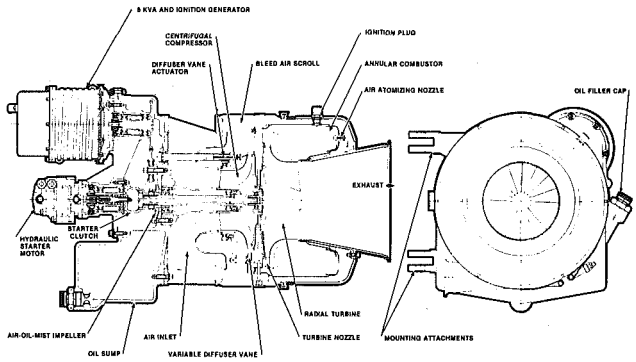


Fig. 13 Complete system envelope

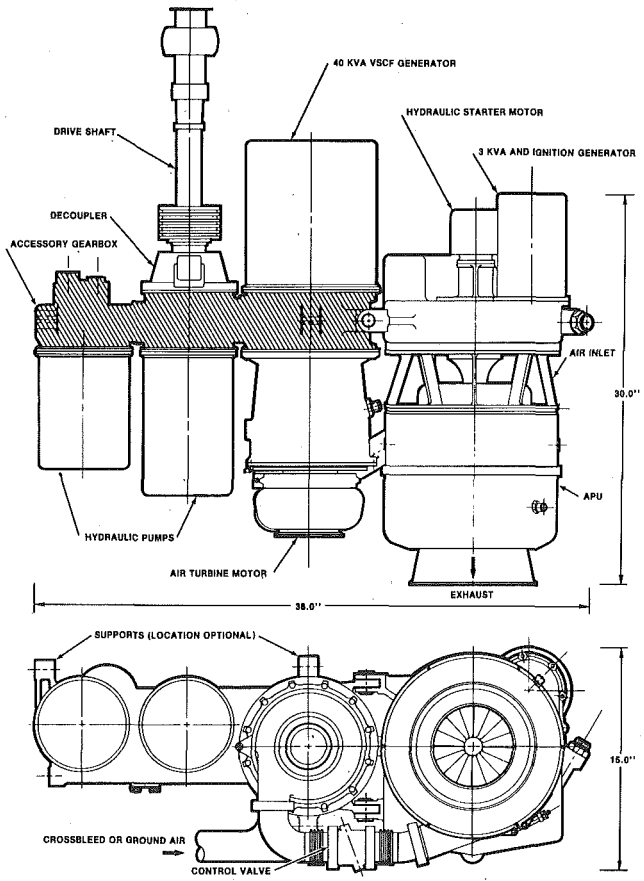


Fig. 12 Pneumatic APU cross-section

Downloaded 01 Jun 2010 to 171.66.16.58. Redistribution subject to ASME license or copyright; see http://www.asme.org/terms/Terms_Use.cfm

This variable diffuser could also be modulated during start to reduce cold cranking aerodynamic drag, if necessary.

The pneumatic link APU is really a cold two-shaft JFS and could therefore be somewhat larger than the conventional two-shaft JFS. The [10] study showed less than ten percent difference in gross weight penalty for a representative fighter mission profile which was attributed to the all pneumatic system in relation to combination mechanical/pneumatic systems. This broad study did not, however, consider the effect of lower starter torque requirements with a Fig. 12 configuration.

Conclusions

The requirements to operate aircraft gas turbines over a large range of environmental conditions prove particularly demanding to the designer, especially when rapid starting of a cold engine is stipulated at sub-zero ambient temperatures.

Cold engine starting torque characteristics are basically controlled by the lubricant viscous drag in the mechanical drive train and accessories. To further complicate matters, this viscous drag is dependent upon the magnitude of the applied start torque. Either actual viscous drag test data or realistic methods of predicting engine cold cranking torque levels with high lubricant viscosity are required before definitive starter specifications can be issued. Experience with hydraulic start systems for small gas turbine APU's had shown that the total accumulator and fluid weight required for successful rapid starting at −65°F can approach the weight of the APU powerhead itself. The same APU, if used as a starter for a larger main propulsion gas turbine, is burdened with the incompatibility of output torque dependent upon air density, yet main engine cranking torque is dependent upon lubricant viscosity.

It is evident that starting torque characteristics of small gas turbines are a function of many interdependent criteria and thus quite synergistic; indeed isolation of the individual cause and effect of many of the criteria involved may be intangible. Nevertheless, an effort has been made to describe these criteria and their apparent effects which may prove sufficiently intriguing to simulate renewed interest in the development of improved starting prediction procedures.

Hopefully, the provisional starting model hypothesis presented can be employed by the gas turbine mechanical or systems engineer to more realistically appraise the complex starting problem issue, and may serve to make him more cognizant of the effects of engine parastic viscous drag sources on starting during the critical engine preliminary design phase.

References

1 Reed, W. E., Murray, J. H., "Use of an Electronic Model to Evaluate Control Concepts for a Regenerative Gas Turbine," *Society of American Engineers*, 767A, 1963.

2 Maccallum, N. R. L., "Effect of Bulk Heat Transfers in Aircraft Gas Turbines on Compressor Surge Margins," *Institution of Mechanical Engineers*, C36/73, April 1973.

3 Rodgers, C., "Performance Development History—10 KW Turboalternator," *Society of Automotive Engineers*, 740849, Oct. 1974.

4 Meyer, W. E., DeCarolis, J. J., Stanley, R. L., "Engine Cranking at Arctic Temperatures," *Society of Automotive Engineers Transactions*, Vol. 63, 1955, Pg. 515

5 Rein, S. W., Cordell, A. D., "Prediction of Engine Cold Cranking Performance of Motor Oils," *Society of American Engineers*, 805B, Jan. 1964.

6 Prizer, C. J., Stringer, H. R., "Component of Engine Oil Viscosity at °F," *Society of Automotive Engineers*, 650444, May 1965.

7 Rhoden, J. A., Scheer, L. E., "Power Systems Study Advanced Fighter/Attack and V/STOL Airplanes," *Naval Air Propulsion Center Report*, 41-1906, Dec. 1977.

8 Needs, J. "Viscosity-Pressure Effect on Friction and Temperature in a Journal Bearing," *Trans., ASME*, 1958, Pg. 109G.

9 Miller, B. C., "Integrated Accessory Systems for Small Gas Turbine Engines," USAAMRDL-TR-75-46.

10 Nicholls, B. H., et. al., "Auxiliary Power System Study for 1975 Fighter Aircraft," *AFAPL*, TR-67-135.

Downloaded 01 Jun 2010 to 171.66.16.58. Redistribution subject to ASME license or copyright; see http://www.asme.org/terms/Terms_Use.cfm

J. C. Napier
Research Staff Engineer.
Solar Turbines International
an Operating Group of International Harvester
P.O. Box 80966 San Diego, CA 92138

Application of All-Ceramic Nozzle to Radial Flow Turbine

An all-ceramic turbine nozzle offers the capability for improved erosion resistance and up-rated turbine inlet temperature. This yields significant improvement in engine durability and performance. Results of ceramic turbine nozzle engine tests and engine simulator tests for a small radial flow gas turbine are presented. The effects of erosive particles and ingested sea salt on the ceramics are included in this work.

Introduction

Development of advanced ceramic materials with improved properties in recent years has opened the potential for their use in the severe, high-temperature environment of gas turbines. The promise of higher turbine inlet temperature and increased resistance to erosion and corrosion has given impetus to work on application of silicon based ceramics to the Gemini radial gas turbine engine used in a portable electrical generating set developed at Solar Turbines International for the U. S. Army Mobility Equipment Research and Development Command (MERADCOM). Fig. 1 shows the unit which is a single-stage back-to-back radial turbine/radial compressor design. The turbine wheel is approximately four inches in diameter and runs at 93,600 rpm. The package is rated to deliver 10 kW of continuous electrical power under the adverse operating conditions of 107°F ambient temperature at 5000 ft altitude.

Since this unit, which has just been qualified in 6000 hr endurance runs for production status, is projected to operate in severe environments with large concentrations of airborne dust, the high erosion resistance of certain ceramics would be of great value in further hardening critical components against erosion. Experience has shown specifically that the nozzle vanes of the single stage radial turbine section are the critical components for erosion of this engine with dust ingestion. The portability of the package also puts incentives for increase of specific power output and improved fuel consumption. Ceramics could fulfill these needs by allowing higher turbine inlet temperature through replacement of the nozzle shroud, exhaust scroll and possibly the combustor with suitably designed ceramic components. Present work at Solar with ceramics, as applied to the Gemini engine package, is described here and includes a ceramic nozzle vane engine demonstration and current progress on development and test of an all-ceramic nozzle section.

Design of Erosion Resistant Ceramic Nozzle

Replacement of nozzle vanes with a highly erosion resistant ceramic material such as hot pressed silicon nitride can substantially extend hot section life in a radial turbine in the event of oversevere erosive conditions. Due to the characteristics of hot section erosion in a radial turbine nozzle, vanes experience more erosive attack than turbine blades or other elements in the hot gas path. Foreign particles entering the turbine section above a given aerodynamic size do not reach full gas stream velocity before they are overcome by turbine blades and slug outward repeatedly against vane trailing edges until they are pulverized to a small enough size to exit inward with the exhaust stream [1]. Engine test results have shown turbine blading to endure artificially induced dust particles much longer than nozzle vanes. Therefore replacement of only nozzle vanes with an erosion resistant material is effective in further hardening the engine package to erosion.

Because of the mechanism for erosion described above, only vane

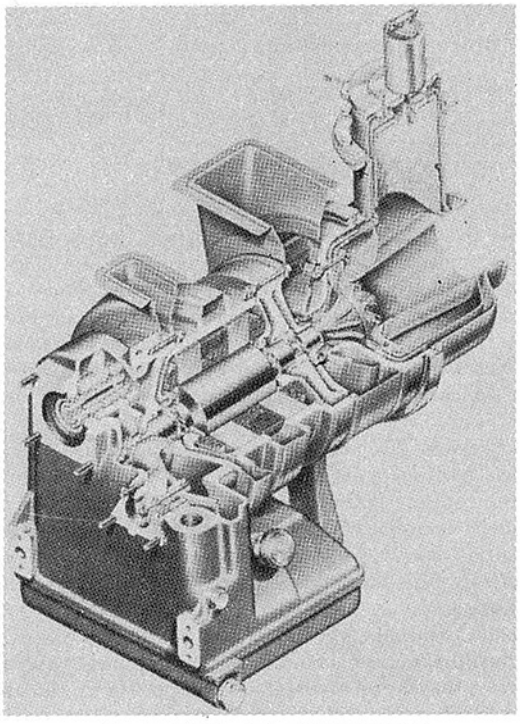


Fig. 1 The Gemini radial gas turbine

Contributed by the Gas Turbine Division and presented at the Gas Turbine Conference and Exhibit and Solar Energy Conference, San Diego, California, March 12–15, 1979 of THE AMERICAN SOCIETY OF MECHANICAL ENGINEERS. Manuscript received at ASME Headquarters December 18, 1978. Paper No. 79-GT-96.

Copyright © 1980 by ASME
Downloaded 01 Jun 2010 to 171.66.16.58. Redistribution subject to ASME license or copyright; see http://www.asme.org/terms/Terms_Use.cfm

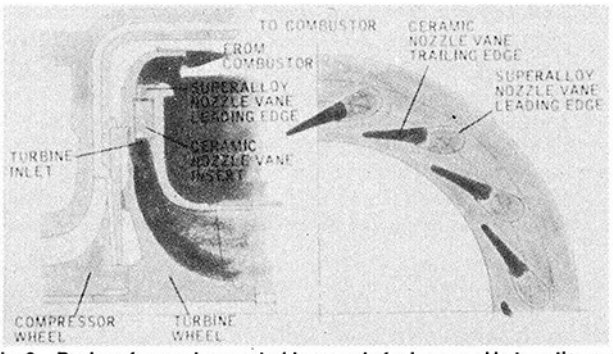


Fig. 2 Design of ceramic vane turbine nozzle for improved hot section erosion

trailing edges need to be ceramic. This allows more latitude in overcoming design problems associated with ceramics integral in a metallic structure.

Fig. 2 shows the design of a ceramic vane nozzle selected for rig and engine test evaluation. This configuration addresses the major ceramic turbine design obstacles which are:

1 thermal expansion coefficient mismatch between ceramics and superalloys,
2 localized contact stresses in ceramics due to normal surface irregularities,
3 manufacturing misfit contact stresses resulting from normal machining tolerances,
4 stresses induced into the assembly due to static and transient thermal distributions.

The ceramic vanes ($HPSi_3N_4$) shown in Fig. 2 are captured in recesses in 713 LC forward and rear shrouds. The recesses are slightly oversized to avoid stresses due to thermal expansion differences and thermal distributions in the nozzle. Accurate nozzle throat size is maintained in this assembly despite oversize recesses because static aerodynamic forces locate each ceramic vane at its furthest inboard downstream position.

A specially developed relaxing glass adhesive is applied at ceramic-vane metal-shroud interfaces to alleviate localized contact stresses due to surface irregularities and assembly mismatches. The glass adhesive is in a high viscosity state at operating temperatures to allow differential growths while providing interface cushion to prevent contact stress failures in the ceramic vanes.

Evaluation of Ceramic Vane Nozzle

Nozzle evaluation included engine simulator rig tests which exposed the ceramic vane nozzle and a reference all superalloy (713 LC) nozzle to dust erosion, sea salt corrosion and thermal shock. This was followed by a 24 hr plus 50 stop/start cycle engine test.

Thermal Shock. The thermal shock test was designed to duplicate the most severe thermal transient condition observed in engine operation. Fig. 3 shows vanes as they progress through one thermal cycle. The temperature indicated in this figure is the local temperature of the vane trailing edge as measured by an optical pyrometer. Five hundred cycles were run and all vanes survived with the exception of one (Fig. 4) which chipped at the trailing edge. This failure was determined to be the result of a lower temperature glass used at that location which generated a longitudinal contact stress on cool-down.

Dust Erosion. The nozzle was eroded in the simulator by means of a special particle impinger with 43–74 μm Arizona road dust with vane temperatures monitored optically to 1700°F for a 10 hr period. Fig. 5 compares erosion of superalloy vanes (713 LC) and hot pressed silicon nitride vanes (NC 132) in the engine simulator rig. The ceramic vanes offer substantial improvement in erosion in this elevated temperature test.

Sea Salt Corrosion. A 70 hr 1700°F, 3 ppm simulated sea salt test was made with the ceramic vane nozzle and reference 713 LC nozzle. Fig. 6 shows that the relative surface attack of 713 LC superalloy is much higher than that of the $HPSi_3N_4$ ceramic.

Engine Test. An engine test of the ceramic vane nozzle consisting

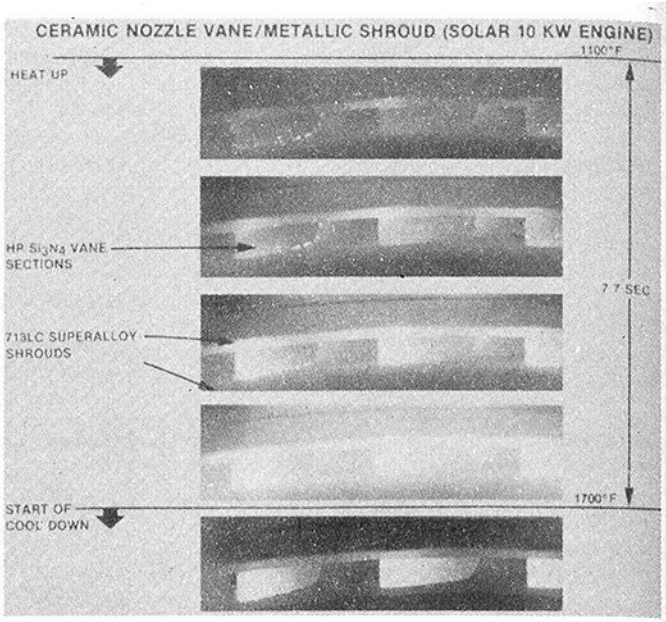


Fig. 3 Thermal shock test cycle for ceramic vane nozzle. ($HPSi_3N_4$ vanes and 713 LC shrouds)

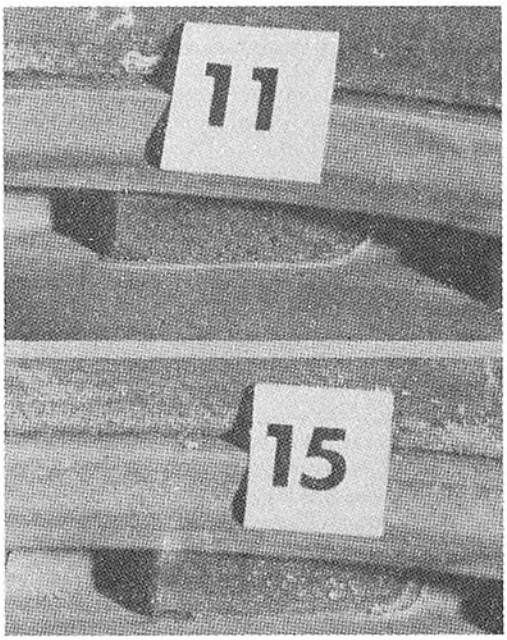


Fig. 4 $HPSi_3N_4$ vanes after 500 thermal shocks (note single failure out of 15 vanes tested at vane No. 15 trailing edge)

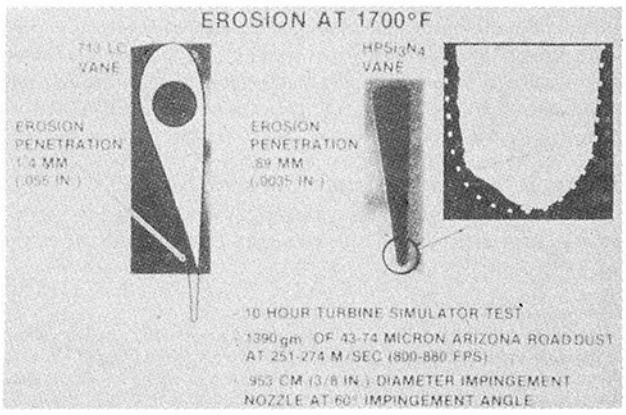


Fig. 5 Results from engine simulator erosion tests

Downloaded 01 Jun 2010 to 171.66.16.58. Redistribution subject to ASME license or copyright; see http://www.asme.org/terms/Terms_Use.cfm

of 24 hr of steady-state running at various loads and 50 start/stop cycles showed the ceramic vane nozzle to perform well with the exception that six vanes had suffered trailing edge fractures. Fig. 7 shows typical fractures [2].

Analysis showed the failures to be a direct result of deformation of the inner diameter lip of the forward shroud due to nozzle assembly loads.

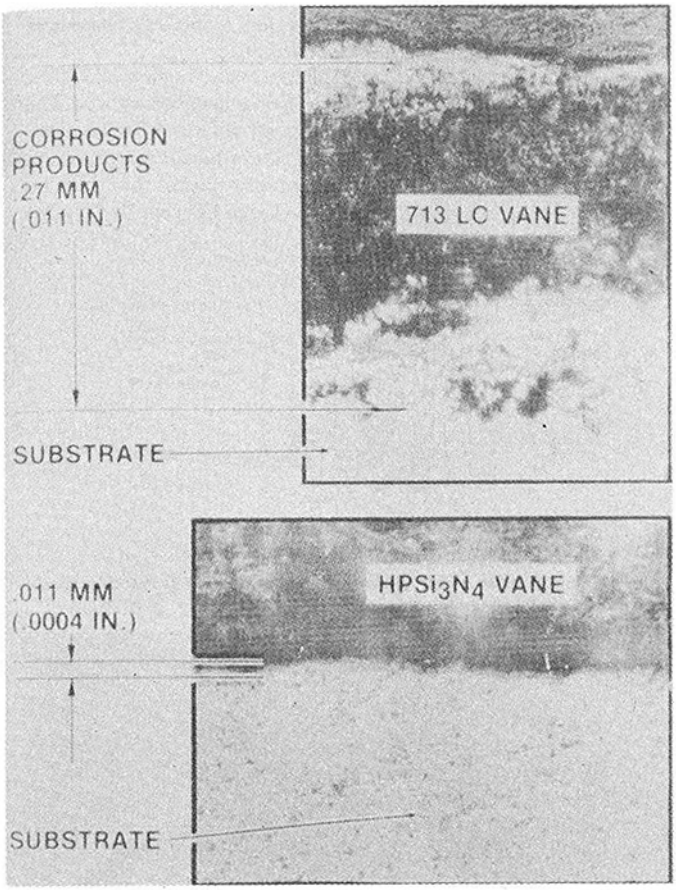


Fig. 6 Sea salt corrosion in engine simulator after 70 hrs

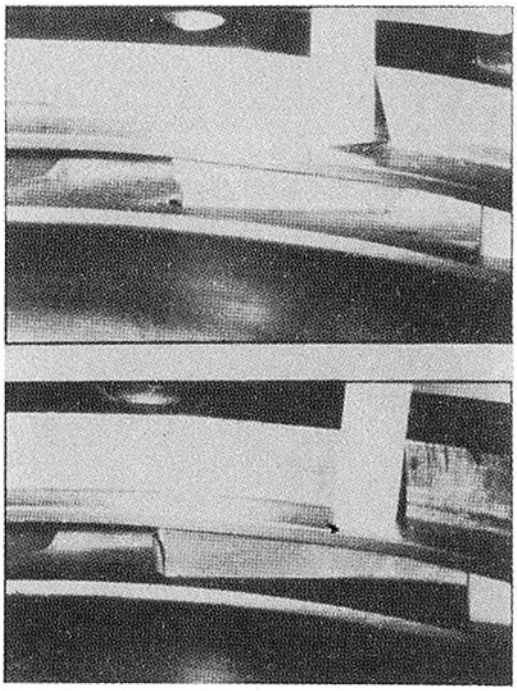


Fig. 7 Typical vane fracture (6 fractures out of 15 vanes) after first engine test

A redesign of the assembly was made (Fig. 8) and a re-run of the engine test gave positive results. The nozzle is shown after test in Fig. 9.

All-Ceramic Nozzle Design

An all-ceramic nozzle must overcome the same design difficulties iterated above.

Three alternate design concepts shown in Figs. 10–12 were chosen for engine simulator evaluation which is to lead to selection of one for engine test.

Design Concept No. 1 (Fig. 10) uses $RBSi_3N_4$ shrouds and cooled 718 superalloy support bolts. The bolts are piloted at the compressor diffuser housing such that they will accurately locate the rear (inner) shroud which must closely match the turbine wheel contour. The bolts are spring loaded in the axial direction to accommodate relative thermal growth. The rear shroud has radial slots at the bolt penetration points to allow for relative thermal growths, which are substantial. The forward (outer) shroud has clearance holes at the penetration point and is located by the seal plate which is made from INCO 903 [3], a low expansion alloy. The net diametrical growth at this junction is well matched to the ceramic shroud because of the

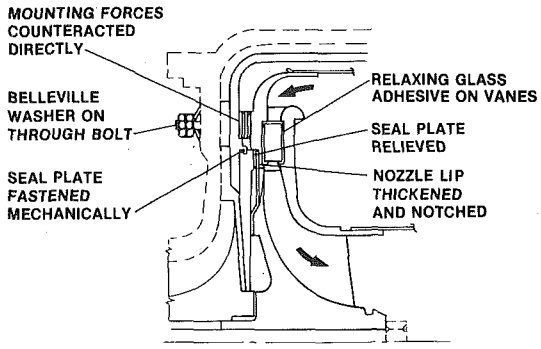


Fig. 8 Design change to ceramic vane nozzle prior to second engine test

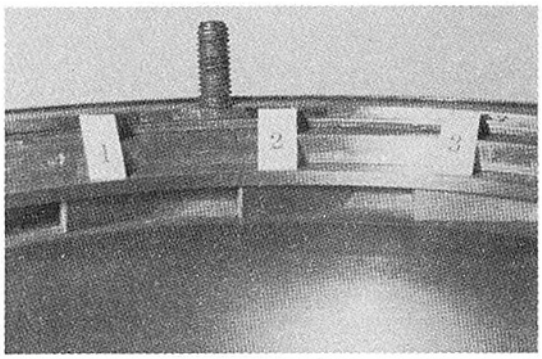


Fig. 9 Hot pressed silicon nitride vanes Nos. 1, 2, and 3 after second engine test

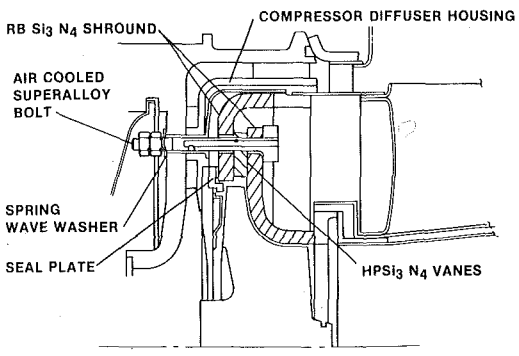


Fig. 10 All-ceramic nozzle design concept No. 1 $RBSi_3N_4$ shrouds, $HPSi_3N_4$ vanes and cooled 718 bolts

Downloaded 01 Jun 2010 to 171.66.16.58. Redistribution subject to ASME license or copyright; see http://www.asme.org/terms/Terms_Use.cfm

lower operating temperature of the seal plate and the low thermal expansion coefficient of the 903 alloy.

Design Concept No. 2 (Fig. 11) is similar to No. 1 except $HPSi_3N_4$ bolts are used in place of the cooled 718 bolts. They are also sprung in the axial position and have spring loaded collets at the external cool position in lieu of nuts. A 0.004 in. pure platinum interface layer has been used successfully at the collet bolt interface to avoid contact stress imposed fracture.

Design Concept No. 3 (Fig. 12) uses silicon filled reaction bonded silicon carbide shrouds and hot pressed silicon carbide vanes. The shrouds and vanes are bonded with a relaxing glass adhesive for contact stress reduction at vanes and for ease of assembly. Aerodynamic forces and a spring loaded exhaust scroll also hold the nozzle in position against the seal plate.

The forward shroud is held in place with a René 41 leaf spring attached to the diffusor housing which pulls the nozzle to the left against the seal plate by attachment to the nozzle retainer ring. The rear shroud has a face seal load applied at its gas exit point by a pressure actuated bellows spring system at the right section of the exhaust scroll (not shown in Fig. 12).

Fig. 13 shows nozzle assembly components which make up each of the three designs.

Evaluation of All-Ceramic Nozzle. Each of the design concepts has been exposed to various engine simulation experiments to evaluate factors such as leakage at seal interfaces and turbine tip clearances under full rated engine operating conditions.

Results have shown that face seal interfaces at ceramic section inlet and exit positions function well without special materials applied. The design provisions which allow compatibility of large differential expansions between ceramics and metal alloys have been proven to function well. Accurate rear shroud centering critical to turbine tip clearance has been demonstrated with Design Concept No. 1 in the

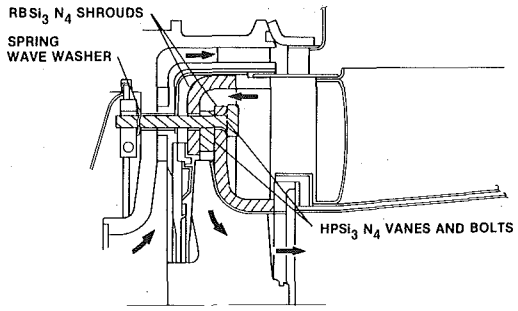


Fig. 11 All-ceramic nozzle design concept No. 2 $RBSi_3N_4$ shrouds, $HPSi_3N_4$ vanes and $HPSi_3N_4$ bolts

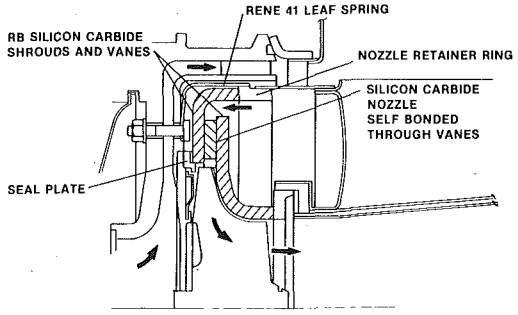


Fig. 12 All-ceramic nozzle design concept No. 3 RBSiC shrouds, HPSiC vanes and vanes bonded to shrouds

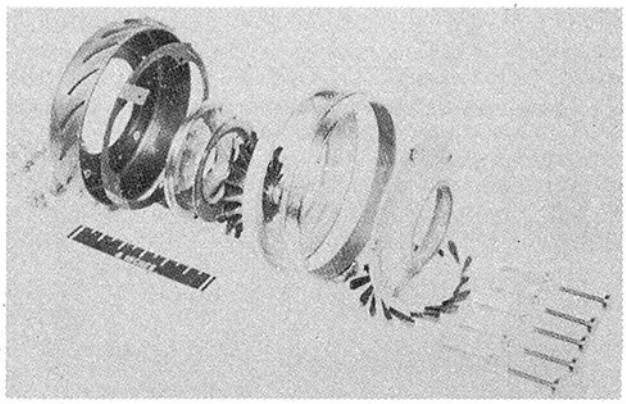


Fig. 13 All-ceramic nozzle assembly components (shown with $RBSi_3N_4$ shrouds)

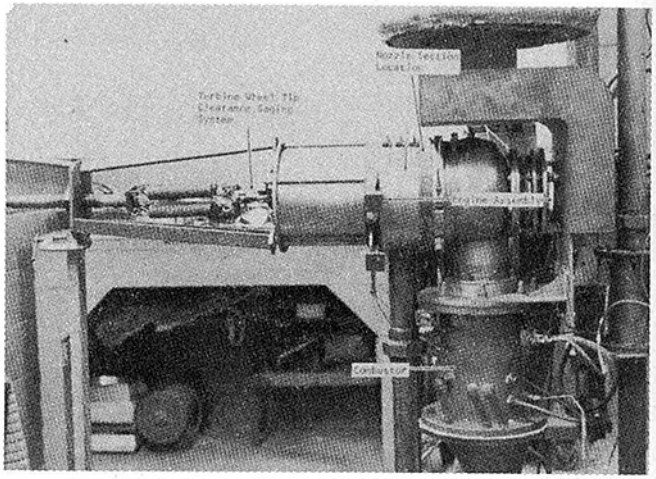


Fig. 14 Engine simulator used in all-ceramic nozzle testing

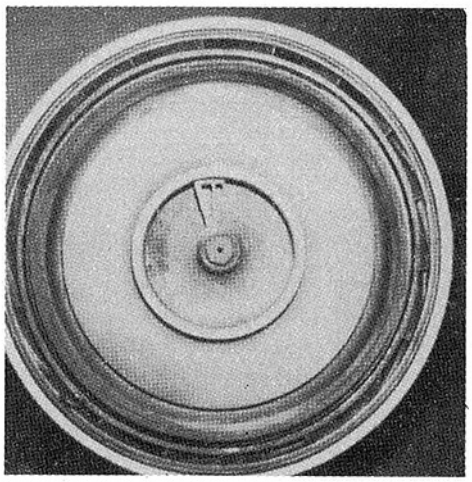


Fig. 15 Design concept No. 3 after engine simulator testing: 4 hr Steady-State at 1700°F and 500 thermal shock cycles

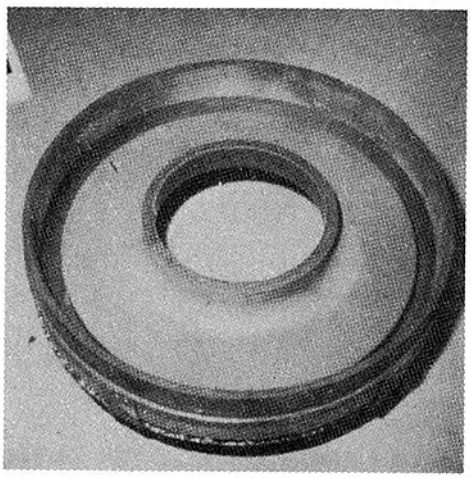


Fig. 16 Design concept No. 3 after engine simulator testing: 4 Hr Steady-State at 1700°F and 500 thermal shock cycles

Downloaded 01 Jun 2010 to 171.66.16.58. Redistribution subject to ASME license or copyright; see http://www.asme.org/terms/Terms_Use.cfm

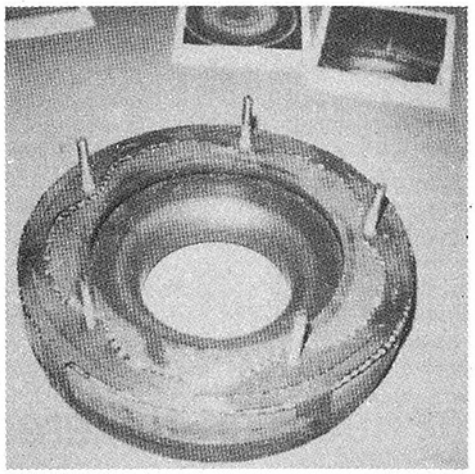


Fig. 17 Design concept No. 3 after engine simulator testing: 4 Hr Steady-State at 1700°F and 500 thermal shock cycles

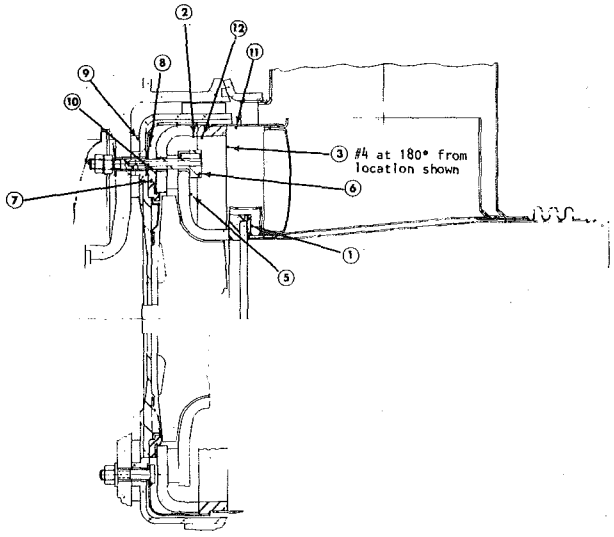


Fig. 18 Thermocouple locations for engine simulator test of ceramic nozzles

engine simulator (shown in Fig. 14) at 1700°F and 2100 fps nozzle throat velocity.

To date, engine simulator testing has successfully demonstrated 4 hr 1700°F steady-state operation and 500 thermal shock cycles with Concept No. 3. This silicon carbide nozzle is shown after this test in Figs. 15, 16 and 17. (See Figs. 18 and 19 for definition of test.)

Engine Simulator testing is still in progress and a 200 hr, 50 stop/start engine test is planned for the near future.

Conclusions

Turbine engine tests have demonstrated feasibility of a ceramic vane nozzle which can further increase engine life in erosion/corrosion severe operating environments.

Work on application of an all-ceramic nozzle for ultimate improvements in fuel economy and engine power to weight-bulk ratios shows promise.

Acknowledgments

The author would like to acknowledge personnel at MERADCOM and Solar for their efforts in conceiving and promoting this project. Special recognition is given to the memory of the late Franklin D. Jordan of MERADCOM who planned and supported much of the work still continuing in this program.

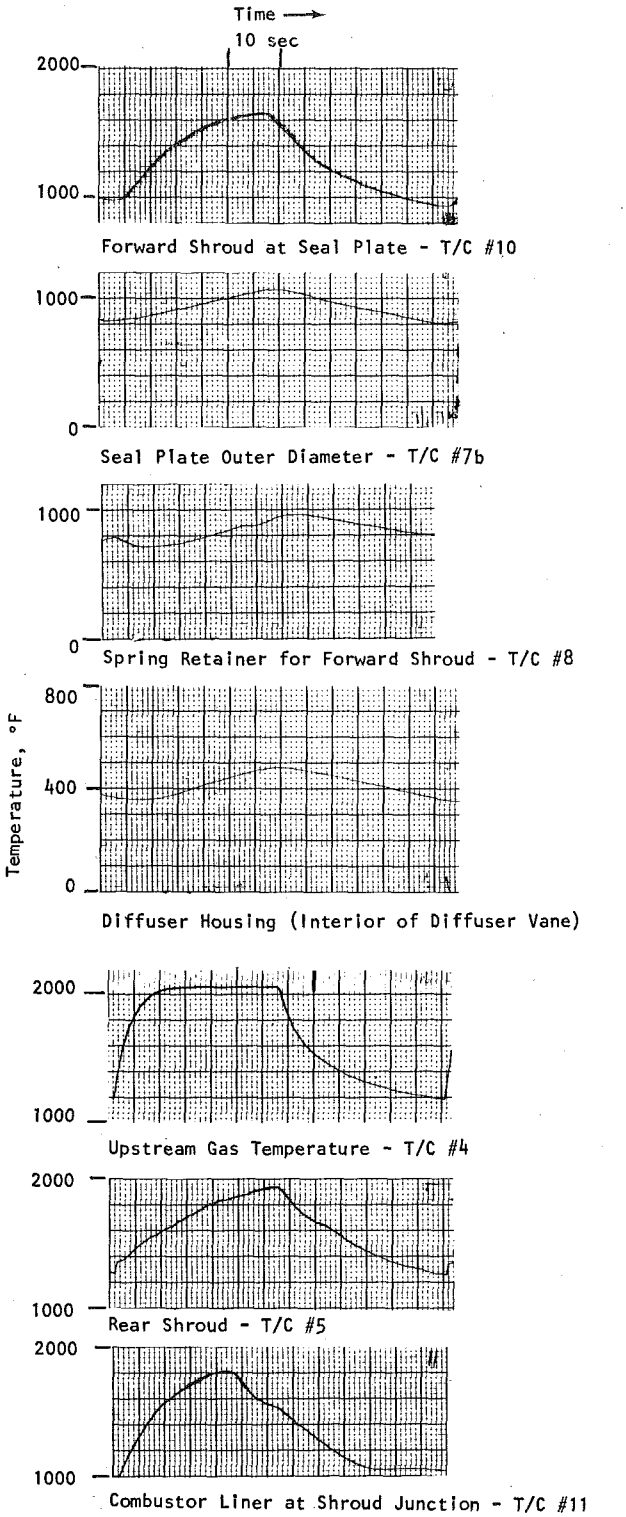


Fig. 19 Temperature time traces for thermal shock cycle of ceramic nozzle in engine simulator (see Fig. 18 for T/C locations)

References

1 Shoemaker, H. E. and Shumate, C. P., "Techniques for Reducing Sand and Dust Erosion in Small Gas Turbine Engines," SAE Paper 700706, Society for Automotive Engineers, Sept. 1970.

2 Jordon, F. D., Napier, J. C., Metcalfe, A. G., and Duffy, T. E., "Application of Ceramics to a radial Inflow Gas Turbine," SAE 770342, Society of Automotive Engineers, 1977.

3 International Nickel Company, Inc.

Downloaded 01 Jun 2010 to 171.66.16.58. Redistribution subject to ASME license or copyright; see http://www.asme.org/terms/Terms_Use.cfm

M. G. Mendiratta
Systems Research Laboratories, Inc.,
2800 Indian Ripple Road,
Dayton, OH 45440

P. L. Land and R. Ruh
Air Force Materials Laboratory,
Wright-Patterson Air Force Base, OH 45433

R. W. Rice
Naval Research Laboratory,
Washington, D. C. 20390

D. C. Larsen
IIT Research Institute,
Chicago, Ill. 60616

Fractography of Reaction-Sintered Si_3N_4

Fractography studies were accomplished on two reaction-sintered Si_3N_4 materials (Norton NC-350 Si_3N_4 and KBI (Kawecki-Berylco) Si_3N_4) which had been tested in four-point bending at room temperature, 1200, 1350, and 1500°C in air. At room temperature NC-350 exhibited uniform planar features representing a transgranular fracture mode, uniformly distributed small pores having a size range of 1–2 μm or less, and a few isolated large pores of ~10 μm. In contrast, the KBI Si_3N_4 at room temperature exhibited nonuniform, diffuse, and ill-defined fracture features, small pores having a size range of 2–5 μm, and many large pores of ~50 μm in size. At high temperatures, the fracture appearance of NC-350 Si_3N_4 was ill defined and diffuse, indicating a change in fracture mode. The fracture originating flaws in NC-350 were primarily the large pores or pore agglomerates. At all temperatures, in the KBI material, it was not possible to observe the mirror and, therefore, the site of fracture initiation. For NC-350, K_{IC} values were 1.2–1.6 $MN/m^{3/2}$ at room temperature and 2.1–2.4 $MN/m^{3/2}$ at high temperatures.

Introduction

Reaction-sintered silicon nitride (*RS* Si_3N_4) has emerged as a leading candidate material for Air Force systems applications such as gas-turbine stators [1], missile heat shields and nozzles [2], radomes, and other applications such as bearings and furnace components. This material is an attractive choice for such applications because it can be easily and economically fabricated into near-net complex shapes by either pressing or slip casting silicon powder and subsequently nitriding the green compacts. In addition, *RS* Si_3N_4 exhibits comparatively good thermal shock, oxidation, corrosion, and erosion resistance and has reasonably high strength at room temperature with good strength retention up to 1400°C; no measurable subcritical crack growth has been detected up to 1400°C.

An extensive property screening and evaluation of *RS* Si_3N_4 is currently being carried out by the IIT Research Institute (IITRI) in Chicago, under the sponsorship of the Air Force Materials Laboratory. One of the properties being measured is the four-point-bend tensile fracture strength, σ_f, as a function of testing temperature. Since there is no measurable plasticity in *RS* Si_3N_4, even at very high temperatures, strength variations can be directly interpreted on the basis of fracture-mechanics considerations involving the size of the critical flaw and the intrinsic materials parameters, which are fracture-surface energy, γ, and Young's Modulus, E. The strength-controlling flaws are introduced by the particular processing and fabrication procedures and machining utilized in *RS* Si_3N_4 obtained from different suppliers; the identification and characterization of these flaws is of extreme importance in understanding the fracture-strength variation as related to processing and fabrication. Fractographic examination of fracture surfaces by scanning electron microscopy (SEM) is emerging as a powerful technique in achieving this understanding in structural ceramics.

The objective of the present study was to perform a comprehensive fractographic investigation on *RS* Si_3N_4 bars fractured in four-point bending at room temperature and at 1200, 1350, and 1500°C. IITRI has carried out strength measurements and other property evaluation on ceramics supplied by two different suppliers—Norton *RS* Si_3N_4 (NC-350 Si_3N_4) and Kawecki-Berylco *RS* Si_3N_4 (KBI Si_3N_4) [3]. Both materials were included in the present fractography study. An understanding of the fracture behavior and the determination of the fracture-mechanics parameters (i.e., relationship between flaw size, fracture mirror size, and strength) are needed to aid in the failure analysis of structural components made from *RS* Si_3N_4.

Materials Studied and Experimental Procedure

The Norton NC-350 *RS* Si_3N_4 used in this study was prepared by cold pressing a large silicon plate which was then nitrided. Samples were diamond machined to a surface finish of ~5 μm RMS. The KBI *RS* Si_3N_4 samples were machined from a cold-pressed silicon block, individually nitrided, and then finished by diamond machining. Surface finish ranged from 20 to 60 μm RMS. Impurity analysis of both materials has been presented previously [3]; in general, the Norton material has a somewhat higher purity. In light of the above differences between the two materials, different microstructural features may govern the fracture behavior. Similar materials from two different suppliers were studied in the hope that a better understanding of the features that control fracture could be gained. The four-point bend strength, elastic modulus, and density of the two materials have been measured and included in the IITRI report [3].

Contributed by the Gas Turbine Division and presented at the Gas Turbine Conference and Exhibit and Solar Energy Conference, San Diego, California, March 12–15, 1979 of THE AMERICAN SOCIETY OF MECHANICAL ENGINEERS. Manuscript received at ASME Headquarters December 18, 1975. Paper No. 79-GT-97.

Copyright © 1980 by ASME
Downloaded 01 Jun 2010 to 171.66.16.58. Redistribution subject to ASME license or copyright; see http://www.asme.org/terms/Terms_Use.cfm

Fracture surfaces were inspected under a 14–60× binocular light microscope to look for the characteristic radiating ridges which are often observed to converge toward the origin of the fracture and frequently to originate in a smooth, sometimes mirror-like region surrounding the flaw. At room temperature, the bars generally broke into two or three pieces. In the NC-350 Si_3N_4 the localized critical flaws could usually be identified with confidence from the fracture markings, but the fracture markings were very ill-defined in the KBI material. At high temperatures, the bars broke in many pieces; and identification of the primary fracture surface and, therefore, the location of the critical flaw were difficult due to missing pieces, damage to the primary feature area, and occurrence of flaws and mirrors at secondary fracture sites with dimensions comparable to those at primary sites. The pieces containing probable critical flaws and several examples of secondary fractures were designated for study in the SEM.

While making observations with the light microscope, the pieces of broken bar were reassembled to determine the position of the critical flaw and to permit tracing of the fracture features. Pieces of the bars were selected for study and photographing in an AMR SEM. These pieces were coated with a thin uniform inner layer of carbon and a thicker outer layer of gold-palladium alloy which is the combination giving the optimum SEM signal and resolution. The SEM examination was usually performed in the secondary-emission mode which is particularly suitable for observing gross three-dimensional features in fracture topography. The backscattered electron mode was also employed selectively; in this mode the high-energy reflected electrons travel in more nearly straight lines and, therefore, the finer topographic features of the fracture are emphasized by shadows in the image.

Results and Discussion

Fracture Modes and Fracture Microstructures. Fracture surfaces of both the NC-350 Si_3N_4 and KBI Si_3N_4 bend bars were examined in the SEM for general fracture features. Representative examples of fracture surfaces for specimens broken at room temperature are shown in the SEM micrographs in Fig. 1 for NC-350 and in Fig. 2 (*a*) and (*b*) for KBI Si_3N_4. As shown in Fig. 1, the fracture surface of NC-350 exhibited uniform, planar features representing the transgranular fracture mode in which the grain size was measured to be ~3–6 μm. A relatively uniform distribution of pores having a size range of 1.5–2 μm can be observed from the micrograph; however, isolated larger pores or pore-coagglomerates having a size of ~10 μm were also observed frequently (shown at locations A and B in Fig. 1). The volume fraction of the porosity having a value of ~20 percent was estimated by standard lineal analysis to be in reasonable agreement with that estimated from the measured density [3].

In contrast to the relatively sharp fracture features in NC-350, the KBI material, in general, exhibited diffuse nonuniform fracture features (see Fig. 2 (*a*) and (*b*)). Fig. 2 (*a*) shows ill-defined features giving a wooly appearance; it is difficult to determine whether the fracture is transgranular or intergranular. Small pores having a size range of ~2–5 μm can be seen in the micrograph. Many large pores showing unreacted material and having a size of ~50 μm were also observed frequently; an example of such a pore can be seen in Fig. 2 (*b*).

The fracture features for the two materials as described above were observed far away from the fracture-originating flaws. These general features were common to most of the bend bars and, therefore, independent of strength distribution. The more uniform fracture features, the flat transgranular fracture mode, and the smaller, more uniform porosity in the NC-350 material indicate that this material had been more completely sintered than the KBI material. For this reason, NC-350 should exhibit less scatter in strength values and a higher mean strength value than that exhibited by the KBI material. The strength data [3] indicate that, indeed, such is the case.

The more undefined and rough features in the fracture surfaces of the KBI bend bars (Fig. 2) indicate that a higher fracture-surface energy may have been expended in propagating the cracks than that in the NC-350 bend bars (Fig. 1). The fracture-surface-energy values calculated from room-temperature K_{IC} data are 15.8 J/m^2 for the KBI material and 11.3 J/m^2 for the NG-350 material [3]. These values and the fracture appearance for the two materials are consistent.

High-Temperature Fracture Appearance. Detailed fractography was carried out for the bars fractured at high temperatures for NC-350 Si_3N_4 only, since NC-350 Si_3N_4 exhibited consistently higher strength than KBI Si_3N_4. The strength at 1200°C in air in-

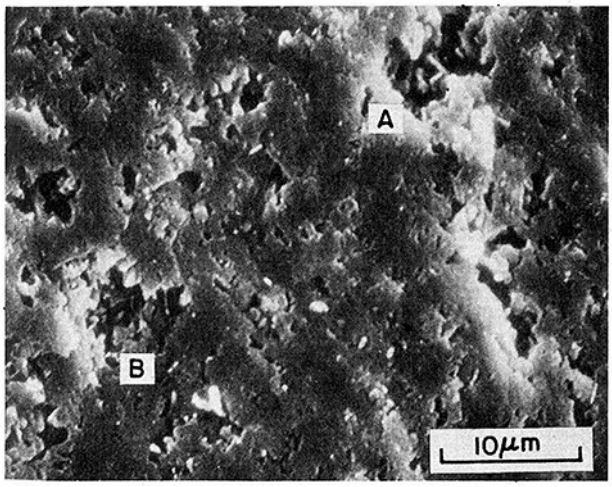
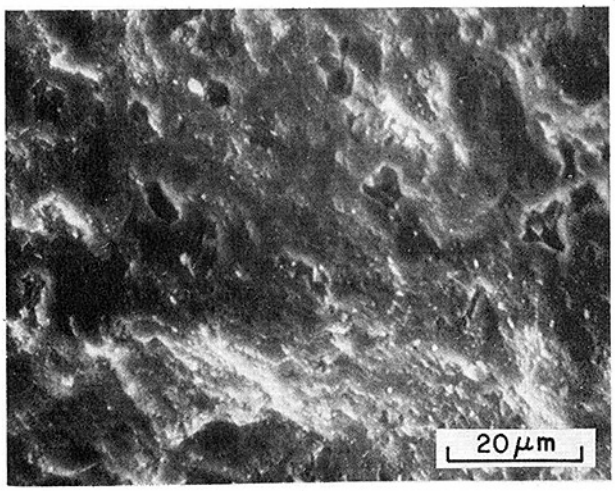
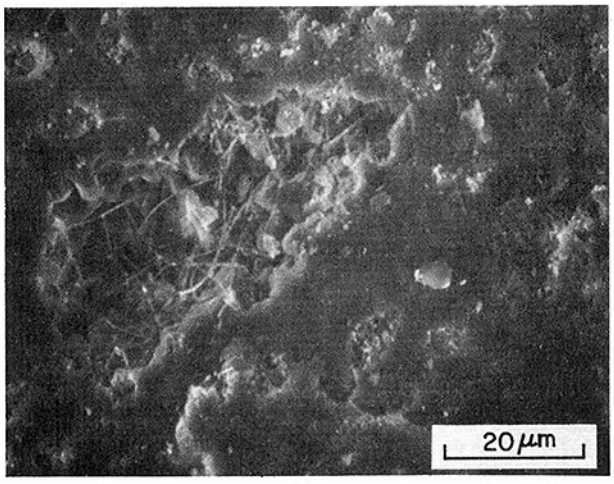


Fig. 1 Fracture surface showing microstructure of NC-350 Si_3N_4 bend bar fractured at room temperature. Secondary electron SEM micrograph



(a)



(b)

Fig. 2 Fracture surface showing microstructure of KBI Si_3N_4 bend bar fractured at room temperature

Downloaded 01 Jun 2010 to 171.66.16.58. Redistribution subject to ASME license or copyright; see http://www.asme.org/terms/Terms_Use.cfm

creased significantly as compared to that at room temperature; above 1200°C the strength dropped slightly but still was higher than that at room temperature. It was hoped that fractography of the bend bars broken at elevated temperatures might give a clue as to the reasons for the increase in strength levels at elevated temperatures.

The fracture surfaces of NC-350 bend bars broken at 1200°C exhibited a marked difference in appearance as compared to those broken at room temperature. The 1200°C fracture surface did not show uniform, planar features; rather it showed diffused, undefined features similar to the room-temperature fracture exhibited by KBI material. Fig. 3 is an SEM micrograph of the fracture surface of a bend bar broken at 1200°C in air. It is difficult to judge whether the fracture mode is transgranular or intergranular. However, in comparison with the room-temperature fracture appearance, the fracture mode has definitely changed.

In order to determine whether oxidation of the fracture surface at 1200°C would obscure the fracture features, two bend bars were broken in four-point loading in a vacuum of 10^{-4} torr. The fracture-strength values are given in Table 1.

The fracture-surface appearance of the bend bars broken at 1200°C in vacuum was very similar to that of the bars broken at 1200°C in air (Fig. 3). Oxidation at 1200°C, therefore, did not obscure the appearance of the fracture surfaces, and it can be stated that there was a definite change in fracture mode at high temperatures as compared to room temperature. However, this change did not seem to affect the strength values; an average strength value of 34 ksi at 1200°C in vacuum was obtained which is very near the average value at room temperature. It appears that the strength increase at 1200°C in air is due to flaw-tip blunting by the formation of a thin layer of silica and the consequent increase in effective fracture-surface energy, γ. The short pretest time (5 min) at 1200°C is not expected to decrease the critical-flaw sizes significantly but could blunt sharp flaws.

Fracture Origins. The sites of fracture origins were located by searching for inner mirrors bounded by rough radiating ridges in the fracture surfaces of the bend bars. The preliminary search for mirrors was made on the binocular light microscope and in the SEM at magnifications below 20×. The fracture-originating flaws were then observed at successively higher magnifications in the SEM. Only in ~40 percent of the bend bars could the fracture mirrors be seen. In the remainder of the fractured bars, either the regions containing the mirrors were chipped away due to multiple fracture or the mechanisms that produce clearly observable mirrors were not operative; e.g., for large flaws and low fracture strength, the crack-growth velocity may be too low for the formation of mirror boundaries [4].

In both NC-350 and KBI Si_3N_4, the most dominant fracture-originating flaws observed following the above procedure were pores and pore agglomerates. However, a number of other types of flaws were also observed. These were:

1 Bands of porosity (pores 10–20 μm in diameter),
2 bands of glassy-looking phase, perhaps indicating local overheating of the material during the fabrication procedure or local chemistry differences,
3 machining flaws, i.e., surface chipping and surface gouging. Only about 10 percent of the fracture surfaces observed indicated that machining flaws were fracture initiating. It appears that machining damage is insignificant in *RS* Si_3N_4.
4 flaked, fibrous band of material, signifying incomplete local nitriding.

Except for machining flaws, the flaws described above are obviously the result of the impurities and particle size distribution of silicon powders used and the nitriding and sintering procedures. Since the materials were obtained from commercial sources, it was not possible to relate the nature of the flaws observed by SEM to the fabrication procedures. Attempts were made to obtain chemistry variations in the immediate vicinity of some of the flaws utilizing the energy-dispersive x-ray technique; however, no significant differences in chemistry could be detected. The number of machining damage flaws was small compared to the significant numbers found in other studies [5, 6].

Fracture Mirrors. Clearly delineated fracture mirrors could be observed only in the NC-350 Si_3N_4. In the KBI material, although vague impressions of a mirror region were observed, it was difficult to measure—even approximately—the size of the inner mirror. Figs. 4, 5, and 6 are SEM micrographs showing mirrors and fracture-originating flaws at room temperature and at 1200 and 1500°C for NC-350 Si_3N_4. The flaws in these examples are pores and unsintered material representing material inhomogeneity and are not caused by machining.

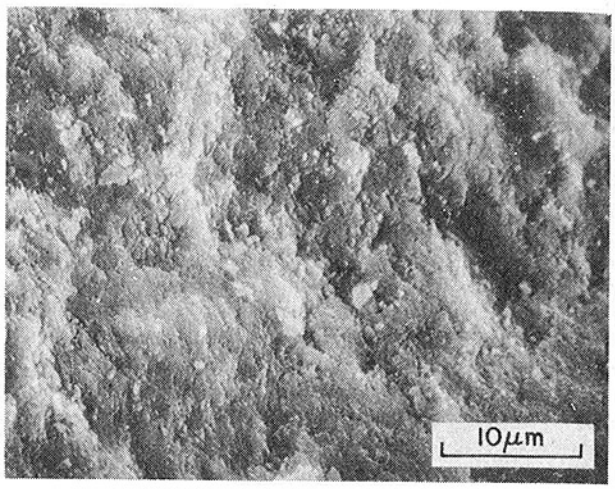


Fig. 3 Fracture surface showing microstructure of NC-350 bend bar fractured at 1200°C in air. Secondary electron SEM micrograph

TABLE 1 Four-point flexural strength at 1200°C for NC-350 Si_3N_4

Test Atmosphere	*Average Strength*
Air	65 ksi (IITRI data)
Vacuum	34 ksi

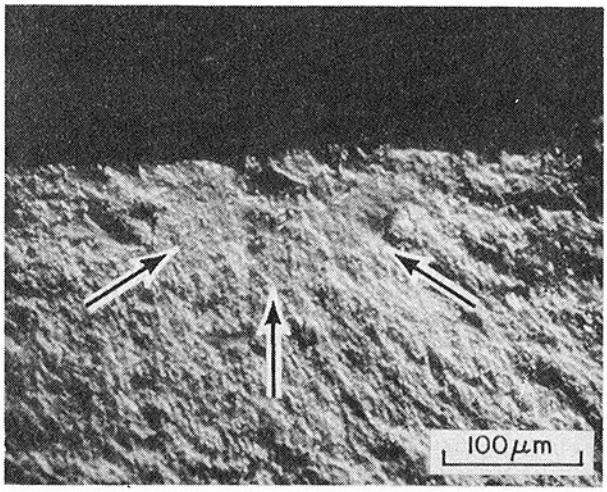


Fig. 4 Fracture originating flaw and associated inner mirror in NC-350 tested at room temperature. Inner mirror shown by arrows

In NC-350 attempts were made to measure mirror sizes and to establish correlation between flaw mirror sizes and between mirror size and strength. In most cases it was difficult to establish the boundaries of the inner, flat, highly reflecting regions (i.e., inner mirrors); it appeared that very fine radiating ridges began forming close to the critical flaws. The measured mirror sizes were very approximate and—independent of testing temperature—had a value of 120 ± 20 μm. The reason for the mirror boundaries not being sharply delineated is not known. The associated critical flaw sizes had a mean value of 25 ± 5 μm, providing a ratio of inner mirror to flaw size of ~5. It has been shown that for many glasses and ceramics, the strength and size of the mirror are related by

$$\sigma_f \sqrt{R} = \text{a constant (for a given material)}$$

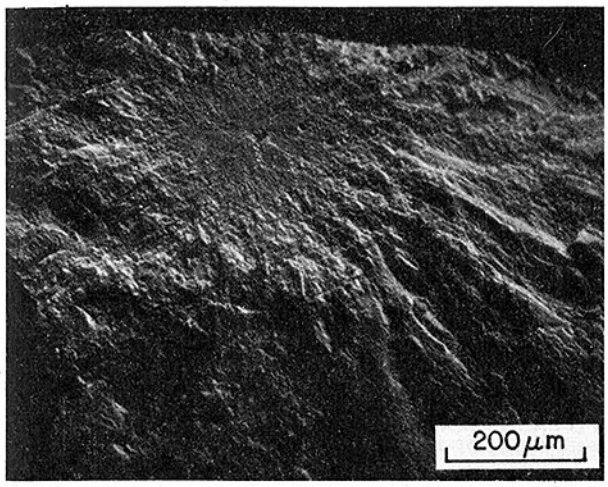
Downloaded 01 Jun 2010 to 171.66.16.58. Redistribution subject to ASME license or copyright; see http://www.asme.org/terms/Terms_Use.cfm

where σ_f is fracture strength and R is the mirror radius. For NC-350 examined in this study the mean value of this parameter was found to be 2.6 $MN/m^{3/2}$ with a variation of as much as ±30 percent. The major uncertainty in the calculation of this parameter was due to ambiguity in establishing precisely the inner mirror boundaries.

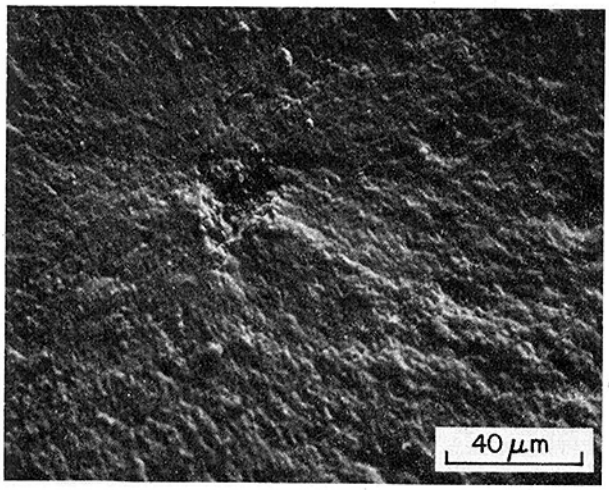
K_{IC} Calculations. Attempts were made to calculate approximately the critical stress-intensity factor, K_{IC}, from fracture-strength values and measured flaw dimensions. The flaws were assumed to be circular flat discs in the depth of bend bars, and in this case the stress-intensity factor is given by [7]

$$K_{IC} = \frac{2}{\sqrt{\pi}} \sigma_f (a)^{1/2}$$

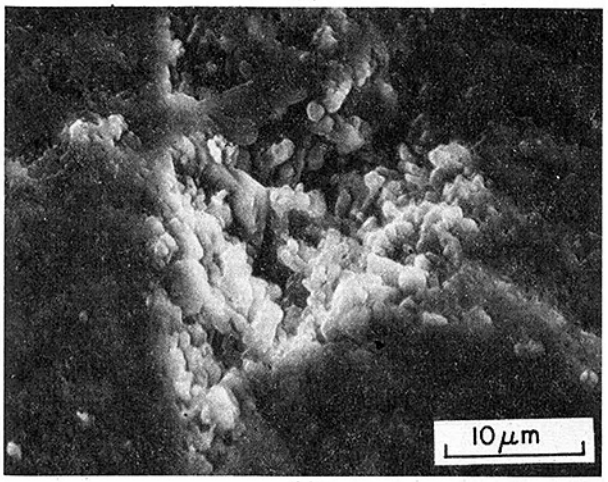
where σ is the tensile stress and a is the radius of the circular flaw. In the depth of the bend bars, the local value of σ was calculated by assuming a linear variation of the stress with depth, with maximum



(a)

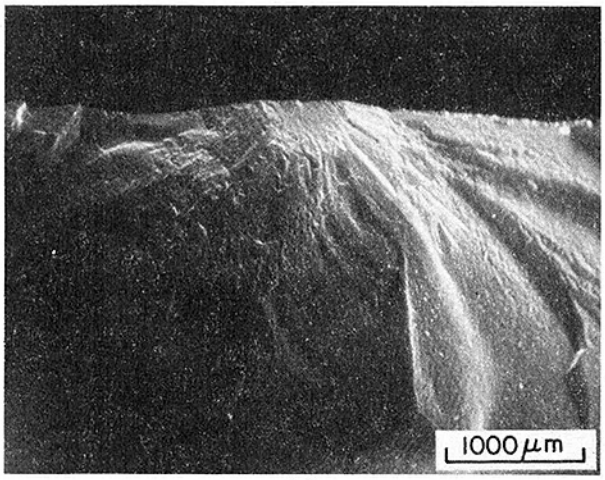


(b)

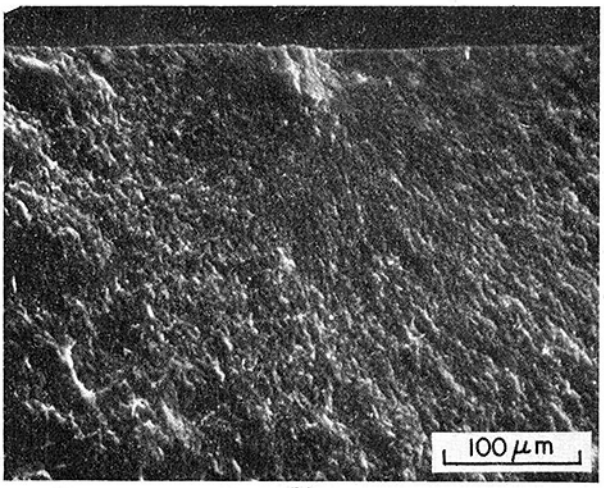


(c)

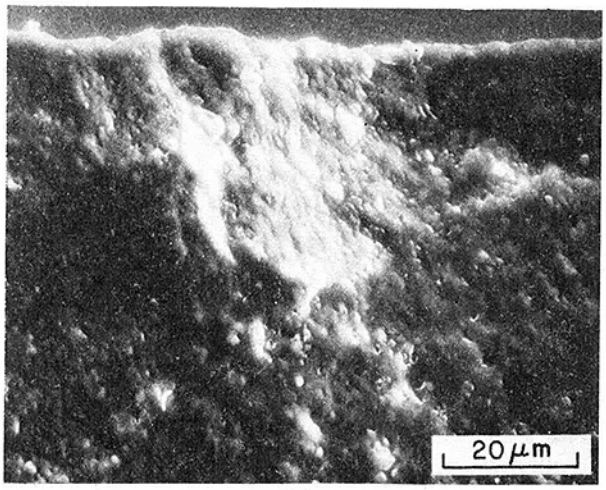
Fig. 5 Fracture-originating flaw in NC-350 Si_3N_4 bend bar fractured at 1200°C in air. (*a*, *b*) backscattering mode, (*c*) secondary electron mode



(a)



(b)



(c)

Fig. 6 Fracture originating flaw in NC-350 Si_3N_4 bend bar fractured at 1500°C in air (secondary electron mode)

Downloaded 01 Jun 2010 to 171.66.16.58. Redistribution subject to ASME license or copyright; see http://www.asme.org/terms/Terms_Use.cfm

value at the surface and zero at the center of the bar, i.e., at the neutral axis. For the flaws which were open to the surface or very near the surface, K_{IC} was calculated from the more precise expression [8]

$$K_{IC} = M\sigma_f \left(\frac{\pi a}{Q}\right)^{1/2}$$

where M is a function of the ratios of flaw depth to bend bar thickness and flaw depth to flaw length and Q is a function of ellipticity, i.e., the ratio of flaw depth to flaw length.

For NC-350 Si_3N_4 the room-temperature values of K_{IC} were found to vary between 1.22 and 1.6 MN/m$^{3/2}$. The double-torsion technique was utilized by IITRI to obtain a room-temperature K_{IC} value for NC-350; a mean value of 2.06 MN/m^2 was reported [3]. This value is somewhat higher than the values calculated in the present investigation. This difference may be due to highly local stress intensification and weak material in the vicinity of small material flaws in contrast to the large artificial crack utilized in the double-torsion technique which averages the microstructural variations. It is interesting to note that average K_{IC} values of 1.87 MN/m$^{3/2}$ were obtained by Wills, et al. [8], who utilized a controlled-surface-flaw technique. In this technique a surface flaw having a depth of ~135 μm was utilized. This crack dimension is about four times larger than the dimensions of the natural critical flaws but is much smaller than the crack front size used in double torsion.

At elevated temperatures, although the strength in air increased substantially, the dimensions of the critical flaws were not different than those at room temperature, i.e., ~25 μm. The calculated values of K_{IC} were found to be 2.1 to 2.4 MN/m$^{3/2}$ at high temperatures (i.e., above 1200°C), with no systematic dependence upon temperature. The increase in K_{IC} at higher temperatures was probably due to increased fracture-surface energy resulting from flaw-tip blunting.

Summary

A fractographic study was carried out on two reaction-bonded silicon nitride materials—Norton NC-350 Si_3N_4 and KBI Si_3N_4 by SEM. The fracture surfaces of the bars fractured in four-point bending at room temperature and at 1200, 1350, and 1500°C were examined. At room temperature the general fracture features in NC-350 Si_3N_4 were uniform, planar features representing the transgranular fracture mode, uniformly distributed small pores having a size range of 1–2 μm or less, and isolated large pores having a size of ~10 μm. In contrast, the KBI material at room temperature exhibited nonuniform, diffuse, and ill-defined fracture features, small pores having a size range of 2–5 μm, and many large pores having a size of ~50 μm. In some regions the KBI material exhibited features similar to those in NC-350 Si_3N_4, i.e., transgranular and uniform fracture, which indicated that the KBI material did not have a uniform microstructure, probably due to inadequate nitriding. The room-temperature strength differences, i.e., higher mean strength and less scatter in strength values in the NC-350 material than in the KBI material, are consistent with the differences in general fracture features in the two materials. At high temperatures the fracture appearance in NC-350 Si_3N_4 was ill-defined and diffuse, indicating a change in fracture mode. However, this change in mode in itself did not seem to increase the fracture-surface energy.

In NC-350 fracture mirrors were frequently observed, although the boundaries of inner mirrors were ill-defined. The fracture-originating flaws in NC-350 were predominantly the large pores or pore agglomerates, although other types of flaws—including bands of small pores, bands of a glassy-looking phase, surface chipping and gouging, and a flaked and fibrous band of material—were present. In the KBI material, because of diffuse and ill-defined fracture features, it was not possible to observe mirrors and, therefore, the sites of fracture initiation.

In NC-350 the measured radius of the inner mirrors had a mean value of 120 ± 20 μm and the size of the associated critical flaw had a mean value of 25 ± 5 μm, thus providing a ratio of the inner mirror to flaw size of ~5. The parameter $\sigma_f \sqrt{R}$ had a value of 2.6 MN/m$^{3/2}$ with a variation of as much as ±30 percent. Thus, in the failure analysis of a component where it may be possible to measure the radius of the inner mirror, the local stress could be predicted to within ±30 percent. At room temperature the values of K_{IC} ranged from 1.22 to 1.6 MN/m$^{3/2}$. At high temperatures, the calculated K_{IC} values were between 2.1 and 2.4 MN/m$^{3/2}$.

Acknowledgments

The authors gratefully acknowledge Joseph Henry and Sarah Morey for assistance with the SEM analysis and Sandra Ehlers and Helen Bailey for preparation of the manuscript.

References

1 McLean, A. F., ASME Paper No. 70-GT-105, New York, May 1970.

2 Godfrey, D. J., "Fabrication and Properties of Silicon Nitride Ceramics and Their Relevance to Aerospace Applications," *J. Brit. Interplanet. Soc.*, Vol. 22, 1969, pp. 353–358.

3 Larsen, D. C., "Property Screening and Evaluation of Ceramic Vane Materials," Report No. IITRI-D6114-ITR-18 (Interim Technical Report No. 3), Air Force Contract F33615-75-C-5196, Feb. 26, 1977.

4 Rice, R. W., "Fracture Topography of Ceramics," in *Surfaces and Interfaces of Glass and Ceramics*, V. D. Frechette, W. C. LaCourse, and V. L. Burdick, eds., Plenum, New York, 1974, pp. 439–472.

5 Rice, R. W., et al., "Fractography of S_{13} LVc and SiC," *Ceramics for High Performance Applications*, Chestnur Hill, MA, 1978, pp. 669–687.

6 Rice, et al., "Fracture Sources in S_{13} and Sic," *Proceedings of the 1977 DARPA/NAVSEA Ceramic Gas Turbine Demonstration Engine Program Review*, MCIC 72-36, Columbus, OH, 1978, pp. 665–688.

7 Brown, W. F., Jr., and Srawley, J. E., ASTM-STP-410, American Society for Testing and Materials, Philadelphia, PA, 1967, pp. 1–15.

8 Wills, R. R., Mendiratta, M. G., and Petrovic, J. J., "Controlled Surface Flaw Initiated Fracture in Reaction Bonded Si_3N_4," *J. Mater. Sci.*, Vol. 11, 1976, pp. 1330–1334.

Downloaded 01 Jun 2010 to 171.66.16.58. Redistribution subject to ASME license or copyright; see http://www.asme.org/terms/Terms_Use.cfm

P. D. Greenhalf
Chief Electrical Engineer,
GEC Gas Turbines Limited,
Whetstone,
Leicester LE8 3LH
England

Recent Developments on Gas Turbine Control Systems

The paper briefly outlines some of the activities undertaken on gas turbine logic and control systems. The frequent requirement for gas turbines to operate in polluted hostile environments has encouraged the development of ancillary equipment which will reliably withstand onerous site conditions. The design requirements, philosophy, component selection and progress made on fuel control and solid state logic systems, specifically introduced to meet arduous service requirements are reviewed. A computer control system designed for more temperate environments is also examined, enabling a comparison of the theoretical reliabilities of the respective systems to be assessed when installed on gas compressor applications.

Introduction

The gas turbine manufacturer is required to review and regularly update the standards of equipment being supplied, in order that the increasingly more onerous design and reliability criteria, which become necessary, are achieved. As more complex control equipment is being installed to provide the additional monitoring and data transmission facilities, for operating the units from centralized remote control rooms, it becomes even more important that the machinery and associated controls are built to the highest standards to insure that reliable unattended operation is obtained.

The machines are often installed in locations experiencing extremes of ambient temperature, sand storms and corrosive atmospheres. When situated in the vicinity of gas and oil well-heads the problems are accentuated by virtue of the dubious quality of the fuel supplies and air pollution from gas flaring causing fouling of the gas turbo compressor, thus reducing starting margins. Notwithstanding the high level of contaminants contained in the fuel or the high environmental temperatures prevailing when air conditioning plant fails, the control equipment is expected to ignore and withstand such conditions, thus ensuring that the machine remains on stream. In this context, the operation of machines forming an integral part of a process is vital, in that an unscheduled outage results in a significant loss of revenue to the operator due to the time taken to re-establish the overall process.

Based on the experience gained over the last few years on machines operating in adverse conditions, considerable efforts have been made to develop standard equipment which is inherently good natured and capable of performing reliably even when subjected to severe maltreatment. In principle, the philosophy adopted at the design stage for overcoming the less predictable events affecting reliability is to utilize superior components and include adequate margins on component ratings, thus catering for failures on equipment beyond the control of the gas turbine vendor.

In the paper that follows potential areas of improvement are reviewed and emphasis placed on:

1 developments surrounding the mechanical aspects of fuel control systems,

2 implementing a computer based control system, having trend analysis potential,

3 development of a solid state control system for service in arduous conditions,

4 reliability assessment problems.

Mechanical Aspects of Fuel Control Systems

Background. While most users will declare that their gas fuel treatment plant will provide fuel gas to an acceptable specification, it frequently transpires that the gas contains quantities of contaminants in both liquid and solid form. These contaminants often contain high levels of hydrogen sulphide which combines with the moisture abstracted from the gas being expanded across the fuel throttle valve, resulting in considerable corrosion occurring on the internal parts of the valve. The problem is compounded by the gas containing extremely fine particles of solid contaminants in the form of dust, having an appearance like face powder with a particle size of less than 5 μm.

In the course of time the pollutants adhere to the internal parts of valves, the combined effect forming an extensive build-up of a substance which appears like very hard scale and which can inhibit and restrict the movement of the fuel valve, see Fig. 1. The problem of dirt manifests itself predominantly on starting, whereby the valve opening is very small for light off and any restraining influence can result in the optimum conditions for light off and subsequent acceleration not being achieved.

The system, which in the past has been in most common use, employs an actuator which responds directly to the governor output and drives the fuel control valve via a CDP (Compressor Discharge Pressure) limiter. The purpose of the limiter is to modify the output of the actuator to ensure that the prescribed fuel scheduling limits are not exceeded during acceleration or deceleration of the machine.

Contributed by the Gas Turbine Division and presented at the Gas Turbine Conference and Exhibit and Solar Energy Conference, San Diego, California, March 12–15, 1979 of THE AMERICAN SOCIETY OF MECHANICAL ENGINEERS. Manuscript received at ASME Headquarters December 18, 1978. Paper No. 79-GT-98.

Copyright © 1980 by ASME

Downloaded 01 Jun 2010 to 171.66.16.58. Redistribution subject to ASME license or copyright; see http://www.asme.org/terms/Terms_Use.cfm

It should be noted that the governor provides the necessary control for normal operation, the limiter forming a second line of defence in the unlikely event of a problem developing on the equipment upstream of the limiter. The system performs satisfactorily providing the fuel gas supply is clean and dry. However, while the actuator/limiter/control valve arrangement is ingenious in concept, its long term stability of operation can be adversely affected by arduous operating conditions of the type noted above.

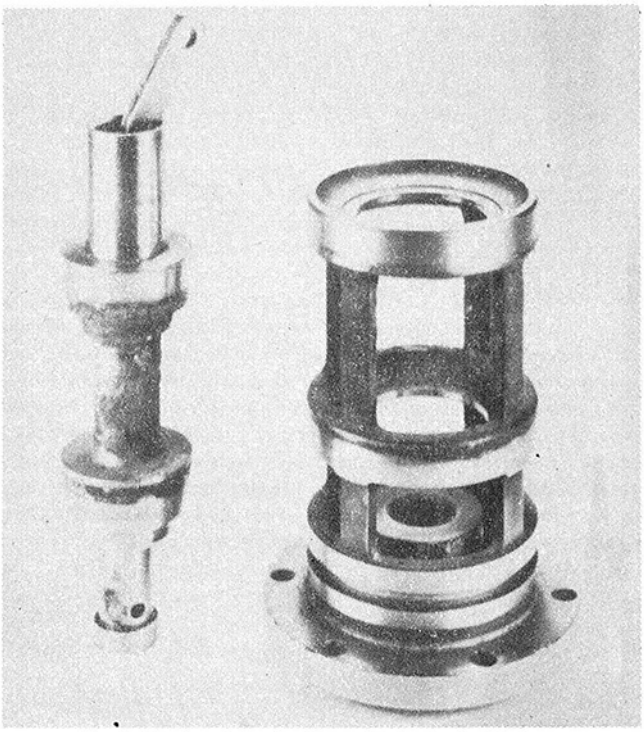


Fig. 1 Fuel control valve demonstrating typical fouling

Direct Acting Throttle. In In order to alleviate the problem and enhance reliability generally, an actuator/throttle valve assembly has been developed which will tolerate considerably higher levels of abuse from the fuel contaminants. In principle, the throttle valve is designed in a manner that limits the exposure of the moving parts to the gas stream, the mechanism being inherently self-cleaning by virtue of the seals and scraper shoes provides. A radical increase in operating torque is necessary to overcome the additional friction created by the sealing arrangement and provide sufficient force to remove any contaminant deposits. With a view to obtaining a further improvement in reliability, acceleration and deceleration fuel scheduling is accomplished within the governor, using electronic techniques to provide the required characteristics.

Simplified system diagrams for a typical gas fuelled machine for both CDP limiter and DAT (Direct Acting Throttle) systems are shown in Fig. 2. Inspection of the diagram shows the basic fuel valve arrangement and the governor systems to be virtually identical, the variation between the two schemes is centered on the replacement of the CDP limiter, including its internal acceleration and deceleration fuel scheduling devices, with an air/fuel controller providing the same features. Thus the throttle now becomes purely a fast acting hydraulically operated valve using a high pressure hydraulic oil system. This arrangement provides a much easier interface for initially setting up the machinery during the commissioning phase, since all controls are located in a non-hazardous area, and subsequently permits any necessary corrections to be made with the machine on line.

Air/Fuel Controller. The Air/Fuel Controller contains all the devices necessary to provide the fuel control and protection limits and reference should be made to Fig. 3 for details of the operational requirements. The shaper modifies the compressor discharge pressure signal to produce a replica of the gas turbine fuel flow/compressor delivery pressure characteristics and by simply exchanging components in the shaper circuitry, the characteristics of any gas turbine can be produced. The acceleration control unit monitors the shaped compressor delivery pressure signal at any operating point on the compressor characteristic against a pre-set limit. In the event of the

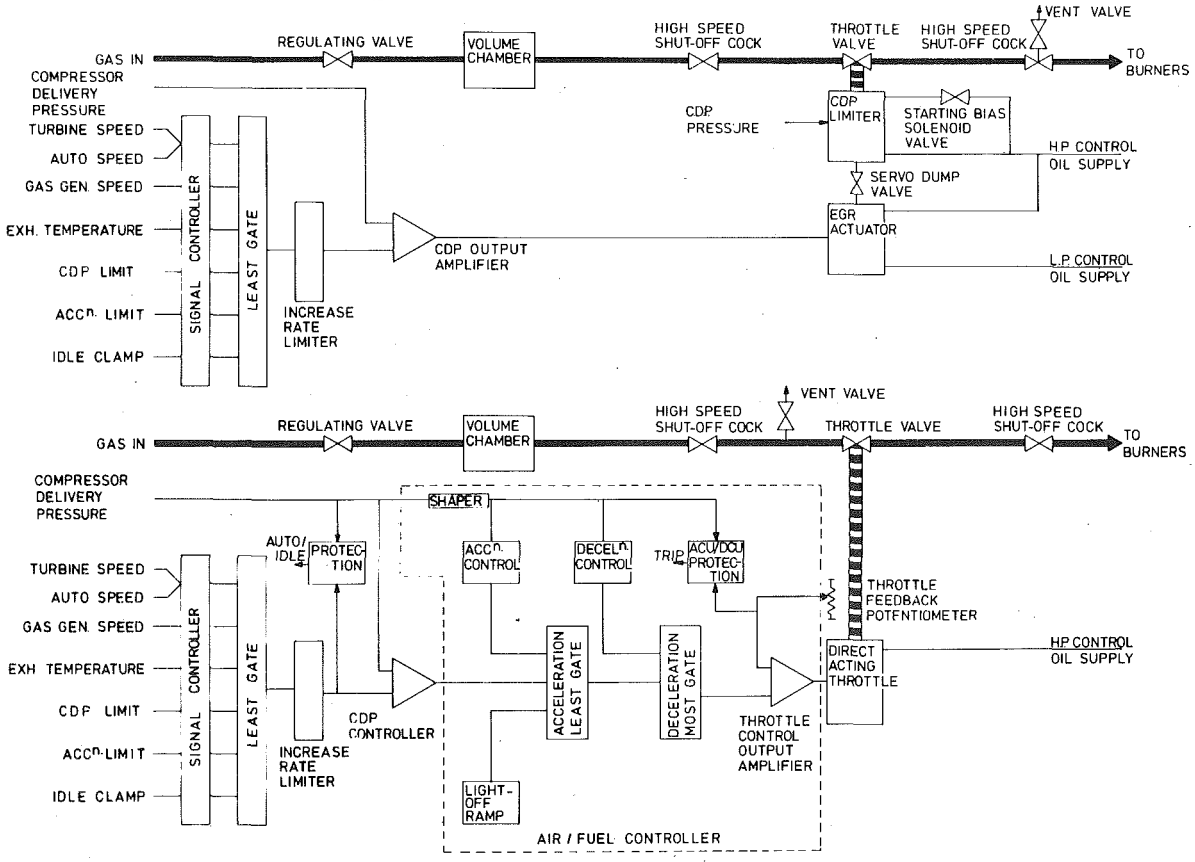


Fig. 2 Comparison of direct acting throttle and CDP limiter fuel control systems

Downloaded 01 Jun 2010 to 171.66.16.58. Redistribution subject to ASME license or copyright; see http://www.asme.org/terms/Terms_Use.cfm

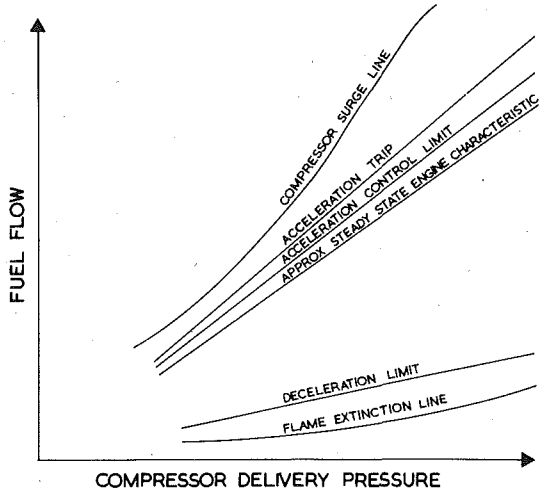


Fig. 3 Typical fuel scheduling characteristic

governor demand signal exceeding the acceleration margin the acceleration controller will take control at the least gate and restrain the output signal to the throttle accordingly, thus precluding overfuelling and the possibility of approaching the compressor surge characteristic.

The deceleration control unit operates in a similar manner, however in this case the controller prevents the fuel flow reducing below a predetermined characteristic during load rejections, thus preventing flame extinction. To insure that the system cannot mal-operate, monitoring facilities are provided at the governor output and the throttle control amplifiers.

Figs. 4, 5, and 6 illustrate the equipment provided to fulfill all necessary governing and fuel scheduling activities.

Light Off Ramp. The direct acting throttle system readily permits the use of "light off to idle ramp" feature whereby, on starting, the throttles are ramped up at a controlled rate to idling speed, which provides a far superior light off and starting characteristic. To achieve this feature an electronic ramp generator is activated at the point in the start sequence when fuel is to be admitted to the machine. During the initial stages of a start the progressively increasing signal from the starting ramp takes precedence, i.e., being lowest at the acceleration least gate since the CDP controller output signal level is set at a value proportional to idling speed, and the acceleration control unit output is high since it is not in control at very low compressor discharge pressures. As the machine achieves idling speed the governor automatically takes control as the ramp passes through the idling datum at which point the ramp is immediately set to a high level so that it cannot subsequently influence the control action of the remaining inputs to the acceleration gate.

Overall System Applications. In order to insure that the overall system is compatible for service with contaminated fuel supplies, improved standards of regulators and fuel shut-off valves have been introduced, with all bearings external to the gas path. The ball type shut-off valves have higher operating forces to combat the effects of scale deposits, which form on the inner surfaces of the valve. The respective devices are considerably more compact, which enables the physical size of the control valve package to be significantly reduced.

While the foregoing discussion has centered on the more exacting requirements associated with gas fuel, the DAT fuel control system is equally applicable to liquid fuel installations, utilizing an identical actuator in conjunction with an appropriate throttle valve. The DAT fuel control system is ideally suited for dual fuel applications, requiring on line change over, in that two completely separate actuator/throttle assemblies are employed, both driven from the common throttle amplifier via a fuel proportioning device. Since the throttles are not fitted with hydraulic fuel scheduling limiters and both share the same drive signal, appropriately proportioned, the fuel change over can be effected without throttle interaction, thus providing a nominally transient-free fuel transfer.

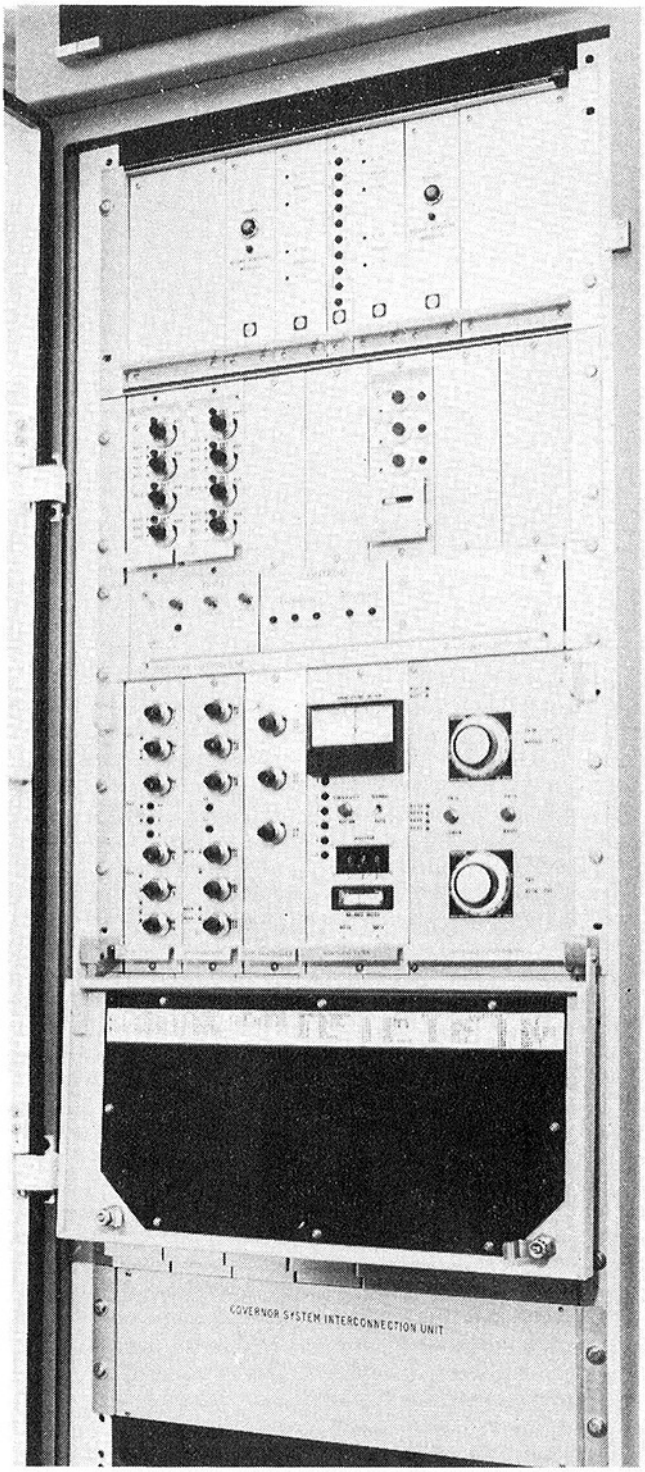


Fig. 4 Governor control cubicle

The superiority of the DAT system may be summarized as follows:

1 high sensitivity, providing superior accuracy of speed control,

2 considerably more tolerant to contaminated fuels,

3 larger number of standard components, hence reduced spares holdings are required,

4 accurate and repeatable electronic fuel scheduling limits,

5 more flexible and permits corrections to be made in the non-hazardous area, with the machine on line,

Downloaded 01 Jun 2010 to 171.66.16.58. Redistribution subject to ASME license or copyright; see http://www.asme.org/terms/Terms_Use.cfm

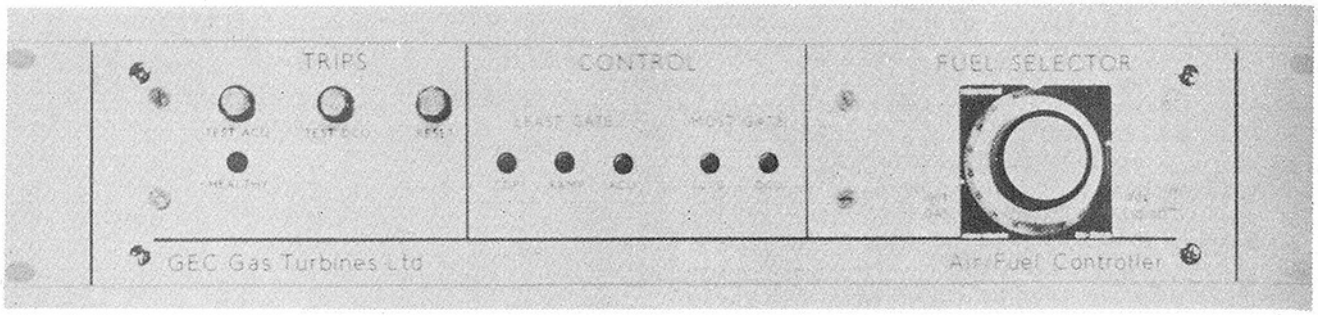


Fig. 5 Air/fuel ratio controller

6 reliable and consistent light offs, with optimum acceleration to idling speed scheduling, thereby reducing thermal stresses,

7 the components mounted adjacent to the engine are robust and few in number,

8 all valves are substantially self-cleaning and selected for their corrosion resistance capability,

9 ideally suited for service on high compression ratio engines,

10 fuel scheduling fully accommodated by electronic means, enabling the system to be used in standard form on engines having widely differing characteristics,

11 does not employ supplementary start bias valves,

12 the separately-driven servo oil pumps to provide throttle actuation during the light off sequence can be duplicated to enhance reliability,

13 the system may be comprehensively commissioned without the necessity of running the engine, which is particularly advantageous when setting up dual fuel systems.

Computer Control Systems

Background. A development program was initiated in 1973 to evaluate the use of digital techniques for turbine control and supervisory functions which consequently resulted in two separate prototype systems being installed on an existing gas turbo compressor set and a generating machine. Each system basically consisted of a programable controller for the logic control functions, operating in conjunction with a mini-computer for analogue control and data logging. The experimental installations entered service in 1974 and performed satisfactorily, although initial problems were encountered in obtaining reliable operation of proprietary input and output interfaces. The installations proved that digital techniques were viable for turbine control and provided the background experience necessary to embark on the development of an integrated digital control system.

As a direct result of the work undertaken on the trial installations, two further programable controller systems were installed and commissioned on a permanent basis, each controlling a group of four turbo-compressors. New input and output interfaces were designed to overcome the problems experienced on the earlier systems and following some three years of testing and operational service, the failure rate has proved to be very small.

It was therefore decided to develop a fully computer controlled system using the same type of mini-computer.

Operating Philosophy. At the design concept stage it was appreciated that some plant operators might have misgivings when operating computer controlled machinery. With a view to alleviating fears of this nature, it was decided to construct the overall system so that all readouts, indications and controls would be presented to the operator in an identical manner to that found on control panels equipped with more conventional control systems.

System Features. The system configuration is shown in Fig. 7 and control of the gas turbine is basically effected by sequentially scanning all status and analogue signals obtained from the various sensors associated with the machine and entering their respective values via an interface into the computer memory. The input interface isolates, filters and converts the signal voltages used externally to a voltage level acceptable to the computer. The analogues are scanned and the output of each channel is further processed by an analogue

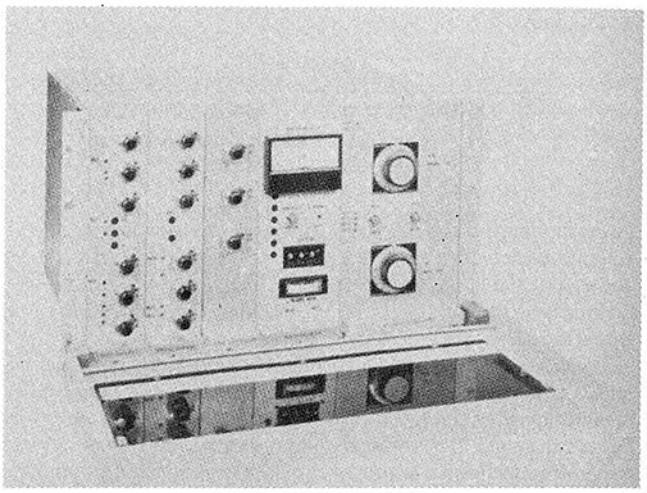


Fig. 6 Unified governor

to digital converter which produces a coded output capable of being understood by the computer. The status inputs are handled in a similar manner, however since the signals are already in digital form no further conversion is necessary and the inputs are multiplexed for economic and space considerations. The stored information is processed by the computer in accordance with the pre-established control program also contained in the memory which basically provides the solution of logical functions and the comparison of analogue points with pre-set values. As each function is solved, the computer establishes from the program whether an action is required and if affirmative, the appropriate output signal is issued and the condition memorized by the computer. The output signal is subsequently isolated and converted, by an output interface, to provide a voltage level suitable for controlling the gas turbine ancillaries or switching the alarm and status indicator lamps. The complete process is accomplished in less than 0.1 s and the input information is then updated and the controlled outputs are revised accordingly during the subsequent operation of the processor.

The remaining interfaces are bi-directional conversion modules which enable the computer to obtain instructions from the teletype keyboard and the tape reader. It also provides information to the tape punch, visual display unit, or the teletype printer, the latter predominantly for data logging.

The machine is initially programed by feeding a works-produced tape through the tape reader, which automatically transfers the information from the tape into the computer memory. Thereafter the memory is accessed via the keyboards provided and simply "typing in" the reference number of the required logic function results in the information being displayed on the visual display unit or a print out obtained on the teletype. The logic functions and pre-set values may be examined and if necessary amended by keying in the required logic or settings and the revised data entered into the memory. The complete memory contents may be transferred onto paper tape by means of the tape punch, which enables a multiple set installation to be readily reprogramed following any program developments that may prove to be necessary.

Downloaded 01 Jun 2010 to 171.66.16.58. Redistribution subject to ASME license or copyright; see http://www.asme.org/terms/Terms_Use.cfm

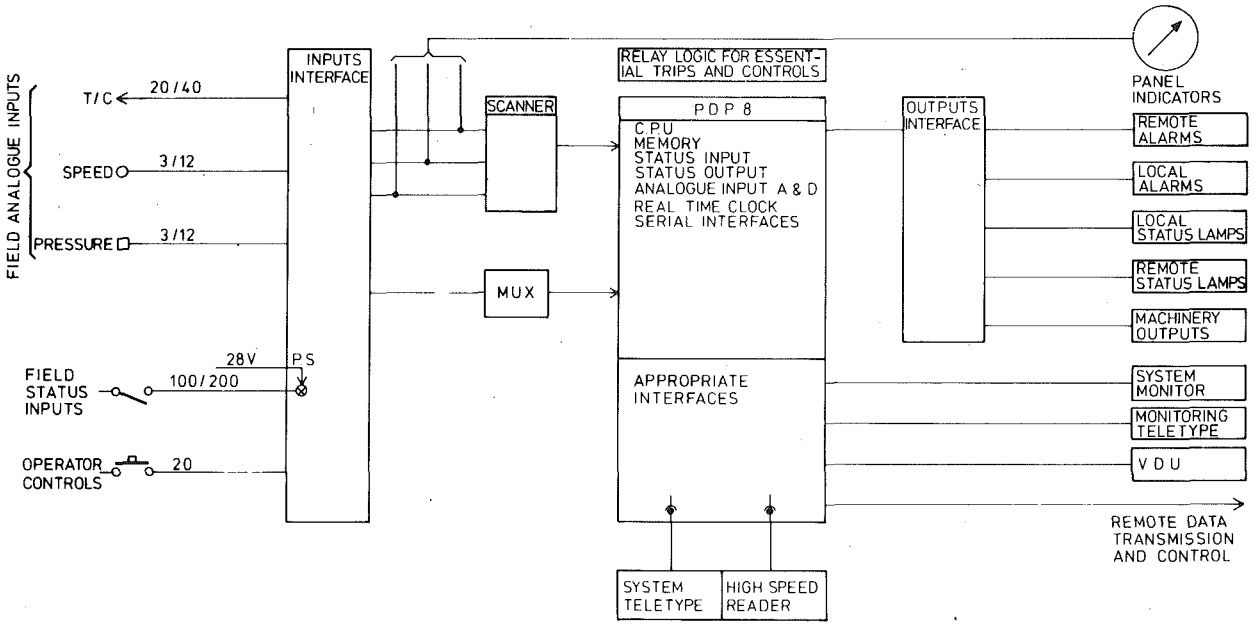


Fig. 7 Basic schematic for mini-computer based unit control system

A system monitor is also included, which provides a method of detecting that the computer is correctly reading the input/output data from the status interface and the analogue to digital convertors. The complete system may also interface with other digital systems to permit overall control of several machines to be performed from one central computer.

By means of the software techniques employed, the computer is arranged to perform logical control functions in a similar manner to a programable controller. Many of the programable controller concepts have been retained and the logical functions are programed by boolean equations, which may be displayed in relay ladder diagram format on a VDU or printed by the computer on listing paper. Complete equations may be deleted or re-written from the VDU or the teletype keyboards. In a similar manner the input and output points may have their states changed, which facilitates maintenance in enabling the logic functions to be completed for sequence checking with the machine shutdown or provides an easy method of switching the controlled devices.

The control system has an addressing capability of 1024 discrete input/output points, which may be either true inputs or outputs, dummy outputs (for storage and reference), timer, analogue, sequence monitor or alarm points. A set of conditional assembly parameters in the executive control program determine the function of each I/O point.

Time delay functions are provided, which may be pre-set within the range of 1–4000 time increments, the increment being programed to equal 0.1, 1.0 or 10 s.

Any analogue channel can have a virtually unlimited number of set points applied to it without incurring a cost penalty. Each set point has a resolution of 0.1 percent full scale, and can clearly be used for pre-set high and low limits as well as providing for example intermediate alarm settings.

Any input/output point may be designated a sequence monitor point, which produces a timed message printed on the system teletype when the selected input/output point changes state. The sequence monitoring points are typically used to provide a log of the attainment of significant events in turbine start and stop sequences.

Alarm points have the same characteristics as a conventional solid state or relay alarm system. The alarm logic is effected in executive software, so that the alarm facia is simply a lamp box assembly. Software routines log each alarm occurrence and provide a timed message on the system teletype.

Programing. The overall transfer function of the system is defined by an English language source program file, "The User Program," from which the binary file may be produced using a compiler. The compiler essentially converts the information contained in the source program file into a binary file, which is meaningful to the computer.

Punched paper tape is used for both the source and object binary files, in order that modifications can be made in the field with simple peripheral equipment. A symbol table is first produced, relating symbolic names to physical input/output point numbers, e.g.:

```
/Start of Symbol Table
1QLX    =  1002     /Lub Oil Control Relay
1QLT    =  1601     /Lub Oil System Timer
STOPPB  =   257     /Stop Push Button
                (remaining definitions)
/End of Symbol Table
```

Boolean equations may then be written linking input and output points in a logical manner, e.g.:

```
/Start of Boolean Equations
STOP = STOPPB * (STOP + /RESET)
                (remaining definitions)
/End of Boolean Equations
```

The VDU is not essential to the operation of the computer control system and is strictly only required for commissioning and diagnostic purposes. The facilities provided by the VDU enable boolean equations, referenced by their respective output numbers, to be displayed in ladder diagram form, inclusive of the status of all contacts associated with the selected output. Alternatively some or all equations in the core may be scanned in either numeric order, core order, or reverse core order. Pre-set values of timers and analogue points may be displayed, together with the real time value of the measured variable.

Trend Analysis. Development work on trend analysis is in progress with the initial effort being concentrated on parameters not directly associated with turbine performance. The system being developed is basically independent of the computer controlling the gas turbine, the only interconnection being the data link which provides the trend analyzer with all the existing status and analogue parameters in digital form, thus minimising further cost and complexity. The operator interfaces with the equipment via a teletype, which enables the operator to request information and receive data from the processor.

The primary objective of the trend analyzer is to monitor data obtained from the gas turbine and inform the operator when any significant deterioration in machinery health, or an impending shutdown condition occurs.

The system under consideration is being developed to:

Downloaded 01 Jun 2010 to 171.66.16.58. Redistribution subject to ASME license or copyright; see http://www.asme.org/terms/Terms_Use.cfm

1 automatically advise which parameter is registering an abnormal condition and, where appropriate, predict the time when a machine shutdown will occur,

2 advise and predict an impending failure when two associated parameters indicate that an abnormal condition prevails. The method of operation is similar to that described in item 1 except that the respective set points are lower,

3 report any abnormal changes in the start sequence times and identify the specific area which has caused the change by comparing the current times against the ideal starting times,

4 provide data logging facilities, which enable the operator to monitor long term deterioration of the gas turbines and assist in scheduling planned maintenance.

The installation of the trend analysis equipment in its unsophisticated form should significantly reduce the machine operating costs by limiting the revenue lost through machine failure, manning levels, and maintenance expenditure.

Solid State Control Systems

Background. It should be appreciated that many countries in the Middle East regularly experience shade temperatures exceeding 50°C and in some locations occasional temperature excursions of 59°C have been recorded. Conversely in extremely cold climates the equipment may be transported to site in the winter months, which necessitates the use of components that will accommodate storage temperatures of typically −50°C.

A study was conducted to investigate what equipment could be obtained which would meet the temperature range and allow sufficient margin to cater for failures of building services.

Design Features. The equipment ultimately chosen exclusively uses semi-conductor devices for all logic, alarm and control functions, including the power outputs to drive field devices. The logic components are mounted on withdrawable printed circuit cards, which are housed in a multiple rack assembly with the power output devices located separately to reduce the possibility of any field generated noise entering the logic section. As the connections to all individual gates are made available at their respective edge connectors, the complete system can be programed on the backplate by simply inter-connecting the appropriate terminal posts. At the manufacturing stage, wiring is accomplished by automatic wire trap techniques which ensures that all units are connected in an identical manner and consistently reliable terminations are obtained. The backplate is subsequently assembled on the racks and requires only the logic cards and field input connectors to be inserted in order to complete the system. From the outset it was recognized that industrial grade semi-conductors would not meet the imposed temperature specification and in consequence Military Standard components were selected on the basis that the ability to manufacture one standard system justified the marginal increase in component cost. The logic components are conventionally mounted on glass fibre boards fitted with proprietary connectors and metal front plates to produce a robust module that can be easily handled. Protection against fungus growth and atmospheric pollution is afforded by gold plating all exposed electrical connections and treating the circuit boards with a lacquer, originally developed for the aero-space industry.

A system can be built to suit any application by selecting an appropriate number of the five standard modules, which provide the following functions: Input, Logic, Timer, Alarm, and Output. The facilities provided on the respective modules are summarized as follows:

1 the input module, shown in Fig. 8, accepts nine separate signals from field contacts and displays their status by means of light emitting diodes. Each channel is optically isolated, incorporating a short time delay and a Schmitt trigger output (which may be inverted if desired) for noise suppression purposes,

2 the logic module, shown in Fig. 9, incorporates the necessary chips to provide 28 individual gates. For ease of application, positive logic is used throughout, hence the components are basically restricted to combinations of AND and OR gates. Module indicators are not provided in this instance, because most of the logic states will automatically be displayed on the output modules. For the more complex logic, where the status of an intermediate point is required, such as unit valve interlocking for permissive starting checks on a gas compressor station, indication is obtained by inserting a standard output module into the logic section of the system and interconnecting the logic points accordingly.

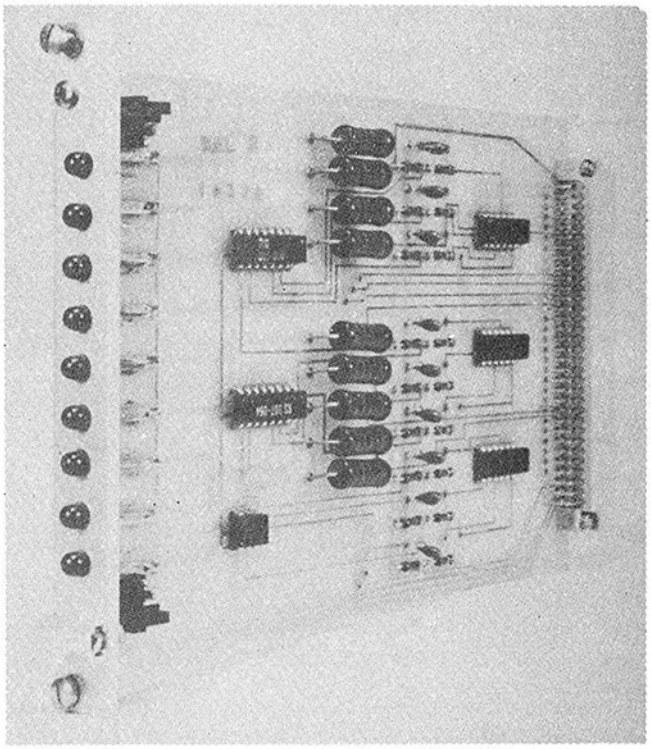


Fig. 8 Input module

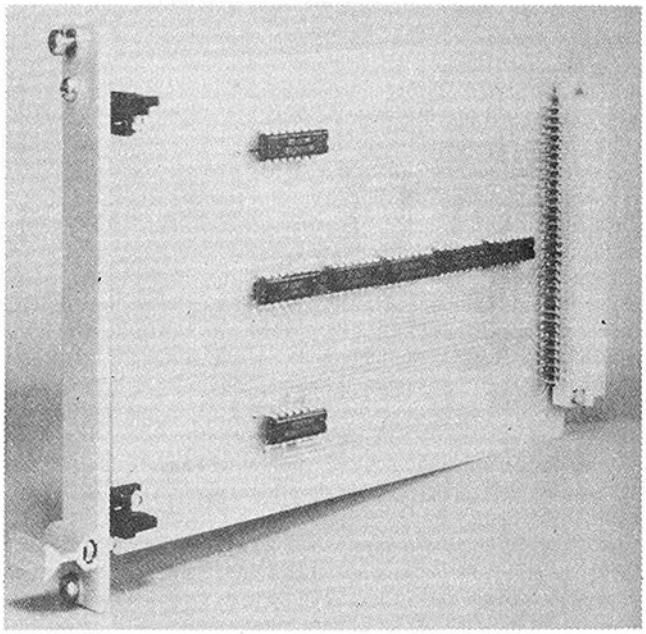


Fig. 9 Logic module

3 the timer module, shown in Fig. 10, provides three independent digital timers, capable of providing on-delay or interval functions. Each timer can be programed to operate over the range of either 0–9.9 alternatively 0–99 s, minutes or hours by interconnecting the appropriate wire wrap spills on the rear of the rack. The set time within the selected range is pre-set by means of the thumbwheel switches and the elapsed time is indicated by the seven-segment LED display.

4 The alarm module, shown in Fig. 11, contains six independent

Downloaded 01 Jun 2010 to 171.66.16.58. Redistribution subject to ASME license or copyright; see http://www.asme.org/terms/Terms_Use.cfm

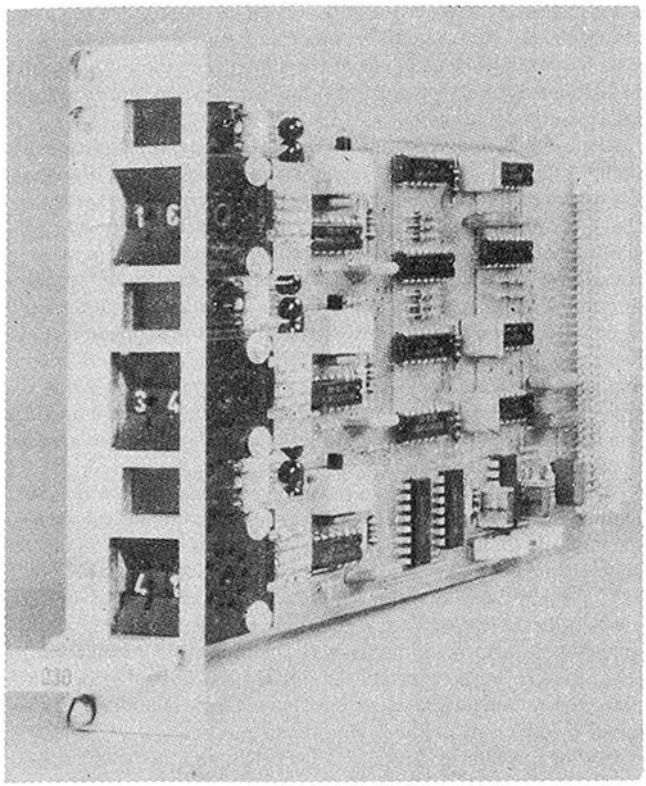


Fig. 10 Timer module

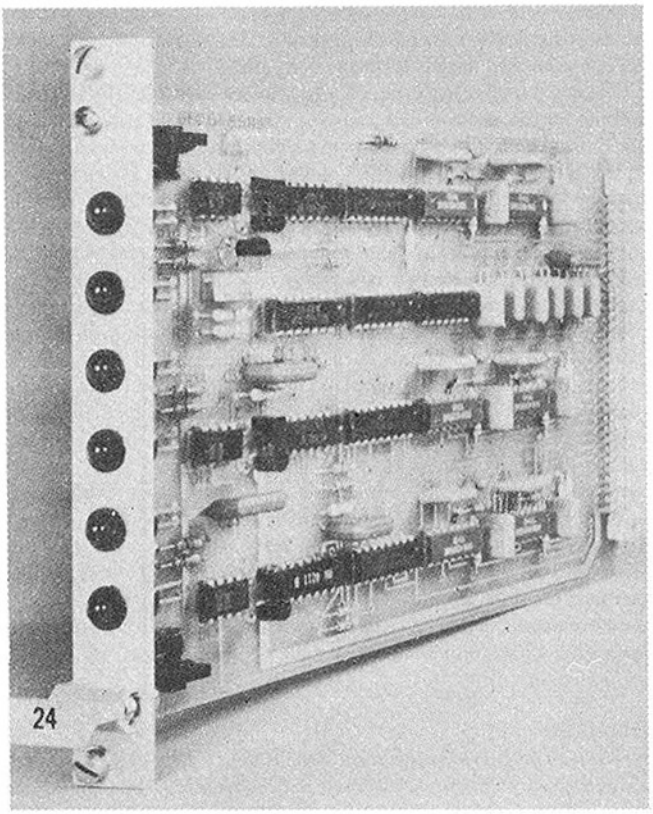


Fig. 11 Alarm module

alarm ways, each channel being provided with input isolation and status indication. The alarm cards interface with a conventional front of panel indicator array and in all other aspects provide the same facilities provided on proprietary equipment.

5 the output module, shown in Fig. 12, contains 21 buffer amplifiers complete with LED input status monitoring. The buffers have sufficient capability to operate indicators but must be used in conjunction with a separately-mounted power amplifier when controlling other equipment.

The overall system is designed to operate from a 24 volt station battery and full account has been taken of the wide voltage ranges normally experienced on such systems. Particular attention has been paid to the power supply unit and a twin channel d-c to d-c converter is incorporated to provide a secure 12 volt isolated output for the CMOS logic modules. Both outputs are provided with short-circuit proof current limiters and two independent regulators complete with over voltage protection, ensuring that the logic system will not be affected by input voltage transients. The respective channels are monitored and an alarm is initiated if a malfunction develops on any section of the power supplies.

A typical gas turbine control system, in which all machine protection, sequencing, alarms and plant control functions are included, would require a five rack arrangement. The individual racks are assigned to provide a specific duty and accommodate modules of the same type.

Reliability

When the designs were finalised and all components selected, theoretical reliability studies were conducted on the respective systems. The studies were based on an application, which included all necessary machine shutdowns, alarms, sequencing and control functions, inclusive of the main process valves, for an unattended gas compressor installation. The assessment utilized a total component count method, which tends to produce a pessimistic result. However, based on actual results obtained on other equipment, the predicted values using this technique provide a more realistic indication of the failure trends.

In an attempt to obtain some practical measure of the calculated

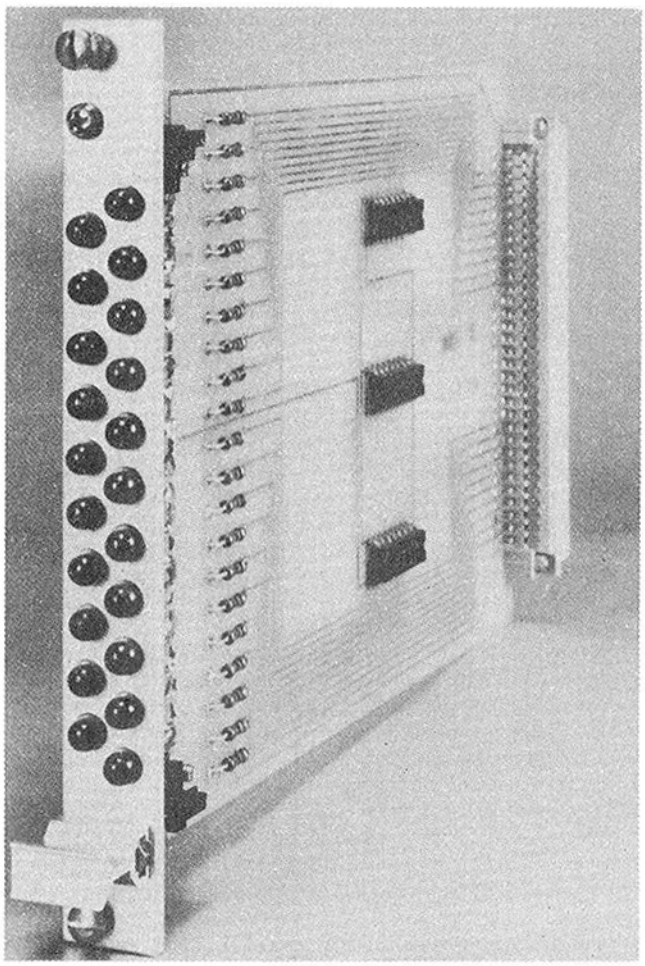


Fig. 12 Output module

Downloaded 01 Jun 2010 to 171.66.16.58. Redistribution subject to ASME license or copyright; see http://www.asme.org/terms/Terms_Use.cfm

reliability values the results were compared with a theoretical assessment for a relay system, which provides basically the same control functions as used in the electronic system studies.

The comparisons with the relay system revealed that the start reliability for the electronic alternatives increased by 0.5 percent based on a typical operating pattern for gas compressor sets, corresponding to one start followed by 140 hr operation per week. However, the comparison of run reliability (mean time between failures) predicts significant improvements, in that the relative reliability for the solid state and the computer systems is higher by 32 percent and 54 percent respectively as compared with the relay system. While the results show that both electronic systems are generally more reliable, the improvements to start reliability are rather disappointing, since the control equipment accounts for a third of the overall start failure contribution. In a similar manner the predicted improvements for run reliability should be tempered with the knowledge that the control systems only provide some ten percent of the overall running failure contribution.

Since both electronic systems are liberally equipped with status indicators, read outs and in the case of the computer system a visual display unit, it is anticipated that the more recent systems to be introduced will be considerably easier to maintain. The monitoring facilities provided should enable the maintenance engineer to diagnose problems quickly on field equipment, which should in the long term produce an improvement in machine availability.

Summary

While it may be argued that it should not be necessary to design equipment to overcome shortcomings in equipment upstream of the fuel control valves, it should be appreciated that in some locations it is not economically feasible to remove all contaminents. The ability of the fuel control system to contend with such situations, without requiring frequent outages to undertake preventative maintenance, has significantly improved the overall machine reliability and availability figures. The operational experience gained on these difficult sites has established a high level of confidence in the system, which has extended to supplying direct acting throttle fuel control systems on all new installations.

The computer control system is expected to be the forerunner of many systems to be commissioned in the next decade. Throughout the design and development of the system, it was always recognized that gas turbine maintenance engineers have wide-ranging responsibilities, often dealing with both mechanical and control aspects. In consequence, considerable attention has been paid to the operator interface with the intention of making the transition to digital control as painless as possible. It is anticipated that once the operators have had the opportunity of utilizing the additional facilities afforded it will lead to a rapid general acceptance of such systems. While the trend analysis system is not intended to be all-embracing, it provides at a realistic cost level a facility which should have considerable appeal to operators and maintenance engineers.

The solid state control equipment is designed in a manner that permits relatively unskilled personnel to understand the logic control functions, in that having appreciated that inputs, outputs and alarm modules may be considered as purely destinations, effectively only the logic and timer modules require to be interrogated when troubleshooting. In this context, attention has been paid to drawing presentation, which in conjunction with the simple module numbering scheme employed, permits faults at chip levels to be readily identified. Since the system only employs five types of logic modules a maintenance by replacement policy is recommended.

The logic system is currently being tested and the results appear to justify the use of high quality, conservatively-rated components, in that no failures have been recorded. From the test evidence available, it is confidently predicted that the equipment will meet the design specification and perform reliably when installed in hostile environments.

Downloaded 01 Jun 2010 to 171.66.16.58. Redistribution subject to ASME license or copyright; see http://www.asme.org/terms/Terms_Use.cfm

R. A. Graziani
Assistant Project Engineer.
Commercial Products Division
Pratt & Whitney Aircraft Group
United Technologies Corporation
East Hartford, CT 06108

M. F. Blair
Research Engineer.
United Technologies Research Center
Mem. ASME

J. R. Taylor
Analytical Engineer.
CPD, Pratt & Whitney Aircraft
United Technologies Corporation

R. E. Mayle
Associate Professor.
Rensselaer Polytechnic Institute
Consultant, Pratt & Whitney Aircraft
East Hartford, Connecticut
Mem. ASME

An Experimental Study of Endwall and Airfoil Surface Heat Transfer in a Large Scale Turbine Blade Cascade

Local rates of heat transfer on the endwall, suction, and pressure surfaces of a large scale turbine blade cascade were measured for two inlet boundary layer thicknesses and for a Reynolds number typical of gas turbine engine operation. The accuracy and spatial resolution of the measurements were sufficient to reveal local variations of heat transfer associated with distinct flow regimes and with regions of strong three-dimensional flow. Pertinent results of surface flow visualization and pressure measurements are included. The dominant role of the passage vortex, which develops from the singular separation of the inlet boundary layer, in determining heat transfer at the endwall and at certain regions of the airfoil surface is illustrated. Heat transfer on the passage surfaces is discussed and measurements at airfoil midspan are compared with current finite difference prediction methods.

Introduction

The continued demand to improve the efficiency of modern aircraft gas turbines is leading to increased turbine inlet temperatures, and high Mach number, low aspect ratio designs. It is well recognized in the aircraft gas turbine industry that these trends require improvements in predicting heat loads to the turbine passage if design goals are to be realized.

For gas turbine application, accurate calculation of local surface heat loads is extremely difficult, requiring knowledge of the local gas driving temperatures and the associated heat transfer coefficients. The problem is further complicated due to the complexity of the three-dimensional flow field which is known to exist in the modern gas turbine passage. This three-dimensional flow field, which arises from turbine passage secondary flows and is largely dependent on the endwall and airfoil viscid-inviscid flow interaction, can be expected to result in complex convective heat transfer coefficient patterns on both the passage endwalls and airfoils. Detailed local heat transfer distribution data, supported by appropriate aerodynamic measurements, are essential in understanding this endwall—airfoil flow interaction on heat transfer.

Numerous aerodynamic studies of the complicated nature of turbine passage secondary flows are available in the literature. A comprehensive review of known cascade secondary flow behavior and its effect on cascade losses up until 1974 is given by Salvage [1]. Included in that review are the secondary flow loss studies of Dunham [2], as well as the work of Came [3] who obtained inlet and exit plane total pressure surveys of a large scale cascade with varying inlet boundary layer thickness and incidence. More recent aerodynamic investigations are the curved channel results of Kenney [4], and the work of Langston, et al. [5] who performed comprehensive and detailed pressure measurements of the flow field within a large scale turbine blade stationary cascade. Waterman and Tall [6] have since extended the aerodynamic data base to include a comparison of total pressure surveys at three axial locations for three large scale, low aspect ratio turbine nozzle configurations. An outline of recent theoretical and experimental studies of secondary flows in both compressors and turbines is presented by Papailiou [7]. In addition, each of the above works contains numerous references to additional studies.

In contrast to the large amount of aerodynamic information available in the literature, documentation of the effect of turbine passage secondary flow on heat transfer is noticeably scarce. Very little information exists which can contribute to an improvement in the calculation of heat loads in the three-dimensional flow regions of a turbine passage. The available works include turbine blade heat transfer coefficient measurements in the presence of secondary flow by Walker and Markland [8]. Louis, et al. [9, 10] have measured heat transfer rates in turbine cascades using short duration methods in a shock tunnel and blowdown facility. Dunn and Stoddard [11] have recently obtained endwall and airfoil heat transfer rate distributions using a similar method. Whereas the above experiments were carried out on near engine size instrumented hardware, Blair [12] obtained detailed heat transfer coefficient data for the endwall of a large scale channel simulating, as closely as possible with channel flow, the aerodynamic conditions found in a turbine passage.

Contributed by the Gas Turbine Division and presented at the Gas Turbine Conference and Exhibit and Solar Energy Conference, San Diego, California, March 12–15, 1979 of THE AMERICAN SOCIETY OF MECHANICAL ENGINEERS. Manuscript received at ASME Headquarters December 18, 1978. Paper No. 79-GT-99.

Copyright © 1980 by ASME
Downloaded 01 Jun 2010 to 171.66.16.58. Redistribution subject to ASME license or copyright; see http://www.asme.org/terms/Terms_Use.cfm

Analytical efforts to provide a complete model which can accurately describe the aerodynamic behavior and heat transfer processes in a turbine passage have met with little success. The uncertainty in the semi-empirical loss correlations and heat transfer calculation methods used by turbine designers attests to this fact. Integral techniques employing boundary layer crossflow models have been proposed by Dring [13] and Booth [14] as solutions for particular regions of the flow field. The three-dimensional differential methods of Patankar and Spalding [15] and Briley [16] hold great potential but the inherent numerical problems and unwieldy application to turbine geometries have not yet been resolved for these methods. The numerical calculation procedure of Dodge [17] is applicable to both 2D and 3D viscous flows and includes predictions of heat transfer rates. There is, nevertheless, some question as to whether sufficient detail in the aerodynamic and heat transfer data is present in the literature to adequately evaluate the completeness of a calculation procedure.

Good agreement in certain regions of the passage has been reported between Dodge's predictions and the data of Dunn and Stoddard [11]. There does not appear to be enough detail in the published data of Dunn and Stoddard, however, to ascertain whether or not important aspects of the flow field such as the saddle point, horseshoe and passage vortices, etc., and their effect on local heat transfer on all of the passage flow path boundaries would be accurately predicted. The trends noted in Blair's endwall heat transfer data were also in agreement with the predictions of Dodge [17]. However, since Blair's data is for channel flow in which only a limited amount of aerodynamic measurements were obtained, there is doubt as to whether the complex three-dimensional aerodynamic aspects of a turbine cascade were realistically modeled.

A review of the literature has thus shown that there exists a need to provide the detailed aerodynamic and heat transfer data necessary for accurate evaluation of proposed calculation techniques, and for understanding the complex flow field resulting from the endwall—airfoil flow interaction of a modern turbine passage. The present work reveals the complex heat transfer pattern on the airfoil and endwall surfaces of a large scale (approximately ten times aircraft engine size) turbine blade rectilinear cascade. Contours of constant heat transfer coefficient over the entire passage surface, and the supporting aerodynamic data necessary to define the flow field, are presented for two inlet boundary layer thicknesses at a Reynolds number typical of gas turbine operation. The measurements were obtained on the same cascade geometry as used by Langston, et al. [5], and complement the aerodynamic results reported there. The accuracy and spatial resolution of the measurements were sufficient to reveal important details of the flow field and provide a needed data base for use in evaluating calculation techniques.

Description of the Passage Flow Field

The cascade geometry and the inlet flow field determine the passage pressure distribution and the nature of the secondary flow. In particular, the streamline curvature of the mainstream flow establishes a strong pressure gradient, from pressure to suction side, which is impressed on the endwall. A fluid particle of low momentum such as that in the inlet boundary layer or in the boundary layer formed within the passage on the endwall, is deflected from the mainstream flow direction by these pressure forces toward the curvature center of the streamlines. It is this low momentum fluid that comprises the endwall secondary flow. The interaction of this secondary flow and the mainstream fluid results in a new passage pressure distribution and flow field, which can be qualitatively examined by addressing the formation and interaction of its main constituents; namely, the horseshoe vortex, saddle point, passage vortex, and endwall boundary layer crossflows.

The horseshoe vortex is formed by a rollup of the inlet boundary layer in accordance with the requirements of vorticity kinematics as

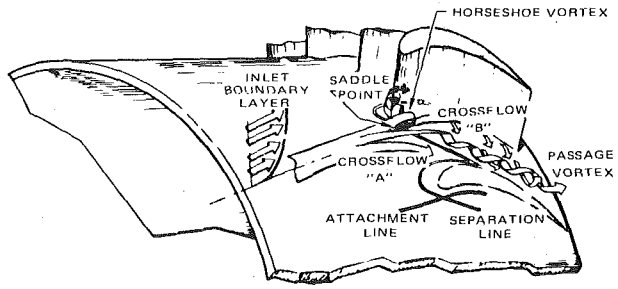


Fig. 1 Endwall secondary flow development

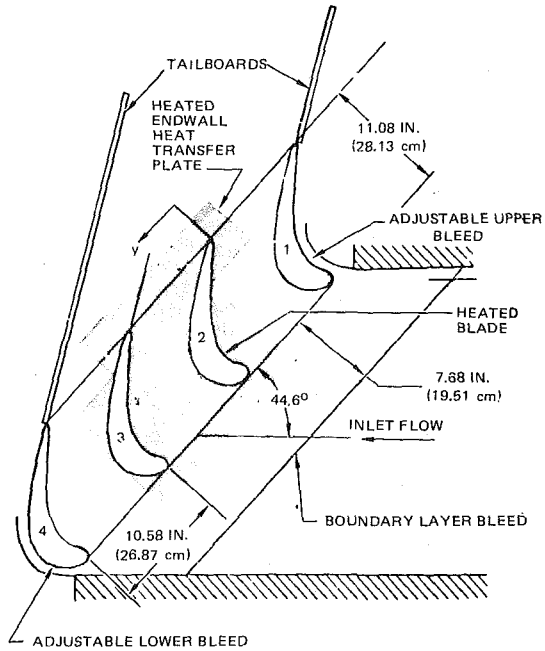


Fig. 2 Schematic of test section

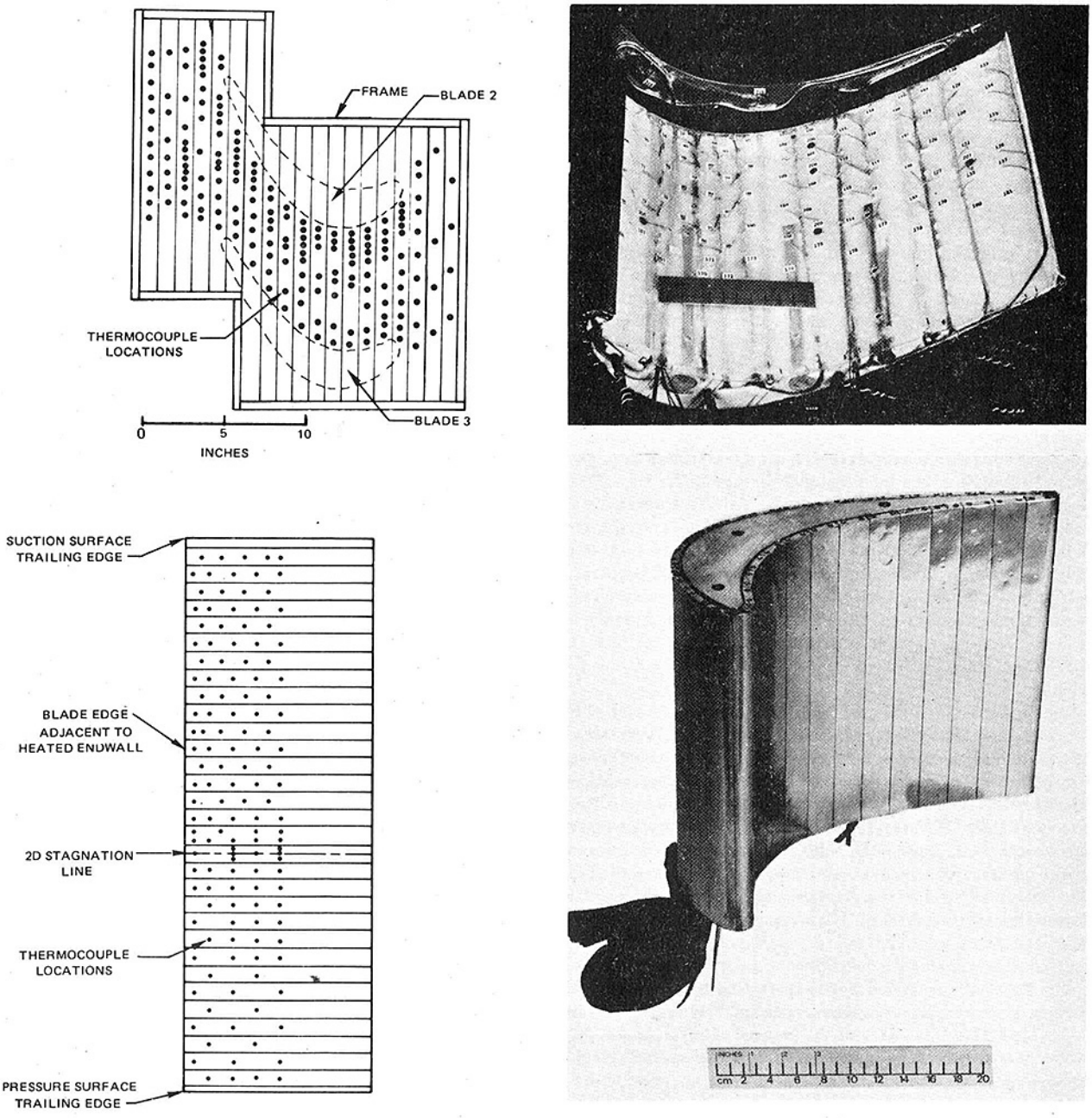
Nomenclature

b = axial chord
c_p = specific heat at constant pressure
C_P = static pressure coefficient = $(P - P_1)/\rho U_0^2/2$
h = heat transfer coefficient = $q_{conv}/(T_W - T_{aw})$
P = local static pressure
P_1 = inlet static pressure
q_{conv} = heat lost by convection per unit surface area exposed to flow
q_{cond} = heat conducted within the instrumented assemblies
q_{gen} = heat generated in the heater strips per unit surface area exposed to flow
q_{rad} = heat lost by radiation per unit surface area
Re = Reynolds number = Ub/ν
Re_θ = momentum thickness Reynolds number = $U\theta/\nu$
S = airfoil surface distance from 2D stagnation line
St = Stanton number = $h/\rho U_0 c_p$
T_{aw} = wall temperature with heating of adjacent passage boundary only
T_w = wall temperature with simultaneous heating of airfoil and endwall
T_∞ = free stream temperature
U = local velocity
U_0 = inlet velocity
U_e = average exit velocity
X = axial distance from blade leading edge
Y = distance perpendicular to the axial chord
Z = airfoil spanwise surface distance
θ = momentum thickness
ν = inlet kinematic viscosity
ρ = inlet air density

Downloaded 01 Jun 2010 to 171.66.16.58. Redistribution subject to ASME license or copyright; see http://www.asme.org/terms/Terms_Use.cfm

it encounters the leading edge of the airfoil. One leg of this vortex is convected around the leading edge to the suction surface and remains close to the suction surface—endwall corner. The other leg proceeds across the passage to the suction side of the opposite airfoil. This split forms a saddle point of separation consisting of the intersection of an attachment line and a separation line, and is identified with a region of high pressure usually located in the vicinity of the leading edge. The separation line, which extends across the passage from the saddle point to the endwall suction surface delineates two distinct regions on the endwall surface as indicated in Fig. 1. The inlet boundary layer below the separation line (Region A), because of the strong lateral pressure gradient, undergoes intense skewing and flows toward the suction surface where it joins the leg of the horseshoe vortex proceeding across the passage and the other leg of the horseshoe vortex which comes around the leading edge of the adjacent passage. Above the separation line (Region B) a new boundary layer forms on the endwall which also undergoes intense skewing and flows toward the suction surface under the influence of the lateral pressure gradient. As this fluid approaches the separation line, however, it gets swept up into the other leg of the vortex that travels across the passage toward the suction side. The combination of this fluid, the boundary layer fluid from Region A, and the mainstream fluid which is entrained by the vortex is known as the passage vortex, and is identified with a growing low pressure region extending across the passage. In the latter part of the passage, the vortex interacts strongly with the airfoil suction surface, lifts off the endwall, and grows rapidly. The exit flow, then, consists of this large vortex over a thin endwall boundary layer, a relatively small counter-rotating vortex which flows along the suction surface corner (this may be rolled up endwall boundary layer fluid or the other leg of the horseshoe vortex), and wake flow from the trailing edge of the airfoils.

It is important to note that the size of the passage vortex, which originates with the rollup of the inlet boundary layer and is dependent on the inlet boundary layer thickness, is instrumental in determining the overall passage flow field pressure distribution. It follows that the passage heat transfer should also be heavily dependent on the inlet



a. DIAGRAM OF ENDWALL AND BLADE INSTRUMENTATION

b. PHOTOGRAPHS OF BLADE HEAT TRANSFER MODEL

Fig. 3 Details of heat transfer model construction

Downloaded 01 Jun 2010 to 171.66.16.58. Redistribution subject to ASME license or copyright; see http://www.asme.org/terms/Terms_Use.cfm

boundary layer thickness and this is, in fact, borne out in the results presented herein.

Experimental Apparatus

The experiment was conducted in the same large scale, low speed, open circuit cascade wind tunnel facility that has been previously described in the aerodynamic investigations [5]. A thick endwall inlet boundary layer (approximately 15 percent airfoil span) was obtained by duplicating the original tunnel configuration of [5]. All heat transfer results presented for the thick boundary layer were acquired with this tunnel configuration. A thin endwall inlet boundary layer (approximately two percent airfoil span) was obtained by shortening the approach duct and installing a boundary layer bleed system upstream and parallel to the cascade inlet plane. Thermal insulation along the sidewall of the inlet duct was added to ensure a flat inlet temperature profile. A diagram of the cascade test section illustrating the important features is presented in Fig. 2.

Surface pressure data in the passage of interest were obtained with rows of static pressure taps located on the airfoil suction and pressure surfaces at 2.3, 12.5, 25, and 50 percent span. Endwall surface pressures were obtained with 220 static pressure taps distributed over the endwall surface. Velocity profile measurements for the thick inlet boundary layer were obtained 26 in. (66 cm) upstream of the leading edge of blade 2 with a pneumatic boundary layer probe. Similar measurements were obtained for the thin inlet boundary layer case at a location 6.8 in. (17.2 cm) upstream of the cascade leading edge plane in the streamwise direction. Flow visualization of the limiting streamlines for both the endwall and blade surfaces was obtained by injecting ink on the surface.

Heat transfer distributions on the endwall and blade surfaces were measured with electrically heated, instrumented, uniform heat flux models. Fig. 3 illustrates the construction details of the heated blade and endwall assemblies. The endwall heat transfer plate consisted of 19 strips of 0.001 in. (.0025 cm) by 1.0 in. (2.54 cm) Chromel-C heater ribbon spaced 0.010 in. (.025 cm) apart and glued with contact cement to a backing of 4.0 in. (10.2 cm) thick rigid urethane foam of low thermal conductivity. A direct current was passed through the constant cross section, constant resistance metal strips wired in series, thus generating a uniform heat flux on the metal surface through resistive heating. Surface temperatures were monitored by 179, 36 gauge, Chromel-Alumel thermocouples welded to the underside and along the centerline of the Chromel-C ribbons. Thermocouple positions were selected to provide high density clusters in areas of expected large surface temperature gradients. The internal temperature distribution through the heat transfer plate was measured with thermocouples cast into the foam at various distances from the test surface. These measurements were used to account for heat flow within the endwall plate in the calculation of the heat transfer coefficient.

The large scale instrumented heat transfer airfoil (Airfoil 2, Fig. 2) was also constructed of the same low thermal conductivity foam with a thin plexiglas .063 in. (.16 cm) sheet molded within the blade along the mean camber line to provide the necessary rigidity and strength. The surface was covered with thirty-one 1.0 in. (2.54 cm) wide by 0.001 in. (.0025 cm) thick stainless steel heater strips spaced approximately 0.017 in. (0.43 cm) apart and attached to the foam with a thin layer of epoxy. Local surface temperatures were measured with 136, 36 gauge Chromel-Alumel thermocouples welded to the underside of the heater strip centerlines. Thermocouple locations on the blade were also selected according to expected regions of large temperature gradients. Blade internal foam temperatures were measured at various locations along the cambered plane between the pressure and suction surfaces. The aerodynamic measurements and blade ink trace results indicated that the symmetry of the passage allowed positioning of most of the blade thermocouples on only one half span of the blade surface. For the same reason, the experiment was conducted with only one heated endwall.

The aerodynamic measurements and flow visualization results also showed that there was no flow interaction between the pressure surface and endwall. Therefore, only one blade (Airfoil 2, Fig. 2) was heated and instrumented, and installed in the cascade with the suction surface adjacent to the heated passage endwall. The measurements obtained with this arrangement of heated blade and endwall were equivalent to measurements taken with an entirely heated cascade passage.

Temperature differences between the surfaces and free stream were obtained at each measurement location using a thermocouple in the free stream as a reference. An ice bath reference was available for measurement of absolute temperatures.

Heat was removed from the heated endwall surface underneath the heated blade by a thin, spring loaded, water cooled copper plate, thus keeping the foam temperature low enough to assure no breakup or distortion of the rigid foam. The maximum surface temperature measured at any point on the heater assemblies was limited to 160°F.

Cascade Geometry and Test Conditions. The cascade geometry and test conditions established for each boundary layer thickness are given in Tables 1(*a*) and 1(*b*), respectively.

The steady state heat transfer boundary condition on the airfoil and endwall heated surfaces was nominally one of constant heat flux. The endwall heat flux commenced 27 percent of axial chord upstream of the leading edge. Slight modification of the constant heat flux boundary condition was caused by surface radiation, heat conduction through the insulating foam, and conduction in the metal strips parallel to the surface. In addition, the thermocouple junction beads

Table 1(*a*)* Cascade Geometry

Axial chord, b	11.08 in. ± 0.01 (28.13 cm)
Chord/axial chord	1.22 ± 0.005
Pitch/axial chord	0.96 ± 0.005
Aspect Ratio (span/axial chord)	0.99 ± 0.005
Airfoil mean camber line angles—measured from y axis	Inlet =44.0 Deg ± 0.2 Exit = 26.0 Deg ± 0.2
Air Inlet Angle	44.6 Deg ± 0.2
Air Exit Angle (Nominal)	26 Deg

* Uncertainty intervals based on 20 to 1 odds

Table 1(*b*)* Test Conditions

Parameter	Thick Boundary Layer [Measured 26 in. (66 cm) Upstream of Cascade]	Thin Boundary Layer [Measured 6.8 in. (17.2 cm) Upstream of Cascade]
Boundary Layer Thickness	1.3 in. ± 0.02 (3.3 cm)	0.16 in. ± 0.003 (0.41 cm)
Displacement Thickness, δ^*	0.148 in. ± 0.002 (0.376 cm)	0.030 in. ± 0.0005 (0.076 cm)
Momentum Thickness, θ	0.110 in. ± 0.002 (0.279 cm)	0.019 in. ± 0.0003 (0.048 cm)
Shape Factor, δ^*/θ	1.35 ± 0.02	1.58 ± 0.02
Momentum Thickness Reynolds No.	5338 ± 100	850 ± 20
Generated Heat Flux, q_{gen} Airfoil	416 Btu/hr-ft^2 ± 5 (0.131 watts/cm^2)	416 Btu/hr-ft^2 ± 5 (0.131 watts/cm^2)
Generated Heat Flux, q_{gen} Endwall	579 Btu/hr-ft^2 ± 7 (0.183 watts/cm^2)	548 Btu/hr-ft^2 ± 7 (0.173 watts/cm^2)
Mainstream Turbulence Intensity	1% ± 0.1	1% ± 0.1
Inlet Velocity	102 ft/s ± 1 (31.1 m/s)	102 ft/s ± 1 (31.1 m/s)
Inlet Reynolds Number = $\frac{U_0 b}{\nu}$	5.5×10^5 ± 0.08×10^5	5.5×10^5 ± 0.08×10^5
Exit Reynolds Number = $\frac{U_e b}{\nu}$	8.8×10^5 ± 0.1×10^5	8.8×10^5 ± 0.1×10^5
Mainstream Gas Temperature	Ambient	Ambient
Tunnel Pressure	Ambient	Ambient

* Uncertainty Intervals Based on 20 to 1 Odds

Downloaded 01 Jun 2010 to 171.66.16.58. Redistribution subject to ASME license or copyright; see http://www.asme.org/terms/Terms_Use.cfm

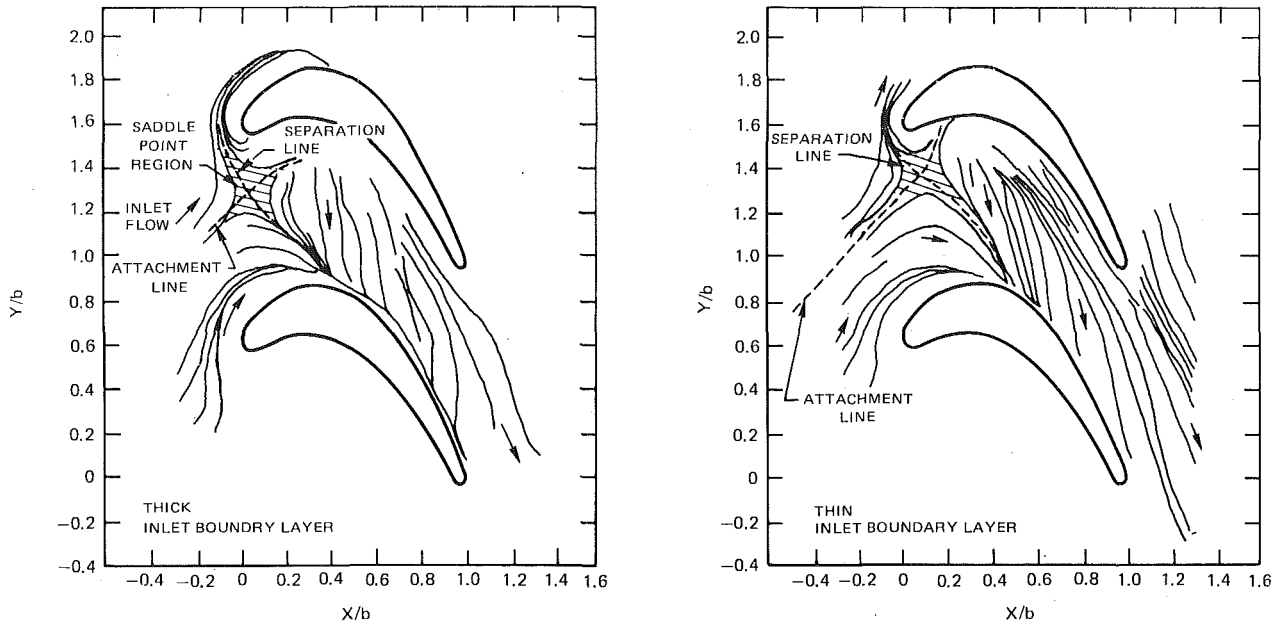


Fig. 4 Endwall limiting streamlines

in thermal contact with the surface acted as a heat sink which resulted in measuring a lower surface temperature than would exist without the bead. These biased effects, along with local variations in strip resistance resulting from local metal temperature differences, were included in the calculation of heat transfer coefficient. The approximate magnitudes of the corrections are as follows: radiation, four percent of q_{gen} on the endwall, two percent on the blade; loss through the insulating foam, 2.5 percent on the endwall, one percent on the blade; heat conduction within the heater strips, less than one percent; thermocouple temperature correction, 1.5 percent of indicated value of $(T_W - T_\infty)$. An error analysis following the procedures of Kline and McClintock [18] was conducted, after accounting for the above biased effects. Uncertainty intervals for each of the factors entering the error analysis were based on 20 to 1 odds that the true value lay within the range defined by the uncertainty interval. This analysis showed the measured heat transfer coefficients to be accurate to within ±3.5 percent based on 20 to 1 odds. In general then:

$$q_{gen} = q_{conv} + q_{rad} + q_{cond}$$

$$\text{where } q_{conv} = h_{conv}\,(T_w - T_{aw})$$

The calculated heat transfer coefficients are for a passage in which the endwall and airfoil are heated simultaneously. The adiabatic wall temperature obtained when only the adjacent surface was heated was the gas temperature used in the heat balance for calculating heat transfer coefficients.

Experimental Results

The following is a presentation and discussion of the flow visualization and pressure field measurements, which were made to define the cascade passage flow field, and of the heat transfer measurements, which are presented as Stanton number contours on the airfoil and endwall surfaces. Although the flow visualization and pressure field measurements for the thick boundary layer case have been previously reported in [5], pertinent results have been included here to facilitate comparison to the thin boundary layer case and to aid in the interpretation of the heat transfer results. The reader is urged to consult that reference for a detailed explanation of the thick inlet boundary layer flow visualization and pressure field measurements, and the inferred flow field characteristics that can be drawn from them.

Flow Visualization. The flow visualization results of the passage surface ink trace limiting streamlines for each inlet boundary layer thickness are shown in Figs. 4 and 5. The intent of these results is to point out the predominant aerodynamic characteristics of the passage

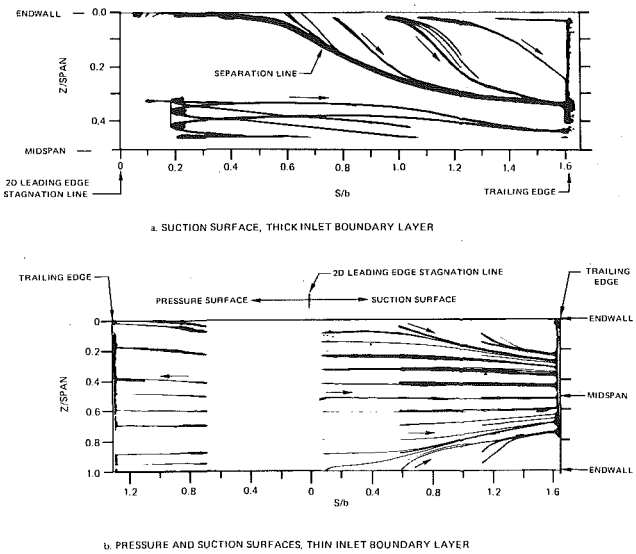


Fig. 5 Limiting streamlines on the airfoil surfaces

flow field that can help to interpret the heat transfer results. Locations of the separation and attachment lines associated with the saddle point and passage vortex have been superimposed to facilitate discussion of the results. Clearly evident in these figures are the saddle point on the endwall, horseshoe vortex, endwall crossflow, and convergence toward midspan of the airfoil suction surface limiting streamlines. Airfoil pressure surface limiting streamlines, although not shown for the thick inlet boundary layer case, exhibit the same apparent two-dimensional pressure surface flow field as indicated by no significant deviation from a straight streamwise surface flow pattern.

Close inspection of the endwall ink traces reveals that the saddle point moves farther back into the passage and closer to the pressure surface for the thin inlet boundary layer. An important observation is the apparent reduction in the severity of the crossflow behind the endwall separation line for the thin inlet boundary layer. There appears to be more of the endwall surface area behind the separation streamline covered with ink traces that exit the passage without crossing over to intersect the airfoil suction surface. Moreover, the ink trace streamline which intersects the trailing edge of the airfoil

Downloaded 01 Jun 2010 to 171.66.16.58. Redistribution subject to ASME license or copyright; see http://www.asme.org/terms/Terms_Use.cfm

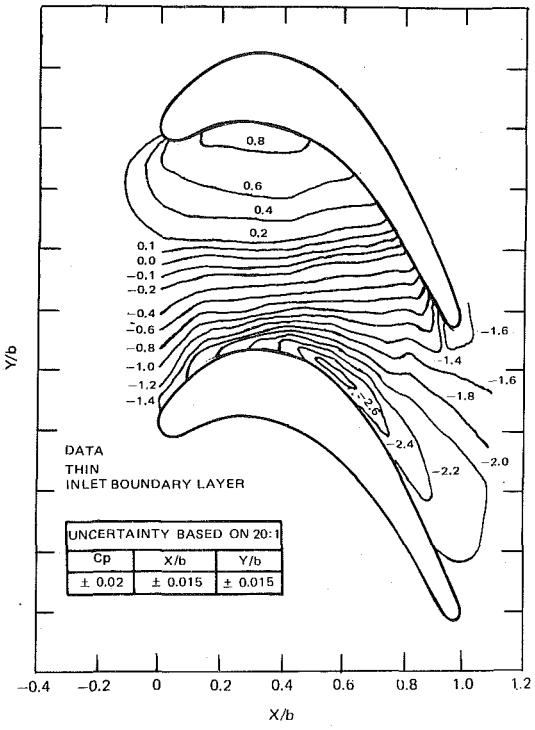
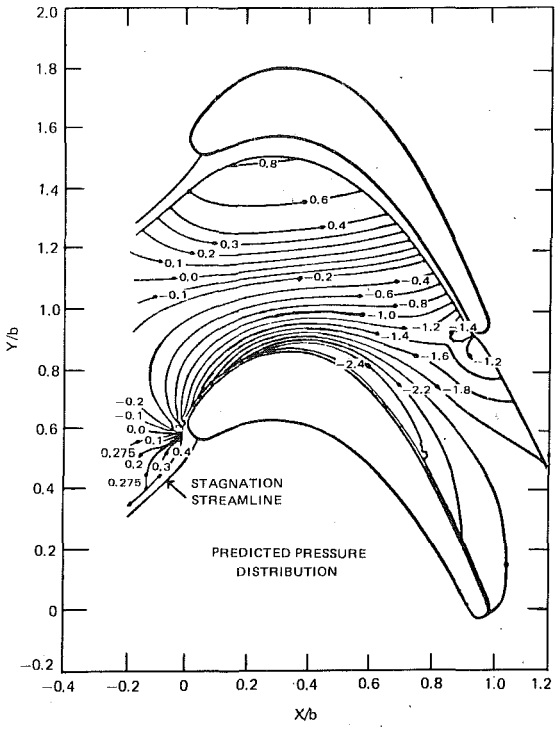


Fig. 6 Endwall static pressure coefficient contours



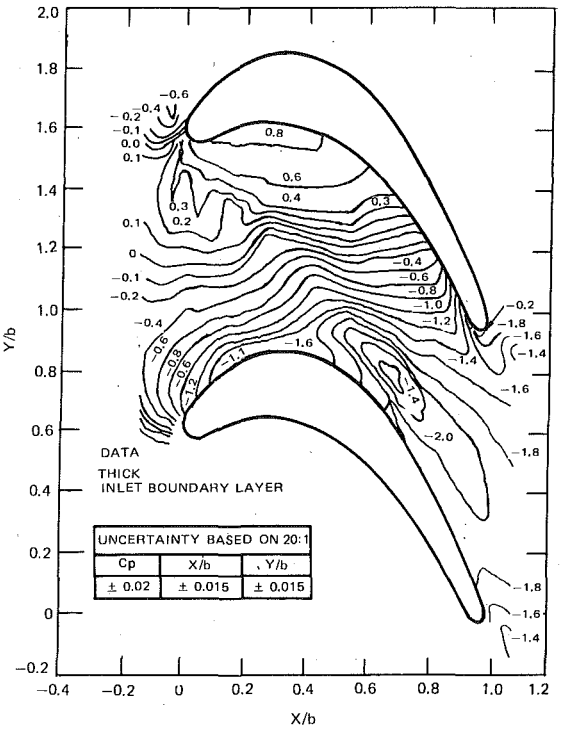


Fig. 6, cont.

suction surface originates much farther up in the passage near the saddle point for the thin inlet boundary layer. It is also noted that for both inlet boundary layers, the separation streamline travels across the endwall and intersects the suction surface near the location of airfoil minimum pressure.

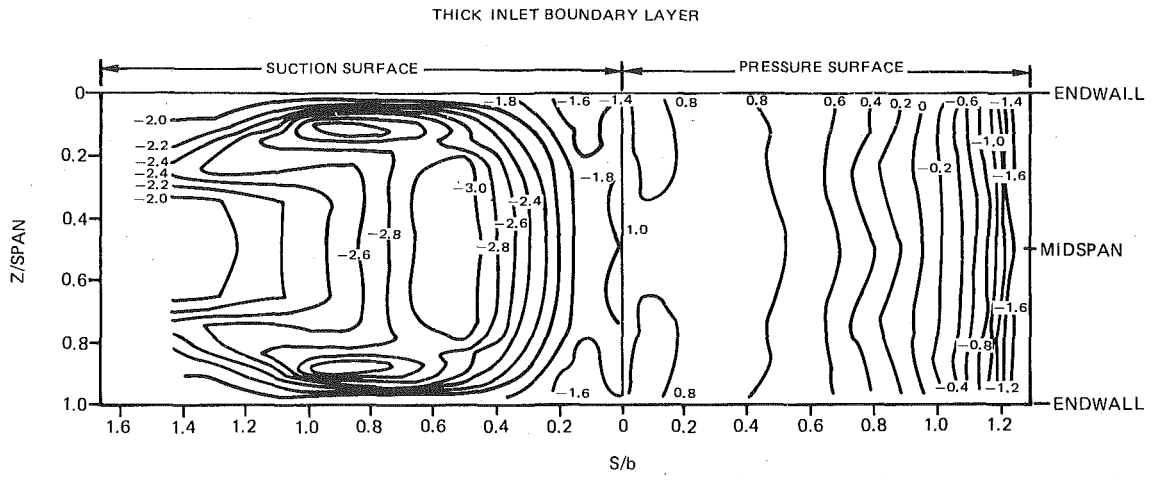
The most notable observation of the ink traces on the airfoil surfaces for both inlet boundary layers is the convergence of the suction surface streamlines toward midspan. Three aspects of this behavior warrant further recognition. The first is that the initiation of the rapid convergence on the suction surface occurs at the same location for both inlet boundary layers and agrees with the location of the intersection of the endwall surface separation line and the suction surface. This agreement, however, should not necessarily be construed to mean that the endwall separation line travels up onto the suction surface. This leads to the second point, namely that there is a separation streamline on the airfoil suction surface across which no surface flow passes. The third important point is the much greater convergence toward midspan of the airfoil separation streamline for the thick inlet boundary layer case. The implication here is that the passage vortex occupies more of the passage in this region, thus subjecting a greater area of the suction surface to secondary flow effects.

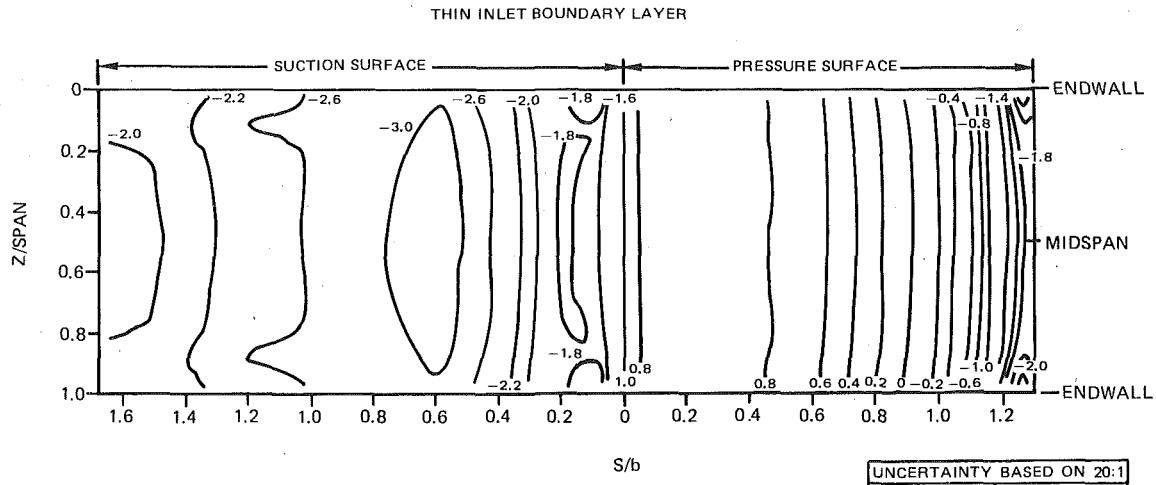
Pressure Measurements. Surface static pressure contours drawn from the measured data for each inlet boundary layer thickness are presented in Figs. 6 and 7. Because the data were obtained on only one half of the span of the airfoil surface, the contours include a reflection of the data to the other half span. Endwall contours and the airfoil surface midspan pressure distribution from a two-dimensional potential flow calculation are also shown for comparison to the data. Comparison of the thick and thin inlet boundary layer endwall contours to the potential flow calculation shows that the pattern for the thin inlet boundary layer case is much closer to the potential flow solution. The only major deviation of the thin inlet boundary layer endwall data from the potential flow pattern is at the low pressure region in the throat near the suction surface. This low pressure region is at the location where rapid growth of the passage vortex occurs as it lifts off the endwall surface when approaching the airfoil suction surface. This region also begins at the point where the endwall separation line intersects the airfoil suction surface, and coincides with the location of the minimum suction surface pressure. Comparison of the thick and thin inlet boundary layer endwall contours to each other shows that the thin inlet boundary layer pattern is much less complex with fewer local distortions.

The saddle point of separation on the endwall, the path of the passage vortex, and the endwall separation line are recognizable only in the thick inlet boundary layer endwall data. Only near the suction surface at the minimum pressure location do the endwall data show evidence of a passage vortex. Another feature common to both endwall contour patterns is the attachment line near the pressure surface. For the thick inlet boundary layer data, however, the ridge pattern formed by the distorted pressure contours around this attachment line is much more pronounced.

Examination of the airfoil surface pressure contours for each inlet

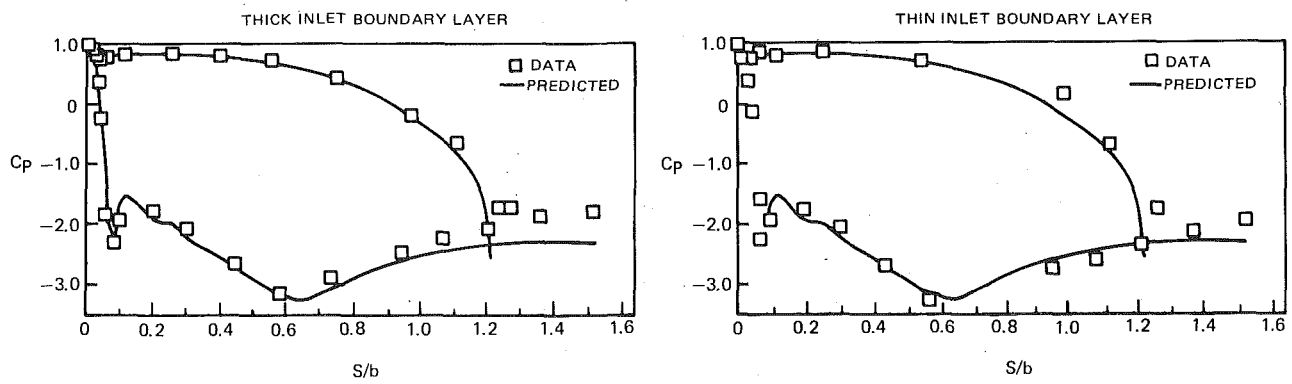
Downloaded 01 Jun 2010 to 171.66.16.58. Redistribution subject to ASME license or copyright; see http://www.asme.org/terms/Terms_Use.cfm





UNCERTAINTY BASED ON 20:1	
C_p	S/b, Z/SPAN
± 0.02	± 0.015

a. BLADE SURFACE PRESSURE COEFFICIENT CONTOURS



UNCERTAINTY BASED ON 20:1	
C_p	S/b
± 0.02	± 0.005

b. BLADE SURFACE MIDSPAN PRESSURE DISTRIBUTION

Fig. 7 Blade surface pressure distribution

boundary layer thickness reveals a highly three-dimensional flow field on the suction surface and an apparent two-dimensional flow field over most of the pressure surface. The apparent two-dimensional flow field on the pressure surface can be inferred from the relatively constant pressure coefficient values in the spanwise direction. The pressure coefficient contours on much of the suction surface, however, show evidence of being greatly affected by the passage secondary flows. The suction surface contours for each inlet boundary layer thickness contain marked deviations from the midspan values in regions near the endwall-airfoil interface, starting at approximately the minimum pressure location and expanding towards midspan as the streamwise distance from the trailing edge is decreased. The extent of these deviations, which are associated with the passage vortex sweeping up onto the suction surface, are in excellent agreement with the flow visualization results in the area below the suction surface separation streamline near the endwall where rapid convergence of the ink traces toward midspan was observed. Furthermore, as in the flow visualization results, this area covers much more of the suction surface for

Downloaded 01 Jun 2010 to 171.66.16.58. Redistribution subject to ASME license or copyright; see http://www.asme.org/terms/Terms_Use.cfm

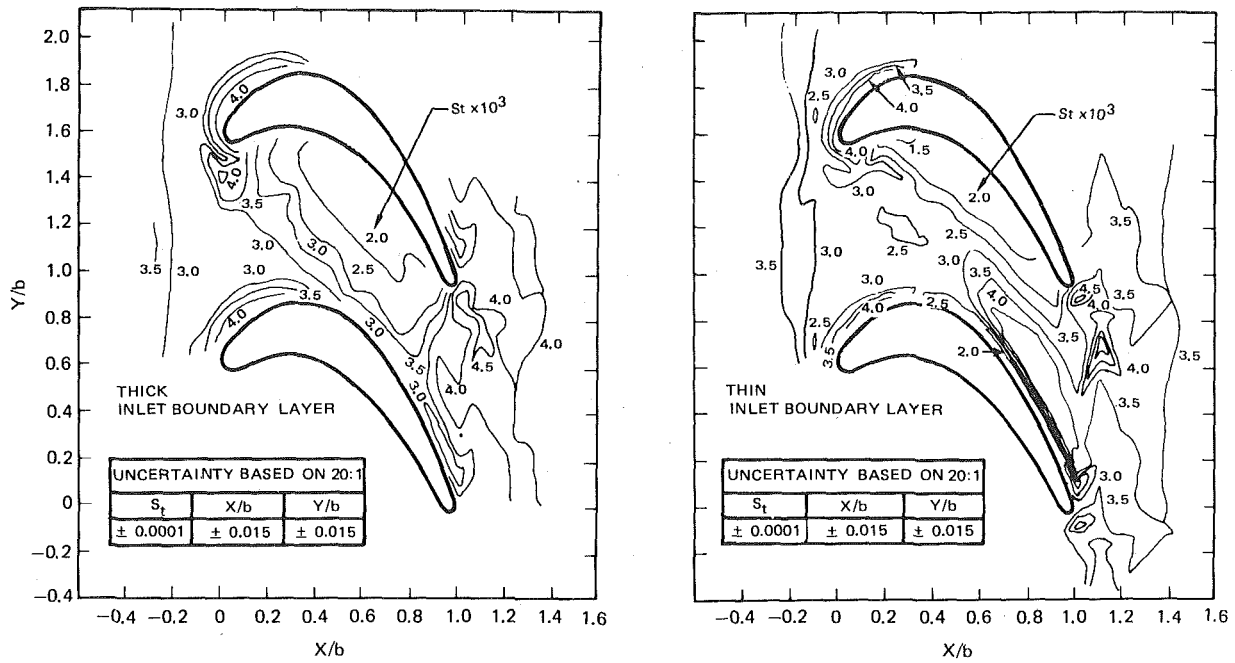


Fig. 8 Endwall Stanton number contours

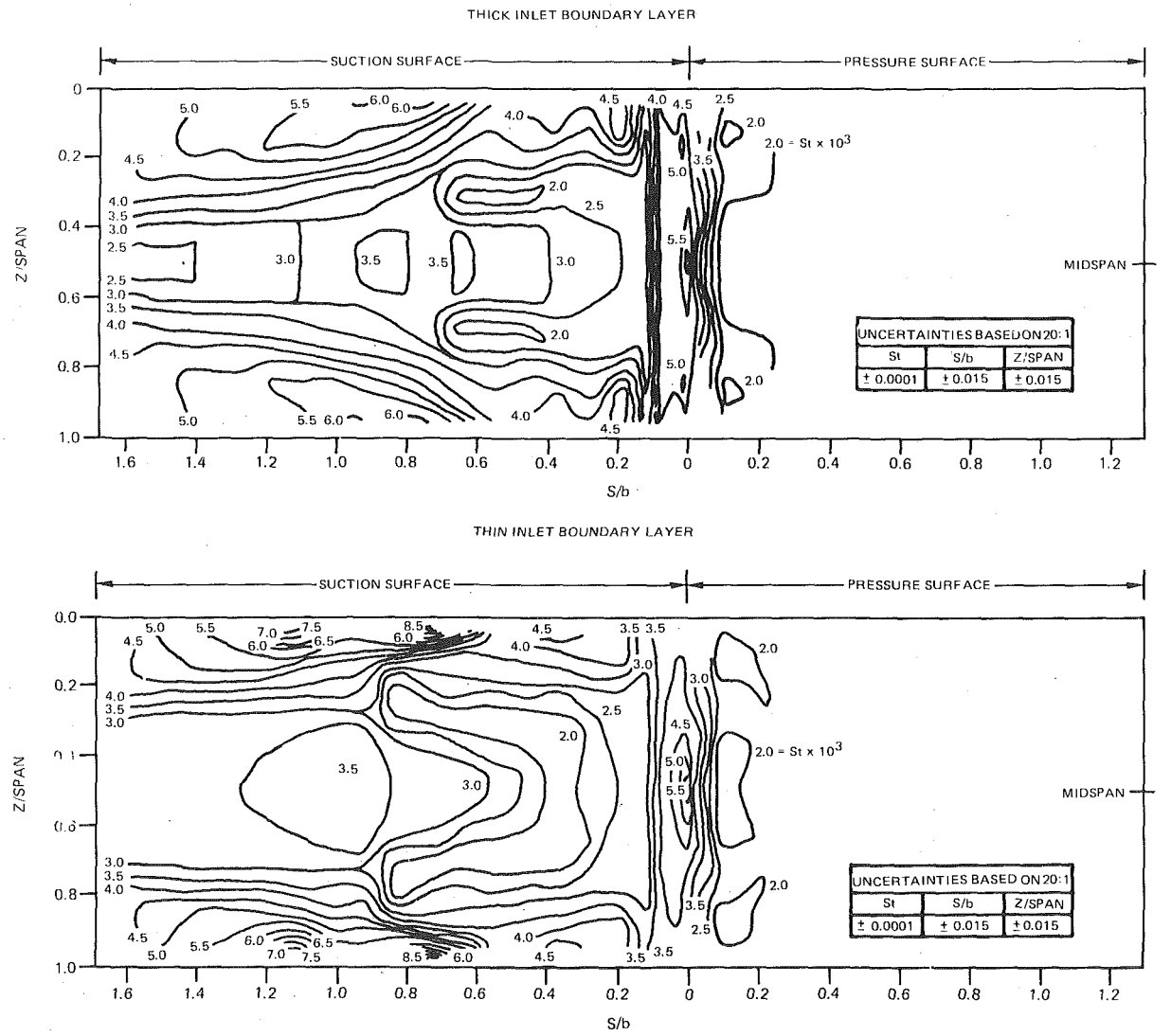


Fig. 9 Blade surface Stanton number contours

Downloaded 01 Jun 2010 to 171.66.16.58. Redistribution subject to ASME license or copyright; see http://www.asme.org/terms/Terms_Use.cfm

the thick inlet boundary layer case. Thus, these pressure coefficient contours indicate that the size of the passage vortex is largely dependent on the size of the inlet boundary layer, and is a significant factor in determining the surface pressure distribution, not only on the endwall surface, but also on a considerable portion of the suction surface. In the leading edge region near the endwall surface, due to the larger horseshoe vortex associated with the thicker inlet boundary layer, the deviation from the midspan values is larger for the thick inlet boundary layer case.

Heat Transfer Results. Contour plots of Stanton number on the endwall and blade surfaces for each inlet boundary layer thickness are presented in Figs. 8 and 9. As with the pressure coefficient contour data, the Stanton number contour plots on the blade surface are based on data taken on one half span and reflected, because of symmetry about midspan, to the other half of the airfoil. The Stanton number lines so presented are based on the mainstream inlet velocity and are, in effect, lines of constant non-dimensional heat transfer coefficient. Except for regions upstream of the leading edge, it is apparent that heat transfer from the passage surfaces is largely determined by the passage secondary flows. Although there are similarities in the heat transfer patterns between the two cases, it is obvious that the inlet boundary layer thickness plays a large role in setting the pattern of heat transfer. Sub-patterns, discernable within the passage for each inlet boundary layer thickness, can be related to particular aspects of the passage flow field as identified from the aerodynamic measurements and flow visualization results.

Endwall. Upstream of the cascade, it is noted in Fig. 8 that the Stanton number contours are parallel to the blade leading edge plane as can be expected for an approaching two-dimensional boundary layer. The Stanton number values and the measured change between the thick and thin inlet boundary layer cases agree well with the flat plate, zero pressure gradient theory of Reynolds, Kays, and Kline [19].

A region of high heat transfer is observed near the airfoil leading edge, where the presence of the horseshoe vortex causes rapid transport of fluid perpendicular to the endwall surface. Comparing the two cases in this region of the endwall, two features are noted: 1) the area of influence of the horseshoe vortex is larger for the thicker inlet boundary layer, and 2) both the minimum and maximum values of Stanton number are nearly the same for the two cases. Referring to the endwall flow visualization, it is seen that the endwall separation line associated with the passage vortex is closer to the airfoil for the thin inlet boundary layer, thus reducing its region of influence. That the maximum Stanton number is the same in each case is an indication of the efficient scouring of the endwall by the vortex.

Heat transfer manifestation in the saddle point region is distinct for the thick inlet boundary layer, and is identified with the closed contour of St = 0.004 near the leading edge of the upper blade. This contour is located above the true saddle point of separation as determined by the intersection of the attachment and separation lines from the flow visualization. The shape of the contour of St = 0.003 located just below the leading edge of the upper blade for the thin inlet boundary layer indicates the same heat transfer mechanism in this region.

A distinct pattern that is observed in the cascade leading edge region is the wedge shaped pattern pointing into the passage in which the heat transfer remains fairly uniform at the approximate level established by the approaching boundary layer. It is interesting to note that in this entrance region, despite nearly an order of magnitude change in inlet boundary layer thickness, the average value of heat transfer is hardly affected.

For the thick inlet boundary layer, the vortex path is clearly marked with a pattern of steep gradients, originating in the saddle point area, and extending across the endwall to the suction surface. Referring to the endwall flow visualization, this path is approximately parallel to, and behind, the endwall separation line. Although the flow visualization for the thin inlet boundary layer also shows an endwall separation line, the Stanton number contours do not reflect the vortex as strongly as the thicker inlet boundary layer. In the suction surface corner, downstream of the point where the separation line intersects the airfoil suction surface, the measurements for both inlet boundary layers show a region of steep heat transfer gradients, with the heat transfer rapidly diminishing toward the suction surface. This corner effect is best shown in the thin inlet boundary layer data, where the Stanton number in the suction surface corner at the rear of the passage falls from 0.004 to 0.002 in a short distance.

The lowest values of heat transfer on the endwall for both inlet boundary layer thicknesses are found near the pressure surface. This low Stanton number region forms a loop, extending from just downstream of the saddle point region, out into the passage, and back towards the pressure surface near the trailing edge. A comparison of endwall and blade heat transfer in this region, close to the endwall-airfoil interface, shows the levels and variation with streamwise distance to be very similar. This similarity is most likely due to the flow in this region being subjected to the same pressure field as the airfoil pressure surface. Since the inlet boundary layer is wrapped up into the horseshoe vortex, a new boundary layer must form within the passage. This new boundary layer is formed along the attachment line, which extends along the endwall near the pressure surface, and is driven by the endwall pressure gradients. It is interesting that the limiting streamlines are nearly perpendicular to the pressure contours of Fig. 6, whereas the endwall Stanton number contours in this area form an angle with the limiting streamlines. The pattern of endwall Stanton contours in Fig. 8 shows that the thickness of the inlet boundary layer plays a large role in determining the size of this region. This may be due to the different location of the vortex over the endwall, which is dependent on the size of the inlet boundary layer, as indicated by the separation lines of Fig. 4.

Near the cascade throat, a complex interaction involving the passage vortex, streamwise accelerations, and the shear-generated endwall crossflow takes place. It is also here that the largest differences between the two inlet boundary layer cases are observed. The Stanton number contours for the thicker inlet boundary layer case suggest that the crossflow boundary layer generated near the pressure surface is able to extend into the throat region before it is swept up into the passage vortex. The corresponding Stanton number contours for the thin inlet boundary layer suggest that the vortex, which is very close to the endwall surface, and the streamwise accelerations dominate the heat transfer in this area, producing a region of very high heat transfer. The complexity of the endwall flow and lack of extensive flow measurements in the throat region, however, preclude any definite conclusions as to the reason for the differences in the two patterns of heat transfer.

For both inlet boundary layer thicknesses in the airfoil wake region, a system of closed Stanton number contours define one of the highest heat transfer regions on the endwall. It should be pointed out, however, that the instrumentation in this area, relative to the spatial scale of the flow phenomenon, was fairly sparse. This necessitated a fair amount of interpolation in drawing the contour lines. With this caution in mind, the Stanton number contours for each inlet boundary layer in the airfoil wake region are found to be nearly identical.

The final definitive region of interest on the endwall surface is downstream of the cascade exit plane, excluding the airfoil wake region just described. The Stanton number contours remain constant over the downstream instrumented portion of the endwall surface. Also, the Stanton number contours for the thin inlet boundary layer are lower than for the thicker inlet boundary layer. Total pressure measurements at the exit plane indicate that the endwall boundary layer at the cascade exit is substantially larger for the thin inlet boundary layer than for the thick inlet boundary layer. Since the hydrodynamic boundary layer is larger at the exit plane, it may be inferred that the thermal boundary layer is also more developed, and is indeed reflected in the lower values of heat transfer observed for the thin inlet boundary layer.

Airfoil. Like the endwall heat transfer results, the airfoil exhibits its own characteristic patterns of heat transfer. Apparent in Fig. 9, for both inlet boundary layer thicknesses, is the striking difference in the pressure and suction surface Stanton number contour lines. While most of the pressure surface shows a heat transfer pattern suggestive of two-dimensional flow, the suction surface heat transfer

Downloaded 01 Jun 2010 to 171.66.16.58. Redistribution subject to ASME license or copyright; see http://www.asme.org/terms/Terms_Use.cfm

patterns, except for a streamwise band on either side of midspan, exhibit the effects of the strong three-dimensional flow field. Furthermore, these patterns show remarkable similarities to, and are consistent with, the aerodynamic measurements of the flow field shown in Fig. 7, and with the flow visualization results of Fig. 5.

Visible for both inlet boundary layer thicknesses are the relatively higher Stanton number values and steep gradients in the three-dimensional flow region on the airfoil suction surface near the endwall. The location of the highest Stanton number values on the entire airfoil surface occurs in this region and coincides with both the location of low pressures and with the initiation of rapid convergence of the surface separation streamline toward midspan. This region and the region downstream near the endwall is associated with the three-dimensional flow of the passage vortex as it travels off the endwall up onto the suction surface. A comparison of the suction surface Stanton number contours for each inlet boundary layer thickness demonstrates that this region for the thin inlet boundary layer case does not cover as much of the suction surface as that for the thicker inlet boundary layer. Consequently, starting with the approximate location of the minimum suction surface pressure, the two-dimensional band of heat transfer on either side of midspan is much wider for the thinner inlet boundary layer. Also note that the airfoil Stanton number contours for the thinner inlet boundary layer show higher heat transfer near the endwall-airfoil suction surface interface. This is attributed to the closer proximity of the passage vortex, relative to the airfoil and endwall surfaces, for the thin inlet boundary layer case.

Upstream of the suction surface minimum pressure location, a complex heat transfer pattern is observed for both inlet boundary layers. The heat transfer on either side of midspan is indicative of two-dimensional flow, which is initially laminar and passes through transition to turbulent. However, the situation rapidly changes as the endwall is approached. One explanation is that the heat transfer interaction of the airfoil and endwall in this region is affected by the horseshoe vortex. Consequently, as with the passage vortex, complex heat transfer patterns are found and heat transfer levels are somewhat higher than midspan values.

A comparison of measured midspan Stanton numbers to predicted values using the finite difference numerical calculation procedure developed by Crawford and Kays at Stanford University [20] is shown in Fig. 10 for each boundary layer thickness. Effects of surface curvature have been included in the predicted values according to the method of Eide and Johnston [21]. The suction surface prediction was obtained by initiating transition at $Re_\theta = 200$, as recommended in [20]. On the pressure surface, however, the adverse pressure gradient in the leading edge region was assumed to initiate transition of the boundary layer at $S/b = 0.038$. Reasonably good agreement between the midspan data and predicted values is observed over much of the region of comparison. The greatest deviation between predicted values and the data occurs on the suction surface downstream of the minimum pressure location for the thick inlet boundary layer case. The reason that the measured values are lower than predicted is thought to be due to flow convergence toward midspan which causes the midspan boundary layer to grow more rapidly. The smaller deviation between predicted values and data for the thin inlet boundary layer case is a consequence of the comparatively diminished convergence of flow toward midspan for this case, as indicated by the surface pressure measurements and flow visualization results.

Fig. 11 is a composite of Figs. 8 and 9 for the thick inlet boundary layer showing the endwall and airfoil heat transfer patterns as would be seen through a wide angle lens looking down into the passage. The Stanton number contours so presented represent an extension of the data in Figs. 8 and 9 to form a consistent pattern for the passage. The resulting composite pattern illustrates the airfoil-to-endwall continuity of the Stanton number contours and the pervading influence of the passage vortex on the endwall and suction surface heat transfer.

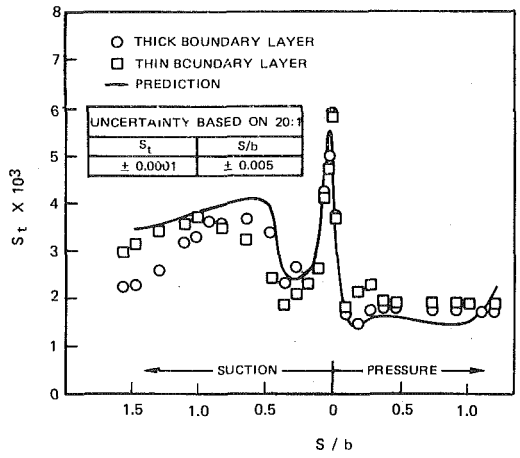


Fig. 10 Measured and predicted midspan heat transfer distributions

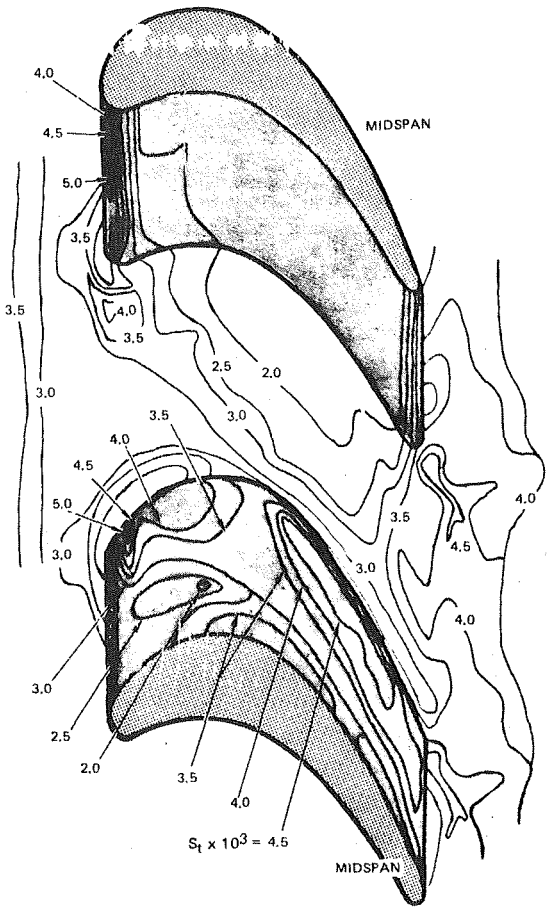


Fig. 11 Stanton number contours on the endwall and blade surfaces for thick inlet boundary layer

Summary and Conclusions

Measurements of local heat transfer coefficient were made on the endwall and airfoil surfaces of a rectilinear turbine blade cascade for two values of inlet endwall boundary layer thickness. The conclusions obtained from these results are:

1 Passage secondary flows greatly influence the heat transfer on the endwall and suction surface of the airfoil.
2 Airfoil pressure surface heat transfer is not affected by these secondary flows.
3 The size of the inlet boundary layer on the endwall has a significant effect on endwall and suction surface heat transfer.
4 Any practical turbine passage heat transfer calculation method must account for the complex flow field produced by the passage vortex.
5 The accuracy, spatial resolution, and completeness of the measurements, which were sufficient to reveal important details

Downloaded 01 Jun 2010 to 171.66.16.58. Redistribution subject to ASME license or copyright; see http://www.asme.org/terms/Terms_Use.cfm

of the flow field, provide a needed data base for use in evaluating calculation techniques.

The blade and endwall geometry and the cascade inlet flow used in this investigation were as simple as possible while retaining most features of a real turbine. Nevertheless, the heat transfer produced on the surfaces formed a complicated pattern beyond present methods of calculation. On the endwall and suction surface there exist large areas where the flow must be considered three-dimensional and where conventional boundary layer assumptions may not be applicable. In addition to providing the first detailed measurements of heat transfer in such a cascade, this work illustrates the difficulties of modeling such flows and adequately predicting heat transfer at the flowpath boundaries.

References

1 Salvage, J. W., "A Review of The Current Concept of Cascade Secondary Flow Effects," von Karman Institute for Fluid Dynamics Technical Note 95, March 1974

2 Dunham, J., "A Review of Cascade Data on Secondary Losses in Turbines," Journal Mechanical Engineering Science, Vol. 12, No. 1, 1970, pp. 48–59.

3 Came, P. M., "Secondary Loss Measurements in a Cascade of Turbine Blades," Instn. Mechanical Engineers, Conference Publ. 3, 1973, pp. 75–83.

4 Kenney, P. S., "An Investigation of Secondary Flow Effects in Curved Channels of Square Cross Section," Thesis, Naval Postgraduate School, Monterey, CA June 1973.

5 Langston, L. S., Nice, M. L., Hooper, R. M., "Three-Dimensional Flow Within a Turbine Cascade Passage," ASME JOURNAL OF ENGINEERING FOR POWER, Vol. 99, No. 1, Jan. 1977.

6 Waterman, W. F., and Tall, W. A, "Measurement and Prediction of 3-D Viscous Flows in Low-Aspect-Ratio Turbine Nozzles," ASME Paper 76-GT-73.

7 Papailiou, K., "Technical Evaluation Report on the 49th (A) Propulsion and Energetics Panel Specialists' Meeting on Secondary Flows in Turbomachines," AGARD Advisory Report No. 109, Nov. 1977.

8 Walker, L. A., and Markland, E., "Calculation of Heat Transfer to Turbine Blading in the Presence of Secondary Flow," *Int. J. Heat Mass Transfer*, Vol. 10, pp. 499–518.

9 Louis, J. F., "Investigation of Factors Affecting Heat Transfer to Turbine End Walls," Air Force Aero-Propulsion Laboratory, TR-73-93, Oct. 1973.

10 Louis, J. F., Dermerjian, A. M., Goulios, G. N. Topping, R. F., Wiedhopf, J. M., "Short Duration Studies of Turbine Heat Transfer and Film Cooling Effectiveness," ASME Paper, 74-GT-131, April 1974.

11 Dunn, M. G., and Stoddard, F. J, "Studies of Heat Transfer to Gas Turbine Components," Air Force Aero-Propulsion Laboratory, TR-77-66, Oct. 1977.

12 Blair, M. F., "An Experimental Study of Heat Transfer and Film Cooling on Large-Scale Turbine Endwalls," ASME *Journal of Heat Transfer*, Nov. 1974, pp. 524–529.

13 Dring, R. P., "A Momemtum-Integral Analysis of the Three-Dimensional Turbine Endwall Boundary Layer," ASME JOURNAL OF ENGINEERING FOR POWER, Vol. 93, Oct. 1971, pp. 386–396.

14 Booth, T. C., "An Analysis of the Turbine Endwall Boundary Layer and Aerodynamic Losses," ASME Paper No. 75-GT-23, March 1975.

15 Patankar, S. V., and Spalding, D. B, "A Calculation Procedure for Heat, Mass, and Momentum Transfer in Three-Dimensional Parabolic Flows," *International Journal of Heat and Mass Transfer*, Vol. 15, 1972d, pp. 1787–1806.

16 Briley, W. R., "Numerical Method for Predicting Three-Dimensional Steady Viscous Flows in Ducts," *Journal of Computational Physics*, Vol. 14, 1974, pp. 8–28.

17 Dodge, P. R., "A Numerical Method for 2-D and 3-D Viscous Flows," AIAA 9th Fluid and Plasma Dynamics Conference, AIAA Paper No. 76-425, July 1976.

18 Kline, S. J., McClintock, F. A., "Describing Uncertainties in Single Sample Experiments," *Mechanical Engineering*, Jan. 1953, pp. 3–8.

19 Reynolds, W. C., Kays, W. M., and Kline, S. J., "Heat Transfer in the Turbulent Incompressible Boundary Layer, III—Arbitrary Wall Temperature and Heat Flux," NASA Memorandum, 12-3-58W, Dec. 1958.

20 Crawford, M. E. and Kays, W. M., "STAN5—A Program for Numerical Computation of Two-Dimensional Internal and External Boundary Layer Flows," NASA CR-2742, Dec. 1976.

21 Eide, S. A., Johnston, J. P., "Prediction of the Effects of Longitudinal Wall Curvature and System Rotation on Turbulent Boundary Layers," Thermo-sciences Report PD-19, Stanford University, 1974.

Downloaded 01 Jun 2010 to 171.66.16.58. Redistribution subject to ASME license or copyright; see http://www.asme.org/terms/Terms_Use.cfm

D. A. Nealy
S. B. Reider

Detroit Diesel Allison
General Motors Corporation
Indianapolis, Ind.

Evaluation of Laminated Porous Wall Materials for Combustor Liner Cooling

Some of the work at Detroit Diesel Allison (DDA) that has been aimed at the synthesis, characterization, and evaluation of a promising porous wall combustor-cooling concept featuring electrochemically etched, multilayer, diffusion-bonded sheet structures (Lamilloy) is briefly reviewed. The specific considerations of cooling effectiveness, design flexibility, fabrication complexity, and special operational and durability problems are considered in light of relevant engine and rig experience.

Introduction

Over the past decade, the problem of combustor liner cooling has received increasing attention, a trend that reflects the continued emphasis on improving turbine engine component performance as well as the concern regarding durability and service life depreciation as operating temperatures are increased. Although attention to cooling problems has traditionally focused on the high-pressure turbine, combustor liner cooling should be viewed as a technical problem of at least equal importance. It must be systematically addressed if projected performance gains and durability improvements (in both combustor and turbine components) are to be achieved.

At the comparatively modest burner outlet temperature levels typical of all but the most recent production turbine engines (BOT $\leq$ 1510 K), experience has shown that liner wall cooling could be effectively achieved with simple film cooling from slots and louvers. In this situation, relatively massive tangential slot flows provide sufficient gas side cooling air film protection that gas-to-wall heat flux levels can be reduced to manageable levels. The system has the inherent advantage of simplicity, and fabrication techniques are well in hand. Furthermore, the large *tangential* slot flows tend to produce a more nearly two-dimensional flow situation in the near-wall region, masking to some extent the troublesome three-dimensional flow field effects always present in combustors.

The principal disadvantage of the pure film cooling approach is that the heat sink potential of the cooling air (in terms of active wall cooling) is not effectively used, and cooling air flows represent a significant portion of the total flow entering the combustor—often as much as 50 to 60 percent of the total. This situation becomes increasingly intolerable as burner outlet temperatures are progressively increased, because the percentage of total airflow required to support combustion (and effectively control burner pattern) soon exceeds available airflow. Consequently, attention must be focused on wall cooling schemes that use cooling air more efficiently, allowing the designer more latitude in overall secondary airflow management.

This paper briefly reviews some of the work at DDA that has been aimed at the synthesis, characterization, and evaluation of a promising porous wall cooling concept featuring electrochemically etched, multilayer, diffusion-bonded sheet structures (Lamilloy[1]). Cooling effectiveness, design flexibility, fabrication complexity, and special operational durability problems are specifically considered in light of relevant engine and rig experience. A brief assessment of the limitations of current analytical design techniques is also made, together with recommendations for improving existing design methodology.

General Liner Cooling Considerations

The principal schemes which, reflecting practical considerations, represent candidate approaches to combustor liner wall cooling are shown conceptually in Fig. 1. As stated previously, simple slot film cooling has traditionally received the most attention in terms of both application and fundamental studies. Because the integrity of the slot air film is the key to cooling performance in these systems, most fundamental work has been focused on characterizing slot jet interaction with the wall and the mainstream and the extent to which mixing destroys the insulating effect of the air film. These studies range from characterization of asymptotic (far downstream) behavior in low turbulence situations [1–4] to more detailed studies of flow/heat transfer behavior in the near slot region, including the effects of slot geometry and mainstream turbulence [5–11]. More recently, studies of film cooling through arrays of holes (as opposed to continuous slots) have been made, although most of these studies are relevant to systems involving more active (internal wall) cooling than is present in pure film cooled liners [12–15]. Detailed studies of circular jet/mainstream flow interactions have also been performed to enhance fundamental understanding of these inherently three-dimensional mixing processes [16–22].

Although the work cited here has greatly enhanced the under-

Contributed by the Gas Turbine Division and presented at the Gas Turbine Conference and Exhibit and Solar Energy Conference, San Diego, California, March 12–15, 1979 of THE AMERICAN SOCIETY OF MECHANICAL ENGINEERS. Manuscript received at ASME Headquarters December 18, 1978. Paper No. 79-GT-100.

[1] Lamilloy is a registered trademark of the General Motors Corporation.

Copyright © 1980 by ASME

Downloaded 01 Jun 2010 to 171.66.16.58. Redistribution subject to ASME license or copyright; see http://www.asme.org/terms/Terms_Use.cfm

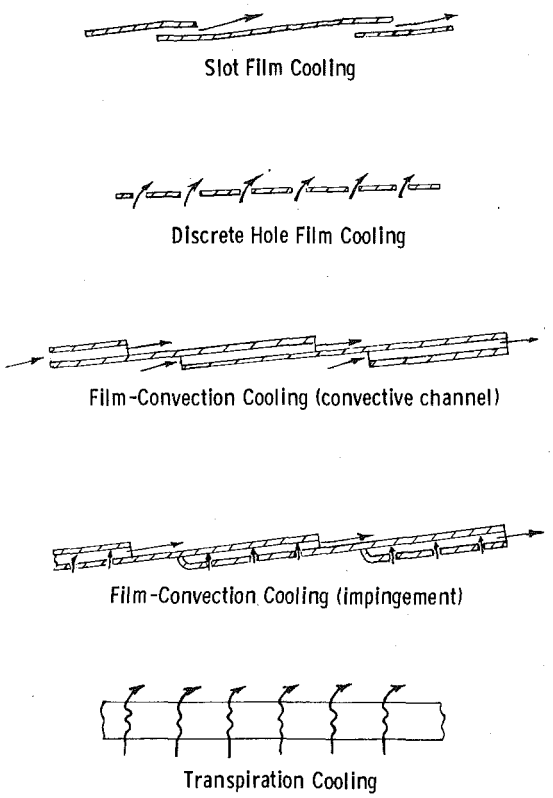


Fig. 1 Combustor cooling approaches

standing of film flow behavior, significant reduction of cooling flows in pure slot film cooled combustors has not been forthcoming. This is, in part, a result of the difficulty in maintaining film integrity in a highly turbulent environment characterized by significant recirculating flows. Another factor limiting the effectiveness of pure film cooling is that the insulating film primarily affects the convective component of heat transfer, and has little effect on the significant radiative heat transfer from the highly luminous gas.[2] Recognizing this basic limitation, it would appear that significant reductions in cooling flow requirements will be achieved only if the heat sink capability inherent in the coolant is more fully used in the active mode prior to injection as a film. This has been clearly pointed out by Colladay [23] and confirmed by our own studies, Fig. 2. The results shown in Fig. 2 should not be interpreted as universal trends, but they do show the large gains to be made if the coolant is used to actively cool the liner wall prior to injection onto the surface as a film.

The motivation for reducing liner cooling flows is illustrated in Figs. 3 and 4 [24], which clearly show that ultimate burner outlet temperature levels are severely constrained by cooling air usage, and that the

[2] An exception is the near slot region where the gas side wall surface may actually be convectively cooled by the slot film (i.e., recovery temperature < wall temperature).

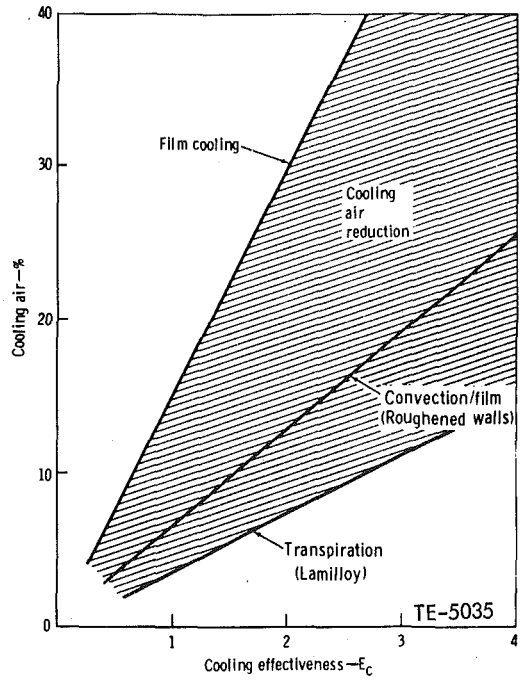


Fig. 2 Cooling performance of film, convection/film, and transpiration

tradeoff between cooling flow and dilution jet flow can significantly affect burner pattern factor. It should also be noted that certain advanced combustor configurations (such as the "fold-back" annular concept) are characterized by larger surface area-to-volume ratios than more conventional types, adding further emphasis to the importance of improving cooling system effectiveness.

The foregoing considerations have led to the development of several alternate liner cooling concepts, which now show considerable promise from a cooling-effectiveness standpoint. In the following sections, one of the most promising approaches is discussed in more detail.

Basic Evaluation of Laminated Porous Wall Materials

General Description. Although transpiration cooling potentially represents the most thermodynamically efficient approach to combustor cooling, practical implementation of the method has been hampered by the limitations of porous materials. In general, conventional porous wall structures have not compared favorably with solid wall structures in terms of strength or oxidation resistance. Considerable difficulty in predicting or controlling local permeability (flow resistance) has also been encountered, and susceptibility to foreign particle clogging continues to be a problem.

Advances in metal-joining techniques over the past several years have led to the development of a multiple-laminate porous structure fabricated from several diffusion-bonded, photoetched metal sheets (Fig. 5). This porous material (Lamilloy) shows considerable promise relative to application in the high-temperature combustor environment.

Nomenclature

Cp_c = coolant specific heat
Cp_∞, Cp_g = mainstream specific heat (used interchangeably)
d = characteristic internal dimension of porous wall
E_c = overall cooling effectiveness defined as $(T_g - T_w)/(T_w - T_c)$
f_w = blowing rate parameter defined in Fig. 11
F = Blowing ratio defined as $\rho_c V_c/\rho_\infty V_\infty$
h = coolant-to-matrix heat transfer coefficient within porous wall
$\rho_c V_c$, G = coolant flow rate per unit surface area (used interchangeably)
P_1 = coolant pressure upstream of porous wall
P_2 = coolant pressure downstream of porous wall
$\rho_\infty V_\infty$ = mainstream mass velocity (flow per unit cross-sectional area)
Pr_c = coolant Prandtl number
R = overall cooling effectiveness defined as $(T_w - T_c)/(T_g - T_c)$
St_0 = convective Stanton number, gas stream to wall, zero injection
T_c, T_{c0} = coolant supply temperature (used interchangeably)
T_s, T_w = wall surface temperature (used interchangeably)
T_∞, T_g = gas stream total temperature (used interchangeably)
β = Inertial flow resistance coefficient for porous wall
ΔT_c = coolant temperature rise through porous wall
η_t = internal thermal effectiveness of porous wall defined as $\Delta T_c/(T_w - T_c)$
μ_c = coolant viscosity
τ = overall thickness of porous wall

Downloaded 01 Jun 2010 to 171.66.16.58. Redistribution subject to ASME license or copyright; see http://www.asme.org/terms/Terms_Use.cfm

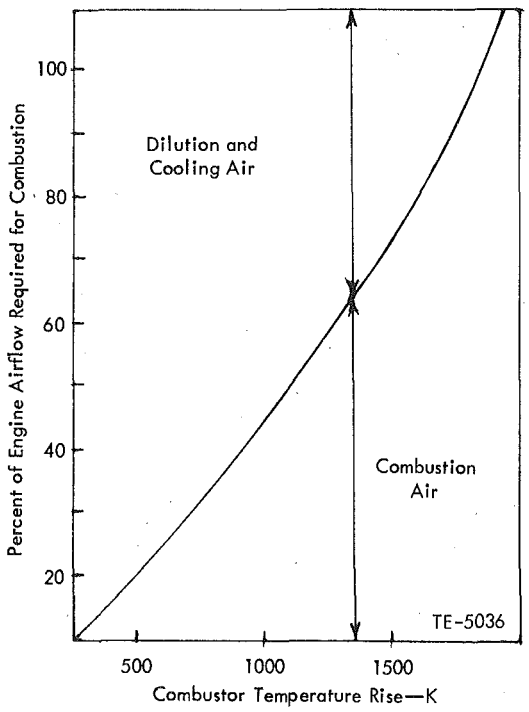


Fig. 3 Combustor air requirements

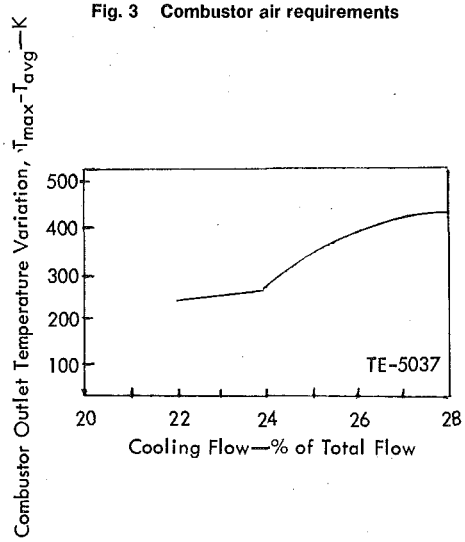


Fig. 4 Effect of cooling air usage on outlet temperature pattern

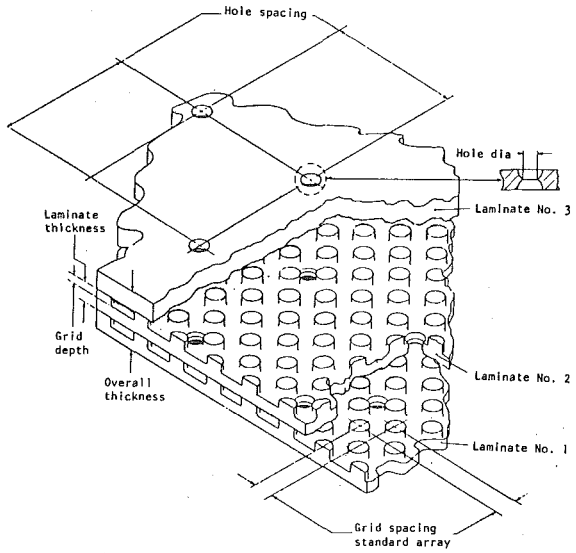


Fig. 5 Typical geometric arrangement of laminated porous wall structure

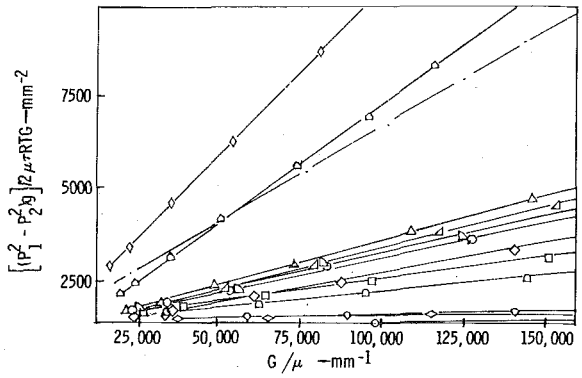


Fig. 6 Typical Lamilloy flow resistance data

This approach provides extraordinary design flexibility relative to flow resistance control and heat transfer performance optimization. Design variables include hole size and spacing (in general different from one laminate to another), laminate thickness, number of laminates, and grid depth, diameter, and spacing. In general, internal surface area densities (internal heat transfer surface area-to-volume ratio) far in excess of more conventional cooling arrangements can be achieved. Larger internal surface area densities, and hence improved thermal effectiveness[3] levels, can be achieved by reducing all dimensions in such a manner that the internal structure approaches that of a fine capillary mesh. In general, however, practical minimum dimensions are dictated by clogging considerations and (to a lesser extent) by fabrication limitations. Improved cooling effectiveness can also be achieved by increasing the number of laminates. In this instance, internal cooled surface area increases directly with no increase in heated (face) area. The principal drawback to this approach is the attendant increase in normal temperature gradient across the structure. Based on experience, the structure can be fabricated from virtually any of the high-temperature wrought alloys currently available commercially.

The development of a thermal design approach involving a structure as complex as Lamilloy has necessarily involved a semiempirical approach to the problem. An overview of the basic experimental work required to characterize heat transfer and fluid-flow behavior is presented in the following section.

Fluid Flow/Heat Transfer Characteristics. The basic flow-resistance characteristics of laminated porous wall structures have been determined using the simple bench test rigs described in [25]. Testing is accomplished at essentially isothermal conditions with ambient temperature air. Mass flow rates are varied by adjusting the upstream pressure level (downstream pressure is essentially ambient). The rig can produce mass flux rates (blowing rates), and therefore internal Reynolds number levels, consistent with actual turbine engine levels. Measurements of upstream and downstream pressures, air temperature, and mass flow rate provide sufficient information to correlate data as shown in Fig. 6. The correlation of porous wall flow resistance in terms of the parameters shown is conventional practice, where the slope and intercept of a given straight line are representative of the respective inertial and viscous resistance coefficients of any given configuration. Configurational differences, therefore, are reflected in differences in the resistance coefficient. Flow data taken at DDA has yielded resistance coefficients for well over 100 different Lamilloy configurations. Considerable effort has been expended in developing correlations between measured flow resistance coefficients and Lamilloy geometric parameters to permit definition of geometric variations required to produce a given flow resistance level. Empirical correlations similar in form to those shown in Fig. 7 have recently been generalized in terms of a simple series resistance flow model of Lamilloy. The development of this semiempirical model has greatly enhanced two elements of design capability—the accurate specification of geometry requirements and the determination of the sensitivity of flow resistance to processing variability.

[3] Thermal effectiveness is defined as actual coolant temperature rise divided by ideal rise, $\Delta T_c/(T_s - T_c)$.

Downloaded 01 Jun 2010 to 171.66.16.58. Redistribution subject to ASME license or copyright; see http://www.asme.org/terms/Terms_Use.cfm

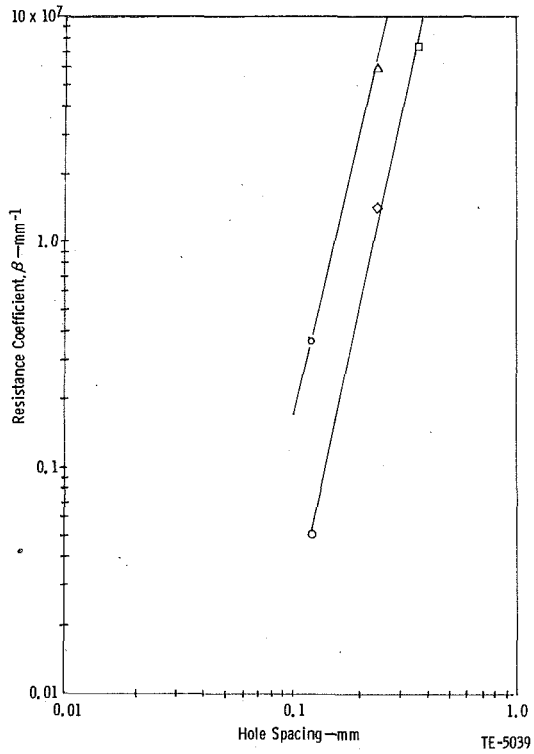


Fig. 7(*a*) Typical cross correlation—inertial resistance coefficient versus hole spacing

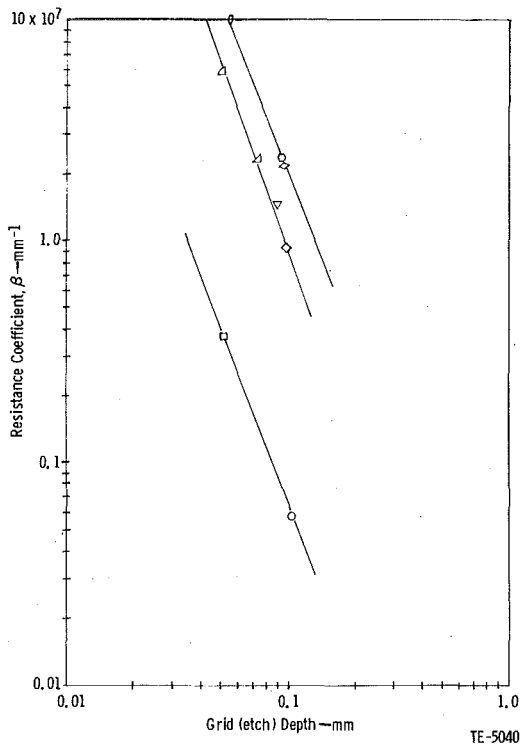


Fig. 7(*b*) Typical cross correlation—inertial resistance coefficient versus grid depth

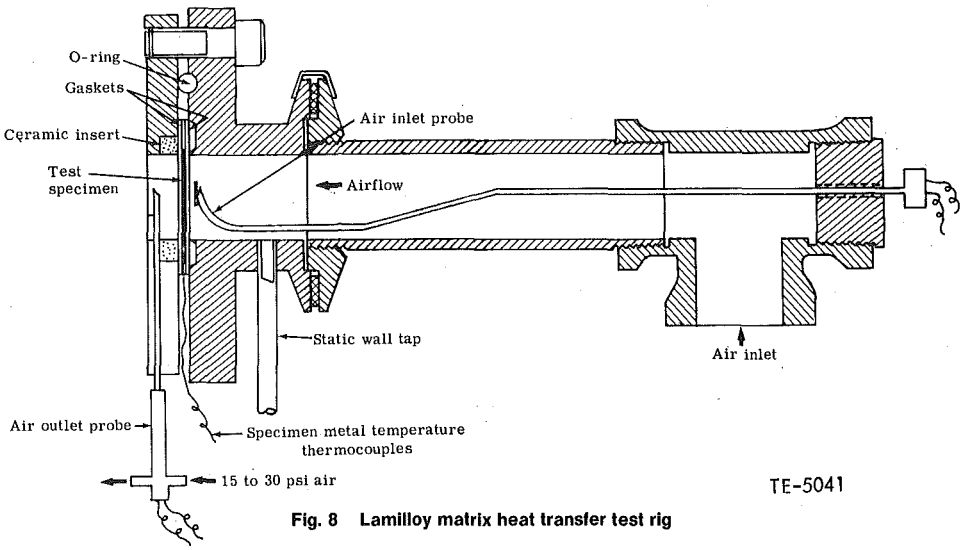


Fig. 8 Lamilloy matrix heat transfer test rig

Knowledge of the internal (matrix) heat transfer characteristics of Lamilloy is an essential empirical input to the design system. The coolant temperature rise through the matrix (thermal effectiveness) and the metal temperature gradient across the structure in the direction of coolant flow are the most useful parameters. A good heat transfer data base is now available for the Lamilloy configurations of interest to the various DDA high-temperature turbine engine programs. The data were obtained by testing simple disk specimens, mounted in a fixture and heated by a high-intensity radiant energy source as illustrated in Fig. 8.

During these tests, measurements were made of coolant flow rate, upstream and downstream pressures, upstream and downstream matrix face temperatures, and coolant inlet and exit temperatures over a range of flow rates at essentially constant heat flux. (The effect of heat flux level on dimensionless heat transfer is negligible when differences in fluid and matrix thermal properties are properly accounted for.) Mass flux rates (internal Reynolds numbers) were held at levels consistent with turbine applications by control of the upstream pressure.

The principal test results of interest (i.e., coolant dimensionless temperature rise and matrix dimensionless temperature gradient) are analyzed using a one-dimensional porous wall thermal exchange model to evaluate the mean matrix-to-coolant heat transfer coefficient and the effective matrix thermal conductivity. Finally, general correlations of the form illustrated in Fig. 9 are established. Combined with the one-dimensional model, correlations such as those shown in Fig. 9 can be used to predict thermal effectiveness (η_t) and matrix temperature gradient under engine conditions.

The boundary layer blockage, or air film protection, resulting from coolant injection through arrays of discrete injection sites represents another, equally important aspect of the overall cooling system. The film protection inherent to systems of this type can significantly reduce gas-to-wall surface heat flux levels, and hence, airflow requirements. Consequently, surface film cooling effectiveness has been investigated for a wide range of Lamilloy configurations.

Film effectiveness data for Lamilloy configurations of interest to this program have been obtained in a subsonic, low-turbulence wind tunnel facility similar to that shown in Fig. 10. During these tests,

Downloaded 01 Jun 2010 to 171.66.16.58. Redistribution subject to ASME license or copyright; see http://www.asme.org/terms/Terms_Use.cfm

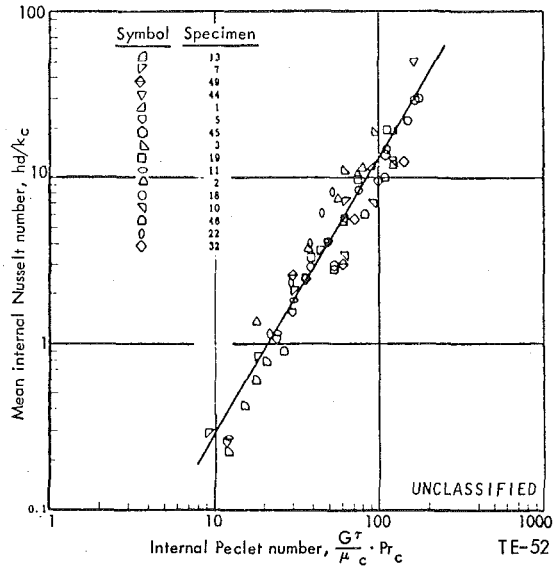


Fig. 9 Lamilloy internal (matrix) heat transfer correlation

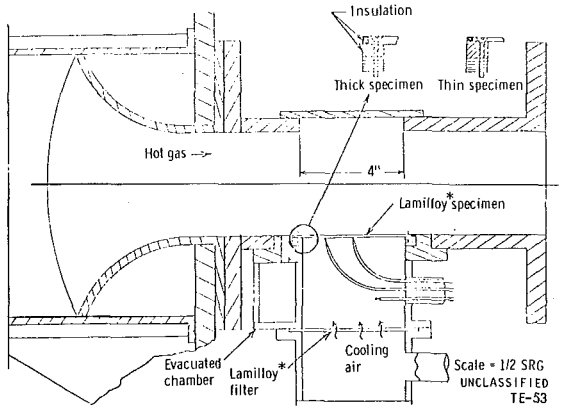


Fig. 10 Schematic of Lamilloy heat transfer tunnel test set-up

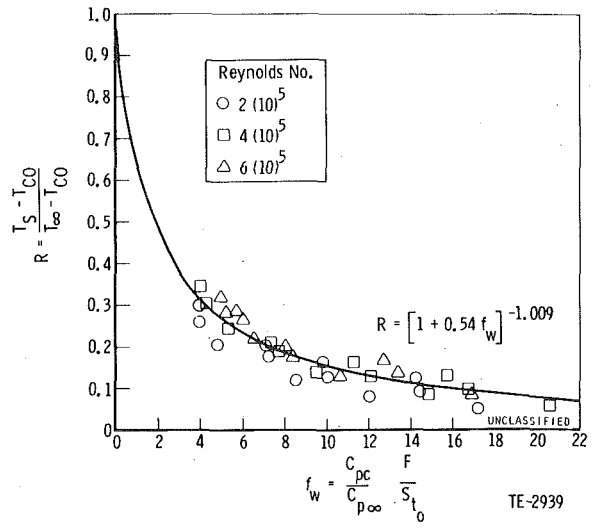


Fig. 11 Overall cooling effectiveness of triply Lamilloy test plate

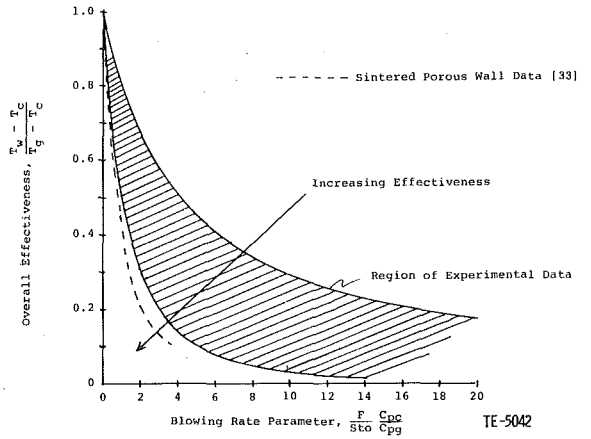


Fig. 12 Overall mass transfer cooling effectiveness for laminated porous walls

instrumented test plates were flush mounted in one wall of the tunnel and convectively heated by vitiated (or otherwise heated) tunnel air. Testing was done in the active mode (i.e., with heat transfer occurring in the Lamilloy passages), and the axial distribution of test plate surface temperature was measured under steady-state conditions.

Primary stream Reynolds number and Mach number levels were established essentially at turbine engine levels. (The Reynolds number was also varied as an independent parameter.) Primary stream and coolant temperature levels were established to simulate engine T_c/T_g ratios, and coolant flow rates were varied over a range consistent with the range of coolant mass velocity-to-free stream mass velocity ($\rho_c V_c/\rho_g V_g$) ratios typical of engine operation. The measured surface temperature distributions (in nondimensional form) then reflect correct primary and secondary stream Mach number, Reynolds number, temperature ratio, and blowing ratio levels.

Typical normalized test plate temperature data represented as a function of dimensionless injection parameter is shown in Fig. 11. Having established internal heat transfer effectiveness characteristics from the bench tests described previously, data in the form of Fig. 11 were combined with an overall energy balance for the cooled test plate to yield the effect of surface injection on gas-to-wall heat flux reduction (film cooling effect). In general, these results have been in reasonable accord with the full coverage film cooling results obtained by the Stanford investigators [13]. Additional details of the DDA work may be found in [15] and [26].

The data band shown in Fig. 12 reflects a wide range of Lamilloy configurations representative of both combustor and turbine cooling applications. As might be expected, those configurations characterized by finer (smaller scale) internal structures exhibit the best performance (lower boundary in Fig. 12) as a result of higher surface area density and more closely spaced injection sites. It should perhaps be noted that the fine structured configurations are more often selected for turbine cooling than for combustor cooling application. This selection is largely made on the basis of clogging considerations—in general, turbine cooling air delivered from the inner compressor flow path is less contaminated than that available for combustor cooling. In addition, local heat flux levels are generally more severe in the turbine airfoil row than in the combustor, requiring somewhat more effective cooling schemes.

The basic analytical design approach used to establish specific cooling geometry arrangements for actual combustor application is outlined in [27]. Little will be said here about the design system except to note that it represents a first-order, two-dimensional approach similar to that proposed in [28] and [29]. The design system has served our purposes reasonably well in those cases where relatively large tangential slot flows have apparently forced the near-wall flows into approximate accord with the simplifying assumptions. However, as cooling flows are introduced more judiciously (e.g., through distributed round hole injection sites), the situation deviates from the assumptions in increasing degree. In fact, strong evidence of three-dimensional effects has been noted in recent transpiration cooled combustor tests (see later sections), indicating the need for improved modeling techniques. Various investigators have noted that numerical, two-equation turbulence modeling schemes (e.g., techniques that solve the turbulent kinetic energy and dissipation equations in addition to the boundary layer momentum and thermal energy equations) may be a necessity in order to properly describe complex mixing phenomena in the near-hole region. Furthermore, since the proper forward marching direction for a numerical solution is not obvious in recirculating three-dimensional flows, simpler parabolic-type so-

Downloaded 01 Jun 2010 to 171.66.16.58. Redistribution subject to ASME license or copyright; see http://www.asme.org/terms/Terms_Use.cfm

lutions may have to yield to three-dimensional elliptic solution approaches. A complete discussion of this aspect of the problem is beyond the scope of this paper, but the reader is referred to some of the recent literature on the subject [16–22, 30].

Mechanical Considerations. Although transpiration cooling for gas turbine systems has for some time been known to be an effective cooling method, pressed sintered wire materials, such as Rigimesh and Poroloy, exhibit marked deterioration in flow at elevated temperature. DDA has conducted comparative contamination tests using Hastelloy X with exposure times to 600 hr. The results shown in Fig. 13 illustrate that at metal temperatures less than 815°C, there is no reduction in flow with Lamilloy after 600 hr of exposure time, whereas the pressed sintered wire materials exhibit a 55 per cent reduction in flow. Similar tests were conducted at metal temperatures of 870 and 1040°C with Lamilloy fabricated from Haynes 188 sheet, to determine changes in permeability, weight, and depth of oxide penetration [31]. The results are shown in Fig. 14. At 870°C essentially no change in permeability after 100 hr exposure was evident. At 1040°C an 18 percent reduction in flow was measured. This reduction could be correlated roughly to the depth of oxide shown in Table 1.

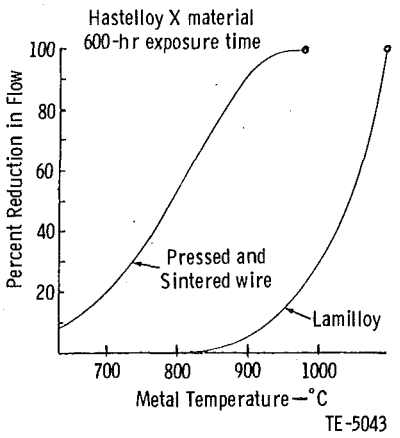


Fig. 13 Oxidation data for Lamilloy and pressed/sintered wire specimens

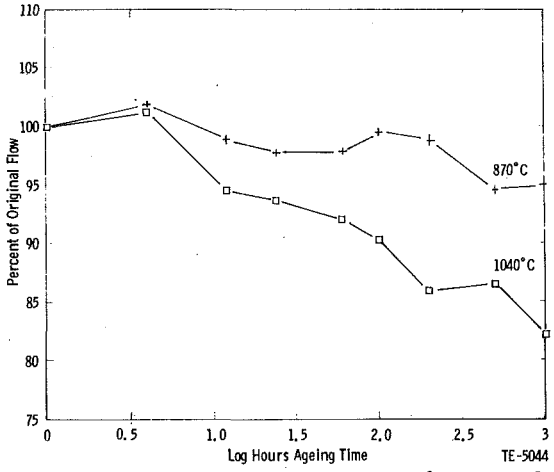


Fig. 14 Permeability of Lamilloy oxidized at 870°C and 1040°C

Table 1 Depth of oxide penetration for HA 188 Lamilloy oxidized for various times at 870°C and 1040°C

Aging time (hr)	Depth of oxide penetration, oxide layer thickness 870°C	1040°C
4	0	0.0002
12	0.0001	0.0004
24	0.0002	0.0004
60	—	—
100	—	0.0012
200	0.0002	—
500	0.0004	0.0020
1000	0.0008	0.0020

The use of a single laminated sheet has certain inherent advantages from a mechanical design standpoint. Recent studies of a large annular combustion system with a pitch diameter of approximately 0.58 m has shown that a substantial weight savings is possible because a single composite sheet is used rather than the multilayered brazed construction used in film and convective-film design. In addition, a life cycle cost study was conducted under an Air Force contract to determine the cost savings of a Lamilloy combustor. Based on 1974 economics, a fleet size of 750 aircraft with a service operational period of 20 yr was used, requiring the production of 2000 engines over a 5.5 yr acquisition phase. The conclusions of this study showed a 43 percent reduction in cost over a film convective cooled combustion system. Experimental quantities rather than production quantities would offer less cost savings, although still on the order of 25 percent.

Lamilloy may be formed into a variety of shapes and sizes. The contour can be successfully rolled, hydroformed, and formed between kirksite dies. It should be noted that limitations in bend radius affect both the structural integrity as well as the porosity; therefore, relatively gentle radii must be considered during the design phase.

Manual gas tungsten arc (GTA) welding has been used to weld liner details because of the process versatility and the ease of adding filler metal. Manipulation of this soft arc has produced solid welds with very little melt-back into the porous structure. Initially, welds were about three times the sheet thickness. However, with technique development and the use of appropriate backup tooling, the weld width has been decreased to only two times the sheet thickness. Work in process is aimed at using automatic GTA welding and appropriate tooling to further reduce weld width and to improve weld uniformity. Some prior work with electron beam and laser beam welding indicated severe problems of cutting or inconsistent melting and burn-back in intermittent patterns of the weld length.

Engine and Rig Experience

Transpiration cooled combustor designs have now been introduced into several development engine and rig tests programs. Fig. 15 is a composite photograph of these demonstrations. These applications cover a wide spectrum of engines including industrial gas turbines such as the IGT 505 and AGT-5 (truck and automotive engines), small gas turbines including Models 250-C20 and -C30 and GMA500, and aircraft turbine engines such as the TF41 and NASA High Pressure Facility. Perhaps the most dramatic illustration of the effectiveness of transpiration cooling has been in the IGT 505 truck engine. The evolutionary comparison shown in Fig. 16 confirms the substantial improvement expected with a transpiration cooled design. Although burner outlet temperature levels are moderate (<1370 K), it should be noted that cooling air temperatures (burner inlet temperatures) are as high as 925 K in this regenerated engine. A total of 10,000 hr

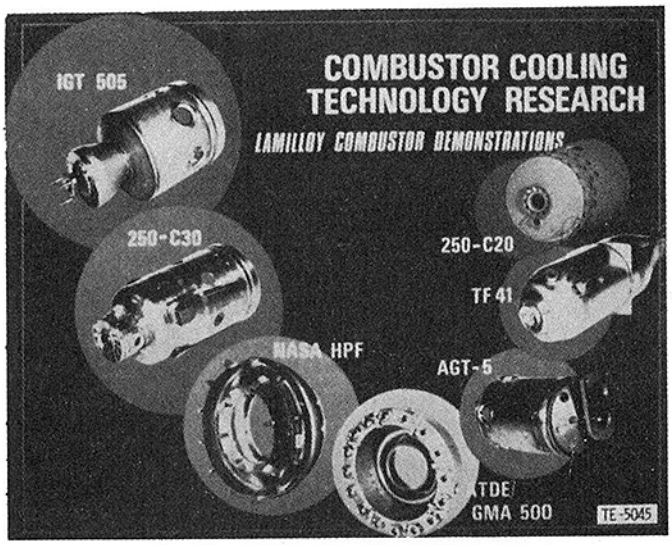


Fig. 15 Lamilloy combustor demonstration

Downloaded 01 Jun 2010 to 171.66.16.58. Redistribution subject to ASME license or copyright; see http://www.asme.org/terms/Terms_Use.cfm

has now been successfully accumulated in field tests on combustors of this type (a single combustor had a total of 3000 hr before it was taken out of service).

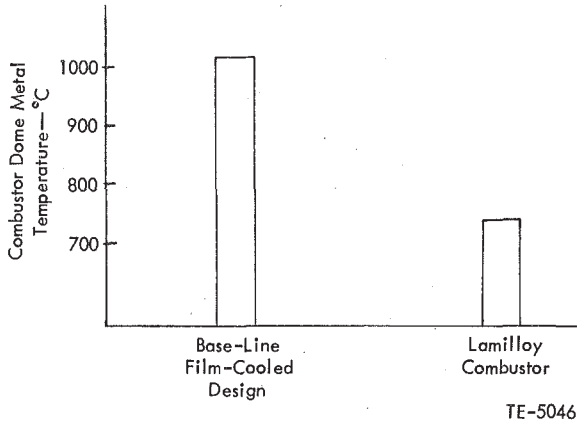


Fig. 16 Cooling effectiveness comparison—IGT 505 combustor

Lamilloy was applied to the 250-C28 combustor after a buckling failure in the primary zone of the conventionally cooled liner. As can be seen in Fig. 17(*a*) the primary zone cooling louver experienced metal temperatures in excess of 1095°C, whereas the Lamilloy replacement (Fig. 17(*b*)) reduced primary zone wall temperatures to approximately 650°C.

A prototype of the small reverse-flow annular combustor (0.28-m pitch diameter) used in the GMA500, an 800-shp gas turbine engine, illustrates the fabricability of Lamilloy structures. As shown in Fig. 18 the contour was readily controlled using a hydroforming process. The combustor surface area of 0.266 m^2 was cooled to an average temperature of 790°C, using 28 percent of the airflow for cooling.

Lamilloy combustors more representative of annular and cannular aircraft turbine engine systems are shown in Figs. 19 and 20. The combustor shown in Fig. 19 was designed and fabricated for NASA for ultimate operation at 4045 kPa and 2478 K burner outlet temperature to replace a conventional stepped louver liner [32]. The liner used 40 percent less cooling air than the more conventional film cooled design. To date, testing has been carried out to temperature levels in

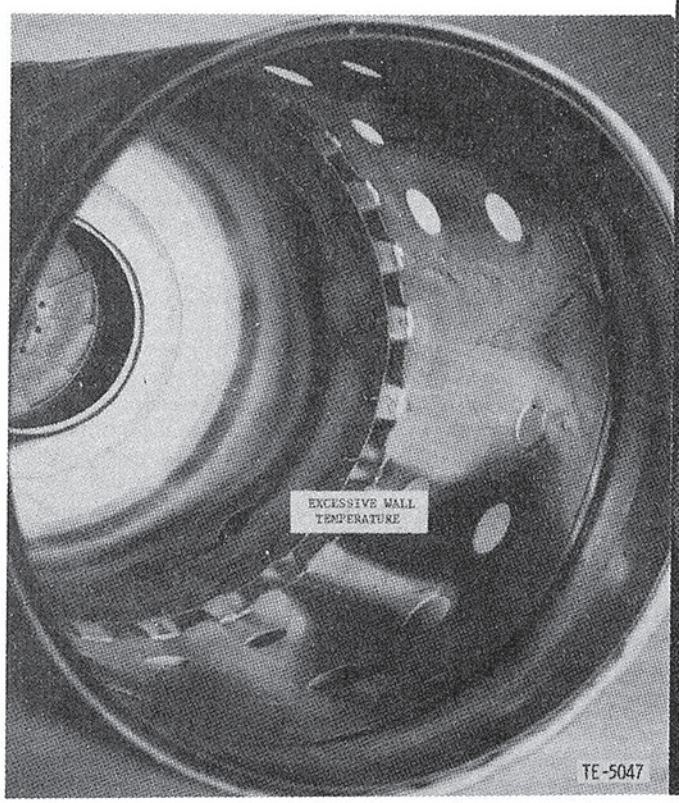


Fig. 17(*a*) Conventional model 250-C28 (film-cooled) combustor

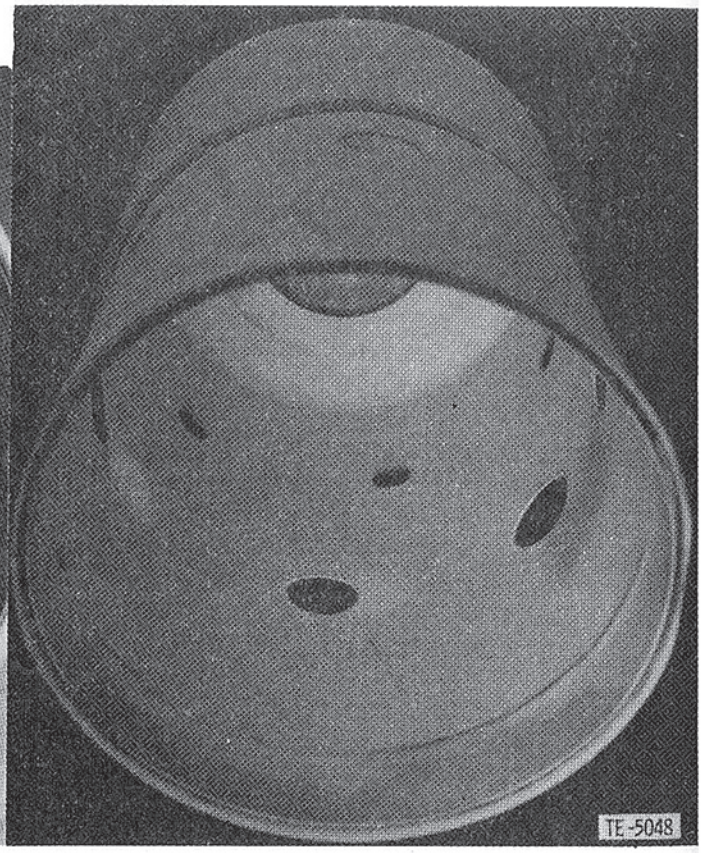


Fig. 17(*b*) Redesigned model 250-C28 (Lamilloy) combustor

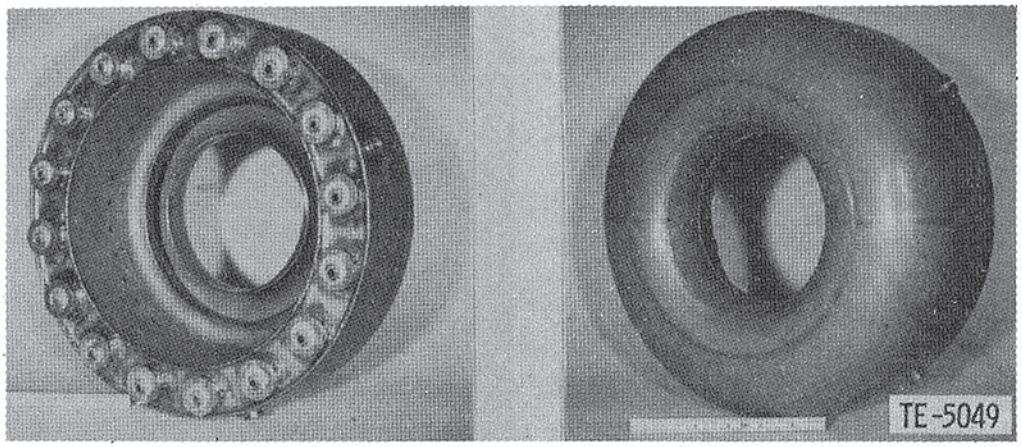


Fig. 18 Prototype GMA500 Lamilloy combustor

Downloaded 01 Jun 2010 to 171.66.16.58. Redistribution subject to ASME license or copyright; see http://www.asme.org/terms/Terms_Use.cfm

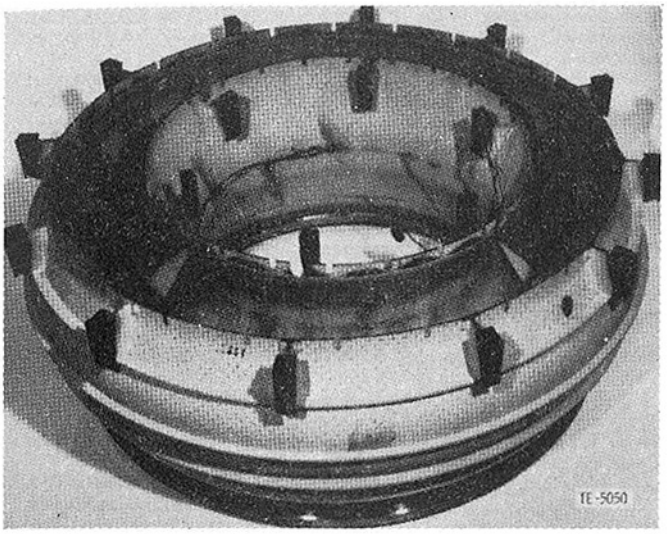


Fig. 19 NASA HPF Lamilloy combustor after 2220 K test

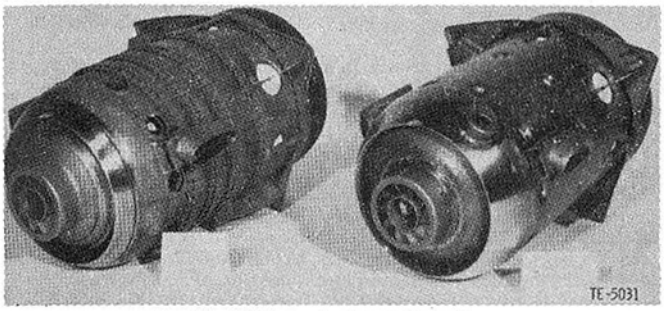


Fig. 20 TF41 combustor configurations

excess of 2220 K at 8 atm pressure with no cooling or durability problems.

The combustor shown in Fig. 20 is being developed for the TF41 turbofan engine as part of a burner pattern factor improvement program. Pattern improvement gains are keyed to a reduction in liner barrel cooling flow and increased pressure drop compared to the existing louvered film cooled design.

Substantial thermal gradients across the Lamilloy structure can be produced as a consequence of the active cooling within the wall, and the relatively large heat transfer rates into the structure, resulting in stresses that could cause thermal fatigue problems. This is a potential problem common to any highly effective cooling system with finite thermal conductivity. Although the problem does not represent a fundamental barrier to the application of transpiration cooling, careful attention must be given to the attendant thermal stress field if designs are to achieve desired low-cycle thermal fatigue life goals. This aspect of the design problem was investigated in a modified Model 250-C30 combustor as shown in Fig. 21. The objective of the test was to demonstrate the viability of the Lamilloy structure, the weld areas required for construction, and two stiffening ring configurations. As shown in Fig. 21, the combustor was elongated by adding a test section consisting of triply HA188 Lamilloy, and both a T and a Z-style stiffening ring. The original combustor was constructed from INCO 601 biply Lamilloy with the permeability of the dome and primary zone identical to the permeability of the new "test section" Lamilloy. The combustor was designed to produce stoichiometric temperatures in the primary zone and test section to maximize the thermal loading of these regions, and thus the thermal gradients experienced by the Lamilloy and the stiffening rings. Both biply and triply were evaluated with thermal gradients as high as 360°C across the triply, and 208°C across the biply. Approximately 1000 thermal cycles were conducted without cracking, either in the Lamilloy or associated welds.

In closing, mention should be made of the three-dimensional flow field effects alluded to earlier. As liner cooling flows are reduced and massive tangential slot flows are eliminated, three-dimensional effects

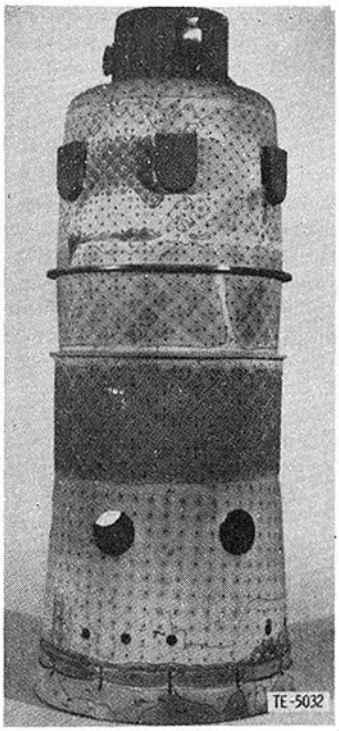


Fig. 21 Modified model 250-C30 combustor used for cyclic stress testing

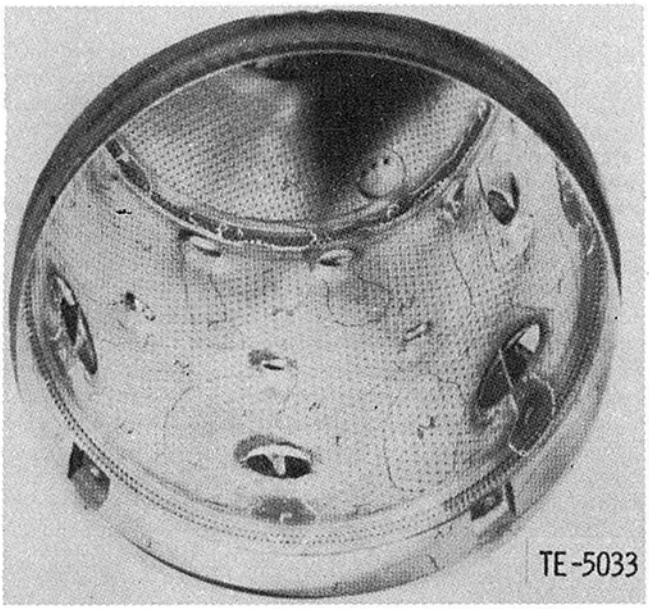


Fig. 22 Combustor showing secondary flow effects behind holes

become more apparent. The thermal paint photograph (Fig. 22) clearly illustrates a strong variation in local wall temperature that can be attributed in large measure to local increases in convective heat flux downstream of large dilution holes. Such flux increases are undoubtedly a result, in part, of flow separation and recirculation induced by the relatively massive normal wall jets. Inferentially, the thermal paint patterns shown in Fig. 22 would indicate local flux increases of as much as 70 percent.

However, problems of this nature do not inhibit the quest for improved cooling techniques as much as they emphasize the need for improved diagnostic and analytical modeling techniques applicable to reacting, three-dimensional turbulent flow fields.

Summary and General Observations

A basic assessment of an advanced porous wall combustor cooling approach has been made, reflecting the specific considerations of cooling effectiveness, design flexibility, fabrication complexity, and

Downloaded 01 Jun 2010 to 171.66.16.58. Redistribution subject to ASME license or copyright; see http://www.asme.org/terms/Terms_Use.cfm

special operational and durability problems. The basic fluid flow and heat transfer characterization studies required to develop a realistic thermal design approach for transpiration cooled liner configurations have been reviewed in some detail, and the fundamental limitations of first-order, semiempirical, two-dimensional thermal design/analysis models have been pointed out.

Our studies have shown that transpiration cooled liner approaches offer the potential of substantial reductions in liner cooling flow requirements. Furthermore, the advanced cooling approaches have demonstrated the capability of successful operation at burner outlet temperatures approaching the near-stoichiometric regime. The payoff of the advanced cooling schemes in terms of outlet pattern improvement and achievable BOT level has been demonstrated in both engine and rig tests.

Although the results are encouraging, it must be recognized that application of the more effective cooling approaches discussed herein has been largely confined to development engines, and several problems still remain. Specifically, further research and development activity is indicated in the following areas:

- Further improvements in fabrication technology will be required to reduce cost, extend cooling design flexibility, and achieve better process tolerance control. For example, recent advances in ECM and laser drilling technology may offer cost, flexibility, and accuracy advantages compared to current electrochemical etching techniques.
- As alternative processes offer additional flexibility in design, better characterization of wall cooling concepts in terms of fluid flow, heat transfer, and mechanical behavior will be required. Relative to the latter, special attention must be given to interactive behavior (creep/fatigue), notch effects, cumulative damage rules, and (perhaps to a lesser extent) fracture mechanics.
- More sophisticated and detailed thermal/structural modeling techniques are required to better represent local temperature and stress distributions throughout the complex cooled wall structure. The eventual achievement of realistic life prediction capability will necessarily require the extension of current finite element methodology to include plastic behavior and creep-fatigue interaction.
- Recent advances in the more sophisticated numerical modeling approaches capable of addressing the three-dimensional turbulent flow field must be fully verified and exploited by the combustor designer. The physics of turbulent shear transport, reflecting the combined effects of three-dimensional wall jets, discrete site coolant injection, inlet swirl, and chemical reaction are clearly beyond adequate description by present first-order analytical techniques.
- The reduction of liner wall cooling flows to minimum acceptable levels will demand that much more careful attention be given to "peripheral" details such as welds, mechanical attachments, scoops, and other flow-path protuberances. Most of the gains (in coolant flow usage) achieved by using advanced cooling techniques can be easily lost through wasteful local cooling "fixes" of poorly conceived mechanical design features.

In summary, much progress in combustor wall cooling technology has been made, but the essential need for ingenuity still prevails.

References

1 Stollery, J., and El Ehwany, A. A. M., "A Note on the Use of a Boundary Layer Model for Correlating Film Cooling Data," *International Journal of Heat and Mass Transfer,* Vol. 8, Jan. 1965, pp. 55–66.

2 Hartnett, J. P., Birkebak, R. C., and Eckert, E. R. G., "Velocity Distributions, Temperature Distributions, Effectiveness and Heat Transfer for Air Injection Through a Tangential Slot Into a Turbulent Boundary Layer," *Journal of Heat Transfer,* Vol. 83, Aug. 1961, pp. 293–306.

3 Librizzi, J., and Cresci, R. J., "Transpiration Cooling of a Turbulent Boundary Layer in an Axisymmetric Nozzle," *AIAA Journal,* Vol. 2, 1964, pp. 617–624.

4 Ross, P. T., "An Experimental Investigation of Adiabatic and Non-Adiabatic Wall Film Cooling With Injection From a Continuous Slot," Detroit Diesel Allison RN 71-14, May 1971.

5 Sivasegarem, S., and Whitelaw, J. H., "Film Cooling Slots: The Importance of Lip Thickness and Injection Angle," *Journal of Mechanical Engineering Science,* Vol. II, No. 1, 1969, pp. 22–27.

6 Kacker, S. C., and Whitelaw, J. H., "The Effect of Slot Height and Slot Turbulence Intensity on the Effectiveness of the Uniform Density, Two-Dimensional Wall Jet," *Journal of Heat Transfer,* Vol. 90, Nov. 1968, pp. 469–475.

7 Kacker, S. C., and Whitelaw, J. H., "An Experimental Investigation of the Influence of Slot-Lip Thickness on the Impervious-Wall Effectiveness of the Uniform Density, Two-Dimensional Wall Jet," *International Journal of Heat and Mass Transfer,* Vol. 12, 1969, pp. 1196–1201.

8 Ballal, D. R., and Lefebvre, A. H. "A Proposed Method for Calculating Film-Cooled Wall Temperatures in Gas Turbine Combustion Chambers," ASME Paper No. 72WA/HT-24, Nov. 1972.

9 Burgraff, F., and Huffmeier, R. W., "Film Effectiveness and Heat Transfer Coefficient Downstream of a Metered Injection Slot," ASME Paper No. 73-HT-31, Aug. 1973.

10 Juhasz, A. J., and Marek, C. J., "Combustor Liner Film Cooling in the Presence of High Free-Stream Turbulence," NASA TN D-6360, July 1971.

11 Seban, R. A., "Heat Transfer and Effectiveness for a Turbulent Boundary Layer With Tangential Fluid Injection," ASME *Journal of Heat Transfer,* Vol. 82, 1960, pp. 303–312.

12 Mayle, R. E., and Camarata, F. J., "Multi-Hole Cooling Film Effectiveness and Heat Transfer," AIAA Paper No. 74–675 and ASME Paper No. 74-HT-9, presented at the AIAA/ASME Thermophysics and Heat Transfer Conference, Boston, July 1974.

13 Crawford, M. E., Kays, W. M., and Moffat, R. J., "Heat Transfer To A Full-Coverage, Film-Cooled Surface With 30-Deg. Slant Hole Injection," Report No. HMT-25, Thermosciences Division, Department of Mechanical Engineering, Stanford University, May 1976.

14. Metzger, D. E., Takeuchi, D. I., and Kuensler, P. A., "Effectiveness and Heat Transfer With Full-Coverage Film Cooling," ASME Paper No. 73-GT-18, April 1973.

15 Anderson, R. D., and Nealy, D. A., "Influence of Surface Injection on Turbulent Heat Transfer for Laminated Porous Materials," Detroit Diesel Allison EDR 6112, Feb. 1969; also in AFAPL TR-69-41.

16 Bergeles, G., Gosman, A. D., and Launder, B. E., "Near Field Character of a Jet-Discharged Through A Wall at 30° To A Mainstream," *AIAA Journal,* Vol. 15, 1977, p. 499.

17 Bergeles, G., Gosman, A. D., and Launder, B. E., "The Near Field Character of a Jet Discharged Through A Wall at 90° To The Mainstream," ASME Paper No. 75 WA/HT-108, Dec. 1975.

18 Patankar, S. V., and Spalding, D. B., "A Calculation Procedure For Heat, Mass, and Momentum Transfer in Three Dimensional Parabolic Flows," *International Journal of Heat and Mass Transfer,* Vol. 15, 1972, pp. 1787–1806.

19 Launder, B. E. and Spalding, D. B., "The Numerical Computation of Turbulent Flows," *Computer Methods in Applied Mechanics and Engineering,* Vol. 3, 1974, pp. 269–289.

20 Ericksen, V. L., and Goldstein, R. J., "Heat Transfer and Film Cooling Following Injection Through Inclined Circular Tubes," ASME *Journal of Heat Transfer,* Vol. 96, 1974, pp. 239–245.

21 Wilson, D. J., Ericksen, V. L., and Goldstein, R. J., "Predicting Heat Transfer Coefficients With Film Cooling From a Row of Holes," ASME *Journal of Heat Transfer,* Vol. 96, 1974, pp. 258–60.

22 Jabbari, M. Y., and Goldstein, R. J., "Adiabatic Wall Temperature and Heat Transfer Downstream of Injection Through Two Rows of Holes," ASME Paper No. 77-GT-50, March 1977.

23 Colladay, R. S., "Importance of Combining Convection With Film Cooling," AIAA Paper No. 72-8, Jan. 1972.

24 Gradon, K., and Miller, S. C., "Combustion Development on the Rolls-Royce Spey Engine," Proceedings of an International Propulsion Symposium, College of Aeronautics, Cranfield, April 1967.

25 Anderson, R. D., and Nealy, D. A., "Evaluation of Laminated Porous Blades—Final Report, Tasks I & II," NASA CR-72281, Jan. 1967.

26 Nealy, D. A., and Anderson, R. D., "Heat Transfer Characteristics of Laminated Porous Materials," AFAPL TR-68-98, Air Force Systems Command, Aug. 1968.

27 Nealy, D. A., "Combustor Cooling—Some Old Problems and New Approaches," Proj. Squid Workshop on Gas Turbine Combustor Design Problems, Lafayette, Ind May 1978 (to be published).

28 *The Design and Performance Analysis of Gas Turbine Combustion Chambers,* Vol. I, Northern Research and Engineering Corp., Cambridge, Mass., and London, England, 1964, pp. 280–340.

29 Lefebvre, A. H., and Herbert, M. V., "Heat Transfer Processes in Gas Turbine Combustion Chambers," *Proceedings of Institution of Mechanical Engineers,* Vol. 174, No. 12, 1960, pp. 463–478.

30 Serag-Eldin, M. A., and Spalding, D. B., "Computations of Three-Dimensional Gas Turbine Combustion Chamber Flows," ASME Paper No. 78-GT-142, April 1978.

31 Spees, J., "Oxidation and Permeability of 0S25 Lamilloy Made from HA188 Sheet," Detroit Diesel Allison Report AV0000-17, Feb. 1978.

32 Wear, J. D., Trout, A. M., Smith, J. M., and Jones, R. E., "Design and Preliminary Results of a Semi-Transpiration Cooled (Lamilloy) Liner for a High-Pressure High-Temperature Combustor," AIAA Paper 78-997, July 1978.

33 Bartle, E. R., and Leadon, B. M., "The Effectiveness as a Universal Measure of Mass Transfer Cooling," *Proceedings, 1962 Heat Transfer and Fluid Mechanics Institute,* Stanford University Press, pp. 27–41.

Downloaded 01 Jun 2010 to 171.66.16.58. Redistribution subject to ASME license or copyright; see http://www.asme.org/terms/Terms_Use.cfm

J. J. Korta
Manager, Mechanical Section,
Westinghouse Canada Ltd.,
P. O. Box 510,
Hamilton, Ontario
Canada L8N 3K2

Mechanical Reliability Considerations in the Modern High Temperature Industrial Gas Turbine

The mechanical design considerations of the CW352 two shaft industrial type gas turbine are discussed with emphasis on achieving a high degree of mechanical reliability based on the extensive service experience of the company's mature 1450°F inlet machines. Problem areas of the early units are discussed and how avoidance of problems has been considered in the design of the CW352.

Introduction

The design of the new generation of high temperature (1850°F TIT) mechanical drive gas turbine as represented by the CW352 two shaft industrial type turbine, Fig. 1, takes advantage of more than two million hours of service experience with company's mature 1450°F inlet machines both in simple cycle and regenerative forms.

Many mechanical features of the 1450°F inlet machines have been retained in the new generation gas turbine equipment because of their sound design philosophy and excellent field history. For example, the axial compressor section with its stable rotor construction comprising keyless disks shrunk on a single compressor spindle and the high hub to tip ratio blading, inherently robust, has shown itself to be very resistant to foreign object ingestion, while still having excellent performance.

However, some features of the older machines produced early field problems. These problems have been resolved or accommodated and the understanding of the hazards leading to the problems and the design philosophy of the solutions have been incorporated in the design of this new generation of turbine.

It is the purpose of this paper to discuss a number of these problems and how the avoidance of them has been considered in the design of the CW352 gas turbine.

Turbine Blading

All stages of turbine blading in the early machines feature free standing blading retained in the disks by a three serration fir tree arrangement, Fig. 2. The serration area is in close proximity to the blade platform, and hence, to the gas path, which was entirely satisfactory in the original design concept of 1350°F firing temperature without rotor cooling. Subsequently, the firing temperature was increased to 1450°F and the provision of serration cooling was added to preserve high temperature creep life in the blade and disk serrations.

These turbines have, on occasion, experienced both vibratory and creep failures in blade and disk serrations. The vibratory problems arose from low order harmonic excitations such as turbine vane and blade ring horizontal joint cooling air leakage, 2H and strut wakes, 5H, in the case of early two shaft engines.

To eliminate horizontal joint excitation, careful maintenance and assembly of diaphragm and blade ring seals was necessary. For retrofit, a new design of joint seal was developed to eliminate this source of excitation and the attendant maintenance. Strut wake problems have been overcome by the addition of upstream straightening air vanes designed to remove gas incidence on the struts.

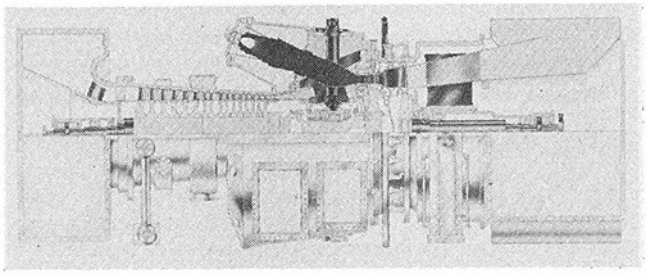


Fig. 1

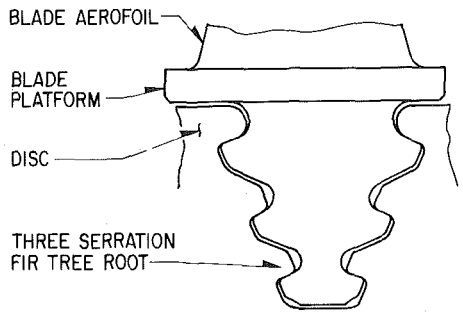


Fig. 2

Contributed by the Gas Turbine Division and presented at the Gas Turbine Conference and Exhibit and Solar Energy Conference, San Diego, California, March 12–15, 1979 of THE AMERICAN SOCIETY OF MECHANICAL ENGINEERS. Manuscript received at ASME Headquarters December 18, 1978. Paper No. 79-GT-101.

Copyright © 1980 by ASME

Downloaded 01 Jun 2010 to 171.66.16.58. Redistribution subject to ASME license or copyright; see http://www.asme.org/terms/Terms_Use.cfm

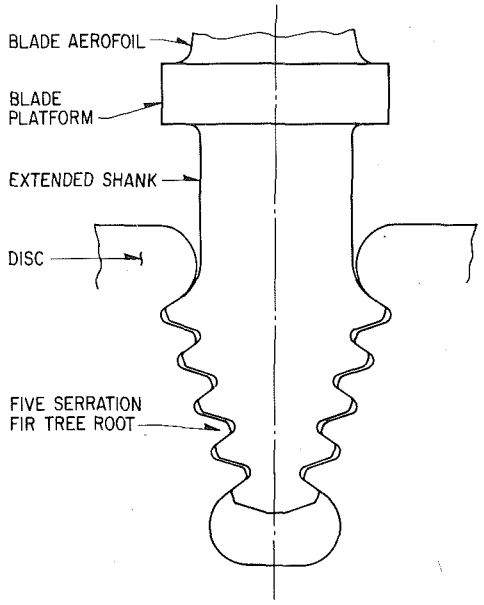


Fig. 3

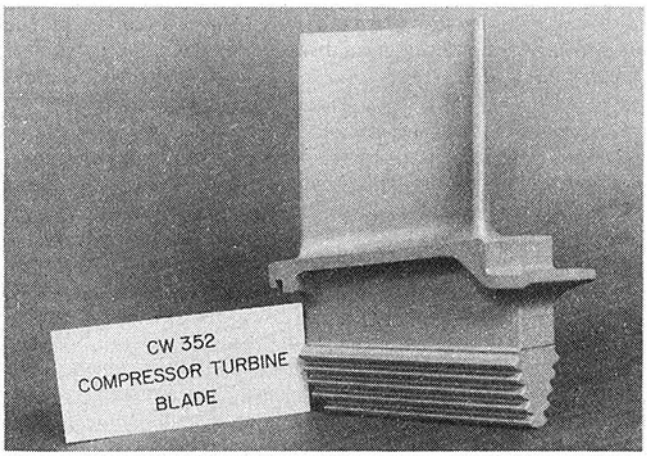


Fig. 4

Some early creep failures in turbine disk serrations were caused by nonuniformity of load sharing on serrations with consequent local overstressing. The solution adopted was to reduce the disk temperature by providing more cooling air to the disk serrations, so that the material was not operating in the creep range.

In the design of the single stage compressor turbine and power turbine blading of the CW352, all the aforementioned factors were considered. To improve the load sharing, a five serration fir tree arrangement is utilized, Fig. 3. This permits better load sharing among serrations because of the inherently smaller and more flexible teeth for a given load capacity.

An extended shank is used to remove the serration area from proximity to the gas path. This, in combination with carefully controlled cooling, results in lower disk metal temperatures in spite of the higher firing temperature of this machine, and effectively removes the disk material from the temperature range where creep strength is a requirement.

The free standing compressor turbine blade, Fig. 4, is of low aspect ratio and does not exhibit low order harmonic interference below 12H in the operating speed range. The higher aspect ratio power turbine blades, Fig. 5, are designed with integral interlocking tip shrouds, which serve to increase blade frequencies sufficiently so that there are no harmonic interferences below 9H in the operating speed range. An additional function of the shrouds is to provide damping to blade vibratory response.

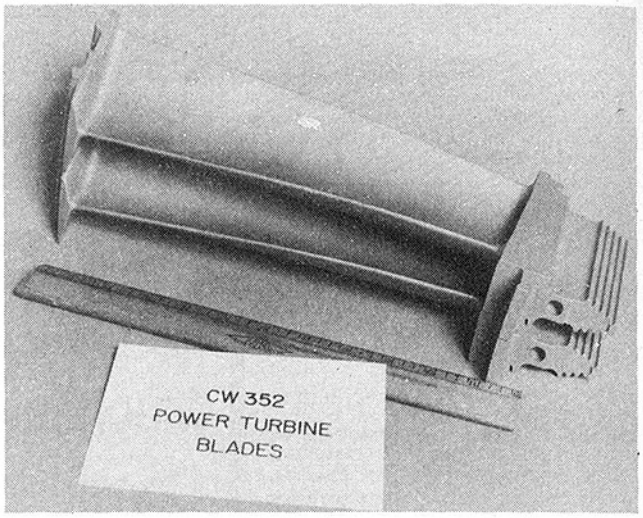


Fig. 5

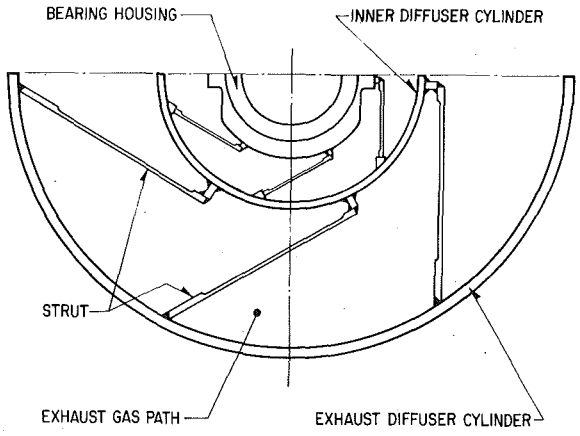


Fig. 6

Exhaust End Bearing Support Structure

Historically, a tangential strut arrangement, Fig. 6, has been used to support the exhaust end bearing housing within the cylinder. Because of the inherent bending flexibility of the struts, this system can be designed to accommodate differential radial expansion between the bearing housing, inner diffuser cylinder, struts and outer turbine casing with acceptable stress levels, while maintaining the bearing housing concentric with the turbine cylinder.

In the early units, where the strut inner and outer casings are exposed directly to gas path temperatures, cases of distorted struts have been reported which produced severe misalignment of the rotor resulting in blade tip rubs which can cause significant degradation of rotor balance and loss of performance. This distortion was traced to abnormal operating conditions such as plugged fuel nozzles and failure to ignite, for example, which exposed the struts to uneven circumferential gas path temperatures during start and stop cycles.

The CW352 turbine retains the basic tangential strut arrangement to support the single stage overhung power turbine rotor. However, recognizing the limitations of earlier designs to cope with uneven gas path temperatures, particularly during abnormal start and stop cycles, the system response to thermal heating has been significantly lowered. To this end, the bearing housing, struts and exhaust cylinder have been totally isolated from the gas path, Fig. 7, with insulated shielding, flexibly supported from the exhaust cylinder.

Another example of tangential strut overloading that caused rotor misalignment problems in early designs was due to loads imposed by the exhaust manifold, Fig. 8. The inner cone of the exhaust manifold casing is directly attached to the struts at the inner diffuser cone and

Downloaded 01 Jun 2010 to 171.66.16.58. Redistribution subject to ASME license or copyright; see http://www.asme.org/terms/Terms_Use.cfm

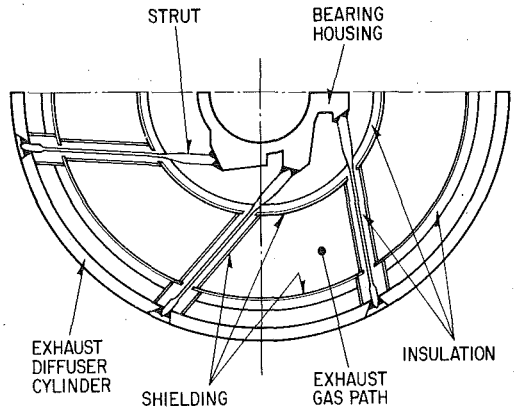


Fig. 7

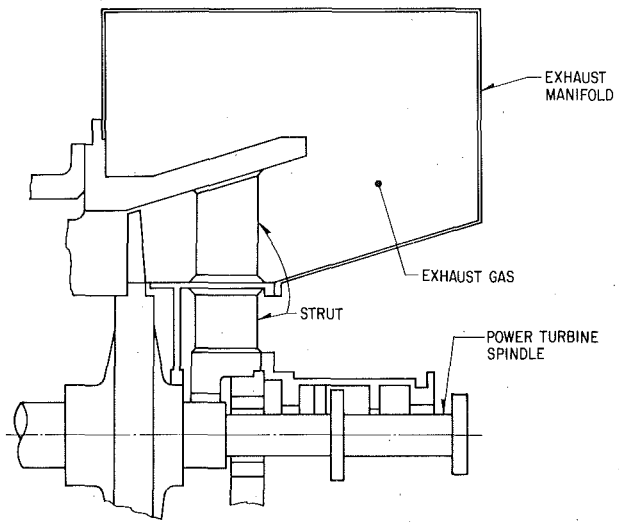


Fig. 8

loads due to thermal misalignment and exhaust back pressure are imposed directly on the struts.

An improved arrangement has been incorporated in the CW352 turbine, Fig. 9. The exhaust manifold is designed to be completely isolated from the strut bearing housing assembly. In addition, any load transfer from the exhaust manifold to the diffuser strut shielding has been eliminated by providing a floating spring loaded seal. The sensitivity of the engine integrity to external and, in many instances, severe forces is, therefore, greatly reduced.

Casing Distortion and Horizontal Joint Leakage

Traditionally, industrial type gas turbine casings are designed with bolted horizontal joints to facilitate inspection and maintenance in the field. Joint leakage has been experienced from combustor cylinders of regenerative units and while the leakage is never of such magnitude as to affect performance, it nevertheless represents a nuisance maintenance item to the customer.

Combustor cylinders of early units were generally arranged as shown in Fig. 10, for regenerative operation. The shell is internally divided into two sections, the cooler compressor discharge section which feeds air to the regenerator and the hotter return section which collects air from the regenerator. Therefore, the casing walls experience severe axial thermal gradients which can cause the casing to distort and the bolted horizontal joints to open in localized areas.

Additionally, the proximity of the combustor baskets to the casing wall causes localized casing hot spots due to radiation. Conduction effects, such as those through the combustor basket transition supports fitted to the casing wall, have also been a source of distortion.

The regenerative combustor shell of the CW352 follows the general arrangement of earlier designs but incorporates several improvements, Fig. 11. As in the past, the cold and hot sections are separated by a

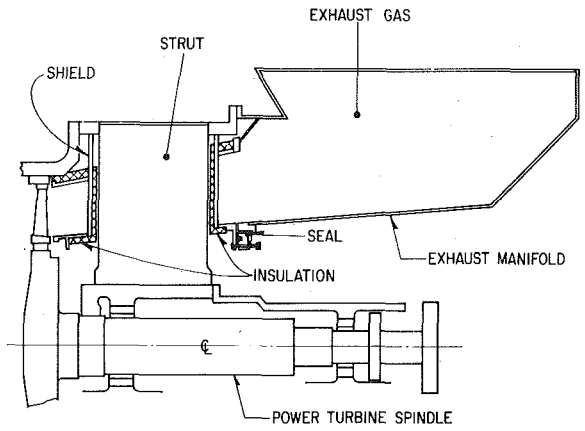


Fig. 9

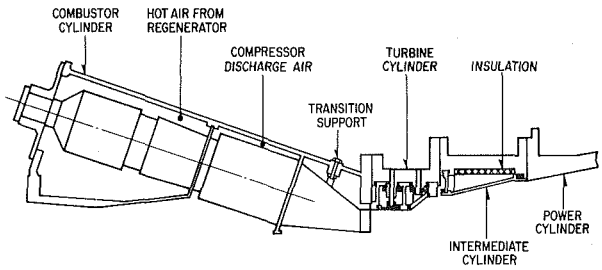


Fig. 10

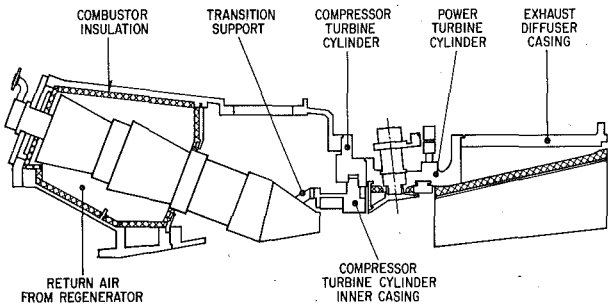


Fig. 11

dividing wall which, rather than being integral with the casing, is now a floating dish to remove redundancy from the shell. The total hot return air section is internally insulated to minimize axial thermal gradients in the casing between hot and cold sections.

Radiation effects from combustor baskets and transitions on the shell are minimized in several ways. The outer wrapper of the casing is positioned remote from the combustion system. The lined hot section insulation and the co-axial flow cones on the primary and secondary sections of the combustor baskets act as effective radiation shields.

Conduction through the transition supports to the outer compressor turbine casing has been isolated by attaching the supports to the cooled inner compressor turbine casing which also supports cooled row one gas path components and by holding the contact surface area between these casings to a minimum.

A further departure of the CW352 combustor shell structural arrangement concerns the primary function of the shell itself. In early units, the shell not only had to act as a pressure vessel but was also a primary structural member of the machine carcass with requirements to maintain both axial and radial alignment between rotor and stationary internal components.

The CW352, because of the single overhung compressor turbine, requires an internal support system for the inboard radial bearing, Fig. 1. This system, consisting of six ribs, is bolted to the discharge

Downloaded 01 Jun 2010 to 171.66.16.58. Redistribution subject to ASME license or copyright; see http://www.asme.org/terms/Terms_Use.cfm

end of the compressor casing and to the end of the compressor turbine casing. The central portion of these ribs is extended radially inwards to the bearing housing support casing. The bridging strut system provides the strength and rigidity to this portion of the cylinder assembly and maintains concentricity of the inboard bearing with the compressor turbine casing. The combustor shell, therefore, need only be designed to contain the hot pressurized gas. The front end wall portion of the casing was arranged so as to provide maximum axial and bending flexibility, thereby minimizing transfer of thermal loading to the strut system.

Turbine Vane Assemblies

Problems with turbine vane assemblies in the early units were associated with low cycle fatigue capability and gas path sealing, giving rise to low order excitation of turbine blades already referred to in the paper.

These earlier turbines feature fabricated turbine vane assemblies consisting of single vanes welded to inner and outer shroud half rings, Fig. 12. The horizontal joints of these half rings are sealed at the outer diameter to prevent loss of cylinder cooling air into the gas path and possible two per rpm excitation of turbine rotating blading. Cantilevered seal strips are used on the inner shroud joints, which, in combination with labyrinth seals, minimize the amount of hot gas path bypassing the turbine vanes through leakage.

Where this style of assembly is still used, care must be exercised when fitting the halves to ensure proper contact and hence sealing of the outer shroud seal strips. For retrofit, a revised joint seal is available similar to that adopted between the power turbine vane segments of the CW352, Fig. 13. Sealing between the shroud segments is accomplished by means of seal strips which are captive in slots of adjacent shrouds. This method utilizes air pressure differences, rather than fit up, to provide gas path sealing.

Low cycle fatigue problems with the early units resulted in vane trailing edge buckling and weld cracking. This was due largely to the constrained nature of the half ring assemblies under thermal gradients during start and stop cycles.

This design was successfully modified some years ago. Along with improvements in the weld design between vanes and shrouds, much of the constraint of this locked up structure was relieved by slotting the inner shrouds between small groups of vanes. The outer shrouds remain as halves and are free to expand circumferentially within their support structure, being pinned at one point only. Low cycle fatigue capability for the CW352 vane arrangement was a prime requisite in view of the higher gas path temperatures in this unit. Vanes are cast with the inner and outer shrouds integral providing greater strength than a welded arrangement. In the case of the compressor turbine, the cooled vane is cast singly and in pairs for the power turbine. Each segment is individually supported and thermally unconstrained by adjacent vanes.

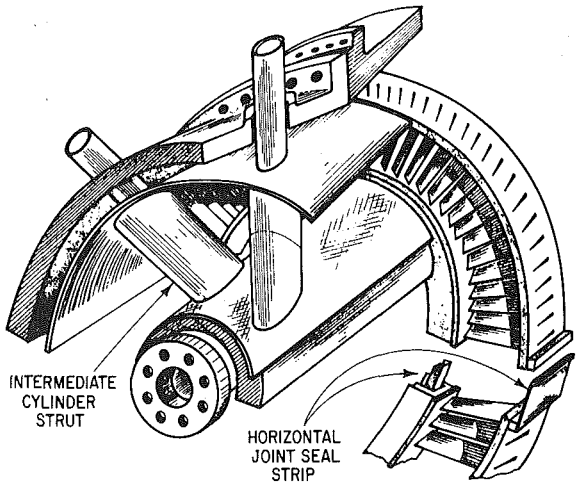


Fig. 12

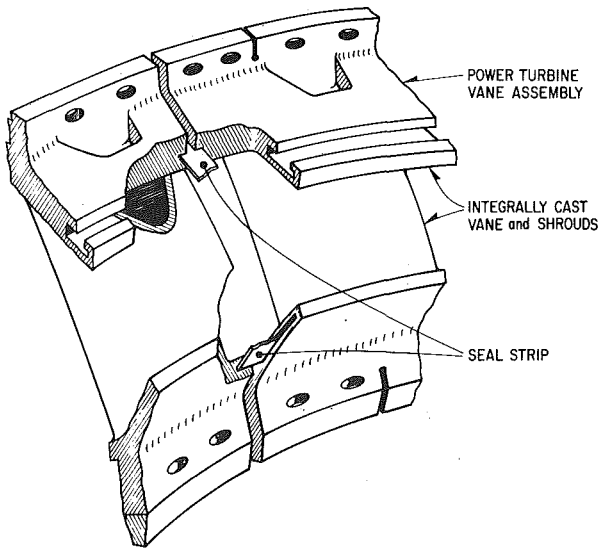


Fig. 13

Turbine Rotor Disk Assembly

Traditionally, turbine rotor assemblies comprise a number of built up components, namely, turbine disks, clamped together by axial through bolts. Disk concentricity is maintained by the curvic clutch mounted on flexible lips at the mating disk interfaces. The through bolts are assembled with a large initial stretch to insure that no loosening can occur at the curvic clutch teeth. This typical construction is illustrated in Fig. 14 for a compressor turbine rotor section of a two shaft turbine which also incorporates a cooling air system for the turbine disk and blade serrations.

The cooling air within the turbine rotor is retained by a seal strip contained in circumferential slots of adjacent turbine disks. This strip was originally manufactured with a single lapped joint to accommodate thermal expansion. During accumulated transient operation, the relative expansions of the seal strip and disks caused high compressive stresses to occur in the strip, resulting in progressive shortening. This cumulative effect, after many cycles, allowed the overlapped joint to open, with loss of serration cooling. This problem has been resolved by fitting a multi-sectional seal strip with lapped joints to reduce the differential growth at the joints, and as well, the strips are chrome plated to reduce friction under thermal growth.

A similar construction to that in Fig. 14 is also used in the two stage power turbine rotors except that no interstage seal strip is required, as no cooling air is supplied through passages in the disks to the blade

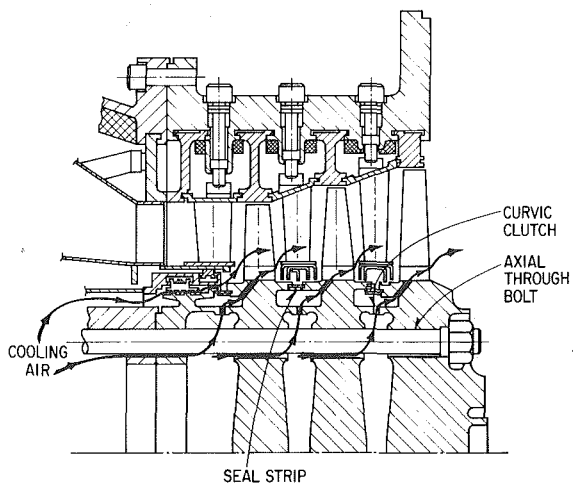


Fig. 14

Downloaded 01 Jun 2010 to 171.66.16.58. Redistribution subject to ASME license or copyright; see http://www.asme.org/terms/Terms_Use.cfm

and disk serrations. During routine inspection of some early units, relaxed through bolting between the two turbine disks was discovered which caused no apparent vibration problems while running. Analysis revealed a mismatch in thermal coefficients of expansion between the bolts and the two dissimilar metals of the disks. Under hot running conditions, the preloaded bolts were overstressed and yielded, resulting in lower than desirable preload at standstill. This was cured by a change to bolting material having thermal expansion properties compatible with the disks so that a satisfactory preload is maintained under all conditions without overstressing.

In the design of the CW352 turbine, it was desirable to minimize the overhang of the single stage compressor turbine and power turbine disks because of whirling critical speed considerations, Fig. 1. Therefore, the curvic clutch arrangement was not adopted. The single stage power turbine disk is forged integrally with the power shaft.

The single stage compressor-turbine disk is attached to the compressor-turbine seal wall disk, Fig. 15. A flexible spigot, located close to the bore of the assembly, where the centrifugal expansion and temperature environment are low, is used to maintain concentricity.

Torque is transmitted through the interface by a series of tangentially fitted, but radially free, drive keys; these allow for some radial thermal mismatch at the interface between disks.

The assembly is clamped using prestretched bolts whose thermal coefficient of expansion is carefully matched to that of the disks to prevent overstressing of the bolts such as occurred on some early 1450°F machines.

The single stage design of compressor turbine and power turbine rotors eliminates the need for interstage sealing as on early units. However, cooling air for the blading is contained on the compressor turbine assembly at the interface between the seal wall disk and the compressor turbine disk by the use of an axially preloaded interface.

Turbine Bearings

Historically, both single and two shaft turbines have employed plain, partial, journal bearings, which have good load, damping and temperature characteristics. These have proven to be extremely reliable in service on units operating as high as 9000 rpm. Bearing pressure, based on projected bearing area has been limited to 200 psi to give satisfactory performance during the low speed turning gear operation.

However, under certain conditions of high speed and/or light load, this class of bearing can exhibit oil whirl, which results in large rotor vibrations. This form of vibration, at a frequency less than one-half the rotational frequency of the rotor, is caused by instability of the hydro-dynamic forces in the oil film. Moreover, conditions can develop which cause stable bearings to exhibit this phenomenon. Among these are foundation and coupling alignment changes, which can unload bearings, particularly where units are coupled with solid shafting.

Oil whirl, due to bearing unloading, has not been a problem in early units, whether solid shafting or flexible couplings have been used between the turbine and driven equipment. Rather, the few problems that did occur were due to the low stability margin inherent in the application of the bearings. For example, cases occurred where an increase in oil viscosity brought about by lowering the oil supply temperature initiated oil whirl. In other cases, the oil supply temperature had to be increased above nominal design to avoid this phenomenon.

Corrective measures to eliminate oil whirl include increasing the pressure, grooving the bearing, decreasing viscosity, reducing the circumferential length of the active bearing arc and reducing bearing length. Circumferential grooving of the bearing was the method adopted on the early units to increase the stability margin.

It is well known that tilting pad radial bearings are completely stable with regard to oil whirl. This was the type finally selected for all bearings in the two shaft CW352 turbine. In addition, this class of bearing possesses a higher degree of damping than plain journals. This damping limits rotor journal motions when passing through rotor whirling critical speeds.

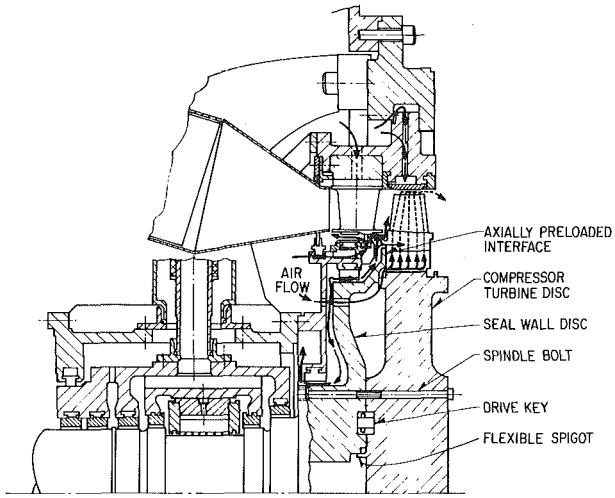


Fig. 15

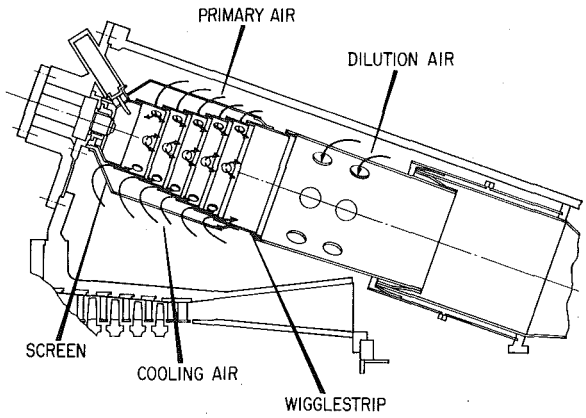


Fig. 16

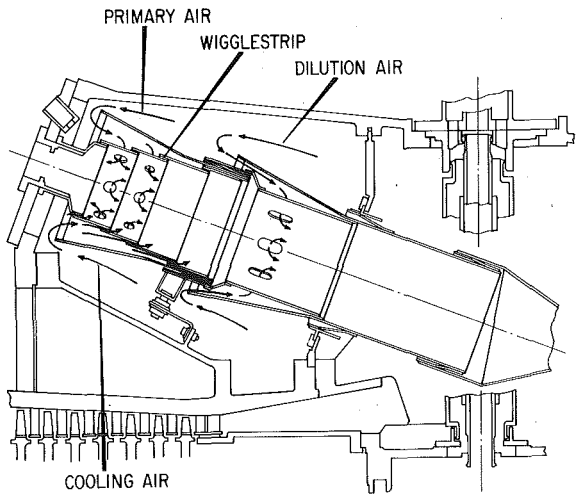


Fig. 17

The journal diameters in the CW352 turbine were mainly governed by bending stiffness requirements of the rotors. Using plain journal bearings in this application would have resulted in unstable bearings because of the low bearing pressures. Therefore, the tilting pad type was selected.

Although tilting pad bearings generally run with lower radial clearance than plain journal bearings, turbine seal clearances may be more affected. It is general practice to orient the multi-shoe bearing with a pair of shoes on either side of bottom dead center to get maximum load capacity and oil film damping in the horizontal plane. Ar-

Downloaded 01 Jun 2010 to 171.66.16.58. Redistribution subject to ASME license or copyright; see http://www.asme.org/terms/Terms_Use.cfm

ranged thus, the journal, at standstill, will wedge itself between the bottom pair of shoes. Hence, larger radial seal clearances through the turbine may be required to eliminate rubs, and of course this will detract from turbine performance. Therefore, in the interest of maintaining the minimum seal clearances possible in the turbine, all bearings were oriented with one pad on bottom dead center.

Combustor Baskets

The allocation of airflow in the design of a combustor basket is a matter of compromise between conflicting requirements. Air must be supplied to the primary end of the combustor to burn the amount of fuel required for the rating of the machine. This primary process results in extremely high gas temperatures, which must be reduced, by a further supply of air in the secondary, or dilution zone, to acceptable levels for the turbine blading. Finally, the remaining air is used to protect the metal walls of the combustor from the high gas path temperatures of the combustion process.

This cooling air must be carefully metered and directed to the critical areas of the basket. It enters through castellated strips (wigglestrips) between cylindrical sections of the basket; maximum cooling air is achieved when this air has the maximum possible axial velocity along the wall of the next cylindrical section. Even circumferential distribution of air into the wigglestrip is vitally important.

Early units, Fig. 16, were equipped with baskets manufactured from 310 stainless steel and no directional control was applied to the cooling air which entered the wigglestrips in a random turning mode, nor was any control of circumferential distribution applied. This was satisfactory at the 1350°F firing temperature but the uprating to 1450°F, reducing the amount of cooling air available, coupled with the higher cooling air temperatures associated with the regenerative cycle, made the use of a better high temperature material, Hastelloy X, necessary. Screens were added to the primary section of the basket to provide some control of circumferential cooling air distribution.

The CW352 turbine, with its 1850°F firing temperature and higher regenerator return air temperatures, demands even closer control of cooling air to achieve basket metal temperatures similar to the earlier units, since the same material is used.

An extensive rig and engine test program has developed a basket which employs cylindrical directional devices to ensure that the air enters the wigglestrips axially with maximum velocity, Fig. 17. These devices also ensure even circumferential distribution of cooling air and help to meter the cooling air, as required, to successive wigglestrips. The basket also features an improved design of wigglestrip which, having a lower blockage ratio, makes more effective use of the cooling air gaps between successive cylinders. This same program has maximized the amount of cooling air available by careful development of methods of injection of primary and dilution air to minimize requirements in these areas.

Concluding Remarks

Mechanical reliability was recognized as an important requirement in the design of the CW352 gas turbine with regard to the intended operation in gas pumping and process duties. To these industries, down time is of critical importance, and the possible operation in remote areas also places a premium on reliability.

The company's earlier generation (1450°F inlet temperature) of gas turbines has accumulated a considerable history in similar operational use, and this experience has been reviewed in depth as part of the design consideration for reliability. A critical examination has been made of these earlier designs and their construction, together with the problems that have arisen.

It has been important to consider the basic causes of these problems and the design philosophy of the applied solutions in the design process for the new turbine. Thus in considering good reliability, we have tried to ask ourselves: have we done this before? Did it work? If not, why didn't it work? How did we reason our way out of the problem? How did we apply the reasoning to an engineering solution? This sort of process is, of course, unconsciously used by any designer. I have tried to show some examples of how we applied it more consciously than may be usual.

Downloaded 01 Jun 2010 to 171.66.16.58. Redistribution subject to ASME license or copyright; see http://www.asme.org/terms/Terms_Use.cfm

K. Bammert
Professor.
Institute for Turbomachinery and Gasdynamics,
University of Hannover,
Hannover, Germany

G. U. Woelk
Head of Design Department Turbines.
Gutehoffnungshütte Sterkrade AG,
Oberhausen, Germany

The Influence of the Blading Surface Roughness on the Aerodynamic Behavior and Characteristic of an Axial Compressor

The conversion of energy in an axial compressor is influenced in great measure by the surface quality of the blading. To achieve low flow losses, the roughness values of the blade surface must be below certain limits. However, the blade surface, which is hydraulically smooth on commissioning of the machine, is in many cases attacked by dirt, corrosion and erosion during operation. For investigation of the influence of the surface quality on the efficiency, flow rate, pressure ratio, and the shifting of the characteristic curves, systematic measurements were taken on a three-stage axial compressor with smooth and uniformly rough blading. The roughness was produced by applying loose emery grain of different grades.

Introduction

The efficiency of energy conversion in a turbo machine is influenced in great measure by the surface quality of the blading. For low flow losses the roughness of the blade surface must be below certain values, which sometimes require extensive manufacturing effort with the correspondingly high cost involved [1]. However, the blade surface, which at the time of commissioning is hydraulically smooth, in many cases undergoes changes during the life of the machine as a result of soiling, corrosion and erosion. These phenomena lead to extensive roughening of the surface often throughout the blade. During operation of axial compressors, soiling and roughening of the blading are caused by dirt and corrosive gas contained in the medium handled.

These changes in the blading, influence the deflection properties and loss coefficients of the cascades and cause considerable changes in the operating data—such as mass flow rate, pressure ratio and efficiency—and also narrow the operating range of the machine. This means that with increasing roughness of the blade surface the controllability of a compressor set decreases and under certain circumstances it is no longer possible to adapt the machine to the required operating conditions.

The effects of soiling, corrosion and erosion can be reduced and the life of the blading can be increased by filtering and wet cleaning of the medium handled however, it is not possible to fully prevent the roughening of the blade surface. It is important therefore to know the quantitative relation between the surface quality of the blade cascades and the aerodynamic behavior of these, i.e., the additional losses due to roughness. This would allow conclusions as to whether the blade layout should include certain reserves or whether it would be expedient to clean, remachine or replace the blading after a certain period of running. For rough turbine cascases, results were available which allow determination of the effects of blade changes on the efficiency, output and characteristic curves of gas and steam turbines [2, 3]. However, these results cannot simply be considered as representative of the aerodynamically much more sensitive retardation cascade of the axial flow compressor.

Measurements taken on plane retardation cascades of large chord length have shown the influence of increasing roughness on the pressure distribution around the profile, on the development of the boundary layer along the profile contour and on the velocity distribution in the boundary layer [4]. With the boundary layers thickened by roughness, there is the danger of flow separation which prevents further pressure development; the result is a marked change in pressure distribution.

In order to obtain quantitative results about the effect of blade roughness on the flow losses and on the operating behavior of axial compressors, systematic measurements were taken on a three-stage model compressor with smooth and uniformly rough blading.

Test Rig

The layout and design of the three-stage model compressor available for the investigations have been previously described [5]. The

Contributed by the Gas Turbine Division and presented at the Gas Turbine Conference and Exhibit and Solar Energy Conference, San Diego, California, March 12–15,1979 of THE AMERICAN SOCIETY OF MECHANICAL ENGINEERS. Manuscript recieved at ASME Headquarters December 18, 1978. Paper No. 79-GT-102.

Copyright © 1980 by ASME
Downloaded 01 Jun 2010 to 171.66.16.58. Redistribution subject to ASME license or copyright; see http://www.asme.org/terms/Terms_Use.cfm

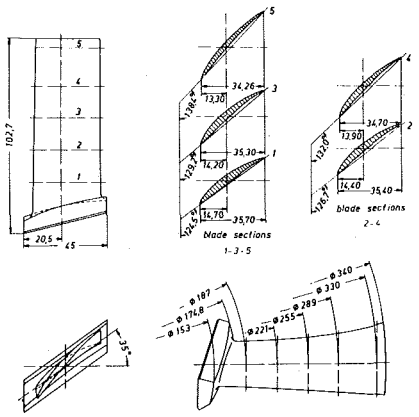


Fig. 1 Rotor blade of the first stage, dimensions in mm

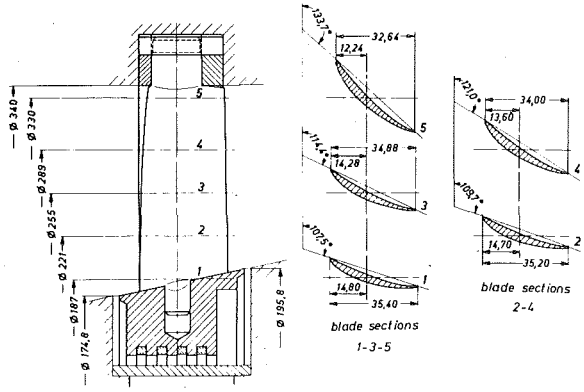


Fig. 2 Guide blade of the first stage, dimensions in mm

design speed of the compressor is n_N = 17,000 rpm, the suction volume flow rate in the design point $\dot{V}_{E,N}$ = 10 m³/s. The total isentropic enthalpy rise resulted from the measurement with smooth blade surface at $\Delta h_{tot,s,N}$ = 67.3 kJ/kg, which corresponds to a total pressure ratio of about 2. The hub-tip radius ratio at the compressor inlet is ν_E = 0.405, with ν being the ratio of inner to outer radius of the blading. With a constant outer radius of the blading of d_a = 340 mm, circumferential velocities of $u_{a,N}$ = 302.6 m/s are developed at the blade tips at the design speed.

The blading of the compressor consists of inlet guide blades and three-stages with the arrangement rotor-guide blades. The inlet guide blades are designed as a slightly deflecting accelerating cascade and impart to the axially entering flow a component in circumferential direction. The blades are designed from profiles of the NACA 65 series. The basic profile of the NACA 65 series has a very thin trailing edge. For the blading of the test compressor the trailing edge was reinforced, for manufacturing and strength reasons, by describing a circle with the radius $r = 0.005 \cdot \ell$ around the point $x/\ell = 0.995$—with ℓ being the chord length of the profile and x the variable longitudinal coordinate—and connecting this by tangents with the basic profile.

In order to achieve a small hub-tip radius ratio a vortex distribution was chosen for the blading which corresponds to a solid-body flow. With this design the total enthalpy h_{tot} is increased with the radius r in the first-stage rotor. In each of the following rotors the total enthalpy is increased by an amount Δh_{tot} which is constant over the blade length, so that the gradient of the total enthalpy $d(h_{tot})/dr$ for the same radii of the rotor is maintained.

Figs. 1 and 2 show the rotor and stator blades of the first stage; the two following stages are of similar design. For each blade section the diameter, stagger angle and axial width of the profiles and a radial line passing practically through the centres of gravity of the blade sections are shown. For the rotor-blade foot a dovetail form was chosen because of the small dimensions and for easy manufacture. The blades were cast from steel by the investment casting process and subsequently ground and polished. The stator blades are fixed by means of a slot in the upper pivot and an adjusting spring. At the hub the blades are supported in rudimentary diaphragms. As the sealing strips extend far into the hub there are only small leakage streams. The stator blades were fitted to the inner and outer channel contours without any clearance. They were machined in the same way as the rotor blades.

Roughness

For roughening the blade surfaces a glueing process was used in which fused corundum in the form of loose emery grain was applied by means of a two-component adhesive on epoxy resin basis. The process was applied in such a manner as to produce an uniformly rough coating with the grains lying in the densest possible arrangement in one layer. After a hardening period of two hours at a temperature of approximately 400 K the adhesive reached the strength required for the machine tests.

The roughness thus produced was removed after completion of the particular series of measurements in a methylene chloride bath. The glueing process chosen offers the advantage over mechanical or chemical roughening that any desired degrees of roughness can be provided one after the other and after the examinations the blades are available again in their original state.

The influence of the roughness on the flow conditions not only depends on the mean grain size k but also on the form of the grains and their distribution on the blade. In order to exclude the latter parameter the blades were uniformly and completely covered with emery grain. The aerodynamic roughness of a surface is usually compared with a standard roughness. For this the equivalent sand grain size k_s has proved satisfactory. The relation between the sand grain size k_s and a number of grain sizes of sandpaper is known from tests [2]. According to [3] this relation also applies to rough surfaces produced by glueing loose emery grain of the same size onto them.

Test Program

For the systematic measurements on the three-stage axial compressor, emery grain of the grades

320 220 and 120

was chosen. Table 1 shows the relation between emery grade number

Nomenclature

d = diameter, mm
k = mean grain size, μm
k_s = equivalent sand grain size, μm
ℓ = chord length, mm
$\dot{m}$ = mass flow rate, kg/s
n = speed, rpm
p = pressure, bar
R = gas constant, J/kg deg K
r = radius, mm
T = temperature, deg K
u = circumferential velocity, m/s
$\dot{V}$ = volume flow rate, m³/s
x = variable coordinate, mm
Δh = enthalpy rise, kJ/kg
η = efficiency
κ = isentropic exponent
ν = hub-tip radius ratio
π = pressure ratio

Subscripts

a = outer
A = outlet, behind the blading
E = inlet, in front of the blading
smooth = hydraulically smooth blade surface
i = internal
N = design point
s = isentropic
tot = total

Downloaded 01 Jun 2010 to 171.66.16.58. Redistribution subject to ASME license or copyright; see http://www.asme.org/terms/Terms_Use.cfm

Table 1 Roughness of blades

emery grade	grain size k in μm	sand grain roughness k_s in μm	sand grain size—chord length ratio $k_s/\ell \cdot 10^3$
320	30	60	1.50
220	60	100	2.51
120	130	180	4.51

and mean grain size k and sand grain size k_s; furthermore the relative roughness k_s/ℓ formed with the mean chord length of the compressor blades of $\ell = 39.9$ mm is given. Fig. 3 shows the rotor blades with emery grade 120. The uniform distribution and dense arrangment of the grains can be clearly seen.

Adhesion of the emery grains to the blade surface was checked several times during the various test series by introducing an endoscope into the flow channel through bores in the compressor casing. This allowed the blades to be viewed without removing the compressor top casing. In none of the test series a visible change to the rough surfaces was noted.

The blades without grain coating are hydraulically smooth, i.e. their roughness is so slight that it is fully covered by the laminar layer of the boundary layer at the blades. Here the relative roughness k_s/ℓ is below $0.15 \cdot 10^{-3}$ on average.

The operating behavior of the compressor was investigated with smooth and rough blades at the speed ratios

$$n/n_N = 0.7 \quad 0.82 \quad 0.9 \quad \text{and} \quad 1.0.$$

With the aid of a throttle valve in the discharge pipe of the test rig the measuring points for the mentioned speed ratios were adjusted in the range between the throttling line and the rotating stall line. The throttling line depends on the resistance characteristic of the discharge pipe with fully opened throttle valve. The rotating stall line is reached on heavy throttling of the compressor; it was assumed to be at the throttle valve position at which blade vibrations in the first rotor blade row were produced as a result of rotating stall. The vibrations were ascertained via a strain gauge on one of the rotor blades with the aid of a telemetry system.

At each measuring point the values for calculating the mass flow, power requirement, pressure ratios, enthalpy rises and efficiencies were measured. In the planes before and behind the blading the flow was measured point by point. The air stream entering the compressor in axial direction was regarded as axisymmetric in the measuring plane before the inlet guide blades so that scanning was only necessary in radial direction. The inhomogeneous field of flow in the measuring plane behind the guide blades of the third stage was scanned, at a free channel height of 43.8 mm, in radial direction on five equidistant radii and in circumferential direction over one blade pitch at each radius in steps of one degree.

The Reynolds number, formed with the inlet velocity and the chord length, proved to be between $3 \cdot 10^5$ and approximately $8.5 \cdot 10^5$, depending on the mass flow. The inlet Mach number of the blading was limited to the value of approximately 0.75 at the design point. The degree of turbulence of the inlet flow was measured with a hot-wire anemometer as 0.7 to 1.1 percent; it decreases with rising mass flow.

Analysis of Measuring Results

The values measured in the planes before and behind the blading are available as a function of the radius or additionally as a function of the blade pitch. Since the results are to be drawn in the form of characteristic curves, representative mean values are to be determined from the local values for the respective flow cross section. The inhomogeneous distribution of the variables of flow is regarded as stationary for this purpose. For determination of the mean values the method proposed by Dzung [6] is used. All variables effective in the system considered are simultaneously changed to mean values in a closed equation system applying the conservation laws to be observed. The variables in the following equations [1–4] are representative mean

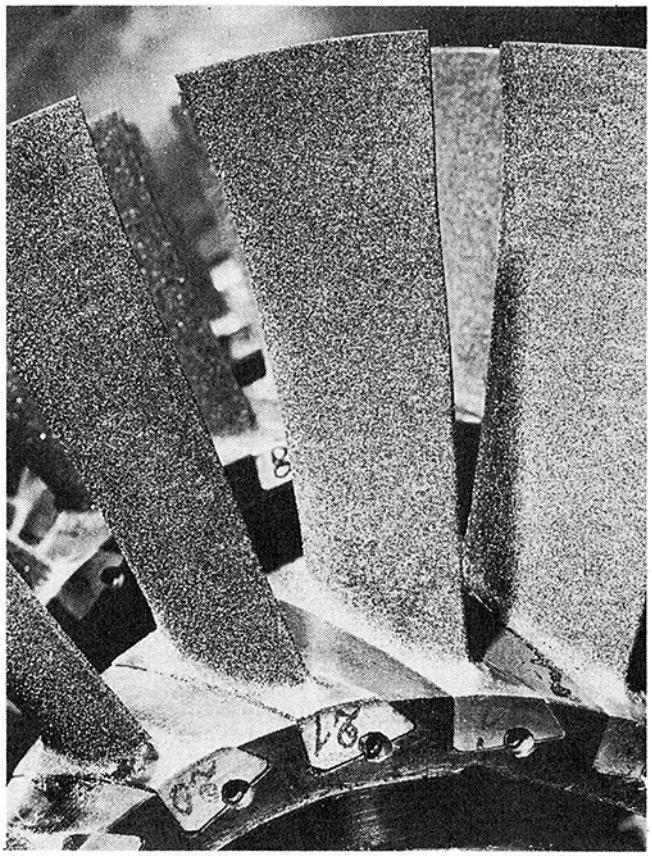


Fig. 3 Roughened rotor blades of the first stage, emery grade 120

values. For representation of the characteristic fields, in addition to the pressure ratios π from the static pressure p or the total pressures p_{tot} in the planes E and A (before and behind the compressor blading),

$$\pi = p_A/p_E \quad \text{and} \quad \pi_{tot} = p_{tot,A}/p_{tot,E} \tag{1}$$

the total isentropic enthalpy rise is used, which according to equation (2) is

$$\Delta h_{tot,s} = \frac{\kappa}{\kappa - 1} \cdot R \cdot T_{tot,E} \cdot (\pi_{tot}{}^{\kappa-1/\kappa} - 1) \tag{2}$$

with κ being the isentropic exponent, R the gas constant, $T_{tot,E}$ the total temperature before the compressor and π_{tot} the total pressure ratio. The total internal efficiency is defined according to equation (3):

$$\eta_{tot,i} = \Delta h_{tot,s}/\Delta h_{tot} \tag{3}$$

where Δh_{tot} is the actual total enthalpy rise of the blading. The suction volume flow rate is given by

$$\dot{V}_E = \dot{m} \cdot R \cdot T_E/p_E \tag{4}$$

with $\dot{m}$ the mass flow rate, and p_E and T_E the static values for pressure and temperature at the compressor inlet.

By applying the laws of similarity the values found under the particular test conditions, i.e., suction conditions, were converted to a uniform reference state, which was given as

$$T_{tot} = 288.15 \text{ K} \quad \text{and} \quad p_{tot} = 1.013 \text{ bar}.$$

Measuring Results

Fig. 4 shows the total isentropic enthalpy rise $\Delta h_{tot,s}$ and the total internal efficiency $\eta_{tot,i}$, each referred to the values at the design point, as functions of the related suction volume flow $\dot{V}_E/\dot{V}_{E,N}$ for smooth blades and blades with different degrees of roughness. Index N designates the values at the design point with smooth blading. The pa-

Downloaded 01 Jun 2010 to 171.66.16.58. Redistribution subject to ASME license or copyright; see http://www.asme.org/terms/Terms_Use.cfm

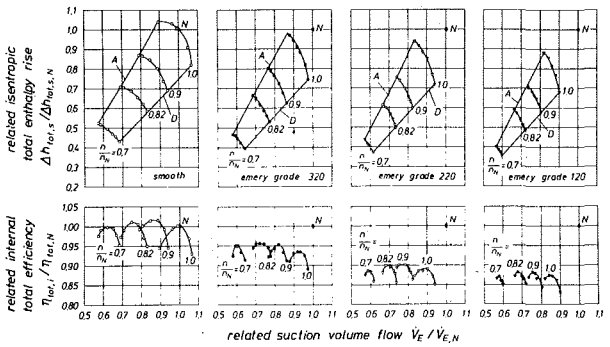


Fig. 4 Characteristic curves of the three-stage axial flow compressor with smooth and roughened blade surfaces: A = rotating stall line, D = throttling line (throttle valve fully opened), N = design point, n/n_N = speed ratio

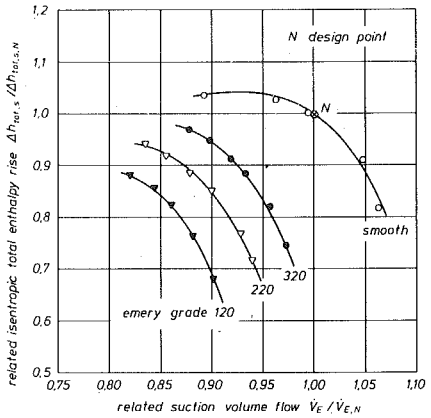


Fig. 5 Characteristic curves of the three-stage axial flow compressor at design speed

rameter in this figure is the speed ratio n/n_N, which in accordance with the test programme is between 0.7 and 1.0. The measuring points on the various speed curves are between the throttle line D and the rotating stall line A. For both smooth and rough blading the design point N is marked.

It can be seen that with increasing roughness, i.e., decreasing emery grade numbers, there is a marked narrowing of the characteristic field and a shift to smaller suction volumes. These points will be dealt with in detail on the basis of the following figures.

From the graphs in the bottom half of Fig. 4 the influence of the blade roughness on the efficiency can be seen. The efficiency decreases at a relative roughness $k_s/\ell = 1.50 \cdot 10^{-3}$ (emery grade 320) by approximately six percent of the nominal value as compared with smooth blading; for the greatest roughness investigated, i.e., $4.51 \cdot 10^{-3}$ (emery grade 120), the difference is about 13 percent. With both smooth and rough blading the influence of the speed on the maximum efficiencies in a test series is small.

The influence of the roughness on the characteristic curves at design speed can be seen from Fig. 5. With rough blading the curves are much steeper than with smooth blading. Already a grade 320 roughness leads to a considerable change in the curve and in the achievable total isentropic enthalpy rise. These changes have their cause in the increasing losses and the smaller deflection angles of the roughened retardation cascades. The suction volume flow rate at the limiting throttle line, which in this figure is marked by the measuring point farthest to the right, decreases by about nine percent for blades with the grade 320 roughness as compared with smooth blades. This decrease refers to the value at the design point. The further stages of roughness each result in an additional shift of three to four percent so that, for instance, with a surface roughness of grade 120 the suction volume at the throttling line is only about the same as that at the rotating stall line with smooth blading. The shift to smaller suction volumes for the measuring points at the rotating stall line is relatively small. The range of the related suction volume covered by the characteristic curves is decreased by about 40 to 50 percent with the chosen degree of roughness as compared with smooth blading. This means that the controllability of a compressor set with rough blading is considerably reduced and adaptation to operating requirements may sometimes no longer be possible.

As shown in Fig. 6, the rough blading not only causes shifting of the operating points to smaller suction volumes but also narrowing of the characteristic field from the throttling line and rotating stall line. Here again the related total isentropic enthalpy rise is shown as a function of the related suction volume with the speed ratio as the parameter. For the sake of clarity only the results of the measuring series with smooth blading and with the smallest and greatest roughness grades, 320 and 120, are shown. The rough blading has an additional throttling effect with the result that the throttling line is shifted so to speak to a line of higher flow resistance. The narrowing from the rotating stall line is due to the fact that the inlet angle range which can be covered without separation of flow decreases with increasing roughness. While the operating points at the rotating stall line have been shifted to smaller suction volumes with rough blading—with the exception of

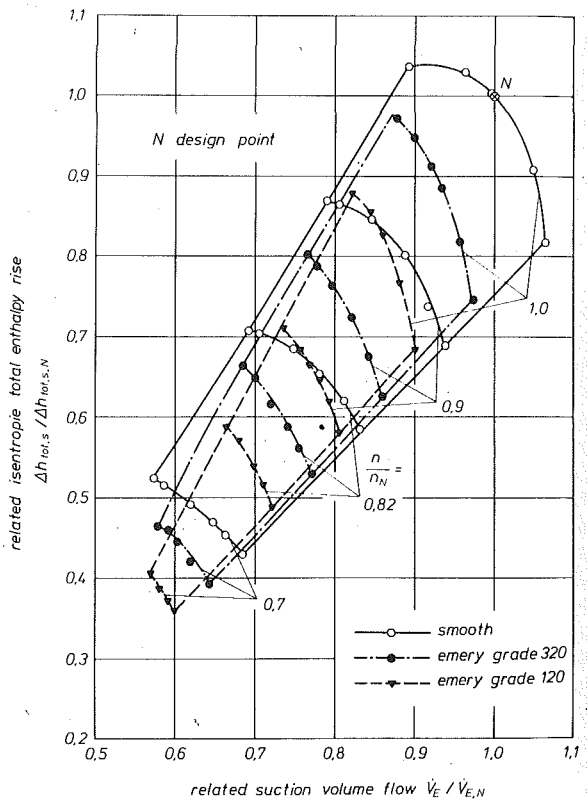


Fig. 6 Shifting of the characteristic curves n/n_N speed ratio

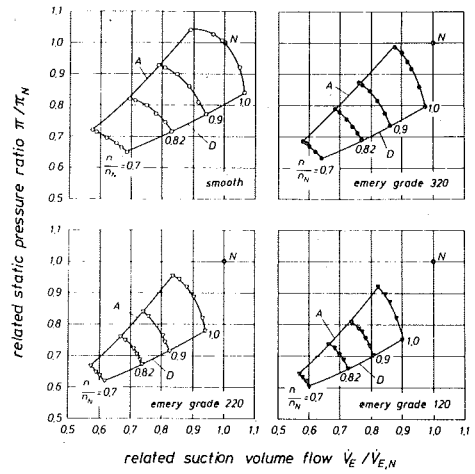


Fig. 7 Pressure lines of the three-stage axial flow compressor with smooth and roughened blade surfaces: A = rotating stall line, D = throttling line (throttle valve fully opened), N - design point, n/n_N = speed ratio

Downloaded 01 Jun 2010 to 171.66.16.58. Redistribution subject to ASME license or copyright; see http://www.asme.org/terms/Terms_Use.cfm

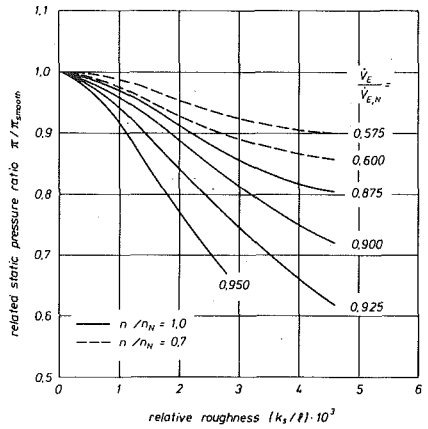


Fig. 8 Influence of the relative roughness on the related static pressure ratio

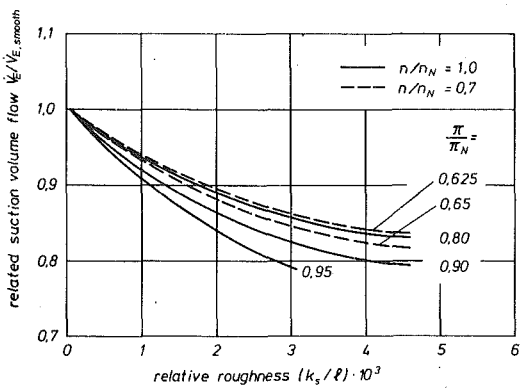


Fig. 9 Influence of the relative roughness on the related suction volume flow

the values for the smallest measured speed ratio $n/n_N = 0.7$—, they are partly far inside the original characteristic field since the total isentropic enthalpy rise or pressure ratio for these operating points are smaller than with smooth blading. Through this it consists the danger with roughened blading to reach or even pass the rotating stall line resp. the surge line during operation.

The static pressure ratio π, which is formed with the static pressures in the measuring planes before and behind the blading and related to the value at the design point of $\pi_N = 1.98$, is shown in Fig. 7 as a function of the related suction volume $\dot V_E/\dot V_{E,N}$. Here again the parameter is the speed ratio n/n_N. With increasing roughening of the blade surface the shifting to smaller suction volumes is accompanied here too by increased steepness of the curves. The pressure ratios achievable with the three-stage blading are considerably reduced.

This is particularly evident from Fig. 8, which shows the influence of the relative roughness k_s/ℓ on the related static pressure ratio π/π_{smooth}. The reference variable π_{smooth} results from the tests with smooth blading at the particular values of the parameter $\dot V_E/\dot V_{E,N}$. The achievable static pressure ratio decreases with increasing relative roughness for constant values of the related suction volume. The gradient is small at first, with relative roughness grades around $1 \cdot 10^{-3}$ it greatly increases and with rising k_s/ℓ values it slowly decreases again. The higher the speed ratio and the larger the related suction volume, the greater the decrease in pressure ratio. For the speed ratio $n/n_N = 0.7$ the reduction with a relative roughness of $k_s/\ell = 4.5 \cdot 10^{-3}$ is 10 to 15 percent as compared with the smooth blading; at design speed, i.e., $n/n_N = 1.0$, this value can rise beyond 30 percent.

Fig. 9 shows the influence of the relative roughness on the related suction volume $\dot V_E/\dot V_{E\text{smooth}}$ with fixed values for the related static pressure ratio π/π_N. The suction volume $\dot V_{E,\text{smooth}}$ was also determined from the tests with smooth blading at the stated values of the parameter π/π_N. The related suction volume decreases with increasing roughness according to the shifting of the previously shown characteristic curves, with the gradient decreasing very quickly with rising k_s/ℓ values. Depending on the related pressure ratio the suction volume decreases with a relative roughness of $4.5 \cdot 10^{-3}$ by about 16 to 22 percent as compared with smooth blading. The influence of the speed ratio is not great as can be seen from the curves for $n/n_N = 0.7$ and 1.0.

Summary

The experimental investigations on a multi-stage axial flow compressor have shown that with increasing roughness of the blade surface the characteristic field is considerably narrowed and the curves, which are steeper than those with smooth blading are shifted to smaller suction volumes. With the chosen roughness grades the suction volume range covered by the characteristic curves is narrowed at the design speed by about 40 to 50 percent as compared with the smooth blading. The achievable static pressure ratio is reduced under these conditions by about 30 percent for a roughness of $k_s/\ell = 4.51 \cdot 10^{-3}$. On the other hand the suction volume decreases at the same roughness according to the static pressure ratio by 15 to 20 percent as compared with smooth blading, with the higher value applying to the higher pressure ratio.

Furthermore the roughness has a great influence on the flow losses in the compressor. The total internal efficiency already decreases at a relative roughness k_s/ℓ of $1.50 \cdot 10^{-3}$ by about six percent as compared with the machine with smooth blade profiles. For the greatest relative roughness investigated, i.e., $4.51 \cdot 10^{-3}$, the difference is approximately 13 percent. In a "transition range", which extends from the surface conditions at which the blades have still a hydraulically smooth appearance to a relative roughness of about $2.5 \cdot 10^{-3}$, the efficiency curve drops relatively steeply and then takes a downward course which is almost proportional to the roughness.

Since even small roughness grades have a great influence on the operating data of axial compressors such as suction volume, pressure ratio and efficiency, the smoothest possible blade surface should be aimed at already in manufacture. If blade roughening during operation cannot be avoided, it can be an advantage to clean or remachine the blades or, in extreme cases, to provide new blading.

References

1 Bammert, K. and Sandstede, H., "Influence of Manufacturing Tolerances and Surface Roughness of Blades on the Performance of Turbines," ASME JOURNAL OF ENGINEERING FOR POWER, Vol. 98, No. 1, 1976, pp. 29–36.

2 Speidel, L., "Influence of the Surface Roughness on the Flow Losses in Plane Blade Cascades," *Forsch. Ing.-Wes.*, Vol. 20, No. 5, 1954, pp. 129–140.

3 Bammert, K. and Sandstede, H., "Measurements Concerning the Influence of Surface Roughness and Profile Changes on the Performance of Gas Turbines," ASME JOURNAL OF ENGINEERING FOR POWER, Vol. 94, No. 3, 1972, pp. 207–213.

4 Bammert, K. and Milsch, R., "Boundary Layers on Rough Compressor Blades," ASME Paper 72-GT-48.

5 Bammert, K. and Turanskyj, L., "Investigations on an Axial Flow Compressor with Low Entrance Hub Ratio and with High Load per Stage in Nuclear Power Plants," *Atomkernenergie*, Vol. 19, No. 2, 1972, pp. 85–91.

6 Dzung, L. S., "Methods of Forming Mean Values in the Theory of Blade Cascades," *Brown Boveri Mitteilungen*, Vol. 54, No. 1, 1967, pp. 37–44.

Downloaded 01 Jun 2010 to 171.66.16.58. Redistribution subject to ASME license or copyright; see http://www.asme.org/terms/Terms_Use.cfm

H. U. Frutschi

Department of Closed-Cycle Gas Turbines,
Brown Boveri and Company, Ltd.,
Baden, Switzerland

The Relationship of Power and Heat Production with Closed Cycle Gas Turbines

As is well known, a part of the waste heat of closed cycle gas turbines can be used without any reduction in power production. However, if the plant is designed for optimal power conversion, the outlet temperatures of the repeatedly intercooled compressors are so low, that only a small part of the removed heat is useful. The closed cycle gas turbine compressor behaves analogous to a heat pump, and therefore an increase of useful heat can be realized without an undue reduction in power production. A moderate increase of the cycle pressure ratio above its optimum, a temperature increase at the compressor inlet and a reduction of the number of intercoolers are good methods for this. Measures, however, which bypass heat from the heater to the precooler, such as recuperator bypass, are not of interest. As far as closed gas turbines are considered, a further degree of freedom is given by the possibility of cycle gas inventory control, as demonstrated in combined power and heat production characteristics. These explanations are not only relevant for fossil fired plants, but also for nuclear high temperature reactors with helium turbines proposed in future.

The Theoretical Background for the Production of Useful Waste Heat

The theoretical ACKERET KELLER Cycle is characterized by an isothermal compression (and expansion) and an infinite recuperator. Fig. 1(*a*) shows the corresponding temperature-entropy diagram. The isothermal compression 1–2*is* consumes the lowest possible power between the two pressures p_1 and p_{2is}, namely

$$P_{1\text{–}2is} = \dot{m}RT_1 \ln\left(\frac{p_{2is}}{p_1}\right) \text{(kW)}$$

The BRAYTON cycle on the other hand is characterized by an isentropic compression (and expansion) 1–2*s*, resulting in a temperature rise from T_1 to T_{2s}. Its power consumption is higher than that of an isothermal compression, namely

$$P_{1\text{–}2S} = \dot{m}cpT_1\left[\left(\frac{p_{2s}}{p_1}\right)^{\kappa-1/\kappa} - 1\right]$$

Since $T_3 = T_{2s}$, this compressor work is useful for heating purposes as $\dot{Q}_{Ho}$.

In reality however, the compressors and recuperators are affected by losses. Whereas the isentropic compression has to be replaced by a polytropic one, the isothermal compression can be subdivided into an infinite number of polytropic ones. The recuperator requires a temperature difference $T_3' - T_3$, see Fig. 1(*b*).

Considering the above irreversibilities, the compressor power consumption is increased to

$$P_{1\text{–}2} = \dot{m}cpT_1\left[\left(\frac{p_2}{p_1}\right)^{\kappa-1/\eta p\kappa} - 1\right]$$

for the polytropic compression and

$$P_{1\text{–}2is_{\text{eff}}} = \frac{1}{\eta_p}\dot{m}T_1R\ln\left(\frac{p_{2is}}{p_1}\right)$$

for the compression with an infinite number of intercooling stages.

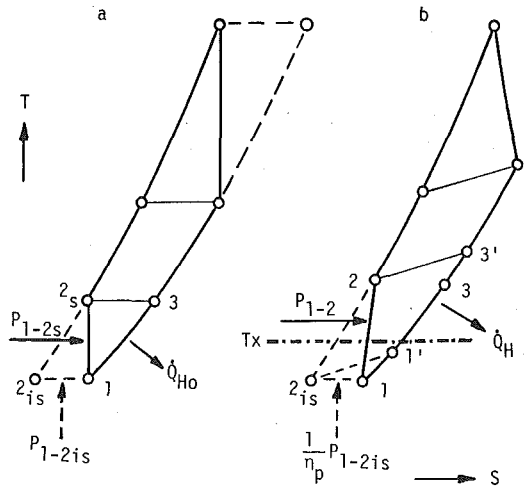


Fig. 1 *T-S* diagrams of closed cycle gas turbines

Contributed by the Gas Turbine Division and presented at the Gas Turbine Conference and Exhibit and Solar Energy Conference, San Diego, California, March 12–15, 1979 of THE AMERICAN SOCIETY OF MECHANICAL ENGINEERS. Manuscript received at ASME Headquarters December 18, 1978. Paper No. 79-GT-103.

Copyright © 1980 by ASME

Downloaded 01 Jun 2010 to 171.66.16.58. Redistribution subject to ASME license or copyright; see http://www.asme.org/terms/Terms_Use.cfm

However, with ΔT Recuperator $= T_3' - T_3$, the useful heat increases to

$$\dot{Q}_H = \dot{m} cp (T_3' - T_x)$$

T_x is the lower limit of the gas temperature for exchanging heat to the water of a district heating network which flows back with the return temperature T_R, as indicated in Fig. 2. T_x is a few degrees higher than T_R.

The process with isothermal compression is giving the maximum power production, but no useful waste-heat as long as $T_3' - T_3 \leqq T_x - T_1$. The process with polytropic compression is giving useful heat but less power.

In the case of heat pumps the so-called coefficient of performance is defined as

$$\epsilon_{HP} = \frac{\dot{Q}_H}{P_e} = \frac{\text{gained heat}}{\text{consumed power}}$$

The same consideration can be made in case of closed cycle gas turbines, if P_e is replaced by ΔP compressor. For the useful heat between the temperatures T_3' and T_X we find

$$\epsilon_{Tx} = \frac{\dot{Q}_H}{\Delta P_{\text{Compr.}}} = \frac{\dot{Q}_H}{(P_{1-2}) - (P_{1-2is\ \text{eff}})}$$

The pressure ratio

$$\Pi_C = \frac{p_2}{p_1} = \frac{p_{2is}}{p_1}$$

has a great influence on ϵ_{Tx} and fixes the possible heating water outlet temperature T_{out}.

Fig. 3 shows ϵ_{Tx}-values for He- and air cycles as a function of the heating water outlet temperature T_{out} under the theoretical sssumption, that the reference cycle is fitted with an infinite number of ideal intercoolers. The heating water return temperature T_R is drawn as parameter. The fixed data are the follows:

T_1		$= 20°C$	see Fig. 2
ΔT_{cold}	$= T_x - T_R$	$= 10°C$	
ΔT_{hot}	$= T_3' - T_{\text{out}}$	$= 20°C$	
$\Delta T_{\text{Recuperator}}$	$= T_3' - T_3$	$= 25°C$	
η_{pol}		$= 0.89$	

The corresponding pressure ratios for He and air are indicated also.

It can be seen that ϵ-values attained with closed-cycle gas turbines are quite satisfactory and much higher than ϵ-values attainable with heat pumps, especially if the high water outlet temperatures which can be reached are considered. This is the consequence of the irreversibilities of the thermodynamic cycles which reduce the performances of heat pumps, but increase those of gas turbines.

Therefore, the compressor of a gas turbine functions as the best heat pump.

Practical Cycles

Intercooling of Compressors. Since isothermal compression can not be realized, an approximation with intercooled compressors is taken into consideration as referred to before. Unfortunately, each intercooler raises the cycle pressure losses, so that the gain of intercooling is outweighed soon. Therefore, for simple closed cycle gas turbines with single heating two intercoolers are the economical

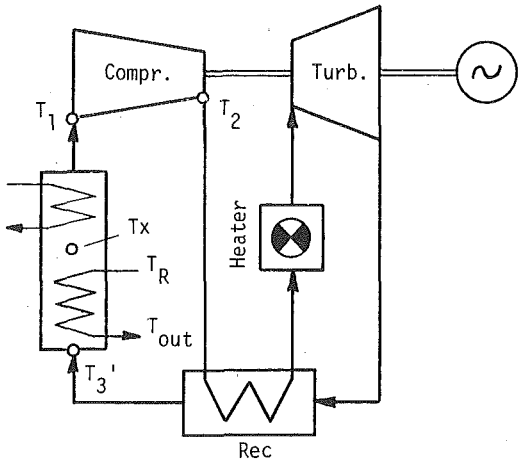


Fig. 2 Cycle diagram of closed cycle gas turbines for waste heat recovery

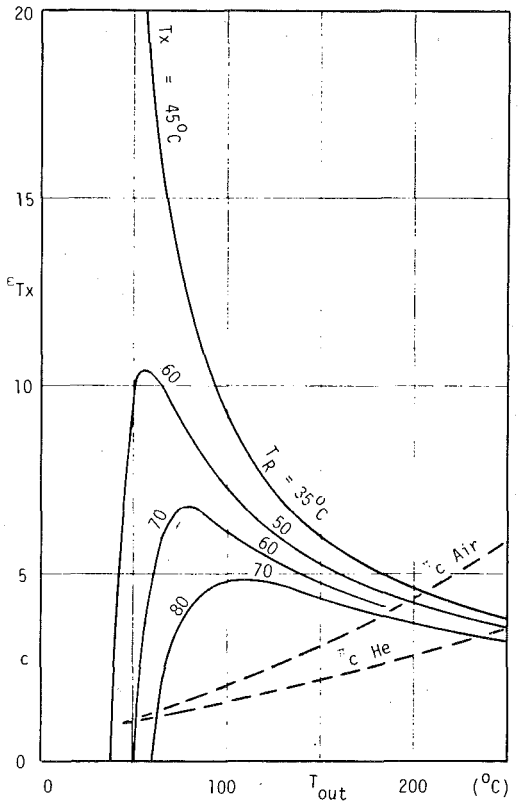


Fig. 3 Coefficients of performance for He and air cycles

maximum, and we define such a cycle now as optimal power production plant.

Fig. 4 shows the thermal efficiencies of closed cycle gas turbine plants without, with one and with two intercoolers as a function of the

Nomenclature

cp = specific heat, kJ/kg, °C
IC = intercooler
$\dot{m}$ = mass flow, kg/s
P = power, kW
p = pressure, bar
$\dot{Q}$ = thermal power, kJ/s
R = gas constant, kJ/kg, °C
T = temperature, K, °C
Δ = difference
ϵ = coefficient of performance
η = efficiency
κ = isentropic exponent
Π = expansion ratio
Π_C = compression ratio

Indices

0 = ideal
1 = compressor inlet
2 = compressor outlet
3 = precooler inlet (ideal cycle)
3′ = precooler inlet
s = isentropic
is = isothermal
p = polytropic
x = point between heating water and cooling water bundles
H = heat
e = electric

Downloaded 01 Jun 2010 to 171.66.16.58. Redistribution subject to ASME license or copyright; see http://www.asme.org/terms/Terms_Use.cfm

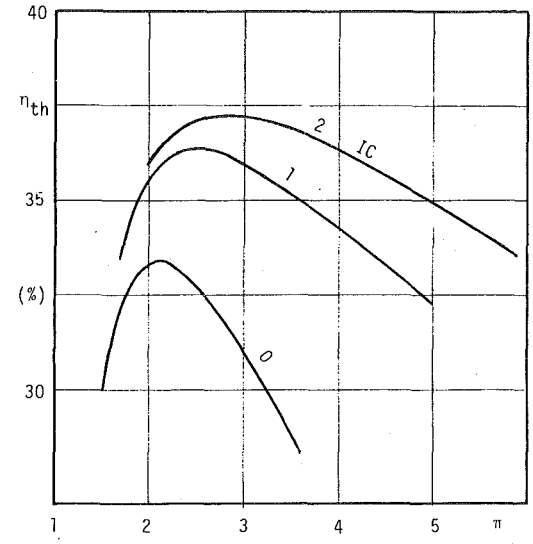


Fig. 4 Thermal efficiencies for different numbers of intercoolers

expansion pressure ratio Π. The cycles are characterized by the following data:

Cycle medium	= He
Turbine inlet temperature	= 750°C
Compressor inlet temperature	= 20°C
Polytropic efficiencies	= 0.89
Recuperator effectiveness	= 90 percent
Heater efficiency	= 90 percent
Relative cycle pressure losses	
0 intercooler	= 8 percent
1 intercooler	= 9 percent
2 intercoolers	= 10 percent
Mechanical and electrical losses	= 5 percent
$T_x - T_R$	= 10°C
$T_3' - T_{out}$	= 20°C

Considering these three cycles with different numbers of intercoolers in their efficiency maxima and computing the energy balances for T_R = 30, 50 and 70°C heating water return temperature, the results of Fig. 5 are obtained.

Because of the higher compressor outlet temperature of the non-intercooled compressor, the useful amount of heat between the temperatures T_3' and T_x is maximum. It is reduced by changing over to intercooled cycles, especially for high T_R-values. For a common heating water return temperature of T_R = 50°C an ϵ_{IC} = 4.6 is to be expected, if changing over from the optimal power production cycle with two intercoolers to cycles with one or even without any intercooler. Also the attainable water outlet temperature rises remarkably, namely from T_{out} = 60°C in the case of two intercoolers to 90°C with one and to 120°C without an intercooler.

Increase of Expansion Ratio. An increase of the turbine expansion ratio above the optimal point results in a higher temperature T_3' and therefore in a greater difference from the lower temperature T_x. More useful heat, a higher water outlet temperature and a small loss of power are the consequences of this measure.

Fig. 6 shows results of calculations in the interesting range of the expansion ratio Π. Especially for higher heating water return temperatures T_R and for cycles with intercoolers, an increase of the expansion ratio can be economically advantageous under certain circumstances. For example, for an increase of Π from Π_{opt} = 2.4 to Π = 3.7 for the cycle with one intercooler, more heat is delivered with an ϵ_Π-value of 5 if T_R = 50°C is considered. For T_R = 70°C, ϵ_Π = 7 is attainable. A moderate increase of the expansion ratio over the optimal value is recommended in all cases, since around Π_{opt} the ϵ_Π-coefficients are very high, as can be seen in Fig. 6.

Temperature Rise at Compressor Inlet. It is evident, that a temperature rise at the compressor inlet increases the useful part of

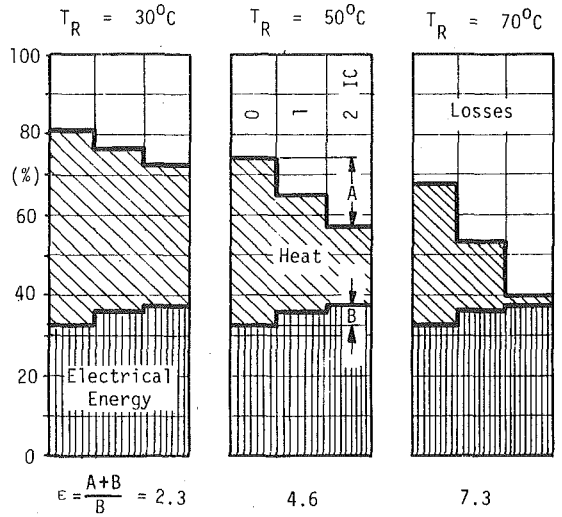


Fig. 5 Energy balances for different numbers of intercoolers

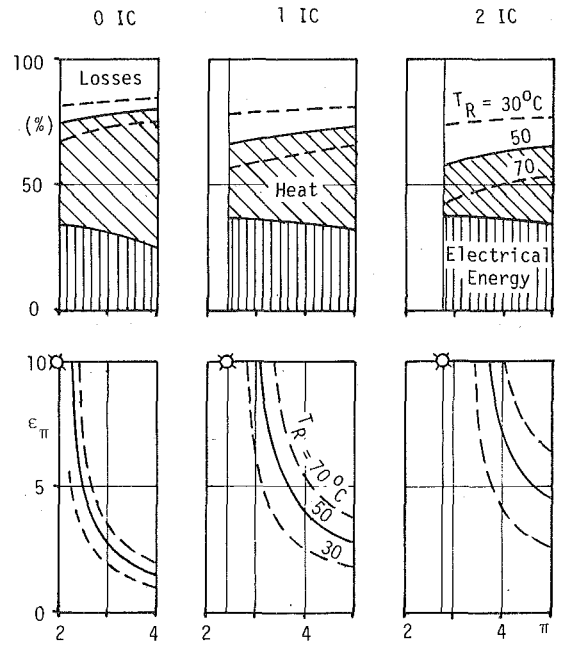


Fig. 6 Energy balances and coefficients of performance for different numbers of intercoolers if the expansion ratio is increased above the optimum ⊠ Efficiency maximum, $\epsilon_\pi \to \infty$

waste heat between T_3' and T_x and reduces the lost part between T_x and T_1 in the same way as a reduction of T_R. However, higher T_1-values reduce the efficiency of the cycle and with this the power production.

For a water return temperature of 50°C and for the optimal expansion ratio of the cycle with one intercooler according to Fig. 4, Fig. 7 shows the resulting energy balance.

We can see that a temperature rise at compressor inlet behaves like a very efficient method to increase the heat production of a given closed cycle gas turbine plant. The loss of power is small, especially if the temperature rise at the water outlet is taken into consideration. T_{out} increases about by the same ΔT as the compressor inlet is lifted. In our example, the temperature T_{out} increases from 120°C (T_1 = 20°C) to 160°C (T_1 = 60°C). For such a water temperature, an ϵ_T-value of 5.6 is hard to exceed.

Recuperator Bypass. As indicated in Fig. 1(*b*), a part of the useful waste heat is produced by the recuperator temperature loss $\Delta T = T_3' - T_3$. Therefore, a further reduction of recuperator effectiveness results in an increase of heat production. This can be easily achieved by bypassing the recuperator either on its low pressure or high pressure side, as indicated in Fig. 8.

Downloaded 01 Jun 2010 to 171.66.16.58. Redistribution subject to ASME license or copyright; see http://www.asme.org/terms/Terms_Use.cfm

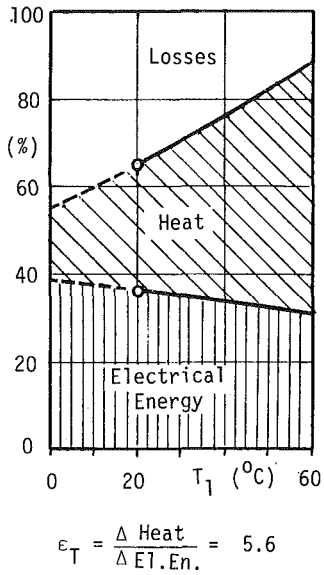


Fig. 7 Energy balance for increased compressor inlet temperature

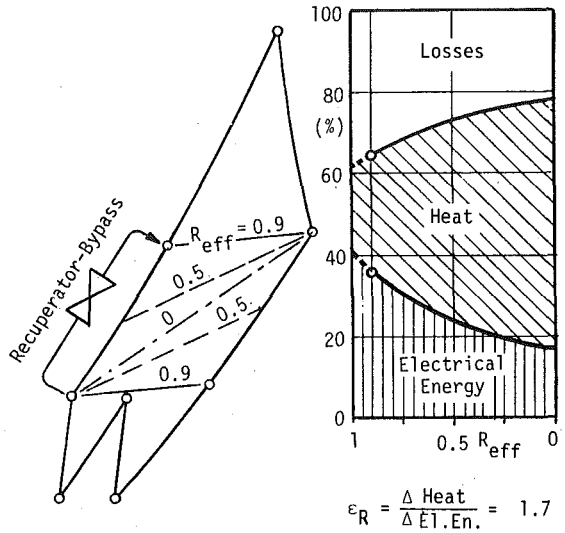


Fig. 8 *T-S* diagram and energy balance for recuperator bypass

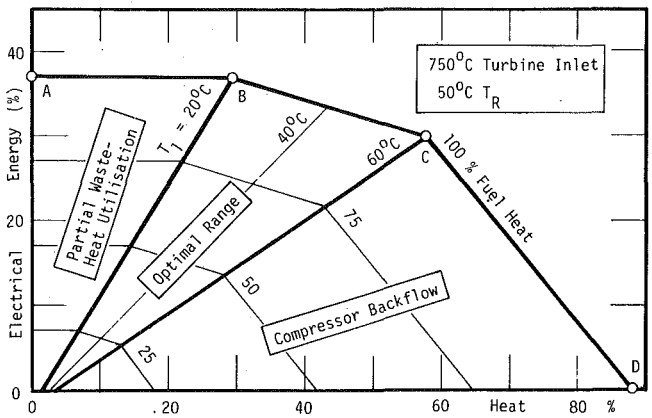


Fig. 9 Characteristics of combined power and heat production with closed cycle gas turbines

However, the corresponding energy balance shows a very poor thermodynamic behavior.

Also for overloading during cold days this method is doubtful since the loss of power is too high.

It is important to remember, that all heat balances in this paper are based on a constant fuel heat (100 percent). In case of recuperator bypass it is possible to maintain the power output constant without overloading the turboset. This will offer much more heat for the district heating system but results in a heavy overloading of the heater, which would have to be taken into account in the design of the heater. However, the production of hot water by means of a costly austenitic heater surface is not lucrative.

Compressor Backflow. Compressor backflow is another method to increase the heat-production at the expense of power. There are three possibilities, namely to provide a backflow to the compressor inlet, to the precooler inlet or to the turbine outlet. All three methods are inadequate in view of the low coefficient of performance, if relatively low compressor inlet temperatures $T_1 \ll T_x$ are considered.

Backflow to the precooler inlet is giving an ϵ_B-value $\ll 1$ and back-flow to the turbine outlet a value <1. Backflow to the compressor inlet is not much better and is not recommended if compressors with intercoolers are considered.

This bad behavior is produced by two effects. First, compressor bypass lowers the pressure ratio noticably, so that T_2 drops. Secondly, the fraction of heat lost between T_x and T_1 is enlarged proportionately to the useful heat between T_3' and T_x respectively between T_2 and T_x for the intercoolers.

In combination with a temperature increase at the compressor inlet up to T_x according to Fig. 7, compressor backflow to the precooler inlet (point 3′) can be considered under certain circumstances to produce more heat with an ϵ_B-value of 1 at the expense of power as shown in the next chapter.

Power and Heat Production Diagram. The closed cycle gas turbine has a further degree of freedom, namely the pressure level. It can be controlled by the cycle gas inventory. Shaft power and heat production are nearly proportional to it, so that a very flat efficiency behavior results. In combination with temperature increase at compressor inlet and compressor backflow to the precooler inlet, the characteristics of Fig. 9 result.

Power production is plotted versus useful heat. A cycle with one intercooler and a heating water return temperature of 50°C are taken into consideration. The relative fuel heat is a parameter.

In point A, the plant produces only electrical power, that is the entire removed heat is wasted. The thermal efficiency is 36 percent. In point B, the maximum amount of heat without reduction of power production is reached. By increasing the compressor inlet temperature (throttling the cooling water flow in the second cooler bundles between T_x and T_1 according to Fig. 7), the heat production can be increased at the expense of power. In point C, the heating network acts as the only heat sink. Maximum fuel utilization is obtained. This good behavior is retained along the 60°C line. For more heat an equivalent reduction of power must be accepted. Under idling conditions of the turboset by compressor backflow, point D with the maximum heat output is reached.

The fuel consumption is nearly proportional to the cycle He-inventory, so that the lines A-O, B-O and D-O are given by gas inventory variation. This results in a very wide field of performance for combined power and heat production with closed cycle gas turbines.

This outstanding operational behavior makes the closed cycle gas turbine an excellent power and heat production installation.

References

1 Keller, C. and Frutschi, H. U., "Closed Cycle Plants-Conventional and Nuclear-Design, Application, Operation," *Sawyer's Gas Turbine Handbook*, Vol. II, 1972.

2 Taygun, F. and Frutschi, H. U., "Conventional and Nuclear Gas Turbines for Combined Power and Heat Production," ASME Paper 70-GT-22.

3 McDonald, C. F., "The Closed-Cycle Turbine-Present and Future Prospectives for Fossil and Nuclear Heat Sources," ASME Paper 78-GT-102.

4 Bammert, K., Boehm, E., and Buende, R., "Nuclear Power Plants With Closed-Cycle Helium Turbine for Industrial Energie Supply," ASME Paper 70-GT-93.

5 Frutschi, H. U., and Müller, W., "Special Operational Properties, Controlability, Waste Heat Recovery and Dry Cooling Tower," NUCLEX Paper A3/10 Basel/CH 1978.

Downloaded 01 Jun 2010 to 171.66.16.58. Redistribution subject to ASME license or copyright; see http://www.asme.org/terms/Terms_Use.cfm

R. S. Holcomb
Engineering Technology Division
Oak Ridge National Laboratory
P.O. Box Y
Oak Ridge, Tenn. 37830

Development Progress on the Atmospheric Fluidized Bed Coal Combustor for Cogeneration Gas Turbine System for Industrial Cogeneration Plants[1]

The Atmospheric Fluidized Bed Coal Combustor Program will develop the technology for a fluidized bed coal combustion system to provide a source of high temperature air for process heating and power generation with gas turbines in industrial plants. The gas turbine has the advantages of a higher ratio of electric power output to exhaust heat load and a higher exhaust temperature than do steam turbines in cogeneration applications. The program is directed toward systems in the size range of 5 to 50 MW(e) and is sponsored by the Department of Energy. A study of industrial energy use has been completed that indicates a large potential market for gas turbine cogeneration systems. Conceptual design studies have been done for typical industrial installations, and some of these results are presented. The conceptual design of a 300 kW(e) test unit has been completed. A number of furnace design firms have been invited to submit their own designs for a 1500 kW(t) (5×10^6 Btu/hr) combustor, from which a final selection will be made. The design of the balance of the test system will proceed in parallel with the combustor design. An engineering design study has been completed by AiResearch Division of Garrett Corporation in which the modifications required to adapt an existing AiResearch 831-200 gas turbine to this cycle for both open and closed cycle operation were determined. Development and testing have been conducted in the areas of fluidization, heat transfer, tube corrosion and coal feeding. Results from heat transfer, tube corrosion, and coal feeding tests are presented.

Introduction

The limited supply of domestic oil and natural gas and the trade imbalance created by importing large quantities of oil make it imperative that oil and gas be replaced by coal in fossil-fired stationary plants to the extent that is practical. The industrial energy consumption amounts to about 40 percent of the total U.S. energy consumption and accounts for about 50 percent of the natural gas and 15 percent of the oil consumed. Thus, very significant savings of gas and oil could be realized if coal were used to supply most of the energy for industry.

Concern for the reduction of environmental pollution has led to strict emission limits being imposed on coal-burning plants. Fluidized bed combustion offers a very promising method for burning a wide range of coals within the emission standards. In fluidized bed combustion, coal is burned in a bed of limestone, which reacts with the sulfur dioxide released from the coal to form calcium sulfate. The bed operates at a temperature of about 870°C (1600°F) so that the coal ash is kept below the fusion temperature, and the calcium sulfate and ash is removed as a dry granular solid which is easily handled for disposal. The lower operating temperature reduces the amount of NO_x formed compared to conventional pulverized coal-fired furnaces.

The environmental effect of coal-fired plants can be further reduced if industrial energy is supplied by cogeneration plants to provide both electricity and process heat, and thus increase the overall thermal efficiency. The gas turbine cycle is very well suited for cogeneration systems, particularly for industrial applications where process heat is required at temperatures of 400°F and higher. The exhaust heat from the gas turbine is available at higher temperatures, and the ratio of electricity to heat is more favorable for gas turbines than for back-pressure steam turbines at these higher temperatures. A fluidized bed coal combustor heating air to drive a gas turbine is an attractive system for industrial cogeneration plants.

[1] Research sponsored by the Department of Energy under contract with Union Carbide Corporation.

Contributed by the Gas Turbine Division and presented at the Gas Turbine Conference and Exhibit and Solar Energy Conference, San Diego, California, March 12–15, 1979 of THE AMERICAN SOCIETY OF MECHANICAL ENGINEERS. Manuscript received at ASME Headquarters December 18, 1978. Paper No. 79-GT-104.

Copyright © 1980 by ASME

Downloaded 01 Jun 2010 to 171.66.16.58. Redistribution subject to ASME license or copyright; see http://www.asme.org/terms/Terms_Use.cfm

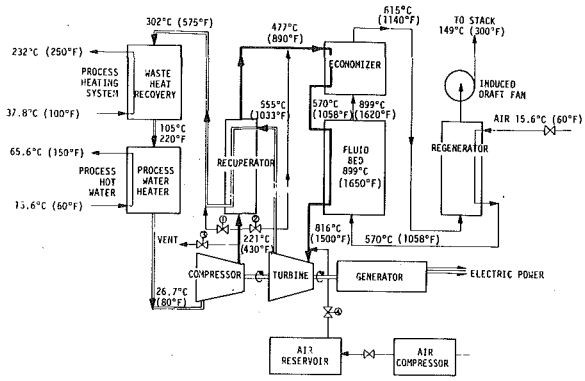


Fig. 1 Flowsheet for a closed gas turbine cycle coupled to a fluidized bed combustor

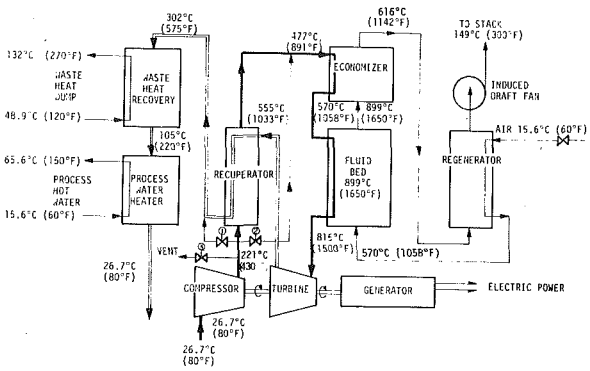


Fig. 2 Flowsheet for an open gas turbine cycle coupled to a fluidized bed combustor

A program for the Department of Energy is underway at the Oak Ridge National Laboratory to develop the technology for a gas turbine cogeneration system coupled to a fluidized bed combustor and to assess the potential market for this type of system. The program entitled "The Atmospheric Fluidized Bed Coal Combustor for Cogeneration (AFBCCC) Program" is directed at developing the technology that can lead to commercial systems in the size range from 5 MW(e) to 50 MW(e).

Description of the Concept

The AFBCCC concept employs a fluidized bed combustor to heat air inside tubes in the bed to drive either an open or closed cycle gas turbine to produce electricity and recover heat for industrial processes from the air leaving the turbine exhaust. In using air rather than flue gases from the bed to drive the gas turbine, the problems of corrosion, erosion, and deposits on the turbine blades are avoided. In addition, the use of the independent turbine air stream permits the use of a closed as well as an open cycle.

The flowsheet for the concept with a closed cycle is shown in Fig. 1. Air from the compressor is preheated in a recuperator and is then sent through the economizer and fluidized bed combustor. After being heated to 816°C (1500°F), the air is admitted to the gas turbine which drives the compressor and electric generator. From the turbine exhaust, the air passes through the hot side of the recuperator to the waste heat exchanger and the process water heater where it supplies heat to the process heating and hot water systems. The air is then returned to the compressor intake. The turbine power output can be varied by changing the closed system pressure by admitting air from the reservoir or venting air. The combustion air is preheated in the regenerator and then is routed to the combustor where it is used to fluidize the bed and burn the coal. The flue gases pass through the economizer and then go to the hot side of the air preheater. Not shown but to be included in the flue gas system is dust removal equipment, including cyclone separators between the economizer and the regenerator, and a bag filter house between the regenerator and the induced-draft fan. Also, a forced-draft fan is to be used on the inlet air to reduce the power for pumping the combustion air.

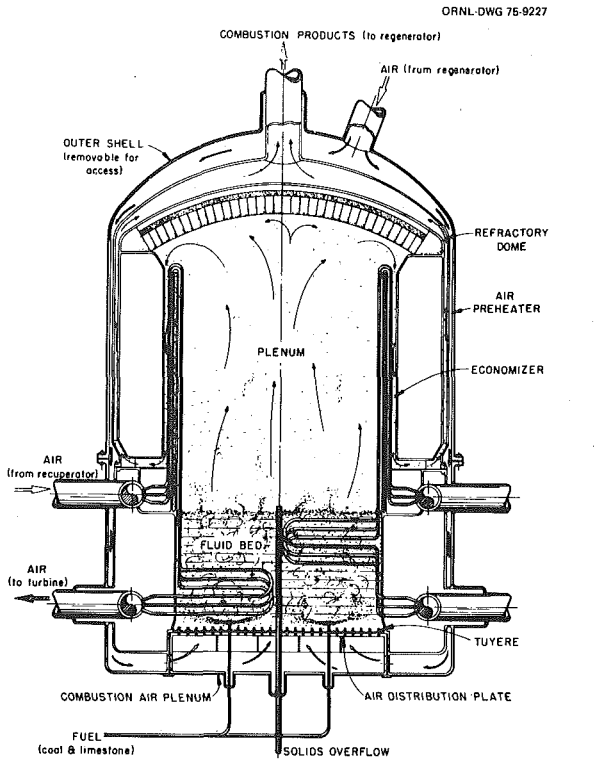


Fig. 3 Conceptual design of a fluidized bed combustor for a gas turbine system

The flowsheet for the concept with an open cycle is given in Fig. 2. The flowsheet is identical except that the turbine system is once-through with the compressor drawing air from the atmosphere and the exhaust air discharged to the stack.

In comparing the closed and open cycle, the closed cycle has two advantages. The first is that the pressure ratio can be selected to yield peak electrical efficiency, and the turbine inlet pressure level can be chosen independently to increase the power density in the system, which may reduce capital cost. The second advantage is that the turbine can follow a changing electrical load by varying the pressure and operate at high efficiency at part load, whereas in the open cycle the turbine inlet temperature must vary, or some air must bypass the turbine which reduces the electrical efficiency at part load. The open cycle has the advantages that existing turbines are more easily adapted for the open cycle concept, and that since the turbine exhaust air is discharged to the atmosphere, it is well suited for direct contact process heating with the hot air.

A conceptual design for a 1.5 MW(t) test combustor is shown in Fig. 3 to illustrate the combustor arrangement for the concept [1]. Combustion air enters at the top of the furnace and passes through the outer annulus to the air plenum at the bottom of the furnace. The air flows through orifices in a large number of nozzles in the distributor plate, and into the 0.6 m (2 ft) deep fluidized bed of limestone and ash where combustion of the coal occurs. The combustion gas flows upward through a plenum where the larger particles blown out of the bed fall back into the bed. The flue gas then flows downward outside the tubes in the economizer section and upward through the annulus in the air preheater zone. The turbine air from the recuperator enters the inlet manifold, passes through the tubes in the economizer and plenum and the heater section in the fluidized bed. The air leaves the outlet manifold and then goes to the turbine.

The fluidized bed is designed for atmospheric pressure and a temperature of 900°C (1650°F). The superficial velocity of the gas through the bed is 0.6 m/s (2.1 ft/s) at design full power of about 1500 kW(t) (5×10^6 Btu/hr). The tube matrix is composed of four bundles with a total of 576 tubes with a 1.3 cm (0.5 in.) OD. The tube matrix is 12 rows deep with a vertical spacing of 3.8 cm (1.5 in.) and a horizontal spacing of 3.8 cm (1.5 in.) in each row.

About a dozen different designs were considered in an effort to

Downloaded 01 Jun 2010 to 171.66.16.58. Redistribution subject to ASME license or copyright; see http://www.asme.org/terms/Terms_Use.cfm

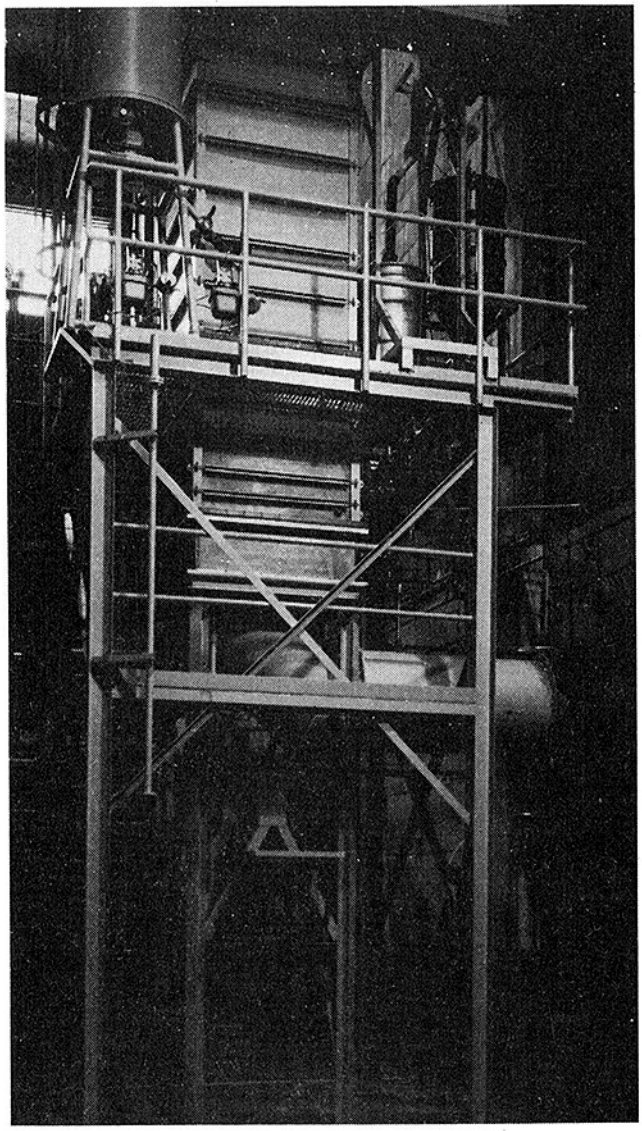


Fig. 4 Fluidized bed cold flow test model

evolve a layout that would best meet the boundary conditions. Of these, fairly detailed layout and analytical studies were carried out for four designs. The various designs and the basic problems are discussed in [2].

Development Program

Program Plan. The overall plan for the CCC program is quite comprehensive. The early phases of the program have included conceptual design, application evaluation and component testing, and technology evaluation. The current program includes commercial-sized reference plant design, test system design, and planned construction and operation, a site specific demonstration plant design and market assessment. The present program places emphasis on participation in all these activities by private industrial firms working with ORNL with the goal of commercial acceptance of the system as early as possible.

Component Test Program. The component test program has been directed toward development and testing in four key problem areas: cold flow model studies on fluidization and solids mixing, coal feed system, fluidized bed heat transfer, and fireside corrosion of tubes in a fluidized bed.

Cold Flow Model. A number of tests were conducted with a 1.3 m (4 ft)-square, 4 m (12 ft)-high Lucite model of the fluidized bed furnace, shown in Fig. 4. The areas of testing include fluidizing velocity, pressure drop, air distribution, coal mixing rate, and tube vibration. The fluidizing velocity tests indicate that it should be possible to

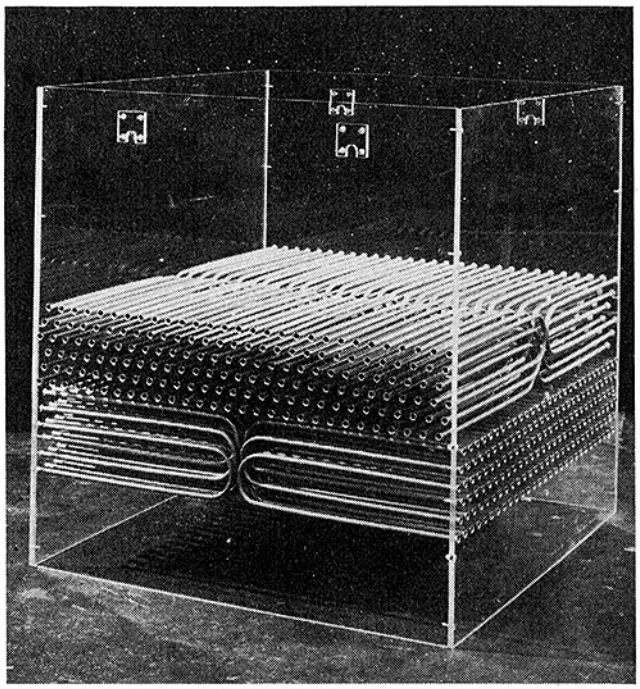


Fig. 5 Tube bundle for cold flow test model

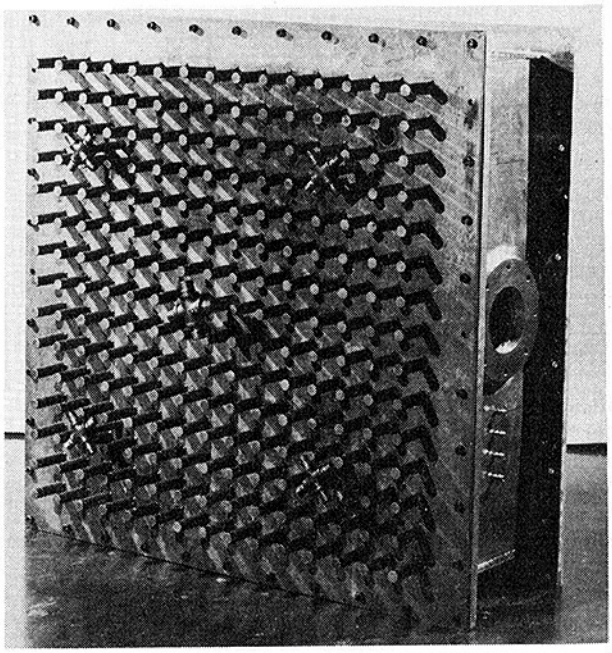


Fig. 6 Air distributor for cold flow test model

operate the furnace at about ⅓ of the full power air flow rate. The coal mixing data showed that adequate horizontal mixing of the coal should be obtained from the four coal feed nozzles at ⅓ of the full power air flow rate. Tube vibration was found having a frequency range of 20–50 Hz, but it was of low amplitude. The natural frequency of a full-length furnace tube was measured and found to be 15 Hz with no support under the horizontal U-bend portion. The results of the vibration test led to the decision to provide supports at the ends of the horizontal U-tubes in the ORNL reference design furnace.

The tube bundle arrangement in the cold flow test model with full-scale diameter tubes is shown in Fig. 5.

A photograph of the model of the air distribution plate is shown in Fig. 6. The air tuyeres are pipe stubs with horizontal holes 90 deg apart to orifice the air. The tuyeres are spaced on a 7.6 cm (3 in.)-square pitch. Coal feed nozzles are located in the four quadrants, and a limestone feed nozzle is located at the center of the plate.

Coal Feed System. Tests have been conducted on components of

Downloaded 01 Jun 2010 to 171.66.16.58. Redistribution subject to ASME license or copyright; see http://www.asme.org/terms/Terms_Use.cfm

three different coal feed systems, and endurance testing has been completed on the system that was selected as the reference design. A coal feed system consisting of a gravity flow splitter feeding four air ejectors for transporting the coal (see Fig. 7) has been tested and found to provide four streams that can be maintained within plus or minus five percent of the mean coal flow rate over the entire operating range with repeatable results. A series of batch flow tests was carried out on this system over a total running time of 175 hrs with good success. The system was selected as the reference design coal feed system and was operated continuously for 1000 hrs without incident.

A coal feed system based on a four-way splitting nozzle in the pneumatic transport line also yielded good test results, although not quite as good as the gravity flow splitter feed system. The split among the four streams was about plus or minus eight percent of the mean value.

Both of these coal feed systems were tested feeding coal of 1600 μm top-size into the fluidized bed cold flow model. Tests were run for coal feed rates and bed superficial velocities corresponding to four power levels from $\frac{1}{3}$ to full power. Both systems gave excellent results over the full range of operating conditions, and no interruption of feed from plugging or other problems were encountered.

Heat Transfer Test. A heat transfer test was run on an air-cooled tube in the FluiDyne Engineering Corporation 45 cm (18 in.)-square fluidized bed furnace at a bed temperature of 900°C (1650°F) over a range of fluidizing velocity of 0.25–0.65 m/s (0.8–2.2 ft/s) with a bed mean particle size of 460 μm. As may be observed in Fig. 8, the heat transfer coefficient from the bed to the tube was found to vary from about 227 W/m^2-°C (40 Btu/hr-ft^2-°F) at a fluidizing velocity of 0.25 m/s (0.8 ft/s) to a value of about 483 W/m^2-°C (85 Btu/hr-ft^2-°F) at a velocity of 0.5 m/s (1.6 ft/s) and was essentially constant at higher velocities [3].

Fireside Corrosion Test. A corrosion test on air-cooled tubes made up of sections composed of 304, 310, 316 stainless steel, Inconel 600, and Incoloy 800 was run in the FluiDyne fluidized bed combustor. The tubes were maintained at a constant maximum wall temperature of about 870°C (1600°F) and an SO_2 level of 300 ppm. The tubes were removed at intervals of 500, 1000, or 1500 hr, and samples were prepared for metallographic examination. The total exposure time was 4500 hr, and examination has been completed for 500, 1000, and 1500 hr exposure.

The results of the examination are encouraging. No evidence of erosion was found, and a thin hard scale composed of about 60 percent $CaSO_4$ was present on the tubes. No measurable loss of wall thickness was found. A metal oxide layer about 0.025 to 0.038 mm (0.001 to 0.0015 in.) was observed on each of the materials. Intergranular oxidation attack for a depth of about 0.03 mm (0.0012 in.) was observed.

No significant increase in the thickness of the metal oxide layer or depth of intergranular attack was found to have occurred between 500 and 1500 hr for the 304, 310, 316 stainless steels and Incoloy 800. Tubes of each of these materials completed the entire 4500 hr test without serious corrosion or tube failures.

Two incidents of high corrosion and wall rupture occurred for Inconel 600 tubes. In both cases, the cause is believed to have been the presence of local reducing conditions at the point of failure. It has been decided that Inconel 600 is too susceptible to corrosion attacks under reducing conditions, and this material was dropped from the test program.

Gas Turbine Evaluation. A survey of gas turbines was made to determine the availability of turbines that could be adapted for use with a coal-fired external heater with a minimum of modification. Only two manufacturers were found that have built gas turbines that have both external combustion chambers and air inlet and outlet ports for a recuperator which would permit adaptation without redesign of the turbine casing. AiResearch Division of Garrett Corporation had built the 500 kW(e) Model 831-200 for the Air Force, and Sulzer-Brown Boveri in Europe has built a number of units in both the 4 MW(e) and 20 MW(e) size.

The AiResearch Model 831-200 turbine was chosen as the reference

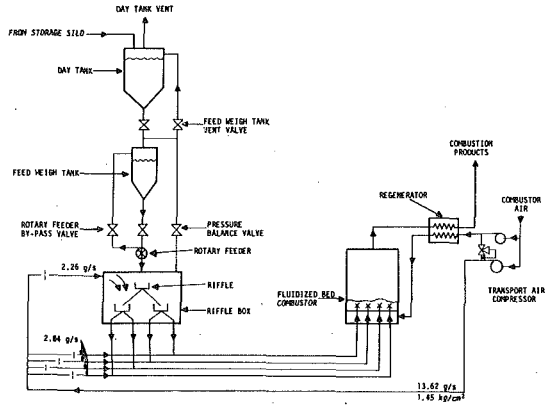


Fig. 7 Flowsheet of coal feed system for the fluidized bed combustor

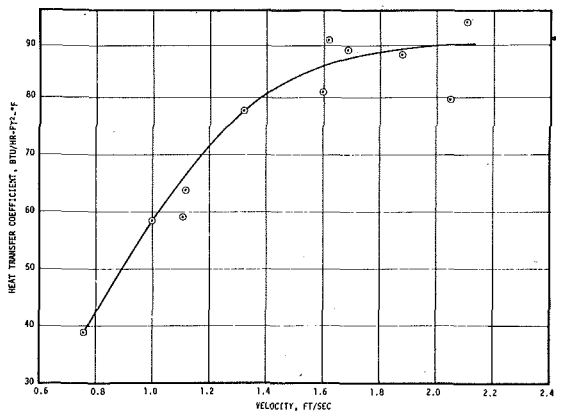


Fig. 8 Heat transfer coefficients to air-cooled tubes in a fluidized bed combustor

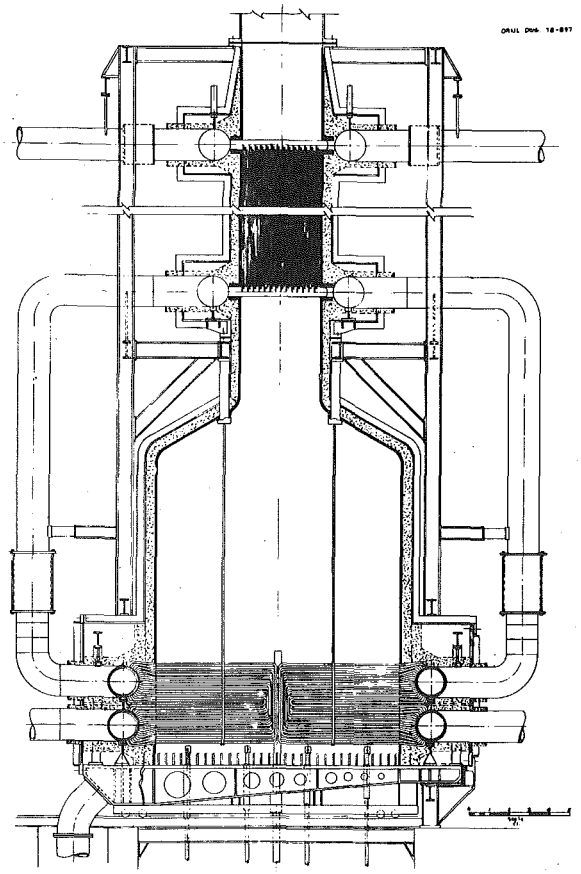


Fig. 9 Conceptual design of a 90 MW(t) fluidized bed combustor for a gas turbine cogeneration system

Downloaded 01 Jun 2010 to 171.66.16.58. Redistribution subject to ASME license or copyright; see http://www.asme.org/terms/Terms_Use.cfm

design for the system test unit. AiResearch was asked to perform an engineering study to evaluate the feasibility of modifying the 831-200 turbine for both open and closed cycle operation with a coal-fired combustor and to determine the modifications that would be required. The study was completed, and they concluded that this turbine could be adapted readily for open cycle operation, and that with somewhat more extensive modification it could also be adapted for closed cycle operation.

Commercial-Sized Plant Conceptual Design. The conceptual design studies of the system included the conceptual design of a 20 MW(e) unit to examine the potential design problems of scaling up to a commercial-sized plant. The primary consideration is the design of the fluidized bed combustor for a heat output of about 90 MW(t) (300×10^6 Btu/hr). This sized unit will require a fairly large area for the fluidized bed. The bed area can be minimized by increasing the bed depth and superficial velocity, but the economical limit for the bed depth of an atmospheric fluidized bed is probably about 1.8 m (6 ft) deep because of the fan power requirements.

The layout drawing for one concept of the combustor is shown in Fig. 9. In this design the bed tube bundle is composed of two bundles of U-tubes that extend halfway across the width of the bed with the turbine air inlet and outlet manifolds on each side of the bed. The combustion plenum, air distributor plate, and tube bundles are designed to be removed as a unit from one side of the combustor by disconnecting the turbine air inlet and outlet pipes and removing bolts from the air plenum flange. In this layout the economizer tube bundle is located above the freeboard. The plenum width is decreased in the economizer region to increase the flue gas velocity through the economizer for improved heat transfer. The combustor is lined with refractory and does not make use of cooling tubes in the combustor walls. The tube bundle is divided into 12 modules to reduce the airflow per manifold. Each bed module has a separate combustion air plenum and air distributor to allow each module to be started up individually to reduce the heating requirements during startup. The principal design parameters are given in Table 1.

Table 1 System parameters for a conceptual design of a 90 MW(t) fluidized bed combustor for a gas turbine cogeneration plant

Turbine air flow, lb/sec	522
(Kg/s)	(237)
Turbine inlet temperature, °F	1500
(°C)	(816)
Compressor outlet pressure, psia	175
(MPa)	(1.2)
Compressor pressure ratio	4.3
Number of tubes in bed	8640
Tube OD, in.	1
(cm)	(2.54)
Tube length in bed, ft	12
(m)	(3.7)
Horizontal tube pitch, in.	2.4
(cm)	(6.1)
Vertical tube pitch, in.	2
(cm)	(5.1)
Number of tube layers in bundle	24
Tube bundle depth, in.	49
(cm)	(124)
Expanded bed depth, in.	58
(cm)	(147)
Freeboard height, ft	12
(m)	(3.7)
Bed width, ft	12
(m)	(3.7)
Bed module length, ft	12
(m)	(3.7)
Number of bed modules	6
Total bed area, ft^2	864
(m^2)	(80)
Superficial velocity, ft/s	5.5
(m/sec)	(1.7)
Bed temperature, °F	1650
(°C)	(900)
Number of coal feed points per bed module	16

System Test Program. It is planned for the test system to be designed as a small-scale version of the commercial-sized reference plant design, both of which are to be designed by a private industrial organization or team. The test system is to be fabricated by a commercial boiler or furnace manufacturing firm.

A test program is to be conducted to obtain operating data that will provide answers to the key technology questions. Performance data will be obtained to establish the combustion efficiency, SO_2 and NO_x emissions of the combustor. Endurance testing will be conducted to determine the corrosion/erosion rates on the tubes in the bed and the reliability of the combustor and the system.

Industrial Energy Assessment. One of the tasks in the program was to survey the use of energy for industrial process heat and electricity. The survey has been completed, and the results have revealed some significant information [4]. A number of industrial energy surveys have been performed, and most of the information required for this program can be obtained from the literature. The energy consumption by industry in 1974 was estimated to be about 28×10^{15} Btu/yr (30×10^{15} J/yr) which amounted to about 39 percent of the total energy used in the United States. Of the energy used by industry, 36 percent was supplied by natural gas, 21 percent by petroleum, 15 percent by coal, and 28 percent by electricity [5]. These data indicate that a considerable amount of natural gas and oil can be conserved as the use of coal for industrial fuel is increased. The amount of electricity used by industry indicates a very good potential application for cogeneration systems.

The use of energy by industry is concentrated in a few industries that are very large users. The industries that are ranked as the six largest consumers of process heat use about 80 percent of the total heat [6]. In order of their ranking by process heat use, these categories are (a) chemicals, (b) primary metals, (c) petroleum refining, (d) pulp and paper, (e) stone, clay, glass, and cement, and (f) food products. In order to have significant impact on industrial fuel use, applications for gas turbine cogeneration systems would need to be found in one or more of these categories of industry.

One of the most important factors in assessing the suitability of the gas turbine cycle for an industrial application is the temperature at which the process heat is used. From one of the surveys on industrial heat use [7], it is estimated that about 30 percent of the process heat is used at temperatures from 177–593°C (350–1100°F), and the remaining 40 percent at temperatures above 593°C (1100°F). In the lower temperature range heat can be supplied easily from either steam or gas turbine systems. The gas turbine cycle is better suited to provide heat with a cogeneration system in the middle range of temperatures. The gas turbine cogeneration system is not adapted to supplying heat at temperatures above about 593°C (1100°F). If the CCC system were used to supply the electricity and the process heat used at temperatures of 593°C (1100°F) or less in the six major industry groups, it would represent a savings of 1.5 million barrels/day of oil and almost 5900 m^3/s (18 billion ft^3/day) of natural gas.

References

1 Fraas, A. P., "Conceptual Design of a Coal-Fired Gas Turbine for MIUS Applications: Phase II Summary Report," (to be published), Oak Ridge National Laboratory, Oak Ridge, Tenn.

2 Fraas, A. P., et al., "Design Study for a Coal-Fueled Closed Cycle Gas Turbine System for MIUS Applications," IEEE Catalog No. 75 CHO 983-7TAB, Oak Ridge National Laboratory, Oak Ridge, Tenn.

3 Holcomb, R. S., "Heat Transfer Performance of an Air-Cooled Tube in a Fluidized Bed Furnace," (to be published), Oak Ridge National Laboratory, Oak Ridge, Tenn.

4 Graves, R. L., Holcomb, R. S., and Tallackson, J. R., "Assessment of an Atmospheric Fluidized Bed Coal Combustion Gas Turbine Cogeneration System for Industrial Application," (to be published), Oak Ridge National Laboratory, Oak Ridge, Tenn.

5 Federal Energy Administration, National Energy Information Center, *Monthly Energy Review*, March, 1976.

6 McDonnel-Douglas Astronautics Co., West, "Industrial Applications of Solar Energy," SAN/1132-1, Jan. 1977.

7 Intertechnology Corporation, "Analysis of the Economic Potential of Solar Thermal Energy to Provide Industrial Process Heat," Vol. 1, Final Report, C0028-1, Feb. 1977.

Downloaded 01 Jun 2010 to 171.66.16.58. Redistribution subject to ASME license or copyright; see http://www.asme.org/terms/Terms_Use.cfm

G. Elmhed
S. Ferm
S. O. Svensson

STAL-LAVAL TURBIN AB
S-612 20 Finspong
Sweden

Industrial Type Gas Turbines for Offshore Applications

The paper discusses, with reference to the power generating gas turbines on the FRIGG TCP-2 platform, the specific and general requirements for offshore gas turbines, and how those sometimes conflicting requirements are met. Furthermore, interesting details of the particular installation on the FRIGG TCP-2 platform are described. The gas turbines on the FRIGG TCP-2 platform are the first ones to be installed in Norwegian water after the Norwegian regulations for "Production and auxiliary systems on production installations, etc." were officially issued in April 1978. Some of these special regulations and their influence on the gas turbine design are discussed.

Introduction

The FRIGG-field located on the 60th parallel athwart the median line between the UK and Norwegian sectors is the first major gas field to be developed in the difficult northern basin of the North Sea. FRIGG, with 200 billion m^3 workable reserves of dry sulphur-free gas, is a resource of considerable significance in the current energy situation.

The development of the field marks a new period of international cooperation between France, Norway and Britain and it is the first field in which all the partners are European.

Elf Aquitaine Norge A/S, a Norwegian subsidiary of the French company "Société Nationale Elf Aquitaine," acts as the main operator for the field development. The other cooperators are Norsk Hydro A/S, Statoil and Total Oil Marine Ltd.

The Joint Venture Kvaerner-Technip acts as the engineering company for compression facilities and associated power generation onboard the TCP-2 platform.

The purchaser of both the UK and the Norwegian produced gas is the British Gas Corporation and the gas is pumped into the UK at the St. Fergus Gas Terminal in northeast Scotland.

The FRIGG-field consists of a complex of five major platforms and a flare stack grouped on both sides of UK/Norwegian median line. On the TCP-2 platform, a CONDEEP construction in the Norwegian sector, the main power supply for the whole field complex will be generated by two gas turbine driven generators with a combined output of 21 MWe.

The two gas turbines are the STAL-LAVAL designed GT 35 manufactured by a consortium formed by NYLANDS VERKSTED of the AKER Group, Oslo, and STAL-LAVAL TURBIN AB, Finspong, Sweden. The two electrical generators are the ASEA GTA 1125.

Requirements for Offshore Gas Turbines

The offshore operations in the North Sea are characterized by the following significant factors:

- hostile environment,
- high cost of space, area and weight on platform,
- continuous operation,
- high cost for loss of production,
- high labor costs,
- hazardous gas area.

All these factors have a great influence on the gas turbine design.

The hostile environment, high winds and seas, and especially the corrosive atmosphere require special precautions.

The high cost of space necessitates a compact unit.

Continuous operation, high cost for loss of production and high labor cost onboard the platform demand a highly reliable unit with maximum accessibility to components. It is also very important to keep the downtime to an absolute minimum. To minimize the downtime, service and repair time has to be short. This is achieved by a design of easily replaceable modules which can be exchanged with minimum disturbance to the surrounding equipment (Fig. 1).

The hazardous gas area implies special design and components for safe operation.

The conflict between some of these requirements will need compromises where the maintenance aspect has a great influence.

The installation of a gas turbine on a platform deck also requires special attention as firstly the erection time should be as short as possible, and secondly the site conditions often can be severe. The solution is a wellproven gas turbine unit which can be preassembled and pretested as much as possible.

GT 35 Gas Turbine Design Characteristics

The GT 35 gas turbine design is a unique combination of the virtues of heavy industrial gas turbines and aircraft derivative engines.

Contributed by the Gas Turbine Division and presented at the Gas Turbine Conference and Exhibit and Solar Energy Conference, San Diego, California, March 12–15, 1979 of THE AMERICAN SOCIETY OF MECHANICAL ENGINEERS. Manuscript received at ASME Headquarters December 18, 1978. Paper No. 79-GT-105.

Copyright © 1980 by ASME

Downloaded 01 Jun 2010 to 171.66.16.58. Redistribution subject to ASME license or copyright; see http://www.asme.org/terms/Terms_Use.cfm

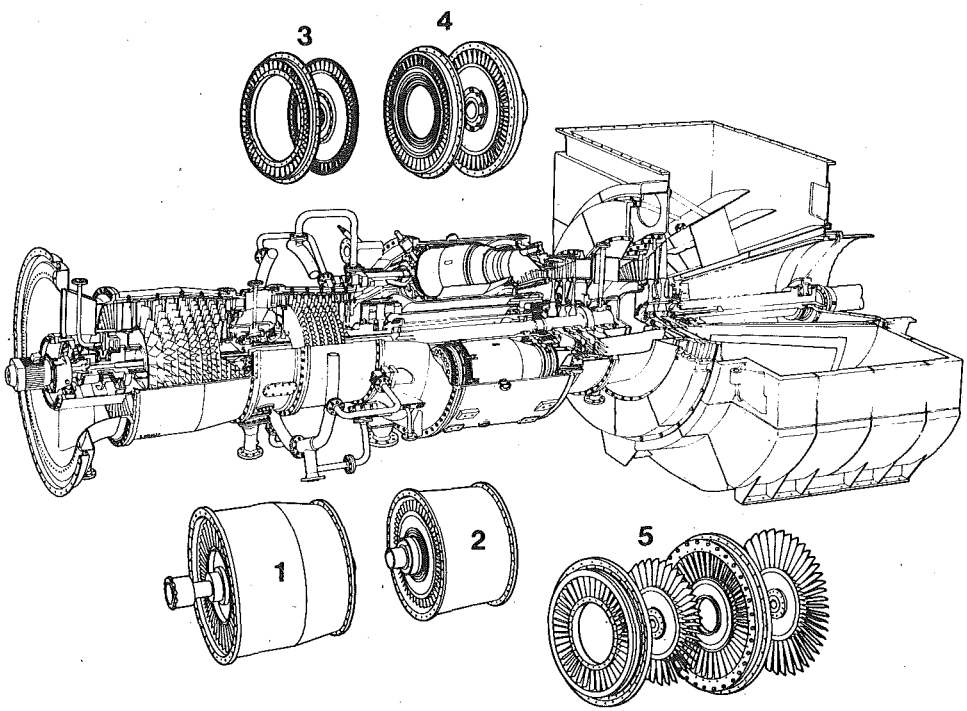


Fig. 1 GT 35 and modules: 1) LP compressor, 2) HP Compressor, 3) HP turbine, 4) LP Turbine, 5) power turbine

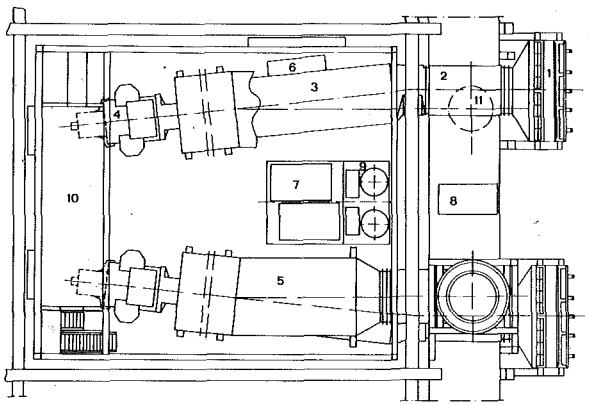


Fig. 2 Gas turbine installation: 1) air intake filter with anti-icing equipment, 2) inlet silencer, 3) gas turbine module, 4) alternator, 5) outlet duct and silencer, 6) fuel and governing unit, 7) lubricating oil tank and coolers, 8) liquid knock out pot unit, 9) starting air module, 10) control room, 11) stack

The GT 35 gas turbine (Fig. 1) consists of a twin-spool industrial type gas generator [1], and a three-stage 3000/3600 RPM power turbine bolted on a common skid and surrounded by a noise attenuating enclosure. Alternatively a two-stage 6000 RPM power turbine can be chosen.

The aerodynamics of the gas generator are very similar to a twin-spool aircraft engine, and give good governing response.

Careful attention to detail has enabled the cold and hot parts to be thermally insulated from each other and has achieved good thermo-flexibility.

Designing compressor and turbine casings as symmetrical shells without longitudinal split allows small tip clearances as distortions during transient thermal conditions are avoided.

Large effectively cooled combustors increase fuel tolerance, decrease thermal stress and give significantly reduced smoke (Bacharach 1 or less). One large fuel nozzle per combustor simplifies maintenance.

There are no wearing parts since seals of the labyrinth type and bearings of the hydro-dynamic tilting pad type are employed. A mineral oil is used throughout the whole gas turbine and generator package.

Separately driven lube oil pumps mean that no power take off gearing is needed on the gas turbine.

Air injector starting involves a large air flow through the gas turbine during the starting period, thus reducing the starting temperature peak giving a lower thermal shock and increased low cycle fatigue life.

Combining a moderate firing temperature with very good turbine material means an inherent reliability. This has also been documented through about 500,000 accumulated hr with the leading turbine having more than 70,000 hr [2].

For the corrosive environment an aluminium based surface coating on the gas generator blades and vanes improves the corrosion resistance.

In addition to this a highly efficient air intake filter arrangement will be used.

A further safeguard is provided by washing not only the compressors but also the turbines separately. The unique combustor windows can be replaced with water injection nozzles for the separate turbine washing.

Gas Turbine Package

The gas turbine enclosure is designed to be compact around the gas generator, but still sufficiently large to allow easy maintenance and inspection work to be carried out.

To allow supervision and service of the auxiliary components during operation the fuel and governing oil systems have been arranged in a separate enclosure alongside the gas turbine enclosure.

On a GT 35 standard package the lube oil module with tank, pumps, filters and coolers is also located beside the turbine enclosure. Due to special installation requirements on the TCP-2 platform the lube oil modules are located separately between the two gas turbine units.

To reduce the influence from platform deck deflections the gas turbine skid is attached to the deck by three main supports which transfer the gas turbine load directly to the deck foundation, using similar techniques to shipboard installations.

Platform Installation

The general restrictions of area and space made the installation rather complicated. In addition the influence of platform structure

Downloaded 01 Jun 2010 to 171.66.16.58. Redistribution subject to ASME license or copyright; see http://www.asme.org/terms/Terms_Use.cfm

and module wall beams necessitated special designs of air intake and exhaust ductings. This gave a unique installation with the two units not parallel to each other and the horizontal part of the exhaust ducting not parallel to the gas turbine itself (Fig. 2).

In the intake duct a corner had to be removed to give space for one of the structure beams. A model test of the air intake arrangement has ensured that a good air flow is still achieved.

Due to the limited height of the platform module, the gas turbine units have been lowered by exclusion of the standard supports. As a consequence of this the lube oil modules have been placed in a recess in the deck in order to give sufficient drainage height.

The exhaust duct is brought horizontally from the turbine outlet above the turbine enclosure to the edge of the platform deck where a vertical 23 m high stack connects. The air intake filter housings are cantilevered from the platform.

As there were definite restrictions for dimensions and weights the operator has required a weight and dimension guarantee. The most critical dimension has been the length, as space for the electrical generator rotor withdrawal must be ensured.

The weight guarantee concerns the total package weight. Weights and centers of gravity of the components were requested at an early design stage as a very careful analysis of the deck structure and load carrying capacity has been necessary.

Environmental Influence

The climate in the northern basin of the North Sea is extremely severe with wind gusts up to 55 m/s and seawaves up to 30 m. The salt content and the humidity of the air are high. The ambient air temperature can during long periods of the year give risk for icing in both the air intake filter and ducting.

The high maintenance cost on an offshore platform has to be considered as well as the extreme difficulty in reaching many of the parts located outside the platform. External maintenance work can on many parts be done only during a few months per year.

Thus, a corrosion resistant material, a 18/12 stainless steel with molybdenum, corresponding to ANSI 316, has been selected for parts such as air intake and exhaust ducting. As no painting is needed, the maintenance work is reduced.

The turbine package is located in an enclosed platform module (Fig. 3).

This module is well ventilated by air taken directly from outside without filtering or heating. That is why many other components are made from the same type of corrosion resistant material as above. For other parts a rigorous surface treatment and painting procedure has been selected.

To protect the internal parts of the gas turbine the intake air is filtered through a four-stage filter. A low velocity filter type has been chosen to reduce the pressure losses in the filter down to 45–50 mm wg in the clean condition. The arrangement consists of an inertial type first stage, a coalescer second stage, and a third and fourth stage combination of a prefilter plus a high efficiency filter of disposable cartridge type. This latter filter combination is used to avoid the possibility of dry salt carry-over. When the relative humidity drops below 75 percent the coalescer pads in stage 2 may begin to dry out and salt particles may leave the coalescer pads. Dry salt crystals in the ambient air may also pass through stages 1–3 at low humidity.

To prevent ice formation in the air intake system, an anti-icing arrangement utilizing exhaust gases has been provided. With a gaseous fuel having low sulphur content, the exhaust gases are clean and can be used to heat the intake air without risk of corrosion. Through a manifold in front of the filter, exhaust gases are evenly distributed to the inlet air. An ejector arrangement is used to transport the exhaust gas. The ejector was chosen instead of a motor-driven fan to reduce maintenance and service of a component which is very awkwardly located.

Gravity operated emergency blow-in doors prevent damage if the intake should be blocked.

Certification of Equipment

General. Equipment on fixed offshore production platforms must be certified as fit for the purpose specified in regulations set up by the authorities in whose jurisdiction the field is located.

The FRIGG-field straddles the boundary of the UK and Norwegian sectors so either British or Norwegian regulations apply. For the TCP-2 platform, in the Norwegian sector, the installed equipment must be approved by the Norwegian Petroleum Directorate (NPD). The applicable detailed regulations were issued in April 1978. Thus the gas turbine generation plant is one of the first plants to be commissioned after the Norwegian detail regulations were officially issued.

Further to the regulations, NPD have for the TCP-2 platform an agreement with Det norske Veritas (DnV) that they inspect and

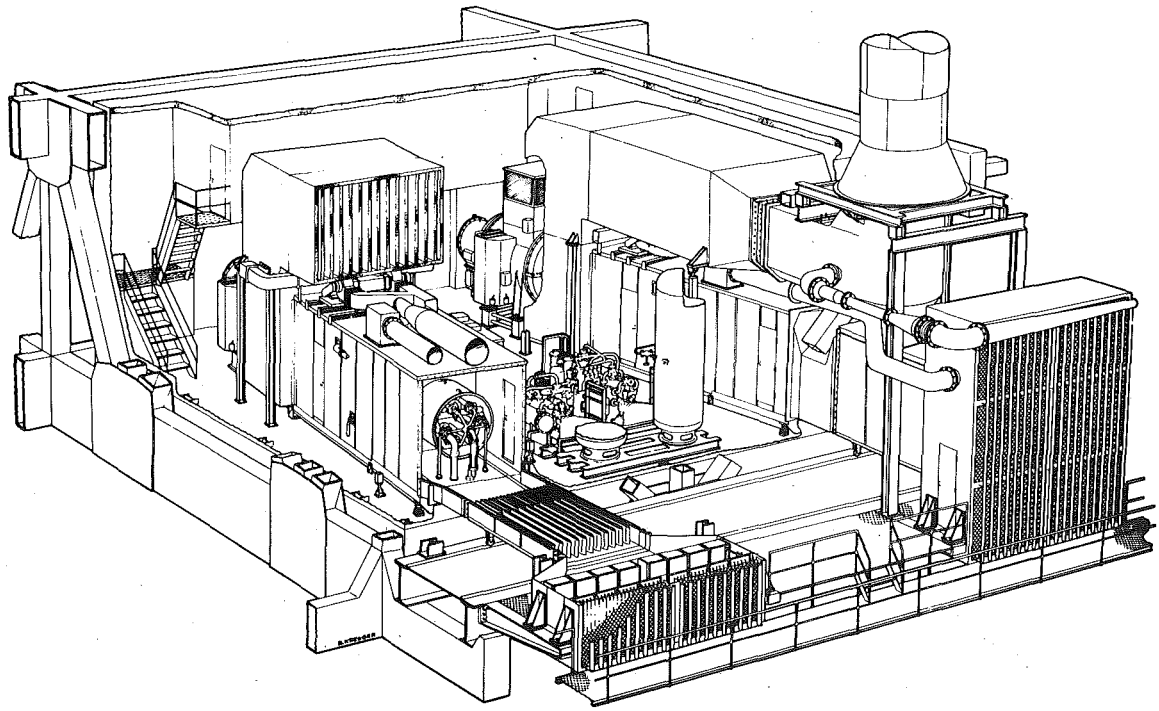


Fig. 3 Platform module

Downloaded 01 Jun 2010 to 171.66.16.58. Redistribution subject to ASME license or copyright; see http://www.asme.org/terms/Terms_Use.cfm

certify the mechanical equipment on behalf of NPD. NPD themselves take care of the systems lay-out and the electrical equipment.

DnV's inspection and certification work is based on the experience and know-how built up from their ship classifications. In addition DnV has issued Process Equipment Recommendations (P.E.R.) and Technical Notes applicable to equipment and systems for oil and gas production facilities on fixed offshore platforms. These P.E.R. and Technical Notes are DnV's interpretations of and additional requirements to internationally accepted codes and standards as ASME, API, BS, Institute of Petroleum, etc.

The operator is responsible for ensuring that the equipment is approved and certified, but has transferred its responsibility to the turbine supplier to comply with these regulations and to obtain design approval as requested by the above authority.

Beyond these official regulations the operators have their own standards and specifications which the supplier must follow. If there should be a conflict between the different regulations the NPD/DnV has the deciding authority.

Gas Turbine Components Subject to Evaluation and Approval. *During planning and design* the following items are subjected to evaluation and comments by NPD/DnV:

Pressure vessels, heat exchangers Turbines, compressors, pumps	DnV only
Area classification Electrical installation Gas detection and alarm system Fire fighting	NPD with assistance from DnV

During the phase of design and engineering: drawings, calculations, welding procedures, general design and fabrication specifications, instrumentation and shut-down systems are subjected to safety evaluation.

During manufacturing and installation: pressure vessels, gas turbines, etc. are subjected to inspection. This inspection work is carried out by DnV as authorized by the NPD.

Area Classification. Type of Equipment

The generation plant is located on the TCP-2 cellar deck in a platform module. Part of the cellar deck is a process area.

The platform module is enclosed with gastight steel walls and well ventilated by forced ventilation to maintain an overpressure and to achieve a safe area classification. Furthermore, the number of gas leakage sources have been kept to a minimum, e.g., no valves and maximum one pair of flanges per fuel gas pipe inside the platform module.

The plant control room is located as a mezzanine arrangement in the platform module. It is well ventilated and classified as safe area.

Inside the platform module each gas turbine is located in an enclosure which is kept at an underpressure compared to the platform module. The fuel and governing oil system is housed in a separate enclosure with underpressure. A differential pressure switch is installed in both enclosures to give an alarm if the pressure difference is less than required.

The gas turbine surface temperature inside the enclosure is higher than 80 percent of the ignition temperature of the fuel gas. According to DnV's Technical Notes the turbine enclosure has to be well ventilated (minimum 90 air changes per hour) to effectively dilute any hazardous gas leakage inside the enclosure.

If the ventilation of the turbine enclosure stops this area will become hazardous and the turbines have to be shutdown. Equipment which must be live after such a shutdown has to fulfil the requirements for Div. 1 Area Classification. Such equipment are post lubrication pumps, emergency ventilation fans, gas detection, fire detection and fire extinguishing equipment. The motor starters for this equipment are housed in sealed, well ventilated boxes and located in a substation at the platform edge, also classified as safe area.

Should the turbine be shut down due to detection of escaped gas, the ventilation of the enclosure has to continue until the turbine surface temperatures have been cooled to a temperature below 80 percent of the ignition temperature of the gas-air mixture present or inert gas has to be released inside the enclosure. The ventilation system which is in operation after a shut down must be supplied from an emergency power source. If the electrical equipment inside the enclosure does not meet Division 2 Area requirement it must not be live after a shutdown.

A "Hot Work Permit" can be given for service jobs on one of the gas turbines where for instance a ducting has to be opened up to the atmosphere thereby destroying the overpressure. Such a "Hot Work Permit" includes extra safety precautions, such as extensive use of gas detectors.

The enclosure around the fuel and governing oil system, where the temperature is below 200°C during operation, should also be well ventilated (12 air changes per hour), and the electrical equipment that is live during normal operation has to meet Division 2 Area requirement.

The gas fuel piping from the fuel treatment plant up to and including the fuel nozzles is designed to allow for a block and bleed ventilation at each turbine stop. The entrapped gas is evacuated outside the platform module to the atmosphere. This ensures that during a standstill no gas leaks into the platform module or turbine enclosure.

Gas detectors have been installed in the turbine enclosure, in the fuel and governing enclosure and in the air intake housing. The detectors in the air intake housing will give a rapid alarm if a major external gas leakage should occur and gas is drawn into the gas turbine inlet. The gas turbine will automatically shut down and, as the extra precaution against reignition of the turbine, a water spray is released into the compressor inlet to extinguish any flames and cool down the hot sections of the gas turbine. The detectors are doubled and strategically located to detect all imminent gas clouds.

The fire extinguishing systems for the turbine and gas fuel enclosures are equipped with Halon 1301 which reduces the amount of agent needed compared with a CO_2 system. In the ventilation ductings dampers have been installed which automatically close when a fire occurs in the corresponding enclosure

To standardize the equipment on the entire platform the gas detection and fire extinguishing equipment has been selected in collaboration with the operator.

Full Load Test

To minimize the adjustment time onboard the platform a full load test ashore has been considered for the gas turbine packages.

To make the test realistic it will be run on methane gas, which was considered to be the only possible alternative as a test with diesel fuel would have made a complete governor resetting necessary on the offshore platform.

Discussions were held regarding the use of other types of gas but the decision was against it as the gas characteristics had to be equivalent to those of the actual FRIGG gas.

Running on propane for instance would have incorporated the risk of introducing gas in a liquid state to the system if not properly heated. The consequences of this would, of course, be fatal.

Maintenance Aspects

Boroscope Inspections. The compressors are inspected through inspection holes in the casings.

Combustors and the high pressure turbine can be inspected through removable combustor windows or fuel nozzles. The nozzles can be removed by undoing four bolts, without disturbing the piping.

Hot Section Inspections. Due to the design of the GT 35, the hot section inspection is carried out with a minimum of dismantling. Fig. 4 shows the operations involved.

The cover around the combustors is moved towards the power turbine to give access to the flame tubes.

Removal of one flame tube allows close inspection of high pressure turbine blades.

The gas generator itself remains undisturbed on its supports.

Modular Maintenance. Of the utmost importance is minimum

Downloaded 01 Jun 2010 to 171.66.16.58. Redistribution subject to ASME license or copyright; see http://www.asme.org/terms/Terms_Use.cfm

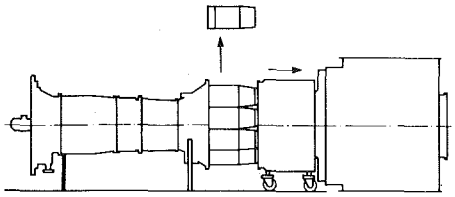


Fig. 4 Removal of flame tube

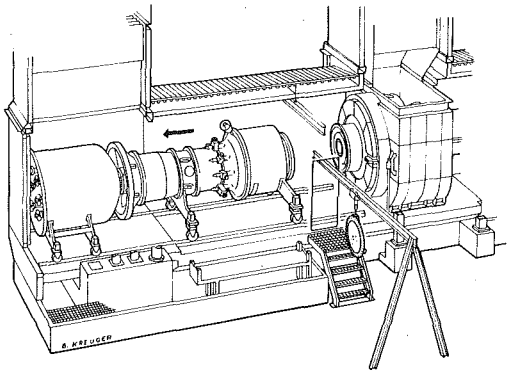


Fig. 5 Removal of low pressure turbine module

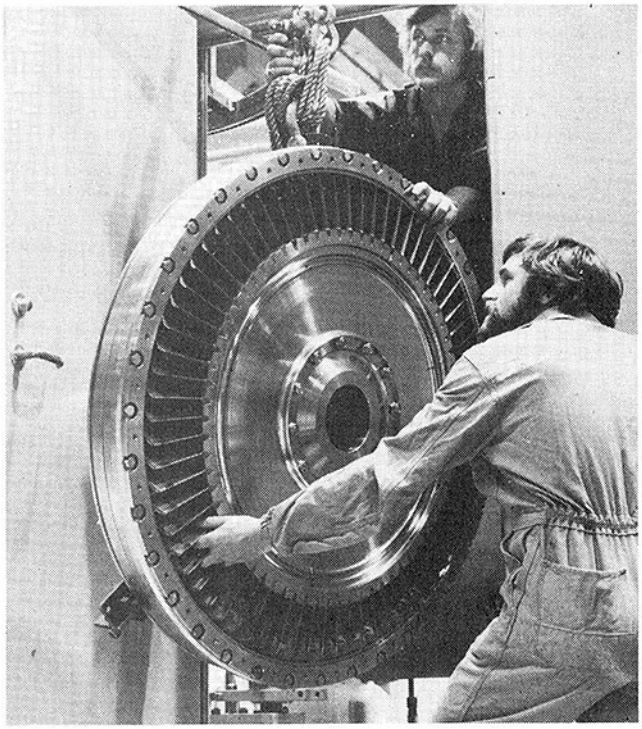


Fig. 6 Low pressure turbine module

downtime for maintenance and repair. This is, of course, primarily achieved by high reliability.

One major difficulty for maintenance onboard a platform is the lack of space. Other factors than the maintainability of the gas turbines are often of higher priority. Thus the need for small and compact modules for maintenance is imperative. This is particularly true for such modules which can be expected to need more repair than others. For example, the high pressure turbine weighs about 250 kg and has a diameter of one meter.

In the TCP-2 platform installation the available space for gas turbines makes the removal and handling of a complete gas generator rather awkward.

The GT 35 design makes it possible to change the gas generator turbine modules through the normal doors in the gas turbine enclosure. The compressor modules can be removed through the inlet ducting.

All dismantling and reassembly can take place within the gas turbine enclosure without the removal of the roof or any wall elements. The lifting tackle is anchored inside the enclosure and an extension rail is fitted outside the enclosure.

The possibility of doing all work inside the enclosure and the removal through a normal door is, of course, of still greater value for applications where the gas turbines are placed on the top deck exposed to the weather.

When the modules have been taken out of the gas turbine enclosure, they can be transported by a special trolley to the maintenance shop on the platform or taken ashore. A replacement module is then taken back on the same trolley and installed. Hence the handling procedure is very simple. Fig. 5 shows the principle for the removal of a low pressure turbine module.

In order to do this the complete gas generator is rolled forward about one meter into the air intake plenum. The wall between the gas generator room and the intake plenum is swung open on its hinges.

The size of the components can be seen in Fig. 6 showing the low pressure turbine module just removed.

The low pressure or high pressure compressor is removed through the inlet ducting after the intake silencer is disconnected and rolled athwartships on two rails. The compressor modules are moved on the same rails directly to the laydown area and replaced by new modules.

Maintenance and overhaul of the electrical generator has also been considered. If necessary, rewinding of the generator stator can be done in the platform module. For removal of the rotor sufficient space has been arranged in the installation lay-out and necessary tackle and tools are provided.

Electrical System Considerations

The small grid on the FRIGG-field complex consists of the two gas turbine plants described here, which in this case provide 10.5 MWe each plus a number of small power plants, mostly acting as standby units.

The power variations on gas production platforms are large with demand for rapid start and unloading of large electrical motors. Thus there is a strict demand on the governing and control of the units to keep frequency and voltage stable. Only after comprehensive dynamic simulation analysis of the grid and of the equipment could the right type of electric generator and exciter be selected. The length of the unit was another factor to consider due to the restricted installation space. These requirements were only met by an ASEA GTA 1125 generator.

When calculating the frequency stability while loading a great advantage was shown in using a twin-spool gas generator with a fast inherent load response. Another advantage in this respect is the electro-hydraulic governor. STAL-LAVAL have been the first to apply electro-hydraulic control on industrial type gas turbines [3] (20 years ago).

The frequency regulator of the gas turbine is equipped with a droop adjustment, which when operating with a droop of a few percent on small grids, automatically increases alternator output at decreasing grid frequency. Normally the frequency is adjusted back to normal by a manual change of the power set point on the turbine governor.

A droop setting of zero gives a frequency that is constant at 50 Hz but this is achieved only by many rapid changes of the gas fuel flow to the one gas turbine acting as frequency stabilizer if the load changes rapidly. In order to avoid rapid changes in the fuel flow and still maintain a constant frequency of 50 Hz the governor is equipped with a load sharing and frequency controlling device.

This device equally divides the load between the two gas turbines and also slowly adjusts the power output in order to keep the frequency constant at 50 Hz.

The grid on the FRIGG-field is laid out to allow the large gas turbines to be separately connected to two sub-grids. The load sharing device is also adopted for this mode of operation and thus two parallel

Downloaded 01 Jun 2010 to 171.66.16.58. Redistribution subject to ASME license or copyright; see http://www.asme.org/terms/Terms_Use.cfm

grids with zero-droop are achieved without a remaining frequency discrepancy.

Conclusion

Gas turbines on offshore production platforms operate in a severe marine environment. The operation duty is long and continuous needing long undisturbed times between overhauls.

The operation of gas turbine for offshore applications is similar to that experienced with gas turbine propulsion ships, an experience where many problems have been encountered.

Extensive development has provided many improvements both in the gas turbine itself and in the installation lay-out including air intake filter designs, operational mode and service.

Due to the high costs on an offshore platform both the erection time and commissioning have to be as short as possible. The gas turbine units will thus be completely installed in the platform module ashore. Further to this a full load test of the units is planned before the module is towed out and lifted onboard the platform.

Acknowledgment

Mr. O. A. Hafnor of Det norske Veritas and Mr. C. Tribout of the Joint Venture Kvaerner Technip have been so kind as to review this paper and have made many valuable comments.

Mr. C. Fischer of STAL-LAVAL has kindly contributed to the chapter Electrical System Considerations.

References

1 Thorén, and Torstenfelt, "Some Technological Aspects of a 15,000 HP Industrial Multipurpose Gas Generator," ASME Paper No. 70-GT-53.

2 Werner, Ekman, and Boltshauser, "Operational and Maintenance Experience of an Industrial Type 14 MW Gas Turbine," ASME Paper No. 77-GT-78.

3 Ljung, "Control Systems for Offshore Turbines Comparing Experience with New Technique, IFAC/IFIP Symposium 1976.

Downloaded 01 Jun 2010 to 171.66.16.58. Redistribution subject to ASME license or copyright; see http://www.asme.org/terms/Terms_Use.cfm

C. F. McDonald
General Atomic Company
P.O. Box 81608
San Diego, CA 92138

The Role of the Ceramic Heat Exchanger in Energy and Resource Conservation

The approaching era of strict energy conservation and eventual energy shortage will have a profound effect on the design of process and power-producing plants, since in the future maximum fuel utilization efficiency will be of the essence. The intrinsic economic worth of industrial reject and exhaust heat is too great to merely discharge to the environment, and means of utilizing this energy by improved process efficiency, or by cogeneration, must be quickly brought to the commercial stage. For future power conversion systems, and in particular open- and closed-cycle gas turbines, emphasis will be placed on maximizing efficiency, and in many cases this can be achieved only by significant increases in operating temperatures. For future gas turbines, process heat plants, chemical plants, basic industries, and waste heat recovery applications, the high level of reject temperature will necessitate the utilization of ceramic heat exchangers for thermal energy recovery. In this paper, current development activities in the field of ceramic heat exchangers for gas turbine applications are discussed, and it is projected that the encouraging results from these programs will stimulate a broader interest in high-temperature waste heat energy recovery. The future role the ceramic heat exchanger will play in energy recovery for different industrial applications is emphasized, and appropriate heat exchanger design criteria, types of construction, surface geometries, and development activities are briefly discussed.

Introduction

It is predicted by many energy experts that the price of fossil fuels will at least double during the next decade. Consequently, heat recovery will become an increasingly important consideration in all industrial operations. Efforts to combat rising fuel prices will be twofold: (1) existing equipment will be modified to recover hitherto wasted reject thermal energy, and (2) design emphasis will be placed on new equipment to improve performance and hence maximize fuel utilization efficiency.

Means of utilizing waste heat by improved process efficiency, or by cogeneration, must be quickly brought to the commercial stage. It is difficult to imagine a device more ubiquitous than the heat exchanger for realizing the industry-wide goal of energy and resource conservation. In the approaching era of strict energy conservation, initial efforts will be concentrated on low- and medium-temperature heat recovery, since existing equipment can be utilized and economic benefits can be realized in the near term.

In the longer term, efforts must be expended to recover high-temperature industrial reject and exhaust heat, which in times of abundant and low-cost clean gaseous and liquid fossil fuel supply was rejected to the environment. In this paper the significant role the heat exchanger can play in high-temperature heat recovery is emphasized. High temperature is defined here as being above 649°C (1200°F).

Contributed by the Gas Turbine Division and presented at the Gas Turbine Conference and Exhibit and Solar Energy Conference, San Diego, California, March 12–15, 1979 of THE AMERICAN SOCIETY OF MECHANICAL ENGINEERS. Manuscript received at ASME Headquarters December 18, 1978. Paper No. 79-GT-106.

For future power conversion systems, and in particular open and closed-cycle gas turbines, emphasis will be placed on maximizing efficiency, and in many cases this can be achieved only by significant increases in operating temperatures. It is projected that for future gas turbines, process heat plants, chemical plants, advanced power conversion systems, basic industries, and many waste heat recovery applications, the high level of reject heat will necessitate the utilization of ceramic heat exchangers for thermal energy recovery. Since development activities are currently under way in the field of ceramic heat exchangers for gas turbine use, this application is stressed herein.

Temperature levels above 649°C (1200°F) in process equipment generally imply gaseous media, and it is projected that the encouraging results from the gas-turbine-related ceramic heat exchanger development programs will stimulate a broader interest in the fields of high-temperature waste heat energy recovery. Since in-depth discussions of ceramic materials have previously been presented in the literature, this paper emphasizes the projected role the ceramic heat exchanger will play in energy recovery for a wide range of different industrial applications. Appropriate heat exchanger design criteria, types of construction, surface geometries, and development activities are briefly discussed. Ceramic heat exchanger technology transfer for the various applications is perhaps the strongest point to be made, since the benefits of high-temperature heat recovery are such that the world-wide efforts to accomplish this should intensify to meet national energy and resource conservation goals.

High-Temperature Waste Heat Recovery

Increasing costs, not only of fuel but also of provisions for rejecting waste heat from a thermodynamic process to the environment, have

Copyright © 1980 by ASME
Downloaded 01 Jun 2010 to 171.66.16.58. Redistribution subject to ASME license or copyright; see http://www.asme.org/terms/Terms_Use.cfm

provided an ever-increasing incentive to improve the efficiency of prime movers. As Carnot demonstrated over a century ago, such improvement implies high peak temperatures in the thermodynamic cycle and hence high-temperature heat exchangers. Obtaining designs that are commercially attractive and yet meet all the boundary conditions is extremely difficult [1]. As temperatures increase, the problems of thermal stress and oxidation become formidable and have a strong effect on important heat exchanger parameters such as cost, structural integrity, reliability, and maintainability.

Heat recovery devices for service at temperatures above 649°C (1200°F) are addressed in this paper, and a number of processes and gas sources in this category are listed in Table 1. This list is far from comprehensive but is presented to illustrate the wide range of processes with high reject gas temperatures that could utilize a ceramic heat exchanger for waste heat energy recovery. It should be pointed out that in many of these processes, waste heat recovery devices are already in service [2, 3].

Approximate operating boundaries for various heat exchanger materials are shown in Fig. 1. For low-grade heat recovery, there is a wide range of materials from which heat exchangers of various types of construction can be fabricated. Over the last few years many articles and papers have been written on heat exchangers for low-temperature heat recovery, so this topic is not discussed in this paper. Instead, emphasis is placed on the possibilities for high-temperature heat utilization/recovery.

For high-temperature heat exchangers, material temperature limits are a major constraining factor. For metallic material use above 649°C (1200°F), the choice is essentially limited to stainless steels and the nickel-base and cobalt-base superalloys with specialized applications for the heat-resistant cast alloys. From Fig. 1 it can be seen that the specific strength (strength/density) of metallic materials decreases very rapidly at elevated temperature. Ceramic materials such as silicon carbide and silicon nitride exhibit excellent high-temperature strength and are obvious candidates for high-temperature heat exchangers. Advanced technology materials such as carbon-bonded carbon filament composites have adequate elevated-temperature mechanical properties, but their applications are limited because they are not usable in the presence of oxygen. The operating islands shown in Fig. 1 are very approximate, and for a particular application the actual properties of the candidate materials must be examined in detail over the operating temperature range.

Fig. 2 was prepared to show, in a simple manner, the possible relationships between heat exchanger materials, applications, and appropriate surface geometries, with emphasis on high-temperature systems. These three topics are covered in more detail in later sections of this paper. Heat sources in the low-temperature (up to about 149°C (300°F)) and medium-temperature (149–649°C (300–1200°F)) ranges use many different working media, involving both single-phase and phase-change modes of heat transfer. Above 649°C (1200°F) most of the applications involve gas-to-gas heat transfer, and several possible applications are identified in Fig. 2. Two classes of applications are shown: (1) those which could benefit immediately from a viable ceramic heat exchanger and (2) advanced systems of the future where high temperatures are inherent in the process. One point to be noted from this figure is the diverse range of applications involving high-temperature operations for which a ceramic heat exchanger could result in energy savings. For each application different types of heat exchanger are suggested, and this subject is discussed in a later section. The transfer of ceramic heat exchanger technology from one application to another will minimize developmental expenditure, which is expected to increase significantly in the next decade.

Table 1 High-temperature waste gases from various industrial process equipment

Type of Process and Gas Source	Waste Gas Temperature Range °F	°C
Gas turbine exhaust	800–1800	427–982
Annealing furnace	1100–2000	593–1093
Cement kiln (dry process)	1150–1500	621–816
Aluminum refining furnace	1200–1400	649–760
Open hearth steel furnace, air blow	1200–1300	649–704
Hydrogen plants	1200–1800	649–982
Fume incinerators	1200–2600	649–1427
Open hearth steel furnace, oxygen blown	1300–2100	704–1149
Ammonia oxidation process	1350–1475	732–802
Zinc refining furnace	1400–2000	760–1093
Copper refining furnace	1400–1500	760–816
Garbage incinerators	1550–2000	843–1093
Sulfur ore processing	1600–1900	871–1038
Copper reverberatory furnace	1650–2000	899–1093
Forge and billet-heating furnace	1700–2200	927–1204
Glass melting furnace	1800–2800	982–1538
Nickel refining furnace	2500–3000	1371–1649
Basic oxygen furnace	3000–3500	1649–1927

Materials for High-Temperature Heat Exchangers

Stainless Steels. Both ferritic and austenitic stainless steels have been successfully used for elevated-temperature heat recovery devices. They have good creep strength and oxidation resistance for long-time service up to temperatures of about 700°C (1300°F). Stainless steels

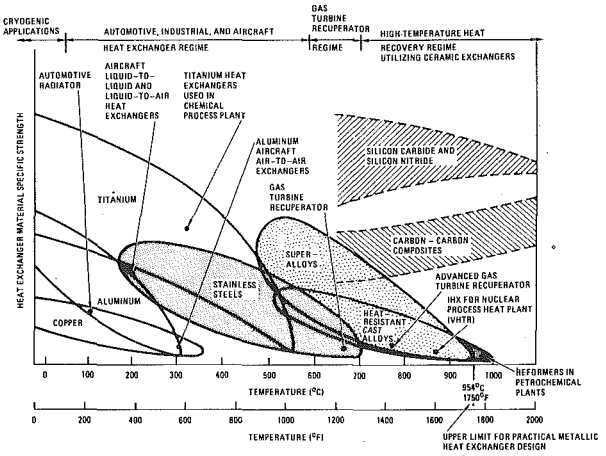


Fig. 1 Approximate operating boundaries for various heat exchanger materials

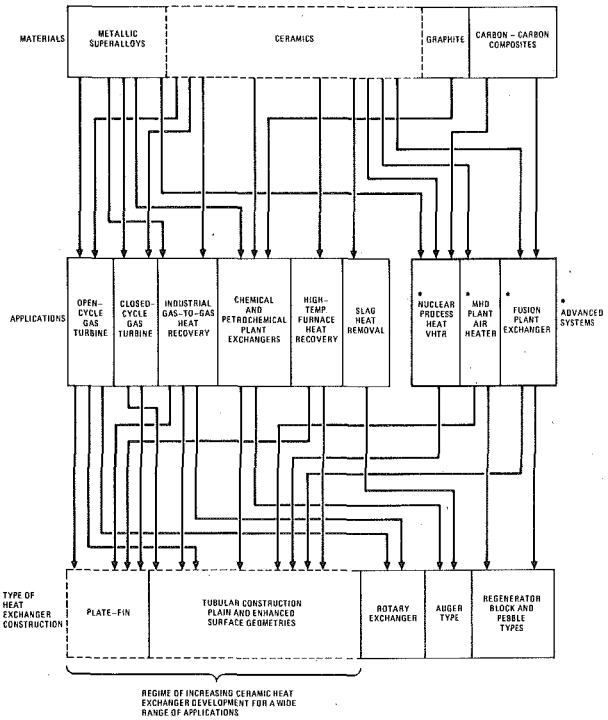


Fig. 2 Heat exchangers for high-temperature waste heat utilization/recovery

Downloaded 01 Jun 2010 to 171.66.16.58. Redistribution subject to ASME license or copyright; see http://www.asme.org/terms/Terms_Use.cfm

in general are readily formable and can be brazed and welded, making them attractive from the standpoint of heat exchanger fabrication.

Superalloys. For high-temperature heat exchangers, material temperature limits are a major constraining factor. Superalloys have been utilized in many high-temperature metallic concepts, and the design and fabrication of superalloy heat exchangers is a well-developed technology. In addition, superalloys are oxidation resistant. Nickel-base and cobalt-base superalloys such as Inconel 600, Incoloy 800, Inconel 807, Incoloy 807, Hastelloy X, and Haynes 188 have been utilized for elevated-temperature service. The upper temperature limit for the Inconels in use today is approximately 899°C (1650°F). Other Inconels, such as Inconel 617, have been considered for tubular heat exchanger designs with peak wall temperatures of 954°C (1750°F). The upper limit for practical metallic heat exchanger design is shown in Fig. 1 as 954°C (1750°F), since this value represents an upper limit for the utilization of the superalloys, which can readily be formed into a variety of heat exchanger surface geometries and construction types.

Heat-Resistant Cast Alloys. In the petrochemical industry, catalytic steam-reforming of hydrocarbon feedstocks for the production of such basic chemicals as ammonia, methanol, and hydrogen requires very high-temperature heat exchangers. Centrifugally cast tubes of 25 Cr/20 Ni steel have been successfully operated in hundreds of plants for many years, and this alloy is still the standard material for the majority of current reformer applications [4]. Cast materials such as HK40, Manaurite 36C, and IN-519 have been in service with tube wall temperatures of slightly over 982°C (1800°F). The centrifugally cast tubes, with about 200-mm (8 in.) diameters about 20 mm (0.8 in.) wall thicknesses, are fabricated for petrochemical plant reformers. This type of tube geometry may be applicable for special purpose metallic heat recovery equipment, and the data in Fig. 1 illustrate that the heat-resistant cast alloys represent the metallic materials with the highest-temperature capability but with limited applications.

Special Purpose Materials. There are several materials (not shown in Fig. 1) which at first sight may seem suitable for high-temperature heat recovery devices but have deficiencies as outlined below. Refractory metals (e.g., molybdenum, niobium, and tungsten) and thoria-dispersed alloys have high-temperature strength capability but are difficult to fabricate (form, weld, braze, etc.) and have little resistance to oxidation, which precludes their use for high-temperature heat exchangers.

Graphite is an excellent high-temperature structural material and has been used as a heat exchanger material for many years, its selection essentially being based on its very high resistance to acid corrosion and attack. Impervious graphite resists a wide range of inorganic and organic chemicals, and heat exchangers of both tubular and block construction have been used extensively in the chemical industry [5, 6]. However, since graphite cannot be welded and there are limits to the possibilities of machining graphite assemblies, the use of cemented joints cannot be avoided. This makes the use of graphite heat exchangers questionable for high-temperature (and high-pressure) service. The role of the graphite heat exchanger is nevertheless an important one for energy recovery in the chemical industry.

For specialized application (such as in High-Temperature Gas-Cooled Reactors), the carbon-fiber-reinforced carbon-based materials have potential for very high-temperature operation. Carbon fiber/carbon composites at 1000°C (1832°F) can have the same or better modulus and strength as steels at room temperature at one fifth of the weight. These composites exhibit virtually no creep and have good fatigue resistance. In recent years, carbon-fiber-reinforced carbon-based materials have been developed which possess very high strength at temperatures of 1000 to 1500°C (1832 to 2732°F). Applications have included aerospace components such as heat shields, rocket nozzles, and thrust chambers which utilize the materials' high-temperature capability, high thermal conductivity, high resistance to thermal shock, low thermal expansion coefficient, high specific heat, and low density. Thus, one can visualize a development of this type of material for specialized industrial applications, starting with components such as ducts and leading to tubular heat excangers. Methods of forming heat exchanger tubes reinforced with carbon fibers are being developed [7], and it is postulated that in coming decades carbon/carbon composites will play a significant role in high-temperature systems.

Ceramic Materials. Because of their high-temperature capability and oxidation resistance, ceramics are obvious candidates for high-temperature heat exchangers. The uncertainties regarding ceramics for this application are their resistance to thermal shock, resistance to thermal fatigue, permeability, and suitability for fabrication and joining techniques.

There are several ceramic candidates for heat exchanger use, and the salient properties for this application are as follows:

- acceptable allowable stress
- low probability of failure
- good thermal shock resistance
- stability at elevated temperature
- low porosity
- low coefficient of thermal expansion
- resistance to high-temperature corrosion and oxidation
- commercial availability
- ability to be fabricated in practical heat exchanger geometries
- adaptability to economic fabrication processes
- low cost

There are three major classifications of engineering ceramics: (1) ceramic oxides, (2) glass ceramics, and (3) carbides/nitrides. These are briefly discussed below.

Ceramic Oxides. Alumina, beryllia, and zirconia are the three oxides used principally as engineering ceramics. Alumina ceramics are inexpensive and easy to produce and can withstand temperatures exceeding 1923°C (3500°F) provided they are not exposed to thermal shock, impact, or highly corrosive atmospheres. Beryllia ceramics are as strong as alumina ceramics, dissipate heat well, and have high thermal shock resistance. However, beryllia is expensive and highly toxic and thus has limited applications. Zirconia ceramics retain strength nearly up to their melting point, which is well over 2204°C (4000°F).

Glass Ceramics. This class of materials are called "glass ceramics" because they contain the same materials found in glass and porcelain but in different proportions. Most of these ceramics are not as strong as alumina, beryllia, or zirconia, and they cost slightly more than alumina. The three common glass ceramics are lithium-aluminum-silicate (LAS), magnesium-aluminum-silicate (MAS), and aluminum-silicate (AS). These materials are stable at high temperature, have a near-zero coefficient of thermal expansion, and resist high-temperature oxidation. These ceramics are nearly as low in cost as alumina and approach the excellent high-temperature properties of beryllia and the corrosion resistance of zirconia. Aluminum-silicate has the best corrosion resistance and strength and is a candidate for high-temperature heat exchangers.

Ceramic Carbides and Nitrides. Silicon carbide and silicon nitride are the strongest ceramics for high-temperature oxidation-resistant service. These materials are either hot-pressed or reaction-bonded into shape. These ceramics are shock resistant and have a fairly low thermal expansion. Although the two materials have significantly different properties, they are both well suited to high-temperature heat exchangers, and extensive development activities are under way with silicon carbide and silicon nitride. From Fig. 1 it can be seen that the specific strength of these materials is far greater than that of even the best metallic materials, and they are expected to play an important role in future high-temperature energy recovery devices.

A silicon-based ceramic in the early stages of development is sialon. This is basically a silicon-nitride ceramic, in which some of the nitrogen is replaced by oxygen and some of the silicon is replaced by aluminum. The constituents—silicon nitride, silica, aluminum oxide, and aluminum nitride (hence the name sialon)—can be sintered at low pressures and temperatures into complex parts. The sintered ceramic is reported to be fully dense, and properties such as thermal shock resistance, low thermal expansion, and corrosion resistance may be superior to silicon nitride, making sialon an excellent potential candidate for high-temperature heat exchangers of the future.

Downloaded 01 Jun 2010 to 171.66.16.58. Redistribution subject to ASME license or copyright; see http://www.asme.org/terms/Terms_Use.cfm

Types of Heat Exchanger Construction

Because ceramic materials have widely different characteristics, each must be closely matched to application conditions. In addition to material choice, the selection of the most appropriate type of construction is an important factor in the design of ceramic heat exchangers for very high-temperature service.

Heat exchangers are an inherent part of almost every industrial process, and their types of construction are essentially tied to important criteria such as (1) thermal duty, (2) working fluids, (3) operating environment, (4) envelope and weight constraints, (5) service life, (6) maintenance considerations, (7) fabricability, and (8) cost, which in many applications is the dominant criterion. Many types of exchanger construction and surface geometries have been utilized [8], ranging from the automobile radiator, one of the simplest applications, to the complex heat exchangers in nuclear power plants.

As mentioned previously, the majority of very high-temperature heat recovery applications involve gas-to-gas heat transfer, and the two most commonly used types of heat exchanger construction involve tubular and plate-fin geometries (shown in a simplified manner in Fig. 3). These two types of geometry are emphasized in this paper, not only because of their adaptability to gas-to-gas applications but because experience has shown they can be fabricated from ceramic materials. Depending upon the application, both tubular and plate-fin types of construction are adaptable to cross-flow, counterflow, and multipass cross-counterflow configurations.

Although plain tubular geometries are simpler than plate-fin variants, they are not as flexible since there is essentially the same surface area on both sides of the exchanger. Flow areas and hydraulic diameters can be changed independently by variations in tube diameter, wall thickness, and tube pitching. The tubes can be oriented in either an in-line or a staggered pattern, although it has been found that the latter gives better heat transfer characteristics and bundle geometries. A compactness array for tubular surface geometries is shown in Fig. 4, where the emphasis is on gas-to-gas exchangers for recuperative gas turbines. As can be seen, differing ceramic tubular geometries are being investigated.

Some flexibility is afforded in the tubular design in that the high-pressure or low-pressure gas can flow inside or outside the tube bundle. The latter case may be of interest to designers of ceramic heat exchangers since the tube walls would be in compression. As will be outlined in a later section, current development activities in the field of tubular ceramic heat exchangers have been directed toward (1) material selection, (2) design, (3) tube-to-header fabrication, and (4) testing to demonstrate structural integrity. In gas-to-gas heat exchangers the heat transfer coefficients are notoriously low, and the use of enhanced surfaces is necessary to improve performance and reduce the size of the heat exchanger. With ceramics in the unfired plasticized condition, a wide variety of surface enhancements in the form of roughening, spiral geometries, local dimpling, and other turbulence-promoting features, together with the utilization of secondary finned surfaces, are under development.

The possible applications for tubular ceramic units outlined in Fig. 3 involve, to a high degree, heat exchangers that must operate with a significant pressure differential between the two working fluids. It is projected that tubular units have the necessary structural integrity for such applications. The tubes would likely be bonded to the header by cementing the joints, thus facilitating repair of heat exchanger elements that may develop leaks in service.

Recent developments in ceramic fabrication techniques have shown that flexible sheets in the green form can be made. These plasticized sheets offer new possibilities in cold or hot forming by extrusion, corrugating, rolling, and molding. Such fabrication techniques permit plate-fin extended surface geometries to be considered for compact ceramic heat exchangers. As shown in Fig. 3, the heat transfer takes place between parallel flat plates or channels which incorporate finned secondary surfaces. Considerable flexibility is afforded with this type of geometry in that passage heights and fin form can be varied independently on both sides of the heat exchanger to provide an optimized

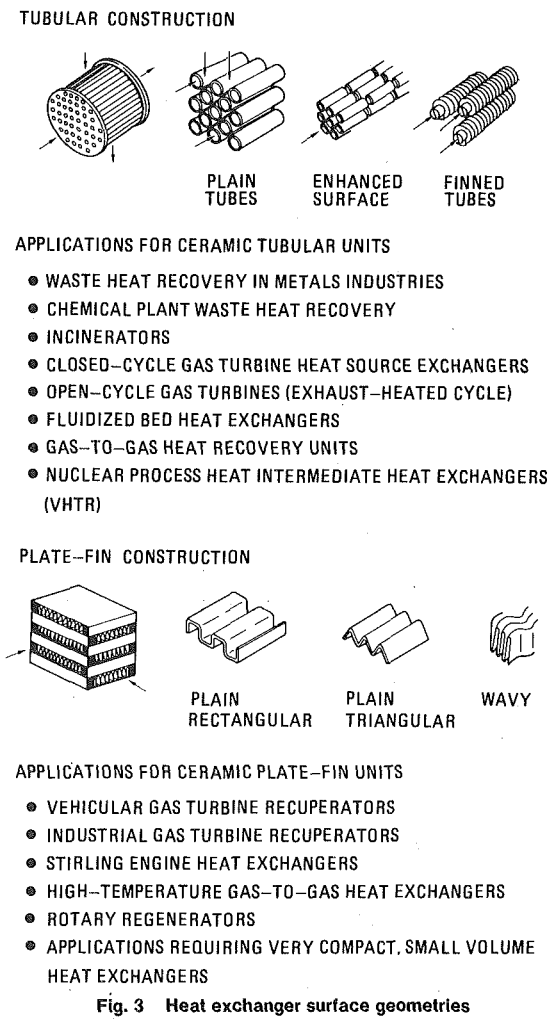


Fig. 3 Heat exchanger surface geometries

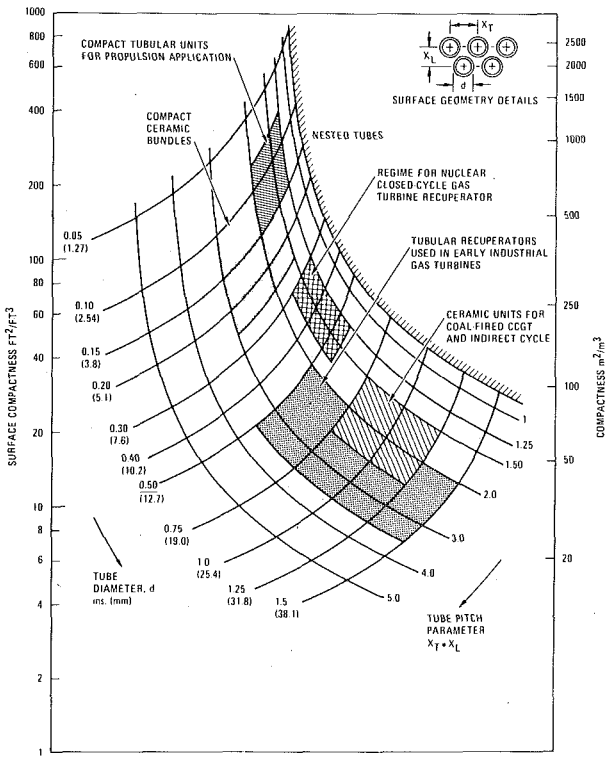


Fig. 4 Surface compactness spectrum for tubular heat exchangers

Downloaded 01 Jun 2010 to 171.66.16.58. Redistribution subject to ASME license or copyright; see http://www.asme.org/terms/Terms_Use.cfm

unit for any particular application. A plot of the range of surface compactness for plate-fin surface geometries is shown in Fig. 5. Extremely compact geometries have been developed for ceramic rotary regenerators for vehicular gas turbine application.

High heat transfer coefficients are not necessarily synonymous with high surface compactness, and while very dense surfaces do result in small heat exchanger volume, some relaxation in compactness is often necessary to obtain acceptable flow frontal area and counterflow lengths. The most interesting development in ceramic plate-fin designs is the promotion of heat transfer through the selection of the fin form. The simplest form is the plain triangular geometry as shown in Fig. 3, but this exhibits poor heat transfer characteristics. As was mentioned for the tubular geometries, surface enhancement is necessary for gas-to-gas heat exchanger applications. In the plate-fin unit, for example, a wavy ceramic fin geometry could be formed so that the periodic change in fluid direction would break up the boundary layer and thus yield higher heat transfer coefficients. The applications for ceramic plate-fin geometries shown in Fig. 3 reflect uses of clean working fluids (to obviate plugging of the compact surfaces with particulate matter, for example) and the need for a small heat exchanger size for compatibility with the prime mover.

The motivation for using compact surfaces is the desirability of gaining high heat transfer performance in a minimum envelope with minimum weight and cost. Designing for ceramics is a new art, and novel surface geometries may well develop for high-temperature heat exchanger applications. Emphasis in this paper is placed on tubular and plate-fin surfaces because they have been demonstrated for a variety of ceramic materials. Initial uses for gas-to-gas heat exchangers embodies plain surfaces, but it is projected that more efficient enhanced surfaces will be used in many applications for energy and resource conservation. As shown in Fig. 2, it is anticipated that tubular and plate-fin ceramic heat exchangers will be used for many high-temperature waste heat recovery processes and for advanced systems of the future.

Ceramic Heat Exchanger Applications

This section covers specific applications for high-temperature heat exchangers and the development activities that are under way to realize viable ceramic heat exchanger configurations. Possible applications for ceramic heat exchangers are outlined in Table 2. Three motivating criteria are given for the utilization of ceramic heat exchangers: (1) high-temperature operation where metallic units are not feasible, (2) hostile and corrosive environments where metallic units would have limited life, and (3) high-temperature applications where metallic units could be used, but the economics of operation favor a lower-cost ceramic alternative.

The information in Table 2 is tentative but clearly shows the motivating element for intensifying ceramic heat exchanger development activities, since the applications spread across the full spectrum of energy intensive industries, high-temperature processes, prime movers, and advanced systems of the future. The three major classes of applications shown in Table 2 encompass the following: (1) near-term possibilities in which ceramic heat exchangers are added to existing processes to improve fuel utilization efficiency, (2) improved prime mover efficiencies of the future (with particular emphasis in this paper on gas turbine applications), and (3) high-technology advanced systems which will play an important role early in the next century, when the clean fossil fuels of today (oil and gas) will be close to depletion and the remaining reserves will be too valuable to merely burn for electrical power generation.

Gas Turbine Applications. Throughout the gas turbine industry, efforts are under way to improve the efficiency of industrial units for a wide range of applications. Rightfully, the bulk of the research and development work is aimed at maximizing the output from the turbomachinery itself by increasing firing temperature, and this leads to the utilization of advanced blade cooling methods (water cooling, for example) or ceramic components, or a combination of both. In addition to these development activities, a role for the ceramic heat exchanger in specialized applications is envisioned [9]. In the future, the electrical power generating gas turbine must be capable of oper-

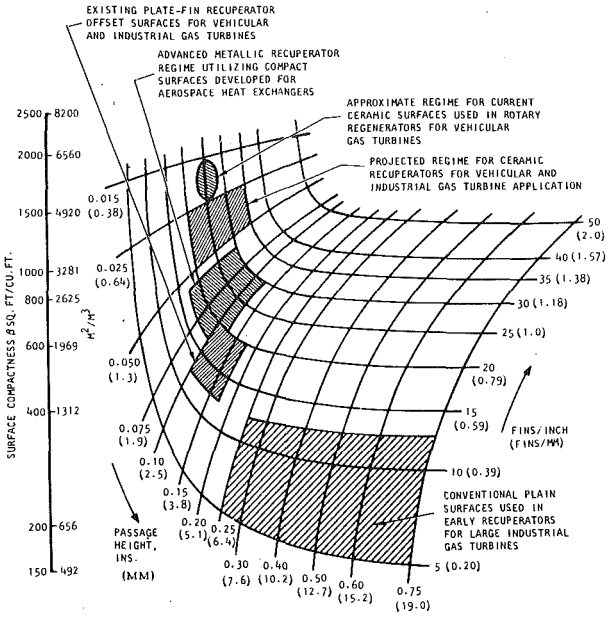


Fig. 5 Surface compactness spectrum for plate-fin heat exchangers

Table 2 Possible ceramic heat exchanger applications

	Applications	High-Temp. Operation	Corrosive Operating Environment	Material Economic Considerations
Near-term possibilities: 5 years	Waste heat recovery			
	Chemical plants	×	×	×
	Basic metal refining industries	×	×	×
	Steel-making soaking pits	×	×	×
	Furnace gases	×	×	×
	Incinerators	×	×	×
	Molten slug heat recovery	×	×	×
	Petrochemical industry			
	Ethylene cracking Reformer tubes	×	×	×
	Power plant combustion air preheaters		×	
Longer-term possibilities: 5–15 years	Gas turbines			
	Vehicular gas turbine recuperators	×		×
	Industrial gas turbine recuperators	×	×	×
	Exhaust-heated cycle exchangers	×	×	
	Coal-fired closed-cycle turbines	×	×	
	Stirling engine exchangers	×		×
	Fluidized bed exchangers	×	×	×
	Advanced solar collectors	×		×
	Coal gasification	×	×	×
Advanced systems	Nuclear process heat			
	Intermediate exchanger for VHTR	×		×
	Reformer tubes	×		×
	Thermochemical water splitting (VHTR and solar)			
	H_2SO_4 exchangers	×	×	×
	Helium-to-H_2SO_4 exchangers	×	×	×
	MHD plant air preheaters	×	×	
	Fusion plant exchangers	×		×

Downloaded 01 Jun 2010 to 171.66.16.58. Redistribution subject to ASME license or copyright; see http://www.asme.org/terms/Terms_Use.cfm

ation on "dirty fuels" which thus far have not been exploited in this type of prime mover, i.e., coal, coal-derived fuels, peat, wood, refuse, etc., and it is in this type of application that the ceramic heat exchanger could make a significant contribution toward the national goal of resource conservation. Gas turbine cycles utilizing a ceramic heat exchanger are shown in Fig. 6 and are briefly described below.

Open-Cycle Gas Turbine. The simplest form of heat exchanger cycle utilizes a recuperator to transfer heat directly from the turbine exhaust to the compressor discharge air before it enters the combustor. This cycle is applicable to industrial and vehicular gas turbines of modest pressure ratio (not much higher than 8 to 1 for maximum benefit). As the cost of clean fossil fuels (oil and gas) continues to increase, the utilization of the recuperative gas turbine is expected to increase significantly [10].

For industrial gas turbine applications the heat exchanger industry has responded to the need for improved recuperator concepts (essentially designs capable of long life in a cyclic environment), and several new types are now entering commercial service [11–13]. As turbine inlet temperatures continue to increase, the introduction of a proven ceramic recuperator for industrial gas turbine application could result in improved engine operating economics [14].

In the case of the industrial gas turbine, the incorporation of a recuperator is at the engine owner/operator's discretion. For the vehicular gas turbine, the exhaust gas heat exchanger is a mandatory component to match the specific fuel consumption of the diesel engine, particularly at part-power. In the case of the small automotive gas turbine, currently under development, legislated automobile minimum fuel consumption to meet the nation's conservation goals will put increasing importance on heat exchanger performance. Perhaps the biggest challenge for the heat exchanger manufacturer is the vehicular gas turbine field, which includes automobiles, trucks, off-highway equipment, and military battle tanks. Utilization of low-cost materials and high-volume manufacturing techniques is necessary to achieve low initial costs.

The many problems associated with heat exchangers for vehicular gas turbines have been discussed previously [15]. For vehicular application, most of the ceramic heat exchanger development work, in the form of rotary regenerator disks, has been done by Corning Glass Works [16]. Significant regenerator advancements have been made in the last few years for small vehicular gas turbines [17]. Early regenerator configurations utilized a drum matrix, but it was found that disks could be better integrated with the turbomachinery, had simpler seal arrangements and drive mechanisms, and were superior from the structural standpoint. A view of a drum matrix and two compact regenerator disks is shown in Fig. 7.

To approach the excellent fuel consumption of the diesel engine, the development trend for vehicular gas turbines is toward high turbine inlet temperature (i.e., on the order of 1371°C (2500°F)), and this necessitates the use of ceramics in all the hot end components. To date, the main emphasis has been placed on use of the ceramic rotary regenerator. However, with the future trend toward higher specific power cycles (increased compressor pressure ratio), the rotary regenerator may lose its advantage because of more severe sealing and support problems.

While still in the early stages of development, the fixed-boundary ceramic recuperator may find acceptance in future vehicular gas turbines. With emphasis on a high degree of compactness (for compatibility with the turbomachinery), ceramic plate-fin geometries are under development, and an example of an early cross-flow module is shown in Fig. 8. An example of a compact, counterflow, ceramic plate-fin recuperator module made from reaction bonded silicon nitride using thin film forming techniques [18] is shown in Fig. 9. An ingenious and novel ceramic recuperator under development in the Federal Republic of Germany [19, 20] embodies a prime surface of

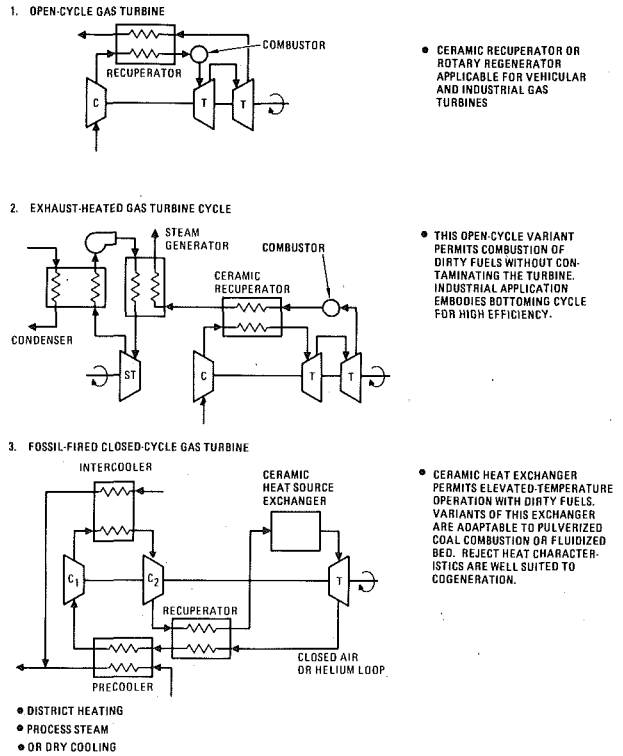


Fig. 6 Gas turbine cycles utilizing a ceramic heat exchanger

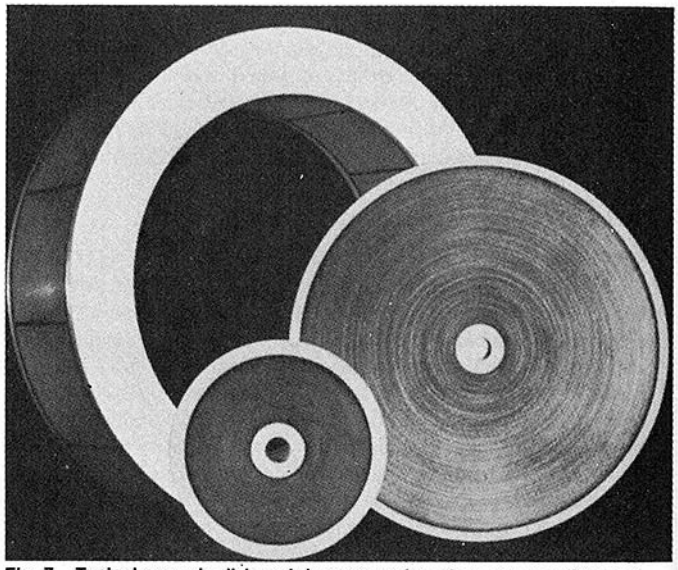


Fig. 7 Typical ceramic disk and drum cores for rotary regenerative heat exchangers

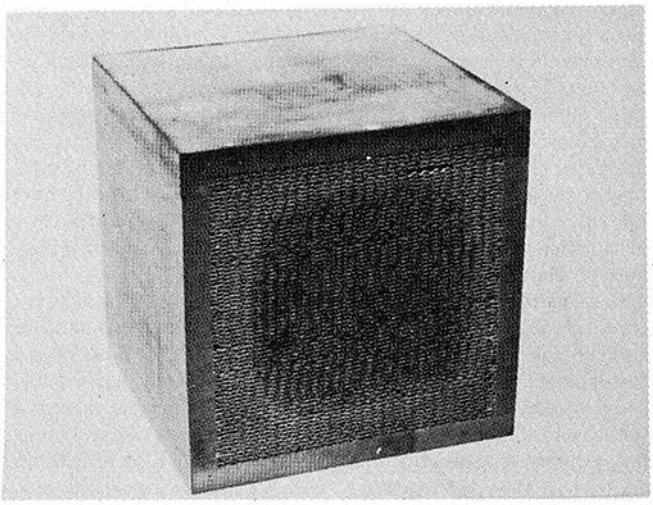


Fig. 8 Developmental ceramic plate-fin heat exchanger module for vehicular gas turbine application

Downloaded 01 Jun 2010 to 171.66.16.58. Redistribution subject to ASME license or copyright; see http://www.asme.org/terms/Terms_Use.cfm

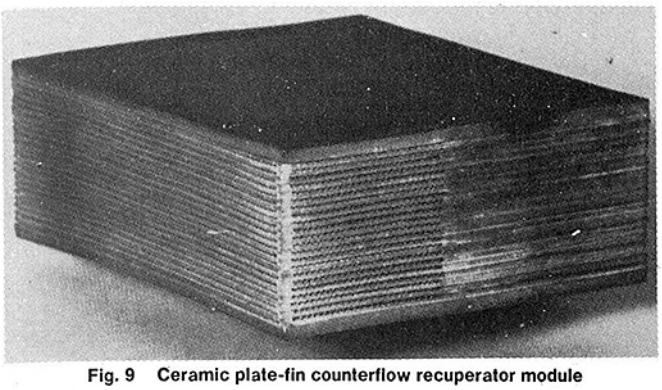


Fig. 9 Ceramic plate-fin counterflow recuperator module

high compactness and is aimed at the vehicular gas turbine market. With fabrication by an extrusion process as the ultimate production method, the initial module shown in Fig. 10 has machined flow channel slots in an isostatically pressed block of silicon nitride. With discrete positioning of the channels in the heat exchanger element, the headering areas are simply formed by local surface machining to give a module with a counterflow configuration.

The motivation for development of a compact ceramic recuperator for vehicular gas turbines is simply that it has the potential for low cost and obviates the seal leakage, drive mechanism, and carry-over loss features of the rotary regenerator. The ultimate recuperator concept is evisioned to be a ceramic element installed in a simple cast structure, with ease of access for inspection or replacement. The utilization of compact plate-fin surfaces has been dealt with here at length because it is felt that ceramic heat exchanger technology from the vehicular gas turbine field will be applicable to many industries where compact units are necessary for high-temperature waste heat recovery.

Exhaust-Heated Gas Turbine Cycle. As shown in Fig. 6, for the exhaust-heated gas turbine cycle the combustor is transposed to a position between the turbine and the heat exchanger. In the exhaust-heated cycle (also known as the indirect cycle), the engine is bulkier and less efficient than in the open cycle by virtue of the mode of heat input to the prime mover. There is substantial renewed interest in this type of cycle [21, 22], although it was first discussed 30 years ago [23] and has been studied in recent years [24, 25]. The current interest relates to the ability of this gas turbine type to burn "dirty fuels" (coal, peat, wood, refuse, for example) without incurring turbine blade erosion and corrosion. This type of cycle necessitates the use of a ceramic heat exchanger since the material temperatures in this component are greater than the turbine inlet temperature. The high reject temperature from this cycle also implies the use of a bottoming cycle or cogeneration for economic viability.

With operation of the exhaust-heated gas turbine on dirty fuels, the particulate matter entering the heat exchanger after combustion obviates the compact plate-fin types of surface geometry. Enhanced ceramic tubular surfaces of reduced surface compactness would be ideally suited for this application, and as will be discussed in a later section, a substantial degree of commonality exists between this application and ceramic heat exchangers under development for high-temperature fossil-fueled furnaces such as slot furnaces, soaking furnaces, preheat furnaces, and melting furnaces.

Closed-Cycle Gas Turbine. With the current emphasis on the use of fuels not previously exploited to a high degree for gas turbine power generation, the closed-cycle gas turbine (pioneered in Europe) is now receiving serious attention in the United States because of its adaptability to various heat sources (fossil, nuclear, solar, isotope, and chemical) and waste heat rejection alternatives (dry cooling, binary cycle, district heating, desalination, process steam, etc.). There are many variants of the basic cycle that have been discussed previously [26], but the one shown in Fig. 6 incorporating an intercooler is perhaps the best known by virtue of the European operating experience. The 20 or so European closed-cycle gas turbine plants have accumulated close to a million hours of operation on a variety of fossil fuels such as coal, oil, coke oven gas, and furnace gases [27].

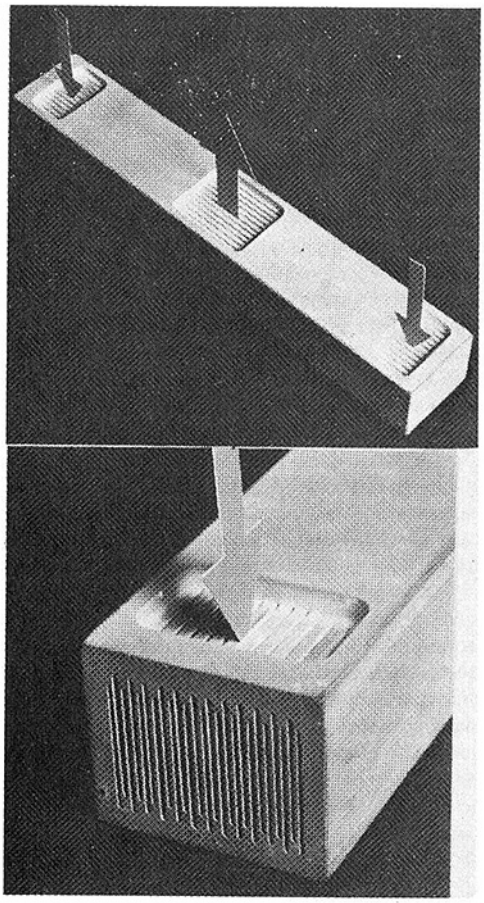


Fig. 10 Modular, counterflow silicon nitride recuperator element

From 1940 to 1977, the increase in turbine inlet temperatures for the closed-cycle gas turbine from 650°C (1202°F) to 750°C (1382°F) has been modest compared with open-cycle industrial gas turbine inlet temperatures. The turbine blading has not limited the temperature, but rather restrictions imposed by the strength of the heater tubes for extended life. For the fossil-fired closed-cycle gas turbine, development efforts are being concentrated on the heat exchanger, with programs under way on fluidized bed and pulverized coal combustion. For turbine inlet temperatures much above 800°C (1472°F), it is projected that a ceramic heat exchanger will be necessary for fossil-fired closed-cycle gas turbines.

Design and experimental work has been under way for several years on air-heater, fluidized bed coal combustion systems for small closed-cycle gas turbines [28, 29]. In this concept, combustion takes place in the fluidized bed with the bulk of the heat of combustion being transferred to the tube matrix, which is immersed in the bed. Development work in this field is expected to intensify, with initial emphasis placed on the use of metallic heat exchangers in the bed. As important, and not yet fully resolved, phenomena such as corrosion and erosion within the bed, together with the desire for higher turbine inlet temperatures, are taken into account, the trend may well be toward the utilization of ceramic heat exchanger surfaces in the fluidized bed.

An alternative to the fluidized bed heat source for the closed-cycle gas turbine is a continuous flow process involving the combustion of pulverized coal, and this necessitates a high-temperature heat exchanger. As described in [30], a ceramic heat exchanger development effort supported by the Electric Power Research Institute (EPRI) is under way. Designed for a turbine inlet temperature of 982°C (1800°F), the ceramic tube walls operate at a temperature in excess of 1093°C (2000°F). For this heat exchanger application, a two-pass cross-counterflow arrangement was selected, the unit being of modular construction. Initial emphasis was placed on the utilization of plain tubes of 25.4 mm (1 in.) diameter and 3.18 mm (0.125 in.) wall

Downloaded 01 Jun 2010 to 171.66.16.58. Redistribution subject to ASME license or copyright; see http://www.asme.org/terms/Terms_Use.cfm

thickness. The candidate material selected was NC-430, a densified form of silicon carbide. Details of a headering approach are shown in Fig. 11. The process used to make such complex shapes is one of slip casting with a subsequent siliconizing operation to produce an impervious strengthened form. The manifolding of a representative (for two-pass cross-counterflow) ceramic heat exchanger module approximately 660 mm (26 in.) high with ceramic joints is shown in Fig. 12. For this high-temperature gas-to-gas exchanger application, the need for enhanced surfaces to reduce the size of the unit for large-scale utility power generation was recognized [30]. Details of a silicon carbide tube embodying secondary surfaces (fabricated by Norton Company) are shown in Fig. 13. With a geometry of 0.2 fins per millimeter (five fins per inch), the effective length of the heat exchanger is about halved. It is projected that advanced ceramic geometries of this type will find acceptance in a wide range of high-temperature heat recovery applications.

Gas Turbines with Solar Heat Source. As outlined above, increasing development attention is being given to developing gas turbines that burn coal and coal-derived fuels for power generation. The other main energy source currently being evaluated for gas turbines of the future is solar energy [31]. Both closed-cycle and open-cycle variants are being evaluated under programs sponsored by EPRI. Both projects envision a central receiver or power tower and an eventual 30 to 100 MW scale for commercial utility service. The use of gaseous working fluids and the high temperatures associated with the Brayton cycle suggest that valuable cost economies may be obtained, since the reject heat characteristics are conducive to economical dry cooling (an important consideration because the major potential sites for solar-thermal plants lack cooling water).

The Boeing closed-cycle concept [32] is based on a helium cycle which operates at a solar-induced temperature of 816°C (1500°F). A heat exchanger embodying U-shaped tubes of a metallic superalloy was selected for this application. The Black & Veatch open-cycle gas turbine design proposes using a regenerative industrial gas turbine that is available today [33]. The point of greatest technical challenge in this power conversion concept is the heat exchanger material, which must withstand temperatures on the order of 980 to 1065°C (1800 to 1950°F). A ceramic heat exchanger using silicon carbide U-tubes, with ceramic-to-ceramic joints, is under development for this solar gas turbine application [34].

From the above discussions of gas turbine applications it can be concluded that a wide variety of ceramic heat exchangers are under development for differing applications of the basic gas turbine cycles shown in Fig. 6. Many of these development activities are still in their infancy, but it is projected that the ceramic heat exchanger will play an important role in the realization of high-efficiency gas turbines in the next decade.

Rotary Heat Exchangers for Industrial Gas-to-Gas Heat Recovery. Rotary regenerative air heaters are widely used in modern fossil-fired boiler plants. Air heaters of the Ljungstrom type [35, 36] make a contribution to plant efficiency, because preheating the combustion air helps the boiler make good use of flue-gas heat which would otherwise be rejected via the stack. Apart from the purely thermodynamic advantages, preheated combustion air is essential for burning lower-grade fuels. In coal-fired plants, it also provides the necessary means of drying the fuel as it passes through the pulverizing mills. Current air heaters operate at modest temperatures which permit the utilization of a matrix embodying closely packed, metallic corrugated surface geometries. Lowering the stack temperature below current values (increasing the quantity of heat transfer) would mean that the heat transfer surfaces would operate at a temperature below the acid dewpoint of the flue gases. The resulting contact of the metallic surfaces with sulfuric acid would lead to severe corrosion problems. Industrial tests and operational experience [37] have shown that promising results can be achieved by utilizing acid-resistant ceramic surface geometries for the heat exchanger matrix packing. This is an example of ceramic heat exchager utilization because of a hostile environment rather than elevated temperatures.

For smaller applications in the industrial market, there is an increasing use of heat wheels for high-temperature heat recovery [38,

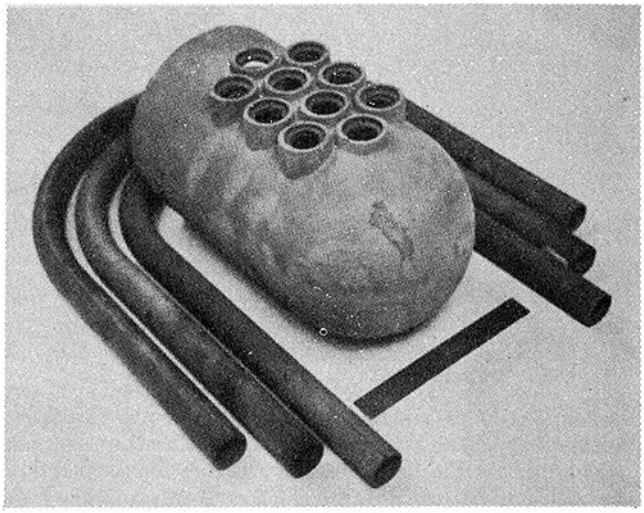


Fig. 11 Silicon carbide heat exchanger subheadering components

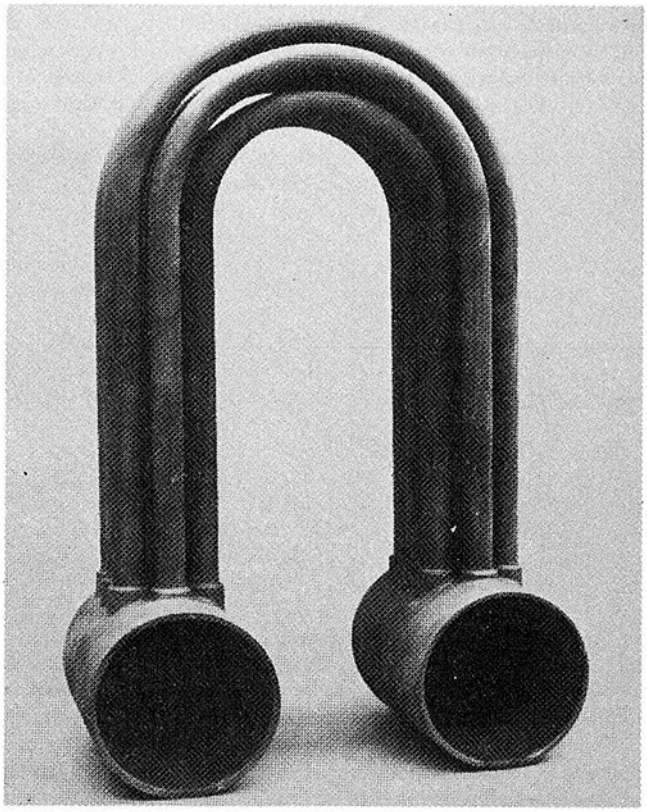


Fig. 12 Manifolding of silicon carbide heat exchanger for coal-fired closed-cycle gas turbine application

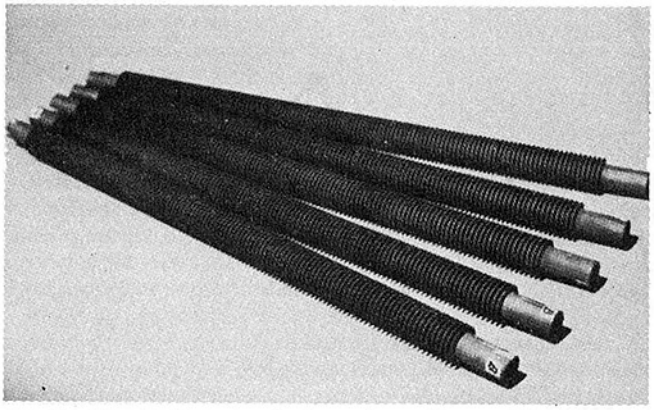


Fig. 13 Finned surface geometry for gas-to-gas silicon carbide tubular heat exchanger

Downloaded 01 Jun 2010 to 171.66.16.58. Redistribution subject to ASME license or copyright; see http://www.asme.org/terms/Terms_Use.cfm

39]. At gas temperatures below 538°C (1000°F), many metal and aluminum wheels have been used. For applications in the fields of incineration, aluminum remelt furnaces, and secondary metal reheat furnaces, with the primary use of the recovered heat being to preheat combustion air, ceramic heat wheels offer a viable solution for temperatures in the range 538 to 1093°C (1000 to 2000°F). An example of a ceramic heat wheel embodying a very compact heat transfer surface is shown in Fig. 14. The slowly rotating wheel is placed between the two gas streams so that the hot exhaust gases pass through one half of the wheel, transferring heat to the cold incoming fresh air. The preheated air can be used as combustion air, and the amount of energy required to bring the air up to combustion temperature is thus reduced. Use of the rotary ceramic heat wheel tends to be limited to applications where there is little pressure differential between the two gas streams because of the leakage problem. Ceramic wheel sizes up to 1778 mm (70 in.) dia have been fabricated by Corning Glass, and several units have been in use for over two yr with over 8000 hr of operation. The high surface compactness of the ceramic heat wheel offers very high efficiency and permits the wheel to be packaged in a small exchanger envelope. As fossil fuel prices continue to increase, it is likely that an increasing number of industrial plants will be retrofitted with ceramic heat wheels to keep the plant economics competitive.

Fixed-Boundary Heat Exchangers for Industrial Gas-to-Gas Heat Recovery. Conventional high-temperature fossil-fueled furnaces for such operations as forging, soaking, preheating, or melting operate between 10 and 15 percent efficiency. In recent years, recuperative heat recovery systems have been developed utilizing both tubular and plate-fin types of surface geometries. Several examples of the utilization of ceramic heat exchangers for high-temperature heat recovery are briefly outlined below.

Tubular Ceramic Heat Exchangers. In the steel industry the efficiency of the fossil-fired soaking heat pits can be considerably improved by incorporation of a high-temperature recuperative heat exchanger. Studies have shown that the utilization of silicon carbide tubes to replace presently used fireclay recuperators would result in increased life because of the improved resistance to thermal shock [40].

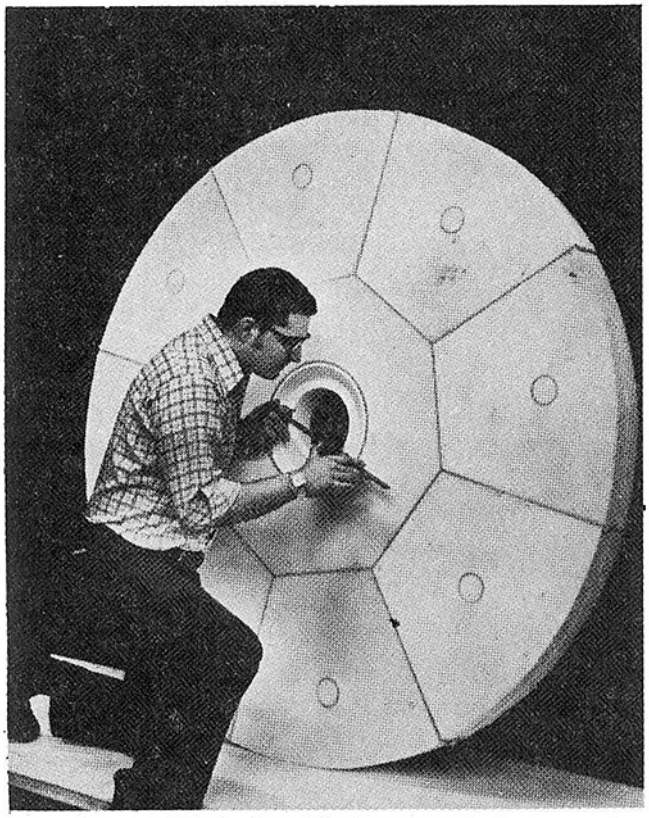


Fig. 14 Ceramic heat recovery wheel

Work has been reported in England [41] covering the design and development of a prototype ceramic tubular recuperator for an oil-fired soaking pit for operating with waste gas temperatures up to 1300°C (2372°F). Both silicon carbide and silicon nitride tubes were evaluated, and a four-pass cross-counterflow unit with plain tubes of 140 mm (5.5 in.) diameter was constructed. The five yr development program included extensive laboratory testing and operating experience in a steel plant, and the results showed a significant fuel savings (between 3 and 20 percent) compared with similar soaking pits using metallic recuperators.

Recognizing the need for improved heat transfer in gas-to-gas heat recovery systems, Hague International has developed a tubular ceramic (silicon carbide) heat exchanger embodying finned surfaces [42]. The ceramic heat exchanger shown in Fig. 15 has been operated for about two yr as a recuperator on a slot furnace and has demonstrated a fuel saving of over 50 percent. This tubular type of exchanger is designed for accepting exhaust gases at 1371°C (2500°F) for operation on oil or gas fuels, but temperatures are limited to a range of 1204 to 1316°C (2200 to 2400°F) because of ash effects associated with operation on dirty fuels such as coal, wood residues, and agricultural waste. Details of the silicon carbide tube, which has a fin outer diameter of 95 mm (3.74 in.). are shown in Fig. 16. This tube, which forms the basic element of the heat exchanger, has both internal and external secondary surfaces. In addition to gas turbine recuperator applications [21, 22], this type of heat exchanger is adaptable to any high-temperature process utilizing direct combustion.

Throughout this paper emphasis has been placed on the utilization of enhanced surface ceramic geometries to improve the performance and reduce the size of gas-to-gas heat exchangers. Excellent examples of ceramic tubes with finned secondary surfaces have been illustrated

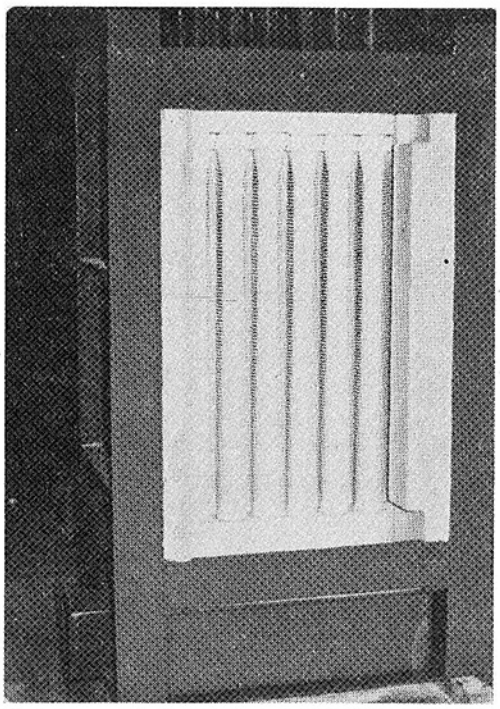


Fig. 15 Tubular ceramic heat exchanger embodying secondary surfaces for high-temperature furnace gas heat recovery

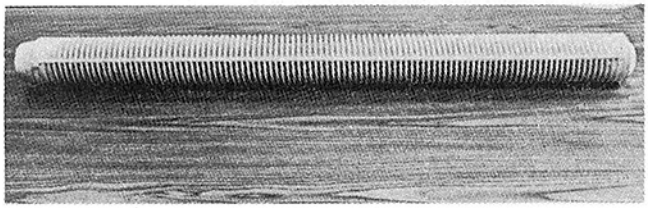


Fig. 16 Silicon carbide tube with internal and external extended surfaces for high-temperature gas-to-gas heat recovery

Downloaded 01 Jun 2010 to 171.66.16.58. Redistribution subject to ASME license or copyright; see http://www.asme.org/terms/Terms_Use.cfm

and described. Other means of surface enhancement aimed at turbulence promotion include ribbing, roughening, fluting, and spiral geometries, and examples of various silicon carbide tubes with enhanced surfaces are shown in Fig. 17.

Plate-Fin Ceramic Heat Exchangers. From comparing the surface compactness values of tubular surfaces (Fig. 4) and plate-fin heat exchangers (Fig. 5), it is clear that the latter have considerably more potential for heat exchanger volume reduction. For applications where minimum exchanger envelope is important, development efforts are under way on the utilization of compact surface geometries, and an example of an early cross-flow plate-fin ceramic module is shown in Fig. 18.

Recently, Thermal Transfer Corporation has developed a compact modular recuperator system which is adaptable to a wide range of gas-to-gas heat recovery applications and can be retrofitted on existing furnaces. As shown in Fig. 19, the basic heat transfer element is an extruded ceramic cube measuring approximately 254 mm (10 in.) on each side. The ceramic module, supplied by G.T.E. Sylvania, consists of rows of small rectangular channels, separated by uniformly thin walls, that are alternately stacked 90 deg in relation to each other. The ceramic cube has very low expansion properties, exhibits excellent resistance to thermal shock, and can withstand hot gas temperatures as high as 1482°C (2700°F). The basic cube is of cross-flow configuration, but elements can be oriented to give multipass cross-counterflow arrangements. Recuperation is often impossible on small industrial furnaces because of space or weight limitations. This compact and novel modular ceramic heat exchanger is well suited to such space-limited applications. The use of a standard cube module provides considerable flexibility, since the elements can be "stacked" depending on the particular application and thermal duty.

High-Temperature Heat Recovery from Molten Materials. Very high-temperature heat recovery essentially implies regenerative heating associated with a variety of furnace applications. There are processes involving high-temperature salts, slags, and granular solids in which large quantities of heat are wasted. For example, heat recovery from molten slag would necessitate the use of special purpose heat transfer equipment, since the use of any static heat exchanger would likely result in local solidification and fouling. A ceramic auger system such as that shown in Fig. 20 is suggested as one solution. The ceramic auger assembly embodies coolant channels for heat removal (water heating, process steam, air preheating, etc.). The ceramic rotor unit would be thermally designed so that surface temperatures are above the slag solidification temperature. The power required to drive the auger, and hence transport the slag, would be small, and slag action on the rotor surface should tend to keep it clean. Auger rotational speed and slag velocities would be selected to minimize erosion, but if problems occurred in service, the ceramic rotating element could be easily replaced. This application is yet another illustration of how ceramic heat exchanger concepts can be applied to very high-temperature heat recovery.

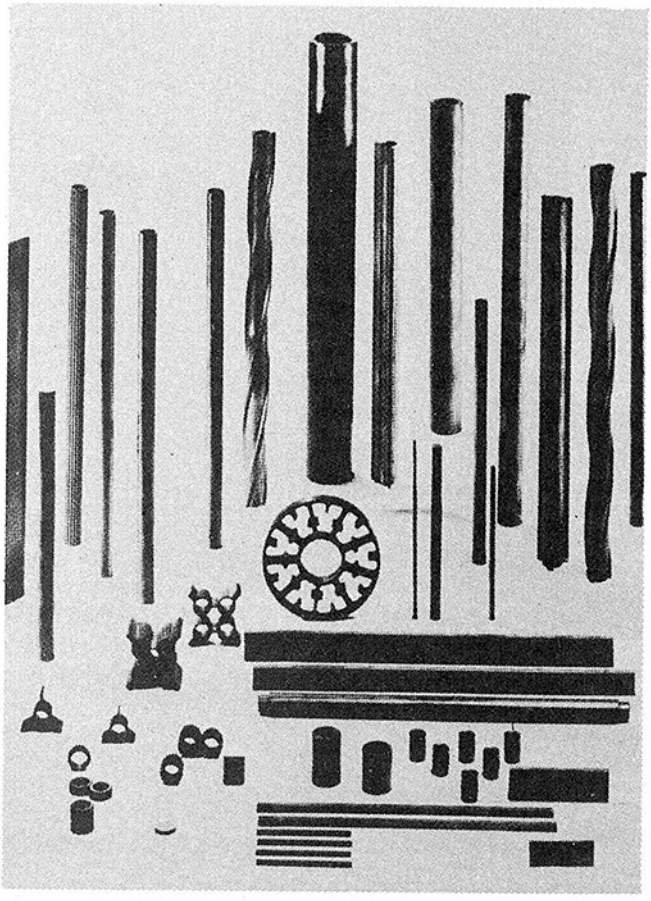


Fig. 17 Silicon carbide tubes with enhanced surfaces

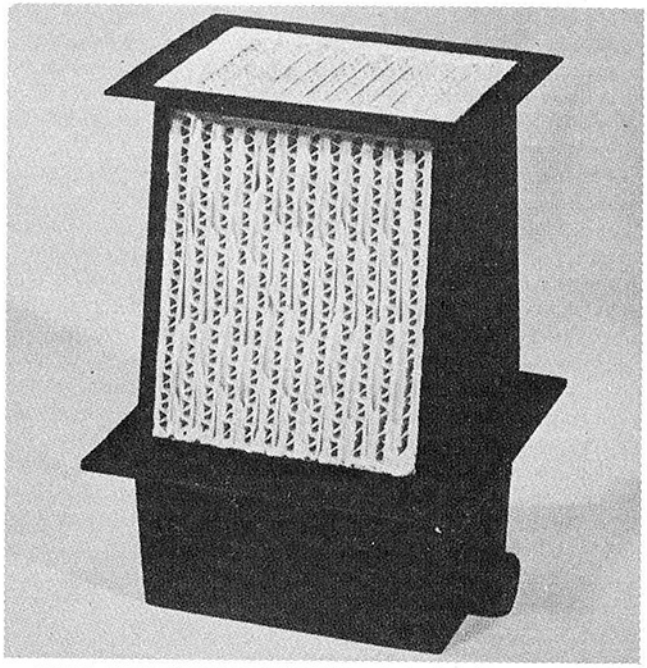


Fig. 18 Early cross-flow plate-fin ceramic heat exchanger model

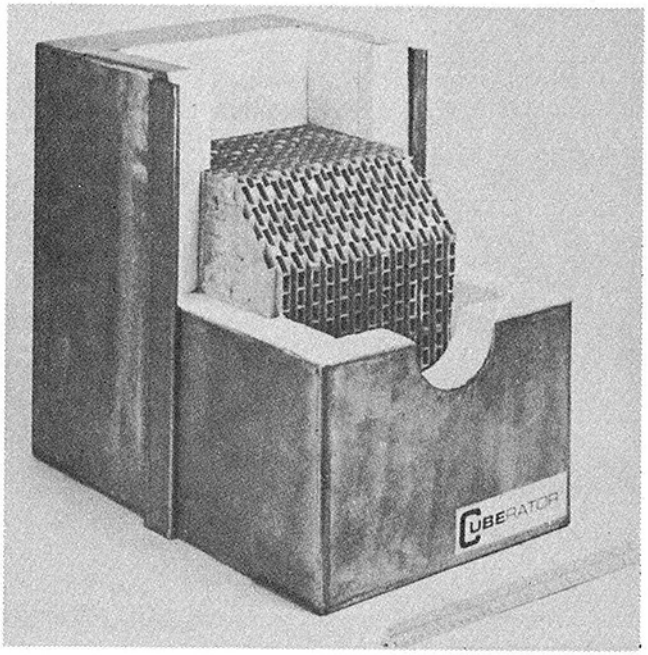


Fig. 19 Modular ceramic recuperator system with extruded surface geometry for high-temperature gas-to-gas heat recovery applications

Downloaded 01 Jun 2010 to 171.66.16.58. Redistribution subject to ASME license or copyright; see http://www.asme.org/terms/Terms_Use.cfm

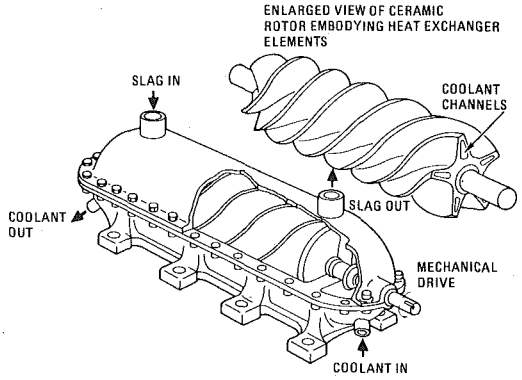


Fig. 20 Ceramic auger heat exchanger concept for high-temperature heat recovery from molten slag

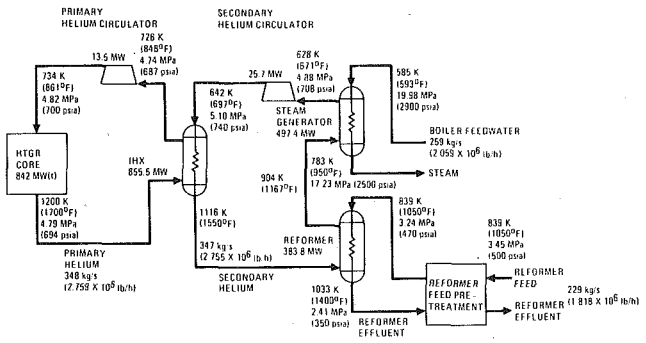


Fig. 21 Flow diagram for nuclear process heat plant with very small VHTR and intermediate loop

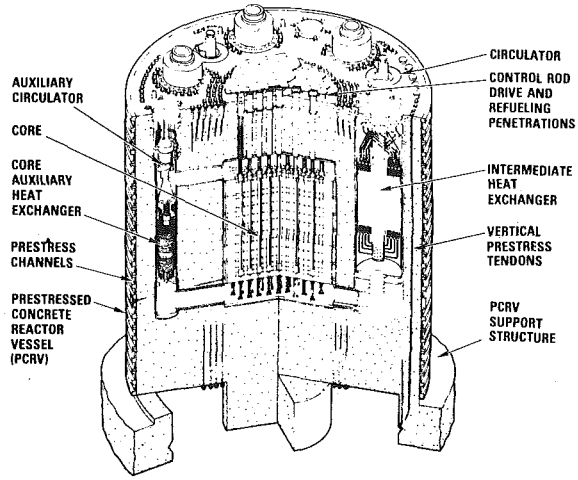


Fig. 22 VHTR nuclear process heat source with intermediate heat exchanger integrated in the concrete reactor vessel

High-Temperature Heat Exchangers in Advanced Systems

In many advanced systems, including power plants and industrial processes related to the utilization of fossil fuels, there is heavy reliance on high-temperature materials for process viability and economic feasibility [43]. It is expected that in the next 20 yr ceramics will play an important role in such systems, and several potential applications are outlined below.

Nuclear Process Heat. The VHTR (Very High-Temperature Gas-Cooled Reactor) coupled with hydrogen processes offers the potential of a large-scale, virtually unlimited source of clean energy for the twenty-first century. The VHTR is the only nuclear reactor type that can achieve the high core outlet temperatures needed to match coal conversion processes. Hydrogen is valuable for converting coal to pipeline gas, removing sulfur, making ammonia, reducing iron ore, providing feedstock to the petrochemical industry, and transporting energy in the future. These process heat applications offer new and exciting uses for a gas-cooled reactor.

The process that has been studied in the United States for several years is based on hydrogasification of coal liquids to produce methane with the hydrogen produced by steam-reforming a portion of the product methane. The latter reaction is endothermic and utilizes nuclear heat. Nuclear heat can be effectively produced by gas-cooled reactors with core outlet temperatures on the order of 900 to 1000°C (1652 to 1832°F). Studies are under way for processes with a secondary loop heat exchanger [44] and have been completed with the steam-methane reformer integrated in the reactor prestressed concrete reactor vessel [45]. The flow diagram for a small VHTR process heat plant concept with a secondary loop is shown in Fig. 21. A reactor concept showing the intermediate heat exchanger (IHX) installed inside the concrete vessel is shown in Fig. 22. For the cycle conditions shown in Fig. 21, the maximum metal temperature in the pressure-balanced intermediate heat exchanger is on the order of 885°C (1625°F), facilitating the use of a superalloy such as Inconel 617 for the tubular heat exchanger. For temperatures much above this level, it will be necessary to utilize ceramics or carbon-carbon composite materials. Details of current metallurgical research programs in support of advanced reactors have been reported previously [46], and the role ceramics could play in heat exchangers for future nuclear process heat plants is described in [47] and [48].

Thermochemical Water Splitting. General Atomic is developing a promising thermochemical water-splitting cycle for hydrogen production [49]. This cycle, which is based on a main reaction involving iodine and sulfur, can be conducted as an all liquid and gas process and has heat requirements that are compatible with the High-Temperature Gas-Cooled Reactor (HTGR). In contrast to many other thermochemical cycles that have been discovered, this cycle requires no solids handling, and its maximum temperature is in the range of 816 to 871°C (1500 to 1600°F). Design of components for the thermochemical decomposition process will require stringent consideration for corrosion compatibility. For several of the heat exchangers (helium to H_2SO_4), the corrosion aspects will be superimposed on the complications of designing for high-temperature service. Current studies indicate that metallic materials (perhaps coated) can be used for the heat exchangers. Candidate materials in the corrosion testing program include ceramics. The use of ceramics for the heat exchangers in this application would satisfy all three of the criteria mentioned earlier in this paper (i.e., high-temperature operation, corrosive operating environment, and material economic considerations).

Fusion Reactor Power Plants. The fusion reactor concept in its present embryonic stage is forcing development to occur in many diverse areas simultaneously, although at this point specific component requirements are difficult to define. Two materials with potential for fusion plants are ceramics and carbon-carbon composites. These materials have potential use in helium heat exchangers and/or support structures for the blanket or first wall. To maintain structural integrity, it is important that they resist thermal shock, crack propagation, fast neutron damage, and high-temperature creep. They must not only maintain structural integrity but in some applications be impermeable to helium.

Air Heater for MHD Power Plants. Successful operation of an open-cycle magnetohydrodynamic (MHD) system depends on preheating the air entering the combustor to a high temperature in order to obtain the required very high combustion temperature and thus system efficiency. Therefore, design of the air preheater is an essential step in meeting these goals [50]. The extremely hostile heater operating environment (high temperature, entrained coal ash, and condensing seed vapor) necessitates the use of ceramic and refractory materials. Preheating air to the 1650°C (3000°F) temperature needed to reach the required 2500°C (4530°F) air/coal combustion temperatures can possibly be done in periodic regenerators in which the heat extracted from the exhaust gases is stored in some solid ceramic materials (cored bricks, pebbles, etc.) to be subsequently released to the air stream. Two different construction designs have been considered for generator systems: moving bed and static bed. The type of regenerator selected will depend on the interaction between economic

Downloaded 01 Jun 2010 to 171.66.16.58. Redistribution subject to ASME license or copyright; see http://www.asme.org/terms/Terms_Use.cfm

operation, construction, and material performance. Development activities aimed at the realization of a viable air preheater have been extensively documented [51–55]. For this application, perhaps more than any other case, the ceramic heat exchanger material is necessary for all three of the major criteria (i.e., high-temperature operation, corrosive operating environment, and economic viability).

In addition to the advanced systems discussed here, there are clearly many other advanced systems, such as coal gasification plant and aerospace components, that will utilize ceramic heat exchangers in the future.

Summary

In this paper an attempt has been made to illustrate the important role ceramic heat exchangers can have in energy and resource conservation for a wide range of applications. The time frame for introduction of ceramic heat exchangers in energy recovery systems is highly dependent on fuel costs, and in the near term increased emphasis will be placed on low- and medium-temperature heat recovery using conventional equipment. This paper is not intended to imply that the technology of ceramic heat exchangers has already been established. In fact, as outlined in Table 3, there are many uncertainties in the areas of structural integrity, performance, and cost, and concentrated development efforts are required to demonstrate the viability of ceramic units, particularly for advanced power conversion systems.

It is encouraging to note that the ceramic heat exchanger can be used for so many diverse applications, since there will be substantial technology transfer and this will minimize development costs. The three main motivations for the introduction of ceramic heat exchangers are (1) their suitability for elevated-temperature service where even the best metallic materials are unsuitable, (2) their ability to operate in hostile and corrosive environments, and (3) their potentially lower capital cost. Examples of applications encompassing these three criteria have been included in this paper. It is projected that the encouraging results from current development programs, for both plate-fin and tubular ceramic units, will lead to more intense efforts to improve performance and reduce exchanger size by utilizing more efficient enhanced surfaces. The ubiquitous metallic heat exchanger has benefited from two centuries of development, while ceramic exchanger technology is still in its infancy. Perhaps the two most important considerations today are (1) the development of design techniques for brittle materials and (2) an accurate assessment of material and fabrication costs. It is expected that these topics will be covered in specialist papers in the near future.

Emphasis in this paper has been placed on the utilization of ceramic heat exchangers for gas turbine applications, including vehicular, industrial, and power-generating uses. Near-term use of ceramic heat exchangers will help keep this type of prime mover economically competitive as fuel prices continue to increase. Clearly, technology transfer from the gas turbine field will be beneficial to the other potential applications outlined in this paper.

The work reported in this paper is only a part of the widespread international efforts to develop ceramic heat exchangers. The projected benefits of ceramic heat exchanger utilization are such that world-wide efforts to make them a reality in the near term should be increased rapidly, since the role they can have in meeting national goals of energy and resource conservation is significant.

Acknowledgments

Appreciation is hereby expressed to the management of General Atomic for permission to publish this paper. This paper has been substantially enhanced by the inclusion of ceramic hardware photographs, and the author wishes to express his thanks to Advanced Materials Engineering, Ltd., American Lava Corporation, Corning Glass Company, Daimler-Benz AG, Hague International, Professor W. Hryniszak of the University of Newcastle Energy Center, Kernforschungsanlage Jülich, Norton Company, and Thermal Transfer Corporation for supplying the many excellent photographs of ceramic heat exchangers. The views expressed in this paper are those of the author and do not necessarily represent any company affiliation.

Table 3 Ceramic heat exchanger synopsis

- Development motivation: energy and resource conservation to meet national goals
- Major advantages
  - Very high-temperature capability and excellent oxidation resistance
  - Potential cost savings compared with use of superalloys and refractory alloys
  - Wide range of applications permitting technology transfer
- Salient material properties
  - Low probability of failure
  - Good thermal shock resistance
  - Low porosity
  - Ability to be fabricated in practical heat exchanger geometries
  - Adaptability to economic fabrication processes
  - Resistance to environmental attack
- Materials of current interest
  - Silicon nitride
  - Silicon carbide
- Types of construction
  - Plate-fin surfaces (very compact surface geometry)
  - Plain tubular surfaces
  - Enhanced tubular surfaces (i.e., finned geometry)
- New design techniques needed for brittle materials
  - Minimize tensile stresses
  - Minimize required amount of ceramic materials
  - Emphasize simplicity of design
  - Develop ability to withstand vibratory loading
- New manufacturing technology required
- Areas of uncertainty requiring resolution
  - Material properties for design purposes
  - Fabrication limitations (sizes, shapes)
  - Dimensional variation of as-fired parts
  - Permeability (coatings necessary, etc., for zero porosity)
  - Service life prediction
  - Design approaches for high-pressure capability (headering, etc.)
  - Projected material and fabrication costs
  - Heat exchanger repair techniques
  - Technology transfer

References

1 Fraas, A. P., "Heat Exchangers for High Temperature Thermodynamic Cycles," ASME Paper No. 75-WA/HT-102, Dec. 1975.

2 "Waste Heat Management Guidebook" *National Bureau of Standards Handbook 121,* U. S. Government Printing Office, Washington, D. C., Feb. 1977.

3 Boyen, J. L., *Practical Heat Recovery,* John Wiley & Sons, New York, 1975.

4 Herda, W., and Rickard, A. J., "Recent Developments in Materials for High-Temperature Service in Petrochemical Process and Refinery Furnaces," *The Metallurgist and Materials Technologist,* July 1973.

5 Bull, J. L., "Recent Development in Graphite Heat Exchangers," Paper C124/72 presented at Institution of Mechanical Engineers Conference on Recent Developments in Compact High Duty Heat Exchangers, London, England, Oct. 12, 1972.

6 Thomas, L., "Graphite in Heat Exchangers," *Chartered Mechanical Engineer,* Vol. 23, No. 10, Nov. 1976, p. 81.

7 Graham, L. W., et al., "Improvements in or Relating to Heat Exchangers," Patent Specification 1 506 489, complete specification published April 5, 1978.

8 Kays, W. M., and London, A. L., *Compact Heat Exchangers,* McGraw-Hill, 2d ed., 1964.

9 McDonald, C. F., "The Role of the Recuperator in High Performance Gas Turbine Applications," ASME Paper No. 78-GT-46, April 1978.

10 McDonald, C. F., "Gas Turbine Recuperator Technology Advancements," ASME Paper No. 72-GT-32, March 1972.

11 O'Reilly, W. J., "A High-Effectiveness Recuperator Design Concept," ASME Paper No. 78-GT-78, April 1978.

12 Cuffe, K. W., et al., "Plate-Fin Regenerators for Industrial Gas Turbines," ASME Paper No. 78-GT-26, April 1978.

13 "Breda Regenerator Does Better Than Guarantee," *Gas Turbine World,* March 1978.

14 McDonald, C. F., "Recuperator Development Trends for Future High Temperature Gas Turbines," ASME Paper No. 75-GT-50, March 1975.

15 Tiefenbacher, E., "Problems of the Heat Exchanger for Vehicular Gas Turbines," ASME Paper No. 76-GT-105, March 1976.

16 Lanning, J. G., and Wardale, D., "The Development of a Glass-Ceramic Axial-Flow Rotary Generator," ASME Paper No. 66-GT-107, 1966.

17 Rahnke, C. J., and Vallance, J. K., "Reliability and Durability of Ceramic Regenerators in a Gas Turbine," ASME Paper No. 77-GT-59, March 1977.

18 Stoddart, D. E., et al., "Silicon Nitride Materials for Gas Turbine Components," ASME Paper No. 73-GT-47, 1973.

Downloaded 01 Jun 2010 to 171.66.16.58. Redistribution subject to ASME license or copyright; see http://www.asme.org/terms/Terms_Use.cfm

19 Forster, S., and Kleeman, M., "Compact Metallic and Ceramic Recuperators for Gas Turbines," ASME Paper No. 78-GT-62, 1978.
20 Krauth, A., et al., "Recuperative Ceramic Heat Exchanger and Stator Parts for Gas Turbine Application," Paper presented at Fifth AMMRC Materials Technology Conference, Newport, R. I., March 1977.
21 Hagen, K. G., and Berg, C., "Wood Residue Fired Gas Turbine Cycle," Paper presented at the Forest Product Research Society Conference, Atlanta, Georgia, Nov. 1976.
22 Most, I. G., and Hagen, K. G., "A Ceramic Heat Exchanger for Exhaust-Fired Gas Turbine Power Cycles," Paper 779034 presented at 12th Intersociety Energy Conversion Engineering Conference, Washington, D. C., Aug. 1977.
23 Mordell, D. L., "The Exhaust-Heated Gas Turbine Cycle," ASME Paper No. 49-F-6, Sept. 1949.
24 Miwa, K., et al., "Analysis and Preliminary Experiments on the Use of a Ceramic Air Heater for Burning Residual Fuels in the Gas Turbine," JSME Paper No. 3, Oct. 1971.
25 Miwa, K., and Miyagi, Y., "A Contribution to the Use of Ceramics for Gas Turbine Heat Exchangers," *Journal of JSME,* Vol. 70, No. 587, 1967.
26 McDonald, C. F., "The Closed-Cycle Gas Turbine—Present and Future Prospectives for Fossil and Nuclear Heat Sources," ASME Paper No. 78-GT-102, 1978.
27 Harmon, R. A., "Operational Status and Current Trends in Gas Turbines for Utility Applications in Europe," Report prepared for Fossil Energy Organization of U. S. Department of Energy, Aug. 16, 1976.
28 Fraas, A. P., "Small Coal Burning Gas Turbine for Modular Integrated Utility System," Paper 769017 presented at 9th Intersociety Energy Conversion Engineering Conference, San Francisco, California, Aug. 26, 1974.
29 Fraas, A. P., "Application of the Fluidized Bed Coal Combustion System to the Production of Electric Power and Process Heat," Paper presented at AIChE Meeting, Kansas City, Missouri, April 11, 1976.
30 Coombs, M. G., "The Development of a Ceramic Heat Exchanger for a Closed-Loop Brayton Cycle," Paper presented at ASME Gas Turbine Conference, San Diego, California, March 11–15, 1979.
31 "Spinning a Turbine With Sunlight," *EPRI Journal,* March 1978, p. 14.
32 Zetner, R. C., and Shannon, R. L., "Thermal Scale Modeling of the Central Receiver of a Helium Brayton Cycle Solar Powerplant," Paper 779031 presented at 12th Intersociety Energy Conversion Engineering Conference, Washington, D. C., Aug. 1977.
33 Grosskreutz, J. C. et al., "Solar Thermal Conversion to Electricity Utilizing a Central Receiver, Open Cycle Gas Turbine Design," Paper 779195 presented at 12th Intersociety Energy Conversion Engineering Conference, Washington, D. C., Aug. 1977.
34 Walton, J. D., and Harris, J. N., "Ceramic Heat Exchanger for Solar Electric Power System Using an Open-Cycle Air Turbine," Paper No. 15-52-77, presented at American Ceramic Society 79th Annual Meeting and Exposition, Chicago, Illinois, Aug. 23–28, 1977.
35 Mac Duff, E. J., and Clark, N. D., "Ljungstrom Air Preheater Design and Operation," *Combustion,* Vol. 47, No. 7 and No. 9, 1976.
36 Chojnowski, B., and Chew, P. E., "Getting the Best Out of the Rotary Air Heaters," *CEGB Research,* No. 7, May 1978.
37 Madoyan, L. G., et al., "An Investigation of the Fouling by Ash of the Ceramic Packing of Regenerative Airheaters of Oil-Fired Boilers," *Thermal Engineering* (English version of *Teploenergetika*), Vol. 24, No. 7, July 1977, pp. 42–44.
38 "Ceramics Improve Heat Wheel Efficiency," *The Industrial Energy Journal,* Vol. 1, No. 1, Spring 1975, p. 2.
39 Phillips, W. A., "Ceramic Fly Wheel Recovers Heat from Stacks," Paper presented at the American Ceramic Society 80th Annual Meeting, Detroit, Michigan, May 10, 1978.
40 Vance, M. W., and McDermott, J. F., "Improvement of Soaking Pit Recuperator Tube Life Using Thermal-Stress Analysis," *Ceramic Bulletin,* Vol. 55, No. 7, 1976, p. 660.
41 Laws, W. R., et al., "The Development and Testing of a Novel High-Temperature Ceramic Recuperator," Paper No. C28/75, presented at Conference on Energy Recovery in Process Plants Organized by The Institution of Mechanical Engineers, London, England, Jan. 29–31, 1975.
42 Bjerklie, J. W., and LaHaye, P. G., "A Practical Ceramic Recuperator System for High Temperature Furnaces," Paper presented at 11th Intersociety Energy Conversion Engineering Conference, Lake Tahoe, Nevada, Sept. 12, 1976.
43 Olds, F. C., "Materials Developments for Power Plants," *Power Engineering,* Vol. 82, Aug. 1978, pp. 34–42.
44 Quade, R. N., and Meyer, L., "High-Temperature Nuclear Heat Source for Hydrogen Production," Paper presented at Second World Hydrogen Energy Conference, Zurich, Switzerland, Aug. 21–24, 1978.
45 Quade, R. N., "The HTGR for Process Heat Applications in the Chemical Industry," Paper presented at Annular Meeting of the Royal Society of Chemical Engineers, Ottawa, Canada, Oct. 4–6, 1976.
46 Nickel, H., "Reactor Materials for Advanced High-Temperature Reactor Systems," *High Temperatures-High Pressures,* Vol. 8, 1976, pp. 123–141.
47 Hryniszak, W., "The Use of Non-Metallic Materials with High Temperature Gas Cooled Reactors with Special Reference to Heat Exchangers for Power and Process Plants," Symposium of British Steel Corporation and British Nuclear Forum, "Strategy for the Development of Nuclear Steel Making in Europe," London, June 6, 1973.
48 Browning, S. C., and Sebastian, J. J. S., "Ceramic Heat Exchangers—For High Temperature Heat Transfer from Helium," *Industrial and Engineering Chemistry,* Vol. 53, No. 3, March 1961, pp. 191–196.
49 Schuster, J. R., and Russell, J. L., "Thermochemical Water Splitting at General Atomic," Paper presented at Eighth Synthetic Pipeline Gas Symposium, Chicago, Illinois, Oct. 18–20, 1976.
50 Postlethwaite, A. W., and Sluyter, M. M., "MHD, Heat Transfer Problems–An Overview," *Mechanical Engineering,* Vol. 100, March 1978, pp. 32–39.
51 Heywood, J. B., and Womack, G. S., *Open Cycle MHD Power Generation,* Pergamon Press, 1969.
52 Horn, G., et al., "Air Heaters and Seed Recovering for MHD Plant," *Philosophical Transactions of the Royal Society of London,* Vol. 261, Series A, 1967, pp. 514–540.
53 Hals, F. A., et al., "Development and Testing of High Temperature Air Preheaters for Open Cycle MHD Power Systems," Paper presented at 6th International Conference on MHD Power Generation, Washington, D.C., June 9–13, 1975.
54 Lindahl, B. C., et al., "Comparison of Indirect and Direct-Fired MHD High Temperature Air Heater Systems," Paper presented at 17th Symposium on the Engineering Aspects of MHD, Stanford, California, March 29, 1978.
55 Smyth, R. R., et al., "Progress in the Testing of Materials and Design Concepts for Direct-Fired MHD Air Heater Service," Paper presented at 17th Symposium on the Engineering Aspects of MHD, Stanford, California, March 29, 1978.

Downloaded 01 Jun 2010 to 171.66.16.58. Redistribution subject to ASME license or copyright; see http://www.asme.org/terms/Terms_Use.cfm

K. Bammert
Professor.
Institute for Turbomachinery
University of Hannover
Hannover, Germany

P. Zehner
Chief Engineer.
Institute of Marine Engineering
University of Hannover
Hannover, Germany

Measurements of the Four-Quadrant Characteristics on a Multi-Stage Turbine

With turbines, operation conditions far from the design range are possible. With gas turbines, in nuclear and solar energy plants in the case of a fault, flow in reverse directions may even occur. For extreme operations insufficient knowledge was available, so measurements were carried out at first on a single-stage turbine and then on a seven-stage turbine, with both the mass flow and the rotor speed systematically varied in the positive (normal direction) and negative ranges (four-quadrant characteristics). The measurement on the seven-stage turbine basically tally with the single-stage measurements. Stage performance curves can be approximately calculated also for four quadrants from the cascade characteristics of the middle section. The calculated curves are compared to the results of the single-stage measurements. During operation far from the design point, the individual stages of a multi-stage turbine work at a wide variety of operating points, so the characteristics of such a turbine have to be determined by the superimposition of the corresponding stage performance curves on each other.

Introduction

The operating behavior of turbines in the range around the design point has been examined frequently both theoretically and experimentally [1]. Usually these works are restricted to one width of the design parameters between 50 and 110 percent of the design values. In this range, the flow is still calculable. Experimental investigations are limited to the range of power output as most turbine test stands are equipped with dynamometrical brakes which cannot deliver power. Also for economic reasons the area near to the design point is the range generally aimed.

During start-up and run-down operation the turbines also pass through operation points outside the above-mentioned range. With turbines driving vehicles a greater operating range is also unavoidable. In the case of great load alterations in closed-cycle gas turbine plants during the control operation for a short time, operating conditions occur where the mass flow is very low and the turbine absorbs power. Ships have a special backward turbine for reversing. For quick reversal of the engine, steam is admitted in counter-direction to the turbine which is still rotating in reverse. In heat-and-power stations when a great deal of heat is required, so much steam is extracted from the turbines that the last stages already start to consume power and have to be cooled by an adequate residual steam flow.

If there have been faults in manufacture or installation or after damage, operation far beyond the normal characteristic field is often necessary. In nuclear power stations with gas turbines in a single-cycle arrangement (HHT plants) safety analyses must not neglect the possibility of a major leak in the main circuit system. In such a case there may be back flow through the turbine.

Within the framework of a development program for high-temperature reactors with helium turbine the turbine test facility of the Institute for Turbomachinery of the University of Hannover was modified for the investigation of turbine characteristic fields during back flow through the turbine. It was possible to carry out wind tunnel experiments on cascades at backward flow conditions [2–5] and to measure the four-quadrant characteristics of a turbine stage [6]. The four-quadrant characteristic field is the characteristic field during operation with mass flow both in normal and in backward directions through the turbine and rotation of the turbine rotor both in normal direction and backwards. The investigations exposed here are the continuation of this work: Publication of results of the seven-stage turbine measurement and comparison of single-stage measurement to single-stage performance calculation on the basis of middle section cascade characteristics.

Test Facility

Fig. 1 shows the layout principle of the turbine test stand. The turbine (*a*) with a maximum output of 1.4 MW is coupled via a gear box (*b*) with a d-c pendulum-type machine (*c*) also with an output of 1.4 MW.

The turbine is supplied with compressed air by means of a compressor set (*d*). The valves of the appertaining piping system are designed such that any direction of flow through the turbine can be set. The air flow rate can be set by adjusting the speed of the compressors and with the aid of a by-pass (*e*). The d-c machine (*c*) is fed via a

Contributed by the Gas Turbine Division and presented at the Gas Turbine Conference and Exhibit and Solar Energy Conference, San Diego, California, March 12–15, 1979 of THE AMERICAN SOCIETY OF MECHANICAL ENGINEERS. Manuscript received at ASME Headquarters December 18, 1979. Paper No. 79-GT-107.

Copyright © 1980 by ASME
Downloaded 01 Jun 2010 to 171.66.16.58. Redistribution subject to ASME license or copyright; see http://www.asme.org/terms/Terms_Use.cfm

Leonard set (f, g, h). Through voltage control and weakening of the field (k) the speed can be adjusted. The direction of rotation is reversed by using the change-over switch (l).

Fig. 2 shows a section through the turbine with seven-stage blading. The casing, which is of grey cast iron, is axially split. The outer contour of the flow channel is formed by exchangeable split ring inserts (a), which also serve as guide blade carriers. The turbine rotor (b) has continuous axial firtree grooves which allow variation of the number of stages and of the axial rotor blade spacing by fitting corresponding intermediate pieces. The guide blade rows (c) are sealed towards the rotor by axially split shroud rings with four sealing strips.

The turbine rotor is supported in multilobe bearings (d, e). The axial bearing (e) is generously sized to ensure safe operation even under extreme conditions. Only at the design point the axial thrust is compensated largely by the compensation piston (f).

The seven-stage blading is designed for potential vortex flow with a 50 percent degree of reaction in the middle section of the last stage.

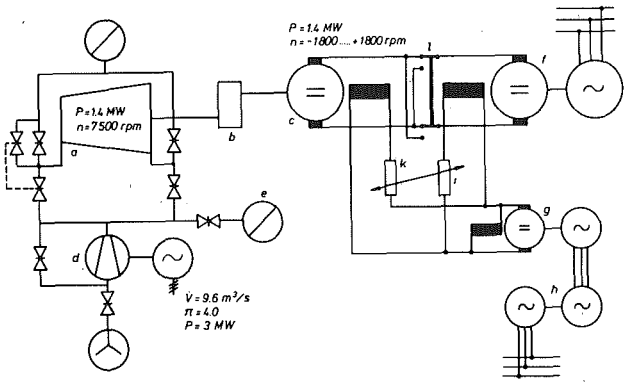


Fig. 1 Principle of layout of the turbine test facility (*a*) turbine, (*b*) gear box, (*c*) d-c machine, (*d*) compressor set, (*e*) bypass, (*f*) armature circuit generator, (*g, h*) field excitation, (*i, k*) speed control, (*l*) reversal of direction of rotation

The impeller outlet whirl is equal to zero. In sections parallel to the axis the blade profiles are the same. Fig. 3 shows the profiles of the guide blades (a) and the rotor blades (c) in six superimposed sections. Section 1 is the root section and section 6 the tip profile. A indicates the axis, U the circumferential direction. The design point velocity triangle (b) for section 3 (middle section) is also shown in the figure. The hub ratio at the outlet is 0.5, the constant hub diameter, 270 mm. The blading is a typical gas turbine blading with a small hub ratio and considerably twisted rotor blades. The material of the blades is sinter aluminium SAP 865.

The design data of the turbine are

coupling power	1,430 kW
speed	7,000 rpm
air flow rate	11.2 kg/s
inlet conditions	4.22 bar
	185 °C
total pressure ratio	0.256
hub ratio at outlet	0.5
degree of reaction middle section outlet	0.5
number of stages	7

The measuring point diagram is shown in Fig. 4. It contains schematically the arrangement of the measuring points.

The mass flow is determined by means of a symmetrical venturi tube (a) with three bores (p) and two window thermoprobes (t) in the middle of the 18 m long turbine inlet pipe, nominal diameter 500. The speed (n) is determined by an impulse counter. For measuring the torque (T) at the turbine shaft, two methods were applied: First, the torque of the pendulum type d-c machine was determined with a balance (b); second, the torque could be obtained from the amount of twisting of a torsion rod (c) between the turbine rotor and the gear box pinion.

The thermodynamic conditions of the flow entering and leaving the turbine were measured with probes (d, e) in the turbine inlet (section A) and outlet (section C). In each plane a triple tube (d) and two wedge probes (e) were installed such that they were radially ad-

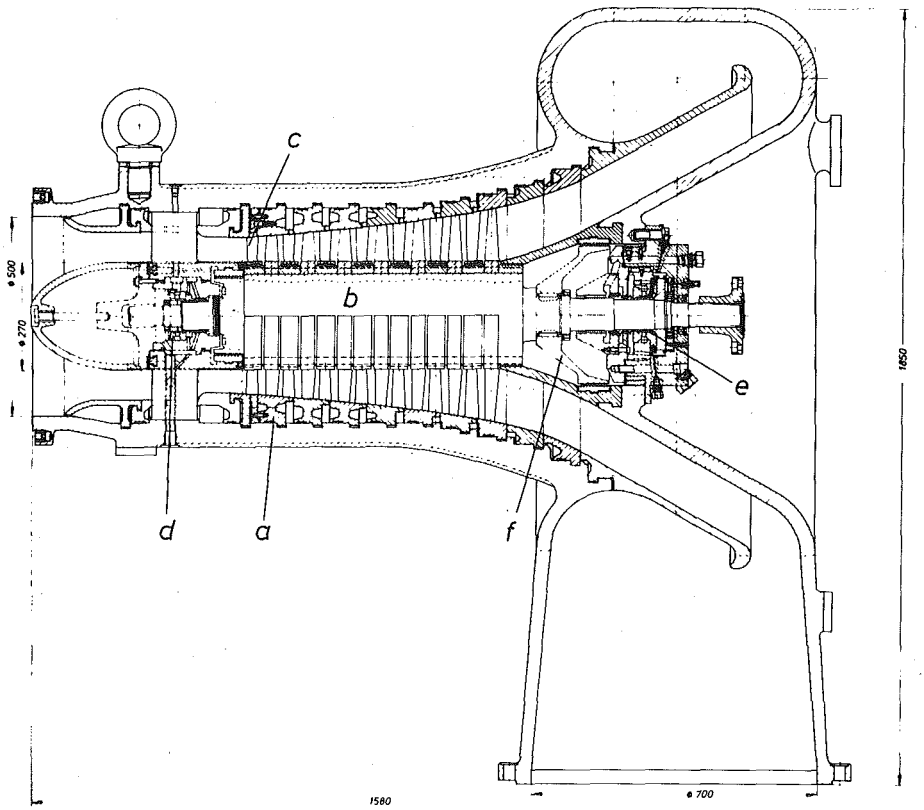


Fig. 2 Sectional drawing of the turbine with seven-stage blading (*a*) guide blade carrier, (*b*) rotor, (*c*) guide blade, (*d*) floating bearing, (*e*) fixed bearing, (*f*) compensation piston

Downloaded 01 Jun 2010 to 171.66.16.58. Redistribution subject to ASME license or copyright; see http://www.asme.org/terms/Terms_Use.cfm

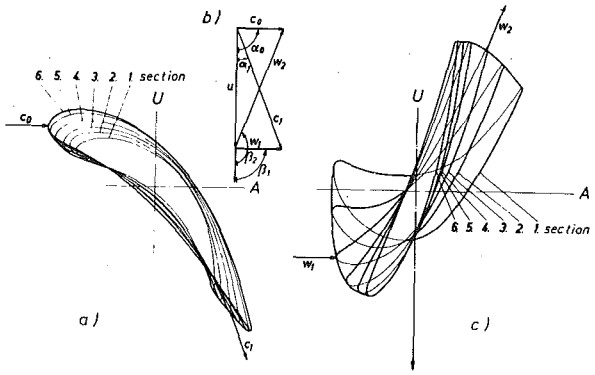


Fig. 3 Superimposed profile sections (*a*) guide blade, (*b*) design point velocity triangle, (*c*) rotor blade (A) machine axis, (*U*) circumferential direction. Section 1: Root profile, section 6: tip profile

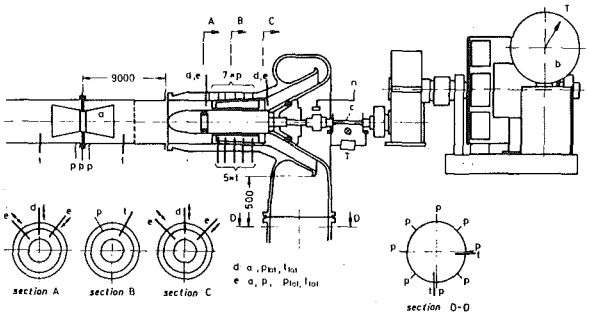


Fig. 4 Diagram of measuring points (*a*) venturi tube, (*b*) torque balance, (*c*) torsion shaft, (*d*) triple tube, (*e*) wedge probe, (*n*) speed measurement, (*p*) pressure measurement, (*t*) temperature measurement, (*T*) torque measurement, (α) angle of flow, (tot) total state

justable and used to determine the angle of flow, the static pressure, the total pressure and the total temperature at nine points on the radius. For adaptation to the varying flow conditions the probes could be turned through 360 deg. Between all seven stages (section B) the total temperature and the static wall pressure were measured by means of window thermoprobes in the middle section and pressure taps.

Test Program

The four-quadrant characteristic was measured within the limits set by the power of the test stand. A test grid was provided in the speed range of $-1.0 \leqq n/n_N \leqq +1.0$ with a step spacing of $n/n_N = 0.25$ and in the area of the mass flow from $-1.00 \leqq \dot{m}/\dot{m}_N \leqq +1.00$ with a step spacing $\dot{m}/\dot{m}_N = 0.125$. The index N marks the design point. Owing to the power limitations of the test facility (maximum pressure ratio and maximum flow rate of the compressor set, admissible torque of the pendulum-type machine, admissible heating-up of the blading) the test range was more restricted than the tests on the single-stage turbine [6].

Starting from the normal characteristic field the tests were extended firstly to cover the range with negative speed and subsequently also negative flow. The tests with positive speed and negative flow were considered the most dangerous on account of the strong vibration excitation of the blades through the distinct jet/dead water zones downstream the cascades with back flow, and were therefore provided to be carried out at last.

The test program could not be carried out in full as at a point with very small load unforeseen total blade damage occurred. The damage was evoked by a fatigue fracture of a blade in the last stage. As on occurrence of the blade fracture there was back flow through the turbine, all rotor blades and the majority of the guide blades were knocked off before the turbine could be stopped by tripping and braking. The cause of the blade fracture was considered to be the asymmetrical admission of flow to the blading during back flow through the turbine outlet diffuser in conjunction with unfavourably small transition radii from the blade leaf to the blade root and notches caused in manufacturing.

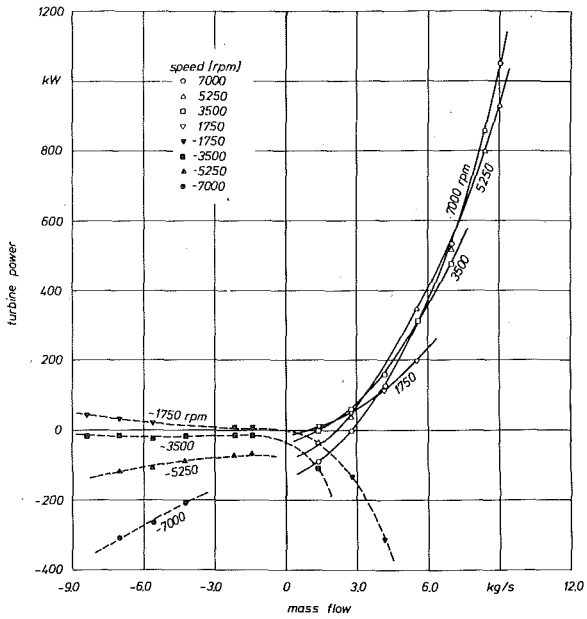


Fig. 5 Turbine power as function of mass flow and speed

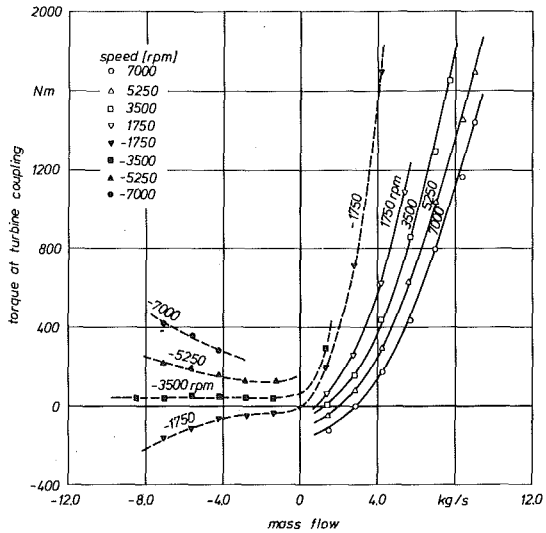


Fig. 6 Torque at turbine coupling as function of mass flow and speed

Results

Figs. 5–9 show some results of the measurements on the turbine with seven-stage blading. Fig. 5 shows the power at the turbine coupling as a function of the mass flow and the speed. The continuous lines represent normal direction of rotation, the broken lines reverse direction of rotation. The power given off by the turbine is considered as positive.

With positive direction of rotation and positive mass flow the power rises with increasing flow rate. The higher the speed the greater the gradient and the higher the minimum mass flow for power output. At nominal speed the zero power point is reached at 25 percent of the nominal mass flow.

With negative direction of rotation and with backward flow the turbine gives off little power only at the lowest speed because in the case of back flow the profile cascades cause considerable losses. With greater negative speeds the turbine consumes power in any case. Power consumption increases pronouncedly only at nominal speed and rising negative mass flow. With average speeds the power consumption is almost equal to the ventilation power.

At positive mass flow but negative direction of rotation the turbine power consumption increases steeply because, as the tests on the single-stage turbine have already shown, even with extreme flow conditions the turbine cascades produce an almost constant outlet

Downloaded 01 Jun 2010 to 171.66.16.58. Redistribution subject to ASME license or copyright; see http://www.asme.org/terms/Terms_Use.cfm

angle. This leads in the case of turning of the turbine rotor in reverse direction to very considerable changes of momentum and a corresponding power consumption. On increasing speed with this multistage blading the point of maximum admissible temperature of the turbine was soon reached.

In Fig. 6 the torque at the turbine coupling as a function of the mass flow and the speed is drawn. Parameter is the speed. One can see the torque increases with rising mass flow and falling speed. As the signs for the speed and the power have already been fixed, there is a positive torque for the same sign of speed and power and a negative torque in the case of differing sign. This definition produces steady lines for the development of the torque. With a turbine rotating backwards the torque rises very quickly with increasing positive mass flow. At 25 percent negative speed the nominal torque is already reached at less than 40 percent of the design flow rate. With negative direction of rotation and negative mass flow the torque is dependent on the flow rate only to a slight extent.

In Fig. 7 the pressure ratio π at the turbine as a function of the relative mass flow and the relative speed is shown. Again the broken lines represent the negative speed. The pressure ratio π is defined as

$$\pi = \frac{p_{\text{tot,O}}}{p_{\text{tot},E}}$$

$p_{\text{tot,O}}$ is the total pressure at the flow outlet and $p_{\text{tot},E}$ the total pressure at the flow inlet. The pressures are measured at the turbine inlet and outlet flanges. The turbine works as a compressor when the pressure of the flow leaving the machine is higher than that entering it. In this case π according to the given definition is greater than 1.

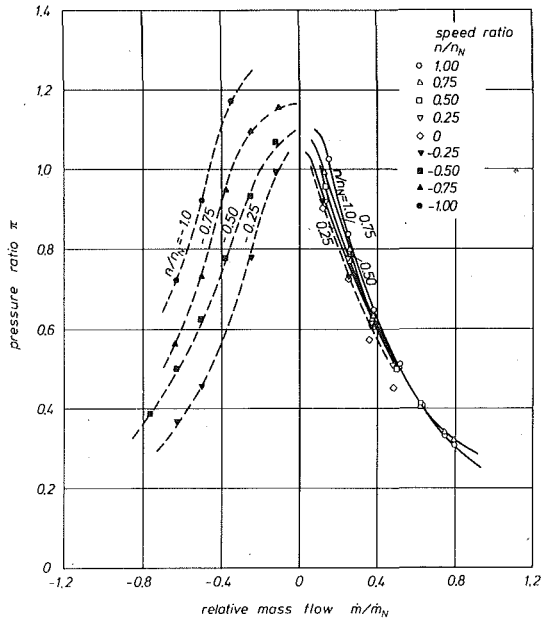


Fig. 7 Pressure ratio π between inlet and outlet flanges of the turbine as function of the relative mass flow $\dot{m}/\dot{m}_N$ and the speed ratio n/n_N (N = nominal point)

The figure illustrates the well-known fact that the absorption behavior of a turbine with normal direction of flow is only slightly dependent on the speed. With back flow, however, a distinct influence can be seen, as the direction of flow onto the trailing edge of the blade is significantly influenced by the speed and thus the flow characteristics of the blade rims.

Fig. 8 shows the development of the temperatures in the turbine, as indicated by the thermoprobes between the stages. These probes were, as measurements in the calibration channel had shown, extremely insensitive to the flow direction. They indicated the total temperature and were mounted on a mean radius dividing the annulus into two equal areas. Plotted is the ratio of the local temperature to the temperature at the flow inlet. As the specific heat of the air flowing through the turbine can be considered as constant in this area, the temperature ratio is a direct measure of the energy supply and removal at the particular stage. The parameters of the curves are the relative speed and the relative mass flow.

With normal flow direction (from stage 1 in the direction of stage 7) with a large mass flow or low speed the energy in the stages is uniformly removed. At higher speeds there is a tendency for the last stages to consume energy. This can be seen particularly clearly in the curve $\dot{m}/\dot{m}_N = 0.375$, $n/n_N = +1.00$. If the mass flow is small and the speed high all stages consume energy; the same is the case with turning of the rotor in reverse direction. At zero speed the temperature must remain constant.

If there is back flow through the turbine (from stage 7 in the direction of stage 1) as a rule all stages consume energy. The part of the last turbine stage is the greatest as here the longest blades operate in the area of the greatest density of the medium flowing through the machine. At large mass flow and low speed the last stages, looking in the direction of flow, supply energy.

The pressure curve, as measured with the wall bores between the pressure stages, is shown in Fig. 9. Plotted is the static pressure of the wall bore divided by the static pressure at the flow inlet. With normal direction of flow the speed has less influence on the pressure drop than the mass flow. With larger mass flow rates the pressure drop is reduced

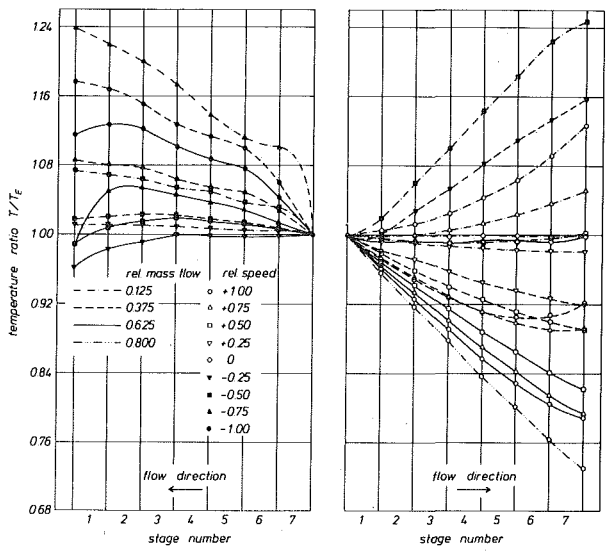


Fig. 8 Temperature ratio measured with total temperature probes between the turbine stages as function of relative mass flow and relative speed at normal flow direction (right) and at backward flow (left) (T) local temperature, (T_E) temperature at flow entrance

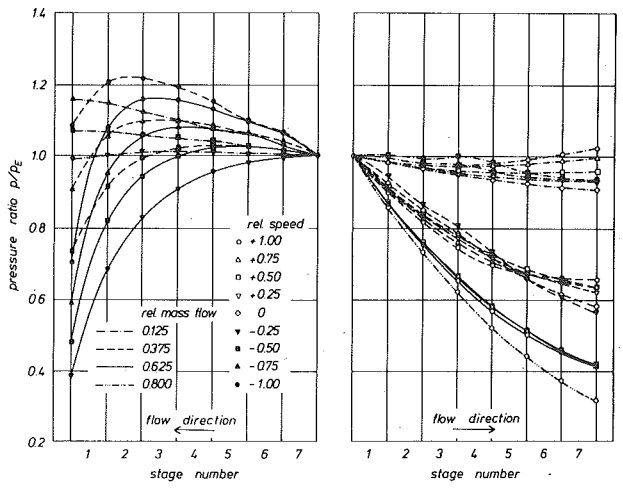


Fig. 9 Pressure ratio measured with wall bores between the turbine stages as function of relative mass flow and relative speed at normal flow direction (right) and at backward flow (left). (p) local static pressure, (p_E) static pressure at flow entrance

Downloaded 01 Jun 2010 to 171.66.16.58. Redistribution subject to ASME license or copyright; see http://www.asme.org/terms/Terms_Use.cfm

quite uniformly. With smaller mass flow rates there is the tendency of a greater pressure drop in the first stages than in the last ones. Taking into consideration the temperature ratios of Fig. 8 this means that at partial load only the first stages of a multi-stage turbine operate with good efficiency. With very small mass flows the last stages work as compressor stages. When the turbine is rotating in reverse direction the tendency is different. Here the pressure drop in the first stages is less than in the last ones.

Informative are the results with back flow. With small flow rates and negative speeds all stages work as compressor stages. With large mass flow rates and small speeds only the first stages, seen in flow direction, are operating as compressor stages; in the last stages the gas expands. As a result of the inappropriateness of the channel contour, the greatest pressure drop always occurs in the last stages. The speed has a much greater influence on the pressure development in the turbine with back flow than with normal direction of mass flow.

Comparison With The Measuring Results on One Stage

Prior to the measurements being carried out on a turbine with seven-stage blading, measurements had been carried out on a single stage, on which a report has already been issued [6]. It can be seen that starting from the cascade characteristics in the middle section of the stage the stage performance curves can be approximately determined [7]. The stage characteristics are the power coefficient λ, the enthalpy coefficient ψ and the efficiency η as a function of the flow coefficient φ.

The power coefficient λ is defined as

$$\lambda = \frac{2\Delta h}{u^2}. \tag{1}$$

Δh is the actual enthalpy drop in the stage, u the peripheral velocity at the flow inlet to the impeller. For λ under simplified conditions the following can be given

$$\lambda = 2\varphi(\cot\alpha_E - \cot\beta_A) - 2, \tag{2}$$

wherein φ is the flow coefficient

$$\varphi = \frac{c_a}{u} \tag{3}$$

and c_a the axial flow velocity. α_E is the angle of the absolute velocity entering the impeller, β_A the angle of the relative outlet velocity countered against the relative peripheral velocity [7]. The peripheral velocity with normal direction of rotation and the axial velocity with normal direction of flow were defined as positive directions. The sign of φ as per equation (3) is dependent on the signs of c_a and u. If λ is positive the stage supplies power. If α_E and β_A can be considered as constant, equation (2) represents the equation of a straight line. With the normal direction of flow that is approximately the case both with positive and negative directions of rotation. With back flow it is more difficult to determine the outlet angles.

As a further stage characteristic, the enthalpy coefficient ψ is used

$$\psi = \frac{2\Delta h_s}{u^2} \tag{4}$$

where Δh_s is the isentropic enthalpy drop at the stage.

For the normal direction of flow ψ can be determined as

$$\psi = \varphi\left[\frac{\varphi}{\sin^2\alpha_1}\left(\frac{1}{\eta'} - 1\right) + \varphi\left(\frac{1}{\eta''\sin^2\beta_2} - 1\right) + 2\cot\alpha_1\right] - 1 \tag{5}$$

and for back flow as

$$\psi = \varphi\left[\frac{\varphi}{\sin^2\beta_1}\left(\frac{1}{\eta''} - 1\right) + \varphi\left(\frac{1}{\eta'\sin^2\alpha_0} - 1\right) - 2\cot\beta_1\right] - 1. \tag{6}$$

α_1 is the angle of the absolute outlet flow at the guide wheel, β_2 that of the relative outlet flow at the impeller, β_1 that of the relative outlet flow at the impeller with back flow and α_0 the angle of the absolute outlet flow at the guide wheel with back flow. η' and η'' are the isentropic efficiencies of the guide wheel and the impeller. The cascade characteristics for back flow can be ascertained with the aid of [4] or [5]. Negative β means operation of the stage in the compressor range. This is always the case for $\varphi = 0$ ($\psi = -1$) and corresponds with the experience gained.

The stage efficiency η is defined for the turbine (positive ψ) as

$$\eta_T = \frac{\lambda}{\psi} \tag{7}$$

and for the compressor (negative ψ) as

$$\eta_V = \frac{\psi}{\lambda}. \tag{8}$$

In Fig. 10 the efficiencies resulting from the measurements on the single-stage turbine [6] and as calculated as per the equations (1–8) and the cascade characteristics as per [4] or [5], are plotted. The efficiency with turbine operation becomes negative when energy is supplied. This is principally the case with negative speed (represented by broken lines).

In the entire four-quadrant range the efficiency curves show good correspondence with the measured values. This means that the stage characteristic curves for four-quadrant operation can approximately be determined with simple equations from the characteristics of the middle section cascades.

To compare the tests on the single-stage turbine and on the turbine with seven-stage blading the results were represented in Figs. 11 and 12 in a characteristic field with Mach similarity. Entered is

$$\frac{\dfrac{\Delta h}{T_E}}{\left(\dfrac{\Delta h}{T_E}\right)_N} = f\left(\frac{\dfrac{\dot m\sqrt{T_E}}{P_E}}{\left(\dfrac{\dot m\sqrt{T_E}}{P_E}\right)_N}, \frac{\dfrac{n}{\sqrt{T_E}}}{\left(\dfrac{n}{\sqrt{T_E}}\right)_N}\right). \tag{9}$$

$\dot m$ is the mass flow, p the pressure, t the temperature and n the speed. Index E characterises the flow inlet, N the nominal point. Simplified the following can be written

$$X^* = f(\mu^*, {}_v{}^*). \tag{10}$$

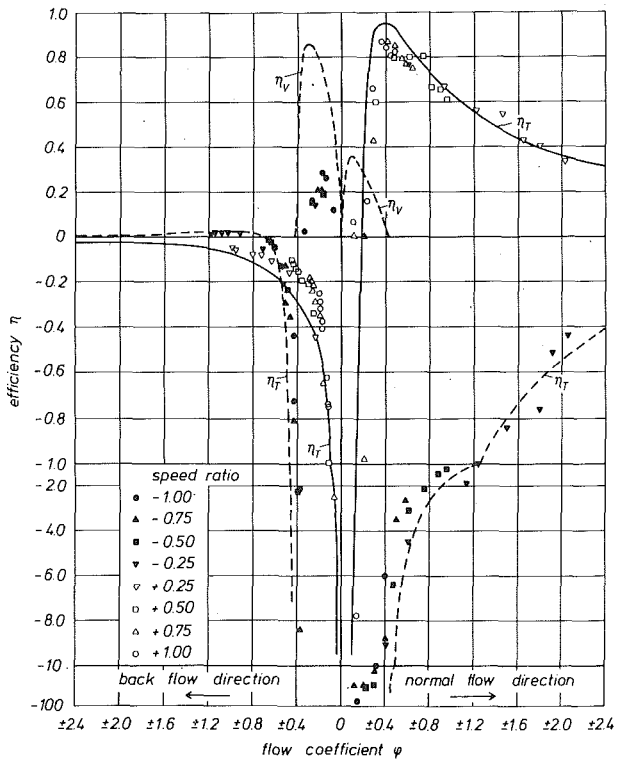


Fig. 10 Turbine stage efficiency as function of the flow coefficient. Points: measuring, lines: calculation: dashed lines: negative speed. η_T efficiency for turbine operation, η_V efficiency for compressor operation

Downloaded 01 Jun 2010 to 171.66.16.58. Redistribution subject to ASME license or copyright; see http://www.asme.org/terms/Terms_Use.cfm

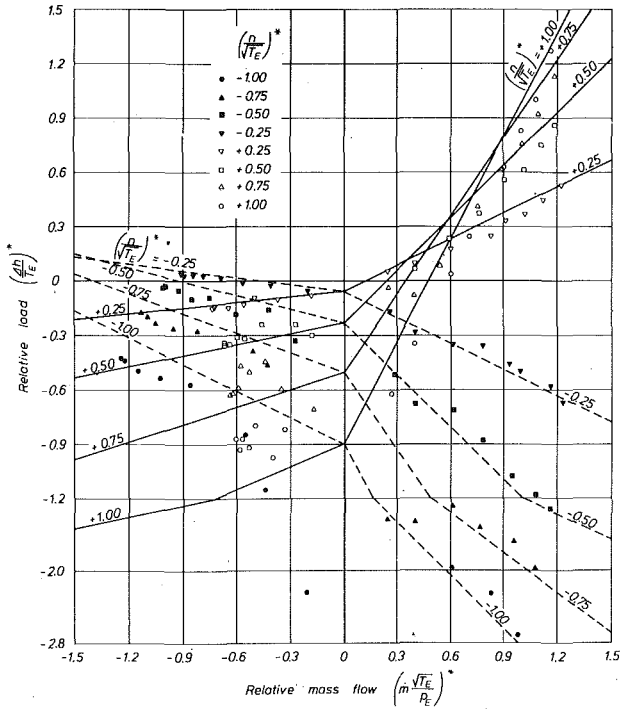


Fig. 11 Performance map with Mach similarity of a turbine stage. Relative load as function of relative mass flow and relative speed. Points: measurements; lines: calculation; dashed lines: negative speed

In Fig. 11 apart from the test points the straight lines as per equation (2) are plotted. Unbroken lines represent positive speeds, broken lines negative speeds.

Between equation (2) and the variables of equation (10) there is the following relationship

$$X^* = \left(k_1 \varphi_N \frac{\mu^*}{\nu^*} - 2\right) \frac{\nu^{*2}}{\lambda_N}. \tag{11}$$

For $\nu^* = \text{const}$ equation (11) is the equation of a straight line. The constant k_1 results as

$$k_1 = 2(\cot\alpha_E - \cot\beta_A)$$

On comparison of Fig. 11 and Fig. 12 it can be seen that calculation of the characteristics as per equation (2), respectively (11) is in some measure possible for the single-stage turbine but not for the multi-stage turbine. In consequence of the different loads of the stages (Figs. 8 and 9) and the reaching of the choking limit, curved characteristics result. Only by the mathematical combination of stages with defined stage characteristics the four-quadrant characteristics of multi-stage turbines can be approximately calculated.

Summary

A report has been made on some results of tests of characteristics on a seven-stage turbine in the four-quadrant range. The four-quadrant range covers positive and negative speed and mass flow direction. In the partial-load and in the back flow range the measuring results showed very different loads for the individual stages of the turbine. Simple equations were given with which the single stage characteristics in the four-quadrant range could be approximately determined from the characteristics of the middle section cascades. A comparison of the performance maps with Mach similarity of the seven-stage and the single-stage turbines showed that the characteristics of the multi-stage turbine can only be determined by successive calculation of adjoining individual stages.

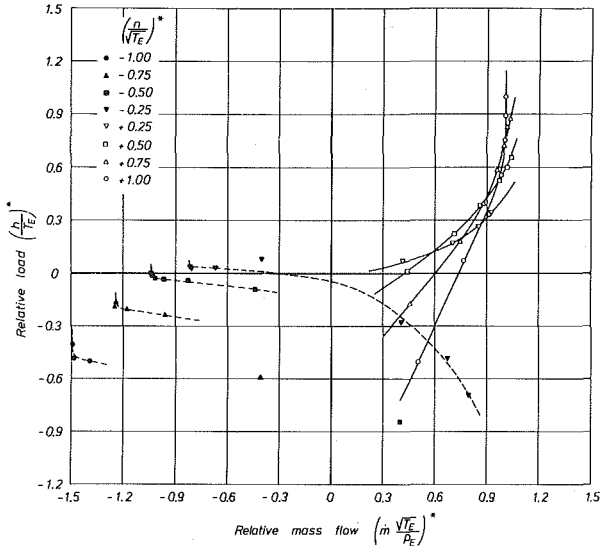


Fig. 12 Performance map with Mach similarity of the seven-stage turbine. All results from measuring. Relative load as a function of relative mass flow and relative speed

Acknowledgment

The work reported in this paper was financially supported by the German Research Association (Deutsche Forschungsgemeinschaft). The authors would like to express their thanks to the DFG.

References

1 Bammert, K. and Brütt, P., "Berechnung und Messung der Kennfelder von mehrstufigen Axialturbinen," *VDI-Forschungsheft,* No. 519, 1967.

2 Bammert, K. and Zehner, P., "Rückströmung an Schaufelgittern von Turbinen." *VDI-Berichte,* No. 193, 1973, pp. 273–283.

3 Bammert, K. and Zehner, P., "Back Flow in Turbines of Nuclear Closed-Cycle Gas Turbine Plants in Case of Circuit Pipe Rupture." ASME JOURNAL OF ENGINEERING POWER, Vol. 97, 1975, No. 2, pp. 189–194.

4 Zehner, P., "Systematische Untersuchungen der Charakteristiken rückwärts durchströmter Turbinengitter." Diss. TU Hannover, 1974.

5 Bammert, K. and Zehner, P., "Back Flow Characteristics of Turbine Cascades." *Atomkernenergie,* Vol. 24, 1974, No. 4, pp. 225–232.

6 Bammert, K. and Zehner, P., "Measurements of the Performance of an Air Turbine Stage at Positive and Negative Mass Flow and Rotational Speed (Four-Quadrant Characteristics)." ASME JOURNAL OF ENGINEERING POWER. Vol. 100, 1978, No. 1, pp. 22–29.

7 Zehner, P., "Vierquadrantencharakteristik einer Turbinenstufe." *Atomkernenergie,* Vol. 32, 1978, No. 4, pp. 292–298.

Downloaded 01 Jun 2010 to 171.66.16.58. Redistribution subject to ASME license or copyright; see http://www.asme.org/terms/Terms_Use.cfm

J. A. Fabunmi
Research Engineer Specialist,
Kaman Aerospace Corporation,
Old Windsor Road,
Bloomfield, CT 06002.

Forced Vibrations of a Single Stage Axial Compressor Rotor

A semi-empirical method, utilizing modal analysis based on experimentally obtained modeshapes has been used to study the vibration response of a 23 bladed axial compressor rotor. The system modeshapes, characterized by the blade deflections at resonance, are more or less irregular depending upon the proximity of the system frequencies to the blade cantilever frequencies. The response of the detuned bladed disk assembly to various types of harmonic excitations are shown to be predictable if sufficient experimental information is available about the resonant modes and frequencies of the system.

1 Introduction

It is the usual practice in turbomachine flutter studies to assume the rotor blades to be identical. Thus the well understood vibration patterns of a tuned bladed disk assembly are taken for granted. These patterns are characterized by a uniform amplitude of vibration of all the blades and a constant phase shift between the generalized displacements of adjacent rotor blades. The consequences of the small differences between the blades of real rotors have been studied extensively by turbomachine vibration researchers [3, 5, 6–11]. Detuned bladed disks have been found to exhibit many more resonances with more complicated modeshapes than those exhibited by a tuned system. Both theoretical and experimental studies have been carried out with the aim of understanding the effects of blade detuning on the vibration characteristics of bladed disks.

As a result of the stiffness and high density of the structure compared to that of air, the flutter modes and frequencies of turbomachine rotors are virtually determined by the vibration characteristics of the structure alone. Reliable flutter calculations cannot be carried out without prior knowledge of the resonant configurations of the given rotor, inasmuch as the onset of flutter in a given rotor depends on the relative motions of the blades during rotor vibrations. On the other hand, computations of these modeshapes from first principles are of limited use, since there is no consistent way of accounting for the small nonuniformities that make so much difference to the response of these structures.

In this study, a semi-empirical method, utilizing modal analysis based on the experimentally determined modeshapes and a linear spring-mass model is used to analyze the vibratory response of an arbitrarily detuned bladed disk assembly. Information about the resonant modeshapes of the 23 bladed experimental compressor rotor was obtained using time averaged holographic technique. The empirical transfer function of the rotor system, based on both the theoretical model and the experimental data was then used to predict the forced response of the rotor to various harmonic excitations.

The present work differs from Ewins' [11–13] in that the method of calculating the forced response of the given rotor is based on the actual, measured resonant modes of the rotor. These modes are properties of the given rotor, and may differ considerably among rotors of the same nominal design.

2 Vibration Characteristics of Bladed Disk Assemblies

Consider the undamped linear system shown in Fig. 1(*a*): m_n and k_n represent the equivalent masses and stiffnesses of the cantilevered blades. M, K and K' simulate the effective mass and stiffnesses of the blade root and section of the rotor disk. It is assumed that the violations of rotational uniformity occur in the blading only.

The natural frequencies and modeshapes of the system are the eigenvalues and eigenvectors of the characteristic value problem:

$$(\overline{K} - \omega^2\overline{M})\overline{q} = 0 \tag{1}$$

where the stiffness $\overline{K}$ and mass $\overline{M}$ matrices are given in Appendix 1.

The eigen values are the solutions of the characteristic equation:

$$\det(\overline{\overline{D}}) = \det(\overline{\overline{K}} - \omega^2\overline{\overline{M}}) = 0 \tag{2}$$

The determinant of $\overline{\overline{D}}(\omega)$ is unchanged if it is postmultiplied by a matrix $\overline{\overline{P}}(\omega)$ also given in Appendix 1, since its effect is to perform elementary operations on the columns of $\overline{\overline{D}}(\omega)$ for $\omega^2 \neq k_n/m_n$, $n = 1, 2, \ldots N$. Thus;

$$\overline{\overline{D}}(\omega) \times \overline{\overline{P}}(\omega) = \overline{\overline{D}}'(\omega) = \begin{bmatrix} \overline{\overline{D}}_{11}'(\omega) & 0 \\ \overline{\overline{D}}_{21}'(\omega) & \overline{\overline{D}}'_{22}(\omega) \end{bmatrix}$$

and $\det(\overline{\overline{D}}) = \det(\overline{\overline{D}}') = \det(\overline{\overline{D}}_{11}')\times\det(\overline{\overline{D}}_{22}')$. Equation (2) is satisfied if $\det(\overline{D}_{22}') = 0$. When all the blades are identical, i.e., in the perfectly tuned case, the diagonal elements of $\overline{D}_{22}'$ are identical and the matrix is circulant, so called because each successive row is a cyclic permutation of the preceding row. Thus for a tuned rotor:

$$\det(\overline{\overline{D}}_{22}'(\omega)_{\text{tuned}}) = \prod_{k=0}^{N-1} (K + 2K' - F(\omega) - K'(\rho_k + \rho_k{}^{N-1})) \tag{3}$$

where $\rho_k = \exp(2\pi ik/N)$, $k = 0, 1, \ldots N-1$. It follows that;

Contributed by the Gas Turbine Division and presented at the Gas Turbine Conference and Exhibit and Solar Energy Conference, San Diego, California, March 12–15, 1979 of THE AMERICAN SOCIETY OF MECHANICAL ENGINEERS. Manuscript received at ASME Headquarters December 18, 1978. Paper No. 79-GT-108.

Copyright © 1980 by ASME
Downloaded 01 Jun 2010 to 171.66.16.58. Redistribution subject to ASME license or copyright; see http://www.asme.org/terms/Terms_Use.cfm

$$\det(\overline{\overline{D}}_{22}'(\omega)_{\text{tuned}}) = \begin{cases} (K - F(\omega)) \prod_{k=1}^{(N-1)/2} (K - F(\omega) + 2K'(1 - \text{Cos}(2\pi k/N)))^2 \\ \qquad\qquad N \text{ odd} \\ (K - F(\omega))(K + 4K' - F(\omega)) \times \\ \quad \times \prod_{k=1}^{N/2-1} (K - F(\omega) + 2K'(1 - \text{Cos}(2\pi k/N)))^2 \\ \qquad\qquad N \text{ even} \end{cases} \tag{4}$$

These equations indicate $(N-1)/2$ (N odd) or $N/2 - 1$ (N even) "double" or paired roots to the frequency equation, meaning that the system possesses two linearly independent modes of vibration at such frequencies.

It can be easily verified that the system modeshapes for the tuned rotor are given by;

$$\underset{(2N \times 1)}{\bar{q}_k} = \underset{(2N \times 1)}{\begin{Bmatrix} \alpha_k(\overline{X}_n)_k \\ (\overline{X}_n)_k \end{Bmatrix}} \qquad n = 1, 2, \ldots N \tag{5}$$

where,

$$\alpha_k = (\omega_{k,s}/\omega_b)^2/(1 - \omega_{k,s}/\omega_b)^2$$

$\omega_{k,s}$ is the kth system frequency,
ω_b is the blade cantilever frequency.
$(\overline{X}_n)_0$ = Constant

$$(X_n)_k = \begin{cases} \text{Cos } (2\pi kn/N) \\ \text{Sin } (2\pi kn/N) \end{cases} \quad k = 1, 2, \ldots \begin{matrix} N/2 - 1 \ (N \text{ even}) \\ (N-1)/2 \ (N \text{ odd}) \end{matrix}$$

$$(X_n)_{N/2} = (-1)^n \ N \text{ even} \tag{6}$$

These modeshapes are best visualized in terms of nodal diameters. The value of k for each mode is the number of nodal diameters associated with the modeshape. Since the sine and cosine functions occur at the same frequency, linear combinations of them are also natural modes at the corresponding frequency. The effect of this is to make the orientation of the nodal diameters arbitrary. Their location will be determined either by the initial conditions, or by the external forcing function. It should also be noted that the blade deflections are just the disk rim deflections amplified by a factor $\alpha_k = (\omega_{k,s}/\omega_b)^2/(1 - (\omega_{k,s}/\omega_b)^2)$. In the tuned rotor, this factor is the same for all the blades and hence the blade configuration faithfully reproduces the nodal diametral patterns of the disk rim.

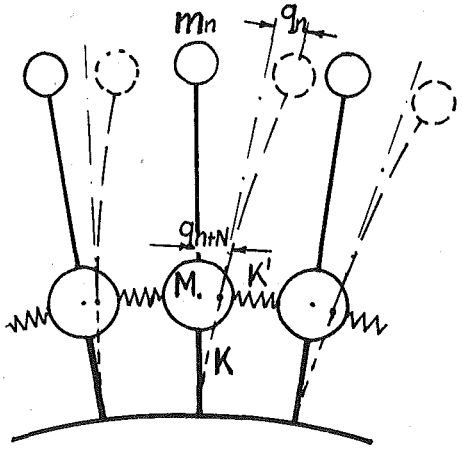


Fig. 1(*a*) Spring-mass model of bladed disk assembly

If the expressions in equations (5) and (6) are substituted into equation (1) for the jth system mode shape, equation (1) is reduced into a 2×2 matrix equation:

$$\begin{bmatrix} \omega_b{}^2 - \omega_{j,s}{}^2 & -\omega_{j,s}{}^2 \\ -\omega_{j,s}{}^2 & \mu\omega_{d,j}{}^2 - (\mu+1)\omega_{j,s}{}^2 \end{bmatrix} \begin{Bmatrix} \alpha_j \\ 1 \end{Bmatrix} = 0 \tag{7}$$

where $\mu = M/m$;

$\omega_{d,j}{}^2 = (K + 2K'(1 - \text{Cos } (2\pi j/N)))/M$, a characteristic frequency of the disk. The characteristic equation, defining $\omega_{j,s}$ from equation (7) is:

$$(\omega_{j,s}{}^2/\omega_{d,j}{}^2 - 1)(\omega_{j,s}{}^2/\omega_b{}^2 - ((\mu+1)/\mu)) - 1/\mu = 0 \tag{8}$$

If the disk is very flexible, the parameter μ is significant and it follows from (8) that there are two families of modes, one with frequencies in the vicinity of $\omega_{d,j}$ and the other in the vicinity of ω_b. $\omega_{d,j}$ can be associated with frequencies at which the motion of the disk rim is significant compared to the blade deflections. For each of the N natural modeshapes defined in equation (6), there are two frequencies, one high, and one low. In all, there are $2N$ natural frequencies, consistent with the degrees of freedom of the model.

In the presence of small physical differences between the blades, the diagonal elements of $\overline{\overline{D}}_{22}'(\omega)$ are not identical anymore. The coincident pairs of roots (double roots) are replaced by pairs of close roots. These roots correspond to pairs of orthogonal modeshapes of the system, occurring at the slightly different frequencies. This phenomenon is usually referred to as "mode splitting." One effect of mode splitting in detuned systems is to increase the number of frequencies at which the system resonances can occur. Another effect of mode splitting is that closely spaced double modes can overlap after splitting. Thus the resultant system resonant modes can contain components with different nodal diametral patterns.

For the general case of detune, the system modeshapes will no more be of the form (5), but of the form:

$$(\bar{q})_{k,\text{detuned}} = \left\{ \frac{(\alpha_{k,n}\overline{X}_n)_k}{(\overline{X}_n)_k} \right\};$$

Nomenclature

N = number of blades
K = equivalent basic stiffness of disk
K' = equivalent coupling stiffness coefficient between blades
M = equivalent lumped mass segment of disk
m, m_n = equivalent lumped mass of cantilevered blade
k, k_n = equivalent stiffness coefficient of cantilevered blade
q_n = coordinate
$\overline{\overline{M}}$ = mass matrix
$\overline{\overline{K}}$ = stiffness matrix
$\bar{(\ )}$ = vector
$\overline{\overline{U}}$ = system modal matrix
Ω = frequency or rotational speed
ω = frequency
α = blade amplification factor
det( ) = determinant of a matrix
γ = structural damping coefficient
μ = mass ratio

Subscripts

n = of the nth blade
n, s = of the nth system mode
k, s = of the kth system mode
n, b = of the nth blade
k = of the kth modeshape
k, n = for the nth blade in the kth system mode
d, j = associated with the disk, in the jth mode

Downloaded 01 Jun 2010 to 171.66.16.58. Redistribution subject to ASME license or copyright; see http://www.asme.org/terms/Terms_Use.cfm

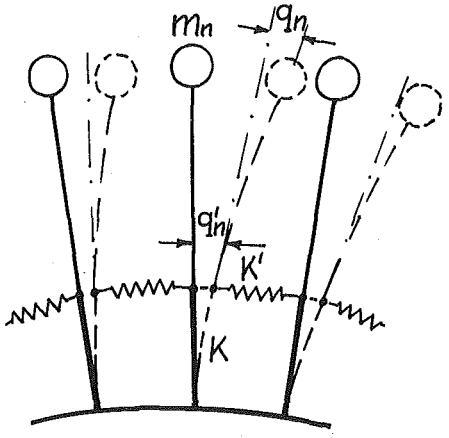


Fig. 1(*b*) Spring-mass model of rotor with stiff disk and flexible blades

with $\alpha_{k,n} = (\omega_{k,s}/\omega_{n,b})^2/(1 - (\omega_{k,s}/\omega_{n,b})^2)$;
$n = 1, 2, \ldots n$; $k = 0, 1, 2, \ldots . N - 1$;
$\omega_{n,b}{}^2 = k_n/m_n$, the cantilever frequency of the nth blade.

It is seen that if the system frequencies occur in the vicinity of the blade cantilever frequencies, then the configurations assumed by the blades at resonance can be largely unlike those assumed by the disk rim, this being the direct result of the different amplification functions for each blade. This is an additional effect that complicates the resonance data of bladed disk assemblies, based on the amplitude of the blade deflections.

The phenomenon of "rogue" blades is very easily explained in this context. It is not necessarily the blade with the worst detune or the lowest cantilever frequency that becomes rogue, rather it is the blade whose cantilever frequency coincides with one of the system frequencies, since $\alpha_{k,n}$ for such a blade is very large.

For the compressor rotor under study, and for most practical rotor designs, the disk is much stiffer than the cantilevered blades, such that $\omega_{d,j} \gg \omega_b$. A more appropriate model is that shown in Fig. 1(*b*). The elastic coupling of the blades through the disk is retained in form of the stiffnesses K and K', while the kinetic energy associated with the motion of the disk is neglected by leaving out the masses M. Only N of the displacement coordinates are independent, and the equation of free motion of the undamped system is;

$$(\overline{\overline{M}}'') \frac{d}{dt^2}(\bar{q}) + \lceil \omega_n{}^2 \rfloor (\bar{q}) = 0 \tag{9}$$

where $(\bar{q})$ is the $N \times 1$ vector of the blade displacement coordinates.

$(\overline{\overline{M}}'')$ is the effective mass matrix, given in Appendix 1; and $\lceil \omega_n{}^2 \rfloor$ is the effective stiffness matrix, which is diagonal, the elements of which are simply the squares of the blade cantilever frequencies; i.e.,

$$\lceil \omega_n{}^2 \rfloor = \begin{bmatrix} \omega_1{}^2 & & 0 \\ & \omega_2{}^2 & \\ & & \ddots \\ 0 & & \omega_N{}^2 \end{bmatrix} \tag{10}$$

3 Experimental Study of Compressor Rotor Vibrations

The compressor rotor under study was an experimental rotor, designed and developed for flutter experiments in a blowdown tunnel under a NASA-MIT Research Contract, directed by Prof. J. L. Kerrebrock of MIT. Excitation of each of the 23 blades of the rotor was achieved by mounting disks of piezoelectric ceramics PZT5H at the base of each blade. The details of the design can be found in [1]. High voltage sinusoidal signals with amplitude, frequency and phase adjustments were applied independently to the PZT's through sliprings, making it possible to specify the amplitude, phase and frequency of the forces exciting the blades.

The first part of the investigation was to find out how much the coupling through the disk affected the response of each blade when it was being forced alone. Two sets of tip deflection versus frequency data were recorded for each blade when that particular blade alone was driven. In one case, the disk was freely supported on a mock up of the rotor shaft. In the other case, the disk rim was uniformly weighed down by heavy flanges. Figs. 2(*a*) and 2(*b*) show the plotted response curves for a typical blade of the assembly. The multiple peaks indicate the participation of the blade in more than one of the system resonant modes when the disk was freely suspended, while only one peak was found when the disk motion was suppressed by the weight of the flanges.

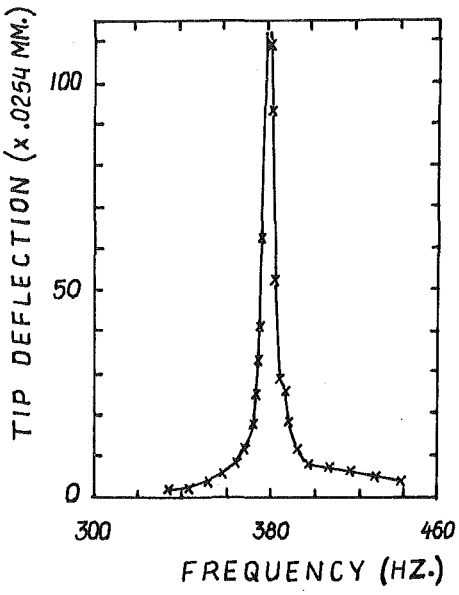


Fig. 2(*a*) Measured response of blade 23 to individual excitation with disk weighted down

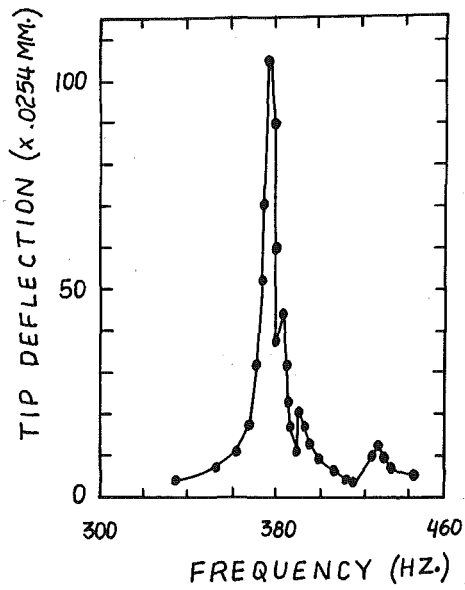


Fig. 2(*b*) Measured response of blade 23 to individual excitation with the disk freely mounted

The second part of the investigation consisted of a procedure for determining the natural modal configurations of the blade disk assembly. It was understood from the results of the preceding sections that these configurations may not have simple nodal diameters, and also that more than one mode may occur at the same frequency, leading to a certain degree of degeneracy which makes any linear combination of these modes also a mode. Since a 23 deg of freedom model is being used, it was necessary to identify 23 independent natural modes, which are orthogonal with respect to both the mass

Downloaded 01 Jun 2010 to 171.66.16.58. Redistribution subject to ASME license or copyright; see http://www.asme.org/terms/Terms_Use.cfm

and stiffness matrices. Thus, the first step was to excite and record 23 linearly independent modal configurations, which can subsequently be orthogonalized with respect to the known stiffness matrix of equation (10), by the Gram-Schmidt procedure.

Different resonant modes were excited by driving the system with different forcing vectors. These modes were recorded holographically.

The complete set of recorded system resonances can be found in [1]. The number of fringes appearing on each blade is a measure of the blade deflection amplitude at that mode. Given the holographic data alone, it is nearly impossible to determine the phase of the blade deflection at resonance, since the hologram indicates only the magnitude of the deflection. Ideally, it is necessary to install sensitive strain gages on all the blades. When this cannot be done, one has to rely on other considerations such as the distribution of the excitation forces, the location of the nodal points and the fundamental modulation of the blade amplitudes. In the case of coincident or closely spaced modes, it is expected that the mode with the least number of nodes will dominate.

Histogram representations of the blade tip amplitudes from the holographic data are presented in [1]. The distribution of the excitation forces can be described as; (Sign(Cos $(2\pi ni/23)$)) Cos ωt, where $n = 0, 1, \ldots 11$ is refered to as the excitation order, and $i = 1, 2, \ldots 23$ is the blade number. The number of resonant frequencies is neither 12 nor 23 which indicates that both mode splitting and resonance coincidence must have occurred. There are 16 resonant frequencies. Most of the resonant frequencies are closely spaced. A number of resonant modes occur at the same frequency. Thus any linear combination of these modes can also be excited at that frequency.

Modal vectors, orthogonal with respect to the stiffness matrix of equation (10), are presented also in histogram form in [1].

4 Modal Analysis of Forced Rotor Response

If proportional hysteretic damping is assumed, the equation of damped forced motion corresponding to equation (9) is:

$$(\overline{\overline{M}}'')\frac{d(\overline{q})}{dt^2} + (1 + i\gamma)\lceil\omega_n{}^2\rfloor(\overline{q}) = (\overline{\overline{M}})^{-1}(\overline{F}) \tag{11}$$

where γ is the damping coefficient, and $\overline{F}$ is the forcing vector. The i in equation (11) is a complex number. In this experiment, the forcing inputs are base accelerations imposed by the piezoelectric exciters. Thus;

$$(\overline{F}) = -(\overline{M})\frac{d(\overline{X}(t))}{dt^2} \tag{12}$$

where $(\overline{X}(t))$ is the vector of input displacements at the blade roots which are proportional to the voltage applied to the piezoelectric ceramics.

If $(\overline{\overline{U}})$ denotes a matrix the columns of which are the orthonormal modes of the system, then:

$$(\overline{\overline{U}})^T\lceil\omega_n{}^2\rfloor(\overline{\overline{U}}) = \lceil I\rfloor, \text{ the identity matrix,}$$

and $$(\overline{\overline{U}})^T(\overline{\overline{M}}'')(\overline{\overline{U}}) = \left\lceil\frac{1}{\omega_{rr}{}^2}\right\rfloor;$$

where ω_{rr} is the rth system natural frequency (not to be confused with the blade cantilever frequencies). For harmonic excitations at a frequency Ω, we can write;

$$(\overline{q}(t)) = (\overline{Q})\exp(i\Omega t),$$

and

$$(\overline{X}(t)) = (\overline{X})\exp(i\Omega t).$$

$(\overline{Q})$ and $(\overline{X})$ are in general complex and are related through the system transfer function $\overline{\overline{G}}(\Omega)$ by:

$$(\overline{Q}) = (\overline{\overline{G}}(\Omega))(\overline{X}) \tag{13}$$

It can easily be shown that;

$$\overline{\overline{G}}(\Omega) = (\overline{\overline{U}})\lceil g_{rr}\rfloor(\overline{\overline{U}})^T \tag{14}$$

where

$$g_{rr} = \Omega^2/((1 - \Omega^2/\omega_{rr}{}^2) + i\gamma).$$

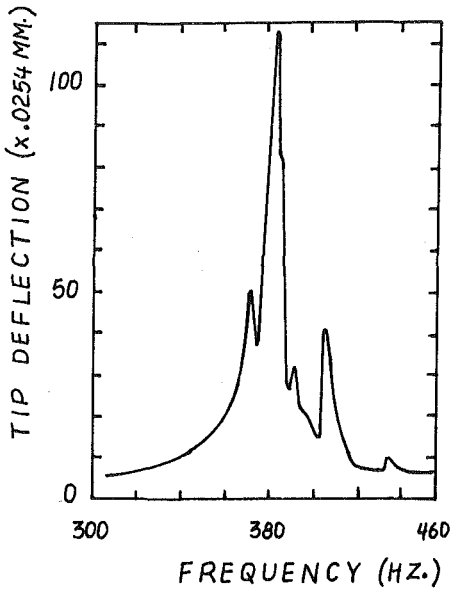


Fig. 3 Computed response of blade 23 to individual excitation

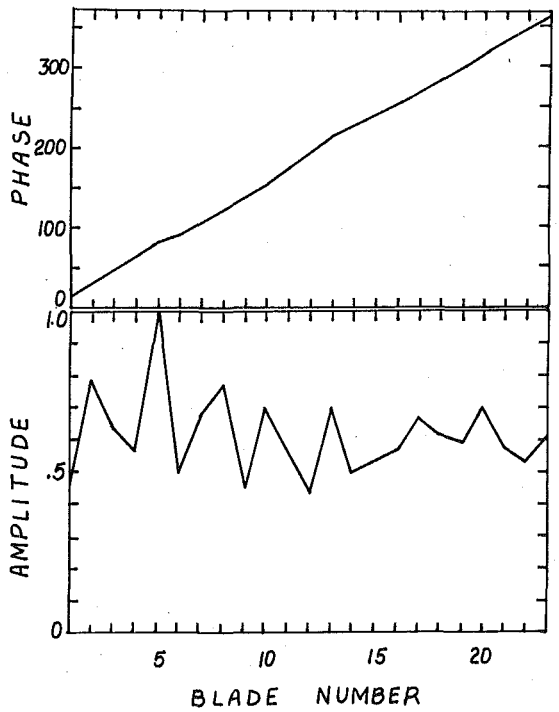


Fig. 4 Computed system response at 340 Hz for $n = 1$

Equation (13) is the numerical analog of the system. $\overline{\overline{G}}(\Omega)$ is determined semi-empirically from the holographic data. Entries into $(\overline{X})$ represent the external forcing. The computed $(\overline{Q})$ yield the complex response of the blades from which the amplitude and phase of the blades can be determined. By entering only one nonzero element into the vector $\overline{X}$, one can simulate the excitation of only one blade in the system. The computed amplitude response of a blade, when only that blade is being driven is shown in Fig. 3. This figure is to be compared to Fig. 2(b), which is the experimentally measured response of the same blade when it was being driven alone.

When all the blades are being driven with a constant interblade phase angle of $2\pi n/23$ radians, the entry into the rth element of $(\overline{X})$ is simply exp $(2\pi nri/23)$ or;

$$\text{Cos}\,(2\pi nr/23) + i\,\text{Sin}\,(2\pi nr/23).$$

Computed amplitude and phase responses of the compressor blades

Downloaded 01 Jun 2010 to 171.66.16.58. Redistribution subject to ASME license or copyright; see http://www.asme.org/terms/Terms_Use.cfm

for $n = 1$ and $\Omega = 340, 380, 427$ and 440 Hz are plotted in Figs. 4–7. 340 Hz is below the band of system frequencies, 440 Hz is above the band of system frequencies, while 380 and 427 Hz fall within the band of system frequencies. Fig. 8 is a plot of the blade cantilever frequencies, measured from the weighted disk experiment.

5 Discussion of results

The computed curve of Fig. 3 exhibits the multiple peak response of the rotor blade similar to that recorded experimentally in Fig. 2(*b*). In fact, by entering zeros into the $(\overline{X})$ vector except for the kth element, from equation (13) and one can write down the expression for the kth element of $(\overline{Q})$:

$$Q_k(\Omega) = \sum_{j=1}^{23} X_k(\Omega^2 U_{k,j}{}^2)/((1 - \Omega^2/\omega_{jj}{}^2) + i\gamma_j) \qquad (15)$$

where ω_{jj} = frequency of the jth system mode, $U_{k,j}$ = amplitude of the kth blade in the jth system normal mode shape, Ω = driving frequency, γ_j = hysteretic damping coefficient of the jth system mode.

Equation (15) governs the curve in Fig. 3. Thus the peaks occur at the system resonant frequencies. The relative amplitude of each peak depends on the damping coefficient of the corresponding system mode and the relative participation of that blade in the system mode shape at that frequency.

The amplitude responses of the blades, computed for the excitation of all the blades at a constant interblade phase angle (see Figs. 4–7) are nonuniform. The phase responses, however show some interesting trends. At 340 Hz, the phase responses of the blades follow those of the forcing functions. At 380 Hz, there is no correlation between the

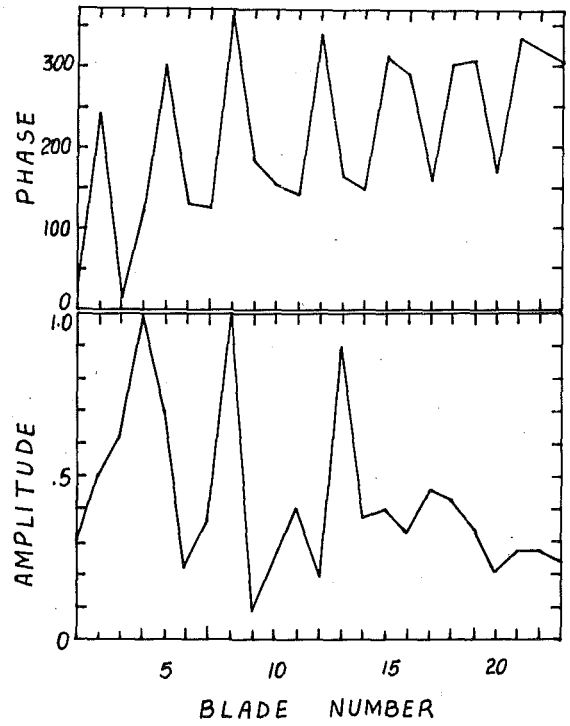


Fig. 5 Computed system response at 380 Hz for $n = 1$

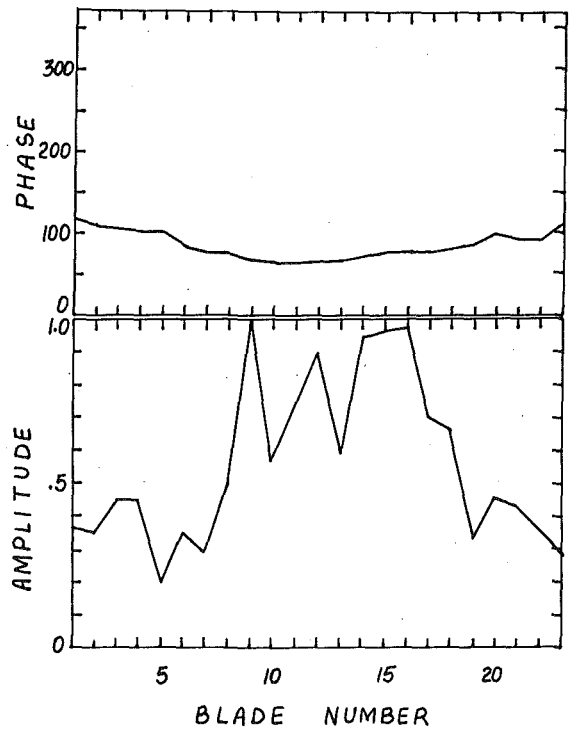


Fig. 6 Computed system response at 427 Hz for $n = 1$

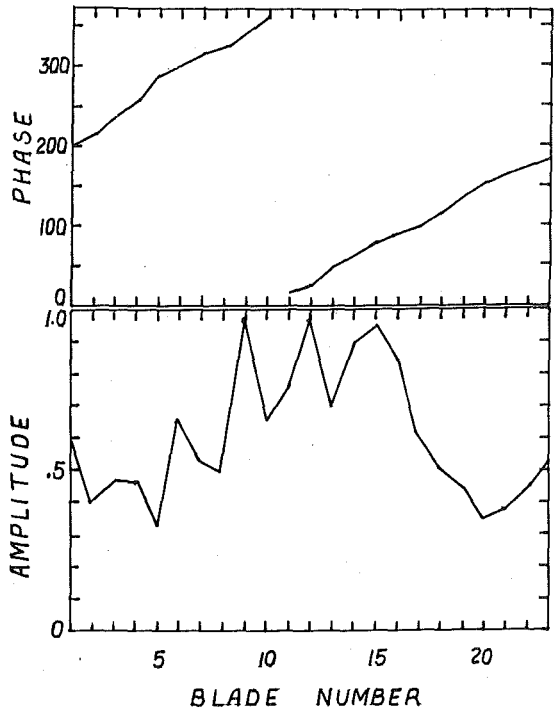


Fig. 7 Computed system response at 440 Hz for $n = 1$

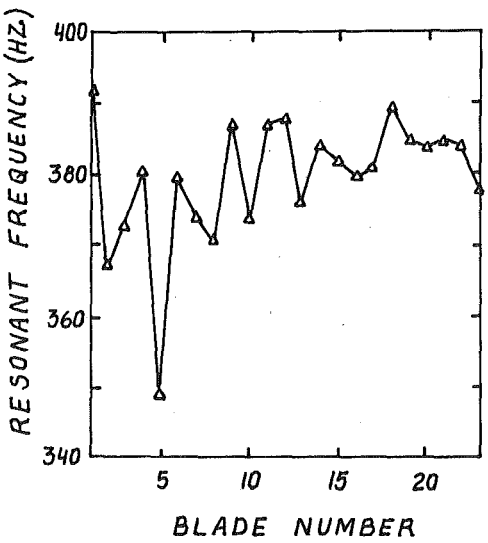


Fig. 8 Variation of blade resonant frequencies

Downloaded 01 Jun 2010 to 171.66.16.58. Redistribution subject to ASME license or copyright; see http://www.asme.org/terms/Terms_Use.cfm

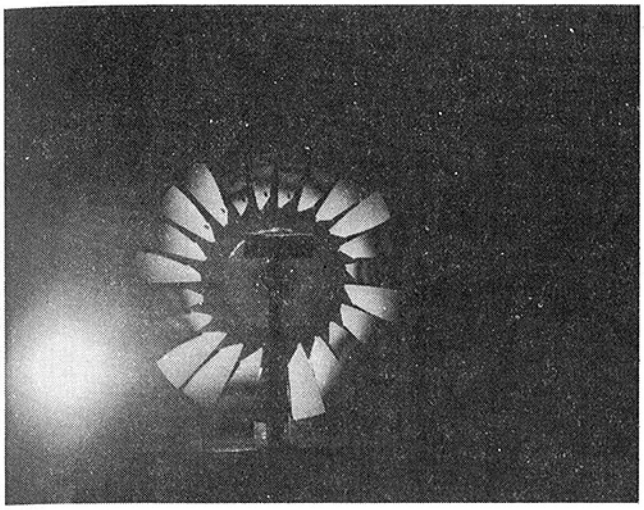


Fig. 9 Holographic reconstruction of vibrating rotor

phase shifts of the blades and those of the forcing functions. At 427 Hz, the phase angles of the blades are almost equal, an evidence of the occurrence of the system "umbrella" mode at 426.5 Hz. Above the system resonances, at 440 Hz, the phase response of each blade is shifted by approximately 180 deg with respect to the forcing function (note that 0 and 360 deg are the same angles). This is consistent with the phase shift associated with the harmonic response of a linear system when forced at frequencies above its resonant frequency.

6 Conclusions

On the basis of the completed analytical and experimental investigations of the vibration characteristics of a single stage axial compressor rotor, the following conclusions are listed:

1 Bladed disk assemblies can exhibit several resonances over a finite range of frequencies. In general, the number of resonant frequencies is not simply related to the number of blades. As the stiffness of the disk increases compared to that of the blades, the range of system frequencies approaches the blade cantilever frequencies.

2 When all the blades are identical, the system mode shapes, characterized by the blade deflections at resonance, can be resolved into circular functions of the blade location, or into so-called "nodal diametral patterns." However, when the blades are slightly different from each other, be it in stiffness or mass, circular functions cease to be the basis for the vector space in which the resonant modes occur. For that matter, each given structure possesses its own unique set of orthogonal vectors. The effective stiffness matrix, with respect to which degenerate modes need be orthogonalized was found to be diagonal with elements equal to the squares of the blade cantilever frequencies.

3 The frequency response of the blades of such assemblies, when forced individually, exhibits a multiple peak behavior. The peaks at the system frequencies. The relative amplitudes of the peaks depend on the damping of the system modes and the participation of that blade in the system normal mode occurring at that frequency. Under arbitrary external forcing, the motion of each blade in the system is governed by the response of the entire system as a whole.

4 When all the blades of a detuned rotor are driven harmonically with uniform amplitude of forcing and constant interblade phase angle, the response amplitudes of the blades are not uniform. At frequencies below the system resonances, the phase angle of each blade follows that of the forcing function. At frequencies above the system resonances, the phase angle of each blade is 180 deg out of phase with the forcing function. At frequencies within the system resonances, the phase response to the blades cannot be correlated with that of the forcing function.

Acknowledgments

The author wishes to express his appreciation of the advice and support of Prof. Jack L. Kerrebrock of the Massachusetts Institute of Technology during the course of the present study.

References

1 Fabunmi, J. A., "Forced Vibrations of a Single Stage Axial Compressor Rotor," Ph.D. Thesis, Massachusetts Institute of Technology, Jan., 1978.

2 Ewins, D. J., "The Vibration of Bladed Discs," Ph.D. Thesis, Cambridge University, 1966.

3 Whitehead, D. S., "Effect of Mistuning on the Vibrations of Turbomachine Blades Induced by Wakes," *Journal of Mechanical Engineering Science,* Vol. 8, No. 1, Mar. 1966.

4 Wagner, J. T., "Coupling of Turbomachine Blade Vibrations Through the Rotor," ASME JOURNAL OF ENGINEERING FOR POWER, Vol. 89, Oct. 1967.

5 Ewins, D. J., "The Effects of Detuning Upon the Forced Vibrations of Bladed Discs," *Journal of Sound and Vibrations,* Vol. 9, No. 1, 1969.

6 Ewins, D. J., "A Study of Resonance Coincidence in Bladed Discs," *Journal of Mechanical Engineering Science,* Vol. 12, No. 5, 1970.

7 Dye, R. C. F., Henry, T. A., "Vibration Amplitudes of Compressor Blades Resulting from Scatter in Blade Natural Frequencies," ASME JOURNAL OF ENGINEERING FOR POWER, Vol. 91, No. 3, 1969.

8 Ewins, D. J., "Vibration Characteristics of Bladed Disc Assemblies", *Journal of Mechanical Engineering Science,* Vol. 15, No. 3, 1973.

9 Ewins, D. J., "Vibration Modes of Mistuned Bladed Disks," ASME Paper No. 75-GT-14, April 1975.

10 El-Bayoumy, L. E., Srinivasan, A. V., "Influence of Mistuning on Rotor-Blade Vibration," *AIAA Journal,* Vol. 13, No. 4, April 1975.

11 Ewins, D. J., "An Experimental Investigation of the Forced Vibration of Bladed Discs due to Aerodynamic Excitation."

12 Ewins, D. J., Sadasiva Rao, Y. V. K., "A Theoretical Study of the Damped Forced Vibration REsponse of Bladed Discs."

13 Srinivasan, A. V., Frye, H. M., "Effects of Mistuning on Resonant Stresses of Turbine Blades," *Structural Dynamic Aspects of Bladed Disc Assemblies,* Presented at the ASME Winter Annual Meeting, New York, NY, Dec. 1976.

APPENDIX 1

Stiffness matrix of equation (1):

$$\overline{\overline{K}}_{2N\times 2N} = \begin{bmatrix} k_1 & & & & & \\ & k_2 & & 0 & & \\ & & \ddots & & & \\ & 0 & & \ddots & & \\ & & & & k_N & \\ & & & & K+2K' & -K' \quad 0\ldots-K' \\ & & & & -K' & K+2K' \quad -K'\ldots 0 \\ & & & & 0 & \\ & 0 & & & \vdots & \\ & & & & -K' & 0\ldots K' \quad K+2K' \end{bmatrix}$$

Mass matrix of equation (1):

Downloaded 01 Jun 2010 to 171.66.16.58. Redistribution subject to ASME license or copyright; see http://www.asme.org/terms/Terms_Use.cfm

$$\overline{\overline{M}} = \underset{2N \times 2N}{\begin{bmatrix} m_1 & & & & m_1 & & & \\ & m_2 & & 0 & & m_2 & & 0 \\ & & \ddots & & & & \ddots & \\ & 0 & & \ddots & & 0 & & \ddots \\ & & & & m_N & & & m_N \\ m_1 & & & & M+m_1 & & & \\ & m_2 & & 0 & & M+m_2 & & 0 \\ & & \ddots & & & & \ddots & \\ & 0 & & \ddots & & 0 & & \\ & & & & m_N & & & M+m_N \end{bmatrix}}$$

The matrix $\overline{\overline{P}}(\ )$ is of the form:

$$\overline{\overline{P}}(\omega) = \underset{2N \times 2N}{\begin{bmatrix} 1 & & & & p_1 & & & \\ & 1 & & 0 & & p_2 & & 0 \\ & & \ddots & & & & \ddots & \\ & 0 & & \ddots & & 0 & & \ddots \\ & & & & 1 & & & p_N \\ 1 & & & & 1 & & & \\ & 1 & & 0 & & 1 & & \\ & & \ddots & & & & 0 & \\ & 0 & & \ddots & & 0 & & \\ & & & & 1 & & & 1 \end{bmatrix}}$$

where,

$$p_n = m_n\omega^2/(k_n - m_n\omega^2).$$

The matrices $\overline{\overline{D}}_{11}'(\omega)$, $\overline{\overline{D}}_{21}'(\omega)$, and $\overline{\overline{D}}_{22}'(\omega)$ are;

$$\overline{\overline{D}}_{11}'(\omega) = \underset{N \times N}{\begin{bmatrix} k_1 - m_1\omega^2 & & & \\ & k_2 - m_2\omega^2 & & 0 \\ & & \ddots & \\ & 0 & & k_N - m_N\omega^2 \end{bmatrix}}$$

$$\overline{\overline{D}}_{21}'(\omega) = \underset{N \times N}{\begin{bmatrix} -m_1\omega^2 & & & \\ & -m_2\omega^2 & & 0 \\ & & \ddots & \\ & 0 & & -m_N\omega^2 \end{bmatrix}}$$

$$\overline{\overline{D}}_{22}'(\omega) = \underset{N \times N}{\begin{bmatrix} K + 2K' - F_1(\omega) & -K' & 0 \ldots 0 & -K' \\ -K' & K + 2K'(\omega) - F_2(w) & -K' \ldots 0 & \\ \multicolumn{4}{c}{\text{---------------------------------------}} \\ \multicolumn{4}{c}{\text{---------------------------------------}} \\ -K'\ 0 \ldots\ldots 0 & -K' & & K + 2K' - F_N(\omega) \end{bmatrix}}$$

where,

$$F_n(\omega) = M\omega^2(\omega_n{}^2(1 + m_n/M) - \omega^2)/(\omega_n{}^2 - \omega^2)$$

and $\omega_n{}^2 = k_n/m_n$.

The mass matrix of equation (9) is of the form:

$$\overline{\overline{M}}'' = \overline{\overline{I}} + (\overline{\overline{K}}')^{-1}\overline{\overline{k}}$$

where $\overline{\overline{I}}$ is an $N \times N$ identity matrix, and;

$$\overline{\overline{K}}' = \underset{N \times N}{\begin{bmatrix} K + 2K' & -K' & 0 \ldots -K' \\ -K' & K + 2K' & -K' \ldots 0 \\ \multicolumn{3}{c}{\text{---------------------------------}} \\ \multicolumn{3}{c}{\text{---------------------------------}} \\ -K' & 0 \ldots . & -K' \quad K + 2K' \end{bmatrix}}$$

$$\overline{\overline{k}} = \underset{N \times N}{\begin{bmatrix} k_1 & & & \\ & k_2 & & 0 \\ & & \ddots & \\ & 0 & & k_N \end{bmatrix}}$$

Downloaded 01 Jun 2010 to 171.66.16.58. Redistribution subject to ASME license or copyright; see http://www.asme.org/terms/Terms_Use.cfm

J. H. Griffin
Senior Design Engineer,
Government Products Division,
Pratt & Whitney Aircraft,
West Palm Beach, Fla. 33402
Mem. ASME

Friction Damping of Resonant Stresses in Gas Turbine Engine Airfoils

The resonant response of a turbine airfoil attenuated through use of a Coulomb damper is analyzed. Parameters that control the damper's effectiveness are identified and characteristics of an optimized system are described. The results of the analysis are confirmed by laboratory tests.

Introduction

Service failures of gas-turbine blades in many instances can be attributed to high cycle fatigue caused by large resonant stresses. In order to avoid such failures, designers of aircraft engines frequently incorporate friction devices into turbine designs to increase damping and reduce vibratory stresses. These devices are frequently of the type designated herein as "blade-to-ground" dampers. A blade-to-ground damper provides a link between a vibrating point on the blade (see Fig. 1) and a relatively rigid structure such as the coverplate. The damper transmits a load through a friction contact which dissipates energy when slip occurs.

The amount of slip at the friction interface depends upon the magnitude of the normal load acting on that surface. As a result, a major design concern has been the determination of an optimum normal load that would dissipate the maximum amount of energy. Various criteria have been used for this purpose, some as simple as the rule of thumb, "the damper normal load should equal a certain percentage of the blade pull," and others much more complex which require computer generated optimums. Laboratory tests in which the damper normal load is varied by a simple lever arrangement (Fig. 5) indicate that such optimums exist (Fig. 6). However, full scale engine tests of dampers of various sizes frequently show little effect from changing damper normal load. One difference between the laboratory and engine tests is that in the engine it is not possible to change the damper normal load without changing the geometry of the damper and consequently its stiffness. Damper stiffness affects the dynamic response only when the damper is stuck during a significant portion of each cycle. As can be seen in Fig. 1, the damper will not slip until the blade's motion compresses the damper to the point that it transmits a load equal to the friction force, μN. The amplitude of vibration at which this occurs can be determined once the mode shape of the blade with a stuck damper is calculated. This was done for a number of blade and damper combinations which had been previously tested. It was found that, under engine test conditions, the dampers were stuck a large part of the time and that variations in damper stiffness significantly altered the system's vibratory response. Consequently, optimum damper weight, easily observed in laboratory tests, was not identified in engine tests because a significant variable, damper stiffness, was uncontrolled. These observations substantiate the need to consider damper stiffness as well as normal load in designing friction devices to optimally control turbine blade vibratory stress.

Previous studies of systems with frictional damping are of two types: those which emphasize the mathematical aspects of solving systems governed by nonlinear differential equation, e.g., [1] and [2], and others which are concerned with a specific design application. Some examples of the latter type are the investigations of root and shroud damping documented in [3] and [4]. In a recent study of vibrating beams with friction dampers, Earles and Williams [5] used a result from Den Hartog's analysis [6] of a single degree of freedom system in which the damper linkage was rigid. Consequently, in their

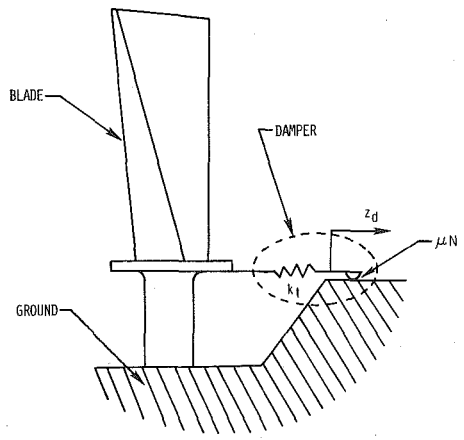


Fig. 1 Blade to ground damper

Contributed by the Gas Turbine Division and presented at the Gas Turbine Conference and Exhibit and Solar Energy Conference, San Diego, California, March 12–15, 1979 of THE AMERICAN SOCIETY OF MECHANICAL ENGINEERS. Manuscript received at ASME Headquarters December 18, 1978. Paper No. 79-GT-109.

Copyright © 1980 by ASME
Downloaded 01 Jun 2010 to 171.66.16.58. Redistribution subject to ASME license or copyright; see http://www.asme.org/terms/Terms_Use.cfm

investigation damper stiffness was not recognized as a parameter and its influence was not studied.

The approach used in this paper assumes that the damper is characterized by two parameters: The force at which it slips and its stiffness. The effect of these parameters on the resonant response of a turbine blade with a blade-to-ground damper is investigated both analytically and experimentally in the following sections.

Analysis

Derivation of Modal Equations. A blade having a blade-to-ground damper is portrayed schematically in Fig. 1. The damper is assumed to be a massless spring of stiffness k_t. The damper slides and dissipates energy when it is deformed to the point that it exerts a force equal to μN on the slip surface. The equation of motion for a discrete model of the blade is

$$M\ddot{U} + C\dot{U} + KU = f_L + f_N \tag{1}$$

where U is the generalized displacement vector; M, C, and K are the mass, viscous damping, and stiffness matrices; f_L and f_N are the linear and nonlinear force vectors acting on the blade, and $\dot{(\ )}$ indicates differentiation with respect to time. Suppose that ϕ_i are the eigenvectors of the nondamped linear system, i.e.,

$$K\phi_i = M\omega_i{}^2\phi_i \tag{2}$$

Assume that the solution to the ordinary differential equation (1) can be represented as the sum of these eigenvectors with time dependent coefficients, τ_i. Letting t^* represent time, U may then be written

$$U = \sum_i \tau_i\,(t^*)\,\phi_i \tag{3}$$

Since eigenvectors which satisfy (2) can be shown to be orthogonal with respect to M, then substitution of (3) into (1) and premultiplication by $\phi_1{}^T$ results in the following differential equation for the first mode response of the damped blade

$$\phi_1{}^T M\phi_1\,(\ddot{\tau}_1 + \omega_1{}^2\tau_1) + \sum_i \phi_1{}^T C\phi_i\dot{\tau}_i = \phi_1{}^T\,(f_L + f_N) \tag{4}$$

This study will focus on the first mode's resonant response, however, the treatment of higher modes is analogous. Thus, consider the situation in which the system is forced sinusoidally at a frequency near the lowest resonant frequency, ω_1. It is reasonable to assume that the single lowest mode will dominate and as a result cross product terms in (4) may be neglected. Then

$$m(\ddot{\tau}_1 + \omega_1{}^2\tau_1) + c\dot{\tau}_1 = f_L + f_N \tag{5}$$

Where m, f_L, and f_N are defined consistent with (4) and

$$c = \phi_1{}^T C\phi_1.$$

The stiffness matrix, K, can be written in two ways, which results in two definitions being possible for the first mode eigenvectors, ϕ_1. If K does not include the effect of the damper stiffness k_t, then ϕ_1 is a modal displacement vector of the free blade unrestrained by a damper. Designate ϕ_1 then as ϕ_f and ω_1 as ω_f. If ϕ_{fd} is the component of ϕ_f at the location that compresses the damper, then (5) becomes

$$m\ddot{\tau}_1 + (k + k_d)\,\tau_1 + c\dot{\tau}_1 = f_L + k_d z. \tag{6}$$

Where

$$k = m_f\omega_f{}^2 \tag{7a}$$

$$k_d = \phi_{fd}{}^2\,k_t \tag{7b}$$

$$z = z_d/\phi_{fd} \tag{7c}$$

and z_d is defined in Fig. 1. For these conditions it may be noted that if F_d is defined as $\mu N\phi_{fd}$ then slip occurs when

$$|\tau_1 - z| = F_d/k_d \tag{8}$$

The second definition of ϕ_1 results whenever K includes the restraint of the damper stiffness; here, ϕ_1 is a modal displacement vector of the blade with a stuck damper. If an s subscript is used analogously to the f subscript to denote stuck parameters, then equations (6) and (8), (7b) and (7c) still hold with s subscripts replacing f subscripts and equation (7a) replaced by

$$k + k_d = m_s\omega_s{}^2. \tag{9}$$

When μN is sufficiently small, the damper slips almost continuously and the first free mode dominates the response of the airfoil. Conversely, if μN is sufficiently large the damper will not slip and the first stuck mode will be dominant. In either case the form of the differential equation is the same, equation (6), the only difference being the value of the coefficients. Thus, the problem can be treated as one in which the differential equation is invariant and the modal values, m, c, etc. depend on the magnitude of the friction force μN. For this reason the single degree of freedom system which is governed by equation (6) is analyzed in the following sections. Using the analysis presented, an approximate solution to equation (6) may be obtained by interpolating the values of modal parameters between their stuck and free values in a manner dependent upon the amount of slip present.

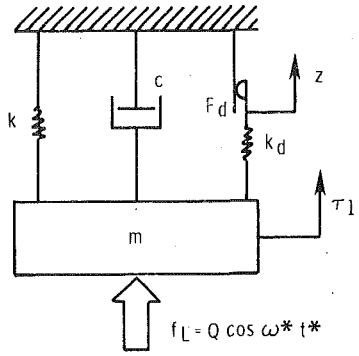


Fig. 2 Equivalent one degree of freedom system

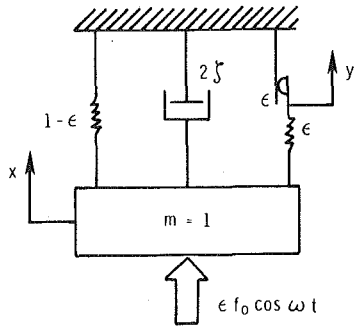


Fig. 3 Dimensionless system

One Dimensional Model. The equation of motion for the system depicted in Fig. 2 is equation (6) in which the blade excitation is assumed to be of the form $Q\cos\omega^* t^*$. It is advisable in nonlinear problems to nondimensionalize the equations to simplify analysis and subsequent parametric studies. If the variables are ratioed to the characteristic time, the square root of $m(k + k_d)$; displacement, F_d/k_d; force, F_d and if

$$\epsilon = k_d/(k_d + k) \tag{10}$$

then (6) implies

$$d^2x/dt^2 + x + 2\zeta dx/dt = \epsilon y + \epsilon f_o\cos\omega t \tag{11}$$

which is the equation of motion for the unit mass system depicted in Fig. 3. The forced response of this system will now be determined using the Ritz method.

Ritz Method. If it is assumed that the steady state response is predominantly sinusoidal, i.e.,

$$x(t) = A\cos(\omega t - \psi) \tag{12}$$

Downloaded 01 Jun 2010 to 171.66.16.58. Redistribution subject to ASME license or copyright; see http://www.asme.org/terms/Terms_Use.cfm

then in order for the average error per cycle to be zero the following condition must be satisfied [7].

$$\int_0^{2\pi} \left[\frac{d^2x}{dt^2} + x + 2\zeta\frac{dx}{dt} - \epsilon y - \epsilon f_o \cos\omega t\right] \begin{Bmatrix}\cos\theta \\ \sin\theta\end{Bmatrix} d\theta = \begin{Bmatrix}0 \\ 0\end{Bmatrix}$$

where

$$\theta = \omega t - \psi \tag{13}$$

Substituting (12) into (13) produces

$$(1-\omega^2)A - \epsilon f_o \cdot \cos\psi = A\epsilon(\pi - \theta^* + \frac{1}{2}\sin 2\theta^*)/\pi \tag{14a}$$

$$\cos\theta^* = 1 - 2/A, \quad 0 \le \theta^* \le \pi \tag{14b}$$

$$-2\zeta\omega A + \epsilon f_o \cdot \sin\psi = A\epsilon(\sin^2\theta^*)/\pi \tag{14c}$$

Equations (14 *a,b,c*) provide an implicit solution to the problem of interest. That is, for a given geometry, ϵ, magnitude of load, f_o, and frequency, ω, the simultaneous constraints of equations (14 *a,b,c*) determine the amplitude, A, and the phase, ψ, of the response.

A Maximum Response. In a rotating structure the excitation frequency is typically an integer multiplier of the rotational frequency, and, over the range of RPM in which the blade strongly vibrates, there is normally little change in the amplitude of the excitation force. Thus, in terms of the variables used here, resonance in airfoils corresponds to a situation in which f_o is held constant and ω is varied until A is a maximum, A_m. Correspondingly, the values of ω and ψ become ω_m and ψ_m. By eliminating ψ from the equations (14*a*) and (14*c*) and examining the resulting equation for A, it can be shown that A_m, ω_m, and ψ_m satisfy the following equations:

$$A_m = \Gamma + \sqrt{\Gamma^2 + 2\epsilon/(\pi\zeta\omega_m)} \tag{15a}$$

and

$$\omega_m = \sqrt{1 - \epsilon(\pi - \theta + .5\sin 2\theta)/\pi} \tag{15b}$$

where

$$\Gamma = \epsilon(f_o - 4/\pi)/(4\zeta\omega_m) \tag{15c}$$

$$\theta = \cos^{-1}(1 - 2/A_m), \quad 0 \le \theta \le \pi, \tag{15d}$$

lastly, as in the case of viscous damping only

$$\psi_m = \pi/2 \tag{15e}$$

Since ω_m is physically restricted to the narrow range $1 - \epsilon \le \omega_m^2 \le 1$, (15) may be solved simply on a digital computer by assuming an initial estimate of ω_m, calculating A_m from (15*a*) and (15*c*), and then computing an improved estimate of ω_m from (15*b*) and (15*d*). This iterative procedure is repeated until the process converges, which, in actual applications, normally occurs in only a few repetitions.

An iterative solution, such as outlined above, can be used as the basis for a damper optimization computer program. In such a program, A_m is determined from equation (15) for various values of damper shear load, μN, and the value of N selected will be that which yields the smallest vibratory stress.

When the amount of viscous damping is small, approximations to optimum values of N, A and ω can be determined explicitly. Such approximations are useful in that they are sufficiently accurate in most cases that they can be used directly for design purposes. In addition, their explicit form reveals basic trends that are of interest. It should be noted, however, that the iterative solution outlined above is of fundamental importance since it must still be used in those cases which require other than optimum damper design; e.g., the damper is required to reduce resonance response for more than one mode.

Choosing the Damper Break Free Force To Minimize Resonant Response. Consider a situation in which all parameters are held constant except the force at which the damper slips, F_d (see Fig. 2). For this case the value of F_d sought is that which will minimize the blade's resonant amplitude. Since the actual displacement is proportional to A_m/f_o and F_d is proportional to $1/f_o$, the objective is to find the value of f_o for which A_m/f_o is a minimum, a goal obstructed by the coupled implicit nature of equations (15 *a,b*). However, for the small amounts of viscous damping usually observed in practice (for example, $\zeta < 0.02$) it can be shown that the resonant amplitude will be approximately a minimum when A_m is 2, θ is $\pi/2$, ψ_m is $\pi/2$ and

$$\omega_m = \sqrt{1 - \epsilon/2} \tag{16a}$$

$$f_o = 2(1 + 2\zeta\pi\omega_m/\epsilon)\pi \tag{16b}$$

For single degree of freedom systems analogous to damped blades, ϵ is small. As a result, from a series expansion of (16*a*) the optimum frequency approximately equals $(1 - \epsilon/4)$. When $F_d = 0$ the blade freely resonates and the resonant frequency is equal to the square root of $1 - \epsilon$, which approximately equals $1 - \epsilon/2$. When $F_d \to \infty$, the damper is stuck and the resonant frequency is one. Thus, the maximum frequency shift that can occur is approximately $\epsilon/2$. Accordingly, if F_d is varied until the minimum resonance occurs, the corresponding frequency shift is half of that possible.

In addition, these results indicate that at optimum F_d the amplitude of the displacement is twice the value at which slip is initiated. Lastly, they imply that for an optimum shear load the damper slips one-half of the time.

The Effect of Damper Stiffness on Amplitude Reduction. From the results of the previous section, the ratio, R, of the displacement amplitude of an optimally damped blade to one with only viscous damping can be found. If ϵ is approximated as $1 - (\omega_f/\omega_s)^2$, then the ratio is given by

$$R = \chi/(1 + \chi)$$

where

$$\chi = 2\pi\zeta\omega_f\omega_s/(\omega_s^2 - \omega_f^2) \tag{17}$$

From (17), it may be observed that if the damper's stiffness is fixed it is always possible to get the same optimum stress reduction. It will occur, however, at different values of μN depending upon the magnitude of the excitation. The optimum value of μN may be approximated as

$$\mu N = \pi Q/[2\phi_d(1 + \chi)] \tag{18}$$

where, ϕ_d is taken as the average of ϕ_{fd} and ϕ_{sd} since at optimum conditions the damper is slipping one-half the time.

The effect of damper stiffness on the modal parameters of an advanced blade was determined by computer simulation. R, the amplitude reduction ratio for ζ equal to one percent is portrayed as a function of damper stiffness in Fig. 4. Here several features can be noted which are typical of all blades. These include the observation that the stiffer the damper the greater the damper's effectiveness, and that the degree of stress reduction asymptotically approaches a limit as the damper's stiffness increases. The latter is true since the stuck modal parameters asymptotically approach those of a blade pinned at the damper location. Thus, the amount of stress reduction possible from a friction damper is an inherent property of the blade's geometry.

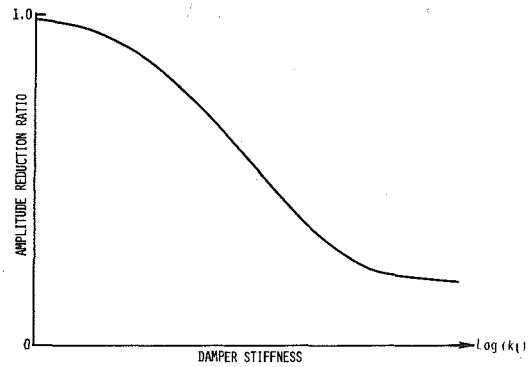


Fig. 4 Amplitude reduction ratio versus damper stiffness

Downloaded 01 Jun 2010 to 171.66.16.58. Redistribution subject to ASME license or copyright; see http://www.asme.org/terms/Terms_Use.cfm

Test Conditions and Procedure

A turbine blade was held in a broach block and vibrated on a shaker table. A damper with a large pivot base was used (Fig. 5) so that the main flexibility could be provided by the small beam extension between the base and the blade. Thus, changes in damper stiffness could be made by pressing extensions of different flexibilities into the pivot base.

The peak vibratory stress and resonant frequency were measured for a range of damper normal loads. Since the results were to be compared with those predicted using the analytical model, a procedure was adopted consistent with the analytical optimization outlined in the preceding section. This procedure was as follows:

1 The shaker table acceleration was maintained at a constant level.

2 For a selected damper normal load the frequency of the excitation was varied until the blade's first mode vibratory stress was a maximum. The resonant frequency and peak vibratory stress were recorded. (For zero normal load the half bandwidth damping was measured as a baseline.)

3 The normal load was then increased and procedure (2) repeated until the entire range of interest was covered.

In order to predict the blade response observed in the tests it was necessary to measure the coefficient of friction. A flat disk of airfoil material was rotated under a pin of damper material in a manner similar to a record player. The resulting frictional force was measured over a range of velocities. After an initial wear-in period, a coefficient of friction relatively independent of velocity was observed; this value was then used to predict vibratory response.

Test Results and Comparisons With Analytical Predictions

In Fig. 6 observed and predicted values of resonant stress amplitudes for dampers of different stiffnesses are plotted as a function of damper normal load. The degree of correlation shown is representative of that observed in tests conducted at other conditions. A result of particular interest to the designer is that values of stress reduction calculated by an iterative solution of equation (15) agreed well with those experimentally observed when the normal load was in the range of maximum interest; i.e., N less than several times the optimum value. In addition, approximate values of optimum normal load and stress reduction as calculated by equations (17) and (18) were not significantly different from those generated iteratively. Thus, these equations provide a good engineering approximation which can be used for optimum damper design. Also of interest to the designer is that, as predicted, a stiffer damper is more effective in reducing vibratory stress.

Experimental and analytical values of resonant frequency are portrayed in Fig. 7. Basically good agreement existed between predicted and observed values. Moreover, as anticipated, the use of a stiffer damper resulted in a larger frequency shift.

An interesting trend is that there is, in general, poorer agreement for larger values of damper normal load. This is more apparent in the results of the flexible damper tests since in a nondimensional sense a larger range of normal load was covered in these experiments. Since the response of the system for a large normal load approaches that of the blade with a stuck damper, it is probable that the associated stuck modal parameters are in error. An initial assumption that affects only stuck modal values is that the mass of the damper is negligible. That this assumption might be the cause of the observed discrepancy is consistent with the fact that the experimentally determined frequencies are less than those predicted when N is large. Fortunately the disagreement occurs in a range of normal load much larger than the optimum and usually would not be of much interest to the designer.

Conclusions

An approximate solution to the problem of determining the resonant response of a turbine blade having a blade-to-ground damper is derived. Values of resonant stress amplitude and frequency for a range of damper slip force are determined experimentally for a blade having dampers of two different stiffnesses. Observed values compare favorably with those theoretically predicted by iteratively solving equations (15a–15d). In addition, the optimum values of slip force and stress reduction were adequately determined from the explicit equations (17) and (18).

The solution presented is based on analyzing a blade having a damper with two properties, a force at which it slips and a stiffness.

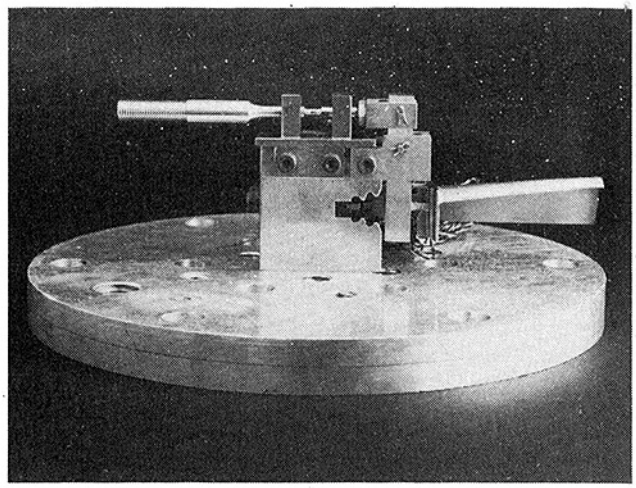


Fig. 5 Test apparatus

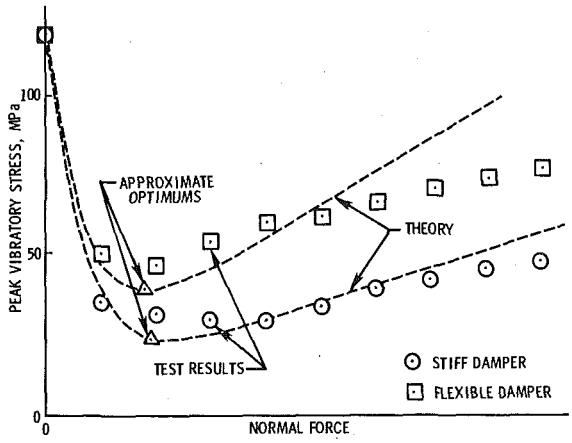


Fig. 6 Stress reduction versus damper load

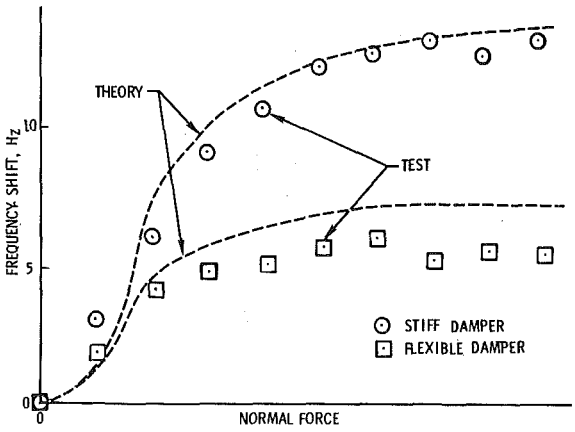


Fig. 7 Frequency versus damper load

Downloaded 01 Jun 2010 to 171.66.16.58. Redistribution subject to ASME license or copyright; see http://www.asme.org/terms/Terms_Use.cfm

Because of the simple form of the approximate solution, certain general conclusions may be made concerning the role of the two damper parameters in affecting resonant response of the blade-damper system. First, consider the case in which only the slip force is varied. If this force is chosen so that the resonant response is minimized, then the resonant frequency is halfway between that of a blade which has a fully slipping damper and one which has a stuck damper. Furthermore, the damper slides and sticks in equal amounts during each cycle. Since this is true for dampers of all stiffnesses, dynamic models of vibrating structures which would optimize friction dampers must be capable of simulating both slip and stick conditions at the damper interface. Secondly, if it is assumed that the damper slip force will be chosen to minimize the blade's resonant response, then the damper's effectiveness in reducing stress will monotonically increase and approach a limit as the damper's stiffness increases. Consequently, the maximum amount of friction damping that can be obtained is an inherent property of the blade's geometry. Hence, by considering the amplitude reduction formula given in equation (17), it is possible to establish guidelines that can be applied in the early stages of blade design. These guidelines can be used to guarantee the possibility of later obtaining adequate friction damping in the final design stage.

Acknowledgment

The author wishes to acknowledge the contribution of J. A. Kramer, J. L. Bearden, and J. H. Doyle in performing the experimental tests cited in this paper.

References

1 Caughey, T. K., "Sinusoidal Excitation of a System With Bilinear Hysteresis," *ASME Journal of Applied Mechanics,* Vol. 27, Dec. 1960, pp. 640–643.

2 Iwan, W. D., "Steady-State Dynamic Response of a Limited Slip System," *ASME Journal of Applied Mechanics,* Vol. 35, June 1968, pp. 322–326.

3 Goodman, L. E., and Klumpp, J. H., "Analysis of Slip Damping with Reference to Turbine Blade Vibration," *ASME Journal of Applied Mechanics,* Vol. 23, Sept. 1956, pp. 421–429.

4 William, E. J., and Earles, S. W. E., "Optimization of the Response of Frictionally Damped Beam Type Structures with Reference to Gas Turbine Compressor Blading," *ASME Journal of Engineering for Industry,* Vol. 96, May 1974, pp. 471–476.

5 Earles, S. W.E, and Williams, E. J., "A Linearized Analysis for Frictionally Damped Systems," *Journal of Sound and Vibration,* Vol. 24, 1972, pp. 445–458.

6 Den Hartog, J. P., *Mechanical Vibrations,* 4th ed., McGraw-Hill, New York, 1956.

7 Timoshenko, S., and Young, D. H., "Systems with Non-linear and Variable Spring Characteristics," *Vibration Problems in Engineering,* 3rd ed., Van Nostrand, 1964, pp. 163–168.

Downloaded 01 Jun 2010 to 171.66.16.58. Redistribution subject to ASME license or copyright; see http://www.asme.org/terms/Terms_Use.cfm

S. Fleeter[1]
W. A. Bennett
R. L. Jay

Detroit Diesel Allison
Division of General Motors Corporation
P.O. Box 894
Indianapolis, Ind. 46206

The Time-Variant Aerodynamic Response of a Stator Row Including the Effects of Airfoil Camber

An experimental investigation was conducted to quantitatively determine the validity and applicability of state-of-the-art transverse gust cascade analyses. This was accomplished by obtaining fundamental time-variant forced response data at realistic values of key parameters in a large-scale, low-speed, single-stage research compressor. The forcing function, the velocity defect created by the rotor blade wakes, was measured with a crossed hot-wire probe. The resulting time-variant aerodynamic response was measured by means of flush mounted high response pressure transducers on both flat plate and cambered airfoil stator vane rows over a wide range of incidence angles. These dynamic data were then analyzed to determine the chordwise variation of the unsteady pressure difference in terms of a dimensionless dynamic pressure coefficient and an aerodynamic phase lag referenced to a transverse gust at the leading edge of the vanes. These dimensionless pressure difference data were all correlated with predictions obtained from a state-of-the-art compressible transverse gust, flat plate cascade analysis. Correlation of the classical flat plate unsteady data with the predictions permitted the range of validity of the analysis to be assessed in terms of incidence angle. Correlation of the cambered vane unsteady data with those for the flat plate and with the predictions allowed the effects of airfoil camber as well as the applicability of the flat plate prediction to realistic cambered airfoils to be quantitatively determined.

Introduction

The dynamic aeroelastic response of turbomachine components to aerodynamic excitations is an area of major concern to manufacturers of turbine engines. These aerodynamically induced vibrations result in high cycle fatigue failures of blading, as exemplified in Fig. 1, and can lead to catastrophic engine failures.

Aerodynamic responses in fans, compressors, and turbines of sufficient magnitude to fail blades have resulted from excitations generated by: upstream vanes, downstream vanes, distortion, rotating stall, bleeds, mechanical sources, and otherwise random sources. Such aerodynamically induced failures are generally not discovered until the engine is well into the prototype and development phase and, hence, are not reported in the open literature.

Failure level vibratory responses occur when a periodic aerodynamic forcing function, with frequency equal to a natural blade resonant frequency, acts upon a blade row. The rotor speeds at which these aerodynamically induced vibrations may occur are currently predicted with frequency-speed diagrams. These display the natural frequency of each blade mode versus rotor speed and, in the same figure, the aerodynamic forcing function frequency versus rotor speed. Wherever these curves intersect, the occurrence of an aerodynamically induced vibration problem is possible. However, no accurate prediction can be made for the amplitude of the resulting stress at these intersections.

Because it is rarely possible to eliminate all natural mode vibration excitation from the operating range of a component, and not possible to predict the amplitude of the resulting stresses with present day technology, the magnitude of the resulting resonant stresses are not known until the first build-up test of engine components. If excessive stresses or failures are then discovered, the result is an extensive and costly re-design, re-build, and re-test program.

For the designer to avoid those critical intersections where high stresses are encountered, his capabilities must be extended to permit the accurate prediction of the amplitude of the response at all of the potential resonance locations predicted with frequency-speed diagrams. Hence the development of a first principles design system for the prediction of aerodynamically induced vibrations has become an item of major interest throughout the turbomachinery industry.

This accurate first principles prediction of the aerodynamically forced response of a blade or vane involves the following elements. Spatially periodic variations in pressure, velocity, and flow direction of the exit flow field of an upstream element appear as temporally varying in a coordinate system fixed to the downstream row. As a

Contributed by the Gas Turbine Division and presented at the Gas Turbine Conference and Exhibit and Solar Energy Conference, San Diego, California, March 12–15, 1979 of THE AMERICAN SOCIETY OF MECHANICAL ENGINEERS. Manuscript received at ASME Headquarters December 18, 1978. Paper No. 79-GT-110.

Copyright © 1980 by ASME

Downloaded 01 Jun 2010 to 171.66.16.58. Redistribution subject to ASME license or copyright; see http://www.asme.org/terms/Terms_Use.cfm

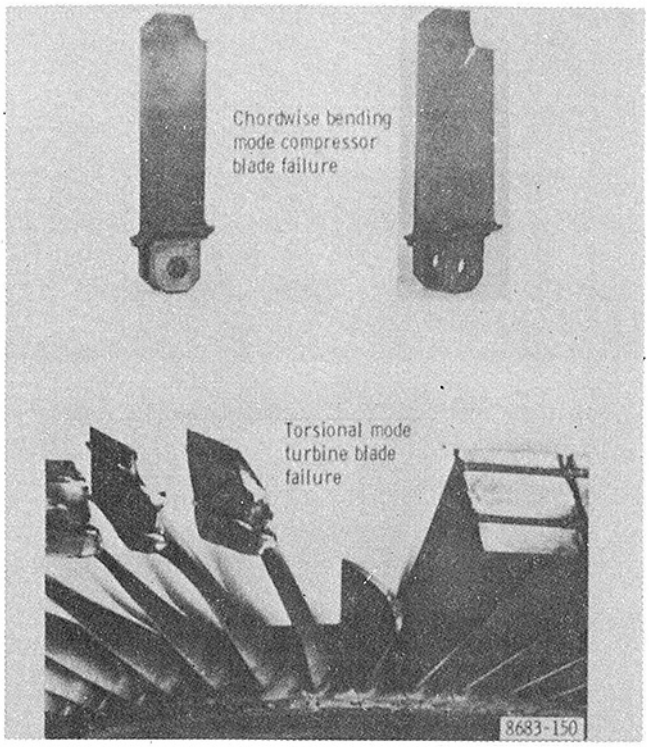


Fig. 1 Example of aerodynamically induced fatigue failure in turbine and compressor blading

result, individual blades are subject to a time-dependent aerodynamic forcing function which can induce vibrations in a number of natural modes, depending on the excitation frequency. Hence, it is necessary to first characterize this aerodynamic forcing function in terms of its harmonics.

The time-variant aerodynamic response of the airfoil surfaces to this forcing function is comprised of two parts. One is due to the disturbance being swept past the non-responding fixed airfoils. The second arises when the airfoil responds to this disturbance. The unsteady pressure distribution on the airfoil surfaces, i.e., the driving force for the airfoil response, is the sum of these two effects. Analytically these effects are modeled by means of two analyses. A gust analysis is used to predict the time-variant aerodynamics of the fixed, non-responding airfoils to each harmonic of the disturbance. An analysis wherein the airfoil cascade is assumed to be harmonically oscillating is then used to predict the additional aerodynamic effect due to the blades responding. Superpositioning of these two effects can be performed only with knowledge of the amplitude of response of the blading because the magnitude of the pressure field resulting from the motion of the responding airfoil is dependent on the amplitude of the motion. Thus, an iterative solution containing the gust analysis, the oscillating airfoil analysis, and the airfoil structural dynamics analysis as key elements is necessary to predict the total response of an airfoil subjected to an upstream generated periodic disturbance.

The aerodynamic gust analysis, as well as the case of harmonic airfoil oscillations, are areas of fundamental research interest. Linearized unsteady aerodynamic small perturbation gust analyses for isolated and cascaded airfoils are appearing in the open literature with regularity. Of direct application to turbomachinery design are the unsteady aerodynamic analyses for cascaded airfoils. Whitehead [1]considered a cascade of thin flat plate airfoils moving through a transverse gust imbedded in an incompressible flow field. This analysis was extended to include the effects of compressibility by Fleeter [2] and Smith [3]. It should be noted that the above analyses by Whitehead, Smith, and Fleeter, also consider the case of harmonic airfoil oscillations in a uniform flow field.

There are obviously many mathematical and physical assumptions inherent in the above analyses. However, only very limited fundamental experimental data exists with which to assess the range of validity of the models or to indicate refinements necessary to develop a valid predictive design model. Ostdiek [4] developed a subsonic cascade wind tunnel capable of generating a variable inlet flow direction. The wind tunnel inlet, which included guide vanes, was oscillated by a motor driven crank. This system is currently limited to very low frequencies of oscillation and, hence, very low reduced frequency values. Bruce and Henderson [5] directly measured the unsteady normal force and pitching moment on a chordwide element of a subsonic rotor blade, rather than the detailed distribution of the unsteady pressure difference across the blades, due to a circumferential inlet flow distortion in a low speed axial compressor. Fleeter, Jay and Bennett [6] determined the incompressible aerodynamically induced fluctuating pressure distribution in a stationary vane row of realistic geometry, with the primary source of excitation being the wakes from the upstream rotor blades. They have also investigated the effects of rotor-stator axial spacing on the fluctuating pressure distribution on the vane [7].

The overall objective of the experimental research program described herein is to quantitatively determine the validity and applicability of the above noted cascade gust analyses. This is accomplished by obtaining fundamental time-variant forced response data at realistic values of the key parameters in a large-scale, low-speed, single-stage research compressor. The aerodynamic forcing functions are the wakes generated by the upstream rotor blades. The resulting time-variant pressure distributions are measured on both a flat plate and a cambered airfoil stator row over a wide range of incidence angles at high reduced frequency values which are of interest to turbomachine applications. The dynamic data are analyzed to determine the dimensionless chordwise variation of the unsteady pressure difference across the flat plate and cambered airfoil vanes. These dimensionless pressure difference data are then correlated with predictions obtained from a state-of-the art, compressible, zero-incidence, transverse gust, flat plate cascade analysis. Correlation of the classical flat plate unsteady data with the predictions permits the range of validity of the analysis to be assessed in terms of the incidence angle. Correlation of the unsteady cambered vane data with those for the flat plate and with the predictions permits the effects of airfoil camber as well as the applicability of the flat plate prediction to realistic cambered airfoils to be quantitatively determined.

Single-Stage Research Compressor

In a turbomachine component, the sources of the aerodynamically induced time-variant vane surface pressures are the wakes from upstream rotor blades, i.e., the rotor wakes define the forcing function to the downstream stator vanes. Hence, it is desirable to experimentally model the significant features which define this forcing function. These include the variation of incidence, the wave form, the velocity (pressure) variation, and the reduced frequency range. These features can be simulated in the Detroit Diesel Allison (DDA) large-scale,

Nomenclature

b = airfoil semi-chord
C = airfoil chord
C_p = dynamic pressure coefficient $\Delta P \Big/ \left(\rho \cdot V^2 \cdot \frac{v}{V}\right)$
L = length
R = radius
V = absolute velocity
S = vane spacing
k = reduced frequency ($k = \omega b/V$)
u = longitudinal perturbation velocity
v = transverse perturbation velocity
β = inlet angle
ϕ = phase lag
ρ = inlet air density
ω = blade passing angular frequency

Subscripts

1 = first harmonic
2 = second harmonic
ABS = absolute
R = rotor

Downloaded 01 Jun 2010 to 171.66.16.58. Redistribution subject to ASME license or copyright; see http://www.asme.org/terms/Terms_Use.cfm

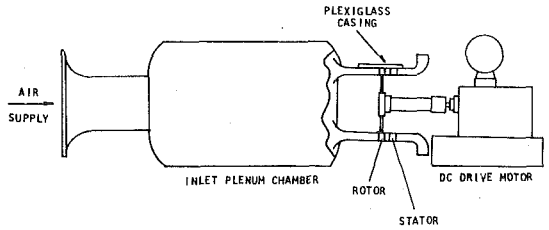


Fig. 2 Schematic of large-scale, low-speed, single-stage, research compressor

low-speed, single-stage research compressor, schematically shown in Fig. 2.

The rotor blades are designed to have aerodynamic loading levels representative of aft stages of modern multi-stage compressors. The geometric characteristics of the rotor blades include high camber, with fairly large deviation angle near the hub region, and a maximum thickness-to-chord ratio which varies from nearly seven percent at the hub to four percent at the tip.

The rotor wake generated unsteady pressures are measured on two separate 40 vane stator rows: one is made up of classical flat plate airfoils while the second consists of cambered (NACA Series 65) airfoils. A view of the rotor and flat plate vane stator row is presented in Fig. 3. Table 1 presents the rotor and stator airfoil mean section characteristics as well as the design point conditions of the compressor.

Instrumentation

The research compressor steady-state instrumentation permits the inlet and exit flow fields to be defined and the compressor map determined. The inlet temperature is measured by means of four thermocouples equally spaced circumferentially in the large stagnation chamber. The rotor inlet velocity profile is determined from the pressure measurements obtained from three equally circumferentially spaced eleven-element total pressure rakes and the average of four hub and four tip static pressure taps. The exit flow field downstream of the stator row is determined from six total pressure rakes, uniformly spaced across an equivalent vane passage, together with hub and tip static pressure taps. The exit temperature is measured with an 11 element rake located circumferentially at the center of the vane passage. The overall compressor aerodynamic performance is evaluated by examining the stagnation tank and stator exit temperature and pressure measurements, with the flow rate computed from the stagnation tank static pressure and total temperature and pressure measurements.

The time-variant quantities of fundamental interest in this experimental investigation include the fluctuating aerodynamic forcing function—the rotor wakes, and the resulting chordwise distributions of the complex time-variant pressure distribution on the downstream stator vane pressure and suction surfaces.

The airfoil surface dynamic pressure measurements are accomplished with flush mounted Kulite thin-line design dynamic pressure transducers. Both surfaces of one flat plate airfoil and one surface of each of two cambered airfoils are instrumented, as seen in Figs. 4 and 5, respectively. The suction and pressure surface transducers in each case are mounted at identical percent vane chord locations which are identified in Table 2. The cambered vane coordinates which specify the profile of this airfoil along the instrumented streamline are presented in Table 3.

The time-variant wake measurements are obtained by means of a cross-wire probe which is calibrated and linearized to 200 ft/s and ±25 deg angular variation. As schematically depicted in Fig. 6 for the flat plate airfoil configuration, the cross-wire probe is located axially immediately upstream of the leading edge of the stator row at mid-stator circumferential spacing in an upstream passage. Fig. 7 presents a view of the cambered airfoil vane row with the cross hot-wire probe and the instrumented vane suction surface clearly visible. The mean absolute exit flow angle from the rotor is determined by rotating the

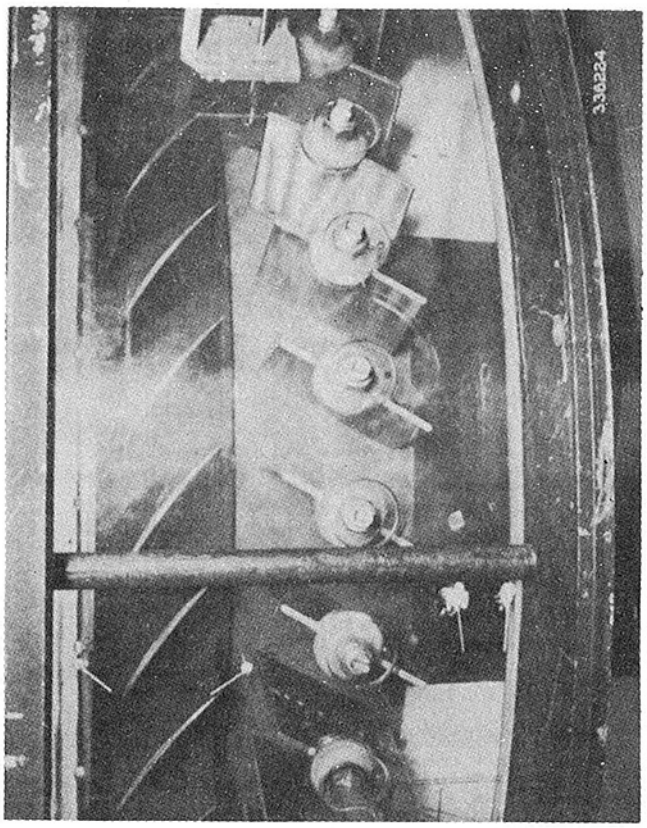


Fig. 3 View of rotor and flat plate stator row

Table 1 Airfoil mean section characteristics and compressor design point conditions

	Rotor	Flat Plate Stator	Cambered Stator
Type of Airfoil	65 Series	Flat Plate	65 Series
Number	42	40	40
Chord, C=in. (cm)	4.589(11.66)	5.089(12.93)	5.089(12.93)
Solidity, $\sigma = C/S$	1.435	1.516	1.516
Camber, ϕ – deg	20.42	0.0	48.57
Aspect Ratio, $AR = S/C$	1.046	0.943	0.943
Loss Coefficient	0.043	—	0.056
Diffusion Factor	0.449	—	0.410
Flow Rate	31.02 lb/s (14.07 Kg/s)		
Tip Speed	183.5 ft/s (5593.1 cm/s)		
Rotational Speed	876.3 rpm		
Stage Pressure Ratio	1.0125		
Inlet Tip Diameter	48.01 in. (121.95 cm)		
Hub/Tip Radius Ratio	0.80		
Stage Efficiency, Percent	88.1		

cross-wire probe until a zero voltage difference is obtained between the two linearized hot-wire signals. This mean angle is then used as a reference for calculating the instantaneous absolute and relative flow angles. The output from each channel is corrected for tangential cooling effects and the individual fluctuating velocity components parallel and normal to the mean flow angle calculated from the corrected quantities.

Data Acquisition and Analysis

In this investigation, both steady-state and time-variant data are acquired. The steady-state data define the points of compressor operation, in terms of overall pressure ratio and corrected mass flow rate, at which the unsteady velocity and surface pressure measurements are obtained. Both the steady and time-variant data acquisition are controlled by an on-line digital computer. The rotor speed is manually controlled by varying the power to the d-c drive motor; a digital

Downloaded 01 Jun 2010 to 171.66.16.58. Redistribution subject to ASME license or copyright; see http://www.asme.org/terms/Terms_Use.cfm

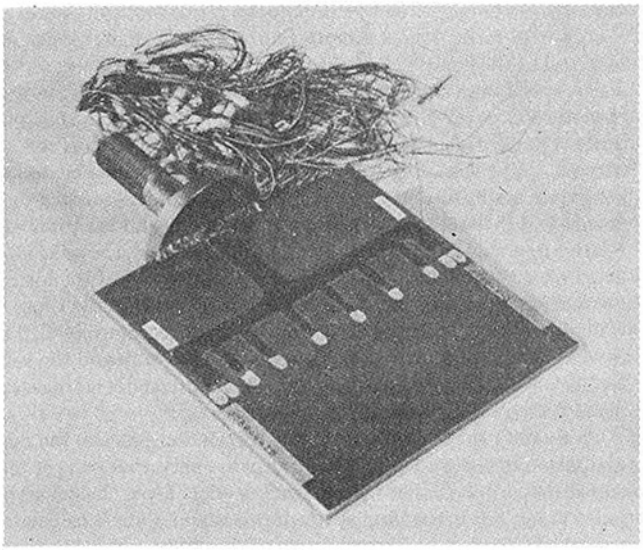


Fig. 4 Flat plate stator instrumented with high response pressure transducers

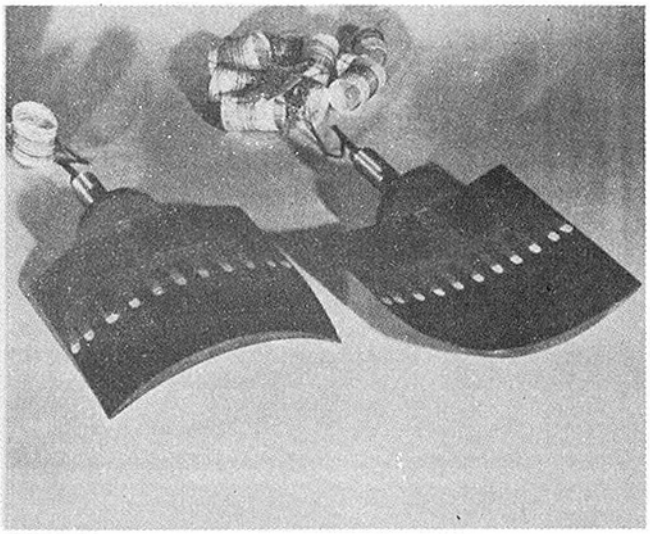


Fig. 5 Cambered airfoil stators instrumented with high response pressure transducers

readout of the rotor speed is provided via a tachometer generated signal.

The steady-state data acquisition follows the standard compressor evaluation procedure. At a selected corrected speed, the compressor is stabilized for approximately five min. Following this period, the on-line computer is used to initiate the acquisition of the temperatures and pressures necessary to generate the corrected mass flow rate, overall pressure ratio, and corrected speed. A scanning of the reduced data is then made to assure data uniformity and to ascertain the operating point.

The time-variant data acquisition and analysis technique used is based on a data averaging or signal enhancement concept. The key to such a technique is the ability to sample data at a preset time. As the signal of interest is generated at the blade passing frequency, an optical encoder, which delivers a square wave voltage signal having a duration of 1.5 ms, was mounted on the rotor shaft. The computer analog-to-digital-converter is triggered from the positive voltage at the leading edge of the pulse, thereby initiating the acquisition of the time unsteady data at a rate of up to 100,000 points per second. The data are sampled for N blade passages and over M rotor revolutions. These rotor revolutions are not consecutive because a finite time is required to operate on the N blade passage data before the computer returns to the pulse acceptance mode which initiated the gathering of the data. For this experimental program, 80 to 100 digitized data points are obtained for each of three blade passages averaged over 400 rotor revolutions ($N = 3$, $M \doteq 400$).

At each steady operating point an averaged time-variant data set, consisting of the hot-wire and Kulite signals, are obtained. Each of these signals is digitized and Fourier decomposed into its harmonics, with only the first two harmonics of the data examined in detail. The reduced frequencies of these data are in the range of turbomachinery experience with forced response problems.

From the Fourier analyses performed on the data, both the magnitude and phase angles referenced to the data initiation pulse are obtained. The wake generated velocity profiles are related to the surface dynamic pressures on the instrumented vanes after examination of the rotor exit velocity triangles. Fig. 8 shows the change in the rotor relative exit velocity which occurs as a result of the presence of the blade. A deficit in the velocity in this relative frame creates a change in the absolute velocity vector as indicated. This velocity change is measured via the crossed hot-wires. From this instantaneous absolute angle and velocity, the rotor exit relative angle and velocity as well as the magnitude and phase of the perturbation quantities are determined.

As noted previously, the hot-wire probe is positioned immediately upstream of the leading edge of the stator row. To relate the time

Table 2 Percent vane chord pressure and suction surface chordwise location of dynamic pressure transducers

Pressure Surface and Suction Surface	
Flat Plate Vane	Cambered Airfoil Vane
4.0	2.94
15.0	10.0
25.0	20.0
40.0	20.0
55.0	30.0
70.0	40.0
85.0	50.0
92.0	50.0
96.0	60.0
	70.0
	80.0
	90.0
	97.0

Table 3 Cambered vane mean profile coordinates

Pressure Surface		*Suction Surface*	
X/C^*	Y/C^*	X/C^*	Y/C^*
−45.04	8.102	55.01	8.184
−44.08	8.550	54.82	7.895
−42.30	8.182	53.68	7.324
−40.45	7.701	47.96	4.655
−38.01	7.029	43.41	2.749
−35.95	6.465	37.76	0.656
−33.77	5.889	33.28	−0.784
−30.90	5.166	28.85	−2.018
−28.48	4.594	23.40	−3.272
−25.94	4.038	19.12	−4.052
−22.60	3.368	14.91	−4.641
−19.81	2.863	9.79	−5.125
−16.15	2.274	5.81	−5.317
−13.10	1.847	.98	−5.341
−9.93	1.460	−2.75	−5.197
−5.61	1.045	−6.35	−4.926
−2.37	0.778	−10.67	−4.417
1.17	0.576	−13.98	−3.893
5.77	0.432	−17.16	−3.278
9.58	0.413	−20.93	−2.401
14.50	0.525	−23.79	−1.631
18.57	0.739	−27.18	−0.595
22.75	1.077	−29.74	0.273
28.12	1.698	−32.16	1.171
32.53	2.376	−34.99	2.323
37.04	3.232	−37.11	3.258
42.80	4.594	−39.10	4.205
47.47	5.940	−41.39	5.402
53.39	7.984	−43.06	6.382
54.58	8.446	−44.57	7.442

* Expressed in percent

Downloaded 01 Jun 2010 to 171.66.16.58. Redistribution subject to ASME license or copyright; see http://www.asme.org/terms/Terms_Use.cfm

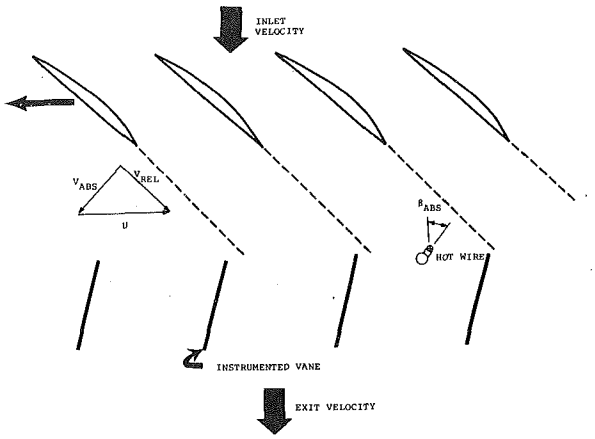


Fig. 6 Schematic of dynamic instrumentation for flat plate stator row

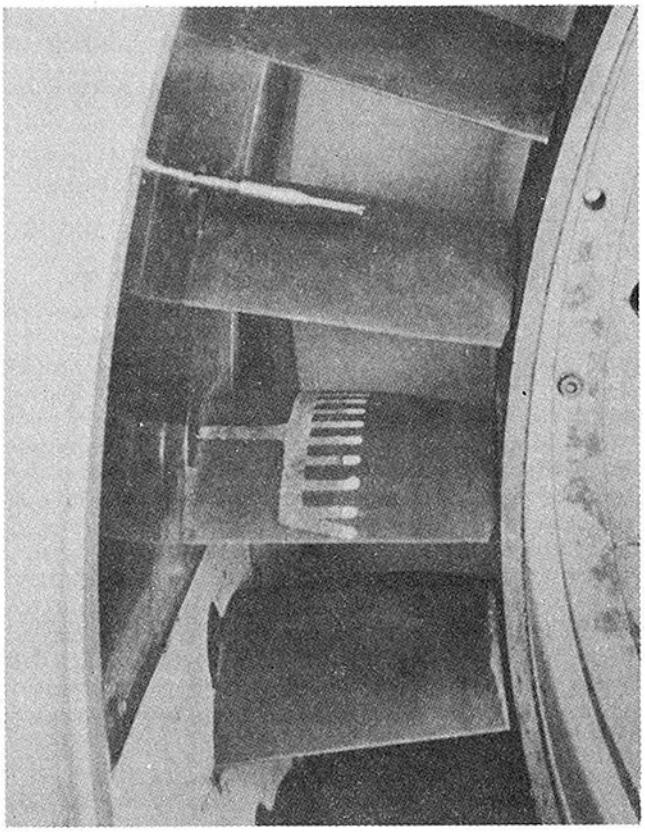


Fig. 7 View of cross hot-wire probe and instrumented cambered vane suction surface

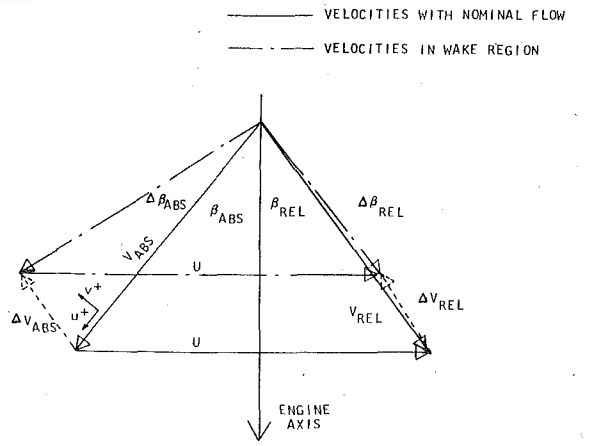


Fig. 8 Reduction in relative velocity generated by blade wake creates corresponding velocity and angular change in absolute frame

based events as measured by this hot-wire probe to the pressures on the vane surfaces, two assumptions are made: (1) the wakes are identical at the hot-wire and the stator leading edge planes; (2) the wakes are fixed in the relative frame. Fig. 9 presents a schematic of the rotor wakes, the instrumented cambered airfoils and the hot-wire probe. The rotor blade spacing, the vane spacing, and the axial spacing between the vane leading edge plane and the probe holder centerline are known quantities. At a steady operating point the hot-wire data is analyzed to determine the absolute flow angle and the rotor exit relative flow angle. Using the two assumptions noted, the wake is located relative to the hot-wires and the leading edges of the instrumented vane suction and pressure surfaces. From this, the times at which the wake is present at various locations is determined. The increment times between occurrences at the hot-wire and the vane leading edge plane are then related to phase differences between the perturbation velocities and the vane surface.

To simplify the experiment-theory correlation process, the data is adjusted in phase such that the transverse perturbation is at zero deg at the airfoil suction surface leading edge. From the geometry indicated in Fig. 9, the time at which this would occur is calculated and transposed into a phase difference. This difference is then used to adjust the aerodynamic phase lag pressure data from the airfoil suction and pressure surfaces.

Following this procedure the equivalent complex pressure difference across a single airfoil at each transducer location is calculated. The magnitude of the pressure difference data is then nondimensionalized with respect to the inlet flow parameter $(\rho \cdot V^2 \cdot v/V)$ where ρ is the inlet air density, V is the stator inlet absolute velocity, and v is the transverse perturbation velocity measured by the cross-wire probe.

Thus, the final form of the unsteady pressure data describes the chordwise variation of the pressure difference across an airfoil and is presented in terms of an aerodynamic phase lag referenced to a transverse gust at the airfoil leading edge and a dynamic pressure coefficient, C_p.

Results

The objective of this experimental investigation was to assess the range of validity of the current state-of-the-art zero incidence, flat plate cascade, transverse gust analyses and to also determine the effects of airfoil camber on the associated fundamental unsteady aerodynamics. This was accomplished by measuring the rotor wake generated harmonic fluctuating pressure distributions on both a flat plate and a cambered airfoil stator row and correlating these data with appropriate predictions as well as with each other.

The state-of-the-art cascade transverse gust analysis used to correlate the nondimensionalized unsteady pressure difference data is that of [2]. This cascade analysis considers the two-dimensional, unsteady flow past a rectilinear flat plate cascade. The basic assumptions are: the fluid is a perfect gas; the flow field is irrotational; and the thin airfoil approximations are appropriate. The flow model

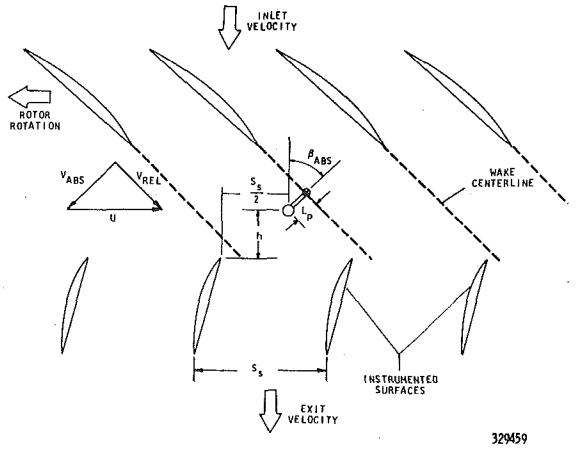


Fig. 9 Schematic of flow field used in dynamic data analysis

Downloaded 01 Jun 2010 to 171.66.16.58. Redistribution subject to ASME license or copyright; see http://www.asme.org/terms/Terms_Use.cfm

assumes a basic uniform compressible flow field past an airfoil cascade, with small unsteady normal velocity fluctuations superimposed. The source of the fluctuations is located upstream with the oscillations in the velocity normal to the airfoil surfaces convected downstream with the uniform flow. The key input parameters included in this analysis are the reduced frequency, the interblade phase angle, the Mach number, the cascade solidity, and the stagger angle. The analysis then predicts the resulting dimensionless chordwise distribution of the complex unsteady pressure difference across a flat plate airfoil in cascade.

The fundamental measured quantities in this experiment are the rotor wakes and the resulting individual surface unsteady pressure distributions. From these, the dimensionless unsteady pressure differential across an airfoil are calculated in the form of a dimensionless dynamic pressure coefficient ($C_p = \Delta P/\rho \cdot V^2 \cdot v/V$) and an aerodynamic phase lag referenced to a transverse gust at the airfoil leading edge, as previously noted. These first harmonic data for both the flat plate and the cambered airfoil vane rows together with the corresponding predictions obtained from the analysis of [2] are presented herein in terms of decreasing incidence angle values. The zero incidence data are presented in Figs. 10 and 11, small negative incidence angle results in Figs. 12 and 13, intermediate negative incidence results in Figs. 14 and 15, and the large negative incidence data in Fig. 16.

Fig. 10 presents the zero incidence angle flat plate airfoil cascade data together with the incompressible and the appropriate compressible (Mach = 0.1) predictions. As indicated, the dynamic pressure coefficient data correlate quite well with the two predictions, which are nearly identical, over the entire vane chord. These data and the predictions decrease in the chordwise direction and attain a near zero value at the airfoil trailing edge (trailing edge transducer at 96.0 percent of the chord). It should be noted that the finiteness of the trailing edge dynamic pressure coefficient data and also its value reflect upon the validity and the application of the Kutta condition for unsteady flows to these high reduced frequency values. It should be emphasized that these data are normalized with respect to a vane inlet velocity and density parameter. Hence, an increase or decrease in C_p implies a corresponding change in the magnitude of the measured unsteady pressure differential.

The zero incidence aerodynamic phase lag flat plate data correlate quite well with the compressible (Mach = 0.1) cascade prediction but not as well with the incompressible one, as also seen in Fig. 10. This relatively large difference in the two predictions, together with the correlation, is somewhat surprising in that the axial velocity past the vane is on the order of 100 ft/s (30.48 m/s), and thus the experiment appears to be incompressible. However, the compressible reduced frequency parameter ($kM/\sqrt{1-M^2}$) is on the order of 0.8 which is well within the range wherein compressibility effects become significant. It should be noted that all of the remaining data presented herein are correlated with the compressible (Mach = 0.1) predictions.

Fig. 11 presents the zero incidence cambered airfoil vane data together with the compressible flat plate prediction. As can be seen, both the dynamic pressure coefficient data and the corresponding prediction decrease along the vane chord. Reasonable correlation is obtained, although not quite as good as that for the flat plate vane. For this cambered airfoil, the ten percent chord dynamic pressure coefficient data appear to be reduced in value as compared to the neighboring data points but are in agreement with the prediction. At the vane trailing edge transducer location (97.0 percent chord) the data are finite, albeit non-zero. Again, this result is of significance with regard to the application of the Kutta condition to unsteady flows at high reduced frequency values.

The cambered airfoil vane cascade aerodynamic phase lag data are seen to correlate well with the flat plate compressible prediction over the front portion of the vane, with the correlation becoming less satisfactory over the rear portion of the vane. This poorer correlation of the data over the rear of the vane is felt to be due to the approximately 49 deg of camber. Comparison of these cambered airfoil vane results, Fig. 11, with those for the flat plate, Fig. 10, demonstrates the effect of airfoil camber and also tends to preclude the possibility of viscous or boundary layer effects yielding the above noted cambered airfoil results.

Figs. 12 and 13 show small negative incidence angle (−2 deg) results for the flat plate and the cambered airfoil vane stator rows respec-

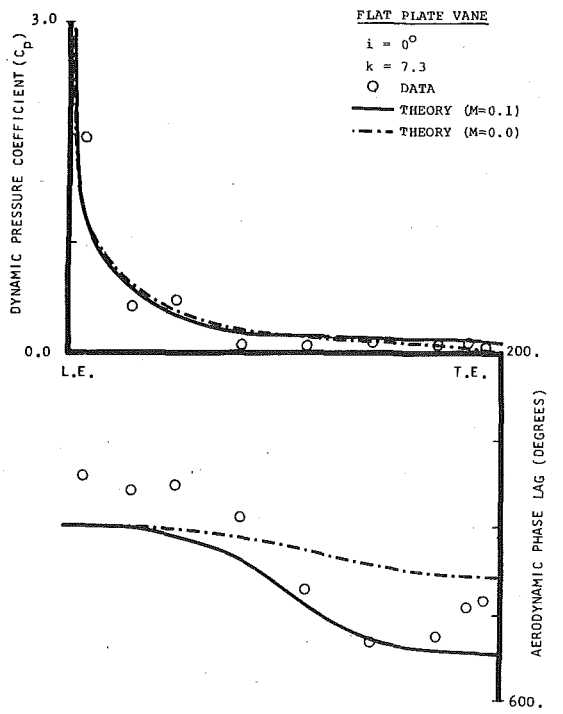


Fig. 10 Correlation of the zero incidence angle flat plate vane row data with incompressible and compressible transverse gust predictions

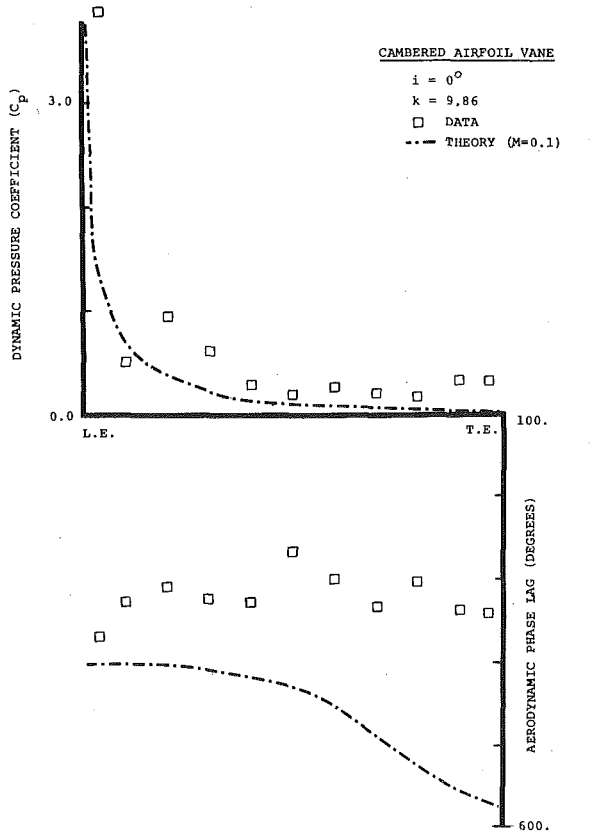


Fig. 11 Correlation of the zero incidence angle cambered airfoil vane row data with the compressible transverse gust prediction

Downloaded 01 Jun 2010 to 171.66.16.58. Redistribution subject to ASME license or copyright; see http://www.asme.org/terms/Terms_Use.cfm

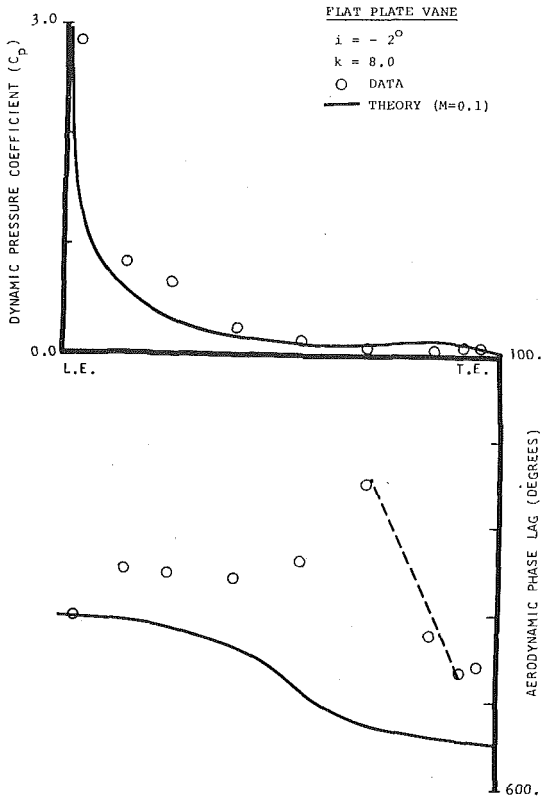


Fig. 12 Correlation of the small incidence angle flat plate vane row data with the compressible transverse gust prediction

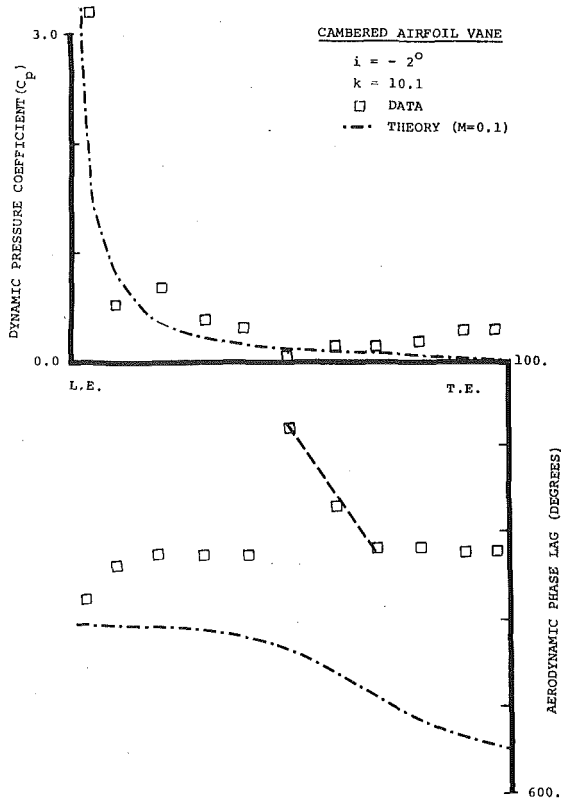


Fig. 13 Correlation of the small incidence angle cambered airfoil vane row data with the compressible transverse gust prediction

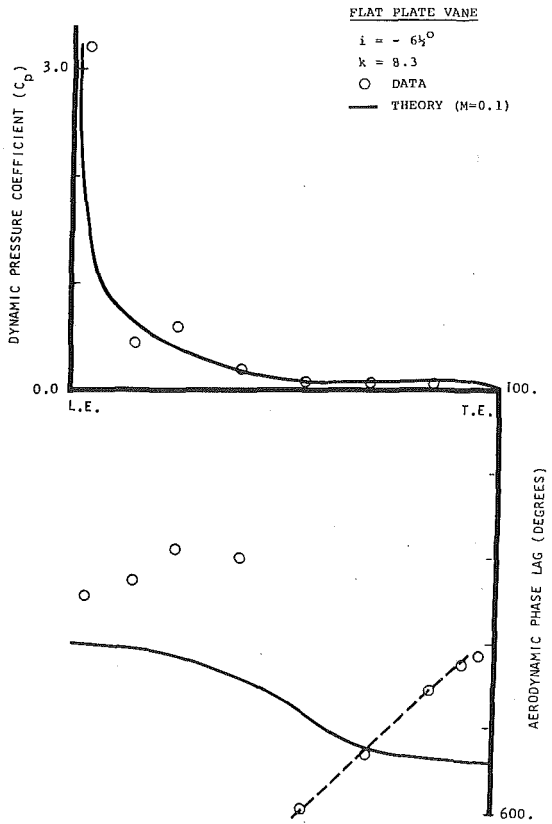


Fig. 14 Correlation of the intermediate incidence angle flat plate vane row data with the compressible transverse gust prediction

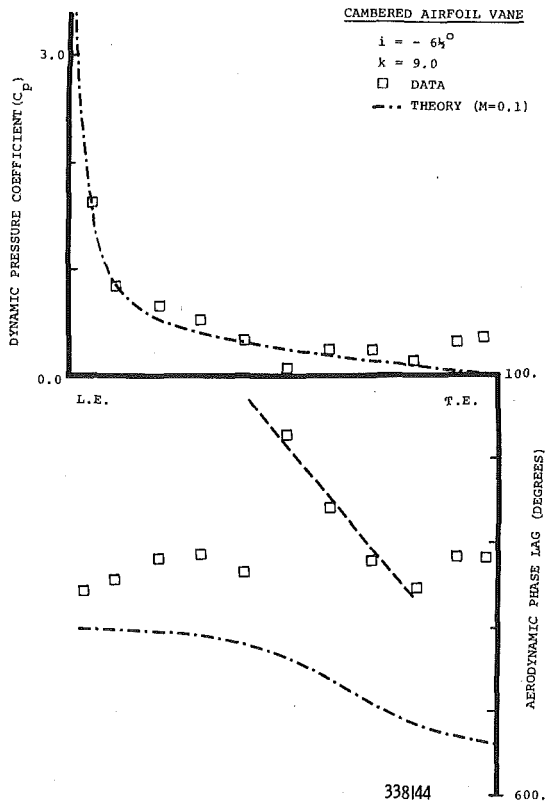


Fig. 15 Correlation of the intermediate incidence angle cambered airfoil vane row data with the compressible transverse gust prediction

tively. As can be seen, the dynamic pressure coefficient data correlates relatively well with the appropriate compressible flat plate predictions. The trailing edge transducer location data are again zero for the flat plate (96 percent chord) and non-zero but finite for the cambered airfoil (97 percent chord).

The aerodynamic phase lag data-theory correlation is much more interesting. For both the flat plate and the cambered airfoils, the phase lag over the front portion of the vane is in good agreement both

Downloaded 01 Jun 2010 to 171.66.16.58. Redistribution subject to ASME license or copyright; see http://www.asme.org/terms/Terms_Use.cfm

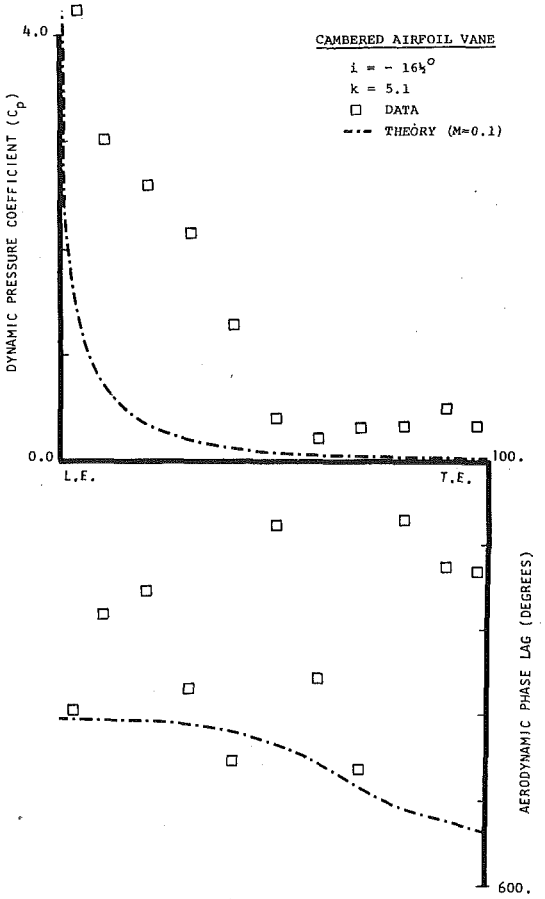


Fig. 16 Correlation of the large incidence angle cambered airfoil vane row data with the compressible transverse gust prediction

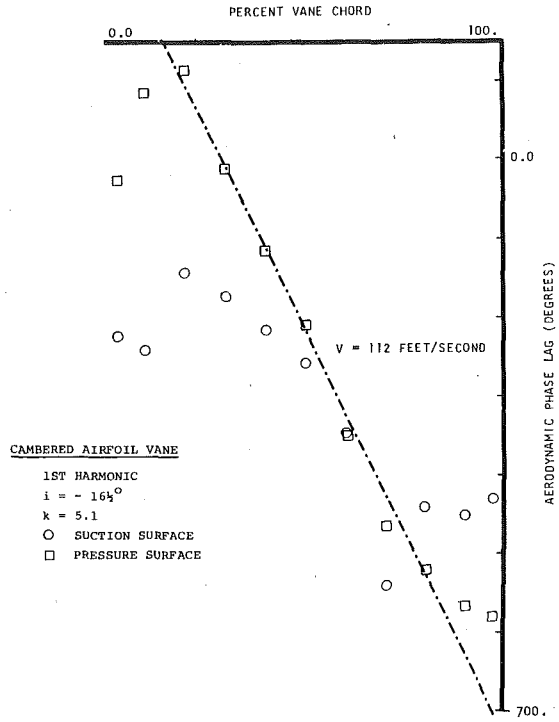


Fig. 17 The chordwise variation of the first harmonic pressure and suction surface aerodynamic phase lag for the cambered airfoil vane row at large incidence angle

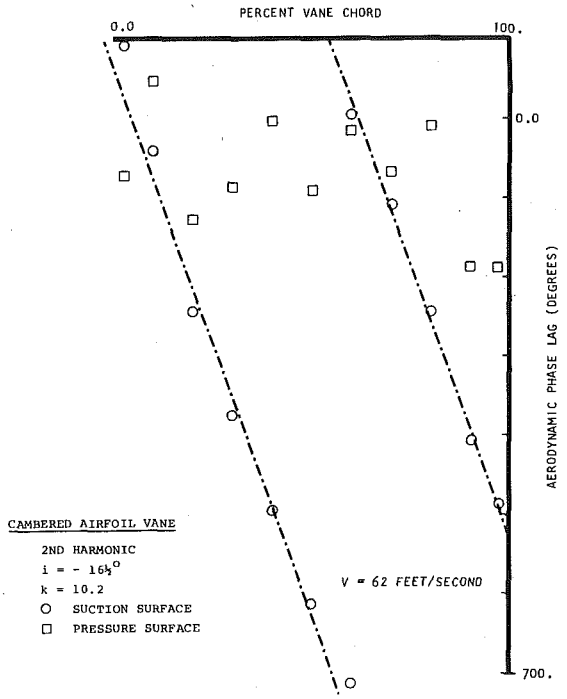


Fig. 18 The chordwise variation of the second harmonic pressure and suction surface aerodynamic phase lag for the cambered airfoil vane row at large incidence angle

with the prediction and with the zero incidence results which were presented in Figs. 10 and 11. Over the rear portion of these airfoils, the trend of the phase lag data departs from the zero incidence results, and a semblance of a linear phase variation begins to become apparent, as is indicated in Figs. 12 and 13.

The incidence angle is further decreased to an intermediate negative value (− 6½ deg) for both the flat plate and cambered airfoil stator rows. The resulting flat plate and cambered airfoil unsteady data and corresponding predictions are presented in Figs. 14 and 15, respectively. Again, the dynamic pressure coefficient data generally correlates well with the prediction, with both decreasing along the vane chord.

The aerodynamic phase lag data over the front portion of both the flat plate and cambered airfoil vanes is in relative agreement with the zero incidence flat plate predictions and unchanged as compared to the zero incidence data. However, the indication of the linear phase lag variation over the rear of the vanes, previously noted for the cases of small negative incidence angle, has now become much more pronounced.

Fig. 16 presents the large negative incidence angle (−16½ deg) results for the cambered airfoil vane row. No analogous results are available for the flat plate vane row. From this figure, it can be clearly seen that there is a large discrepancy between the flat plate dynamic pressure coefficient prediction and the theory over the major portion of the vane chord. Even so, it is interesting to note that the pressure difference data tends toward a zero, or at least finite, value at the vane trailing edge.

The previously described trends of the aerodynamic phase lag data with decreasing values of the incidence angle have now reached an apparent limit. The good correlation with theory over the front of the vane is now limited to the leading edge pressure transducer (2.94 percent of the vane chord). The linear variation of the phase lag, previously apparent only over the rear portion of the vane, now dominates the major portion of the vane. This linearly increasing phase lag variation is signficant in that it means that an event occurring at one station occurs at a later time at some downstream station. This time and distance can be used to determine a convected wake speed which agrees well (within five percent) with the mass averaged axial velocity.

An examination of the aerodynamic phase lag data on the individual surfaces of the cambered airfoil vane at this large negative incidence angle reveals an interesting phenomenon. Figs. 17 and 18 present this

Downloaded 01 Jun 2010 to 171.66.16.58. Redistribution subject to ASME license or copyright; see http://www.asme.org/terms/Terms_Use.cfm

chordwise variation of the aerodynamic phase lag data for the first and second harmonics. As is indicated, the first harmonic phase lag data demonstrate that a convected wake traveling at approximately 62 ft/s (18.90 m/s) dominates nearly the entire pressure surface, but not the suction surface. The second harmonic phase lag data, on the other hand, shows that a convected wake traveling at approximately 112 ft/s (34.14 m/s) dominates the entire suction surface, but not the pressure surface. Thus, not only does a convected wake phenomena exist over the entire cambered airfoil vane chord at large negative incidence angles, but these wakes are convected at different velocities along each surface.

Summary and Conclusions

The rotor wake generated harmonic time-variant pressure distributions on both a classical flat plate and a cambered airfoil stator row have been determined over a wide range of incidence angle values at realistic reduced frequency. These dynamic data were all correlated with predictions obtained from a state-of-the-art compressible, zero incidence, flat plate cascade, transverse gust analysis to determine its range of validity and to quantitatively assess the effects of airfoil camber.

This data-theory correlation quantitatively demonstrated the following.

- Compressibility is significant at high reduced frequency and low Mach number values (unit order compressible reduced frequency values).
- The zero incidence flat plate vane data correlate very well with the compressible flat plate predictions.
- The zero incidence cambered airfoil vane row dynamic pressure coefficient data corrleate well with the compressible flat plate prediction over the entire vane chord whereas the phase lag data correlate only over the front portion of the vane, i.e., the effect of airfoil camber is to increase the aerodynamic phase lag over the rear portion of the vane.
- As the incidence angle is decreased from zero, the flat plate and cambered airfoil aerodynamic phase lag were affected prior to the dynamic pressure coefficient.
- As the incidence angle is decreased from zero towards large negative values, a wave phenomenon not modeled by the analysis becomes apparent on both the flat plate and cambered airfoil vane rows. This wave phenomenon first appears at the rear of the vane, and moves forward as the incidence angle decreases.
- At large negative incidence angle values, the wave phenomena exhibits different velocities on the pressure and suction surfaces of the cambered airfoil, a result not modeled in the analysis.
- The value of the dynamic pressure coefficient at the trailing edge was zero for the flat plate and non-zero but finite for the cambered airfoil vane rows, even at large negative incidence angle values. This reflects upon the validity of the Kutta condition for unsteady flows at high reduced frequency values.

Acknowledgment

This research was sponsored, in part, by the Air Force Office of Scientific Research (AFSC), United States Air Force. Acknowledgment is also made to the General Motors Corporation for permission to include the flat plate cascade data.

References

1 Whitehead, D. S., "Force and Moment Coefficients for Vibrating Airfoilds in Cascade," *Aeronautical Research Council R and M 3254*, Feb. 1960.

2 Fleeter, S., "Fluctuating Lift and Moment Coefficients for Cascaded Airfoils in a Nonuniform Compressible Flow," *AIAA Journal of Aircraft*, Vol. 10, No. 2, Feb. 1973.

3 Smith, S. N., "Discrete Frequency Sound Generation in Axial Flow Turbomachines," University of Cambridge, Department of Engineering Report CUED/A-Turbo/TR 29, 1971.

4 Ostdiek, F. R., "A Cascade in Unsteady Flow," Ph.D. Thesis, The Ohio State University, 1975.

5 Bruce, E. P. and Henderson, R. E., "Axial Flow Rotor Unsteady Response to Circumferential Inflow Distortions," Project SQUID Technical Report PSU-13-P, Sept. 1975.

6 Fleeter, S., Jay, R. L., and Bennett, W. A., "Rotor Wake Generated Unsteady Aerodynamic Response of a Compressor Stator," ASME Paper No. 78-GT-112, April 1978.

7 Fleeter, S., Jay, R. L., and Bennett, W. A., "The Unsteady Aerodynamic Effects of Decreased Compressor Stage Axial Spacing," Air Force Office of Scientific Research Report, DDA EDR 9379, Dec. 1977.

Downloaded 01 Jun 2010 to 171.66.16.58. Redistribution subject to ASME license or copyright; see http://www.asme.org/terms/Terms_Use.cfm

chordwise variation of the aerodynamic phase lag data for the first and second harmonics. As is indicated, the first harmonic phase lag data demonstrate that a convected wake traveling at approximately 62 ft/s (18.90 m/s) dominates nearly the entire pressure surface, but not the suction surface. The second harmonic phase lag data, on the other hand, shows that a convected wake traveling at approximately 112 ft/s (34.14 m/s) dominates the entire suction surface, but not the pressure surface. Thus, not only does a convected wake phenomena exist over the entire cambered airfoil vane chord at large negative incidence angles, but these wakes are convected at different velocities along each surface.

Summary and Conclusions

The rotor wake generated harmonic time-variant pressure distributions on both a classical flat plate and a cambered airfoil stator row have been determined over a wide range of incidence angle values at realistic reduced frequency. These dynamic data were all correlated with predictions obtained from a state-of-the-art compressible, zero incidence, flat plate cascade, transverse gust analysis to determine its range of validity and to quantitatively assess the effects of airfoil camber.

This data-theory correlation quantitatively demonstrated the following.

- Compressibility is significant at high reduced frequency and low Mach number values (unit order compressible reduced frequency values).
- The zero incidence flat plate vane data correlate very well with the compressible flat plate predictions.
- The zero incidence cambered airfoil vane row dynamic pressure coefficient data corrleate well with the compressible flat plate prediction over the entire vane chord whereas the phase lag data correlate only over the front portion of the vane, i.e., the effect of airfoil camber is to increase the aerodynamic phase lag over the rear portion of the vane.
- As the incidence angle is decreased from zero, the flat plate and cambered airfoil aerodynamic phase lag were affected prior to the dynamic pressure coefficient.
- As the incidence angle is decreased from zero towards large negative values, a wave phenomenon not modeled by the analysis becomes apparent on both the flat plate and cambered airfoil vane rows. This wave phenomenon first appears at the rear of the vane, and moves forward as the incidence angle decreases.
- At large negative incidence angle values, the wave phenomena exhibits different velocities on the pressure and suction surfaces of the cambered airfoil, a result not modeled in the analysis.
- The value of the dynamic pressure coefficient at the trailing edge was zero for the flat plate and non-zero but finite for the cambered airfoil vane rows, even at large negative incidence angle values. This reflects upon the validity of the Kutta condition for unsteady flows at high reduced frequency values.

Acknowledgment

This research was sponsored, in part, by the Air Force Office of Scientific Research (AFSC), United States Air Force. Acknowledgment is also made to the General Motors Corporation for permission to include the flat plate cascade data.

References

1 Whitehead, D. S., "Force and Moment Coefficients for Vibrating Airfoilds in Cascade," *Aeronautical Research Council R and M 3254*, Feb. 1960.

2 Fleeter, S., "Fluctuating Lift and Moment Coefficients for Cascaded Airfoils in a Nonuniform Compressible Flow," *AIAA Journal of Aircraft*, Vol. 10, No. 2, Feb. 1973.

3 Smith, S. N., "Discrete Frequency Sound Generation in Axial Flow Turbomachines," University of Cambridge, Department of Engineering Report CUED/A-Turbo/TR 29, 1971.

4 Ostdiek, F. R., "A Cascade in Unsteady Flow," Ph.D. Thesis, The Ohio State University, 1975.

5 Bruce, E. P. and Henderson, R. E., "Axial Flow Rotor Unsteady Response to Circumferential Inflow Distortions," Project SQUID Technical Report PSU-13-P, Sept. 1975.

6 Fleeter, S., Jay, R. L., and Bennett, W. A., "Rotor Wake Generated Unsteady Aerodynamic Response of a Compressor Stator," ASME Paper No. 78-GT-112, April 1978.

7 Fleeter, S., Jay, R. L., and Bennett, W. A., "The Unsteady Aerodynamic Effects of Decreased Compressor Stage Axial Spacing," Air Force Office of Scientific Research Report, DDA EDR 9379, Dec. 1977.

DISCUSSION

T. H. Okiishi[1]

Of the several useful aspects of this paper, I am particularly interested in the authors' conclusions related to convected wake segment (rotor wake segment in the present case) transport through a chopping blade row (stater row in the present case). They have shown in this and an earlier paper [8], that the convection of chopped wake segments along a chopping blade section, suction and pressure surfaces occurs at different velocities; they also suggested that this kind of wake action may be important enough to consider if more accurate analytical predictions of the unsteady effects involved are desired. An approproximate description of the wake chopping and transport process in a turbo-machine has been proposed by several investigators [9–14] and detailed measurements including fluid velocities and particle pathlines seem to support the general model involved.

There appears to be an inconsistency between the wake segment convection velocities reported in the present paper and those reported earlier [8] and I would appreciate the authors' comments on this particular matter.

In the present paper, the authors have concluded from chopping blade (stater blade) surface pressure aerodynamic phase lag data that convected wake segments traveling at approximately 112 ft/s (34.14 m/s) dominate the pressure surface while convected wake segments traveling at approximately 62 ft/s (18.9 m/s) dominate the suction surface. In the earlier paper, the authors concluded from individual chopping blade surface pressure transducer signals, unsteady chopping blade surface pressure differential data and timing traces that the chopped wake segment convection velocity was between 60 to 62.2 ft/s (18.3 to 19.0 m/s) on the pressure surface and 105.6 to 110 ft/s (32.2 to 33.5 m/s) on the suction side. In both papers, the authors concluded that the first harmonic of the chopping blade unsteady pressure data is dominated by wake segment transport over the pressure surface of the chopping blade section and that the second harmonic of the unsteady pressure data is dominated by wake segment transport over the suction surface.

[1] Professor, Mechanical Engineering Department, Iowa State University, Ames, Iowa 50011.

Additional References

8 Fleeter, S., Jay, R. L., and Bennett, W. A. "Rotor Wake Generated Unsteady Aerodynamic Response of a Compressor Stator," ASME, JOURNAL OF ENGINEERING FOR POWER, Vol. 100, 1978, pp. 664–675.

9 Meyer, R. X. "The Effect of Wakes on Transient Pressure and Velocity Distributions in Turbomachines," *Trans ASME*, Vol. 80, 1958, pp. 1544–1552.

10 Smith, L. H., Jr., "Wake Dispersion in Turbomachines," ASME *Journal of Basic Engineering*, 1966, pp. 688–690.

11 Kerrebrock, J. L., and Mikolajczak, A. A., "Intra-Stator Transport of Rotor Wakes and its Effect on Compressor Performance," ASME JOURNAL OF ENGINEERING FOR POWER, 1970, pp. 359–368.

12 Brandone, B., and Bernard, P., "Visualization par Analogie Hydraulique de L'Ecoulement dans une Grille D'Aubes Plane Mobile," *La Recherche Aerospatiale* 141, No. 1971–2, 1971, pp. 125–128.

13 Walker, G. J., and Oliver, A. R., "The Effect of Interaction Between Wakes from Blade Rows in an Axial-Flow Compressor on the Noise Generated by Blade Interaction," ASME JOURNAL OF ENGINEERING FOR POWER, 1972, pp. 241–248.

14 Lockhart, R. C., and Walker, G. J., "The Influence Viscous Interactions on the Flow Downstream of an Axial Compressor Stage," *Proceedings of the 2nd International Symposium on Air Breathing Engines*, 1974.

15 Wagner, J. H., Okiishi, T. H., and Holbrook, G. J., "Periodically Unsteady Flow in an Embedded Stage of a Multistage Axial-Flow Turbomachine," ASME, JOURNAL OF ENGINEERING FOR POWER, Vol. 101, 1979, pp. 42–51.

Copyright © 1980 by ASME

Downloaded 01 Jun 2010 to 171.66.16.58. Redistribution subject to ASME license or copyright; see http://www.asme.org/terms/Terms_Use.cfm

Authors' Closure

We appreciate Dr. Okiishi's interest in this effort and also for pointing out the inconsistency in the reported convected velocities of the wake segments. The inconsistency comes from writing a textual conclusion from a mislabeled plot. Fig. 17 should have a labeled velocity of 62 ft/s and Fig. 18 should be labeled 112 ft/s with the text also reflecting this change. This can be readily checked by obtaining the slope of the phase lag as a function of percent chord and calculating the convected velocity of 70 percent design speed (613 rpm). From the published plots one can easily obtain 65 ft/s for Fig. 17 and 105 ft/s for Fig. 18, which is well within tolerance one may expect for an unlined plot.

The conclusion, for our purpose, remains unchanged in that the apparent chopped wake segments travel at different convected velocities along the pressure and suction surfaces and this difference should be incorporated into the analytical model.

Downloaded 01 Jun 2010 to 171.66.16.58. Redistribution subject to ASME license or copyright; see http://www.asme.org/terms/Terms_Use.cfm

H. Atassi
Professor.

T. J. Akai
Assistant Professor.

Department of Aerospace and Mechanical Engineering
University of Notre Dame
Notre Dame, Ind. 46556

Aerodynamic and Aeroelastic Characteristics of Oscillating Loaded Cascades at Low Mach Number

Part I: Pressure Distribution, Forces, and Moments[1]

A complete theory is developed in Part I of these two papers for the analysis of oscillating airfoils in cascade in uniform incompressible flows. The theory fully accounts for the geometry of the airfoils and cascade parameters. It is shown that the strong mean velocity gradient near the leading edges of the airfoils significantly affects the unsteady pressure, forces and moments acting upon the airfoils. In Part II the aeroelastic characteristics of a loaded cascade are investigated for one and two degrees of freedom oscillations.

Introduction

A complete first order theory was developed in [1] for the analysis of oscillating airfoils in cascade in uniform incompressible flows. The geometry of the blades is arbitrary. The angle of attack of the mean flow, and the parameters of the cascade, i.e., stagger, solidity, and interblade phase angle can assume any general set of values. The mathematical formulation leads to two singular integral equations in the complex plane for the density distribution of singularities along the airfoils' contours and their wakes. The two equations are coupled by the Kutta condition at the trailing edges of the airfoils.

The authors in [2] and [3] developed a numerical computation procedure for the integral equations and presented preliminary results about the unsteady aerodynamic forces and moments. It was noted then that a nonlinear coupling between the steady and unsteady flow fields introduces a term in the boundary conditions proportional to the mean velocity gradient which is singular at the trailing edge for non-cusped airfoils and is inversely dependent on the radius of curvature at the leading edge of the airfoil. This term was then neglected because it creates major difficulties in the numerical computation and as shown by Whitehead [4] in a discussion of [2], it does not significantly alter the aerodynamic lift for unloaded blades at zero interblade phase angle. However, this term substantially affects the pressure near the leading and trailing edges. Furthermore, it will be shown that for a non-zero interblade phase angle it also has a significant effect on the aerodynamic forces and moments.

In Part I, the authors will introduce an analytical solution which accounts for the singular behavior of the mean velocity gradient and modify their numerical procedure so that all the terms of the boundary conditions at the surface of the airfoil are properly and completely accounted for.

A study of the unsteady pressure distribution, forces and moments for typical airfoil geometry and cascade parameters will then be presented. The results will be compared with cases studied previously. The basic characteristics of the unsteady pressure near the leading edge will be investigated in view of its importance to flow separation and bubble formation.

In Part II the authors will use the aerodynamic results to investigate the flutter and instability boundaries for unstalled loaded cascades.

Mathematical Formulation

In view of the modification of the mathematical procedure for solving the problem described in [2] we briefly outline the basic concepts of the theory.

The geometrical configuration of the problem is shown in Fig. 1. A two-dimensional cascade of airfoils of chord length, c, is placed in a uniform flow, U_∞, at an angle of attack α. The airfoils have a small harmonic oscillation about their mean position with a constant interblade phase angle σ. We consider translational oscillations of the

[1] Research supported by a grant from the Air Force Office of Scientific Research, No. AFOSR-F49620-79-C-0014.

Contributed by the Gas Turbine Division and presented at the Gas Turbine Conference and Exhibit and Solar Energy Conference, San Diego, California, March 12–15, 1979 of THE AMERICAN SOCIETY OF MECHANICAL ENGINEERS. Manuscript received at ASME Headquarters December 18, 1978. Paper No. 79-GT-111.

Copyright © 1980 by ASME

Downloaded 01 Jun 2010 to 171.66.16.58. Redistribution subject to ASME license or copyright; see http://www.asme.org/terms/Terms_Use.cfm

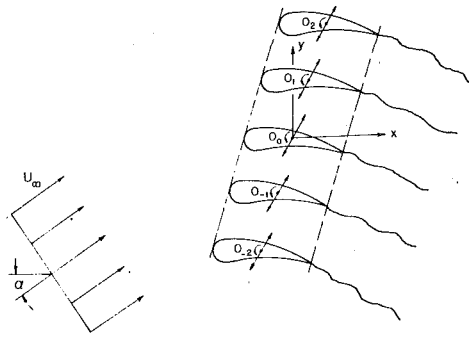


Fig. 1 Schematic of an oscillating cascade in a uniform flow

airfoils in the direction, γ, defined by $\epsilon\vec{H}_m$, where ϵ is a small number and m refers to the particular airfoil considered. Also, we suppose that every airfoil has a rotational oscillation about O_m which can be obtained from O_0 by a translation parallel to the spacing-stagger vector $\vec{S}$ of the cascade. Hence, the motion of a point, $M_s^{(m)}$, of airfoil m is defined by $\epsilon\vec{A}_m(t)$, where

$$\vec{A}_m(t) = \vec{H}_m + \vec{\Omega}_m X O_m \vec{M}_S{}^{(m)}. \tag{1}$$

$\vec{\Omega}_m$ is the rotation vector of airfoil m perpendicular to the xO_oy plane.

The velocity field is expanded as follows

$$\vec{q}(x, y; t) = \vec{q}_0(x, y) + \epsilon\vec{q}_1(x, y; t) + \dots \tag{2}$$

Both $\vec{q}_0$ and $\vec{q}_1$ are assumed to be irrotational and solenoidal. The boundary condition at the surface of the airfoil is that the normal velocity of the flow is equal to that of the airfoil surface. This condition is linearized and transferred to the mean position to yield

$$V_n{}^{(m)} = \vec{q}_1 \cdot \vec{n}_m = \frac{\partial}{\partial t}(\vec{A}_m \cdot \vec{n}_m) - \frac{\partial}{\partial n_m}(\vec{A}_m \cdot \vec{q}_0), \tag{3}$$

where $\vec{n}_m$ is the unit vector normal to airfoil m.

The boundary-value problem for $\vec{q}_1$ can therefore be formulated in terms of sectionally analytic functions satisfying condition (3) on the airfoils and a jump condition along the airfoils' wakes. We introduce the customary complex notations, $z = x + iy$, with $i = \sqrt{-1}$. Because of the periodic nature of the oscillatory motion of the airfoils, only one Fourier component will be considered. Thus the time dependence of $\vec{A}_m$ is of the form $\exp[j(\nu t + m\sigma)]$ where ν is the circular frequency, σ is the interblade phase angle, and $j = \sqrt{-1}$ for time. In the following the same letters denoting vector quantities will be used to denote their complex affixes. Thus, we have

$$A_m = (he^{i\gamma} + i\omega z)e^{jm\sigma}, \tag{4}$$

where h and ω are the time-dependent magnitudes of $\vec{H}$ and $\vec{\Omega}$, respectively. Note that A_m is a hypercomplex function which depends on two independent imaginary numbers i and j representing the direction of the y-axis in the plane, and the time phase, respectively. Because the motions of the airfoils differ only by a phase factor $\exp(jm\sigma)$ we shall drop, for the sake of simplicity, the index m, and consider only the oscillatory motion of the base airfoil (index o). The boundary condition (3) then becomes

$$V_n = jk\mathrm{Re}\{n\overline{A}\} - \omega\,\mathrm{Re}\{in\overline{q}_0\} - \mathrm{Re}\left\{nA\frac{d\overline{q}_0}{dz}\right\}. \tag{5}$$

Here lengths, velocities, and time are normalized with respect to $c/2$, U_∞, and $c/2U_\infty$, respectively, $k = \nu c/2U_\infty$ is the reduced frequency, and the overbar is for the complex conjugate. Note that the last term of the right-hand side of equation (5) is proportional to the gradient of the mean velocity of the flow. It is singular for noncusped airfoils at the trailing edge. At the leading edge, it is inversely dependent on the radius of curvature at this point and hence inversely dependent on the square of the thickness of the airfoil. Therefore for a typical airfoil thickness it becomes very large near the leading edge. This characteristic destabilized the matrix obtained in the numerical procedure used in [2] and [3] and led us to neglect this term in the preliminary results previously obtained. Note that this term introduces a strong coupling between the steady-state solution $\vec{q}_0$ and the unsteady solution $\vec{q}_1$.

The other boundary condition of the problem is the tangential discontinuity of $\vec{q}_1$ along the wakes which represents the vortex shedding due to the motion of the airfoil and the imposition of the Kutta condition. The expression of the jump of $\vec{q}_1$ was derived in [1]

$$\vec{q}_1{}^+ - \vec{q}_1{}^- = \frac{C_0}{\overline{q}_0}e^{jk(t-\phi)} \tag{6}$$

with

$$\phi = \int_{T.E.}^{z}\left(\frac{dz}{\overline{q}_0}\right)_W \tag{7}$$

where C_0 is a constant to be determined by the use of Kelvin's theorem [4], and the line integral of equation (7) is taken along the mean wake line W.

Splitting the Solution. Let $u_1 + iv_1$ be the complex velocity representing $\vec{q}_1$. Then $u_1 - iv_1$ is a sectionally analytic function in the

Nomenclature

A = displacement of a point on the airfoil surface
c = chord length
D = unsteady aerodynamic drag
F = unsteady aerodynamic force
$\vec{H}$ = translational motion of the airfoil
i = unit imaginary number for space
j = unit imaginary number for time
$k = \nu c/2U_\infty$, reduced frequency
K = kernel function defined in equation (9)
L = unsteady aerodynamic lift
M = unsteady aerodynamic moment
$\vec{n}$ = unit normal to airfoil
n = complex unit normal to airfoil
O = origin of the coordinate system; also center of rotational oscillation for airfoil
P = unsteady pressure
q = complex velocity
$\vec{S} = \vec{O_0O_1}$ in Fig. 1, defines solidity and stagger
S = complex representation of $\vec{S}$
t = time
u = x-component of velocity
v = y-component of velocity
x = coordinate direction parallel to chord
y = coordinate direction perpendicular to chord
$z = x + iy$
$\mathcal{D}$ = linear operator yielding drag from velocity
$\mathcal{F}$ = linear operator yielding force from velocity
$\mathcal{L}$ = linear operator yielding lift from velocity
$\mathcal{M}$ = linear operator yielding moment from velocity
α = angle of attack with respect to x-axis
γ = angle between $\vec{H}$ and the x-axis
δ = stagger angle measured from y-axis ($\pi/2$ − arg S)
ε = small parameter for linearization
μ = density distribution; defined in equation (8)
σ = interblade phase angle
τ = point on the airfoil surface in its mean position
ϕ = Lagrangian time function; defined by equation (7)
Γ = circulation around airfoil
Ω = rotational motion or airfoil
$z^* = (\tau - z)/S$
C_0 = constant defined in equation (24)
U_∞ = freestream velocity
V_n = normal velocity of flow at airfoil mean position
β_1 = camber angle/2

Subscripts

m = index identifying blades in cascade
o = denotes steady state
A = airfoil contour
I = denotes instantaneous solution
W = wake line; also denotes wake solution
1 = denotes unsteady location

Downloaded 01 Jun 2010 to 171.66.16.58. Redistribution subject to ASME license or copyright; see http://www.asme.org/terms/Terms_Use.cfm

multiply-connected domain outside of the airfoils' contours. This function can be represented by a density distribution, $\mu(\tau)$, along the boundaries of the problem which are here the airfoils' contours and their wakes. We shall choose μ to be real with respect to the space variables (see Muskhelishvili [5] and Gakhov [6]) and complex with respect to time. Note, however, that because we have airfoils with finite thickness, μ is not simply a distribution of vortices along the airfoils' surfaces. Then we have

$$u_1 - iv_1 = \frac{1}{2\pi i} \sum_{m=-\infty}^{m=+\infty} \int_L \frac{\mu(\tau) e^{jm\sigma}}{\tau + mS - z} d\tau. \tag{8}$$

The path of integration L comprises the contour A of the base airfoil (index 0) and its wake W. After summation with respect to m (8) can be written as

$$u_1 - iv_1 = \frac{1}{2\pi i} \int_L K(z^*)\mu d\tau, \tag{9}$$

where

$$K(z^*) = \frac{\pi}{S} \frac{e^{j(\pi-\sigma)z^*}}{\sin \pi z^*}, \tag{10}$$

with $z^* = (\tau - z)/S$.

The solution is split as follows

$$u_1 - iv_1 = (u - iv)_I + C_0(u - iv)_W, \tag{11}$$

where $(u - iv)_I$ is an analytic function satisfying condition (5) on the airfoil surface.

$$\mathrm{Re}\{(u - iv)_I \cdot n\} = V_n, \tag{12}$$

and $(u - iv)_W$ is a sectionally analytic function satisfying

$$\mathrm{Re}\{(u - iv)_W \cdot n\} = 0. \tag{13}$$

along the airfoils' surfaces.

Using a representation of $(u - iv)_I$ and $(u - iv)_W$ of the form (9) will define two singular integral equations for the density functions μ_I and μ_W. However, the last term of the right-hand side of (5) may be singular at the trailing edge and exhibits large values at the leading edge. This feature produced a great difficulty in the numerical procedure employed to solve the singular integral equation. We removed this difficulty by finding an analytical solution satisfying the last term of (5), namely, $\mathrm{Re}\{nAd\bar{q}_0/d\tau\}$.

Using Cauchy's formula for a multiply connected domain, it can be shown (see [1] for details) that at the surface of the airfoils

$$A\frac{d\bar{q}_0}{dz} = \frac{-1}{iS} \int_A \left(A\frac{d\bar{q}_0}{d\tau}\right) \cot \pi t^* d\tau \tag{14}$$

where $t^* = z^*$ for z on the airfoil surface. Therefore, we seek a representation for $(u - iv)_I$ at the surface of the airfoils as

$$(u - iv)_I = (u - iv)_I^{(1)} + (u - iv)_I^{(2)} + (u - iv)_I^{(3)} \tag{15}$$

$$(u - iv)_I^{(1)} = \frac{1}{2\pi i} \int_A K(z^*)\mu_I d\tau \tag{16}$$

$$(u - iv)_I^{(2)} = \frac{-1}{2\pi i}\left(\frac{\pi}{S}\right) \int_A \left(A\frac{d\bar{q}_0}{d\tau}\right) \left[\cot \pi t^* - \frac{e^{j(\pi-\sigma)t^*}}{\sin \pi t^*}\right] d\tau \tag{17}$$

$$(u - iv)_I^{(3)} = -\left(A\frac{d\bar{q}_0}{dz}\right) \tag{18}$$

Note that the integral of the right-hand side of (17) is not singular. Moreover, because of (14) the interblade phase relationship (4) is satisfied by $(u - iv)_I$ represented in (15).

The integral equation to be satisfied by μ_I is then

$$\mathrm{Re}\{(u - iv)_I^{(1)} \cdot n\} = V_n - \mathrm{Re}\{u - iv)_I^{(2)} \cdot n\} + \mathrm{Re}\{nAd\bar{q}_0/dz\}, \tag{19}$$

with

$$[\mu_I{}^+ - \mu_I{}^-]_{T.E.} = 0. \tag{20}$$

This eliminates the term proportional to $d\bar{q}_0/dz$ in V_n and the numerical difficulties associated with it. Another interesting feature of this form of the solution is the convenient way the solution can be transferred back from the mean position of the airfoil to its instantaneous position. This will be discussed later as we derive the expression for the pressure on the airfoil.

Now we turn to determine the sectionally analytic function satisfying the homogeneous equation (13) and the boundary condition (6) along the wakes. We first determine a sectionally analytic function satisfying (6) for $C_0 = 1$. This is obtained by the use of Plemelj's formula (see Gakhov [6], p. 25). After summation along the wakes, this solution can be reduced to

$$u - iv = \frac{1}{2\pi i} \int_W \frac{e^{jk(t-\phi)}}{q_0} K(\tau - z) d\tau. \tag{21}$$

Such a function does not satisfy, however, the zero normal velocity condition along the airfoil surface. We then add to it an analytical function of the form (9) and defined by an unknown density function μ_W. Thus we consider the wake solution

$$(u - iv)_W = \frac{1}{2\pi i}\left\{\int_W \frac{e^{jk(t-\phi)}}{q_0} K(\tau - z) d\tau + \int_A \mu_W K(\tau - z) d\tau\right\}, \tag{22}$$

which should satisfy equation (13) with

$$[\mu_W{}^+ - \mu_W{}^-]_{T.E.} = -e^{jkt}/|q_0|_{T.E.}. \tag{23}$$

The constant C_0 should be determined by the condition that the total circulation around the airfoil and its wake is zero. That is

$$C_0 = \frac{\int_A \mu_I d\tau + i\omega\Gamma_0}{\frac{j}{k} e^{jkt} - \int_A \mu_W d\tau}, \tag{24}$$

where Γ_0 is the steady circulation round the airfoil taken clockwise. Note that both the numerator and denominator of (24) are only complex with respect to the unit imaginary number, j, associated with the time phase. The term $i\omega\Gamma_0$ in the numerator of C_0 is exactly cancelled by a term obtained from the integration of μ_I. It is also important to note that the numerator of C_0 represents the quasi-steady circulation in the clockwise direction around the airfoil of index zero.

$$\Gamma_{Q.S.}^{(1)} = \int_A \omega_I d\tau + i\omega\Gamma_0 \tag{25}$$

The splitting of the unsteady velocity field as given by (11) is different from the one carried out by Theodorsen [7] and von Karman and Sears [8] in classical airfoil theory. Their splitting consisted of considering a non-circulatory solution and a circulatory one. Here both solutions $(u - iv)_I$ and $(u - iv)_W$ are circulatory. Conditions (20) and (23) are indeed necessary to insure finite solutions at the trailing edge and to avoid singular behavior in μ which would have made the numerical computations much more difficult to carry out.

Numerical Procedure. The integral equations (13) and (19) are solved numerically by collocation. The numerical procedure uses complex variables and was outlined in detail in [2].

Unsteady Pressure Distribution

The unsteady pressure distribution along the airfoil surface is obtained in terms of $\bar{q}_0$ and $\bar{q}_1$ by integrating Euler's equation along the contour of the airfoil. After transfer to the instantaneous airfoil position we find

$$P - P_{T.E.} = -\mathrm{Re}\left\{q_0\left(\bar{q}_1 + A\frac{d\bar{q}_0}{dz}\right)\right\} + \mathrm{Re}\left\{q_0\left(\bar{q}_1 + A\frac{d\bar{q}_0}{dz}\right)\right\}_{T.E.^+} - jk\int_{T.E.^+}^{\tau} \mathrm{Re}\{\bar{q}_1 dz\} \tag{26}$$

Note that $Ad\bar{q}_0/dz$ accounts for the transfer of the pressure value from a point at the mean position of the airfoil to its instantaneous position.

Downloaded 01 Jun 2010 to 171.66.16.58. Redistribution subject to ASME license or copyright; see http://www.asme.org/terms/Terms_Use.cfm

The pressure expression in (26) is normalized with respect to $\epsilon\rho U_\infty{}^2$ for both translational and rotational oscillation. This normalization is identical to the one used by Sears [9] and Whitehead [10] for rotational oscillation. But it differs by a factor jk from the one used for translational oscillations. This is mainly due to the term $(u - iv)_I{}^{(2)}$ given by equation (17) which does not vanish as $k \to 0$. Physically, it is a consequence of the fact that for a cascade of nonflat plate airfoils the velocity field q_0 is modified by an amount equal to $Ad\bar{q}_0/dz$ as the airfoil moves a distance A from its initial position. For the same reason the torsional and bending lifts will be also both normalized with respect to $\frac{1}{2}\epsilon\rho U_\infty{}^2 c$.

Table 1 shows the characteristics of the cascades studied. Figs. 2 to 9 are plots of the real (in-phase) and imaginary (out-of-phase) components of the pressure along the surface of the base airfoil. Starting from the trailing edge, every pressure distribution loop is drawn in the direction indicated by the arrow to represent first the unsteady pressure along the suction surface of the airfoil and then goes back to the trailing edge describing the pressure along the pressure surface. Figs. 2 and 3 represent the pressure along an airfoil in cascade C_5 having a plunging oscillation perpendicular to the chord for three different values of the reduced frequency $k = 0.1, 0.5, 3$. The distribution of the imaginary component of the pressure which, in our representation, is the component out-of-phase with the airfoil displacement, appear to follow the same pattern for this range of frequency. Note that this component divided by k would represent the pressure component normalized with respect to the airfoil oscillatory velocity and would be in-phase with it.

Table 1 Figure symbols and parameters for Joukowski airfoils and cascades studied

Cascade	Symbol	Percent Thickness	Camber Angle	α (deg)	δ (deg)	σ (deg)
C_1	○	5	0	0	0	90
C_2	△	11.25	0	0	0	90
C_3	□	11.25	32	0	0	90
C_4	◇	11.25	32	16	0	90
C_5	▽	11.25	32	16	37.5	90
C_6	●	11.25	32	16	37.5	180

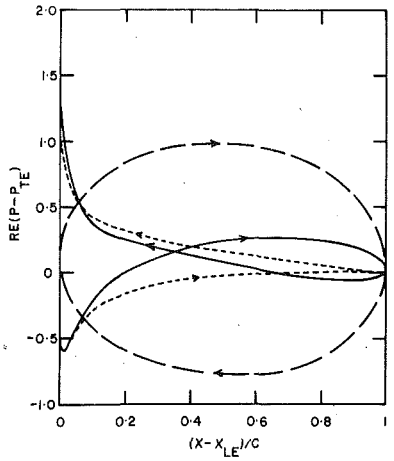


Fig. 2 Real component of the unsteady pressure distribution for plunging oscillation. Cascade C_5; - - -, $k = 0.1$; —, $k = 0.5$; — —, $k = 3.0$. For $k = 3$, the scale of the ordinate is reduced by a factor of 10.

The distributions of the real component of the pressure do not display such a simple pattern for various frequencies. A reversal in the sign of the pressure occurs for k at about 0.5 and higher. This is usually followed by a change in sign of the corresponding lift component. This results in shifting the center of pressure rearward and eventually producing a positive aerodynamic damping.

Figs. 4 and 5 show plots of the pressure distribution for the same cascade, C_5, in a rotational oscillation. The conditions are the same as for Figs. 2 and 3. Note the important change which occurs in the out-of-phase component of the pressure as k increases from 0.1 to 3. At low reduced frequency the pressure pattern is dominated by its shape near the leading edge. The center of pressure is forward of the center of the airfoil. However, as k increases the value of the pressure increases along the surface of the airfoil and the relative importance of the leading edge area is reduced.

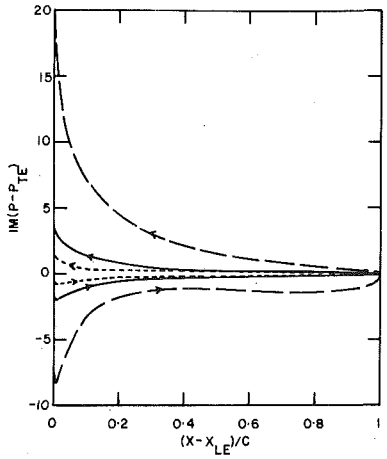


Fig. 3 Imaginary component of the unsteady pressure distribution for plunging oscillation. Cascade C_5; - - -, $k = 0.1$; —, $k = 0.5$; — —, $k = 3.0$

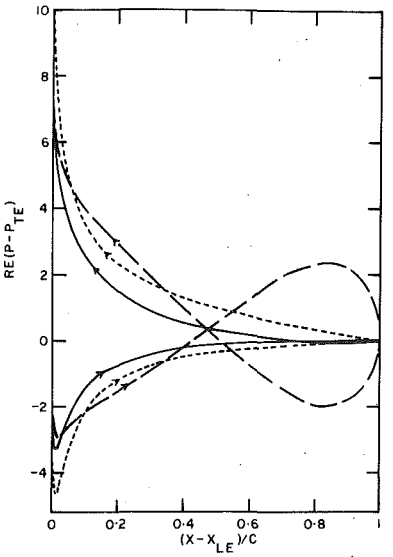


Fig. 4 Real component of the unsteady pressure distribution for rotational oscillation. Cascade C_5; - - -, $k = 0.1$; —, $k = 0.5$; — —, $k = 3.0$

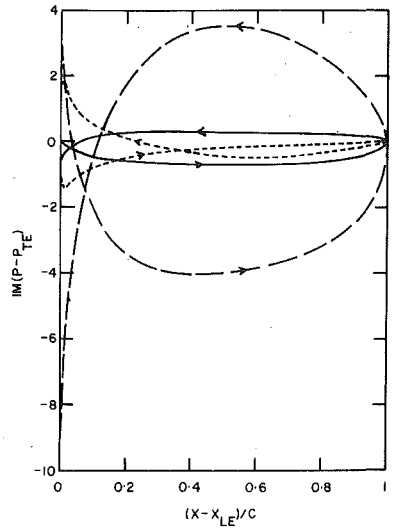


Fig. 5 Imaginary component of the unsteady pressure distribution for rotational oscillation. Cascade C_5; - - -, $k = 0.1$; —, $k = 0.5$; — —, $k = 3.0$

Downloaded 01 Jun 2010 to 171.66.16.58. Redistribution subject to ASME license or copyright; see http://www.asme.org/terms/Terms_Use.cfm

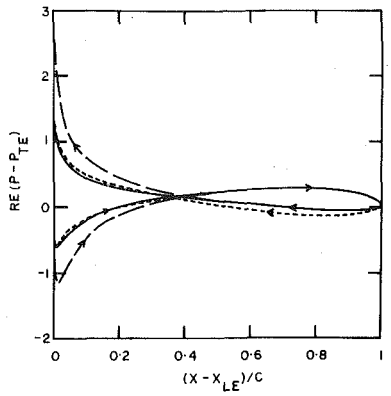


Fig. 6 Real component of the unsteady pressure distribution for cascades C_4, C_5 and C_6 in plunging oscillation at $k = 0.5$; - - -, C_4; —, C_5; — —, C_6

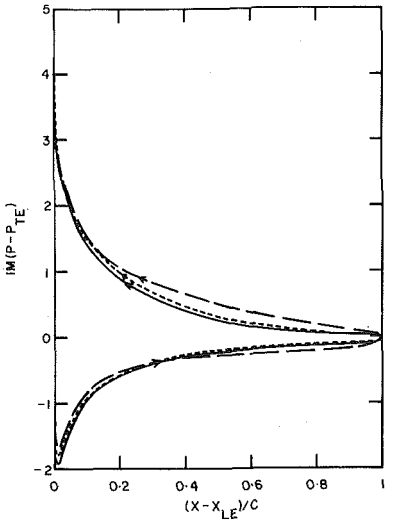


Fig. 7 Imaginary component of the unsteady pressure distribution for cascades C_4, C_5 and C_6 in plunging oscillation at $k = 0.5$; - - -, C_4; —, C_5; — —, C_6

Figs. 6 to 9 show plots of the unsteady pressure for cascades C_4, C_5, and C_6 at the same reduced frequency $k = 0.5$. It is remarkable to observe that for both plunging and rotational oscillations the imaginary component of the pressure is only slightly affected by the stagger of the cascade and the interblade phase angle of the oscillatory motion. The real component of the unsteady pressure for plunging oscillations shows more dependence on the interblade phase angle, while for rotational oscillations the stagger of the cascade produces larger effects.

Pressure Gradient at the Leading Edge. The unsteady pressure gradient at the leading edge plays an important role in the formation of the leading edge separation bubble. Since it is difficult to appreciate its magnitude and variation from the pressure plots in Figs. 2 to 9, we have calculated its values at the leading edge and plotted them versus the reduced frequency in Figs. 10 to 13 for cascades C_1 to C_6.

Fig. 10 shows the imaginary component (in-phase with the velocity) of the unsteady pressure gradient for a plunging oscillation. The linear dependence of $\mathrm{Im}\{dP/ds\}$, where s is the length of the arc along the airfoil, suggests a quasi-steady behavior of the pressure except at very low frequency where interference from the wake effects and other cascade blades produces a non-zero limit for $\mathrm{Im}\{dP/ds\}$ as $k \to 0$. In fact a simple quasi-steady analysis leads to

$$\frac{dP}{ds} \sim (\rho U_\infty \dot{h}) \frac{1}{R^{3/2}} \text{ where } \dot{h} = jkh, \text{ represents the plunging velocity}$$

and R the radius of curvature at the leading edge of the airfoil. This result correlates well with the pressure gradients shown in Fig. 10 for different airfoils. The quasi-steady behavior of this unsteady pressure component is due to the fact that where the flow has strong velocity

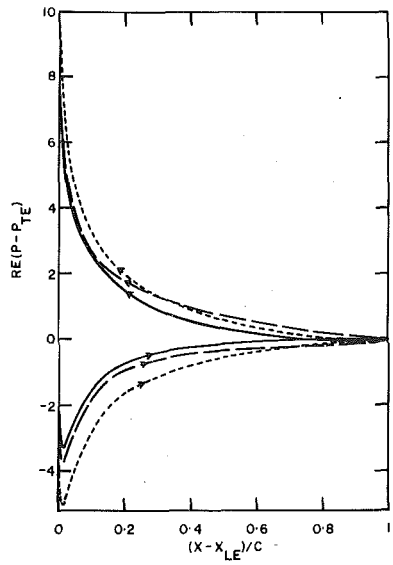


Fig. 8 Real component of the unsteady pressure distribution for cascades C_4, C_5 and C_6 in rotational oscillation at $k = 0.5$; - - -, C_4; —, C_5; — —, C_6

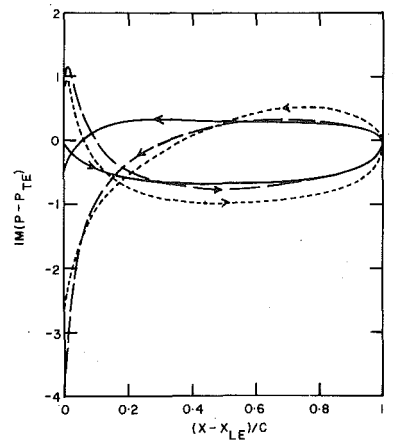


Fig. 9 Imaginary component of the unsteady pressure distribution for cascades C_4, C_5 and C_6 in rotational oscillation at $k = 0.5$; - - -, C_4; —, C_5; — —, C_6

gradients resulting from the local geometry, the unsteady flow is also essentially dominated by the local geometry.

The real component of the pressure gradient (in-phase with the displacement h) is shown in Fig. 11. One notes that its magnitude is, in general, smaller than that of the imaginary component. Also, one notes that this component depends strongly on the interblade phase angle σ, the stagger of the cascade, and the thickness of the airfoil. This suggests that contrary to the imaginary component which mainly depended on the local geometry, the value of the real component seems to be the result of interaction among the various parameters of the problem.

The analysis of the results of the unsteady pressure gradient at the leading edge for a rotational oscillation is more complicated. Figs. 12 and 13 show their plots versus the reduced frequency. Though at large k we have similar patterns for the imaginary component as for the plunging case, at low frequency the pressure gradient is very much influenced by the change of the effective angle of attack due to the rotation of the airfoil.

Unsteady Aerodynamic Forces and Moments

The unsteady aerodynamic force and moment are given in term of the pressure by

$$F = i \int_A P dz, \tag{28}$$

and

Downloaded 01 Jun 2010 to 171.66.16.58. Redistribution subject to ASME license or copyright; see http://www.asme.org/terms/Terms_Use.cfm

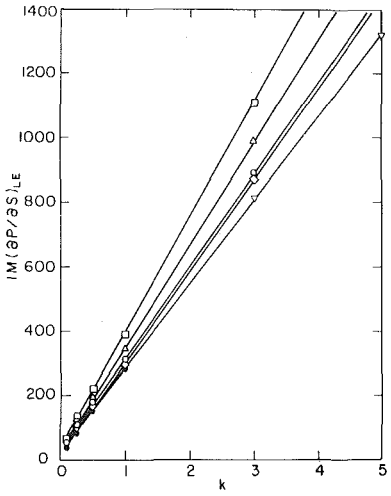


Fig. 10 Imaginary component of the unsteady pressure gradient at the leading edge for cascades C_1 to C_6 in plunging oscillation versus the reduced frequency. C_1, ○; C_2, △; C_3, □; C_4, ◇; C_5, ▽; C_6, ●. For C_1, the scale of the ordinate is reduced by a factor of 10.

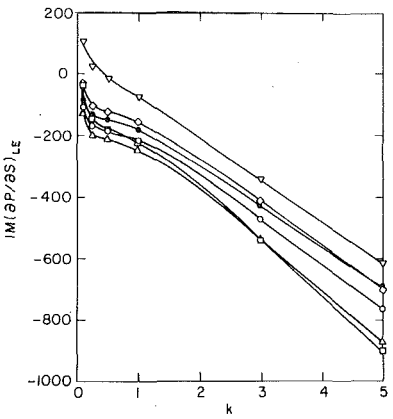


Fig. 12 Imaginary component of the unsteady pressure gradient at the leading edge for cascades C_1 to C_6 in rotational oscillation versus the reduced frequency. C_1, ○; C_2, △; C_3, □; C_4, ◇; C_5, ▽; C_6, ●. For C_1, the scale of the ordinate is reduced by a factor of 10.

$$M = \mathrm{Re} \int \bar{z} P dz. \tag{29}$$

Substituting the expression of P given by (26) into (28) and (29), we get

$$F = \mathcal{F}\{u_1 - iv_1\} = i\omega F_0 + i \int_A (z - z_{T.E.}) \,\mathrm{Re}\,\{\bar{q}_1 dz\} - i \int_A \mathrm{Re}\left\{q_0 \left(\bar{q}_1 + A \frac{d\bar{q}_0}{dz}\right)\right\} dz, \tag{30}$$

$$N = \mathcal{M}\{u_1 - iv_1\} = \frac{1}{2} \int_A (z\bar{z} - z_{T.E.}\bar{z}_{T.E.}) \,\mathrm{Re}\,\{\bar{q}_1 dz\} - \int_A \mathrm{Re}\left\{q_0 \left(\bar{q}_1 + A \frac{d\bar{q}_0}{dz}\right)\right\} \mathrm{Re}\,\{\bar{z} dz\}, \tag{31}$$

where $\mathcal{F}$ and $\mathcal{M}$ are linear operators yielding the aerodynamic force and moment, respectively, when applied on the unsteady velocity $(u - iv)_1$. They are defined by equations (30) and (31). $z_{T.E.}$ is the affix of the trailing edge. Following the same normalization as for the velocity, length, and time, the forces and moments are respectively normalized with respect to $\epsilon\rho U_\infty{}^2 h$ and $\frac{1}{2}\epsilon\rho U_\infty{}^2 hc$ for plunging oscillations and to $\frac{1}{2}\epsilon\rho U_\infty{}^2 c\omega$ and $\frac{1}{4}\epsilon\rho U_\infty{}^2 c^2\omega$ for rotational oscillations. F_0 is the mean flow lift.

Note that F is a hypercomplex number in the sense that it contains two pure imaginary numbers—i for space and j for the time phase. P and M are only complex and contain j to account for the shift in phase with respect to time. The lift and drag are calculated from F, and we have

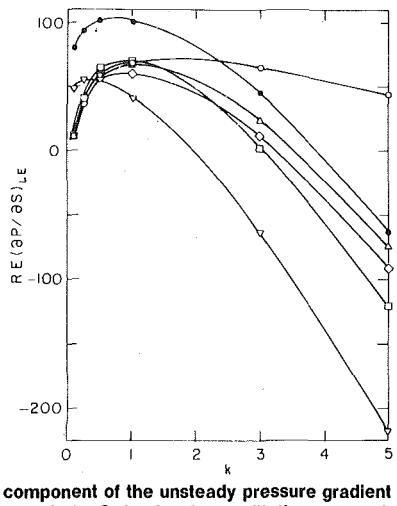


Fig. 11 Real component of the unsteady pressure gradient at the leading edge for cascades C_1 to C_6 in plunging oscillation versus the reduced frequency. C_1, ○; C_2, △; C_3, □; C_4, ◇; C_5, ▽; C_6, ●. For C_1, the scale of the ordinate is reduced by a factor of 10.

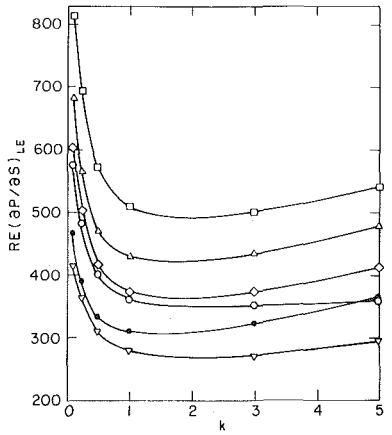


Fig. 13 Real component of the unsteady pressure gradient at the leading edge for cascades C_1 to C_6 in rotational oscillation versus the reduced frequency. C_1, ○; C_2, △; C_3, □; C_4, ◇; C_5, ▽; C_6, ●. For C_1, the scale of the ordinate is reduced by a factor of 10.

$$L = \mathcal{L}\{u_1 - iv_1\} = Im\,\{\mathrm{Fe}^{-i\alpha}\}, \tag{32}$$

$$D = \mathcal{D}\{u_1 - iv_1\} = \mathrm{Re}\,\{\mathrm{Fe}^{-i\alpha}\}, \tag{33}$$

where $\mathcal{L}$ and $\mathcal{D}$ are the linear operators yielding the lift and drag, respectively.

If we further split $u_1 - iv_1$ according to (11), we arrive at

$$L = L_I + L_W, \tag{34}$$

$$D = D_I + D_W, \tag{35}$$

$$M = M_I + M_W, \tag{36}$$

where

$$L_I = \mathcal{L}\{(u - iv)_I\}, \tag{37}$$

$$D_I = \mathcal{D}\{(u - iv)_I\}, \tag{38}$$

$$M_I = \mathcal{M}\{(u - iv)_I\}, \tag{39}$$

$$L_W = \Gamma^{(1)}_{Q.S.} L_W{}^* \tag{40}$$

$$D_W = \Gamma^{(1)}_{Q.S.} D_W{}^* \tag{41}$$

$$M_W = \Gamma^{(1)}_{Q.S.} M_W{}^* \tag{42}$$

with

$$L_W{}^* = \mathcal{L}\{(u - iv)_W\} \Big/ \left(\frac{j}{k} e^{jkt} - \int_A \mu_W d\tau\right), \tag{43}$$

Downloaded 01 Jun 2010 to 171.66.16.58. Redistribution subject to ASME license or copyright; see http://www.asme.org/terms/Terms_Use.cfm

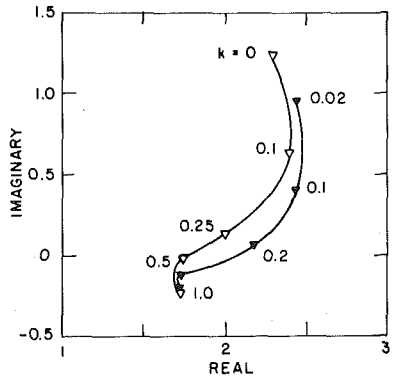


Fig. 14 Moment for C_5 in rotational oscillation compared to the results of [2]. The reduced frequency is varied from 0 to 1. Present study, ▽; [2], ▼.

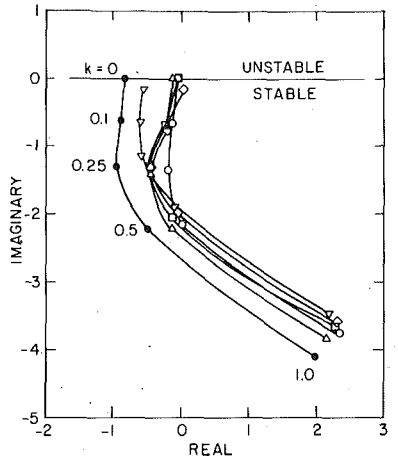


Fig. 15 Unsteady lift for cascades C_1 to C_6 in plunging oscillation. The reduced frequency is varied from 0 to 1. C_1, ○; C_2, △; C_3, □; C_4, ◇; C_5, ▽; C_6, ●.

$$D_W^* = \mathcal{D}\{(u - iv)_W\}/\left(\frac{j}{k}e^{jkt} - \int_A \mu_W d\tau\right), \tag{44}$$

$$M_W^* = \mathcal{M}\{(u - iv)_W\}/\left(\frac{j}{k}e^{jkt} - \int_A \mu_W d\tau\right), \tag{45}$$

The functions L_W^*, D_W^*, and M_W^* are independent of the particular oscillatory motion of the airfoils. They represent the lift, drag, and moment induced by the wake per unit quasi-steady circulation. Thus they are not affected by the particular type of boundary conditions applied at the airfoil surface. L_W^* and M_W^* were studied for typical cascade parameters in [2] and [3].

The total lift, L, drag, D, and moment M are however affected by the new boundary conditions through L_I, D_I, M_I, and $\Gamma_{0_S}^{(1)}$. In order to illustrate the effect of the last term of condition (5), namely, $\mathrm{Re}\{nAd\bar{q}_0/dz\}$, which we have neglected in the preliminary results presented in [2] and [3], we have compared in Fig. 14 the results for the aerodynamic moment for cascade C_5 in rotational oscillation about the origin calculated as in the present paper taking all terms of (5) into account and those obtained from our previous results in [2] neglecting this term. It is remarkable that the difference between the two results is quite significant. Of great interest is the fact that in the new results the negative aerodynamic damping, i.e., $\mathrm{Im}\{M\}$, is positive up to a reduced frequency of 0.5, while in the previous incomplete results the stability boundary was at $k \sim 0.25$. If we consider a natural frequency of 500 radians per second we see that for a typical compressor blade of chord length 15 cm flutter could occur for a flow Mach number larger than about 0.25. Flutter and instability boundaries will be discussed in more detail in the second part of this paper.

Figs. 15 to 18 show the unsteady lifts and moments for cascades C_1 to C_6, in plunging and torsional oscillations. Note that because of the term $(u - iv)_I$ [2] and defined by (17) the plunging lift, normalized here with respect to the airfoil displacement and not oscillating velocity,

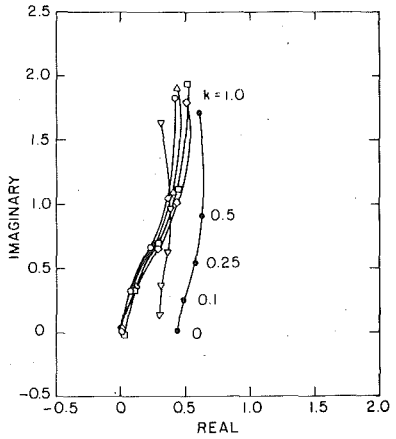


Fig. 16 Unsteady moment for cascades C_1 to C_6 in plunging oscillation. The reduced frequency is varied from 0 to 1. C_1, ○; C_2, △; C_3, □; C_4, ◇; C_5, ▽; C_6, ●.

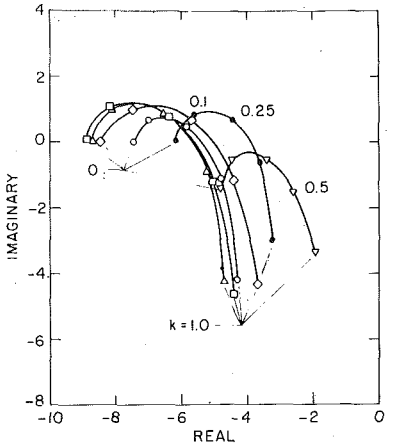


Fig. 17 Unsteady lift for cascades C_1 to C_6 in rotational oscillation. The reduced frequency is varied from 0 to 1. C_1, ○; C_2, ▽; C_3, □; C_4, ◇; C_5, ▽; C_6, ●.

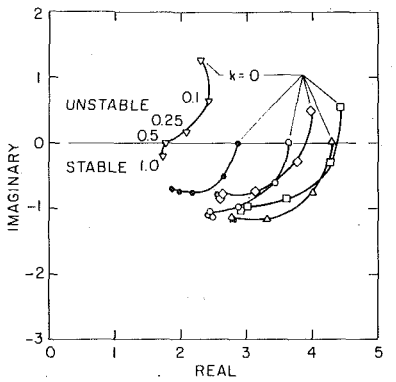


Fig. 18 Unsteady moment for cascades C_1 to C_6 in rotational oscillation. The reduced frequency is varied from 0 to 1. C_1, ○ 0; C_2, △; C_3, □; C_4, ◇; C_5, ▽; C_6, ●.

does not vanish as $k \to 0$. Its value at vanishing k depends strongly on the interblade phase angle σ as suggested by (17). In the case of a bending flutter, the imaginary component of the lift represents the negative aerodynamic damping. For the flow conditions of C_1 to C_6, Fig. 15 rules out any possibility of flutter since the aerodynamic damping is always positive. Fig. 18 contains plots of the rotational moments for C_1 to C_5. Note the destabilizing effect of camber at very low reduced frequency for unstaggered cascades. For staggered cascades the interblade phase angle has a very strong effect on the rotational lift and moment.

Downloaded 01 Jun 2010 to 171.66.16.58. Redistribution subject to ASME license or copyright; see http://www.asme.org/terms/Terms_Use.cfm

Conclusions

The theory presented in this paper gives a complete analysis of the unsteady aerodynamics of an infinite cascade of airfoils oscillating with interblade phase angle and subject to a uniform incompressible flow. The results obtained for the unsteady pressure distribution, lifts, and moments show strong interactions between the many parameters entering the problem, i.e., airfoil geometry, cascade stagger and solidity, angle of attack of the mean flow, and interblade phase angle of the oscillatory motion.

The present analysis has basically two important applications. First, the aerodynamic coefficients which we have derived and calculated are used in Part II of this paper to investigate stability and flutter boundaries for compressor and turbine cascades subject to strong loading. The introduction of the interblade phase angle of the oscillatory motion of the airfoils in our analysis allows us, using the results of Lane [11], to reduce the cascade system of blades to one single equivalent blade in the analysis of instability and flutter conditions. The results obtained and reported in Part II show very significant effects of blade geometry and mean flow incidence on the critical flutter speed.

The second important application of the present analysis lies in the utilization of the detailed pressure distribution obtained particularly near the leading edge area for analyzing the onset of the boundary layer separation which eventually could lead to the stalled flutter phenomenon.

References

1 Atassi, H., "A Complete First-Order Theory for the Unsteady Aerodynamics of Oscillating Airfoils in Cascade," University of Notre Dame, Aerodynamics Group, TR-772, 1977.

2 Atassi, H., and Akai, T. J., "Aerodynamic Force and Moment on Oscillating Airfoils in Cascade," ASME Paper No. 78-GT-181, April 1978.

3 Atassi, H., and Akai, T. J., "Effect of Blade Loading and Thickness on the Aerodynamics of Oscillating Cascades," AIAA Paper 78-227, Jan. 1978.

4 Whitehead, D. C., Discussion of [2], April 1978, London, England.

5 Muskhelishvili, N. I., *Singular Integral Equations*, P. Noordhoff, 1953.

6 Gakhov, F. D., *Boundary Value Problems*, Pergamon Press, 1966.

7 Theodorsen, Th., "General Theory of Aerodynamic Instability and the Mechanism of Flutter," NACA, TR-496, 1935.

8 von Kármán Th., and Sears, W. R., "Airfoil Theory for Non-Uniform Motion," *Journal of Aeronautical Sciences*, Vol. 5, No. 10, Aug. 1938, pp. 379–390.

9 Sears, W. R., "Same Aspects of Non-Stationary Airfoil Theory and its Practical Applications," *Journal of Aeronautical Sciences*, Vol. 8, No. 3, pp. 104–188, 1941.

10 Whitehead, D. S., "Force and Moment Coefficients for Vibrating Airfoils in Cascade," British A. R. C., RSM, No. 3254, Feb. 1960.

11 Lane, F., "System Mode Shapes in the Flutter of Compressor Blade Rows," *Journal of the Aeronautical Sciences*, Vol. 23, No. 1, Jan. 1956, pp. 54–66.

Downloaded 01 Jun 2010 to 171.66.16.58. Redistribution subject to ASME license or copyright; see http://www.asme.org/terms/Terms_Use.cfm

T. J. Akai
Assistant Professor

H. Atassi
Professor

Department of Aerospace and Mechanical Engineering
University of Notre Dame
Notre Dame, Ind. 46556

Aerodynamic and Aeroelastic Characteristics of Oscillating Loaded Cascades at Low Mach Number

Part II: Stability and Flutter Boundaries[1]

The aerodynamic coefficients obtained from the analysis developed in Part I of this paper are utilized here to investigate stability and flutter boundaries for loaded cascades of airfoils with finite thickness. Combined bending and torsional oscillations for different stiffness ratios are studied for compressor and turbine cascades. The results show very significant effects of blade geometry and mean flow incidence on the stability and flutter boundaries. These effects are basically the consequence of strong coupling between the steady and unsteady aerodynamics of the cascade.

Introduction

The present trend in axial flow turbomachine design is to increase the blade loading. In this part of the paper the aeroelastic stability of highly loaded blades in coupled bending-torsional vibrations is analyzed using the aerodynamic theory developed in Part I [1]. This is the case often referred to as classical flutter [2, 3].

In our analysis the blade row is approximated by a linear cascade of blades of infinite span. Lane [4] has shown that such a blade system can be replaced with no loss of generality by a single equivalent blade when this blade is under a special form of influence from all other blades. This condition is that all other blades oscillate with the same blade mode and with a constant interblade phase angle. It is exactly this type of aerodynamic force that has been derived in Part I of this paper.

In what follows we first formulate the bending-torsion flutter problem for the single "equivalent" blade. We also define the parameters of the cascades studied.

The corresponding aerodynamic coefficients are then presented and discussed for the plunging and rotational motions. Finally, we present stability and flutter boundaries for compressor and turbine cascades and compare these results with those of Whitehead [5] for flat plate cascades and Dieckelman [6] for a single airfoil.

Bending-Torsional Flutter

We consider here the two-dimensional model of a blade undergoing small bending and torsional vibrations with frequency ν. Bending is simulated by oscillations of amplitude ϵH perpendicular to the chord line and torsion by rotational oscillations of angular amplitude $\epsilon\omega$ about some axis Z_A with $\epsilon \ll 1$. A schematic of the problem showing the sense in which the lift L and moment M are taken is given by Fig. 1. The static mass unbalance D is also shown in this figure. The instantaneous position of a point on the blade is therefore found from

$$Z = Z_0 + \epsilon\{iH + i\omega(Z_0 - Z_A)\}e^{j\nu t},$$

in which Z_0 is the mean position of the point, and i is the unit imaginary number associated with space. We assume that a simple harmonic process has been going on indefinitely and remove the factor $\exp(j\nu t)$ from all unsteady quantities. Nondimensionalization with respect to the fluid density ρ, the semichord B, and the inlet free-stream velocity U_∞ is carried out. In particular, we define

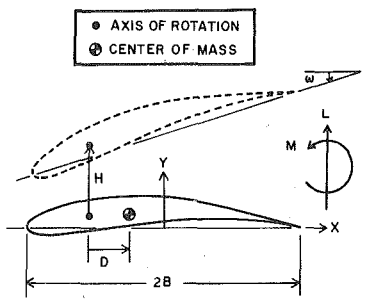


Fig. 1 Schematic of the problem

[1] Research supported by a grant from the Air Force Office of Scientific Research, No. AFOSR-F49620-79-C-0014.

Contributed by the Gas Turbine Division and presented at the Gas Turbine Conference and Exhibit and Solar Energy Conference, San Diego, California, March 12–15, 1979 of THE AMERICAN SOCIETY OF MECHANICAL ENGINEERS. Manuscript received at ASME Headquarters December 18, 1978. Paper No. 79-GT-112.

Copyright © 1980 by ASME

Downloaded 01 Jun 2010 to 171.66.16.58. Redistribution subject to ASME license or copyright; see http://www.asme.org/terms/Terms_Use.cfm

$$[h,d] = [H,D]/B, \tag{1}$$

$$[k_H, k_\omega, k] = [\nu_H, \nu_\omega, \nu]\, B/U_\infty, \tag{2}$$

$$L = \epsilon\rho U_\infty{}^2 B\{hC_{L_H} + \omega C_{L_\omega}\}, \tag{3}$$

and

$$M = \epsilon\rho U_\infty{}^2 B^2\{hC_{M_H} + \omega C_{M_\omega}\}. \tag{4}$$

The subscripts H and ω denote bending and torsion, respectively, ν_H and ν_ω are the bending and torsional natural frequencies, and C_L and C_M are the lift and moment coefficients. In addition,

$$\text{Mass of Blade} = \rho B^2 m,$$

$$\text{Moment of Inertia} = \rho B^4 m r_A{}^2,$$

and

$$K = k_H/k_\omega \tag{5}$$

Moments and the polar moment of inertia are measured about the axis of rotation.

The derivation of the equations of motion for the system described is well known (see, for example, [7]). They are expressed in nondimensional form by

$$\begin{bmatrix} \{C_{L_H} + m(k^2 - K^2k_\omega{}^2)\} & \{C_{L_\omega} + mdk^2\} \\ \{C_{M_H} + mdk^2\} & \{C_{M_\omega} + mr_A{}^2(k^2 - k_\omega{}^2)\} \end{bmatrix} \begin{Bmatrix} h \\ \omega \end{Bmatrix} = 0 \tag{6}$$

or in the more concise form by

$$[A]\,[h\ \omega]^T = 0. \tag{7}$$

The conditions for flutter are obtained from the relation

$$|A| = 0. \tag{8}$$

Since the elements of $[A]$ are complex in time, this relation yields two real equations. For pure bending, these simplify to

$$\text{Im}\{C_{L_H}\} = 0 \tag{9}$$

and

$$k_H{}^2 = k^2 + \text{Re}\{C_{L_H}\}/m, \tag{10}$$

and in pure torsion,

$$Im\{C_{M_\omega}\} = 0 \tag{11}$$

and

$$k_\omega{}^2 = k^2 + \text{Re}\{C_{M_\omega}\}/(mr_A{}^2). \tag{12}$$

For this study, the blade is assumed to be solid and homogeneous, and the axis of rotation is constrained to lie on the camber line. The origin of the coordinate system is at midchord. We choose as independent variables m, k, and K, and use equation (8) to solve for x_A and k_ω in the general case. Note that

$$d = d(x_A) = x_C - x_A \tag{13}$$

and

$$r_A{}^2 = r_A{}^2(x_A) = r_C{}^2 + (x_C - x_A)^2 + (y_C - y_A(x_A))^2 \tag{14}$$

where the subscript C denotes the center of mass, $y_A(x_A)$ describes the camber line, and r_C is the radius of gyration about the center of mass.

This investigation focuses on two cascades: a compressor configuration with stagger angle of 37.5 deg oscillating with a constant interblade phase angle of 54 deg and a turbine configuration with stagger angle of −37.5 deg and interblade phase angle of 306 deg. The phase angles were chosen on the basis of earlier studies [5, 8, 9] which indicate the occurrence of maximum torsional instability near these values. The blade geometry for the two cascades is identical and is obtained from the unit circle denoted by $\zeta = \exp(i\theta)$ in the complex plane by the Joukowski transformation

$$z = \left[\zeta + \zeta_0 + \frac{c'^2}{\zeta + \zeta_0}\right]\Big/ B, \tag{15}$$

where $\zeta_0 = -b + im$. The numerical values of the parameters are given in Table 1. The leading and trailing edges correspond to $\theta = 187.90978$ deg and $\theta = -7.90978$ deg, respectively. The airfoil profile and center of mass location are as shown in Fig. 1. The geometry of the two cascades is shown in Fig. 2. The angle of attack (to the chord line) is 16 deg in both cases. For comparison, an isolated airfoil of the same geometry and angle of attack as in the cascades, and a flat plate cascade at zero angle of attack with 37.5 deg stagger and 54 deg interblade phase angle are also considered. Note that for an unloaded flat plate cascade the unsteady lifts and moments are the same for opposite stagger angle (here −37.5 deg) and complementary interblade phase angle with respect to 2π (here 306 deg). These four cases are summarized in Table 1.

Aerodynamic Coefficients

The unsteady forces and moments (taken about the midchord) for plunging and sliding oscillations as well as rotational oscillations about an axis at the midchord are calculated according to the theory presented in Part I [1] of this paper for reduced frequencies ranging from 0 to 5. If the subscripts P, R, and S are used to denote coefficients for plunging, rotation, and sliding, the coefficients appearing in the matrix $[A]$ can be obtained from

$$C_{L_H} = C_{L_P}, \tag{16}$$

$$C_{L_\omega} = C_{L_R} - x_A C_{L_P} + y_A C_{L_S}, \tag{17}$$

Nomenclature

b = Joukowski thickness parameter
B = airfoil semichord
$d = D/B$
D = static mass unbalance, $X_C - X_A$
$h = H/B$
H = amplitude of plunging oscillation
i = unit imaginary number associated with space
j = unit imaginary number associated with time
k = reduced frequency, $\nu B/U_\infty$
$K = k_H/k_\omega$
L = unsteady lift (in y-direction)
m = blade mass/ρB^2; also, Joukowski camber parameter
M = unsteady moment (counterclockwise)
r = radius of gyration
t = time
$x = X/B$
X = Cartesian coordinate in direction of chord
$y = Y/B$
Y = Cartesian coordinate perpendicular to chord
$z = x + iy$
$Z = X + iY$
ϵ = small parameter for linearization
$\zeta = \exp(i\theta)$
θ = polar coordinate locating a point on a circle centered at the origin
ρ = fluid density
ν = frequency of oscillation
ω = angular amplitude of rotational oscillation
c' = Joukowsky parameter, $\sqrt{1-m^2} - b$
C_D = unsteady drag coefficient (in x-direction)
C_L = unsteady lift coefficient (in y-direction)
C_M = unsteady moment coefficient (counterclockwise)
$k_H = \nu_H B/U_\infty$
$k_\omega = \nu_\omega B/U_\infty$
U_∞ = magnitude of freestream velocity
$\zeta_0 = -b + im$
ν_H = natural frequency in bending
ν_ω = natural frequency in torsion
$[A]$ = coefficient matrix defined in equation (6)

Subscripts

A = axis of rotation
C = center of mass
H = bending
0 = mean position of airfoil
P = plunging oscillation
R = rotational oscillation about midchord
S = sliding oscillation
ω = torsion about axis at Z_A

Downloaded 01 Jun 2010 to 171.66.16.58. Redistribution subject to ASME license or copyright; see http://www.asme.org/terms/Terms_Use.cfm

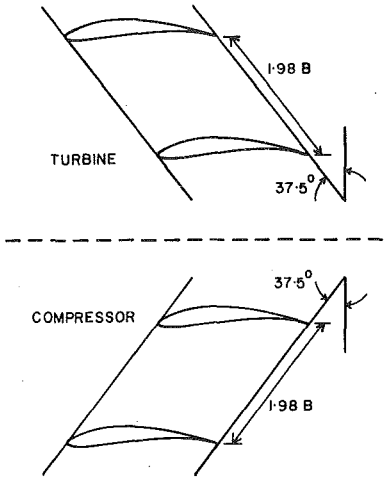


Fig. 2 Geometry of the cascades

Table 1 Comparison of parameters for the cases studied

	Compressor	Turbine	Single Airfoil	Flat Plate Cascade
Thickness (percent chord)	11.25	11.25	11.25	0
Camber (percent chord)	6.95	6.95	6.95	0
Camber Angle (deg)	31.64	31.64	31.64	0
Angle of Attack (deg)	16.0	16.0	16.0	0
Solidity	1.01	1.01	0	1
Stagger (deg)	37.5	−37.5	−	±37.5
Interblade Phase Angle (deg)	54	306	−	180 ∓ 126
x_C	−.2479	−.2479	−.2479	0
y_C	.1045	.1045	.1045	0
$r_C{}^2$	.1938	.1938	.1938	.3333
m	2000	2000	2000	2
Steady Load	0.76	1.48	2.79	0
Flow Deflection (deg)	23.76	25.92	0	0
Discharge Velocity	0.68	1.38	1.0	1.0
Joukowski Parameters				
b	0.08473	0.08473	0.08473	0
m	0.13761	0.13761	0.13761	0
c'	0.82039	0.82039	0.82039	1
B	1.82487	1.82487	1.82487	2

$$C_{M_H} = C_{M_P} - x_A C_{L_P} + y_A C_{D_S}, \tag{18}$$

$$C_{M_\omega} = C_{M_R} - x_A(C_{M_P} + C_{L_\omega}) + y_A\,(C_{M_s} + C_{D_R} - x_A C_{D_P} + y_A C_{D_S}). \tag{19}$$

The coefficients for the single airfoil are obtained from Dieckelman [6] for the same frequency range, and those for the flat plate cascade from Whitehead [5] up to a reduced frequency of 1. The dominant coefficients C_{L_P}, C_{L_R}, C_{M_P}, and C_{M_R} are plotted in Figs. 3–6.

The aerodynamic coefficients to be used in the flutter calculation (equation (6)) are defined by equations (16–19). They are in fact combinations of the various aerodynamic coefficients plotted in Figs. 3–6. Thus even if C_{L_P}, C_{L_R}, C_{M_P} and C_{M_R} do not suggest at a given frequency the occurrence of instability, their coupling could produce instability conditions. Nevertheless it is quite interesting to see their dependence on the reduced frequency.

Figs. 3 and 4 show plots of the plunging lift and moment versus the reduced frequency for the four cases. It is remarkable to observe the significant difference between the compressor and turbine cascades. Recalling that no difference exists for flat plate cascades at zero-incidence, this significant effect is essentially due to the geometry and steady loading of the airfoil blades.

Figs. 5 and 6 show similar plots for rotational oscillations about the midchord. Again we observe the significant difference between the compressor and turbine cascades. In Part I, we have studied the same compressor cascade but at interblade phase angles of 90 deg and 180 deg. Our choice of $\sigma = 54$ deg in the present case was taken because

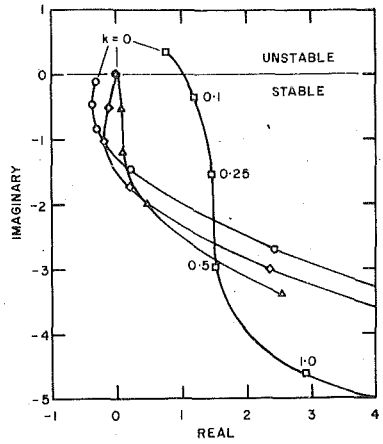


Fig. 3 Unsteady lifts for a plunging motion. The reduced frequency is varied from 0 to 1. compressor, ○; turbine, □; single airfoil, ◇; flat plate cascade, △

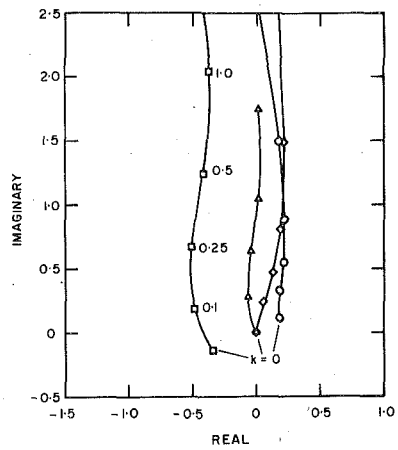


Fig. 4 Unsteady moments for a plunging motion. The reduced frequency is varied from 0 to 1. compressor, ○; turbine, □; single airfoil, ◇; flat plate cascade, △

it corresponds to the maximum of the negative aerodynamic damping in pure torsion given in [8]. Fig. 6 indeed shows that torsional instability occurs for larger reduced frequencies up to 0.77 as compared to a maximum value of about 0.5 at $\sigma = 90$ deg. In contrast with the plunging oscillation where the turbine exhibited more instability than the compressor, in rotational oscillation the turbine instability extends only to $k = 0.19$.

The previous results are all given at midchord location. They cannot be construed as general trends for other axis location. The interaction of the aerodynamic coefficients for other axis location could yield quite different flutter and stability characteristics as will be shown in the following section.

Instability in Pure Bending and Pure Torsion

Flutter and instability boundaries in pure bending are governed by equations (9) and (10). Fig. 3 shows that of the four cases studied only the turbine configuration has a frequency range of instability. This instability, however, occurs below a reduced frequency of 0.051. The inverse flutter speed k_H at which flutter can occur is also approximately 0.051 since the term $\mathrm{Re}\{C_{L_H}\}/m$ in equation (10) is negligible due to the large value of the mass parameter m. Lower values of m would result in flutter at higher values of k_H since $\mathrm{Re}\{C_{L_H}\}$ is positive in the case of the turbine.

As pointed out in Part I [1] of this paper, the unsteady coefficients for plunging oscillations at such low frequencies are dominated by the steady velocity gradient and the effects of interblade phase difference.

Bellenot and D'Epinay [10] and Whitehead [11] pointed out the requirement of strong steady flow deflection for bending flutter to occur. This is confirmed by our present results. However, we should emphasize that steady flow deflection *per se* cannot be considered as

Downloaded 01 Jun 2010 to 171.66.16.58. Redistribution subject to ASME license or copyright; see http://www.asme.org/terms/Terms_Use.cfm

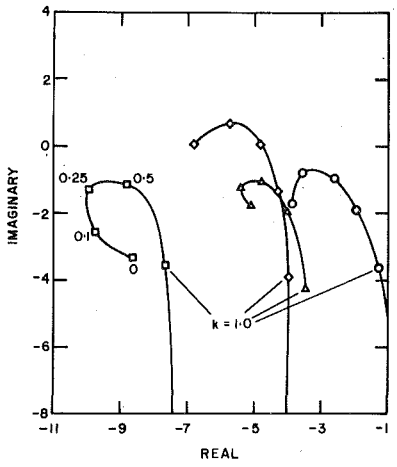


Fig. 5 Unsteady lifts for a rotational motion. The reduced frequency is varied from 0 to 1. compressor, O; turbine, □; single airfoil, ◇; flat plate cascade, △

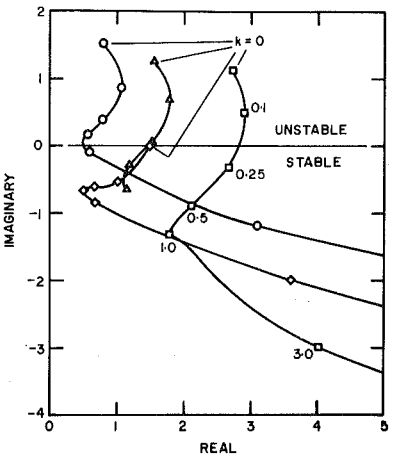


Fig. 6 Unsteady moments for a rotational motion. The reduced frequency is varied from 0 to 3. compressor, O; turbine, □; single airfoil, ◇; flat plate cascade, △

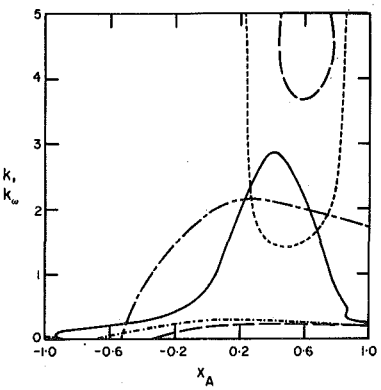


Fig. 7 Flutter and instability boundaries in pure torsion. compressor,—; turbine,——; single airfoil, ---; flat plate cascade; k,·····; k_ω, ——

a primary parameter in producing bending flutter. Evidence of this is shown in Table 1 where the steady flow deflections for the compressor and turbine are seen to be nearly the same.

Flutter and instability boundaries in pure torsion are obtained by applying equations (11) and (12) and are summarized in Fig. 7. For all cases except the flat plate cascade, k_ω is very nearly equal to k as a result of the large value of m. In order to illustrate the effect of m on the values of k_ω we have considered a flat plate cascade for which we have assigned a relatively small value for m. The term $\mathrm{Re}\{C_{M_\omega}\}/(mr_A{}^2)$ in equation (12) becomes then significant and results in k_ω values that are much larger than k. Naturally such a small value for m is not realistic.

The boundaries in Fig. 7 are shown as a function of the location of

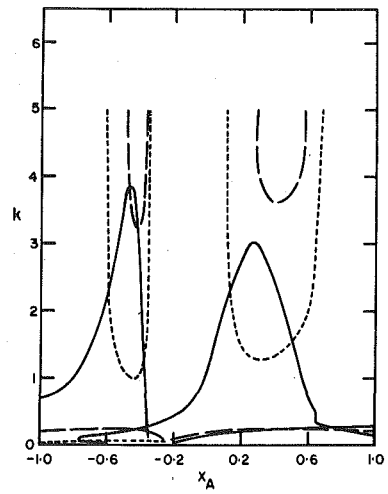


Fig. 8 Instability boundary for $K = 2$. compressor, —; turbine ——; single airfoil, ---

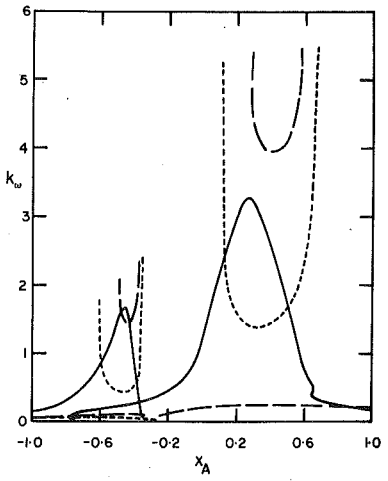


Fig. 9 Flutter boundary for $K = 2$. compressor, —; turbine, ——; single airfoil, ---

the axis of motion. The isolated airfoil is unstable at very low frequencies for axis locations on the forward part of the airfoil and also exhibits instability at higher frequencies for a range of axis locations near the three quarter chord point. The region of instability for the cascades extends rearward from points located on the forward part of the airfoil. The stability boundary for the compressor has a maximum at about 70 percent of the chord from the leading edge while the turbine has a pocket of instability at even higher frequencies. Typically, the real part of C_{M_ω} is negative for the far forward axis locations up to about the quarter chord point and positive for other axis locations. Therefore, examination of equation (12) shows clearly that if instability occurs at forward axis locations, a lower mass parameter tends to reduce k_ω and thus produces higher flutter speed. If, however, instability occurs aft of the point at which $\mathrm{Re}\{C_{M_\omega}\}$ becomes positive, a lower mass parameter results instead in lowering flutter speeds and enhances the possibility of flutter.

Results for Combined Bending and Torsion

Flutter and stability boundaries for combined bending and torsional oscillations at the same reduced frequency k are obtained from equation (8) for the compressor, turbine, and single airfoil. The results are for stiffness ratios K (equal to k_H/k_ω) of 2, 1, and 0.5.

The stability and flutter bounds for $K = 2$ are shown in Figs. 8 and 9. The plots of k versus x_A in Fig. 8 shows regions of instability at rearward axis locations very much like that for pure torsion. The maximum value for k in the instability region occurs at axis locations slightly forward of those in the pure torsion case and k_ω/k is generally slightly greater than unity. For $K = 2$, however, another major region of instability occurs at forward axis locations in the region of the

Downloaded 01 Jun 2010 to 171.66.16.58. Redistribution subject to ASME license or copyright; see http://www.asme.org/terms/Terms_Use.cfm

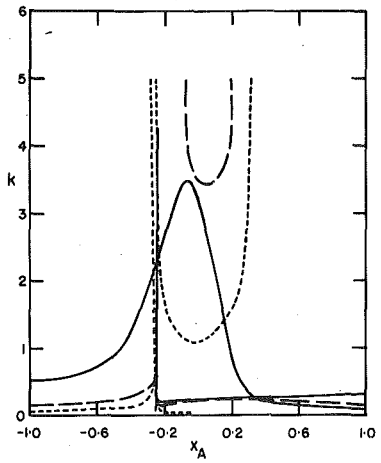


Fig. 10 Instability boundary for $K = 1$. compressor, —; turbine, ——; single airfoil, ---

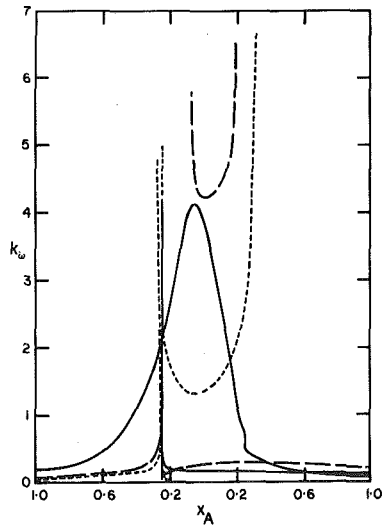


Fig. 11 Flutter boundary for $K = 1$. compressor, —; turbine, ——; single airfoil, ---

quarter-chord point. At these locations k_ω is greatly reduced but is still significant. At the higher frequencies, the bending and torsional modes have a difference of phase of nearly 180 deg with each other, torsion lagging behind bending.

Figs. 10 and 11 show k and k_ω versus x_A for $K = 1$. The rearward region of instability and flutter which we have found for $K = 2$ exists also here but is now shifted forward to the neighborhood of the mid-chord and the forward region shifts to a narrow range of axis positions near the center of mass. The latter behavior is similar to that for $m = \infty$ which gives a solution of $k = k_H = k_\omega$ when $x_A = x_C$.

At $K = 0.5$, k and k_ω are confined to much lower values as shown in Figs. 12 and 13 (note the change of scale). K values of this order represent the typical stiffness ratios for the first bending and torsional modes.

Although instability is absent in pure bending except for the turbine at very low frequencies, the coupling of bending and torsion results in flutter speeds that are lower than those in the case of pure torsion at certain stiffness ratios. In particular, higher bending modes than the first coupled with the first torsion mode can result in flutter at low speeds at typical torsion axis locations. As pure torsion is approached, the region of instability is confined mainly to rearward axis locations that might be the case in torsion modes higher than the first. Although

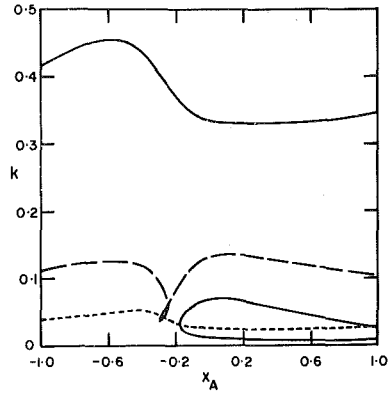


Fig. 12 Instability boundary for $K = 0.5$. compressor, —; turbine, ——; single airfoil, ---

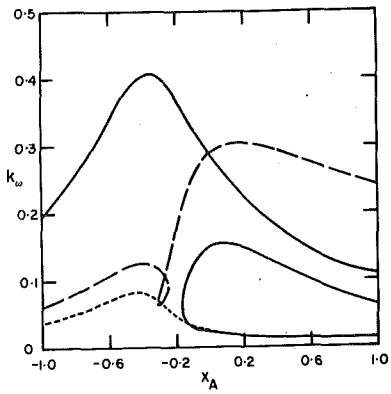


Fig. 13 Flutter boundary for $K = 0.5$. compressor, —; turbine, ——; single airfoil, ---

this analysis does not treat torsion modes other than the first, the results suggest the investigation of flutter be extended to include these higher modes.

References

1 Atassi, H., and Akai, T. J., "Aerodynamic and Aeroelastic Characteristics of Oscillating Loaded Cascades at Low Mach Number. Part I. Pressure Distribution, Forces, and Moments," ASME JOURNAL OF ENGINEERING FOR POWER, Vol. 102, No. 2, pp. 344–351.

2 Theodorsen, Th., and Garrick, J. E., "Mechanism of Flutter, a Theoretical and Experimental Investigation of the Flutter Problem" NACA Rept. 685, 1940.

3 Schnittger, J. R., "Flutter Problems in Gas Turbine," in *Design and Performance of Gas Turbine Power Plants, High Speed Aerodynamics and Jet Propulsion*, Vol. XI, Ed. Hawthorne, W. R., and Olson, W. T., 1960.

4 Lane, F., "System Mode Shapes in the Flutter of Compressor Blade Rows," *Journal of the Aeronautical Sciences*, Vol. 23, No. 1, Jan. 1956, pp. 64–66.

5 Whitehead, D. S., "Force and Moment Coefficients for Vibrating Airfoils in Cascades," British A.R.C., R & M. No. 3254, Feb. 1960.

6 Dieckelman, R. J., "Flutter Analysis of a Single Degree of Freedom Airfoil System Undergoing a Pitching Oscillation," University of Notre Dame, M.S. Thesis, 1978.

7 Bisplinghoff, R. L., Ashley, H., and Halfman, R. L., *Aeroelasticity*, Addison-Wesley, 1955.

8 Atassi, H., and Akai, T. J., "Aerodynamic Force and Moment on Oscillating Airfoils in Cascade," ASME Paper No. 78-GT-181, April 1978.

9 Hanamura, Y., "Flutter of Cascading Blade Row," Institute of Space and Aeronautical Science, University of Tokyo, Report No. 459, Vol. 36, No. 1, 1971, pp. 1–36.

10 Bellenot, C. and D'Epinay, J. L., "Self Induced Vibrations of Turbomachine Blades," *Brown Boveri Review*, Vol. 37, 1950, p. 368.

11 Whitehead, D. S., "Bending Flutter of Unstalled Cascade Blades at Finite Deflection," British A.R.C., R&M No. 3386, Oct. 1962.

Downloaded 01 Jun 2010 to 171.66.16.58. Redistribution subject to ASME license or copyright; see http://www.asme.org/terms/Terms_Use.cfm

H. A. Nied
General Electric Company
Gas Turbine Division
Schenectady, New York
Mem. ASME

Modal Analysis of Gas Turbine Buckets Using a Digital Test System

A modal analysis was conducted on gas turbine buckets using a digital Fourier analyzer. This digital test/computer system measures a set of frequency response functions for broadband impulse excitation at successive locations on the bucket airfoil. From the set of frequency response functions, the analyzer computes the modal parameters used to determine the natural frequencies, critical damping ratio and mode shapes of the turbine buckets. An animated display of the mode shapes for a discrete experimental model graphically revealed compound modes due to coupling. The test has shown that the digital modal analysis using the impulse excitation technique is a rapid and precise experimental method to determine the modal parameters of turbine buckets with a high degree of repeatability.

Introduction

It is important to determine the natural frequency and mode shapes of gas turbine buckets during the design of a turbine to assure that the bucket will not be subjected to a resonant condition. The chief source of excitation is due to nozzle and combustor passing frequencies. Proper design of the bucket will avoid a resonance vibration condition which can lead to HCF crack initiation and propagation in the bucket.

The natural frequencies and mode shapes of turbine buckets have been obtained by many experimentalist using various techniques. Carnegie [1] conducted vibration tests on blading to determine the natural frequencies and nodal patterns from 20 to 5000 Hz using an electromagnetic excitation method. The blade was vibrated over the specified frequency range and when a normal mode was excited, sand was sprinkled along the blade length which collected at the nodal lines. Plunkett [2] conducted vibration tests on flat and tapered rectangular plates representative of turbine blading. These plates clamped on a mounting block were excited using an electromagnet near the free end which was driven by an audio oscillator. The vibratory response was obtained using a crystal pickup which was connected to an oscilloscope. The resonant frequencies were found by tuning the oscillator and observing the Lissajous figure formed on an oscilloscope by the transducer and oscillator signals. Resonances were defined as the frequencies where the measured response amplitude reached a relative maximum and the phase angle varied rapidly. The mode shapes were also found by sprinkling dry sand on the vibrating plate which collected at the nodal lines. The extension of this test method, commonly called *vibration bench test*, has been used for numerous years in the turbine industry. The technique is different from the previously described methods in that Chladni sand patterns are not used to obtain node line profiles. With this method strain gaged buckets are excited using an electromagnet and power amplifier. Usually a frequency domain of 0–5000 Hz is manually swept through the spectrum using the audio oscillator. The resonant frequencies are determined from the strain gage peak responses. When the strain survey is completed, the gages are removed and a modal analysis is conducted. The nodal patterns are determined by manually scanning the surface of a bucket with a crystal pickup for the previously determined natural frequencies. When the filtered signal from the pickup is connected to the vertical input of the oscilloscope and the signal from the oscillator is fed to the horizontal input, a U-shaped Lissajous signal is observed on the scope. The amplitude of the signal will decrease as the crystal pickup is moved closer to a node line. When the signal is on a node line, the signal on the scope will be a horizontal line. As the pickup is moved beyond the node line, the signal amplitude will increase with a 180 deg phase shift. By this means, the experimenter can map out the node lines for the natural frequencies of interest. It is apparent that these methods are tedious and highly dependent on the skill of the experimenter.

Currently more sophisticated methods are available which can be used to determine turbine bucket natural frequencies and mode shapes. The holographic technique using the time averaging method can be used to photographically determine the mode shape of bucket vibrations. The state-of-the-art for the holographic method is vividly described in [3]. Another advanced method was used by Jones and Muszyńska [4] to obtain modal parameters of a compressor blade. In this test a harmonic excitation was applied at the tip in the fundamental mode of vibration. This harmonic force was applied by means of a magnetic transducer and the response was measured by successively locating a miniature accelerometer at various points on the blade. The data then provided the transfer impedance as a function of frequency at each location on the airfoil. From these transfer functions the mode shapes could be constructed.

In this paper a modal analysis was conducted on gas turbine buckets using a digital Fourier analyzer which directly measures the frequency response functions when the bucket is subjected to an impulse excitation at successive locations on the bucket airfoil. This experimental method described in references [5, 6, 7] has been successfully applied

Contributed by the Gas Turbine Division and presented at the Gas Turbine Conference and Exhibit and Solar Energy Conference, San Diego, California, March 12–15, 1979 of THE AMERICAN SOCIETY OF MECHANICAL ENGINEERS. Manuscript received at ASME Headquarters December 12, 1978. Paper No. 79-GT-124.

Copyright © 1980 by ASME
Downloaded 01 Jun 2010 to 171.66.16.58. Redistribution subject to ASME license or copyright; see http://www.asme.org/terms/Terms_Use.cfm

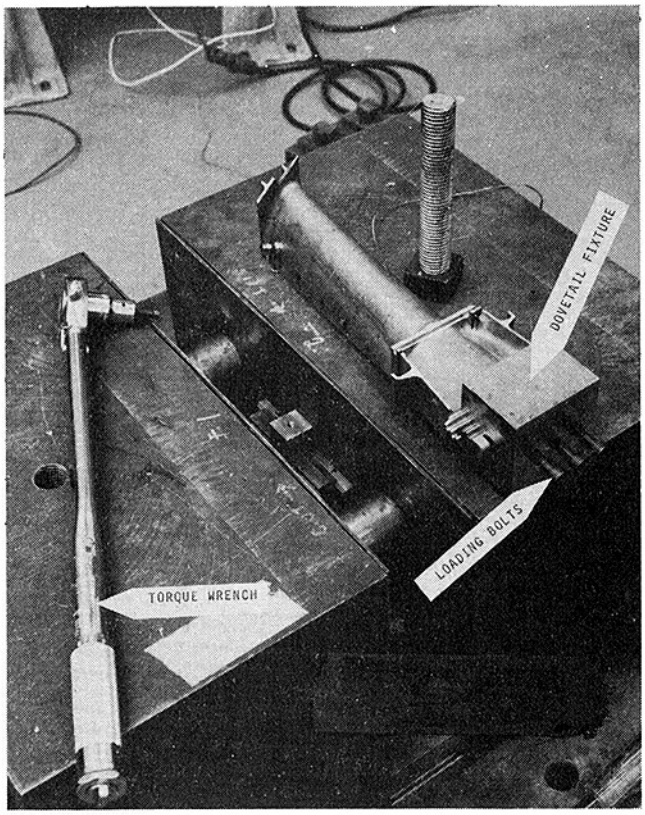


Fig. 1 MS-6001 stage 2 bucket showing accelerometer and dove tail fixture

for determining the vibratory response of structures in the aircraft and automotive industries.

An analytical and experimental program was initiated to determine the natural frequencies and mode shapes of the MS-6001 Stage 2 turbine bucket. A 3-D ANSYS finite element model was constructed to conduct both vibration and stress analysis. As a part of this overall program, an experimental analysis was conducted to determine the natural frequencies and mode shapes, using the Hewlett-Packard Fourier and Modal Analyzer, which is located in the Gas Turbine Development Laboratory. This equipment is a test measurement and post processing digital system that can be used to determine the modal parameters by measuring the transfer functions of a mechanical system. The major modal parameters of a structure such as the natural frequencies, damping ratio, damping coefficient and mode shapes can be readily obtained with a high degree of precision.

It was the purpose of this test to compare the vibration characteristics of the MS-6001 and MS-7001 Stage 2 buckets. This test method was found to be particularly suited to determine the natural frequencies of these two gas turbine buckets and to compare their mode shapes. The MS-7001 Stage 2 bucket would serve as a "bench mark" since considerable test and field experience has been compiled for this component. Both turbine buckets had been previously vibration bench tested to determine the natural frequencies and mode shapes using the manual crystal pickup mapping method. The test results obtained by using these two methods were compared and it was shown that the digital modal analysis method is more rapid and precise.

Test Configuration

A modal analysis was conducted on both an MS-6001 and MS-7001 Stage 2 bucket in succession. These buckets were considered to be representative of production quality components. The buckets were fully machined and had no known defects. Each bucket was instrumented with a PCB 304A piezoelectric accelerometer which had a sensitivity of 3.6 mv/g measured at 100 Hz under 8 g-s zero-to-peak excitation. The accelerometer axis was located near the trailing edge

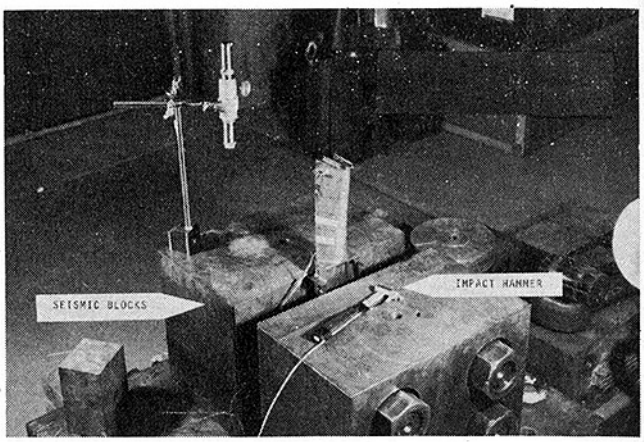


Fig. 2 MS-6001 stage 2 bucket showing seismic mount

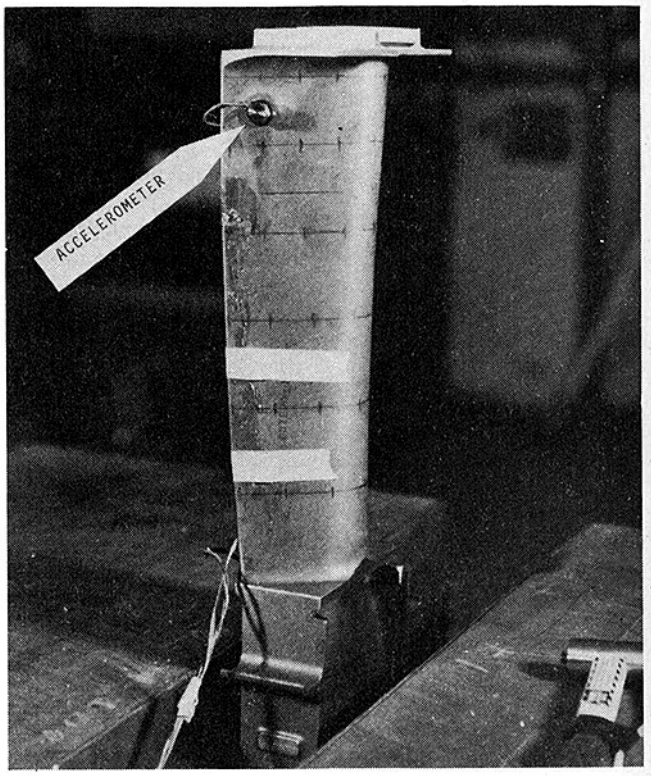


Fig. 3 MS-6001 stage 2 bucket modal analysis test configuration showing strike points

below the tip shroud as shown in Figs. 1–3.

Each bucket was mounted into a mating dovetail fixture (see Fig. 1). Three load bolts in the bottom of the fixture were used to apply the necessary force to engage the bucket in the dovetail fixture. A torque wrench was used to distribute the load equally between the three bolts. This test configuration provided a suitable load to seat the bucket in the fixture representative of the mounting achieved in a rotating turbine wheel. The bucket mounted in the dovetail fixture was securely clamped between two large seismic blocks as shown in Fig. 2. The tip shroud for this modal analysis was free. The data obtained from this test was to provide the comparison between the MS-6001 and MS-7001 Stage 2 buckets mounted similarly for a fixed-free boundary condition.

Test Procedure

Test measurements were obtained from the bucket by using an instrumented hammer which has a force transducer mounted in the head. Fig. 2 shows the instrumented hammer. Early in the application of this test technique for modal analysis of buckets, it was found

Downloaded 01 Jun 2010 to 171.66.16.58. Redistribution subject to ASME license or copyright; see http://www.asme.org/terms/Terms_Use.cfm

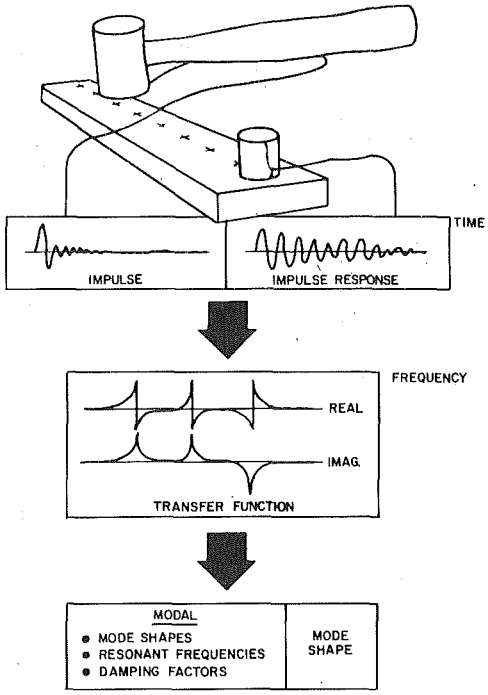
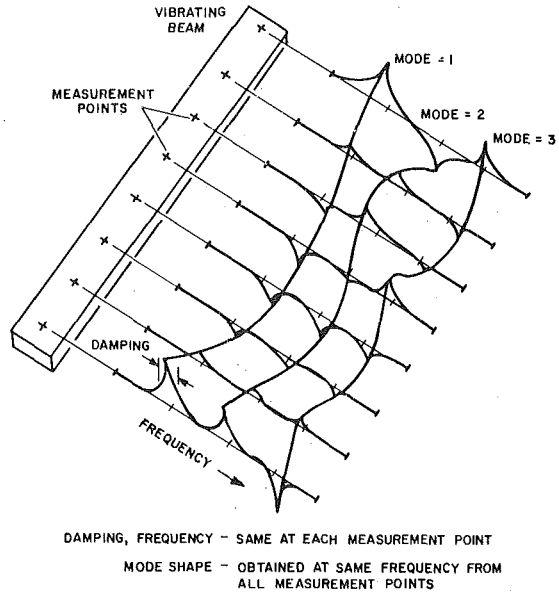


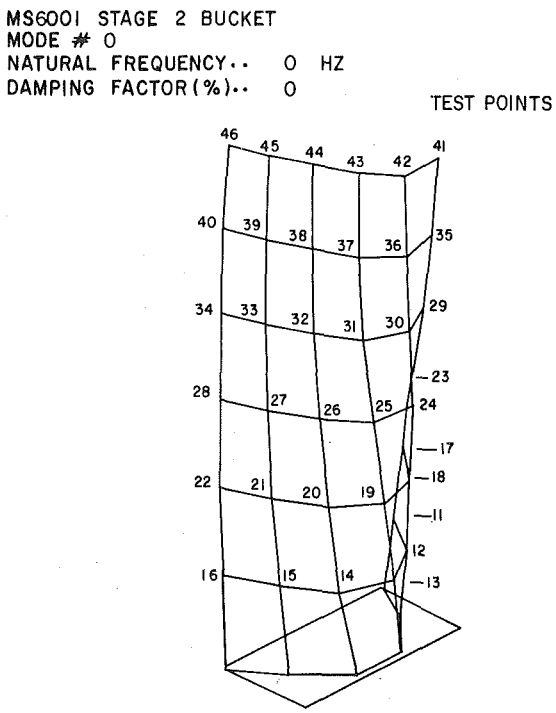
Fig. 4 Measurement and display process



DAMPING, FREQUENCY – SAME AT EACH MEASUREMENT POINT

MODE SHAPE – OBTAINED AT SAME FREQUENCY FROM ALL MEASUREMENT POINTS

Fig. 5 Modal data from transfer functions



GAS TURBINE DEVELOPMENT LABORATORY

Fig. 6 Experimental model of the MS-6001 stage 2 bucket

necessary to design a new type of impact head. The details are described in Appendix A. Fig. 3 shows a closeup of the strike points scribed on the bucket to be tested. The bucket to be tested has been discretized to provide a sufficiently refined model for determining the bucket mode shapes. The test is conducted by striking the bucket at the test points marked on the bucket. Both the acceleration response and impact signals are measured simultaneously and the ratios of the Fourier transforms are computed in the frequency domain to provide the measured transfer function. The mathematical theory and governing equations associated with this test technique are described in Appendix B. The impact of the hammer provides the necessary broadband response needed to determine the modal parameters of the bucket over a large frequency range. The hammer is used to strike the bucket at all the measurement points defining the bucket geometry and to measure the force impulse. Only a single accelerometer is needed to measure the bucket response. Figs. 4 and 5 depict the test procedures just described leading to the determination of the mode shapes of the structure which is the ultimate objective of the test. The block diagrams in Fig. 4 show the transformation of the analog data (time domain) to transfer function data (frequency domain) which is then used to compute the modal parameters of mode shape, resonant frequency and damping factors by the software in the HP system. Fig. 5 shows pictorially how the mode shapes are constructed from the transfer function measured at each test point on the structure. In this figure the transfer function data is plotted along the frequency axis for each test point. The mode shape is a global response along the spatial axis of the structure. Connecting these peaks along the spatial axis at the resonant frequency associated with the mode of interest will provide the mode shape. A crucial step for determining the mode shapes is the principle that the modal vectors can be computed from the single row of measurements of the transfer function instead of the NXN matrix of the system transfer functions. It is shown in Appendix C that a single response sensor in conjunction with a roving force impulse on a structure can be used to measure the modal vectors of the bucket. The mathematical statement of this principle is that only *one row* or *column* of the transfer function matrix needs to be measured in order to determine *all* the mode vectors.

A modal analysis using the HP 5451B Modal Analyzer requires conducting five operational steps. They are (1) set-up, (2) measurement, (3) mode identification, (4) print and (5) modal display.

Set-Up Step. In the set-up step for the HP-system prior to making test measurements, the user enters the test parameters into the system. This input information includes the number of transfer functions to be measured, the location for storing the data on the disk, the data block size to be allocated on the disk, how the polar transfer functions are to be stored, the transducer sensitivity and the amplifier gain.

Measurement Step. The transfer function data is taken and entered in the system during this step. The system has the software capability for making measurements with either impulse or random excitation. As previously described, the impulse technique with a hammer was used to produce and measure the broadband excitation at all the measurement points defining the geometry of the bucket. The real time Fourier Transforms (FFT) of the response and excitation are measured simultaneously and used to compute the transfer function from the ratio of the cross power spectrum and the input

Downloaded 01 Jun 2010 to 171.66.16.58. Redistribution subject to ASME license or copyright; see http://www.asme.org/terms/Terms_Use.cfm

power spectrum. See Appendix B for details of theory and the applicable equations. Each time a data point is acquired, it can be viewed on the scope to determine its quality and acceptability. During the acquisition of data, the coherence function is also viewed on the scope to determine the linearity of response to excitation. At each test point on the structure, repeated measurements are made and the average computed. The system will accept up to 500 measurements at a test point. For the test on the bucket a statistical average of ten measurements was computed. The experimental model consisted of 46 points for display. Measurements were made on 36 test points located on the bucket airfoil, with the remaining ten points used to represent the platform for display only. The actual test points on the bucket are shown in Fig. 3, while Fig. 6 shows the experimental model with test point identification numbers.

Mode Identification Step. During this step the modal parameters in each transfer function are identified. The identification process begins by displaying the measured transfer function that had been previously stored on the disk. It can be viewed in either the polar or rectangular form. Continuing the evaluation, the transfer function data can be refined by a smoothing process built into the system which will sharply identify the peaks and remove the noise. The error between the measured and smooth form of the data can be directly displayed. The smoothing process is continued until the desired error level is achieved. When the iterative feature of the system is used, a least squares routine is used to construct a curve fit for the transfer function. The details of this least squares technique used in the HP system is described in Appendix D. The user has control over the number of iterations and can refine it to his satisfaction. The user can then instruct the system to autofit all the other measured transfer functions to the same iterative process he had originally controlled. As a final decision in this operational step, the curve-fitted transfer functions are saved on the disc storage. It is in this step that the resonant frequencies, damping coefficient and the residue matrix are computed which will be used to extract the mode vectors. The equations and method of solution used for calculating the four unknown modal parameters are described in Appendix D.

Print Step. In this step permanent copies of the modal frequencies, damping ratio, damping coefficient and the mode vectors can be obtained by printing on the Varian Printer/Plotter Stratos 42. Fig. 7 shows a typical print out of data obtained at this operational step. It should be noted that the residues of the transfer function can be printed out also at this step. These residues can be used to construct the full $N \times N$ transfer function matrix if analysis beyond simply obtaining the mode shapes is desired.

Display Step. Up to now the transfer function data were obtained for numerous measurement points without describing the geometry of the structure. These data must now be assigned to the proper point on the analytical model which will be used in the animated display. The coordinates of points that define the model in Cartesian or cylindrical systems are specified in this step. The points that describe this model are identified with the proper measurement point transfer function data that has been stored. This system has the option for constructing the display model before measurements were actually taken and the model data put on disc storage if it is desired.

Once the measurement data are identified with the appropriate point in the model, the structural response can be viewed on the scope as an isometric animated display. There are many features in the system to view the mode shapes. The undeformed and deformed shape can be displayed and viewed from any direction desired. The motion can also be stopped and resumed by the operator.

After the mode shapes have been viewed, selected modes and views can be stored on the disc and then hard copied. The transfer functions needed to evaluate the structural response at critical locations can also be stored and hard copied to complete the documentation of the modal test.

Results

The results of the modal analysis are shown in Figs. 6–23. The modal parameters and mode shapes for the MS-6001 Stage 2 bucket are shown in Figs. 6–14. The corresponding data for the MS-7001 Stage 2 bucket are shown in Figs. 15–23.

STORAGE: TEMP=10, PERM=10

AVERAGE MODAL FREQUENCIES AND DAMPING

* * * * * * * * *

MODE	NAT. FREQ. (HZ)	DAMP. FACT. (%)	DAMP. COEFF. (RAD/SEC)
1	314.8651	.5503	10.8862
2	633.1643	.2383	9.4783
3	1195.8545	.3384	25.4257
4	1399.1929	.0988	8.6848
5	1760.7222	.0946	10.4611
6	2778.8306	.3561	62.1750
7	2847.5103	.0529	9.4658
8	3452.1514	.4695	101.8317
9	3858.6147	.1756	42.5757
10	4670.1006	.2625	77.0283

PRINT(1), DROP(2), SAVE(3), RECALL(4), MSD(5), FINISH(6)?

Fig. 7 Natural frequencies and damping characteristics—MS-6001 stage 2 bucket

Table 1 Natural frequency comparison of MS-6001 second stage bucket (fixed-free boundary condition)

Mode	HP Modal Test	Bench Test
1	314.8 (Hz)	322 (Hz)
2	633.2	662
3	1196.0	1242
4	1399.2	1406
5	1760.7	1803
6	2778.8	2754

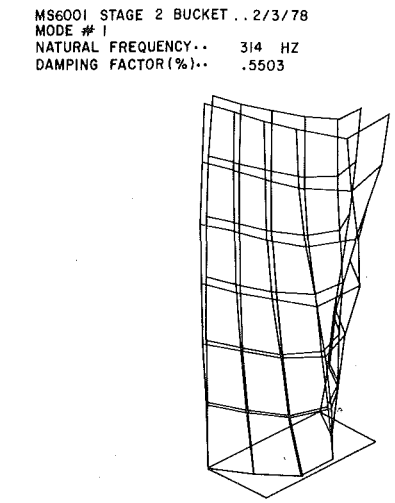


Fig. 8 MS-6001 stage 2 bucket mode No. 1

Fig. 6 shows the experimental model used for this test. A total number of 46 points were used to describe the airfoil and platform. In this model, measurements were taken at 36 points which were identified as points 11–46. The test point locations of this model in the XYZ coordinate system were obtained directly from bucket drawings by using the Gerber Model 24 plotter/digitizer.

Fig. 7 is a table of the natural frequencies, damping factor and damping coefficient obtained at the Print step in the test. The natural frequencies have been computed from the transfer function data by a peak picking algorithm. These natural frequencies compare well with those obtained by conventional bench testing. A frequency comparison of results for the first six modes is contained in Table 1.

Both of these tests were conducted with the tip shroud free. This modal test does not provide the frequencies and mode shape for comparison with a wheel box or machine test since the boundary and physical conditions are different. It does, however, provide information on the characteristic vibration response of the bucket. For the test described, the bucket was held securely in a dovetail fixture as previously described. For the bench test, the bucket was welded to a steel block which was securely clamped between two heavy seismic

Downloaded 01 Jun 2010 to 171.66.16.58. Redistribution subject to ASME license or copyright; see http://www.asme.org/terms/Terms_Use.cfm

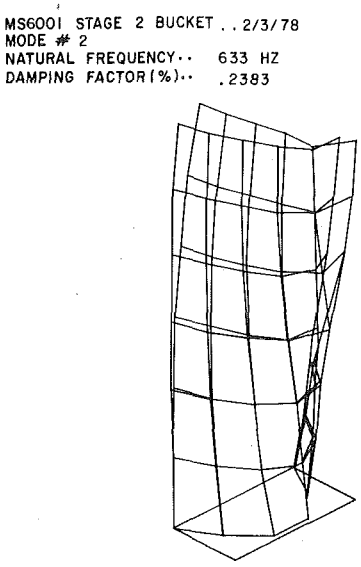


Fig. 9 MS-6001 stage 2 bucket mode No. 2

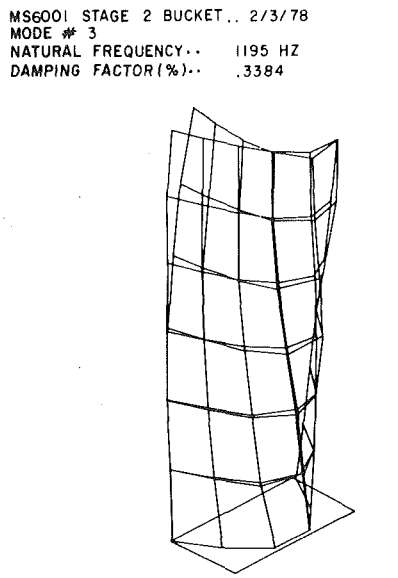


Fig. 10 MS-6001 stage 2 bucket mode No. 3

blocks. The frequencies obtained by the HP-modal analysis are slightly lower than those obtained by bench test since some flexibility exists in the dovetail mounting used in the former test.

Fig. 8 shows the first mode shape of the bucket superimposed on the undeformed mesh. In turbine jargon this mode is called the first tangential bending mode. In reality, since the elastic and inertia axes do not coincide, the mode is actually a compound mode with primarily a larger tangential bending component. This mode is the most heavily damped mode and will have the lowest Q value of the first ten frequencies.

Fig. 9 shows the second mode shape of the bucket. This was the principle mode of interest during the test and was studied from all major view angles to identify the modal displacement field. In turbine jargon this mode is called the first axial bending. This test indicated that this is also a compound mode. For this mode the torsional component, identified by out-of-phase displacement between the trailing and leading edges, was larger than the axial bending mode.

Fig. 10 shows the third mode shape. It is clear that this vibration mode is chiefly a displacement of the upper corner of the trailing edge. When observed in the animated display, the motion is a "flapping" of the trailing edge with little displacement of the leading edge.

Fig. 11 shows the fourth mode of vibration. This mode shape was clearly identified as chiefly a torsional mode. The damping factor is low and it therefore will have a high Q value.

Fig. 12 shows the fifth mode of vibration. This mode shape is the next higher order of mode No. 1. Consequently it can be identified as the second tangential bending mode. The characteristic of this mode is substantial bending at the trailing edge approximately $\frac{1}{3}$ the span below the tip shroud. The damping ratio for this mode is low; therefore, the Q-value will be high.

Transfer function data were obtained and hard copied for each of the 36 measurement points. Both acceleration and displacement transfer functions were plotted from the test data. Fig. 13 is a typical plot of the acceleration transfer function, while Fig. 14 is a plot of the displacement transfer function for the same location on the model; namely, measurement point No. 46. The acceleration transfer function (Fig. 13) is called inertance. It provides the magnitude and phase angle of the acceleration due to a unit vibratory excitation force. The units of this function are G-s/lb force. The displacement transfer function (Fig. 14) is called the compliance. It provides the magnitude and phase angle of the displacement for a unit excitation force. The units of this transfer function are in./lb force. All of these functions show peaks at the resonant frequency. In general, higher frequency modes tend to exhibit smaller displacements than at lower natural frequencies. Since the first mode of this bucket has the highest damping ratio, it is reasonable that the magnitude will be small compared to the next

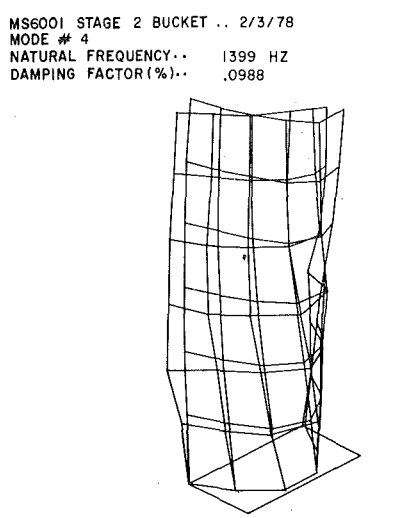


Fig. 11 MS-6001 stage 2 bucket mode No. 4

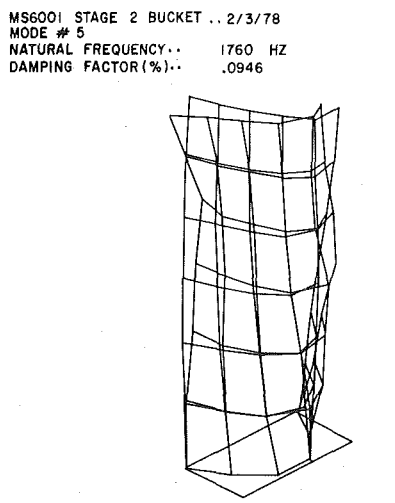


Fig. 12 MS-6001 stage 2 bucket mode No. 5

Downloaded 01 Jun 2010 to 171.66.16.58. Redistribution subject to ASME license or copyright; see http://www.asme.org/terms/Terms_Use.cfm

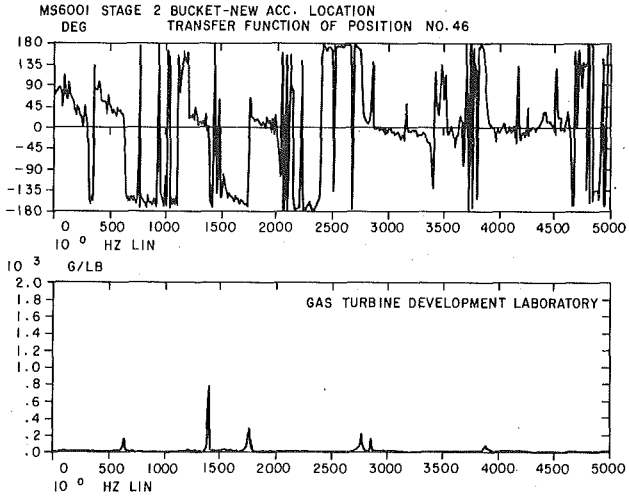


Fig. 13 Acceleration transfer function—point 46

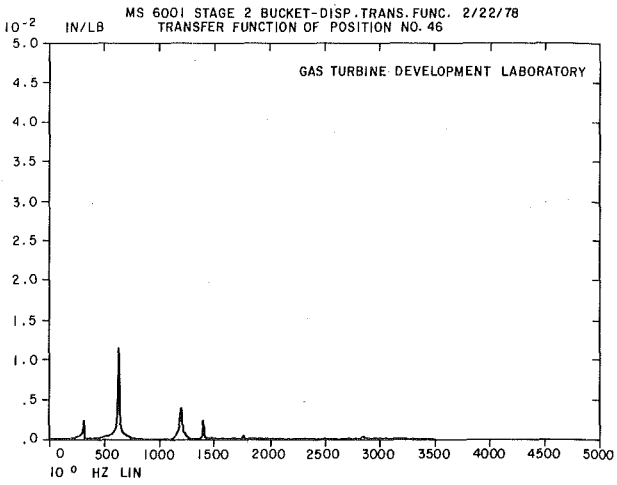


Fig. 14 Displacement transfer function—point 46

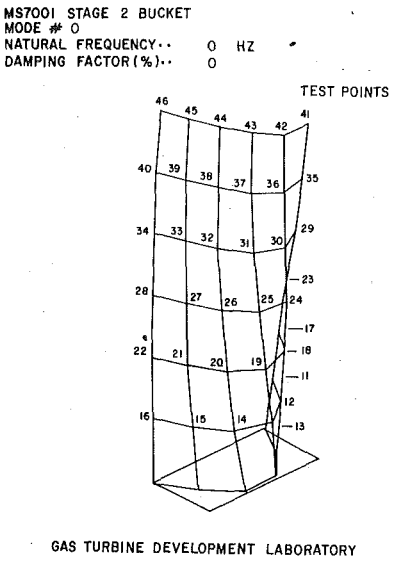


Fig. 15 Experimental mode of the MS-7001 stage 2 bucket

AVERAGE MODAL FREQUENCIES AND DAMPING

MODE	NAT.FREQ.	DAMP.FACT.	DAMP.COEFF.
1	180.3539	3.3268	37.7200
2	422.7847	.4111	10.9215
3	721.3254	.2088	9.4614
4	861.9922	.2125	11.5065
5	1111.8582	.3557	24.8467
6	1538.2014	.1247	12.0550
7	1826.2683	.1034	11.8682
8	2088.4922	.1551	20.3465
9	2555.0381	.1241	19.9234
10	2943.7764	.0833	15.4112

PRINT(1),DROP(2),SAVE(3),RECALL(4),MSD(5),FINISH(6)?

Fig. 16 Natural frequencies and damping characteristics—MS-7001 stage 2 bucket

Table 2 Natural frequency comparison of MS-7001 second stage bucket (fixed-free boundary condition)

Mode	HP Modal Test	Bench Test
1	180.4 (Hz)	190 (Hz)
2	422.8	464
3	721.3	
4	862.0	834
5	903.7	920

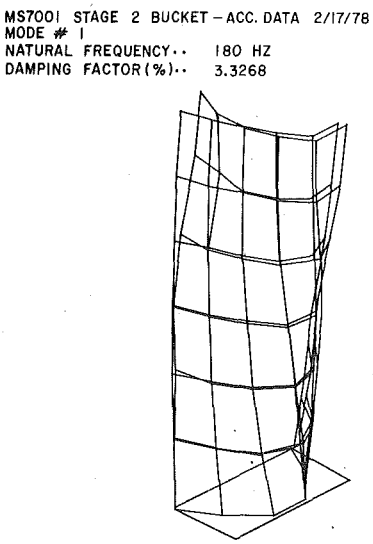


Fig. 17 MS-7001 stage 2 bucket mode No. 1

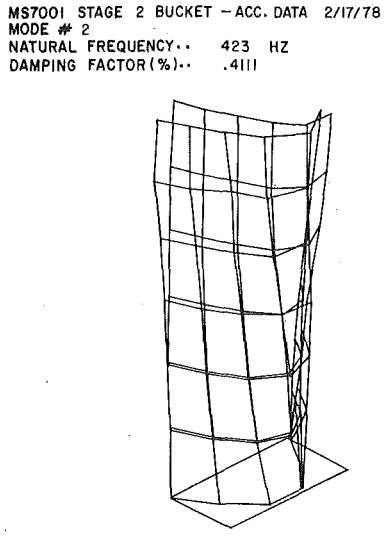


Fig. 18 MS-7001 stage 2 bucket mode No. 2

Downloaded 01 Jun 2010 to 171.66.16.58. Redistribution subject to ASME license or copyright; see http://www.asme.org/terms/Terms_Use.cfm

higher modes (see Fig. 14). On the other hand, since the magnitude of the acceleration transfer function is biased in proportion to the frequency squared, the magnitude of this function could be larger than the lower modes in some circumstances. If these functions are known for the entire structure, all the modal information needed to predict the global vibratory response is available. Since the transfer function of a structure is a basic parameter, it can be used to compare the response between different structures since this function is normalized with the excitation force.

The results of the modal analysis conducted on the MS-7001 Stage 2 Bucket are shown in Figs. 15–23. The model configuration shown in Fig. 15 was used to display the transfer function and mode shapes for this component. This experimental model is the same as that used for the MS-6001 shown in Fig. 6 since the airfoil is a scale geometry. Fig. 16 is a print out of the natural frequencies, damping factor and damping coefficient for the MS-7001 Stage 2 Bucket. Since the MS-7001 bucket is proportionately longer than the MS-6001 bucket, its natural frequencies will be lower than those exhibited on Fig. 7. The frequencies obtained from the HP Modal Analysis were compared to bench test data. This comparison is shown in Table 2 below.

The earlier bench test had identified the frequencies and mode as follows:

First Tangential	190 (Hz)
First Axial	464
First Torsional	834
Complex (Torsion + Bending)	920

The HP Modal Analysis which is a more precise experimental technique than bench testing, is able to detect resonances with high modal density. The bench test which used foil type strain gages mounted on the shank and upper tang of the dovetail missed the third mode at 721 Hz. This may be partly due to the location of the strain gages and instrumentation which could not discriminate in regions of high modal density.

Comparison of Figs. 8 and 17 show that both buckets have essentially the same first mode which is primarily a tangential bending component.

Comparison of Figs. 9 and 18 show that the second mode shapes are the same; namely, a compound mode with a dominant torsional component.

Comparison of mode 3, Figs. 10 and 19, show that the modes are very similar except the MS-7001 bucket has a higher tangential bending component than the MS-6001. However, the dominant component in this mixed mode is a trailing edge flap for both buckets.

It is obvious that mode 4 is a torsion mode when Figs. 11 and 20 are compared. It is interesting to note that the axes of torsional vibration is essentially the same for both these buckets.

Figs. 12 and 21 show that the 5th modes are quite different. Mode No. 5 for MS-6001 is the next higher tangential bending mode. This mode shape for higher order bending does not appear until the 6th mode for the MS-7001 at 1112 Hz.

In summary, it may be stated that the first four mode shapes of the MS-6001 and MS-7001 Stage 2 Buckets are the same. This detail in resolution between the mode shapes of two entirely different buckets could not have been made very easily by bench tests.

Finally, a comparison of transfer functions will be made at the same proportionately scaled location, point 46. Comparison of Figs. 13 and 22 of the acceleration transfer functions shows the structural response differences of these two buckets. The torsional response, mode 4, of the MS-6001 bucket has a magnitude nearly four times higher than the comparable mode for the MS-7001 bucket. However, comparison of the damping factors at the 4th modes from Figs. 7 and 16 shows that the damping is much larger at this mode for the MS-7001 bucket, which may be the explanation for the difference in magnitude. A comparison of Figs. 14 and 23 discloses the differences in trailing edge displacement response. The largest magnitude occurs at the second mode for both these buckets. However, the scale is different in these two figures. The displacement at point 46 of the MS-6001 bucket is nearly three times larger than the corresponding point on the trailing edge of the MS-7001 bucket when the same unit load excitation is applied. This infers that the MS-6001 Stage 2 Bucket has a higher

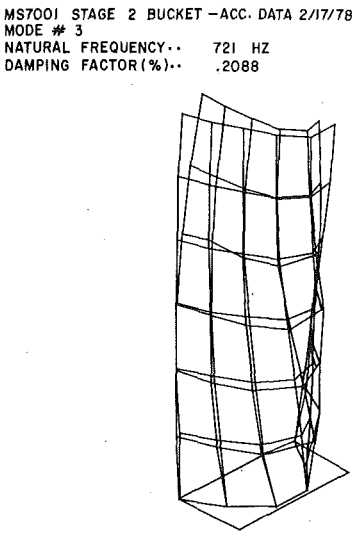


Fig. 19 MS-7001 stage 2 bucket mode No. 3

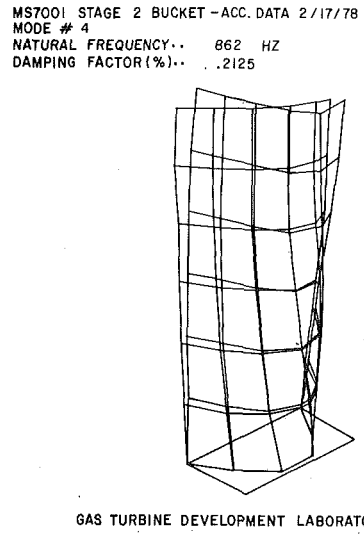


Fig. 20 MS-7001 stage 2 bucket mode No. 4

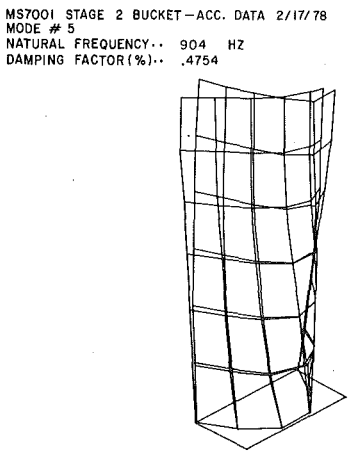


Fig. 21 MS-7001 stage 2 bucket mode No. 5

Downloaded 01 Jun 2010 to 171.66.16.58. Redistribution subject to ASME license or copyright; see http://www.asme.org/terms/Terms_Use.cfm

compliance at mode 2 when compared to the similar mode of the MS-7001 bucket.

Summary and Conclusions

The experimental modal analyses conducted on the MS-6001 and MS-7001 Stage 2 Buckets using the HP Fourier and Modal Analyzer have revealed the following:

1 The method is currently the most accurate and reliable technique available for determining the natural frequency, damping characteristics and mode shapes of gas turbine buckets.

2 The measured data are obtained on a statistical basis which provides a reliable average of the modal parameters.

3 Testing on turbine buckets has shown that this test system determines modal characteristics with repeatability.

4 The method is currently the fastest method available for determining the natural frequencies, damping characteristics and mode shapes of turbine buckets.

5 High cycle fatigue (HCF) problems can be quickly identified by observing the animated modal display.

6 This method has the potential for conducting forced vibration analyses using the measured transfer functions.

7 The transfer functions obtained by this method which are the dynamic structural property of the component can be used as a criterion for comparing the structural response of turbine components.

Acknowledgment

This writer gratefully acknowledges the contribution of Greg Maxwell, Test Engineer, and Ralph Bush, Specialist, both of the Gas Turbine Laboratory for conducting the tests. The adaption of this modal analysis technique to the turbine buckets required experimental work. Their help and cooperation to demonstrate the feasibility of this digital test method is greatly appreciated.

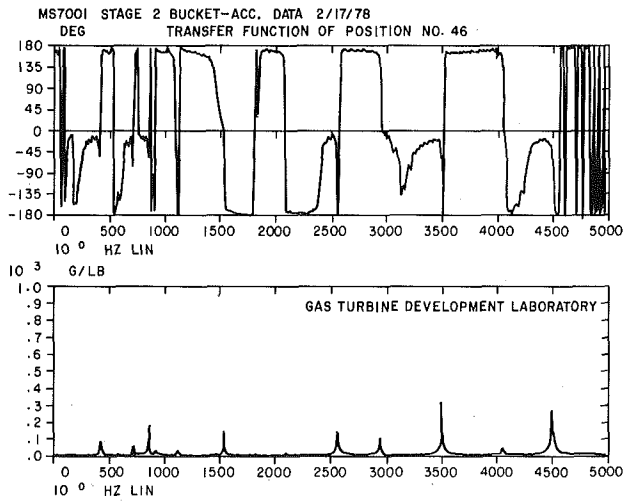


Fig. 22 Acceleration transfer function—point 46

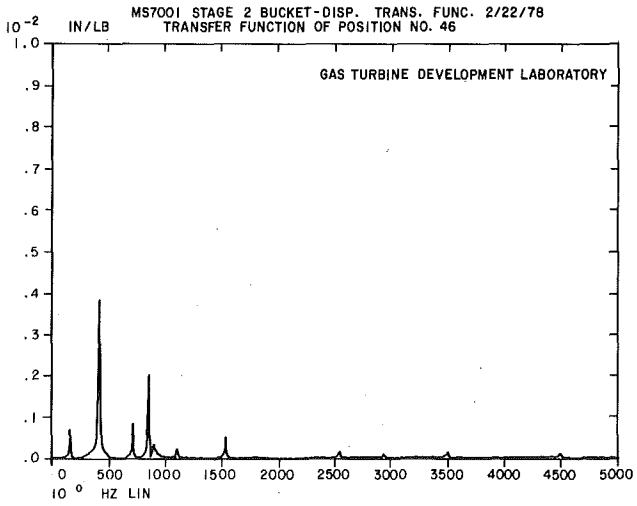


Fig. 23 Displacement transfer function—point 46

APPENDIX A

Modified Impact Hammer Head

Early in the development testing conducted on gas turbine buckets, it was determined that the screw-on plastic impact heads supplied with the test hammer did not provide the desired impact signal clarity. The curvature of the impact surface on the head was too large for the airfoil curvature. This made it extremely difficult to precisely hit the measurement point on the bucket pressure side. The problem was overcome by using a modified impact head which consisted of a $\frac{1}{8}$ in. dia ball bearing brazed onto the end of an Allen head screw.

The use of this impact head which screws onto the force sensor, provided a clear input excitation to the bucket with a high degree of repeatability. The sketch below shows the modified head used for this test.

APPENDIX B

Structural Dynamics Model for *N*-Dimension

The Hewlett-Packard digital test system became a practical experimental technique for determining the mode shapes of a structural component with the advent of the real time Fast Fourier Transform (FFT). The Fourier Analyzer which is a key component of the HP-5451B provides a means for real time spectral analysis of a test signal. This equipment can process the input and response time signals measured simultaneously with the FFT algorithm to provide a spectral transfer function. See page 150 of [8] which describes the basic theory and algorithm of the Fast Fourier Transform. The spectral transfer function contains all of the necessary modal parameters to be able to characterize the natural frequency response of a mechanical system.

The major assumption that this test system is based on is that the structure can be considered an array of simple linear spring-mass-damper components. The governing equation for a simple spring-

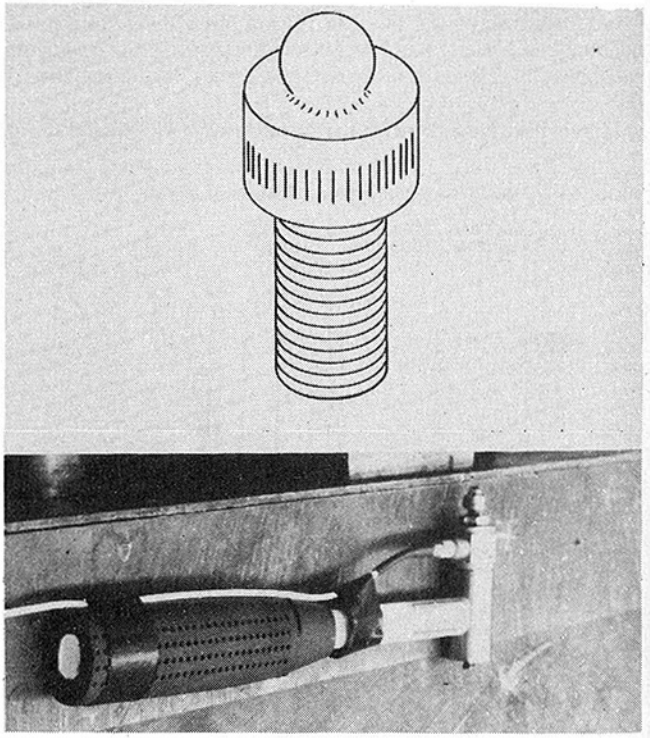


Fig. A (Appendix A) Impact hammer showing modified head attached to force sensor

Downloaded 01 Jun 2010 to 171.66.16.58. Redistribution subject to ASME license or copyright; see http://www.asme.org/terms/Terms_Use.cfm

mass-damper system is given by:

$$M\frac{d^2x(t)}{dt^2} + c\frac{dx(t)}{dt} + kx(t) = f(t) \tag{1}$$

where $f(t)$ = applied excitation, $x(t)$ = displacement vector, M = mass, c = damping coefficient, and k = stiffness.

The approach used by Hewlett Packard is the identification of the modal parameters by measurements of the transfer function. Much of the theory used in the formulation of the software for the HP system has its foundation in control theory and the utility of the transfer function to describe a linear system. See [9]. The spectral transfer function is a complex function with real and imaginary parts. To better understand the underlying principles, it will be necessary to consider the equations in the complex plane. Consequently, consider the operations using the Laplace transform. [10–12] have good detailed descriptions on the basic theory.

By definition, the transform of a time dependent function $f(t)$ to a function in the complex s-plane is given by the following relationship.

$$F(s) = \int_0^\infty e^{-st} f(t)dt = \mathcal{L}[f(t)] \tag{2}$$

where $F(s)$ is the new variable in the s-plane. The function s is a complex variable. Note that the operator which produces the transform is an exponential. The symbol $[\mathcal{L}]$ refers to the operation of taking the Laplace transform of a time dependent function

Consider the Laplace transforms of the left side of equation (1), the result will be:

$$\mathcal{L}[x(t)] = X(s) \tag{3}$$

$$\mathcal{L}[\dot{x}(t)] = sX(s) - X(0) \tag{4}$$

$$\mathcal{L}[\ddot{x}(t)] = s^2X(s) - sX(0) - \dot{X}(0) \tag{5}$$

The dot over the dependent function denotes time derivative according to the usual notation. The transforms $X(0)$ and $\dot{X}(0)$ are the initial displacement and velocity transforms at $t = 0$. Assuming that the initial conditions are zero, equation (1) will become:

$$[Ms^2 + cs + k]\, X(s) = F(s) \tag{6}$$

Taking the Laplace transform of the linear differential equation (1) results in the much simpler algebraic equation (6) in the complex domain. See [12]. This complex s-domain is the frequency domain. Let

$$B(s) = Ms^2 + cs + k \tag{7}$$

Then equation (6) becomes the simple equation

$$B(s)\, X(s) = F(s) \tag{8}$$

When both sides of equation (8) are premultiplied by the inverse matrix $B^{-1}(s)$, the following equation is obtained:

$$X(s) = H(s)\, F(s) \tag{9}$$

where $H(s)$ is defined as the transfer function

$$H(s) = B^{-1}(s) = \frac{1}{Ms^2 + cs + k} \tag{10}$$

Much of the discussion uses the common notation of matrix theory described in [13]. For N-dimensional space the transfer function $H(s)$ is an NXN matrix. Using the usual matrix notation

$$H(s) = \begin{bmatrix} H_{11}(s) & \cdots & H_{1N}(s) \\ \vdots & & \vdots \\ \vdots & & \vdots \\ H_{N1}(s) & \cdots & H_{NN}(s) \end{bmatrix} \tag{11}$$

Equation (9) is a simple statement of cause and effect for a linear system [9].

$$\xrightarrow{F(s)} \boxed{H(s)} \xrightarrow{X(s) = H(s)\, F(s)}$$

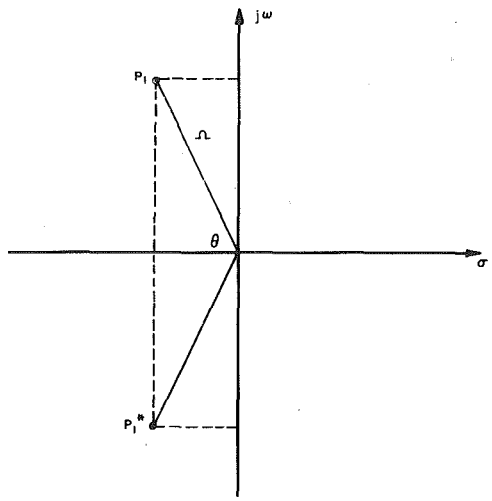


Fig. 24 Representation of Point *P* in the complex *S*-plane

This relationship can be used to determine the response $X(s)$ of any linear system for a given input or excitation $F(s)$. The spectral transfer functions $H(s)$ is the system parameter which describes how the structure will behave.

From equation (9), the transfer function $H(s)$ can be determined simply as the ratio of output to input.

$$H(s) = \frac{X(s)}{F(s)} \tag{12}$$

The transfer function of $H(s)$ is determined by the HP-5451B system by experimentally measuring response and force input. Both these measurements are made simultaneously with the FFT and the complex division according to equation (12) is performed in the complex domain. The result is a digital form of the transfer function with real and imaginary parts.

To obtain a better understanding of the functional representation in the s-domain or complex plane, consider Fig. 24, Argand Diagram. The objective is to represent resonance as a point in the complex plane. The real axis is the damping coefficient, σ, and the imaginary axis is the frequency axis, ω. In the complex plane the point P_1 has the complex conjugate P_1*. The symbol * denotes the complex conjugate throughout this development. These points plotted in Fig. 24 would correspond to a damped harmonic oscillation. If point P_1 and its conjugate fall on the imaginary axis, the representation would be for undamped vibration. If the point P_1 and its conjugate are plotted with a positive component of σ, the representation is for a critically damped system. Continuing the discussion for the interpretation of representing a function in the complex domain, consider Fig. 25 which is a three-dimensional plot of the real part of the transfer function for a single degree of freedom system. The peaks in this plot correspond to the point P projected on to the s-plane shown in Fig. 24. These peaks are the resonance points and are called the poles. If a cutting plane is passed through the origin along the imaginary axis, the thick lined curve will be obtained. This plot of the function through the origin (damping coefficient, σ, is zero), is actually a plot of the Fourier transform. The HP system obtains the digital form of the Fourier transform of the transfer function from the measured output and input transforms, thereby, providing the curve of H as a function of frequency. If the possibility of noise pickup is remote, then the transfer function could be computed directly from equation (12). However, since noise sources are prevalent and unpredictable under most test conditions, it is more accurate to compute the transfer function using the power spectrum method.

The Fourier transform of the input and output are obtained by the definition

$$S_f = F[f(t)] = \int_0^\infty f(t)\, e^{-j\omega t}dt \tag{13}$$

$$S_x = F[x(t)] = \int_0^\infty x(t)\, e^{-j\omega t}dt \tag{14}$$

Downloaded 01 Jun 2010 to 171.66.16.58. Redistribution subject to ASME license or copyright; see http://www.asme.org/terms/Terms_Use.cfm

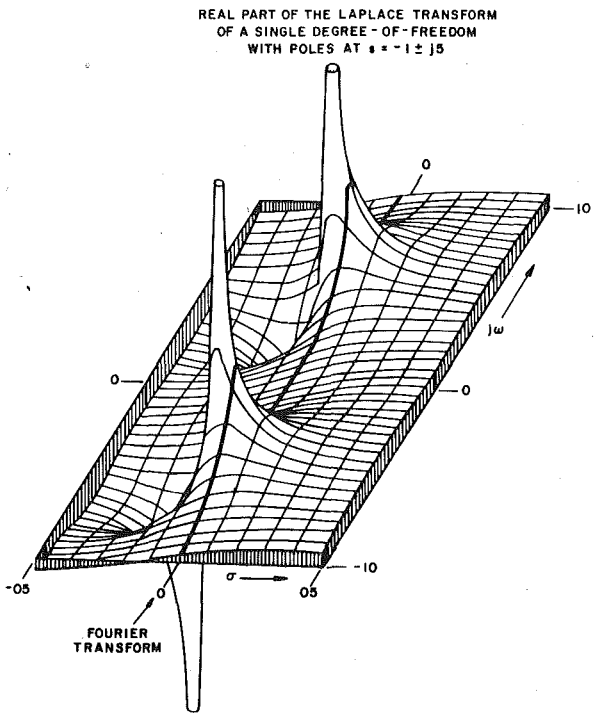


Fig. 25 Real part of a transfer function

Note the similarity of this transform with the Laplace transform given by (2). The Fourier transform is a special case of the Laplace transform. [11] has a good discussion on the differences between the Laplace and Fourier Transforms in Section 23–27. Note that the S parameter in the Laplace domain is given by

$$S = -\sigma + j\omega \tag{15}$$

In the limit as $\sigma \to 0$, the Laplace transform will yield the transform operator $e^{-j\omega t}$ which is precisely the Fourier transform operator. The average power spectrum $\overline{G_{ff}}$ is computed by the product of the excitation Fourier transform and its complex conjugate (see [11] Section 27-5).

$$\overline{G_{ff}} = S_f S_f^* \tag{16}$$

The average cross power spectrum $\overline{G_{fx}}$ is computed by:

$$\overline{G_{xf}} = S_x S_f^* \tag{17}$$

Finally, the transfer function is computed from the ratio of the power spectrums by the relationship:

$$\boxed{H(s) = \frac{\overline{G_{xf}}}{\overline{G_{ff}}}} \tag{18}$$

When the HP system is used to determine the transfer function, the software system takes the average of test measurements made at a point. As the number of measurements taken at a point in the structure is increased, the error in the noise is reduced. See section which describes the measurement step. The HP system will accept a number of measurements up to 500 to compute the average power spectrum.

The coherence function γ^2 is a measure of the linearity of the system and can be used to detect cause/effect characteristics of a system. (See [11], Section 27-6 for the basic theory associated with this function.) The coherence function is determined by the following equation:

$$\gamma^2 = \frac{|\overline{G_{xf}}|^2}{|\overline{G_{ff}}|\ |\overline{G_{xx}}|} \tag{19}$$

Throughout the acquisition of data, the coherence function can be viewed to determine the quality of the measurements being taken. For our test data acceptance is based on coherence function range of:

$$.8 < \gamma^2 < 1.0 \tag{20}$$

APPENDIX C

Modal Vector Determination from Transfer Function

The HP Fourier and Modal Analysis System determines the modal vectors from only one row or column of the transfer function matrix. It is the objective of this section to show that these mode vectors can be completely defined from data used to compute either a row or column of the transfer function.

The full transfer function matrix given by equation (11), can be written in partial fraction form. (See [9] and [12] for the analytical theory of partial fraction expansion of a function in terms of its poles.)

$$H(s) = \sum_{k=1}^{2N} \frac{a_k}{s - p_k} \tag{21}$$

where

p_k = kth root of the determinant $|B(s)|$ (commonly referred to as the pole of $H(s)$)

a_k = residue for the kth root

Fig. 24 shows only a single pole. In the complex domain, multiple poles may be represented. The kth pole and its conjugate are specified as:

$$p_k = -\sigma_k + j\omega_k \tag{22}$$

$$p_k^* = -\sigma_k - j\omega_k \tag{23}$$

From this figure it is easily seen that the resonant frequency Ω_k is determined by:

$$\Omega_k = \sqrt{\sigma_k^2 + \omega_k^2} \tag{24}$$

The damping factor or percent of critical damping associated with the kth mode is given by:

$$\zeta_k = \cos\theta_k = \frac{\sigma_k}{\Omega_k} \tag{25}$$

The damping characteristics can be specified in terms of the amplification factor Q which is a reciprocal function of ζ.

$$Q_k = \frac{1}{2\zeta_k} \tag{26}$$

The kth modal vector u_k is the solution of the homogeneous equation from [8].

$$B(p_k)u_k = 0$$

or using indicial notation

$$\boxed{B_k\, u_k = 0} \tag{27}$$

(See [11], Section 28-14, for the formulation of the eigenvalue problem in matrix notation.)

It is well known that the determination of the natural frequencies and mode vectors of a linear system can be formulated in turns of an eigenvalue and eigenvector problem. This usually is reduced to solving a set of homogeneous equations. Premultiply the transfer function relationship of equation (21) by the matrix $B(s)$ and then operate on this result by the vector $(s - p_k)$

$$(S - P_k)B(s)H(s) = B_k(a_k) \tag{28}$$

Since $B(s)$ is the inverse matrix of the transfer functior matrix $H(s)$ according to (10), then:

$$B(s)\, H(s) = I \tag{29}$$

where I is the identity matrix. Therefore, the left side of (28) can be rewritten and the limiting process taken as the Laplace variable (s) approaches the pole (p_k).

$$\lim_{s \to p_k} (s - p_k)I = 0 \tag{30}$$

Downloaded 01 Jun 2010 to 171.66.16.58. Redistribution subject to ASME license or copyright; see http://www.asme.org/terms/Terms_Use.cfm

Consequently, the right hand side of (28) will be zero when $s \rightarrow p_k$. Therefore,

$$\boxed{B_k\, a_k = 0} \tag{31}$$

Consider this as condition No. 1 on the residue matrice a_k which in a system with N degree of freedom will be an $N \times N$ matrix. Comparison of the result (31) with (27), shows that every column of the residue matrix a_k contains the modal vector u_k.

A second condition on the residue matrix can be established by post multiplying the transfer function (21) by the matrix $B(s)$

$$H(s)\, B(s) = \frac{a_k}{s - p_k} B_k \tag{32}$$

The left side reduces to the identity matrix by virtue of (29).

$$I = \frac{a_k}{s - p_k} B_k \tag{33}$$

Again multiply by the vector $(s - p_k)$ and take the limit as (s) approaches the (p_k) pole.

$$\lim_{s \rightarrow p_k} (s - p_k) I = a_k\, B_k = 0 \tag{34}$$

Therefore

$$a_k\, B_k = 0 \tag{35}$$

In [14] it is shown that this result can be expressed in transpose matrix form.

$$B_k{}^T a_k{}^T = 0 \tag{36}$$

Since B_k is a symmetric matrix, the relationship (36) becomes

$$\boxed{B_k\, a_k{}^T = 0} \tag{37}$$

Specify this result as condition No. 2 on the residue matrix a_k. If (37) is now compared to (27), then each row of the residue matrix must contain a modal vector. Based on conditions (31) and (37), it then follows that the most general form of the residue matrix can be expressed in terms of the modal vectors by:

$$a_k = A_k\, u_k\, u_k{}^T \tag{38}$$

where A_k is an arbitrary coefficient. When (38) is substituted into (21), the final expression for the transfer function becomes:

$$H(s) = \sum_{k=1}^{2N} \frac{A_k u_k u_k{}^T}{(s - p_k)} \tag{39}$$

This result proves a major property of the residue matrix which is obtained from frequency response measurements. It is only necessary to determine one row or column of the residue matrix to completely define the mode shape for a particular pole p_k. From the test point of view, this means that one only has to measure one row or column of the transfer function of the system to completely define the mode shapes of that system. If the response sensor remains fixed and a roving excitation is used, then a row of the system transfer function is being measured by this test technique. On the other hand, if the force excitation remains fixed and the response sensor is moved to various locations, then essentially a column of the system transfer function is being measured.

APPENDIX D

Determination of Modal Parameters from Measured Transfer Functions

The HP system contains software which computes the modal parameters such as the resonant frequencies and damping coefficients for each mode of the system. The procedure used is to curve fit the digital transfer function data to the analytical model of an N degree linear system based on a simple linear spring-mass-damper components previously described. For that purpose, the expression (21) of the transfer function is rewritten into the following form:

$$H(s) \sum_{k=1}^{N} \frac{a_k}{s - p_k} + \frac{a_k{}^*}{s - p_k{}^*} \tag{40}$$

where $a_k = N \times N$ complex residue matrix, p_k = pole location of kth mode, and * = denotes complex conjugate.

The residue can be defined in the following form which will simplify later computations.

$$a_k = 2\, j\, r_k \tag{41}$$

When (41) is substituted into (40), the final form of the transfer function is obtained.

$$H(s) = \sum_{k=1}^{N} \frac{r_k}{2j(s - p_k)} - \frac{r_k{}^*}{2j(s - p_k{}^*)} \tag{42}$$

In [5], Richardson describes the various techniques used to extract the modal parameters from the digital data by using some form of equation (42). This includes estimation of mode shape by quadrature response, by circle fit, by complex division, by difference formula and by least square curve fit. The most precise method is the least square estimation. Hewlett-Packard has applied an iterative least square error technique by using equation (42) in conjunction with the transfer function data. The iterative equations arise from the extremum of the error function.

$$\epsilon = \sum_{k=1}^{N} [H_k - H(p_k)]^2 \tag{43}$$

where H_k = measured data at frequency ω_k, $H(p_k)$ = analytical model, equation (42), N = degree of freedom.

At each kth mode, there are four unknowns: (1) the resonant frequency, ω_k, (2) and damping coefficient, σ_k, (3) and (4) the amplitude and phase angle of the residue, r_k.

The least squares method is a well known numerical technique (see [13] and [14] for an analytical curve fit to data). By minimizing the error with respect to unknown coefficients, the set of simultaneous equations are obtained from

$$\frac{\partial \epsilon}{(\partial \alpha_n)_k} = [H_k - H(p_k)] \frac{\partial}{(\partial \alpha_n)_k} [H_k - H(p_k)] = 0 \tag{44}$$

where the index, k, identifies the mode and, α_n is the unknown modal parameter with $n = 1, 2, 3$, or 4.

The method used in the HP system is to use a computerized peak picking procedure to obtain starting estimates of the modal damping, frequency and residue. With each iteration of the algorithm new values of the four unknowns for each mode are computed to reduce the error between the measured and the analytical expression for the transfer function. In the HP5451B system there is a large degree of user control during the iterative process in the mode identification step to reduce the error difference between the measured and curve fit until the operator is satisfied. During this iterative procedure, the error can be viewed on the oscilloscope to determine if a sufficient number of iterations were made.

References

1 Carnegie, W. "Vibrations of Pre-Twisted Cantilever Blading," *Proc. Instn. Mech. Engrs.*, London, 1959, 173, pp. 343.

2 Plunkett, R. "Natural Frequencies of Uniform and Non-Uniform Rectangular Cantilever Plates," *Jour. Mech. Engineering Science*, Vol. 5, No. 2, 1963, pp. 146.

3 *Holographic Non Destructive Testing*, edited by Robert K. Erf, Academic Press, 1974, Chap. 8.10 "Turbine Blade Inspection" by R. K. Erf, pp. 343.

4 Jones D. I. G. and Muszyńska, A. "Effect of Slip on Response of a Vibrating Compressor Blade," presented at the ASME Winter Annual Meeting of the Gas Turbine Div., Atlanta, Ga., Nov. 27–Dec. 2, 1978, Paper No. 77-WA/GT-3.

5 Richardson, M. "Modal Analysis Using Digital Test Systems," *Seminar on Understanding Digital Control and Analysis in Vibration Test Systems*, 1975.

6 Ramsey, K. A. "Effective Measurements for Structural Dynamics Testing," Part 1, Vol. 9, No. 11, Nov. 1975, pp. 24 and Part 11 Vol. 10, No. 4, Apr. 1976, pp. 18, *Sound and Vibration*.

7 Halvorsen, W. G. and Brown, D. L. "Impulse Technique for Structural Frequency Response Testing," Vol. 11, No. 11, Nov. 1977, pp. 8, *Sound and Vibration*.

8 Newland, D. E. *An Introduction to Random Vibrations and Spectral*

Downloaded 01 Jun 2010 to 171.66.16.58. Redistribution subject to ASME license or copyright; see http://www.asme.org/terms/Terms_Use.cfm

Analysis, Longman, 1975.
9 Gardner, M. F. and Barnes, J. L. *Transients in Linear Systems,* Vol. I, John Wiley and Sons, 1942.
10 Meirovitch, L. *Elements of Vibration Analysis* McGraw-Hill, 1975.
11 Harris, C. M. and Crede, C. E. *Shock and Vibration Handbook,* 2nd ed., McGraw-Hill, 1976.
12 Thomson, W. J. *Laplace Transformation—Theory and Engineering Applications,* Prentice-Hall, 1950.
13 Hildebrand, F. B. *Methods of Applied Mathematics,* Prentice-Hall 1961.
14 Pennington, R. H. *Introductory Computer Methods and Numerical Analysis,* MacMillan, 1965.

Downloaded 01 Jun 2010 to 171.66.16.58. Redistribution subject to ASME license or copyright; see http://www.asme.org/terms/Terms_Use.cfm

K. Bammert
Professor.
Institute for Turbomachinery and Gasdynamics
University of Hannover, Hannover
Germany

R. Staude
Head of Department for Mechanic and Thermodynamic Design of Turbomachines.
Gutehoffnungshütte Sterkrade AG., Oberhausen, Germany

Optimization for Rotor Blades of Tandem Design for Axial Flow Compressors

The tandem cascades investigated consist of two retarding cascades closely arranged behind one another. The influences of the flow interference for the pressure distribution at the profiles, for the losses and the outlet angle are discussed. Various cascade configurations are theoretically and experimentally investigated to find out the optimum range of the axial spacing and for the displacement in circumferential direction. An example shows how rotor blades of tandem design can be optimized for minimal profile losses. The aim is to find the optimum configuration for each of the design sections of the rotor blades. A further condition is to avoid additional bending stresses due to centrifugal forces, so that tandem rotor blades can run with relatively high speed.

Introduction

The energy transformation of axial flow compressors can be considerably increased by the selection of suitable tandem cascades. Tandem cascades consist of two retarding cascades arranged closely one behind another, cascade 1 and cascade 2 (Fig. 1).

The arrangement of two single cascades to form a tandem cascade is fixed by the displacement, b, of the two cascades in circumferential direction and by their axial spacing, a (Fig. 1). With infinitely large cascade spacing, a, the two cascades behave as two independent cascades. On the other hand a close configuration of the two cascades cause influencing of the flow by both cascades. The influence of the flow interference becomes greater on reduction of the spacing and increase of the displacement.

Relatively high degrees of reaction between 80 and 100 percent permit tandem cascades to be used to advantage in multi-stage axial flow compressors. The energy transformation is considerably increased by the configuration of tandem cascade rotors and one row stator blades. As against comparable axial flow compressors of conventional single cascade design, the number of blades with the tandem cascade design with approximately the same aerodynamic loading for the individual rotor blade profiles can be reduced to about 40 percent. Further, with the tandem cascade design there is a reduction in the length of the bladed part of the shaft of approximately 30 percent (Fig. 2). The shorter length and the reduced number of blades results basically from the fact that, as compared with the conventional signal cascade design, over two stages a row of stator blades can be omitted (Fig. 2). The stator blades have smaller pitch ratios than the rotor blades [1, 2, 3].

The tandem cascade rotor blades should have almost optimum cascade configurations over their height in all radial sections. The tandem configuration defined by a certain relative cascade spacing a/ℓ_1 and a certain relative cascade displacement h/t is optimum for minimum profile losses. Using a theoretical calculation method, the aim is to determine the optimum cascade configuration for any tandem cascade. The comparison of theoretically calculated values with measurements on two-dimensional cascades shows the applicability of the method for the optimization of compressor blading. For an example it is finally shown how the tandem cascade rotor blades for

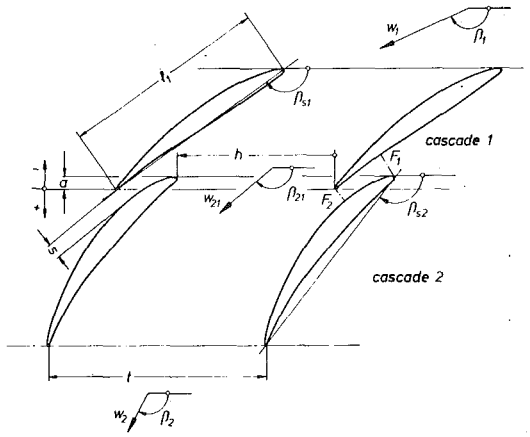


Fig. 1 References on tandem cascade: t pitch, ℓ_1 chord length, a cascade spacing, h cascade displacement, s gap width, β_{s1} stagger angle, cascade 1, β_{s2} stagger angle, cascade 2, β_1 inlet angle, β_{21} outlet angle, cascade 1 and inlet angle, cascade 2, β_2 outlet angle, w_1 inlet velocity, w_{21} outlet velocity, cascade 1 and inlet velocity, cascade 2, w_2 outlet velocity, F_1 inlet area gap, F_2 outlet area gap

Contributed by the Gas Turbine Division and presented at the Gas Turbine Conference and Exhibit and Solar Energy Conference, San Diego, California, March 12–15, 1979 of THE AMERICAN SOCIETY OF MECHANICAL ENGINEERS. Manuscript received at ASME Headquarters December 26, 1978. Paper No. 79-G7-125.

Copyright © 1980 by ASME

Downloaded 01 Jun 2010 to 171.66.16.58. Redistribution subject to ASME license or copyright; see http://www.asme.org/terms/Terms_Use.cfm

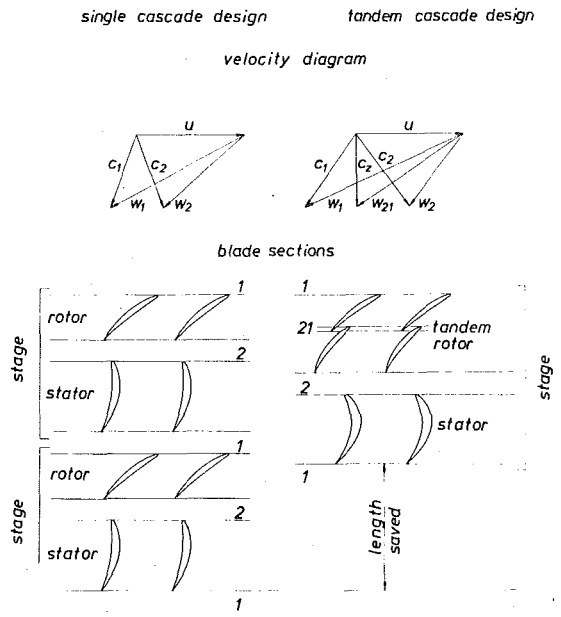


Fig. 2 Comparison of single cascade and tandem cascade design

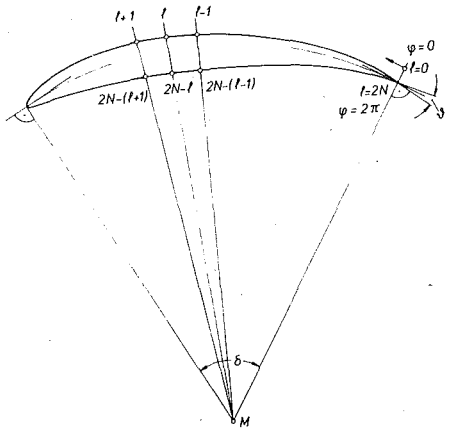


Fig. 3 Determination of the fixed points

a multi-stage test compressor were optimized throughout the blade height for the smallest profile losses.

Optimization Method

The cascade investigations published up to now have shown that for the relative cascade spacing a/ℓ_1 and the relative cascade displacement h/t of the optimum cascade configurations no generally valid values can be given.

This is due to fact that the optimum cascade configuration via the geometry of the gap depends on the profile form and on the stagger angles β_{s1} and β_{s2} of the cascades 1 and 2 (Fig. 1). The stagger angles β_s are influenced by the flow coefficient, the degree of reaction and the chosen vortex distribution of the blading to be designed. To take into account these different influences a potential theory method for calculation of the static pressure distributions with incompressible flow for any tandem cascade is chosen [4]. The influence of the flow interference is also taken into consideration for various spacings and displacements of the cascades.

The determination of the pressure distribution is followed by a boundary layer calculation for ascertaining the profile losses [5].

Pressure Distributions

The method chosen is based on a continuous vortex distribution of the profile contour. The basis of this is the consideration that the vortex strength applied to the profile contour induces certain velocities on each of the fixed points of the profile. These velocities are dependent on the particular influence point and its distance from the considered fixed points. The profile contour (Fig. 3) is given by

$$x = x(\varphi), \qquad y = y(\varphi). \tag{1}$$

It is assumed that the fractions $x(\varphi)$ and $y(\varphi)$ for profiles with a sharpened trailing edge must be explained in an open interval

$$0 < \varphi < 2\pi.$$

With the exception of the trailing edge point the derivations $\dot{x}(\varphi)$ and $\dot{y}(\varphi)$ may not be simultaneously equal to zero at any point. The transformed vortex strength $\gamma(\varphi)$ is defined by the equation

$$\gamma(\varphi) = w(\varphi) \cdot \sqrt{\dot{x}^2(\varphi) + \dot{y}^2(\varphi)} \tag{2}$$

and corresponds to the vortex distribution on the contour. $w(\varphi)$ is the velocity distribution to be ascertained. For the desired function $\gamma(\varphi)$ in [4] the following equation system is given

$$\left.\begin{aligned} &\gamma(\ell) - \frac{1}{2N}\sum_{k=1}^{2N-1}\left[K(1,\ell,k) + \frac{2\pi}{t}\dot{y}(1,\ell)\right]\gamma(k) \\ &\quad - \frac{1}{2N}\sum_{k=2N}^{4N-2}\left[K(2,\ell,k) + \frac{2\pi}{t}\dot{y}(2,\ell)\right]\gamma(k) \\ &= 2w_1[x(1,\ell)\sin\beta_1 - y(1,\ell)\cos\beta_1] \quad \ell = 1, 2, \ldots 2N-1 \end{aligned}\right\} \tag{3}$$

$$\left.\begin{aligned} &\gamma(\ell) - \frac{1}{2N}\sum_{k=1}^{2N-1}\left[K(4,\ell,k) + \frac{2\pi}{t}\dot{y}(1,\ell)\right]\gamma(k) \\ &\quad - \frac{1}{2N}\sum_{k=2N}^{4N-2}\left[K(3,\ell,k) + \frac{2\pi}{t}\dot{y}(2,\ell)\right]\gamma(k) \\ &= 2w_1[\dot{x}(2,\ell)\sin\beta_1 - \dot{y}(2,\ell)\cos\beta_1] \quad \ell = 2N, \ldots 4N-2. \end{aligned}\right\} \tag{4}$$

The range from 1 to $2 \cdot N - 1$ indicates the points of cascade 1; the range from $2 \cdot N$ to $4 \cdot N - 2$ belongs to the points of cascade 2 (Fig. 3). With the functions $K(2, \ell, k)$ and $K(4, \ell, k)$ the fixed points and influence points are at different cascades. The indices 1 and 2 in the derivations of x and y indicate the cascades 1 and 2. For the stagnation point at the trailing edge the vortex strength is fixed as zero. If in the equation system (3) and (4) the equations for $\ell = 2N - 1$ and $\ell = 4N - 2$ are replaced by the conditions

$$\gamma(2N-1) = -\gamma(1) \tag{5}$$

and

$$\gamma(4N-2) = -\gamma(2N) \tag{6}$$

one gets a linear independent equation system for the unknown vortex strength $\gamma(\ell)$.

As per equation (2) the pressure distribution for the profiles of the tandem cascades can then be given according to the equation

$$c_p(\ell) = 1 - \left(\frac{w(\ell)}{w_1}\right)^2 \tag{7}$$

with the dimensionless pressure coefficient c_p.

With the relations

$$\Gamma_1 = \frac{\pi}{N}\sum_{\ell=1}^{2N-1}\gamma(\ell), \quad \Gamma_2 = \frac{\pi}{N}\sum_{\ell=2N}^{4N-2}\gamma(\ell) \tag{8), (9}$$

for the circulation Γ_1 and Γ_2 of the cascades 1 and 2 the outlet angle of the homogeneous flow downstream of both cascades can be determined. For the outlet angle β_{21} downstream the cascade 1, with the symbols per Fig. 1

$$ctg\,\beta_{21} = \frac{\Gamma_1}{t w_1 \sin\beta_1} + ctg\,\beta_1 \tag{10}$$

is obtained.

The outlet angle β_2 of the tandem cascade is thus

$$ctg\,\beta_2 = \frac{\Gamma_1 + \Gamma_2}{t w_1 \sin\beta_1} + ctg\,\beta_1. \tag{11}$$

Profile Losses

The profile losses are determined on the basis of a boundary layer

Downloaded 01 Jun 2010 to 171.66.16.58. Redistribution subject to ASME license or copyright; see http://www.asme.org/terms/Terms_Use.cfm

calculation per Truckenbrodt [5]. The method is used for single as for tandem cascades. The pressure distributions determined as per the potential theory method are used as a basis. As the boundary layer calculation to Truckenbrodt can generally be assumed to be known, a detailed representation of the calculating procedure is not being given. Further information and addenda for determining the transition point as well as the separation losses can be found in [3].

With the calculated boundary layers the values for the displacement thickness δ_{1HK} and for the momentum thickness ζ_{HK} at the trailing edges (index HK) of the profiles are given.

For the dimensionless displacement thickness Δ^* and the dimensionless momentum thickness θ at the trailing edge as per [6] the following abbreviations are used

$$\Delta^* = \frac{\delta_{1HK,S} + \delta_{1HK,D}}{t \cdot \sin \beta'_2}, \tag{12}$$

$$\theta = \frac{\zeta_{HK,S} + \zeta_{HK,D}}{t \cdot \sin \beta'_2}, \tag{13}$$

$$\chi = \frac{1 - \theta - \Delta^*}{(1 - \Delta^*)^2}. \tag{14}$$

Herein the indices S and D refer to the suction and pressure sides of the profile. β'_2 is the outlet angle in the trailing edge plane. According to Schlichting and Scholz [6] it can be equated in the mean with the outlet angle β_{2id} of the potential flow. The outlet angle β_{2id} was previously determined with the calculation for the pressure distribution of the tandem cascade configuration. The profile losses can be calculated by the application of the impulse theorem to the upstream flow. The loss coefficient is given by

$$\zeta' = \frac{2\Delta^* - \Delta^{*2}}{(1 - \Delta^*)^2} - 2(\chi - 1)\sin^2 \beta_{2id} - (\chi^2 - 1)\cos^2 \beta_{2id}. \tag{15}$$

On determination of the loss coefficient the trailing edge loss is considered by adding in equation (12) the thickness of the trailing edge analogously to the displacement thicknesses at the trailing edge. Instead of equation (12) the equation

$$\Delta^* = \frac{\delta_{1HK,S} + \delta_{HK,D} + S_{HK}}{t \cdot \sin \beta'_2} \tag{16}$$

is now used.

For the single cascades 1 and 2 of the tandem cascade the loss coefficients ζ'_1 and ζ'_2 as per equation (15) were determined. These loss coefficients are defined by

$$\zeta'_{1,2} = \frac{\Delta g_{1,2}}{q_{21,2id}} \tag{17}$$

with the differences of the total pressures Δg_1 and Δg_2 for cascade 1 and cascade 2. q_{21id} and q_{2id} represent the dynamic pressures of the nonviscous outlet flow of the two cascades. However, it is usual for retarding cascades to refer the loss coefficient to the dynamic pressure of the inlet flow. Therefore the loss coefficients ζ'_1 and ζ'_2 are converted as per the relations

$$\zeta_1 = \zeta'_1 \left(\frac{\sin \beta_1}{\sin \beta_{21}}\right)^2, \tag{18}$$

$$\zeta_2 = \zeta'_2 \left(\frac{\sin \beta_1}{\sin \beta_2}\right)^2. \tag{19}$$

Thus the loss coefficients ζ_1 and ζ_2 correspond to the definition

$$\zeta_{1,2} = \frac{\Delta g_{1,2}}{q_1}. \tag{20}$$

This further has the advantage that from the loss coefficients thus determined for both cascades, as per the relation

$$\zeta = \zeta_1 + \zeta_2 \tag{21}$$

the loss coefficient for the tandem cascade can be easily ascertained.

Taking into consideration the friction the outlet angle β_{2id} ascertained by the potential theory method alters. For the cascades 1 and 2 of the tandem cascade the actual outlet angle β_{21} resp. β_2 is calculated using equation (14) with the relation

$$ctg\ \beta_{21,2} = ctg\ \beta_{21,2id}\chi. \tag{22}$$

β_{21id} and β_{2id} represent the outlet angle for both cascades with potential flow.

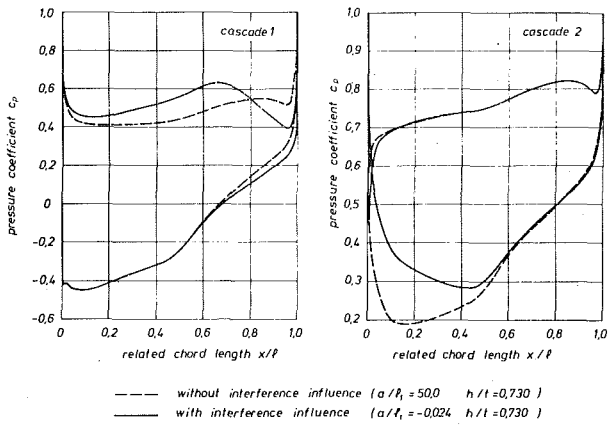


Fig. 4 Pressure distribution for the examined tandem cascade

Table 1 Design data tandem cascade

Reference	Dimension	cascade 1	cascade 2
ℓ	mm	55.5	57.0
t	mm	62.7	62.7
t/ℓ	-	1.13	1.10
d/ℓ	-	0.088	0.088
β_1, β_{21}	deg	155.5	146.5
β_{21}, β_2	deg	146.5	127.8
$\Delta\beta_1$, $\Delta\beta_2$	deg	9.0	18.7
w_{21}/w_1	-	0.75	-
w_2/w_{21}	-	-	0.70
β_s	deg	147.1	133.3
$\Delta\beta$	deg	27.7	
w_2/w_1	-	0.525	

Results

The optimization calculations were carried out by a FORTRAN computer program for the incompressible flow. The influence of the boundary layers on the pressure distributions remains unconsidered. This is admissible as long as the boundary layers at the profiles are relatively thin and the flow has not separated. Moreover, an influencing of the boundary layer development at the cascade 2 by the wake zone of cascade 1 was not acquired. It only occurs with a few configurations with positive cascade spacing a, which has, however, not been further investigated here.

The influence of flow interference on the tandem cascades, pressure distributions were compared with that of single cascades 1 and 2 which are marked by an infinitely large cascade spacing from each other. In this case mutual influencing of the flow by cascades 1 and 2 can no longer occur. Fig. 4 shows the pressure distributions for the chosen tandem cascade, determined by calculation both with and without flow interference. The investigated tandem cascade corresponds with the mean section of the tandem cascade rotor blade of a test compressor (Table 1). The pressure distributions were each calculated with 20 fixed points on the suction and pressure side of the profiles. For the case without the influence of interference the pressure distributions were determined with the relative cascade spacing a/ℓ_1 of 50.0. This value is large enough since on the basis of several calculations, influences of interference by the potential theory method were found only for relative cascade spacings a/ℓ_1 up to 0.8. Thus the pressure distributions calculated with the relative cascade spacing

Downloaded 01 Jun 2010 to 171.66.16.58. Redistribution subject to ASME license or copyright; see http://www.asme.org/terms/Terms_Use.cfm

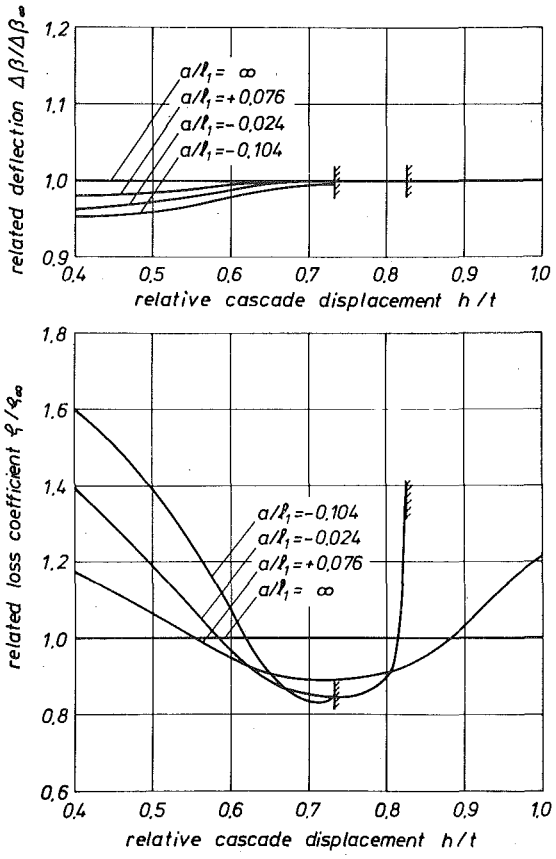


Fig. 5 Deflection and loss coefficient as a function of the relative cascade displacement for the examined tandem cascade, $Re_1 = 3{,}5 \cdot 10^5$

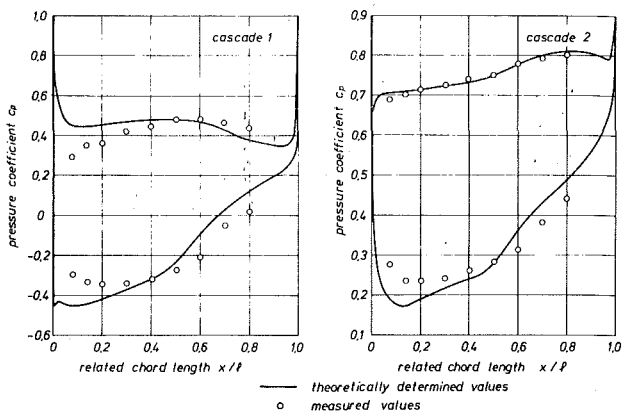


Fig. 6 Comparison of measured and calculated pressure distributions for the examined tandem cascade, $a/\ell_{1min} = -0.024$, $h/t = 0{,}73$

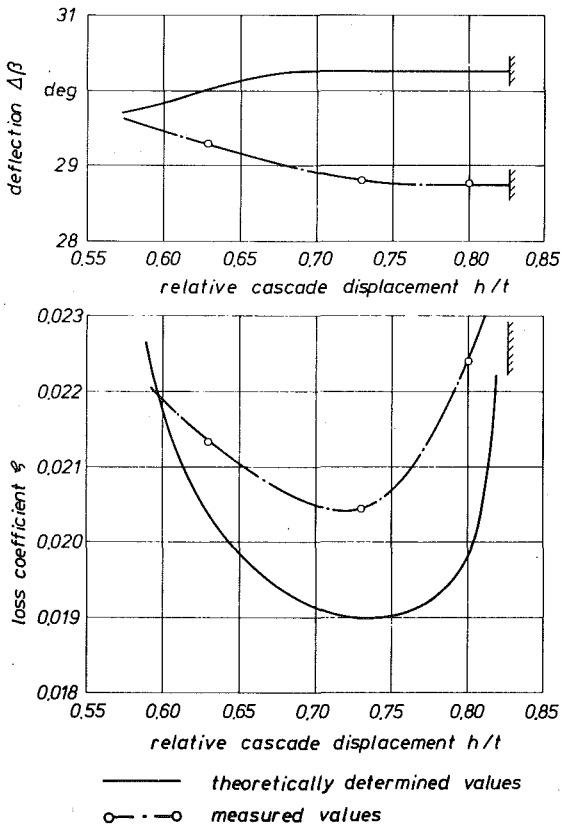


Fig. 7 Comparison of measured and calculated values for the deflection and loss coefficient of the examined tandem cascade, $Re_1 = 4.21 \cdot 10^5$, $\beta_1 = 155.5$ deg, $a/\ell_{1min} = -0{,}024$

a/ℓ_1 of 50.0 correspond to the pressure distributions with an infinitely large cascade spacing.

From Fig. 4 it can be seen that the static pressure on the pressure side of the first cascade is, as a result of the stagnation effect of the second cascade, at first above the static pressure with relatively large spacing if they behave like two single cascades without mutual influence.

With the investigated tandem cascades in close configuration the static pressure in the vicinity of the trailing edge was reduced somewhat as a result of the slight acceleration of flow in the gap which shows the channel geometry of a nozzle. This causes reduction of the boundary layer on the pressure side of the profiles of cascade 1 thus resulting in smaller losses for the cascade 1. Contrary to this for the second cascade a relatively great influence of interference was determined on the suction side of the profile. This effects a reduction in the maximum velocities on the suction side of the cascade 2 and thus a reduction in the aerodynamic load for this cascade.

It can be seen from Fig. 4 that the static pressure distributions of the tandem cascade with close configuration differ considerably from the pressure distributions of a tandem cascade with very large cascade spacing. This shows that the influence of interference may not be neglected for the design of the tandem cascade.

Fig. 5 shows the results of pressure distribution and boundary layer calculations for the examined tandem cascade which for various cascade configurations basically supply the outlet angle β_2 and/or the deflection $\Delta\beta$ and the loss coefficient ζ. The calculations were carried out for inlet Reynolds numbers of 3.5×10^5. Fig. 5 gives the related deflection $\Delta\beta/\Delta\beta_\infty$ and the related loss coefficient ζ/ζ_∞ as a function of the relative cascade displacement h/t with the relative cascade spacing a/ℓ_1 as a parameter. The flow deflection $\Delta\beta_\infty$ thus results according to the relation

$$\Delta\beta_\infty = \Delta\beta_1 + \Delta\beta_2 \tag{23}$$

as the sum of the deflections $\Delta\beta_1$ and $\Delta\beta_2$ for the cascades 1 and 2 with an infinitely large cascade spacing. ζ_∞ is then with the equation

$$\zeta_\infty = \zeta_1 + \zeta_2 \tag{24}$$

the sum of the loss coefficients of both noninfluenced cascades 1 and 2. Thus the quotients $\Delta\beta/\Delta\beta_\infty$ and ζ/ζ_∞ represent the values (index$_\infty$) related to the theoretically infinitely large cascade spacing a for the deflection $\Delta\beta$ and for the coefficient of the profile losses ζ. For numerical reasons the variables for the infinitely large cascade spacing were calculated again with a maximum relative cascade spacing a/ℓ_1 of 50.0. The upper part of the graph shows that the influence of the tandem cascade configuration on the deflection $\Delta\beta$ in the range of optimum relative cascade displacements is relatively small. From Fig. 5 it can further be seen that the profile losses within a range of differing relative displacements h/t can be minimized. Fig. 5 also shows that the profile losses with the optimum tandem cascade configuration can be approximately 10 to 18 percent below the values of the corresponding single cascades without interference influence. This result was confirmed by measurements by Ihlenfeld [7] and Pal [4] which

Downloaded 01 Jun 2010 to 171.66.16.58. Redistribution subject to ASME license or copyright; see http://www.asme.org/terms/Terms_Use.cfm

were carried out on similar tandem cascades with comparable close cascade configuration.

In Fig. 5 curves exist only in the range of the relative cascade displacement h/t and of the relative cascade spacing a/ℓ_1, in which the profiles of the cascades 1 and 2 do not touch. Fig. 5 further shows that the losses of the tandem cascades outside the optimum range, in particular towards smaller relative cascade displacements h/t, increase considerably and can in principle exceed the losses of the corresponding single cascades ($a/\ell = \infty$). Depending on the cascade spacing and displacement, losses can reach up to 100 percent.

As could be expected, the influence of the flow interference on the deflection and on the losses of tandem cascades increases when the cascade spacing becomes smaller and the cascade displacement greater (Fig. 5).

Comparison with Measuring Results

Measurements with quasi-incompressible flow for the tandem cascade were compared with the theoretically determined values. In addition to the general boundary layer data and the cascade parameters, the Reynolds number Re_1 known from the tests and the investigated inlet angle β_1 were used in the calculation.

In Fig. 6 the measured and the calculated static pressure distributions for the examined tandem cascade are shown. It can be seen that the calculation correctly reproduces the influencing of the static pressure distribution which is caused in the case of close tandem configurations by flow interference basically on the pressure side of cascade 1 and on the suction side of the tandem cascade 2. It can be concluded from this that the pressure distribution of the tandem cascades for the investigated range of the cascade spacings and cascade displacements can be acquired with the above procedure to the potential theory method.

Fig. 7 shows for the examined tandem cascade the curves of the calculated and measured values for the deflection $\Delta\beta$ and for the loss coefficient ζ as a function of the relative cascade displacement h/t.

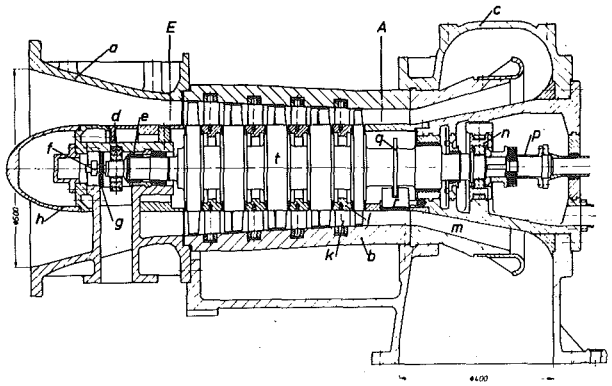


Fig. 8 Tandem cascade compressor: a = inlet casing, b = stator blade carrier, c = outlet casing, d = journal bearing, e = labyrinth seal, f = co-rotational transmitter, g = receiving antenna, h = locking cap, k = stator blade, l = shroud, m = diffuser, n = double thrust bearing, p = coupling, q = collar for monitoring axial play, r = measuring coil, t = rotor with rotor blades, E = plane blading inlet, A = plane blading outlet

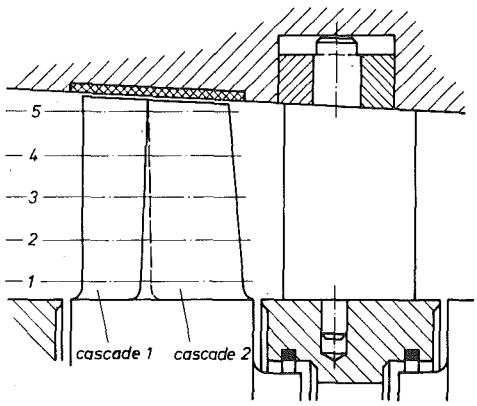


Fig. 9 Compressor stage

Compared with the calculation the measurements have shown that with increasing relative cascade displacement h/t the deflection of the tandem cascades decreases slightly. This is due to the influencing of the boundary layers increasing with the cascade displacement, at the suction sides of the profiles of cascade 2 on account of the wakes of cascade 1. The calculated deflections are on average 1.0 to 2.0 deg greater than the measured values (Fig. 7). These deviations are due to the fact that the reduced deflection caused by friction was not completely reproduced by the calculation.

In all, four different tandem cascades with deflections $\Delta\beta$ between 19.6 and 48.3 degrees were recalculated. The comparison of the measurements with the calculated values shows that the method of calculation used correctly reproduces the curve of the measured loss coefficients ζ and the minimum of losses as a function of the cascade configuration. This method is thus suitable to be applied for the aerodynamic optimization of tandem cascade blades.

Optimization of a Tandem Cascade Rotor Blade

It is shown how a tandem cascade rotor blade for a multi-stage axial flow compressor can be optimized with the above method of calculation over the entire blade height for the smallest possible profile losses. The method is applied to the radial sections of the tandem cascade rotor blade.

Compressor Stage

The tandem cascade axial flow compressor used is designed for a

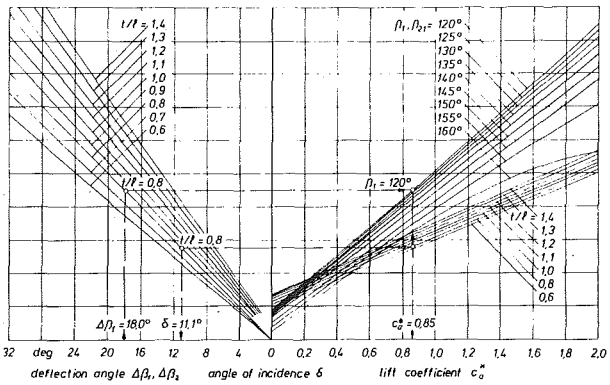


Fig. 10 Layout nomogram

Table 2 Profile and cascade data tandem cascade rotor blade cascade 1

Sections	Dimension	1	2	3	4	5
r	mm	114.5	127.0	139.5	152.0	164.5
t	mm	34.25	38.0	41.8	45.4	49.25
ℓ	mm	35.0	36.0	37.0	38.0	39.0
t/ℓ	-	0.978	1.056	1.130	1.195	1.263
β_1	deg	155.5	155.0	155.5	156.7	158.6
β_{21}	deg	141.0	143.8	146.5	148.6	150.5
$\Delta\beta_1$	deg	14.5	11.2	9.0	8.1	8.1
c_a^*	-	1.06	0.81	0.71	0.68	0.72
β_s	deg	144.0	145.4	147.1	148.8	150.6
d/ℓ	-	0.100	0.094	0.088	0.082	0.076

Table 3 Profile and cascade data tandem cascade rotor blade cascade 2

Sections	Dimension	1	2	3	4	5
r	mm	114.5	127.0	139.5	152.0	164.5
t	mm	34.25	38.0	41.8	45.4	49.25
ℓ	mm	35.0	36.5	38.0	39.5	41.0
t/ℓ	-	0.978	1.041	1.100	1.150	1.201
β_{21}	deg	141.0	143.8	146.5	148.6	150.5
β_2	deg	109.0	119.4	127.8	134.1	139.0
$\Delta\beta_2$	deg	32.0	24.4	18.7	14.5	11.5
c_a^*	-	2.12	1.70	1.37	1.11	0.92
β_s	deg	121.6	128.0	133.3	137.6	141.0
d/ℓ	-	0.100	0.094	0.088	0.082	0.076

Downloaded 01 Jun 2010 to 171.66.16.58. Redistribution subject to ASME license or copyright; see http://www.asme.org/terms/Terms_Use.cfm

degree of reaction of 100 percent (Fig. 8). For the axial flow compressor designed a homogeneous blading based on the free vortex was selected. The compressor stages each consist of a tandem cascade rotor and a single cascade stator (Fig. 9). The axial flow compressor for which the optimization of a tandem cascade rotor blade is represented has been designed for the fluid air. The data for the design point are: pressure ratio $\pi_{tot} = 2.5$, mass flow rate $\dot{m} = 6.6$ kg/s, speed $n = 11{,}000$ rpm, number of stages $z = 4$.

The tandem cascade rotor blade to be optimized was designed with five radial sections (Fig. 9). The curve of the flow angle as a function of the blade height is fixed on the basis of the thermodynamic design of the compressor with a multi-section method [3]. NACA 65 profiles were selected. For the given flow angle the layout nomogram (Fig. 10) with the pitch ratio t/ℓ supplies the lift coefficient c_a* and the stagger angle β_s (Tables 2 and 3). The layout nomogram is based on numerous cascade measurements on NACA profiles [8].

Optimum Cascade Configurations

For an optimum tandem cascade rotor blade if possible all radial sections must show optimum tandem cascade configurations over the blade height. The task of optimization is to determine the relative cascade spacing a/ℓ_1 and the relative cascade displacement h/t for the sections 1 to 5 (Fig. 9) such that the resultant tandem cascade configurations give the smallest possible profile losses. The following condition should apply here that the center of gravity for the profiles of any radial section of both cascades must lie on the radial vectors to avoid additional bending stresses in the blade as a result of centrifugal forces.

Optimizaiton of the tandem cascade rotor blade is started at the lowest section of the blade, section 1. For section 1 the optimum cascade configuration is determined using the calculation method. With the corresponding profile and cascade data (Tables 2 and 3) section 1 of the tandem cascade rotor blade can be drawn. To fulfil the above condition all the centers of gravity for the profiles of the cascades 1 and 2 must be on radial vectors. They run through the centerline of the rotor (Fig. 11). For optimization of the blade sections 2 and 5 it must be considered that the displacement h of the cascades 1 and 2 in the circumferential direction alters due to the arrangement of the profile centers of gravity on radial vectors and due to the twist of the blades over the blade height. It is recommended that firstly the optimum tandem cascade configuration is to be determined for the tip section, section 5. As the stagger angles β_s have been fixed by the profile layout the optimum cascade displacement h/t_{opt} can only be achieved for section 5 if one chooses greater chord lengths as compared with the hub section. In this case the chord lengths increase lineally for both cascades from the hub to the tip section. The values for the cascade spacings a can be seen from the drawings for sections 2 to 4. With the relative cascade spacings a/ℓ_1 thus determined the pressure distribution and boundary layer calculations are carried out for each section using the above described method. The results of these optimization calculations for all five sections of the tandem cascade rotor blade can be seen from Fig. 12. Here the related deflection $\Delta\beta/\Delta\beta_\infty$ and the related loss coefficient ζ/ζ_∞ for the above determined cascade spacings a/ℓ_{1min} of sections 1 to 5 are shown as a function of the relative displacement h/t. The optimization calculation is based on a Reynolds number of 3.5×10^5. In the lower part of Fig. 12 the connection between the radial sections and the relative cascade displacement h/t is given. For the radial sections it can be seen from the diagram for the related loss coefficient ζ/ζ_∞ that all sections give optimum cascade arrangements with minimum losses. The reduction of the profile losses if compared with single cascades decreases from section 1 with 24 to section 5 to 12 percent.

Since it has been shown that larger gaps rather than smaller ones are of advantage, for section 1 of the tandem cascade rotor blade an optimum relative displacement h/t_{opt} was selected which compared with the corresponding value determined from Fig. 12 is 5 percent points smaller.

Optimization has shown that for the selection of the optimum tandem cascade configurations for the hub and the tip sections the tandem cascades of all sections between them are also optimum. Si-

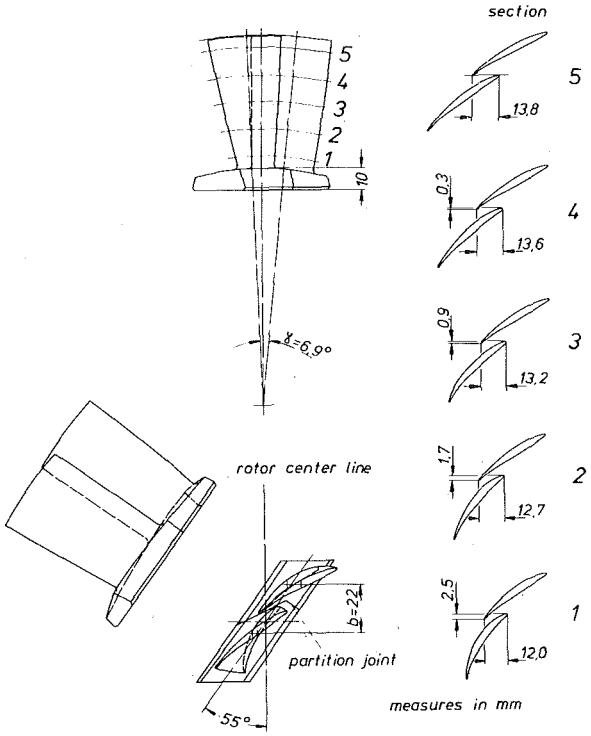


Fig. 11 Tandem cascade rotor blade

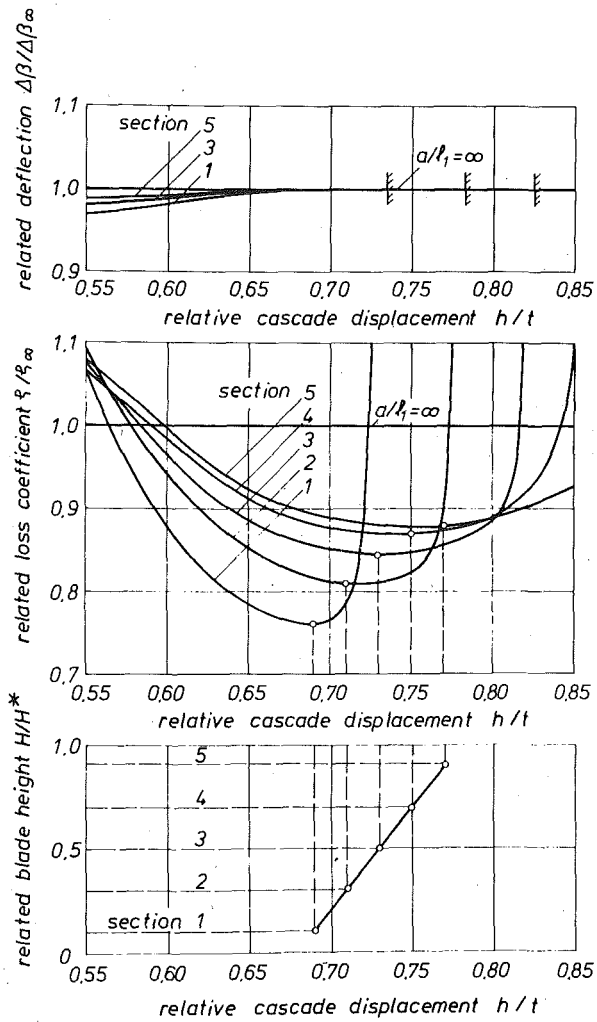


Fig. 12 Optimum cascade configurations for a tandem cascade rotor blade: section 1) $a/\ell_{1\,min} = -0.071$, section 2) $a/\ell_{1\,min} = -0.047$, section 3) $a/\ell_{1\,min} = -0.024$, section 4) $a/\ell_{1\,min} = -0.008$, section 5) $a/\ell_{1\,min} = 0$

Downloaded 01 Jun 2010 to 171.66.16.58. Redistribution subject to ASME license or copyright; see http://www.asme.org/terms/Terms_Use.cfm

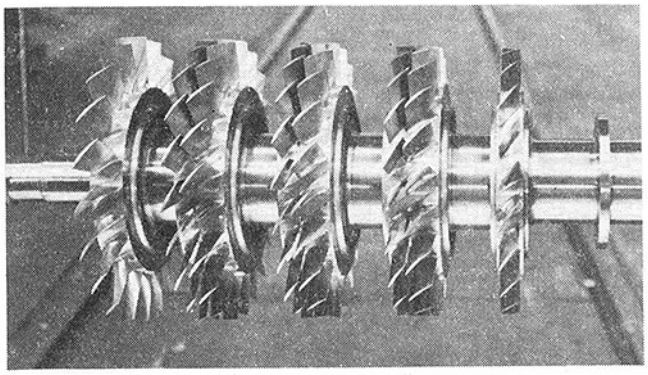


Fig. 13 Rotor of tandem cascade compressor

multaneously the condition for the centers of gravity of all profiles to lie on radial vectors could be fulfilled. Thus tandem cascade rotor blades can also run with relatively high circumferential speed.

The chosen tandem cascade rotor blade was optimized with the above method for the smallest possible profile losses. Since per Ihlenfeld [7] in addition to the profile losses the secondary and wall boundary layer losses which occur in the area of the casing wall and in the vicinity of the hub are favorably influenced by the optimum tandem cascade configuration.

The last two Figs. 13 and 14 show the rotor and the above optimized tandem cascade rotor blade of the test compressor. This compressor was designed and investigated by the Institute for Turbomachinery Hannover University in Germany. It was manufactured by GHH Sterkrade, Germany.

Summary

A procedure is presented to determine the pressure distribution, profile losses and outlet angles for different configurations of tandem cascades for axial flow compressors. The pressure distributions and profile losses of tandem cascade with close configurations differ considerably from the flow through tandem cascades with large axial spacing. It was found that the interference effect should not be neglected for the design of tandem cascades. Using an example it is shown how the tandem rotor blades for a multi-stage test compressor were optimized over the height for minimum profile losses.

References

1 Bammert, K., and Staude, R. "Experimentelle Untersuchungen an ebenen verzögernden Tandemgittern," *VDI-Berichte* No. 264, 1976, pp. 81/89.

2 Bammert, K. and Ahmadi, B., "Investigations on Impulse Blade Cascades with Medium Deflection," ASME JOURNAL OF ENGINEERING POWER, Paper No. 78-GT-12.

3 Staude, R., "Zur Optimierung von ebenen verzögernden Tandemgittern," Diss. TU Hannover, 1975.

4 Pal, P., "Untersuchungen über den Interferenzeinfluß bei Strömungen durch Tandem-Schaufelgitter," *Ing.-Archiv* 34, No. 3, 1965, pp. 173/193.

5 Truckenbrodt, E., "Ein Quadraturverfahren zur Berechnung der laminaren und turbulenten Reibungsschicht bei ebener und rotationssymmetrischer Strömung," *Ing.-Archiv* 20, No. 4, 1952, pp. 211/228.

6 Schlichting, H. and Scholz, N., "Über die theoretische Berechnung der Strömungsverluste eines ebenen Schaufelgitters," *Ing.-Archiv* 19, No. 1, 1951, pp. 42/65.

7 Ihlenfeld, H., "Strömungsvorgänge an stark verzögernden Spaltflügelgittern," Maschinenbautechnik 14, No. 7/8, 1965, pp. 361/65 and 420/424.

8 Herrig, L. J.; Emery, J. C. and Erwin, J. R., "Systematic Two-Dimensional Cascade Tests of NACA 65-Series Compressor Blades at Low Speeds," NACA TN 3916, 1957.

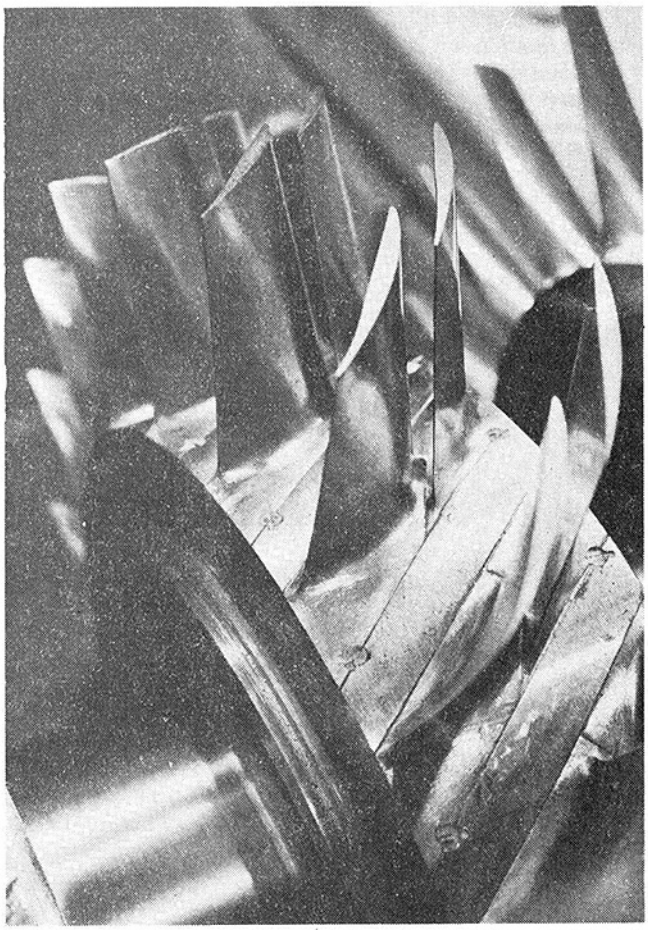


Fig. 14 Rotor blade of tandem design

Downloaded 01 Jun 2010 to 171.66.16.58. Redistribution subject to ASME license or copyright; see http://www.asme.org/terms/Terms_Use.cfm

R. A. J. Ford[1]
C. A. Foord
Mem. ASME

Advanced Research Laboratory,
Rolls-Royce Ltd.,
P.O. Box 31,
Derby, England

An Analysis of Aeroengine Fan Flutter Using Twin Orthogonal Vibration Modes

Flutter prediction methods for aeroengine fans at present typically combine a complex aerodynamic analysis with a simple model of the mechanical behavior of the fan. In this paper a more sophisticated model of the mechanical response is used to investigate flutter and provide additional insight into the physical mechanisms involved. The model incorporates twin orthogonal modes, which are two independent vibration patterns similar in shape and resonant frequency but displaced 1/4 wave circumferentially in space. Flutter can be thought of as a self excited vibration in which the response of each blade in one mode generates aerodynamic forces on the blades which drive the twin mode—and vice versa. The flutter frequency can be determined by considering the phasing between the twin modes; whether flutter does actually occur (at this frequency) depends upon the relationship between the aerodynamic force coefficients and the amplitude response of each mode. The greatest tendency to flutter occurs when the twin modes are identical in frequency. For the more practical case of a frequency split between the modes the tendency to flutter decreases with increased frequency separation, and the vibration pattern becomes non-uniform. The non-uniformities include unequal blade amplitudes, unequal interblade phase angles, variation from blade to blade in the temporal phase between twist and flap within each individual blade, and a deflected shape which is not sinusoidal circumferentially.

Introduction

Supersonic unstalled flutter in aeroengine fans is a self excited unstable vibration which imposes a limit to the maximum speed of the fan. Prediction methods are needed for assessing whether flutter will occur within the operating speed range of a particular fan design. It is also necessary to know how to modify a fan which is susceptible to flutter so that the problem can be eliminated in the most effective manner.

Flutter occurs when a mechanical vibration of the fan gives rise to unsteady aerodynamic forces which feed energy into the fan and sustain (or increase) the vibration amplitude [1, 2, 3]. There are two aspects to the phenomenon:

1 The mechanical behavior of the fan. Flutter is very sensitive to the deflected shapes of the individual blades of the fan, and the relative motion between them.
2 The unsteady aerodynamic behavior of the fan. This determines the unsteady aerodynamic forces generated in response to unsteady motion of the blades.

Any flutter analysis must model both aspects. Current published methods, e.g., [1], use a simplified mechanical model of the fan with advanced aerodynamics. This paper describes an alternative approach in which a more rigorous mechanical model is combined with simplified aerodynamics. It was originally developed to enable experimental studies of stationary vibrating fans [4] to be related more effectively to flutter, but in addition, the understanding to be gained from this approach is a further step towards a complete analysis in which the aerodynamics and vibrations are both modelled accurately.

The mechanical model to be used is based on twin orthogonal modes. Experimental studies of real fans reveal pairs of spatially orthogonal vibration modes which have similar shapes but slightly different natural frequencies. These independent vibrations can occur simultaneously so that each blade in the fan responds to both modes (but differently in each) and the total response of the blade is the sum of two components. The resultant motion depends upon the relative phase and amplitude of these two components. In a previous paper [4] each disk mode was studied in isolation and the modes added vectorially to produce the blade motions seen in flutter. In that study the values of relative phase and amplitude used were chosen according to the analysis described in this paper.

Flutter can be thought of as an interaction between the modes of

[1] Now at: School of Mechanical and Industrial Engineering, The University of New South Wales, P.O. Box 1, Kensington, N.S.W. 2033, Australia.

Contributed by the Gas Turbine Division and presented at the Gas Turbine Conference and Exhibit and Solar Energy Conference, San Diego, California, March 12–15, 1979 of THE AMERICAN SOCIETY OF MECHANICAL ENGINEERS. Manuscript received at ASME Headquarters December 18, 1978. Paper No. 79-GT-126.

Copyright © 1980 by ASME

Downloaded 01 Jun 2010 to 171.66.16.58. Redistribution subject to ASME license or copyright; see http://www.asme.org/terms/Terms_Use.cfm

an orthogonal pair, in which the response of each blade in one of the twin modes produces aerodynamic forces on the blades which drive the second mode, and vice versa [5]. This is shown in the feed-back loop of Fig. 1. This loop is unstable for a fan in a flutter condition and any disturbance to the system will initiate a self excited vibration which will persist, without external forcing, after the disturbance is removed (note, the location of the disturbance on the block diagram is arbitrary and does not affect the stability boundary of the system). The unstable self excited vibration occurs if the aerodynamic forces due to mode I provided suitable and sufficient excitation for driving mode II while at the same time the aerodynamic forces due to mode II provide suitable and sufficient excitation for mode I. This requires:

1 correct phasing between the two modes,
2 forces which are large enough to sustain the motion.

The following analysis shows that phasing determines the frequency at which flutter will occur if it occurs at all, whereas whether flutter actually does occur depends upon the relationship between the aerodynamic forces and the mechanical response of the fan.

Behavior of Twin Orthogonal Fan Modes

The spatial arrangement of twin orthogonal modes is shown in Fig. 2. The circumferential mode shapes are assumed to be simple sinusoids.

The orthogonal modes are independent, and can therefore be excited independently. If each mode is excited at an antinode the exciters are 1/4 wave displaced circumferentially as shown in Fig. 2 and, as an antinode of one mode is a node of its twin, each exciter can excite only one of the two modes.

The response of each mode to sinusoidal excitation can be represented by a rotating vector (phasor) diagram. Fig. 3 shows the behavior of a pair of lightly damped modes for which the natural frequencies are only slightly different. For each pair of phasor diagrams the excitations for the two modes are in phase and of the same frequency. Changing this common frequency changes the magnitude and phase of each response as shown. The phase angle between the two responses can be seen for each frequency, and at any frequency it depends on the frequency separation between modes and the degree of damping.

Orthogonal Modes and Flutter

Aerodynamic Forces. For the purposes of this paper the unsteady aerodynamic forces due to a vibrating blade will be simplified to two components (see Appendix):

1 Bending forces due to bending deflections. These are in temporal phase with velocities (i.e., in temporal quadrature with deflections).
2 Bending forces due to twisting deflections. These are in temporal phase with deflections.

These are generally the major contributions, however extra terms can be added if required at the expense of some additional complexity.

It is further assumed that the aerodynamic forces for each mode are independent of motion in the other mode.

A net energy input (or output) for the vibration modes can be provided only by those force components in phase spatially with similar deflections. For example, bending forces in phase spatially with bending deflections can excite or damp the motion, whereas bending forces in spatial quadrature with bending deflections have no net effect.

Consider the clapper ring of a fan (the ring formed by the locked part span shrouds or snubbers) as shown in Fig. 4. Within each mode, the spatial phase between twist and flat waves is 90 deg (1/4 wave). It can be seen from the figure that in each mode bending forces due to twist are spatially phased such that they drive the twin, thus deflections in one mode produce forces phased to drive the other. Bending forces due to bending deflections are in spatial phase with their own deflections, i.e., in spatial quadrature with the twin mode, and cannot couple the modes, but provide "damping" (+ or −) within each mode (force proportional to velocity).

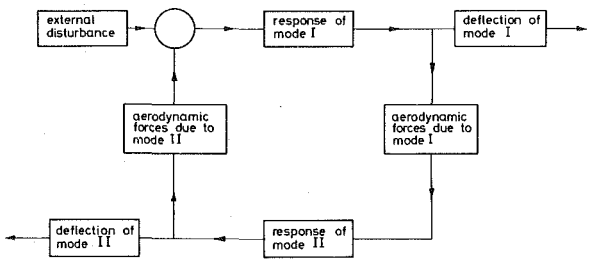


Fig. 1 The interaction of orthogonal modes to give flutter.

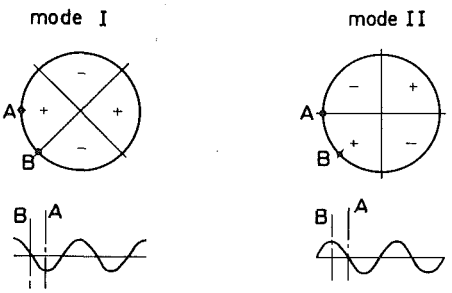


Fig. 2 The geometry of twin orthogonal modes. A and B show exciter positions 1/4 wave displaced.

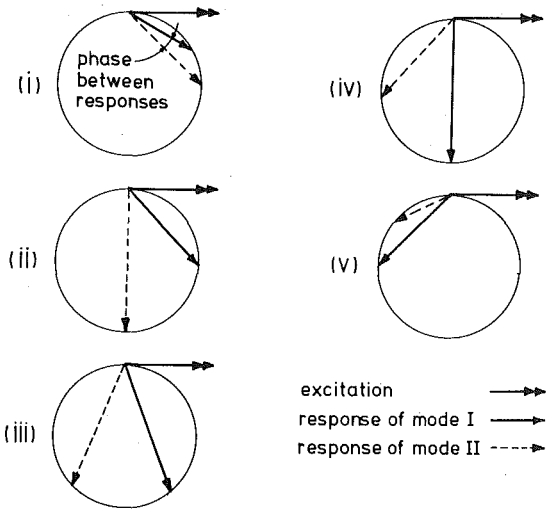


Fig. 3 Phasor diagrams for a pair of orthogonal modes at five frequencies. Frequency increases through the numbered sequence. Mode I has the higher natural frequency.

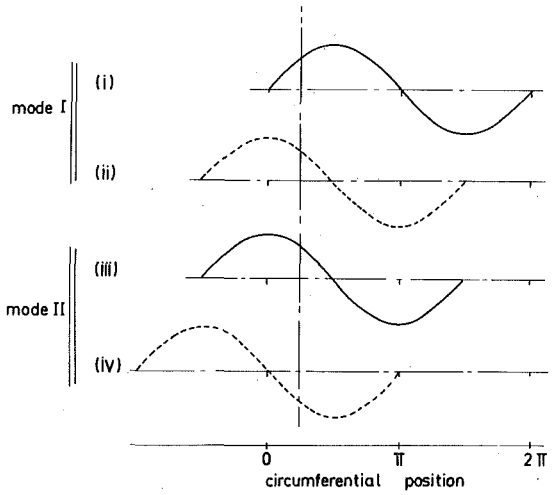


Fig. 4 Displacements and forces at the clapper ring. (i) Mode I: Flap and (in temporal quadrature) force due to flap, (ii) Mode I: Twist and force due to twist, (iii) Mode II: Flap and (in temporal quadrature) force due to flap, (iv) Mode II: Twist and force due to twist.

Downloaded 01 Jun 2010 to 171.66.16.58. Redistribution subject to ASME license or copyright; see http://www.asme.org/terms/Terms_Use.cfm

If we now consider the tip, Fig. 5, the spatial phase between the twist and flap waves is not generally 90 deg [4]. In this case, the force in bending due to twist must be resolved into two components. One component is ¼ wave displaced from the flap wave and couples the two modes as before; the other component is in spatial phase with the flap wave, and in temporal phase too, and its effect is to alter the effective stiffness of the mode.

Thus for an elemental annulus at any radius the integrated (circumferential) effects of the two classes of forces are:

1 Force due to bending: a velocity damping term within each mode,
2 Force due to twist; *a*) an additional stiffness term within each mode due to the spatial in phase component. *b*) an excitation of the other mode (cross coupling) due to the spatial quadrature component.

The overall behavior of the fan is the result of the integrated effect of conditions at all radial stations.

Mode Description. The interaction of the two modes can be examined by considering them to be two single-degree-of-freedom systems as below.

Effective mass m_1; m_2

Damping term $(2c/c_0)_1$; $(2c/c_0)_2$: mechanical damping plus (1) above

Stiffness term K_1; K_2: mechanical stiffness plus (2) above

Predicting the Flutter Frequency and Deflection Pattern

For flutter to occur the aerodynamic forces which couple the two modes must be suitably phased; that is the aerodynamic bending force due to twist in mode I must be in temporal phase with the bending deflection of mode II while simultaneously the force due to twist from mode II is in temporal phase with the bending deflection of mode I.

The nature of the coupling between modes can be seen from Fig. 6. The only forces shown are those due to twist; the other aerodynamic forces are included as damping and stiffness in the mode descriptions. In this model the forces due to twist are in phase with the twist, but aerodynamic phase lag can be readily incorporated if required.

Fig. 6 indicates that in one mode twist is in phase with flap whereas in the other mode it is 180 deg out of phase with flap. This results from the two modes being ¼ wave displaced as can be seen in Fig. 4, where at the blade position shown by the vertical line, twist and flap have the same sign for mode I and the opposite sign for mode II. Which of the two modes has the 180 deg phase shift depends upon the position chosen on the fan.

Fig. 6(*a*) shows the two modes with excitations in phase. However, as the modes are independent the phasing between excitations can be varied and this can be represented by rotating one phasor diagram relative to the other. In Fig. 6(*b*) the second phasor diagram has been rotated to bring the force due to twist in mode II in phase with the excitation required by mode I. In this condition mode II can drive mode I. It can now be seen from the figures that if angle β equals angle γ the force due to twist in mode I is in phase with the excitation required by mode II, and in this situation the twin modes are suitably phased to drive each other simultaneously.

Angles β and γ depend upon the frequency of excitation, the frequency split between the modes, the undamped natural frequency $[\sqrt{K/m}]$, and the amount of damping. Thus, given the mode description, the flutter frequency can be calculated.

For this model (no aerodynamic phase lag), flutter occurs at the frequency which puts each mode an equal amount, in terms of phase angle, away from resonance. This can be seen from Figs. 6(*c*) and (*d*), where with $\beta = \gamma$, the angles marked (90-β) and (90-γ), which measure the phase angle from resonance, are also equal in magnitude. In this case the amplitudes of the two modes are also the same. The phase angle between modes (i.e., between flap responses) is (180 deg-β) and is shown in Fig. 7 for a range of conditions.

If aerodynamic phase lags are introduced into the analysis, for example if force due to twist lags twist, then the two modes are not an equal amount from resonance and are not of equal strength.

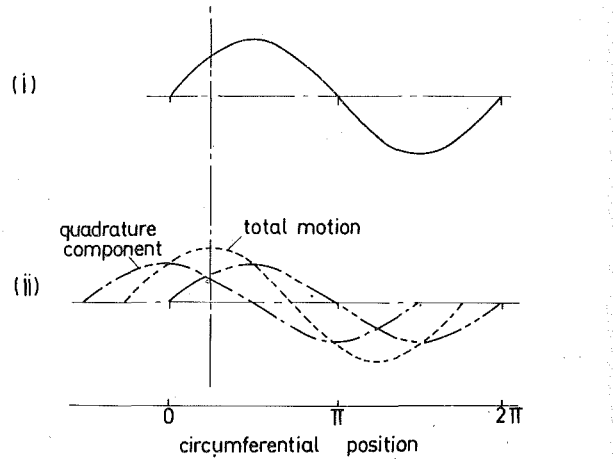


Fig. 5 Displacements and forces at the tip of fan. (i) Flap and (in temporal quadrature) force due to flap, (ii) Twist and force due to twist showing in phase and quadrature components.

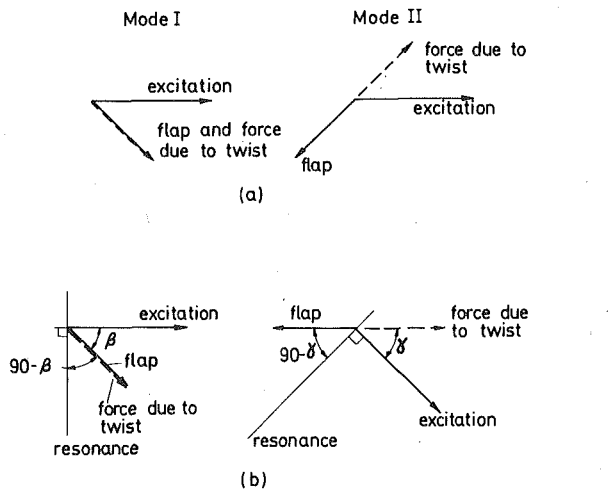


Fig. 6 Phasing of twin modes for flutter to occur

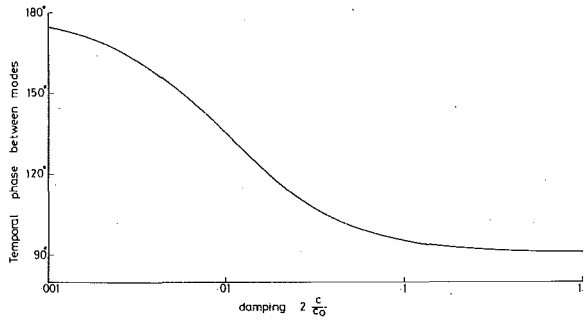


Fig. 7 Temporal phase between modes versus damping in each mode. ω_1/ω_2 = .99; p/ω_1 = 1.005.

Once the frequency at flutter and the relative amplitudes of the two modes are known, the deflected shape of a fluttering fan assembly (at a particular radius) can be calculated by vectorially adding the appropriate waves for the two modes.

It is only when the twin modes have identical natural frequencies that the total motion gives identical amplitudes for each blade, a constant interblade phase angle around the fan, and the temporal phase between twist and flap within each blade equal to 90 deg at the clapper radius, as assumed by the simplified mechanical model used in published flutter analyses [1].

Fig. 8 describes the total motion for one condition representative

Downloaded 01 Jun 2010 to 171.66.16.58. Redistribution subject to ASME license or copyright; see http://www.asme.org/terms/Terms_Use.cfm

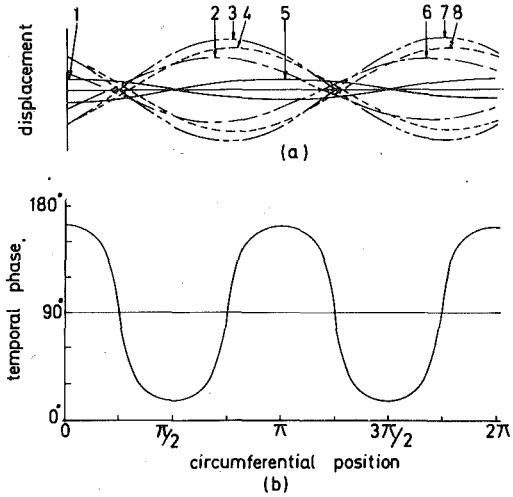


Fig. 8 Vibration behavior of a fluttering fan. Equal mode strengths: $\omega_2/\omega_2 = .99$; $2(c/c_0) = .003$. a) Displacements. Time intervals between successive curves $\pi/4$. Figures denote time sequence, b) Temporal phase between twist and flap in a single blade.

of a fluttering fan:

$$\frac{\omega_1}{\omega_2} = .99 \qquad 2c/c_0 = .003$$

The corresponding temporal phase angle between modes is:

$$\phi = 163 \text{ deg}$$

Fig. 8(*a*) shows the deflected shape at various times in the vibration cycle. This behavior shows that the motion can be thought of as a stationary wave and a traveling wave. These together produce a variation in vibration amplitude, from blade to blade, which is fixed relative to the fan. Thus the blade stresses vary from blade to blade.

The figure also shows that the wave does not move equal distances in equal time periods. Hence the interblade phase angle, which is important for the aerodynamic analysis, varied from blade to blade.

Fig. 8(*b*) shows that the time phase between twist and flap for a single blade at the clapper ring is not generally 90 deg and varies significantly around the disk at twice the spatial frequency of the flap wave. The phases at other radial stations can also be obtained but the analysis is complicated by the way in which the spatial phase between twist and flap in each of the twin modes varies with radial station.

The addition of orthogonal modes to give the total motion of a fluttering fan is analyzed in more detail in [4].

Predicting the Onset of Flutter

Phase considerations determine the frequency at which a fan will flutter if it flutters, and also the phase between modes and their relative amplitudes. Whether or not the fan does flutter at all is determined by the degree of aerodynamic coupling between the modes.

Interaction of Twin Orthogonal Modes. Fig. 1 shows a fan as a feed back loop; flutter corresponds to instability in this system. This can readily be analyzed using classical Automatic Control Theory, but, in the following treatment an alternative approach is used with the aim of providing additional insight into the physical mechanisms involved.

Each vibration mode is represented by a single-degree-of-freedom spring/mass/damper system. The mode descriptions and notation are as follows:

	Mode I	Mode II
Peak displacement	X_1	X_2
Peak exciting force	F_1	F_2
Natural frequency $\left(\sqrt{\frac{K}{m}}\right)$	ω_1	ω_2

Both modes have the same damping ratio c/c_0 and are driven at the same frequency p.

The steady-state amplitude for forced vibration of this kind is given by the standard relationship:

$$X = \frac{F}{k} \frac{1}{\sqrt{\left(1 - \left(\frac{p}{\omega}\right)^2\right)^2 + \left(2\frac{c}{c_0}\frac{p}{\omega}\right)^2}} \tag{1}$$

If X is less than the value given by equation (1) the amplitude must increase until the relationship is satisfied. Thus the equations below specify the conditions under which the vibration of each fan mode will be steady (equality) or increasing (inequality).

$$\left.\begin{aligned} \frac{X_1}{F_1} &\leqslant \frac{1}{K_1\sqrt{\left(1 - \left(\frac{p}{\omega_1}\right)^2\right)^2 + \left(\frac{2c}{c_0}\right)^2\left(\frac{p}{\omega_1}\right)^2}} \\ \frac{X_2}{F_2} &\leqslant \frac{1}{K_2\sqrt{\left(1 - \left(\frac{p}{\omega_2}\right)^2\right)^2 + \left(\frac{2c}{c_0}\right)^2\left(\frac{p}{\omega_2}\right)^2}} \end{aligned}\right\} \tag{2}$$

The definition of a mode contains a complete description of the deflected shape, so for each mode the degree of twist is proportional to flap amplitude, and the force due to twist (excitation for the other mode) is proportional to twist, so

$$F_1 = A_1X_2 \quad \text{and} \quad F_2 = A_2X_1 \tag{3}$$

where A_1, A_2 are constants describing the aerodynamic response to unsteady blade motion.

Substituting (3) in (2) gives:

$$\frac{X_1}{A_1X_2} \leqslant f\left(\frac{p}{\omega_1}\right); \quad \frac{X_2}{A_2X_1} \leqslant f\left(\frac{p}{\omega_2}\right) \tag{4}$$

Hence:

$$\frac{1}{A_1A_2} \leqslant f\left(\frac{p}{\omega_1}\right) \times f\left(\frac{p}{\omega_2}\right)$$

or

$$\frac{K_1K_2}{A_1A_2} \leqslant \frac{1}{\sqrt{\left(1 - \left(\frac{p}{\omega_1}\right)^2\right)^2 + \left(\frac{2c}{c_0}\frac{p}{\omega_2}\right)^2}} \times \frac{1}{\sqrt{\left(1 - \left(\frac{p}{\omega_2}\right)^2\right)^2 + \left(\frac{2c}{c_0}\frac{p}{\omega_2}\right)^2}} \tag{5}$$

or

$$C \leqslant M$$

where C denotes the left hand side and M the right hand side of (5). C is a dimensionless measure of the aerodynamic coupling between modes which is present in the vibration; strong coupling is represented by low values. M prescribes the degree of cross coupling that must be present before flutter occurs, and is proportional to the product of the receptances of the twin modes. Low values of M represent a lower likelihood of flutter. Fig. 9 plots M (calculated at the flutter frequency as determined earlier) against $(2c/c_0)$ for several values of mode frequency ratio (ω_1/ω_2).

Effect of Speed. From equation (5) flutter occurs when $C \leqslant M$. C and M both depend on fan speed. Typically they decrease as speed is increased, but C decreases faster than M and ultimately the flutter condition $C \leqslant M$ is reached.

The flutter condition can arise at any value of M, if C is low enough. However, the shapes of the curves in Fig. 9 are quite different at high and low damping, and this affects flutter behavior. In particular, the degree of damping determines the phase between the two modes, as discussed above, and therefore affects the shape of the total motion of the fan. Hence the absolute magnitudes of M and C are important as well as the relative magnitudes.

Downloaded 01 Jun 2010 to 171.66.16.58. Redistribution subject to ASME license or copyright; see http://www.asme.org/terms/Terms_Use.cfm

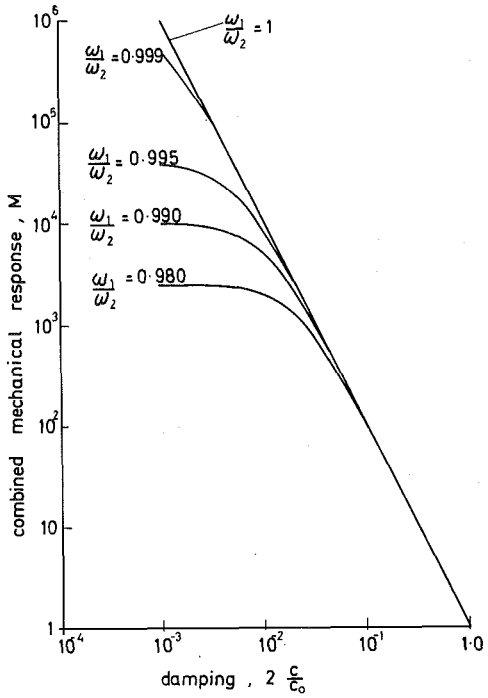


Fig. 9 ***M*** **versus damping:**

$$M = \frac{1}{\sqrt{\left(1-\left(\frac{p}{\omega_1}\right)^2\right)^2 + \left(\frac{2c}{c_0}\frac{p}{\omega_1}\right)^2}} \times \frac{1}{\sqrt{\left(1-\left(\frac{p}{\omega_2}\right)^2\right)^2 + \left(\frac{2c}{c_0}\frac{p}{\omega_2}\right)^2}}$$

For a given fan and mode, M depends solely upon the total damping in that mode $(2c/c_0)$, as shown in Fig. 9. (Note (ω_1/ω_2) is a fixed property of the fan.) The total damping comprises aerodynamic and mechanical damping. Flutter behavior can be studied by making the following simplifying assumptions for the two components.

Aerodynamic damping:	Dependent upon fan speed. Independent of vibration amplitude.
Mechanical damping:	Independent of fan speed. Dependent upon vibration amplitude.

With the simplified aerodynamic model the aerodynamic damping term is provided solely by the lift-due-to-bending component, and, for a given fan and mode, this is proportional to air inlet velocity, u, (see Appendix) giving:

$$\frac{2c}{c_0} = \left(\frac{2c}{c_0}\right)_{\text{mech}} + B(u) \tag{6}$$

where B is a constant. This relationship enables M to be found as a function of speed (from equation (5)).

With the simplified aerodynamic model, C is provided solely by the lift-due-to-torsion term. For a given fan and mode the lift-due-to-torsion is proportional to u^2 (see Appendix) so the dependence of C on speed becomes:

$$A \propto u^2$$

giving

$$C = \frac{K_2 K_2}{A_1 A_2}$$

and for

$$A_1 = A_2$$

$$C \propto \frac{1}{u^4} \tag{7}$$

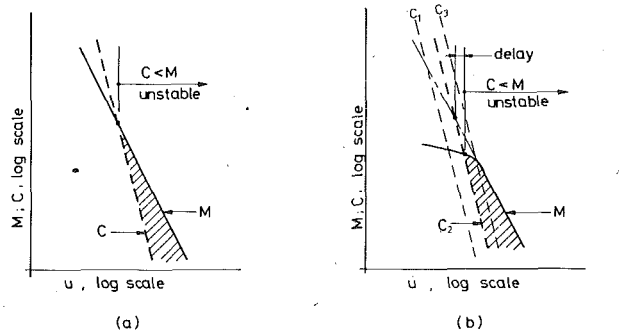


Fig. 10 The interrelationship of *C* and *M* as a function of speed. (a) $\omega_1/\omega_2 = 1$: (b) $\omega_1, \omega_2 \neq 1$

Application to Three Models of the Mechanical System.

1 Two Identical Modes ($\omega_1 = \omega_2$); no mechanical damping.

This represents the simplified mechanical model used in published flutter analyses, e.g., [1].

In this case the flutter frequency, p, is the common natural frequency of the undamped modes, (i.e., $p/\omega_1 = p/\omega_2 = 1$), and M reduces to

$$M = \frac{1}{\left(\frac{2c}{c_0}\right)^2}$$

now $c/c_0 \propto u$ so

$$M \propto \frac{1}{u^2}$$

Also $C \propto 1/u^4$ (equation (7)).

Hence, as speed, u, increases C decreases much more quickly than M so that a flutter condition is eventually reached. This is shown in Fig. 10(*a*).

2 Frequency Split ($\omega_1 \neq \omega_2$): no mechanical damping.

In this case M is given by Fig. 9. Equation (6) with no mechanical damping gives $u \propto 2c/c_0$ so with a suitable change of scale Fig. 9 can be replotted as M versus u. As before $C \propto 1/u^4$. An example of the resulting behavior is given in Fig. 10(*b*) which shows that the onset of flutter is delayed by the frequency split. The size of the delay depends upon the relative positions of the C and M lines, for example, the delay for the line C_1 in the figure is significantly larger than for C_2 and for C_3 the delay has disappeared.

3 Frequency Split ($\omega_1 \neq \omega_2$); mechanical damping present.

If mechanical damping is included then

$$u = \left[\left(\frac{2c}{c_0}\right) - \left(\frac{2c}{c_0}\right)_{\text{mech}}\right] \div B.$$

The curve of M against u is still broadly similar to M against $(2c/c_0)$ but is shifted to the left and (because of the logarithmic scale) is distorted. The figure is similar in form to Fig. 10(*b*), but is different in detail. Increasing the mechanical damping makes the fan more stable.

The following points arise from the analysis of these three conditions:

1 A fan with a frequency difference between the two orthogonal modes is less likely (in general) to flutter than a fan with two identical modes (perfect symmetry).

2 The scale of the effect depends upon the total amount of damping in each mode. With large damping the effect disappears.

3 Increasing the frequency split increases the effect and the range of damping over which it is significant.

Actions which Extend the Flutter Boundary. In the terms of the above analyses these can be seen as:

1 Shift the C curve to the right, for example by altering the mode shape so that the ratio twist/flap is reduced and the lift-due-to-torsion term reduced for a given linear displacement. Increasing the mechanical stiffness of the fan also shifts the

Downloaded 01 Jun 2010 to 171.66.16.58. Redistribution subject to ASME license or copyright; see http://www.asme.org/terms/Terms_Use.cfm

curve to the right.

2 Shift the M curve to the left, for example by altering the mode shape to increase the aerodynamic damping for a given linear displacement.

3 Change the shape of the M curve. Adding mechanical damping and increasing the frequency separation of the modes both have a favorable effect.

The first approach corresponds to reducing the gain of the system while leaving the nature of the response unchanged. The second two approaches correspond to altering the nature of the response while leaving the gain unchanged.

Conclusions

Fan flutter has been analyzed in terms of twin orthogonal vibration modes, (independent vibrations which are similar in shape but have slightly different natural frequencies) and simplified aerodynamic theory. Published flutter analyses use advanced aerodynamic models, but with simplified mechanical models. The alternative approach has shown that aspects of fan vibration which are ignored by the simplified models can significantly alter flutter behavior.

Flutter onset speed is shown to be affected by the natural frequency ratio of the two modes, as well as by the degree of damping present.

Blade behavior is shown to be non-uniform around the fan. This non-uniformity appears as:

1 Unequal blade amplitudes, hence unequal stresses
2 Unequal interblade phase angles
3 A variation from blade to blade in the temporal phase between twist and flap in each individual blade
4 Non-sinusoidal deflection patterns.

The nature and extent of the non-uniformity is determined by the natural frequency ratio of the twin modes, and the degree of total damping in each mode (aerodynamic plus mechanical).

The twin mode analysis clarifies the relationship between tests made on stationary fans, in which a standing wave is usually generated, and flutter, where the vibration propagates around the fan. Now that experimental techniques such as laser holography [4, 6] are providing a great deal of detailed information on fan vibration, it is becoming increasingly important that improved mechanical models are used in flutter analysis so that full use can be made of the new data.

The alternative viewpoint provided by the twin mode analysis provides additional insight into the physical mechanism of flutter. This is valuable in itself and also facilitates the next step, which is to combine the twin mode model with the latest developments in unsteady aerodynamic theory.

Acknowledgments

The authors wish to thank Rolls-Royce for permission to publish this paper. The authors also wish to acknowledge the work of the Vibration Group in Bristol which first related fan flutter to twin orthogonal modes. Finally they would like to thank colleagues in Derby and Bristol who contributed to the study through their discussions.

References

1 Carta, F. O., "Coupled Blade-Disk-Shroud Flutter Instabilities in Turbojet Engine Rotors," ASME JOURNAL OF ENGINEERING FOR POWER, Vol. 89, July 1967, pp. 419–426.

2 Mikolajczak, A. A., et al., "Advances in Fan and Compressor Blade Flutter Analysis and Prediction," *Journal of Aircraft*, Vol. 12, April 1975, pp. 325–333.

3 Halliwell, D. G., "The Characteristics Prediction and Test Analysis of Supersonic Flutter in Turbofan Engines," I. Mech. E., Paper C187/76, Conference on Vibrations in Rotating Machinery, Sept. 1976.

4 Hockley, B. S., Ford, R. A. J., and Foord, C. A., "Measurement of Fan Vibration Using Double Pulse Holography," ASME Paper No. 78-GT-111, Presented at the Gas Turbine Conference, London, England, April 1978.

5 Armstrong, E. K., Private communication.

6 Stetson, K. A., "The Use of an Image Derotator in Hologram Interferometry and Speckle Photography of Rotating Objects," *Experimental Mechanics*, Vol. 18, Feb. 1978, pp 67–73.

APPENDIX

Unsteady Aerodynamic Forces

The analysis of the unsteady aerodynamic forces acting on an aerofoil executing simple harmonic motion in a steady airstream is reviewed in [1]. The forces can be described in terms of four components:

Lift force due to bending	$= (P_{LH})H$
Lift force due to twist	$= (P_{L\theta})\theta$
Moment due to bending	$= (P_{MH})H$
Moment due to twist	$= (P_{M\theta})\theta$

where P represents unsteady force coefficients for lift, L, or moment, M, as functions of bending, H, or twist, θ.

In general the P terms are complex, but in order to demonstrate the method of twin orthogonal modes, the following simplifications have been made:

$P_{MH} = P_{M\theta} = 0$

P_{LH} = Imaginary term only (i.e., lift dependent upon bending velocity)

$P_{L\theta}$ = Real term only (i.e., lift dependent upon twist displacement)

The dependence of the P terms on free stream velocity, u, has been simplified to give:

$$P_{L\theta} \propto u^2$$

$$P_{LH} \propto u$$

These relationships can be obtained by simplifying the unsteady force equations or from incidence considerations as below.

For small vibrations the change in lift can be approximated by

$$\Delta(\text{Lift}) = E\frac{1}{2}\rho u^2 \times \Delta(\alpha)$$

where α = incidence angle

E = constant of proportionality.

For a twisting blade $\Delta(\alpha)$ equals the angle of twist, θ, giving

$$\Delta(\text{Lift}) = E\rho\theta u^2$$

For a flapping blade $\Delta(\alpha) = \dot{H}/u$ where $\dot{H}$ = flap velocity giving

$$\Delta(\text{Lift}) = E\rho\dot{H}u$$

If the behavior is such that E is approximately constant over the required range these relationships give the required results.

It should be noted that although these approximations are significant they are not prerequisites for the analysis. They have been made in this instance to enable aspects of the twin mode approach to be demonstrated more clearly.

Downloaded 01 Jun 2010 to 171.66.16.58. Redistribution subject to ASME license or copyright; see http://www.asme.org/terms/Terms_Use.cfm

M. W. Johnson
J. Moore

Engineering Department
Cambridge University
Trumpington Street
Cambridge CB2 1PZ
England

The Development of Wake Flow in a Centrifugal Impeller

Three-dimensional flow, leading to the formation and the growth of a wake in a centrifugal impeller, has been studied. Results of flow measurements in a 1 m dia, shrouded, centrifugal compressor impeller running at 500 rpm are presented. Relative velocities and rotary stagnation pressures ($p^* = p + {}^1/_2\rho W^2 - {}^1/_2\rho\omega^2 r^2$) were measured, on five cross-sectional planes between the inlet and outlet of the impeller, using pressure probes which were traversed within the rotating impeller passage. Particular attention was given to the convection of low p^* fluid by secondary flows and to the formation of the wake in the shroud/suction-side corner region of the passage.

Introduction

Wake Formation and Development. The 'jet-wake' model for the outlet flow from a centrifugal impeller was first proposed by Carrard [1, 2] in 1923. In many experimental investigations which have been made since [3, 4, 5], this jet-wake flow has been observed. The wake formation has been found to vary with the impeller geometry and also with the flow rate and operating speed, but even today, its position, size and shape can not be predicted reliably. Eckardt [6], with his detailed measurements, showed that potential flow theory was capable of describing the jet flow, but to understand the development of the wake, it is necessary to investigate in more detail, the secondary flows, which contribute to the thickening of the suction side and shroud wall boundary layers.

Wake Flow Measurements of Eckardt. Some light was thrown on these secondary flows by Eckardt, who used a Laser-2-Focus Velocimeter to study his impeller flow. With this technique, Eckardt measured statistically-averaged mean values of a flow velocity and a flow angle and hence, obtained two velocity components (approximately in the meridional and circumferential directions) in a complex three-dimensional flow. The two measured velocity components were perpendicular to the optical axis of the laser beams, and therefore no information was obtained about the third component of velocity, in the hub-to-shroud direction. Thus, Eckardt obtained a remarkably complete picture of the meridional component of velocity, on five cross-sectional planes between the inlet and the outlet of the impeller, together with an incomplete, but nonetheless informative picture of the three dimensionality of the flow.

Eckardt's measured distributions of meridional velocity clearly showed the formation and growth of a wake flow in the shroud/suction-side corner region of his impeller channels. Furthermore, the measured circumferential components of velocity were consistent with the well-known concept of the wake flow as an accumulation of low momentum fluid. Eckardt was therefore able, to construct a qualitative picture of the three-dimensional flows, which convected boundary layer fluid and tip leakage fluid towards the shroud/suction-side corner region. In this picture, flows in the hub-to-shroud direction contribute significantly to the flow pattern. It is interesting to speculate therefore, whether the formation of the wake in Eckardt's impeller, which was observed to occur in a region of high meridional curvature, could have been influenced by the convection of blade boundary layer fluid towards the shroud wall. Eckardt observed that the circumferential velocities were still relatively low in the cross-sectional plane where the wake first appeared and also, that there was a reduction of turbulence intensity immediately upstream of the wake incidence location. However, both these observations could be consistent with a picture of the wake formation being due to three-dimensional flow towards the shroud in the boundary layers on the blade surfaces, with a consequent accumulation of low-momentum fluid on the shroud wall.

Contribution of the Present Paper. Clearly, as concluded by Eckardt, further measurements are necessary to improve the understanding of the wake formation process. It is the object of this paper to contribute to this discussion the results of some measurements of three-dimensional flow and wake development in a De Havilland Ghost centrifugal impeller, operating at low speed (500 rpm). This Ghost impeller, in common with Eckardt's impeller, has a strong curvature from the axial to the radial direction. In the present, incompressible flow study therefore, the authors measured all three, mutually-perpendicular velocity components and the rotary stagnation pressure, $p^* = p + {}^1/_2\rho W^2 - {}^1/_2\rho\omega^2 r^2$. Results are presented, showing the convection of low p^* fluid along the blades from the hub to the shroud, and the authors conclude that this convection has a dominant influence on the development of the wake flow, described in the present paper.

The Development of Secondary Flow. Before describing the experimental program and the test results, let us consider the qualitative features of secondary flow in centrifugal impellers. Let us consider the departures of real impeller flows from ideal potential flow and let us ask how such departures can influence the location of wake flow in the exit planes of centrifugal impellers.

We are interested in the generation of a streamwise component of vorticity in flows in curved and rotating passages and it is sufficient

Contributed by the Gas Turbine Division and presented at the Gas Turbine Conference and Exhibit and Solar Energy Conference, San Diego, California, March 12–15, 1979 of THE AMERICAN SOCIETY OF MECHANICAL ENGINEERS. Manuscript received at ASME Headquarters January 3, 1979. Paper No. 79-GT-152.

Copyright © 1980 by ASME

Downloaded 01 Jun 2010 to 171.66.16.58. Redistribution subject to ASME license or copyright; see http://www.asme.org/terms/Terms_Use.cfm

for present purposes to restrict our attention to the inviscid development of flow containing vorticity, initially oriented perpendicular to the flow direction. This will give a quantitative understanding of the development of the secondary flow in regions where viscosity is unimportant, and a qualitative picture of secondary flow elsewhere.

The equation governing the development of streamwise vorticity along a streamline in incompressible flow in a rotor, which was derived by Smith [7], has recently been presented in the following simple form by Hawthorne [8];

$$\frac{\partial}{\partial s}\left(\frac{\Omega_s}{W}\right) = \frac{2}{\rho W^2}\left(\frac{1}{R_n}\frac{\partial p^*}{\partial b} + \frac{\omega}{W}\frac{\partial p^*}{\partial z'}\right). \quad (1)$$

Here, $p^* = p + \frac{1}{2}\rho(W^2 - \omega^2 r^2)$ is the rotary stagnation pressure, W is the fluid velocity relative to the rotor and ωr is the rotor tangential velocity; and the equation is expressed in streamline co-ordinates, where s is the streamwise direction, n the normal direction and b the binormal direction. The two terms contributing to the generation of the streamwise vorticity Ω_s, are due to curvature of the streamlines with radius R_n, and due to rotation with angular velocity ω about the axis of rotation z'. They are associated with gradients of p^* in the binormal and axial directions, respectively.

Rotary Stagnation Pressure, p^*. The rotary stagnation pressure, p^*, is conserved along a streamline in steady, inviscid, incompressible flow in a rotor. Even in viscous flow, for small distances along streamlines, one may identify a fluid particle by its value of p^*. This is particularly useful in complex three-dimensional flows, as it offers a method of following the development of the flow by following fluid particles, in addition to the more usual approach of measuring flow direction. The migration and accumulation of low p^* fluid can thus, be observed directly.

p^* is the sum of the dynamic pressure $\frac{1}{2}\rho W^2$, and the reduced static pressure, $p_r = p - \frac{1}{2}\rho\omega^2 r^2$. The action of viscosity reduces p^*, especially in boundary layers, where the relative velocity decreases. In a boundary layer with uniform reduced static pressure, the lowest value of p^* occurs at the wall and equals p_r. The large gradients of p^*, which are found in boundary layers, give rise to secondary flows as indicated by equation (1).

Stable Location of Low p^* Fluid. Under the action of secondary flows, fluid with low p^* migrates towards regions of low reduced static pressure, which Johnson [9] has termed the "stable locations" for such fluid. As discussed by Johnson, the low p^* fluid does not necessarily accumulate in the regions of low p_r, as it can be convected to regions of higher p_r, by the inertia of the secondary flows. However, a knowledge of the stable location at each section of an impeller passage, gives an approximate indication of where wake flow will develop.

Secondary Flow in Centrifugal Impellers. In the Ghost impeller and Eckardt's impeller, there are two bends, the inducer bend and the axial-to-radial bend. In the inducer bend, secondary flow develops on the shroud and hub surfaces, convecting fluid with low p^* from these boundary layers towards the suction surface. In the axial-to-radial bend, secondary flows in the suction and pressure surface boundary layers, convect low p^* fluid towards the shroud.

Rotation induces a streamwise component of vorticity, whenever there is a gradient of p^* in the axial direction. In a centrifugal impeller, such gradients occur particularly in the inducer, on the blade surfaces, and in the radial part towards the exit of the impeller, on the hub and shroud surfaces. Inducer flow has recently been investigated by Anand and Lakshminarayana [10], who observed the convection of low momentum boundary layer fluid, towards the shroud, on both the suction and pressure surfaces of their axial-inducer blades. This flow is similar to the flow due to the axial-to-radial bend. The influence of rotation on the flow in the radial part of the impeller passage however, causes low p^* fluid to be convected to the suction side of the passage; such flow was investigated by Moore [11], in a rotating radial-flow channel. In this radial section of the impeller passage, it is interesting to note that the rotation and the curvature of the axial-to-radial bend do not cause similar three-dimensional flows, but compete for the dominating influence on the stable location of low p^* fluid. This competition contributes to the observed differences in wake locations at the exit of centrifugal impellers.

A measure of the relative influences of curvature and rotation may be obtained by evaluating the Rossby number, $W/\omega R_n$. In impellers with low Rossby numbers, the flow will probably be dominated by rotation, and this suggests that the wake fluid will be found on the suction surface, whereas, in impellers with high Rossby numbers, the wake fluid is to be expected on the shroud wall at the impeller exit, since influences of curvature will probably dominate the flow.

Both the Ghost impeller and Eckardt's impeller have Rossby numbers of approximately unity, suggesting that in these impellers, curvature in the axial-to-radial bend, and rotation are of approximately equal importance. It is therefore, to be expected that the overall features of the wake development in the two impellers, will be similar and that the wake will be found in the shroud/suction-side corner in both impellers, as indeed was observed by Eckardt.

Current design methods for centrifugal impellers give little assistance in predicting the size and location of wakes, but clearly this information will be of value in diffuser design and in optimising centrifugal compressor stages. It will be useful also, to have data on wake development in two impellers of known geometry [12], in order to provide test cases for flow modellers.

The Test Rig

A schematic diagram of the centrifugal impeller rig is shown in Fig. 1. The impeller is from a De Havilland Ghost engine, and details of the geometry of the impeller are given in Appendix 1. A glass fiber shroud is bolted to, and therefore rotates with, the impeller, which is driven by an 11 hp d-c electric motor; the running speed of 500 rpm is controlled by a Ward Leonard set. The actual running speed is recorded by a frequency counter to ±0.1 rpm. The air flow is delivered to the impeller through a duct containing several wire mesh screens and a honeycomb, which insure a uniform inlet flow without swirl. A

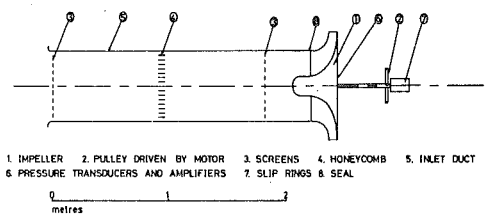


Fig. 1 Schematic of test rig

Nomenclature

a,b,d = constants in equation (A1)
p = static pressure
p_r = reduced static pressure, $p_r = p - \frac{1}{2}\rho\omega^2 r^2$
p^* = rotary stagnation pressure, $p^* = p + \frac{1}{2}\rho W^2 - \frac{1}{2}\rho\omega^2 r^2$
P = dimensionless static pressure, equation (2)
P_r = dimensionless reduced static pressure, equation (3)
P^* = dimensionless rotary stagnation pressure, equation (4)
r,θ,z' = cylindrical polar co-ordinates
r_0,R,z''_0 = constants in equation (A3)
R_n = radius of curvature of streamline
s,n,b = streamwise, normal and binormal directions—streamline co-ordinates
W = relative velocity
$\overline{W}$ = mean relative velocity
x/x_0 = meridional inlet-to-outlet co-ordinate, measured along the shroud
y/y_0 = pressure-side to suction-side co-ordinate
z/z_0 = hub-to-shroud co-ordinate
z' = direction of axis of rotation
z'' = axial distance upstream of impeller hub at outlet
ϕ = blade angle, Appendix 1
ω = angular velocity
Ω_s = component of absolute vorticity along streamline
ρ = fluid density

Subscripts

min = minimum value
max = maximum value

Downloaded 01 Jun 2010 to 171.66.16.58. Redistribution subject to ASME license or copyright; see http://www.asme.org/terms/Terms_Use.cfm

rubber seal attached to the duct, and running on the outside of the shroud, prevents air leakage at the impeller inlet. The boundary layers are tripped by emery paper on the passage walls, at the impeller's inlet, to ensure that they are turbulent. No diffuser is fitted, so the impeller exhausts directly into the atmosphere, but the compressor flow rate can be adjusted by the number of screens in the inlet duct.

A traversing gear, see Fig. 2, driven by a small electric motor is used to move a measuring probe across one of the 19 impeller passages, which was chosen for detailed flow investigation. The traversing gear can be mounted at five stations see Figs. 3 and 4 and at several positions at each station, so that the entire passage cross-section can be covered by probe traverses, at less than 1 cm intervals. The depth of the probe, below the shroud, during a traverse, is recorded by counting the pulses from a microswitch, which closes once for every revolution of the traversing gear's leadscrew. This gives the probe's position within ±1 mm. The probe access holes are sealed, except the one in use, to prevent leakage. The blockage of the probe varies according to its depth below the shroud, the typical blockage is 200 mm^2 or 2 percent of the passage area. The co-ordinates of the locations of the five stations are given in Appendix 2.

The differential pressures from the probe are converted to electrical signals by three sensitive pressure transducers, mounted on the back of the impeller flange with their diaphragms perpendicular to the axis of rotation to minimise the effect of the centrifugal loading. The signals are amplified and pass through slip rings and a smoothing circuit (time constant: 2 s), to a digital voltmeter. Pressure differences are measured with an accuracy of ±10 N/m^2.

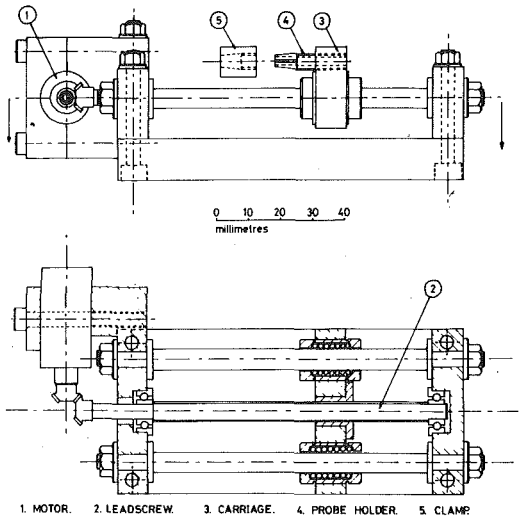


Fig. 2 Traversing gear

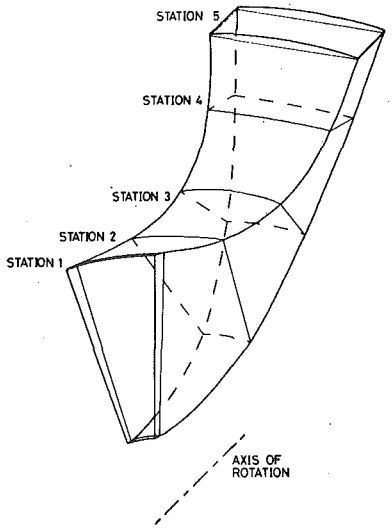


Fig. 3 Impeller passage with measurement planes

Measurements

Relative Velocities. A five hole probe, with an outside diameter of 2 mm, is used to measure the flow velocities. The probe is calibrated for flow direction and velocity. The three, mutually-perpendicular velocity components are calculated using the calibration, and are corrected to standard atmospheric pressure, temperature and running speed (0.101325 MN/m^2, 288.15 K; 500 rpm). The estimated accuracy is ±1 m/s in relative velocity, at 10 m/s and ± 5 deg in flow direction.

Pressures. A Kiel probe, of 3 mm OD was used to measure the rotary stagnation pressure, $p^* = p + \frac{1}{2}\rho(W^2 - \omega^2 r^2)$, relative to atmospheric pressure from a tapping on the shaft. This is corrected to standard atmospheric pressure, temperature and running speed, and the estimated accuracy of p^* is ±10 N/m^2.

The reduced static pressure, $p_r = p - \frac{1}{2}\rho\omega^2 r^2$, is calculated from the measured values of p^* and relative velocity, and the estimated accuracy of p_r is ±40 N/m^2, in the wake region, and ±20 N/m^2, elsewhere.

Integrations. The experimental results, at the measurement points, are extrapolated onto a 50 × 50 grid, covering the measurement plane, and these extrapolated values are integrated, to calculate the flow rate and mass-averaged flow properties.

Experimental Results and Discussion

The results presented show details of the flow development in one passage of the Ghost impeller. The mass flow rate through the passage was 0.17 (±0.01) kg/s. The particular flow rate investigated is equivalent to a total flow rate of 3.3 kg/s, through the impeller, and this is higher than the flow rate of 2.5 kg/s, which would give zero incidence at the blade leading edges. In fact, the measured flow angles near the leading edge plane (Station 1), shown in Fig. 5, show a negative incidence angle over most of the blade, with a value as high as −20 deg, at $z/z_0 = 0.8$.

Characteristic Values of p^*. The uniform, axial, inlet flow gave a flow with a uniform value of $p^* = -250$ (±20) N/m^2 gauge, at the impeller inlet. This is the highest value of p^* measured throughout the impeller flow, and is subsequently referred to as p^*_{max}. p^*_{max} was less than atmospheric pressure, because of the stagnation-pressure drop, through the screens and the honeycomb in the inlet duct. This pressure drop corresponds to the pressure rise achieved in the impeller and in the diffusion beyond the impeller outlet.

The fluid with the lowest values of p^* in the impeller, is fluid with low relative velocity in regions of low reduced static pressure. As

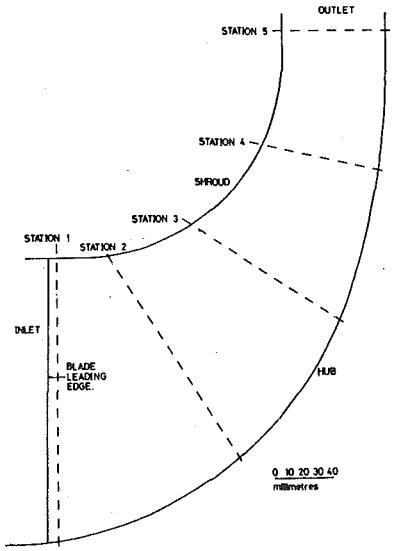


Fig. 4 Meridional cross-section of impeller with locations of measurement planes

Downloaded 01 Jun 2010 to 171.66.16.58. Redistribution subject to ASME license or copyright; see http://www.asme.org/terms/Terms_Use.cfm

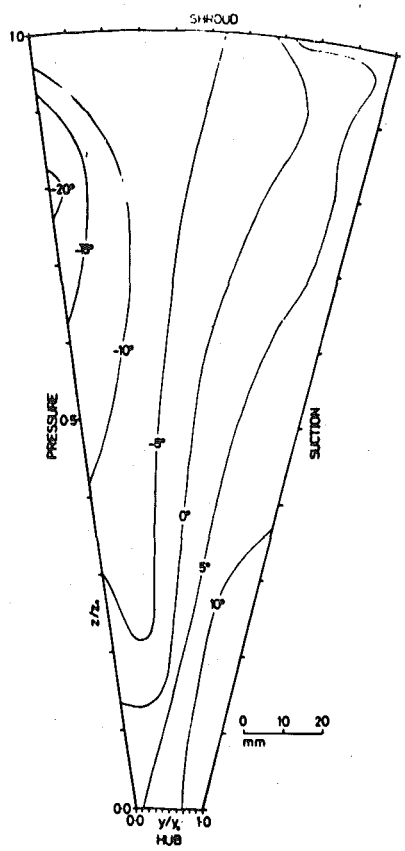


Fig. 5 Station 1: incidence angles at impeller inlet

discussed below, the lowest values of p_r were found adjacent to the regions of highest velocity of the potential flow, which occurred near the shroud in the inducer. From these measurements, it is estimated that the minimum value of p^* (p^*_{min}) was -650 (± 30) N/m^2 gauge. Also, it is clear that the pressure difference, $p^*_{max} - p^*_{min}$, corresponds to the maximum dynamic pressure of the potential flow, which is often used to characterise pressure recovery in centrifugal impellers.

Dimensionless Pressures. The characteristic values, p^*_{max} and p^*_{min}, are used to define a dimensionless static pressure, P, a dimensionless rotary stagnation pressure, P^*, and a dimensionless reduced static pressure, P_r, such that

$$P = \frac{p - p^*_{min}}{p^*_{max} - p^*_{min}}, \tag{2}$$

$$P^* = \frac{p^* - p^*_{min}}{p^*_{max} - p^*_{min}}, \tag{3}$$

$$P_r = \frac{p_r - p^*_{min}}{p^*_{max} - p^*_{min}}. \tag{4}$$

Both P^* and P_r can vary between zero and one, in the impeller. The maximum value of P^* is associated with the inviscid, potential flow, and the maximum value of P_r occurs due to stagnation of the potential flow, at the blade leading edges, for example.

Contours of the measured values of P^* and P_r are presented on measurement planes through the impeller.

Relative Velocities. Velocities are presented in Figs. 6, 9, 12, 15, 18 for the five stations; contours represent the velocity component perpendicular to the measurement plane, and the remaining component in the measurement plane is represented by an arrow, at each measurement point.

The measurement planes are not perpendicular to the passage walls, so in the inducer bend (Stations 1, 2, 3), a component of velocity is always present in the suction-side to pressure-side direction. The suction and pressure surfaces diverge and the shroud and hub surfaces converge, so there are velocity components in the measurement plane, perpendicular to the passage walls. As measurements were not made close to the wall, the velocities in the diagrams, are not zero at the wall.

Station 1. The air enters the impeller, and as the blockage of the blade leading edges is greatest at the hub (46 percent at the hub, one percent at the shroud), most of the air enters the top half of the passage. Fig. 6 shows the lower axial velocity in the lower half of the passage, and the corresponding hub-to-shroud component of velocity. The velocities are higher on the pressure side, because of the large negative angles of incidence, shown in Fig. 5. With this incidence, the blades are initially unloaded up to approximately 60 percent of their height, and negatively loaded towards the shroud, as shown by the reduced static pressure diagram (Fig. 7). The low reduced static pressure ($P_r < 0.05$), in the shroud/pressure-side corner, corresponds to the high relative velocities of the potential flow, and represents one of the lowest reduced static pressures measured in the passage.

The distribution of P^* at Station 1, was found to be uniform, (1.0 $\pm$ 0.02), except close to the corners, where some loss of P^* had occurred, particularly close to the shroud/pressure-side corner, where the flow could have been locally separated at the leading edge.

Station 2. The P^* diagram (Fig. 8) shows that the suction side boundary layer is thickening. The velocity diagram (Fig. 9) suggests that this fluid, with reduced p^* ($P^* = 0.85 - 0.95$), is being convected from the corner towards the centre of this wall. The regions of low p^* flow, on the pressure side near the hub and shroud corners, are probably associated with the incidence at the blade leading edge; the low p^* fluid in the shroud/pressure-side corner region covers a significant area.

The reduced static pressures, shown in Fig. 10, indicate that most of the work is being done in the top half of the passage, where the blades are now loaded. The low static pressure, in the shroud/suction-side corner ($P_r < 0.05$), is of similar magnitude to that occurring in the shroud/ pressure-side corner, at Station 1. These are the two regions of lowest reduced static pressure, found adjacent to the walls in this passage, and as discussed above, they are the locations where fluid with the lowest p^* may be found.

The cross velocities, shown in Fig. 9, near the shroud wall, are parallel to the shroud wall, but because of the convergence of the hub and shroud walls, they have a shroud-to-hub component.

Station 3. At Station 3, the air is about halfway through the impeller, and the flow has been turned through about 58 deg by the

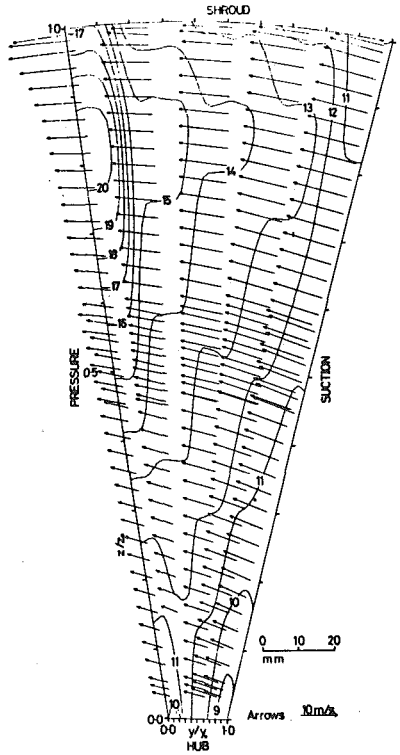


Fig. 6 Station 1: relative velocities—contours in m/s

Downloaded 01 Jun 2010 to 171.66.16.58. Redistribution subject to ASME license or copyright; see http://www.asme.org/terms/Terms_Use.cfm

axial-to-radial bend. The velocity measurements, presented in Fig. 12, show that this bend is strongly influencing the secondary flow pattern. On both the suction and pressure side walls, the low p^* fluid in the boundary layers, is moving towards the shroud. The movement on the suction side is considerably stronger, as there is more low p^* fluid due to the thickening of the boundary layer, as noticed at Station 2. The secondary flow pattern is dominated by two opposing passage vortices; one with anticlockwise motion, on the suction side, and another with clockwise motion, on the pressure side of the passage. This is the pattern, which would be expected in a stationary axial-to-radial bend, but in addition here, there is a strong secondary flow along the shroud, towards the suction side corner, which is generated by Coriolis forces due to the passage rotation. The effects of the convergence of the shroud and hub walls and the divergence of the suction side and pressure side walls, can again be seen in the cross velocities near the walls.

The P^* diagram, in Fig. 11, shows that most of the low p^* fluid observed at Station 2 on the shroud and on the suction side, has moved into the corner. The lowest measured value of P^* (0.48) is much lower than that seen at Station 2, because although fluid with this low value was present at Station 2, the boundary layers were too thin for measurements within them, with the probes used in the present study. This accumulation of low p^* fluid, in the shroud/suction-side corner region, provides the first indication of wake flow in the present flow. It coincides with the first indication, in the velocity diagram, of a large-scale departure from potential flow, and, as such, it corresponds

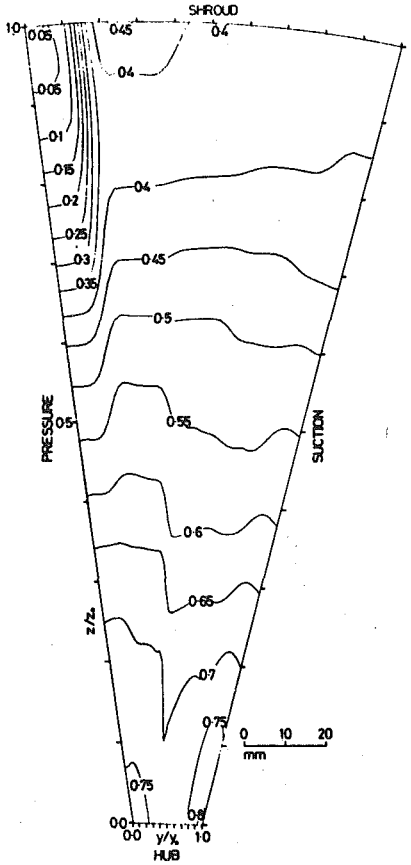


Fig. 7 Station 1: dimensionless reduced static pressure, P_r

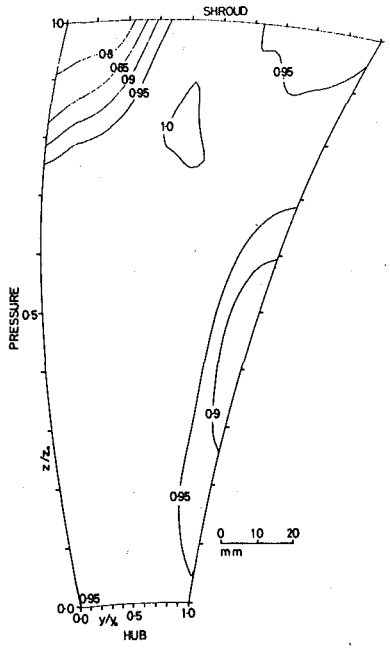


Fig. 8 Station 2: dimensionless rotary stagnation pressure, P*

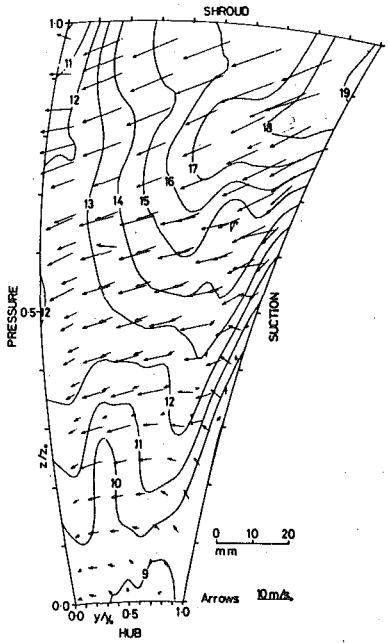


Fig. 9 Station 2: relative velocities—contours in m/s

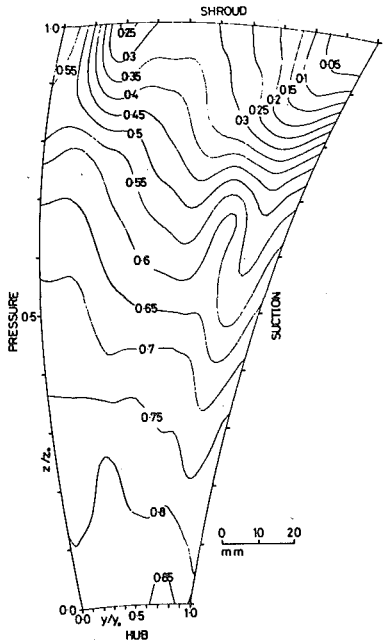


Fig. 10 Station 2: dimensionless reduced static pressure, P_r

Downloaded 01 Jun 2010 to 171.66.16.58. Redistribution subject to ASME license or copyright; see http://www.asme.org/terms/Terms_Use.cfm

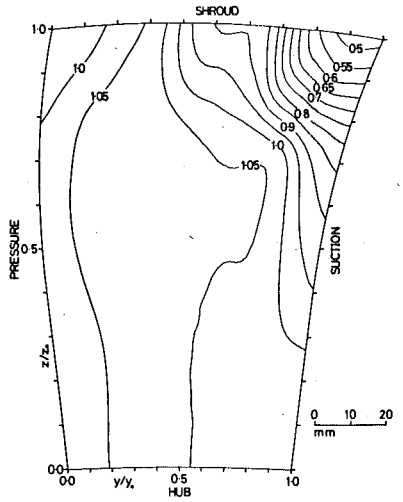


Fig. 11 Station 3: dimensionless rotary stagnation pressure, P^*

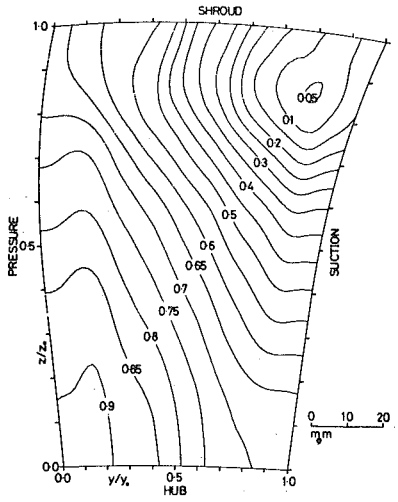


Fig. 13 Station 3: dimensionless reduced static pressure, P_r

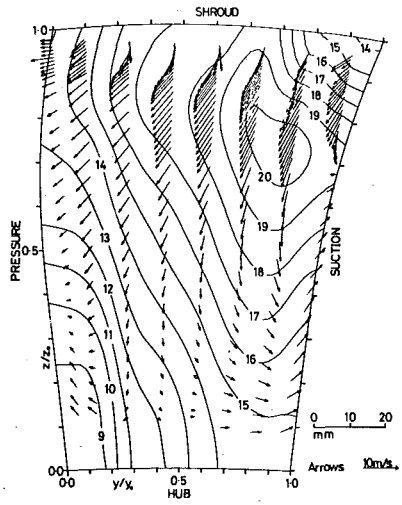


Fig. 12 Station 3: relative velocities—contours in m/s

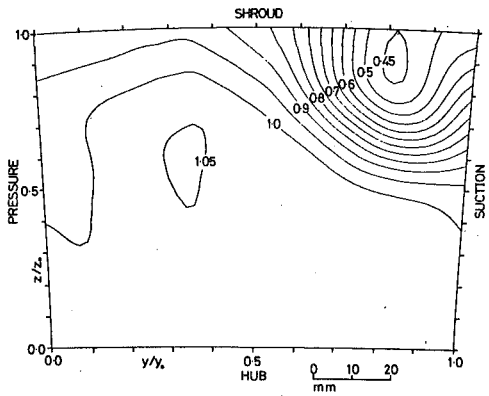


Fig. 14 Station 4: dimensionless rotary stagnation pressure, P^*

remarkably closely with Eckardt's first observation of the wake, in his impeller at his operating condition, at his Station 3. In this investigation, however, evidence of the build-up of low p^* fluid has already been found at Station 2, and we have observed the migration of this fluid to the wake.

The impression gained from the velocity diagram (Fig. 12), that the blades are fully loaded at Station 3, is confirmed by the reduced static pressures in Fig. 13, in which the blades are seen to be loaded at the root, and the highest value of P_r occurs in the hub/pressure-side corner.

Station 4. At Station 4, the passage has turned, almost completely, to the radical direction. The reduced static pressure distribution is dominated by the tangential gradient of static pressure, due to the Coriolis acceleration of the fluid. This is confirmed by the reduced static pressures, presented in Fig. 16, which show the static pressure falling, almost linearly, from the nearly uniform maximum pressure, on the pressure-side wall, to the lowest pressures, on the suction side.

Let us compare the measured difference in reduced static pressure with the result of a simple calculation, which models the flow as a radial flow with a mean velocity $\overline{W} = 15$ m/s. The tangential pressure gradient is given by the simple expression

$$\frac{1}{r}\frac{\partial p}{\partial \theta} = -2\rho\omega\overline{W},$$

and the tangential distance, between the suction and pressure sides, is 0.11 m; hence, we obtain a simple estimate of ΔP as 0.53. This agrees well with the measured pressure difference, $\Delta P \simeq 0.5$.

The stable location for low p^* fluid, in this radial section of the passage, is the region of lowest reduced static pressure, which we have seen, in Fig. 16, occurs on the suction surface as in a straight rotating channel. However, although the axial-to-radial bend has only a small lingering influence on the static pressure distribution, at Station 4, its influence is retained in the inertia of the twin secondary-flow vortices, observed at Station 3. The P^* diagram, in Fig. 14, shows that the low p^* fluid, in the wake flow, has moved further along the shroud, towards the pressure side, between Stations 3 and 4, even though the stable location for low p^* fluid, has moved the other way! This migration is due to the inertia of the passage vortex, on the suction side of the passage , which was induced by the axial-to-radial bend.

The twin vortex system has two main influences on the wake development. Firstly, the anticlockwise vortex on the suction side, causes a strong secondary flow, along the suction surface towards the shroud. And secondly, the clockwise vortex creates a secondary flow along the shroud towards the suction surface; this is augmented by the action of Coriolis forces. The low p^* fluid in these two flows, collides at $y/y_0 \simeq 0.8$, and moves away from the wall. Near the hub wall, it can be seen that the twin vortices result in secondary flow, which is nearly symmetrical about the centre, at $y/y_0 = 0.5$.

It is noteworthy that a high shear occurs between the wake and the jet, and that the wake's core has relatively low radial momentum.

Station 5. Station 5 is close to the impeller exit and the passage is still radial, as may be seen in Fig. 3.

The P^* diagram (Fig. 17) shows that the wake area has increased dramatically between Stations 4 and 5. The minimum observed P^* has also increased between Stations 4 and 5. This may be due to a slight increase in the reduced static pressure in the wake region, which further reduces the low radial momentum of the fluid. This slow moving, low p^* fluid may now mix with fluid of a higher p^*, possibly brought to it by the passage vortex, still present in the shroud/suction-side corner region ($y/y_0 = 0.7 - 1.0$, $z/z_0 = 0.7 - 1.0$), in order to reach the impeller outlet. A combination of the increase in wake

Downloaded 01 Jun 2010 to 171.66.16.58. Redistribution subject to ASME license or copyright; see http://www.asme.org/terms/Terms_Use.cfm

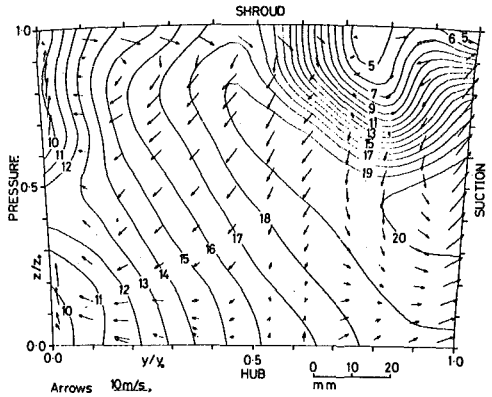


Fig. 15 Station 4: relative velocities—contours in m/s

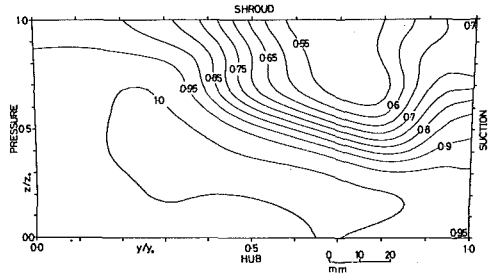


Fig. 17 Station 5: dimensionless rotary stagnation pressure, P^*

fluid due to the mixing, together with the reduction in radial momentum, can explain the observed increase in the wake area.

The wake has continued to be displaced along the shroud wall, away from the suction side, and the centre of the wake is now located close to $y/y_0 = 0.67$. But, there is now a tendency for the fluid with lowest p^* to move towards the stable location on the suction surface. This movement can be seen in the velocity diagram (Fig. 18), but it is also clear that the flow up the suction surface persists and prevents the bulk of the wake fluid from reaching its stable location.

The P_r diagram, in Fig. 19, shows that the blades are almost unloaded and that the reduced static pressure in the wake region is quite uniform, with a value of P_r between 0.45 and 0.5. In the jet, the value of P_r varies between 0.45, in the shroud/pressure-side corner region, and 0.6 − 0.65, along the hub wall; but at the boundary between the jet and the wake, the reduced static pressure is nearly uniform, with a value of $P_r \simeq 0.5$. As discussed above, P_r corresponds to the pressure coefficient of jet fluid, which has diffused from the maximum relative velocity in the potential flow in the inducer. This pressure coefficient is used by many designers as a simple criterion, for two-dimensional boundary layer growth in a diffusing impeller flow. Clearly, the boundary layer flow in the present passage is not two-dimensional, but nonetheless, it is interesting that a pressure coefficient of 0.5 is representative of the magnitude of pressure coefficient necessary to cause the separation of a two-dimensional turbulent boundary layer.

Mass-Averaged Pressures. After considering the details of the reduced static and rotary stagnation pressure distributions, it is interesting to evaluate the mass-averaged pressures at each of the five stations. These are presented in Fig. 20.

The reduced static pressure varies very little, after an initial small pressure rise between the inducer throat, close to Station 1, and Station 2; these small changes are within the limits of experimental accuracy. The rise in static pressure then represents only a centrifugal pressure rise.

The only station, at which the mass-averaged p^* is significantly different from unity, is Station 5, and the reduction between Stations 4 and 5, could be due to increased mixing in the wake region, near the exit of the impeller.

Conclusions

1 The development of the wake flow in the Ghost impeller, with a tip speed of 23.8 m/s, observed in the present study, is very similar

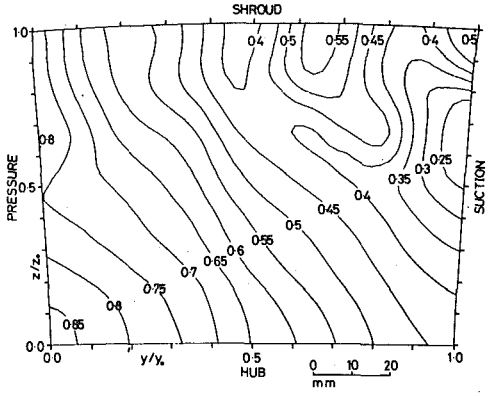


Fig. 16 Station 4: dimensionless reduced static pressure, P_r

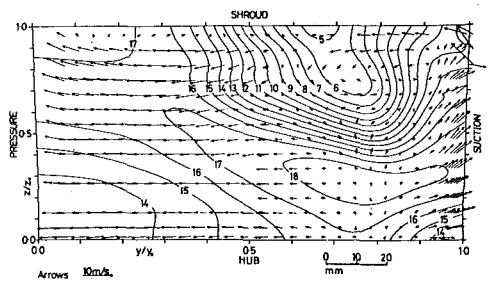


Fig. 18 Station 5: relative velocities—contours in m/s

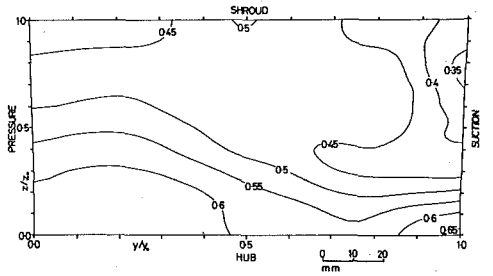


Fig. 19 Station 5: dimensionless reduced static pressure, P_r

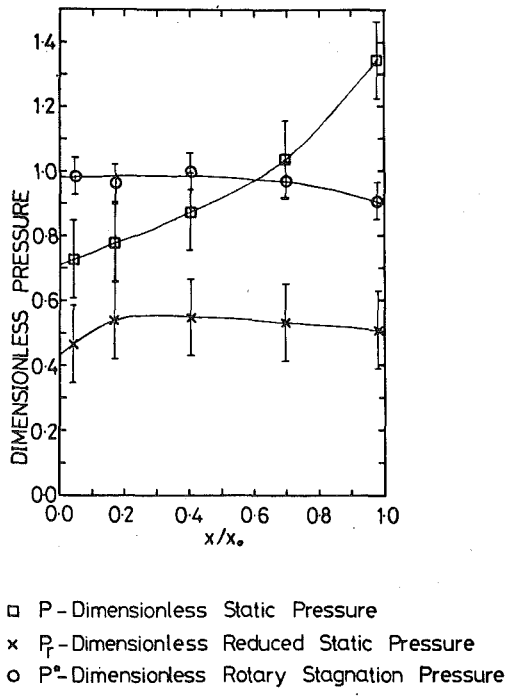


Fig. 20 Mass-averaged dimensionless pressures through the impeller

Downloaded 01 Jun 2010 to 171.66.16.58. Redistribution subject to ASME license or copyright; see http://www.asme.org/terms/Terms_Use.cfm

to that in Eckardt's impeller [6], with a tip speed of 293. m/s. This is because the influences of curvature and rotation are of approximately equal importance in the two flows. The wake is an accumulation of fluid, with low rotary stagnation pressure p^*, which forms in the shroud/suction-side corner region of the impeller passage.

2 Evidence of the build-up of low p^* fluid is found upstream of the point, where the first large scale departures from potential flow are observed, in the contours of meridional velocity. The accumulation of this low p^* fluid, to form the wake, is observed by measuring the three mutually-perpendicular velocity components and by following the motion of fluid, with a particular value of p^*, between measurement stations (p^* is approximately conserved along a streamline). It is concluded therefore, that secondary flows have a dominant influence on the formation of the wake flow in the present study.

3 The axial-to-radial bend dominates the secondary flow pattern through most of the impeller. Two opposing passage vortices are induced, one on the suction side and one on the pressure side of the passage. On the suction side, low p^* fluid is carried by the vortex along the wall to the wake region. The passage vortex on the pressure side, creates a secondary flow, along the shroud towards the suction surface; this flow is enhanced by the action of Coriolis forces, due to passage rotation. The low p^* fluid in these two flows, collides in the wake region and moves away from the shroud wall.

4 The stable location of wake fluid, in the radial section of the passage, is on the suction-side wall, but the wake remains on the shroud, because of the inertia of the suction-side passage vortex. This vortex continues until the impeller outlet and feeds fluid into the wake, where it may mix with low p^* fluid, to raise the lowest value of p^* observed at the outlet.

5 We have studied wake formation and development experimentally by measuring three mutually-perpendicular velocity components, measuring rotary stagnation pressure, and then calculating reduced static pressure. In a certain sense, we have used the stagnation pressure to judge what has arrived at our measuring location, we have used the velocity to determine where it is going, and we have used the static pressures as an indication of where it is trying to get to!

Acknowledgments

The authors wish to thank Rolls-Royce (1971) Ltd., for their financial support of this project, and especially, Mr. P. H. Timmis of the Rolls-Royce Helicopter Engine Group and Mr. P. Clark of Rolls-Royce, Bristol, for their encouragement.

References

1 Carrard, A., "Sur le Calcul des Roues Centrifuges," *La Technique Moderne*, T. XV No. 3, pp. 65–71, and No. 4, Feb. 1923, pp. 100–104.

2 Carrard, A., "On Calculations for Centrifugal Wheels," translation by J. Moore, C.U.E.D./A-Turbo/TR73/1975.

3 Cheshire, L. J., "Centrifugal Compressors for Aircraft Gas Turbines," *Proc. I. Mech. E.* Vol. 153, 1945, p. 440.

4 Hamrick, J. T., "Some Aerodynamic Investigations in Centrifugal Impellers," *Trans. ASME*, April 1956, pp. 591–602.

5 Hamrick, J. T., Mizisin, J. and Michel, D. J., "Study of Three-Dimensional Flow Distribution Based on Measurements in a 48-Inch Radial-Inlet Centrifugal Impeller," NACA TN 3101, 1954.

6 Eckardt, D., "Detailed Flow Investigations within a High-Speed Centrifugal Compressor Impeller," ASME *Journal Fluids Eng.*, Vol. 98, 1976, pp. 390–402.

7 Smith, A. G. "On the Generation of the Streamwise Component of Vorticity for Flows in a Rotating Passage," *Aeronautical Quarterly*, Vol. 8, 1957, pp. 369–383.

8 Hawthorne, W. R., "Secondary Vorticity in Stratified Compressible Fluids in Rotating Systems," C.U.E.D./A-Turbo/TR63/1974.

9 Johnson, M. W., "Secondary Flow in Rotating Bends," ASME JOURNAL OF ENGINEERING FOR POWER, Vol. 100, No. 4, pp. 553–560.

10 Anand, A. K. and Lakshminarayana, B., "An Experimental Study of Three-Dimensional Turbulent Boundary Layer and Turbulence Characteristics Inside a Turbomachinery Rotor Passage," ASME JOURNAL OF ENGINEERING FOR POWER, Vol. 100, No. 4, pp. 676–690.

11 Moore, J., "A Wake and an Eddy in a Rotating, Radial-Flow Passage," ASME JOURNAL OF ENGINEERING FOR POWER, Vol. 95, July 1973, pp. 205–219.

12 Moore, J., "Eckardt's Impeller—A Ghost from Ages Past," C.U.E.D./A-Turbo/TR83/1976.

APPENDIX 1

Ghost Impeller Geometry

In this section linear dimensions are given in mm.

The main dimensions of the impeller are:

outside diameter = 909.3,
inlet diameter = 571.5,
hub diameter = 177.8.

The impeller has 19 blades which have radial sections. The camber-line geometry is defined by Moore [12], in a cylindrical co-ordinate system (r,ϕ,z''), where z'' is taken as the axial distance upstream of the impeller hub at the outlet. The variation of the blade angle, ϕ, with z'' is represented by an ellipse;

$$\left(\frac{\phi}{a}\right)^2 + \left(\frac{z'' - d}{b}\right)^2 = 1, \text{ for } z'' \geq d, \tag{A1}$$

and by

$$\phi = a, \text{ for } 0 \leq z'' \leq d, \tag{A2}$$

where a = 31.983 deg, b = 182.73 and d = 72.39.

The shroud profile is defined by a circular arc;

$$(r - r_0)^2 + (z'' - z''_0)^2 = R^2, \quad \text{for } 72.39 \leq z'' \leq 212.09, \tag{A3}$$

where r_0 = 425.45, z''_0 = 212.09 and R = 139.7,

and by

$$r = 285.75, \quad \text{for } 212.09 \leq z'' \leq 237.49, \tag{A4}$$

and

$$z'' = 72.39, \quad \text{for } 425.45 \leq r \leq 454.66. \tag{A5}$$

The hub profile is defined by two circular arcs, of the form of equation (A3), where

r_0 = 342.90, z''_0 = 266.19 and R = 254.00, for $25.4 \leq z'' \leq 241.3$,

r_0 = 416.56, z''_0 = 482.60 and R = 482.60, for $0 \leq z'' \leq 25.4$,

and by

$$z'' = 0, \quad \text{for } 416.56 \leq r \leq 454.66. \tag{A6}$$

APPENDIX 2

Measurement Stations

Co-ordinates of the intersections of the measurement planes with the hub and shroud walls are presented in Table 1. The intersections are shown in Fig. 4, but the accuracy of the co-ordinates is only ± 2 mm, since they represent intersections between planes and a surface of revolution. The total meridional distance, x_0, along the shroud, from inlet to outlet of the impeller, is 274. mm.

Table 1 Measurement-plane co-ordinates, dimensions in mm.

Station	x/x_0	Shroud		Hub	
		r	z''	r	z''
1	0.02	285.8	232.	91.2	232.
2	0.17	287.3	191.	148.	103.
3	0.41	311.	132.	240.	28.
4	0.69	372.	83.	344.	5.5
5	0.97	447.	72.4	447.	0.

Downloaded 01 Jun 2010 to 171.66.16.58. Redistribution subject to ASME license or copyright; see http://www.asme.org/terms/Terms_Use.cfm

DISCUSSION

N. A. Cumpsty[1]

The authors have presented details of the flow in impellers; but future discussion on the nature of such flows should be held on the basis of much firmer evidence. I find particularly striking the discrepancy between the apparent position of the vortex from, for example, the tightly closed contours of total pressure in Fig. 14 and the true circulatory motion evident from the velocity vectors in Fig. 15. This discrepancy has been commented on elsewhere but a reminder may be helpful.

A paper by Senoo, et al. [13] drew attention to anomalies in the static pressure contours measured on the shroud of a high speed machine. The sign of the circumferential pressure gradient was observed to change in some places, principally towards the pressure surface and near the end of the inducer. It is interesting that similar behavior can be seen in the results at Station 2, Fig. 10.

Referring to Fig. 6, the authors appear to attribute the lower axial velocities near the hub to the blockage; this is improbable, whereas meridional curvature is likely to affect the axial velocity at inlet.

In interpreting the results, I am unable to follow all of the authors' descriptions. For example, referring to Station 3, Fig. 12, the authors draw attention to the movement of low p^* fluid in the suction and pressure side boundary layers towards the shroud; this is evident only near the hub on the pressure side. It is not evident on either side near the tip and does not appear to be a dominant motion. Again at Station 3, the authors describe a *strong* secondary flow along the shroud towards the suction side corner; this is not apparent to me and I wonder if it could be clarified.

The velocity vectors do not appear to explain the motion of the center of low relative stagnation pressure fluid, which I find rather surprising. Indeed the gross pattern in the movement that I can detect is that the low stagnation pressure region at Station n is approximately where there was abnormally low reduced static pressure at Station n-1. This "rule" works after a fashion from Stations 2 through 5. One expects the low stagnation pressure flow to migrate to the low static pressure but might expect this to be more evident in the crossflow velocities.

The development of the mass averaged pressure through the impeller is interesting (Fig. 20), particularly since it shows that losses in reduced stagnation pressure occur primarily through mixing in the wake near the end of the impeller. The application of this to typical machines at high speed requires caution on two counts: First the tests were carried out at negative incidence. Second, the high speed impeller used for these tests was run at low speed without modification to correct for the reduction in volume flow towards the exit expected at high speed.

[1] Visiting Associate, California Institute of Technology, Pasadena, CA 91125.

Additional Reference

13 Senoo, Y., Hayami, H., Kinoshita, Y. and Yumasaki, H., "Experimental Study of Flow in a Supersonic Centrifugal Impeller," ASME JOURNAL OF ENGINEERING FOR POWER, Vol. 1, No. 1, Jan. 1979, pp 32–39.

Authors' Closure

The authors thank Dr. Cumpsty for his comments and hope that the following discussion will aid his interpretation of their results.

Flow perpendicular to the measurement planes can be better understood with the help of Figs. 3 and 4. For example, at Station 3, flow perpendicular to the measurement plane near the shroud indicates flow towards the shroud and towards the suction surface. Also at Station 3, there are significant changes in flow direction within the boundary layers on the shroud, pressure side and suction side walls, as low p^* fluid moves towards the shroud/suction-side corner. The change in flow angle in the shroud wall boundary layer is seen, in Fig. 12, to be at least 30 deg and could have been greater as measurements were not taken within 3mm of this wall. These flow features are taken by the authors to be strong evidence of significant secondary flows.

The authors agree that meridional curvature is also likely to induce a lower axial velocity at the hub close to the inlet.

Copyright © 1980 by ASME

Downloaded 01 Jun 2010 to 171.66.16.58. Redistribution subject to ASME license or copyright; see http://www.asme.org/terms/Terms_Use.cfm

F. O. Carta
Supervisor, Aeroelastics.

Mem. ASME

A. O. St. Hilaire
Research Engineer.

United Technologies Research Center, East Hartford, Conn. 06108

Effect of Interblade Phase Angle and Incidence Angle on Cascade Pitching Stability[1]

A comprehensive test program was performed at low subsonic velocity on a linear cascade of airfoils oscillating in pitch about their midchords for incidence angles up to 10 deg, reduced frequencies up to 0.193, and over a range of interblade phase angles from $\sigma = -60$ deg to +60 deg. The test conditions represent significant changes in blade loading and dimensionless frequency, and the range of interblade phase angle includes those values usually encountered in actual turbomachines. The measured pressure time histories over the airfoil chord were used to calculate the stability parameters of the system including the unsteady pitching moment coefficient and the aerodynamic damping parameter. For the range of parameters tested it was found that the interblade phase angle is the most important parameter affecting the stability of oscillating cascaded airfoils. The system was unstable for most positive values of σ over the entire range of loading and frequency. This was similar in behavior (but not in magnitude) to the predictions of available potential flow cascade theories and suppports the observation that blade stall need not be present for torsional "stalled" flutter to occur. System stability for negative values of σ was more dependent on loading and frequency and conformed more closely with the observed behavior of stalled flutter. Specifically, for $\sigma < 0$ deg stability increased with frequency and decreased with loading. A preliminary evaluation of the pressure time histories shows that a second harmonic behavior renders the 1.2 percent chord station ineffective in contributing to the blade damping. Under these circumstances it is surmised that the induced damping is associated mainly with the first harmonic component of the pressure response at the 6.2 percent chord station.

Introduction

Until recently it was commonly believed that the single-degree-of-freedom subsonic torsional flutter of turbomachinery blades occurring at part speed near surge was inextricably associated with blade stall and flow separation [1, 2, 3]. As seen in the compressor map of Fig. 1, this region of instability has traditionally been called the subsonic stalled flutter region. This choice of label was based on the tacit assumption that stall and separation were present during flutter as in the case of high incidence stall flutter of isolated propeller or helicopter rotor blades [4, 5]. However, as a result of careful time-averaged flow measurements taken downstream of a fluttering research fan stage it was found that aerodynamic losses behind the rotor do not increase measurably as the so-called stall flutter region is penetrated [6]. These authors further observed that "... in some instances the stall flutter boundary has been observed to occur near maximum compressor efficiency indicating that stalling is not an essential condition for 'stalled' flutter, although it could be the most severe condition. The above observations indicate that the influence of flow incidence on the unsteady aerodynamic forces will have to be considered in the prediction of the flutter boundary."

Over the past four years, an experimental Oscillating Cascade Wind Tunnel (OCWT) has been built and checked out at the United Technologies Research Center (UTRC) with the specific objective of measuring the unsteady aerodynamic response of a cascade of os-

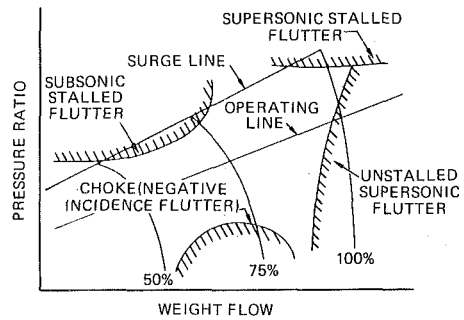


Fig. 1 Compressor map showing flutter boundaries of four types of flutter

[1] This research was supported by Project SQUID under ONR Contract No. N00014-75-C-1143, Subcontract No. 8960-19. Permission to present this material is gratefully acknowledged.

Contributed by the Gas Turbine Division and presented at the Gas Turbine Conference and Exhibit and Solar Energy Conference, San Diego, California, March 12–15, 1979 of THE AMERICAN SOCIETY OF MECHANICAL ENGINEERS. Manuscript received at ASME Headquarters January 3, 1979. Paper No. 79-GT-153.

Copyright © 1980 by ASME

Downloaded 01 Jun 2010 to 171.66.16.58. Redistribution subject to ASME license or copyright; see http://www.asme.org/terms/Terms_Use.cfm

cillating blades subjected to aerodynamic loading under carefully controlled variations in oscillatory frequency and interblade phase angle. The early experiments in this facility were devoted to developing the instrumentation and investigating the characteristics of the surface flow [7]. More recently the emphasis has been to make unsteady pressure measurements on the surface of the center blade [8, 9], and the effort has culminated in a parametric study of the effects of mean camber line incidence angle, α_{MCL}, interblade phase angle, σ, and reduced frequency, k. Tests at a moderate loading condition of $\alpha_{MCL} = 8$ deg were performed under U.S. Air Force sponsorship [10], and tests at low and high loading, at $\alpha_{MCL} = 6$ deg and 10 deg, were recently completed under U.S. Navy sponsorship through Project SQUID. Results for all three values of α_{MCL} are included in the present paper.

In contrast to the results presented in [8, 9], the current results and those of [10] were obtained using an expanded wind tunnel instrumentation capability. This improvement allowed the tunnel flow adjustment to be significantly refined, and in reviewing the previous results in [8, 9] it was determined that the data were inadvertently obtained in the presence of a distorted inlet flow, caused by a misaligned inlet honeycomb. Current results indicate that the actual values of α_{MCL} in [8, 9] are lower than the published values by approximately 2 to 4 deg. Although this indicates a change in the specific flow geometry of the test, the basic primary results presented in [9] are believed to remain valid if the numerical values of $\alpha_{MCL} = 8$, 10, 12 deg are replaced by the more general terms, low, medium, and high loading, respectively.

Experimental Equipment and Procedures

The OCWT has been described in detail in [8, 9] together with discussions of operating procedures and data handling techniques. Therefore, the present discussion will be confined to changes and additions to the previously published work, together with a limited definition of the model geometry for the convenience of the reader.

OCWT Improvements. Considerable care was taken prior to the current tests and those of [10] to adjust the upstream honeycomb to provide uniform, parallel inlet flow, and to rebalance the flow in the sidewall suction plenums to remove the sidewall boundary layer more uniformly than previously. After several preliminary runs to make these necessary adjustments it was found that an upstream cross-tunnel wedge probe, inserted between the sidewall boundary layer slot and the cascade leading edge locus, was sufficient to insure proper operation of the OCWT. The revised procedure now required the wedge probe to be placed at the desired flow angle, and the tailboard and sidewall suction adjustments to be made to yield zero wedge probe unbalance as well as uniform upstream and downstream static pressure distributions along the cascade inlet and exit planes. A further discussion of the procedures employed and the results obtained in these preliminary tests will be found in [10].

Test Airfoils. As before the cascade configuration consisted of 11 NACA 65-series airfoils, each having a chord of $c = 15.24$ cm (6 in.) and a span of $L = 25.4$ cm (10 in.), with a 10 deg circular arc camber and a thickness to chord ratio of 0.06. Fig. 2 is a schematic drawing depicting four of the 11 blades as they were mounted in the wind tunnel. The relative positions shown are properly scaled but the blade geometry has been exaggerated for clarity in describing the blade

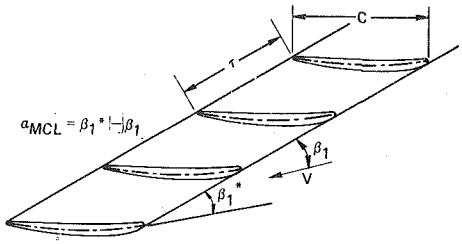


Fig. 2 Blade nomenclature

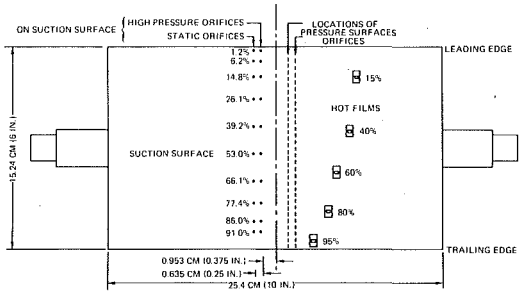


Fig. 3 Schematic plan view of instrumented airfoil

shape parameters. The slant gap, measured along the blade-to-blade stagger line, is $\tau = 0.1143$m (4.5 in.) so the gap-to-chord ratio is $\tau/c = 0.75$.

For these tests the blade stagger angle, β_1^*, measured between the tangent to the blade mean camber line at the leading edge and the leading edge locus line, is 30 deg. (Note that this angle is the complement of the NASA blade angle defined on pp. 184, 185 of [11].) The blade inlet angle, β_1, is measured between the inlet velocity, V, and the leading edge locus line. Hence, the mean camber line incidence angle is defined as $\alpha_{MCL} = \beta_1^* - \beta_1 = 30 \text{ deg} - \beta_1$.

Instrumentation. In addition to conventional wind tunnel instrumentation [8, 9, 10], ten miniature high-response transducers were placed on each surface of the center blade to obtain measurements of unsteady surface pressures along the chord. In addition, static pressure taps, coincident in chord position with each high response orifice, provided a zero frequency reference for each unsteady pressure. Finally, five hot-film transducers were bonded to the blade suction surface to monitor detectable changes within the boundary layer (although none of these measurements are reported on herein). A schematic planform view of the instrumented blade is shown in Fig. 3. Here it is seen that the orifices for both the pressure transducers and the static taps were placed along the chord near the span centerline. The specific chordwide locations, from 1.2 to 91.0 percent, were arranged in a Gaussian array to maximize the accuracy in the numerical integration of the induced pressure distributions [12].

Oscillatory Drive System. The entire set of airfoils was coherently driven in a sinusoidal pitching motion with an amplitude of $\bar{\alpha} = 2$ deg about α_{MCL} for a variety of prescribed frequencies and over a wide range of interblade phase angle, σ. This parameter is defined as positive for an equivalent forward travelling wave around the rotor. In the case of a stationary cascade, as shown in Fig. 2, a positive interblade phase angle is simulated by any blade in the pack leading its

Nomenclature

a = dimensionless location of pivot axis aft of leading edge
C_M = pitching moment per unit span
$\bar{C}_{M1}$ = amplitude of first harmonic component of pitching moment
c = blade chord, m
f = oscillatory frequency, cps
k = reduced frequency, $= c\omega/2V$
L = blade span, m
M = pitching moment per unit span, N-m
p = pressure, N/m^2
Δ_p = pressure difference, N/m^2
q = dynamic pressure, N/m^2
T = period of oscillation, s
t = time, s
V = velocity, m/s
x = chord position, m
Z_p = total pressure wake loss coefficient
α = incidence angle, deg
α_{MCL} = mean camber line incidence angle, deg
$\bar{\alpha}$ = amplitude of motion, deg
β_1 = blade inlet angle, deg
β_1^* = blade stagger angle, deg
$\Delta\theta$ = turning angle, deg
Ξ = aerodynamic damping parameter
ρ = fluid density, N-s^2/M^4
σ = interblade phase angle, deg
τ = slant gap, m
ϕ_{M1} = first harmonic moment phase angle
ω = oscillatory frequency, rad/s

Subscripts

R = real part
s = steady state
u = unsteady

Downloaded 01 Jun 2010 to 171.66.16.58. Redistribution subject to ASME license or copyright; see http://www.asme.org/terms/Terms_Use.cfm

upper adjacent neighbor by the value of σ. For further details of the system the reader is referred to [8, 9, 10].

Test Program

Test Plan. Three parameters were varied to construct the test matrix employed in these tests; α_{MCL}, f (and hence k), and σ. The reduced frequency, k, was determined uniquely by f because the velocity, V, was held constant at 61 m/s (200 ft/s) throughout the test. The incidence-frequency matrix of test points is shown in Table 1 and the incidence-interblade phase angle matrix is shown in Table 2. Tests were conducted for all combinations of the parameters denoted by X with a few noted exceptions. The first test program, described in [10] was run at α_{MCL} = 8 deg for the three frequencies shown and over a complete range of interblade phase angle. In the current program it was decided to run these tests at somewhat higher frequencies, as indicated in Table 1. The frequencies f = 16.2 and 17.9 cps were originally intended to be equal and were set in each test at f = 17.1 cps (or T = 58.5 m/s) on a digital counter. However, it was subsequently determined that the counter was inherently inaccurate at the low frequency end of its range which accounts for the difference observed relative to the nominal value desired.

Steady-State Data. As a preliminary step to each test sequence at constant α_{MCL} a series of steady-state measurements were made to verify the correctness of the test condition (flow uniformity, blade-to-blade periodicity, etc.), and to provide reference steady-state data for the cascade configuration. The pressure distributions corresponding to the three values of α_{MCL} are shown in Fig. 4. It is seen that the major differences show up at the leading edge suction peak (note actual values rather than faired curves), and that the distributions are otherwise similar. Other steady-state data taken were total pressure wake loss (with a wake rake), blade static pressure rise coefficient (extrapolated to the trailing edge), and flow turning (with upstream and downstream wedge probes). All three parameters are plotted versus α_{MCL} in Fig. 5.

Table 1 Incidence–frequency matrix of test points

f	α_{MCL} = k	6 deg	8 deg	10 deg
4.6	.037		X	
9.4	.073	X		X
11.5	.090		X	
16.2	.127	X		X
17.9	.140		X	
24.6	.192	X		X

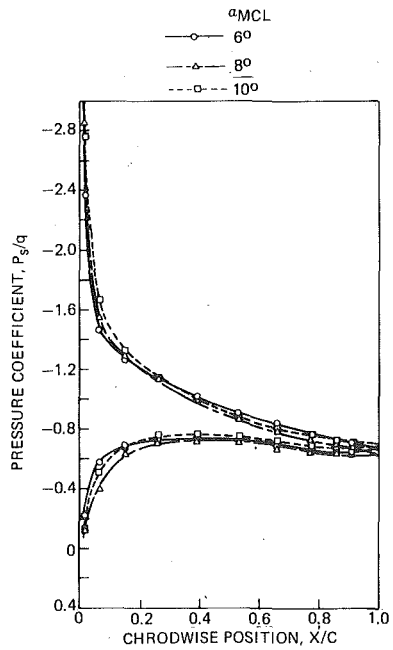


Fig. 4 Steady-state chordwise pressure distribution

The blade geometry used here was predicted to have a minimum loss of approximately Z_p = 0.02 at α_{MCL} = 6 deg. In addition, at α_{MCL} = 8 deg the cascade correlation system (unpublished) predicted a turning angle of $\Delta\theta$ = 11.5 deg and a static pressure rise coefficient of $\Delta p/q$ = 0.48 [10]. Thus there is good agreement between the cascade correlation and the present experiment for both Z_p at α_{MCL} = 6 deg and for $\Delta\theta$ at α_{MCL} = 8 deg. As noted in [10], the deviation of $\Delta p/q$ at α_{MCL} = 8 deg is possibly caused by the buildup of sidewall boundary layer within the blade passage and flow convergence downstream of the cascade. An examination of these results shows that the loss increases monotonically from its minimum value at α_{MCL} = 6 deg to more than twice the minimum loss at α_{MCL} = 10 deg, while the other two parameters peak at α_{MCL} = 8 deg and then decrease at α_{MCL} = 10 deg. Because pressure rise and turning are generally associated with "good" flow conditions, these decreases indicate that a deterioration of the flow, possibly associated with blade stall, may be occurring at or just below α_{MCL} = 10 deg. However, the pressure distributions of Fig. 4 do not show this stall-like behavior as α_{MCL} is increased from 8 to 10 deg and it is seen that the only obvious change is a diminution in the leading edge suction peak response.

For the purposes of this paper and the points that will ultimately be made with regard to the effects of the parameter variations on blade stability, it is sufficient to interpret these steady results to yield the following interim conclusions: 1) at α_{MCL} = 6 deg the system is at or near minimum loss; 2) at α_{MCL} = 8 deg we have modest loading, little

Table 2 Incidence–interblade phase angle matrix of test points

α_{MCL} = σ	6 deg	8 deg	10 deg
−60	X	X	X
−45	X	X	X
−30	X	X	X
−20	X	X	X
−10	X	X	
−5	X(*a*)	X	
0	X	X	X
5	X(*b*)	X	
10	X	X	
20	X	X	X
30	X	X	X
45	X	X	X
60	X	X	X

(*a*) except k = .073
(*b*) except k = .192

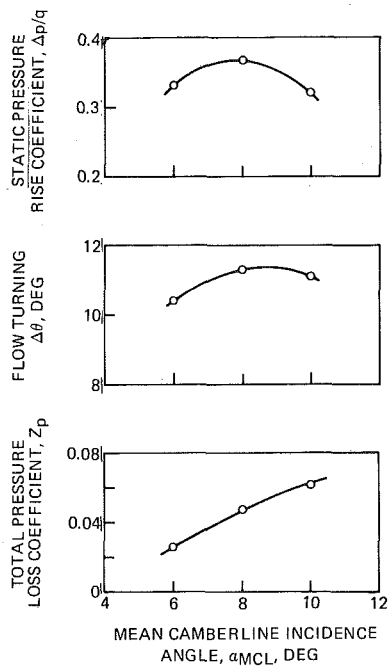


Fig. 5 Steady-state performance parameters

Downloaded 01 Jun 2010 to 171.66.16.58. Redistribution subject to ASME license or copyright; see http://www.asme.org/terms/Terms_Use.cfm

or no indication of blade stall, and good agreement with predicted flow turning; 3) at $\alpha_{MCL} = 10$ deg we have increased loading, increased loss, and deteriorating turning and pressure rise coefficient, but there is still no indication of substantial flow deterioration on the blade.

Results

Summary of Relevant Equations. The data reduction procedure employed in this test is generally well known and has been adequately described in previous reports on this work [8, 9, 10]. The relevant equations are basically simple and are repeated here for reference and for the reader's convenience. First, the unsteady pressure difference time history is obtained from the expression

$$\Delta p(x, t) = -[(P_u + P_s)_{\text{upper}} - (P_u + P_s)_{\text{lower}}] \quad (1)$$

where the subscripts u and s denote the unsteady and steady-state values, respectively. The unsteady pitching moment about an axis at ac (measured from the leading edge) is

$$M(t) = \int_0^c \Delta p(x, t)(ac - x)dx \quad (2)$$

or in coefficient form,

$$C_M(t) = \frac{M(t)}{\frac{1}{2}\rho V^2 c^2} \quad (3)$$

The real part of the pitching displacement about the mean angle is defined[2] as

$$\alpha_R = \bar{\alpha} \sin \omega t \quad (4)$$

The corresponding real part of the first harmonic component of the induced moment is given by

$$C_{MR} = \bar{C}_{M1} \sin(\omega t + \phi_{M1}) \quad (5)$$

where ϕ_{M1} is the phase angle lead relative to the blade motion and the subscript 1 denotes the first harmonic component. Then, as shown in [9], the aerodynamic damping parameter becomes

$$\Xi = -\frac{\bar{C}_{M1}}{\bar{\alpha}} \sin \phi_{M1} \quad (6)$$

These equations were used to produce the results described in the remainder of this paper.

Discussion of Stability. According to the equation cited above, the stability of the system depends only on the algebraic sign of ϕ_{M1} because the moment amplitude, $\bar{C}_{M1}$, is always positive. Thus, the phase angle range $180 < \phi_{M1} < 360$ deg corresponds to positive damping, and hence stability, whereas the phase angle $0 < \phi_{M1} < 180$ deg indicates negative damping or instability. The magnitude of the damping parameter is determined by both $\bar{C}_{M1}$ and ϕ_{M1}. A summary of the data taken in these tests is presented in terms of these parameters in Figs. 6–9.

In Figs. 6, 7, and 8 the data are arranged to show the respective variations of $\bar{C}_{M1}(\sigma)$, $\phi_{M1}(\sigma)$, and $\Xi(\sigma)$ with increasing α_{MCL} from top to bottom, and with increasing k from left to right. At $\alpha_{MCL} = 6$ deg (top row), it is seen that changes in k produce only minor changes in the $\bar{C}_{M1}(\sigma)$, $\phi_{M1}(\sigma)$, and $\Xi(\sigma)$ distributions. This will subsequently be interpreted to mean, on a preliminary basis, that loading effects are minimal (but not absent). In contrast to this, at $\alpha_{MCL} = 10$ deg (bottom row), changes in k produce substantial changes in the forms of $\bar{C}_{M1}(\sigma)$, $\phi_{M1}(\sigma)$, and $\Xi(\sigma)$ which will be interpreted to mean that loading effects are significant. Similarly, a vertical scan of any column for comparable values of k will show large changes at the smallest k and small changes at large k. (Theoretical results are also shown in Fig. 8 which will discussed presently.)

To establish the basis for this reasoning the reader is referred to

[2] Note that this is 90 deg out of phase with respect to the usual mathematical definition of the real part, and has been chosen for convenience in visualizing the time histories by placing the zero displacement point at the origin of coordinates.

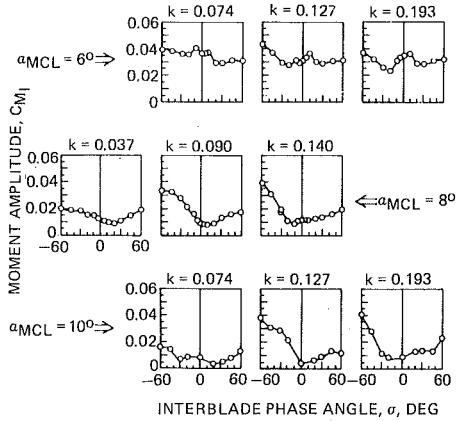


Fig. 6 Variation of first harmonic moment amplitude with interblade phase angle

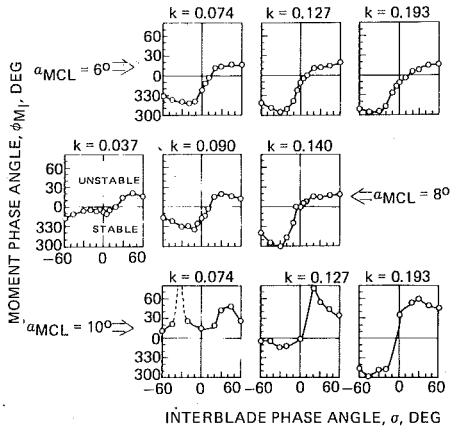


Fig. 7 Variation of first harmonic moment phase angle with interblade phase angle

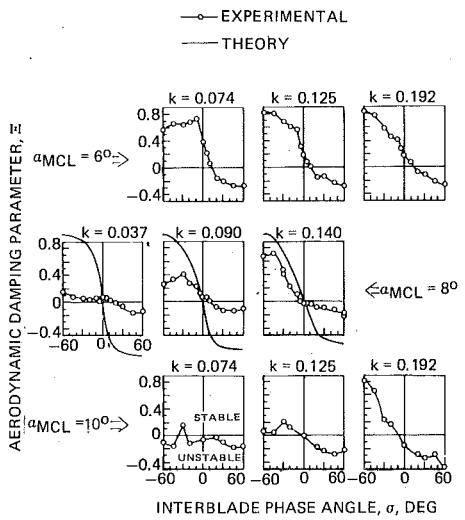


Fig. 8 Variation of aerodynamic damping parameter with interblade phase angle

any of a number of reports and papers on the unsteady aerodynamics of dynamically stalled isolated airfoils (e.g., [5, 13]). In these and other research efforts several basic principals have been established as follows: 1) At low load, and hence in the absence of stall, increasing the frequency has a minimal effect on changing the character of the unsteady blade response. Specifically, the moment hysteresis loops generated by the blade response are qualitatively similar while exhibiting regular and systematic changes with frequency. 2) At high load, and hence in the presence of stall, increasing the frequency has a profound effect on the character of the unsteady blade response. At low frequency, the dynamic stall phenomenon manifests itself in

Downloaded 01 Jun 2010 to 171.66.16.58. Redistribution subject to ASME license or copyright; see http://www.asme.org/terms/Terms_Use.cfm

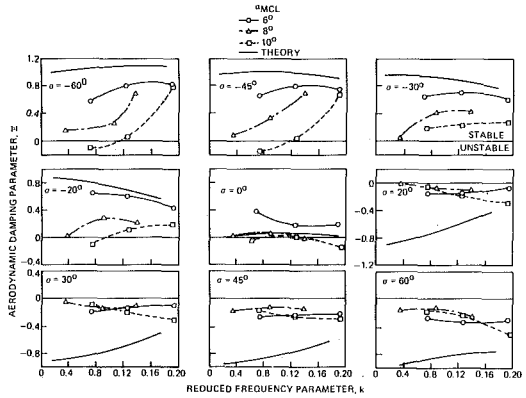


Fig. 9 Variation of aerodynamic damping parameter with reduced frequency

distorted hysteresis loops and higher harmonic reactions. At high frequency, the loops become similar to the potential flow loops, even when the stall regime is deeply penetrated. 3) Thus, at constant low reduced frequency, an increase in load will produce strong dynamic stall effects while at constant high reduced frequency, increasing the load will not necessarily produce dynamic stall on the airfoil. 4) If the isolated airfoil becomes unstable in single-degree-of-freedom torsional motion, it will do so at high load and low frequency. Increasing the frequency will tend to stabilize the motion.

We shall now consider each of these figures in detail. First, in Fig. 6, the first harmonic component of the moment amplitude, $\overline{C}_{M1}$, is plotted versus interblade phase angle. In the first row for $\alpha_{MCL} = 6$ deg, there is a slight trend toward smaller values as k is increased, but in general, all three curves are similar. Larger trend variations are experienced for $\alpha_{MCL} = 8$ and 10 deg. Here the overall level of $\overline{C}_{M1}$ is small at low frequency, and varies strongly with σ at high frequency. Although $\overline{C}_{M1}$ has no impact on the determination of stability, it does have an effect on damping level (cf. equation 6)) as will be seen in subsequent results.

The curves in Fig. 7 can be directly used to determine stability. Here the first harmonic moment phase angle, ϕ_{M1}, is plotted versus σ. As noted earlier, $0 < \phi_{M1} < 180$ deg implies an instability (upper half of each panel).

As before, there is no significant change with frequency at the lowest load condition, $\alpha_{MCL} = 6$ deg, and all three curves follow substantially the same pattern. However, there is an important difference between these results and those of an isolated airfoil in that a single-degree-of-freedom torsional instability can exist at low load over a range of σ values. This will be discussed in more detail below. A similar situation exists for the moderate load condition, $\alpha_{MCL} = 8$ deg. Here the trends are the same as for the low-load condition, but the stable portion over negative σ at the lowest k is considerably diminished, implying the possibility of deteriorating flow effects at the lowest frequency. Finally, at the highest load condition, $\alpha_{MCL} = 10$ deg, the motion is unstable over the entire range of σ tested at low k and appears to recover over the negative range of σ as k is increased. At $\alpha_{MCL} = 10$ deg, $k = 0.74$, and $\sigma = -30$ deg where $\phi_{M1} = 238$ deg appears to be the only result which deviates from what is otherwise a regular trend. The data leading to this result appear to be correct but additional data would be needed to confirm this outcome.

The aerodynamic damping parameter, Ξ, is obtained from equation (6) by combining the results of the previous two figures. In essence, a picture similar to Fig. 7 emerges, but the plots of Ξ versus σ in Fig. 8 now represent a quantitative measure of stability. As before, the influence of increasing k at the low-load condition of $\alpha_{MCL} = 6$ deg is minimal, with stability over negative values of σ and instability for positive σ. The same pattern of stability-instability is observed for $\alpha_{MCL} = 8$ deg, but the level of damping at negative values of σ is strongly affected by frequency. At $k = 0.037$ this is a combination of diminished moment amplitude and small values of ϕ_{M1}. For the highest loading condition, the widespread unstable region over σ persists to higher values of k, and only at the highest value of reduced frequency is the recovery of the Ξ variation substantial. Note that the exceptional point in Fig. 7 shows up as a stable peak in Fig. 8, but also note the occurrence of several other peaks at or near $\sigma = -30$ deg in neighboring panels, which lends credence to the validity of the peak at $k = .074$.

Also shown in Fig. 8 are some theoretical predictions calculated from the flat plate cascade theory of Whitehead [14] using the procedures developed by Smith [15].[3] They were calculated only at $k = 0.035$, .086, and .134 and have been superimposed on the three panels for $\alpha_{MCL} = 8$ deg for convenience. It is seen that the general trends for the theory are similar to the experimental results for low loading or for high frequency although the magnitude of Ξ does not agree. This is hardly surprising because even at $\alpha_{MCL} = 6$ deg the results of Fig. 5 show that significant turning has occurred, and the theory is derived for a flat plate cascade at zero incidence angle. Nevertheless, theory and experiment both agree in their prediction of instability for positive interblade phase angles, even under low load conditions. Furthermore, the crossover from stability to instability at values of $\sigma \approx 0$ deg are in reasonable agreement.

In each of these three figures, it appears that we can draw a diagonal line through the entire set of panels from upper left to lower right to separate the region behaving like low loading from the region behaving like high loading. This is precisely the effect one experiences in isolated airfoil response, as described earlier. The system trends toward low-loading behavior as frequency is increased, and trends toward low-frequency behavior as loading is increased. Furthermore, in the upper right diagonal region of Fig. 8 the experimental curves are all similar to one another and strongly resemble the theoretical curves for the flat plate cascade. Thus, within this context, and supported by the steady-state trends in pressure rise, turing, and loss shown in Fig. 5, we can presume that the deterioration of stability for negative σ is probably associated with the deterioration of flow quality under high load, and that this effect is mitigated by an increase in frequency. However, of equal importance is the persistent region of cascade instability at positive interblade phase angle over all values of σ. Although it is beyond the scope of the present paper to provide a basic understanding of the instability, the next section will present additional observations in which some of the details of the induced loading are discussed.

Before proceeding to the next section, it is useful to consider Fig. 9, which is a crossplot of Fig. 8 and presents Ξ as a function of k for several values of σ. In each panel, the three loading conditions are distinguished by appropriate symbols. Also included here are crossplots of the theoretical predictions from Fig. 8. The plots of Fig. 9 show the experimental trends described earlier in another form. At negative interblade phase angles, the widely varying values of Ξ for the three incidence angles tend to converge toward the theoretical value at high damping as k increases. This is particularly true at $\sigma \approx -60$ and -45 deg where the results are reminiscent of isolated airfoil experience. Although the theoretical values are generally far removed from the measured results, there is a tendency for the low-loading condition at $\alpha_{MCL} = 6$ deg to approach the theory. In contrast to this, it is seen in all panels for $\sigma \geq 20$ deg that the cascaded blade remains unstable for all k and for all values of α_{MCL}. In this range of σ the experimental values of Ξ show little variation in magnitude with k, while the theoretical curves are strongly dependent on k, tending toward stability as k increases. (It should be noted that use of the tabulated values in [14] shows the system to be stable for $k \geq 0.25$.)

These results further emphasize the difference between the isolated airfoil and the cascade. The isolated airfoil has never been known to be unstable in subsonic single-degree-of-freedom torsional flutter except under high-load condition whereas the cascades can be unstable for a variety of conditions including low loading and even potential flow. Further, the inability of the existing cascade theory to predict the damping behavior with any reasonable accuracy, even at low loading may be attributed to the limitations of flat plate theory and its inability to model the actual flow past a cascade of cambered,

[3] The authors are indebted to Dr. R. H. Ni of the Pratt & Whitney Division of United Technologies Corporation for making the calculated values available.

Downloaded 01 Jun 2010 to 171.66.16.58. Redistribution subject to ASME license or copyright; see http://www.asme.org/terms/Terms_Use.cfm

6 percent thick experimental airfoils, and points up the need for additional research in this area.

Pressure Time Histories. In the previous section it has been shown that the interblade phase angle, σ, is the dominant parameter affecting cascade stability. Since the interaction between adjacent blades is believed to be strongly dependent on σ, it might be surmised from the present results that cascade stability and blade interaction are closely linked. It is also worth noting the effect of σ on the pressure time histories near the leading edge. Fig. 10 illustrates this over a range of σ for $\alpha_{MCL} = 8$ deg and $k = 0.14$. The most revealing observation is the increasing dominance of the second harmonic component of the pressure response near the leading edge (1.2 percent chord station) as σ increases in the positive direction. This second harmonic trough occurs at peak incidence angle and has all of the outward appearances of the loss in suction peak associated with dynamic stall. However, from a computational point of view, this strong second harmonic behavior at the leading edge does not contribute to the damping by orthogonality because the damping parameter involves an integration over one period of the product of the motion and the moment-weighted chordwise load distribution. (For further details, see p. 34 of [8].) Furthermore, it is seen that this second harmonic behavior in the response is completely absent at the 6.2 percent chord station.

A comparison of these events with those displayed in Figs. 7 or 8 reveals that the quenching of the first harmonic component (relative to the second harmonic component) at the leading edge for $\sigma > 5$ deg coincides closely with the onset of instability. In addition, since most of the induced loading occurs in the forward 10 percent region of the blade suction surface [8, 9], it is clear that as the impact of the first harmonic component of the leading edge response is diminished (when $\sigma > 5$ deg), the load response at the 6.2 percent location becomes the predominant contributor to the first harmonic component of the integrated moment and thus the aerodynamic damping coefficient. An examination of Fig. 10 shows that there is a phase shift from lead to lag at this station (relative to α) as σ decreases, which has been confirmed by a harmonic analysis of the data (not included here). It is easily shown by analysis that the system instability is a direct consequence of this phase shift.

The logical conclusion to be drawn, based on the observations cited above, is that an analysis attempting to relate cascade stability (as a function of σ) to the corresponding events in the leading edge region of the blade may be fruitful. This is an ongoing effort and has already yielded some correlative relationships between the various parameters. Ultimately, an understanding of how these events are related would provide the additional physical intuition needed for developing a refined analytical study of subsonic cascade flutter.

Summary of Findings

The work reported on herein is a continuation of the research described earlier in [8, 9]. In view of the more extensive program that has been conducted it is now felt that the tentative findings of the previous work have been largely validated and extended, and that a basis has been established for a continuing research program in this field. The following are the findings of this study.

Primary Findings

1 For all values of α_{MCL} and k tested the cascade is unstable for positive interblade phase angles greater than $\sigma = 10$ deg.

2 As α_{MCL} is increased at low to moderate reduced frequency the aerodynamic damping becomes negative for negative interblade phase angles.

3 Thus, as stated in [9], for the range of parameters tested, the interblade phase angle is the most important parameter affecting the stability of oscillating cascaded airfoils.

4 The results of this investigation verify the statement made in [6] that blade stall is not an essential condition for "stalled" flutter of airfoils in cascade, and indicate that a more appropriate term might be loaded blade flutter.

Secondary Findings

5 Steady-state blade pressure distributions for all three values of α_{MCL} show no signs of stall, although other steady parameter measurements (static pressure rise, turning, and loss) indicate some flow deterioration at $\alpha_{MCL} = 10$ deg.

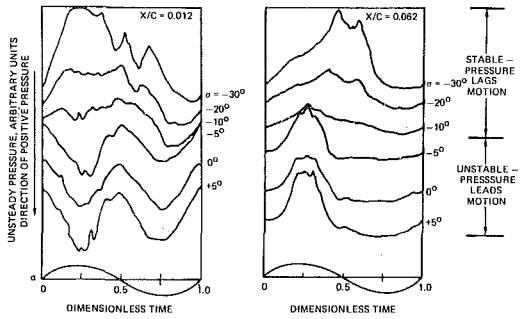


Fig. 10 Time-averaged pressure wave forms from airfoil suction surface for several interblade phase angles

6 For the case analyzed herein, the unsteady pressure at the 6.2 percent chord station lags the motion for $\sigma < -5$ deg and leads for $\sigma > -5$ deg, and appears to be a controlling factor in determining the stability of the system.

7 Also for this single case the unsteady pressure at the 1.2 percent chord station shifts from a predominant first harmonic behavior for $\sigma < -30$ deg to a predominant second harmonic response for $\sigma > -5$ deg and can therefore contribute little to the damping of the primary sinusoidal motion of the system.

8 The pressure trough of the second harmonic time history at 1.2 percent chord occurs at peak incidence angle and has the outward appearance of the loss in suction peak associated with dynamic stall, although steady parameters do not indicate the presence of significant stall.

9 For low loading and/or high frequency the experimental damping behavior is similar to that predicted by flat plate theory. The wide discrepancy in damping level between theory and experiment is tentatively ascribed to the difference between the flat plate theoretical model and the real 6 percent thick cambered blades.

References

1 Carter, A. D. S. and D. A. Kilpatrick, "Self-Excited Vibration of Axial-Flow Compressor Blades," *Proceedings of the Institution of Mechanical Engineers,* Vol. 171, 1957, pp. 245–281.

2 Kilpatrick, D. A., A. D. S. Carter, and L. O'Neill, "Blade Vibratory Stresses in a Multi-Stage Axial-Flow Compressor," A.R.C. R. & M. No. 3181, Jan. 1958.

3 Sisto, F. and R. H. Ni, "Research on the Flutter of Axial-Turbomachine Blading," Stevens Institute of Technology. Technical Report ME-RT 72005, May 1972.

4 Baker, J. E., "The Effects of Various Parameters, Including Mach Number, on Propeller-Blade Flutter with Emphasis on Stall Flutter," NACA TN 3357, Jan. 1955.

5 Carta, F. O. and C. F. Niebanck, "Prediction of Rotor Instability at High Forward Speeds," Vol. III, *Stall Flutter.* USAAVLABS TR 68-18C, Feb. 1969.

6 Mikolajczak, A. A., R. A. Arnoldi, L. E. Snyder, and H. Stargardter, "Advances in Fan and Compressor Blade Flutter Analysis and Predictions," *AIAA Journal of Aircraft,* Vol. 12, No. 4, April 1975, pp. 325–332.

7 Carta, F. O., "Unsteady Surface Flow Behavior on a Cascade of Airfoils Oscillating Below Stall," Project SQUID Technical Report UTRC-1-PU, September 1975.

8 Carta, F. O. and A. O. St. Hilaire, "An Experimental Study on the Aerodynamic Response of a Subsonic Cascade Oscillating Near Stall," Project SQUID Technical Report UTRC-2-PU, July 1976.

9 Carta, F. O. and A. O. St. Hilaire, "Experimentally Determined Stability Parameters of a Subsonic Cascade Oscillating Near Stall," ASME JOURNAL OF ENGINEERING FOR POWER, Vol. 100, No. 1, Jan. 1978, pp. 111–120.

10 Arnoldi, R. A., F. O. Carta, R. H. Ni, W. N. Dalton, and A. O. St. Hilaire, "Analytical and Experimental Study of Subsonic Stalled Flutter," U. S. Air Force Report AFOSR-TR-77-0854, July 1977.

11 Johnson, I. A. and R. O. Bullock, "Aerodynamic Design of Axial Flow Compressors," NASA SP-36, 1965.

12 Davis, E. L., Jr., "The Measurement of Unsteady Pressures in Wind Tunnels," AGARD Report 169, March 1958.

13 McAlister, K. W., L. W. Carr, and W. J. McCroskey, "Dynamic Stall Experiments on the NACA 0012 Airfoil," NASA Technical Paper 1100, Jan. 1978.

14 Whitehead, D. S., "Force and Moment Coefficients for Vibrating Aerofoils in Cascade, "A. R. C. R. & M. No. 3254, 1962.

15 Smith, S. N., "Discrete Frequency Sound Generation in Axial Flow Turbomachines," A.R.C. R. & M. No. 3709, 1971.

Downloaded 01 Jun 2010 to 171.66.16.58. Redistribution subject to ASME license or copyright; see http://www.asme.org/terms/Terms_Use.cfm

S. H. D. Lee
I. Johnson
Chemical Engineering Division,
Argonne National Laboratory,
Argonne, Ill.

Removal of Gaseous Alkali Metal Compounds from Hot Flue Gas by Particulate Sorbents

Six commercially available materials have been tested as granular sorbents to be used in granular-bed filters for the removal of gaseous alkali metal compounds from the hot (1073 to 1153 K) flue gas of pressurized fluidized-bed combustors (PFBC) for proposed combined-cycle power generation. Tests were performed using a simulated dry flue gas of PFBC in a laboratory-scale, fixed-bed combustor. Diatomaceous earth and activated bauxite were found to be the two most promising sorbents. The experimental results of screening tests are presented, along with the effects of temperature and superficial velocity and space velocity of the flue gas on the sorption performance for the two sorbents. Possible sorption mechanisms, applications of the sorbents and preliminary cost evaluations are discussed.

Introduction

Pressurized fluidized-bed combustion (PFBC) in combined-cycle power generation systems provides a direct combustion process of coal with the potential for improved thermal conversion efficiency, reduced costs, and acceptable environmental impacts [1]. Past experiences obtained from operating gas turbines with hot flue gas from the combustion of liquid fuels [2] and from the direct combustion of pulverized coal [3] have indicated that particulates of unburned coal and ash and alkali metal compounds (such as chlorides and sulfates of sodium and potassium) in the flue gas cause catastrophic erosion, corrosion, and fouling of gas turbine hardware. Of these corrosive agents alkali metal compounds in the flue gas are thought to cause hot corrosion of turbine hardware [4, 5]. Therefore, for the successful operation of combined-cycle power plants, cleanup of the hot flue gas to remove particulates and alkali metal compounds is imperative.

Sodium and potassium compounds exist in coal in similar chemical forms. Sodium and potassium chlorides are present in saline ground water permeating the rock and filling pores and cracks in the coal bed. Both sodium and potassium are also constituents of clay minerals in coal, such as illite and montmorillonite. NaCl is a principal form of sodium in coal; potassium in coal, in contrast, occurs largely as nonvolatile alumino-silicates. However, potassium can be released from silicates as KCl through exchange reactions with NaCl vapor [6–8]. Since both NaCl and KCl have appreciable vapor pressures (0.4 and 0.7 kPa, respectively, at 1173 K) at the fluidized-bed combustion temperature range, their vapors are expected to be in the flue gas of PFBC. Thermodynamic calculations indicate that gaseous NaCl and KCl are the major sodium and potassium carriers, respectively, present in the flue gas of a fluidized-bed combustion of coal [9]. Alkali metal sulfates can be formed by the reactions of alkali chlorides with gaseous sulfur compounds.

For the elimination of the hot corrosion problem, the concentration of alkali metal compounds in flue gas have to be reduced to a tolerable level of gas turbines. Combustion Power Company has demonstrated that the addition of an aluminum silicate clay to the combustion zone of PFBC's effectively reduces the emission of alkali vapors [10]. The chemical reactions involved in the fixation of alkali chlorides by an aluminum silicate clay have been well established [11]. For high-temperature and high-pressure (HTHP) particulate cleanup of flue gas, commercially reliable and economically feasible HTHP gas purification equipment is not yet available [12]. Granular-bed filters are among the many devices being actively developed for this application. They hold great promise based on their potential advantages over other devices for particulate removal [13]. With a suitable bed material, the granular-bed filter will allow simultaneous removal of particulates and alkali metal compounds.

Research work has been under way at Argonne National Laboratory to develop effective granular sorbents that can be used as bed material in a granular-bed filter for the removal of alkali metal compounds from the hot flue gas of PFBC. Presented in this paper are experimental results obtained on the screening of six commercial products and the subsequent parametric tests of the two most promising substances. In these experiments, gaseous alkali metal compounds transported in simulated dry flue gas of PFBC were used. Possible sorption mechanisms and applications for the two most promising substances are discussed.

Experimental

In this study, various materials have been evaluated as sorbents for the removal of gaseous alkali metal compounds from a hot gas having the composition expected from pressurized fluidized-bed coal combustors. Screening tests were performed on six commercial products (Table 1) using gaseous NaCl. The two most promising

Contributed by the Gas Turbine Division of The American Society of Mechanical Engineers and presented at the Gas Turbine Conference and Exhibit and Solar Energy Conference, San Diego, Calif., March 12–15, 1979. Manuscript received at ASME Headquarters January 3, 1979. Paper No. 79-GT-154.

Copyright © 1980 by ASME
Downloaded 01 Jun 2010 to 171.66.16.58. Redistribution subject to ASME license or copyright; see http://www.asme.org/terms/Terms_Use.cfm

Table 1 Sources and major composition of materials tested

Sorbent	Source	Major Composition
Alundum	Norton Company, Massachusetts	α-Al_2O_3 (99.5 percent)
Celatom MP-91 Diatomaceous Earth	Eagle-Picher Industries, Inc., Ohio	SiO_2 (92.0 percent); Al_2O_3 (5.0 percent)
Silica Gel	Fischer Scientific Company, N. J.	SiO_2
Burgess No. 10 Pigment	Burgess Pigment Company, Georgia	SiO_2 (44.8–45.3 percent) Al_2O_3 (37.5–39.7 percent)
Attapulgus Clay	Engelhard Minerals and Chemicals Corp., N. J.	SiO_2 (68.0 percent) Al_2O_3 (12.0 percent) MgO (10.5 percent)
Activated Bauxite	Engelhard Minerals and Chemicals Corp., N. J.	SiO_2 (10.0 percent) Al_2O_3 (81.5 percent)

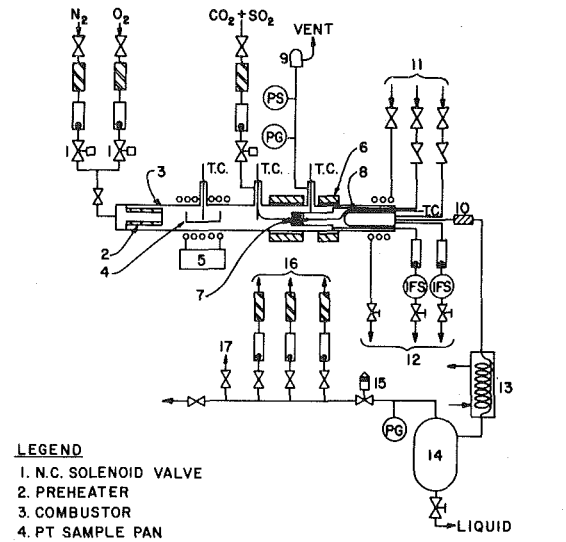
substances were then tested as sorbents for gaseous KCl and K_2SO_4. With the exception of Burgess No. 10 pigment, the material tested were −8 + 10 mesh particles obtained by sieving. The sorbents were preheated in a flowing air stream at 1173 K to remove volatile alkali metal compounds. The fine-powder Burgess No. 10 pigment was formed into cylinders (2.5 cm dia by 3 cm long), heat-treated, and then crushed; −8 + 10 mesh particles were used in the tests.

A laboratory-scale, batch-type, fixed-bed combustor system was used to test sorbents for gaseous sodium and potassium chloride. Fig. 1 is a schematic diagram of the combustor system. A detailed description of the system has been reported elsewhere [14]. The combustor is a 8.9 cm ID 1.8 m long horizontal stainless steel pipe and consists of four sections: preheating, combustion, filtration, and cold-trap sections. The sorbent is placed between two perforated steel plates in a stainless steel tube, which is fastened on the upstream side of a cold trap tube into which a cold finger is inserted; thus, the sorbent is at the filtration section of the combustor. A weighed pure alkali metal compound is heated at the combustion section of the combustor (that is heated by induction heating) and is vaporized. The vapor is carried by preheated flowing gas downstream through the sorbent bed and finally is condensed on the cold trap tube, cold finger, and the backup filter (i.e., the glasswool filter).

For tests using gaseous potassium sulfate, a small-scale sorption test rig was used (Fig. 2). In this test rig, a known amount of potassium sulfate contained in a Pt sample pan is vaporized inside a pure Al_2O_3 tube that is heated by a tubular furnace. The preheated simulated PFBC flue gas then carries the alkali metal sulfate vapor downstrown through a bed sorbent to be tested and a condenser, and finally is vented to an exhaust. The sorbent bed is supported by a Pt gauze and quartz tubing that is inserted concentrically inside the Al_2O_3 tube. The Al_2O_3 tube is capped on both ends with lava end caps.

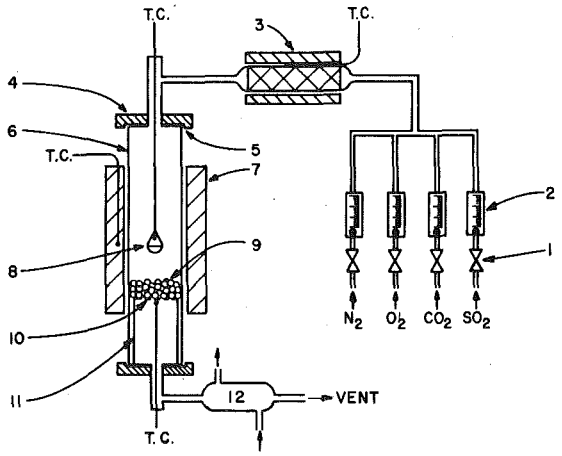
All tests conducted in this study were performed at atmospheric pressure. Except in screening tests for gaseous NaCl for which air was used, sorbents were tested using simulated dry flue gas of PFBC. The volumetric composition of the simulated dry flue gas was 3 percent O_2, 16 percent CO_2, ~180 ppm H_2O, ~300 ppm SO_2, ~80 ppm alkali metal compound vapor, and the balance N_2 for tests with NaCl and KCl vapors. As compared with the estimated alkali concentration in the flue gas of PFBC (~10 ppm), a flue gas with a fairly high alkali concentration was used in this work so that a detectable amount of alkali vapor could be obtained within a reasonable experimental period. For the tests with K_2SO_4 vapor, the average concentration of K_2SO_4 vapor in the flue gas is 3 ppm.

At the end of each experiment, the weight loss of alkali metal compound in the sample pan was measured; the condensates were collected by washing with distilled water and were analyzed for the alkali metals of interest. The sorbent was evaluated by measuring its effectiveness in removing gaseous alkali metal compounds from flue gas. Sodium in the water solution was analyzed by flame emission



LEGEND
1. N.C. SOLENOID VALVE
2. PREHEATER
3. COMBUSTOR
4. PT SAMPLE PAN
5. INDUCTION HEATING UNIT
6. FURNACES
7. SORBENT BED
8. COLD FINGER
9. RELIEF VALVE
10. GLASS-WOOL FILTER
11. COOLING AIR AND WATER INLETS
12. COOLING AIR AND WATER OUTLETS
13. CONDENSER
14. SEPARATOR
15. BACK PRESSURE REGULATOR
16. TO EFFLUENT GAS ANALYZERS
17. SAMPLING PORT
NEEDLE VALVE
CHECK VALVE
ON-OFF BALL VALVE
FLOW METER
DRYER
PG PRESSURE GAUGE
PS PRESSURE SWITCH
IFS INTERLOCKING FLOW SWITCH
T.C. THERMOCOUPLE

Fig. 1 Schematic of batch fix-bed combustor system



LEGEND
1. VALVES
2. FLOWMETERS
3. PREHEATER
4. LAVA END CAP
5. CERAMIC FIBER SEAL
6. PURE Al_2O_3 TUBE
7. TUBULAR FURNACE
8. PT SAMPLE PAN
9. SORBENT BED
10. PT GAUZE
11. QUARTZ TUBING SUPPORT
12. CONDENSER

Fig. 2 Schematic of sorption test apparatus

spectrometry, and potassium by atomic absorption spectrometry. For the analysis of chloride ion, a potentiometric method was used.

Results and Discussion

Six commercial products (Table 1) were first screened by measuring their effectiveness for the removal of NaCl vapor from hot NaCl vapor-bearing flowing air. The two most promising substances were then tested as sorbents for KCl and K_2SO_4 vapors using a simulated flue gas of PFBC. Tests were then made to investigate the effects of some parameters on the sorption performance of gaseous NaCl.

Screening Tests

NaCl vapor tests. Two sets of tests, the first at 1143K in air flow and the second at 1153K in simulated dry flue gas, were completed.

Downloaded 01 Jun 2010 to 171.66.16.58. Redistribution subject to ASME license or copyright; see http://www.asme.org/terms/Terms_Use.cfm

Table 2 Material balances for NaCl from testing sorbents for NaCl vapor capture

Experiment No., HGC—	3	4	5	6	7	8	11	11R	12R	13
Sorbent	Alundum	Diatomaceous Earth	Silica Gel	Burgess No. 10 Pigment	Attapulgus Clay	Activated Bauxite	Diatomaceous Earth	Diatomaceous Earth	Activated Bauxite	Burgess No. 10 Pigment
Flowing Gas	Air	Air	Air	Air	Air	Air	S.F.G.[a]	S.F.G.	S.F.G.	S.F.G.
Experiment Duration, min	180	180	180	180	180	180	100	100	100	100
	Total NaCl, mg									
Input (1) NaCl Transported[b]	92	91	91	92	95	96	242	303	245	252
Output (2) NaCl Collected by										
(a) Cold Traps	71	18	40	15	25	6	6	8	3	26
(b) Glass-wool filter	24	6	15	5	9	2	4	4	5	13
(3) Total	95	24	55	20	34	8	10	12	8	39
(4) Percent NaCl Capture by Sorbent 100 × [(1)–(3)]/(1)	−3	74	40	78	64	92	96	96	98	85

[a] Simulated dry flue gas
[b] Amount of NaCl vapor transported to the sorbent bed

For these two sets of tests, the superficial gas velocity and the gas hourly space velocity (GHSV) of the flowing gas passing through the bed were 8 cm/s and 3,500 h^{-1}, and 25 cm/s and 12,000 h^{-1}, respectively. GHSV is defined as the volumetric flow rate of flue gas in units of sorbent volumes per hour.

Table 2 shows the material balances of NaCl from testing the six commercial products for NaCl vapor capture, and Fig. 3 presents plots of cumulative pore volume against pore diameter for these products. Inert alundum was used to test the experimental system. The good material balance obtained from experiment HGC-3 demonstrated that there was no purely physical condensation of NaCl vapor on the sorbent under the experimental conditions. In comparison to alundum, Celatom MP-91 diatomaceous earth effectively captured 74 percent of the NaCl vapor passing through it. Nelson and Lisle [15] reported that silica gel, with its large internal structures, was the most effective of all silicates tested as corrosion-inhibiting additives for high-temperature liquid phase corrosion in coal-fired boilers. However, when silica gel was used as a sorbent in these tests, it showed only moderate effectiveness in tying up NaCl vapor. This was due to the loss of porosity of the silica gel (Fig. 3) caused by the preheat-treatment of the sample.

Burgess No. 10 pigment has been shown to be a very effective "getter" for alkali metals [10]. Although this pigment and Attapulgus clay effectively captured NaCl vapor in this test system, they became fragile after the tests. Fragility is not an acceptable property because fine particles would be produced, increasing the particulate loading in flue gas. Among the six products tested, activated bauxite is the most effective. Table 2 also shows that in the second set of tests, the efficiencies of NaCl vapor capture of diatomaceous earth, activated bauxite, and Burgess No. 10 pigment were significantly increased—to 96, 98, and 85 percent capture, respectively. This increase is the result of the combined effects of (1) shorter experiment duration, (2) higher NaCl vapor concentration in the flue gas, and (3) the higher superficial velocity of the flue gas that increases the mass transfer of NaCl vapor from the bulk of flue gas to the surface of the sorbent; thereby increasing the sorption of NaCl vapor by the sorbent. When the results in Table 2 are compared with those in Fig. 3, it is noticed that the effectiveness of a sorbent for NaCl vapor capture is generally related to its internal surface area, which is primarily contributed by small pores.

KCl vapor tests. In each of this set of tests, the sorbent was tested at an average bed temperature of 1153K for 100 min in a simulated dry flue gas at a superficial gas velocity of 25 cm/s and a GHSV of 12,000 h^{-1}. Table 3 indicates that diatomaceous earth and activated bauxite captured KCl vapor as effectively as they did NaCl vapor. The KCl vapor capture for diatomaceous earth and activated bauxite were 98 and 95 percent, respectively. In comparison with those two sor-

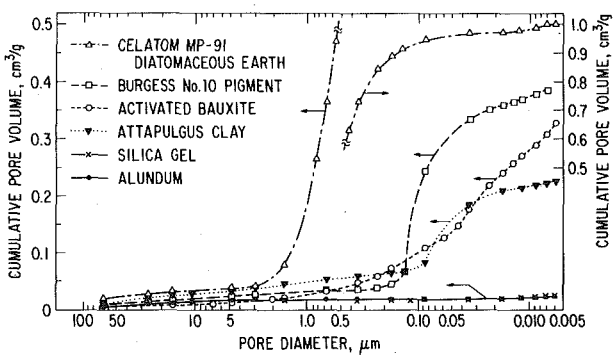


Fig. 3 Cumulative pore volume as a function of pore diameter for six commercial products

Table 3 Material balances for KCl from testing sorbents for KCl vapor capture

Experiment No. HGC—	16	17	18
Sorbent	Diatomaceous Earth	Activated Bauxite	Burgess No. 10 Pigment
	Total KCl, mg		
Input (1) KCl Transported[a]	321	271	263
Output (2) KCl Collected by			
(a) Cold Traps	3	10	45
(b) Glass Wool Filter	1	4	22
(3) Total	4	14	67
(4) Percent KCl Captured by Sorbent 100 × [(1)–(3)]/(1)	98	95	74

[a] Amount of KCl vapor transported to the sorbent bed

Downloaded 01 Jun 2010 to 171.66.16.58. Redistribution subject to ASME license or copyright; see http://www.asme.org/terms/Terms_Use.cfm

bents, Burgess No. 10 pigment was less effective (74 percent KCl capture). This is also true for NaCl vapor capture, as shown in Table 2. The similar sorption activity of these sorbents toward both NaCl and KCl vapor is not surprising because of the similar chemical properties of NaCl and KCl.

K_2SO_4 vapor tests. Tests were conducted using the small scale sorption test rig (Fig. 2). The material balances of K_2SO_4 are given in Table 4 for diatomaceous earth and activated bauxite tested at 1123K for 24 h at the superficial gas velocity of 27 cm/s and a GHSV of 62,000 h^{-1}. As shown in Table 4, 93 and 72 percent of the total K_2SO_4 vapor was captured by activated bauxite and diatomaceous earth, respectively. The sorbent was tested at a fairly high gas hourly space velocity of 62,000 h^{-1}, or a contact time of only about 0.05 s; therefore an increase in capture efficiency can be expected by increasing the contact time of the flue gas with the sorbent. The capabilities of these sorbents for retaining K_2SO_4 vapor from hot flue gas appears to be comparable to their capabilities of retaining alkali metal chloride vapors, as demonstrated previously. Based on the similar chemical properties of K_2SO_4 and Na_2SO_4, it is reasonable to expect that the capabilities of these sorbents for retaining Na_2SO_4 vapor are similar.

Effect of Sorbent Bed Temperature. Diatomaceous earth and activated bauxite were tested for NaCl vapor removal at average bed temperatures of 1073 and 1153K as a function of experiment duration. Tests were conducted using a simulated dry flue gas of PFBC at a superficial gas velocity of 25 cm/s and a GHSV of 67,000 h^{-1}. Fig. 4 shows the amount of NaCl captured per gram of sorbent plotted against the experiment duration in hours.

As can be seen in Fig. 4, the amount of NaCl captured by diatomaceous earth is substantially greater than that captured by activated bauxite on a weight basis (i.e., milligrams of NaCl per gram of sorbent). This is due to the activated bauxite being more dense than diatomaceous earth. On a volume basis (i.e., milligram of NaCl per milliliter of sorbent), the sorption capacity of activated bauxite is greater than that of diatomaceous earth. Fig. 4 also shows that the amount of NaCl captured by diatomaceous earth increases with the sorbent bed temperature. In contrast, activated bauxite behaves in the opposite way to diatomaceous earth with temperature. Fig. 4 also shows that the amounts of NaCl captured by both diatomaceous earth and activated bauxite increase nonlinearly with the experimental duration. This suggests that under the experimental conditions, the rates of NaCl capture by both diatomaceous earth and activated bauxite are not controlled by the mass transfer of NaCl vapor from the bulk of flue gas to the external surfaces of the sorbents [16].

Table 4 Material balances for K_2SO_4 from testing diatomaceous earth and activated bauxite for K_2SO_4 vapor capture

Experiment No., KSO—Sorbent	4 Activated Bauxite	5 Diatomaceous Earth
	Total K_2SO_4, mg	
Input		
(1) K_2SO_4 Vaporized	346	264
Output		
(2) K_2SO_4 Collected from		
(a) Combustion Tube	8	23
(b) Downstream Line Condenser	2	3
(3) K_2SO_4 Captured by Sorbent	322	191
Total	332	217
(4) K_2SO_4 Loss	14	47
(5) Percent K_2SO_4 Capture [100 × (3)/(1)]	93	72

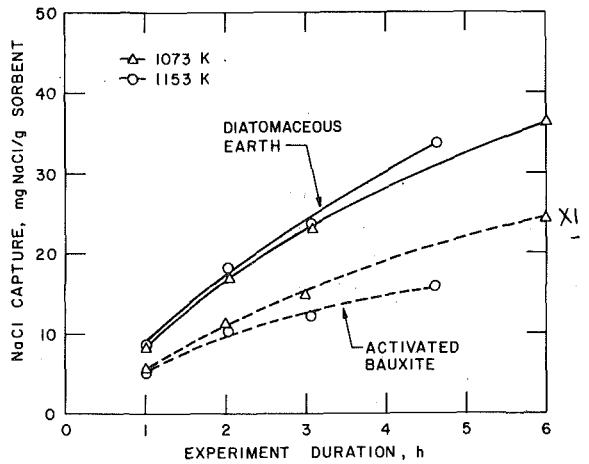


Fig. 4 Effect of sorbent bed temperature on NaCl capture as a function of experiment duration

Effect of Superficial Velocity of Flue Gas at Constant GHSV. In gas-solid reactions, such as the system involved in the present study, the effect of the superficial velocity of flue gas on the rate of NaCl capture provides another means of measuring the role played by the mass transfer of NaCl vapor from the bulk of flue gas to the external surfaces of the sorbent. For mass-transfer-controlled reactions, an increase in superficial gas velocity increases the mass transfer coefficient, thereby increasing the extent of reaction. The superficial gas velocity is also an important parameter when designing a sorber because it determines the bed cross-sectional area of a sorber for a given volumetric flow rate of flue gas to be treated. Based on these reasons, a series of tests was conducted 1073 K using a simulated flue gas at superficial gas velocities of 25, 66, and 155 cm/s and a constant GHSV of 67,000 h^{-1}. The rate of NaCl capture by diatomaceous earth and activated bauxite versus the superficial gas velocity is plotted in Fig. 5.

Within the limits of experimental and analytical errors, the rates of NaCl capture hold constant irrespective of the superficial gas velocity for both diatomaceous earth and activated bauxite. These results verify the conclusion (drawn previously) that under the experimental conditions, the rates of NaCl captured by both diatomaceous earth and activated bauxite are not controlled by the mass transfer of NaCl vapor from the bulk of the flue gas to the external surfaces of the sorbent. Rather, the rate of NaCl capture is controlled by either the diffusion of NaCl vapor through internal pores, the adsorption of NaCl vapor on the active sites of the sorbent, or the chemical kinetics.

Also shown in Fig. 5 are the rates of NaCl capture for both sorbents calculated from results of experiments HGC-4 and HGC-8 in Table 2 on the basis that the amounts of NaCl vapor transported were similar to those transported in the 25 cm/s series of experiments. For those two experiments, sorbent was tested at 1143K in an air flow at

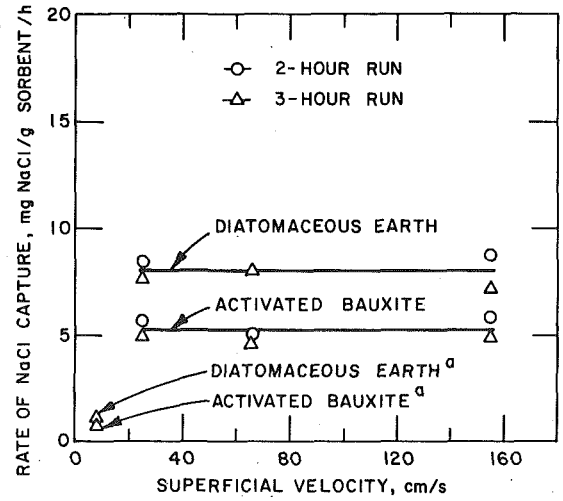


Fig. 5 Effect of superficial gas velocity on rate on NaCl capture. Data calculated from results of experiments No. HGC-4 and HGC-8 in Table 2 on the basis that amounts of NaCl vapor transported were similar to those in the 25 cm/s series of experiments.

Downloaded 01 Jun 2010 to 171.66.16.58. Redistribution subject to ASME license or copyright; see http://www.asme.org/terms/Terms_Use.cfm

a superficial gas velocity of 8 cm/s and with a GHSV of 3500 h^{-1}. Because the sorbents in those two experiments were not tested under quantitatively comparable experimental conditions to those at high superficial gas velocities, the results are included in the figure for qualitative comparison. It is seen that the rate of NaCl capture is substantially lower at a linear velocity of 8 cm/s than at high superficial gas velocities. This indicates that at such a low superficial gas velocity, the rate of NaCl capture by these sorbents was probably mass transfer controlled.

Effect of GHSV of Flue Gas at Constant Superficial Gas Velocity. The gas hourly space velocity (GHSV) is defined as the volumetric flow rate of flue gas in units of sorbent volumes per hour. The reciprocal of the GHSV, which is space time, is related to the contact time of flue gas with the sorbent bed. The GHSV determines the sorbent volume required for a given volumetric flow rate of flue gas to be treated. Both diatomaceous earth and activated bauxite were tested as a function of GHSV at 1073 K and a constant superficial gas velocity of 66 cm/s for 2 h. Fig. 6 is a plot of percent NaCl vapor capture as a function of GHSV (or the contact time in seconds). Fig. 6 indicates that as expected, the increase in contact time of flue gas with the sorbent bed increases NaCl vapor capture for both sorbents. At the fairly short contact time of about 0.2 s and 2 h duration of experiment, 98.5 and 97 percent removal of NaCl vapor from hot flue gas by activated bauxite and diatomaceous earth, respectively, can be achieved.

Sorption Mechanisms. For the purpose of obtaining an insight into the mechanism of NaCl capture by these sorbents, a water-leaching study has been carried out on the sorbents, both fresh and with NaCl absorbed. Leaching was performed using gently boiling (~368 K) distilled water. The leachant was then analyzed for sodium ion and sometimes for chloride ion.

As shown in Table 5, the Na^+ concentrations in diatomaceous earth, Burgess No. 10 pigment, and Attapulgus clay were only slightly higher in the leachants from NaCl-absorbed sorbents than in those from fresh sorbents. This indicates that NaCl vapor was primarily tied up by these sorbents in chemical forms that are not soluble in water. Clay minerals are known to be effective getters for alkali metal compounds [2, 10, 11, 15]. Burgess No. 10 pigment is essentially a kaolin clay; therefore, it is concluded that NaCl vapor was retained by Burgess No. 10 pigment and Attapulgus clay through chemical reactions to form water-insoluble products such as sodium aluminum silicates.

Diatomaceous earth is a sedimentary rock of marine or lacustrine deposition. Chemically, it consists primarily of silicon dioxide and various amounts of impurities such as clay, carbonaceous matter, iron oxide, sand, etc. As shown in Table 1, the Celatom MP-91 diatomaceous earth contains 92 percent SiO_2, 5 percent Al_2O_3, and other impurities. The reaction of

$$2\,NaCl\,(g) + H_2O\,(g) + n\,SiO_2\,(S)$$
$$= Na_2O \cdot n\,SiO_2\,(s) + 2\,HCl\,(g)$$
$$\Delta H_{1073K} = -5.71\ \text{kcal mol}^{-1} \text{ for } n = 1$$

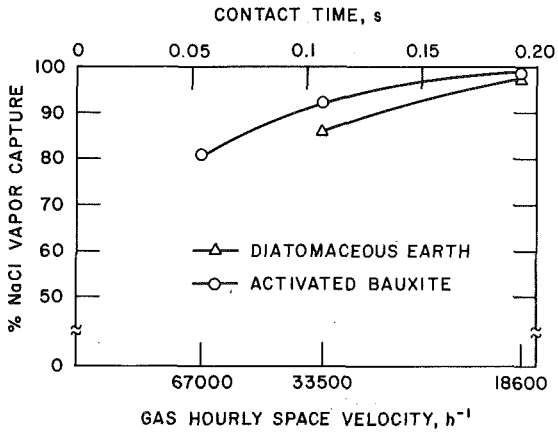


Fig. 6 Effect of GHSV of flue gas on NaCl vapor capture

is well known and has been studied [17, 18]. In the present work, the NaCl vapor is believed to primarily react with diatomaceous earth according to the above reaction to form sodium silicates that are not readily soluble in water. The solubility of an alkali metal silicate depends on the ratio of silica to alkali metal oxide and is also controlled by the amount of impurity present [19]. Part of the NaCl vapor may also react with clays present as impurities in diatomaceous earth. In an investigation of the kinetics of the above reaction, Chirkov [18, 20] reported that between 1113 and 1213K, the rate of the above reaction increases with the temperature according to the Arrhenius equation. The rate of reaction of NaCl with diatomaceous earth in the present system is also noted to increase with temperature, as shown in Fig. 4.

In contrast to these three sorbents, the NaCl captured by silica gel and activated bauxite was readily leached out by water, as shown in Table 5. Within the limits of experimental and analytical errors, the mole ratio of sodium to chloride is close to unity. These results appear to indicate that capture of NaCl vapor by these two sorbents was primarily due to a physical action—an adsorption process. A similar observation was reported by Nelson and Lisle [15] who attributed the inhibiting capability of silica gel for high temperature alkali sulfates liquid phase corrosion in coal-fired boilers to a physical adsorption mechanism. Bauxite is a principal ore of aluminum; it consists mainly of aluminum oxide and other impurities including SiO_2 and clay minerals. Activated bauxite used for this study contains more than 10 percent SiO_2 and clay minerals (Table 1). Chemical reactions of these amounts of impurities with NaCl vapor may also play a role in NaCl vapor capture.

The amount of NaCl vapor adsorbed at equilibrium on activated bauxite at 1073K and atmospheric pressure has been obtained using the sorption test apparatus (Fig. 2). It was found to approach 25 mg NaCl per gram of activated bauxite. Fig. 4 shows that the adsorption of NaCl vapor on activated bauxite approaches the equilibrium amount at the end of 6 h, and the equilibrium amount of NaCl vapor captured is noted to decrease with increasing temperature. Since an adsorption process is always exothermic, the amount of adsorbate adsorbed at equilibrium must always decrease with increasing temperature according to the principle of Le Chatelier; consequently, the present observation clearly substantiates the argument made previously that NaCl vapor is primarily captured by activated bauxite through an adsorption process.

Sorbent Applications. In a proposed PFBC combined-cycle power generation system, the PFBC combustor is combined with an open-cycle gas turbine to achieve improved thermal conversion efficiency. The potential problems associated with the operation of the gas turbine are erosion, fouling, and corrosion of turbine hardwares caused by the presence of particulates and alkali metal compounds in flue gas. The state-of-the-art on the development of HTHP particulate control has been reviewed [12, 21]. Among the many devices presently under the active development of HTHP removal of particulate from flue gas is the granular-bed filter [22–24]. This device is potentially superior to conventional particulate collection devices.

Table 5 Comparison of sodium and chloride ion concentrations in leachants from fresh and NaCl-absorbed sorbents

Experiment No. HGC—	Sorbent	Concentration, mole × 10^6/g Sorbent: Fresh Sorbent Na^+	Fresh Sorbent Cl^-	NaCl-Absorbed Sorbent Na^+	NaCl-Absorbed Sorbent Cl^-
3	Alundum	2.21	N.A.[a]	1.52	N.A.
4	Celatom MP-91 Diatomaceous Earth	0.91	0.11	1.20	0.15
5	Silica Gel	0.47	0.03	1.78	1.39
6	Burgess No. 10 Pigment	0.04	N.A.	0.09	N.A.
7	Attapulgus Clay	0.04	N.A.	0.11	N.A.
8	Activated Bauxite	0.05	N.A.	2.76	2.83

[a] N.A., not analyzed

Downloaded 01 Jun 2010 to 171.66.16.58. Redistribution subject to ASME license or copyright; see http://www.asme.org/terms/Terms_Use.cfm

With appropriate selection of bed material, it will allow simultaneous removal of particulates and alkali metal compounds.

Experimental results presented above demonstrate the effectiveness of diatomaceous earth and activated bauxite as granular sorbents for the capture of alkali metal compounds from hot flue gas. Both diatomaceous earth and activated bauxite have inherent properties of stability at high temperatures and resistance to attrition. With these specific characteristics, these two sorbents hold great promise for the use as filter media in granular-bed filters for accomplishing the simultaneous cleanup of particulate and alkali corrodents from hot flue gas of PFBC.

A low-Btu gasification combined cycle has been identified as an alternative to the PFBC combined cycle for efficient power generation. Because of the effective alkali removal capability, the high temperature stability, and the attrition resistance of diatomaceous earth and activated bauxite, a granular-bed filter with such a sorbent may also be applicable for HTHP removal of particulates and alkali corrodents from the hot flue gas of a low-Btu gasification combined-cycle system, which has similar potential gas turbine hardware problems as the PFBC combined-cycle. These two sorbents should be tested for this application.

Preliminary Cost Evaluations. The cost evaluation presented here is intended as a preliminary estimate of the cost of diatomaceous earth and activated bauxite when used as granular sorbents for the removal of alkali vapors from the hot flue gas of PFBC's. Under the assumption that a typical Illinois coal with a heating value of 29×10^3 J/g is combusted with 20 percent excess air using Tymochtee dolomite at Ca/S mole ratio of 1.5 for 80 percent sulfur removal, the costs for using diatomaceous earth and activated bauxite to achieve 90 percent removal of alkalis from the hot flue gas generated from a 200-MW demonstration plant with 40 percent over-all cycle efficiency are estimated to be 0.07 and 0.53 cents per kilogram of coal burned, respectively. These costs may be compared with 0.26 cents for the cost of the SO_2 sorbent. Although the cost for activated bauxite is more than seven times that of diatomaceous earth, activated bauxite can be regenerated. The cost of regeneration and the number of cycles that activated bauxite can be regenerated without losing its sorption activity are not known.

Conclusions

Experimental results obtained from this work show that both diatomaceous earth and activated bauxite are very effective granular sorbents for the removal of gaseous alkali metal compounds from the hot (1073–1153K) simulated dry flue gas of PFBC's. The retention of gaseous alkali metal compounds by diatomaceous earth is attributed to chemical reactions with alkali metal compounds to form water-insoluble alkali metal silicates. In contrast, activated bauxite primarily captures the gaseous alkali metal chlorides by an adsorption mechanism. The capture capabilities for these two sorbents were found (1) to relate to their internal surface areas, (2) to increase with temperature for diatomaceous earth, but decrease with temperature for activated bauxite, and (3) to increase with a decrease of the gas hourly space velocity of flue gas passing through the sorbent bed. The rates of NaCl capture by both diatomaceous earth and activated bauxite are independent of the superficial velocity of flue gas in the range of 25 to 155 cm/s, indicating that the capture rate is not mass transfer controlled. The potential application of these two sorbents is as filter media in granular-bed filters for the simultaneous cleanup of particulates and alkali metal compounds from hot flue gas of PFBC.

Acknowledgments

The authors wish to express their appreciation to R W. Bane for flame emission and atomic-spectrometry analyses and to A. A. Jonke for helpful discussions. These studies were carried out under the auspices of the U.S. Department of Energy and the U.S. Environmental Protection Agency.

References

1 "Comparative Evaluation of Phase I Results from the Energy Conversion Alternatives Study (ECAS)," NASA Report TM-X-71855, 1976.

2 Reid, W. T., ed., *External Corrosion and Deposits—Boilers and Gas Turbines*, 1st ed., American Elsevier Publishing Comp., New York, 1971.

3 Interdepartment Gas Turbine Steering Committee, "The Coal-Burning Gas Turbine Project," Department of Minerals and Energy, Department of Supply, Australia, Australian Government Publishing Service, Canberra, 1973.

4 Lunt, H. H., "Hot Corrosion in Gas Turbine," ASME Paper 77-WA/Fu-3, 1977.

5 Beltran, A. M., and Shores, D. A., "Hot Corrosion," Chapter II from *Superalloys*, Sims, C. T., and Hagel, W. C., eds., Wiley, 1972.

6 Jackson, P. J. and Ward, J. M., "Operational Studies of the Relationship between Coal Constituents and Boiler Fouling," *J. Inst. Fuel*, Vol. 29, 1956, pp. 154–164; Discussion, p. 441.

7 Jackson, P. J., and Duffin, H. C., "Laboratory Studies of the Deposition of Alkali-Metal Salts from Flue Gas," *Proceedings of the International Conference on the Mechanism of Corrosion by Fuel Impurities*, Central Electricity Generating Board, Marchwood, England, 1963, pp. 427–442.

8 Raask, E., "The Behavior of Potassium-Containing Silicate Minerals in Pulverized-Coal-Fired-Boilers," *Mitteilungen Ver. Grosskesselbetr*, Vol. 48, 1968, pp. 348.

9 "An Investigation of Hot Corrosion and Erosion Occurring in a Fluid Bed Combustion-Gas Turbine Cycle Using Coal as Fuel," FE/1536-2, May 1977.

10 Phillips, K. E., "Energy Conversion from Coal Utilizing CPU-400 Technology," FE-1536-A-2, Annual Report for July 1975–June 1976, Combustion Power Company, Menlo Park, CA.

11 Wall, C. J., Graves, J. T. and Robert, E. J., "How to Burn Salty Sludges," *Chem. Eng.*, April 14, 1975, pp. 77.

12 Meyer, J. P. and Edwards, M. S., "Survey of Industrial Coal Conversion Equipment Capabilities: High-Temperature, High-Pressure Gas Purification," ORNL/TM-6072, June 1978, Oak Ridge National Laboratory, Oak Ridge, TN.

13 Zenz, F. A., and Krockta, H., "The Evolution of Granular Beds for Gas Filtration and Adsorption," *Brit. Chem. Eng. & Proc. Tech.*, Vol. 17, No. 3, 1972, pp. 224–227.

14 Vogel, G. J., *et al.*, "A Development Program on Pressurized Fluidized-Bed Combustion," Annual Report, July 1975–June 1976, ANL/ES-CEN/1016, Argonne National Laboratory, Argonne, IL.

15 Nelson, W., and Lisle, E. S., "High-Temperature External Corrosion on Coal-Fired Boilers: Siliceous Inhibitors," *J. Inst. Fuel*, Vol. 38, 1965, pp. 179–186.

16 Szekely, J., Evans, J. W., and Sohn, H. T., *Gas-Solid Reactions*, 1st ed. Academic Press, New York, 1976, pp. 21.

17 Vail, James G., ed., *Soluble Silicates—Their Properties and Uses*, 1st ed., Reinhold Publishing Corporation, N. Y., 1952.

18 Iler, R. K. and Tauch, E. J., "Sodium Silicate and Hydrochloric Acid from Sand, Salt and Steam," *Trans. Am. Inst. Chem. Engrs.*, Vol. 37, 1941, pp. 853–877.

19 Kirk-Othmer, *Encyclopedia of Chemical Technology*, 2nd Ed., Vol. 18, Interscience Publishers, New York, 1963, p. 134.

20 Chirkov, S. K., "The Preparation of Water Glass without the Use of Alkalies," *J. Chem. Ind.*, Moscow, Vol. 13, 1936, pp. 469–474.

21 "Particulate Control for Pressurized Fluidized Bed Combustion," HCP/T220-16, May 1978, Prepared by Gilbert/commonwealth for U.S. Department of Energy.

22 Wigton, H. and Wade, G., "Granular Bed Filter Development Program—Theoretical Analysis of Granular Bed Filtration Principles and Performance Prediction," FE-2579-18, Jan., 1978, Combustion Power Company, Menlo Park, CA.

23 Hoke, R. C., *et al.*, "Miniplant Studies of Pressurized Fluidized-Bed Coal Combustion," EPA-600/7-78-069, Third Annual Report, April, 1978, Exxon Research and Engineering Company, Linden, NJ.

24 Johnson, I., *et al.*, "Supportive Studies in Fluidized Bed Combustion," ANL/CEN/FE-78-10, Annual Report for July 1977–June, 1978, Argonne National Laboratory, Argonne, IL.

Downloaded 01 Jun 2010 to 171.66.16.58. Redistribution subject to ASME license or copyright; see http://www.asme.org/terms/Terms_Use.cfm

W. S. Blazowski

Exxon Research and Engineering Company,
Corporate Applied Research Laboratories,
Linden, NJ 07036

Dependence of Soot Production on Fuel Blend Characteristics and Combustion Conditions

Liquid synthetic fuels derived from nonpetroleum resources will play a major role in meeting future national energy demands. In the case of gas turbine applications, it is known that the different properties of these fuels can result in substantially altered combustion performance. Most importantly, decreased fuel hydrogen content resulting from an increased aromatic content has been observed to result in increased exhaust smoke and particulates as well as greater flame luminosity. This paper contributes empirical information and insight which allows the greater soot formation tendencies of low hydrogen content fuels to be better understood. A small scale laboratory device which simulates the strongly backmixed conditions present in the primary zone of a gas turbine combustor is utilized. The Jet Stirred Combustor provides for very rapid mixing between a premixture of vaporized fuel and air and the combustion products within a 5.08 cm dia hemispherical reactor. Results to be presented are gaseous combustion product distributions, incipient soot limits, and soot production (mg/ℓ) for a variety of fuels. The influences of combustor inlet temperature and reactor mass loading have been evaluated and the sooting characteristics of fuel blends have been studied. These results have been analyzed to develop useful correlations which are in general agreement with existing mechanistic concepts of the soot formation process.

Introduction

Characteristics of the basic feedstocks from which the future liquid fuels will be made are significantly different from typical petroleum properties. Liquid synfuels, especially those derived from coal, are likely to be more aromatic and have significantly decreased hydrogen content. In the case of gas turbines these characteristics can be expected to result in increased soot formation, increased flame radiation (which can affect the integrity of combustor hardware), and increased deposit forming tendency, possibly resulting in plugging and fouling of equipment. Another significant difference between conventional petroleum and synthetic crudes is nitrogen content. Depending on the extent of refining performed, increased NO_x emission from fuel bound nitrogen may also be a problem. Finally, as a result of the generally lower volatility of synthetic crudes, synfuels might be expected to be less volatile than petroleum-derived fuels thereby causing problems associated with fuel evaporation or droplet burning.

In his plenary session paper, "Synthetic Fuels and Combustion," for the 16th International Combustion Symposium, J. P. Longwell discussed the rationale for the utilization of synthetic liquid fuels without extensive refining [1]. The incentives for following this route were shown to be very significant from the standpoints of energy conservation and cost. For combustion engineers and researchers, the task at hand is one of evaluating the impact of changes in fuel character and defining the range of fuel characteristics within which the system can operate. With this expanded insight, new fuel-flexible designs might be developed which allow operation with minimum cost and energy consumption.

The U. S. Air Force has initiated one such program for defining future military aircraft fuels [2]. The combustion effects of future fuels are to be characterized along with other system factors (e.g., fuel tank design, pumps, handling requirements, etc.) and fuel processing information is to be acquired. A trade-off analysis will then determine the characteristics (a future fuel specification) which will result in minimum total operating cost and adequate availability without significant sacrifice in safety, performance, or environmental impact. With respect to availability, geographic variability in the staple recourse and in refining capability will cause combustion system flexibility to be an important asset.

In the case of gas turbines for future electric power generation, the potential for combined cycle operation makes it imperative that technology be developed to allow operation on liquid synfuels with minimum refining [3]. Development of such fuel-flexible gas turbines will encourage the utilization of synthetic fuels as they enter the marketplace, have major impact on future conservation of petroleum supplies, and reduce the cost of power production.

An analysis of the combustion research requirements brought about by the need for development of fuel-flexible engines [4] indicates that the problem of soot formation resulting from utilization of low hydrogen content, highly-aromatic fuels should receive high priority. The present paper addresses this need. A small-scale combustion device, the Jet Stirred Combustor, has been used to study the soot formation process under strongly backmixed combustion conditions similar to that occurring in the primary zone of a gas turbine combustor. Most previous studies of soot formation involve laminar pre-mixed or diffusion flames—aerodynamic situations far removed from that occurring in the gas turbine combustor—and the present results are believed to be more applicable to gas turbine soot formation. Reference [4] contains an extensive listing of previous publications.

Previously reported Jet Stirred Combustor results [5] concerned the fuel rich combustion and soot formation characteristics of a number of pure hydrocarbons. It was found that all hydrocarbons tested might be grouped into three categories as follows:

Contributed by the Gas Turbine Division of The American Society of Mechanical Engineers and presented at the Gas Turbine Conference and Exhibit and Solar Energy Conference, San Diego, Calif., March 12–15, 1979. Manuscript received at ASME Headquarters January 3, 1979. Paper No. 79-GT-155.

Copyright © 1980 by ASME

Downloaded 01 Jun 2010 to 171.66.16.58. Redistribution subject to ASME license or copyright; see http://www.asme.org/terms/Terms_Use.cfm

Group 1	Group 2	Group 3
Ethylene	Toluene	1-methyl-napthalene
Hexane	O-xylene	
Cyclo-hexane	M-xylene	
N-octane	P-xylene	
Iso-octane	Cumene	
1-octene	Tetralin	
Cyclo-octane	Dicyclopentadiene	
Decalin		

The first group produced large amounts of exhaust hydrocarbons (i.e., many percent based on equivalent flame ionization detector response to methane) without sooting and in no case was significant (i.e., measurable in terms of mg/ℓ) soot observed. The second group produced measurable soot. For these fuels, the leanest mixture ratio at which soot is observed (the incipient soot limit) was found to correspond to the conditions at which significant concentrations of exhaust hydrocarbons were first detected (hydrocarbon breakthrough). In these cases the measured hydrocarbon concentration was less than one percent at the incipient limit. Another commonality in the second group is that the amount of soot produced as fuel-air mixture ratio was increased beyond the incipient sooting limit was similar (within a factor of two) for all the hydrocarbons. 1-methyl-napthalene was significantly different in this respect producing much higher soot quantities than those in the second category.

The purpose of this paper is to present additional experimental results which concern soot formation characteristics of fuel blends and the impact of operating conditions on soot formation. The fuel blend evaluation considered a two-component mixture composed of a Group 1 and a Group 2 hydrocarbon. Operating characteristics which were evaluated included reactor mass loading (mass flow into the reactor) and inlet temperature. Information presented below is organized into four further sections. Section II concerns the experimental system, Section III presents results, Section IV discusses the experimental findings, and Section V is a summary.

Experimental

The experimental program reported here focused on study of fuel-rich combustion and soot formation processes using the Jet-Stirred Combustor (JSC). This device is a modification of the Longwell-Weiss reactor [6] with hemispherical geometry. The JSC has been used extensively in fluid mechanic and combustion modeling because combustion rates are limited by chemical kinetics as opposed to transport effects. A key advantage of the JSC for the present program is that the strongly backmixed nature of this combustion process provides a simulation of the recirculating characteristics of the gas turbine primary zone. It is in this zone where mixture conditions are sufficiently rich to produce soot. Consequently, the JSC allows study of soot formation in an aerodynamic situation relevant to gas turbine systems. Another advantage of the stirred combustor is that the reactor is homogeneous in species concentration as well as temperature; each operating condition is characterized by a *single set* of temperature and concentration data rather than profiles of these parameters. This simplifies the tasks of obtaining and interpreting data.

The reactor (Fig. 1) consists of an outer shell of castable refractory shaped as two halves of a sphere, 15.2 cm in diameter. Materials used in fabricating these reactors are Super Castable 3200, Fractocrete 3400, or Castable 141A, all products of Combustion Engineering Refractories. The upper hemisphere is solid with the exception of the hole through which the reactants are brought to the injector. The lower portion is hollowed out to a hemispherical reaction zone of 5.08 cm dia and has 25 holes of 3.2 mm dia through which the burned mixture exhausts. Combustion experiments are conducted at atmospheric pressure with a range of residence times from 0.6 to 4 ms.

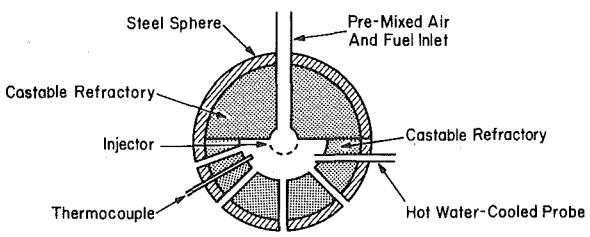


Fig. 1 The jet stirred combustor

Fuel and air are metered separately through calibrated rotameters, preheated to the desired inlet temperature and then mixed before entering the combustor. Air and fuel heating to temperatures of 350°C (and fuel prevaporization in the case of liquids) is accomplished in an aluminum block heater. Separate coils for fuel and air are embedded in the solid aluminum block which is wrapped with electrical resistance heaters. In the case of liquid fuels, a small flow of N_2 is maintained through the fuel coil to atomize the fuel and provide for smooth vaporization. Atomization is achieved at the entrance to the heater with a Spraying Systems Company 1/4 JSS air atomizing nozzle. In this configuration, a central jet (0.2 mm dia) of fuel is atomized by the strong shearing forces caused by a co-axial jet (between diameters of 1.2 and 1.6 mm) of N_2.

The temperature of the fuel/air stream is determined immediately before injection. This measurement is input to a digital controller which provides power to the block heater to maintain injector inlet temperature within ±10°C of the set point. The fuel-air mixture enters the reaction zone through an Inconel injector which is a hemisphere of 1.27 cm dia into which are drilled forty radial holes of 0.5 mm dia. Reactants enter the reaction zone as small sonic jets which stir the reactor contents and produce a mixture of essentially uniform temperature and composition in a characteristic time which is very short compared with the average residence time.

A probe is inserted through one of the twenty-five exhaust ports to extract a sample. Special care has been taken to prevent condensation of water or unburned hydrocarbons within the probe and sample lines, as high concentrations of these constituents are expected at mixture ratios of interest in this study. The sampling probe is hot-water (~80°C) cooled and has a constant-area cross section two mm in diameter. Sample flow is 1–2 ℓ/min. The gas sample is transferred through electrically-heated sample lines to a sample conditioning oven containing all filters, valves, and pumps. The lines and oven are maintained at 150°C.

Gas analysis is accomplished with conventional process instrumentation. A filter within the oven removed particulates from the sample stream sent to the gas analysis instrumentation. A first gas stream leaving the oven is transferred through hot (~150°C), electrically-heated lines to a Beckman Model 402 flame ionization detector for total hydrocarbon (THC) measurement. This instrument has a vast dynamic range allowing determination of hydrocarbon concentrations ranging from the parts-per-million level through tens of mole percent. The hydrocarbon instrument was calibrated with a mixture containing CH_4 and all reported THC results are "as methane." A second sample gas stream leaving the oven is chilled to eliminate condensable water (to a dew point of about 10°C) and hydrocarbons prior to introduction into NDIR analyzers for CO and CO_2 measurements.

The particulate sampling system uses different filters located within the sample-conditioning oven. Two 47 mm filters sealed in a stainless steel holder were used in "series." The first was a Millipore Mitex (Teflon) filter with a 5 μm pore size; the second was a Gellman Type AE with a 0.3 μm pore size. The Teflon filter was found to be necessary to prevent the glass fiber material from sticking to the Viton O-Ring sealing the filter holder. Nearly all the soot collected was found on the first (Teflon) filter.

The incipient soot formation equivalence ratio was the simplest determination of sooting characteristics pursued during this program. For this information, data are taken at increasing equivalence ratio[1] increments of 0.1 until a filter deposit is observed. Results presented will, therefore, represent an equivalence ratio value midway between test points at which soot was observed.

[1] Equivalence ratio, ϕ, is the actual fuel-air ratio divided by the stoichiometrically correct fuel-air ratio. Values less than one correspond to lean operation while values greater than one indicate fuel rich operation.

Downloaded 01 Jun 2010 to 171.66.16.58. Redistribution subject to ASME license or copyright; see http://www.asme.org/terms/Terms_Use.cfm

Soot production (mg soot/liter) was determined by a differential weighing procedure. The Teflon filters were not preconditioned to drive off moisture—it was experimentally found that this is not necessary. The glass-fiber filters were conditioned by overnight drying in an oven at 150° followed by at least four hours in a desiccator. The Teflon and dried glass-fiber filters were then pre-weighed together and stored in the desiccator until actual use. After soot collection the samples were kept in a desiccator overnight to drive-off moisture remaining from the combustion gases which has passed through. Final weighing was then performed on a Metler H20 balance. In general, 10 standard liters of gas passed through each filter produced a collection of soot sufficient for weighing. A wet test meter was used to determine this total volume throughput which usually required less than ten minutes to accomplish.

Under many conditions it was evident that significant soot had deposited along the inner wall at the probe tip during sampling. In these cases the deposited soot was limited to a few mm of the probe tip and was removed with a fine wire to be included with the filters in the differential weighing procedure. Under lightly-sooting conditions the fraction of the total soot determination attributed to the deposit was a small fraction of that on the filters. However, at highly-sooting conditions, the deposit weight could be equivalent to the filter contribution.

Results

The previously reported results of this program [5] concerned detailed soot formation information for ethylene and toluene and the conclusion that these fuels behave in distinctly different ways. Data to be discussed below concern the dependence of sooting characteristics for these two fuels on reactor mass flow and inlet temperature. In addition, results will be presented which provide new information regarding the soot formation characteristics of fuel blends. Mixtures of iso-octane and toluene (from Groups 1 and 2 as described in the Introduction) were evaluated as was a commercial Jet A fuel.

Sooting Dependence on Operating Conditions. Ethylene was the first fuel studied under fuel-rich conditions at which soot may form. However, the amount of soot produced with ethylene is very small and no measurements of soot production were made. Experimental observations are limited to the incipient soot mixture ratio and the gas species concentrations in the neighborhood of the incipient soot limit.

The dependence of the incipient soot formation limit on reactor inlet mixture flow rate and inlet *temperature* was determined. Fig. 2 illustrates the dependence of the incipient soot formation limit on inlet mass flow rate for ethylene-air combustion at an inlet temperature of 25°C. The flow rate effect appears to be significant with soot limit equivalence ratio increasing from 1.85 to 2.25 over the flow range tested (70–160 gm air/min). It can be postulated that residence time effects—particularly the effect of reduced burnedness as JSC loading is increased—are important to ethylene's soot formation process in the well mixed situation. This will be discussed further in Section IV.

Data presented in Table 1 indicate that the temperature effect on the incipient soot limit is not measurable over the range of ethylene air combustion conditions investigated (25–300°C). Wright [7, 8] reported a continuous increase in incipient soot equivalence ratio with increasing temperature in a JSC experiment but considered a broader range of temperatures and identified the critical O/C by observing flame color.

A notable temperature effect observed during this testing was that the darkness of the filter observed at the lowest sooting equivalence ratio increased with mixture inlet temperature. At 25°C the darkness of the soot deposit was very light with increased darkness as temperature was elevated. Another observation was that at mixture ratios richer than the soot limit the soot deposit on the filter first became darker but then lighter as the blowout mixture ratio was approached.

The incipient soot limit behavior of toluene was determined as a function of inlet mass flow and inlet mixture temperature (at 200, 250, and 300°C). No distinct relationship between the incipient soot limit and these parameters was uncovered. Using the same technique used in evaluating C_2H_4—leanest operation at which a soiled filter was observed—the limit was consistently found to be 1.35.

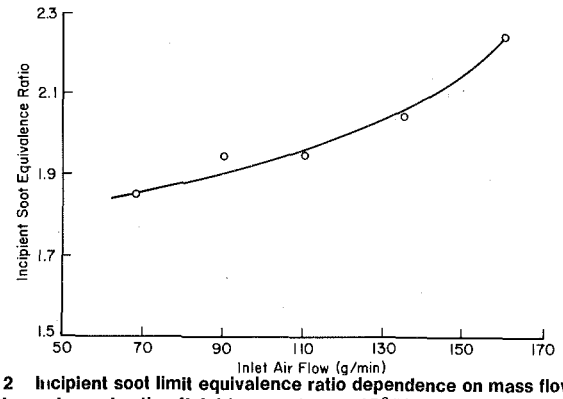


Fig. 2 Incipient soot limit equivalence ratio dependence on mass flow for ethylene-air combustion (inlet temperature = 25°C)

Table 1 Incipient soot limit dependence on inlet temperature for ethylene-air combustion

	(m_{air} = 110 g/min)	
Temp.	ϕ	Percent HC
25°C	1.95	5.0
100°C	1.85	3.2
200°C	1.95	4.3
300°C	1.95	3.4

Fig. 3 illustrates the dependence of soot production on mixture inlet temperature for toluene-air mixtures. As has been noted previously, the incipient soot limit was not substantially influenced by inlet temperature. However, these data illustrate that mixture inlet temperature (and flame temperature) increases result in greater soot production at the higher equivalence ratios.

The influence of reactor loading on toluene soot production is shown in Fig. 4. These data correspond to operation at air mass flows of 50, 80, and 112.5 gm/min and at an inlet mixture temperature of 300°C. Note that while the incipient soot limit was not significantly affected by mass flow, soot production was substantially less at the lower air mass flow condition. An explanation of this behavior and interpretation of the practical implications of these findings is reserved for the discussion section which follows. The results of Fig. 4 also indicate that soot production increases very significantly as the mixture equivalence ratio increases. However, translation of the data to fraction of fuel carbon as soot indicates that, even at the worst condition, less than 1 percent of the fuel carbon is converted to soot.

These results for toluene and ethylene indicate a number of potentially important differences between the effects of operating conditions on the soot formation processes of the Group 1 and Group 2 hydrocarbons:

1 Toluene soots at a much lower equivalence ratio (1.35) than ethylene (1.95) and the amount of soot formed with ϕ beyond the incipient limit is much larger.

2 The incipient soot limit for ethylene was found to vary with mass flow, but this was not the case for toluene.

Results presented previously [5] provide a third important difference between Groups 1 and 2 which complement those above. Namely, in the case of Group 1 hydrocarbon combustion, significant amounts of hydrocarbons (about 3–8 percent as CH_3) were present at equivalence ratios leaner than the soot limit but with the Group 2 hydrocarbons the incipient soot limit corresponded approximately to the equivalence ratio for the initial presence of hydrocarbons in the combustion products.

Sooting Characteristics Of Fuel Blends. Blends of iso-octane and toluene were tested to determine the behavior of a two-components mixture with like-C_2H_4 and like-$C_6H_5CH_3$ hydrocarbons. These results are shown in Fig. 5 and Table 2. Mixtures with 50 or more percent toluene produced soot while a 25 percent toluene blend did not. Clearly, for the mixtures which did soot, increases in the volume percent toluene result in increased soot production at all equivalence

Downloaded 01 Jun 2010 to 171.66.16.58. Redistribution subject to ASME license or copyright; see http://www.asme.org/terms/Terms_Use.cfm

ratios. It was also determined that with less toluene in the blend, the concentration of hydrocarbons at the incipient limit tended to increase. For example, with 50 percent toluene, the hydrocarbon concentration was 2.4 percent, while with 100 percent toluene this value was 0.20 percent. These results indicate a combination of Group 1 and 2 behaviors and imply that a combination of the analytical descriptions for toluene and iso-octane might be a reasonable approach for prediction of the sooting characteristics of such fuel blends.

A commercial aviation turbine fuel, Jet A, was also tested. This fuel produced soot, but in amounts less than the 50 percent toluene/50 percent iso-octane blend discussed above. Further, the incipient soot limit equivalence ratio was found to be greater than that of the 50 percent blend (ϕ = 1.7 versus 1.5). These results are consistent with the previous observations in that the Jet A has a hydrogen content of about 13.9 percent, midway between the 50 percent toluene blend (11.9 percent) and the 25 percent toluene blend (14.6 percent) which did not soot.

Attempts to test two coal liquids were made. These were both COED samples supplied by FMC of Princeton, New Jersey. The first was produced from Utah Coal while the second utilized a Western Kentucky coal. Both tests failed as these fuels were found to plug the atomizing nozzle utilized in the fuel prevaporizer. The 0.2 mm dia fuel orifice became plugged with a gum-like substance which prevented fuel flow.

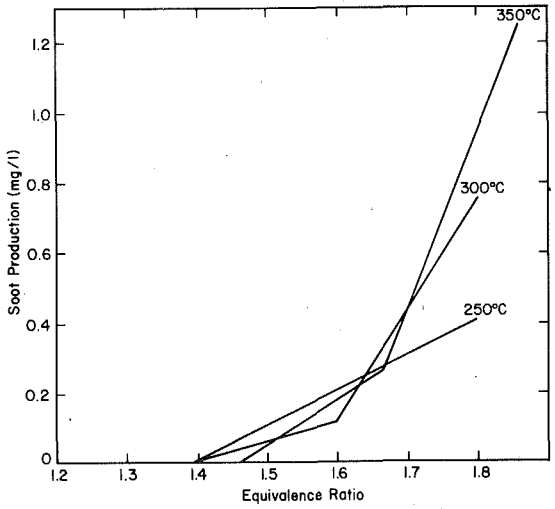


Fig. 3 Effect of inlet temperature on soot production of toluene

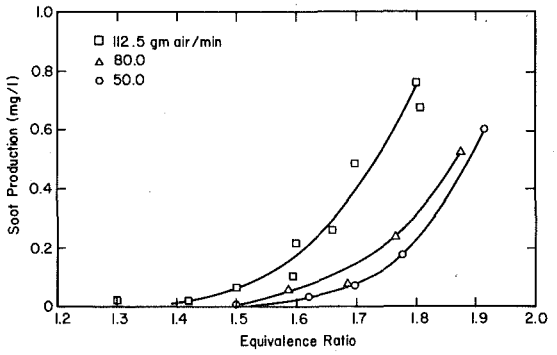


Fig. 4 Dependence of toluene soot production on mass loading (inlet temperature = 300°C)

Discussion

The discussion below provides further interpretation of these results. Key items addressed are:

- Correlation of fuel blend soot production results with blend overall hydrogen content
- Assessment of soot production trends with exhaust product THC
- Comparison of current results with soot formation theories.

Hydrogen Content Correlation. The toluene/iso-octane soot production data illustrated in Fig. 5 may also be examined to evaluate the effect of fuel hydrogen content, a parameter often reported as useful in correlating sooting characteristics. At constant equivalence ratios of 1.6 and 1.8, an excellent correlation implying a linear relationship is evident (see Fig. 6). Actual gas turbine combustor testing has also found an approximately linear relationship between fuel hydrogen content and soot production [9] and the results discussed here indicate an important similarity between sooting in the well-characterized JSC and that in an actual combustor.

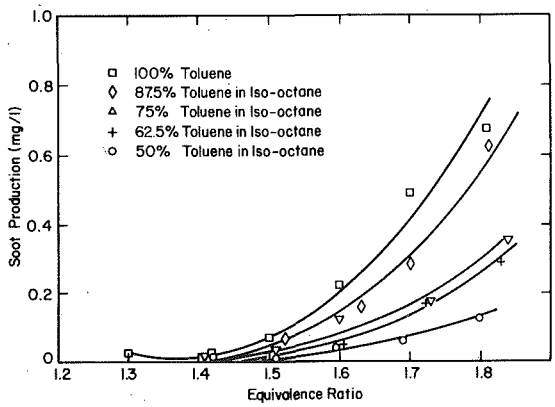


Fig. 5 Soot production versus equivalence ratio for toluene and toluene/iso-octane blends at 300°C inlet temperature and 112.5 gm/min air flow

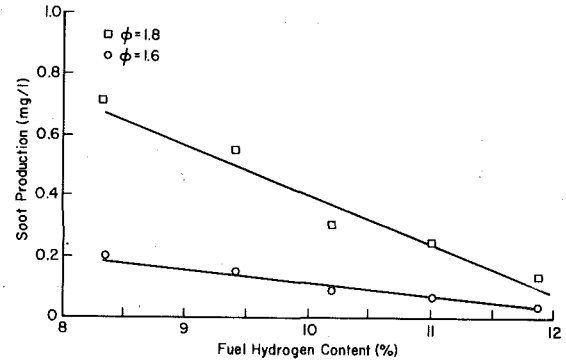


Fig. 6 Dependence of soot production on hydrogen content of toluene/iso-octane blends

Table 2 Fuel blend screening results

Fuel	Incipient Soot Limit[1] ϕ	Incipient Soot Limit[1] Percent HC	S_T[2] @ ISL + 0.2ϕ mg/l	S_T[2] @ ISL + 0.2ϕ Percent HC	S_T @ ISL + 0.4ϕ mg/l	S_T @ ISL + 0.4ϕ Percent HC
100 percent toluene	1.39	0.20	0.118	1.72	0.765	5.88
87.5 percent toluene/12.5 percent iso-octane	1.41	0.15	.160	2.2	0.63	5.25
75 percent toluene/25 percent iso-octane	1.40	1.21	.122	4.88	4	
62.5 percent toluene/37.5 percent iso-octane	1.49	0.82	.165	3.85	4	
50 percent toluene/50 percent iso-octane	1.50	2.4	.060	6.75	4	
25 percent toluene/75 percent iso-octane	1.61[3]	7.12				
10 percent toluene/90 percent iso-octane	1.51[3]					

[1] Incipient soot limit (ISL) is condition at which soot was first noted on a clean filter
[2] S_T = Total soot combination of soot on filter and in probe
[3] Does not soot—highest equivalence ratio value bbtained prior to blowout
[4] Rich blowout occurred before condition could be reached

Downloaded 01 Jun 2010 to 171.66.16.58. Redistribution subject to ASME license or copyright; see http://www.asme.org/terms/Terms_Use.cfm

Another interesting implication of the Fig. 6 correlation is that the JSC might be a tool useful in better relating fundamental fuel characteristics to combustion behavior. In this context, it will be useful to examine the Fig. 6 correlation for other two component blends and for three and four component blends. This should provide the means of combining semi- or quasi-global models of the soot formation process for various hydrocarbon types to describe a fuel blend (see [3] and [4] for a description of this approach). For example, it may be that an iso-octane/1-methyl-napthalene blend will produce a steeper soot production/hydrocarbon content trend than is evident for the toluene/iso-octane blend. Work of this type might result in new insight regarding the ranking of the soot production potential of various continuous combustion system fuels.

Trends with THC. Throughout this paper and [5] the concept that exhaust total hydrocarbon content is a key parameter in soot formation has been proposed. In analyzing the data obtained it has been found that useful correlations can be developed. Before presentation of this information, however, it is necessary to more closely examine the data which has been produced very near the rich blowout point. It will be concluded below that some of the data corresponded to operation beyond the rich blowout point. In these cases, the reactor operated sporadically with fuel passing through uncombusted at times and the system behaving as a pyrolysis or coker system.

Data for which this situation existed have been identified by close examination of the temperature information obtained. Close review of the results indicate that in many cases the measured and/or calculated reactor temperature is less than that of the thermocouple embedded furthest within the castable refractory. That is, the reactor is hotter than the combustion products and, therefore, must be supplying heat to the reactants. Naturally, this is an unstable process which leads to the sporadic combustion which was observed. These data must be considered as not directly relevant to the current study and have been discriminated against in the correlations which are to be discussed below.

The correlation involving THC as the key parameter involves the previously-reported results for toluene soot production variation with JSC mass loading (Fig. 4). It was determined that these data for 50, 80, and 112.5 gm air/min could be correlated with combustion product total hydrocarbon concentration. These results are illustrated in Fig. 7. The shaded data points in this graph correspond to operating conditions believed to be beyond the rich blowout point and are not considered in developing the correlation. The implication of the trend pictured in Fig. 7 is that regardless of residence time the factor most important to soot production is the reactor hydrocarbon concentration. Consequently, reduced reactor mass loading (longer residence time) causes increase reactedness (or combustion efficiency) and the decrease in hydrocarbon soot precursors results in less soot production. This information has the practical implication that soot production (and flame luminosity) in gas turbines can be minimized by reducing primary zone mass loading.

Comparison with Theory. Many mechanistic models for soot formation have been proposed [10–28]. Generally, it is recognized that condensed ring aromatic hydrocarbons can produce soot via a different mechanism than do aliphatic hydrocarbons. A simplified mechanism following Graham, et al. [18, 19] is shown in Fig. 8.

Aromatic hydrocarbons can produce soot via two mechanisms: (1) condensation of the aromatic rings into a graphite-like structure, or (2) breakup to small hydrocarbon fragments which then polymerize to form larger, hydrogen deficient molecules which eventually nucleate and produce soot. Based on his shock tube studies, Graham concludes that the condensation route is much faster than the fragmentation/polymerization route. According to this simple model, aliphatics produce soot via the fragmentation/polymerization mechanism only. As a result, these hydrocarbons do not form the quantities of soot produced by the aromatics. Indeed, during the fuel rich combustion of a fuel blend composed of aromatics and aliphatics, the aromatic hydrocarbons would produce the major quantity of soot. Combustion of the aliphatic portions of the fuel would influence temperature and hydrocarbon fragment concentration but soot formation via fragmentation/polymerization would be minimal.

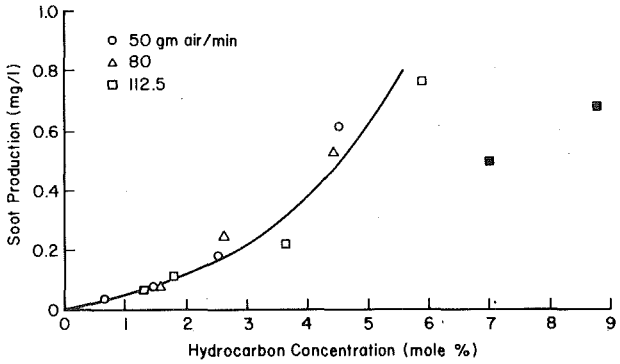


Fig. 7 Correlation of Fig. 4 soot production data with hydrocarbon concentration (shaded data points indicate operation beyond rich blowout)

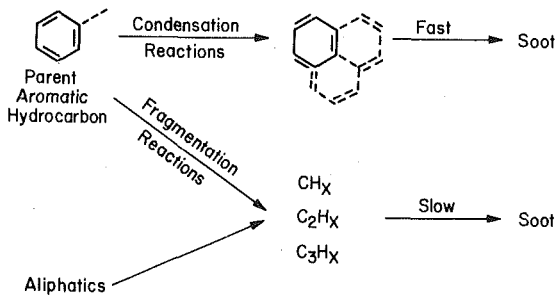


Fig. 8 Simplified soot formation mechanism

The experimental results presented here are consistent with this model. As the amount of toluene in the toluene/iso-octane fuel blends increased, more soot was formed and the incipient limit equivalence ratio decreased with increasing percent toluene. Moreover, the quantity of hydrocarbons present at the soot limit increased as the amount of iso-octane in the blend increased. This implies that ex st hydrocarbons produced by breakdown or pyrolysis of iso-octane produce soot by the slow polymerization route while the breakthrough hydrocarbons with toluene produce soot much more effectively by the ring condensation route. Furthermore, the presence Group 1 and Group 2 behavior evident here indicates that a combination of the analytical descriptions for the two categories might be a reasonable approach for predictions involving fuel blends.

In the variable air flow experiments with toluene (Fig. 8) soot production is closely related to hydrocarbon presence in the exhaust. If we assume that these hydrocarbons maintain their aromatic character, this observation reflects the fast kinetics of the ring-building or condensation reactions. Unfortunately, the present results involve flame ionization detector measurements of total hydrocarbons only. Future efforts to determine the nature of these hydrocarbons are necessary to evaluate this important assumption.

These experimental/mechanism comparisons are not intended to firmly establish the validity of any theory. For example, an equally suitable mechanism can be postulated where the aromatic pyrolysis process supplies very large C_2H_2 concentrations which then can result in substantial soot formation. The observations are presented to illustrate that the results do complement existing simplified views of the soot formation process. Most importantly, the current results lend optimism to the simple engineering approach of quasi-global modeling of the soot formation process.

Summary

Liquid synthetic fuels of the future will be substantially lower in hydrogen content than those currently utilized. Optimal utilization of this resource will involve devising means of altering combustion systems to allow the use of these resources with minimum processing for upgrading. This paper presents results concerning soot formation in a strongly back-mixed combustion device which is representative of gas turbine primary zones.

The influences of combustor inlet temperature and reactor mass loading have been evaluated and the sooting characteristics of fuel

Downloaded 01 Jun 2010 to 171.66.16.58. Redistribution subject to ASME license or copyright; see http://www.asme.org/terms/Terms_Use.cfm

blends have been studied. It was shown that toluene (representative of aromatic constituents in fuels) has an incipient soot formation limit which is not dependent on mass flow while that for ethylene (representative of the aliphatic constituents of fuel) was a function of this parameter. Incipient sooting limits did not vary with inlet temperature, but soot production (at equivalence ratios beyond the limit) for toluene did increase with inlet temperature. Toluene soot production does depend on reactor mass loading in a manner which implies that minimization of soot formation within the primary zone of a gas turbine requires that the zone not be highly loaded.

Fuel blend investigations involved study of toluene/iso-octane blends, Group 1 and Group 2 mixtures; [5] established the distinctly different sooting characteristics of these two hydrocarbon categories. Soot production increased and incipient soot limit equivalence ratio decreased with more toluene in the blend. A correlation between fuel hydrogen content and soot production was established and testing of a commercial Jet A proved consistent with these results. Collectively, these results strongly support the use of the Jet Stirred Combustor for fundamental studies of soot formation in continuous combustion systems. The findings also imply that the JSC may be a useful tool in assessing the soot production potential of various fuels.

All results described here were found to be consistent with a simple soot formation mechanism. While these comments do not prove or confirm the validity of the mechanism, confidence that simple, quasi-global soot formation mechanisms might be developed for use in analytical models of combustion systems is gained by the agreement.

Finally, a note of caution must be expressed. The present results involve a very well mixed system with a vapor fuel. Complications arising from droplets within the combustion zone and turbulence/chemistry coupling via unmixedness which are present in real systems must be taken into account. Future experiments in this program are oriented towards obtaining information to address these questions.

Acknowledgment

This work was supported by the U. S. Department of Energy, Power Systems Division (Contract No. EC-77-C-03-1543). Dr. J. Birkeland of DOE is the responsible Program Manager and Drs. R. Dean Pierce and J. Fischer of Argonne National Laboratory are the technical program monitors. The author is grateful to Mr. Robert Schroeder of Exxon Research and Engineering Company for his contributions to the design of the experimental system and performance of the experimental program.

References

1 Longwell, J. P., "Synthetic Fuels and Combustion," 16th Symposium (International) on Combustion, 1976, pp. 1–15.

2 Churchill, A. V., Delaney, C. L., and Lander, H. R., "Future Aviation Fuels," *J. Aircraft,* Vol. 15, No. 11, Nov. 1978, pp. 731–735.

3 Cooper, V., and Duncan, R., "Baseload Reliability in a Combustion Turbine?", *EPRI Journal,* June 1978, pp. 17–21.

4 Blazowski, W. S., Bellan, J. R., Harsha, P. T., and Edelman, R. B., "Fundamental Characterization of Alternate Fuel Effects in Continuous Combustion Systems," Technical Progress Report No. 1, Contract EC-77-C-03-1543, Jan. 1978.

5 Blazowski, W. S., "Dependence of Soot Production on Fuel Structure in Backmixed Combustion," to be published in *Combustion Science and Technology,* 1979.

6 Longwell, J. P., and Weiss, M. A., *Ind. Eng. Chem.,* 47, 1634, 1955.

7 Wright, F. J., "The Formation of Carbon Under Well-Stirred Conditions," *12th Symposium (International) on Combustion,* The Combustion Institute, Pittsburgh, PA, pp. 867–875, 1968.

8 Wright, F. J., "Carbon Formation Under Well-Stirred Conditions, Part II," *Combustion and Flame,* Vol. 15, pp. 217–222, 1970.

9 Jackson, T. A., and Blazowski, W. S., "Fuel Hydrogen Content as an Indicator of Radiative Heat Transfer in an Aircraft Gas Turbine Combustor," in *Gas Turbine Combustion and Fuels Technology,* ASME, New York, N. Y., Nov. 1977, pp. 59–65.

10 Cullis, C. F., "Role of Acetylenic Species in Carbon Formation," *ACS Symposium Series,* 21, 1976, pp. 348–357.

11 Daniels, P. H., "Carbon Formation in Premixed Flames," *Combustion and Flame,* Vol. 4, pp. 45–49, 1960.

12 Fenimore, C. P., and Jones, G. W., "Comparative Yields of Soot from Premixed Hydrocarbon Flame," *Combustion and Flame,* Vol. 12, No. 3, June 1968, pp. 196–200.

13 Fenimore, C. P., and Jones, G. W., "Coagulation of Soot to Smoke in Hydrocarbon Flames," *Combustion and Flame,* Vol. 13, No. 3, June 1969, pp. 303–310.

14 Fenimore, C. P., Jones, G. W., and Moore, G. E., "Carbon Formation in Quenched Flat Flames at 1600 K," *6th Symposium (International) on Combustion,* pp. 242–246, 1956.

15 Gaydon, A. G., and Wolfhard, H. G., "Solid Carbon in Flames," Chapter VIII in *Flames,* pp. 175–210.

16 Graham, S. C., Homer, J. B., and Rosenfeld, J. L. J., "The Formation and Coagulation of Soot Aerosols Generated by the Pyrolysis of Aromatic Hydrocarbons," *Proc. Roy. Soc. London A.,* Vol. 344, 1978, pp. 259–285.

17 Graham, S. C., Homer, J. B., and Rosenfeld, J. L. J., "The Formation and Coagulation of Soot Aerosols," *Int. Shock Tube Symposium, 10th Proceedings,* July 1975, pp. 621–631.

18 Hein, K., "Recent Results on the Formation and Combustion of Soot in Turbulent Oil and Gas Flames," *Combustion Science and Technology,* Vol. 5, 1972, pp. 195–206.

19 Holderness, F. H., and MacFarlane, J. J., "Soot Formation in Rich Kerosene Flames at High Pressure," Paper No. 18, AGARD Conference Proceedings No. 125, *Atmospheric Pollution by Aircraft Engines,* April 1973.

20 Homann, K. H., "Carbon Formation in Premixed Flames," *Combustion and Flame,* Vol. 11, pp. 265–287, 1967.

21 Howard, J. B., "On the Mechanism of Carbon Formation in Flames," *12th Symposium (International) on Combustion,* 1968, pp. 877–887.

22 Jensen, D. E., "Prediction of Soot Formation Rates: A New Approach," *Proc. Roy. Soc. London A.,* 338, 1974, pp. 375–396.

23 MacFarlene, J. J., Holderness, F. H., and Whiteher, F. S. E., "Soot Formation Rates in Premixed C_5 and C_6 Hydrocarbon-Air Flames at Pressure Up to 20 Atmospheres," *Combustion and Flame,* Vol. 8, pp. 215–229, 1964.

24 Palmer, H. B., and Cullis, C. F., "The Formation of Carbon from Gases," Chapter 5 in *Chemistry and Physics of Carbon,* ed. P. L. Walker, 1965.

25 Stehling, F. C., Frazee, J. D., and Anderson, R. C., "Carbon Formation from Acetylene," *6th Symposium (International) on Combustion,* pp. 247–254, 1956.

26 Street, J. C., and Thomas, A., "Soot Formation in Premixed Flames," *Fuel,* Vol. 34, pp. 4–36, 1955.

27 Tesner, P. A., "Formation of Dispersed Carbon by Thermal Decomposition of Hydrocarbons," *7th Symposium on Combustion,* 1959.

28 Thomas, A., "Carbon Formation in Flames," *Combustion and Flame,* Vol. 6, March 1962, pp. 46–62.

Downloaded 01 Jun 2010 to 171.66.16.58. Redistribution subject to ASME license or copyright; see http://www.asme.org/terms/Terms_Use.cfm

B. M. Huggett
Manager.

D. R. Ingham
Assistant Manager (Design).

Machinery Department
British Gas,
London, England

Improvements in the Utilization of Gas Turbine Compression Plant

The paper reviews the technical developments and changes in philosophy currently underway in British Gas to improve the utilisation of existing and future gas compressor plants. These developments have two main objectives, first to improve the operation of all plants, with corresponding reductions in operating costs, and second to reduce capital investment in future plants by good design and accurate planning. The paper considers in some detail machinery selection including the possibility of a short-term peak operation of plant and the use of waste heat recovery schemes. Improvements in machinery operating efficiency are also reviewed with particular emphasis on performance testing, computer based health monitoring schemes and reliability investigations. The influence of the various technical developments in relation to the investment in new and standby plants is considered.

Introduction

Over the past decade or so dramatic changes have taken place in the gas industry in Britain. With the discovery of natural gas offshore, the Industry has developed from a regional manufacturing and supply concern to a national transmission and distribution system.

The main British Gas transmission system can now handle peak flows up to 200 million m^3/day. The natural gas is transmitted along 5000 Km of high pressure pipelines incorporating 12 compressor stations, and supplied to Regional systems. Currently there is 470 MW installed power and this is expected to increase to 900 MW over the next seven years. The development of the British Gas system has been described in [1].

The pipeline system in England is often described as a high pressure distribution system, rather than a true transmission system, because of the relatively low compressor load factors. The new pipelines transmitting gas from the Frigg and Brent fields are the first real transmission lines with compressors being required to operate on a high load factor. This change in operating mode has provided an additional incentive to reconsider the design, planning and operational strategy. This paper describes the current British Gas philosophy on the utilization of compression equipment and some of the technical developments underway designed to improve the utilization.

Machinery Selection

The Transmission system has been developed primarily with the Avon gas generator providing the hot gases to power a variety of gas compressor/power turbine combinations. Machinery selection involves matching power requirements to the most appropriate machines and adding on extra standby units. The standby policy has always been to add a minimum of one extra unit, of the same type as the primary unit, to the basic station requirement. This means for system requirement of one unit two would be installed; for a requirement of between one and two units, three would be installed. In the case of larger stations the standby installed would depend on a number of considerations including phasing of station development, load factor and the critical nature of the station to the grid. This method of planning was considered essential to obtain quick and reliable operation in what was a completely new system. Circumstances have changed, and planning of compressor stations, whilst being more refined, is also more complicated. Fig. 1 illustrates some of the factors which influence Machinery selection and utilisation at the moment and will continue to do so in the future. Some of the changes are a result of changing philosophies others are a result of technical developments.

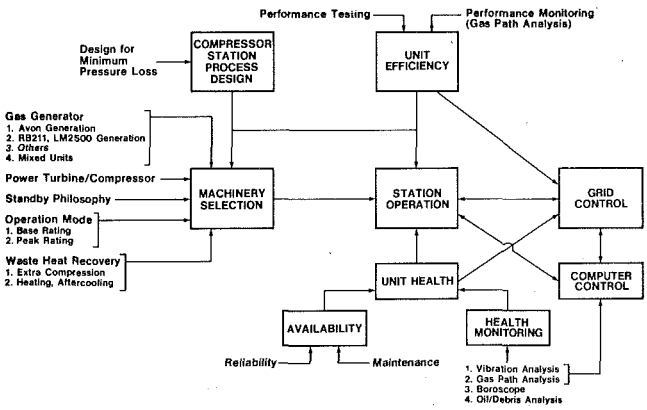


Fig. 1 Factors affecting utilization of compressor plant

Changes in philosophy will in the future influence standby requirements. The concept of mixed units with, for example, an RB211 with a Maxi-Avon operating on peak as standby represents a significant departure from established practice. This will be discussed later.

Contributed by the Gas Turbine Division of The American Society of Mechanical Engineers and presented at the Gas Turbine Conference and Exhibit and Solar Energy Conference, San Diego, Calif., March 12–15, 1979. Manuscript received at ASME Headquarters January 3, 1979. Paper No. 79-GT-156.

Copyright © 1980 by ASME

Downloaded 01 Jun 2010 to 171.66.16.58. Redistribution subject to ASME license or copyright; see http://www.asme.org/terms/Terms_Use.cfm

Standby should no longer be viewed as purely a station concept but should be viewed as a grid concept with the cost of the lost gas being balanced against the installation of extra units.

The technical aspects which influence machinery selections are reviewed in this paper, and broadly speaking, then can be split into three categories:

1 selecting the most cost effective machinery,
2 improvements in basic machinery operating efficiency,
3 improvements in methods of controlling machinery availability.

Selection of the most cost effective machinery solution for a particular requirement is of course the primary concern which in fact interacts with the other categories. For stations with low utilisation it may involve the selection of lower efficiency machinery with lower capital costs. Alternatively it may involve running machines at their peak rating (rather than base rating) thereby offsetting the increased overhaul cost and reduced carcase life by reduced fuel consumption.

Improvements in operating efficiency can be achieved in certain situations by (1) selecting advanced machinery, (2) minimizing energy loss by waste heat recovery schemes, (3) monitoring efficiency of individual machines, (4) optimizing operational efficiency of particular stations and the grid by preferentially running certain machines, and (5) minimizing system pressure losses to reduce machinery power requirements and running costs.

Machinery availability depends upon the inherent machinery reliability, knowledge of the state of health of the machinery, the maintainability of the machinery and the maintainance procedures applied. The inherent reliability can only be improved by a design change, and the strategy is to monitor reliability and, by co-operation with the manufacturer, to insure this is fed back into new designs. The other aspect, which will be discussed later, is to insure that reliability performance matches design reliability. In order to insure the condition or health of the machine is known at any time a computer based health monitoring scheme coupled with regular manual inspections using boroscopes and oil analysis techniques is the proposed strategy. The introduction of computers for unit control has provided an extra incentive for introducing sophisticated health monitoring methods. Certainly the cost and complexity of extending a computer control system to health monitoring is much less than installing a new system.

The object of the reliability studies and the application of health monitoring schemes is to minimise capital expenditure on standby plant by insuring cost effective, quantifiable reliability, while maintaining supply. This new approach is reflected in the remainder of the paper.

Improving Power Output of Machinery

The compression equipment on the national grid is characterised by two primary gas generator sets, the Avon set with an overall efficiency of about 26 percent and the RB211 with an efficiency of 34 percent. At the moment, with heavy industrial gas turbines not presenting a viable alternative for BGC operation, two primary options exist for selection of machinery viz. whether to go for lower efficiency machinery with lower capital cost or higher efficiency machinery with higher capital cost. However, there are more options when thinking in terms of mixed units, peak operation and waste heat recovery. This section considers the added design flexibility possible with this type of option.

Peak Rating. Rolls Royce Avon gas generators supplied to BGC have a base rating and a peak rating. The base rating is intended to give maximum engine life compatible with maximum output available for continuous duties. The peak rating is intended to be the maximum recommended power at which reduced life could be expected. Many of the compressor sets installed in our compressor stations have a peak capability, this capability was regarded as an emergency facility only, because of its adverse effects on engine life. In fact until recently the capability had never been used. The effect of peak operation is to increase power output by up to 30 percent whilst reducing overhaul life of the gas generator from 24,000 to 6000 hr and the power turbine from 100,000 to 20,000 hr. When operating above base load the increased costs associated with more frequent overhauls can be offset by the reduced operating costs. This reduction in operating costs is due to the significantly higher efficiency of running a single machine, as opposed to running two machines at part load. In addition the extra horsepower available could reduce capital investment by deferring or eliminating the purchase of new machinery.

Peak operating experience of gas fueled Avons was limited although, for electrical peak lopping, some very encouraging results had been obtained. These results together with the fact that the likely operating regime would involve excursions above base, rather than continuous peak running, suggested that peak operation should be considered and that the reduction in overhaul life would be significantly less than the peak continuous case. Bearing in mind these factors a machine originally installed for emergency peak operation was subject to a peak trial. Whenever the station power requirement exceeded base load for one machine, instead of starting another, peak operation was selected. The trial was very encouraging and approximately 500 hr running above base load was accrued in three months operation. The machine had accumulated some 15,000 hr running in total and was due for overhaul, but before the trial was discontinued, the power turbine suffered a blade failure. It is now certain that peak operation did not cause the failure although the coincidence was unfortunate. Further peak trials are planned to establish cab cooling requirements, to confirm increases in power and efficiency, and to investigate detrimental effects such as increased noise, vibration or gas emissions. Initial tests suggested there were no such problems.

Based on these limited trials together with peak lopping experience a decision was made to install a peak rated Maxi-Avon removed from an existing station to act as standby to an RB211 on a new station. The Maxi-Avon had been replaced by an RB211 and was surplus to requirements. The move made commercial sense in that the Maxi-Avon was available and, even at first cost, saved over a quarter of a million pounds on the purchase of a second RB211. The real saving by avoiding the purchase of a second machine was about 650,000 pounds. The load requirement for the station concerned is shown in Fig. 2. The maximum power output from the peak rated machine is 14.5 MW compared with 19.4 MW from the RB211-22. This compares with a maximum power requirement of 16.4 MW. The decision to install this machine combination was based on the assumption that the RB211 would always be run as the lead machine with the peak rated lower efficiency machine acting as standby. Under these circumstances high efficiency operation, with almost full standby, can be achieved with minimum capital cost. To ensure that peak excursions are adequately recorded and to increase confidence, the Maxi-Avon operation will be monitored using a torquemeter.

Waste Heat Recovery. We have been investigating the feasibility of recovering waste heat from the power turbine exhaust gases. The possible uses of the waste heat are manifold ranging from process heating, to the generation of process steam, to the use of combined cycles involving steam or propane.

Feasibility studies have concluded that the most convenient

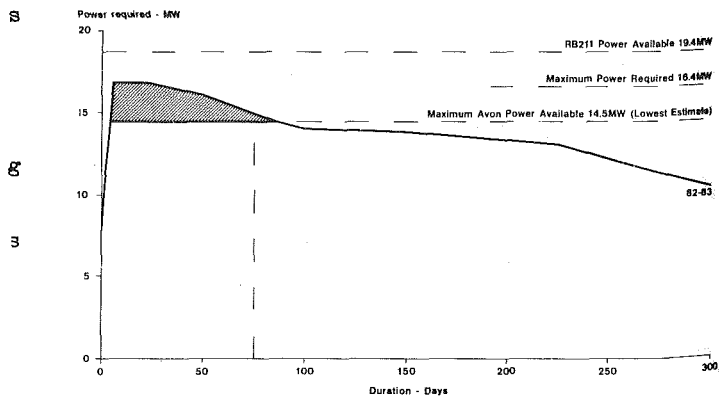


Fig. 2 Load profile requirement for future compressor stations

Downloaded 01 Jun 2010 to 171.66.16.58. Redistribution subject to ASME license or copyright; see http://www.asme.org/terms/Terms_Use.cfm

methods of harnessing waste heat is by either using steam in a combined cycle for generating extra compression power or by using the extra energy for aftercooling the gas. The methods are put forward as alternatives although the possibility of sharing the recovered power to incorporate both applications has been considered. A further study has shown that the optimum gas transmission temperature in the grid is 20°C and aftercooling would be required at compressor stations to achieve this temperature. Although the study reached only tentative conclusions, if the energy to cool the gas was obtained by waste heat recovery methods the proposition could be attractive. The variation of load factors between stations will require each future station to be studied separately to determine the economic viability of waste heat recovery schemes.

Fig. 3 shows a typical cost benefit analysis for a station running for up to 330 days per year at a demand power of between 14.9 MW and 32 MW. This analysis is based on the RB211-24 gas generator and assumes that the waste energy is used to provide extra compression power. For demand powers exceeding the base load operation of one RB211 either a second machine would be required or alternatively waste heat recovery could be used. In this case the starting of the second RB211 could be deterred until the power requirement reached 28.3 MW. The economics are sensitive to the amount of running in the regime between base load power of one RB211 and base load power plus waste heat recovery for one RB211. Although there are revenue savings possible throughout the power range, maximum savings are achieved if the starting of a second RB211 is avoided. Payback period for revenue savings, over the increased capital cost of waste heat machinery, would be about four years based on the operating profile shown. This could, however, extend to fifteen years for a significantly different load profile. The reliability of the cost studies on waste heat recovery can only be as accurate as the plans for future loading of the grid. These plans are sensitive to changes in national and corporation policy, to new gas finds, and to a prevailing supply and demand situation a few years hence. However, as a result of these studies it is now proposed to invite tenders with a view to installing waste heat units, on a future station, for extra compression power.

The installation of aero derivative gas turbines with waste heat recovery would reduce the number of machines required either by providing more primary power or reducing the number of standby machines.

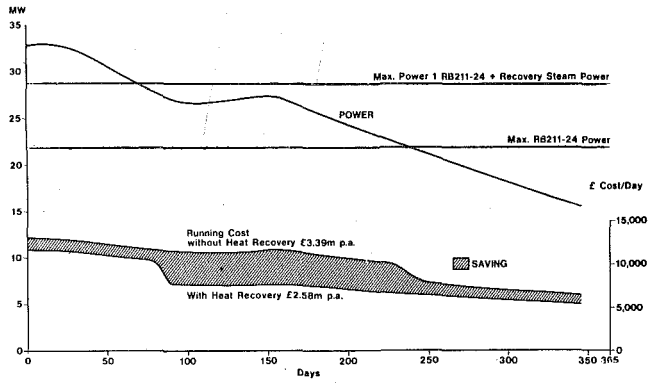


Fig. 3 Cost/benefit analysis for waste heat recovery—extra compression

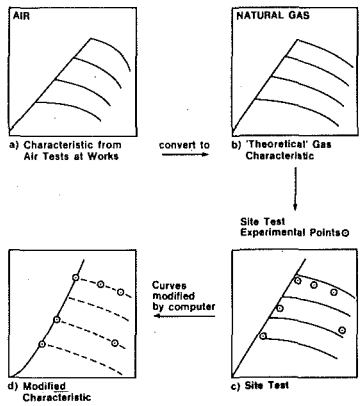


Fig. 4 Performance testing strategy

Performance Testing

British Gas has embarked on a test program aimed at accurately measuring the performance of compression plant.

Performance testing has three main functions in the British Gas context:

1 to insure that machines as supplied meet contractual performance,
2 to insure continued efficient machinery operation,
3 provision of accurate machinery power for planning purposes.

In the past works tests have been carried out on compressors prior to shipment but these results have never been accurately confirmed on site. The primary reasons for the lack of accurate site results are the limitations of the installed instrumentation and methods of measurement, and the inability to establish required test flow conditions. Prevailing grid conditions frequently limit the range of test conditions unless some provision is made to permit variations in gas flow and pressure, and this is discussed below.

In order to insure that machines as supplied meet contractual performance it is necessary to achieve the following objectives:

1 to confirm the guarantee point,
2 to establish the surge line and set up the surge control system,
3 to assess compressor/power turbine matching,
4 to establish operating characteristics of the compressor.

Performance Testing Strategy. The BGC Machinery specification requires a machinery contractor to carry out a performance test in accordance with PTC10 [2] with a class 3 test as a minimum. Further stipulations are made governing the number of speed lines, test points, derivation of flow profiles, ambient conditions, etc., which may vary slightly from PTC10. In addition a BGC test procedure has been drafted based on PTC10 but relating to site tests. At the moment the standard of the works test is considered adequate although in the light of the more precise performance tests on site, it is possible they will be reviewed.

The strategy which will be followed in performance testing is depicted in Fig. 4. Figs. 4(*a*) and 4(*b*) indicate conversion of compressor air test characteristics to gas characteristics. Although both items of information will be supplied by the contractor, BGC will also carry out the conversion as accurately as possible using the real thermodynamic properties of the gas at any point. Performance tests on site are then necessary. In the case of new stations it is anticipated that these will be carried out during or immediately following commissioning. Because of station and grid conditions, only a limited number of experimental points may be achievable although many points may not be necessary. Fig. 4(*c*) shows the comparison of a limited number of experimental points with the derived gas characteristic from air tests at the works. These comparisons are used in two ways, firstly for feedback to the manufacturer and secondly for deriving a "base line" characteristic for future comparison as shown in Fig. 4(*d*). It is hoped that in this way reliable characteristics may be generated from relatively few site test points.

For existing stations the base line characteristic will update the characteristic used by operational departments, give an indication of the state of the Machinery and will form a reference for performance trending associated with health monitoring as discussed later. The performance test results would be regarded as an absolute level for comparison with the results, recorded at the same time by the health monitoring equipment. The health monitoring approach may involve different methods of determining power and efficiency (e.g., torquemeter methods), although it is hoped discrepancies in the two methods will form a "qualitive datum" for repetitive trend monitoring.

Downloaded 01 Jun 2010 to 171.66.16.58. Redistribution subject to ASME license or copyright; see http://www.asme.org/terms/Terms_Use.cfm

The frequency of repeat performance testing has not been established, although in the case of stations with health monitoring it will be infrequent. Current thinking suggests that a repeat test may be required where unacceptable deterioration has been indicated on the permanently installed systems and, prior to action such as replacement or refurbishment, a confirmatory test would be carried out. On existing stations with no health monitoring equipment the frequency of site testing will be based on cost effectiveness, i.e., the amount of money that can be saved for a given test frequency.

The role of the machinery contractor is extremely important in the performance investigations. He is required to carry out the works tests which are witnessed by BGC. He is also requested to approve the site test carried out in-house.

The outcome of the performance test program will be to confirm or otherwise the works test is satisfactory and, if it is not, to persuade the contractor to improve his test method.

Site Tests—Measurement and Control. The critical factors affecting site performance testing are the provision of accurate instrumentation and good flow control to permit establishment of test points. In the early compressor stations no deliberate provision was made for controlling flow and pressure within stations. Achieving test points without provision or some method of control, in or close to the station, depends critically on grid operation. The absence of any special provisions makes guarantee point testing and confirmation of compressor characteristics very difficult. Some stations had inadvertent flow control facilities available either due to an adjacent pressure reduction station or a valve which had become redundant.

On two of the most recent stations to be built the first specific provisions for throttling flow during testing have been installed. This together with a station bypass enabled a range of flow and pressure conditions to be achieved. On the first station a 36 in. ball valve was installed. This station could also operate without grid influence (see Fig. 5). The second station has a control valve installed in a station bypass loop as indicated in Fig. 5(*a*). In all future stations provision should be made for flow control to permit performance testing.

Flow Measurement. Flow measurement in compressor stations can be achieved by various methods. In the early compressor stations orifice plates were installed but were rarely used, involved substantial first costs and, unless they were installed in a separate metering loop, increased the pressure drop across the station. For these reasons their use was discontinued. Elbow meters have been installed in recent stations and have proved satisfactory for machinery control and flow balancing although their accuracy is low. Another alternative, insertion meters, have been used extensively in the Industry for testing purposes. There is currently no common practice for flow measurement on compressor stations but as the performance test procedure is finalised new design rules will be formulated. It was felt that the apparent accuracy of existing metering could be improved if some accurate means of checking were available.

A method is available which has been adopted both for checking filtration efficiencies of scrubbing equipment and for flow checking. This method is illustrated in Fig. 6. An irradiated tracer is injected at a measured distance downstream and the time of travel is measured giving the flow velocity. Using a calibrated density cell and accurately measuring the internal diameter of the pipe permits accurate flow measurement. The technique is too expensive to use as the primary means of flow measurement, but it can be justified to check either an insertion meter, installed for the duration of tests, or normal orifice metering.

Typical Test Results. A typical test result is shown in Fig. 7. This particular result has been obtained from the station depicted in Fig. 5. Control of test conditions was achieved by the use of a 36 in. ball valve installed in the suction line to the compressor. Total flexibility of operation could not be achieved although meaningful test results were obtained. Some problems were encountered due to pulsations, introduced by the valve, affecting the metering but by appropriate valve positioning this could be overcome. In addition, although temperature measurement of gas flow at inlet and outlet of the compressor is accurate, a significant profile exists across the ducts making efficiency determination difficult. This area is to be investigated further. An alternative approach is the deduction of efficiency from torquemeter measurements. This is the preferred approach for health monitoring although more work is needed to establish confidence in the reliability and accuracy of torquemeter methods. Generally site results were fairly consistent with works tests for the compressor, although the surge line and flow capacity is different to that obtained

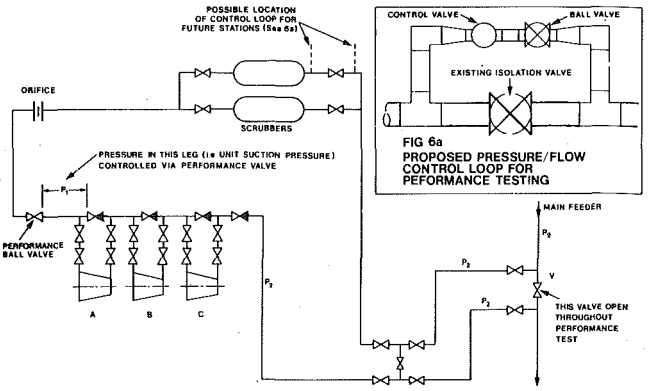


Fig. 5 Typical compressor station showing pressure/flow control provisions

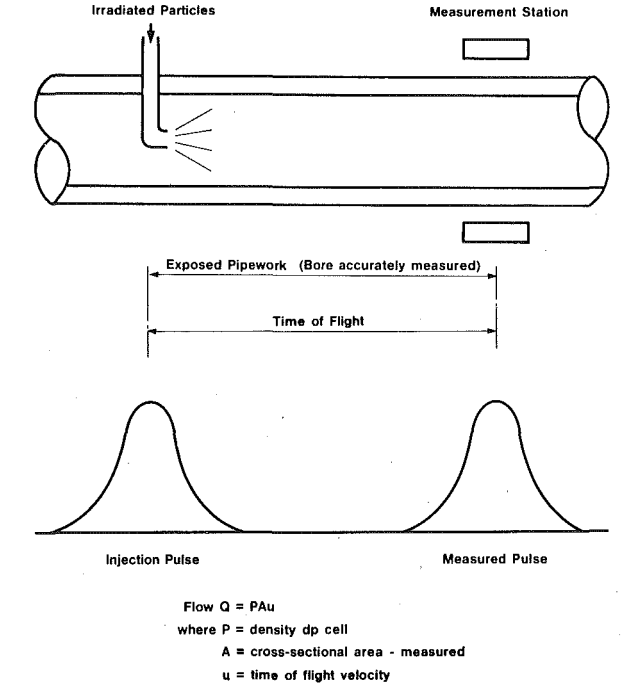


Fig. 6 Method for checking flow metering devices

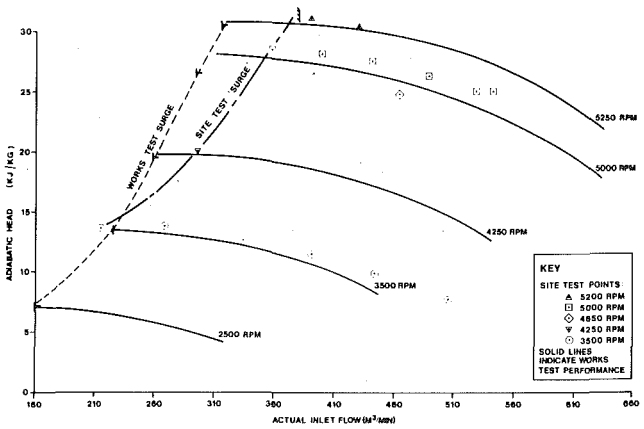


Fig. 7 Typical site performance test—compared with converted works air test

Downloaded 01 Jun 2010 to 171.66.16.58. Redistribution subject to ASME license or copyright; see http://www.asme.org/terms/Terms_Use.cfm

by works test. Power measurement using aerodynamic data from the power turbine gave very similar results (to within 2½ percent) of those obtained from the torquemeter.

Computer Unit Control

The first station supervisory computer control system was installed at the BGC terminal at St. Fergus commissioned in 1977. This system has a multi functional role. Its specification and installation followed successful trials at two compressor stations. Two further stations have been designed for unit computer control both based on the DEC PDP 8 computer.

Initially the trial installations had hard wired logic systems with the computer duplicating all the major unit control functions. This trial demonstrated that computer unit control systems can be successful but at the same time operators would select their preferred system for primary maintenance. The operators' choice depended on familiarity and inevitably this ended with the partial rejection of the computer system. Apart from the obvious cost disadvantages of duplicating, in order to introduce technically advanced control systems it is considered essential to reject entirely alternative systems to gain maximum benefit.

BGC have not yet extended their use of computer control to governor control or integrated station and unit control but these are seen as future developments. Similarly the use of micropressor technology, because of its inherent cheapness, compactness, and capability will come in due course. British Gas does not consider itself even now irrevocably committed to computer control, alternative equipment being evaluated on its merit. In evaluating tenders for a recent compressor station contract, the balance was tipped from a solid state electronics system to a computer based system by the following considerations:

1 A theoretical reliability analysis which indicated that the inherent reliability of the computer system was almost twice that of the alternative. (This represents about a 10 percent improvement in the overall reliability of a compressor unit).
2 The capability of more readily incorporating data logging and sophisticated health monitoring techniques into an existing computer system.

It could be that for a station noncritical to the grid and with a low load factor these would not have carried as much weight. On the other hand contractors inevitably reject "old" technology when they sense that the satisfied user is ready for the complete break.

The move towards computer control of most of the major control functions is almost certain, probably based on microprocessor technology. The increased capability of such systems in terms of monitoring equipment is a very important factor. On the other hand there is no rush to introduce microprocessor technology and indeed, with the current emphasis on flexibility and reliability, it is essential to gain operational experience in a limited number of installations before rejecting established methods. If however, the real reliability of the computer system can be shown to exceed the more conventional technology, as a theoretical assessment suggests, then further commitment is inevitable.

Health Monitoring

The techniques of Health Monitoring have merited a good deal of attention in recent years. In the BGC context Health Monitoring consists of noting the trends of certain parameters, by regular measurement, and relating these to established criteria. By this method, changes in the condition of a machine or its components, can be noted and assessed.

The approach to date has been to carry out regular maintenance and to manually log performance data on an hourly basis. Any attempt to trend plot the deterioration of machinery using this technique is laborious and provides a very coarse analysis, as the data available to the operator are limited.

Computer based health monitoring methods do not have these inherent limitations, in that the computer has the advantage of rapid recording and analysis of a large number of machine parameters.

Benefits of Health Monitoring. By extensive monitoring of machine parameters, utilizing a computer based system, it is believed possible to achieve the following advantages:

1 provide early indication of a fault which, if left undetected, could well cause extensive secondary damage,
2 permit "on condition" maintenance, thereby saving costs of a major overhaul,
3 minimize the number of unscheduled outages and allow maintenance to be preplanned,
4 promote greater confidence with machines operating in a remote control mode,
5 permit greater confidence in those compressor stations which may be designed to operate with reduced standby capacity,
6 provide early detection of a fall off in machine efficiency and thereby optimisation, of both Grid operation and individual machine selection, within a plant,
7 provide sufficient data which, in the event of a failure occurring, may be used to perform diagnostic analysis.

On the basis of these advantages a financial case for a pilot health monitoring scheme was prepared and subsequently approved. It was considered that health monitoring has two primary functions:

1 to indicate the thermodynamic efficiency of the machine,
2 to indicate the mechanical condition of the machine.

The initial proposal for a computer health monitoring trial considered both of these functions. The cost arguments were based on the likely failures provided from the experience of other users of gas turbine plant, since they had logged many more hours of operation than BGC. The potential economic advantages of health monitoring were demonstrated with reference to possible savings in planning, plant operations and grid control. For units with over 2000 hr running per annum, the estimated maximum cost savings resulting from health monitoring range from 10,000 to 50,000 pounds per year per unit, for base load rated Avon units, and 22,000 to 55,000 pounds per year per unit for RB211 powered units. These savings can amount to 0.8m pounds in the life of a unit. As the machine costs and load factor rise, the economic advantages of health monitoring increase. On base load machines, the majority of the estimated savings would be those associated with fuel costs. These savings can be achieved by optimising the efficiency of single units and by selecting the most efficient combination of units to run on the grid. On peak rated machines with a shorter overhaul period, maintenance savings become appreciable.

On the new Scottish stations transmitting gas from the Frigg field, it is predicted that the load factor will be high. It is envisaged that the application of health monitoring will permit the selection of the optimum machine or combination of machines to suit Grid requirements.

This argument also applies to other existing units when the machines are nearing their overhaul life. By monitoring every unit, the most suitable one may be selected, thus reserving others for standby. This method of obtaining maximum utilisation from existing machinery should minimise maintenance expenditure as overhaul would only occur when required. Elimination of a single major overhaul could save 50,000 pounds per unit at todays prices.

As machinery approaches the limit of its useful carcase life, complete replacement of the unit may be required. This could be avoided by the use of health monitoring with a possible saving of 350,000 to 600,000 pounds. By knowing the condition of the machine, deterioration to a state requiring replacement would be averted. In addition, the possibility of catastrophic failure, which increases with age, would be reduced.

For future stations, large savings may result by the application of health monitoring techniques. The improved reliability and greater confidence in maintenance frequency selection, should reduce standby requirements, thereby minimizing capital expenditure. By acceptance of peak operation, coupled with health monitoring, it may be possible to eliminate one unit with a possible 2m to 3m pounds cost saving. The small risk involved by using peak load operation can be minimised by the additional confidence gained from health monitoring. Additional savings could also be made at the planning stage if the present operating margins assumed for existing and future machinery could

Downloaded 01 Jun 2010 to 171.66.16.58. Redistribution subject to ASME license or copyright; see http://www.asme.org/terms/Terms_Use.cfm

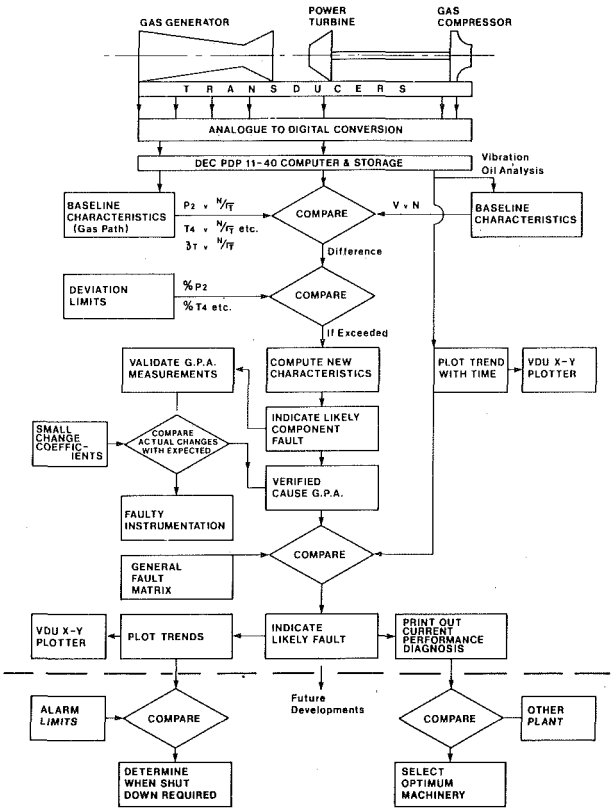


Fig. 8 Health monitoring pilot scheme

be reduced. For example, the power margin of 8 percent at present included for deterioration in machine performance, may be limited to say 4 percent by monitoring the efficiency of the machine and by taking corrective action at the appropriate time.

Methods of Health Monitoring. Preliminary studies have shown that the methods likely to be most effective in health monitoring of gas compressor sets are (1) vibration analysis and monitoring, (2) gas path analysis, (3) debris formation and oil consumption, (4) boroscopic and external visual inspection.

These methods are complementary and will all be included in the BGC health monitoring scheme which is depicted in Fig. 8.

Experience obtained to date using the vibration monitoring equipment installed on existing machinery, has shown that the coarse vibration measurements currently indicated are not sufficient to detect many faults and quite serious failures have occurred without prior warning. More sophisticated analysis possibly involving real time analysis methods are considered necessary and these will be integrated into the computer system.

The provision of transducers in the gas path through the turbine driven units and the gas compressor, will enable continual monitoring of performance parameters. Considerable fuel savings can result from day to day optimisation of plant and from the identification of plant deterioration. Performance measurements must be analysed using a computer to minimise the manual effort required.

By using both on line and in line techniques, the rate of debris formation can be monitored. This can indicate impending failure of bearings and gears well before significant secondary damage can occur. The analysis of oil provides secondary information regarding the state of bearing components etc., and can also indicate rates of wear. In conjunction with the health monitoring exercize oil sampling is being carried out.

Boroscopic monitoring is considered to be an important device for providing information on the condition of the unit being monitored. It can be used to confirm evidence inferred from other methods and British Gas are gearing up to carry out regular inspections.

Pilot Health Monitoring Scheme. The majority of the stations currently operating on the grid cannot necessarily justify the installation of individual computer based health monitoring systems, although future stations on the Scottish feeders almost certainly could. In the period during which flows along the Scottish lines build up, breathing space exists in which to establish the most appropriate methods and procedures and to optimise the design of a health monitoring system. This is to be achieved by carrying out a pilot health monitoring scheme. Complete health monitoring packages providing the hardware and computer software can be bought. Several of these systems are based on a DEC PDP11 computer. However, the purchase of a complete system is not considered to be the best approach, because of the high cost involved and because much of the experitise would remain external to British Gas.

It is considered that we have the capability of producing our own health monitoring package and, for the trial, advantage can be taken of existing equipment and where possible, BGC software developed inhouse. This approach will minimise the cost and insure that the necessary expertise is retained.

At stations where computers are to be used for unit control, it is intended to incorporate health monitoring into the computer in the future at little additional cost. For new stations, instrumentation will be specified for the health monitoring in the original design and so minimize the installation costs. Retrospective action on existing stations to install health monitoring equipment could only be justified on an individual station basis when a suitable system had been developed.

Unit Availability

The availability of existing compressor units will influence the number of main and standby units planned for future stations. Reductions in the amount of standby plant can only be justified on the grounds of acceptable and demonstrable high plant availability.

Plant availability depends upon plant reliability and maintenance outages, this section will concentrate on unit reliability. The subject of reliability of compressor sets has been discussed in a previous British Gas paper [3].

For a given type of machinery the maximum reliability achievable will relate to the theoretical reliability. The actual reliability of a particular unit may of course be more or less than this theoretical value. The theoretical reliability is arrived at by combining the average known reliability of its component parts (or similar components). Whether this level is achieved or even exceeded on a particular unit will be influenced by component quality, maintenance and chance. It follows, however, that for average chance with predictable component reliability and careful maintenance, reliability can only be improved by improved design. It is essential, therefore, for the equipment manufacturer to be aware of the performance, or lack of performance, of his equipment to provide the information and inducement necessary to improve the design reliability of his product. In underlining these requirements the difficulty in the user improving the reliability beyond a certain point is apparent. Because both the user and the manufacturer play a vital role both have to be reliability orientated. There is always an incentive to the user because downtime involves increased revenue costs or capital costs for standby plant. On the other hand, the manufacturer is market oriented and may be complacent or satisfied with his product and therefore reluctant to look at the reliability of his design.

However, in association with a manufacturer, a reliability programme has been initiated. Through the BGC defect data collection schemes, starting and running reliability of compressor sets has been carefully monitored over a number of years and the reasons for unreliability noted. On the basis of these data a reliability specification has been agreed for the whole compression unit and associated systems. This specification describes two requirements:

1 a cumulative starting probability of 95 percent,
2 a required growth in MTBF (mean time between failures) to an agreed level.

The data collection scheme has indicated that both starting probability and MTBF first falls after the initial start up and then increases and this is reflected in the details of the specification (see Fig. 9). In the agreed reliability programme monitoring the starting

Downloaded 01 Jun 2010 to 171.66.16.58. Redistribution subject to ASME license or copyright; see http://www.asme.org/terms/Terms_Use.cfm

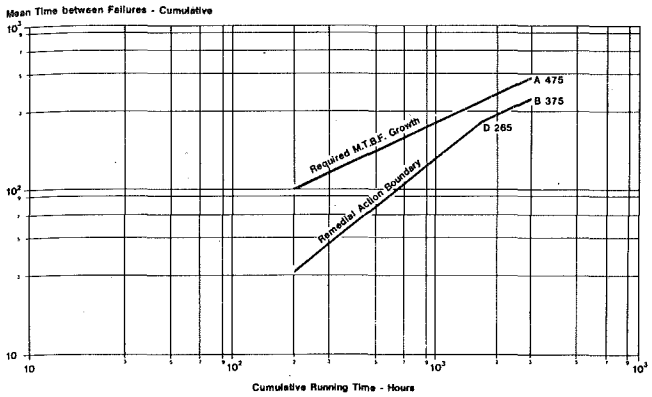


Fig. 9 Reliability specification

probability commences on the twentieth start up and is completed either on the two-hundreth start up or when the previous 100 first time start attempts have been completed with five or less failures. The cumulative MTBF agreement commences when the unit has achieved 200 operating hr and is terminated after 1500 hr provided that an MTBF of 325 hr has been achieved, it will then be continued to 3000 hr. The target requirement is an MTBF of between 375 and 475 hr after 3000 hr operation. The MTBF requirement is illustrated in Fig. 9.

Regular meetings are held with the contractor to monitor the first compressor units to which the specification agreement applies. The areas which the meeting considers are. (1) predictive design analysis, (2) problem areas, (3) investigations and tests, (4) review of trip requirements.

BGC has carried out some reliability predictions but the major input in this area comes from the manufacturer who, because he controls the design, must carry out predictive analysis to gain the confidence and conviction to improve his designs. Problem areas must be identified, recorded and corrective action taken. An identified problem will influence the reliability study in two ways: firstly the failure itself is a statistic which demonstrates how reliable the unit is, but secondly it identifies an area in which improvements should be considered. Investigations and tests will be necessary to establish the reason for problems occuring or for evaluation of new or existing components or assemblies.

It was felt necessary to review existing trips which stop the machine in the event of a particular parameter being exceeded. This has resulted in the elimination of a significant number of trips. The reason for having trips is to avoid a situation which could be either potentially hazardous or costly. The trip evaluation indicated that certain trips could be changed to alarms since it was by no means certain that if the parameter concerned exceeded a permitted level either of the consequences would result, and even if it did it would not occur quickly. In addition in some cases it was discovered that some other parameter would also have to be exceeded first, if damage or danger was to occur, and a trip on this parameter would suffice. The trip review investigated the effect of the trip, both real and spurious, on reliability and whether it was really necessary.

We feel that this reliability agreement is a major step forward in insuring maximum plant utilization. Undoubtably, the outcome will eventually be a more contractually binding specification agreement. Only by this method, together with good machinery surveillance and maintenance, can the level of plant availability improve and the level of standby be reduced.

Summary

This paper has reviewed some of the technical developments currently underway to improve the utilization of existing and future gas compressor plants. These developments have two main objectives, firstly to improve the operation of all plants, with corresponding reductions in operating costs, and secondly reducing capital investment in future plants by accurate planning. New machinery on site is to be performance tested to insure that it meets its guarantee and to establish base line measurements for future comparison. Comprehensive health monitoring, trending both mechanical and performance parameters, would then indicate the condition and deterioration of the machine at any time. The use of computer unit control within BGC will provide a facility for extension to computer based health monitoring systems. The current approach to testing, monitoring and computer utilization has been described and the advantages of these techniques in planning and operation are discussed.

At the planning stage factors affecting specification of new machinery include the available power installed, the power rating of the various new machinery options, and the prevailing standby philosophy. The power rating of the new equipment can be increased by operating in the peak regime or by greater utilization of existing energy through waste heat schemes. The application of these techniques are discussed in the paper. The amount of standby equipment installed in new stations depends upon the prevailing standby philosophy. This philosophy can only be changed if the BGC strategy for maintenance of supply is not affected. The development of health monitoring methods and improvements in the availability of machinery will permit a reduction in the level of standby. In the paper, improvements in availability are considered with reference to the new approach to reliability. An agreement between BGC and a contractor is described where both parties are aiming to improve the reliability of machinery. In conclusion improvements in plant utilization can be produced by continued technical developments. BGC consider it important to keep abreast of such developments to insure efficient gas pumping operations.

Acknowledgment

The authors would like to thank their colleagues in the Machinery Department and the other departments within British Gas whose assistance and contributions have made this paper possible. Thanks are also due to the British Gas Corporation for permission to publish this paper.

References

1 Huggett, B. M., and Austin, C. J., "Prospects for the Gas Turbine in the U.K. Gas Transmission System," ASME Paper 78-GT-53.
2 PTC 10 ASME Power Test Codes—Compressors and Exhausters.
3 Harrison, R. A., and Weatherilt, P. F., "The Reliability of Gas Turbine Compressor Units", ASME JOURNAL OF ENGINEERING FOR POWER, Jan. 1979, pp. 73–78.

Downloaded 01 Jun 2010 to 171.66.16.58. Redistribution subject to ASME license or copyright; see http://www.asme.org/terms/Terms_Use.cfm

D. R. Ballal
Visiting Associate Professor.

A. H. Lefebvre
Professor and Head.

School of Mechanical Engineering,
Purdue University,
West Lafayette, Ind.

Weak Extinction Limits of Turbulent Heterogeneous Fuel/Air Mixtures

Experimental and theoretical studies are made of the factors governing the weak extinction limits of stabilized flames supplied with flowing mixtures of liquid fuel drops and air. The test program includes wide variations in inlet air pressure, velocity and turbulence level, and also covers wide ranges of fuel volatility and mean drop size. The influence of flameholder size and blockage is also examined. An equation is derived for predicting weak extinction limits which shows good agreement with the corresponding experimental values.

Introduction

An essential feature of most gas turbine combustors is the toroidal flow reversal which is created and maintained in the primary combustion zone by air entering through swirl vanes located round the fuel nozzle, supplemented by air jets injected through one or more rows of holes in the walls of the liner. In addition to its main role as the major heat release zone of the chamber, the other important function of the primary zone is to recirculate combustion products to mix and burn with the incoming air and fuel. By this means a mechanism of continuous ignition is established, and combustion can be sustained over wide ranges of pressure, velocity and fuel/air ratio.

An alternative method of stabilizing a flame in a high velocity stream of combustible mixture is by means of a bluff body, such as a rod, cone or "vee"-gutter, which produces in its wake a low-velocity recirculatory flow in which combustion can be initiated and maintained. The propagation of flame to other regions of the flow is rendered possible by the transport of heat from the boundaries of the recirculation zone to the adjacent fresh mixture. This method of flame stabilization has been widely used in the afterburner systems of turbojet engines.

With both types of stabilization, a parameter of considerable importance is the weak extinction limit, i.e., the minimum fuel/air ratio below which the flame is extinguished. The precise determination of weak extinction limits is assuming increasing importance at the present time due to the incentive to operate combustion systems at weak mixture strengths in order to minimize the emissions of smoke and nitric oxides.

Recently Ballal and Lefebvre [1] derived an equation for predicting the weak extinction limits of stabilized flames supplied with turbulent flowing mixtures of uniform, gaseous composition. Predictions of weak extinction equivalence ratio based on this equation were found to be in close agreement with the corresponding experimental values, measured over wide ranges of pressure, temperature, velocity and turbulence level.

The purpose of the present investigation is to extend the scope of the previous study to include heterogeneous mixtures, i.e., to derive an equation for weak extinction equivalence ratio, ϕ_{WE}, that is valid for fuel/air mixtures in which the fuel is present in the form of multitudinous liquid drops of varying size. Most practical combustion devices, burning liquid hydrocarbon fuels, employ mixtures of this latter type.

Experimental

The apparatus employed is shown schematically in Fig. 1. Essentially, it comprises a circular pipe, 25 cm in diameter, through which metered air flows into a large settling chamber housing a number of flow-smoothing grids. To the downstream flange of the settling chamber is connected the working section, which is also a circular pipe of 25 cm in diameter, fitted with small quartz windows to facilitate observation of the flame. The flameholder is in the form of a hollow cone of 45 deg included angle, which is mounted on three thin stays at the center of the pipe with its apex pointing upstream. Four geo-

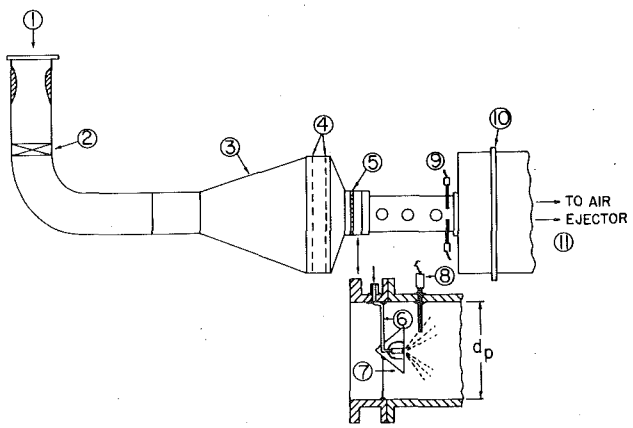


Fig. 1 Arrangement of the test rig (1) air flow, (2) regulating valve, (3) settling chamber, (4) flow smoothing grids, (5) turbulence grids, (6) stay, (7) conical baffle with spray nozzle, (8) spark plug, (9) flame detector, (10) nitrogen spray ring, (11) air ejector connection.

Contributed by the Gas Turbine Division of The American Society of Mechanical Engineers and presented at the Gas Turbine Conference and Exhibit and Solar Energy Conference, San Diego, California, March 12–15, 1979. Manuscript received at ASME Headquarters January 4, 1979. Paper No. 79-GT-157.

Copyright © 1980 by ASME

Downloaded 01 Jun 2010 to 171.66.16.58. Redistribution subject to ASME license or copyright; see http://www.asme.org/terms/Terms_Use.cfm

metrically similar cones were manufactured to give the following values of blockage ratio, B_g. [Note: B_g = (cone dia/pipe dia)^2]

Cone dia	Blockage ratio, B_g
5.0 cm	0.04
8.3 cm	0.11
12.5 cm	0.25
14.6 cm	0.34

Ignition is accomplished by means of an electric spark. After each ignition the spark plug is withdrawn to avoid disturbance to the flowing stream. Flame ionization probes are mounted at the downstream end of the working section to assist flame detection at low combustion pressures. The combustion products discharge into a large circular exhaust duct which is connected to an air-ejector facility to permit studies at subatmospheric pressures. Liquid nitrogen is sprayed into the combustion products at entry to the exhaust duct in order to reduce their temperature to an acceptable level for satisfactory and reliable operation of the ejector rig.

Perforated plates located 20 cm upstream from the base of the cone provide near-isotropic turbulence in the flow entering the recirculation zone varying between 5 and 15 percent in intenstiy. Details of plate geometry and corresponding turbulence levels are listed in Table 1.

Turbulence intensities and scales are measured with a DISA 55D01 constant temperature, hot-wire anemometer at a plane just upstream of the base of the cone. For test runs with minimum turbulence, the perforated plates are replaced by a fine mesh wire gauge. With this arrangement the turbulence level in the air stream approaching the cone is less than 2 percent.

Air metering is provided by fitting a venturi section in the pipe, the static depression at the throat being measured by means of a water (or alcohol) manometer. The fuel flow is metered and controlled using a series of Fischer-Porter flowmeters.

Table 1 Details of turbulence-promoting grids

Grid No.	Mesh Size, cm	Hole diam, cm	Intensity u′/U %	Scale L, cm
1	1.45	1.27	5.5	0.40
2	1.70	1.27	7.8	0.58
3	2.00	1.27	12.2	0.73
4	2.20	1.27	14.7	0.90

The fuel nozzle is mounted inside the hollow cone flameholder with its discharge orifice just protruding beyond the base of the cone, as illustrated in Fig. 1. Ten different simplex atomizers, varying in flow number from 0.15 to 0.80 US gallons/hr(psi)$^{0.5}$, (note that flow number in liters/hr (N/m^2)$^{0.5}$ = 0.0456 × flow number in US gallons/hr(psi)$^{0.5}$) are used in order to cover wide ranges of air velocity, air pressure and mean drop size (SMD). Drop sizes are measured using the light-scattering technique in the form developed by Lorenzetto [2]. All measurements are carried out by spraying the fuel downwards into still air at normal atmospheric pressure and temperature. The influence of variation in air pressure on mean drop size is accommodated by employing the relationship, SMD $\propto P_a^{-0.1}$ [3].

In a series of tests carried out on a similar hollow cone plus pressure atomizer configuration, Plee and Mellor [4] observed that, under certain conditions, the fuel spray penetrated right through the recirculation zone to produce a tongue of flame downstream. This problem of loss of fuel drops from the wake region is much less serious in the present experiments since spray penetration is relatively low at the low fuel-flow rates associated with weak extinction limits. Moreover, by comparing the time required for a fuel drop to traverse the wake region (using the values of drop discharge velocity from a pressure swirl atomizer as measured by York and Stubbs [5]) with the calculated evaporation lifetime of the same drop, it can be shown that, except for the combination of the smallest flameholder with drop sizes in excess of 150 μm, the fuel spray is fully confined to the recirculation zone.

The test program includes several different hydrocarbon fuels, representing a wide range of transfer number as indicated by the transfer number, B [6]. The main properties of interest for these fuels are listed in Table 2. The values of B quoted in this table are calculated for conditions of stoichiometric combustion in air at normal room pressure and temperature.

The heavy fuel oil is too viscous to be pumped at normal room temperature. However, by heating it to a temperature of 350 K, it is possible to achieve fine atomization without resorting to excessively high fuel injection pressures.

The test conditions are: mainstream velocity = 15 to 75 m/s, air pressure = 0.2 to 1.0 10^5 N/m^2, air temperature = 290 K, turbulence intensity = 2 to 14.7 percent, blockage ratio = 0.04, 0.11, 0.25 and 0.34, fuel transfer number, B = 1.5 to 6.1, fuel drop diameter (SMD) = 40 to 160 μm

The test procedure, for any given flameholder/fuel nozzle combi-

Table 2

Fuel	Stoichiometric Fuel/Air Ratio by Weight	Carbon/ Hydrogen Ratio	Specific Gravity at 293 K	Kinematic Viscosity m^2/sec × 10^{-6} at 293 K	Spalding Transfer Number B
Iso-octane	0.066	5.33	0.692	0.77	6.10
Kerosine (AVTUR)	0.068	6.10	0.775	1.30	3.75
Gas Oil	0.068	6.40	0.837	5.00	3.10
Diesel Oil	0.070	7.00	0.900	14.5	2.80
Light Fuel Oil	0.072	7.40	0.930	165.0	2.50
Heavy Fuel Oil	0.073	7.70	0.970	860.0	1.50

Nomenclature

$\dot{W}$ = mass flow rate, kg/s
U = mainstream velocity, m/s
u' = r.m.s. value of fluctuating velocity, m/s
Tu = percentage turbulence intensity, (100 u′/U)
T_0 = initial air temperature, K
ρ = density, kg/m^3
ν = kinematic viscosity, m^2/s
μ = dynamic viscosity, kg/ms
k = thermal conductivity, W/mK
c_p = specific heat at constant pressure, J/kg, K
Pr = Prandtl number = $(c_p\mu/k)$
D = drop size
Re_D = Reynolds number $(u'D/\nu)$
D_{32} = Sauter mean diameter, m
D_{10} = mean diameter, m
D_{20} = mean surface diameter, m
D_{30} = mean volume diameter, m
C = experimental constant
$C_1 = D_{20}/D_{32}$
$C_2 = D_{10}/D_{32}$
$C_3 = D_{30}/D_{32}$
$\mathrm{Re}_{D_{32}} = u'D_{32}/\nu$
P = air pressure, N/m^2
q = fuel/air ratio, by weight
ϕ = equivalence ratio
ϕ_{WE} = weak extinction value of equivalence ratio
V = volume of combustion zone, m^3
A = c.s.a. of combustion zone, m^2
B = fuel mass transfer number
d = baffle diameter, m
d_p = pipe diameter, m
B_g = flameholder blockage $(d/d_p)^2$
n = number of drops in spray
f = fraction of fuel in vapor state
E = fraction of total air entrained in wake region

Subscripts

a = air
f = fuel
g = gas

Downloaded 01 Jun 2010 to 171.66.16.58. Redistribution subject to ASME license or copyright; see http://www.asme.org/terms/Terms_Use.cfm

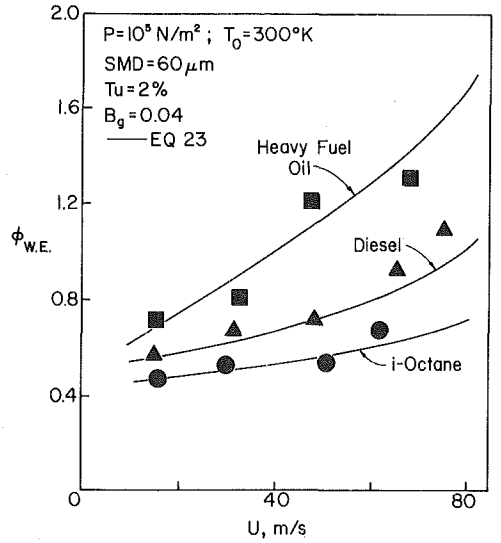


Fig. 2 Influence of mainstream velocity on weak extinction equivalence ratio for a conical baffle of low blockage ratio

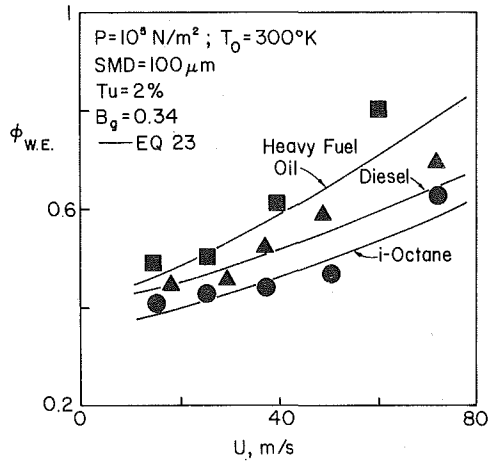


Fig. 3 Influence of mainstream velocity on weak extinction limits for the case of high blockage ratio

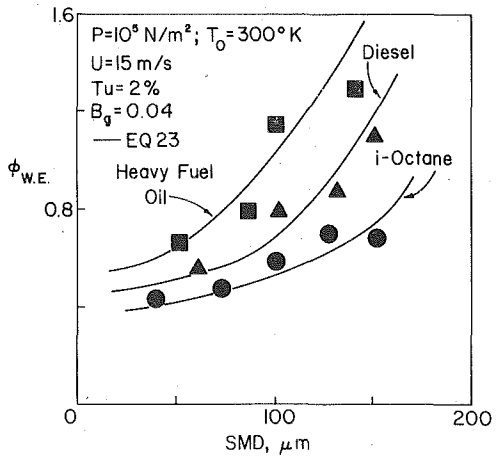


Fig. 4. Effects of spray drop size (SMD) on weak extinction limits for a low blockage ratio.

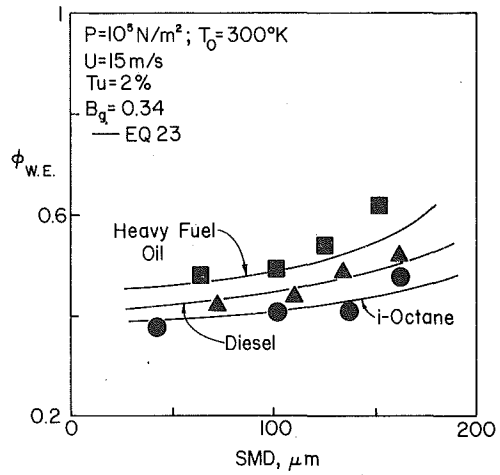


Fig. 5 Effects of spray drop size (SMD) on weak extinction limits for a high blockage ratio

nation, is first to establish the desired flow conditions of air pressure, velocity and turbulence, and then to gradually increase the fuel flow until the onset of ignition. Having stabilized the flame on the conical baffle, the spark plug is withdrawn to lie flush with the duct wall, and the supply of fuel is slowly reduced until flame extinction occurs. The fuel flow at this condition is recorded. This procedure is repeated for all fuels over the entire range of test conditions in order to study the separate effects on weak extinction limits of variations in pressure, velocity, turbulence intensity, flameholder size, flameholder blockage, fuel volatility anf fuel drop size.

The results obtained are shown plotted in Figs. 2–10. They demonstrate that weak extinction limits are improved, i.e., extended to lower values of equivalence ratio, by increases in flameholder size, fuel volatility and air pressure, and by reductions in mainstream velocity and mean drop size.

The influence of turbulence intensity on ϕ_{WE} is complex. For highly volatile fuels ϕ_{WE} always increases with increase in turbulence, due to the additional air that is entrained into the wake region, which reduces the time available for combustion. However, for less volatile fuels, such as heavy fuel oil, the beneficial effect of turbulence in accelerating fuel evaporation rate can often outweigh this effect and lead to a reduction in ϕ_{WE} with increase in turbulence intensity, as illustrated for heavy fuel oil in Fig. 10.

Theory

In a previous publication Ballal and Lefebvre [1] showed that weak extinction limits for flames supplied with premixed gases could be expressed in terms of the combustion volume, pressure, initial temperature and mass flow rate, by the relationship

$$\phi_{WE} = \left[\frac{a\dot{W}_a}{VP^n \exp\,(T_0/b)}\right]^c \tag{1}$$

in which the values for the constants a, b, and c are determined by the collision factor C_F, the activation energy, E, and the global reaction order, n, respectively.

From analysis of available reaction rate data from well-stirred reactors, it was concluded that the weak extinction equivalence ratio for hydrocarbon-air mixtures is given by

$$\phi_{WE(\text{premixed})} = C\left[\frac{\dot{W}_a}{VP^{1.25} \exp\,(T_0/150)}\right]^{0.16} \tag{2}$$

where C is a mixing factor which depends on the stabilizer configuration and the turbulence level of the fresh mixture, and must be determined experimentally for each individual combustor.

Equation [2] is satisfactory for premixed gaseous fuel-air mixtures and also for premixed/prevaporized liquid fuel-air mixtures. However, it cannot be used for heterogeneous liquid fuel-air mixtures unless the rate of fuel evaporation is sufficiently high to ensure that all the fuel is fully vaporized within the combustion zone. If the fuel does not fully vaporize, then clearly the "effective" equivalence ratio will be lower than the nominal value. However, if the fraction of fuel that is vaporized is known, or can be calculated, it can then be combined with equation [2] to yield the weak extinction value of equivalence ratio, i.e.,

$$\phi_{WE(\text{heterogeneous})} = \phi_{WE(\text{premixed})} \times f^{-1} \tag{3}$$

Downloaded 01 Jun 2010 to 171.66.16.58. Redistribution subject to ASME license or copyright; see http://www.asme.org/terms/Terms_Use.cfm

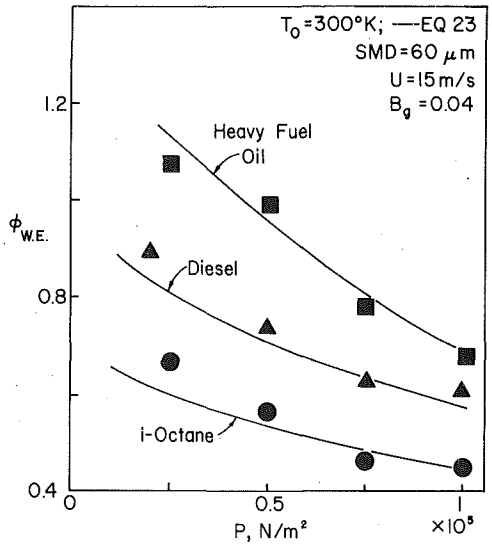


Fig. 6 Influence of pressure on weak extinction limits for a low blockage ratio

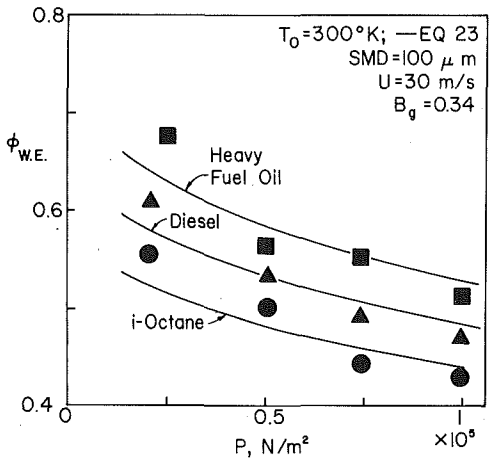


Fig. 7 Influence of pressure on weak extinction limits for a high blockage ratio

where f is the fraction of fuel that is vaporized in the combustion zone.

Now, for a single drop in stagnant gas the average rate of fuel evaporation during the lifetime of the drop is given by [6]

$$\dot{W}_f = 1.33\pi D(k/c_p)_g \log(1+B) \tag{4}$$

where D is the initial drop diameter

Since the fuel drops are usually quite small, when injected into a flowing air stream they tend to remain airborne, and their velocity relative to that of the air stream is insufficient to enhance appreciably the rate of fuel evaporation. However, if the flow is turbulent, the fuel drops are subjected fully to the fluctuating components of velocity. Under these conditions, the average rate of fuel evaporation is given by

$$\dot{W}_f = 1.33\pi D(k/c_p)_g \log(1+B)(1+0.25\mathrm{Re}_D{}^{0.5}) \tag{5}$$

where $\mathrm{Re}_D = (u'D/\nu)$

Thus, for a flame zone of volume, V, containing n fuel drops of diameter, D, equation (5) becomes

$$\dot{W}_f = 1.33\pi nD(k/c_p)_g \log(1+B)(1+0.25\mathrm{Re}_D{}^{0.5}) \tag{6}$$

For a fuel/air ratio in the flame zone, q, we have

$$q = \frac{\text{mass of fuel}}{\text{mass of air}} = \frac{\rho_f n(\pi/6)D^3}{\rho_a V} \tag{7}$$

hence $n = (6/\pi)(\rho_g/\rho_f)(V/D^3)q$ (8)

Substitution of n from (8) into (6) yields

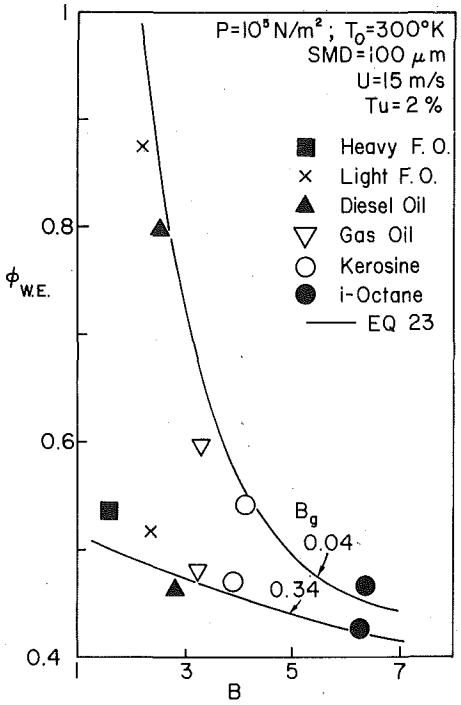


Fig. 8 Influence of fuel transfer number B on weak extinction limits

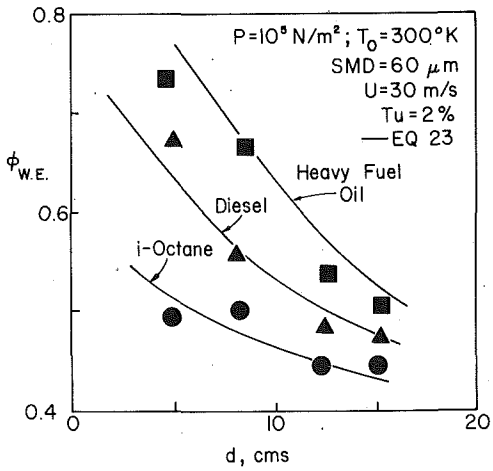


Fig. 9 Effects of the flameholder dimensions on weak extinction limits

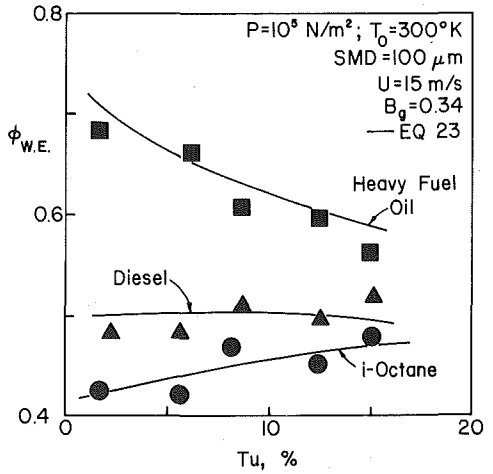


Fig. 10 Influence of mainstream turbulence intensity on weak extinction limits

Downloaded 01 Jun 2010 to 171.66.16.58. Redistribution subject to ASME license or copyright; see http://www.asme.org/terms/Terms_Use.cfm

$$\dot{W}_f = 8q(\rho_g/\rho_f)(k/c_p)_g \log (1 + B)(V/D^2)\,(1 + 0.25\mathrm{Re}_D{}^{0.5}) \quad (9)$$

Of the total fuel supplied to the combustion zone, the fraction, f, that is vaporized within the zone is given by

$$f = \dot{W}_f/q\dot{W}_a \quad (10)$$

Substituting $\dot{W}_f$ from equation (9) into (10) leads to

$$f = 8.0(\rho_g/\rho_f)(k/c_p)_g \log (1 + B)(V/\dot{W}_a D^2) \times (1 + 0.25\mathrm{Re}_D{}^{0.5}) \quad (11)$$

Hence, from equations (2, 3) and (11) we have

$$\phi_{WE(\text{heterogeneous})} = C\left[\frac{\dot{W}_a}{VP^{1.25}\exp(T_0/150)}\right]^{0.16} \times \left[\frac{\rho_f c_{p_g}\dot{W}_a D^2}{8\rho_g k_g V \log (1 + B)(1 + 0.25\mathrm{Re}_D{}^{0.25})}\right] \quad (12)$$

It should be noted that equation (11) allows f to exceed unity. However, when this occurs, it simply means that fuel evaporation is not limiting to performance, i.e., $f = 1.0$ and $\phi_{WE(\text{heterogeneous})} = \phi_{WE}(\text{premixed})$.

In the above equations, it is assumed that all the fuel drops are of uniform size. For a polydisperse spray of the type produced by most practical atomizing devices, some modifications are needed to account for the distribution of drop sizes in the system. Thus, equations (6) and (8) become, respectively,

$$\dot{W}_f = 1.33\pi C_1 D_{32}(k/c_p)_g \log (1 + B) \times (1 + 0.25C_2{}^{0.5}\mathrm{Re}_{D_{32}}{}^{0.5})(\text{where } \mathrm{Re}_{D_{32}} = u'D_{32}/\nu_g) \quad (13)$$

and

$$n = (6/\pi)(\rho_g/\rho_f)[V/(C_3/D_{32})^3]q \quad (14)$$

where D_{32} = Sauter mean diameter, $C_1 = D_{20}/D_{32}$, $C_2 = D_{10}/D_{32}$, $C_3 = D_{30}/D_{32}$

Following the same procedure as before leads to

$$f = 8.0(C_1/C_3{}^3)(\rho_g/\rho_f)(k/c_p)_g \log (1 + B)(V/\dot{W}_a D_{32}{}^2) \times (1 + 0.25C_2{}^{0.5}\mathrm{Re}_{D_{32}}{}^{0.5}) \quad (15)$$

From inspection of this equation, it is clear that some simplification is possible for the two important practical cases of low and high $\mathrm{Re}_{D_{32}}$

Low $\mathrm{Re}_{D_{32}}$

When $\mathrm{Re}_{D_{32}} \ll 1.0$, equation (15) reduces to

$$f = 8.0(C_1/C_3{}^3)(\rho_g/\rho_f)(k/c_p)_g \log (1 + B)(V/W_a D_{32}{}^2) \quad (16)$$

This is the appropriate expression for estimating the fraction of fuel that is vaporized within the combustion volume under conditions of low pressure and low turbulence.

Ideally, the values of C_1 and C_3 should be determined from analysis of the drop-size distribution for each individual spray. This could be a tedious and time-consuming process, but fortunately, as demonstrated by Simmons [7], the sprays produced by well-designed atomizers of various types have several important features in common. Based on their analysis of drop-size data, the present authors concluded that, for simplex and airblast atomizers, $C_1 = 0.31$ and $C_2 = 0.21$. Inserting these values into (16) yields

$$f = 25.6(\rho_g/\rho_f)(k/c_p)_g \log (1 + B)(V/W_a D_{32}{}^2) \quad (17)$$

High $\mathrm{Re}_{D_{32}}$

When $\mathrm{Re}_{D_{32}} \gg 1.0$, by substituting in equation (15) for $u' = (Tu/100)U = (Tu/100)\dot{W}_a/\rho_g A$, and $(c_p\mu/k)_g = \mathrm{Pr}$, it reduces to

$$f = 2.0(Z/\mathrm{Pr})(\rho_g/\rho_f) \log (1 + B)V[(Tu/100) \times \mu_g/\dot{W}_a D_{32}{}^3 A]^{0.5} \quad (18)$$

where $Z = (C_1/C_2{}^{0.5}/C_3{}^3) \simeq 1.46$ for most practical sprays. Substituting this value of Z into (18) gives

$$f = (2.9/\mathrm{Pr})(\rho_g/\rho_f) \log (1 + B)V[(Tu/100) \times \mu_g/\dot{W}_a D_{32}{}^3 A]^{0.5} \quad (19)$$

This expression is most relevant to conditions of high pressure and high turbulence, such as exist, for example, in the primary zones of modern gas turbine combustors.

The weak extinction equivalence ratio for any combustion zone supplied with a heterogeneous liquid fuel-air mixture is obtained by substituting into equation (3) the corresponding value for a homogeneous mixture, along with an appropriate value of f from equations (15–19). For example, the weak extinction limit for a gas turbine combustor under normal operation is obtained from equations (2, 3) and (19) as

$$\phi_{WE} = C\left[\frac{\dot{W}_a}{VP^{1.25}\exp(T_0/150)}\right]^{0.16} \times \left[\frac{\rho_f}{\rho_g V \log (1 + B)}\right]\left[\frac{\dot{W}_a D_{32}{}^3 A}{(Tu/100)\mu_g}\right]^{0.5} \quad (20)$$

It should be noted that equations (15–20) embody the assumption that the fuel spray comprises a multi-droplet mist whose overall evaporation characteristics are identical to those of a single evaporating drop. Thus, droplet interaction is ignored, and this could appreciably affect the overall rate of fuel evaporation. Another potential source of error is the combustion volume, V. Due to the physical space occupied by air jets and recirculating burned products, the actual reaction zone is normally appreciably less than that indicated by the liner dimensions. Thus, the constant, C, should be determined experimentally for each particular liner/nozzle combination.

In order to apply equation (20) to baffle-stabilized flames, it must be modified to allow for the fact that only a small fraction of the flowing air stream is entrained into the wake region. Thus equation (20) becomes

$$\phi_{WE} = C\left[\frac{E\dot{W}_a}{VP^{1.25}\exp(T_0/150)}\right]^{0.16} \times \left[\left(\frac{\rho_f}{\rho_g V \log (1 + B)}\right)\left(\frac{E\dot{W}_a D_{32}{}^3 A}{(Tu/100)\mu_g}\right)^{0.5}\right] \quad (21)$$

where E represents the fraction of the total air flow, $\dot{W}_a$, that is entrained into the recirculation zone.

From analysis of the fluid dynamics of this region, and examination of the experimental data obtained on the weak extinction limits of premixed flames, Ballal and Lefebvre [1] concluded that the entrainment factor, E could be expressed as

$$E \propto [B_g/(1 - B_g)][1 + 0.12Tu] \quad (22)$$

Substituting for E from (22) into (21), and also for $\dot{W}_a = \rho AU$ leads to

$$\phi_{WE} = C_4\left[\frac{U(1 + 0.12Tu)}{P^{0.25}d(1 - B_g)T_0\exp(T_0/150)}\right]^{0.16} \times \left[\left(\frac{\rho_f}{d \log (1 + B)}\right)\left(\frac{UD_{32}{}^3(1 + 0.12Tu)}{\rho_g\mu_g(Tu/100)B_g(1 - B_g)}\right)^{0.5}\right] \quad (23)$$

In the present study a value for C_4 of 0.005 was found to give a good fit to all the experimental data.

Discussion

The validity of the proposed model for determining the weak extinction limits of flames supplied with flowing heterogeneous fuel-air mixtures may be tested by comparing measured values of weak extinction equivalence ratio with the corresponding predicted values from equation (23). This is done in Figs. 2–10, in which the full lines represent theoretical values determined from equation (23). It is observed that the level of agreement between theory and experiment is generally very satisfactory, thus confirming the basic premise of the proposed model.

Of special interest are the results obtained on the influence of turbulence on ϕ_{WE}, as illustrated in Fig. 10. According to equation (23), for fuels that vaporize rapidly, the first term on the right-hand side is equal to unity, and ϕ_{WE} increases with turbulence intensity according to the relationship, $\phi_{WE} \propto (1 + 0.12Tu)^{0.16}$. In this situation, where the fuel-air mixture is effectively homogeneous, the effect

Downloaded 01 Jun 2010 to 171.66.16.58. Redistribution subject to ASME license or copyright; see http://www.asme.org/terms/Terms_Use.cfm

of an increase in turbulence intensity is to raise ϕ_{WE} by increasing the amount of air entrained in the recirculation zone, thereby reducing the time available for combustion. Thus, for fuels of relatively high volatility such as isoctane, equation (23) predicts that ϕ_{WE} should increase continuously with increase in turbulence intensity, and this is borne out by the experimental data for iso-octane, shown plotted in Fig. 10.

For less volatile fuels, there are many operating conditions at which the rate of heat release within the wake region is limited, not only by reaction kinetics, but also by rates of fuel evaporation. In this situation, we have, from equation (23)

$$\phi_{WE} \propto (1 + 0.12Tu)^{0.66}/Tu^{0.5}$$

And thus, ϕ_{WE} diminishes with increase in turbulence, as shown in Fig. 10 for heavy fuel oil. For diesel oil, at the conditions tested, the beneficial effect of an increase in turbulence in promoting fuel evaporation is outweighed by the accompanying adverse effect of a reduced residence time for combustion. This is evident from Fig. 10 which shows that, for diesel oil, ϕ_{WE} is sensibly independent of Tu.

Summary and Conclusions

From analysis of the processes governing the rates of fuel evaporation and chemical reaction in a combustion zone supplied with heterogeneous liquid fuel-air mixtures, it is concluded that the weak extinction equivalence ratio is given by

$$\phi_{WE(\text{heterogeneous})} = \phi_{WE(\text{premixed})} \times f^{-1} \text{ where}$$

$$f = 8.0(C_1/C_3^3)(\rho_g/\rho_f)(k/c_p)_g \times \log(1 + B)(V/\dot{W}_a D_{32}^3)(1 + 0.25C_2^{0.5}\text{Re}_{D_{32}}^{0.5})$$

For the important practical cases of low and high droplet Reynolds number the above expression simplifies to

(a) $\text{Re}_{D_{32}} \ll 1.0$, (low pressure, low turbulence)

$$f = 8.0(C_1C_3^3)(\rho_g/\rho_f)(k/c_p)_g \log(1 + B)(V/\dot{W}_a D_{32}^2) \text{ and}$$

(b) $\text{Re}_{D_{32}} \gg 1.0$, (high pressure, high turbulence)

$$f = (2.0/\text{Pr})(C_1C_2^{0.5}/C_3^3)(\rho_g/\rho_f) \times \log(1 + B)V[(Tu/100)\mu_g/\dot{W}_a D_{32}^3 A]^{0.5}$$

Recommended values of C_1, C_2 and C_3 for practical atomizers of the simplex and airblast type are 0.31, 0.21 and 0.46, respectively. (For nondisperse sprays, $C_1 = C_2 = C_3 = 1.0$, by definition).

For the highly turbulent primary zones of gas turbine combustion chambers, the weak extinction equivalence ratio is given by

$$\phi_{WE} = C\left[\frac{\dot{W}_a}{VP^{1.25}\exp(T_0/150)}\right]^{0.16} \times \left[\frac{\rho_f}{\rho_g V \log(1 + B)}\right]\left[\frac{\dot{W}_a D_{32}^3 A}{(Tu/100)\mu_g}\right]^{0.5}$$

For baffle-stabilized flames the role of turbulence is more complex because it affects not only the rate of fuel evaporation, but also the rate of entrainment of air into the wake region. Either effect could predominate but, in general, ϕ_{WE} increases with turbulence intensity for fuels of high volatility and decreases with increase in turbulence intensity for fuels of low volatility. For this type of flame ϕ_{WE} is given by

$$\phi_{WE} = \left[\left(\frac{0.005\rho_f}{d \log(1 + B)}\right)\left(\frac{UD_{32}^3(1 + 0.12Tu)}{\rho_g\mu_g(Tu/100)B_g(1 - B_g)}\right)^{0.5}\right] \times \left[\frac{U(1 + 0.12Tu)}{P^{0.25}d(1 - B_g)T_0\exp(T_0/150)}\right]^{0.16}$$

The theory predicts, and the experimental data confirm, that for heterogeneous mixtures of fuel drops and air, the weak extinction limit may be extended to lower values of equivalence ratio by increases in combustor size, fuel volatility, air pressure temperature, and by reductions in air mass flow rate and mean drop size.

References

1 Ballal, D. R., and Lefebvre, A. H., "Weak Extinction Limits of Turbulent Flowing Mixtures," ASME Gas Turbine Conference, London, England, Paper No. 78-GT-144, April, 1978.

2 Lorenzetto, G. E., "Influence of Liquid Properties on Plain-Jet Airblast Atomization," Ph.D. thesis, School of Mechanical Engineering, Cranfield, 1976.

3 Ballal, D. R. and Lefebvre, A. H., "Ignition of Liquid Fuel Sprays at Subatmospheric Pressures," *Combustion and Flame,* Vol. 31, 1978, pp. 115–126.

4 Plee, S. L. and Mellor, A. M., "Flame Stabilization in Simplified Prevaporizing, Partially Vaporizing and Conventional Gas Turbine Combustors, Paper No. 78-1038, AIAA/SAE 14th Joint Propulsion Conference, Las Vegas, Nev. July, 1978.

5 York, J. L. and Stubbs, H. E., "Photographic Analysis of Sprays," Trans ASME, Vol. 74, 1952 pp. 1157–1162.

6 Spalding, D. B., *Some Fundamentals of Combustion,* Butterworths, London, 1955.

7 Simmons, H. C., "The Correlation of Drop-Size Distributions in Fuel Nozzle Sprays," ASME JOURNAL OF ENGINEERING FOR POWER, July, 1977, pp. 309–319.

Downloaded 01 Jun 2010 to 171.66.16.58. Redistribution subject to ASME license or copyright; see http://www.asme.org/terms/Terms_Use.cfm

J. Odgers
I. White
D. Kretschmer

Dépt. Génie Mécanique,
Université Laval,
Québec, Canada

The Experimental Behavior of Premixed Flames in Tubes:

The Effects of Diluent Gases

One of the problems facing gas turbine users is the proliferation of gaseous fuels which may be available. These are so many that a comprehensive rig/engine study would be far too costly to undertake. The present studies represent an attempt to quantify the behavior of such fuels in a simple environment. Measurements of the rates of flame travel and the stability limits have been made for propane/oxygen mixtures diluted with nitrogen, carbon dioxide, helium or argon. The results have been used to forecast the laminar flame speed of mixtures, and rates of flame travel for the various mixtures have been correlated with groups representative of reaction rate and gas transport properties.

1 Introduction

The introduction of gaseous fuels (high, medium and low calorific values) to gas turbines has given rise to questions regarding the compatibility of fuels of differing composition, required to be burned within the same combustion system. As usual, many of the problems are being solved in the field by means of combustor development, and doubtless this will continue. However, the properties of possible fuels, whether primary fuels (e.g., methane) or derived from industrial processes (e.g., medium calorific gases) or produced as waste products (e.g., low calorific gases), are so diverse that information pertinent to their combustion properties may only be obtained (economically) by detailed studies using laboratory scale apparatus. The results of such studies should then be relatable to full scale industrial equipment.

As the first stage of a wide program of such studies, observations have been made of a range of mixtures burned within a series of transparent tubes. These notes present the experimental findings of the studies and some reflections on their significance. A full theoretical analysis of the combustion behaviors will follow at a later date when further experiments have been done to confirm the observed trends.

2 Apparatus and Method

A schematic diagram of the equipment is given in Fig. 1. The gaseous mixture is prepared by metering the various gases separately and then passing them through a mixing section prior to their entering the combustion tube. Leaving the combustion tube, the gases pass to a Meker burner where they are burned. This continues until the combustion tube is sufficiently purged of any previous mixture (minimum purging quantity of gas to tube volume of 20 to 1 was used).

After purging, bypass valves are used to isolate the mixture in the combustion tube. At one end of the latter, a small electric spark may be induced to ignite the mixture. For many experiments, as the flame travelled down the tube, it passed a number of thermocouples (four) upon which it imposed a transient temperature rise. The resultant current was detected by a UV recorder which charted the impulses. A chart speed was selected so as to enable the time intervals to be deduced for the passage of the flame between the thermocouples. For other tubes, the time for the passage between two marked points was measured by direct observation, using a stop watch. Most of the tests were done using tubes of lengths 1.1 m, but others were done using tubes measuring 3.07 m. Using the thermocouple technique, for the faster flames (up to 2.5 m/s) the timing error was estimated as ±10 ms which represented an error of about ±2.5 percent in the flame

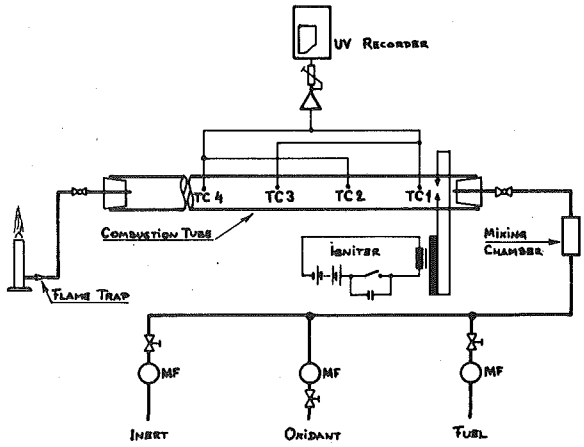


Fig. 1 Schematic of apparatus

Contributed by the Gas Turbine Division of THE AMERICAN SOCIETY OF MECHANICAL ENGINEERS and presented at the Gas Turbine Conference and Exhibit and Solar Energy Conference, San Diego, Calif., March 12–15, 1979. Manuscript received at ASME Headquarters January 4, 1979. Paper No. 79-GT-168.

Copyright © 1980 by ASME

Downloaded 01 Jun 2010 to 171.66.16.58. Redistribution subject to ASME license or copyright; see http://www.asme.org/terms/Terms_Use.cfm

travel determination. This is well below the overall error of a determination, which was generally ±10 percent.

The tubes could be fired either vertically or horizontally. Only small differences were noted between the two modes of firing. There was a tendency for the horizontally fired tubes to yield slightly faster rates of flame travel and slightly wider combustion limits than the ones fired vertically downward. The differences are attributed to flame convection effects. In addition, the horizontal mode of propagation tended to yield more erratic results than the vertical one. However, both sets of results fell within a general scatter band. Because of laboratory height restrictions the longer tubes were always fired in the horizontal mode. For both modes of firing, immediately prior to ignition, the bung sealing the firing end of the tube was removed in order to prevent pressure build-up during the combustion phase. Even so, one had to be very careful not to produce atmospheric disturbances adjacent to the tube, or else irregular flame travel could result. It is because of this tendency to instability that most of the experimental scatter arises.

In addition to the measurement of the rate of flame travel, the stability limits (rich and weak) were determined for each tube. The repeatability of the weak (fuel lean) mixtures was fairly good, but the rich mixtures exhibited considerable scatter, and, in some instances (using horizontal tubes), a pronounced "tail" was observed for rich mixtures (see Fig. 5). This tail lay outside the normal limits. In other instances, "partial" light-ups were noted which may have been caused by air diffusing into the open mouth of the tube. There is also the possibility that some of the over-rich light-ups could be associated with possible cool flame phenomena. Even more plausible, in the case of the horizontal tubes, are the possible effects of convection currents which may function as a sort of preheat. The likelihood of this latter effect is supported by the fact that the largest discrepancies occurred with the tubes having the larger diameters.

In order to establish confidence in the technique, a limited number of tests were performed using methane/air mixtures at conditions similar to those of other workers' [1, 2]. The results are indicated in Fig. 2, and they are considered to exhibit satisfactory agreement, bearing in mind the small differences in technique, tube materials, purity of gases, humidity of the gases, etc. The only arguable differences occur with the rich mixtures cited in [2] and those of the present experiments.

3 Experimental

Table 1 summarizes the range of experimental data considered for this paper. Similar data are being accumulated for other inert gases and other gaseous fuels and, at a later date, mixed fuels will be considered. The similarity in the form of the present results and those of other fuel/oxygen/inerts mixtures not considered here, suggests that any analysis procedure obtained for propane fuel will probably apply to other fuels.

Space limitations do not permit the presentation of all the results obtained for propane mixtures, and for the most part presentation will be limited to summary curves. Fig. 3 shows a typical stability loop obtained for a propane/air mixture. For comparison, results given by other workers are also given. The curve cited is the "best-fit" obtained for all the stability data for all modes of propagation and for all diameters. It will be noted that the original (horizontal) data obtained by White [3] tend to lie slightly outside the loop. Additionally, the results demonstrate the wider scatter experienced with rich mixtures.

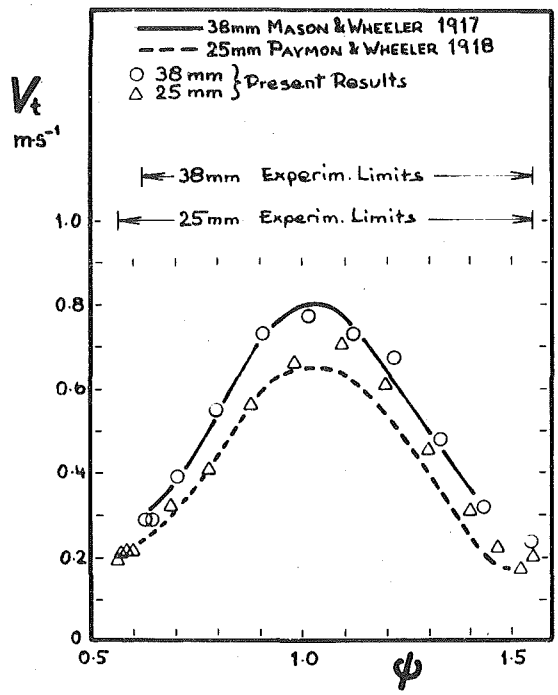


Fig. 2 Rates of flame travel—comparison of present results with existing data, ambient conditions

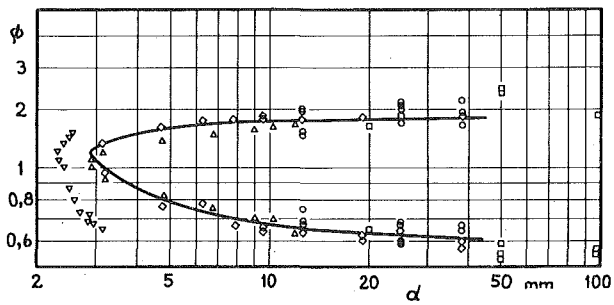


Fig. 3 Stability/quenching limits of propane/air mixtures at ambient conditions. ◊ This work ○ [3] horizontal propagation, □ [4] upwards propagation, △ [5] quenching, ▽[6] quenching

The effects of both, diameter and inert content, are demonstrated in Fig. 4. For ease of reading, the experimental points have been omitted; the scatter of Fig. 4 is similar to that of Fig. 3.

The bulk of the work was directed towards the determination of the rates of flame travel and a set of results is exhibited in Fig. 5. The loop is typical for a large diameter (38 mm) tube, and the ofttimes exhibited burning outside the normal rich limit is well indicated, as also the typical scatter due to lack of repeatability and reproducibility. Fig. 6 summarizes the effects of tube diameter, equivalence ratio upon the rates of flame travel in the tubes. Once again, for clarity of reading, the experimental points have been omitted.

Nomenclature

C = function of activation energy, E/R, K
C_p = molar heat capacity at constant pressure, J/(mol.K)
d = diameter, mm
E = activation energy, J/mol
l = length, m
M = molar mass, kg/mol
m = ratio inerts to oxygen (molar)
N = gas mass flow into a reactor, mol/s
n = overall reaction order, (equals 2ϕ for weak, $2/\phi$ for rich mixtures)
p_0 = pressure, atm
R = gas constant, J/(mol.K)
S_u = burning velocity, m/s
T_0 = inlet temperature, K
T_{eq} = equilibrium temperature after combustion, K
V = volume, l
v_t = flame travel velocity, m/s
β = correlation group $= \lambda M\, e^{-C/T}/C_p\, \rho\, T^{n-0.5}$ $m^2\, kg^{0.5}\, K^{0.5-n}\, mol^{-0.5}\, s^{-1}$
λ = thermal conductivity, W/m K
ρ = density, kg/m³
ϕ = equivalence ratio: stoichiometric oxygen, fuel ratio divided by the actual oxygen, fuel ratio

Downloaded 01 Jun 2010 to 171.66.16.58. Redistribution subject to ASME license or copyright; see http://www.asme.org/terms/Terms_Use.cfm

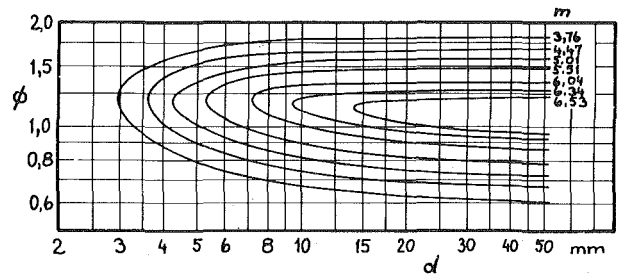


Fig. 4 The effects of tube diameter and inert content on flame stability ($C_3H_8/O_2/N_2$ at ambient)

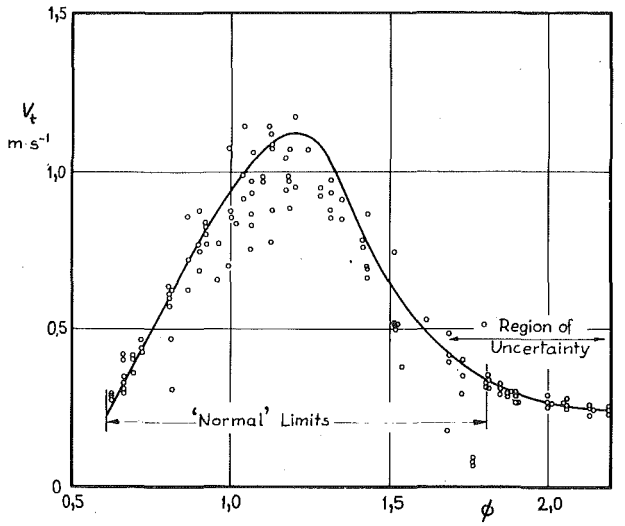


Fig. 5 Rates of flame travel. Typical experimental data for a single tube $C_3H_8/O_2/N_2$, $m = 3.76$, $d = 38$ mm, $T_0 \simeq 300$ K, p_0 atmospheric

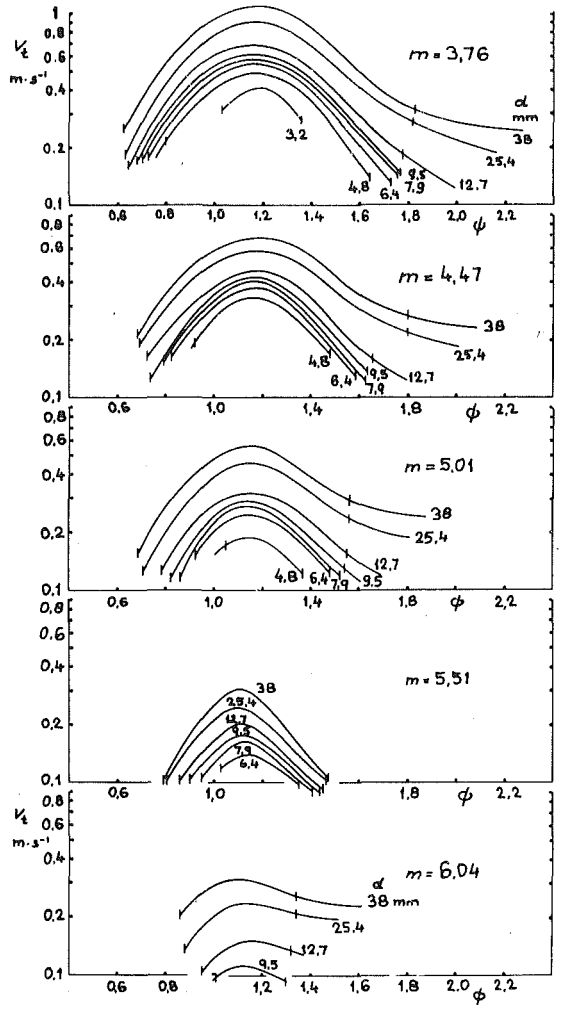


Fig. 6 Flame travel in tubes—effect of tube diameter and inert content. $C_3H_8/O_2/N_2$ ambient conditions

4 Discussion of Results

4.1 Combustion limits. In an unconfined space, mixtures of fuel and oxidant burn within fairly well-defined limits. As the degree of containment increases, these limits become narrower (as typified by Fig. 3), until a limiting diameter is reached, below which the mixture will not burn at all. Generally, if the ignition is within the tube, these limits are said to be stability (of burning) limits. If the flame approaches the tube from an outside source (e.g., burner experiments) and is then extinguished, this is termed "flame quenching." At the same experimental conditions, these two effects should be similar, the small differences observed being generally attributed to the ignition energy source, or to the approaching flame front or to small differences in aero-thermo-dynamics. The degree of coincidence is brought out in Fig. 3 and may be considered as satisfactory.

Flame extinction (quenching), or failure to ignite, may be due to heat losses (by conduction, convection or radiation from the flame zone) or to third-body collisions at the surface of the wall which will effectively quench the chain-initiating and/or branching reactions. In the case of an unconfined flame, the principal reason for extinction is probably due to radiative losses. For this type of flame, near the limits, the temperature corresponding to the peak reaction rate is close to the adiabatic flame temperature, and hence, a relatively small heat loss will occasion extinction. For most hydrocarbon/air mixtures the unconfined limits approximate to $\phi = 0.5$ (weak limit) and $\phi = 2.0$ (rich limit) at ambient conditions. At these conditions (air temperature 300 K), it can be shown [7] that the adiabatic flame temperatures are 1500 K and 1565 K, respectively, and that a heat loss of approximately 3 percent can bring about flame extinction. It is noteworthy that this temperature region (1500–1600 K) represents the temperature region at which most hydrocarbon flames are extinguished. For a flame to sustain a greater heat loss, the adiabatic flame temperature will have to be higher, and it follows that the limits will narrow.

Within tubes of varying diameter, the rate of heat loss from a flame will be a function of the diameter, with relatively greater losses occurring in the narrower bore tubes. Hence there will come a time when the heat loss exceeds the possible heat release by the flame of the most stable mixture. At this point, the loop will close and flame will not propagate in tubes of any smaller diameter. If, as is often supposed, the walls bring about the termination of the chain branching reactions of combustion, then the heat loss effect will be abetted. The difficulty is in allocating the magnitudes of the two effects.

If nitrogen plays the role of an inert gas, then the stability should be related to the expression of the nitrogen content as an equivalent heat loss. It could also be anticipated that the flame extinction would occur at a common temperature for any given tube diameter. The experimental results obtained to date suggest that this is so, but further data and analysis are required to establish the point quantitatively.

4.2 Rates of flame travel.

4.2.1 Propane/oxygen/nitrogen mixtures. A typical set of data for flame travel is given in Fig. 5. The experimental scatter can be seen to be substantial; the reasons for the scatter being those mentioned previously as also the reasons for the tail at the rich conditions.

For convenience, the experimental points have been omitted from the curves of Fig. 6. Some irregularities will be noted with respect to these curves. This is because each curve was drawn individually through the relevant experimental points and no attempt has been made to "smooth-out" the resulting composite curves. Using these curves, if a cross-plot is made of log v_t versus log d, then a straight line relationship is obtained for any specific value of equivalence ratio. This line, extrapolated to the stability limit (quenching diameter), yields a value for the laminar flame speed of the mixture (S_u) [8]. For mixtures of propane/air, the values of S_u obtained from the present

Downloaded 01 Jun 2010 to 171.66.16.58. Redistribution subject to ASME license or copyright; see http://www.asme.org/terms/Terms_Use.cfm

Table 1 Range of experimental data

Experiment	Mixture	Inerts/Oxygen m	Equivalence Ratio ϕ	Number of Experimental Points	Tube Diameters d mm	Remarks
Verification of Experimental Equipment	CH_4/Air	3.76	0.56 to 1.55	26	38–25.4	Comparison with data of other workers
Combustion Limits	$C_3H_8/O_2/N_2$	3.76 to 6.43	0.66 to 2.02	121	44–38–25.4 19.1–12.7 9.5–8–6.4 4.8–3.2	Used to determine the effect of tube diameter upon flame limits
Flame Travel Velocity Measurements Series I	$C_3H_8/O_2/N_2$	3.76 to 6.04	0.67 to 2.0	≃550	38–25.4 19.1–12.7 9.5–8–6.4 4.8–3.2	Used to determine the effect of tube diameter upon v_t and also to determine S_u
Flame Travel Velocity Measurements Series II	$C_3H_8/O_2/N_2$ C_3H_8/Air/CO_2 C_3H_8/Air/Ar C_3H_8/Air/He $C_3H_8/O_2/CO_2$ C_3H_8/O_2/Ar C_3H_8/O_2/He	3.76 to 6.03 4.38 to 5.48 4.47 to 6.3 5.02 to 5.55 1.83 to 3.73 3.51 to 4.72 3.39 to 5.08	0.65 to 2.1 0.75 to 1.9 0.7 to 2.0 0.9 to 1.7 0.5 to 2.2 0.45 to 2.7 0.7 to 1.5	≃550	25.4	Used to correlate flame travel data with different inert gas combinations

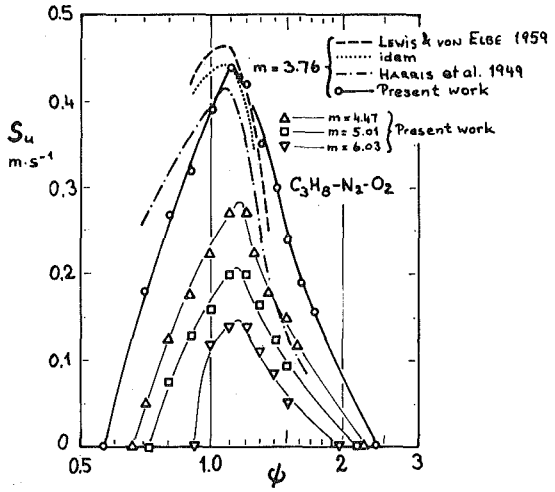


Fig. 7 Flame speeds—propane/air. Comparison of values obtained by different techniques

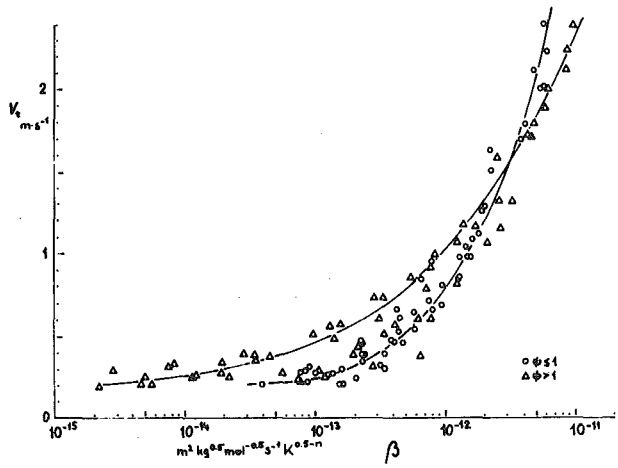


Fig. 8 Correlation of the rates of flame travel for propane/oxygen/inert mixtures using a 25.4 mm tube

work are given in Fig. 7. For comparison, results of other workers are also given [5, 8–10]. The measure of agreement is not very good, but it falls within the scatter band which has been observed for flame velocities determined by different techniques for other hydrocarbon fuels (e.g., see [11] for methane/air mixtures). As more data become available, using other diluents, the present results will be reappraised. However, by using the data given in Fig. 6, and the technique outlined above, the laminar flame velocity for any propane/oxygen/nitrogen mixture may be deduced from $m = 3.76$ to $m = 6.5$.

4.2.2. Propane/oxygen/inert mixtures. Some of this work was done in part fulfillment of an MS thesis [3] and, for a single tube diameter, a correlation was obtained which linked the rate of flame travel to the various physical and chemical properties of the mixtures involved. The range of data is given in Table 1.

Since (for a constant tube diameter) the rate of flame travel is dominated by the rate of chemical reaction, then the flame temperature of the gas could be expected to assume a very significant role. This is easily established in a qualitative manner. For a given equivalence ratio, as the amount of diluent was increased (i.e., flame temperature decreased), the rate of flame travel diminished. Similarly, for a constant amount of inerts in a mixture, the rate of flame travel increased as the mixture went from the weak limit towards stoichiometric, and then decreased as the rich limit was approached. If air is accepted as a 'standard' inerts/oxygen ratio, then one would anticipate that a mixture of propane/oxygen/carbon-dioxide would propagate flame at a slower rate than the air mixture having the same inerts to oxygen ratio, due to the increased specific heat of carbon dioxide. This was verified experimentally, as was the corresponding (but opposite) effects due to dilution with helium and argon. However, although the rates for both helium and argon mixtures were faster than those for nitrogen mixtures, those with helium were much faster than those with argon despite the fact that the mixtures possessed the same specific heats. Obviously then, factors other than temperature affect the rates of flame travel and it seems likely that the differences could be occasioned by the different transport properties of the mixtures. With this in mind, a correlation group was sought which would be representative of both, reaction and transport phenomena.

It was decided that the reaction group should be represented by $e^{-C/T}/T^{n-0.5}$ and it remained to select the appropriate values of C and n. For each equivalence ratio, the values of both parameters were obtained from the tables given by Kretschmer, et al. [7]. As anticipated, this group alone was insufficient to correlate the data and a term was sought which would be representative of the transport properties of the mixtures. Eventually, the group $\lambda M^{0.5}/C_p \rho$ was adopted as being satisfactory. The reaction rate group was evaluated at the adiabatic equilibrium temperature, and the transport group was evaluated at the temperature corresponding to the arithmetic mean of the flame temperature and the inlet temperature. Fig. 8 represents the rate of flame travel (v_t) plotted against the product of the two groups, for the data yielded by the 25.4 mm tube. The correlation appears to be fairly satisfactory, but as in the work discussed above, there is more scatter with rich mixtures, and there are

Downloaded 01 Jun 2010 to 171.66.16.58. Redistribution subject to ASME license or copyright; see http://www.asme.org/terms/Terms_Use.cfm

two distinct lines, one for rich conditions, the other for weak conditions. As more data become available for other tubes and other fuel/oxygen/inert mixtures, it is hoped to extend the correlation so as to make it of general application.

4.3 General Discussion. The relationship between the measured rates of flame travel and the laminar flame speed has already been established. Evidence that this sort of relationship extends to the more exotic diluents is given in Fig. 9 which relates v_t to S_u for propane/oxygen/helium mixtures. The laminar flame speed data are from Morgan et al. [12], the values of v_t are from the present work.

The measured rates of flame travel also correlate with spherical combustor performance as shown in Fig. 10 for stoichiometric conditions. The data for the spherical combustor are taken from [13]. This relationship is of particular significance since the data from spherical combustors have been used to derive equations found to be useful in the modelling of gas turbine combustors.

With respect to possible application to combustor design, it is anticipated that the present work will relate to several topics. It should have some bearing on the design of interconnectors for the transfer of flame in cannular combustion systems. Thus, to have maximum possibility of flame transference, the diameter of the interconnectors should at least correspond to the tube diameter above which there is no further widening of combustion limits. A knowledge of the rate of flame passage will enable the time of transfer to be calculated. To meet a given transfer requirement, this may necessitate the use of a tube of larger diameter than that indicated by the first consideration.

The data might also suggest a minimum flame tube diameter (or annulus width), beyond which flame quenching will be significant due to wall effects. This could have considerable importance in the design of future low-pollution combustors.

The current shortage of conventional gas turbine fuels has created a need for new sources of fuels. One response has been the advent of gaseous fuels having medium or low calorific values. In order to burn these fuels successfully, it is necessary to modify the combustion system so as to cater for the new limits and rates of combustion, as well as to modify the fuel injection system so as to cater for the increased volume of fuel gases. As the present work progresses to complex mixtures of fuels and inerts, it should be possible to specify the limits of combustion with good accuracy even for complex mixtures. Some knowledge of the rates of combustion will also be forthcoming, probably in the form of global kinetic equations relating to the estimation of the laminar flame speed. A knowledge of such flame speeds would then enable the designer to scale the combustor appropriately.

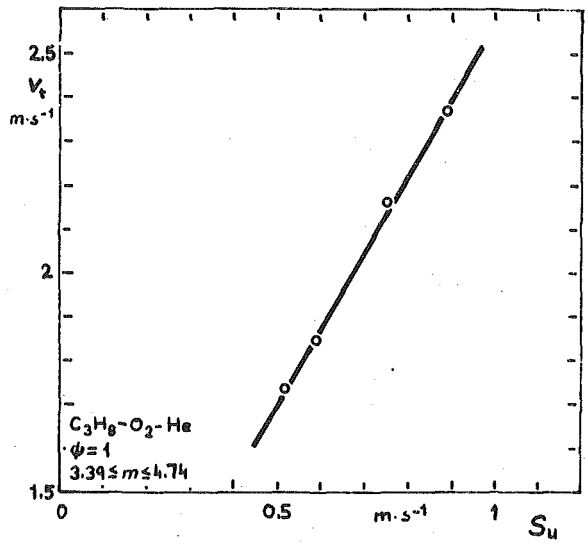


Fig. 9 Dependence of flame travel velocity upon burning velocity

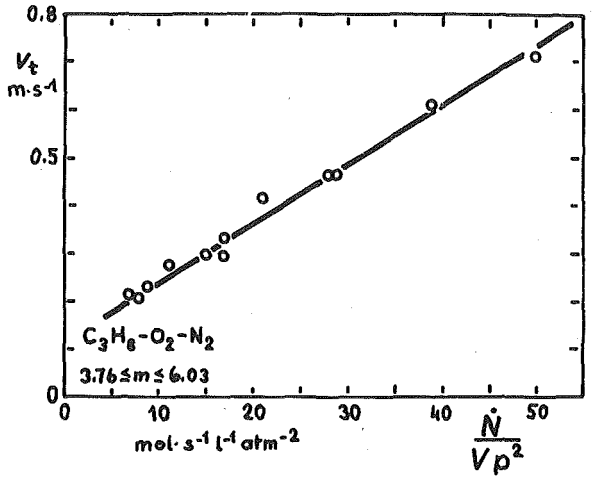


Fig. 10 Flame travel velocity versus kinetic air loading within a spherical combustor

5 Conclusions

An apparatus has been developed suitable for the measurement of the rates of flame travel in tubes of different diameters. The limits of combustion may also be determined using the same equipment.

From the rates of flame travel, the laminar flame speeds have been estimated by plotting v_t versus d and extrapolating to the diameter at which flame extinction occurs. At this point the value of v_t corresponds to S_u.

For a given tube diameter, a correlation has been established between the rate of flame travel and the correlation parameter β, where $\beta = (\lambda M^{0.5}/C_p \rho)(e^{-C/T}/T^{n-0.5})$.

As more data become available, there would appear to be a considerable potential for application to the design of gas turbine combustors and associated components.

Acknowledgments

Thanks are due to the National Research Council of Canada for the granting of funds which enabled this project to be carried out, and for their continued support which is enabling the work to be extended.

References

1 Mason, W., and Wheeler, R. V., "The Uniform Movement During the Propagation of a Flame," *J. Chem. Soc.* 111, 1917, p. 1044.

2 Paymon, W., and Wheeler, R. V., "The Propagation of Flame through Tubes of Small Diameter," *J. Chem. Soc.* 115, 1918, p. 656.

3 White, L., "The Propagation of Flames within Tubes," MSc thesis, Université Laval, Québec, 1978.

4 Coward, H. F., and Jones, G. W., "Limits of Flammability of Gases and Vapours," Bulletin 503, Bureau of Mines, US Government Printing Office, Washington, 1952.

5 Harris, M. E., Grumer, J., von Elbe, G., and Lewis, B., "Burning Velocities, Quenching and Stability Data on Nonturbulent Flames of Methane and Propane with Oxygen and Nitrogen," 3rd Symp. (Int.) on Combustion, Williams and Wilkins, 1949, pp. 80–98.

6 Gibbons, L. C., Barret, H. C., and Gerstein, M. "Effect of Molecular Structure on Combustion Behaviour," *I & E C*, 1954, No. 10.

7 Kretschmer, D. and Odgers, J., "Modelling of Gas Turbine Combustors—A Convenient Reaction Rate Equation," ASME JOURNAL OF ENGINEERING POWER, 1972, pp. 173–179.

8 Lewis, B., and von Elbe, G. *Combustion, Flames and Explosions of Gases,* Academic Press, 1959, 3rd. Ed., 317 pp.

9 Dugger, G. L. and Graab, D. D., "Flame Velocities of Hydrocarbon-Oxygen-Nitrogen Mixtures," 4th Symp. (Int) on Combustion, Williams and Wilkins, 1953, p. 336.

10 Leason, D. B., "The Effect of Gaseous Additions on the Burning Velocity of Propane/Air Mixtures," 4th Symp. (Int) on Combustion, Williams and Wilkins, 1953, p. 369.

11 Andrews, G. E., and Bradley, D., "The Burning Velocity of Methane-Air Mixtures," *Combustion & Flame,* Vol. 19, 1972, pp. 275–278.

12 Morgan, G. H., and Kane, W. R., "Some Effects of Inert Diluents on Flame Speeds and Temperatures," 4th Symp. (Int) on Combustion, Williams and Wilkins, 1953, p. 313.

13 Clarke, A. E., Odgers, J., Stringer, F. W., and Harrison, A. J., "Combustion Processes in a Spherical Combustor," 10th Symp. (Int) on Combustion, The Combustion Institute, 1956, p. 1151.

Downloaded 01 Jun 2010 to 171.66.16.58. Redistribution subject to ASME license or copyright; see http://www.asme.org/terms/Terms_Use.cfm

R. M. Clayton
Jet Propulsion Laboratory
California Institute of Technology,
Pasadena, CA

A Partial Oxidation Staging Concept for Gas Turbines Using Broadened Specification Fuels

A concept is described for using a very fuel-rich partial oxidation process as the first stage of a two-stage combustion system for onboard processing of broadened specification fuels to improve their combustion characteristics. Results of an initial step in the experimental verification of the concept are presented, where the basic benefits of H_2 enrichment are shown to provide extended lean-combustion limits and permit simultaneous achievement of ultralow levels of NO_x, CO, and HC emissions. The H_2 required to obtain these results is within the range available from a partial oxidation precombustion stage. Operation of a catalytic partial oxidation reactor using a conventional aviation turbine fuel (JP5) and an unconventional fuel (blend of JP5/xylene) is shown to produce a "fuel gas" stream with near-theoretical equilibrium H_2 content. However, a number of design considerations indicate that the precombustion stage should be incorporated as a thermal reaction.

Introduction

Recent large price increases for aircraft turbine engine fuels and possible future fuel shortages have led to increased interest in widening the spectrum of fuels (including those from coal and oil shale syncrudes) acceptable for aviation turbine engine operation. It is expected that a broader spectrum of acceptable fuels would lead to substantial fuel cost savings in the total life cycle costs of operating those engines. However, it is also expected that the combustion behavior of these fuels, particularly regarding pollutant emissions, will be poorer because aromatics content will be greater, fuel-bound N_2 will be greater, and vaporization rates will be lower. Thus, development of new combustor design concepts is warranted if low emission levels are to be retained with the relatively poorer fuels.

A potential means of accomplishing this is through onboard fuel processing which, in principle, has the effect of decoupling the properties of the raw turbine fuel from the main combustion processes of the engine. The process of present interest is partial oxidation where a large portion of the fuel (not necessarily all of the fuel) to the engine would be reacted with a small portion of the air to the engine in a precombustion stage of an overall two-stage combustion system. Such a processing stage would generate H_2-bearing gaseous products whose composition is dependent on the fuel richness of the reaction and on the hydrogen content of the fuel.

The notion of staged combustion for turbine engines is not new [1], but an objective of maximizing H_2 generation in the precombustion stage for the purpose of emission control is believed to distinguish this scheme from others. Yamagishi, et al. [2] reports a similar scheme applied to an atmospheric pressure burner.

With fuels having hydrogen-to-carbon ratios of approximately 1.9, air-to-fuel ratios in the range of 5–6 theoretically produce a gas stream consisting of over 20 percent by volume of both H_2 and CO, the remainder of the products consisting mainly of N_2. A "fuel gas" of this composition exhibits combustion characteristics superior to those of the initial raw hydrocarbon fuel by virtue of (1) its H_2 content, which provides a reduced lean flammability limit, broadening the margin between the leanness required for control of thermally generated NO_x and that providing adequate flame stability; and (2) its fully gaseous state, which provides the potential for higher mixing and combustion rates, as well as reduced thermal radiation to the combustor walls. Moreover, experimental results reported in [2] suggest the potential of well premixed, very fuel-rich reactions ($A/F < 7$) for suppressing the formation of intermediate nitrogen compounds (HCN, NH_3, etc.) which are involved in the formation of NO from fuel-bound N_2. Thus, processing a substantial portion of fuel (containing fuel-bound N_2) through a precombustion stage may also inhibit the production of fuel-generated NO_x during the final combustion stage.

It is envisioned that ultimately this processing stage could be physically integrated with the combustor. The partial-oxidation products would then be directed into the combustor where they would be mixed with additional air, and any remaining fuel, and burned in the combustor.

This paper summarizes the most current results from an ongoing experimental program to establish the practical feasibility of the concept. Ultralow levels of emissions have been adopted as targets. These targets are, in terms of emission index (g pollutant species/kg total fuel), 1.0 for NO_x and CO, and 0.5 for HC. The experiments are conducted using combustor inlet air state conditions typical of high-performance turbofan aviation engines.

The work has proceeded from using neat H_2 (bottled H_2 source)/JP5 admixtures to establish the basic benefits of H_2 enrichment, to the use of a simulated, partial-oxidation product gas mixture (also from a bottled source) substituted for the neat H_2. This step is incomplete but is being undertaken as an expedient means of achieving a timely verification that the benefits of neat H_2 will be retained. It is necessary because a very fuel-rich precombustion reaction suitable for operation under gas turbine inlet air conditions is not yet available. In this regard, exploratory work has been done with a catalytic reactor. Demonstration of an integrated two-stage combustion system is a future goal of the work.

A description of the concept and progress toward its experimental verification is presented.

Contributed by the Gas Turbine Division of The American Society of Mechanical Engineers and presented at the Gas Turbine Conference and Exhibit and Solar Energy Conference, San Diego, Calif., March 12–15, 1979. Manuscript received at ASME Headquarters January 4, 1979. Paper No. 79-GT-169.

Copyright © 1980 by ASME
Downloaded 01 Jun 2010 to 171.66.16.58. Redistribution subject to ASME license or copyright; see http://www.asme.org/terms/Terms_Use.cfm

Theoretical Considerations

Partial Oxidation Products. Although the partial-oxidation process can be carried out either thermally or catalytically, the theoretical, adiabatic, equilibrium composition of the product gases are identical for the same initial reaction conditions. Details of the paths of the combustion chemistry for either reaction scheme are complex and not fully understood and their discussion is beyond the scope of this paper. Suffice to say that the overall process occurs with an excess of fuel and that the consumption of the available oxygen by a portion of the fuel provides heat, CO_2, and H_2O that react with the remainder of the fuel to produce a final product gas whose composition is a function of the particular fuel stock and the reaction mixture ratio.

Fig. 1 shows the results of one-dimensional, equilibrium-thermochemical calculations giving product composition (molar basis) and temperatures for a typical conventional turbine fuel with a hydrogen-to-carbon ratio of 1.92, over a range of fuel-rich air-to-fuel ratios and at an operating condition in the range of interest to the present work (nitrogen concentrations are not shown). The calculations were made using the computer program described in [3].

Note that solid carbon (C_s) is predicted with A/F ratios less than about 5.2 and that the product gas temperature increases rapidly at A/F ratios greater than 5.2. Carbon monoxide, one of the two major combustibles in the product gas, reaches a peak at about this A/F ratio, whereas the other major combustible, H_2, shows an increasing volumetric concentration in the A/F region of C_s formation. However, in terms of the mass of H_2 produced per unit mass of hydrocarbon fuel, it can be shown that H_2 mass productivity of the fuel also peaks at about the A/F ratio of 5.2, as illustrated in Fig. 2.

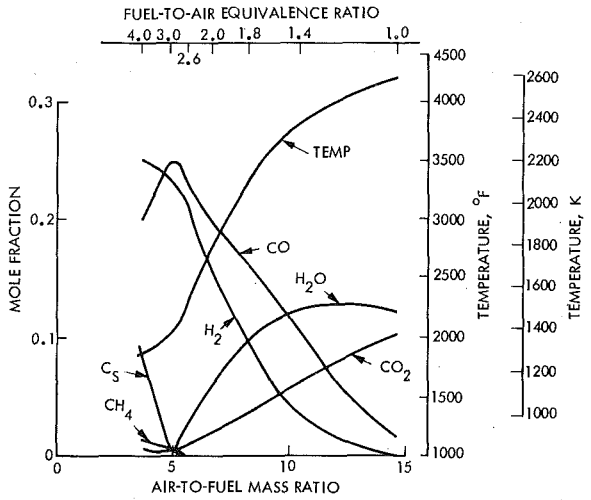


Fig. 1 Theoretical equilibrium composition and temperature of fuel-rich products for inlet air at 778 K (940°F) and 25.3 × 10^5 N/m² (25 atm); fuel H/C = 1.92

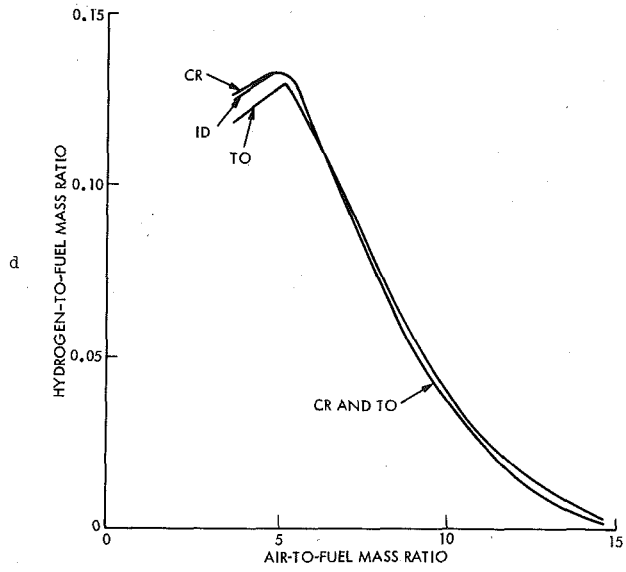


Fig. 2 Theoretical hydrogen-to-fuel mass ratio for various inlet air conditions typical for gas turbines: (TO) 778 K (940°F), 25.3 × 10^5 N/m² (25 atm); (CR) 717 K (830°F), 8.1 × 10^5 N/m² (8 atm); (ID) 422 K (300°F), 3.0 × 10^5 N/m² (3 atm); fuel H/C = 1.92

Thus, from a theoretical standpoint, the optimal A/F ratio for sootless H_2 production is about 5.2, where the H_2 content of the product gas is about 6 percent of the mass of the combustibles in the gas. The lean flammability limit of the total product gas when mixed with additional air is estimated to occur at an overall A/F ratio of about 57 based on the procedure for fuel gas mixtures (at ambient temperature) outlined in [4], taking the H_2, CO, and CH_4 as combustibles and the H_2O, CO_2, and N_2 as inerts. The substantially reduced A/F lean limit of 57 for the product gas compared to about 24 for turbine fuels is of course the central argument for the subject concept.

Integrated Combustion System. Assuming that the technology for providing an optimized partial-oxidation reactor existed, integrating it into a two-stage combustion system has a substantial impact on present combustor design practices. However, a rudimentary conceptual design analysis serves to outline projected operational requirements and identifies potential design options that could accommodate the broad combustion range needed for aviation gas turbine engines.

A two-stage combustion system is depicted schematically in Fig. 3, where the various fuel and air flows are also identified. It is assumed that the precombustion stage is to be operated at its optimal A/F ratio of 5.2. The basic operational and control consideration is how the total system flows should be split between the two stages. For present purposes, the fuel and air splits are defined as $\dot{m}_{fg}/\dot{m}_{ft}$ and $\dot{m}_{ag}/\dot{m}_{at}$, respectively. From these definitions and the constant mixture ratio constraint for the first stage, it can be shown that the required fuel split to the first stage is related to the overall system equivalence ratio (based on $\dot{m}_{ft}/\dot{m}_{at}$) as shown by the straight lines and the right-hand ordinate in Fig. 4. Each line represents an arbitrarily selected constant value of air split to the first stage. For a particular total air flow to the

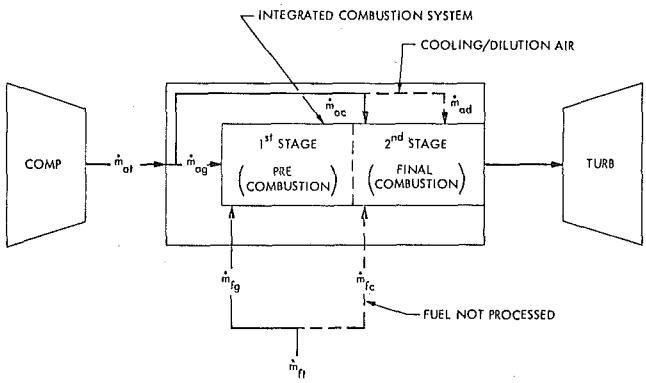


Fig. 3 Schematic of two-stage combustion system

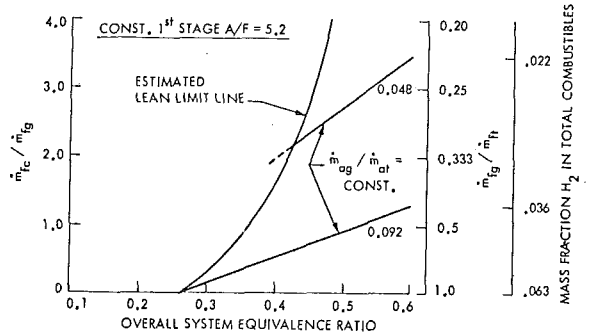


Fig. 4 Conceptual operating map for two-stage combustion system

Downloaded 01 Jun 2010 to 171.66.16.58. Redistribution subject to ASME license or copyright; see http://www.asme.org/terms/Terms_Use.cfm

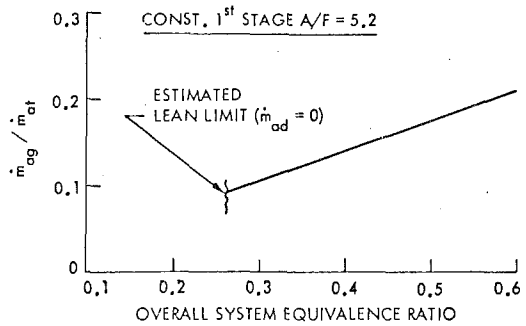


Fig. 5 Variation of air split for all fuel through the first stage

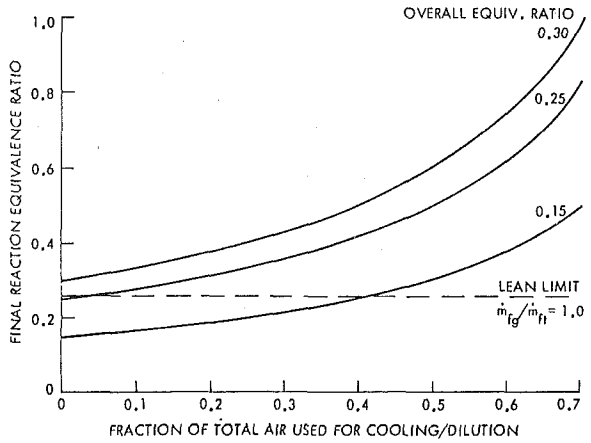


Fig. 6 Variation of final reaction equivalence ratio with air used for cooling and dilution

combustion system (i.e., a particular engine power level), each of these lines also represents a constant total throughput for the precombustion stage.

If all the system fuel is directed through the first stage, then operation of the combustion system lies along the abscissa and the air split no longer can remain constant. The required air split for all fuel through the first stage is shown as a function of system equivalence ratio in Fig. 5.

The curved line shown on Fig. 4 is an estimated lean limit line based on considering the first-stage product gas stream as a fuel gas mixture having a composition and lean limit specified from the theoretical calculations discussed above. When all the raw fuel is processed through the first stage, this fuel gas mixture is the only "fuel" burned in the second stage; therefore, the system lean flammability limit is at its minimum value. When lesser amounts of raw fuel are processed (fuel split ratios < 1.0), the system lean limit increases by virtue of the increased limit of the raw fuel that bypasses the first stage and enters the combustion process in the second stage without prior processing.

The lean limit line represents a theoretical combustion limit, but not necessarily a lean blowout limit, since blowout is also a function of flame stabilization technique and reactant premixedness. Nevertheless, all other combustor factors fixed, fuels or fuel mixes with substantially lower flammability limits can be expected to provide substantially leaner blowout limits.

If the final combustion is to be carried out totally premixed with all the air to the second stage ($\dot{m}_{ad} = 0$), then only the system equivalence ratio region to the right of the limit line, shown in Fig. 4, is theoretically viable for completing the combustion reaction started in the precombustion stage. If a portion of the total air flow is to be used for film-cooling and dilution ($\dot{m}_{ad} > 0$), as would be required for an engine combustor, the final combustion reaction would necessarily be richer and the overall equivalence ratio could lie to the left of the limit line so long as the final *reaction* equivalence ratio was to the right of the limit line. In that case, the final reaction equivalance ratio depends on the fraction of the total system air used for cooling and dilution and on the overall equivalence ratio required for a particular engine operating condition. An evaluation of this relationship is shown in Fig. 6 for overall equivalence ratios of 0.30, 0.25, and 0.15, which are typical for maximum, cruise, and idle power, respectively. For all fuel through the first stage, air fractions of 0.45 or greater would keep the final reaction equivalence ratio above the lean limit for all power conditions.

Table 1 Comparison of two-stage operational schemes

Operational scheme	Air split	Fuel split	Advantage
1) All fuel through first stage	Variable	Constant at 100 percent	Greatest benefit for alternate fuels
2) Constant air split to first stage	Constant	Variable	Simpler control
3) Parallel the lean limit line	Variable	Variable	None
4) Constant fuel split to first stage (<100 percent)	Variable	Constant	None

From the foregoing discussion and a further inspection of Fig. 4, four distinct schemes for system operation can be defined and are shown in Table 1. Scheme 1 would provide the greatest benefit for application to broadened specification fuels. But scheme 2 might also be used depending on how poor the fuel is and whether processing only a portion of it would be adequate. Scheme 2 would be simpler to implement because variable fuel split control is probably easier than variable air split control, although compressor bleed might also be needed at low power to throttle system air mass flow while maintaining combustion stability.

Progress in Experimental Verification

The Benefits of H_2 Enrichment. It was deemed important to establish the basic benefits of H_2 enrichment as the first step in the overall process of experimentally verifying the utility of the two-stage combustion concept.[1] The rationale for expecting significant combustion enhancement with admixtures of H_2 and jet fuel is described in [5] and [6] along with interim experimental results. These results showed that the targeted ultralow emission levels could be achieved simultaneously, but that the proportion of H_2 required (10–12 mass percent in the total fuel) was greater than the maximum theoretically available from a partial oxidation precombustion stage (~ 6 percent).[2] It was concluded from those results that improved premixing (H_2, jet fuel, and air) was necessary to decrease the H_2 requirement.

Subsequent modifications to the fuel injector and flameholder for the JPL MOD 2 burner resulted in the version shown schematically in Fig. 7. Pertinent design parameters are summarized in Table 2. Although the burner was not intended to be a scale version of the G.E. CF6-50 combustor, analogous design parameters for a production version are shown for reference. The experimental burner has about 4 percent of the mass throughput and about 40 percent of the combustion space rate of the engine combustor.

For testing, the burner is housed within a heavy-walled pressure vessel which also serves as a plenum chamber for a preheated inlet-air supply. (See [6] for a description of the test facility.) The burner is designed to utilize 100 percent of the air flow in the combustion process; thus air film cooling and air dilution, which are normally used in an engine combustor, are omitted. In this way, combustion effects from air injection are avoided for the concept evaluation. The cylin-

[1] Hydrogen enrichment of jet fuel can be considered to be a combustion enhancement scheme distinct from the two-stage combustion concept if the H_2 is available as a second fuel.

[2] It was expected that a similar H_2 proportion of the total combustibles would be required to achieve similar suppression of flammability limits regardless of the proportion of CO and jet fuel, since CO and jet fuel have similar lean flammability limits on an equivalence ratio basis.

Downloaded 01 Jun 2010 to 171.66.16.58. Redistribution subject to ASME license or copyright; see http://www.asme.org/terms/Terms_Use.cfm

drical combustion chamber is water-cooled, as are the inlet/flameholder assembly, sonic exhaust nozzle, and gas sample probe.

The burner is intended to operate with a near homogeneous fuel/air mixtures. This is accomplished in the mixing duct, where gaseous H_2, finely atomized jet fuel, and the air are combined. The interfacial component between the combustion and premixing zones is an axisymmetric, combination step/bluff-body flameholder. A torch igniter provides ignition but is inactive once steady burning is obtained.

Fuel Injection/Premix Section. As is seen from Fig. 7, premixing is carried out via a coaxial flow scheme where the fuels are injected at the bell-mouthed entry to a 5.22 cm (2.07 in.) dia straight cylindrical duct, 10.16 cm (4.0 in.) long. The flow area provides a space velocity of about 140 m/s (460 ft/s) for the cruise power condition. This results in a residence time in the premixing section of about 1.6 ms.

Table 2 JPL Mod 2 burner design specifications and comparison with typical production engine burner[a]

Specification item	Mod 2 burner[b]	Engine burner[b]
Air total pressure	30.39×10^5 N/m^2 (30 atm)	30.39×10^5 N/m^2 (30 atm)
Air total temperature	812 K (1460 R)	821 K (1477 R)
Air flow rate	4.6 kg/s (10 lbm/s)	103.4 kg/s (228 lbm/s)
Chamber reference velocity	18.3 m/s (60 ft/s)	25.9 m/s (85 ft/s)
Chamber dwell time (no recirculation)	5.0 ms	2.6 ms
Chamber L/D (shape)	1.7 (cylindrical)	3.0 (annular)
Combustion length	30.5 cm (12.0 in.)	34.8 cm (13.7 in.)
Combustion space rate[c]	0.88×10^6 J/hr-m^3-N/m^2 (2.4×10^6 Btu/hr-ft^3-atm)	2.2×10^6 J/hr-m^3-N/m^2 5.9×10^6 Btu/hr-ft^3-atm)
Combustion equivalence ratio	LBO < ER < 1.0	>1.0
Overall equivalence ratio	LBO < ER < 1.0	0.34
Air split for cooling	N.A.	30 percent
Air split for dilution	N.A.	38 percent
Premix reference velocity	157.8 m/s (518 ft/s)	N.A.
Premix Mach number	0.28	N.A (0.27 at compressor discharge)
Premix dwell time	1.4 ms	N.A.
Premix length	22.3 cm (8.8 in.)	N.A.

[a] G. E. CF6-50. Data from [8], [b] Takeoff conditions, [c] At overall equivalence ratio = 0.34

The fuel injector is a JPL-fabricated device designed to inject liquid jet fuel and gaseous H_2 into the air stream from 15 pairs of coaxial tubes arranged to provide a near-uniform initial distribution of flow over the cross section of the mixing duct. The exit end of each pair of injector tubes is located approximately at the throat station of the bell-mouthed entry. This positioning of the injection tube ends, combined with an appropriate location of the conical surface of the injector body, provides an arrangement where the fuels are injected into a region of near-axial air flow. Turbulence and recirculating flows are thus deliberately avoided in the mixing duct in order to reduce flame holding tendencies under the high temperature and pressure of the inlet air.

Atomization of the liquid fuel streams is accomplished by reversing the usual scheme for pressure atomizers where high-velocity fuel is injected into low-velocity air. In the present scheme, advantage is taken of the high-velocity air which is required for short premix residence times, and the fuel is injected at low velocities: of the order of 3 m/s (10 ft/s). Thus a large velocity gradient is available for fuel atomization. The coaxial arrangement of the injected flows also assures that the initial fuel distribution will be insensitive to variations in all flow rates as operating conditions are varied.

Combustion Chamber Inlet/Flameholder Assembly. The design criteria adopted for the combination step/bluff-body flameholder were to keep the mixture velocity through the annular flow area around the 7.6-cm (3.0 in.) dia, semi-ellipsoidal centerbody equal to the approach velocity from the mixing duct, and to direct the mixture flow so as to establish roughly equivalent flameholding recirculation zones behind the annular step and the centerbody. Thus the premixed reactants are introduced to the combustion zone as an axially directed annular jet with velocities of the order of 140 m/s (460 ft/s), which provides adequate resistance to flashback yet imposes no more than a reasonable (for concept evaluation) 7–8 percent total pressure loss. Communication between the inner and outer flameholding zones is provided in the wake region behind four 1.27 cm (0.5 in.) wide struts that support the centerbody.

The centerbody and struts are water-cooled over the last 1.27 cm (0.5 in.) of length at the chamber end. The cavity in the centerbody serves to reduce heat transfer rates to the uncooled portion. The downstream face of the step portion of the inlet assembly is also water-cooled.

Acoustic cavities of quarter-wave slot configuration are positioned around the periphery of the inlet section, adjacent to the chamber wall. Half of them are sized for the first tangential acoustic mode frequency of the chamber and the other half tuned for the second

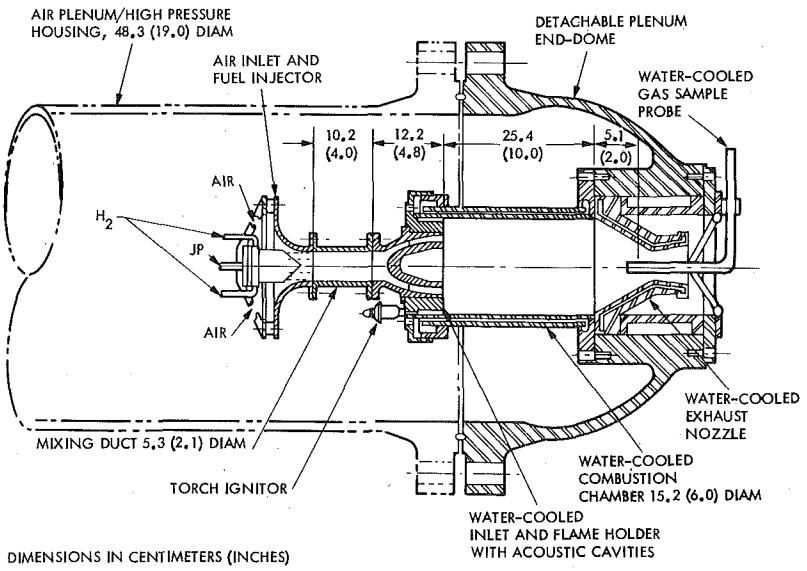


Fig. 7 MOD 2 research combustor installed in burner housing

Downloaded 01 Jun 2010 to 171.66.16.58. Redistribution subject to ASME license or copyright; see http://www.asme.org/terms/Terms_Use.cfm

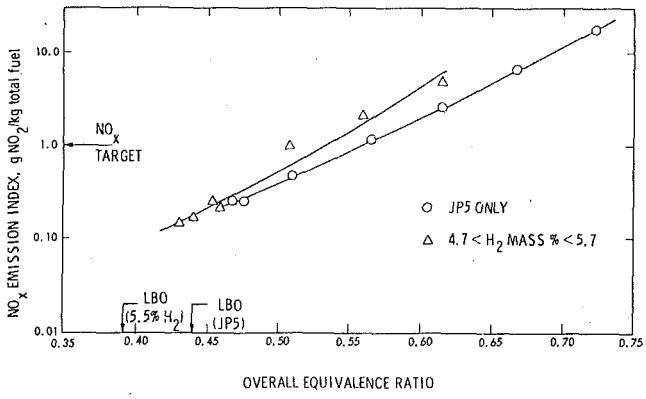


Fig. 8 NO_x emissions with and without hydrogen. Cruise power inlet air conditions: 728 K (850°F) 12.2 × 10^5 N/m^2 (12 atm)

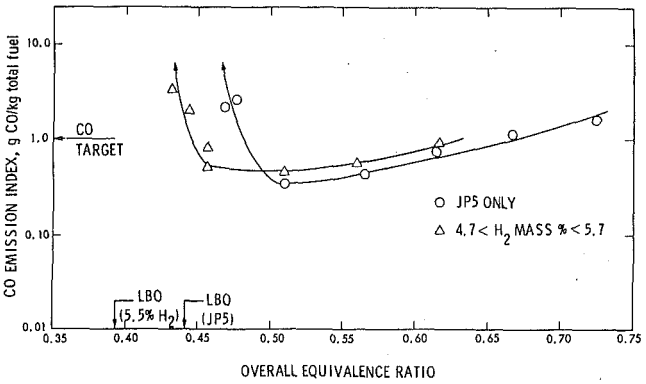


Fig. 9 CO emissions with and without hydrogen. Cruise power inlet air conditions; 728 K (850°F), 12.2 × 10^5 N/m^2 (12 atm)

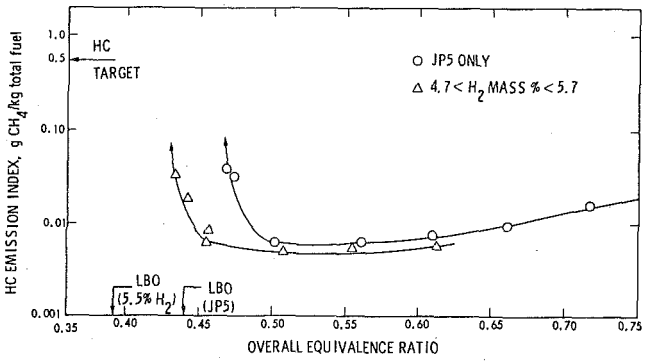


Fig. 10. HC emissions with and without hydrogen. Cruise power inlet air conditions; 728 K (850°F), 12.2 × 10^5 N/m^2 (12 atm)

tangential mode. This cavity design was found to be adequate to control high-frequency (3–5 KHz) combustion resonance.

Results. Salient emission results for this burner are shown for a typical cruise-power operating condition in Figs. 8–10 where it can be seen that:

1 The ultralow emission goals are simultaneously achieved or bettered over an equivalence ratio (based on H_2 + jet fuel) range of 0.45 to 0.52 using 4.7–5.7 mass percent H_2 (H_2 in total fuel.)

2 The lean blowout limit (LBO) is reduced from an equivalence ratio of 0.44 for jet-fuel-only to 0.39 with 5.5 percent H_2.

These data also show that the target emissions are simultaneously achievable with JP5 alone in the 0.48 to 0.55 equivalence ratio range with the good premixing obtained with the current injection/mixing configuration. However, the high level of mixedness produces a high LBO ($\phi_{LBO} \sim 0.44$), and the HC and CO levels are very sensitive to equivalence ratio as LBO is approached. Addition of the relatively small amounts of H_2 used here broadens the margin between acceptable blowout stability and acceptable emission levels. This

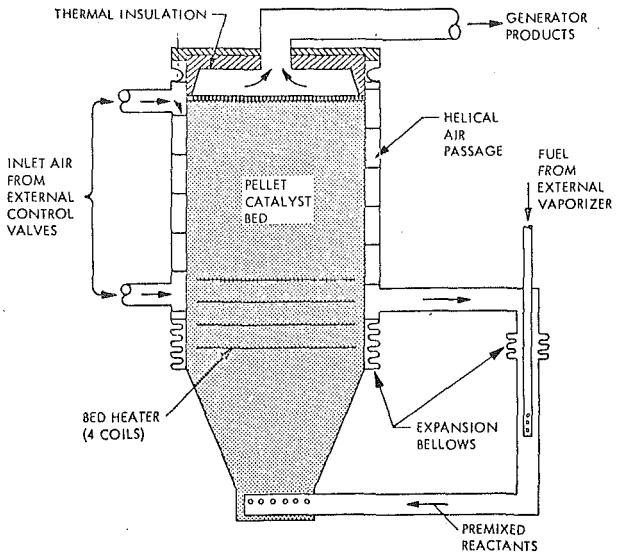


Fig. 11 Schematic of generator L

broadened margin would be highly significant in a full-scale premixed combustor where gross fuel and air maldistributions exist.

The 4.7–5.7 percent H_2 used to obtain these results represents better than a 50 percent reduction in required H_2 from previous results [5], and is within the range theoretically available from a very fuel-rich precombustion stage.

Generating the H_2. A catalytic, partial-oxidation reactor, designated H_2 generator L, has been used to explore the potential utility of this scheme as a design concept for a precombustion stage [7]. The generator was operated over the pressure range of 3.45 to 4.66 × 10^5 N/m^2 (3.4 to 4.6 atm) and with inlet air temperatures of approximately 422 K (300°F). Total mass flow through the generator ranged from 15 to 26 × 10^{-3} kg/s (0.034 to 0.058 lbm/s). Aviation turbine fuel JP5 was used for the bulk of the experiments, but a blend of JP5 and xylene (C_8H_{10}) was also used to provide a fuel with a significantly increased aromatics content (~35 percent). In all experiments, the product gas was analyzed for its H_2, CO, CO_2, and CH_4 content.

Generator Description. Generator L is shown schematically in Fig. 11. Inlet air enters the ports (one or both, as controlled by external valves), is directed around the bed liner through the helical air passage and exits from the single port opposite the inlet ports. The purpose of the two inlet ports is to permit a variable amount of additional air preheat as the air absorbs the heat rejected by the bed. This preheat is greatest when all of the air enters the uppermost port, and least when all of the air enters the lower inlet port. In practice, the air is directed through the upper port for startup, and is changed to the lower port as the reaction stabilizes at a steady-state condition. Further modulation of the air split was not used in these experiments.

After leaving the preheating passages, the air is mixed with fuel vapor (from an external vaporizer) in the induction passage and the fuel/air mixture is ducted to the generator inlet, where the mixture is diffused into the bed through an array of 18 holes in the wall of the induction tube. The fuel vapor is introduced into the air through an array of nine holes near the end of the fuel injection tube. Final mixture temperatures were generally in the range of 561–589 K (550–600°F).

The premixed fuel and air enter the bed at the conical transition section, which is filled with catalyst pellets, as is the cylindrical part of the generator. Reaction occurs throughout the bed and the resulting gaseous products are discharged through the duct at the top of the bed.

The catalyst used in all of the experiments is a pellet type, with pellets 6.4 mm (0.25 in.) dia and 6.4 mm (0.25 in.) long. All catalyst material is manufactured by Girdler Division of Chemtron Corporation of Louisville, Kentucky. The bulk of the work was conducted using a catalyst loading consisting of a less reactive material in the conical section than for the cylindrical section of the generator. For

Downloaded 01 Jun 2010 to 171.66.16.58. Redistribution subject to ASME license or copyright; see http://www.asme.org/terms/Terms_Use.cfm

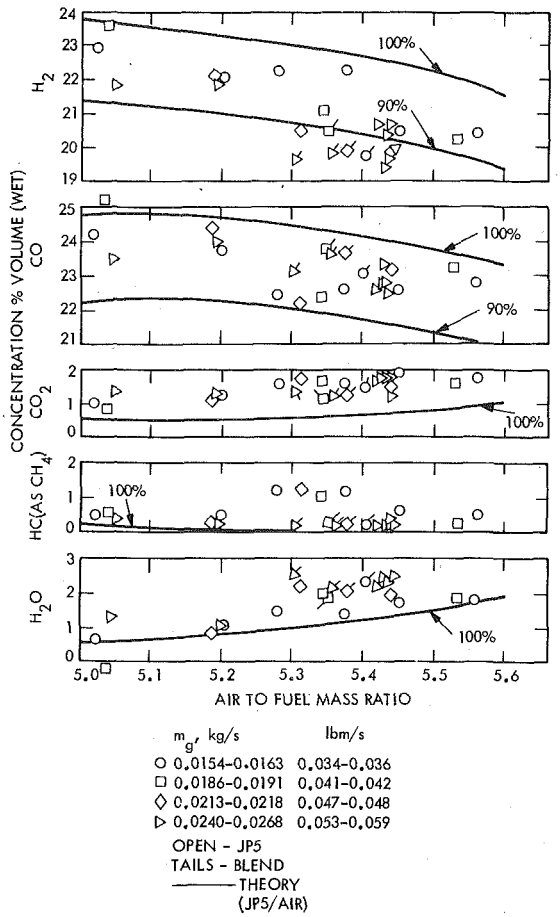


Fig. 12 Product composition for generator L

this loading, approximately 1.18 kg (2.6 lbm) of G90B pellets were used in the conical section and 4.4 kg (9.7 lbm) of G90C pellets were loaded in the cylindrical section. These catalysts have 11 and 15 percent nickel by mass, respectively, and use an alumina substrate.

For startup, a portion of the catalyst bed is electrically preheated with a heating element composed of four coils of Inconel-sheathed, Nichrome wires as indicated in Fig. 11. The coils are supplied with a total of 1350 to 1600 kw of dc electrical power. This power range is adequate to heat the bed locally to 811 K (1000°F) in about 10 minutes.

Results. The concentrations of the four measured species in the product gas as a function of metered generator A/F ratio is shown for four levels of throughput and two fuels in Fig. 12. Concentrations are based on dry, soot-free volumetric concentrations using metered air flow rates and standard species balance procedures for estimation of water content. The estimated water concentrations are also shown in Fig. 12. The JP5/air theoretical equilibrium composition curves for 3.0×10^5 N/m^2 (3 atm), 422 K (300°F) air are shown for reference. Theoretical calculations for the blended fuel were no made.

Considerable data scatter is apparent, but taken as whole, the data for JP5 follow the trends for H_2 yield expected from theoretical considerations, with the yield generally within 90 percent of theoretical. Some reduction in H_2 yield is apparent as the throughput was increased to the highest value tested. But whether this was the result of a true bed capacity limitation or the effects of soot deposition is uncertain. The highest throughput levels not only gave indication of high soot production, but also occurred late in the runs when accumulated deposits were probably already present.

The data for the run with the fuel blend show somewhat less H_2 yield than for the JP5 fuel, but this is expected since the hydrogen content of the blend is approximately 12.8 percent by mass compared to the nominal 13.8 percent for JP5.

The trend for CO yield was also consistent with the theoretical trend and was generally within 90 percent of theoretical equilibrium.

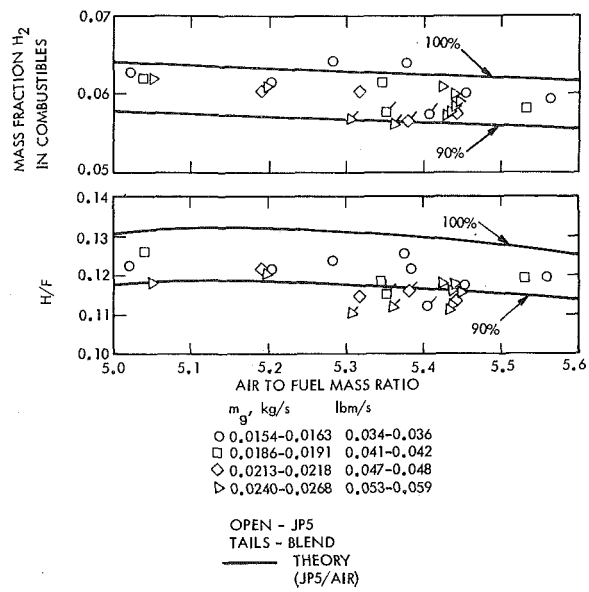


Fig. 13 Hydrogen yield indices for generator L

The concentrations of CO_2 and unconverted hydrocarbons (as CH_4) in the product gas stream were always somewhat greater than expected from theoretical considerations. This reflects the nonequilibrium performance of the generator that are apparent in the less than theoretical yield of H_2 and CO previously mentioned.

Since the H_2 content of the product gas is considered to be the most influential factor in the concept of improving the combustion properties of the raw fuel by onboard fuel processing, the quantity of H_2 produced per unit quantity of fuel (H/F) and the fraction of H_2 in the total combustibles are important indices of generator performance. Maximizing these indices would provide the optimal application of the partial oxidation process to the two-stage concept for broadening acceptable fuel specifications. The H/F mass ratios and H_2 fraction in the combustibles observed in these tests are shown in Fig. 13, where they again compare favorably with theoretical equilibrium values. As did the volumetric H_2 yields, the H/F ratios for JP5 fuel generally fall within 90 percent of the theoretical values, with some reduction indicated for the higher throughput levels. The fuel blend, of course, exhibits a reduced H_2 mass production due to its smaller initial hydrogen content.

In summary, the fuel gas stream produced by the catalyzed partial oxidation process, and in particular by the generator tested, using a conventional and an unconventional turbine fuel, appears to be near the theoretical gaseous composition attainable. The utility of this fuel gas stream in application to a second stage of combustion in a continuous-flow, turbine-engine-like burner system of course remains to be demonstrated.

Concluding Remarks

A partial oxidation staging concept for gas turbine combustors using broadened specification fuels has been described and elements of its experimental verification have been presented. The concept is proposed as a means of controlling gaseous pollutant emissions to ultralow levels while maintaining acceptable lean blowout limits.

While the practical feasibility of the concept is as yet incompletely demonstrated due to the lack of a satisfactory partial oxidation reactor, the following conclusions can be stated from results to date.

1 Admixtures of H_2 and conventional JP5 jet fuel used in an experimental premix combustor of quasi-prototype functional design provide a significant extension of the lean blowout limit.

2 The proportion of H_2 in the total combustibles required to achieve ultralow levels of emissions simultaneously with the extended lean limits is within the theoretical capabilities of a very fuel-rich partial oxidation process.

Downloaded 01 Jun 2010 to 171.66.16.58. Redistribution subject to ASME license or copyright; see http://www.asme.org/terms/Terms_Use.cfm

3 A catalytic process can produce near theoretical equilibrium products under very fuel-rich operating conditions, but considerations of simpler startup, greater durability, lack of abrasive particulates, and greater tolerance to soot production make thermal processes potentially more attractive.

4 Soot production is likely to be a persistent problem with very fuel-rich precombustion, especially with fuels with high aromatics content. However, unreported JPL results with rich thermal reactors indicate that sooting tendencies can be minimized by thorough premixing and high preheat.

Acknowledgments

The author expresses appreciation to all individuals who have contributed to the progress of this investigation. Particular gratitude is due to Roy Bjorklund and Milton Noel, test engineers, Donald Cerini, principal designer and consultant for the catalytic H_2 generator, and Clarence Tuttle, engineering assistant and test facility operator.

This paper presents the results of research carried out at the Jet Propulsion Laboratory, California Institute of Technology, for NASA under Contract NAS7-100, and for the Air Force Aero Propulsion Laboratory by agreement with NASA.

References

1 Roffe, G., and Ferri, A., "Prevaporization and Premixing to Obtain Low Oxides of Nitrogen in Gas Turbine Combustors," NASA CR-2495, March 1975.

2 Yamagishi, K., et al., "A Study of NO_x Emission Characteristics in Two Stage Combustion," 15th Symposium (International) on Combustion, The Combustion Institute, 1975, pp. 1157–1166.

3 Gordon, S., and McBride, B. J., "Computer Program for Calculation of Complex Chemical Equilibrium Compositions, Rocket Performance, Incident and Reflected Shocks, and Chapman-Jouguent Detonations," NASA SP-273, Lewis Research Center, Cleveland, Ohio, 1971.

4 Coward, H. F., and Jones, G. W., "Limits of Flammability of Gases and Vapors," Bulletin 503, Bureau of Mines, Washington, D. C., 1952.

5 Clayton, R. M., "Hydrogen Enrichment for Low Emission Jet Combustion," *Evaporation-Combustion of Fuels*, Advances in Chemistry Series No. 166, American Chemical Society, 1978.

6 Clayton, R. M., "Reduction of Gaseous Pollutant Emissions from Gas Turbine Combustors Using Hydrogen-Enriched Jet Fuel-A Progress Report," Technical Memorandum 33-790, Jet Propulsion Laboratory, Pasadena, California, Oct. 1, 1976.

7 Clayton, R. M., "Performance Evaluation of a Catalytic Partial Oxidation Hydrogen Generator Using Turbine Engine Fuels," AFAPL-TR-77-62, June 1977.

8 Rudey, R. A., "Status of Technological Advancement for Reducing Aircraft Gas Turbine Engine Pollutant Emissions," NASA TMX-71846, Lewis Research Center, Cleveland, Ohio, Dec. 1975.

Downloaded 01 Jun 2010 to 171.66.16.58. Redistribution subject to ASME license or copyright; see http://www.asme.org/terms/Terms_Use.cfm

K. D. Mach
AFAPL/TBC,
Wright-Patterson Air Force Base, OH

Improving Turbine Component Efficiency

The thermal efficiency of a gas turbine engine depends on the cycle pressure and temperature ratio and on the aerodynamic efficiencies of the gas path components. Maintaining and/or improving structural integrity and aerodynamic efficiency in this high pressure, high temperature environment is the preeminent problem of the turbine designer. High gas temperatures require at least some of the metal structure to be cooled, yet cooling air is a loss to the cycle and its consumption must be kept to a minimum. Research into cooling techniques and boundary layer behavior on airfoils and endwalls and into test procedures for obtaining heat transfer data are providing some of the answers the designer needs. Increased operating pressures generate increased mechanical stresses. Finite element analyses and automated design procedures are proving to be powerful aids to the designer. Improving aerodynamic efficiency requires careful control of the flow in three dimensions, particularly in low aspect ratio machines. The first practical computation method for three-dimensional, viscous, transonic flows became available in late 1977 and has made this one of the most exciting areas of turbine technology. Additional gains in aerodynamic efficiency can be realized by controlling leakages, especially those over the rotor tip, by accounting for the transient interactions between rotor and stator; and by careful control of discharged coolant flow. This paper briefly describes the turbine cooling research conducted by the Air Force Aero Propulsion Laboratory and describes more extensively the AFAPL programs in turbine aerodynamics, including applications of three-dimensional flow analysis.

Introduction

The thermal efficiency and specific output of a gas turbine engine depend on the cycle pressure and temperature ratios and on the aerodynamic efficiencies of the gas path components. Cycle efficiency increases with compressor pressure ratio and specific output increases with the ratio of turbine inlet temperature to compressor inlet temperature, hence the continuous striving for higher compressor pressure ratios and higher turbine inlet temperatures.

Aerodynamic inefficiencies in the gas path degrade the cycle efficiency on at least a one-to-one ratio. For example, in a simple turbojet with compressor pressure ratio of 20:1 and temperature ratio (turbine inlet to compressor inlet) of 4.0, and all gas path efficiencies set to unity, the cycle efficiency is 57.5 percent. If we decrease the turbine efficiency, the cycle efficiency decreases 1.4 times as fast, reaching zero when the turbine efficiency is 59 percent. The efficiencies of other gas path components exert similar, if not greater, influences. It is clear, therefore, that the achievement of maximum component efficiency is imperative.

In order to design an efficient turbine, today's designer must contend with three major interrelating problems. He must provide an efficient three-dimensional flow path, and he must provide some means of blade and endwall cooling, at least in the first stages, while accounting for the effect of discharged coolant on the main flow. Finally, he must provide sufficient structural strength to withstand the high pressures and temperatures, allowing space for internal coolant flow, and holding weight to a minimum.

Succeeding paragraphs of this paper will examine some of these problems in more detail and describe some of the research activities directed toward their solution. The paper concludes with a projection of the state-of-the-art of turbine design in the 1980's.

Contributed by the Gas Turbine Division of The American Society of Mechanical Engineers and presented at the Gas Turbine Conference and Exhibit and Solar Conference, San Diego, Calif., March 12–15, 1979. Manuscript received at ASME Headquarters January 8, 1979. Paper No. 79-GT-176.

Description

Broadly speaking, the turbine design process consists of a cycle of preliminary aerodynamic and stress analyses followed by detailed and elaborate analyses. The preliminary analyses are iterative and serve to delimit the various design parameters—the flow path, the vector diagrams, the airfoil sections, the heat load on the airfoils, the required coolant, and the stress levels.

Preliminary Design. The actual nature of preliminary design and analysis calculations has not changed significantly over the years because the governing principles and the steps of their implementation have long been known. What has changed is the method of executing the solution procedure and to some extent the magnitude of the problem.

The digital computer afforded a significant increase in designer productivity because of its speed. Problems which took days with a slide rule or desk calculator could be solved in minutes with—assuming a thoroughly debugged program—no errors. The introduction of interactive computer graphics yielded another major increase in designer productivity because he could obtain both graphic and printed output almost instantly. A preliminary design system of this type is described in the next section, and with greater detail in [6]. With it, a designer can analyze a complete stage-root, pitch, and tip sections—from vector diagrams to the estimated life over a given mission—in half a day.

Much more needs to be done in the area of preliminary design methods because the advancing state-of-the-art has made the design problem more complex and more aspects need to be considered in the preliminary phase. Cooling system design is an example.

Turbine cooling is expensive. The coolant is lost to the cycle when it is extracted from a compressor stage and is discharged from the

Copyright © 1980 by ASME
Downloaded 01 Jun 2010 to 171.66.16.58. Redistribution subject to ASME license or copyright; see http://www.asme.org/terms/Terms_Use.cfm

turbine. The discharge interferes with the mainstream flow. The need to provide flow paths through the engine and into the blades and vanes increases the complexity and cost of the machine. The designer naturally wants to use the smallest quantity of coolant possible and he would like to define that quantity as early as possible in the design cycle in order, for example, to be sure that the airfoils have sufficient internal flow area to pass the coolant. From an aerodynamic loading viewpoint, the turbine airfoils need to be slender. From a low heat transfer viewpoint, the opposite is desirable. Unfortunately, the current state-of-the-art puts this kind of calculation out of the area of preliminary analysis. There is no fast and yet accurate method of determining the heat transfer to airfoils and endwalls and the available test data are far from comprehensive. Flow passages inside the airfoils are so complex that it is almost impossible to calculate the heat transfer coefficients. When the coolant is finally discharged, either as a film or through the trailing edge of a blade, the current state of knowledge does not permit an accurate prediction as to how it interacts with the free stream flow. The designer, therefore, must make do with a very preliminary estimate, with a view to improve it in the detailed design phase.

Detailed Design. The need for detailed design calculations has been recognized from the very early days of the gas turbine development. The turbine flow field is, after all, three-dimensional, with heat transfer, mass addition, thick boundary layers, and transonic velocities; whereas the preliminary design calculations are essentially one-dimensional. Before the early 1950's, detailed design consisted of applying empirical corrections to the preliminary design.

The complexity of the flow field and the Navier-Stokes equations precluded any analysis in greater depth. Closed form solutions were not (and still are not) apparent and the sheer magnitude of the calculations required put any numerical solution out of reach of the desk top calculators then available.

In the early 1950's, two events significant to gas turbine design occurred [2]. Wu published his theory of S_1-S_2 stream surfaces, on which the flow is two-dimensional, and the second event was the emergence of the digital computer. The S_1-S_2 concept led to the development of radial equilibrium and streamline curvature analyses in the meridional plan for which the digital computers could generate solutions in a few hours. By the early 1960's, streamline curvature methods had been highly developed and were in everyday use, as indeed they are today, and computers could generate solutions in a few minutes. Turbine and compressor designers could economically obtain a much more accurate picture of the flow field which relied less extensively on empirical corrections.

Still streamline curvature methods are limited in accuracy because they attempt to solve a three-dimensional problem by a series of two-dimensional approximations. Therefore, the need for a fully three-dimensional Navier-Stokes solution continued to be pressing, awaiting only a sufficiently powerful computer and the necessary skill to develop a tractable algorithm. Numerous investigators attempted solutions and by the early 1970's reasonably accurate solutions of turbomachinery flow fields were obtained from incompressible viscous flows with no heat transfer. One of the most successful is described in [5]. Figs. 1 and 2 show some typical predictions of this program. Fig. 1 is a contour plot of the kinetic energy loss at the exit plane of a turbine stator and Fig. 2 is a plot of the "mixed out" (average blade-to-blade) efficiency at the same plane as compared with test data from a half inch downstream. The comparison can be seen to be quite good. In addition to aerodynamic performance, the program predicts heat transfer.

The case shown required about 40 min of CDC 6600 time and cost about 1000 dollars. This may seem expensive until one considers the cost of a test project to determine the equivalent aerodynamic and heat transfer information. One can readily see that three-dimensional fluid flow computations are now economically feasible as well as technically necessary, as is evidenced by its rapid adoption by the turbine engine industry.

Beyond dispute, three-dimensional fluid flow computations are here to stay and extensive further growth is expected. Rapid advances at least through 1985 are projected with some serious obstacles yet

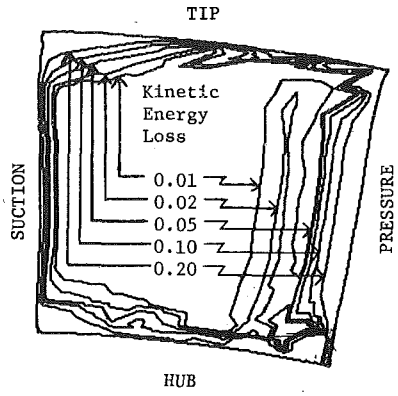


Fig. 1 Exit plane survey

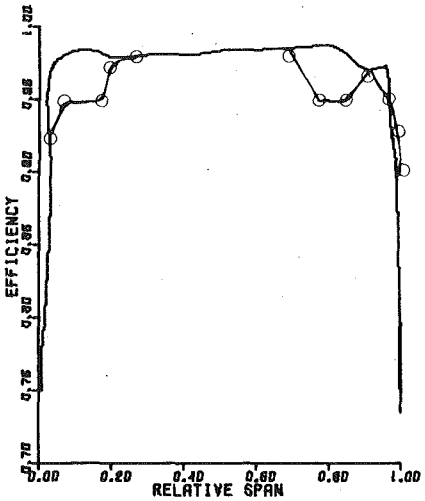


Fig. 2 Mixed-out efficiency

to be tackled. For example, the boundary layers in turbomachinery are not well understood for the two-dimensional case and much less so in three-dimensional cases. We have only begun to explore the phenomenon of rotor-stator interaction, which profoundly influences both the free stream and the boundary layer flow (and thereby, the heat transfer), and we will have to learn to account for the effect of discharged coolant on both flows. Naturally, we will want extensive experimental verification of all analytical methods.

Approach

The Air Force Aero Propulsion Laboratory (AFAPL), the NASA, the Army, the Navy, other Government agencies, and industry are conducting numerous research projects, both experimental and analytical, directed toward improving gas turbine component efficiencies. Some typical AFAPL programs are described below.

In response to the need to minimize coolant flow and provide aerodynamic and heat transfer data for design use and validation of prediction methods, the AFAPL in partnership with the NASA Lewis Research Center is sponsoring a program to measure heat transfer to the endwalls of typical turbine cascades. Measurements will be taken at a variety of operating conditions, with and without coolant flow.

Steady state heat transfer tests are expensive and time-consuming and it is very difficult to simulate engine conditions in a test rig, much less keep instrumentation intact at typical engine temperatures. Dunn and Stoddard [3] demonstrated the capability of obtaining detailed heat transfer measurements to a turbine stator at actual engine conditions by using a shock tube as the hot gas source. They further showed the potential capability of obtaining aerodynamic measurements with the same apparatus. There is, however, some uncertainty with regard to the boundary layer fluctuation or intermittency phenomenon which may not be present in the short duration shock tube environment. They are currently engaged in applying the same technique to a complete stage. A fast, inexpensive technique such as

Downloaded 01 Jun 2010 to 171.66.16.58. Redistribution subject to ASME license or copyright; see http://www.asme.org/terms/Terms_Use.cfm

this allows rapid comparisons of alternative designs, and because of the detailed heat transfer map it provides, allows the designer to put the coolant flow where it is needed without risk of over or undercooling.

Research on airfoil boundary layers and cooling methods has provided the first photographic evidence of Taylor-Goertler vortices on the pressure surface of a turbine airfoil, and is yielding valuable insights on the transition from laminar to turbulent boundary layer flow. Another program has shown for the first time the trajectories of coolant flows discharged from a turbine rotor.

Turbine aerodynamic and analytical research led to the development of the first viable three-dimensional viscous flow analysis, and to the LART stator, the first to be designed using a three-dimensional flow analysis. A high pressure stage made up of this stator and a conventional rotor developed 92 percent efficiency at the design point, which vividly demonstrates the benefits to be obtained from such a design tool [4, 5]. The current program seeks to develop a three-dimensional analysis in rotary coordinates, to design a rotor using this analysis, and to build the rotor and test it with the existing stator. In other phases of the program, tip leakage flow fields and the transient region between rotor and stator will be measured and analytical models developed.

Other analytical work includes the Turbine Design System [6], a set of preliminary design analyses designed to be used through an interactive graphics terminal. A schematic is shown in Fig. 3. Such a system increases designer productivity markedly because it eliminates the labor of punching data cards and it eliminates the wait for job turnaround. Once the preliminary design is satisfactory, the user can produce an input set for both the three-dimensional flow analysis and the three-dimensional structural analysis. Additions to produce tapes for numerically controlled machine tools are feasible and are coming into use in some industries [7].

Outlook and Conclusions

Turbine design is entering a period of rapid and profound change caused by the simultaneous arrival of interactive graphics methods and a viable three-dimensional flow analysis. By 1985, the typical preliminary design and analysis system will resemble that shown in Fig. 3, with extensive use of graphics along the way. The detailed analysis will be fully three-dimensional and account for rotation, heat transfer, mass addition, leakage flows, rotor-stator interactions, boundary layer transition, etc. It will be linked to the preliminary system as shown in Fig. 4 and will be in daily use as a partial substitute for rig tests. Given a sufficiently robust computer, it may be possible to predict the flow through, and performance of, a complete stage.

Interactive graphics techniques and viable three-dimensional methods in both fluid flow and structural analyses will together greatly increase the designer's productivity and reduce the need for development testing of new designs. This means that component efficiencies can be achieved at significantly reduced time and cost.

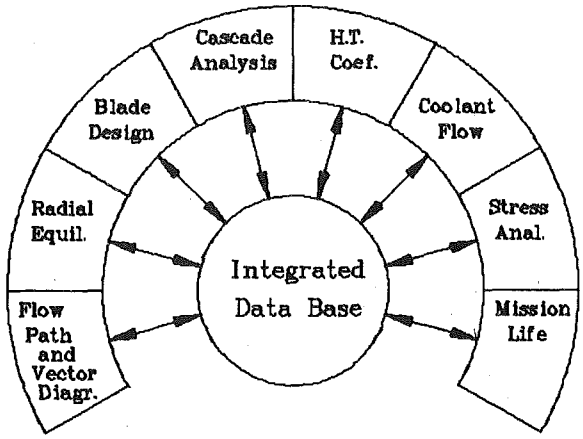


Fig. 3 Turbine design system schematic

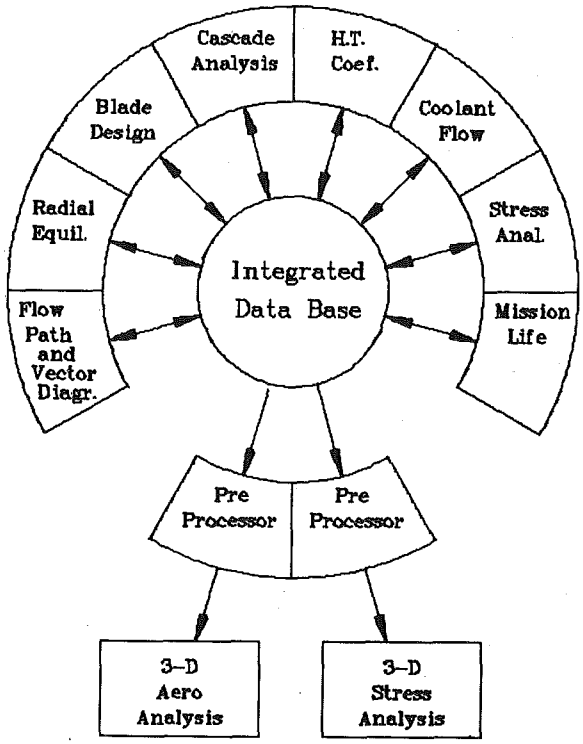


Fig. 4 Advanced turbine analysis system

References

1 Zucrow, M. J., *Aircraft and Missile Propulsion*, Vol. II, New York, John Wiley and Sons, 1964.

2 Serovy, G. K., ed., "Fluid Dynamics of Turbomachinery," Course notes for ASME short course—*Fluid Dynamics of Turbomachinery*, July 1973, Ames, Iowa.

3 Dunn, M. G. and Stoddard, F. J., "Measurement of Heat-Transfer Rate to a Gas Turbine Stator," ASME 78-GT-119, 1978.

4 Tall, W. A., "Understanding Secondary Flows," *Secondary Flows in Turbomachines*, AGARD Conference Proceedings No. 214, 1977, pp. 14-1–14-12.

5 Dodge, P. R. "3-D Heat Transfer Analysis Program," AFAPL-TR-77-64, 1 Oct 77, Air Force Aero Propulsion Laboratory, Wright-Patterson Air Force Base, OH.

6 Wysong, R. R., et al., "Turbine Design System," AFAPL-TR-78-92, Sept 78, Air Force Aero Propulsion Laboratory, Wright-Patterson Air Force Base, OH.

7 Roberts, D. I., "3-D Interactive Graphics Assist Diesel Engine Design," *Mechanical Engineering*, Vol. 100, No. 3, March 1978, pp. 40–45.

8 Goldman, L. J. and McLallin, K. L., "Cold-Air Annular-Cascade Investigation of Core-Engine-Cooled Turbine Vanes," NASA TM X-3224, April 1975, NASA Lewis Research Center, Cleveland, OH.

Downloaded 01 Jun 2010 to 171.66.16.58. Redistribution subject to ASME license or copyright; see http://www.asme.org/terms/Terms_Use.cfm

P. J. Coty
Project Engineer,
AFAPL,
Wright-Patterson AFB, Ohio

A. D. Lane
Supervisor,
Static Structures,
Mechanical Component Design

J. B. Lee
Engineering Specialist,
Aerodynamics Turbine Group
Assoc. Mem. ASME

L. J. Meyer
Supervisor,
Turbine Design,
Mechanical Component Design

AiResearch Mfg. Company of Arizona,
Phoenix, Ariz.

A Design Review of Ceramic Components for Turbine Engines

This paper summarizes a program (AFML/APL Contract No. F33615-77-C-5171) to evaluate the application of ceramic materials in small, limited-life turbine engines. Advanced ceramics technology is employed in the program to achieve an affordable, reliable, high-performance capability for turbine engines in a missile application. The paper presents design and material considerations for ceramic rotor blades and stator vanes in addition to aerodynamic flow path analyses for ceramic components in high temperature environments. An iterative materials/design analysis was made with use of probabilistic design methods to predict the survivability of the ceramic components. Materials for both rotor blades and stator vanes were evaluated and selected based on mechanical and thermal stresses imposed by the optimum component design. A number of design concepts for the primary components are reviewed. These concepts include segmented-vane configurations and rotor airfoil shape and attachment schemes.

Introduction

Small gas turbine engines are at a critical point in their development since turbine inlet temperature (TIT) must be substantially increased to provide the performance improvements required in volume-limited applications. Since increased performance in small turbine engines is also characterized by higher turbine operating stresses, new components must have greater strength as well as higher temperature capability. The higher cycle temperatures necessitate the development of either improved materials, (and fabrication techniques), or improved cooling technology. The new, exotic metallic alloy combinations will provide only a temporary solution. Cooling, as a method of increasing the useful operating temperature range of these superalloys, means sacrificing gains in engine performance and, in the case of small engines, is extremely difficult to incorporate because of small component size.

Because of their excellent strength properties above 2100°F, ceramics offer a potential solution. Their high temperature properties obviate the requirement for cooling. Some structural ceramic materials, easily fabricated by net or near-net shape processing, have great potential as reliable components. Structural operational stability combined with low cost and plentiful raw material supplies make ceramics attractive materials for further development for nonmanrated, limited-life turbine engines.

The United States Air Force is sponsoring a program at AiResearch to demonstrate the feasibility of using ceramic materials for structural, rotating, and static components in the hot section of a small gas turbine engine. The objective of this program is to provide affordable, reliable, uncooled, ceramic turbine vanes and blades that will operate at average material temperatures of 2250°F (1232°C) or greater in a small, limited-life gas turbine engine, and to demonstrate this capability in a realistic turbine-engine environment. Specific objectives of the program are (1) to develop the combined brittle-materials design methodology, manufacturing techniques, and NDE/proof-test schemes required; (2) to design and build turbine components using ceramic materials; and (3) to test them both as components and in a demonstrator engine.

In order to accomplish these objectives, the seven month analytical phase of this program addressed each aspect of turbine engine design including material trade-offs and the manufacturing capabilities of each component. The aerodynamic design, mechanical design, and materials selection activities completed during this study phase are discussed in the following sections.

Ceramic Turbine Aerodynamic Design

In order to produce a component that is comparable or superior to a cooled metallic turbine, special considerations in aerodynamic design must be adopted to compensate for the unique mechanical properties and manufacturing limitations of ceramic materials. The mechanical property limitations of ceramics place restrictions on blade height, number, and twist. Low blade height results in lower centrifugal loads while reduced blade number contributes to reduced attachment stresses. Minimum airfoil twist results in reduced bending stresses in the blades. Of these, the blade height and number restrictions are most significant since they lead directly to low aspect-ratio designs and attendant high secondary flow losses. The reduction of these losses is a primary aerodynamic goal. Manufacturing limitations are introduced by the requirement for diamond grinding to produce the airfoil shape. These limitations are imposed primarily by the size of the grinding wheel. A large wheel has longer life, grinds faster and can use a larger, thus stiffer, supporting shaft for better tolerance control. This requires blades with low twist and the largest possible radius of curvature on the pressure surface. (As will be discussed in a later section, mechanical design alternatives were considered which would allow the use of materials that could be fabricated by net-shape manufacturing methods. However, these were shown to have inadequate strength for high performance balde applications.)

Vector Diagram and Flowpath. The ceramic turbine design point conditions are listed in Table 1. With these as a starting point, a vector diagram and flowpath were initiated. To expedite this effort, two levels of iteration between the aerodynamic and structural design

Contributed by the Gas Turbine Division of The American Society of Mechanical Engineers and presented at the Gas Turbine Conference and Exhibit and Solar Energy Conference, San Diego, Calif., March 12–15, 1979. Manuscript received at ASME Headquarters January 10, 1979. Paper No. 79-GT-183.

Copyright © 1980 by ASME
Downloaded 01 Jun 2010 to 171.66.16.58. Redistribution subject to ASME license or copyright; see http://www.asme.org/terms/Terms_Use.cfm

requirements were used. The initial level fixed the flowpath height and its radial location. This was accomplished by considering attachment stresses due to centrifugal loads of linearly tapered blades derived from a free vortex type vector diagram. With the flowpath fixed, the second level optimized the vector diagram such that airfoils derived would satisfy all the design criteria. A total of six alternative designs were evaluated before a satisfactory solution was achieved.

The final vector diagram and flowpath are shown in Table 2, and Fig. 1, respectively.

The distinguishing feature of the vector diagram is the parabolic stator exit flow angle distribution as shown in Fig. 2. Since the flow turning with this approach is reduced at both the hub and shroud, there is a favorable reduction in secondary end wall losses. The reduction in turning at the shroud also allows a tip section to be designed with a larger minimum radius of curvature on the pressure surface. This is important from a manufacturing point of view, as shown in Fig. 3, since it is this curvature which determines the maximum allowable grinding wheel diameter. The reduction in turning at the hub section permits a higher stagger angle resulting in a low twist blade and thus, minimum overhang.

Stator and Rotor Airfoil Design. Stator airfoils were designed to obtain satisfactory aerodynamic loading. Due to the parabolic stator exit flow angle distribution, a total of four design sections were analyzed. Both subsonic and transonic analyses were performed at each design section to determine velocity distribution around the airfoils. Fig. 4 shows the final profiles and tip section aerodynamic loading. The final design used fifteen vanes to preclude vane-wake-induced vibration of the blades. In addition, end wall contouring and 26 deg of compound airfoil lean were incorporated to simulate the stator design of the LART Program [1].

The rotor design also consisted of four design sections at which subsonic and transonic analyses were performed. Final blade shapes and hub section loading are shown in Fig. 5. The blade number was set at 26 to satisfy aerodynamic loading and structural requirements.

A summary of turbine design characteristics is given in Table 3.

Turbine Performance Estimate. The efficiency level used in the chosen vector diagram is consistent with the losses established by a standard iteration procedure which takes into account two-dimensional and three-dimensional losses. Additional efficiency decrements due to rotor-tip clearance losses were predicted based upon in-house correlations.

In spite of stringent manufacturing and stress requirements, a predicted efficiency meeting the original cycle value of 0.85 was achieved at a rotor tip running clearance of 0.020 inch. This is due

Table 1 Ceramic turbine design point conditions

Inlet temperature, °F (°C)	2300 (1260)
Inlet pressure, psia (N/cm^2)	120.58 (83.14)
Pressure ratio (total-to-total)	2.532
Stage work-Btu/lbm (J/kg)	134.83 (313,406)
Corrected flow - $\frac{W\sqrt{\theta}}{\delta}$ - lbm/sec (kg/sec)	1.718 (0.7792)
Stage efficiency (total-to-total)	0.85
Rotational speed, rpm	41,730

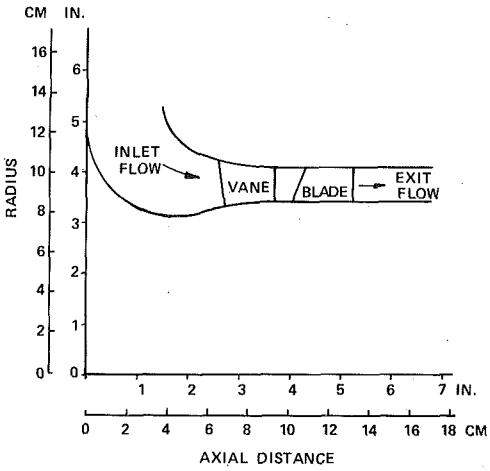


Fig. 1 Ceramic turbine flow path

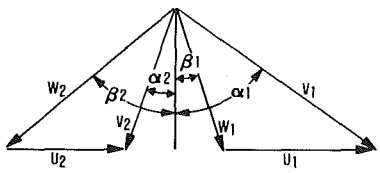


Table 2 Ceramic turbine vector diagram

	HUB		MEAN*		TIP	
	INLET	EXIT	INLET	EXIT	INLET	EXIT
RADIUS IN. (CM)	3.4 (8.64)	3.4 (8.64)	3.758 (9.55)	3.774 (9.59)	4.095 (10.40)	4.118 (10.46)
α (DEG)	60.72	-24.44	71.90	-24.64	69.62	-23.09
β (DEG)	50.07	-58.23	48.18	-61.17	33.78	-62.34
V/A'_{cr}	1.075	0.562	0.981	0.529	0.915	0.545
U/A'_{cr}	0.535	0.586	0.592	0.653	0.645	0.713
$W//A''_{cr}$	0.642	0.928	0.481	0.954	0.402	0.998
REACTION (%)	26.26		39.45		48.28	

*50% STREAMLINE

Nomenclature

A'_{cr} = critical velocity based on absolute total temperature
A''_{cr} = critical velocity based on relative total temperature
A_{HUB}/A_{TIP} = blade hub section area divided by the tip section area
CP = center of pressure
C_P = specific heat
CPF = cumulative probability of failure
CPS = cumulative probability of success
C_x = axial chord
E = Youngs modulus
FD = fully dense
G = shear modulus
g = gravitational constant
H = enthalpy
h = blade or vane height
HP = hot pressed
Hz = hertz
J = joules constant
K = thermal conductivity
KSI = one-thousand pounds force per square inch
LER = blade leading edge radius
N_B = blade number
R = radius
RB = reaction bonded
R_{HUB} = blade hub radius
R_{TIP} = blade tip radius
S = pitch or blade spacing
TER = blade trailing edge radius
U = wheel velocity
V = absolute velocity
W = physical flow or relative velocity
α = linear thermal expansion coefficient or flow angle in the absolute frame
β = flow angle in the relative frame
δ = ratio of pressure to standard pressure of 14.696 psi
θ = ratio of temperature to standard temperature of 518.688°R.
ν = Poissons ratio
ρ = density
σ = stress or strength
$\sigma_{avg\ hub}$ = blade hub average radial stress

Subscripts

m = mean
T = tip
x = axial

Downloaded 01 Jun 2010 to 171.66.16.58. Redistribution subject to ASME license or copyright; see http://www.asme.org/terms/Terms_Use.cfm

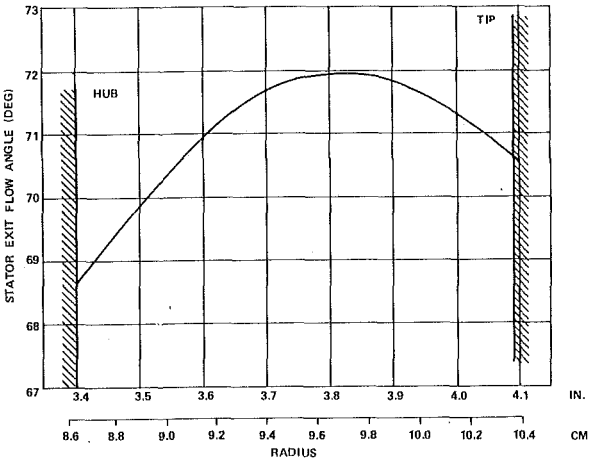


Fig. 2 Ceramic turbine radial distribution of stator exit flow angle

- MINIMUM RADIUS OF GRINDING WHEEL SET BY MAXIMUM OVERHANG AND SHAFT DIAMETER REQUIREMENTS (0.093 IN. MINIMUM)
- MAXIMUM RADIUS OF GRINDING WHEEL SET BY MINIMUM PRESSURE SURFACE RADIUS, R

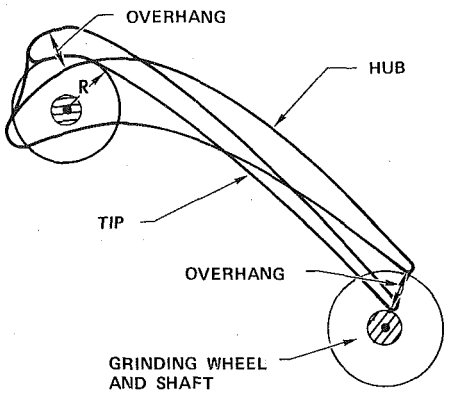


Fig. 3 Ceramic blade machining limitations

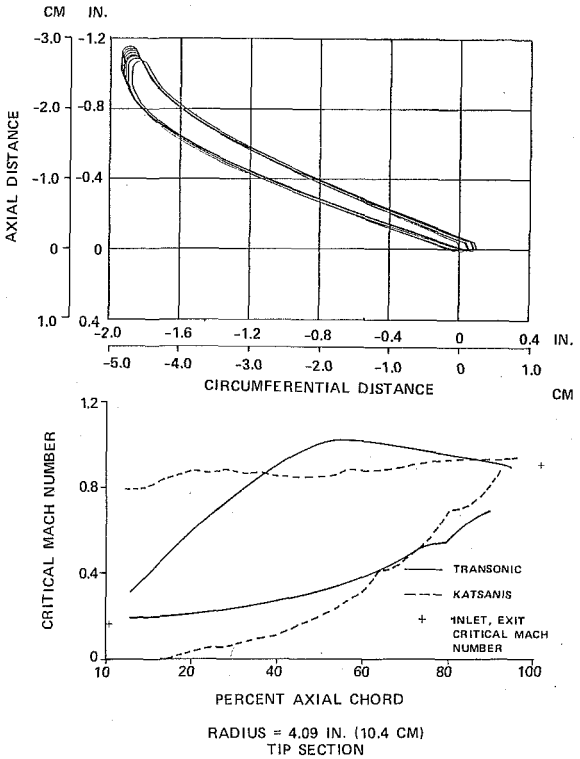


Fig. 4 Ceramic stator profiles and tip aerodynamics loading

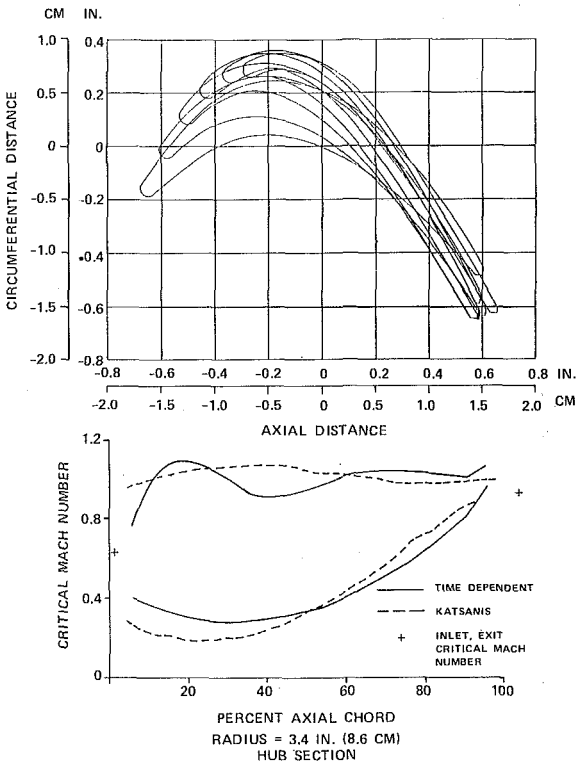


Fig. 5 Cermic rotor profiles and hub aerodynamic loading

	Stator	Rotor
Aspect ratio, $(h/C_x)_{mean}$	0.657	0.665
Solidity, $(C_x/S)_{mean}$	0.668	1.187
Zweifel loading coefficient	0.834 (tip)	1.109 (hub)
Mean exit critical Mach no.	0.981	0.954*
Work coefficient, $\lambda_m = \frac{gJ\Delta H}{U_m^2}$	1.810	
Flow coefficient, $\phi_m = \frac{V_x}{U_m}$	0.741	
Tip speed, U_T, ft/sec (m/sec)		1493 (455)

*Relative critical Mach number

Table 3 Relevant turbine design characteristics

primarily to the implementation of an advanced, low aspect-ratio design philosophy.

Rotor Mechanical Design and Materials Selection

Rotor Design Objectives and Mechanical Design. The scope of design possibilities for the limited-life ceramic turbine comprised a wide range of materials, processes, and configurations, including options not currently available but having short-term future potential. Innovative design concepts based on low-cost materials with reduced strength, multi-material concepts, and formed near net-shape configurations were considered. Emphasis was placed on designs that would accept material or process substitutions that might offer future cost reductions.

A constraint placed upon the design selection was the requirement for scalability of the rotor tip diameter in the range of six to nine inches. This constraint limits minimum and maximum material thicknesses and influences blade count for an inserted blade design. The mechanical design conditions for the rotor include an average TIT of 2300°F, a 100 percent rotor design speed of 41,730 rpm, and a mission life of 50 hr.

At the outset, the material and design concept candidates for the rotor included all reasonable design approaches used in previous

Downloaded 01 Jun 2010 to 171.66.16.58. Redistribution subject to ASME license or copyright; see http://www.asme.org/terms/Terms_Use.cfm

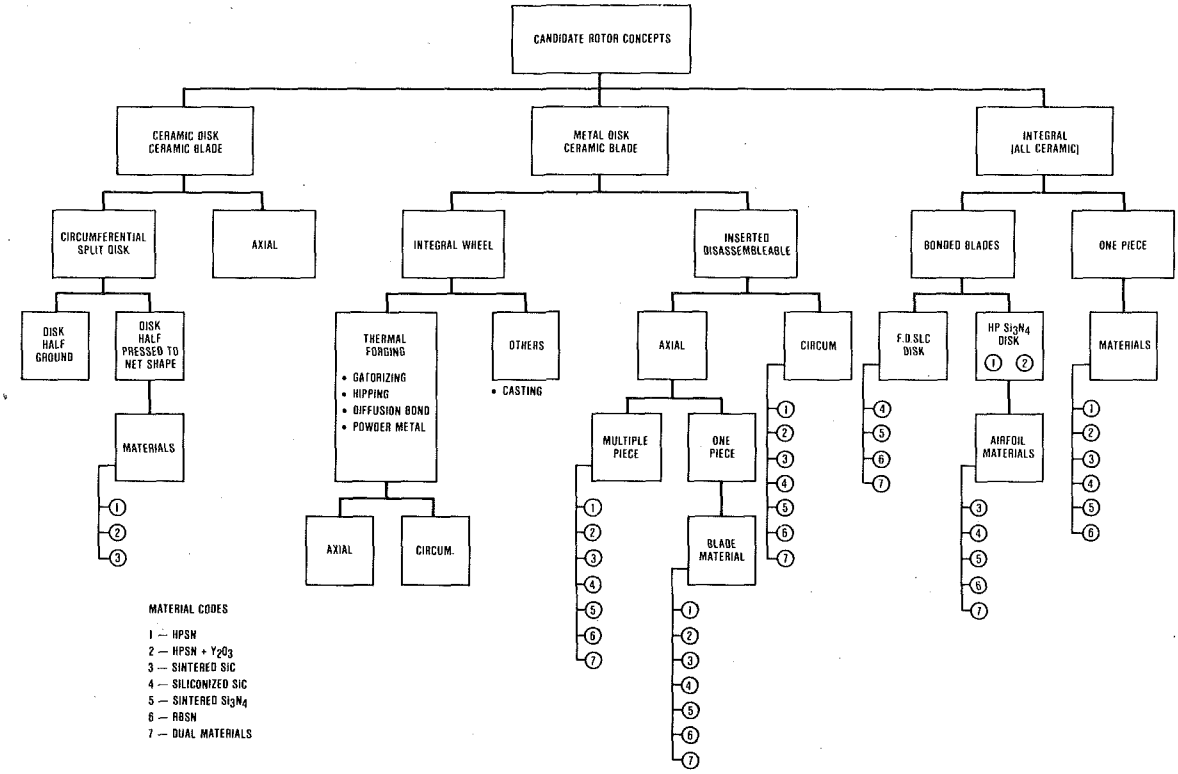


Fig. 6 Rotor Design activity network

Table 4 Integral ceramic rotor study

Disk Material	Current Values For 4 Pt. Flexure Strength/Modulus	CPS(A)	CPS(B)	Required 4 Pt. Flexure(B) Strength For CPS >0.98	Comments
HP Si_3N_4	95.4 ksi/12.6	0.9824	0.835	>110 ksi	
HP Si_3N_4+Y_2O_3	100 ksi/12.6	0.9853	0.840	>110 ksi	
FD SiC	50 ksi/8.0	0	0	>150 ksi	
Si SiC	50 ksi/5.0	0	0	>120 ksi	Machined Properties
Sintered Si_3N_4	65 ksi/8.0	0	0	>110 ksi	Machined Properties
RBSN	34 ksi/10.0	0	0	> 90 ksi	

(A) 70°F Uniform Temperature

(B) Mild Bore-To-Rim Temperature Gradient

Rotor Speed = 41,730 rpm

turbine designs. The candidate ceramic materials were:

- Hot-pressed silicon nitride (with and without oxide additives)
- Sintered (fully dense) silicon carbide
- Siliconized silicon carbide
- Sintered silicon nitride
- Reaction-bonded silicon nitride

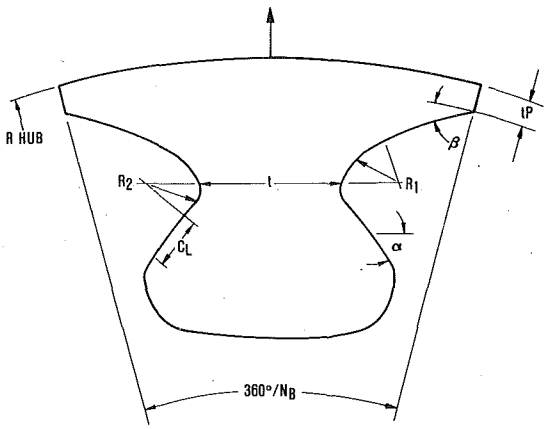
The rotor design candidates are listed in Fig. 6. The design objective was to reduce the list of acceptable approaches to the optimum candidate with respect to cost, reliability, and manufacturing technology.

Rotor Design Concept Studies. To evaluate the configurations listed in Fig. 6, a study of the integral ceramic rotor was conducted. The disk portion of the rotor was examined to assess its ability to withstand rotational loads and thermal stresses. The disk geometry was optimized (consistent with the flow path size studies) for maximum cumulative probability of success (CPS) and was analyzed to determine its CPS level for the various ceramic material candidates. Results summarized in Table 4, indicate that only hot-pressed silicon nitride has acceptable room-temperature CPS levels at design speed. However, the CPS is unacceptable when a mild bore-to-rim thermal gradient, which is typical for a gas turbine with these temperature levels, is imposed. Consequently, for this turbine application and flow path, an integral ceramic rotor is not considered feasible. Based on these analytical results, the ceramic disk/ceramic blade is also not considered viable.

The remaining design approaches were confined to ceramic blades inserted in a metallic disk. Attachment studies were initiated to optimize the turbine flow path selection. The attachment parameters studied, illustrated in Fig. 7, apply to an axially inserted ceramic blade. A technique, based on experience gained from previous axially inserted designs, was developed to describe the flow path envelopes shown in Fig. 8. At a selected blade hub radius and airfoil load, a range of blade numbers is feasible. The extremes are limited by platform mass increase on the lower end and disk post area decrease on the upper end. Increased loads imply larger attachments and fewer blades. These results were used in an iterative process to select flow path dimensions and later, the detailed airfoil geometry.

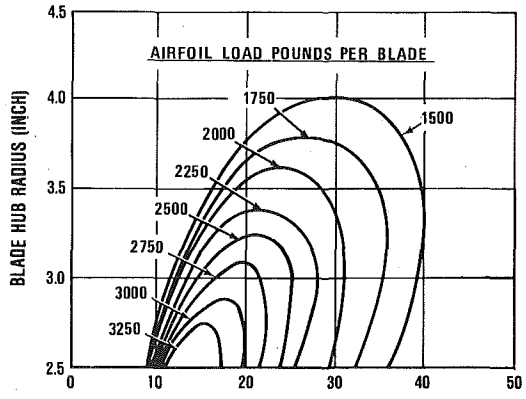
Use of a circumferentially oriented, inserted, ceramic blade was considered to determine the attachment stress impact of airfoil-to-platform and platform-to-attachment orientation. Three-dimensional finite-element analyses indicated that a circumferential attachment would have greater average attachment stresses over an equivalent axially inserted design because of increases in platform mass and larger stress concentrations due to airfoil orientation and overhang. The design of a disk member to support the circumferential attachment is extremely difficult due to the high separating loads on the disk posts and the severe bending stresses generated. Efforts to counterbalance the load result in a very thick rim region, an awkward disk geometry, and high stress levels throughout the disk. The result is an unacceptable combination of blade attachment stress and disk

Downloaded 01 Jun 2010 to 171.66.16.58. Redistribution subject to ASME license or copyright; see http://www.asme.org/terms/Terms_Use.cfm



- FOR ANY BLADE LOAD t IS SIZED FOR ALLOWABLE STRESS
- C_L IS SIZED FOR 55,000 PSI CONTACT STRESS
- THE MATERIAL USED BY THE ATTACHMENT DETERMINES THE AVAILABLE DISK POST NECK THICKNESS

Fig. 7 Parameters that determine allowable attachment design



$\sigma_{CERAMIC\ MAX}$ = 43,800 PSI — R_1 = 0.09 INCH
σ_{DISK} = 60,000 PSI AVERAGE — β = 15°
BROACH = 23°
CHORD = 1.2 INCH
SPEED = 41,730 RPM

Fig. 8 Flow path selection envelope rotor design

stresses. Consequently, the circumferentially inserted blade approach was eliminated.

An integrally inserted design, such as a thermal forging approach, was considered next. This concept has the advantage of forming surface-to-surface contact between ceramic and metal to minimize point loading. Its feasibility has not been demonstrated for axially oriented attachments. In the circumferential configuration, this technique possesses all of the stress problems discussed previously. In addition, maintenance of an interference fit during engine operation is questionable since the high disk-post temperatures and the separating loads associated with a circumferential design will certainly result in creep deformation of the disk posts. Based on these potential difficulties, the thermal forging approach was eliminated for lack of near-term feasibility.

With the candidate list narrowed to an inserted, axial design that can be disassembled, it became increasingly important to evaluate low cost, lower strength ceramic materials. Approaches such as material removal from low stress regions to reduce blade mass and the use of less conventional attachment shapes including multi-tang, reverse dovetail and curved attachments to match airfoil camber, were considered. Platformless blade concepts, such as those shown in Fig.

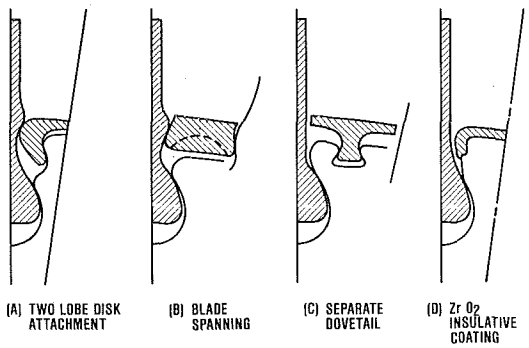


Fig. 9 Platformless blade concepts

ATTACHMENT INCLUDES PLATFORM AND AIRFOIL FOR STRAIGHT AXIAL DESIGN

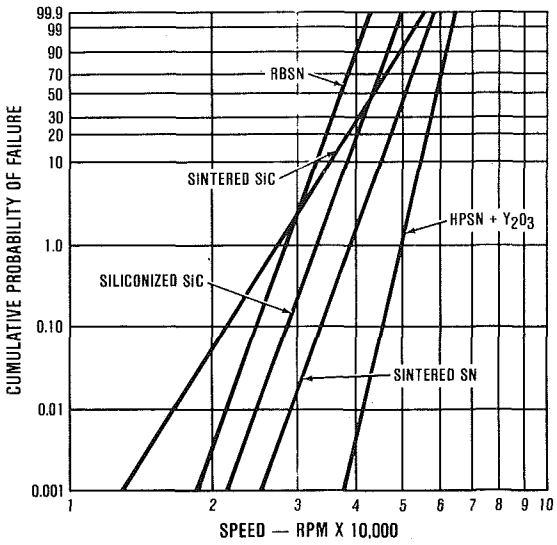


Fig. 10 Material risk comparisons for a common blade rotor design

9, are undesirable because of cost and increased areas of ceramic-to-ceramic or ceramic-to-metal interface. Dual material blade concepts can employ lower density material in lower stress regions, but manufacturing complexity and cost are high. Therefore, the single material, one-piece-blade design remained the preferred approach from cost and reliability standpoints.

The selection of the lowest risk ceramic material for the axial, inserted, one-piece-blade design necessitates the use of probabilistic analytical methods to account for material strength scatter and component size effects. For the intended application, failure under the fast fracture mode is the governing criterion. Time dependence of material characteristics is not considered. Fig. 10 presents a Weibull model cumulative probability of failure (CPF) prediction of the selected blade configuration with five material candidates. This prediction is based on current assessments of four-point flexure and tensile strength material data. Fig. 11 factors in cost to identify the overall best material candidate as a function of engine operating speed.

The conclusion from this study is that the optimum design, based on reliability and cost, is to use a metallic disk with axially inserted hot-pressed silicon nitride ceramic blades that can be disassembled from the disk.

Rotor Blade Design and Analysis. A significant task in the overall design was the iterative process by which an airfoil shape is selected to meet the often conflicting requirements of aerodynamic performance and mechanical integrity. While this process is somewhat common to all gas turbine blade designs, it is further complicated for ceramic airfoils by machinability considerations, which can be quite restrictive for high performance blading. Final airfoil shape parameters are:

Downloaded 01 Jun 2010 to 171.66.16.58. Redistribution subject to ASME license or copyright; see http://www.asme.org/terms/Terms_Use.cfm

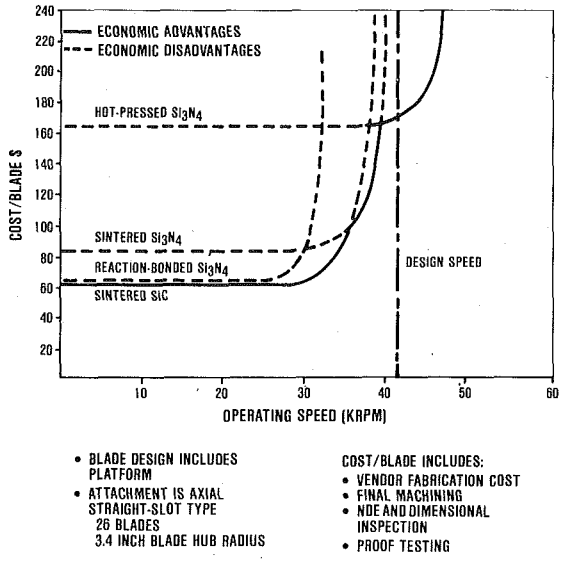
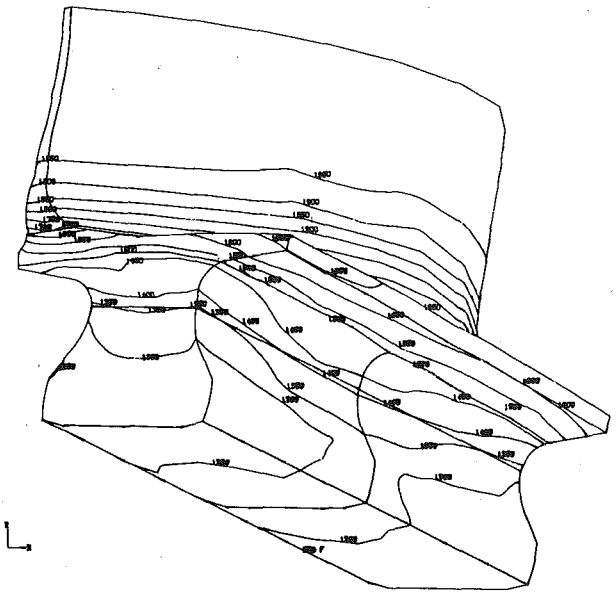


Fig. 11 Material selection cost preference ranges in operating speed



VIEWED FROM TRAILING EDGE, SUCTION SIDE, TEMPERATURES IN DEGREES F

Fig. 12 Blade temperatures at full power, steady-state conditions

R_{Tip}	= 4.10 in.
R_{Hub}	= 3.40 in.
Cx_{Tip}	= 0.86 in.
Cx_{Mid}	= 1.05 in.
Cx_{Hub}	= 1.18 in.
LER	= 0.06 in.
TER	= 0.04 to 0.034 in.
A_{Hub}/A_{Tip}	= 2.0
Load per Airfoil	= 1750 lbs
Average Hub	= 10.8 ksi

In the airfoil and flow path selection processes, vibrational considerations play a significant role because of the necessity to avoid blade resonances in the engine operating range. The low aspect-ratio of this design, coupled with the inherently high elastic modulus-to-density ratio of ceramics, are desirable features with respect to blade resonance problems. The blade first natural frequency is predicted to be 12,300 Hz. A satisfactory margin results with respect to the 15 vane stator passing frequency of 10,430 Hz at operating speed.

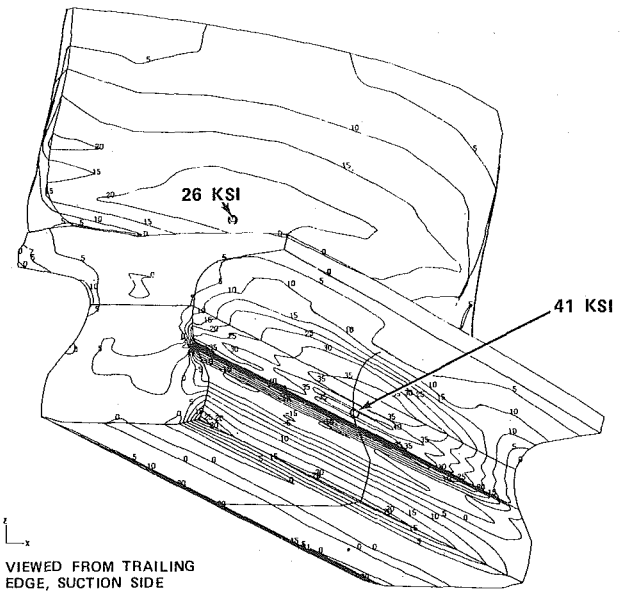


Fig. 13 Blade maximum principal stresses at full power, steady-state conditions

The detailed attachment design was initiated with profile parameter studies using two-dimensional analysis methods. Based on the two-dimensional results, a dovetail angle of 30 deg from a radial line was determined to be optimum. From this work, a basic dovetail shape was achieved and a three-dimensional finite-element stress analysis of the entire blade, attachment, and airfoil was begun. The initial stress analysis work was accomplished for the 100 percent design speed room-temperature condition since rotational effects dominate the rotor blade stress distribution. The airfoil maximum principal stress was found to be 26 ksi and occurs on the suction surface. The attachment maximum principal stress is 56 ksi and occurs at the contact zone. This peak stress is very localized and is moderated by the compliant layer and disk-post flexibility.

Finite-difference thermal analysis of the rotor disk and blade was conducted at the steady-state full power condition. The resulting blade temperature distribution is given in Fig. 12. These temperatures were then used for combined thermal and centrifugal three-dimensional stress analysis. The results are presented in Fig. 13. The trailing edge attachment stress is relieved due to thermal bending of the attachment and the stress peak shifts towards the mid-chord with a peak value of 41 ksi. Airfoil stresses are shown to be approaching 20 ksi in the trailing edge region.

The computed stresses were used to make a probabilistic assessment of risk for the blade design. This assessment is illustrated in the Weibull diagram in Fig. 14 which shows less than 0.01 percent CPF per blade at design speed, and 1.0 percent CPF at a proof speed of 130 percent. A summary of the rotor blade design is presented in Table 5 which shows that a satisfactory configuration has been achieved.

The turbine static structure contains three reaction-bonded silicon nitride ceramic components: a stator vane, stator inner support ring, and turbine tip shroud. These components, along with the metallic support structure, are illustrated in the turbine cross section illustrated in Fig. 15. The 15 individual stator vane segments are simply supported at their inner and outer platforms by the adjacent metallic structure. During engine/rig operation, the vanes are loaded against the metallic support structure by the aerodynamic forces acting on the vanes. To support the vanes against the metallic structure when the engine is not running, a wave washer spring is installed at the outer platform to provide a positioning load against the stators. Since the stator is simply supported at both the inner and outer platforms, the design must be capable of allowing relative axial and radial motion between the inner and outer metallic structure due to thermal growth. Fig. 15 shows the magnitude of relative motion that the design must accommodate.

Downloaded 01 Jun 2010 to 171.66.16.58. Redistribution subject to ASME license or copyright; see http://www.asme.org/terms/Terms_Use.cfm

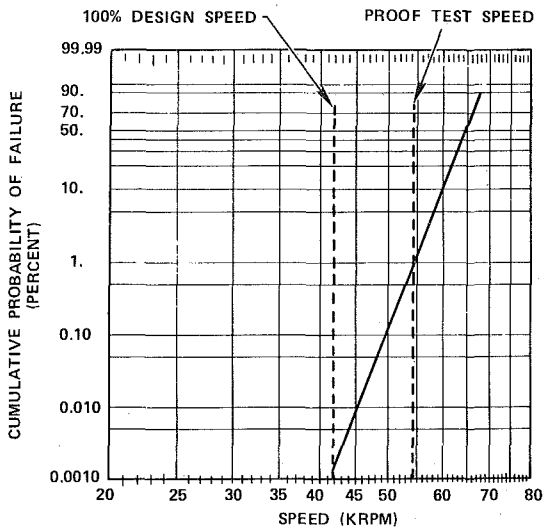
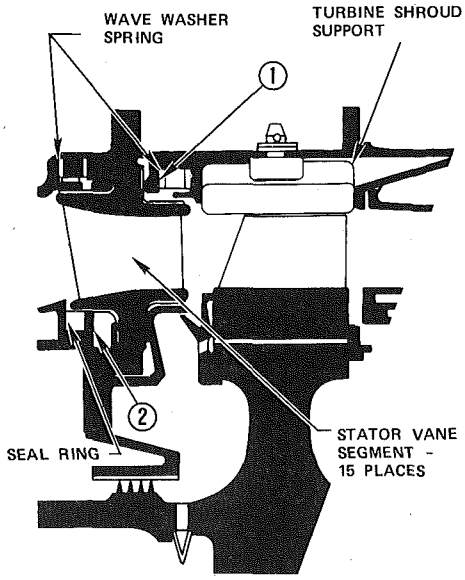


Fig. 14 Ceramic rotor blade cumulative probability of failure, rotation only

Table 5 AFML/APL ceramic rotor blade cumulative probability of failure, rotation only

Material	NC-132
Cumulative probability of survival, CPS	99.99
Design goal, CPS	99.8
Peak temperature	2000°F
Creep extension	$<10^{-4}$ In.
Airfoil average tensile stress	10.8 ksi
Attachment average tensile stress	12 ksi
Maximum local stress	56 ksi rotation at 41730 rpm 41 ksi full power
Flexure strength at 1400°F	
Characteristic	94.3 ksi
Weibull modulus	11.3
Tensile strength at 1400°F	
Characteristic	76.4 ksi
Weibull modulus	10.5
Frequency margin	18% nominal 10% *minimum*



MAXIMUM DEFLECTIONS, INCHES		
LOCATION	AXIAL	RADIAL
1	±0.015	±0.055
2	±0.020	±0.027

Fig. 15 Turbine stator vane and support structure

Table 6 Design criteria and goals, static components

• Probability of survival, fast fracture	
Ceramic turbine vanes	99.8%
Other ceramic structure	98.0%
• Contact stresses	Maximum 75 lb load at each stator vane support lug to prevent chipping
• Limited life design	Slow crack growth not considered
• Low cost	Consistent with functional success
• Performance	Acceptable leakage characteristics
• Design conditions stator inlet temperature	2300°F average 2550°F hot spot

The turbine shroud is a continuous, reaction-bonded silicon nitride ring which mounts to the metallic structure by means of three radial metal pins and matching radial ceramic lugs. These radial pin joints serve to pilot the turbine shroud radially, while at the same time allowing the relative motion between the ceramic and metal components which must occur as a result of differential thermal expansion.

Ceramic static structure design considerations and procedures. The objective of the design process was to provide a sound structure suitable for the intended mission. The design goals required predicted probabilities of survival for the ceramic components in the range of 98.0 to 99.8 percent (depending on the component), as summarized in Table 6 along with other design criteria and goals.

Analyses were conducted to verify that clearance changes in the hot end, which result from engine operation through the entire speed and power range, would not produce rubbing conditions except in those areas specifically designed to accommodate contact. All large-scale calculations were based on typical thicknesses. Finite-element analyses were conducted for both steady-state and transient loading conditions. Three-dimensional finite element techniques were employed, except for metallic components for which two-dimensional analysis methods were considered suitable. Thermal analyses were performed to provide temperature distributions for each component. Three-dimensional thermal analyses were accomplished to support three-dimensional finite-element stress analyses.

Steady-state and transient temperatures were calculated for all ceramic and metallic structural components. Conditions analyzed included steady-state operation under maximum power conditions and transient cycles from start to maximum power for all components and from maximum power to shutdown for the metallic structure.

The results of the finite-element analyses were used to calculate the probability of survival for each component. The CPS goals for various components, listed in Table 6, were selected by considering risk to the engine system in the event of failure of the part concerned. In reality, the probability of survival is only obtainable as a result of engine use. Satisfaction of the CPS goals must be interpreted as indications of when analysis may stop and component fabrication begin, not as absolute values. Actual CPS values will be affected by factors such as the potential for improvement afforded by proof and development tests.

Materials Selection. Four materials were evaluated as candidates for stator fabrication: reaction-bonded silicon nitride, sintered silicon nitride, siliconized silicon carbide, and sintered silicon carbide. A representative three-dimensional finite-element model was used to perform a comparative analysis of the four candidate materials. Steady-state and start-up transient operating temperatures were calculated for each of the materials for a 10 second start cycle with 2300°F average and 2551°F hot streak steady-state stator-inlet gas temperature. These temperatures were then used to calculate corresponding thermal stresses and probabilities of survival.

Material properties used in the analyses are listed in Table 7. The resulting stress distribution for the start-up transient, which yielded higher stresses than the steady-state condition, is shown in Fig. 16.

Downloaded 01 Jun 2010 to 171.66.16.58. Redistribution subject to ASME license or copyright; see http://www.asme.org/terms/Terms_Use.cfm

Table 7 Design properties used for static structure

DESIGN PROPERTIES USED FOR SILICONIZED SiC								FOUR POINT FLEXURE	
T °F (°C)	E psi (MN/cm^2)	α $10^{-6}/°F$ ($10^{-6}/°C$)	ν in./in.	G psi (MN/cm^2)	K Btu/hr. ft °F (W/m°C)	Cp Btu/lb. °F (J/kg/°C)	ρ Lbm/in^3 (g/cm^3)	σ ksi (MPa)	Projected for 1983 σ ksi (MPa)
78 (25.6)	55×10^6 (37.9)	-	0.24	-	-	-	0.112 (3.1)	58 (399.9)	75 (517.1)
500 (260)	-	1.7 (3.06)	-	-	47 (25.1)	0.24 (1005)	-		
1000 (538)	-	2.1 (3.78)	-	-	36 (19.2)	-	-	60 (413.7)	75 (517.1)
1500 (816)	-	2.3 (4.14)	-	-	27 (14.4)	-	-	63 (434.4)	75 (517.1)
1800 (982)	50×10^6 (34.5)	2.37 (4.27)	-	-	23 (12.3)	-	-		
2000 (1093)	-	2.42 (4.36)	-	-	20 (10.7)	-	-	67 (461.9)	75 (517.1)
2200 (1204)	44×10^6 (30.3)	2.45 (4.41)	-	-	18 (9.6)	-	-		
2400 (1316)								55 (379.2)	75 (517.1)
2550 (1371)								23 (158.6)	30 (206.8)
DESIGN PROPERTIES USED FOR SINTERED SiC (CARBORUNDUM SiC)									
78 (25.6)	58.9×10^6 (40.6)	-	0.15	25.6×10^6 (17.7)	50 (26.7)	0.16 (670)	0.112 (3.1)	45-66 (310.3-455)	90 (620.5)
500 (260)	57.9×10^6 (39.9)	1.8 (3.24)	-	25.4×10^6 (17.5)	39 (20.8)	0.23 (963)	-	48 (330.9)	-
1000 (538)	56.5×10^6 (39)	2.3 (4.14)	-	25.0×10^6 (17.2)	31 (16.5)	0.264 (1105)	-	-	-
1500 (816)	55.3×10^6 (38.1)	2.6 (4.68)	-	24.7×10^6 (17)	25 (13.3)	-	-	-	-
1800 (982)	54.5×10^6 (37.6)	2.71 (4.88)	0.11	24.5×10^6 (16.9)	-	-	-	55-64 (379.2-441.3)	95 (655)
2000 (1093)	54.0×10^6 (37.2)	2.78 (5.00)	- -	24.4×10^6 (16.8)	-	-	-	-	-
2200 (1204)	53.5×10^6 (36.9)	2.83 (5.09)	-	-	-	-	-	58-65 (399.9-448.2)	-
2400 (1316)	53×10^6 (36.5)	2.88 (5.18)	-	-	-	-	-	-	-
2500 (1371)								60-63 (413.7-434.4)	100 (689.5)
DESIGN PROPERTIES USED FOR REACTION-BONDED Si_3N_4									
78 (25.6)	25.0×10^6 (17.2)		0.17	10.7×10^6 (7.4)	8.6 (4.6)	0.170 (712)	0.094 (2.6)	35-40 (241-276)	45-50 (310-345)
500 (260)	24.9×10^6 (17.2)	0.9 (1.62)	0.17	10.6×10^6 (7.3)	7.7 (4.1)	0.209 (875)	0.094 (2.6)	-	-
1000 (538)	24.8×10^6 (17.1)	1.3 (2.34)	0.18	10.5×10^6 (7.2)	6.8 (3.6)	0.247 (1034)	0.094 (2.6)	45 (310.3)	55 (379.2)
1500 (816)	24.6×10^6 (17)	1.45 (2.61)	0.18	10.4×10^6 (7.2)	6.1 (3.3)	0.277 (1160)	0.094 (2.6)	-	-
1800 (982)	24.3×10^6 (16.8)	1.55 (2.79)	0.17	10.4×10^6 (7.2)	5.8 (3.1)	0.293 (1227)	0.094 (2.6)	49 (337.8)	58 (399.9)
2000 (1093)	24.1×10^6 (16.6)	1.59 (2.86)	0.17	10.3×10^6 (7.1)	5.6 (3.0)	0.304 (1273)	0.094 (2.6)	-	-
2200 (1204)	23.7×10^6 (16.3)	1.63 (2.93)	0.15	10.3×10^6 (7.1)	5.4 (2.9)	0.313 (1311)	0.094 (2.6)	53 (365.4)	60 (413.7)
2400 (1316)	22.8×10^6 (15.7)				5.1 (2.7)	0.320 (1340)			-
2500 (1371)								56 (386.1)	62 (427.5)
FLEXURE STRENGTH (σ) VERSUS TEMPERATURE FOR SINTERED Si_3N_4									
38 (3.33)								80* 65** (552)(448)	100 (689)
2000 (1093)								70* (483)	90 (621)
2250 (1232)								35** (241)	80 (552)
2400 (1316)								60* (414)	70 (483)

*GTE supplied data (1978 material)
**AiResearch supplied data on GTE specimens (1976 material)

Downloaded 01 Jun 2010 to 171.66.16.58. Redistribution subject to ASME license or copyright; see http://www.asme.org/terms/Terms_Use.cfm

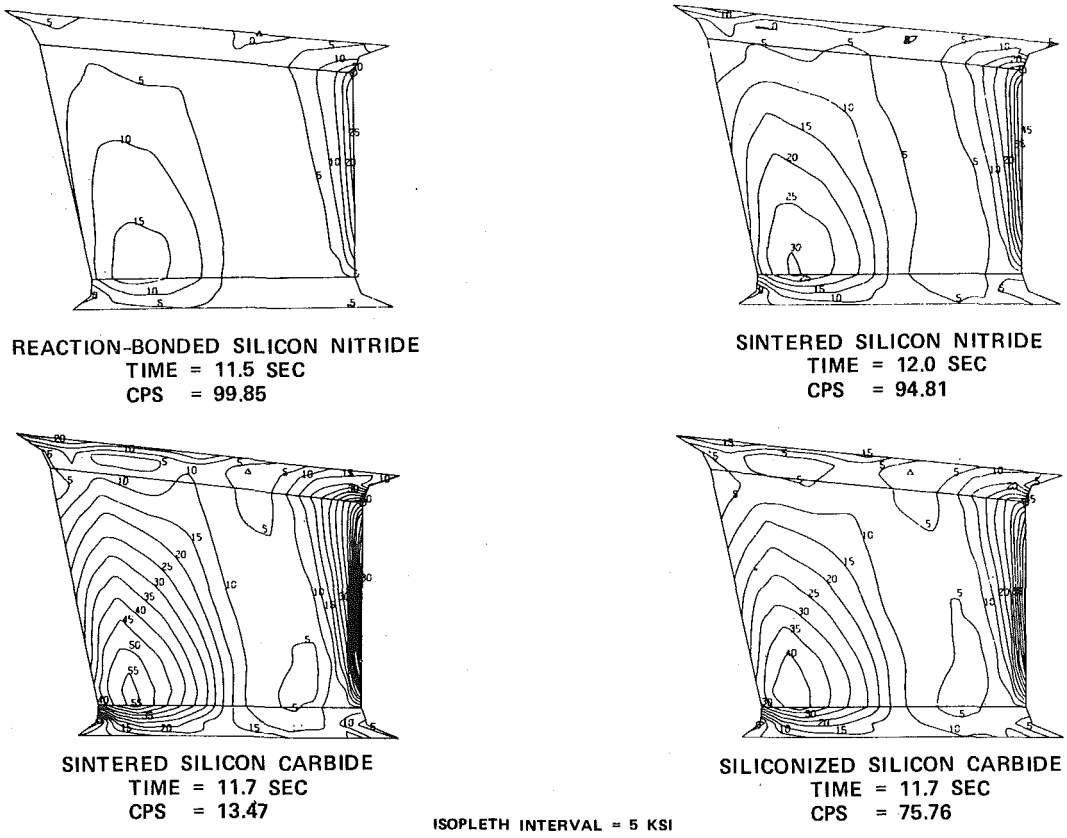


Fig. 16 Stator principle stresses—start-up transient

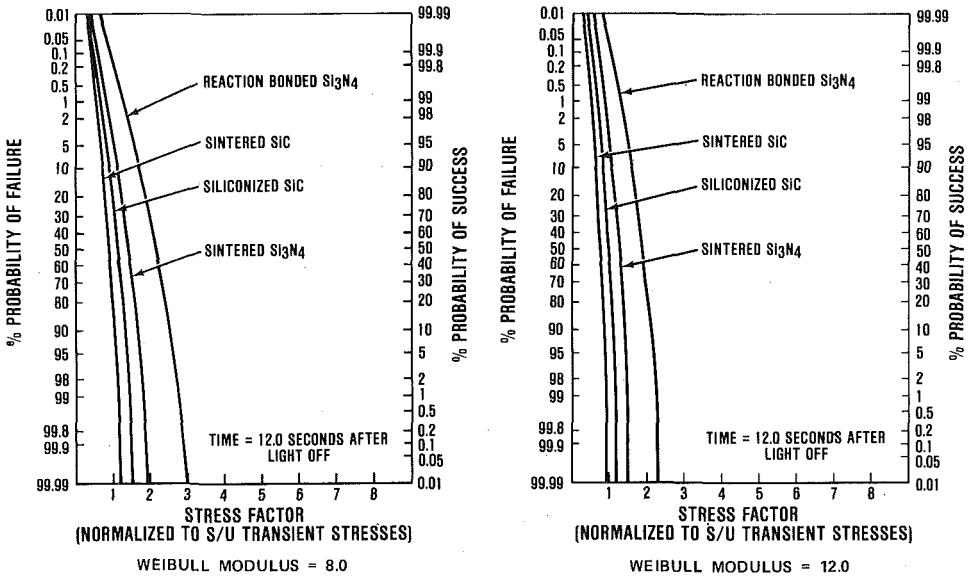


Fig. 17 Candidate ceramic material study results start-up transient results

The probabilities of survival calculated for each candidate material are plotted in Fig. 17 as a function of stress factor, where a stress factor of one corresponds to the calculated stresses and a factor of two would be twice the calculated stress.

As a result of these studies, reaction-bonded silicon nitride was identified as the only material that could meet the design goal of 99.8 percent CPS per vane for a 10 second start cycle.

Stress Analysis. Once the stator airfoil had been designed to achieve the desired aerodynamic characteristics, a configuration study was made to determine what type of design would yield a structurally satisfactory stator at the lowest possible cost. The range of configurations considered is shown in Fig. 18. A single vane segment was selected over the other approaches because it offered the best compromise between cost, stress, and vibration.

A stress analysis of the selected concept was perfomred to ensure that the vane would be capable of withstanding the imposed aerodynamic loads and thermally induced stresses. The loads and reactions resulting from the aerodynamic forces are shown in Fig. 19.

Downloaded 01 Jun 2010 to 171.66.16.58. Redistribution subject to ASME license or copyright; see http://www.asme.org/terms/Terms_Use.cfm

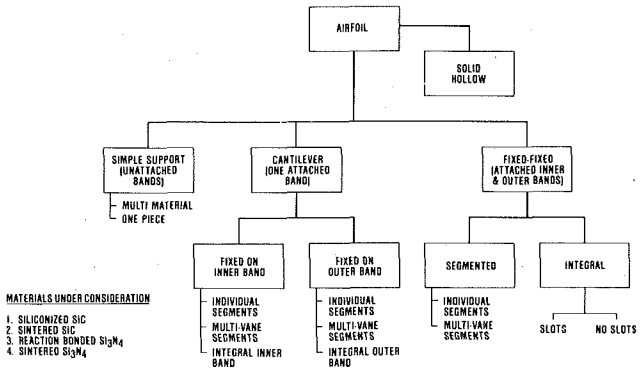


Fig. 18 Airfoil-band attachment matrix

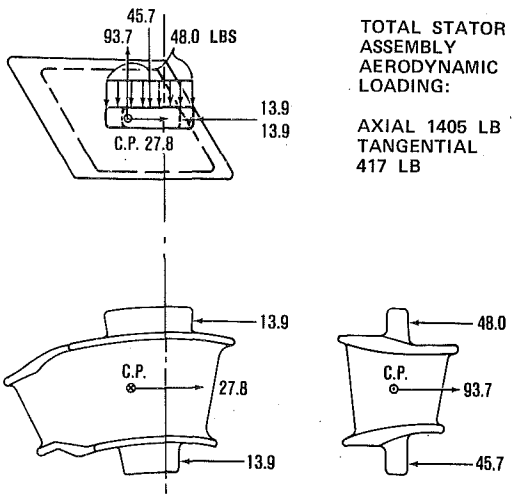
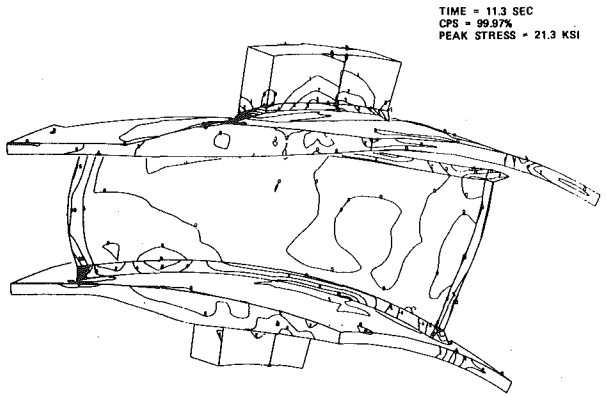
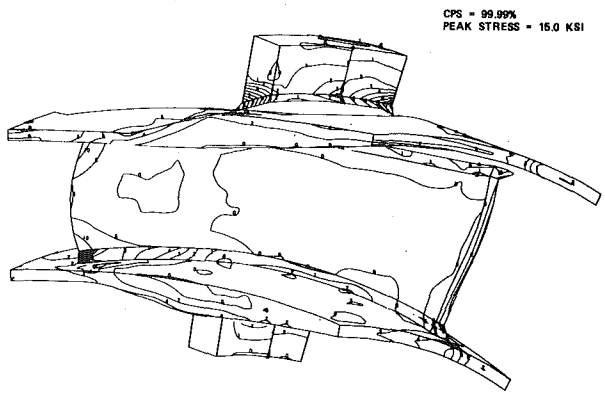


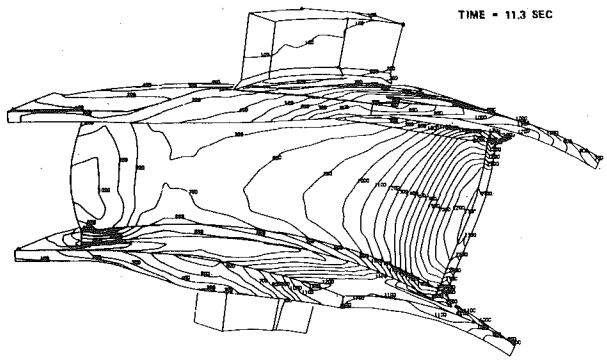
Fig. 19 Turbine stator vane free body diagram



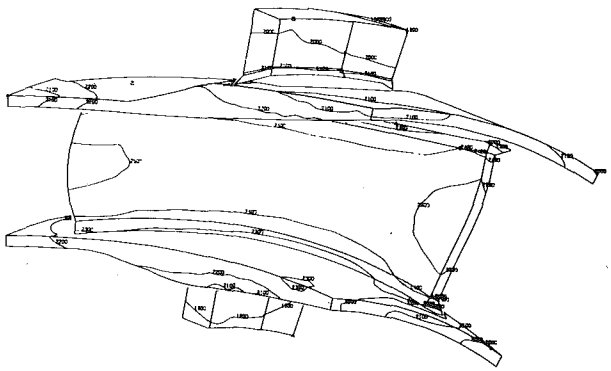
STATOR VANE PRINCIPAL STRESSES FOR START-UP TRANSIENT



STATOR VANE PRINCIPAL STRESSES - STEADY STATE



STATOR VANE START-UP TRANSIENT TEMPERATURES



STATOR VANE STEADY-STATE TEMPERATURES

Fig. 20 Stator stresses and temperatures

Steady-state and start-up transient temperature distributions for the duty cycle were calculated using three-dimensional finite-difference heat transfer models of the selected vane. The predicted temperature and stress distributions are shown in Fig. 20. The startup transient condition yielded the highest stresses. The corresponding probability of success is plotted in Fig. 21 as a function of stress factor, and shows that the stator design meets the design goal of 99.8 percent CPS per vane. Similar analyses were performed for the ceramic inner support ring and the turbine shroud. The finite element models and predicted CPS for these components are shown in Fig. 22 and 23.

Since the stator segments are supported at both the inner and outer platforms by metallic structure, it is essential that the relative motions due to thermal growth are known so that the mount points can be designed to accommodate this motion. A thermal deflection analysis of the entire metallic structure was performed for a startup transient and for steady-state operating conditions. The predicted deflections are shown in Fig. 24.

In summary, all three reaction-bonded silicon nitride ceramic components have been shown to meet or exceed all design goals in this application for the worst operating conditions.

Downloaded 01 Jun 2010 to 171.66.16.58. Redistribution subject to ASME license or copyright; see http://www.asme.org/terms/Terms_Use.cfm

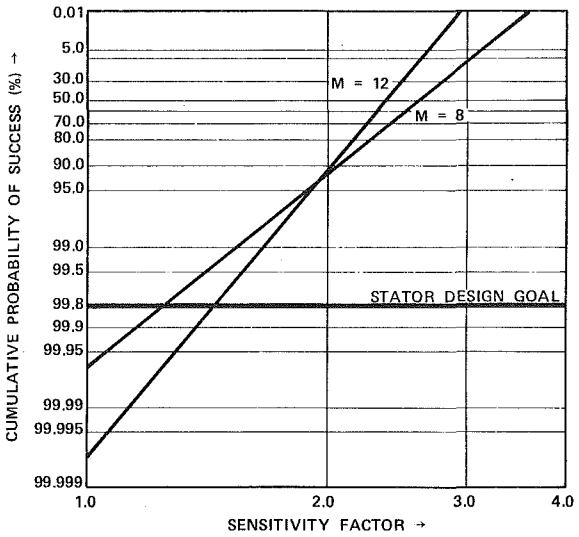
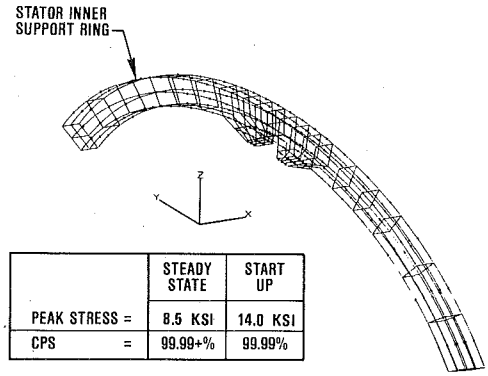


Fig. 21 Stator probability of success start-up transient (11.3 s)



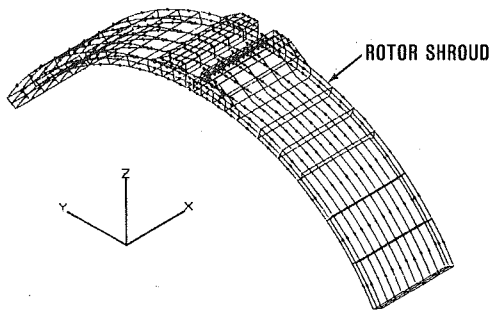
	STEADY STATE	START UP
PEAK STRESS =	8.5 KSI	14.0 KSI
CPS =	99.99+%	99.99%

Fig. 22 Stator inner support ring stress analysis

Conclusions

This paper has presented some of the design considerations for ceramic materials for hot-section components of a gas turbine engine. The immediate concerns when designing a ceramic airfoil for a small, limited-life engine are: the number of blades that the diameter-limited rotor can accept, the aspect ratio, and structural integrity. Manufacturing techniques for ceramic materials also constrain the design of blades and vanes. If the components are to be machined, the size of the grinding wheel limits the amount of twist and the radius of curvature of the airfoils.

A linear stator-exit flow-angle distribution was found to produce excessive suction-side leading-edge overhang, pressure-side trailing-edge overhang, and a small pressure-side radius of curvature of the blade. These difficulties lead to the introduction of a parabolic stator-exit flow- angle distribution which, when optimized, met all of the stress, aerodynamic, and manufacturing constraints within acceptable limits. A comprehensive study was performed on an array of rotor configurations and materials. The selected design consisted of a hot-pressed silicon nitride ceramic blade and a metallic disk. Blade attachment to the disk is axial dovetail. Each blade can be disassembled from the disk. The ceramic static components, vanes, inner support ring and the turbine tip shroud, were similarly analyzed. A slip cast reaction-bonded silicon nitride vane will be used.



	STEADY STATE	START UP
PEAK STRESS =	6.0 KSI	18.9 KSI
CPS =	99.99+%	99.99%

Fig. 23 Turbine shroud stress analysis

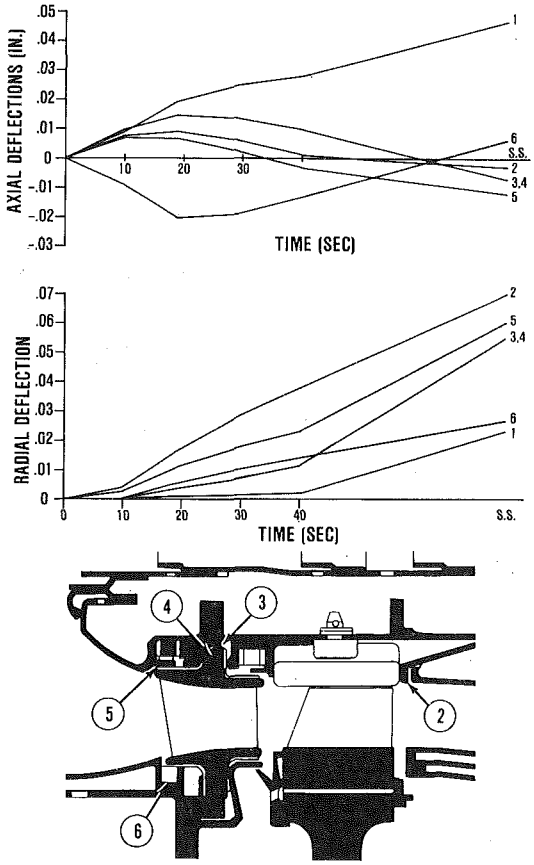


Fig. 24 Static structure deflections

Reference

1 Waterman, W. F., et al., "The Low Aspect Ratio Turbine Technology Program," sponsored by AFAPL, Final report for Phase II: AiResearch Report No. 75-21170 (2), March, 1977.

Downloaded 01 Jun 2010 to 171.66.16.58. Redistribution subject to ASME license or copyright; see http://www.asme.org/terms/Terms_Use.cfm

H. Mokelke
Motoren- und Turbinen-Union München GmbH
Postfach 50 06 40
8000 München 50
Germany

The Prediction of Steady, Circumferential Pressure and Temperature Distortions in Multistage Axial Flow Compressors

A small perturbation theory is presented for the prediction of the decay of steady circumferential pressure, temperature and velocity distortions in multistage axial flow compressors. The mathematical model which is employed replaces the blade rows of the compressor by actuator disks. A closed solution for the linearized equations describing the two-dimensional, inviscid and compressible flow between the disks is derived and appropriate matching conditions at the disks (assuming a quasi-steady blade response) are determined. An efficient calculation procedure is presented which allows the rapid computation of the distortion development through any compressor configuration, i.e., through any combination of rotors, stators and axial clearances including the core engine compression system. The theory can be applied to the mean section of the compressor or separately from stream surface to stream surface. Due to the assumption of a two-dimensional flow, however, it is restricted to purely circumferential distortions in compressors with sufficiently high hub-to-tip ratios where radial flow redistributions can be expected to be small. The validity of the small perturbation theory is demonstrated by comparing the theoretical results with experimental data. In addition, the theory is used to study the effect of Mach-number and flow rate on the decay of the distortions through two compressor configurations. Suggestions are made how to utilize the theory for the design of distortion-tolerant compressors.

Introduction

Axial flow compressors operating with a steady circumferentially distorted inlet flow generally show a decrease in pressure ratio, corrected mass flow and efficiency. The inlet distortion also tends to cause premature compressor stall and, due to fluctuating blade forces, there is a possibility of blade vibration and blade failure. Additionally the disturbances may persist right through the compressor and, as a result of different work input by the compressor, can cause turbine overheating.

In order to gain some insight into these effects, small perturbation theories have been developed which allow the propagation of the distortion through the compressor to be predicted. These mathematical models replace the blade rows (in some cases the stages or the entire compressor) by either actuator disks or semi-actuator disks or distributed body-forces and regard the perturbed flow to be composed of small perturbations superimposed upon the mean values.

Ehrich [1] presented such a theory for the computation of the perturbed two-dimensional steady velocity flow field of a constant density fluid upstream and downstream of a single blade row. Rannie and Marble's analysis [2] additionally allows the perturbed pressure field to be determined. Their theory also includes losses and outlet flow angle variations, both being neglected by Ehrich. Katz [3] then extended Rannie/Marble's method to multistage machines. Another two-dimensional imcompressible small perturbation actuator disk theory has been presented by Dunham [4]. The analysis (extended by Whitehead [5] to allow for any gap length between the blade rows within the compressor) yields the same results as those obtained by Katz. It uses, however, the more efficient concept of transfer functions which is also utilized in the theory described in this paper.

In an attempt to include the unsteady rotor blade response, Seidel [6] extended Rannie and Marble's theory by assuming that the blades of the rotor behave like single aerofoils subjected to transverse and streamwise gusts. In [7], Fabri included the unsteady effect due to the inertia of the fluid in the blade passage.

Dunham's two-dimensional small perturbation theory was modified in [8] to accomodate turbulent mixing. The modified theory was then used to predict the decay of sinusoidal distortions of various order through a multistage compressor.

Ehrich's two-dimensional analysis was extended by Krzywoblocki [9] to allow for a compressible fluid. Another two-dimensional small perturbation analysis which permits the fluid to be compressible is presented by Elder [10]. In Elder's analysis the blade rows are replaced by an appropriate distribution of body forces. Wells, Tabakoff and Savell [11] also used a compressible two-dimensional small perturbation analysis to predict the propagation of steady circumferential distortions through a rotor, the rotor itself being replaced by a semi-actuator disk.

The theory of the author falls into the group of [9–11] in the sense that the flow is also assumed to be two-dimensional and compressible and the perturbations are small compared to the mean values. It has in common with [9] that in the model the blade rows are replaced by actuator disks, however, it allows for losses and exit flow angle vari-

Contributed by the Gas Turbine Division of The American Society of Mechanical Engineers and presented at the Gas Turbine Conference and Exhibit and Solar Energy Conference, San Diego, Calif., March 12–15, 1979. Manuscript received at ASME Headquarters January 11, 1979. Paper No. 79-GT-184.

Copyright © 1980 by ASME
Downloaded 01 Jun 2010 to 171.66.16.58. Redistribution subject to ASME license or copyright; see http://www.asme.org/terms/Terms_Use.cfm

ations not considered in [9]. In addition, it permits the propagation of the distortion through any number and configuration of rotors, stators and axial clearances to be calculated. In [10] and [11] only pressure and velocity perturbations in the flow outside the blade rows are considered. However, even if the distortion at compressor inlet is assumed to consist only of a total pressure distortion with a uniform total temperature, the circumferential difference in work addition by the rotor creates a temperature distortion at rotor exit which has to be accounted for. The theory described below accounts for this effect.

Mathematical Model

It is desired to predict the circumferential pressure, temperature and velocity perturbations upstream, between the blade rows and downstream of a multistage, high hub-to-tip ratio axial flow compressor subjected to a steady combined total pressure/total temperature inlet flow distortion. For this purpose an analytical model is employed which replaces the blade rows of the compressor by actuator disks, located at the semi-chord position, Fig. 1. Due to this arrangement of the disks, the circumferential crossflow between the blade rows is over-estimated but this is neglected.

The restriction to a high hub-to-tip ratio compressor with a purely circumferential distortion allows to neglect radial variations in flow properties so that the problem reduces to a two-dimensional one. Although the theory to be derived strictly only holds for a cylindrical annulus of zero height with a constant radius r, to a first degree of accuracy it can be applied to the mean section of the compressor or separately from stream surface to stream surface.

The Flow Outside The Actuator Disks. The fluid is assumed to be a perfect, inviscid gas and a stationary co-ordinate system x, θ is introduced, Fig. 1. The total axial velocity component of the flow may be composed of a mean value $\bar{c}_x$ and a superimposed perturbation $c_x'(x, \theta)$, hence $c_x = \bar{c}_x + c_x'$. Similarly the tangential velocity component, the static pressure, the density, the entropy and the static temperature are $c_\theta = \bar{c}_\theta + c_\theta'$, $P_s = \bar{P}_s + P_s'$, $\rho = \bar{\rho} + \rho'$, $s = \bar{s} + s'$ and $T_s = \bar{T}_s + T_s'$. The mean quantities are constant within one flow régime but have different values for different flow régimes. (A flow régime may be the upstream or downstream flow field of the compressor or the flow field between two actuator disks.)

With the assumption that the perturbation quantities are small compared with the mean quantities, the equations describing the flow may be linearized and (with the notation $c_x^* = c_x'/\bar{c}_x$, $c_\theta^* = c_\theta'/\bar{c}_x$, $P_s^* = P_s'/\bar{P}_s$, $\rho^* = \rho'/\bar{\rho}$, $T_s^* = T_s'/\bar{T}_s$) the result is:

$$\frac{\bar{a}}{r}\frac{\partial c_x^*}{\partial \theta} + \frac{\partial c_x^*}{\partial x} = -\frac{1}{\gamma \bar{M}_x^2}\frac{\partial P_s^*}{\partial x} \tag{1}$$

$$\frac{\bar{a}}{r}\frac{\partial c_\theta^*}{\partial \theta} + \frac{\partial c_\theta^*}{\partial x} = -\frac{1}{\gamma r \bar{M}_x^2}\frac{\partial P_s^*}{\partial \theta} \tag{2}$$

$$\frac{\bar{a}}{\bar{r}}\frac{\partial \rho^*}{\partial \theta} + \frac{\partial \rho^*}{\partial x} + \frac{1}{r}\frac{\partial c_\theta^*}{\partial \theta} + \frac{\partial c_x^*}{\partial x} = 0 \tag{3}$$

$$\frac{\bar{a}}{r}\frac{\partial s'}{\partial \theta} + \frac{\partial s'}{\partial x} = 0 \tag{4}$$

$$s' = c_p\left(T_s^* - \frac{\gamma - 1}{\gamma}P_s^*\right) \tag{5}$$

$$P_s^* = \rho^* + T_s^* \tag{6}$$

In these equations, $\bar{a}$ is the tangent of the absolute mean flow angle, Fig. 1, i.e., $\bar{a} = \bar{c}_\theta/\bar{c}_x = \tan\bar{\alpha}$ and $\bar{M}_x = \bar{c}_x/\sqrt{\gamma \bar{P}_s/\bar{\rho}} = \bar{c}_x/\sqrt{\gamma R \bar{T}_s}$ is the axial component of the mean flow Mach number.

Equations (1) and (2) represent the x and θ-momentum equation, respectively, and equation (3) is the continuity equation. The energy equation, equation (4), implies that the entropy perturbation is constant along the mean streamlines (with different values from streamline to streamline). Equation (5), sometimes referred to as Gibbs equation, is a fundamental thermodynamic equation and equation (6) is the equation of state.

Equation (6) combined with equation (5) yields

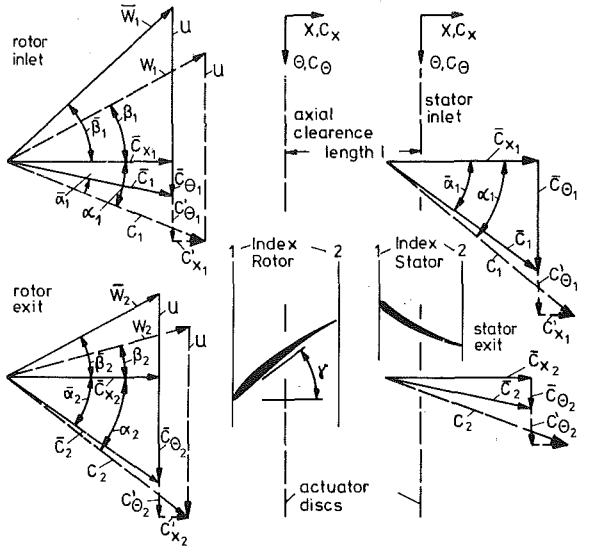


Fig. 1 Replacement of rotors and stators by actuator disks. Velocity diagrams of the mean and perturbed flow (schematic)

$$s' = c_p\left(\frac{1}{\gamma}P_s^* - \rho^*\right) \tag{7}$$

By introducing equation (7) into equation (4) it is found that

$$\frac{\bar{a}}{r}\frac{\partial}{\partial \theta}\left(\frac{1}{\gamma}P_s^* - \rho^*\right) + \frac{\partial}{\partial x}\left(\frac{1}{\gamma}P_s^* - \rho^*\right) = 0 \tag{8}$$

The isentropic equation P_s/ρ^γ = constant written in linearized form yields $P_s^* - \gamma\rho^* = 0$. This equation, which was used for example in [10], satisfies equation (8). Equation (7) shows, however, that in this case $s' = 0$. Since the analysis has to include combined pressure/temperature distortions, a solution implying $s' = 0$ is not suitable.

The system of equations (1–3) and (8) is linear and thus the principle of superposition holds. It is therefore assumed that the solutions can be represented as a Fourier series. The Fourier series will be expressed in complex notation where the real part represents the physical quantity. The perturbation quantities then take the general form

$$f^*(x, \theta) = \sum_{n=1}^{j} F_n(x)e^{in\theta} \tag{9}$$

where $F_n(x)$ are the complex harmonic coefficients. The solution must be periodic in θ therefore n must be integer.

After substitution of equations (9) into equations (1–3) and (8) and dropping the summation sign, four simultaneous ordinary differential equations are obtained. For these a nontrivial solution for the different values of n can be found. This solution reintroduced into equations (9) finally yields for the perturbations

$$c_x^* = \sum_{n=1}^{j}(A_{n1}e^{R_{n1}x} + R_{n2}A_{n2}e^{R_{n2}x} + R_{n3}A_{n3}e^{R_{n3}x})e^{in\theta} \tag{10}$$

$$c_\theta^* = \sum_{n=1}^{j}\left(\bar{a}A_{n1}e^{R_{n1}x} + \frac{in}{r}A_{n2}e^{R_{n2}x} + \frac{in}{r}A_{n3}e^{R_{n3}x}\right)e^{in\theta} \tag{11}$$

$$P_s^* = \gamma\bar{M}_x^2\sum_{n=1}^{j}[-(R_{n2} - R_{n1})A_{n2}e^{R_{n2}x} - (R_{n3} - R_{n1})A_{n3}e^{R_{n3}x}]e^{in\theta} \tag{12}$$

$$\rho^* = \sum_{n=1}^{j}[-(R_{n2} - R_{n1})\bar{M}_x^2A_{n2}e^{R_{n2}x} - (R_{n3} - R_{n1})\bar{M}_x^2A_{n3}e^{R_{n3}x} + A_{n4}e^{R_{n1}x}]e^{in\theta} \tag{13}$$

where

$$R_{n1} = -in\bar{a}/r \tag{14}$$

$$R_{n2,3} = \frac{n}{(1 - \bar{M}_x^2)r}[i\bar{a}\bar{M}_x^2 \pm \sqrt{1 - \bar{M}_x^2(1 + \bar{a}^2)}] \tag{15}$$

Downloaded 01 Jun 2010 to 171.66.16.58. Redistribution subject to ASME license or copyright; see http://www.asme.org/terms/Terms_Use.cfm

The complex constants A_{n1}, A_{n2}, A_{n3} and A_{n4} may be determined from the boundary conditions.

The perturbed flow is fully described by the derived quantities c_x^*, c_θ^*, P_s^* and ρ^*. For a more convenient application of the theory, however, the total temperature perturbations, $T_t^* = T_t'/\overline{T}_t$ and the total pressure perturbations $P_t^* = P_t'/\overline{P}_t$ will also be determined. They will then "replace" the quantities P_s^* and ρ^*. From

$$T_t = T_s + (c_x^2 + c_\theta^2)/2c_P \tag{16}$$

it is obtained with $T_t = \overline{T}_t + T_t'$, $T_t' \ll \overline{T}_t$, by linearization

$$T_t^* = (\overline{T}_s/\overline{T}_t)[T_s^* + (\gamma - 1)\overline{M}_x^2(c_x^* + \bar{a}c_\theta^*)] \tag{17}$$

where

$$\overline{T}_s/\overline{T}_t = \left[1 + \frac{1}{2}(\gamma - 1)\overline{M}_x^2(1 + \bar{a}^2)\right]^{-1} \tag{18}$$

Similarly, from

$$P_t/P_s = (T_t/T_s)^{\gamma/(\gamma-1)} \tag{19}$$

it is obtained with $P_t = \overline{P}_t + P_t'$, $P_t' \ll \overline{P}_t$, by linearization

$$P_t^* = P_s^* + [\gamma/(\gamma - 1)](T_t^* - T_s^*) \tag{20}$$

Equations (10–13) (observing equation (6)) introduced into equation (17) yields

$$T_t^* = (\overline{T}_s/\overline{T}_t) \sum_{n=1}^{j} [(\gamma - 1)\overline{M}_x^2(1 + \bar{a}^2)A_{n1} - A_{n4}]e^{R_{n1}x}e^{in\theta} \tag{21}$$

Introduction of equations (6, 12, 13) and (21) into equation (20) yields

$$P_t^* = \gamma\overline{M}_x^2(1 + \bar{a}^2)(\overline{T}_s/\overline{T}_t) \sum_{n=1}^{j} \left(A_{n1} + \frac{1}{2}A_{n4}\right) e^{R_{n1}x}e^{in\theta} \tag{22}$$

The Gap Transfer Matrix. The perturbed flow at any axial location of the compressor (including the upstream and downstream flow field) can be described by

$$P_t^* = \sum_{n=1}^{j} P_n e^{in\theta} \tag{23a}$$

$$T_t^* = \sum_{n=1}^{j} T_n e^{in\theta} \tag{23b}$$

$$c_x^* = \sum_{n=1}^{j} U_n e^{in\theta} \tag{23c}$$

$$c_\theta^* = \sum_{n=1}^{j} V_n e^{in\theta} \tag{23d}$$

where P_n, T_n, U_n and V_n are complex harmonic coefficients. The column matrix

$$[S_V] = \begin{bmatrix} P_n \\ T_n \\ U_n \\ V_n \end{bmatrix} \tag{24}$$

will be called a state vector. Once the state vector is known (for all harmonics), the flow perturbations can be calculated using equations (23).

As previously mentioned, the analysis is linearized and the various harmonic components do not interact. In the following, therefore, only one component given by the integer n will be considered and the index n will be dropped.

The relationship between the components of the state vector describing the flow somewhere within a flow régime (index 2) at a distance x from the flow régime inlet and the complex harmonic constants A_1, A_2, A_3 and A_4 is found by equating equation (23a) with (22), (23b) with (21), (23c) with (10) and (23d) with (11). The result is

$$\begin{bmatrix} P_2 \\ T_2 \\ U_2 \\ V_2 \end{bmatrix} = \begin{bmatrix} y_{11} & 0 & 0 & y_{14} \\ y_{21} & 0 & 0 & y_{24} \\ 1 & R_2 & R_3 & 0 \\ \bar{a} & in/r & in/r & 0 \end{bmatrix} \begin{bmatrix} A_1 e^{R_1 x} \\ A_2 e^{R_2 x} \\ A_3 e^{R_3 x} \\ A_4 e^{R_1 x} \end{bmatrix} \tag{25}$$

where

$$y_{11} = \gamma\overline{M}_x^2(1 + \bar{a}^2)(\overline{T}_s/\overline{T}_t)$$

$$y_{14} = (\gamma/2)\overline{M}_x^2(1 + \bar{a}^2)(\overline{T}_s/\overline{T}_t)$$

$$y_{21} = (\gamma - 1)\overline{M}_x^2(1 + \bar{a}^2)(\overline{T}_s/\overline{T}_t)$$

$$y_{24} = -\overline{T}_s/\overline{T}_t$$

The relationship between the components of the state vector describing the flow at the flow régime inlet (index 1) and the complex harmonic constants A_1, A_2, A_3 and A_4 is obtained from equations (25) by putting $x = 0$. The result is

$$\begin{bmatrix} P_1 \\ T_1 \\ U_1 \\ V_1 \end{bmatrix} = \begin{bmatrix} y_{11} & 0 & 0 & y_{14} \\ y_{21} & 0 & 0 & y_{24} \\ 1 & R_2 & R_3 & 0 \\ \bar{a} & in/r & in/r & 0 \end{bmatrix} \begin{bmatrix} A_1 \\ A_2 \\ A_3 \\ A_4 \end{bmatrix} \tag{26}$$

Equations (26) solved with respect to A_1, A_2, A_3 and A_4 yields

$$\begin{bmatrix} A_1 \\ A_2 \\ A_3 \\ A_4 \end{bmatrix} = \begin{bmatrix} w_{11} & 1/2 & 0 & 0 \\ w_{21} & w_{22} & w_{23} & w_{24} \\ w_{31} & w_{32} & w_{33} & w_{34} \\ w_{41} & -1 & 0 & 0 \end{bmatrix} \begin{bmatrix} P_1 \\ T_1 \\ U_1 \\ V_1 \end{bmatrix} \tag{27}$$

where

$$w_{11} = 1/[\gamma\overline{M}_x^2(1 + \bar{a}^2)]$$

$$w_{21} = -\tilde{R}_3/[(n/r)\tilde{R}_{23}\gamma\overline{M}_x^2(1 + \bar{a}^2)]$$

$$w_{22} = -\tilde{R}_3/[2(n/r)\tilde{R}_{23}]$$

$$w_{23} = 1/\tilde{R}_{23}$$

$$w_{24} = iR_3/[(n/r)\tilde{R}_{23}]$$

$$w_{31} = \tilde{R}_2/[(n/r)\tilde{R}_{23}\gamma\overline{M}_x^2(1 + \bar{a}^2)]$$

$$w_{32} = \tilde{R}_2/[2(n/r)\tilde{R}_{23}]$$

$$w_{33} = -1/\tilde{R}_{23}$$

$$w_{34} = -iR_2/[(n/r)\tilde{R}_{23}]$$

$$w_{41} = (\gamma - 1)/\gamma$$

$$\tilde{R}_2 = i\bar{a}R_2 + n/r$$

$$\tilde{R}_3 = i\bar{a}R_3 + n/r$$

$$\tilde{R}_{23} = R_2 - R_3$$

The relationship between the components of the state vector describing the flow somewhere within the flow régime and those describing the flow at the flow régime inlet is obtained by introducing equations (27) into (25). The result is

$$\begin{bmatrix} P_2 \\ T_2 \\ U_2 \\ V_2 \end{bmatrix} = \begin{bmatrix} g_{11} & 0 & 0 & 0 \\ 0 & g_{22} & 0 & 0 \\ g_{31} & g_{32} & g_{33} & g_{34} \\ g_{41} & g_{42} & g_{43} & g_{44} \end{bmatrix} \begin{bmatrix} P_1 \\ T_1 \\ U_1 \\ V_1 \end{bmatrix} \tag{28}$$

The (non-zero) elements $g_{11}, g_{22}, \ldots$ of the transfer matrix are given in the Appendix.

The state vector $[S_V]_2$ at the exit of a gap with a length ℓ (axial clearance between two actuator disks, Fig. 1) is obtained from the state vector $[S_V]_1$ by

$$[S_V]_2 = [G][S_V]_1 \tag{29}$$

Downloaded 01 Jun 2010 to 171.66.16.58. Redistribution subject to ASME license or copyright; see http://www.asme.org/terms/Terms_Use.cfm

where the elements of the gap transfer matrix $[G]$ are obtained from $g_{11}, g_{22}, \ldots$ by putting x equal to the gap length ℓ.

Matching Conditions at the Blade Rows. The flow fields upstream and downstream of a blade row have to be matched at the blade row, contracted to an actuator disk. The four matching conditions are derived from the following requirements

1 specified total pressure change
2 total temperature change
3 continuity of mass flow
4 specified flow outlet angle

Matching Conditions at a Stator Blade Row. *(1) Specified Total Pressure Change.* It is common practice to define a total pressure loss coefficient, which in the case of a stator takes the form [12]

$$\omega_S = (P_{t1} - P_{t2})/(P_{t1} - P_{S1}) = f(\alpha_1) \tag{30}$$

The indices 1 and 2 refer to the stator inlet and outlet, respectively. The loss coefficient is assumed to be a function of the absolute air inlet angle α_1 only. Equation (30) solved with respect to P_{t2} yields

$$P_{t2} = P_{t1} - \omega_S(P_{t1} - P_{S1}) \tag{31}$$

This equation may be linearized and the result is

$$P_{t2}^*(\overline{P}_{t2}/\overline{P}_{t1}) = P_{t1}^* - \omega_S'[1 - (\overline{P}_{s1}/\overline{P}_{t1})]\,(c_{\theta 1}^* - \overline{a}_1 c_{x1}^*) - \overline{\omega}_S[P_{t1}^* - (\overline{P}_{s1}/\overline{P}_{t1})P_{s1}^*] \tag{32}$$

where, from equation (31) (which is assumed to hold for the mean flow as well),

$$\overline{P}_{t2}/\overline{P}_{t1} = 1 - \overline{\omega}_S(1 - \overline{P}_{s1}/\overline{P}_{t1}) \tag{33}$$

The pressure ratio $\overline{P}_{s1}/\overline{P}_{t1}$ is given by

$$\overline{P}_s/\overline{P}_t = \left[1 + \frac{1}{2}(\gamma - 1)\overline{M}_x{}^2(1 + \overline{a}^2)\right]^{-\gamma/(\gamma-1)} \tag{34}$$

The loss coefficient $\overline{\omega}_S$ is to be obtained from the (normally measured) loss vs. air inlet angle curve (Fig. 2) at the mean absolute air inlet angle tangent, $\tan \overline{\alpha}_1$. The quantity

$$\omega_S' = d\omega_S/d(\tan\alpha_1) \tag{35}$$

is equivalent to the slope of the loss versus inlet angle curve at $\tan \overline{\alpha}_1$.

Elimination of T_s^* from equation (17) and (20) yields for the static pressure perturbation

$$P_s^* = P_t^* + \frac{\gamma}{2}\overline{M}_x{}^2(1 + \overline{a}^2)T_t^* - \gamma\overline{M}_x{}^2 c_x^* - \gamma\overline{M}_x{}^2\overline{a}c_\theta^* \tag{36}$$

which may be introduced into equation (32). The final result is

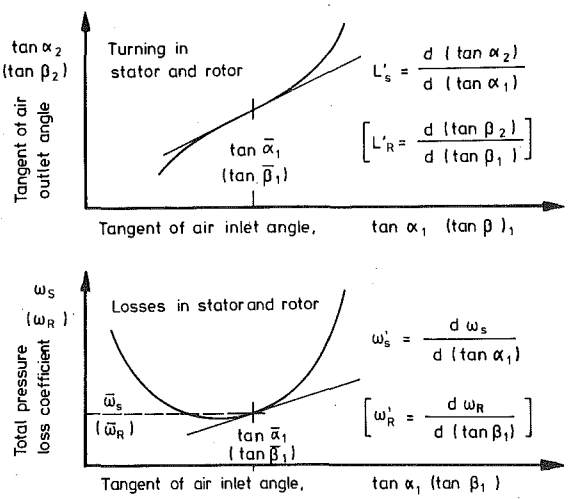


Fig. 2 Total pressure losses and outlet versus inlet angle variations including mean flow conditions (schematic)

$$P_{t2}^* = P_{t1}^* + f_{12}T_{t1}^* + f_{13}c_{x1}^* + f_{14}c_{\theta 1}^* \tag{37}$$

where

$$f_{12} = \frac{\frac{\gamma}{2}\overline{\omega}_S\overline{M}_{x1}{}^2(1 + \overline{a}_1{}^2)(\overline{P}_{s1}/\overline{P}_{t1})}{1 - \overline{\omega}_S(1 - \overline{P}_{s1}/\overline{P}_{t1})}$$

$$f_{13} = \frac{(\gamma\overline{\omega}_S\overline{M}_{xt}{}^2 + \overline{\omega}_S'\overline{a}_1)(\overline{P}_{s1}/\overline{P}_{t1}) - \omega_S'\overline{a}_1}{1 - \overline{\omega}_S(1 - \overline{P}_{s1}/\overline{P}_{t1})}$$

$$f_{14} = \frac{(\gamma\overline{\omega}_S\overline{M}_{x1}{}^2\overline{a}_1 - \omega_S')(\overline{P}_{s1}/\overline{P}_{t1}) + \omega_S'}{1 - \overline{\omega}_S(1 - \overline{P}_{s1}\overline{P}_{t1})}$$

(2) Total Temperature Change. For a stator row, $T_{t2} = T_{t1}$, which in terms of perturbation quantities, yields

$$T_{t2}^* = T_{t1}^* \tag{38}$$

(3) Continuity of Mass Flow. This requirement is expressed by $\rho_2 c_{x2} = \rho_1 c_{x1}$. By linearizing this equation it is found that

$$\rho_2^* + c_{x2}^* = \rho_1^* + c_{x1}^* \tag{39}$$

The combination of equation (6, 17) and (20) yields

$$\rho^* = P_t^* - \left[1 - \frac{1}{2}\overline{M}_x{}^2(1 + \overline{a}^2)\right]T_t^* - \overline{M}_x{}^2 c_x^* - \overline{a}\overline{M}_x{}^2 c_\theta^* \tag{40}$$

Introducing equation (40) into (39) obtains

$$P_{t2}^* + d_{32}T_{t2}^* + d_{33}c_{x2}^* + d_{34}c_{\theta 2}^* = P_{t1}^* + f_{32}T_{t1}^* + f_{33}c_{x1}^* + f_{34}c_{\theta 1}^* \tag{41}$$

where

$$d_{32} = -\left[1 - \frac{1}{2}\overline{M}_{x2}{}^2(1 + \overline{a}_2{}^2)\right]$$

$$d_{33} = 1 - \overline{M}_{x2}{}^2$$

$$d_{34} = -\overline{a}_2\overline{M}_{x2}{}^2$$

$$f_{32} = -\left[1 - \frac{1}{2}\overline{M}_{x1}{}^2(1 + \overline{a}_1{}^2)\right]$$

$$f_{33} = 1 - \overline{M}_{x1}{}^2$$

$$f_{34} = -\overline{a}_1\overline{M}_{x1}{}^2$$

(4) Specified Flow Outlet Angle. The tangential velocity components at stator outlet and inlet are given by (Fig. 1)

$$c_{\theta 2} = c_{x2}\tan\alpha_2 \tag{42a}$$

$$c_{\theta 1} = c_{x1}\tan\alpha_1 \tag{42b}$$

Equations (42) linearized and the results suitably combined yields

$$d_{43}c_{x2}^* + c_{\theta 2}^* = f_{43}c_{x1}^* + f_{44}c_{\theta 1}^* \tag{43}$$

where

$$d_{43} = -\overline{a}_2$$

$$f_{43} = -\overline{a}_1 L_S'$$

$$f_{44} = L_S'$$

The quantity

$$L_S' = d(\tan\alpha_2)/d(\tan\alpha_1) \tag{44}$$

is equal to the slope of the flow outlet angle versus inlet angle curve (Fig. 2) at $\tan \overline{\alpha}_1$.

The Stator Transfer Matrix. The stator matching conditions, given by equations (37, 38, 41) and (43) summarized in matrix notation,

Downloaded 01 Jun 2010 to 171.66.16.58. Redistribution subject to ASME license or copyright; see http://www.asme.org/terms/Terms_Use.cfm

$$\begin{bmatrix} 1 & 0 & 0 & 0 \\ 0 & 1 & 0 & 0 \\ 1 & d_{32} & d_{33} & d_{34} \\ 0 & 0 & d_{43} & 1 \end{bmatrix} \begin{bmatrix} P_{t2}^* \\ T_{t2}^* \\ c_{x2}^* \\ c_{\theta 2}^* \end{bmatrix} = \begin{bmatrix} 1 & f_{12} & f_{13} & f_{14} \\ 0 & 1 & 0 & 0 \\ 1 & f_{32} & f_{33} & f_{34} \\ 0 & 0 & f_{43} & f_{44} \end{bmatrix} \begin{bmatrix} P_{t1}^* \\ T_{t1}^* \\ c_{x1}^* \\ c_{\theta 1}^* \end{bmatrix} \quad \ldots \quad (45)$$

By linear combination of equations (45) and introduction of equations (23), the state vector at the stator outlet can be calculated from the state vector at the stator inlet by the system of equations

$$\begin{bmatrix} P_2 \\ T_2 \\ U_2 \\ V_2 \end{bmatrix} = \begin{bmatrix} 1 & s_{12} & s_{13} & s_{14} \\ 0 & 1 & 0 & 0 \\ 0 & s_{32} & s_{33} & s_{34} \\ 0 & s_{42} & s_{43} & s_{44} \end{bmatrix} \begin{bmatrix} P_1 \\ T_1 \\ U_1 \\ V_1 \end{bmatrix} \quad (46)$$

which (by use of equation (24)) may be written in the form

$$[S_V]_2 = [S][S_V]_1 \quad (47)$$

The elements $s_{12}, s_{13}, \ldots$ of the stator transfer matrix $[S]$ are given in the Appendix.

Matching Conditions at a Rotor Blade Row. The matching conditions at the rotor blade row are derived by assuming a quasi-steady rotor blade response to the distorted inlet flow.

(1) Specified Total Pressure Change. It is common to define a total pressure loss coefficient for a rotor [12],

$$\omega_R = (P_{tr1} - P_{tr2})/(P_{tr1} - P_{s1}) = f(\beta_1) \quad (48)$$

where P_{tr1} and P_{tr2} are the relative total pressures at rotor inlet and exit. The loss coefficient is assumed to be a function of the relative air inlet angle β_1 only. Equation (48) solved with respect to P_{tr2} yields

$$P_{tr2} = P_{tr1}\{1 - \omega_R[1 - (P_{s1}/P_{tr1})]\} \quad (49)$$

With

$$P_{tr} = P_t(T_{tr}/T_t)^{\gamma/(\gamma-1)} \quad (50)$$

and $T_{tr2} = T_{tr1}$, where T_{tr} is the total temperature relative to the rotor, equation (49) can be rewritten as

$$P_{t2}T_{t2}^{-\gamma/(\gamma-1)} = P_{t1}T_{t1}^{-\gamma/(\gamma-1)}\left[1 - \omega_R\left(1 - \frac{P_{s1}}{P_{tr1}}\right)\right] \quad (51)$$

This equation may be linearized and the result is

$$P_{t2}^* + h_{12}T_{t2}^* = P_{t1}^* + k_{12}T_{t1}^* + k_{13}c_{x1}^* + k_{14}c_{\theta 1}^* \quad (52)$$

where

$$h_{12} = -\gamma/(\gamma - 1)$$

$$k_{12} = \left[\frac{1}{2}\gamma\bar{\omega}_R\overline{M}_{x1}^2(1 + \bar{b}_1^2)(\overline{P}_{s1}/\overline{P}_{tr1})(\overline{T}_{s1}/\overline{T}_{tr1}) \times (\overline{T}_{t1}/\overline{T}_{s1})\right]/[1 - \bar{\omega}_R(1 - \overline{P}_{s1}/\overline{P}_{tr1})] - \gamma/(\gamma - 1)$$

$$k_{13} = -\frac{\gamma\bar{\omega}_R\overline{M}_{x1}^2(\overline{P}_{s1}/\overline{P}_{tr1}) - \omega_R'\bar{b}_1(1 - \overline{P}_{s1}/\overline{P}_{tr1})}{1 - \bar{\omega}_R(1 - \overline{P}_{s1}/\overline{P}_{tr1})}$$

$$k_{14} = \left\{\gamma\bar{\omega}_R\overline{M}_{x1}^2\left[\bar{b}_1 - \frac{1}{2}(\gamma - 1)\overline{M}_{x1}^2(1 + \bar{b}_1^2)\bar{a}_1\right](\overline{P}_{s1}/\overline{P}_{tr1}) \times (\overline{T}_{s1}/\overline{T}_{tr1}) + \omega_R'(1 - \overline{P}_{s1}/\overline{P}_{tr1})\right\}\Big/[1 - \bar{\omega}_R(1 - \overline{P}_{s1}/\overline{P}_{tr1})]$$

and

$$\overline{T}_{s1}/\overline{T}_{tr1} = 1/\left[1 + \frac{1}{2}(\gamma - 1)\overline{M}_{x1}^2(1 + \bar{b}_1^2)\right] \quad (53)$$

$$\overline{P}_{s1}/\overline{P}_{tr1} = (\overline{T}_{s1}/\overline{T}_{tr1})^{\gamma/(\gamma-1)} \quad (54)$$

$$\bar{b}_1 = \tan\bar{\beta}_1 = 1/\bar{\phi}_1 - \tan\bar{\alpha}_1 \quad (55)$$

The loss coefficient $\bar{\omega}_R$ is to be obtained from the (normally measured) loss versus air inlet angle curve (Fig. 2) at the mean relative inlet angle tangent $\tan\bar{\beta}_1$. The quantity

$$\omega_R' = d\omega_R/d(\tan\beta_1) \quad (56)$$

is equivalent to the slope of the loss versus inlet angle curve at $\tan\bar{\beta}_1$. The temperature ratio $\overline{T}_{t1}/\overline{T}_{s1}$ is given by equation (18).

(2) Total Temperature Change. The total enthalpy rise across a rotor is equal to the work done per unit mass. Hence, with the assumption of a perfect gas

$$c_p(T_{t2} - T_{t1}) = u(c_{\theta 2} - c_{\theta 1}) \quad (57)$$

where u is the rotor speed at the radius, r. In terms of perturbation quantities, equation (57) can be written as

$$c_pT_{t2}' - uc_{\theta 2}' = c_pT_{t1}' - uc_{\theta 1}' \quad (58)$$

Equation 58 suitably expended and introducing the flow coefficient for the mean flow, $\bar{\phi} = \bar{c}_x/u$, it is finally found that

$$h_{22}T_{t2}^* + h_{24}c_{\theta 2}^* = k_{22}T_{t1}^* + k_{24}c_{\theta 1}^* \quad (59)$$

where

$$h_{22} = \bar{\phi}_2^2(\overline{T}_{t2}/\overline{T}_{s2})/[(\gamma - 1)\overline{M}_{x2}^2]$$

$$h_{24} = -\bar{\phi}_2$$

$$k_{22} = \bar{\phi}_1^2(\overline{T}_{t1}/\overline{T}_{s1})/[(\gamma - 1)\overline{M}_{x1}^2]$$

$$k_{24} = -\bar{\phi}_1$$

Again the temperature ratio $\overline{T}_t/\overline{T}_s$ is given by equation (18).

(3) Continuity of Mass Flow. This requirement is identical to that for the stator, equation (41). It will be repeated here for completeness,

$$P_{t2}^* + h_{32}T_{t2}^* + h_{33}c_{x2}^* + h_{34}c_{\theta 2}^* = P_{t1}^* + k_{32}T_{t1}^* + k_{33}c_{x1}^* + k_{34}c_{\theta 1}^* \quad (60)$$

where h_{32} corresponds to d_{32} etc.

(4) Specified Flow Outlet Angle. The tangential velocity components at the rotor outlet and inlet are given by

$$c_{\theta 2} = u - c_{x2}\tan\beta_2 \quad (61a)$$

$$c_{\theta 1} = u - c_{x1}\tan\beta_1 \quad (61b)$$

Equations (61) linearized and the results suitably combined yields

$$h_{43}c_{x2}^* + c_{\theta 2}^* = k_{43}c_{x1}^* + k_{44}c_{\theta 1}^* \quad (62)$$

where

$$h_{43} = \bar{b}_2 = \tan\bar{\beta}_2 = 1/\bar{\phi}_2 - \tan\bar{\alpha}_2$$

$$k_{43} = \bar{b}_1L_R'$$

$$k_{44} = L_R'$$

The quantity

$$L_R' = d(\tan\beta_2)/d(\tan\beta_1) \quad (63)$$

is equal to the slope of the flow outlet versus inlet angle curve (Fig. 2) at $\tan\bar{\beta}_1$.

The Rotor Transfer Matrix. The rotor matching conditions given by equations (52, 59, 60) and (62) summarized in matrix notation

$$\begin{bmatrix} 1 & h_{12} & 0 & 0 \\ 0 & h_{22} & 0 & h_{24} \\ 1 & h_{32} & h_{33} & h_{34} \\ 0 & 0 & h_{43} & 1 \end{bmatrix} \begin{bmatrix} P_{t2}^* \\ T_{t2}^* \\ c_{x2}^* \\ c_{\theta 2}^* \end{bmatrix} = \begin{bmatrix} 1 & k_{12} & k_{13} & k_{14} \\ 0 & k_{22} & 0 & k_{24} \\ 1 & k_{32} & k_{33} & k_{34} \\ 0 & 0 & k_{43} & k_{44} \end{bmatrix} \begin{bmatrix} P_{t1}^* \\ T_{t1}^* \\ c_{x1}^* \\ c_{\theta 1}^* \end{bmatrix} \quad (64)$$

Downloaded 01 Jun 2010 to 171.66.16.58. Redistribution subject to ASME license or copyright; see http://www.asme.org/terms/Terms_Use.cfm

By linear combination of equations (64) and introduction of equations (23), the state vector at the rotor outlet can be calculated from the state vector at the rotor inlet by the system of equations

$$\begin{bmatrix} P_2 \\ T_2 \\ U_2 \\ V_2 \end{bmatrix} = \begin{bmatrix} 1 & r_{12} & r_{13} & r_{14} \\ 0 & r_{22} & r_{23} & r_{24} \\ 0 & r_{32} & r_{33} & r_{34} \\ 0 & r_{42} & r_{43} & r_{44} \end{bmatrix} \begin{bmatrix} P_1 \\ T_1 \\ U_1 \\ V_1 \end{bmatrix} \tag{65}$$

which (by use of equation (24)) may be written in the form

$$[S_V]_2 = [R][S_V]_1 \tag{66}$$

The elements $r_{12}, r_{13}, \ldots$ of the rotor transfer matrix [R] are given in the Appendix.

The Transfer Matrix for the Compressor. From the above derived transfer matrices for a gap, a stator and a rotor, the transfer matrix for the whole compressor can be calculated. As an example, consider the four-stage compressor described in [8]. Using equation (47), the state vector at the exit of the stator belonging to the fourth stage is related to the state vector at inlet to that stator by

$$[S_V]_2 = [S][S_V]_1 \tag{67}$$

Similarly, using equation (29), the state vector at the exit of the gap preceding that stator can be related to the state vector at inlet to the gap by

$$[S_V]_2 = [G_S][S_V]_1 \tag{68}$$

Similarly, for the rotor preceding that gap, equation (66),

$$[S_V]_2 = [R][S_V]_1 \tag{69}$$

Similarly, for the gap preceding that rotor, equation (29),

$$[S_V]_2 = [G_R][S_V]_1 \tag{70}$$

The state vector at the exit of the fourth stage consisting of gap, rotor, gap, stator can be related to the state vector at inlet to that stage by combining equations (67–70). Hence

$$[S_V]_2 = [\mathrm{St}_4][S_V]_1 \tag{71}$$

where

$$[\mathrm{St}_4] = [S][G_S][R][G_R] \tag{72}$$

For a combination of four stages, the state vector at exit is related to the state vector at inlet by

$$[S_V]_2 = [\mathrm{St}_4][\mathrm{St}_3][\mathrm{St}_2][\mathrm{St}_1][S_V]_1 \tag{73}$$

The four stages of the compressor described in [8] are preceded by inlet guide vanes and followed after a large gap, by outlet guide vanes. The state vector at the exit of the compressor is then related to the state vector at the inlet to the compressor by

$$[S_V]_2 = [T][S_V]_1 \tag{74}$$

where the compressor transfer matrix is

$$[T] = [\mathrm{OGV}][G_B][\mathrm{St}_4][\mathrm{St}_3][\mathrm{St}_2][\mathrm{St}_1][\mathrm{IGV}] \tag{75}$$

For other compressor configurations, the compressor transfer matrix can be calculated correspondingly.

Far Upstream And Downstream Boundary Conditions. Equation (10) shows that for the perturbations to remain finite far upstream of the compressor ($x = -\infty$) it is required that $A_3 = 0$. From the third of equations (27), this is equivalent to the requirement that the harmonic coefficients at the inlet to the upstream flow field (which is identical to the compressor inlet, hence the index 1) satisfy the equation

$$(w_{31})_1 P_1 + (w_{32})_1 T_1 + (w_{33})_1 U_1 + (w_{34})_1 V_1 = 0 \tag{76}$$

Correspondingly, for the perturbation to remain finite far downstream of the compressor, $A_2 = 0$. From the second of equations (27) this is equivalent to the requirement that the harmonic coefficients at the inlet to the downstream flow field (which is identical to the compressor outlet, hence the index 2) satisfy the equation

$$(w_{21})_2 P_2 + (w_{22})_2 T_2 + (w_{23})_2 U_2 + (w_{24})_2 V_2 = 0 \tag{77}$$

The State Vector at the Compressor Inlet. Equation (74) is equivalent to the following set of equations

$$P_2 = t_{11}P_1 + t_{12}T_1 + t_{13}U_1 + t_{14}V_1 \tag{78a}$$

$$T_2 = t_{21}P_1 + t_{22}T_1 + t_{23}U_1 + t_{24}V_1 \tag{78b}$$

$$U_2 = t_{31}P_1 + t_{32}T_1 + t_{33}U_1 + t_{34}V_1 \tag{78c}$$

$$V_2 = t_{41}P_1 + t_{42}T_1 + t_{43}U_1 + t_{44}V_1 \tag{78d}$$

where $t_{11}, t_{12}, \ldots$ are the (generally complex) elements of the compressor transfer matrix, $[T]$. Equations (78) introduced into equation (77) yields

$$q_1P_1 + q_2T_1 + q_3U_1 + q_4V_1 = 0 \tag{79}$$

where

$$\begin{aligned} q_1 &= (w_{21})_2 t_{11} + (w_{22})_2 t_{21} + (w_{23})_2 t_{31} + (w_{24})_2 t_{41} \\ q_2 &= (w_{21})_2 t_{12} + (w_{22})_2 t_{22} + (w_{23})_2 t_{32} + (w_{24})_2 t_{42} \\ q_3 &= (w_{21})_2 t_{13} + (w_{22})_2 t_{23} + (w_{23})_2 t_{33} + (w_{24})_2 t_{43} \\ q_4 &= (w_{21})_2 t_{14} + (w_{22})_2 t_{24} + (w_{23})_2 t_{34} + (w_{24})_2 t_{44} \end{aligned} \tag{80}$$

There are now two conditions imposed on the harmonic coefficients P_1, T_1, U_1 and V_1 at the compressor inlet which are expressed by equation (76) and (79). These equations can be combined with each other to eliminate U_1 and V_1, respectively, and the result is

$$U_1 = -\{[(w_{31})_1 q_4 - (w_{34})_1 q_1]P_1 + [(w_{32})_1 q_4 - (w_{34})_1 q_2]T_1\}/D \tag{81}$$

$$V_1 = \{[(w_{31})_1 q_3 - (w_{33})_1 q_1]P_1 + [(w_{32})_1 q_3 - (w_{33})_1 q_2]T_1\}/D \tag{82}$$

where

$$D = (w_{33})_1 q_4 - (w_{34})_1 q_3$$

Summary of the Calculation Procedure. (1) It is assumed that a circumferential total pressure and total temperature distortion exists at the compressor inlet, specified in the form

$$(P_t - \overline{P}_t)/\overline{P}_t = P_t'/\overline{P}_t = f_1(\theta)$$

and

$$(T_t - \overline{T}_t)/\overline{T}_t = T_t'/\overline{T}_t = f_2(\theta)$$

Using equations (23 *a*, *b*), a Fourier series approximation then yields the harmonic coefficients P_1 and T_1 at the compressor inlet. (2) The stator transfer matrices are calculated from $\overline{M}_{x1}, \overline{M}_{x2}, \overline{\alpha}_1, \overline{\alpha}_2, L_S', \overline{\omega}, \omega_S'$. (3) The rotor transfer matrices are calculated from $\overline{M}_{x1}, \overline{M}_{x2}, \overline{\alpha}_1, \overline{\alpha}_2, \overline{\phi}_1, \overline{\phi}_2, L_R', \overline{\omega}_R, \omega_R'$. (4) The gap transfer matrices for each harmonic are calculated from $\overline{M}_x, \overline{\alpha}, r, l, n, \gamma$. Since the quantities of the mean flow do not change within a particular gap, some of the quantities listed under (2), (3) and (4) are identical. (5) The compressor transfer matrix is calculated from the transfer matrices of rotors, stators and gaps. (6) To complete the state vector at the compressor inlet, the harmonic coefficients for the axial velocity, U_1, and for the tangential velocity, V_1, are to be determined. With $\overline{M}_x, \overline{\alpha}, \gamma, n, r$ for the flow fields upstream and downstream of the compressor and with the elements of the compressor transfer matrix, they are found from equations (81) and (82), respectively. (7) With the transfer matrix of the first blade row and the known state vector at the inlet of the compressor, the state vector at the exit of the first blade row can be found. Applying the same procedure through the whole compressor using the appropriate matrices for the various gaps and blade rows, the state vectors may be calculated everywhere. (8) Once the state vectors for all harmonics are known, the total pressure, total temperature, axial velocity and tangential velocity perturbations in the various planes of the compressor can be determined from equations

Downloaded 01 Jun 2010 to 171.66.16.58. Redistribution subject to ASME license or copyright; see http://www.asme.org/terms/Terms_Use.cfm

(23). (9) The static pressure, static temperature, density and entropy perturbations then follow from equations (36, 20, 6) and (5), respectively. (10) The perturbed flow angles in the absolute and relative system may be calculated from

$$\alpha(\theta) = \arctan\,[(\bar{a} + c_\theta^*)/(1 + c_x^*)] \tag{83}$$

and

$$\beta(\theta) = \arctan\,\{[1/\bar{\phi} - (\bar{a} + c_\theta^*)]/(1 + c_x^*)\} \tag{84}$$

respectively.

Application of the Model to Simple Compressor Configurations

In this application, the above theory will be used to solve a problem which slightly differs from the one considered in the previous section. Here it is requested to determine the attenuation of a sinusoidal total pressure perturbation through a compressor. The attenuation of the distortion will be described in terms of the ratio of the total pressure perturbation amplitude at the compressor exit to that at the compressor inlet.

The sinusoidal total pressure distortion at the compressor exit is given by

$$P_{t2}^* = (P_t'/\bar{P}_t)_2 = P_2 e^{in\theta} \tag{85}$$

Correspondingly, at the compressor inlet

$$P_{t1}^* = (P_t'/\bar{P}_t)_1 = P_1 e^{in\theta} \tag{86}$$

Denoting the distortion amplitude by $\Delta P_t'/\bar{P}_t$, the ratio of outlet to inlet distortion amplitudes is then

$$\frac{(\Delta P_t'/\bar{P}_t)_2}{(\Delta P_t'/\bar{P}_t)_1} = \left|\frac{P_2 e^{in\theta}}{P_1 e^{in\theta}}\right| = \left|\frac{P_2}{P_1}\right| \tag{87}$$

The ratio of the harmonic coefficients, P_2/P_1, is found from equation (78a). Hence, with the assumption of a constant total temperature at the compressor inlet, $T_1 = 0$,

$$\left|\frac{P_2}{P_1}\right| = |t_{11} + t_{13}(U_1/P_1) + t_{14}(V_1/P_1)| \tag{88}$$

The ratios U_1/P_1 and V_1/P_1 in equation (88) are obtained from equations (81) and (82), respectively, bearing in mind that $T_1 = 0$. Equation (87) combined with equation (88) then yields the required perturbation amplitude ratio,

$$\frac{(\Delta P_t'/\bar{P}_t)_2}{(\Delta P_t'/\bar{P}_t)_1} = |t_{11} - t_{13}[(w_{31})_1 q_4 - (w_{34})_1 q_1]/D + t_{14}[(w_{31})_1 q_3 - (w_{33})_1 q_1]/D| \tag{89}$$

Isolated Rotor. Equation (89) will be used to determine the total pressure attenuation rate of an isolated rotor. It is assumed for this example that the losses in the rotor are negligible ($\bar{\omega}_R = \omega_R' = 0$) and that the relative flow outlet angle is constant, $L_R' = 0$. In addition, the mean flow upstream and downstream of the rotor is purely axial, $\bar{a}_1 = \bar{a}_2 = 0$, i.e., the rotor is windmilling in the flow and the mean lift on the rotor blades is zero. Hence also $\bar{P}_{t2} = \bar{P}_{t1}$. With these assumptions and remembering that the compressor transfer matrix in this case is equivalent to the rotor transfer matrix, equation (89) yields for the total pressure attenuation ratio, through an isolated windmilling rotor

$$\Delta P_{t2}'/\Delta P_{t1}' = \sqrt{Z_1/Z_2} \tag{90}$$

where

$$Z_1 = 4(1 - \overline{M}^2)\bar{\phi}^2 + \left\{2(1 - \overline{M}^2)\left(1 + \frac{\gamma - 1}{2}\overline{M}^2\right)^{-1} - [(1 - \overline{M}^2)(1 + \bar{\phi}^2) - \overline{M}^2]\right\}^2$$

$$Z_2 = 4(1 - \overline{M}^2)\bar{\phi}^2 + [(1 - \overline{M}^2)(1 + \bar{\phi}^2) - \overline{M}^2]^2$$

For the case that the mean Mach number $\overline{M}$ reduces to zero, equation (90) simplifies to the result obtained in [13] for incompressible flow.

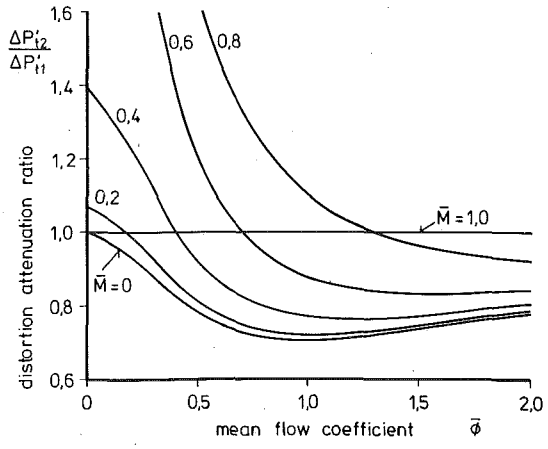


Fig. 3 Total pressure attenuation ratio for an isolated windmilling rotor

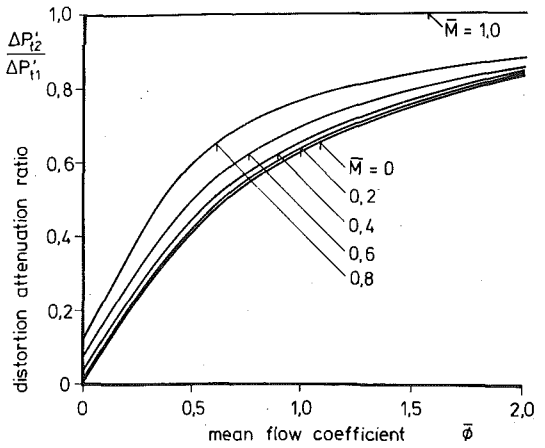


Fig. 4 Total pressure attenuation ratio for a single stage with a windmilling rotor

The attenuation ratio for the isolated rotor given by equation (90) is presented in Fig. 3. The figure shows that the highest achievable distortion attenuation decreases with increasing Mach-number. At $\overline{M} = 1$, a value of unity is obtained for all flow coefficients. It is further recognized that in order to achieve the highest possible decay rate, the flow coefficient has to be increased with increasing Mach number. This means that the rotor blades have to be opened up with increasing Mach-number, beginning with a blade stagger angle of 45 deg for $\overline{M} = 0$. Finally, it is noticed from the figure that for some combinations of $\overline{M}$ and $\bar{\phi}$ the distortion amplitude at rotor exit is higher than that at rotor inlet.

Single Stage Compressor. The isolated rotor row of the previous example may be followed by a stator row with no axial clearance between the two blade rows. It is assumed that the losses of the stator are negligible ($\bar{\omega}_S = \omega_S' = 0$) and the flow outlet angle is no function of the inlet angle, $L_S' = 0$. The blades of the stator are unstaggered and uncambered so that the mean flow enters and leaves the stator purely axial.

Equation (89) will be used again to determine the total pressure attenuation ratio through the single stage. The required single stage transfer matrix is obtained from

$$[T] = [S][R] \tag{91}$$

where the rotor transfer matrix corresponds to that of the previous example and the stator transfer matrix is obtained from the equations in the Appendix considering the assumptions made above. The result is

Downloaded 01 Jun 2010 to 171.66.16.58. Redistribution subject to ASME license or copyright; see http://www.asme.org/terms/Terms_Use.cfm

$$\frac{\Delta P_{t2}'}{\Delta P_{t1}'} = \sqrt{\frac{\bar{\phi}^2 + (1-\bar{M}^2)\left[\left(1+\frac{\gamma-1}{2}\bar{M}^2\right)^{-1} - (1+\bar{\phi}^2)\right]^2}{\bar{\phi}^2 + (1-\bar{M}^2)(1+\bar{\phi}^2)^2}} \quad (92)$$

For the case that the Mach-number $\bar{M}$ reduces to zero, equation (92) simplifies to the result obtained in [13] for incompressible flow.

The total pressure attenuation ratio of the single stage (equation (92)) is presented in Fig. 4. The figure shows that (contrary to the isolated rotor) the ratio $\Delta P_{t2}'/\Delta P_{t1}'$ has no minimum but increases continuously for all Mach-numbers with increasing flow rate. It is further recognized that the attenuation of the distortion for a specified flow rate decreases with increasing Mach number.

Application of the Model to an Eight-Stage Compressor

The model has further been applied to predict the propagation of a first-order cosine-wave total pressure distortion through an eight-stage compressor. The amplitude of the distortion at inlet is chosen to be 10 percent of the mean value and the compressor is assumed to operate at its design conditions.

The free-vortex compressor is equipped with IGVs and has a hub-to-tip ratio at compressor inlet and exit of 0.75 and 0.9, respectively. The Mach number at inlet is M = 0.6 and at exit it is M = 0.33.

The model is applied on five different radii of the compressor, including the hub, mean and tip section. The required input data for the small perturbation theory such as Mach-numbers, absolute flow angles, flow coefficients and blade row losses is directly taken from the design analysis. Since, at design conditions, all blade rows operate at the flat part of the "horse-shoe" loss curve, values of $\omega_R' = \omega_S' = 0$ have been chosen for all blade rows and blade sections. The quantities L_R' and L_S' have been (somewhat arbitrarily) assigned values which increase linearly between hub and tip from 0.06 to 0.3.

Fig. 5 shows the predicted development of the total pressure, static pressure and total temperature perturbation amplitudes along the mean section of the eight-stage compressor. It is apparent from the figure that only the rotors achieve a significant amount of total pressure distortion attenuation whereas little attenuation takes place in the stators. It is also remarkable that contrary to the behavior of the compressor described in [8] the rotors belonging to the later stages achieve a higher distortion attenuation than the rotors belonging to the front stages. At compressor exit, the total pressure distortion amplitude is only 1.3 percent of the corresponding mean value.

Contrary to the total pressure, the static pressure distortion decay is somewhat higher in the stator blade rows than in the rotor blade rows.

The lower part of Fig. 5 shows the expected build-up of a total temperature distortion in conjunction with the total pressure distortion attenuation. Of course, the total temperature distortion amplification only takes place across the rotors. At compressor exit, the total temperature distortion has an amplitude which is about 2.6 percent of the corresponding mean value.

In order to show radial differences in the distortion development due to radial variations in mean flow, losses and deviations, the model has been applied (as mentioned previously) to five different radii. For the first-order cosine-wave total pressure distortion (with a constant amplitude in radial direction) prescribed at the compressor inlet, the total temperature distortion pattern which has established itself in the plane at the compressor exit is shown by the contour-map, Fig. 6. (For an easier interpretation, the hub-to-tip ratio in this map has been expanded artificially to 0.5). The figure shows the usually observed "twisting" of the temperature "patches" defined by a given distortion intensity range.

Comparison between Theory and Experiment

Due to the lack of suitable experimental distortion data from high-speed multistage axial flow compressors with high hub-to-tip ratios, a comparison between theory and experiment has been performed for an isolated rotor and a single-stage compressor for which

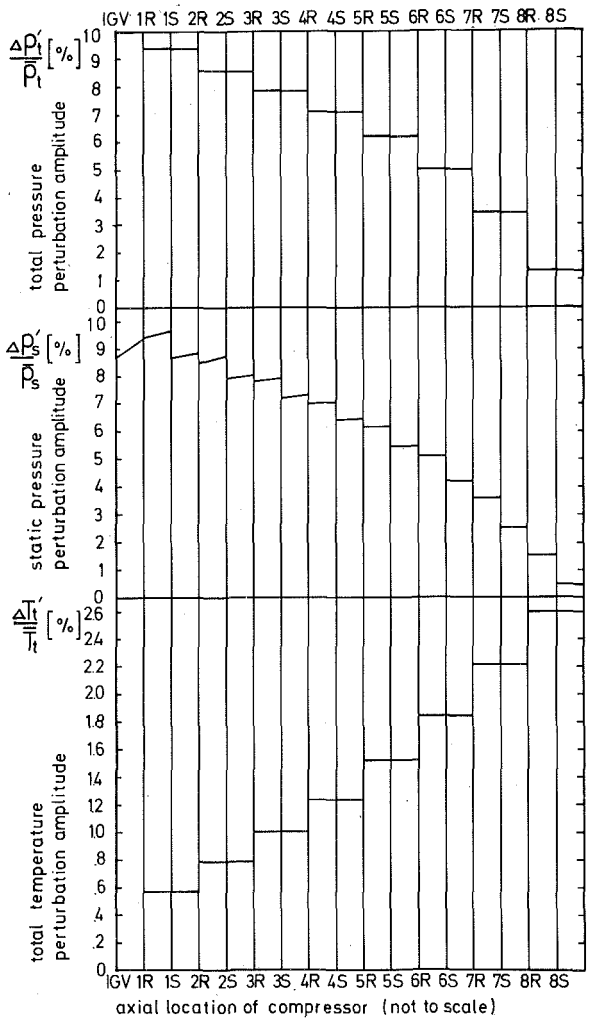


Fig. 5 Predicted development of the total pressure, static pressure and total temperature perturbation amplitudes along the mean section of an eight-stage compressor

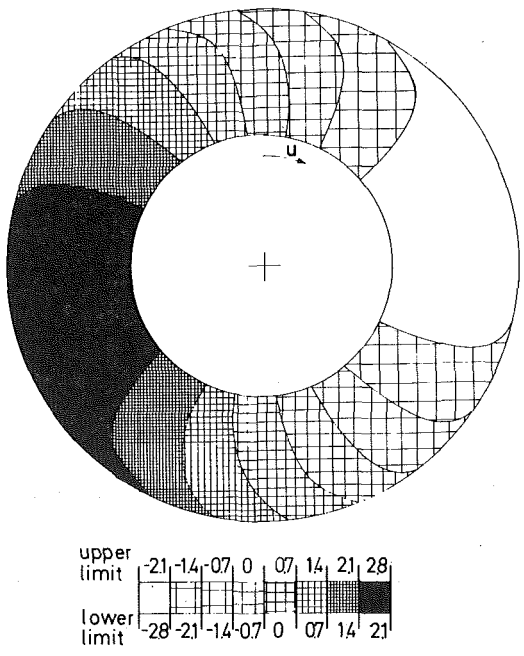


Fig. 6 Predicted contour map of the total temperature distribution downstream of an eight-stage compressor

Downloaded 01 Jun 2010 to 171.66.16.58. Redistribution subject to ASME license or copyright; see http://www.asme.org/terms/Terms_Use.cfm

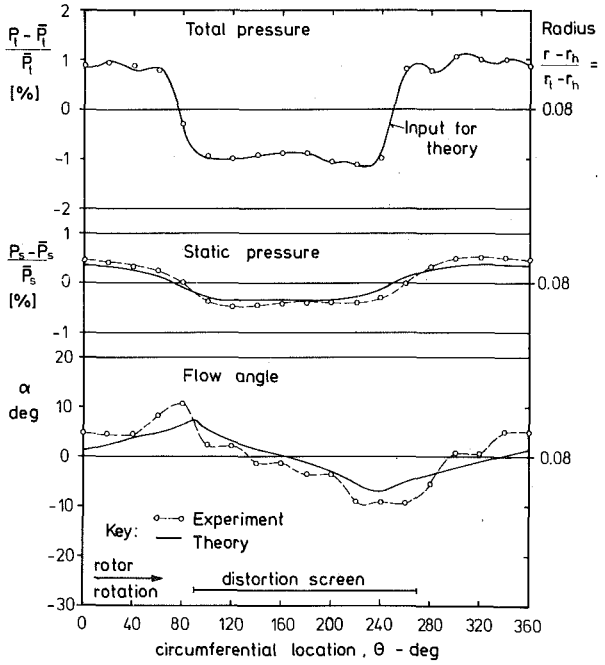


Fig. 7(*a*) Predicted and measured circumferential total pressure, static pressure and flow angle distributions at $(r - r_h)/(r_t - r_h) = 0.08$ upstream of an isolated rotor

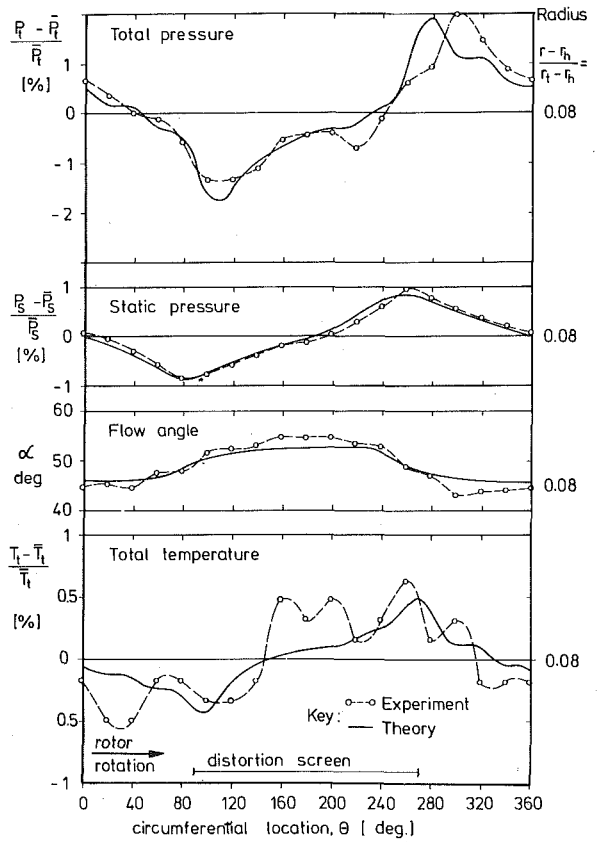


Fig. 7(*b*) Predicted and measured circumferential total pressure, static pressure, flow angle and total temperature distributions at $(r - r_h)/(r_t - r_h) = 0.08$ downstream of an isolated rotor

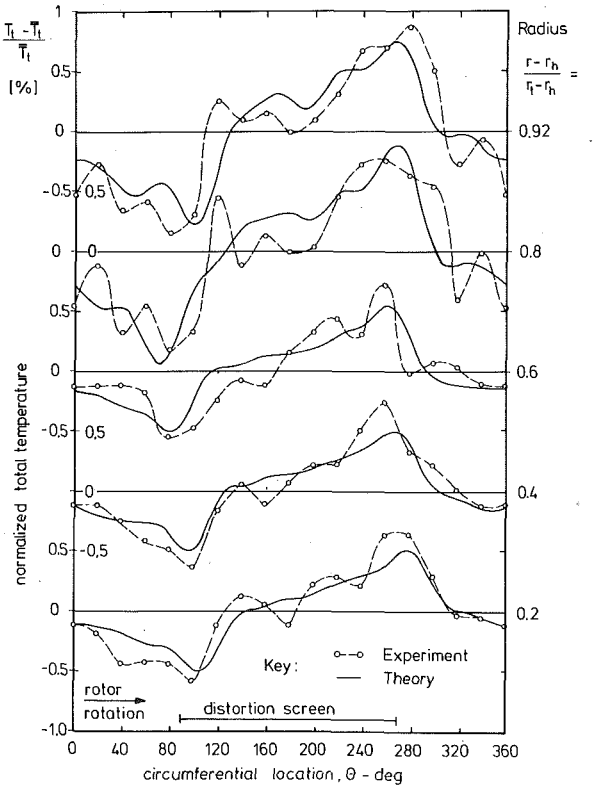


Fig. 7(*c*) Predicted and measured circumferential total temperature distributions at various radii downstream of an isolated rotor

experimental data were available. Both machines have a hub-to-tip ratio which is too low for the theory to be fully valid in these cases.

Isolated DFVLR-Rotor. The isolated rotor, used by the DFVLR for the experiments [14], has a cylindrical annulus with a hub-to-tip ratio of 0.5. The 180 deg total pressure distortion was generated by a screen about three rotor mean radii upstream of the rotor blade. Measurements were performed in planes normal to the axis 0.27 rotor mean radii upstream and downstream of the blade semi-chord position (location of the actuator disk). Readings of total pressure, total temperature and flow angles from probes in these planes were taken at the different normalized radii of $(r - r_h)/(r_t - r_h) = 0.08, 0.2, 0.4, 0.6, 0.8$ and 0.92. The static pressure in these two measuring planes was obtained from outer wall static pressure tappings. The distorted rotor was operated close to its design point. The comparison between experimental and theoretical results is restricted to the normalized radius of 0.08 (except for the total temperature). A wall-near radius was chosen so that wall static pressure measurements could be used for the comparison. The input data required for the theory was obtained from the circumferential averages of the measured distortions and also from measurements of the undistorted rotor at various mass flows.

The upper part of Fig. 7(*a*) shows the experimental points of the upstream circumferential total pressure distribution together with a Fourier-series approximation of $j = 9$ which serves as an input for the theory. Fig. 7(*a*) also shows the predicted and measured circumferential static pressure and flow angle variations upstream of the rotor.

The experimentally and theoretically obtained circumferential distributions in total pressure, static pressure, flow angle and total temperature downstream of the isolated rotor are compared in Fig. 7(*b*).

Corresponding results for the total temperature downstream of the rotor at other radii are presented in Fig. 7(*c*). It is clear from the comparison between the two-dimensional theory and the experiments that some of the differences between the measured profiles are solely due to radial variations in the mean flow, losses and deviation characteristics.

Single-stage NASA-compressor. Experimental results obtained from a single-stage compressor subjected to a 90 deg total pressure distortion are presented in [15], where a description of the experimental apparatus and test procedure can be found.

Downloaded 01 Jun 2010 to 171.66.16.58. Redistribution subject to ASME license or copyright; see http://www.asme.org/terms/Terms_Use.cfm

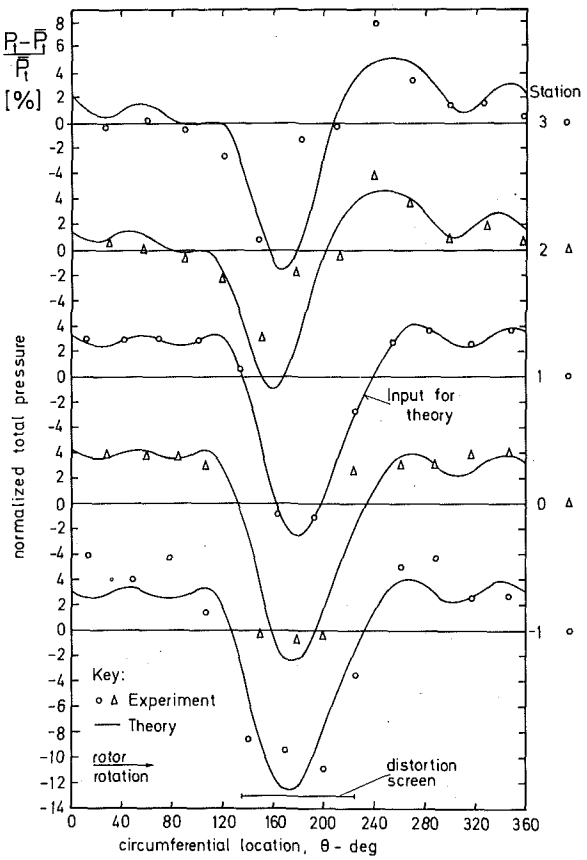


Fig. 8(*a*) Predicted and measured circumferential total pressure distributions at various axial stations of a single-stage compressor

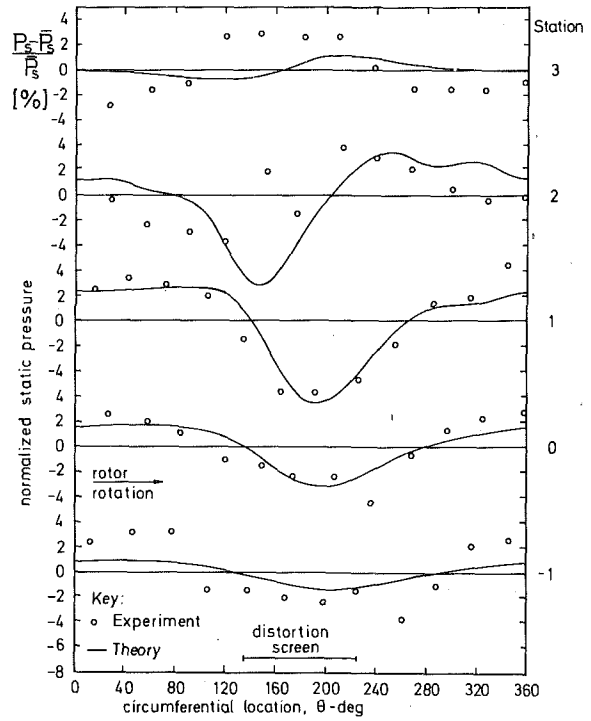


Fig. 8(*b*) Predicted and measured circumferential static pressure distributions at various axial stations of a single-stage compressor

Measurements were taken in five axial planes (stations) of the compressor at different normalized radii. Of the experimental data for the various compressor operating conditions reported in [15], only the data obtained at a normalized radius of $(r_t - r)/(r_t - r_h) = 0.45$ for 100 percent of the design speed at maximum flow was used for a comparison with theoretical results.

Fig. 8(a) shows the circumferential distribution of the total pressure measured at station 1 upstream of the compressor. A Fourier-series approximation with $j = 5$ serves as an input for the theory. The experimentally obtained total pressure distortions further upstream (stations 0 and −1), between rotor and stator (station 2) and downstream of the compressor (station 3) are compared in Fig. 8(a) with theoretical results. (Since the experimental points are further apart here than in the previous case, no attempt has been made to draw a curve through these points).

The predicted and experimental static pressure perturbations at the various axial stations of the compressor are compared in Fig. 8(b). A larger discrepancy between experiment and theory exists at the compressor exit.

In Fig. 8(c) the circumferential flow angle distributions measured at stations 1, 2 and 3 and the total temperature distribution measured at station 2 are presented together with theoretical results.

Discrepancies between experiments and theory can be attributed to three-dimensional effects, to the unsteady rotor blade response, to viscous effects and to nonlinear large perturbation effects not allowed for by the theory. In addition there may be inaccuracies in the input data for the theory as well as in the measurements.

Conclusions

A model has been developed which allows to predict the propagation of steady pressure, temperature and velocity perturbations through high-speed multistage compressors of high hub-to-tip ratio.

The model can be used for designing compressors tolerant to steady

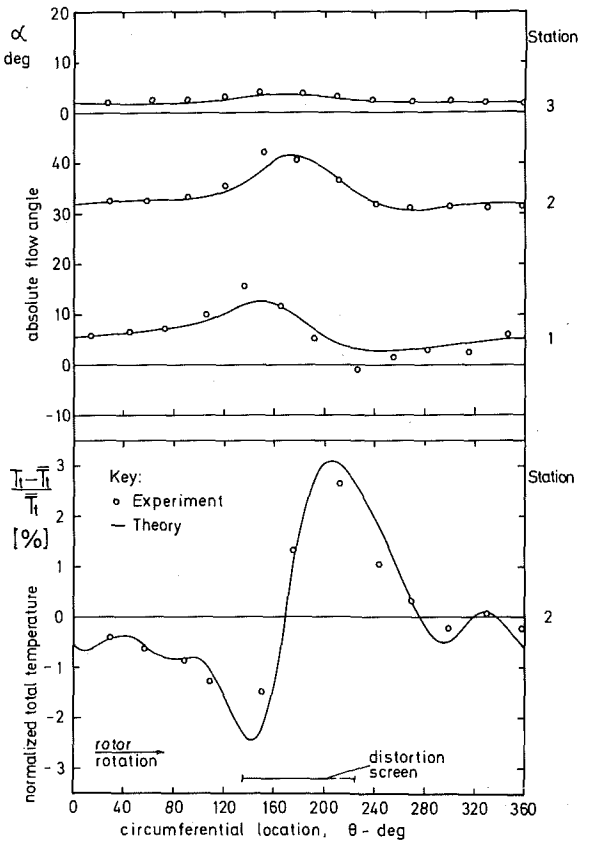


Fig. 8(*c*) Predicted and measured circumferential flow angle and total temperature distributions at various axial stations of a single-stage compressor

Downloaded 01 Jun 2010 to 171.66.16.58. Redistribution subject to ASME license or copyright; see http://www.asme.org/terms/Terms_Use.cfm

distortions. It is customary for a conventional compressor design (not accounting for distortion effects) to place a limit on the deceleration of the flow in the blade passages by imposing a safe value for, say, the diffusion factor in all radial sections of all blade rows. The above theory now provides a means to extend this rule to compressors subjected to an inlet flow distortion of prescribed intensity. Since the theory permits the circumferential variation of the diffusion factor for any blade row within the compressor to be calculated, one may now require that a safe value for the diffusion factor is not exceeded in any section of the blade row anywhere around the circumference. Variations in the basic design parameters such as blade loading, reaction ratio, Mach-number level, axial clearances between blade rows, presence of inlet guide vanes etc. can be used to achieve this goal. Because of the strong coupling between multispool compressors in the case of an inlet maldistribution, it is advisable to perform this optimisation procedure for the whole core compression system of a turbine engine.

Acknowledgments

The work reported herein was supported by the Bundesministerium der Verteidigung under Contract-No. MTU-ZTL-4.05/7 and 4.05/8. The permission to publish the results is gratefully acknowledged.

References

1 Ehrich, F., "Circumferential Flow Distortions in Axial Flow Turbomachinery," *Journal of Aeronautical Sciences*, Vol. 24, pp. 413–417, 1957.

2 Rannie, W. D., and Marble, F. E., "Unsteady Flows in Axial Turbomachines," Communication aux Journées Internationales de Science Aeronautique, ONERA, Paris, France, May 1957.

3 Katz, R., "Performance of Axial Compressors with Asymmetric Inlet Flows," Daniel and Guggenheim Jet Propulsion Center, Calif. Inst. of Tech. Report, June 1958 AFSOR-TR-58-59 AD 162-112.

4 Dunham, J., "Non-Axisymmetric Flows in Axial Compressors," *Mech. Eng. Sci. Monograph No. 3*, 1965.

5 Whitehead, D. S., "The Decay of Inlet Disturbances in the Q.E.2 H.P. Turbine," Unpublished report, Cambridge University Eng. Dept., 1969.

6 Seidel, B. S. "Asymmetric Inlet Flow in Axial Turbomachines," ASME JOURNAL OF ENGINEERING FOR POWER, Vol. 86, No. 1, 1964.

7 Fabri, J., "Growth of a Perturbation in an Axial Flow Compressor," ASME JOURNAL OF ENGINEERING FOR POWER, Vol. 101, No. 4, 1979, pp. 87–94.

8 Mokelke, H., "The Effect of Turbulent Mixing on the Decay of Sinusoidal Inlet Distortions in Axial Flow Compressors," *AGARD-CP-177*, Paper 22, 1975.

9 Krzywoblocki, M. Z., "Compressibility Effects in Circumferential Inlet Distortion in Axial Compressors," *Öster. Ing.-Archiv:* Pt. I: Vol. 13, No. 4, p. 214, 1959.

10 Elder, R., "Propagation of Time Varying Spatially Distorted Flows through Axial Flow Compressors," presented at the 6th Thermodynamic and Fluid Mechanic Convention, Durham, England, Institute of Mechanical Engineers, April 1976.

11 Wells, W. R., Tabakoff, W., and Savell, C. T., "Transmission of Circumferential Inlet Distortion Through a Rotor," AGARD-CP-177, Paper 20, 1975.

12 Johnsen, I. A. and Bullock, R. O., ed. "Aerodynamic Design of Axial-flow Compressors," NASA SP-36, 1965.

13 Mokelke, H., "Dynamic Stall Detection and Design Aids for Distortion Tolerant Compressors Using Quasisteady Actuator Disc Analysis," in *Proceedings of a Workshop* held at United Aircraft Research Laboratories, Hartford, CT, July 11, 12, 1974.

14 Lecht, M., "Experimentelle Untersuchung einer Axialverdichterstufe bei gestörter Zuströmung," DFVLR-IB352/78/6, 1978.

15 Sanger, N. L., "Performance of a 1.57-Pressure-Ratio Transonic Fan Stage with a Screen-Induced 90° Circumferential Inlet Flow Distortion," NASA TN D-8163, Feb. 1976.

APPENDIX

The (non-zero) elements of the transfer matrix (which for $x = l$ becomes the gap transfer matrix) are:

$$g_{11} = g_{22} = e^{R_1 x}$$

$$g_{31} = [(n/r)\tilde{R}_{23}e^{R_1 x} - R_2\tilde{R}_3 e^{R_2 x} + R_3\tilde{R}_2 e^{R_3 x}]/[\gamma\overline{M}_x{}^2(1+\bar{a}^2)(n/r)\times \tilde{R}_{23}]$$

$$g_{32} = [(n/r)\tilde{R}_{23}e^{R_1 x} - R_2\tilde{R}_3 e^{R_2 x} + R_3\tilde{R}_2 e^{R_3 x}]/[2(n/r)\tilde{R}_{23}]$$

$$g_{33} = (R_2 e^{R_2 x} - R_3 e^{R_3 x})/\tilde{R}_{23}$$

$$g_{34} = iR_2R_3(e^{R_2 x} - e^{R_3 x})/[(n/r)\tilde{R}_{23}]$$

$$g_{41} = (\bar{a}\tilde{R}_{23}e^{R_1 x} - i\tilde{R}_3 e^{R_2 x} + i\tilde{R}_2 e^{R_3 x})/[\gamma\overline{M}_x{}^2(1+\bar{a}^2)\tilde{R}_{23}]$$

$$g_{42} = (\bar{a}\tilde{R}_{23}e^{R_1 x} - i\tilde{R}_3 e^{R_2 x} + i\tilde{R}_2 e^{R_3 x})/(2\tilde{R}_{23})$$

$$g_{43} = i(n/r)(e^{R_2 x} - e^{R_3 x})/\tilde{R}_{23}$$

$$g_{44} = (-R_3 e^{R_2 x} + R_2 e^{R_3 x})/\tilde{R}_{23}$$

The elements of the stator transfer matrix are:

$$s_{12} = f_{12}$$

$$s_{13} = f_{13}$$

$$s_{14} = f_{14}$$

$$s_{32} = (f_{32} - d_{32} - f_{12})/(d_{33} - d_{34}d_{43})$$

$$s_{33} = (f_{33} - f_{13} - d_{34}f_{43})/(d_{33} - d_{34}d_{43})$$

$$s_{34} = (f_{34} - f_{14} - d_{34}f_{44})/(d_{33} - d_{34}d_{43})$$

$$s_{42} = -d_{43}s_{32}$$

$$s_{43} = f_{43} - d_{43}s_{33}$$

$$s_{44} = f_{44} - d_{43}s_{34}$$

The elements of the rotor transfer matrix are:

$$r_{42} = h_{43}[h_{22}(k_{32} - k_{12}) - k_{22}(h_{32} - h_{12})]/D$$

$$r_{43} = h_{22}[h_{43}(k_{33} - k_{13}) - h_{33}k_{33}]/D$$

$$r_{44} = \{h_{43}[h_{22}(k_{34} - k_{14}) - k_{24}(h_{32} - h_{12})] - h_{22}h_{33}k_{44}\}/D$$

$$D = h_{43}[h_{22}h_{34} - h_{24}(h_{32} - h_{12})] - h_{22}h_{33}$$

$$r_{32} = -r_{42}/h_{43}$$

$$r_{33} = (k_{43} - r_{43})/h_{43}$$

$$r_{34} = (k_{44} - r_{44})/h_{43}$$

$$r_{22} = (k_{22} - h_{24}r_{42})/h_{22}$$

$$r_{23} = -h_{24}r_{43}/h_{22}$$

$$r_{24} = (k_{24} - h_{24}r_{44})/h_{22}$$

$$r_{12} = k_{12} - h_{12}r_{22}$$

$$r_{13} = k_{13} - h_{12}r_{23}$$

$$r_{14} = k_{14} - h_{12}r_{24}$$

Downloaded 01 Jun 2010 to 171.66.16.58. Redistribution subject to ASME license or copyright; see http://www.asme.org/terms/Terms_Use.cfm

B. A. Folsom
C. W. Courtney
M. P. Heap

Energy and Environmental Research Corporation
Santa Ana, CA 92705

The Effects of LBG Composition and Combustor Characteristics on Fuel NO_x Formation

The low Btu gas (LBG) combined gas and steam turbine power cycle is a potentially attractive alternative to the direct coal fired steam cycle because of the potential for low sulfur emissions and high overall cycle efficiency. However, LBG may contain ammonia (NH_3) which could be converted to nitrogen oxides (NO_x) under typical combustion conditions. This paper examines the effects of LBG composition and combustor design on NO_x emissions. Low Btu gases of varying compositions were synthesized from bottled gases and fired in three atmospheric pressure flame reactors: diffusion flame reactor, flat flame reactor and catalytic reactor. Nitrogen oxide emissions were found to be most sensitive to the concentrations of NH_3 and hydrocarbon fuel gas in the synthetic LBG. Lowest NO_x emissions were produced by the diffusion flame reactor operating at near stoichiometric conditions and the catalytic reactor operating fuel rich.

Introduction

This paper examines the effects of fuel composition and combustor design on NO_x emissions from low Btu gas (LBG) fired combined gas and steam turbine (COGAS) power cycles. Although it is accepted that this country must make more use of its most abundant source of fossil fuel, coal, environmental constraints present technical and economic problems which must be overcome. The efficient utilization of coal has the potential to degrade the atmosphere due to the formation of three primary pollutants: sulfur oxides (SO_x), particulate matter and nitrogen oxides (NO_x). Because coal contains sulfur, SO_x formation is a natural consequence of the combustion process which must take place to generate steam in conventional direct-fired power plants. Coal gasification and the subsequent combustion of the product gas in a high-efficiency COGAS power cycle offers a potentially attractive alternative to direct coal combustion in conventional plants. The integrated gasifier, LBG-fired COGAS power cycle has the potential advantage that it is more economic to remove sulfur compounds from a fuel gas than from the products of complete combustion in a conventional plant. Although there are energy losses associated with gasification and fuel gas cleanup, these losses can be more than offset if the clean LBG is fired in a high-efficiency COGAS power cycle [1, 2].

A simplified schematic diagram of an integrated-gasifier, COGAS power cycle is shown in Fig. 1. The system consists of a gas turbine topping cycle with exhaust heat transferred to a steam turbine bottoming cycle through a waste heat recovery boiler. A gasifier supplied with coal, compressed air from the gas turbine air compressor and steam from the bottoming cycle produces a LBG which is cleaned before being burned in an adiabatic gas generator. Depending upon the method of LBG cleaning and the turbine inlet temperature, systems such as this are projected to have overall cycle efficiencies significantly higher (ten percentage points) than conventional direct-fired steam power plants with flue gas scrubbing [3–6].

The adiabatic gas generator and the LBG cleanup system are two of the major potential sources of atmospheric pollutants in the power cycle shown in Fig. 1. The composition and temperature of the LBG leaving the gasifier will depend upon gasifier design and operating

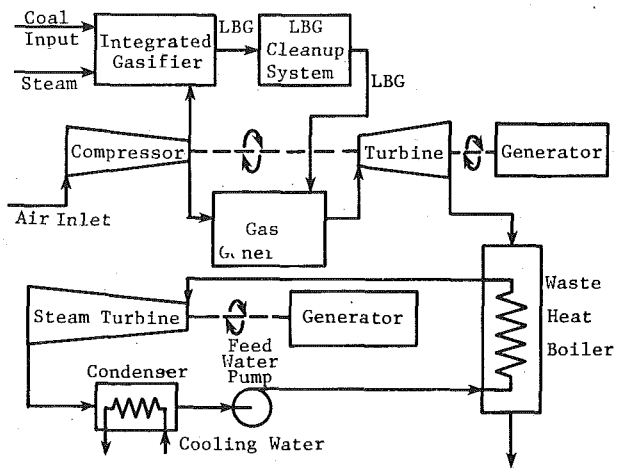


Fig. 1 Simplified schematic of basic LBG fired combined cycle power plant

conditions. The temperature of the product gas may be as high as 1370 K and will contain fuel gases such as carbon monoxide (CO), hydrogen (H_2), and hydrocarbon gases, as well as diluents such as water vapor (H_2O), carbon dioxide (CO_2), and nitrogen (N_2) [7]. The raw LBG is processed through a gas cleanup system to reduce the concentrations of sulfur compounds to levels which will give acceptable concentrations in the effluent streams. Particulates such as carbon, tars and ash must be removed from the raw LBG to prevent damage to the turbine blades, as well as to preclude their emission into the atmosphere. The raw LBG may also contain ammonia (NH_3) produced from the nitrogen bound in the organic portion of the coal being gasified. Unless suitable measures are taken to control emissions, this NH_3 is a potential source of NO_x in the combustion products of the adiabatic gas generator.

The concentration of NH_3 in the raw LBG will depend upon gasifier design and operating parameters. It may be as high as 0.38 percent by volume of the product stream [2]. If all of this NH_3 were converted to NO_x it would result in approximately 2000 ppm NO_x at dry stoichiometric conditions or 1370 ng/J (3.2 lb/10^6 Btu) NO_x, expressed as NO_2. Although there are no presently promulgated emission standards for LBG fired COGAS power cycles, it is expected that these systems will be required to at least meet the current standard for

Contributed by the Gas Turbine Division of The American Society of Mechanical Engineers and presented at the Gas Turbine Conference and Exhibit and Solar Energy Conference, San Diego, Calif., March 12–15, 1979. Manuscript received at ASME Headquarters January 11, 1979. Paper No. 79-GT-185.

Copyright © 1980 by ASME

Downloaded 01 Jun 2010 to 171.66.16.58. Redistribution subject to ASME license or copyright; see http://www.asme.org/terms/Terms_Use.cfm

stationary gas turbines (262 ppm NO_x) or perhaps the current standards for gaseous fuel fired steam generators (86 ng/J (0.2 lb/10^6 Btu) NO_2) [8]. However LBG fired COGAS power cycles will commence operation in the future when environmental restrictions may be much more restrictive than at present and thus their design goals should be to minimize emissions rather than to meet current emission standards.

There are two alternate approaches to controlling NO_x formation during LBG combustion in a COGAS power cycle. One involves removal of the NH_3 prior to combustion and the other relies upon combustor design to minimize NO_x formation. Several gas cleanup systems have been developed or are under development to remove sulfur compounds and particulates from LBG [9]. Water based gas cleanup systems, which involve cooling the LBG to near ambient temperatures (400 K), also remove a substantial amount of NH_3. Residual NH_3 levels from 100 to 400 ppm have been reported [5, 6]. The sensible heat removed from the LBG may be used for a variety of purposes, but it effectively bypasses the gas turbine topping cycle and contributes to reduced cycle efficiency. Several studies have illustrated the potential gains in cycle efficiency resulting from the use of a high temperature gas cleanup system, and subsequent utilization of the clean, high temperature LBG in the adiabatic gas generator [10, 11]. However, the high temperature cleanup systems under development at the present time remove very little or no NH_3. Thus, there are considerable economic advantages to be gained from the control of NO_x emissions via the second alternative-optimized combustor design.

Several investigators have considered the design and operation of low NO_x combustors for LBG-fired COGAS power cycles [5, 6, 10–13]. One distinguishing feature of the investigation discussed in this paper is an attempt to establish the lower bounds of pollutant emissions limited by chemistry and practical mixing constraints and not necessarily restrained by current gas turbine design constraints, which are to some extent, dictated by evolution from aircraft gas turbine systems. Although the investigation involves parallel analytical and experimental studies, the following sections are restricted to a series of experiments designed to define the influence of LBG composition and combustor characteristics upon NO_x formation from NH_3. The results of these investigations are currently being used to design bench-scale combustors for operation at pressures typical of adiabatic gas generators for COGAS power cycles.

Combustor Concepts to Minimize NO_x Formation

Nitric oxide (NO) can be formed from two sources during concombustion: the oxidation of N_2 (thermal NO_x) and the oxidation of chemically bound nitrogen contained in the fuel (fuel NO_x). As the name implies, the formation of thermal NO_x is extremely sensitive to temperature, and its formation can virtually be eliminated by restricting peak temperatures to below 1800 K. In LBG fired COGAS power cycles, thermal NO_x is usually not a severe problem. Water injection into the gasifier and heat losses from the gasifier and gas cleanup system usually result in a low LBG flame temperature and hence low thermal NO_x. However high gas turbine inlet temperatures, high compression ratios and high temperature gas cleanup systems increase residence times at high temperatures leading to increased thermal NO_x formation.

Fuel NO_x formation is relatively insensitive to temperature, and is dependent upon the quantity of fuel-bound nitrogen and the method of fuel/air contacting. Several studies have shown that the fraction of fuel nitrogen converted to fuel NO_x decreases with increasing fuel nitrogen content, and that fuel nitrogen conversion is very sensitive to reactant stoichiometry. It is generally recognized that fuel nitrogen can undergo two competing series of reactions under combustion conditions [14]. Although the precise mechanisms are unknown, these reaction series result in the formation of either N_2 or XN (where XN represents bound nitrogen species such as NO, NH_3 or hydrogen cyanide (HCN). In premixed gaseous systems almost complete conversion of the fuel nitrogen to NO has been reported under oxygen rich conditions, whereas under oxygen-deficient conditions considerable quantities of N_2 can be formed. The challenge to the designer of a combustor firing a fuel with fuel nitrogen compounds is to maximize the production of N_2, minimizing NO_x.

The conventional method of controlling fuel NO_x formation is to operate a combustor in a staged heat release mode. Heat is released in the first stage under oxygen-deficient conditions before second stage air addition completes the heat release process. Thus, the fuel nitrogen compounds initially react under oxygen-deficient conditions and temperature, stoichiometry and residence time can be optimized to maximize N_2 production. Thermal NO_x can be minimized by interstage heat removal which will minimize peak temperatures during second stage burnout.

Minimum NO_x emissions from a staged heat release process will occur if: the products of the first stage contain the minimum total XN (ΣXN) concentration, the second stage heat release process allows the minimum conversion of these XN species to NO and thermal NO_x is minimized. Thermodynamic equilibrium represents one limit on XN production in a fuel-rich primary stage and Fig. 2 shows equilibrium ΣXN concentrations as functions of reactant stoichiometry for a typical LBG composition. It can be seen that ΣXN is strongly dependent upon reactant stoichiometry, and that a minimum ΣXN concentration occurs at approximately 65 percent theoretical air. On the rich side of this minimum the XN species are primarily NH_3 and HCN, whereas on the lean side the XN species are almost totally NO. Reactant temperature will influence both the minimum ΣXN concentration and the stoichiometry at which the minimum occurs, and under lean conditions the equilibrium ΣXN concentration is very strongly dependent upon reactant temperature. The curve in Fig. 2 is typical of all hydrocarbon fuels with minimum ΣXN concentration typically below 10 ppm. This is at least an order of magnitude lower than NO_x measured in staged heat release systems involving fuels containing bound nitrogen. In real systems this difference may be due to either a kinetic limit on the decay of XN species, imperfect fuel/air mixing producing a range of reactant stoichiometries, or a combination of both of these effects.

Tyson, et al. [15] have assembled a kinetic reaction set which describes the formation of NO and N_2 in combustible mixtures of CO, H_2 and methane (CH_4). This reaction set was developed by: combining reaction subsets prepared by several investigators, tuning recommended reaction rates (within the published estimated error bands) to obtain good agreement between kinetic predictions and experimental flame data, and eliminating reactions which are not important for combustion conditions. The key reactions in this set involving XN species are listed in the following column to illustrate how under rich conditions nitrogen which is originally present in the form of NH_3 may be converted to HCN, NO, N_2 or back to NH_3.

Ammonia Breakdown

$$NH_3 + H \rightarrow NH_2 + H_2 \quad (1)$$

$$NH_2 + H \rightarrow NH + H_2 \quad (2)$$

$$NH + H \rightarrow N + H_2 \quad (3)$$

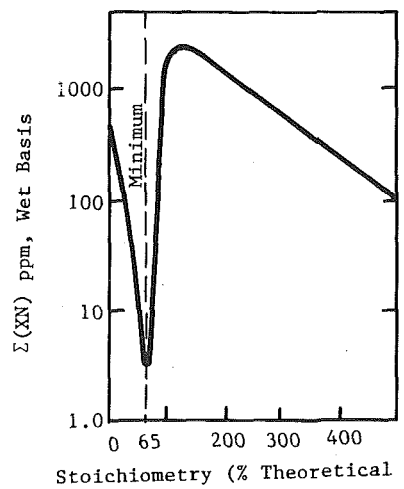


Fig. 2 Equilibrium $\Sigma(XN)$ for a typical LBG under adiabatic conditions

Downloaded 01 Jun 2010 to 171.66.16.58. Redistribution subject to ASME license or copyright; see http://www.asme.org/terms/Terms_Use.cfm

Nitric Oxide Formation

$$N + O_2 \rightarrow NO + O \quad (4)$$

$$N_2 + O \rightarrow NO + N \quad (5)$$

$$N + OH \rightarrow NO + H \quad (6)$$

Hydrogen Cyanide Formation

$$CH_3 + NO \xrightarrow[\text{and } CH_2NOH]{\text{via } CH_3NO} HCN + \ldots \quad (7)$$

$$CH + NO \rightarrow HCN + O \quad (8)$$

$$CH + N_2 \rightarrow HCN + N \quad (9)$$

XN Specie Exchange

$$HCN + OH \rightarrow CN + H_2O \quad (10)$$

$$CN + OH \rightarrow NCO + H \quad (11)$$

$$NCO + H \rightarrow NH + CO \quad (12)$$

$$NH + H_2 \rightarrow NH_2 + H \quad (2R)$$

$$NH_2 + H_2 \rightarrow NH_3 + H \quad (1R)$$

Nitrogen Formation

$$N + NO \rightarrow N_2 + O \quad (5R)$$

$$NH_2 + NO \rightarrow N_2 + H_2O \quad (13)$$

Ammonia breakdown occurs via hydrogen abstraction allowing NO formation by the oxidation of any of the XN fragments. Under fuel-lean conditions reaction (4) predominates, and the major portion of the initial fuel nitrogen compound is converted to NO. Under fuel-rich conditions NO might still be formed via reaction (4) if all the oxygen has not been consumed, or by reaction (6). Hydrogen cyanide has been observed by several investigators, and for high temperature flames, Morley [16] has shown that regardless of their nature, nitrogen compounds are quantitatively converted to HCN in the reaction zones of premixed rich hydrocarbon flames. Hydrogen cyanide formation from NO could be possible by reactions such as (7) and (8). Hydrogen cyanide could also be produced from N_2 via reaction with hydrocarbon radicals [17]. The subsequent oxidation of HCN allows the interchange of XN species since NH is one of the species formed as HCN is oxidized via the intermediary NCO. Once NH is present then the reverse of reactions (1–3) allows the formation of NH_3. Nitrogen (N_2) formation can occur via the reverse of reaction (5), or by reaction with NO and other XN species. Although reaction (13) is included there is some question as to whether a reaction of this type can take place. Since N_2 is thermodynamically favored at certain reactant stoichiometries and temperatures, the objective of the combustor designer is to provide the most favorable temperature and stoichiometry histories to maximize N_2 production and minimize the ΣXN species at the exit of the rich first stage.

Except for the practical considerations of the fuel/air contacting process, it would appear that several combustor concepts might minimize ΣXN exiting a fuel-rich combustor. These concepts can be represented by combinations of idealized, well-stirred and plug flow reactors involving heat and/or product feedback. Fig. 3 illustrates four combustor concepts which have been utilized in numerical experiments and have shown the potential for low NO_x emissions [15].

The simplest concept, A, involves a well-stirred ignition reactor followed by a long residence time plug flow reactor. The ignition reactor provides the feedback of heat and radical species for flame stabilitization. The plug flow reactor operates at an optimum stoichiometry (ϕ) allowing XN species to decay toward low equilibrium concentrations via the reactions above. Interstage heat loss between the exit of the rich first stage and the second stage burnout prevents thermal NO_x formation during the final heat release. The decay of the XN species in the plug flow reactor of concept A is kinetically limited. Since many of the reactions included have high activation energies, the rate of XN decay can be accelerated by increasing the reactant temperature [18]. Concept B involves heat feedback in the rich first stage to provide higher temperature in a rich combustion zone and maximize N_2 production.

Kinetic calculations [15] suggest that the rate of decay of XN species is initially dependent upon reactant stoichiometry; the distributed air addition concept (C in Fig. 3) allows progressive air addition with residence times at several stoichiometries. Numerical experiments with this concept have shown that progressive air addition increases the overall ΣXN decay rate over that obtained at any single stoichiometry.

The formation of N_2 from fuel nitrogen compounds might well be maximized by contacting certain species which do not normally occur simultaneously in a series staged combustor. This could be achieved by dividing the total combustor into two parallel systems with different stoichiometries, and then contacting the product streams prior to secondary burnout. This concept is termed parallel staging and is shown as concept D in Fig. 3.

Although in the limit, kinetic considerations dictate the ultimate conversion of fuel nitrogen to N_2 or NO_x, conversions in practical systems are dictated by the realities of the fuel/air mixing process. The reactants can be premixed to ensure that reaction takes place at a single stoichiometry or the fuel and air may be supplied to the combustor separately, thus allowing reaction to take place over a range of stoichiometries which will depend upon the intensity of the mixing process.

The completion of combustion in the second stage involves mixing of the rich combustion products from the first stage with additional air to complete combustion and dilute the products to the correct turbine inlet temperature. This mixing process can also occur in several stages. Since the optimum combustor design may not achieve complete minimization of XN species in the first stage, the design of the burnout reactor may be important.

The approach of this study is to build reactors which approximate the ideal reactor sequences shown in Fig. 3 in an attempt to simulate in practice the results achieved in numerical experiments. However, the designer of practical combustors must take account of practical constraints such as combustor cost, maintainability, and operability. Pressure drops must be minimized since they represent energy losses, and combustor volumes (and therefore residence times) must be kept

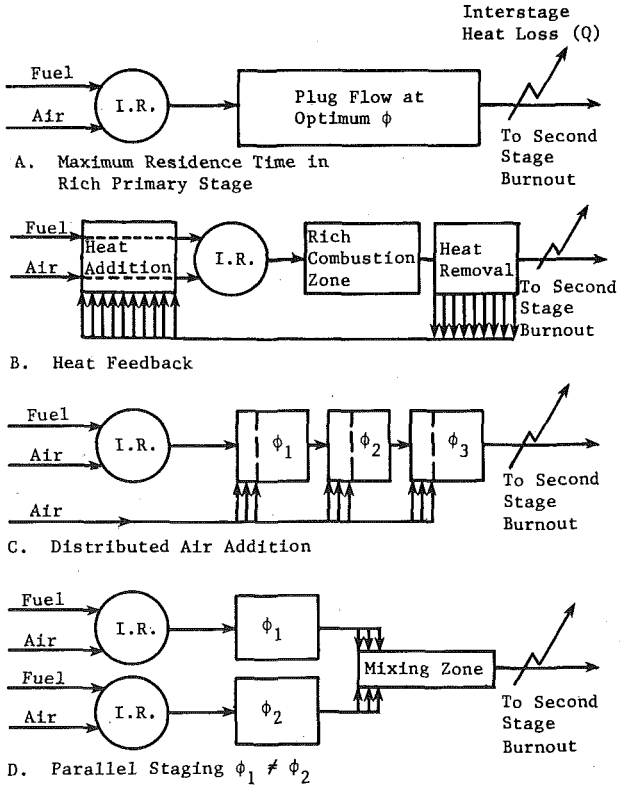


Fig. 3 Idealized low NO_x combustor concepts

Downloaded 01 Jun 2010 to 171.66.16.58. Redistribution subject to ASME license or copyright; see http://www.asme.org/terms/Terms_Use.cfm

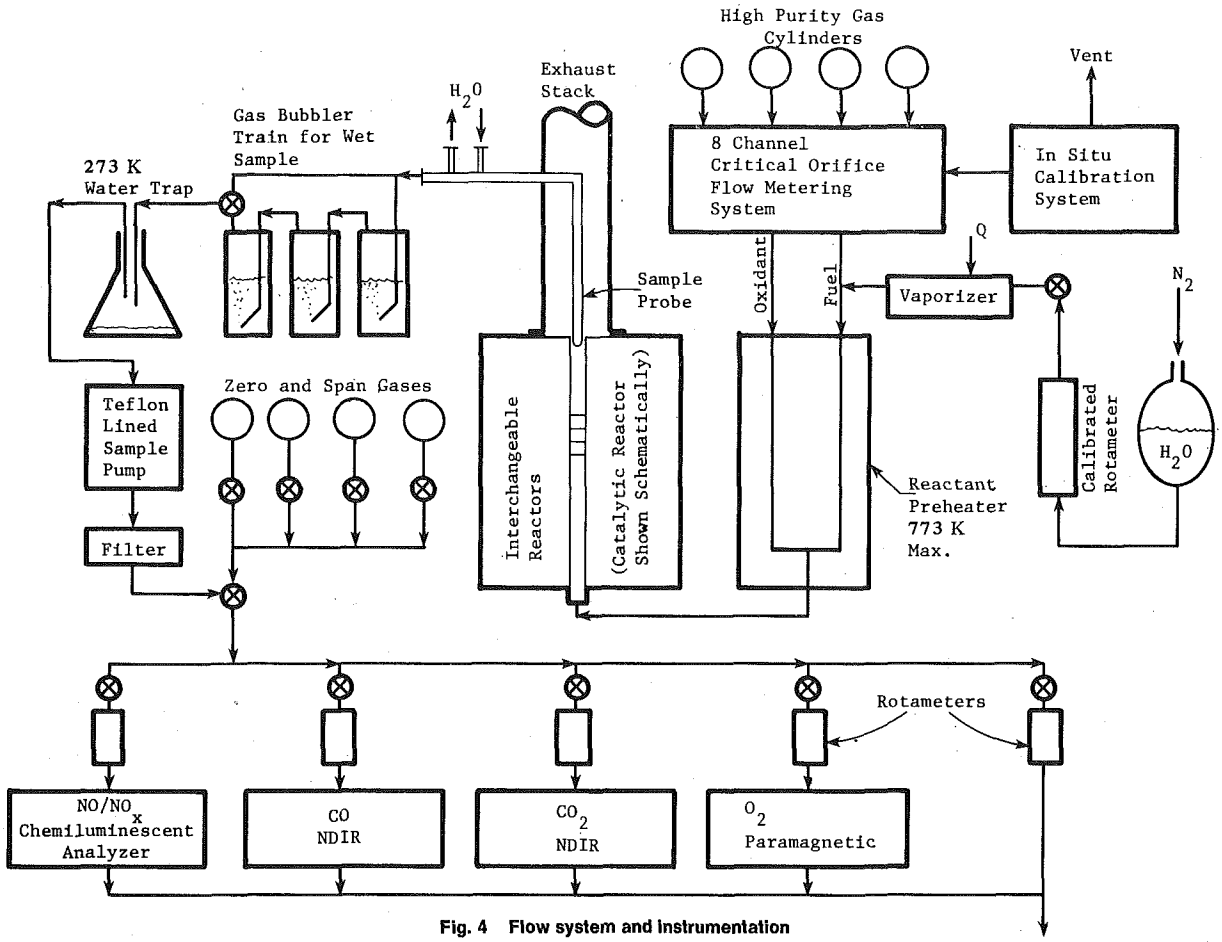


Fig. 4 Flow system and instrumentation

within bounds to reduce combustor cost and the potential for heat loss. Thus, the idealized reactor combustors must be translated into practical bench-scale combustors which satisfy practical requirements. Before the bench-scale combustors can be constructed it is necessary to establish the parameters controlling conversion of fuel nitrogen compounds in LBG to N_2. The LBG composition will vary with gasifier design, operating conditions and feedstocks and therefore one of the objectives of the initial experimental investigations has been to establish to what degree it is necessary to simulate the exact composition of a particular LBG. A second objective has been to investigate simple fuel/air contacting systems to provide information on how these systems process fuel nitrogen species. The simple combustors considered to date are: diffusion flame reactor, flat flame reactor and catalytic reactor. The XN species included in these investigations were NH_3, HCN and NO. Hydrogen cyanide and NO were included because they are representative of the XN species which might exit an initial first stage, thus providing information on second stage reactor performance.

Experimental Systems

The experimental equipment used in this investigation includes a reactant flow system, interchangeable flame reactors, and an analytical train. These components are shown schematically in Fig. 4.

Reactant Flow System. The LBGs were synthesized by blending high purity gases from cylinders. All gases were 99.7 percent purity or better with the exception of CO (99.0 percent). NH_3, NO and HCN were supplied as ±2.0 percent accuracy mixtures in N_2 to facilitate metering. The oxidant was supplied as dry air (an O_2/N_2 mixture). All gases were metered with sapphire jewel, critical orifices. Pressures upstream of the orifices were measured with high accuracy (±0.11 percent full-scale) variable-capacitance pressure transducers. The downstream pressures were maintained constant. These transducers were calibrated periodically against a common laboratory reference, and the flow rate through each orifice was calibrated by filling an evacuated reservoir. The estimated total inaccuracy in each gas flow rate was 0.5 percent. All reactants were preheated to 366 K. For the investigations involving the catalytic reactor, it was necessary to dilute the reactants with N_2 to lower the adiabatic flame temperature below the maximum operating temperature of the catalyst.

Variations in LBG H_2O content were achieved by metering distilled water with a calibrated rotameter and prevaporizing before mixing with the other reactant gases. The mixture was maintained well above the dewpoint to prevent subsequent condensation.

Interchangeable Flame Reactors. The diffusion flame reactor utilized in these experiments is shown in Fig. 5. Fuel gases entered through a stainless steel tube centered in a sintered stainless steel disk. Air passed through the sintered disk and mixed with the fuel gases by laminar diffusion. The fuel tube was 0.63 cm OD and 0.55 cm ID. A fully developed velocity profile was assured by a tube length greater than 100 diameters. Once ignited, the flame was stabilized on the fuel tube lip. The sintered disk and the surrounding enclosure were 5.0 cm dia. The surrounding tube was 91 cm long and enclosed by a water jacket to control heat losses. Combustion products exiting the reactor were mixed by several rows of stainless steel water cooled tubes normal to the flow. Samples were withdrawn for analysis downstream of this mixing section through a water cooled stainless steel probe. All water cooled surfaces were maintained at 343 to 363 K.

In the experiments reported here, the fuel flowrate was 167 cm^3/s at 366 K and atmospheric pressure. The air flowrate was adjusted as required by fuel composition to achieve 150 percent theoretical air. The resulting flames were observed with a quartz tube replacing the water cooled enclosure. All flames were laminar with lengths from 23 to 51 cm depending upon fuel composition. The Reynolds number based on average fuel velocity and fuel tube inside diameter was 1321.

The flat flame reactor is shown in Fig. 6. The premixed reactants passed through a 4.6 cm dia stainless steel sintered disk. The small pore size (20 μ) produced a uniform velocity profile. Once the reactants were ignited a thin planar flame stabilized approximately 1.0 mm above the disk. The disk was water cooled. The flat flame reactor

Downloaded 01 Jun 2010 to 171.66.16.58. Redistribution subject to ASME license or copyright; see http://www.asme.org/terms/Terms_Use.cfm

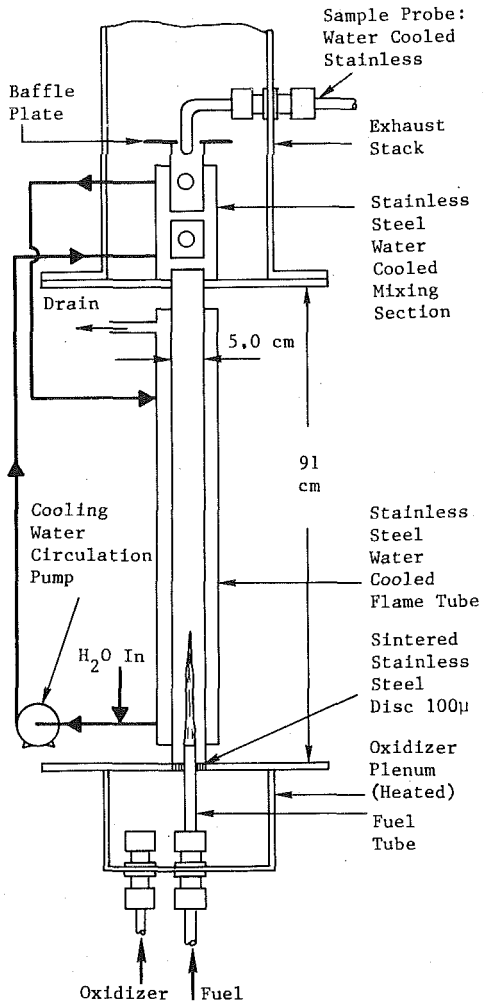


Fig. 5 Diffusion flame reactor

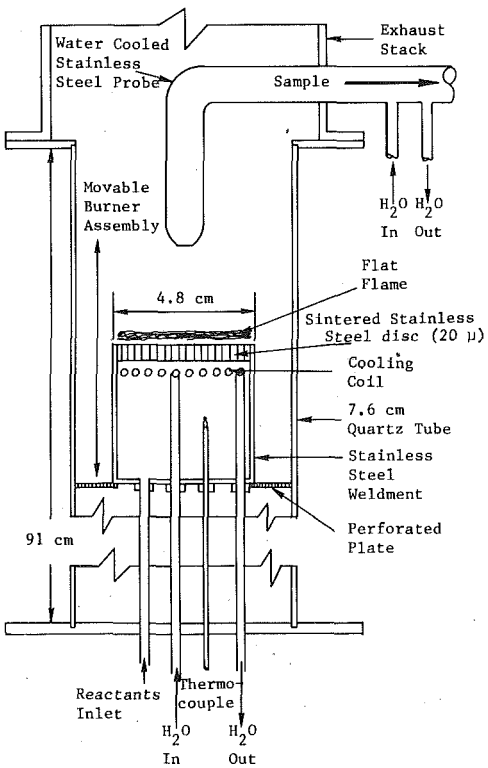


Fig. 6 Flat flame burner

was enclosed by a 7.6 cm dia quartz tube; combustion products were sampled with stationary probes. The flat flame reactor was movable axially; combustion product samples could be obtained at any desired distance downstream from the flame front.

The catalytic reactor is shown in Fig. 7. The catalyst used in these tests was a platinum coated graded cell monolith supplied by the Acurex Corporation. The desirable features of the graded cell catalyst have been discussed previously [19]. The monolith was 2.5 cm dia and included three 2.5 cm long segments of varying cell sizes. Each segment consisted of a hexagonal cell alumina monolith washcoated with alpha alumina and subsequently loaded with platinum. The maximum recommended temperature for this catalyst is 1588 K. Type K thermocouples were cemented in two of the cells in the downstream segment to monitor maximum monolith temperature.

To approximate adiabatic conditions and minimize heat loss, the catalyst was mounted in a refractory tube which was electrically backheated. The temperature between the refractory tube and the heating element was measured with a thermocouple and the heating power was controlled to maintain this temperature near the equilibrium adiabatic flame temperature of the reactants.

The reactants passed through a sintered stainless steel disk immediately upstream of the catalyst. The combustion products discharged into a 10.0 cm exhaust stack and a water-cooled stainless steel sample probe was installed to measure combustion product concentrations. The probe tip was 4.4 cm from the downstream catalyst face.

Additional details of this reactor's construction and operation are documented in [20].

Analytical Train. The same sampling and analysis systems were used for all flame reactor studies. Combustion products were sampled with a rapid quench water-cooled stainless steel probe and analyzed for O_2, CO, CO_2, NO, NO_x, NH_3 and HCN by the instruments shown in Fig. 4. Comparisons were made under fuel-rich conditions between the water-cooled stainless steel probe and an uncooled quartz sampling probe, and no effect of probe design was observed. The sample train components were constructed entirely of stainless steel, glass and teflon.

NH_3 and HCN were measured by bubbling known volumes of combustion products through three water baths in series. The absorbed NH_3 and HCN concentrations were then measured by ion specific electrodes. The other product species were monitored con-

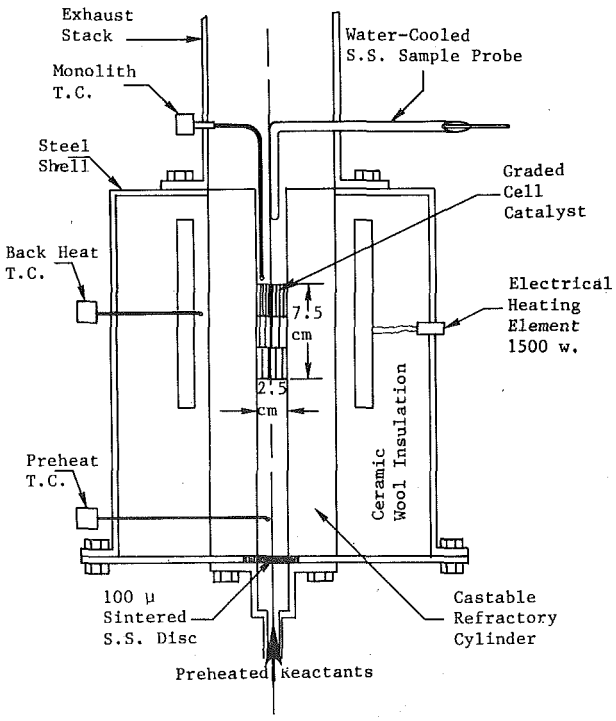


Fig. 7 Catalytic reactor housing

Downloaded 01 Jun 2010 to 171.66.16.58. Redistribution subject to ASME license or copyright; see http://www.asme.org/terms/Terms_Use.cfm

tinuously. The sample was dried to a dewpoint of 273 K in a cyclone water trap located close to the sample probe to minimize residence time between probe and trap. NO_x concentrations were measured after the sample had passed through a stainless steel converter operating at 1073 K. This converter could not be operated under oxygen-deficient conditions because of the well-known reduction of NO.

Results

The Effect of LBG Composition on Fuel Nitrogen Conversion. The experiments involving the effect of LBG composition on the formation of fuel NO_x were carried out in the diffusion flame reactor described in the previous section. Operating at 150 percent theoretical air the results presented in Figs. 8–10 show the percentage conversion of dopant in the LBG to NO_x in the combustion products. Fuel NO_x was determined to be the difference between total NO_x measured with and without dopant under the given conditions. Thermal NO_x was typically less than 50 ppm in the dry combustion products.

The presence of a hydrocarbon fuel in the LBG was found to have the most significant effect upon the conversion of NH_3 to NO_x (see Fig. 8). Without CH_4, percentage conversions were typically 5 percent of the dopant. This rapidly increased to greater than 20 percent when the fuel gas contained 5 percent CH_4. Above this concentration, further increases in CH_4 content did not have a significant effect upon fuel nitrogen conversion. It can also be seen in Fig. 8 that the influence of CO/H_2 ratio was minimal compared to that of the presence of hydrocarbon. A preliminary series of tests was also carried out with ethylene (C_2H_4) as the hydrocarbon specie. The influence of C_2H_4 on NH_3 conversion was similar to that of CH_4; however, maximum conversions were lower, typically of the order of 20 percent for an LBG containing 10 percent C_2H_4.

The partial products of combustion of the first stage in a staged heat release combustor can contain several XN species (NO, NH_3 and/or HCN) as well as CO, H_2 and a hydrocarbon fuel. The results in Fig. 8 show that the processing of a given nitrogenous specie in a LBG is dependent upon the nature of the fuel nitrogen specie. At small dopant concentrations high conversion of HCN to NO_x and high NO retention (conversion of NO to NO_x) were measured almost independent of hydrocarbon content. However at the same dopant concentration, the conversion of NH_3 to NO_x was strongly affected by hydrocarbon content.

Fig. 9 shows the effects of hydrocarbon content and dopant concentration on NH_3 and NO conversion to NO_x. With the exception

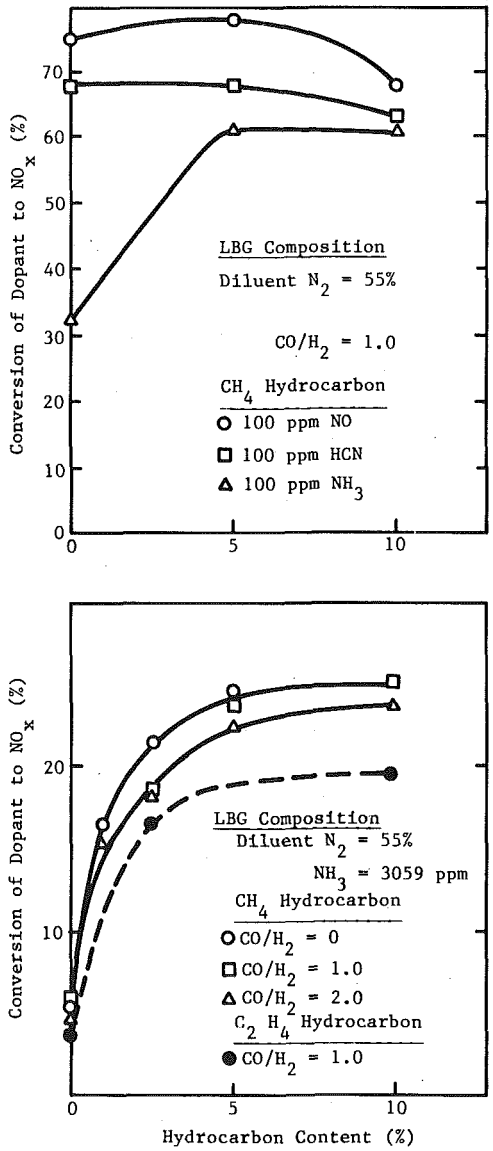


Fig. 8 Diffusion flame processing of XN as a function of hydrocarbon content and CO/H_2 ratio

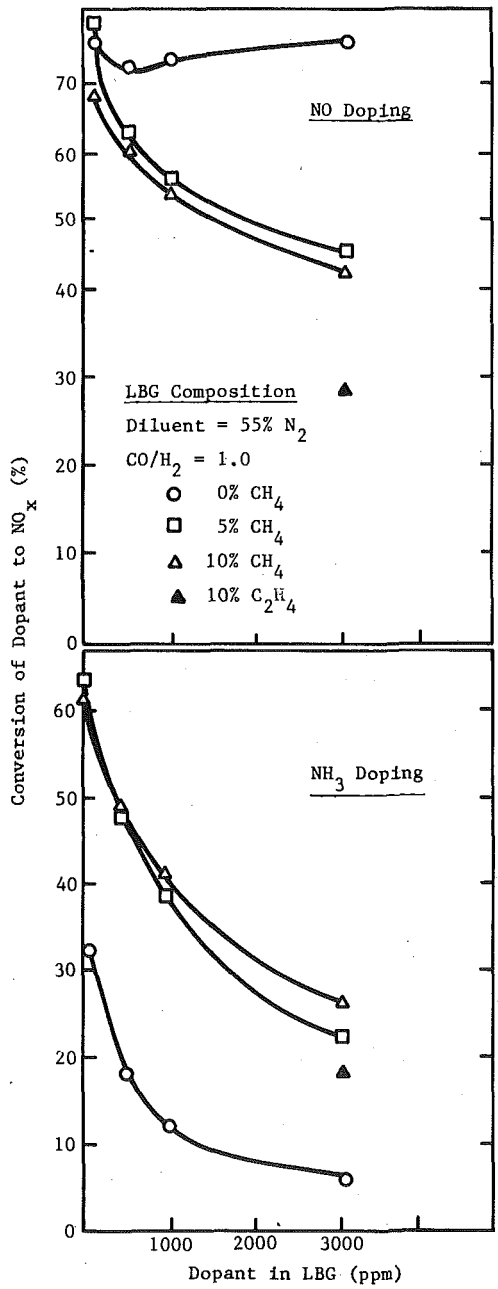


Fig. 9 Diffusion flame processing of XN as functions of dopant and hydrocarbon concentrations

Downloaded 01 Jun 2010 to 171.66.16.58. Redistribution subject to ASME license or copyright; see http://www.asme.org/terms/Terms_Use.cfm

of NO as the dopant and 0.0 percent CH_4, percentage conversion of dopants decreased as the dopant levels increased. However, the decrease in conversion was insufficient to counter the increase in XN available for conversion, and total NO_x emissions increased with dopant level. At NO dopant levels greater than 500 ppm there was a significant influence of hydrocarbon content upon fuel nitrogen conversion (NO to NO_x). This suggests that if the effluents of a rich primary contained a hydrocarbon fuel gas and NO, as the only bound nitrogen specie, significant reductions in emissions might be achieved in a lean secondary burnout stage.

The effect of a hydrocarbon fuel on the conversion of NH_3 to NO can be explained by consideration of the reactions listed above. In a laminar diffusion flame, NH_3 breakdown occurs on the fuel-rich side of the heat release zone, and N_2 formation can occur by reaction of the XN fragments. Any NO that is produced can react with these XN fragments, producing N_2 as in reaction (13). When a hydrocarbon fuel is present HCN can be produced from NO via reactions such as (7) and (8), thus effectively removing nitrogen species from the zone in which they can be more easily converted to N_2. Once HCN is produced, the XN specie exchange reactions allow the regeneration of NO as oxygen diffuses into the reaction zone.

LBG fuel gases can contain various diluent fractions. A series of investigations was carried out to check the influences of diluent composition and concentration of NH_3 conversion to NO_x in a laminar diffusion flame. Fig. 10 shows the influence of replacing N_2 diluent by either CO_2 or H_2O for a CO/H_2 ratio of 1.0 and three CH_4 concentrations. It can be seen that for both diluents there was a small increase in fuel NO_x formation as the N_2 was replaced either by CO_2 or H_2O. The heat capacity of both these diluents is greater than N_2 and the thermal NO_x decreased as the fuel NO_x increased. This slight increase in fuel nitrogen conversion could be associated with the temperature effect but is more likely due to a change in the H, O and OH concentrations in the reaction zone. Tests were also carried out varying the higher heating value of the LBG from 28,700 to 61,500 J/m by changing the percentage of N_2 in the LBG. In the absence of CH_4, a variation in heating value had little effect upon percentage conversion of NH_3 to NO_x. With 5 percent CH_4 the conversion increased from 17 to 22 percent as the heating value decreased.

The Effect of Combustor Characteristics on Fuel NO_x Formation. To measure the effects of fuel/oxidant contacting conditions on fuel NO_x formation a LBG with the composition listed was fired over a wide range of reactant stoichiometries in the three reactors described previously.

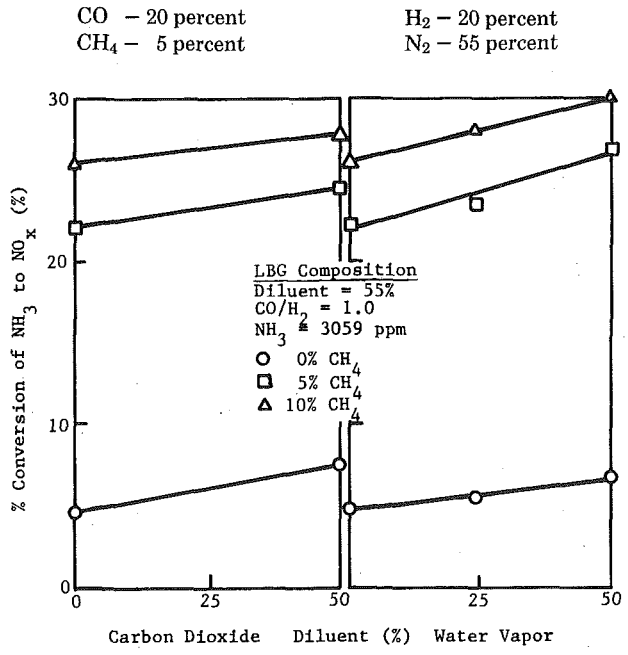


Fig. 10 Diffusion flame processing of NH_3 as a function of diluent and hydrocarbon concentration

Measured concentrations of NO, NH_3 and HCN are presented in Fig. 11. For the diffusion flame and catalytic reactors, combustion products were sampled downstream of the mixing device described previously. For the flat flame reactor, combustion products were sampled on the axis approximately 45 ms from the primary reaction zone. Axial probing traverses showed no significant variation in these concentrations over a product residence time range of 2 to 50 ms.

The results in Fig. 11 are similar for all reactors: as the percentage of theoretical air decreased, the concentration of NO in the products decreased, while the NH_3 and HCN concentrations increased.

For the diffusion flame reactor, the majority of the XN species was NO at stoichiometric conditions and NH_3 for rich conditions. Hydrogen cyanide was always small. The high NH_3 concentrations under rich conditions are probably due to flame quenching on the cold reactor walls.

In the flat flame reactor the majority of the XN species was NO from 60 to 80 percent theoretical air. Ammonia was very low and HCN increased substantially as percentage theoretical air was reduced.

With the catalytic reactor NO was the major XN specie under fuel lean conditions but decreased substantially for fuel rich conditions. Both NH_3 and HCN increased substantially as percentage theoretical air was reduced. The concentrations of HCN measured in the flat flame and catalytic reactors were almost identical.

The catalytic reactor data in Fig. 11 were obtained with the mixing device located 36.1 cm above the catalyst bed. Measurements were also made without the mixing section with the probe on the axis 4.4 cm above the catalyst bed. Fig. 12 shows a comparison between the results of these two experiments. The observed differences are difficult to explain at present, but may be associated with catalyst aging, radical variations in reactant concentrations across the catalyst bed, or reactions in the ceramic secondary tube.

Discussion

The LBG fired COGAS power cycle is a potentially attractive alternative for the efficient use of coal. One of the environmental considerations associated with this type of plant is the atmospheric pollutant emissions from the gas turbine burning the LBG. The LBG may contain NH_3 in concentrations up to 0.38 percent depending upon the method of fuel gas cleaning. This NH_3 is a potential source of NO_x in the gas turbine combustion products. It is known that the conversion of NH_3 to NO_x can be restricted by modifying the combustion process in such a way as to insure that the NH_3 reacts initially under fuel-rich conditions. The results presented in this paper represent the initial portion of a study to develop combustor concepts to minimize NO_x emissions of LBG-fired combustors. Before the development of bench-scale combustors can commence it is necessary to ascertain the parameters controlling fuel NO_x formation in LBG-fired combustors. The LBG composition will vary depending upon the gasifier design and operating parameters. Thus, if the combustor concepts are to be universally applicable then it is necessary to establish whether the combustor must be tailored to the particular fuel gas being produced. The results indicate that by far the most significant effect of LBG composition on fuel NO_x formation is the presence of a hydrocarbon gas.

Combustors which minimize fuel NO_x formation will involve some method of staged heat release. One of the design features of low NO_x combustors will be a fuel-rich primary zone designed to maximize N_2 formation from the initial fuel nitrogen specie. Kinetic considerations suggest that optimum temperature/stoichiometry histories exist to maximize N_2 production. However the practical considerations involved in fuel and oxidant mixing provide the potential for different types of combustors. A series of simple reactor experiments has been carried out with synthesized LBG to determine the influence of combustor characteristics on the processing of NH_3 in LBG. Fig. 13 compares the ΣXN (measured rich) and NO_x (measured lean) for the three reactors firing a LBG with 5 percent CH_4 doped with NH_3 and similar data for the diffusion flame reactor firing a LBG with no hydrocarbons. For the LBG containing CH_4, the diffusion flame and catalytic reactors produce comparable minimum conversions and the flat flame reactor produced much higher conversion over the range

Downloaded 01 Jun 2010 to 171.66.16.58. Redistribution subject to ASME license or copyright; see http://www.asme.org/terms/Terms_Use.cfm

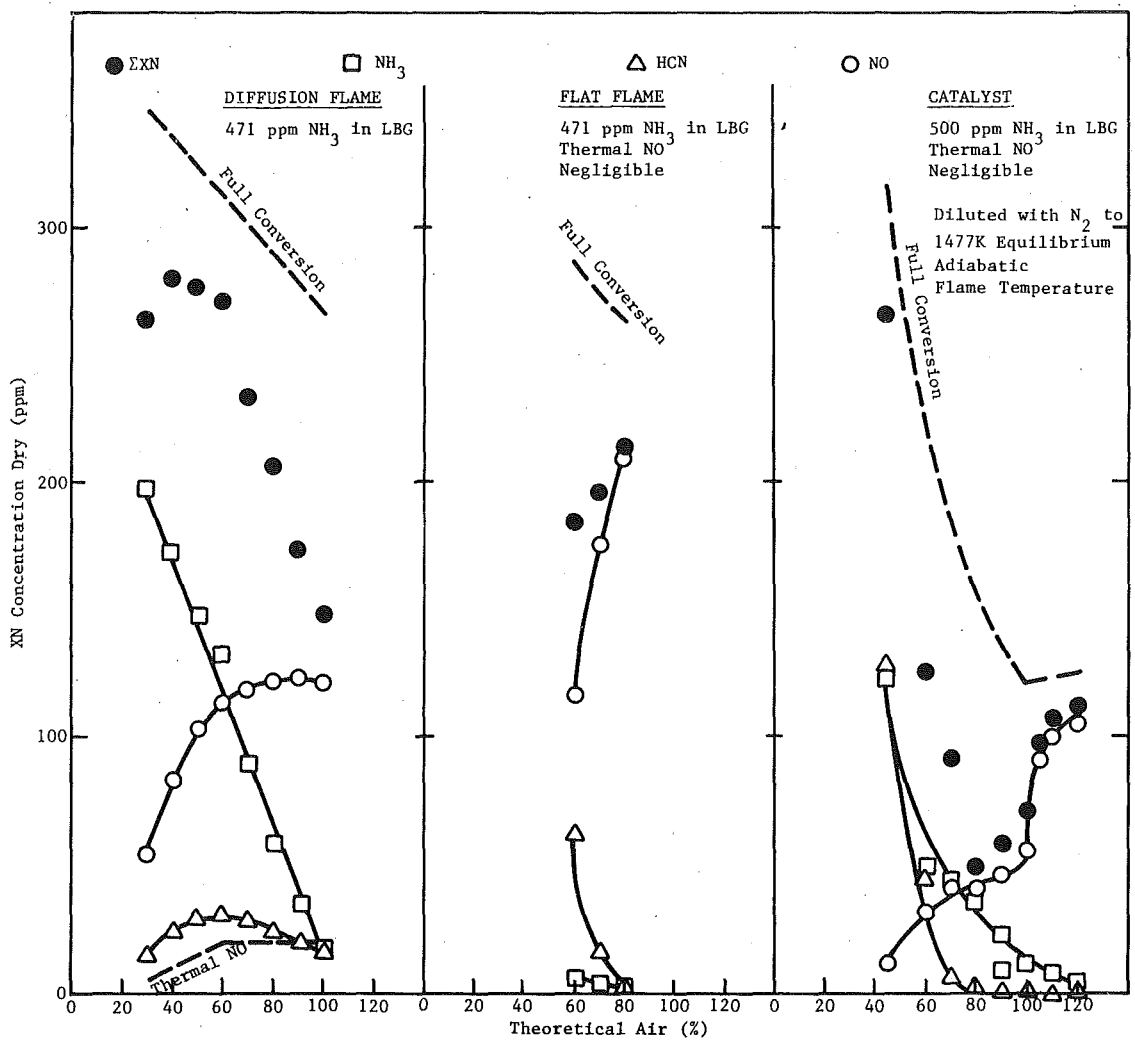


Fig. 11 NH_3 processing in three flame reactors

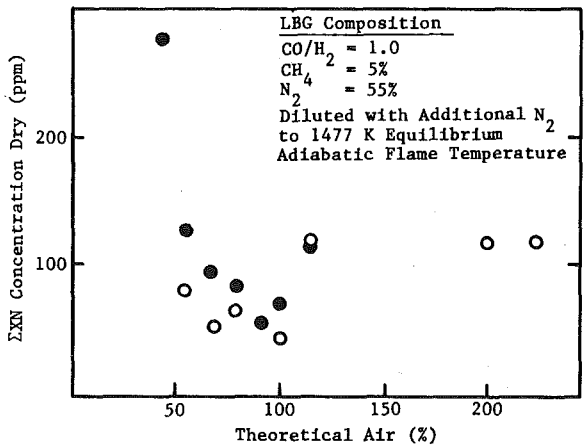


Fig. 12 Comparison of catalyst data for two sampling configurations

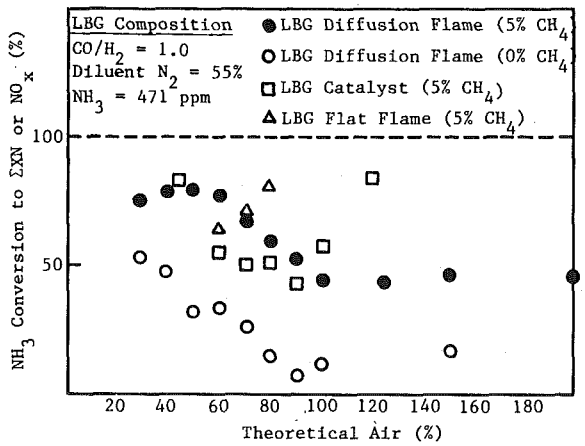


Fig. 13 NH_3 conversion to ΣXN for three reactors

of stoichiometries tested. (It could not be operated richer than 60 percent theoretical air due to flame stability.)

It is difficult to compare results from three reactors since their operational characteristics are different. The maximum operating temperature of the catalyst was 1588 K, and the undiluted reactants could not be burned between 40 and 230 percent theoretical air. Therefore, to obtain the results shown in Figs. 11–13 it was necessary to dilute the reactants with N_2 to insure that this maximum temperature was never exceeded. In a practical system this would require recirculation of cooled combustion products or heat loss from the primary section. The effectiveness of the diffusion flame is associated with its laminar condition. Fenimore, et al. [21] have carried out similar experiments with Mache-Hebra nozzles and have shown that as the flow becomes turbulent fuel nitrogen conversion increases. The results shown in Fig. 13 refer to a Reynolds number of 1321. Increasing the Reynolds number to 5286 produced a visibly turbulent flame but did not appreciably increase the conversion of NH_3 to NO_x. This can be explained only if it is accepted that at these turbulence levels the turbulent flame front provides a continuous reaction zone around the fuel stream. If turbulence levels were increased to such levels that the reaction zone were stretched and extinguished then fuel/oxidant mixing could take place without reaction and the subsequent for-

Downloaded 01 Jun 2010 to 171.66.16.58. Redistribution subject to ASME license or copyright; see http://www.asme.org/terms/Terms_Use.cfm

mation of fuel NO_x would increase. Heat release rates in conventional practical combustors are such that this phenomena is most likely to occur. Other studies [15] have shown that fuel nitrogen conversion in both liquid and solid fuels is minimized if combustion can take place in long turbulent diffusion flames anchored at the fuel injectors, and this type of naturally staged system offers one potential for low NO_x combustion systems.

The comparison presented in Fig. 13 also includes results for an LBG which does not contain a hydrocarbon. It can be seen that under these circumstances low ΣXN species concentrations are possible. It should be noted that all of the concentrations presented in Fig. 13 are in excess of the equilibrium values, indicating that the design of the post-reaction zone system is inadequate to maximize N_2 production.

Conclusions

Synthesized LBGs have been burned in simple flame reactors to investigate the influences of LBG composition and combustor characteristics on fuel NO_x formation. The most significant fuel composition effect is the hydrocarbon content of the LBG. Fuel NO_x formation from NH_3 is minimized if the hydrocarbon content is zero. However, if the initial fuel nitrogen specie is NO then its reduction to N_2 is maximized by the presence of a hydrocarbon gas. This difference between NH_3 and NO has significance for the design of second stage burnout combustors. The LBG diluent and CO/H_2 ratios were found to have a minimal effect on fuel NO_x formation.

Acknowledgment

The work upon which this publication is based was conducted under Contract No. 68-02-2196 with the Environmental Protection Agency. The authors wish to express their appreciation to Messrs. J. Johnsen and J. Keene of Energy and Environmental Research Corporation for their assistance in various portions of the work.

References

1 Fluor Engineers and Constructors, Inc., "Gasification-Combined-Cycle Power Plants," *EPRI Journal*, July/Aug. 1978, pp. 43.

2 Robson, F. L., Blecher, W. A., and Giramonti, A. J., "Combined-Cycle Power Systems," EPA-600/2-76-149, U. S. Environmental Protection Agency, Washington, DC, 1976, pp. 359.

3 "Evaluation of Phase 2 Conceptual Designs and Implementation Assessment Resulting from the Energy Conversion Alternatives Study (ECAS)," prepared under Interagency Agreement E(49-18)-1751, NASA Report No. TM X-73515.

4 Shaw, H., Cerkanowicz, A. E., and Tung, S. E., "Environmental Assessment of Advanced Energy Conversion Technologies—Interim Report, Vol. 1, State-of-the-Art," Contract No. 68-02-2146, U. S. Environmental Protection Agency, Cincinnati, OH, 1977.

5 Harris, L. P., and Shah, R. P., "Energy Conversion Alternatives Study (ICAS), General Electric Phase II Final Report: Vol. II, Advanced Energy Conversion Systems—Conceptual Designs: Part 3, Open Cycle Gas Turbines and Open Cycle MHD," General Electric Report No. SRD-76-064-2, NASA Report No. NASA CR-123929, 1976.

6 Beecher, D. T., et al., "Energy Conversion Alternative Study (ECAS), Westinghouse Phase II Final Report: Vol. II—Combined Gas-Steam Turbine Plant Using Coal-Derived Fuel," Westinghouse Report No. 76 9E9-ECAS-R2v.2, NASA Report No. NASA CR-134942, 1976.

7 Boodle, W. W., "Introduction to Modern Processes," Clean Fuels from Coal Symposium, published by Institute of Gas Technology, 1973.

8 Environmental Protection Agency Title 40, Chapter 1, Subcharter C, Part 60-Standards of Performance for New Stationary Sources, Federal Register, Vol. 36, No. 247, Dec. 23, 1971.

9 Dravo Corporation, *Handbook of Gasifiers and Gas Treatment Systems*, NTIS Report No. FE-1772-11, Feb. 1976.

10 Tyson, T. J., et al., "Low NO_x Combustion Concepts for Advanced Power Generation Systems Firing Low-Btu Gas," EPA-600/2-77-235, U. S. Environmental Protection Agency, Washington, DC, 1977.

11 Folsom, B. A., et al., "Evaluation of Combustor Design Concepts for Advanced Energy Conversion Systems," *Proceedings of the Second Stationary Source Combustion Symposium*, Vol. 5, Addendum, EPA-600/7-77-073, July 1977.

12 Martin, G. B., "NO_x Considerations in Alternate Fuel Combustion," EPA-600/1-76-149, U. S. Environmental Protection Agency, Washington, DC, 1976, pp. 373.

13 Heap, M. P., et al., "Environmental Aspects of Low Btu Gas Combustion," 16th Symposium on Combustion, The Combustion Institute, 1977, p. 535.

14 De Soete, G., "La Formation Des Oxydes D'Azote Dans La Zone D'Oxydation Des Flammes D'Hydrocarbures," No. 23 309, Institut Francais De Petrole, France, June 1975.

15 Tyson, T. J., et al., "Fundamental Combustion Research Applied to Pollutant Control," First Annual Report, EPA Contract 68-02-2631. In preparation.

16 Morley, C., "The Formation and Destruction of Hydrogen Cyanide from Atmospheric and Fuel Nitrogen in Rich Atmospheric-Pressure Flames," *Combustion and Flame*, Vol. 27, 1976, pp. 189–204.

17 Myerson, A. L., "The Reduction of Nitric Oxide in Simulated Combustion Effluents by Hydrocarbon-Oxygen Mixtures," 15th Symposium (International) on Combustion, The Combustion Institute, Pittsburgh, PA, 1975.

18 Sarofim, A. F., Pohl, J. H., and Taylor, B. R., "Mechanisms and Kinetics of NO_x Formation Recent Developments," Paper presented at 69th Annual Meeting AIChE, Chicago, Nov. 1976.

19 Kesselring, J. P., Krill, W. V., and Kendall, R. M., "Design Criteria for Stationary Source Catalytic Combustors," EPA-600/7-77-073c, U. S. Environmental Protection Agency, Washington, DC, July 1977, pp. 193.

20 Folsom, B. A., Courtney, C., and Heap, M. P., "Environmental Aspects of Low Btu Gas-Fired Catalytic Combustion," *Proceedings of the Third Workshop on Catalytic Combustion*, Oct. 3–4, 1978.

21 Fenimore, C. P., "Effects of Diluents and Mixing on Nitric Oxide from Fuel-nitrogen Species in Diffusion Flames," 17th Combustion Symposium published by the Combustion Institute, pp. 1065.

Downloaded 01 Jun 2010 to 171.66.16.58. Redistribution subject to ASME license or copyright; see http://www.asme.org/terms/Terms_Use.cfm

J. Stringer
Project Manager.

S. Ehrlich
Program Manager.

W. W. Slaughter
Project Manager.

A. C. Dolbec
Program Manager.

Fossil Fuel and
Advanced Systems Division,
Electric Power Research Institute,
Palo Alto, CA

Assessment of Hot Gas Clean-Up Systems and Turbine Erosion/ Corrosion Problems in Pfbc Combined Cycle Systems

Alternative methods of producing electricity from coal while maintaining acceptable environmental standards are currently being examined in detail. One such method involves the fluidized bed combustion of coal at elevated pressure, using an acceptor in the fluidized bed to remove the sulfur. Steam is raised using heat exchangers within and above the bed, and the hot combustion gases are expanded through a gas turbine. A serious limitation on this system is the ability to reduce the particulate loading in the combustion gases to a level at which a gas turbine having acceptable life can be constructed. The turbine may be either a new design or a modification of a currently available engine, and palliatives include lowering the turbine inlet temperature, lowering the gas velocity through the turbine, and "hardening" the turbine by the selection of appropriate materials or claddings for the vanes and blades. In this paper, the various degradation processes are considered, with emphasis on erosion, and the probable limits of particulate loading in the gas stream are estimated. These estimates are discussed in relation to existing hot gas particulate removal systems, and directions for further study are suggested.

Introduction

The electric utility industry's objective in developing a coal-fired combined-cycle power plant is to provide a more efficient alternative to the conventional coal-fired power plant equipped with flue gas desulfurization. Three systems are being evaluated by three different EPRI programs:

1 A direct coal-fired ceramic heat exchanger with a closed-cycle turbine [1].

2 Coal gasification combined with a high-temperature clean-gas turbine [2].

3 A pressurized fluidized-bed combustion (pfbc) boiler combined with a pressure recovery turbine, operating on a moderately dirty gas [3].

It seems to us too early to compare these three technologies (although some have tried [4]); each offers potential advantages. The gasification route should offer higher overall efficiency, the direct-fired heat exchanger may offer simplicity, and the pfbc may offer lower capital costs.

EPRI recently initiated a pfbc subprogram, partly as a response to the potential impact of new air quality regulations on conventional pulverized-coal (pc) boilers. Data show that SO_x and NO_x emissions can be low without the addition of a post-combustion clean-up system. However, particulate emissions present a potential problem: EPA has discussed a standard of 0.03 lb/10^6 Btu (approximately 0.02 gr/scf; 0.04 g/sm^3; 36 ppm), which is 70 percent lower than the existing New Source Performance Standard. However, the gas clean-up requirements for a technically feasible pfbc plant may be even more stringent, because the pressure recovery turbine might not survive a dust loading as high as that, although this has yet to be established. It follows that if the pfbc plant costs stay relatively constant, the pfbc option will become more attractive as the cost of conventional plants increases with the addition of more post-combustion clean-up equipment. In addition, under the elevated pressure conditions present in some pfbc concepts, regeneration of the spent SO_2 sorbent may be technically and economically feasible. This is becoming an increasingly important requirement because of emerging regulations affecting by-product disposal and land use. The regeneration of lime at elevated pressures does not appear feasible [5], but there has been a very encouraging result with MgO [6].

Fig. 1 shows the essential features of a pfbc combined-cycle plant. Coal and a sorbent (usually a dolomitic limestone or high-calcium lime; but in view of the result referred to above MgO may be preferable) are crushed to size (~2 mm) and are fed to a pressure lock for transport into the pfbc boiler. At the bottom of this boiler furnace is an air distributor. The fluidized bed, made up of particles of coal ash and sorbent, has some liquid-like properties (even though the particles, of course, remain solid). For example, the fluidized bed flows around the heat exchange (steam generating) tubes almost as if the bed were a liquid.

Coal will burn in a fluidized bed when the temperature of the bed particles is above 600°C (1112°F). Start-up is accomplished by spinning the gas turbine and igniting the oil-fired start-up burner just

Contributed by the Gas Turbine Division of The American Society of Mechanical Engineers and presented at the Gas Turbine Conference and Exhibit and Solar Energy Conference, San Diego, Calif., March 12–15, 1979. Manuscript received at ASME Headquarters January 15, 1979. Paper No. 79-GT-195.

Copyright © 1980 by ASME

Downloaded 01 Jun 2010 to 171.66.16.58. Redistribution subject to ASME license or copyright; see http://www.asme.org/terms/Terms_Use.cfm

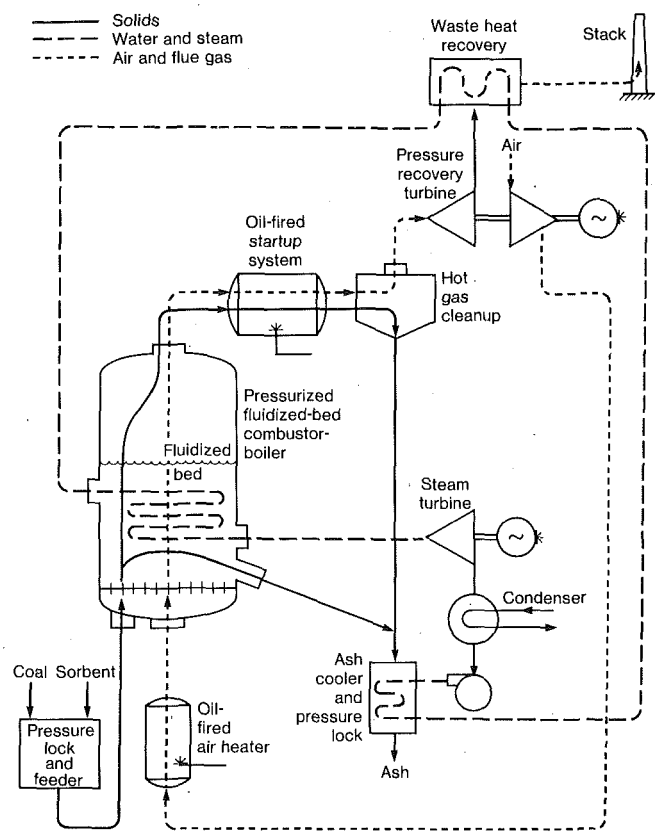


Fig. 1 Pfbc power plant system, showing the hot gas cleanup system for protecting the pressure recovery turbine

as if it were a conventional combustion turbine. The compressed air is heated with a second oil burner before it reaches the fluidized bed, and the bed temperature rises. Once coal flow starts, the bed temperature rapidly reaches design temperature, usually in the range 800–900°C (1472–1652°F). Obviously, this is an over-simplification, but the fundamentals should now be clear.

Exhaust from the pfbc

The gas composition of the exhaust from a pfbc depends on the excess air. For an afbc a value of approximately 20 percent is not uncommon. At the other extreme an adiabatic pfbc, in which there is no heat exchange surface in the bed and the bed temperature is controlled by the air flow, may have 300 percent excess air. Because of the low combustion temperature the concentration of nitrogen oxides will be low, typically 150 ppm. The presence of the acceptor results in a relatively low SO_x concentration: a typical value is 300 ppm. However, because of the low combustion temperature it seems possible that the SO_3/SO_2 ratio may be higher than in a pc boiler: since this reaction is sluggish the ratio is seldom at equilibrium for any combustion system. Several equilibrium thermodynamic calculations have been performed for fbc off-gases: Fig. 2 shows a typical example taken from the work of Keairns, et al. [7]. From the point of view of gas turbine corrosion the alkali metals are very important. The alkali metals are present in coal as chlorides and in clay minerals, for example illites and feldspars. It is believed that at the low combustion temperatures in the fbc the minerals will not be decomposed, although this does not seem to have been clearly established. The chlorides however (and perhaps some of the other alkali metal salts) can be carried in the gas stream, either as the vapor phase or as aerosol particles. Attempts have been made to analyze the content in the gas streams from several combustors: typical values lie in the range 0.3–3 ppm combined Na + K; in industrial gas turbine practice 1 ppm would be regarded as the maximum normally possible in the fuel, corresponding to 0.3 ppm or less in the exhaust gases. This subject was discussed at length in the program conducted by Combustion Power Company (CPC) [8]. More recently, Spacil and his colleagues at G.E.

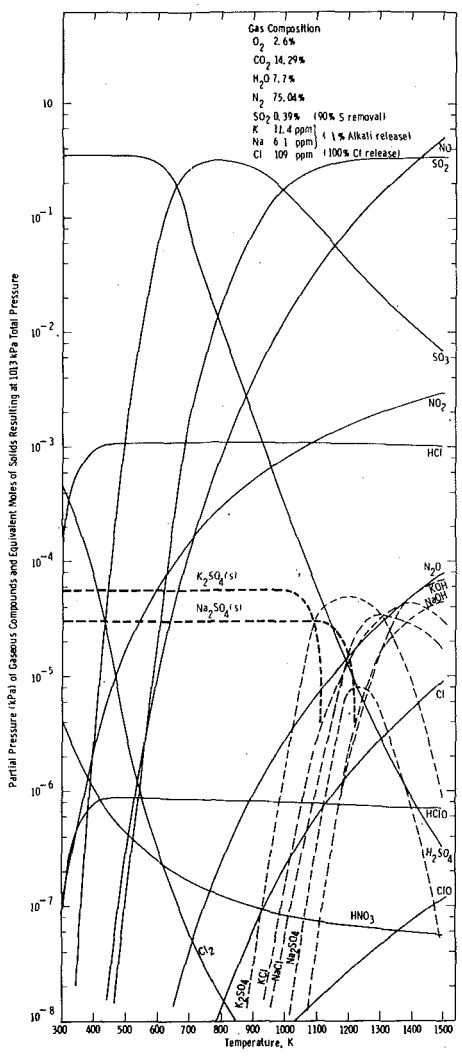


Fig. 2 Equilibrium species concentration in fluidized bed combustion gaseous effluent

have conducted a theoretical study of the alkali release processes, and have concluded that the alkali metal content of the gas is a function of the chlorine content of the coal: Fig. 3 shows their results [9] compared with experimental data from the pfbc at the Coal Utilization Research Laboratories (CURL) of the National Coal Board (NCB) in the U.K.

The particulate loading in the off-gas varies greatly with the fluidizing velocity, the detailed design of the combustor, the height of the freeboard and so forth. A typical value is 25 gr/scf (55 g/sm^3). The particulates in the off-gas have a composition not greatly different from that of the bed: a typical composition for a bed using a limestone acceptor would be 10 percent CaO, 40 percent $CaSO_4$, 25 percent SiO_2, 15 percent Fe_2O_3, 10 percent Al_2O_3 (the carbon content is normally less than 1 percent). Some of the Al_2O_3 and SiO_2 may be combined as alumino silicates. In a pfbc the acceptor would normally be dolomite, but apart from the additions of magnesium compounds the composition should not be too different. Unlike the fly ash from pc boilers the ash particles from the fbc have not been fused, and will have undergone fewer chemical changes: it is generally believed that this will make them less abrasive, although the evidence for this is not conclusive.

Degradation Mechanisms in the Turbine

There are three possible degradation mechanisms in the turbine: erosion, fouling and corrosion. They are not independent, and indeed positive synergisms have been demonstrated. For the purposes of the present paper only the erosive damage will be reviewed in detail, since this largely determines the demands on the particle removal

Downloaded 01 Jun 2010 to 171.66.16.58. Redistribution subject to ASME license or copyright; see http://www.asme.org/terms/Terms_Use.cfm

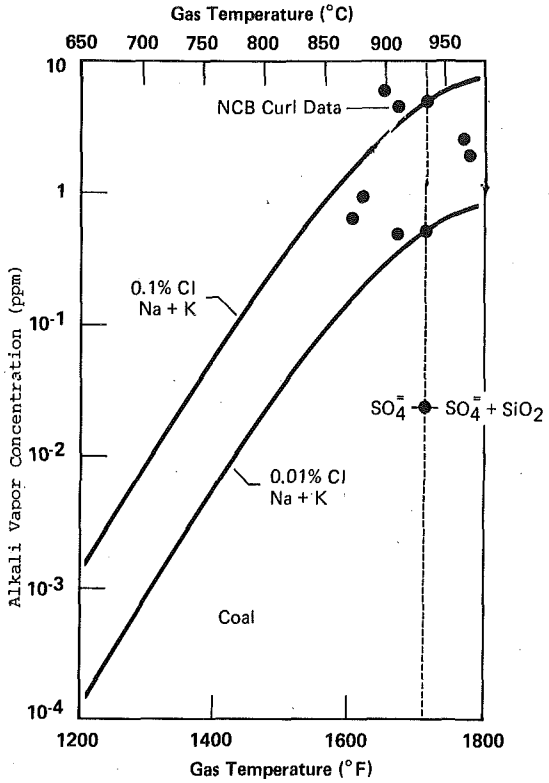


Fig. 3 Alkali vapor concentration Na + K as a function of gas temperature for PFBC

system.

There is quite an extensive experience with erosion in coal-burning gas turbines, which has been summarized in some detail by Lackey [10]. The early work in the United States was conducted by the Locomotive Development Committee (LDC) of Bituminous Coal Research Inc. The later stages of this work used an Allis Chalmers gas turbine designed for locomotive use. Between 1951 and 1958 this operated for more than 4000 hr at a turbine inlet temperature of 1250°F (677°C) but three partial rebladings due to erosion damage were required in that period. However, reducing the turbine inlet temperature to 1050°F (566°C) resulted in negligible fouling or erosion in 500 hr operation. In 1959 the engine was transferred to the U. S. Bureau of Mines research center at Morgantown, W. Va., and G.E. designed and constructed new blades. The early testing had frequently resulted in very severe localized erosion, and this was attributed to the concentration of the particles into a small part of the gas stream due to centrifuging action at bends in the gas path. Redesigning the gas path and the use of shields has helped to combat this. At Morgantown, a pulverized coal combustor was used, followed by a multicyclone designed to reduce the particle loading to 0.12 gr/scf of particles between 2 and 20 μm in size, but it partially plugged during at least some of the tests.

The changes recommended by G.E. [10, 11] are, firstly, to encourage ash to concentrate at the outer sidewall rather than at the roots of the rotor blades since wear at the rotor blade tips is less damaging than at the highly stressed roots and, secondly, to use titanium carbide wear strips at certain key locations.

Detailed changes designed to accomplish the first of these objectives included:

(1) Provision of an axial space between the first-stage stator and rotor blades to centrifuge ash particles towards the outer casing by main stream gas flow. This was achieved by removing rotor row 1 and stator row 2 from the six-stage turbine, converting it to a five-stage turbine.

(2) Redesign of the stator blades to minimize flow separation and end whirls by the use of new profile shapes and a higher solidity.

(3) Increasing the thickness of the trailing edge of the rotor blades to the maximum value (3.0 mm) consistent with turbine efficiency to encourage ash flow radially outward from the inner diameter.

The modified turbine operated for 878 hr with a turbine inlet temperature of 666°C (1230°F); the run was ended by the build-up of deposits on the first-stage stator blading. The turbine was cleaned, and a second test of 1085 hr run under the same conditions. After the first period, the first-stage stator blades showed little visible evidence of erosion. Blades in stages 2 to 5 were significantly eroded at the outer sidewall bases. Large curlicues of hard bonded ash gradually built up between the bases of the first stage stator blades, eventually blocking the gas flow and forcing an end to the test. The rotor blades were in excellent condition. After the second test the results followed a similar pattern: the ash build-up was not as heavy, but the erosion of the stator blades was more severe. This increase in erosion was attributed to the multicyclone blocking referred to above.

The effective lifetime of the rotor blades was estimated to be 20,000 hr and that of the stator blades 5000 hr. These figures were estimated to be 50 percent higher for a properly operating multicyclone. It was concluded that a satisfactory operation (minimal deposits and erosion) for a direct coal-fired gas turbine could be obtained for a particulate loading of approximately 100 ppm (0.06 gr/scf) with a size range of 10–15 percent plus 10 μm and 1–2 percent plus 20 μm at a turbine inlet temperature of 740–1060°F (394–571 °C).

Margulis [12] reported on some early work of Alco to test the erosion resistance of a range of alloys for a coal-burning gas turbine. The test assembly was the turbo supercharger of the Alco four-cylinder diesel engine; the turbine wheel consisted of 53 small blades. The test was a "rainbow" test in which the blades were made from a number of different alloys: generally four blades of each alloy were tested, mounted 90 deg apart on the wheel. The turbine inlet temperature was in the range 1250–1300°F (677–704°C). The turbine was driven by the exhaust gas from the diesel engine, and fly ash was injected into the gas stream. Approximately 42 percent of the ash was over 20 μm, 39 percent below 10 μm; this relatively coarse ash was used with the deliberate intention of accelerating the test. The ash flow density was calculated to be approximately 1 gr/scf (1800 ppm). The relative mean blade gas velocity was computed at 770 fps (235 m/s).

Of the alloys studied, austenitic steels and nickel base alloys generally exhibited poor erosion resistance; cast alloys such as Haynes Stellite 3 (Co-30Cr-12W-2C) were usually much better than the wrought alloys. Of the usual gas turbine alloys, Haynes Stellite 31 (Co-25Cr-10Ni-7.5W-0.5C) was the best; its performance was further improved by carburizing the surface. Diffusion coatings of chromium were also very effective in reducing wear, although they were brittle and had a tendency to spall. Margulis nevertheless concluded that the results were sufficiently encouraging to predict that "blade life of commercially acceptable levels can be obtained in turbines which are specifically designed for this application."

The Aeronautical Research Laboratory (ARL) of the Department of Supply, Melbourne, Australia conducted a program on coal-burning gas turbines over the period 1948–1970 [10, 13] using a Ruston and Hornsby TA turbine. The early work used a coal-fired test rig based on an aircraft supercharger, and produced little evidence of erosion, but revealed a serious ash deposition problem; this was however believed to be sensitive to the blade design. In 1958 the TA turbine was installed, and run with a maximum turbine inlet temperature of 650°C (1202°F).

After 20 hours running, the power output had decreased 2.5 percent; inspection revealed a severe build-up of ash on the stator leading edge. Erosion of the stator and rotor blades occurred in both stages of the compressor and power turbine: the first row averaged 0.62 mg/cm^2 hr (approximately 6 mm/yr recession rate), the second row averaged 2.15 mg/cm^2/hr (2.2 cm/hr). The power turbine was also eroded, but the extent was less.

Incomplete combustion very greatly increased the deposition rate of the ash. A second test of the same duration was run using a multicyclone separator. The material entering the separator was approximately 50 percent carbon; that leaving was virtually pure ash; the dust loading of the exit gas was 340 ppm (0.19 gr/scf), with 4 percent above 20 μm and 26 percent above 10 μm. The deposition was changed

Downloaded 01 Jun 2010 to 171.66.16.58. Redistribution subject to ASME license or copyright; see http://www.asme.org/terms/Terms_Use.cfm

considerably, with none of the hard sintered deposit on the first row stators found in the first test. Erosion was also much reduced, and confined to a "scouring" process over the trailing half of the pressure (concave) face of the blade. The average erosion rates of the two rotors in the compressor turbine was reduced to 0.04 mg/cm^2/hr (0.4 mm/yr recession rate).

Next, a 203 hr test was run, in which the turbine was cleaned by water washing while feeding crushed apricot stones for two minutes every ten hours. In general, the erosion rate was less in the longer test, although there were some localized increases which were attributed to the changes in blade shape as a consequence of all the earlier testing. The Nimonic 80A (Ni-20Cr-2Ti-1A1) blades exhibited clear signs of corrosion beneath the ash deposit near the blade tips.

The early tests were performed with a brown coal; the following series was with a low ash bituminous coal. At the end of the first 17 hr test there was damage to eight of the cyclones caused by after burning within the separator; these were blanked off. The erosion rates in the compressor turbine were some four times those with the brown coal. As an example, the particulate loading in the better tests was of the order of 300 ppm with a mean particle size at the entry to the first stage stator of 6–8 μm; the particle size at the entry to the third stage (the power turbine) was 5–7 μm. Of the materials examined, the original Nimonic 80A exhibited the highest erosion rate; a hard chromium plating gave the best results; but some surface failures occurred due to thermal cracking and crazing of the chromium layer.

As a result of the initial testing, it appeared that, using a low ash coal and ash separation, the life of blades in the compressor turbine would be between 2500 and 5000 hr. The life in the power turbine was at least an order of magnitude greater, and it was noted that the major difference between the two was the gas velocity, which was approximately 1100 fps (355 m/s) in the compressor turbine and 800 fps (244 m/s) in the power turbine. The compressor turbine was accordingly redesigned to have velocities of approximately 800 fps (244 m/s). This involved extending the compressor turbine to three stages. The work output was shared equally between the three stages, because this results in approximately equal velocities in each stage. In addition, the trailing edge thickness of both stator and rotor blades was increased to 0.060 in. (1.5 mm). To reduce the tendency of the ash to separate to the inner diameter, mid-span stator wake fences were built into the stator blades. The rotor blade platform was extended, and the stator blade tips were recessed into the inner boundary below the level of the rotor blade root, so that most erosion caused by the particles in the tip vortices would occur on the blade platform rather than on the blade itself. Finally, the Nimonic 80A material of the original was replaced with Haynes Stellite 31.

The erosion rate was initially high, but quickly levelled off to a steady-state rate: in the first stage this was approximately 0.020 mg/cm^2/hr (2 mm/yr recession rate), with some 20 kg per hr ash passing through the turbine. Chromized HS31 blades eroded at a rate approximately one-fifth of this. Based on a detailed examination of the wear patterns and a criterion for useful life of a reduction in the trailing edge thickness to zero, the estimated mean lifetime for the rotor blades was a minimum of 31,000 hr, and for the stators a minimum of 25,000 hr for untreated HS31 blades. A similar quantitative estimate was not possible for the chromized components since their wear did not appear to have stabilized. It was noted that the wear pattern varied around the stator row, demonsfrating the importance of the inlet volute design in gas turbines operating on dirty gases.

A pressure recovery turbine was first used in conjunction with a catalytic regenerator in an oil refinery in 1950. The first unit was installed by the Elliott Company in Ohio, and at the end of 750 hr operation the single-stage turbine was considered virtually useless [10, 14]. No separation equipment was installed ahead of the turbine, although presumably there were two stages of internal cyclones within the regenerator itself. In 1957 the Shell Oil Development Company installed a gas turbine driven air compressor in the East Montreal refinery [10, 15]; a separator was installed ahead of the turbine. The inlet temperature was 1100°F (594°C) and the unit was operated for 4000 hr, at the end of which there was only minor polishing of the blades. To demonstrate the effect of the separator it was removed, and the engine run again; after 650 hr the turbine efficiency dropped from 79 to 49 percent. There was severe erosion of both stator and rotor blades. In 1962 the Shell Oil Company began installation of power recovery turbines in both new and existing refineries. The particle loading entering these turbines is of the order of 150 ppm (0.1 gr/scf). Blades have been fabricated from tungsten carbide flame coated A-286 (Fe-26Ni-15Cr-2Ti-1Mo-0.3V) for 620°C (1150°F) service, and Inconel X (Inconel X-750? Ni-15Cr-7Fe-2Ti-1Nb-0.7A1) for 650°C (1200°F), and have a life expectancy of 25,000–35,000 hr without significant power reduction caused by erosion.

The Combustion Power Company [8] has used an adiabatic pfbc to combust coal in conjunction with a Ruston and Hornsby TA-1500 gas turbine; the bed temperature was approximately 1570°F (854°C) and the turbine inlet temperature was 1400°F (760°C). The particle separation system consisted of three stages: in one test the first stage had two 36 in. tangential entry cyclones; the second stage two 30 in. cyclones; and the final stage 100 3 1/2 in. reverse flow inertial tubes. A variety of separator configurations was examined. There was persistent trouble with plugging in the final stage, and for the latter tests the inertial tubes were removed. It is interesting to note that holes were worn in some of the separators, presumably due to erosion.

The dust loading to the turbine was of the order of 2–3 lbs/10^6 Btu (approximately 1–2 gr/scf). The erosion of the stator blades showed a very considerable peak opposite the point of entry; in the second stage stator this peak was displaced about seven blades (approximately 33 deg). The highest rates observed were approximately 0.3 mg/cm per kg of dust ingested: the values in the Australian work in the same units varied from 0–0.07 in the original (unmodified) turbine. Little variation was observed in the different alloy and alloy/coating combinations tried, but at these really rather high rates in untypically severe conditions that is scarcely surprising. It does imply, however, that the efflux from the pfbc may not be noticeably less erosive than conventional pc fly ash.

Barkalow and Pettit [16] have developed a simulator rig for studying gas turbine erosion and combined erosion/hot corrosion. The rig consists of a small combustor burning distillate fuel: the exhaust gases pass over a group of cylindrical specimen pins arranged radially; the specimen assembly can be rotated about the axis of the apparatus and, if necessary, individual specimens may be cooled by means of air blown down axial holes. This apparatus has been used for studying erosion processes using a number of typical gas turbine alloys and coatings. The metal temperature for most of the early tests was 871°C (1600°F); the nominal gas velocity at the specimen was 275 m/s (900 fps), but the blocking effect of the fully loaded specimen holder reduced this to 200 m/s (655 fps). The abrasive medium in the early tests was alumina (Al_2O_3) with average particle sizes of 20 μm, 2.5 μm and 0.3 μm; tests were also run with 8 μm MgO and several fly ashes and fbc dusts. The 20 μm particles (size range 8–38 μm) at a loading of 130 ppm (0.07 gr/scf) produced severe erosion: the alloys lost between 200 and 400 mg/cm^2 in 50 hr. This corresponds to an average recession rate of approximately 4–8 cm/yr; however, the rate of removal is markedly dependent on impingement angle, the maximum loss occurring at an impact angle of about 40 deg; below 15 deg no erosion is apparent. As a result, local erosion rates were as high as 20 cm/yr.

With 2.5 μm alumina (size range 0.3–7 μm) at a loading of 300 ppm (0.16 gr/scf) the weight losses were significantly reduced; but specimens still lost between 30 and 80 mg/cm^2 in 30 hr (1–3 cm/yr). Whereas with the coarse erodent there was little systematic difference between the different materials systems, with the finer powder those systems forming Al_2O_3 oxide scales were eroded significantly less than those forming Cr_2O_3 oxide scales. The 0.3 μm alumina particles caused no erosion. Instead, they deposited on the leading edges of the specimens.

The 8 μm MgO produced erosion one-half to one-sixth of that produced by the 2.5 μm Al_2O_3. M_gO was selected because its hardness (Mohs 4½) was believed to be closer to that of the particulates in coal combustion gases than α-Al_2O_3 (Mohs 9). It appears probable that the particle hardness does indeed have a substantial effect on erosion,

Downloaded 01 Jun 2010 to 171.66.16.58. Redistribution subject to ASME license or copyright; see http://www.asme.org/terms/Terms_Use.cfm

but that even the softer particles can result in unacceptable damage rates.

The initial experiments with fbc particulates failed because they were injected into the gas stream at a position where the temperature was high enough to melt them: they then deposited on the specimen surfaces. The injection system has been changed to allow injection further down the gas stream, and examination of the particles before and after passing through the rig confirms that no melting appears to have taken place. With dust taken from the second cyclone of a pfbc having an average particle size of 20 μm there was substantial build-up of ash on the leading edge [17] similar to that observed with the 0.3 μm alumina. Adjacent areas showed superficial signs of erosion, but the amount did not seem to be substantial; however these tests are still in progress and the evaluation is far from complete. Barkalow and Pettit also noted that when a mixture of sodium and potassium sulfates was injected into the combustion gases together with 2.5 μm Al_2O_3 to simulate combined erosion and hot corrosion, the damage was significantly greater than the sum of the damage produced by the erosive and hot corrosive environments separately.

At BCURA, a test was run [18] in which the combustion gases from a 6 atm pfbc were expanded through a gas turbine nozzle guide vane cascade and over a set of pin specimens. The gas was passed through two cyclones and at the cascade contained 250 ppm particulate (0.14 gr/scf); the gas temperature was 871°C (1600°F) and the velocity at the cascade 407 m/s (1338 fps). The size distribution of the particulates was quoted as 95 percent less than 10 μm, 85 percent less than 5 μm. After 204 hr operation no erosion of either the blade cascade or the pins was observed, although hot corrosion was experienced.

However, Zellars, et al. [19] exposed four alloys as wedge-shaped specimens to the exhaust gases from the NASA pfbc; this operated at 0.58 MPa (84 psia); the local gas velocities were 150 and 270 m/s (500 and 885 pfs); the temperatures 730 and 795°C (1350 and 1460°F); the solids loading was 2–4 g/m^3 (1–2 gr/scf); the particulates were in the range 1–30 μm. All the materials suffered both erosion and hot corrosion under these conditions. The surface recession rates were as high as 75 cm/yr at the higher velocity. Reducing the velocity by a factor of 1.8 reduced the erosion rate by a factor of between 3 and 7.

General Electric has exposed airfoil shaped specimens to the exhaust from the Exxon miniplant pfbc during a 100 hr shakedown test [20]. The gases were passed through particulate separation devices before entering the turbine test section, where the particle loading was 0.04 gr/scf (75 ppm) particles 5 μm and above; smaller particles totalled about 0.1 gr/scf. Very significant erosion was observed. However, later testing has resulted in very little apparent erosion [21].

Westinghouse reviewed the problem of using dust-laden gases in gas turbines [22, 23]. The gas stream was assumed to contain 0.01 gr/scf (18 ppm) of particulates, 80 percent of which were below 1 μm, 1.25 percent in the range 5–10 μm, and none above 10 μm. This gas was then considered to have passed through the 60 blade first stage of a typical industrial turbine, at a gas temperature of 870°C (1600°F) and a pressure of 1.0 MPa (150 psia), for gas velocities of 500 pfs (~150 m/s) and 1000 fps (~300 m/s). The surface recession rates were then calculated to be 1 and 10 mils per year (0.02–0.2 mm/yr). The higher value was regarded as unacceptable.

Westinghouse has also developed computerized models for evaluating erosion and deposition in gas turbines [24]. An important point which emerges from this work is that reducing the size of components by geometrical scaling increases the erosion rate; for a large utility turbine, one-fourth scale first stage vanes can experience three times the erosion of the full-scale vane for 9 μm particles. In discussion Tabakoff [25] questioned the use of the Westinghouse model, and remarked that a major source of damage of the first stage blades is rebound particles from the second stage.

General Electric specifications for fuel gases for turbines [26] require that they should not contain more than 30 ppm (0.017 gr/scf) of solid materials, and of this not more than 1 percent by weight shall have a terminal settling velocity in air of 14 in. per minute (this is about 7 μm dia particles for a material with density 4 g/cm^3), and not more than 0.1 percent have a settling velocity in excess of 23 in. per min (9 μm).

To summarize: it appears that acceptable lives of gas turbine vanes and blades can be obtained with particulates in the gas stream. However, the particle loading may have to be even lower than that likely EPA limits, perhaps as low as 0.01 gr/scf. Since the off-gas from the combustor can be as high as 25 gr/scf, this implies an efficiency of 99.96 percent in the particulate removal system. It is generally agreed that erosive damage diminishes abruptly below a certain size; it seems likely that 10 μm particles can produce erosion, and 1 μm particles will result in little damage where the limiting value is dependent on the detailed characteristics of the particles themselves. Hard particles cause more erosion than soft particles, but the differences are not very great in the hardness range likely to be encountered in different ashes and dusts.

Design aspects are of great significance. The flow of gas has to be designed to avoid concentration of the particulates both at the inlet from the combustor and within the turbine itself. The erosion does not seem to depend greatly on temperature within the typical range for industrial gas turbines, but it does depend very much on velocity: redesigning to reduce the maximum gas velocity (to perhaps 800 fps) would clearly be beneficial but may not be cost effective.

Under very severely erosive conditions there are only limited differences between different metallic materials, but as the conditions become less severe significant differences begin to emerge, suggesting that optimization of materials, and in particular of surface coatings or treatments, may result in useful extensions of lives. This also points out the danger of using unduly severe conditions in developmental testing in the hope of reducing test times.

The limited information available suggests that ceramic materials such as silicon nitride have very much better erosion resistance than any metallic material.

This summary has concentrated on erosion. Fouling is clearly also a problem, and it appears that it can occur even at temperatures well below the particulate melting temperature for very small particles. Because the very smallest size particles are of the greatest importance in fouling, and these are the most difficult to remove, this problem should it prove to be important may have to be dealt with by appropriate turbine cleansing procedures.

Hot corrosion has been discussed at length in several recent publications, and is not expressly considered here except to note that it has been observed in pfbc off-gases after quite short times; turbine materials will have to have adequate resistance to this form of attack. In addition, the presence of a corrosive medium greatly accelerates erosion.

Hot Gas Clean-Up Systems

Several hot gas cleaning techniques are currently being considered to reduce the particulate loading in the pfbc combustor effluent to the levels indicated in the previous section. There are four basic techniques: centrifugal separation, filtration, electrostatic precipitation, and wet scrubbing; and work is currently underway in all but the last of these: wet scrubbing is thought to require too high an economic penalty in cooling and reheating the combustion gases between the combustor and the turbine. The following discussion will be concerned only with the three techniques currently being evaluated.

System Requirements. I *Performance Criteria.* Three basic performance criteria will be required for a hot gas clean-up system for a pfbc power plant:

1 The equipment must be capable of capturing the particulates in the combustor effluent at an efficiency acceptable for the turbine specifications.

2 If the system performance degrades with time, it must be capable of being regenerated to an acceptable level.

3 It must be possible to remove the captured particulate from the high temperature, high pressure environment to safe disposal.

The previous section has described the various experimental results on which the criterion concerned with the level of particle removal would be based. Fig. 4, prepared by Brooks and Peterson of G.E., il-

Downloaded 01 Jun 2010 to 171.66.16.58. Redistribution subject to ASME license or copyright; see http://www.asme.org/terms/Terms_Use.cfm

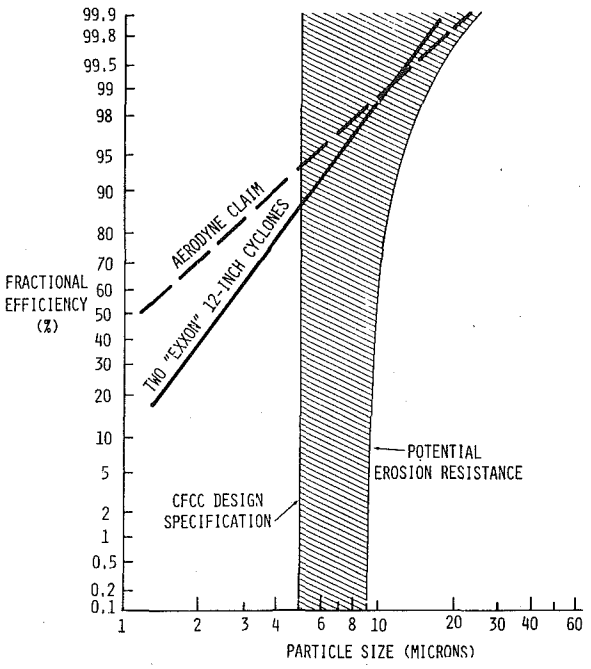


Fig. 4 Particulate cleanup efficiencies required for 25,000 hour erosion lifetime

lustrates two specifications for the degree of gas clean-up necessary for successful gas turbine operation of 25,000 hr [27]. The below 5 μm specification is based on General Electric's standard turbine practice, while the potential upper size limit is based on their interpretation of the coal-fired locomotive testing at Morgantown. Currently work is being sponsored by EPRI at Westinghouse to update turbine life specifications for specific pfbc configurations at present under development.

The problem of maintaining hot gas clean-up system performance continuously is a major concern. Filtration devices must be regenerated in some way to maintain their efficiency. Inertial and electrostatic devices, if used alone, must be capable of preventing damage to the turbine during periods of off-specification performance of the combustor.

Design of equipment to remove the captured particulate from the pfbc environment is not straightforward. Because of the uncharacterized and potentially changing physical and electrostatic properties of the pfbc effluent at high temperatures and pressures, flow characteristics of the captured particulate may present problems in designing the required valving and flow paths.

Any pressure drop between the combustor and the turbine carries performance, and hence economic, penalties. The pressure drop may change with time, and this may determine the frequency with which the captured particulate must be removed to regenerate the original characteristics of the separator.

II *Economic Criteria.* Assuming that a given hot gas clean-up system has demonstrated the required performance criteria, the cost of the system must still be low enough to maintain an overall economic advantage for the pfbc power plant over alternative systems. Because of the lack of definition of the performance criteria, the costs of a suitable system are still uncertain. A project is currently being formulated at EPRI to quantify the risk of various pfbc design approaches versus the economic return. As the hot gas clean-up system/turbine interface is the most risk-intensive section of a commercial pfbc plant, the study will attempt to identify the economic rewards of increased sophistication in order to give a better indication of how much R&D effort is justified in developing these systems.

Cyclones. Cyclones continue to be of great interest to pfbc process developers due to their potential for straightforward design and scale-up, and relatively low capital and operating costs. In a similar process situation, multiple cyclones have been used in the petroleum industry preceeding the power recovery turbine, as described above. In this service, typical outlet concentrations as reported by Worthen

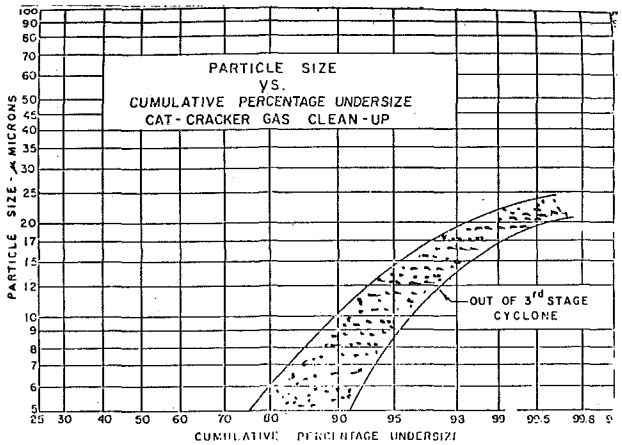


Fig. 5 Particle size versus cumulative percentage undersize

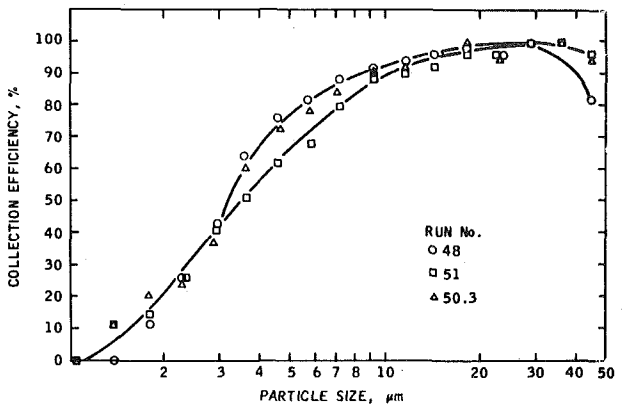


Fig. 6 Secondary cyclone efficiency versus particle size

of Ingersoll-Rand are shown in Fig. 5 for a turbine inlet dust concentration of 0.07 gr/scf (125 ppm) at up to 1300°F (704°C) and a pressure of 40 psig (0.38 MPa) [28]. Although good lifetimes have been achieved with these units, current pfbc designs aim at much higher efficiencies, and (as indicated above) improved particulate removal is required. As a consequence, there has recently been interest in producing improved cyclones. There is also the matter of the size of these units—for example, one of the current large industrial gas turbines in the 70–80 MW range would require some 1000 12 in. cyclones.

The Exxon miniplant pfbc also has used two stages of cyclones and has reported satisfactory operation with efficiencies as shown in Fig. 6.

As described above, the Combustion Power Company used various combinations of cyclones during their tests. The banks of high efficiency 3½ and 6 in. inertial tubes were particularly prone to plugging and had to be replaced by lower efficiency 30 in. diameter cyclones.

Recent work on advanced cyclones has focused on the Aerodyne tornado cyclone, with testing at various pfbc simulation and test rigs. This cyclone, which predicts up to 70 percent removal of 1 μm particles under suitable conditions [30], utilizes two counter-current high velocity vortices. Preliminary unpublished results have not so far indicated that significantly better performance can be obtained than that of two conventional cyclones in series for pfbc applications [31], although additional testing is currently underway at several locations. In summary:

1 Cyclones of conventional form are straightforward in design and operation, but rapidly lose efficiency at particle sizes of less than 10 μm.

2 Fouling and erosion have been encountered when using banks of smaller, high efficiency multiclones.

3 Engineering design of banks of hundreds of small diameter, high efficiency cyclones is not straightforward. Flow distribution problems

Downloaded 01 Jun 2010 to 171.66.16.58. Redistribution subject to ASME license or copyright; see http://www.asme.org/terms/Terms_Use.cfm

and particle removal piping will require careful analysis.

Granular Bed Filters. Filtration of pfbc combustor effluent by granular beds of sand or other similar inert media continues to be theoretically appealing as a way of meeting the most stringent turbine requirements for small particulates. In the conceptual ECAS study published in 1976 [32, 33], both General Electric and Westinghouse specified a Ducon granular bed filter as a third stage clean-up device following two stages of cyclones. However, testing of this filter at the Exxon miniplant has not been encouraging [34]. Although collection efficiencies of 90–95 percent were measured in initial operation, the inability to regenerate the filter media limited operation of the device to several hours.

Test programs are currently underway to test alternative granular bed filtration systems at Combustion Power Company and at the Coal Research Establishment of the National Coal Board. This latter program, a test of a design developed by Squires and co-workers at CCNY, will be operated in conjunction with a gasifier development program, although the results will be of relevance to pfbc applications.

To summarize the situation for granular bed filters:

1 Operational problems have not yet allowed adequate characterization of their behavior at high temperatures and high pressures.

2 The design and operation of granular bed filters for a large commercial system will be complex and of relatively high cost.

3 Despite the disadvantages, this is the only advanced separation technique which has been considered by designers in detailed design studies of potential commercial pfbc power plants (other than the advanced cyclone designs referred to above).

Baghouse, Electrostatic Precipitation, and other Advanced Concepts. The use of baghouses at relatively low stack gas temperatures is a relatively well-known positive filtration technique capable of achieving very high collection efficiencies down to submicron particle size. Baghouses were successfully installed in the early '70's in a utility application at the Sunbury Station of Pennsylvania Power and Light. Recent developments of refractory fibers make it possible to fabricate bags capable of withstanding the temperatures and gas compositions encountered in pfbc exhausts, and this has stimulated interest in this technique for hot gas clean-up. Tests of a 1.5 ft^2 surface area bag fabricated of saffil alumina with a small high temperature, high pressure pfbc simulator at Acurex Corporation for the Environmental Protection Agency have demonstrated efficiencies of 99.9 percent and above during 200 hr of operation [35].

While these tests are very encouraging from the point of view of developing materials for bag filtration, there remain very considerable problems in conceiving and designing a potential commercial system; there is consequently great uncertainty in estimating the size, cost, and viability of a high-temperature baghouse.

Electrostatic precipitation is another technique which is well-established for the removal of particles from cool gases; it is often regarded as being impossible for high temperature gases, although this is being re-examined. However, the possibility of electrostatic enhancement for other forms of separation, in particular cyclones and granular bed filters, is currently being studied at General Electric (cyclone) and Stanford University (granular bed). One of the problems with any separation system is the removal of very fine particles: the efficiency of the removal can thus be increased if the particles are agglomerated.

Potential Commercial Systems. Table 1 lists those industrial organizations which have active development of hot gas clean-up systems for pfbc applications. The two preferred system designs are:

1 Two or three stages of multiclones (AEP, Curtiss Wright)

2 Two stages of cyclones followed by a granular bed filter (G.E., Westinghouse, CPC).

A small pilot unit planned in Germany will use an electrostatic precipitator as the sole means of gas clean-up [36]; but the design of this equipment has not yet been disclosed.

Table 1 Industrial projects in hot-gas clean-up

Inertial Separators (Cyclones)
- —CPC
- —Exxon
- —NCB/CURL
- —GE/CFCC
- —MTI
- —Curtiss-Wright

Enhanced Inertial Separators
- —GE/CFCC (Electrostatics)

High-Temp Baghouse
- —Acurex
- —Buhl

High Pressure, Hot Electrostatic Precipitator
- —Research Cottrell
- —Babcock BSH

Fixed Granular Bed Filter
- —Ducon/Exxon
- —Squires Panel Bed Filter/NCB CRE (Gasifier)

Moving Granular Bed Filter
- —CPC

Electro-Fluidized Bed
- —EFB, Inc.

Summary

The designing of an acceptable pfbc/gas turbine system will require the selection of an optimum solution from the integration of the various points discussed above.

1 The particle concentration in the off-gas must be reduced very significantly, and it seems likely that only low levels of particles above 4 μm can be tolerated. Since simple cyclones fall off significantly in efficiency below 20 μm, it follows that some improvement over current practice may be necessary, perhaps by one of the methods outlined above. Clearly more work is required on techniques for the removal of particulates from hot high pressure gases, and on the design of practical systems employing the advanced techniques.

2 The turbine materials must be selected to be as resistant as possible to erosion; it is probable that they will also have to be resistant to hot corrosion. It appears that the variation in structural materials is not very great, although the carbide dispersion strengthened cobalt-base alloys seem rather better than the nickel-based alloys, and (in the absence of hot corrosion) alloys forming alumina scales are better than alloys forming chromia scales. Unfortunately, there is no carbide dispersion strengthened cobalt-base alloy which is also an alumina former. The most promising results seem to have been produced by coatings or surface treatments, although hard coatings which are also brittle may degrade the mechanical properties of the blades unacceptably. Further work is required on coatings for this purpose and an EPRI contract, RP1337, has recently been awarded to General Electric on this topic. More work is also required on the mechanisms of erosion and erosion/corrosion in particulate-containing gases, the effect of particulate size, velocity, and hardness and the response of alloys to this type of environment. EPRI has a contract, RP979-4, with United Technologies which addresses these problems.

3 The turbine must be designed to be as tolerant of particulates as possible. The hot gas ducting to the turbine inlet must be designed to eliminate so far as possible the concentration of the particulates in one part of the gas stream or at one part of the first stage stator vanes. The concentration of particulates towards the highly-stressed roots of the rotating blades must be avoided; designs which centrifuge the particulates out to the blade tips akin to the methods used to remove water droplets at the low pressure end of steam turbines would be desirable. The vanes and blades can be designed so that the more erosive parts of the gas stream strike the platforms or shrouds rather than the airfoils. Increased spacing between stages may facilitate the centrifuging of the particles. Lowering the relative gas velocities and compensating by adding additional stages would seem to be helpful. Increasing the thickness of the trailing edge of the blades would lengthen the lifetime of the components.

Many of these possible modifications are expensive, particularly if they require changes in the main frame, and some also carry

Downloaded 01 Jun 2010 to 171.66.16.58. Redistribution subject to ASME license or copyright; see http://www.asme.org/terms/Terms_Use.cfm

penalties in reduced efficiency. Work needs to be done on the conceptual design of large utility gas turbines tolerant of particulate-containing gas streams, and on estimation of the costs involved.

References

1 Air Research Manufacturing Company of Arizona, "Coal Fired Prototype High Temperature Continuous Flow Heat Exchanger—Final Report," EPRI AF-684, Feb. 1978.

2 Gluckman, M. J., "Gasification-Combined Cycle Power Plants," *EPRI Journal,* July/Aug. 1978, p. 43.

3 Ehrlich, S., "Fluidized-Bed Combustion," *EPRI Journal,* June 1978, p. 39.

4 "Energy Conversion Alternatives Study (ECAS)—Summary Report," ASA TM-73871, Sept. 1977. "Comparative Study and Evaluation of Advanced Cycle Systems—Final Report," EPRI AF-664, General Electric Company, Feb. 1978.

5 Newby, R. A., Katta, S. and Keairns, D. L., "Regeneration of Calcium Based SO_2 Sorbents for Fluidized-Bed Combustion: Engineering Evaluation," EPA-600/7-78-039, March 1978.

6 Kan, G. L., Graff, R. A., Squires, A. M., "Cyclic Use of (I) Half Calcined Dolomite for Removal of Hydrogen Sulfide and (II) Magnesium Oxide for Removal of Sulfur Dioxide from Gases at Elevated Pressure," The Clean Fuels Institute, CUNY, New York, July 1976.

7 Keairns, D. L., et al., "Corrosion/Deposition in Fluidized Bed Combustion Power Plant Systems" in *Ash Deposits and Corrosion Due to Impurities in Combustion Gases,* ed. R. W. Bryers, Hemisphere Publishing, Washington, 1977, p. 497.

8 Phillips, K. E., "Energy Conversion from Coal Utilizing CPU-400 Technology," Final Report on U.S. ERDA Contract No. EX-76-C-01-1536, March, 1977.

9 McCarron, R. L., Beltran, A. M., Spacil, H. S., and Luthra, K. L., *Proceedings of the Fifth International Conference on Fluidized Bed Combustion,* Dec. 1977 (to be published).

10 Lackey, M. E., "Summary of the R & D Effort on Open Cycle Coal-Fired Gas Turbines," Oak Ridge National Laboratory Report (to be published).

11 Smith, J., et al., "Bureau of Mines Coal-Fired Gas Turbine Research Project: Tests of New Turbine Blade Design," BM-RI-6920, Bureau of Mines, U. S. Department of the Interior, 1967.

12 Margulis, W., "High Temperature Abrasion Resistance of Gas Turbine Alloys," Alco Products Inc. Report, Aug. 1956.

13 "The Coal-Burning Gas Turbine Project—Report of the Interdepartmental Steering Committee," Department of Minerals and Energy—Department of Supply, Australian Government Publishing Service, Canberra, 1973.

14 Stettenbenz, L. M., "Power-Recovery Gas Expander Gains in FCC Cycle," *The Oil and Gas Journal,* Dec. 18, 1972, p. 60.

15 Wilson, J. G., *The Oil and Gas Journal,* April 18, 1966, p. 77.

16 Barkalow, R. H., and Pettit, F. S., "Design of Materials for Use Under Erosion-Corrosion Conditions at High Temperature in Coal Gasification and Coal Combustion Systems," Final Report in EPRI Contract No. RP 979-4 (in press).

17 Barkalow, R. H., and Pettit, F. S., "Erosion and Corrosion of Materials by High-Velocity Combustion Gases Containing FBC Particulates," Report to EPRI in Contract No. RP 979-4 (in preparation).

18 "Pressurized Fluidized Bed Combustion," R & D Report No. 85, prepared by the National Research and Development Corporation of London, England, for the Office of Coal Research, Department of the Interior, Washington, D.C., 1973.

19 Zellars, G. R., Rowe, A. P., and Lowell, C. E., *NASA Technical Paper 1274,* July 1978.

20 General Electric Company, Report to Department of Energy on Contract EX-76-C-01-2357, 1978.

21 Bertrand, R. R., et al., "Hot Corrosion/Erosion Testing of Material for Application to Advanced Power Conversion Systems Using Coal-Derived Fuels. Task II—Fluidized Bed Combustion," Second Task Report prepared for the Department of Energy on Contract No. EX-76-C-01-2652, Sept. 1978.

22 Menguturk, M., and Sverdrup, E. F., "Calculated Tolerance of a Large Electric Utility Turbine to Erosion Damage by Coal Gas Ash Particles," presented to ASTM Symposium on Erosion: Prevention and Useful Applications, Vail, Colo., Oct. 1977.

23 Sverdrup, E. F., Archer, D. H., and Menguturk, M., "The Tolerance of Large Gas Turbines to Rocks, Dusts, and Chemical Corrodents," Westinghouse R & D Center Report 77-1E3-CEDRM-R1, October 1977.

24 Wenglarz, R. A., and Sverdrup, E. F., "Modelling of Turbine Flow Path Degradations Due to Particle Laden Expansion Gases," presented to workshop on Mechanisms of Erosion in Hot Flowing Media, Fort Myers, Fla., May 1978.

25 Tabakoff, W., Discussion of reference [24].

26 Foster, A. D., Doering, H. von E., and Hickey, J. W., "Fuel Flexibility in GE Gas Turbines," General Electric Gas Turbine Reference Library, GET-222L, 1977.

27 Brooks, R. D., and Peterson, J. R., "General Electric Pressurized Fluidized Bed Powerplant Status," presented at the Fifth International Conference on Fluidized Bed Combustion, Washington, D. C., Dec. 14, 1977.

28 Worthen, R., "Equipment Needs in Coal Gasification and Liquefaction Plants," Ingersoll-Rand Research, Inc., Fourth Annual International Conference on Coal Gasification, Liquefaction and Conversion to Electricity, Pittsburgh, PA, Aug. 4, 1977.

29 Hoke, R. C., et al., "Miniplant Studies of Presurized Fluidized Bed Coal Combustion: Third Annual Report," Contract No. 78-GT-40 for U. S. E.P.A., Exxon, April 1978, p. 64.

30 "Purification of Hot Fuel Gases from Coal or Heavy Oil," Interim Report, EPRI-243-1, Stone and Webster, Nov. 1974, p. 5-5.

31 Thoennes, C. M., Energy Systems Programs Dept., General Electric Co. Private communication, Dec. 14, 1978.

32 Bass, R. R., et al., "Energy Conversion Alternatives Study, General Electric Phase II Final Report," NASA CR-134949, General Electric Co., Dec. 1976.

33 Beecher, D. T., et al., "Energy Conversion Alternatives Study, Westinghouse Phase II Final Report," NASA CR-134942, Westinghouse Electric Corporation, Nov. 1, 1976.

34 "Purification of Hot Fuel Gases from Coal or Heavy Oil," Interim Report, EPRI-243-1, Stone and Webster, Nov. 1974, p. 6.

35 Shakleton, Michael A., "Barrier Filtration for HTHP Particulate Control," Acurex Corporation, *Symposium on the Transfer and Utilization of Particulate Control Technology,* Denver, Colo., July 24–28, 1978.

36 Schilling, H., Schreckenberg, H., and Wied, E., "Design of a Gas Turbine Plant with a Pressurized Fluidized Bed Combustor," Bergbau-Forschung Gmblt and Vereinigte Kesselwerke AG, Fifth International Conference on Fluidized Bed Combustion, Washington, D. C., Dec. 14, 1977.

Downloaded 01 Jun 2010 to 171.66.16.58. Redistribution subject to ASME license or copyright; see http://www.asme.org/terms/Terms_Use.cfm

J. R. Newman
Senior Machinery Design Engineer,
326 High Holborn,
British Gas, London,
England

K. I. McEwan
Assistant Compressor Operations Manager,
British Gas, Hinckley,
England

Low Frequency Gas Turbine Noise

British Gas have experienced problems at some installations from low frequency turbine noise. The paper describes how the low frequency noise problems were investigated and then resolved by aerodynamic modifications and a silencer extension.

Introduction

The design of British Gas (B.G.C.) gas turbine exhaust silencers has been developed over eight years of compressor operation. The problems and experience gained in the suppression of low frequency noise have been reflected in the requirements of the current B.G.C. purchase specification for exhaust silencers. The low frequency noise problem was first highlighted in 1973, some years after the first compressor station was commissioned. The extensive investigation which followed and the methods used to reduce the effect of the low frequency noise are discussed in this paper.

Background

The levels of low frequency noise generated at three British Gas Compressor Stations was sufficient to cause complaints from local residents. In each case the noise described was similar in character, being a barely audible rumble with a distinct steady "beat." In some instances energy levels were sufficient to excite resonances causing windows, doors and crockery to vibrate. At a very early stage in the investigations it was clear that the problems stemmed from high levels of airborne noise in the 31.5 Hz octave band, originating from the gas turbine exhausts.

All three stations employed aero-derivative gas turbine driven compressor sets housed in steel fabricated, weatherproof acoustic enclosures with vertical exhaust stacks. The machinery and acoustic equipment at these three stations was supplied by various vendors and these are listed in Table 1. This table also includes two further stations which were investigated for comparative purposes.

Although at one of the stations the complaint was judged to be marginal, in all cases B.G.C. undertook to seek methods of reducing noise levels. This approach was consistent with a good neighbour policy which has always maintained, as an objective, that the existing background noise level should not be significantly affected by the new installations. This policy has in the past enabled a harmonious coexistence to be maintained between B.G.C. and site neighbours [1].

All three of the stations involved were amongst the earliest constructed for B.G.C. and the acoustic design criteria for the exhaust silencers were based upon the use of NR curves [2, 3]. These include the 31.5 Hz octave band and approximate to curves of equal annoyance. Although it was appreciated at the time that their use might allow low frequency noise levels of a magnitude sufficient to provoke complaints, knowledge was insufficient to take account of this in the exhaust silencer criteria. In all three cases the measured dBA noise levels were such that no complaints should have been likely. The fact that low frequency noise can result in annoyance to an extent not simply related to loudness levels has subsequently been observed by others [4–6].

Typical residual noise levels specified for the early B.G.C. stations were NR 30 or NR 35 per gas turbine unit at 100 m. Thus levels of 74 dB and 78 dB, respectively, in the 31.5 Hz octave band were permitted. It will be shown later that for stations where houses exist within 0.5 Km of the machines, lower levels are required if complaints are to be avoided.

Table 1 Equipment suppliers

Station	Machinery	Silencing Equipment
1	Cooper Bessemer	Cullum Detuners
2	Cooper Bessemer	Cullum Detuners
3	GEC—Gas Turbines	Burgess Industrial Silencing
4	Cooper Bessemer	Burgess Industrial Silencing
5	GEC—Gas Turbines	Burgess Industrial Silencing

Measured Low-Frequency Community Noise Levels

At the three stations concerned, 31.5 Hz octave band sound pressure level (SPL) measurements were obtained at the houses of the complainants. A summary of the noise measurements carried out at these community locations is given in Table 2. A brief description of the three community locations is given below.

Compressor Station 1. Complaints were received from the occupants of a bungalow 385 m South of the station and a two storey house 620 m North East of the station. Although an inn was sited almost adjacent to the bungalow complaints were never received from its occupants. The topography around the station is flat with the exhaust stacks visible from all the houses.

Compressor Station 2. Complaints have been received from only one house 1300 m to the South of this station. The house is one of several in a village street and other houses are located nearer to the station. The local topography is gently undulating but the houses in the village street including the complainants are screened by rising ground and the exhaust stacks are not visible. This Compressor Station is a peak load station with limited usage basically restricted to spells of cold weather, which in the U.K. frequently coincide with northerly winds. The complainant's house is, under these conditions, immediately down wind of the station and it was clear that wind direction was a significant factor in justifying a complaint.

Contributed by the Gas Turbine Division of The American Society of Mechanical Engineers and presented at the Gas Turbine Conference and Exhibit and Solar Energy Conference, San Diego, Calif., March 12–15, 1979. Manuscript received at ASME Headquarters January 15, 1979. Paper No. 79-GT-196.

Copyright © 1980 by ASME
Downloaded 01 Jun 2010 to 171.66.16.58. Redistribution subject to ASME license or copyright; see http://www.asme.org/terms/Terms_Use.cfm

Compressor Station 3. The topography around the station is very flat and complaints were received from several residents living about 500m from the station. Further complaints came from the occupant of a residential caravan located 380 m from the station.

Investigation of Low Frequency Sources

Comparative Noise Surveys—Different Gas Turbines. As a first step in the analysis of the problem, it was decided that low frequency noise surveys should be carried out to establish whether different gas turbines emitted different levels of low frequency noise. It was suspected that this was the case even for nominally similar gas turbines by the same manufacturer.

Of the stations with complaints, stations 1 and 2 had identical gas turbines which were supplied by a different manufacturer to those at station 3. The three units at station 3 also differed amongst themselves. Units A and B were identical whilst unit C had a modified power turbine diffuser and volute design.

Low frequency noise measurements were also performed at two other stations from which no complaints had been received and these have been identified as stations 4 and 5.

In all cases the gas turbine was operating at as near full power as possible. A single position at 50 m from the exhaust stack center line and at right angles to the axis of the machine was chosen for the measurements. However, at station 1, 100 m was used at eight compass positions. The data are generally presented in the form of octave band levels at 100 m but in addition some narrow band analysis was undertaken. The results of the surveys are summarized in Table 3 while narrow band analysis of the surveys are shown in Figs. 1 and 2.

A feature of the results is the substantial differences in low frequency noise emission between the various gas turbines. Reference to the narrow band analysis noise spectra shows that in both cases for the gas turbines provoking complaints a distinct peak existed in the region 25 Hz to 35 Hz.

Subsequent measurements have shown that if the peak can be reduced not only will the magnitude of the noise be lessened but a reduction in the modulated quality of the noise will occur, i.e., the beat will be less noticeable and the noise considered subjectively more acceptable.

During the comparative noise surveys the effects of running condition were also investigated, to check that maximum noise emission occurred at full power as was suspected. Accordingly during the tests at station 1, a gas turbine was run up from idling to full power in stages, with a recording of low frequency noise being taken at each stage. Analysis of the results showed:

1 Maximum noise emission occurred at full power.
2 A reduction of 17 dB in spectral peak level occurred between the full load and idle condition.
3 The spectral peak is much less prominent at idle conditions.
4 The frequency of the peak is reduced at idle conditions.

Narrow band analysis of the low frequency noise at full power and idle conditions is shown in Fig. 3. Similar effects to those listed in 1–4 were noted for A/B units at station 3, where a difference of 13 dB in spectral peak levels occurred. For the quieter station 3 Unit C, however, a difference of 7 dB in spectral peak levels occurred.

Low Frequency Noise Sources. When considering the results of the comparative noise surveys, it was felt that the influence of the existing exhaust silencers on emitted levels of low frequency noise could be ignored. Although there were some variations in silencer shape and configuration all the silencers were of the same length and designed for broad band silencing only. It was, therefore, assumed that their low frequency performance was comparable and that the observed differences in low frequency noise levels could be attributed to differences in source level.

It was judged that one reason for the differences in low frequency noise levels was the variations in turbulence and instability in the various arrangements of power turbine diffuser and volute. Differences in the geometry of these items might therefore be expected to result in variations in the low frequency noise generated.

The geometry of a typical power turbine diffuser volute, transition piece and silencer is shown on Fig. 4. Review of the various arrangements, and the noise survey results suggested that if the turbine exhaust gas flow is directed away from the back wall of the volute and is more evenly distributed at entry to the silencer than a reduction in low frequency noise could be expected to occur. This was found to be the common factor in the installations with the lowest levels of low frequency noise.

At station 4 the exhaust gases are deflected away from the volute rear wall by the geometry of the volute and the offset relationship of

Table 2 Low frequency noise measurements at complainants' houses

Station No	Location	31.5 Hz SPL	Annoyance
1	*Bungalow*		
	Outside	80	yes
	"	65	yes
	Bedroom 1	49	no
	House		
	Outside	72	yes
	Conservatory	78	yes
	Living Room	62	yes
	Conservatory	60	no
2	Outside House	72	yes
	" "	61	yes
	Kitchen	64–68	yes
	Living Room	44–58	yes*
	" "	43–46	no
3	Outside House	78	yes
	" "	60	no
	Caravan-Bedroom	74	yes
	Outside Caravan	78	yes
	" "	60	no

* Depending on position in room

Notes:
1 In some instances for the indoor measurements, standing waves were observed in some rooms and the 31.5 Hz levels stated indicate the highest levels present. Other levels are mean values, fluctuations of up to 3 dB typically occurring.
2 Background 31.5 Hz noise levels with gas turbines shut down were typically in the range 45 dB to 58 dB.

Table 3 Summary of results of noise surveys at various stations with units in original unmodified condition

Station	31.5 Hz SPL at 100 m dB re 2×10^{-5} N/m^2	Comments
1—Unit A	87*	Identical Units
1—Unit B	87*	
4—Unit A	70	Identical units (By same supplier as station 1, but different volute/diffuser design).
4—Unit B	75	
3—Unit B	80	Different supplier to stations 1 & 4
3—Unit C	69	Identical Units (By same supplier as station 3—unit B, but different
5—Unit A	73	volute/diffuser design).

* Mean values from data at eight locations. All other results from single measurement positions only.

Downloaded 01 Jun 2010 to 171.66.16.58. Redistribution subject to ASME license or copyright; see http://www.asme.org/terms/Terms_Use.cfm

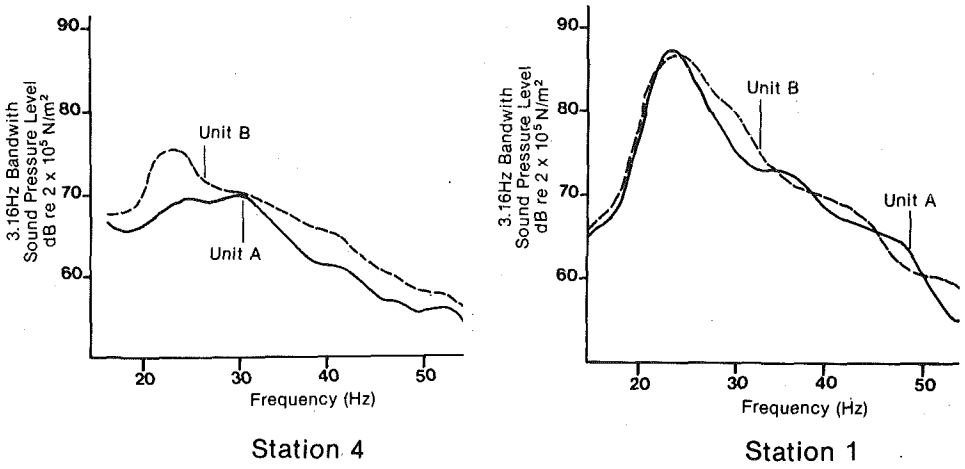


Fig. 1 Narrow band analysis low frequency noise at 100 m—full power operation

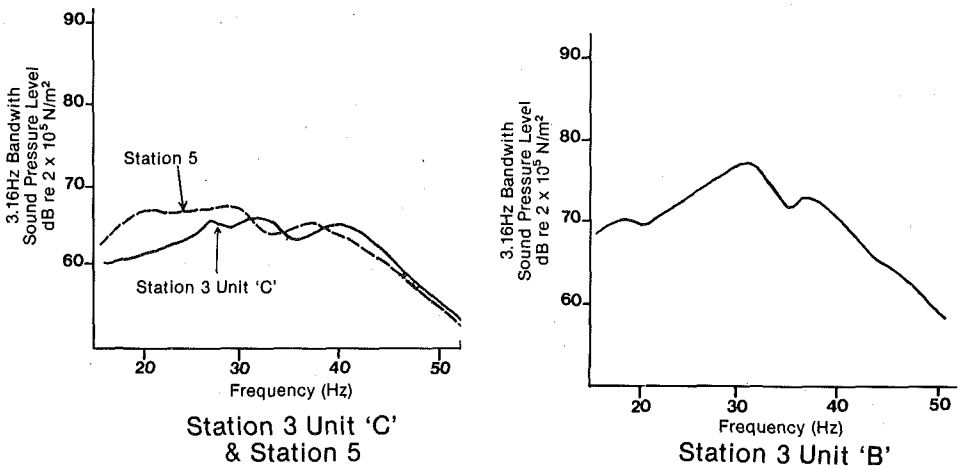


Fig. 2 Narrow band analysis low frequency noise at 100 m—full power operation

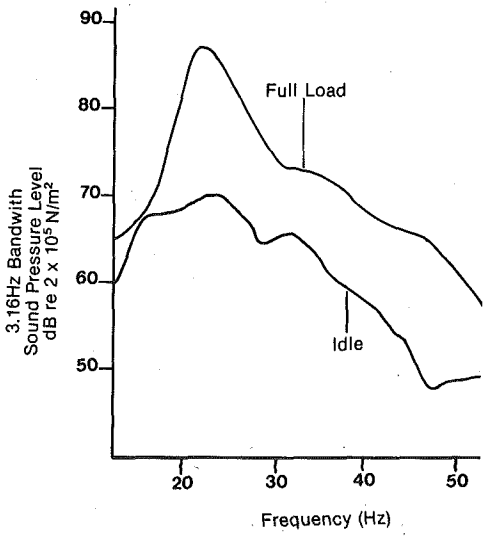


Fig. 3 Narrow band analysis low frequency noise at 100 m—effect of varying power output

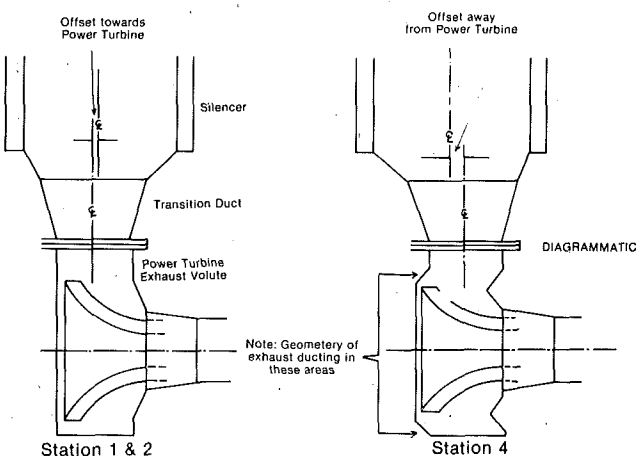


Fig. 4 Typical power turbine exhaust volute and silencer arrangements

the silencer to the volute as shown in Fig. 4. For station 5 and station 3 Unit C, this is achieved by aerodynamic improvements.

Low Frequency Noise Reduction

Following the comparative noise surveys and investigations it was proposed by the silencing equipment and machinery suppliers that efforts at achieving reductions in low frequency noise should initially be concentrated in the area of aerodynamic modifications, using devices that would improve the exhaust flow distribution into the silencer and at the same time reduce turbulence and vortices in the power turbine volute. This approach had the advantage that it appeared to offer a good chance of a worthwhile noise reduction at low cost and the work could also be quickly carried out. Speed was important as the complaints occurred generally at the start of the winter running season which meant that no long outages could be tolerated.

Downloaded 01 Jun 2010 to 171.66.16.58. Redistribution subject to ASME license or copyright; see http://www.asme.org/terms/Terms_Use.cfm

It was also important from the view point of relationships with the complainants that some improvements were quickly achieved.

Aerodynamic Modifications. The aerodynamic modifications employed were essentially either flow straightening devices or flow control devices in the volute and transition duct area. In all instances the devices were simple ad-hoc modifications which could easily be fitted. Time did not permit any development or test work, such as model testing.

Tables 4 and 5 present a summary of the low frequency noise reductions achieved by various devices. The values are corrected to estimated full load conditions in some cases, to facilitate comparisons. In detail the following aerodynamic devices were evaluated:

Flow Straightening Grids. The flow straightening grids were installed at the exit of the exhaust duct transition sections. These grids gave a reduction in the outlet transition duct free area and a resulting calculated power loss of 1/2 to 1 percent although this has not been checked.

Flow Control Devices in Volute Area. Following the success of the grids a further attempt was made to re-direct flow from the exhaust volute rear wall by the use of various flow control devices in the power turbine volute area.

At station 3 a flow deflector plate installed at the inlet to the transition duct was tried in conjunction with a straightening grid. At stations 1 and 2 both the deflector plate and a deflector cone within the volute were each tried in combination with a flow straightening grid and then all three devices together.

The deflector plate and grid combination was not successful. At station 3 a further low frequency noise reduction of only 2 dB occurred but at the expense of a significant power loss as a consequence of which the plate was removed. At stations 1 and 2, zero additional low frequency noise reduction was achieved. The deflector cone and grid combination at stations 1 and 2 was also unsuccessful with no further noise reduction being obtained.

However the combination of grid, deflector plate and volute cone gave a further noise reduction of approximately 5 dB. It is possible that this resulted from the deflector plate interfering with and modifying the production of vortices along the back wall of the volute.

Volute Aerodynamic Improvements. Investigation of unit C at station 3 which is the quietest unit, indicated that the most likely reason for the lower noise levels was aerodynamic improvements in the volute. A decision was therefore made to modify the volutes on the other two units at this station, a further attraction being a probable improvement in power turbine efficiency.

The evaluation showed that the aerodynamic improvements gave approximately a 5 dB reduction in low frequency noise when compared with the noise level of the unit in its original condition.

For the gas turbine which already had a flow straightening grid installed, a further 2 dB was achieved.

Exhaust Silencer Modification. The aerodynamic modifications described previously were sufficient to alleviate the complaints at stations 2 and 3. At station 1, however, it became clear, after evaluating the grid and deflector plate combination, that the desired low frequency noise reduction was unlikely to be achieved by further aerodynamic means.

B.G.C. estimated that a further noise reduction of 11 dB in the 31.5 Hz octave band was required to achieve a solution and the silencing supplier proposed that this could be obtained most economically by modifying and extending the exhaust silencer. The design offered for evaluation was to be similar to an exhaust silencer supplied by the same manufacturer, which had also been designed for low frequency noise suppression. This silencer was the same length as the proposed extended silencer and had been installed on a compressor station which was not commissioned. Its performance was therefore unknown.

An earlier attempt had been made to achieve some noise reduction by the installation of an outlet restrictor to the top of an exhaust silencer giving a 45 percent reduction in silencer outlet area. No reduction was in fact achieved and the restrictor was subsequently removed.

At the time the silencer extension was contemplated, there were few known installations around the world where gas turbine exhaust silencers had been specifically designed for substantial low frequency noise reduction. However a very large tuned silencer with dissipative side branches had been stated to achieve a 16 dB insertion loss in the 31.5 Hz octave band [7]. It was also known that a similar low frequency gas turbine noise problem in Holland had been solved by the addition of a purpose designed silencer for low frequencies on top of the existing silencers.

Because of the limited operational experience available at the time, it was agreed between B.G.C. and the silencing contractor that some limited test work would improve confidence in the likelihood of the modified and extended silencers achieving their target noise reduction.

B.G.C. felt that experimental confirmation of the low frequency performance of the silencer was desirable and it was considered that this could be assessed by the use of loudspeakers. For the original si-

Table 4 Summary of performance achieved by various low frequency noise reducing devices—compressor stations 1 and 2

Noise Reduction Device	Mean 31.5 Hz Octave Band SPL at 100 m dB re 2×10^{-5} N/m^2 Full Load*			
	STATION 1		STATION 2	
	Unit A	Unit B	Unit A	Unit B
Original unmodified condition (All units identical)	89*	89*	—	—
Silencer outlet restrictor	89*	—	—	—
Flow straightening grid	—	82*	86	84
Grid plus volute deflector cone	—	—	—	84
Grid plus deflector plate	83*	83*	—	—
Grid plus deflector plate plus volute cone	79*	—	—	79
Grid plus deflector plate plus volute cone plus silencer extension	66	—	—	—
Grid plus deflector plate plus silencer extension	—	67	—	—

*adjusted to estimated full load values

Table 5 Summary of performance achieved by various low frequency noise reducing devices—compressor station 3

Noise Reduction Device	Mean 31.5 Hz Octave Band SPL at 100 m dB re 2×10^{-5} N/m^2		
	Unit A	Unit B	Unit C
Original Unmodified Condition (Units A & B Identical)	—	80	69
Flow Straightening Grid	—	74.5	—
Volute Aerodynamic Improvements	75	—	—
Volute Improvements Plus Grid	—	73	—
Deflector Plate (375 mm Extension)	78		

Downloaded 01 Jun 2010 to 171.66.16.58. Redistribution subject to ASME license or copyright; see http://www.asme.org/terms/Terms_Use.cfm

lencer a single loudspeaker was located in an access opening provided in the exhaust transition duct below the silencer. Using a broad band white noise input a static attenuation of only 2 dB in the 31.5 Hz 1/3 octave was indicated. This was then compared with the performance of the low frequency silencer on the uncommissioned compressor station. The performance of this silencer was also assessed using loudspeakers located in the exhaust transition section. A static attenuation of 14 dB in the 31.5 Hz 1/3 octave band was indicated. It was appreciated that when operating, the actual silencer performance would be changed due to the high temperatures and velocities involved.

It was thought by the silencer supplier that there would probably be a level at which the insertion loss of the modified extended silencer would be controlled by self noise. To assess this, various parts of the internals of the original silencer were removed or blanked off to give varying velocities, and the gas turbine operated at full power. Measurements of low frequency noise were made for each condition. As a consequence of these tests, it was concluded that expected self noise would be within the required noise limits for the 31.5 Hz octave band for the design velocity chosen.

The results of the loudspeaker and velocity tests gave confidence that a reasonable low frequency noise reduction would follow from the rebuilt silencers at station 1, and the extensions were subsequently carried out.

The low frequency silencer after modification is shown diagrammatically in Fig. 5. It is circular, like the original, but is longer, while the attenuating elements in the original silencer were replaced by a new single element. The low frequency performance is derived from the large diameter central absorption section.

Reference to Table 4 will show the silencer to have been successful with an insertion loss of approximately 13 dB for one unit and 16 dB for the other.

Conclusions

General. The investigations into the noise complaints have enabled a number of conclusions to be drawn regarding low frequency gas turbine exhaust noise. Generally it can be said that the design of exhaust volutes and ductwork has an important influence on low frequency noise source levels. Maximum noise emission occurs at full power and can be reduced to acceptable levels by careful application of aerodynamic modifications or by the installation of purpose designed silencers.

Further conclusions can be drawn regarding the propagation of low frequency noise, factors affecting complaints and community noise criteria as follows:

Propagation of Low Frequency Noise. Propagation of low frequency noise measurements carried out appeared to confirm that over flat terrain and under calm or light wind conditions, attenuation with distance follows the inverse square law, i.e., 6 dB per doubling of distance from source.

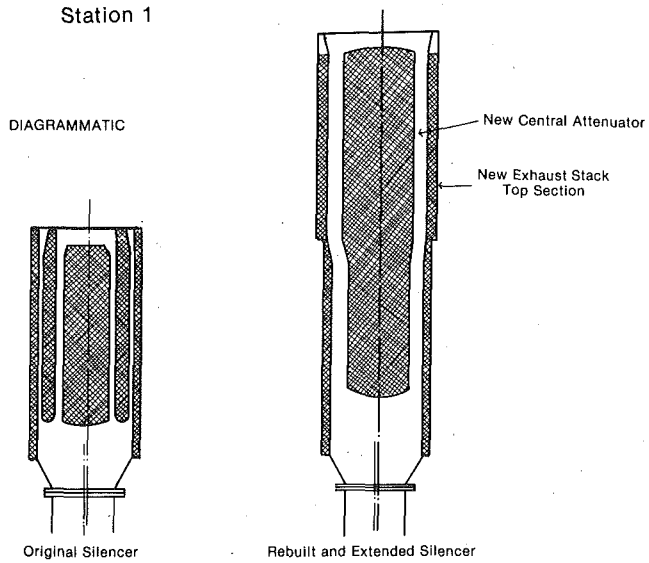


Fig. 5 Compressor station—silencer extensions

Winds blowing from the direction of the source towards the receiver significantly reduces inverse square law attenuation. Failure to obtain full inverse square law reduction by as much as 9 dB over a distance of 1300 m has been noted.

Factors Affecting Complaints. Consideration of the complaints experienced has led to the view that many factors are involved in determining whether a complaint will be caused by low frequency noise from gas turbine exhausts.

Some of these factors cannot easily be taken account of in design. For example, room resonances in neighboring houses arising from the room dimensions, the sensitivity of residents, and the frequency of night operation (difficulties in sleeping were cited as causing particular annoyance in all but one of the low frequency noise complaints arising from the compressor stations).

To be reasonably certain that no low frequency noise complaints will be caused by a new installation a noise emission criterion should be established which includes the low frequencies. Such a criterion will now be discussed.

A Community Criterion for Low Frequency Noise. In proposing a community criterion for low frequency gas turbine noise one particular feature of the complaints should be noted. In all instances once the noise had been experienced by the recipients, noise reduction down to inaudibility was required before the complaints ceased. This seems to stem from the recipients becoming attuned to the noise and the lack of masking in background noise spectra. Unlike higher frequencies, no significant noise reduction can be achieved by closing windows and this no doubt reinforces the annoyance.

The criterion now used by B.G.C. when specifying noise control for gas turbines, is 60 dB in the 31.5 Hz octave band at the nearest dwelling. This value has been determined by review of the noise levels which the complainants considered satisfactory. Although more complex criteria could doubtless be devised involving narrow band analysis, the use of octave bands is preferred for contractual purposes.

It should be noted that design to the criterion stated does not in fact necessarily achieve inaudibility as defined in the Minimum Audible Field Threshold curve, recommended by the International Organization for Standardization [8]. For the 31.5 Hz octave band, the hearing threshold is given by this curve as 67 dB and 43 dB for the cut off frequencies of 22 Hz and 44 Hz, respectively.

The B.G.C. criterion can be compared with a similar criterion which has been used for some years by the U.K. Electricity Generating Board and has helped to successfully minimise low frequency noise problems on their installations. Further comparisons can be made with the value of 65 dB in the 31.5 Hz octave band suggested by Hoover [7], and the example of a gas turbine electric power generation plant in Portland, Oregon. There, a level of 60 dB in the 31.5 Hz octave band at a nearby house eliminated a complaint of excessive low frequency noise.

Future Prospects

The paper has described how the low frequency noise problems were overcome by a combination or relatively cheap aerodynamic modifications and more costly silencer extensions.

On current and future compressor stations the low frequency noise criterion is now the controlling parameter in the design of gas turbine exhaust silencers, overiding the broad band silencing requirements. Hence the costs of exhaust silencers are now effectively set by the low frequency criterion.

It is therefore important in the future that gas turbine manufacturers pay special attention to the reduction of low frequency noise at source. This requires that some weight be given to the low frequency noise characteristics of the exhaust volute and ductwork system. Similarly, silencer manufacturers should be looking for more effective and cheaper ways of attenuating low frequency noise.

An example of such a method might be 'active attenuation' whereby additional sound is generated to interfere with and cancel the offending frequencies. The technique is ideally suited to low frequency

Downloaded 01 Jun 2010 to 171.66.16.58. Redistribution subject to ASME license or copyright; see http://www.asme.org/terms/Terms_Use.cfm

noise where the sound field is simply plane waves and where conventional absorption silencers are inefficient. Application of the technique to gas turbine exhaust silencers would mean that they would only need to be designed for broad band silencing and could therefore be drastically reduced in length.

Research on the application of the technique to gas turbine exhaust silencers is currently being carried out in the U.K. and B.G.C. will be following the progress of this with interest.

Acknowledgments

The equipment described in this paper was designed and installed under contract by the machinery and silencing equipment suppliers. Much of the acoustic measurements and analysis were carried out by the Engineering Research Station of B.G.C.

The authors wish to acknowledge the contribution made by the vendor companies to the work described and for permission to publish the results. The authors would also like to acknowledge the assistance given by colleagues with B.G.C.

This paper is published with the consent of B.G.C.

References

1 Dixon, P. H., and McEwan K. I., "Operational Plant in the Rural Scene—How to Live With Your Neighbours," The Institution of Gas Engineers, Communication 1047, 1977.

2 Grettum, R. S., "Meeting Europe's Low Noise Requirements for Compressor Stations," ASME Paper No. 71-GT-87.

3 Cleveland, A., "Noise and Other Environmental Considerations in the Design and Planning of Gas Compressor Stations in the U.K.", ASME Paper No. 72-GT-110.

4 Bryan, M. E., *Annoyance Effects Due to Low Frequency Sound Proceedings of British Acoustical Society,* Vol. 1 and 3, Summer 1972.

5 Vasudevan, R. N., and Gordon, C. G., "Experimental Study of Annoyance Due to Low Frequency Environmental Noise," *Applied Acoustics,* Jan. 1977, p. 57–69.

6 Tempest, W., "Loudness and Annoyance Due to Low Frequency Noise," *Acoustica* 29, 1973, pp. 205–9.

7 Hoover, R. M., "Beware Low Frequency Gas Turbine Noise," *Power Magazine,* May 1972.

8 International Organisation for Standardisation, "Normal Equal-loudness Contours for Pure Tones and Normal Threshold of Hearing Under Free Field Listening Conditions," ISO/R 226–1961.

Downloaded 01 Jun 2010 to 171.66.16.58. Redistribution subject to ASME license or copyright; see http://www.asme.org/terms/Terms_Use.cfm

I. Oliker
Supervising Mechanical Engineer,
Burns and Roe, Inc.
496 Kinderkamack Road,
Oradell, N. J. 07649
Mem. ASME

Steam Turbines for Cogeneration Power Plants

Steam turbines for cogeneration plants may carry a combination of industrial, space heating, cooling and domestic hot water loads. These loads are hourly, weekly, and seasonally irregular and require turbines of special design to meet the load duration curve, while generating electric power. Design features and performance characteristics of one of the largest cogeneration turbine units for combined electric generation and district heat supply are presented. Different modes of operation of the cogeneration turbine under variable load conditions are discussed in conjunction with a heat load duration curve for urban heat supply. Problems associated with the retrofitting of existing condensing type turbines for cogeneration applications are identified.

Introduction

Combined generation of heat and power offers one of the major fuel conservation opportunities and a significant reduction of air pollution, when compared with separate electrical and heat production. In a cogeneration power plant, a substantial part of the throttle steam is expanded in the turbine to generate electricity before the steam is extracted at a pressure and temperature which can supply the required thermal loads. The extracted steam may be directly used as a heating medium and supplied by a piping system to the customers. Another method is to condense the extracted steam in closed-type heat exchangers at the power plant, thereby producing hot water, which can then be pumped to customers. Hot water as a heating medium offers a number of advantages in comparison to steam, which are discussed in detail in [1].

The most effective use of fuel is achieved when the cogeneration plant serves both industrial customers needing high pressure process steam, and urban customers, who require hot water from a district heating network. In order to economically supply steam at high pressure the cogeneration plant has to be situated close to the industrial complex. Hot water can then be pumped for a substantial distance to the urban customers. However, such an integrated cogeneration system depends on many factors and can not always be accomplished. Therefore a cogeneration power plant serving either only industrial customers (industrial cogeneration) or urban customers (district heating cogeneration) is more usually the case.

Most of the existing power plants in the U.S. are of the single purpose, condensing type, and are not designed for the extraction of large amounts of steam that are required to supply the thermal load.

Extracting additional heat from an existing turbine involves some reduction in electrical generation. The electricity lost depends directly on the extracted steam flowrate, pressure, and the number of extractions.

When considering the conversion of existing turbines for cogeneration operation, the possibility of extracting up to 15 to 20 percent of the throttle steam flow from the crossover point of the turbine could be considered. An additional pressure control system may have to be installed at the crossover pipe to provide reliable operation of the turbine.

It has to be emphasized that the retrofitting of existing turbines to extract the required steam flow is very difficult and involves a significant redesign of the turbine and its control system, and consequently, a substantial outage time may be necessary for modification.

One of the major differences also, between an existing turbine and a specially designed cogeneration turbine is that in the former, all the low pressure extraction piping is located inside the condenser. For modification of existing turbines, provision must be made for routing this enlarged diameter extraction piping out of the condenser.

To avoid the problems discussed above, different types of cogeneration turbines have been developed and are commercially available. The existing cogeneration turbine designs can be categorized according to the following features:

1 with one controlled space heating extraction
2 with one controlled industrial steam extraction
3 with two space heating extractions
4 with two controlled extractions, industrial and space heating
5 with controlled industrial and two space heating extractions
6 with three controlled extractions—one industrial and two space heating
7 with back pressure operation
8 with back pressure operation and controlled industrial extraction

The purpose of this paper is to discuss the technical features and modes of operation of only one type of the above turbines, namely large cogeneration turbines for district heating applications.

Control of the District Heating Load

The maximum effect of cogeneration is achieved when the turbine is designed to match the heat consumption which varies substantially during the year. The capability of the turbine design to follow closely a variable heat load is very important in achieving high performance characteristics.

A typical space heating and domestic hot water load duration curve for an urban district is presented in Fig. 1(*b*). When the outdoor temperature increases the load decreases and becomes a constant

Contributed by the Power Division of THE AMERICAN SOCIETY OF MECHANICAL ENGINEERS and presented at the Joint ASME/IEEE/ASCE Power Generation Conference, Dallas, Texas, September 10–14, 1978. Manuscript received at ASME Headquarters June 27, 1978. Paper No. 78-JPGC/Pwr-16.

Copyright © 1980 by ASME
Downloaded 01 Jun 2010 to 171.66.16.58. Redistribution subject to ASME license or copyright; see http://www.asme.org/terms/Terms_Use.cfm

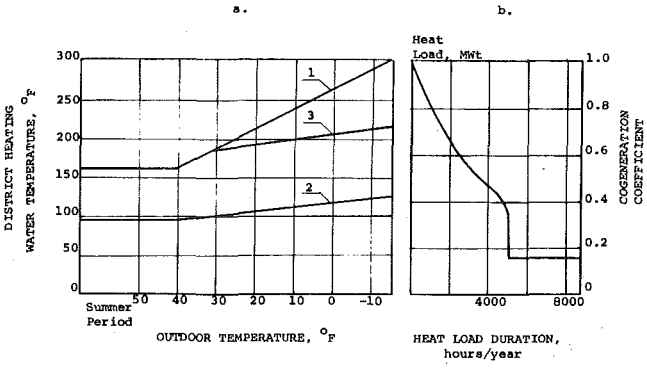


Fig. 1 (*a*) Dependence of the district heating supply (1) and return (2) temperatures on the outdoor temperatures. (3) district heating supply temperature provided by the turbine heat exchangers. (*b*) the load duration curve for space heating and domestic hot water supply

value in the summer for only domestic hot water supply.[1]

Different methods of controlling the heat supply in district heating systems have been developed. The simplest and most widely used is the central temperature control system. In this case, the required amount of heat is provided to the customer by varying the temperature in the supply network line at the power plant as a function of the outdoor ambient temperature. This means that the flow rate of water circulated in the district heating system is almost constant during the heating period.

The maximum temperature of the district heating water is determined by feasibility analysis. By increasing the delivery temperature in the network, the cost of the piping system is reduced. However, as a result, the extraction pressure at the turbine is increased and the electrical generation reduced. Therefore a cogeneration turbine is usually designed for base load operation and does not supply the peak load. The optimal cogeneration coefficient for a district heating system is determined by feasibility analysis.[2]

The type of heat load control and the cogeneration coefficient determine the temperature of the hot water supply. In the Fig. 1(*a*) the dependence of the temperatures in the district heating system on the outdoor temperature is presented.

It is evident that to provide the required network temperature the pressure of the steam extracted for district heating purposes should change correspondingly. Therefore the cogeneration turbine must be designed to closely follow the district heating system loads. In addition to the district heating modes the cogeneration turbine will operate also in á pure condensing mode. Therefore the turbine should provide the optimal economical operation during the year taking into account both cogeneration and condensing modes.

The specific features of cogeneration turbines for district heating applications may be summarized as follows:

1 suitable openings in the turbine cylinders for extraction of large amounts of low pressure steam

2 capability to control concurrently and independently the electrical load and the steam extractions over a wide range of combined electrical and thermal load demands

3 capability to operate in the condensing mode

4 heating in stages, of the district water, in series extraction heat exchangers

5 minimum throttling of extraction steam. This insures optimal operation of the bleed system over a wide range of parameters

6 maximum utilization of the steam entering into the condenser

In the following section one of the largest cogeneration turbines for district heating which has been in operation in the USSR since 1972, is discussed [2–4].

[1] Supply of cooling loads are not discussed in this paper.

[2] Cogeneration coefficient is the ratio of heat load supplied by the cogeneration turbine to the maximum peak demand.

Cogeneration Turbine for District Heating

This turbine is selected for discussion because it meets most of the previously stated requirements. The turbine has a nominal electric capacity of 250 MWe and nominal heat capacity of 385 MWt [2, 3]. The maximum electrical capacity of the turbine with the district heat load disconnected is 300 MWe.

The throttle flow for the turbine is 2,100,000 lbs/hr with steam parameters of 3400 psig and 1040/1049F. A longitudinal section of the machine is presented in Fig. 2.

The turbine is tandem compound with four cylinders: high pressure (*HP*), intermediate pressure No. 1 (*IP*1), and No. 2 (*IP*2), and low pressure (*LP*). Main steam from the boiler is supplied to two valve blocks, located each side of the HP element. Each block is a combination of the one stop and three control valves.

The *HP* cylinder has a double-wall counterflow arrangement. The blading of the *HP* cylinder has 12 stages. From the *HP* cylinder the steam is supplied to the intermediate superheat section of the boiler from which the steam is directed into *IP*1 through two valve blocks. Each valve block consists of an intercept and control valves. The *IP*1 cylinder is of the single flow, single wall type and has 10 stages. From *IP*1 the steam with pressure at about 78.2 psia at nominal load is supplied to *IP*2 which is double-flow with six stages in each flow, in which four stages are located before the upper extraction stage and two stages between the upper and lower stages. After *IP*2 a part of the steam may be supplied to the lower extraction point and the rest enters the *LP* cylinder via two crossover pipes. The pressure after *IP*2 is about 11.4 psia in the nominal condensing mode.

The *LP* cylinder is double-wall, double-flow, each flow having three stages, including the control stage. The steam supply into the *LP* cylinder is controlled by a grid type diaphragm. The moving blades of the last stage of the *LP* cylinder have a length of 37 in. with a mean diameter of 94 in., which corresponds to an area for both exhausts into the condenser of 152 square feet. From the *LP* section the steam is supplied into one condenser with a surface area of 150,000 ft^2 via a field welded connection.

The anchor point of the turbine is located on the side frames of the *LP* exhaust section.

The turbine is provided with an automatic control and protection system. The working fluid in the control system is condensate at a pressure of between 282 and 341 psia, which is provided from special pumps or from the condensate pumps. The flow diagram for the machine is presented in Fig. 3.

The district heating water is heated in the gland steam condenser and in two district heat exchangers in series, supplied with steam from the lower and upper space heating extraction points from *IP*2. These heat exchangers are of the horizontal type, with surface areas of 53,800 ft^2 each with stainless steel tubes. The condensate after the district heat exchangers, is pumped forward into the feedwater system.

The feedwater cycle of the turbine includes five low pressure heaters, a deaerator of 85 psia and three high pressure heaters. The turbine thus has seven noncontrolled extractions; the low pressure heaters No. 2 and 3 are supplied with steam from the space heating extractions.

The boiler feed pump is turbine driven by steam supplied from the extraction point of the turbine after the fourteenth stage. The steam after the feedwater turbine returns to the main turbine between the *IP*1 and *IP*2 and is partially extracted to the low pressure heater number 5.

The operating modes of the turbine are discussed in the following section.

Description of Operating Modes

The *HP* cylinder of the turbine is designed for steam flow in the nominal heating mode, and the low pressure cylinder for the condensing mode. By operating with nominal electrical and heat loads the steam flow to the *LP* section is restricted. Therefore it is possible to increase the electrical generation more than nominal by increasing the steam flow into the *LP* cylinder and at the same time decreasing the controlled extraction load. The maximum electrical generation

Downloaded 01 Jun 2010 to 171.66.16.58. Redistribution subject to ASME license or copyright; see http://www.asme.org/terms/Terms_Use.cfm

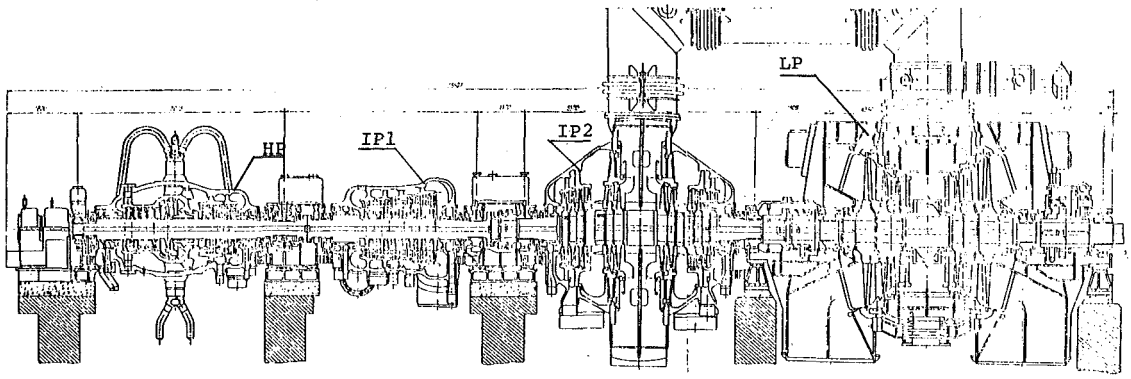


Fig. 2 A longitudinal section of the 250 MWe turbine

in the turbine is achieved when the full steam flow is passing through all sections, *HP*, *IP* and *LP* and a disconnected heat load. For the modern district heating turbine the maximum electrical generation is approximately 110–125 percent higher than nominal and depends on the type of the turbine, steam parameters, controlled extraction pressures and the capacity of the electrical generator. For the turbine discussed, the maximum electrical generation is 20 percent higher than at the nominal load. The nominal heating load of the turbine is equal to the sum of both space heating extractions, while the maximum heating load includes also, the heat utilized in the condenser.

As described above, the turbine has two space heating extractions utilized for heating of the district water in series. The turbine has one pressure regulator for space heating extraction consisting of a grid type diaphragm, located in the *LP* cylinder. The pressure may be controlled in only one of the two extraction stages: in the upper stage with two operating heat exchangers or in the lower stage with only the lower heat exchanger in operation. It should be noted that there are no control valves in the extraction piping.

The space heating extractions have the following pressure range: upper 8.5–38.5 psia, lower 7.2–21.3 psia. Distribution of the heating load between the upper and lower extraction stages is determined by the temperatures of the district heating water before and after the heat exchangers, the flow rate of the district heating water and the electrical load and can not be changed without a change in the mode of operation. The steam flow to the lower extraction stage cannot be reduced below that required for stage cooling purposes. Such a flow condition could obtain when only the upper heater is in operation. To prevent such a mode of operation, the district heat load must be distributed equally between the two extraction stages. To insure this condition district heating water must pass through the heaters in series at the same flow. Therefore the operation of the upper heater only, with the lower out of service is not allowed.

The series heating of the district water is similar to feedwater heating. However, in district heat exchangers the temperature difference between entering and leaving water is relatively small, 72–90°F, as compared to 270–450°F in a regenerative feedwater system. Another feature, is that in this system 70–80 percent of throttle steam is used for district heating, whereas only 20–30 percent is utilized in a regenerative feedwater system. This condition imposes a number of difficulties on the turbine design. Therefore, optimization of the series heating system is more important for the performance characteristics of the turbine when compared with the feedwater heating system of a condensing turbine.

The effectiveness of the series heating depends on a number of factors: number of stages, distribution of the load between stages, the load level, flow rate and temperature of the district heating water, changes in these parameters during the year, type of heat load control, climatic conditions of the district served, cogeneration coefficient, throttle steam conditions, type of turbine and auxiliary equipment. As an example, in Fig. 4 the dependence of the optimal distribution of the heat load between the heating stages on the terminal temperature difference in each stage is presented.

The maximum heat load from both extractions takes place when the control diaphragm in the *LP* element is closed. In these conditions the pressure in the controlled extraction increases, and the flowrate

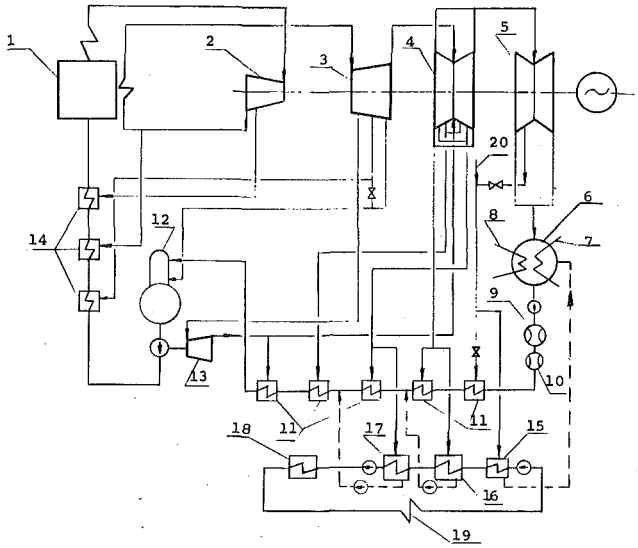


Fig. 3 A flow diagram of the 250 MWe congeneration turbine: (1) boiler, (2) *HP* cylinder, (3) *IP*1 cylinder, (4) IP2 cylinder, (5) *LP* cylinder, (6) condenser, (7) circulating cooling water bundle, (8) district heating bundle, (9) main ejector cooler, (10) cooler of the gland condenser ejector, (11) low pressure heaters, (12) deaerator, (13) boiler feedpump, (14) high pressure heaters, (15) gland steam condenser, (16) lower stage district heat exchanger, (17) upper stage district heat exchanger, (18) water heating peaking boiler, (19) district heating load, (20) steam from the gland system

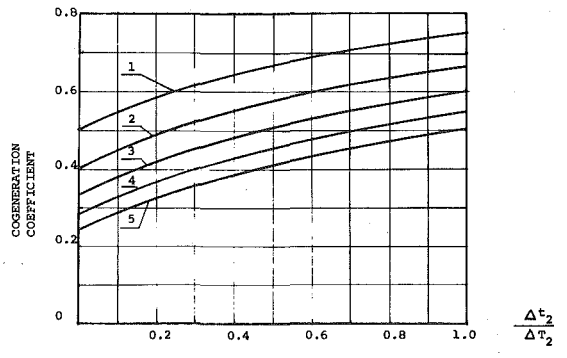


Fig. 4 The dependence of the optimal distribution of the heat load on the terminal temperature difference in each extraction stage

$$\frac{\Delta t_1}{\Delta T_1}: \quad \begin{matrix} 1-0;\ 2-.25;\ 3-0.5; \\ 4-0.75;\ 5-1.0 \end{matrix}$$

Δt_1 and Δt_2—terminal temperature difference for the lower and the upper stage, respectively. ΔT_1 and ΔT_2—temperature difference between the entering and leaving district water in the lower and upper district heat exchanger, respectively

Downloaded 01 Jun 2010 to 171.66.16.58. Redistribution subject to ASME license or copyright; see http://www.asme.org/terms/Terms_Use.cfm

of the cooling steam into the *LP* section increases in proportion to the pressure in front of the closed diaphragm. When the extraction pressure decreases, the cooling steam flow also decreases. In Fig. 5 the variations of the pressure in the extraction stages for a similar district heating turbine with two space heating extractions is presented. From this figure one can see that the pressure in the upper extraction stage varies during the heating period between 7.1–18.0 psia and in the lower extraction in the range 3.5–9.0 psia. If the cogeneration coefficient increases, the pressure in the stages increases accordingly. When the extraction pressure changes the heat load is redistributed between the district heat exchangers and affects the steam flow in the upstream stages. The efficiencies of these stages change accordingly. Substantial changes of the extraction pressures and volumetric flows take place for the upstream stages when the seasonal heating period changes, or the turbine operates in the condensing mode. Taking into account the variable conditions of upstream stages the design of the bleed system of the turbine should provide the maximum effectiveness during an annual period.

The use of steam control devices in the turbine increases the possibility of a pressure increase in the *IP* and *LP* cylinders as a result of control system malfunction. Therefore the extraction stages are supplied with safety devices. The extraction pipe from the upper stage is also supplied with nonreturn valve to prevent overspeed of the turbine.

The cogeneration turbine in the district heating mode of operation provides steam flow for cooling the *LP* stages and this flow enters the condenser. The minimal cooling flow requirements are determined by the turbine design features such as type of the *LP* bleeds, control diaphragm leakage and operation factors (such as pressure in the extraction stage and the condenser).

The following features are incorporated in the turbine design to utilize the cooling steam flow:

1 Installation in the condenser of a separate tube bundle, in which the return or make-up district water may enter and pick-up heat.

2 Construction of the turbine tail-end with a cooling system capable of working with a low steam flowrate, elevated vacuum and temperature.

When utilizing the cooling steam flow in the condenser this flow is obviously limited. In this situation the condenser is cooled only by the return district heating water and the pressure in the condenser is elevated, which increases the temperature of the turbine exhaust. When operating in the condensing mode the circulating cooling water is supplied both to the main surface and the district bundle of the condenser. District water is not provided in this situation.

When the cooling steam flow is being utilized, the grid diaphragm in the low pressure elements is closed and the turbine is working in a mode similar to that of back-pressure operation, that is, all heat supplied to the turbine except for mechanical generator and radiation losses, is used for electrical and heat generation. However, the possibility of controlling the heat and the electrical loads independently is restricted in this mode.

The design of the condenser with a district heating bundle, having separate water boxes in the same steam space permits changes of the turbine modes without shutting down the turbine and reducing the capacity.

In single purpose turbines there is a proportional relationship between the steam flowrate through the turbine, and the amount of drain and pressure drop between the feedwater heaters. This provides in most of the operation modes a reliable cascading of the drains from one feedwater heater to another.

In the cogeneration turbine such relationship does not exist. When operating with controlled extraction the flowrate through the *LP* cylinders is reduced. However, the throttle flow in the turbine increases. When the extraction stages are operated with small steam flowrates, the pressure difference between the interconnected heaters is not enough to provide the cascading of the drains from one heater to another. Therefore in this type of turbine the cascading mode of operation is limited and drain pumps are often used.

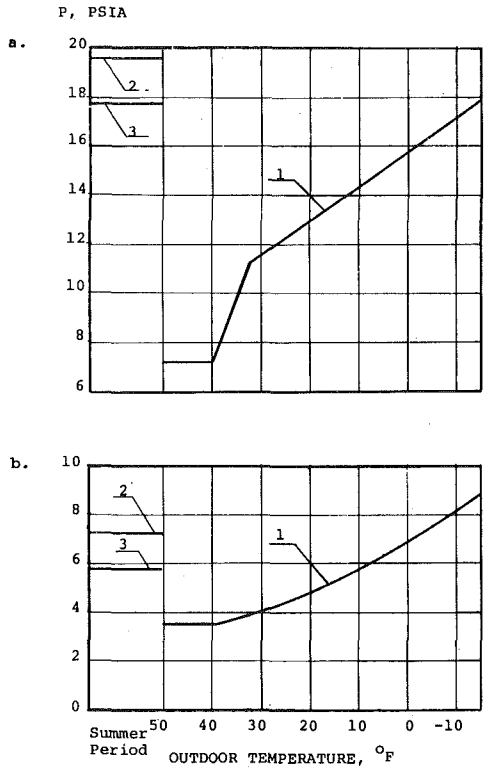


Fig. 5 Dependence of the stream pressure in the upper (*a*) and lower (*b*) extraction stages on the outdoor temperature. Design temperatures in the supply and return lines of the district heating system are 300°F and 150°F, *respectively; the cogeneration coefficient is 0.5.* (1) *heating period,* (2) summer period with the domestic hot water load, (3) condensing mode

Another specific feature of the cogeneration turbines is when the turbine is running with high heat load, the flowrate of the steam entering into the condenser is low and therefore there is not enough condensate to cool the gland steam condenser and the ejector. Therefore, in this mode, a recirculation line from the feedwater system is provided back to the condenser.

Conclusion

From the foregoing it is evident that the operating modes of cogeneration turbines are somewhat more complex than for single purpose machines. It is therefore necessary to recognize this characteristic and design the cogeneration turbine in conjunction with the district heating system to be served.

References

1 Oliker, I., and Philipp, J., "Technical and Economic Aspects of District Heating Systems Supplied From Cogeneration Power Plants," 40th Annual American Power Conference, Chicago, IL, 1978.

2 Rishkin, V. Ya., *Thermal Power Plants,* Energiya, Moscow, 1966.

3 Benenson, E. I., and Ioffe, L. S., *Steam Turbines for District Heating,* Energiya, Moscow, 1976.

4 Greil, A. D., and Sacharov, A. M., "Results of The Performance Test of the Turbine T-250/300-240 UTMZ," *Teploenergetica,* No. 2, 1977.

Downloaded 01 Jun 2010 to 171.66.16.58. Redistribution subject to ASME license or copyright; see http://www.asme.org/terms/Terms_Use.cfm

R. J. Zoschak
Mem. ASME

S. F. Wu
Mem. ASME

Foster Wheeler Development Corporation
Livingston, N. J.

D. N. Gorman
Mem. ASME

Martin Marietta Corporation
Denver, Colo.

Design and Testing of a Cavity-Type, Steam-Generating, Central Receiver for a Solar Thermal Power Plant

This paper focuses on the design and operating aspects of a 10-MWe cavity-type, natural-circulation, steam-generating receiver for a central-receiver thermal power plant. The development of the receiver concept and the basic design features are described. The solar energy input analysis, thermal/hydraulic performance, and structural design of the receiver are discussed along with its control concept and transient operation. The design, construction, and testing of a 5-MWt scaled-down version of the 10-MWe receiver are summarized with emphasis on test objectives, scaling criteria, and design similarities to the full-scale receiver.

Introduction

Phase I of the Central Receiver Solar Thermal Power System (CRSTPS) program, authorized by the Division of Solar Energy, ERDA, Washington, D.C., was the two-year initial phase of the Central Receiver Solar Thermal Power Development and Demonstration program which includes the construction and operation of a 10-MWe pilot plant and, ultimately, a commercial demonstration plant.

Phase I, the preliminary design of the CRSTPS, was broadly divided into three major activities:

- The baseline design definition for the commercial plant and the pilot plant which would best serve as the development vehicle for the commercial plant.
- The parallel design, fabrication, and testing of subsystem research experiments to demonstrate feasibility of the solar-unique subsystems (collector, receiver, and thermal storage).
- The completion of the pilot-plant preliminary design, which included further reexamination of basic features resulting from more detailed studies and data obtained from the subsystem research experiment (SRE) test programs.

The work reported here was part of a complete Phase I program performed by a team of organizations with complementary capabilities. Martin Marietta Corporation was the team leader, responsible for program management, system integration of the CRSTPS commercial and pilot plant designs, the collector subsystem design, and the collector SRE.

Foster Wheeler Energy Corporation designed the steam-generating receiver for the full-scale solar plants and designed, fabricated, and erected the 5-MWt SRE receiver.

Georgia Institute of Technology was responsible for the thermal storage subsystem design and the thermal storage SRE.

Bechtel Corporation had design responsibility for the Electric Power Generation subsystem and the architect and engineering features of the plants.

The CRSTPS plant is made up of five major subsystems: the collector, receiver, and thermal storage, which are unique to the solar application; and the electrical power generation and plant control, which are currently commercial. Energy flow through the plant starts with the solar energy intercepted by the heliostats of the collector subsystem. The solar energy is reflected in concentrated beams to the receiver. Within the receiver subsystem, the solar energy is converted to thermal energy in the form of superheated steam and is transmitted to the thermal storage and electrical power generation subsystems. Conversion of thermal energy from either the receiver or the storage system to electricity takes place in the turbine and generator of the electrical power generation subsystem. Energy flow in the thermal storage subsystem is from steam to sensible heat in the storage fluids during charging and from the sensible heat of the fluids to steam during discharge.

Basic features of the Martin Marietta team's solar power plant concept, shown pictorially in Fig. 1, have been established to achieve a practical utility-scale solar plant with the highest performance consistent with the goals of:

- Minimized capital and operating costs
- Safe, flexible, reliable, and long-life application features
- Timely development of solar power technology.

The purpose of this paper is to describe key design and performance features of the receiver concept, including fabrication, testing, and evaluation of the 5-MWt SRE receiver.

Basic Design

Design Requirements. An abundance of design and operating requirements from several sources shaped the receiver subsystem

Contributed by the Power Division for publication in the JOURNAL OF ENGINEERING FOR POWER. Manuscript received at ASME Headquaters December 4, 1978.

Copyright © 1980 by ASME

Downloaded 01 Jun 2010 to 171.66.16.58. Redistribution subject to ASME license or copyright; see http://www.asme.org/terms/Terms_Use.cfm

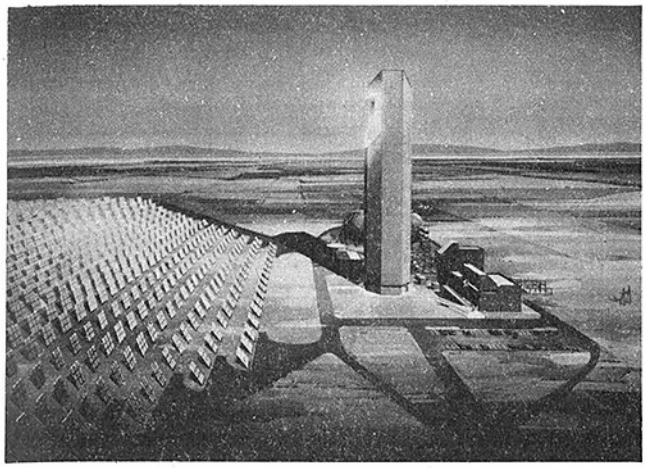


Fig. 1 Artist's rendition of preliminary design of 10-MWe pilot plant

design concept and evaluation. Many requirements changed during the course of the Phase I effort, as the total system and the subsystems became more clearly defined and the operating interfaces became more firmly established. The major requirements that directly guided the design of the pilot-plant receiver subsystem are given in Table 1.

Basic Features and Arrangement. The Martin Marietta CRSTPS Commercial Plant design features 15 modular collector/receiver subsystems, each capable of converting 52 MW of solar energy into useable steam flow. The pilot-plant version is powered by a collector/receiver module that is identical in size, output, and water/steam statepoint requirements to one commercial-plant module. This elimination of scaling uncertainties allows a direct evaluation of commercial-plant receiver design, operating, and economic characteristics at the pilot-plant level.

The commercial/pilot-plant receiver subsystem consists of a single-drum, natural-circulation, side-opening-cavity receiver supported by an enclosed and roofed structural-steel tower.

The essential instrumentation, valving, and controls of the receiver are shown in the schematic flow diagram (Fig. 2). A simplified cutaway drawing of the receiver is shown in Fig. 3. All walls of the cavity are vertical. The rear wall and a large portion of both side walls are covered with 38.1-mm OD carbon-steel boiler tubes on 44.5 mm centers, using MONOWALL™ construction in which the tubes are joined together along their length by continuous-weld integral fins to form flat panels. This construction was adopted because it is structurally rigid, can be handled in shipment and during erection with relative ease, and is impenetrable to solar flux.

The superheater consists of six passes in series, two passes on each of the sidewalls and two on the rear wall. Each pass is made from a number of parallel 25.4 mm OD austenitic stainless steel tubes arranged side by side on 28.6 mm centers to form one or more platens. These tube platens are placed in front of the waterwall panels (on the cavity side). Because of the heat-flux pattern, the passes on all three walls must be approximately aligned horizontally at two elevations. All superheater headers and transfer lines between passes are located behind the waterwall panels. Superheater tubes penetrate through openings in the water-wall panels at the inlet and outlet of each pass and at intervals along each pass where expansion loops and intermediate supports are located. These openings are made by offsetting the required number of adjacent waterwall tubes outward into the cavity a sufficient distance to provide clearance for the superheater tubes. The offset waterwall tubes serve to shield the openings from the incident solar flux.

The inner surfaces of the cavity that are not lined with boiler tubes are lined with either steel coated with reflective material or refractory, depending on the intensity of incident solar flux on the particular surface. The outside surface of the entire cavity, as well as the steam drum and exterior piping, is encased in weatherproofed insulation.

The entire receiver is suspended from a structural steel grid made

Table 1 Pilot-plant receiver requirements

Site Location	Barstow, California
Aperture Elevation (centerline)	90 m above ground level
Aperture Opening	7.498 m square
Maximum Solar Energy to Receiver	52.3 MWt
Feedwater Input:	
Flow Rate	20.76 kg/s
Pressure	13,460 kPa
Temperature	193°C/229°C
Receiver Output:	
Flow Rate	20.55 kg/s
Temperature	516°C
Pressure	10,687 kPa
Cycle Life:	
Diurnal Cycles	13,000
Cold Starts	1,300
Start-Up Time:	
Overnight	45 min
Cold	6 hr
Winds (Ground Level)	3.5 m/s Maximum Operating 40.0 m/s Maximum
Ambient Temperature	−29°C/49°C
Seismic Activity (Ground Level)	0.25 *g*

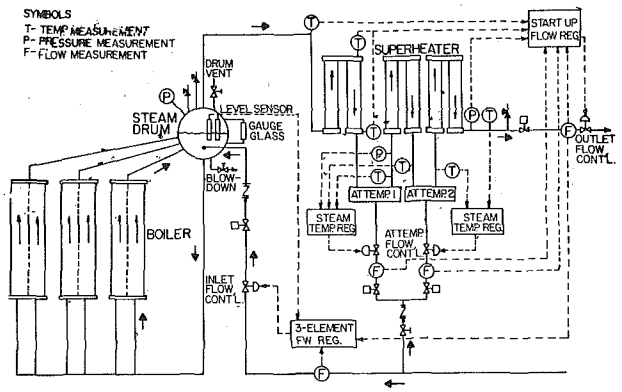


Fig. 2 Schematic flow diagram of the receiver

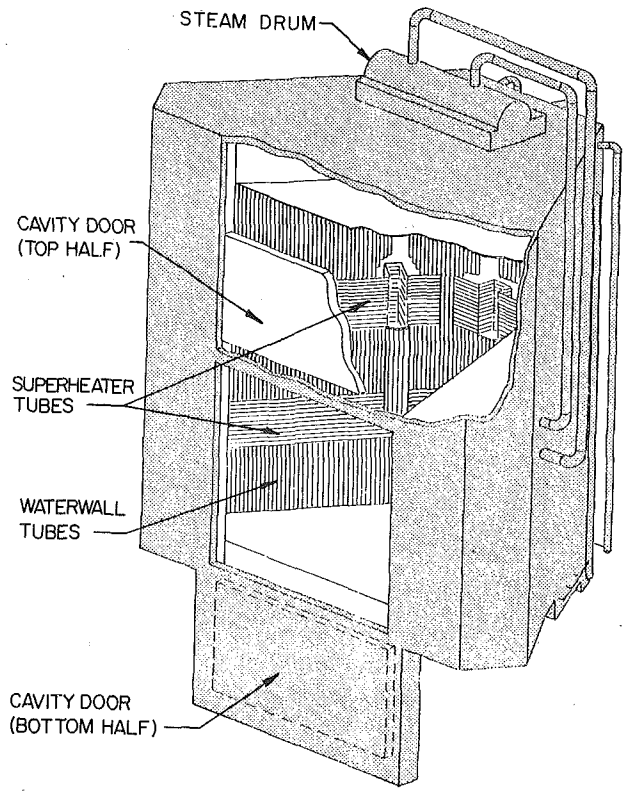


Fig. 3 Simplified cut-away drawing of the receiver

Downloaded 01 Jun 2010 to 171.66.16.58. Redistribution subject to ASME license or copyright; see http://www.asme.org/terms/Terms_Use.cfm

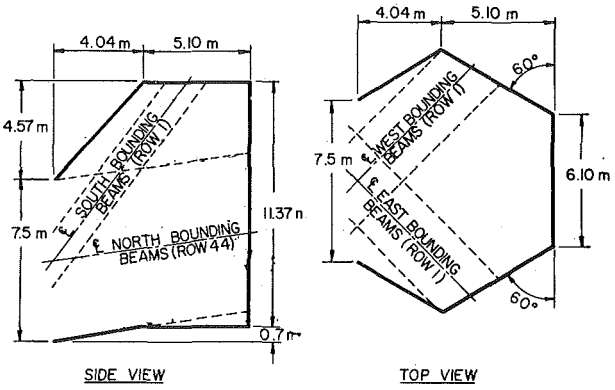


Fig. 4 Commercial/pilot-plant receiver cavity configuration

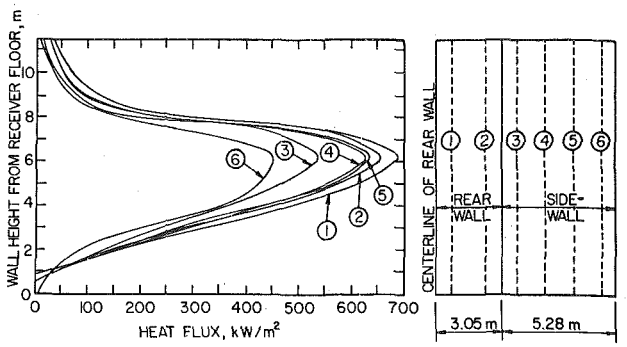


Fig. 5 Incident heat-flux distribution on active surfaces of receiver, 1200 winter solstice

up of large girders that are attached to the columns of the tower. The receiver is free to expand downward from the support grid, rearward from the front, and sideward about its centerline. The waterwalls are held in position and braced against externally applied loads (wind and seismic) by horizontal, structural-steel buckstays located at five elevations. These buckstays also support the enclosure. The superheater headers are supported by brackets welded to the enclosure. Support points for the superheater tubes are located at the expansion loops and where the tubes penetrate the waterwalls. Mechanical snubbers attached to the buckstays transmit seismic loads to the tower structure while still permitting movement of the receiver parts caused by thermal expansion.

The aperture of the cavity is provided with an insulated door that can be closed to minimize heat loss and resultant cooling when the receiver is out of service. This door is mounted inside the receiver enclosure and is made from two pieces which abut each other at the horizontal centerline of the aperture when the door is closed.

Cavity Characteristics

Configuration. Geometrical design of the cavity was accomplished in an iterative procedure along with layout of heliostats in the collector field. Optimum size, shape, and orientation of energy-absorption surfaces, as well as design of the aperture, are dependent upon specific location of heliostats and the pattern of their projected radiation vectors.

Fig. 4 depicts the selected cavity configuration with projections of heliostat solar beams which bound the directly insolated surfaces. Energy is absorbed by the entire rear wall and most of the adjacent sidewall surfaces. The forward sides (adjacent to aperture), floor, and ceiling receive little direct insolation.

The aperture was optimally sized to allow the maximum amount of reflected energy from all heliostats to enter while minimizing direct radiation and convection losses from the cavity. The 7.498 m square aperture selected captures an annual average of 97.7 percent of the energy from the heliostat field and loses about 6 percent by radiation and convection.

The depth and width of the cavity and the orientation of the three active walls with respect to the aperture were established to attain a reasonable compromise between receiver size and active surface heat-flux distribution. A larger cavity could result in lower peak heat fluxes and a somewhat more uniform distribution of energy over the active walls, but it would also be heavier (a detriment to tower design), costlier, and less efficient as a result of increased heat losses through the insulated walls.

Radiant Energy Input Analysis. An accurate prediction of heat-flux patterns within the cavity is vital to the proper design of the receiver. First, the available active wall area (that which receives direct solar flux from the field) must be divided into boiler and superheater zones so that the total energy into each of those zones is compatible with specified steam-generation rates, pressures, and temperatures. The second important factor is knowing the magnitude and location of peak heat fluxes, which can induce excessive temperatures and thermal stresses within individual superheater tubes. The complexity and quantity of calculations to be performed dictated the use of a computerized math model based on the Thermal Radiation Analysis System (TRASYS) developed by Martin Marietta.

TRASYS locates the sun at any given time of day and day of year, orients each heliostat in azimuth and elevation to project the focused solar image toward the specified aiming point (i.e., center of cavity aperture), and then determines the resultant heat-flux distribution upon the receiver surfaces. Receiver and heliostat mirror surfaces can be divided into any desired number of finite-sized elements. The effect of spherical aberration on projected solar image size can be approximated by a programmed factor based on mirror size and angle of incidence.

Incident heat-flux profiles were calculated for the three active heat-absorbing surfaces of the receiver cavity at several selected times of day and year. The heat-flux distribution at 1200 on the winter solstice is shown in Fig. 5, along with a sketch depicting the right half of the rear and sidewall surfaces which receive the incident energy. The vertical heat-flux gradients are characteristically quite sharp, while the horizontal gradients are much less severe.

The cavity heat-flux profiles were a key consideration in defining the sizes and locations for superheater surfaces. A specific proportioning of total energy between boiler and superheater zones was established to meet steam output state-point requirements. Some imbalance in those proportions will occur since the heat-flux patterns shift as a function of time, but it was desirable to minimize the excursions from the standpoint of steam temperature-control design.

Table 2 Energy proportions on superheater panels

Day of Year	Time of Day (h)	Percentage of Energy on Superheater Panels (Passes 1 Through 6)						
		1	2	3	4	5	6	Total
Spring Equinox	800	4.9	7.6	7.4	3.5	4.4	2.6	30.4
	1200	6.9	7.9	6.3	3.1	4.0	2.5	30.8
	1600	8.1	7.6	4.5	3.0	4.4	2.8	30.4
Summer Solstice	600	3.4	6.7	8.0	4.6	4.8	2.0	29.5
	1200	6.7	7.6	6.1	3.4	4.3	2.8	30.9
(Pilot-Plant Design Point)	1400	7.8	7.5	5.1	3.2	4.4	3.1	31.1
	1800	8.7	6.7	3.1	2.4	4.8	3.8	29.5
Winter Solstice	800	5.4	6.7	7.2	3.3	4.2	2.6	29.5
(Commercial-Plant Design Point)	1200	6.9	8.0	6.4	3.0	3.6	2.5	30.5
	1600	7.7	6.7	5.0	3.1	4.2	2.8	29.5

Downloaded 01 Jun 2010 to 171.66.16.58. Redistribution subject to ASME license or copyright; see http://www.asme.org/terms/Terms_Use.cfm

The superheater surfaces are sized in accordance with the minimum anticipated proportion of energy incident upon them, and the spray attemperator system is designed to accommodate increases in that proportion. Table 2 summarizes the direct-incident energy distribution for several extreme time points during the year. Although the proportion of energy falling on a given pass can vary considerably with time, the total percentage falling on all six passes changes only slightly—from 29.5 to 31.1 percent.

Cavity Thermal Losses. The cavity concept was selected for the commercial/pilot-plant receiver to minimize thermal losses during operation and overnight or cloudy-day shutdown periods. Heat loss occurs in three basic ways:

- Radiation through the aperture
- Convection through the aperture
- Conduction through the cavity walls and supports

Radiation includes reflected solar energy and infrared energy emitted from the hot internal surfaces. Convection stems from temperature-induced air-density gradients in and around the receiver and from wind. Both radiation and convection losses are minimized by the cavity enclosure during operating periods and are eliminated entirely by the aperture door when the receiver is shut down. Conduction loss through the cavity walls and aperture door is limited by 0.2 m-thick mineral-wool insulation. Loss by conduction through the supports was calculated to be about 15 percent of the cavity insulation loss.

Radiation and conduction losses are easily analyzed and subject to a relatively small degree of uncertainty. Convection, however, requires substantial empirical data to accurately define heat-transfer coefficients for the cavity geometry and mass-transfer coefficients for the cavity geometry and mass-transfer characteristics through the aperture for various wind and temperature conditions. Results from some limited experimental work performed at Martin Marietta [1] using an electrically heated, small-scale cavity receiver was used as the basis for predicting convection loss.

Radiation, convection, and conduction losses were calculated at different energy input levels. At the design-point energy input of 40.5 MW, the radiation loss is 2.8 percent, or 1.13 MW. The convection and conduction losses are 1.31 and 0.11 MW respectively. Therefore, the total thermal loss at the design point is 2.55 MW, or 6.3 percent of the cavity input energy. The convection and conduction losses are nearly independent of receiver power level at operating steam conditions and will vary by only about 5 percent of their maximum values from zero to maximum steam output.

Overnight cool-down of the receiver is governed by conduction heat loss and thermal capacity of the insulated "hot" part of the unit. The insulated cavity door prevents any radiation and convection losses at night. A design goal was restriction of the overnight drop in water/steam saturation temperature to a maximum of 83°C.

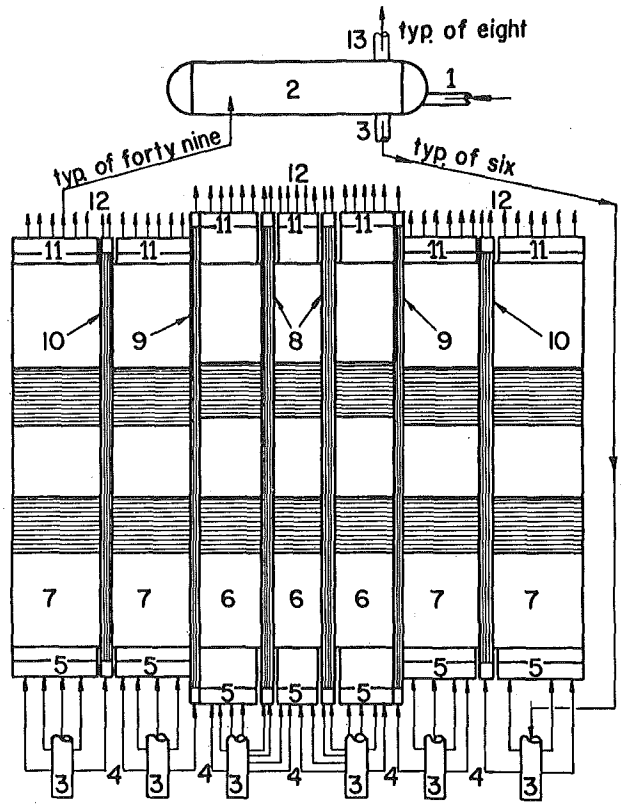


Fig. 6 Boiler circuitry of commercial/pilot-plant receiver (1: feedpipe, 2: drum, 3: downcomers, 4: feeders, 5: headers, 6,7: rear and side walls, 8–10: screen panels, 11: headers, 12: risers, 13: steam outlets)

Receiver Design and Analyses

Thermal/Hydraulic. The boiler circuitry design and circulation analysis were iterative in nature. The arrangement selected for the preliminary receiver design is shown schematically in Fig. 6. Fig. 7 shows typical profiles of steam quality, heat-transfer coefficient, and incident heat flux along the boiler heating surface of the rear wall screen panel, which receives the highest rate of heat input.

To assess the part-load circulation performance, calculations were also made at 75, 50, 25, 10, and 5 percent of the maximum heat input to the receiver. Each part-load calculation was based on drum pressure corresponding to the full superheater outlet pressure of 10,687 kPa. The total circulation flow rate, the steam-generating rate, and the ratio of the former to the latter (circulation ratio) are presented in Fig.

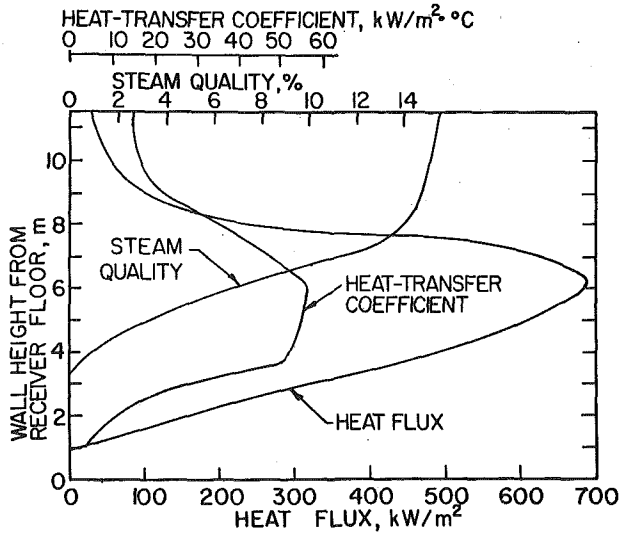


Fig. 7 Typical steam quality, heat-transfer coefficient, and incident heat-flux profiles along the boiler wall

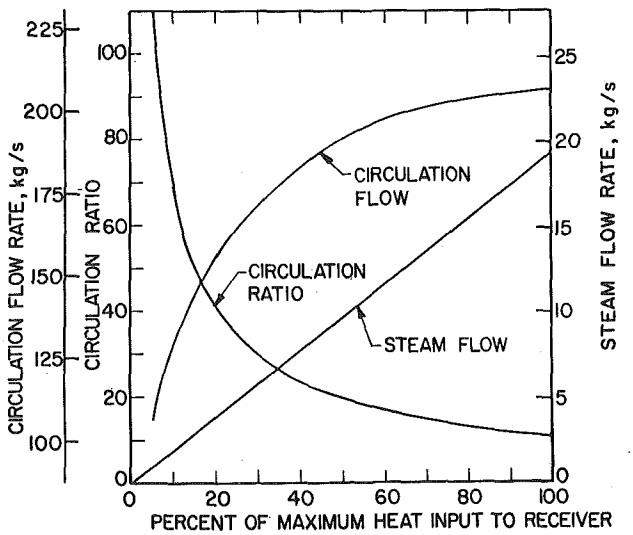


Fig. 8 Circulation characteristics at different load conditions

Downloaded 01 Jun 2010 to 171.66.16.58. Redistribution subject to ASME license or copyright; see http://www.asme.org/terms/Terms_Use.cfm

8 as functions of the heat input.

The heating surface in the receiver cavity must be correctly proportioned between superheater and boiler sections to obtain the designed superheater outlet conditions. Because of the uneven heat-flux distribution on the heating surfaces, a system of multiple superheater panels was necessary, and a trial-and-error design had to be followed. For each proposed arrangement, the procedure was first to ensure that the total energy absorbed by the superheater surface met requirements. The superheater surface was then divided into a suitable number of passes connected in a desired order so that sufficiently high steam mass velocity could be obtained without exceeding the allowable pressure drop across the entire superheater. For each superheater pass, the average fluid-bulk temperature and film coefficient were calculated. With this information and heat-flux values taken from the distribution curves, thermal stresses were spot-checked for the critical locations. If the stresses were too high, the flow arrangement was revised, and the procedure was repeated.

The final selected superheater surface arrangement, containing six passes, is shown schematically in Fig. 9. In this arrangement all passes are divided into two subpasses each, and steam flow is divided into one upper and one lower subpass, as shown in this figure. This division reduces the vertical heat-flux variation in each pass and effects a more uniform flow distribution and steam-temperature rise among the tubes.

At the maximum insolation condition, the predicted pressure drop across the superheater is 1620 kPa, of which 138 kPa is the loss through the two attemperators. At the design condition, the total pressure drop across the superheater is 1103 kPa.

Structural. The solar receiver is a power boiler; hence the minimum requirements and criteria for its design are those given in *ASME Boiler and Pressure Vessel Code,* Section I. The design philosophy of Section I is to set the wall thickness necessary to keep the basic hoop stress below the tabulated allowable stress. Section I does not require a detailed evaluation of the higher, more localized stresses known to exist, but instead allows for these by the safety factor and a set of design rules. In addition, Section I has no criteria to evaluate thermal stresses, creep, and fatigue. Past experience shows that this approach has worked reasonably well in the case of conventional power boilers. However, the loading conditions in the solar receiver are different from those of the conventional boilers, because the solar receiver is subjected to diurnal start-up and shutdown cycles. The creep and fatigue associated with thermal cycling are important failure modes in a solar receiver, but Section I does not have explicit criteria to evaluate these failure modes. In the design of the receiver, Section I was supplemented with the criteria given in Section VIII-Division 2. The high-temperature fatigue curves given in ASME Code Case 1592 were also used.

To insure the structural integrity, lifetime requirements, and performance characteristics of the receiver, detailed structural analyses of superheater, boiler waterwall, and other pressure parts were made. These are discussed in detail in [2]. The superheater tube-support arrangement selected for this receiver design is shown schematically in Fig. 10. The superheater tubes are welded to headers at both ends, with intermediate supports located at the expansion loops. This arrangement allows the superheater tubes, heated by solar radiation from one side, to bow out laterally and stretch axially and, consequently, reduces the thermal stresses.

Transient Consideration. A comparison of start-up and shutdown transients showed that the former imposed much more severe temperature and stress conditions on the receiver. Therefore, analytical studies were concentrated on start-up transients, specifically:

- Hot start-up after overnight shutdown
- Restart after cloud passage
- Cold start-up from ambient condition.

Hot start-up is a diurnal morning start-up of the receiver after overnight shutdown. Since the receiver cavity insulation is designed to limit the drop in saturation temperature to 83°C during a 12-hr shutdown period, it can be restarted each morning from a relatively hot standby state. To utilize all available insolation during the start-up period, it is desirable to bring up the receiver with the full solar energy input anticipated for any day of the year or, simply phrased, "start up with the sun." This method minimizes the control functions required for the collector subsystem but incurs more operational restraints on the receiver subsystem. Among all the parameters affecting a hot start-up transient, the most important and governing parameter is the rate of drum pressure increase.

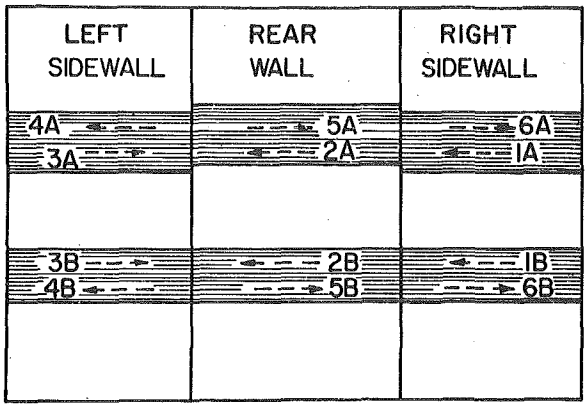


Fig. 9 Arrangement of superheater passes, commercial/pilot-plant receiver

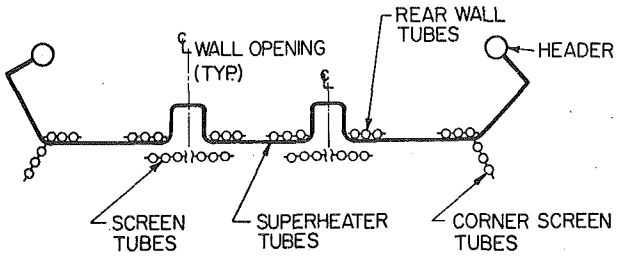


Fig. 10 Superheater tube-support arrangement

The receiver, which was operating at the normal load condition before being shut down by cloud cover, must restart as soon as the cloud disappears. Because the receiver is expected to be started up from its full pressure condition, the rate of increase of incident energy becomes the dominant parameter for this type of restart. Although the solar energy to the receiver can conceivably be brought up from zero to the peak intensity in $\frac{1}{2}$ min by the collector subsystem, such a rapid rate cannot be accepted by the receiver.

Cold start-up is anticipated when the receiver is first put into operation or is started after a shutdown longer than 72 hr. The receiver is assumed to be at the ambient condition before starting. When starting from this condition, the receiver cannot absorb the fully concentrated solar energy without overheating components, especially during the early period of start-up when no steam is being generated. Thus the incident energy to the receiver must be greatly reduced by defocusing the heliostats. After the receiver begins to generate steam, the incident energy intensity can be gradually increased, accompanied by a gradual increase in drum pressure. Therefore, the rates of increase of both incident energy and drum pressure govern this type of start-up.

The study of start-up transients involved the development of a computer program for transient overall receiver heat balance calculation and the use of a finite-element program, ANSYS, for local tube temperature and stress evaluations. The overall heat-balance program uses a group of lump-mass nodes as a receiver model, approximates a transient period by a sequence of steady-state intervals, and performs a simplified heat-balance calculation for each time interval. The results of a typical hot start-up are shown in Fig. 11. This is an acceptable hot start-up on the winter solstice, which is more critical than on any other day of the year because the rate of increase of solar energy to the receiver is fastest. As shown in the figure, full rated temperature is reached earliest—50 min after starting. Full pressure of the outlet steam is reached in 60 min.

Downloaded 01 Jun 2010 to 171.66.16.58. Redistribution subject to ASME license or copyright; see http://www.asme.org/terms/Terms_Use.cfm

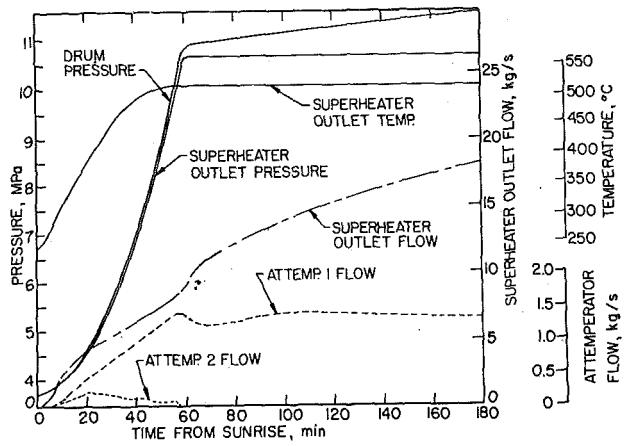


Fig. 11 Predicted transient results for an acceptable hot start-up

Control. During normal operation the receiver delivers steam to the Electrical Power Generation Subsystem and Thermal Storage Subsystem at controlled superheater outlet conditions of 10,687 kPa and 516°C. The amount of steam delivered at any instant is a function of the incident energy, feedwater temperature, and receiver losses, assuming quasi-steady-state operation. True steady state is never achieved because the incident energy is constantly changing as the sun changes position. Therefore, there is some thermal capacitance lag between incident energy and steam generation rate.

Control of superheater outlet steam temperature is required during normal operation because of the diurnal variations in incident heat-flux distribution between superheater and boiler surfaces and the effect of thermal capacitance on the relationship between steam flow and heat flux incident on the superheater. A two-stage attemperation system is used for steam temperature control. Referring back to Fig. 2, the first-stage attemperator is located between Superheater Passes 2 and 3, and the second-stage attemperator between Passes 4 and 5. The two attemperators operate in parallel. The first stage is set to control the temperature leaving Pass 4 at some fixed predetermined value, and the second stage controls the temperature at the superheater outlet. Pressure sensed at the outlet of the first-stage attemperator is used in the control logic to determine the saturation temperature at the attemperator outlet.

Feedwater flow is controlled during normal operation by a conventional three-element feedwater regulator responsive to drum water level, steam flow, and feedwater flow.

Since the receiver must be started up at least once a day, the start-up must be automated to bring the receiver on line in a minimum time consistent with safe operation. The fundamental requirement during start-up is to maintain sufficient steam flow through the superheater during the pressure ramp-up to keep superheater tube temperatures and front-to-back tube-wall temperature differences within safe limits.

Based on experience gained in the SRE tests, a simple, automatic start-up control system has been devised. This control system will ramp up receiver pressure at an optimum rate consistent with safe superheater temperatures for any hot restart no matter what pressure prevails in the receiver at the outset of the ramp-up. The start-up flow regulator, shown in Fig. 2, controls flow through the superheater by modulating a valve in the superheater outlet line. Inputs to the regulator are steam flow, attemperator water flows, saturation temperature at the drum, steam temperature rise across Superheater Pass 2, and superheater outlet steam pressure. The control system operates in response to a start-up function which relates the acceptable drum water temperature rise to the instantaneous heat absorbed and the drum water temperature. The operation of this control system will have to be tuned during preliminary operation of the receiver.

As is apparent, the start-up control system responds to but does not control the energy input to the receiver. Based on the analyses and on the SRE test experience, it is anticipated that this control system can start up the receiver on diurnal hot restarts as the receiver starts up with the sun. On cold starts or other hot restarts begun during the day when insolation is high, the focusing of heliostats on the receiver must be programmed to obtain an acceptable rate of increase of solar flux.

Subsystem Research Experiment (SRE) Receiver

Objectives and Requirements. The objectives of the SRE were to confirm thermal/hydraulic performance, structural design, and operation of controls and to simulate pilot-plant operating transients, steady-state operation at design point and reduced loads, and steady-state operation at peak heat flux.

The need for simulating the pilot-plant receiver operating conditions resulted in the following basic requirements for the receiver experiment:

- Delivery of steam at the same pressure and temperature
- A structural arrangement similar to that of the pilot-plant receiver in critical zones
- Use of the same materials of construction
- The distribution of absorbed heat flux with the same pattern over the heating surfaces
- An experimental receiver subjected to start-up and other transients typical of those predicted for the pilot plant

Scaling. Because the pilot-plant receiver design could not be split up into identical modules, one of which could be tested, it had to be scaled down as a unit. However, complete geometric similarity was neither possible nor even desirable, because it was important to maintain full scale in certain critical areas.

It was important that the SRE receiver cavity be a scaled-down version of the pilot-plant design. First, a geometrically similar cavity facilitates duplication of the heat-flux patterns. Second, the attainment of valid operational data from testing with an actual heliostat field is very dependent upon the similarity of cavity geometry.

Identical heat-flux densities were maintained at corresponding points so that heating surface arrangement, ratio of superheater surface to steam-generator surface, and location of peak heat-flux density on both superheater and steam-generator surfaces were not changed when scaling down. This criterion was satisfied by geometric similarity and by having the energy per unit of internal area of SRE receiver cavity equal to that in the pilot-plant receiver. The SRE receiver was designed to accept 5-MWt input energy at the normal operating design point and 6.7 MWt at a peak insolation of 1.02 kW/m^2, representing a power (capacity) scale-down of approximately 8 to 1.

Drum diameter and thickness were made the same to obtain the same stress intensities under equivalent transient temperature and pressure conditions.

Identical diameters and thicknesses of tubes were used together with a tube-support scheme and spans between supports as nearly identical as scaled-down dimensions would allow, so that similar stresses and strains would be developed in the tubes under similar operating conditions.

Steam/water circulation (velocity and steam fraction) could not be made identical for two reasons. First, the heat input per tube is lower in the SRE receiver because the tubes have the same diameter as in the pilot-plant receiver and the total number of tubes in the SRE receiver is scaled down in proportion to the square root of the energy input rather than directly. Second, the elevation of the drum relative to the entrance of the upflowing circuits is less in the SRE steam generator because of the scaling down of linear dimensions, thus reducing the natural circulation head available in the downcomers. As a result there were lower entrance velocities and lower exit qualities (steam fractions) in the tubes of the SRE boiler section. The lower entrance velocities indicate that the SRE boiler design is more critical than that of the pilot plant. Experimental verification that the entrance velocity is adequate in the SRE receiver would automatically prove the same or better for the pilot-plant receiver. The lower exit qualities predicted for the SRE steam generator, on the other hand, suggest the opposite. Therefore, provision was made in the SRE receiver design to bias the heat-flux density pattern to provide equal heat input per tube to a selected number of tubes so that the extreme

Downloaded 01 Jun 2010 to 171.66.16.58. Redistribution subject to ASME license or copyright; see http://www.asme.org/terms/Terms_Use.cfm

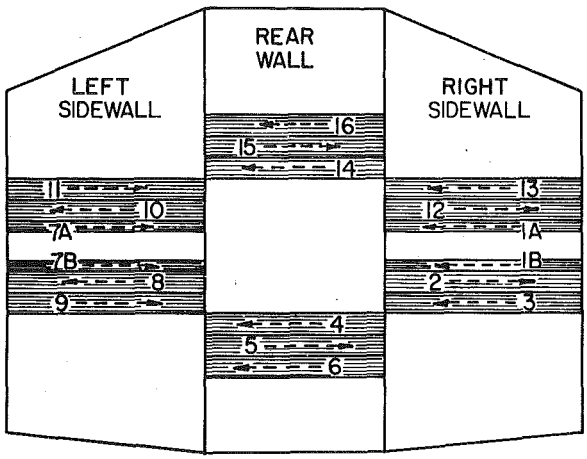


Fig. 12 Arrangement of superheater passes, SRE receiver

steam quality versus heat-flux intensity condition expected for the pilot-plant receiver could be simulated in the SRE receiver.

In a similar vein, it was not possible to duplicate steam temperature profiles and mass velocities in the superheater. To obtain desired mass velocities, fewer tubes in parallel, and hence a greater number of passes, had to be used in the superheater of the SRE receiver.

Design Description. The SRE receiver is geometrically and structurally similar to the pilot-plant receiver in most respects. The most significant differences are:

- The SRE superheater has 16 passes rather than 6.
- Design exit pressure for the SRE is 9136 kPa rather than 10,687 kPa because of a pilot-plant design change after the SRE design was frozen.
- The SRE cavity tilts at a 20 deg angle to the vertical, consistent with the pilot-plant design prior to a change to vertical receiver attitude late in the pilot-plant design phase.
- The second-stage attemperator was eliminated for the tests using electrical radiant heaters. This attemperator will be added to the SRE receiver for the planned solar testing at the Solar Thermal Test Facility.

The arrangement of superheater passes is shown schematically in Fig. 12. There are 16 passes located in six zones of the rear and sidewalls. These zones resemble the six superheater panels of the pilot-plant receiver. Since the SRE cavity tilts at a 20 deg angle to the vertical, the heat-flux distribution on the heat-absorbing surfaces is somewhat different than in the pilot-plant receiver, where the cavity is suspended vertically. To avoid the peak heat-flux zone, the two rear wall superheater panels in the SRE receiver were separated proportionately farther away from each other than those in the pilot-plant receiver.

Superheater tubes are of the same size as those of the pilot-plant receiver (i.e., 25.4 mm OD by 2.77 mm minimum wall). The superheater tubes in the SRE receiver span the complete width of the heated walls, making the spans nearly equal to those in the pilot-plant receiver, where there are two intermediate supports, and hence three spans, across the rear wall. Passes 2 and 3 (as shown in Fig. 12) across the lower right sidewall of the SRE receiver have an expansion loop and intermediate support at the midpoint of the wall to check the functioning of the expansion loop and to compare the effectiveness of different span lengths.

The same size boiler tubes, 38.1 mm OD by 3.76 mm minimum wall were used for the SRE waterwalls, and the steam generator circuitry arrangement resembles, again, many features of the pilot-plant receiver. The length of the drum has been shortened in proportion to steaming capacity, while the drum diameter is the same.

The important physical data of the SRE and the pilot-plant receivers are compared in Table 3. The heating surface distributions between the boiler and the superheater are approximately identical for the two receivers. To compare the responses of the receivers with start-up transients in terms of their respective heat capacities, the dry weight of all pressure parts and the volume of water contained in the boiler are also listed in this table. The weight and water volume of the SRE receiver are greater than would be obtained by direct scale-down in proportion to heat input and indicate that the SRE receiver will take more time than the pilot-plant receiver to heat up under the same heat input condition. A comparison of receiver performance data is shown in Table 4. The design-point load corresponds to the heat input to the receiver at 1400 on summer solstice at an insolation of 0.95 kW/m^2, and the maximum load corresponds to that at 1200 on winter solstice at an insolation of 1.02 kW/m^2.

Fabrication and Erection. The various subassemblies of the SRE receiver were fabricated in the shops of Foster Wheeler Energy Corporation using the same equipment and methods normally used in fabricating utility and marine steam generators. All materials and workmanship were in accordance with the applicable sections of the *ASME Boiler and Pressure Vessel Code* as witnessed and certified by the National Board of Boiler and Pressure Vessel Inspectors.

The receiver was erected at the Sandia Laboratories-Albuquerque Radiant Heat Facility by local craft labor under the supervision of a Foster Wheeler Energy Corporation erection superintendent. Test instrumentation was installed as erection proceeded. The heated surfaces of the waterwalls and all surfaces of the superheater panels were painted with special black, heat-absorbing paint prior to assembly. An array of quartz radiant heat lamps arranged to duplicate, as nearly as possible, the anticipated solar flux pattern, was installed by Sandia Laboratories after the assembly of heating surfaces and

Table 3 Comparison of physical parameters of receiver

Parameter	SRE	Commercial/ Pilot Plant
Total heating surface,* m^2	29.3	191.9
Boiler surface,* m^2	22.6	143.5
Superheater surface,* m^2	6.7	48.3
Superheater surface/total surface, percent	22.86	25.17
Estimated total receiver weight, Mg	83.9	419.4
Estimated dry weight of pressure parts, Mg	21.0	82.6
Estimated volume of water contained, m^3:		
Boiler:		
Drum full	4.3	14.5
Drum at normal water level	2.8	11.6
Superheater	0.6	5.1

* Projected

Table 4 Comparison of receiver performance data

Parameter	SRE		Commercial/Pilot plant	
	Design	Maximum	Design	Maximum
Thermal duty, MW	4.63	6.19	37.90	49.6
Steam flow, kg/s	1.82	2.43	15.70	20.55
Superheater outlet pressure, kPa	9,136	9,136	10,687	10,687
Superheater outlet temperature, °C	516	516	516	516
Average heat-flux densities, kW/m^2				
Boiler surface	147.68	197.50	178.10	223.31
Superheater surface	193.56	258.86	274.00	343.57
Peak heat flux densities, kW/m^2				
Boiler surface	540.03	699.44	487.30	678.50
Superheater surface	451.83	536.28	408.37	568.50

Downloaded 01 Jun 2010 to 171.66.16.58. Redistribution subject to ASME license or copyright; see http://www.asme.org/terms/Terms_Use.cfm

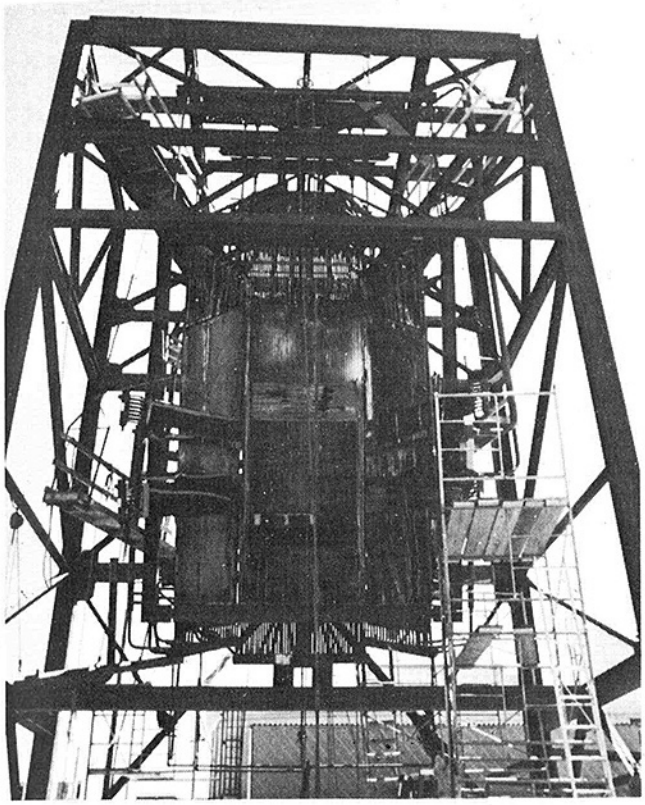


Fig. 13 Front view of SRE receiver during construction, showing superheater panels in place in front of water-walls

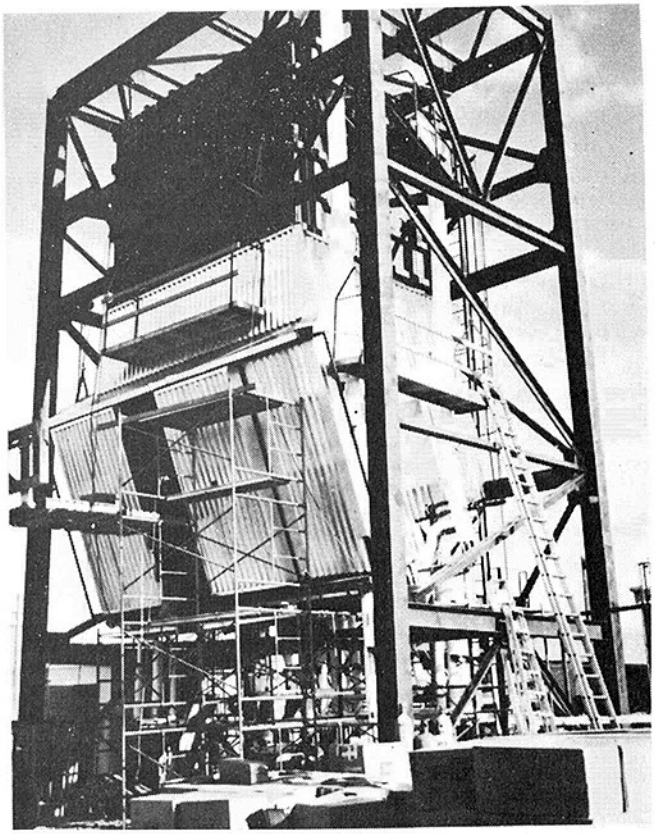


Fig. 14 Front view of completed SRE receiver

cavity was complete. Fig. 13 shows the front of the receiver after installation of the waterwalls and initial emplacement of the superheater panels. Some of the risers, feeders, and downcomers are also visible in this photograph. Fig. 14 is a view of the front and right-hand side of the receiver, complete except for lagging of the piping. Erection was completed early in January 1977.

Testing. Tests were conducted between February and May 1977. The receiver was subjected to a wide variety of simulated solar operating conditions, including cold starts, hot restarts, cloud interruptions, partial cloud obscurations, solar day simulations, reduced power conditions, and steady-state operations. Approximately 231 hr of operating time was accumulated and 53 test runs were made.

A summary of steady-state operating points recorded during the final month of testing is shown in Table 5. The maximum available electrical power was 5.15 MW, resulting in 3.55 MWt absorbed into generation of steam. The major conversion loss was to the cooling water circulating in the radiant lamp reflector panels. Electrical power was purposely restricted to less than 4.0 MW thereafter to reduce lamp failures, which were excessive during maximum power operation. Steam output ranged between 0.32 and 1.41 kg/s, or 18 to 78 percent of design flow. The receiver circulation and control characteristics were very stable through this range, and no operational problems were encountered.

Nine cold start-up tests were performed with progressively shorter ramp-up periods. The results showed that 3½ to 4 hr were generally required for the receiver to reach the full steam temperature and drum

Table 5 Steady-state operating summary during the final month of testing

				Receiver Operating Conditions				
		Energy Input, MW		Steam	Drum	Superheater Outlet	Superheater Outlet	Feedwater
		Total	Into	Flow,	Pressure,	Pressure,	Temperature,	Temperature,
Date	Time	Electrical	Steam	kg/s	kPa	kPa	°C	°C
4/30/77	1905	4.53	3.14	1.11	9377	8964	528	145
5/2/77	2000	5.15	3.55	1.41	9791	8991	506	199
5/2/77	2207	4.91	3.35	1.24	9432	8867	518	160
5/2/77	2258	4.76	3.20	1.22	9460	8888	516	188
5/3/77	0124	4.52	3.12	1.14	9529	9026	513	160
5/4/77	2030	3.91	2.80	1.07	9370	8922	508	205
5/4/77	2150	3.48	2.59	0.92	9384	9046	502	144
5/4/77	2359	3.15	2.06	0.79	9239	8964	523	194
5/5/77	0207	2.55	1.60	0.62	9232	9046	521	202
5/5/77	0315	1.62	0.71	0.32	9108	9026	483	277
5/9/77	2220	3.66	2.31	0.90	9377	9115	513	205
5/10/77	2105	3.67	2.42	0.92	9508	9143	516	181
5/12/77	0050	3.72	2.41	0.88	9391	9143	518	163
5/18/77	2050	3.36	2.10	0.86	9391	9163	519	277
5/19/77	2335	2.97	1.84	0.75	9343	9198	515	202
5/20/77	0125	4.63	3.14	1.24	9653	9177	510	205
5/21/77	0510	2.48	1.47	0.62	9274	9177	499	246
5/21/77	0638	1.82	0.85	0.32	9308	9101	520	149
5/21/77	1030	3.63	2.26	0.86	9412	9191	506	183

Downloaded 01 Jun 2010 to 171.66.16.58. Redistribution subject to ASME license or copyright; see http://www.asme.org/terms/Terms_Use.cfm

pressure after initial application of power. Eight hot restarts were tested with a minimum ramp-up time of 35 min actually achieved.

Eleven runs were conducted to simulate various types of partial and total cloud obscurations of a collector field. These runs were performed by cutting power from all or part of the receiver after a steady-state run, holding for variable durations from 5 min to 1 hr, then reapplying full power. A typical test run showed that steam pressure and flow were fully recovered within 5 min and steam outlet temperature in about 20 min.

One of the most severe tests performed was the simulation of intermittent, partial cloud obscurations. This test was performed over a 5½ hr span with entire sections of steam generator and superheater zones being powered down for short periods of time. The receiver operation was smooth and very stable throughout this test. Although circulation flow was stopped in entire steam-generator circuits whenever power to the circuits was terminated, the flow responded immediately to the resumption of power. No signs of instability or localized overheating were detected.

Conclusions

The results of the design and analysis effort on the 10 MWe pilot-plant receiver and the successful 5 MWt SRE radiant-heat test program established the capabilities of the cavity/natural-circulation steam receiver. In particular, the test results substantiate the following conclusions:

- The thermal/hydraulic and structural design characteristics of this receiver have been proven over a wide range of operational conditions.
- The receiver design for an operational northfield cavity central-receiver power plant has been confirmed.
- The natural-circulation steam generator has been demonstrated to be stable, easily controlled, and highly responsive over wide ranges of severe start-up and variable input power transients.

References

1 Martin Marietta Corporation, "Final Report, Solar Power System and Component Research Program," MCR-75-9, Jan. 1975, p. VI-58.

2 Martin Marietta Corporation, "Preliminary Design Report, Central Receiver Solar Thermal Power System, Phase 1," MCR-77-156, Apr. 1977, Vol. IV, pp. IV-54-84.

Downloaded 01 Jun 2010 to 171.66.16.58. Redistribution subject to ASME license or copyright; see http://www.asme.org/terms/Terms_Use.cfm

B. F. Williams

Director,
Energy Systems Research,
RCA Laboratories,
Princeton, NJ 08540

Do Photovoltaics have a Future?

While there are several commercial businesses selling photovoltaic power supplies, the applications are all in places where conventional electric power is unavailable. The present interest in solar cell electricity for widespread terrestrial use has led to an intense activity exploring the opportunities for significant cost reduction. In this paper obstacles to cost reduction will be identified and the programs addressing techniques for overcoming those obstacles will be presented.

Introduction

Photovoltaic power supplies have proven reliable and effective as sources of electricity in remote applications. There is no question of the economic viability of these power supplies for selected situations. There is major concern, however, as to the economic practicality of widespread terrestrial use because of the high cost of the photovoltaic arrays themselves. Based on their high efficiency, photovoltaic collectors should be one of the cheapest forms of energy generators known.

Fig. 1 compares the relative cost of energy from some familiar forms of solar collectors [1]. In this figure, the cost of energy derived from the various sources shown is plotted against the conversion efficiency of the various options. The entries for biomass and photovoltaic or thermal collectors are shown in their approximate location based on the efficiency of these processes. In the case of meat, cows convert the grain to meat with about ten percent efficiency. In this case, the energy efficiency is 10^{-5} and the cost is about a dollar/kWh. As the efficiency of the collection increases the costs of the energy reduce in a linear fashion so that for forests, the cost of energy is reduced to 0.01 dollar/kWh. The costs of coal and oil are also shown. It is an interesting coincidence that the present day cost of coal is very close to what it would be in its non-fossilized form.

If this interesting trend were to continue for higher conversion efficiencies, the costs of the energy produced would be very low. Present day photovoltaic devices have conversion efficiencies of about ten percent. According to Fig. 1, the cost of energy produced should be on the order of 0.0001 dollar/kWh. The present cost of electricity produced from photovoltaic devices is about four orders of magnitude higher than this.

Because of the diffuseness of the solar energy, the key to low cost collection is low materials costs. In the case of the linear portion of Fig. 1, the materials costs are low; the collector grows out of the ground as a result of the sunshine. The high cost of photovoltaics is due to the high materials costs associated with the construction of the panels themselves.

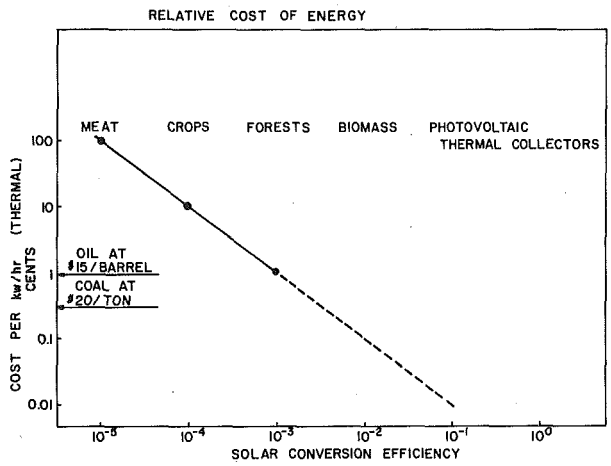


Fig. 1 Relative cost of energy

Present Technology

The present panels use single crystal silicon wafers as the photovoltaic material. Fig. 2 is a photograph of a typical such panel. The panel shown is four feet square and is designed to produce about 8.5 A at 28 V, or about 150 W. An exploded schematic of this panel is shown in Fig. 3. This figure indicates the materials content of the panel shown. Table 1 is a summary of costs of a manufacturing process which will produce such a state-of-the-art photovoltaic panel [2]. We have used present day material costs of 60 dollar/kg for the polycrystalline silicon and advanced manufacturing processes which are under development for all the process steps. The figure highlights significant material costs.

The costs in Table 1 are all expressed in terms of cents/peak Watt. In order to compare these costs to those in Fig. 1 we will assume that the average insolation is 20 percent of the peak insolation. From Table 2 we see that if the purchase price of this panel were 2.40 dollars/peak Watt the cost of electricity produced by this panel would be 0.20 dollar/kWh. In order to have electricity cost less than 0.10 dollar/kWh, a selling price for the panels of less than 0.50 dollar/peak Watt is required.

The costs shown in Table 1 are the manufacturing costs, however, and not the selling prices. If we include an after-tax profit (return on assets) of 15 percent, a cost of sales of 25 percent of the selling price

Contributed by the Solar Energy Division and presented at the Gas Turbine Conference and Exhibit and Solar Energy Conference, San Diego, California, March 12–15, 1979, of THE AMERICAN SOCIETY OF MECHANICAL ENGINEERS. Manuscript received at ASME Headquarters December 6, 1978. Paper No. 79-Sol-7.

Copyright © 1980 by ASME

Downloaded 01 Jun 2010 to 171.66.16.58. Redistribution subject to ASME license or copyright; see http://www.asme.org/terms/Terms_Use.cfm

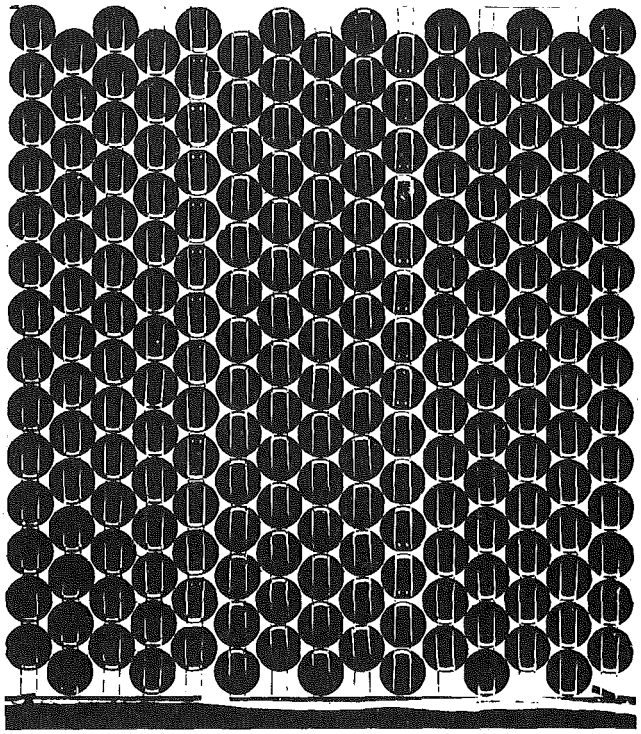


Fig. 2 Typical state-of-the-art panel

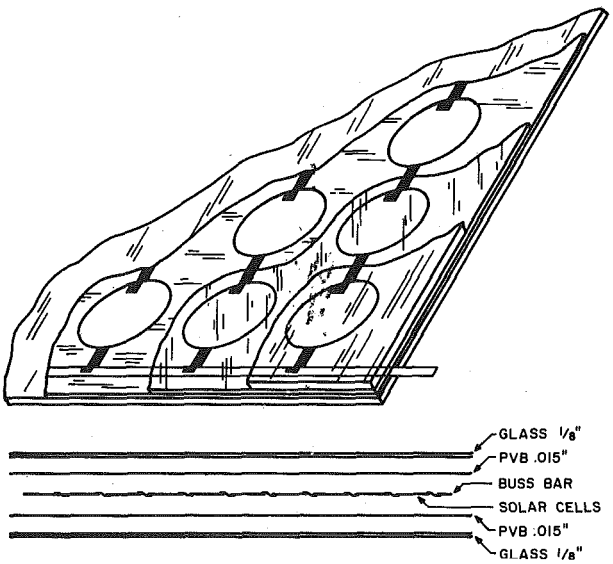


Fig. 3 Detail of typical panel

Table 1 Solar panel costs in cent/peak watt

	MATERIAL & EXPENSE	LABOR & O.H.	INTEREST & DEPREC.	TOTAL
CRYSTAL GROWING	110.0	18.0	5.0	133.0
WAFER PREPARATION	28.0	26.0	6.0	60.0
JUNCTION FORMATION	4.3	9.0	3.1	16.4
METALLIZATION	9.1	3.0	2.0	14.1
AR COATING	---	0.5	0.5	1.0
INTERCONNECT	---	2.0	0.5	2.5
ENCAPSULATION	21.0	2.5	0.5	24.0
	172.0	61.0	18.0	251.0

Table 2 Cost of electricity

Initial Cost	$2.51/pk Watt	$12,550/average kilowatt
Installation	$50/M^2	$ 2,500/average kilowatt
Lifetime	20 yrs	
Interest Rate	10%	
Annual Cost		$ 1,750/average kilowatt
Annual Output	8760 hrs	8,760 kilowatt/hr
Electricity Cost		20¢ kilowatt/hr

Table 3 Concentrator costs

	SILICON (16%)	GaAs (20%)	
	$17/WATT X190	$1000/WATT X1700	$100/WATT X500
CELLS	10%	34%	16%
HEADER	4%	2%	3%
LENS	7%	3%	4%
STRUCTURE & DRIVE	73%	57%	73%
TRACKING & CONTROL	6%	4%	4%
COMPLETE ARRAY COST	$1.05/WATT	$2.00/WATT	$1.40/WATT

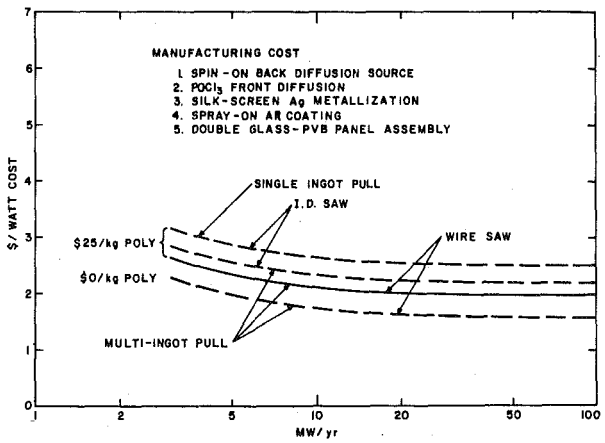


Fig. 4 Cost as a function of manufacturing volume with wafer preparation and polysilicon cost as parameters

and complete factory level overhead, then a selling price of about 4 dollars/W is realized.

How low could the price go if we stay with single crystal silicon Czochralski technology? We have estimated the effect of factory size, single and multiple crystal pulling, changes in polycrystalline silicon cost, and new saving technology on the manufacturing cost. This is shown in Fig. 4 [2]. With presently forecastable technology improvements, a manufacturing cost of about 1.50 dollars/peak Watt seems a minimum.

As we see in Table 1, if we can eliminate the costs associated with the crystal growth and slicing and the encapsulation costs, the manufacturing cost would drop to about 0.30 dollar/peak Watt. The R&D programs in the photovoltaic area are designed to do just this.

Concentrating Systems

One alternative for reducing the materials cost of photovoltaic arrays is to concentrate the sunlight with relatively inexpensive concentrators onto a limited area of the more expensive solar cell material. A recent detailed GE study done for EPRI indicated that simple fixed tilt flat plate collectors had the most potential for utility systems [3]. However, high efficiency high concentration ratio systems also were shown to have "great potential." In Table 3 we compare the costs of concentrator systems using GaAs and silicon cells for a range of cell costs. The system used here was a passively cooled fresnel lens concentrator developed by RCA [4]. The concentration ratio of the system was optimized in each case based on the cost of the solar cells themselves. The cost of the cells shown in the figure was estimated based on the requirement of the high performance shown. In the case of GaAs we have used a range of costs for the cells themselves which reflects manufacturing costs using known technologies. As can be seen from Table 3, a cost of about 1 dollar/W appears feasible. This is less than the projected costs for flat plate collectors using Cz silicon technology by about a factor of two.

Downloaded 01 Jun 2010 to 171.66.16.58. Redistribution subject to ASME license or copyright; see http://www.asme.org/terms/Terms_Use.cfm

Thin Film Flat Plate Devices

Crystalline. The Department of Energy is sponsoring research on evaluating the performance of almost every semiconductor material which has a bandgap in the proper range for photovoltaic devices, i.e., from about 1–2 eV. There are basically two classes of crystalline materials, high cost high performance materials and low cost low performance materials. The objective of the programs is to reduce the cost of the high performance materials and/or increase the performance of the low cost materials. In general, the cost of the high performance materials, i.e., GaAs or Si, is the cost of the substrate on which the active layer rests. The programs for the most part are attempts to manufacture low cost starting materials on inexpensive substrates or to grow ribbons directly with no substrate at all. Since the materials are crystalline, and large grain sizes are desired, a substrate which lattice matches the growing layer is desirable. This has not proved to be an easy task for inexpensive substrates. A very active and promising program is under way addressing these problems.

Also materials with poorer performance but which may be grown on inexpensive substrates are under study. These are mainly II-VI compounds or thin films of II-VI compounds on top of III-V materials. CdTe p-n junctions or CdS-InP heterojunctions are examples of these devices. By far the most advanced is the Cu_2S-CdS solar cell which has been under investigation for about 20 years. An efficiency of nine percent has been reported for a laboratory version of this cell [5].

A principal concern with the CdS-Cu_2S technology has been an instability apparently associated with a reaction of the Cu layer with oxygen. This reaction suggests the active layer must be isolated from air to such an extent that the all glass encapsulation system used in the cost estimate of the single crystal silicon panel (see Table 1) may be necessary. Correcting the costs for the reduced efficiency observed, the manufacturing costs shown in Table 4 are developed. The costs in Table 4 were estimated assuming no cost at all for the thin film CdS-Cu_2S film itself. The result is a manufacturing cost of ~0.50/W, with a projected selling price somewhat higher.

Although the costs of depositing the CdS-Cu_2S layer itself are assumed to be zero, the importance of developing a cell which can exhibit long term reliability without an expensive encapsulation system are emphasized by Table 4.

Amorphous. While there has been much interest in amorphous solar cell developments, actual data on operating cells have been published by only a few organizations [6–8]. The published work is on hydrogenated amorphous silicon.

This is a relatively new semiconductor material, which has optical and electrical properties totally different from crystalline silicon. It is because amorphous silicon has such a high optical absorption and because it is amorphous that it is of interest for solar cells. Its high optical absorption means it will absorb a large fraction of the incident sunlight even though it is deposited in a very thin film. As a result, the deposition times are very short and the consumed material is minimal. That it is an amorphous film means that its properties are insensitive to the substrate on which it is deposited. Inexpensive substrates of glass, plastic, or metal foils have been used with some success [9].

A major problem with amorphous silicon for photovoltaics is the low conversion efficiency which has been observed, six percent. A major plus is the remarkable stability of even unencapsulated solar cells. The cost of a photovoltaic module based on amorphous silicon is shown in Table 5. Note that in this case cost reductions compared to the single crystal panel are due to the reduced cost encapsulation system. At six percent efficiency, a manufacturing cost of less than 40 cents/W is projected. The widespread concern that the balance of system costs requires a higher efficiency (on the order of ten percent) is a major stumbling block for this technology. The effect on the cell costs themselves of improving the basic efficiency of the amorphous silicon cells is shown by the column in parentheses in Table 5. It is this hoped-for efficiency improvement which is the driving force behind the amorphous silicon programs.

Table 4 Solar panel costs in cent/peak watt (nine percent efficient glass encapsulated 10 MW)

	MATERIAL & EXPENSE	LABOR & O. H.	INTEREST & DEPRECIATION	TOTAL
ACTIVE LAYER FORMATION				
METALLIZATION	6.0	4.0	2.7	12.8
AR COATING		.7	.7	1.3
INTERCONNECT		2.7	.7	3.3
ENCAPSULATION	28.0	3.3	.7	32.0
	34.0	10.8	4.7	49.4

Table 5 Solar cell panel costs in cent/watt (amorphous silicon 10 MW)

	MATERIAL & EXPENSE	LABOR & O. H.	INTEREST & DEPRECIATION	TOTAL 6% (12%)
PATTERN SUBSTRATE & DEPOSIT LAYERS	9.3	6.4	6.1	21.8 (17)
METALLIZATION & TEST	.6	3.2	1.6	5.4 (3.5)
INTERCONNECT	.4	2.2	.5	3.1 (2.1)
ENCAPSULATION	4.2	1.7	.7	6.6 (4.4)
	14.5	13.5	8.9	36.9 (27.0)

Conclusions

Present photovoltaic panels are violating the trend of lower costs with increasing efficiency due to their reliance on expensive materials. While developing solar cells which can produce energy at costs which are consistent with historic trends seems unlikely, a medium technology solution should provide electricity competitive with the existing medium to high technology energy generators such as oil, coal, gas, and nuclear fission thermal plants.

Programs to cost reduce silicon and develop reliable thin film materials both have a realistic chance of producing such cost effective photovoltaic panels.

References

1 Rose, A., "A Global View of Solar Energy in Rational Units," *Phys. Status Solidi* (in press).

2 D'Aiello, R. V., "Automated Array Assembly," Final Report, DOE/JPL 954352-77/4.

3 "Requirements Assessment of Photovoltaic Power Plans in Electric Utility Systems," Technical Report ER-685, prepared by General Electric Company.

4 Napoli, L. S. and D'Aiello, R. V., "Design and Development of a 300-Watt Solar Photovoltaic Concentrator," Final Report, SAND78-7027.

5 Barnett, A., *Proc. of Photovoltaic Specialist Conference,* Washington, D.C., June 1978.

6 Carlson, D. E. and Wronski, C. R., *Appl. Phys. Lett. 28,* 1976 p. 671; Carlson, D. E., IEEE Trans. *Electron Dev. ED-24,* 1977, p. 449.

7 Wilson, S. B., McGill, J., and Kinmond, S., *Nature,* No. 272, 1978, p. 152.

8 Okamoto, H., Nitta, Y., Adachi, T., and Hamakawa, Y., "Glow Discharge Produced Amorphous Silicon Solar Cells," presented at ICSFS, Tokyo, Japan, July 1978.

9 Carlson, D. E., "Amorphous Silicon Solar Cells," Annual Report, PRRL-77-CR-32, Contract No. EY-76-C-03-1286.

Acknowledgment

This research was supported in part by the Department of Energy under Contract No. E(04-3)-1286; JPL under Contract No. 954352; and RCA Laboratories, Princeton, NJ 08540.

Downloaded 01 Jun 2010 to 171.66.16.58. Redistribution subject to ASME license or copyright; see http://www.asme.org/terms/Terms_Use.cfm

G. Bergeles
National Technical University,
Athens, Greece

A. D. Gosman
Imperial College,
London, England

B. E. Launder
Department of Mechanical Engineering,
University of California,
Davis, CA 95616

Double-Row Discrete-Hole Cooling: an Experimental and Numerical Study

Double-row discrete-hole cooling arrangements offer several advantages over single-row systems yet the detailed cooling mechanism is less completely understood than for the single-row. This is partly because there have been fewer studies of this geometry and partly because the flow structure is more complex. The present paper presents detailed flow-field and concentration measurements around the injection holes for double-row injection on a flat plate at 30 deg to the mainstream. The experiments span values of the blowing injection mass velocities from 0.25 to 1.0 times the free stream mass velocity and for two boundary layer thicknesses just upstream of the injection. In contrast to single-row injection the cooling effectiveness rise monotonically with M over the range studied. Computer simulation of these flows and similar experiments of [7] has been made using a three-dimensional finite-difference code that embodies a semi-elliptic treatment of the flow field in the neighborhood of the injection holes in conjunction with a two-equation turbulence model with non-isotropic effective transport coefficients. It emerged from the calculations, that, for injection velocities up to 50 percent of the free stream value, levels of film-cooling effectiveness are extremely well predicted beyond about 10 diameters behind the leading row of holes. Around the holes themselves, however, there are certain discrepancies which become more serious as the injection level is raised.

Introduction

Discrete hole cooling has for a number of years been recognized as a technically feasible and attractive method of protecting the surface of turbine blades from hot gaseous combustion products. To assist the development of practical discrete-hole cooling arrangements numerous fundamental experimental studies have been made to help delineate the effects of the basic flow parameters. The main attention has been given to arrangements either with a single spanwise row of holes [1–3] or with numerous rows [4–6]; the latter are commonly known as full-coverage cooling systems. The intermediate cooling scheme—that of a double row of holes—has until recently received relatively little attention [7]; yet this approach would appear to offer superior cooling coverage than with a single-hole arrangement while posing less serious problems of manufacture than a full coverage system.

Until recently nearly all studies of discrete-hole cooling had been experimentally based. In [8], however, the authors have reported the development of a three-dimensional calculation scheme for discrete-hole configurations which has been applied to single-row injection into laminar and turbulent flows [3, 9]. Comparisons of predictions with experiments suggested that for injection through 30 deg holes the calculation scheme was highly satisfactory for injection velocities up to 30 percent of the free-stream velocity and gave tolerably good predictions of the far-field cooling effectiveness even for velocity ratios up to unity; thus the approach could be usefully applied over much of the interesting range of injection rates for discrete-hole cooling. As implied, there was a gradual deterioration of accuracy with increasing injection rates. This was due partly to the use of a semi-elliptic numerical procedure which could not accommodate regions of flow reversal in the streamwise direction and partly to the diminishing accuracy of the model of turbulent transport in the increasingly complex strain field created by the injection.

A primary aim of the work reported hereunder was to provide detailed experimental data of the flow and species concentration fields created by injection through a double row of holes. With this information it was hoped to make a searching assessment of how well the above computational scheme could simulate this kind of cooling arrangement. Experience with single-row calculations had shown us that defects in the predictions appeared first in the immediate vicinity of the injection holes. This is a crucially important region because it is there that stress concentrations will occur due partly to the rapid temperature variations in the blade and partly to the presence of the holes themselves. Hitherto available experiments [7] have not examined this region; accordingly, the focus of the present experimental studies has been the near-field behavior of the jets.

Experimental Program

The experiments were performed in the same open circuit wind tunnel described in [10]. The test section was of rectangular section 250mm × 115mm while the length was 950mm. All the walls of the test section were Plexiglas. The lower wall, forming the test plates, was drilled to admit two rows of aluminum tubes (internal diameter 19.05mm) machined flush with the surface, the tube axes making an angle of 30 deg with the plate surface and lying in the x-y plane. The

Contributed by the Gas Turbine Division and the Heat Transfer Division and presented at the Winter Annual Meeting, San Francisco, California, December 10–15, 1978 of THE AMERICAN SOCIETY OF MECHANICAL ENGINEERS. Manuscript received at ASME Headquarters March 13, 1979.

Copyright © 1980 by ASME

Downloaded 01 Jun 2010 to 171.66.16.58. Redistribution subject to ASME license or copyright; see http://www.asme.org/terms/Terms_Use.cfm

arrangement of the injection holes is shown in Fig. 1, the lateral and streamwise distances between adjacent hole centers being 2.67 and 3.50 diameters respectively. Around the central injection holes, where constructional limitations permitted, static pressure tappings were drilled. These were also used for sampling the wall concentration of helium (contained in the injectant stream).

The primary air flow was provided by a 15 hp centrifugal blower and was supplied to the test section by way of a diffuser section, a settling chamber and a high contraction ratio nozzle. The entrance to the test section was designed to bleed the boundary layer formed on the bottom wall of the nozzle. All tests were conducted at a nominal flow velocity of 26 m/s. In operation the roof of the test section (which was hinged near the upstream end) was raised slightly to minimize the variation of static pressure along the test plate.

The laboratory compressed air supply provided the source of the injectant flow. The air was passed through a pressure regulator into a mixing chamber from which individual pipes, each with its own control valve, led to the injectant tubes. Helium tracer gas (approximately 0.5 percent by volume) was added to the air supply upstream of the mixing chamber to ensure complete mixing. The flow rate to each injection pipe was measured with calibrated orifice plates of diameter 12.5mm or 6.3mm depending on flow rate. In operation the valves were adjusted to give the same indicated flow rate through each tube.

The mean velocity distributions in the boundary layer on the plate were obtained with standard pitot static probes, the probe diameters being 1.7mm and 2.2mm. In regions where the streamwise static pressure gradients were large separate traverses were made to obtain the dynamic and static pressure profiles at precisely the same location. In all cases the velocity levels were found to be reproducible within 3 percent even in the vicinity of an injection hole. A statistical analysis of potential errors [11] indicates an overall uncertainty of velocity levels not exceeding 5 percent except immediately behind an injection hole; there low streamwise velocities and high turbulence intensities lead to unquantifiable uncertainties.

The wall concentration of helium tracer was found by slowly withdrawing samples of the air-helium mixture through a static pressure tap and passing them through an on-line thermal conductivity cell housed in an oven maintained at 50°C. A detailed analysis of possible error sources [11] indicates that when the wall concentration is 80 percent or more of that at the pipe discharge uncertainties do not exceed 2 percent. This level increases gradually, however, as the wall concentration diminishes; for levels of concentration below 5 percent of the discharge level the uncertainty is estimated at 20 percent.

Summary of Mathematical and Physical Model

The mathematical and physical model has been described in detail in [8] and [11]; here, therefore, a summary may suffice.

Solutions are obtained by solving the following three-dimensional continuity, momentum and energy (or species concentration) equations for stationary turbulent flow in which x denotes the streamwise direction and y the direction normal to the plane wall:

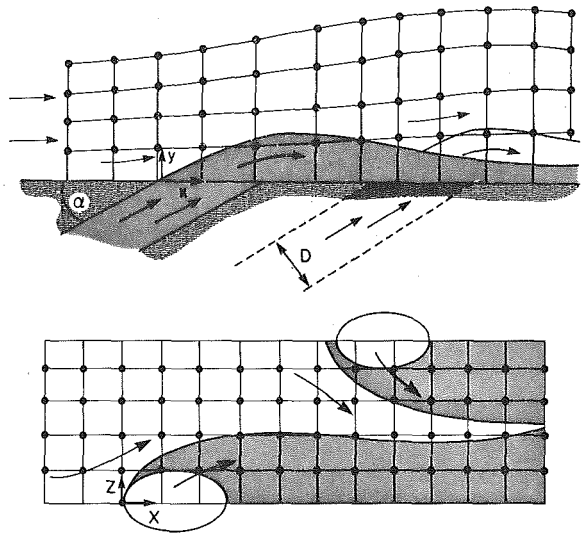


Fig. 1 Flow topography and solution domain

$$\frac{\partial \rho U}{\partial x} + \frac{\partial \rho V}{\partial y} + \frac{\partial \rho W}{\partial z} = 0 \tag{1}$$

$$\left.\begin{aligned} \rho U\frac{\partial U}{\partial x} + \rho V\frac{\partial U}{\partial y} + \rho W\frac{\partial U}{\partial x} &= -\frac{\partial p}{\partial x} + \frac{\partial \tau_{yx}}{\partial y} + \frac{\partial \tau_{zx}}{\partial z} \\ \rho U\frac{\partial V}{\partial x} + \rho V\frac{\partial V}{\partial y} + \rho W\frac{\partial V}{\partial z} &= -\frac{\partial p}{\partial y} + \frac{\partial \tau_{yy}}{\partial y} + \frac{\partial \tau_{zy}}{\partial z} \\ \rho U\frac{\partial W}{\partial x} + \rho V\frac{\partial W}{\partial y} + \rho W\frac{\partial W}{\partial z} &= -\frac{\partial p}{\partial z} + \frac{\partial \tau_{yz}}{\partial y} + \frac{\partial \tau_{zz}}{\partial z} \end{aligned}\right\} \tag{2}$$

$$\rho U\frac{\partial \phi}{\partial x} + \rho V\frac{\partial \phi}{\partial y} + \rho W\frac{\partial \phi}{\partial z} = \frac{\partial J_{\phi,y}}{\partial y} + \frac{\partial J_{\phi,z}}{\partial z} \tag{3}$$

Here ϕ denotes either specific enthalpy or the mass fraction of an inert species and $J_{\phi,y}$ and $J_{\phi,z}$ denote the corresponding y and z-direction diffusional fluxes of heat or chemical species. The other symbols, which take their conventional meaning, are defined under Nomenclature.

We note that x-gradients of shear stresses and diffusive fluxes are omitted from equations [2] and [3]. This omission is entirely acceptable because, over nearly all the flows, rates of change in the x direction are between one and two orders of magnitude less than those in the y direction. Moreover, around the injection holes themselves, where x gradients are fairly steep, the Reynolds stresses are entirely overshadowed by *pressure* gradients. We shall see in the section following that the neglect of these terms allows great simplification of the numerical treatment.

Nomenclature

D = diameter of injection hole
f = anisotropy factor weighting stresses and fluxes due to z-direction gradients
k = turbulence kinetic energy
$J_{\phi,y}$, $J_{\phi,z}$ = diffusive fluxes associated with ϕ in y z directions
M = normalized injection rate $\rho_j V_j/\rho_\infty U_\infty$
p = static pressure
P = production rate of turbulent kinetic energy
S_x = x-direction distance between centers of holes in first and second row
S_z = z-direction distance between centers of adjacent holes in first and second row
U = local mean velocity in x direction
V = local mean velocity in y direction
V_j = jet injection velocity
$\overline{v^2}$ = mean square velocity fluctuation in y direction
W = local mean velocity in z direction
$\overline{w^2}$ = mean square velocity fluctuation in z direction
x = streamwise direction coordinate with origin at upstream edge of leading row
y = coordinate direction normal to plate with origin at surface
z = lateral distance coordinate
Γ = molecular diffusion coefficient for transport of ϕ in y direction
Γ_t = turbulent diffusion coefficient for transport of ϕ in y direction
δ_1 = boundary layer displacement thickness
ϵ = dissipation rate of turbulence energy
η = film cooling effectiveness $\phi_w - \phi_\infty/\phi_j - \phi_\infty$
$\bar{\eta}$ = laterally average effectiveness $(1/S_z)\int_0^{S_z}\eta dy$
μ = molecular viscosity
μ_t = effective turbulent viscosity
$\tau_{\ell m}$ = turbulent plus viscous stress acting in the m direction on a face whose normal points in the ℓ direction
ϕ = chemical species specific enthalpy

Subscripts

j = jet-exit conditions
w = wall value
∞ = free stream conditions

Downloaded 01 Jun 2010 to 171.66.16.58. Redistribution subject to ASME license or copyright; see http://www.asme.org/terms/Terms_Use.cfm

The stresses and fluxes are obtained from the following non-isotropic form of the high Reynolds number $k \sim \epsilon$ model of turbulence:

$$\left.\begin{aligned} \tau_{yx} &= (\mu + \mu_t)\frac{\partial U}{\partial y} \\ \tau_{zx} &= (\mu + f\mu_t)\frac{\partial U}{\partial z} \\ \tau_{yy} &= 2(\mu + \mu_t)\frac{\partial V}{\partial y} \\ \tau_{zy} = \tau_{yz} &= (\mu + \mu_t)\frac{\partial W}{\partial y} + (\mu + \ell\mu_t)\frac{\partial V}{\partial z} \\ \tau_{zz} &= 2(\mu + \mu_t)\frac{\partial W}{\partial z} \end{aligned}\right\} \quad (4)$$

$$\left.\begin{aligned} J_{\phi,y} &= (\Gamma + \Gamma_t)\frac{\partial \phi}{\partial y} \\ J_{\phi,z} &= (\Gamma + \ell\Gamma_t)\frac{\partial \phi}{\partial z} \end{aligned}\right\} \quad (5)$$

where the turbulent viscosity is expressed via the local turbulence energy and dissipation rate:

$$\mu_t = 0.09\rho k^2/\epsilon \quad (6)$$

and the enthalpy or mass-diffusion coefficient is obtained as

$$\Gamma_t = \mu_t/0.9 \quad (7)$$

The anisotropic function ℓ, which appears in the z direction diffusion, varies across the boundary layer according to:

$$\begin{aligned} \ell &= 3.5 - 2.5y/\Delta \quad y \le \Delta \\ \ell &= 1 \qquad\qquad\quad y > \Delta \end{aligned} \quad (8)$$

where Δ is the height above the wall at which the velocity in the boundary layer reaches 90 percent of the local free stream velocity. This variation of ℓ is intended to approximate the variation of $\overline{w^2}/\overline{v^2}$ across the boundary layer; further discussion is provided in [8].

Finally, the turbulence kinetic energy and dissipation rate are obtained from transport equations as follows

$$\rho U\frac{\partial k}{\partial x} + \rho V\frac{\partial k}{\partial y} + \rho W\frac{\partial k}{\partial z} = \frac{\partial}{\partial y}\left((\mu + \mu_t)\frac{\partial k}{\partial y}\right) + \frac{\partial}{\partial z}\left((\mu + \ell\mu_t)\frac{\partial k}{\partial z}\right) + P - \rho\epsilon \quad (9)$$

$$\rho U\frac{\partial \epsilon}{\partial x} + \rho V\frac{\partial \epsilon}{\partial y} + \rho W\frac{\partial \epsilon}{\partial z} = \frac{\partial}{\partial y}\left(\frac{(\mu + \mu_t)}{1.3}\frac{\partial \epsilon}{\partial y}\right) + \frac{\partial}{\partial z}\left(\frac{(\mu + \ell\mu_t)}{1.3}\frac{\partial \epsilon}{\partial z}\right) + 1.44\frac{P\epsilon}{k} - 1.9\rho\frac{\epsilon^2}{k} \quad (10)$$

where P is the turbulence kinetic energy production rate which, with x-gradient terms omitted, may be written:

$$P = \mu_t\left\{\left(\frac{\partial U}{\partial y}\right)^2 + 2\left(\frac{\partial V}{\partial y}\right)^2 + \left(\frac{\partial W}{\partial y}\right)^2\right\} + \ell\mu_t\left\{\left(\frac{\partial U}{\partial z}\right)^2 + \left(\frac{\partial V}{\partial z}\right)^2 + 2\left(\frac{\partial W}{\partial z}\right)^2\right\} \quad (11)$$

The Numerical Solution Procedure

The numerical task is that of solving for appropriate boundary conditions the system of seven coupled partial differential equations: (1–3, 9, 10) together with the indicated auxiliary equations in order to determine the variation through the flow of the dependent variables $U, V, W, p, \phi, k,$ *and* ϵ.

The computer program developed for this purpose incorporated the solution strategy of Patankar and Spalding [12] and Pratap and Spalding [13]. Here only an outline of the main features of the method will be given (fuller accounts are provided in [8] and [11]):

1 The dependent variables are computed on grids superimposed on the solution domain indicated in Fig. 1. While the scalar variables p, ϕ, k and ϵ share the same location, the velocity components are situated midway between the pressures which drive them. The grid is nominally Cartesian but may expand or contract at the external stream boundary to conform with the boundary-layer profile.

2 For all variables except the pressure, finite-difference equations (*fde*'s) are derived which relate each variable at a point to its nearest neighbors in the same cross-stream plane and to the adjacent upstream (but *not* downstream) neighbor. In the case of the velocity equations the neighboring pressures in the directions of the component appear as well.

3 Pressure is obtained from its own equation, derived by combining the fde's for momentum and continuity. Unlike the other members of the set, this equation relates to the nearest grid neighbors in *all* directions, including downstream.

4 Starting from initial guesses for the dependent variables, the procedure operates by scanning the cross-stream planes one by one, beginning from the upstream end and solving at each plane for all variables, on the assumption that the values on neighboring planes are known. Thus, provided that the pressures were correctly specified, one scan of the field would secure the solution to the problem (this of course is precisely the way conventional boundary-layer methods operate). In practice, the effects of injection will necessitate that adjustments be made to the pressures and hence the velocities and other dependent variables; thus, the scanning procedure is repeated in an iterative fashion using the pressure field of the previous iteration until a satisfactory solution is achieved.

5 The procedure therefore preserves as far as possible the limited-storage requirements of boundary-layer methods, requiring only that the static pressure, whose influence is transmitted in all directions, be stored three-dimensionally. The approach is therefore referred to as a "semi-elliptic" treatment.

6 The following practices were followed in assigning boundary conditions:

a) *Symmetry planes.* gradients of dependent variables normal to plane set to zero except for the normal mean component of velocity (W) whose value was set to zero.

b) *Free stream boundary.* prescribed free stream velocity and species concentration. Very small values of k and ϵ (sufficiently small to have no effect on the predictions yet large enough to avoid "overflow" in the computations).

c) *Inlet boundary.* prescribed distributions of U and V; $W = 0$; k and ϵ estimated from mixing length hypothesis (see [8]).

d) *Test plate (excluding injection holes).* mean velocity parallel to wall matched to generalized law of wall. Corresponding specification for k and ϵ; detailed presentation given in [8]. Adiabatic condition on ϕ, i.e., $\partial\phi/\partial y = 0$.

e) *Injection holes.* inlet velocity V_j assumed uniform over hole with x and y components as implied by injection angle. Inlet levels of turbulence energy and energy dissipation rate assigned uniform values corresponding with typical averaged values in pipe flow.

f) *Downstream.* extrapolation of pressure from the last two interior nodes, [8]. No downstream boundary condition on any other variable.

7 Sufficiently far behind the injection holes pressure variations across the boundary layer become sufficiently small for the external-stream pressure gradient dp_∞/dx to replace the local value in the x-momentum equation. (Local pressure gradients in the y and z directions must still be retained because these are necessarily of the same magnitude as the dynamic pressure gradients associated with motion in the y-z plane.) This simplification allows the computation to proceed entirely without iteration. This is exactly the scheme proposed by Patankar and Spalding. In the computations presented in Section 5 this non-iterative "parabolic" treatment begins at $x/D = 9.0$.

Presentation and Discussion of Results

Experimental Study. Some measured characteristics of the velocity and concentration fields are first considered. Thereafter comparison will be drawn with a number of computer simulations of experiments of Jabbari [7] and the present study.

Downloaded 01 Jun 2010 to 171.66.16.58. Redistribution subject to ASME license or copyright; see http://www.asme.org/terms/Terms_Use.cfm

Figs. 2(*a*) and (*b*) show the development of the mean velocity profile along the plate at two lateral positions for the case where the mean injection velocity is 50 percent of the free-stream velocity. The origin for x is at the *upstream* end of the leading row of holes and the second row of holes begins at $x/D = 3.5$. The broken lines on the figure relate to measurements at the corresponding geometrical position for a test of a *single* row of holes operating at the same injection rate and with the same approaching boundary layer on the test plate. Evidently, from Fig. 2(*a*), along the line $z/D = 0.53$ the velocity profiles up to $x/D = 3.8$ are essentially the same as for single-row injection. Further downstream fluid is squeezed between the second row of holes however producing substantially higher near-wall velocities than in the single row experiment. For $z/D = 1.33$, which passes through the center of the second-row hole, the development shown in Fig. 2(*b*) is again seen to be very little different from that of the boundary layer downstream of a single-row of holes.

This pattern is confirmed by the wall film-cooling-effectiveness pattern shown in Fig. 3. The variation of η measured along $z/D = 1.33$, i.e., directly behind the second row of holes, is indistinguishable from that measured in our earlier single-row study [3]. The situation is quite different along $z/D = 0$: the squeezing of the flow between the second row of holes produces a more rapid falling off of the film cooling effectiveness vis à vis the single row case due—so the predicted flow field suggests—to the pressure and vorticity fields created by the

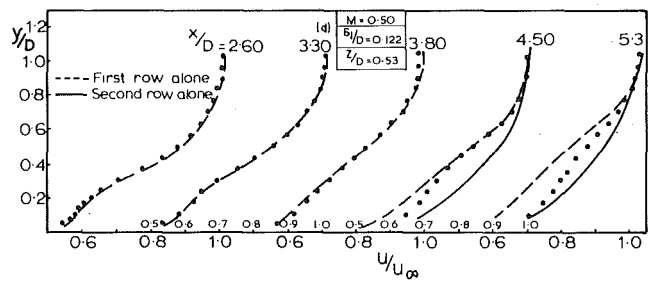


Fig. 2(*a*) $z/D = 0.53$

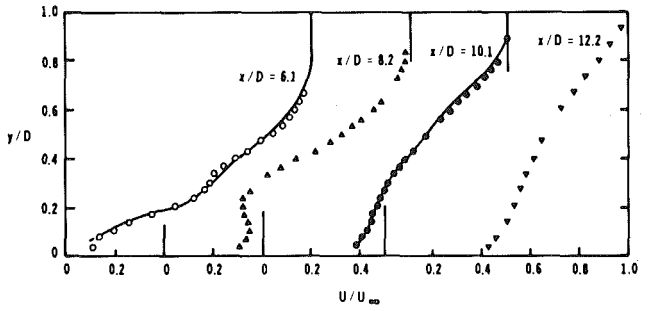


Fig. 2(*b*) $z/D = 1.33$

Fig. 2 Mean velocity profiles downstream of double-double-row injection at $M = 0.50$

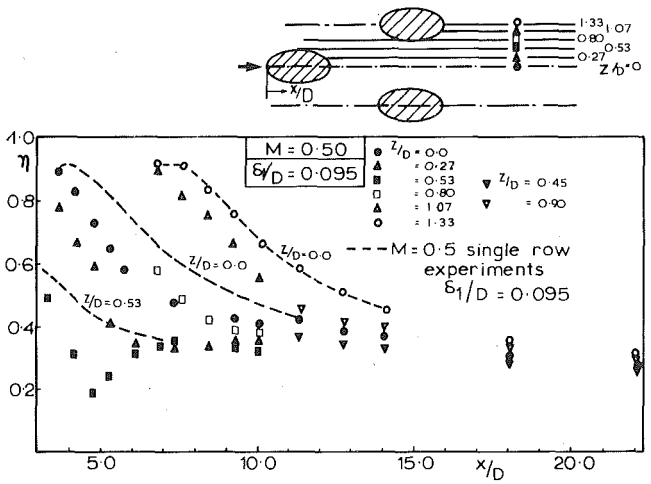


Fig. 3 Near-field film cooling effectiveness $M = 0.5$

second-row injection tending to lift the upstream jet off the surface. Along $z/D = 0.53$ the effectiveness falls to only 0.2 at $x/D \simeq 5.0$, less than half the single-row level; this dramatic fall is again due to the lateral displacement of fluid around the second row. On an actual blade, conduction within the blade would reduce significantly the variations in temperature implied by the present "adiabatic wall" study; nevertheless the region between the second row of holes is clearly one where steep temperature gradients will occur and hence where one may expect serious thermal stresses to be present. Further downstream the lateral variations in η are 0.37 and 0.29 while for a single row at $M = 0.5$ the corresponding values were 0.31 and 0.08.

The behavior observed at $M = 0.25$ is qualitatively very similar to that for $M = 0.50$ (this case will be examined in connection with the computer simulations). Some interesting differences emerge, however, when the injection velocity is raised to that of the primary stream. It is seen in Fig. 4 that along $z/D = 0$ the effectiveness is now very similar to the single row case (suggesting the downstream row is now having little effect on the trajectory). Moreover the effectiveness behind the second row (i.e., along $z/D = 1.33$) is now significantly higher than recorded for the single row; apparently the jets from the upstream row help to keep the second row jets on the surface. Consequently, the far-field behavior is markedly superior than for $M = 0.5$ even though concentrations are lower in the immediate vicinity of discharge. This feature emerges strongly in Fig. 5 which shows the laterally averaged film cooling effectiveness at the three injection rates together with those for two single-row studies. The superiority of the double-row arrangement may be noted by comparing the single-row curve for $M = 0.5$ with the double-row curve for $M = 0.25$ (both schemes involving the same total mass flow rate of coolant); even more startling is the comparison between the single row operation for $M = 1.0$ and the double row for $M = 0.5$.

Bergeles [11] reports a further complete set of effectiveness measurements for identical conditions to those examined above except that the boundary layer displacement thickness ahead of the hole was 20 percent less ($\delta_1/D = 0.078$). For $M = 1.0$ and 0.25 the effects of the thinner boundary layer were small; at $M = 0.5$, however, the laterally averaged film-cooling effectiveness was raised by up to 20 percent in the vicinity of the holes and by about 10 percent at $x/D = 20$. Single row studies have shown that the jet is on the verge of breaking away from the surface at $M = 0.5$ and it is for this reason that the cooling pattern is then so sensitive to even small changes in the primary stream. The earlier double row study of [7] at the same nominal in-

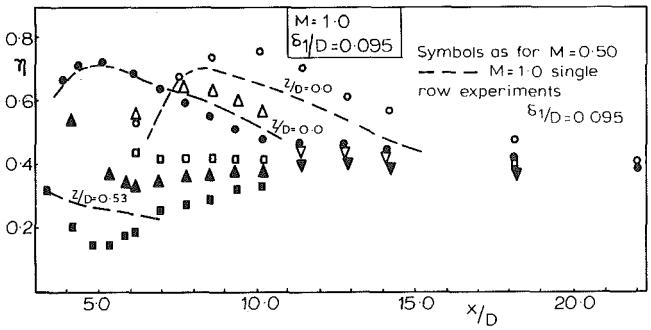


Fig. 4 Near-field film cooling effectiveness $M = 1.0$

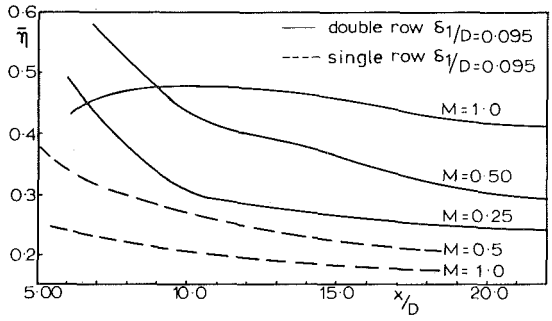


Fig. 5 Laterally averaged film cooling effectiveness-comparison of single- and double-row cooling

Downloaded 01 Jun 2010 to 171.66.16.58. Redistribution subject to ASME license or copyright; see http://www.asme.org/terms/Terms_Use.cfm

jection rate in which δ_1/D had been 0.18, reported levels of $\bar{\eta}$ between 12 and 5 percent below those of the present study for $\delta_1/D = 0.095$ depending upon downstream distance. While consistent with the trend found here it should be said that the hole configuration, though similar to, was not exactly the same as in the present study.

Numerical Simulations. The double-row configurations required approximately 45 min central processor time on an IBM 360-190 computer to achieve grid-independent, converged solutions. In view of this large execution time it was not practical to study such an extensive range of flow conditions as for the single-row arrangement. Three cases were selected corresponding to experiments for injection rates of 0.25, 0.33, and 0.47 drawn from the present study and those of [7].

We first compare the calculated near-field behavior with measurements. Fig. 6 shows for $M = 0.25$ the downstream variation of effectiveness directly behind the two injection holes (i.e., $z/D = 0.0$ and $z/D = 1.33$) and along the line $z/D = 0.53$ passing between the holes. Agreement between calculations and measurements in the first two cases is satisfactorily close. Along $z/D = 0.53$, however, the predictions exhibit a much stronger "recovery" than do the measurements; consequently at $x/D = 6.0$ the predicted level of η is almost 50 percent too high. We note that the overall level of agreement of calculations with experiment is markedly worse than for injection through a *single* row of holes at the same dimensionless injection rate [3]. Moreover, [3] reported that when M was raised to 0.5 serious discrepancies were evident in the *single* row predictions in the near field. Three factors contributing to these errors were identified:

1 uncertainties in the velocity profile at exit from the injection holes,

2 the patching over technique used to obliterate the small reverse flow region behind the holes [8],

3 the assumption that the ratio of lateral to transverse diffusivities was unaffected by the injection process [8].

We may conclude that, due to the more complex flow fields created in the present study these same factors lead to inaccuracies in the near field prediction for double-row injection at lower levels of injection than for the single-row case.

The single-row computations [3] had shown that, despite the discrepancies in the near field, the *far* field predictions ($x/D > 10$) were satisfactory, at least for M up to 0.50. The same turns out to be the case for double-row injection as may be seen from Fig. 7 which shows the calculated and measured effectiveness patterns for two of Jabbari's [7] experiments. The computed results were obtained by applying the semi-elliptic procedure to the region up to $x/D = 9.0$ and then employing the non-iterative parabolic scheme for the remainder of the flow. Despite the difference in injection rates the two tests display a similar development. At $x/D = 10$ (the closest to the injection holes at which Jabbari reports measurements) the predicted levels of effectiveness range from $0.51 - 0.35$ and $0.53 - 0.36$, respectively, for $M = 0.33$ and 0.47. The lateral variations decrease smoothly with distance downstream (more steeply for $M = 0.33$) until for $x/D > 21$ the wall concentration has become essentially just a function of x. In general the experimental data support this predicted pattern very closely, the maximum difference between the calculated and measured point values being 8 percent, which is comparable with the experimental uncertainty.

Summarizing Remarks

The present experiments have provided new data of the pattern of film-cooling effectiveness created by double-row injection at 30 deg to the surface. The results confirm the superiority of this pattern of cooling over single-row arrangements. By comparing the present results with those of [11] it is deduced that the cooling performance is highly sensitive to the thickness of the external boundary layer when the injection velocity is close to 50 percent of the external stream value but is only slightly influenced at $M = 0.25$ and $M = 1.0$. A particularly beneficial characteristic of double-row injection is that the mean effectiveness downstream of the holes increases monotically as the injection rate is raised, at least up to $M = 1.0$ (in contrast, for single row injection [3], the peak mean effectiveness was reached for $M \simeq 0.5$;

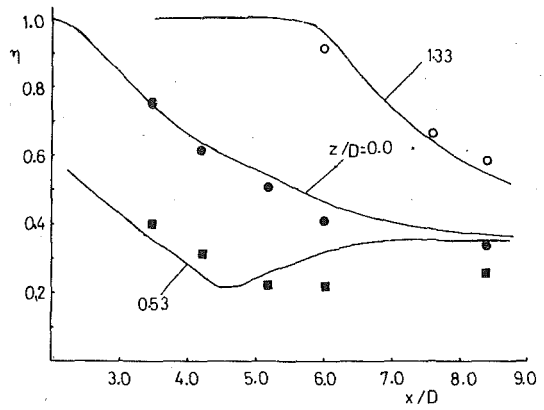


Fig. 6 Predicted and measured near-field cooling effectiveness

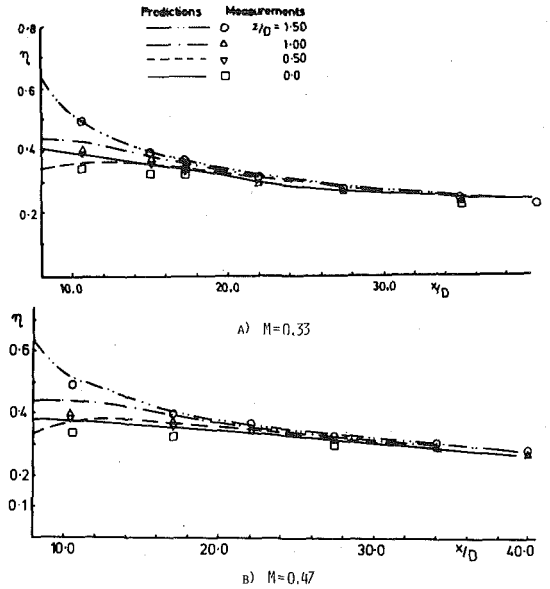


Fig. 7 Prediction of far-field effectiveness—comparison with measurements of [7]

at $M = 1.0$ the overall level of $\bar{\eta}$ had fallen by 50 percent from this value). The cause of this behavior seems to be that the streamwise vorticity field created by the leading row of jets helps to keep the second row of jets impressed on the surface.

The numerical simulations of the experiment for $M = 0.25$ has indicated that the near-field effectiveness is predicted moderately well but not as successfully as for single-row injection [3]. In fact the quality of the predictions may be expected to deteriorate appreciably as the injection velocity is raised since, even for single-row injection, rather poor agreement has been observed at $M = 0.5$. Nevertheless, despite the shortcomings in predicting the flow character in the immediate neighborhood of injection, the smoothing out of the wall effectiveness beyond ten diameters from the start of injection is very satisfactorily predicted for injection velocities up to 50% of that of the mainstream.

Acknowledgments

The research has been supported with interest and understanding by the U.K. Ministry of Defence (Procurement Executive) and by Rolls Royce (1971) Ltd. The numerical computations have been performed at the Imperial College and University of London Computer Centers and at the SRC's Rutherford Laboratory. The authors' names appear alphabetically.

References

1 Pedersen, D., "Effect of Density Ratio on Film-Cooling Effectiveness for Injection through a Row of Holes and a Porous Slot," University of Minnesota, Mechanical Engineering Department, Ph.D. thesis, 1975.

2 Kadotani, K., "Effect of Mainstream Variables on Heated and Unheated Jet Issuing from a Row of Inclined Holes," University of Minnesota, Mechanical

Downloaded 01 Jun 2010 to 171.66.16.58. Redistribution subject to ASME license or copyright; see http://www.asme.org/terms/Terms_Use.cfm

Engineering Department, Ph.D. thesis, 1975.

3 Bergeles, G., Gosman, A. D., and Launder, B. E., "The Prediction of Discrete-Hole Cooling Processes—2: Turbulent Flow," to appear in ASME JOURNAL OF HEAT TRANSFER, 1979.

4 Launder, B. E. and York, J., "Discrete-Hole Cooling in the Presence of Free-Stream Turbulence and Strong Favorable Pressure Gradient," *Int. J. Heat and Mass Transfer,* Vol. 17, 1974, Vol. 1403.

5 Metzer, D. E., Takenchi, D. I., and Krentler, D. A., "Effectiveness and Heat Transfer with Full Coverage Film Cooling," ASME paper 73-GT-18, April 1973.

6 Yavuzkurt, S., Moffat, R. J., and Kays, W. M., "Full Coverage Film Cooling: Three Dimensional Measurements of Turbulence Structure and Prediction of Recovery Hydrodynamics," Stanford University, Thermo-Sciences Division, Rep. HMT-27, 1977.

7 Jabbari, M. Y., "Film Cooling and Heat Transfer with Air Injection through a Staggered row of Holes into an Accelerating Flow," University of Minnesota, Mechanical Engineering Department, Ph.D. thesis, 1973.

8 Bergeles, G., Gosman, A. D., and Launder, B. E. "The Turbulent Jet in a Cross-Stream at Low Injection Rates: a Three-Dimensional Numerical Treatment," *Numerical Heat Transfer,* Vol. 1, 1978.

9 Bergeles, G., Gosman, A. D., and Launder, B. E., "The Prediction of Three-Dimensional Discrete-Hole Cooling Processes—1: Laminar Flow," ASME JOURNAL OF HEAT TRANSFER, Vol. 98, 1976, p. 379.

10 Bergeles, G., Gosman, A. D., and Launder, B. E., "Near-Field Character of Jet Discharged through a Wall at 30 deg to a Mainstream," *AIAA Journal,* Vol. 15, 1977, Vol. 499.

11 Bergeles, G., "Three-Dimensional Discrete Hole Cooling Processes: An Experimental and Theoretical Study," Ph.D. thesis, Faculty of Engineering, University of London, 1976.

12 Patankar, S. V. and Spalding, D. B., "A Calculation Procedure for Heat, Mass and Momentum Transfer in Three-Dimensional Parabolic Flow," *Int. J. Heat and Mass Transfer,* Vol. 15, 1787, 1972.

13 Pratap, V. S. and Spalding, D. B., "A Calculation Procedure for Partially Parabolic Flow Situations," Imperial College, Mechanical Engineering Department Report HTS/74/35, 1974.

Downloaded 01 Jun 2010 to 171.66.16.58. Redistribution subject to ASME license or copyright; see http://www.asme.org/terms/Terms_Use.cfm

S. Lin
Associate Professor.

R. Bhardwaj
Postgraduate Student.

Department of Mechanical Engineering,
Concordia University,
Montreal, Canada

The Effect of Material Properties on the Thermal Efficiency of the Minto Solar Wheel

The characteristic of the thermal performance of the Minto solar wheel is that its thermal efficiency is strongly dependent on the material properties of the working fluid. For a specified working fluid, the thermal efficiency of the ideal cycle of the Minto solar wheel is dependent only on the mean diameter of the wheel. To study the effect of the material properties of the working fluid on the ideal thermal efficiency, 14 working fluids are selected, and their thermal efficiencies as functions of the mean diameter of the wheel are calculated and compared with each other. Among these fluids, R-12, R-115, R-500, R-22 and R-13B1 achieve better thermal performance than the others.

Introduction

The Minto solar wheel is a vapor-power engine operating on a small temperature difference between a heat source and sink. Fig. 1 shows a schematic diagram of the Minto solar wheel. The engine consists of many pairs of metallic containers. A low-boiling liquid, such as Freon or propane, fills one container of each pair. The opposite container is evacuated. The liquid collects in the lower container which is in contact with hot (solar-heated) water. Heat transferred from the hot water vaporizes the liquid in the container and forces part of it up through the connecting tube and into the other container on top. Due to an unbalanced force, the heavier container on top starts down, the lighter container in the water goes up. As each pair shuttles its liquid mass back and forth, the whole system turns and repeats the process continually [1, 2].

It can be seen that the energy transfer process in the Minto solar wheel starts from the change of thermal energy to potential energy, and then from potential energy to mechanical energy. The new engine is novel in concept, which does not operate on the Rankine cycle. An analysis of the thermodynamic cycle of the Minto Solar wheel was recently conducted [3]. The characteristic of the thermal performance of the Minto solar wheel is that its thermal efficiency is strongly dependent on the material properties of the working fluid. An increase of the diameter of the solar wheel does not mean an increase of the thermal efficiency. The study of the effect of the material properties on the thermal efficiency of the Minto solar wheel is the subject of the present paper.

The Ideal Cycle of the Minto Solar Wheel

The ideal cycle of the Minto solar wheel can be analyzed as follows:

We consider only one pair of the containers of the engine and assume that the volume of the connecting tube and the volume occupied initially by vapor in the lower container are negligibly small in comparison with the volume of the container. The change of the density in the liquid phase may be neglected.

We consider also that the lower container filled with a low-boiling liquid, is located at the lowest position of the engine, and that the total liquid in the lower container is as a closed thermodynamic system. Heat transferred from the hot water to the system results in an increase of temperature, pressure, internal energy and potential energy, and causes the system to do work on the vapor located above the system. The details of the processes are described as follows:

1 **Change of the Internal Energy.** At the beginning of the heat-transfer process, heat transferred from the hot water evaporates a very small amount of the liquid into vapor, in the lower container, which forces a small part of the liquid into the connecting tube. The static pressure at the bottom of the connecting tube increases by an amount of $\rho_\ell gL$ due to the liquid column existing in the connecting

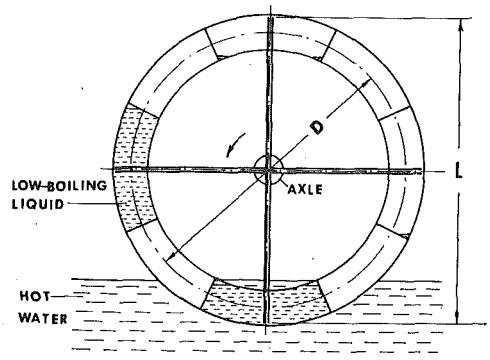


Fig. 1 Schematic diagram of Minto solar wheel

Contributed by the Solar Energy Division for publication in the JOURNAL OF ENGINEERING FOR POWER. Manuscript received at ASME Headquarters March 23, 1979.

Copyright © 1980 by ASME

Downloaded 01 Jun 2010 to 171.66.16.58. Redistribution subject to ASME license or copyright; see http://www.asme.org/terms/Terms_Use.cfm

tube, where ρ_ℓ is the density of the liquid, g the gravitational acceleration, and L the length of the connecting tube. The increase of the pressure results in an increase of the saturated temperature from T_1 to T_2 as shown on T-s diagram in Fig. 2. The increase of the internal energy of the system, caused by the increase of the temperature, is given by

$$\Delta U_{12} = \rho_\ell V(u_2 - u_1), \tag{1}$$

where V is the volume of the liquid in the container. After the liquid reaches the temperature, T_2, further transfer of heat evaporates more of the liquid into vapor which forces all of the liquid in the lower container up into the upper container. The mass of the liquid evaporated is given by

$$m = \rho_{v3} V, \tag{2}$$

where ρ_{v3} is the density of the vapor at state 3. The change of the internal energy during the evaporation of the liquid mass, m, can be expressed as

$$\Delta U_{23} = \rho_{v3} V(u_3 - u_2). \tag{3}$$

Point 3 in Fig. 2, represents the state of the saturated vapor.

2 Change of the Potential Energy. When all the liquid in the lower container is forced up into the upper container, it causes the change of the potential energy of the system,

$$\Delta E_p = (\rho_\ell - \rho_{v3}) VgD, \tag{4}$$

where D is the mean diameter of the engine.

3 Work Done by the System. When the liquid is raised from the lower container into the upper container, the vapor existing in the upper container is therefore compressed. Due to the slow motion of the engine, the vapor compression process can be taken as an isothermal process in the wet vapor region. Therefore, the compression work can be expressed as

$$W_{41} = p_1 \left(1 - \frac{\rho_{v3}}{\rho_\ell}\right) V, \tag{5}$$

where p_1 is the pressure in the upper container.

We consider now that the heavier container on top starts down, and the lighter container at the bottom goes up. The engine rotates. The lower container leaves the hot water and enters its ambient air. For an ideal cycle the temperature of the ambient air is assumed to be equal to T_1 which is lower than the temperature, T_2, in the container. Heat is then transferred from the vapor in the container to the ambient air. During this cooling process, there is no change in volume in the system. When the lower container reaches the top position of the engine, the temperature and pressure inside the container must reduce to T_1 and p_1, respectively, because the working fluid undergoes an ideal cycle. In Fig. 2, the state at point 4 represents the end state of the isochoric cooling process. During this cooling process, the amount of heat transferred from the system is given by

$$\Delta U_{34} = \rho_{v3} V(u_4 - u_3). \tag{6}$$

Heat is now transferred from the hot water to the other container located at the lowest position of the engine. The processes described above start to repeat. The vapor in the upper container is then compressed by the liquid raised by the vapor pressure in the lower container. This is an isothermal compression process as indicated above, which closes the cycle as shown in Fig 2. During this isothermal compression process the total amount of heat transferred from the system is expressed as

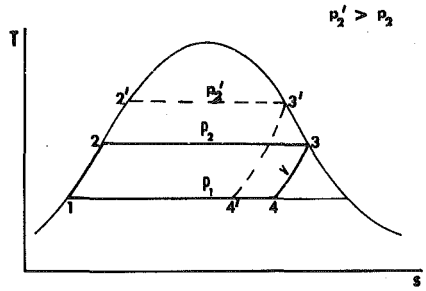


Fig. 2 The ideal cycle of the Minto solar wheel: 1→2 saturated heating, 2→3 isobaric expansion, 3→4 isochoric cooling, 4→1 isothermal compression

$$Q_{41} = \Delta U_{41} + W_{41} = \rho_{v3} V(u_1 - u_4) + (\rho_\ell - \rho_{v3}) V(u_1 - u_2) - p_1 \left(1 - \frac{\rho_{v3}}{\rho_\ell}\right) V. \tag{7}$$

The second term on the right-hand side of equation (7) represents that the liquid raised from the lower container, having the temperature T_2 must be cooled down to T_1 in order to achieve thermal equilibrium with the fluid existing in the upper container. The minus sign written for the third term is due to the fact that heat transferred from the system has a negative value.

From Fig. 2, it is seen that the ideal cycle of the Minto solar-powered engine consists of the following four processes: 1→2, saturated heating, 2→3, isobaric expansion, 3→4, isochoric cooling, and 4→1, isothermal compression.

It should be noted that in processes 2→3 and 3→4, only the vapor part of the system is involved in the heat transfer. However, in processes 1→2 and 4→1, the total fluid in the container is involved in the heat transfer. Physically, this means that only the vapor part of the fluid, having the mass of $\rho_{v3} V$, undergoes a complete cycle. Heat transferred to the other part of the fluid having the mass of $(\rho_\ell - \rho_{v3})V$ in process 1→2, in the amount of $(\rho_\ell - \rho_{v3}) V(u_2 - u_1)$, represents practically the loss of energy.

In the cycle, the energy used for the increase of the internal energy and potential energy, and for doing the external work must come from the hot water. Therefore, the total heat supplied from the hot water to the system is then

$$Q = \Delta U_{12} + \Delta U_{23} + \Delta E_p + W_{41} = \rho_\ell V(u_2 - u_1) + \rho_{v3} V(u_3 - u_2) + (\rho_\ell - \rho_{v3}) VgD + p_1 \left(1 - \frac{\rho_{v3}}{\rho_\ell}\right) V. \tag{8}$$

Only the potential energy, ΔE_p (equation (4)), obtained during the expansion process, 2→3, can be converted into useful mechanical work. Therefore, the ideal thermal efficiency of the engine cycle can be expressed as follows:

$$\eta_{th} = \frac{W_{\text{useful}}}{Q} = \frac{\left(1 - \frac{\rho_{v3}}{\rho_\ell}\right) gD}{(u_2 - u_1) + \frac{\rho_{v3}}{\rho_\ell}(u_3 - u_2) + \left(1 - \frac{\rho_{v3}}{\rho_\ell}\right)\left(gD + \frac{p_1}{\rho_\ell}\right)}. \tag{9}$$

Nomenclature

D = mean diameter of the Minto solar wheel
E_p = potential energy
g = gravitational acceleration
m = mass
p = pressure
Q = heat
T = temperature
u = specific internal energy
U = total internal energy
V = initial liquid volume in the lower container
W = work
X = defined in equation (11)
η_{th} = thermal efficiency
ρ = density

Subscripts

1, 2, 3, 4 = thermodynamic states
2′, 3′, 4′
ℓ = liquid
v = vapor

Downloaded 01 Jun 2010 to 171.66.16.58. Redistribution subject to ASME license or copyright; see http://www.asme.org/terms/Terms_Use.cfm

From equation (9), it can be seen that the thermal efficiency of the ideal cycle is essentially influenced by the material properties of the working fluid.

The Effect of Material Properties on the Ideal Thermal Efficiency

In order to pursue a systematic study of the effect of the material properties of different working fluids on the thermal efficiency of the ideal cycle, equation (9) is written in the following form,

$$\eta_{th} = \frac{gD}{X + \frac{p_1}{\rho_\ell} + gD}, \tag{10}$$

where

$$X = \frac{\rho_\ell(u_2 - u_1) + \rho_{v3}(u_3 - u_2)}{\rho_\ell - \rho_{v3}}. \tag{11}$$

For the purpose of comparison, the initial state of the cycle, state 1 in Fig. 2, is fixed at a saturated liquid temperature of 21.1°C (70°F). The pressure at state 2 can be determined by an increase of a static pressure of $\rho_\ell gD$ from the pressure at state 1. For the calculation of the thermal efficiency the value of the liquid density, ρ_ℓ, is taken as the average value of the density at state 1 and state 2. That is

$$\rho_\ell = \frac{\rho_{\ell_1} + \rho_{\ell_2}}{2}. \tag{12}$$

Therefore, for a specified working fluid, the value of X in equation (11) is dependent only on the mean diameter of the Minto solar wheel D. Fig. 3 shows the value of X as a function of D, for the following 14 selected working fluids: (1) R-11–Trichlorofluoromethane, (2) R-12–Dichlorodifluoromethane, (3) R-13B1–Bromotrifluoromethane, (4) R-22–Chlorodifluoromethane, (5) R-40–Methyl Chloride, (6) R-113–Trichlorotrifluoroethane, (7) R-114–Dichlorotetrafluoroethane, (8) R-115–Chloropentafluoroethane, (9) R-152a–Difluoroethane, (10) R-290–Propane, (11) R-500–Azeotrope of Refrigerants 12/152a, (12) R-600–Butane, (13) R-600a–Isobutane, (14) R-717–Ammonia [4].

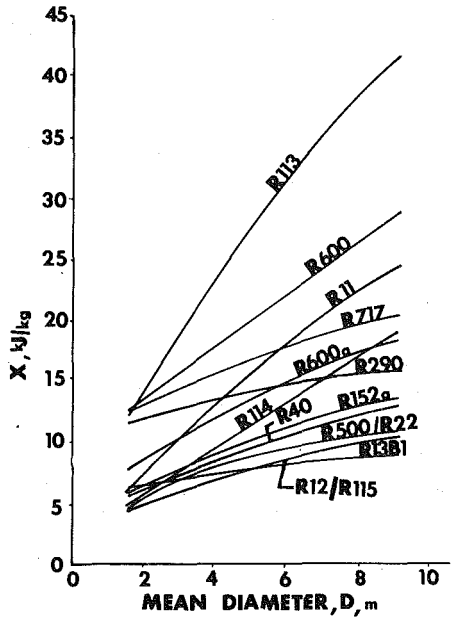


Fig. 3 The factor X as a function of the mean diameter of the Minto solar wheel for 14 selected working fluids with the fixed saturated liquid temperature, T_1 = 21.1°C (70°F)

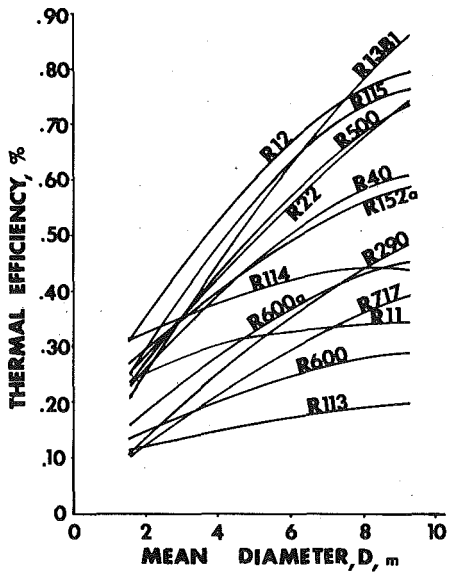
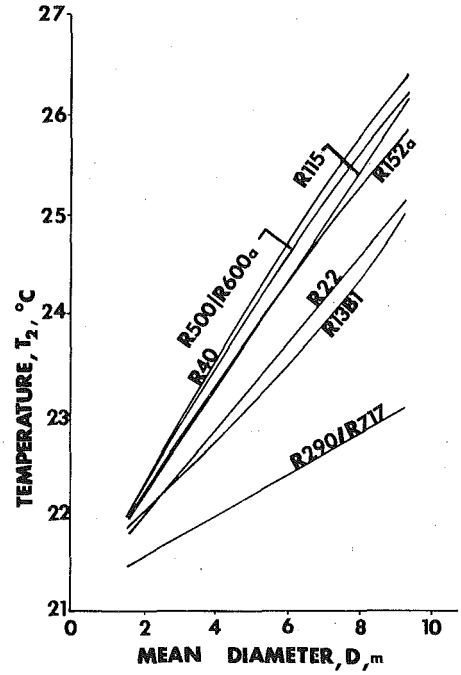


Fig. 4 The thermal efficiency of the ideal cycle as a function of the mean diameter of the Minto solar wheel for 14 selected working fluids with the fixed saturated liquid temperature, T_1 = 21.1°C (70°F)



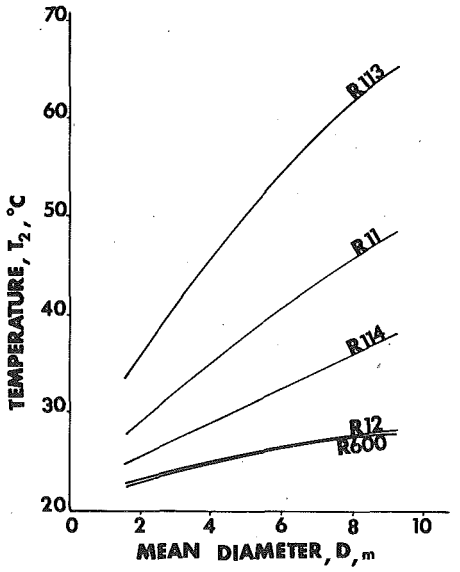


Fig. 5 The temperature at the end of the saturated heating process, T_2, as a function of the mean diameter of the Minto solar wheel for 14 selected working fluids with the fixed saturated liquid temperature, T_1 = 21.1°C (70°F)

Downloaded 01 Jun 2010 to 171.66.16.58. Redistribution subject to ASME license or copyright; see http://www.asme.org/terms/Terms_Use.cfm

Because X is in the denominator of the thermal efficiency equation, equation (10), the lower is the value of X, the higher is the thermal efficiency for a given diameter of the solar wheel. Fig. 3 shows the value of X is largest for R-113. Consequently, this working fluid has the lowest thermal efficiency. On the other hand, the refrigerants R-12, R-115 and R-13B1 give low values of X, and thus these refrigerants when used as the working fluid in the Minto solar wheel tend to increase the thermal efficiency. Fig. 4 shows the thermal efficiency as functions of the mean diameter of the Minto solar wheel for the fourteen selected working fluids. It is shown that the steeper is the X-curve in Fig. 3, the steadier is the corresponding thermal efficiency in Fig. 4.

The wide range of the variation of the X-value is due to the fact that different materials have different material properties and different increments of the temperature from state 1 to state 2 (Fig. 2). Fig. 5 shows the relationship between the temperature increase from state 1 to state 2 and the increase of the mean diameter of the solar wheel for the fourteen working fluids. The higher is the temperature increase, the higher is the amount of heat, $(\rho_\ell - \rho_{v_3})V(u_2 - u_1)$, required to raise the temperature of the liquid in the lower container, which represents practically the loss of energy as indicated in the preceding section. It is shown that R-113 has the highest temperature increase and it has the lowest thermal efficiency.

From Fig. 2 it can be seen that by an increase of the upper temperature limit from T_2 to T_2', the ratio of the useful works, (area 12′3′4′)/(area 1234), is smaller than the ratio of the temperature differences, $(T_2' - T_1)/(T_2 - T_1)$. However, the ratio of the losses, $(u_2' - u_1)/(u_2 - u_1)$, is approximately proportional to the ratio of the temperature differences. Therefore, it is expected that for a fixed value of the lower temperature limit with the increase of the upper temperature limit, the thermal efficiency of the Minto solar wheel increases first rapidly and then gradually slowly. After a certain value of the upper temperature limit the thermal efficiency will then decrease. The curves presented in Fig. 4 verify this conclusion. The curve for R-114 is a typical one with a drop of the thermal efficiency after D = 7.62m (25 ft).

It is evident that working fluid used for the Minto solar wheel has to be selected in order to obtain a good thermal performance of the engine. Among the 14 selected working fluids, R-12, R-115, and R-500, R-22 and R-13B1 achieve better thermal performance than the other fluids as shown in Fig. 4. In general, a working fluid having a small temperature increase from state 1 to state 2 of the ideal cycle of the Minto solar wheel, has the advantage that a heat source, with a relatively low temperature, which supplies heat to the working fluid, may be used to operate the engine.

Conclusions

The characteristic of the thermal performance of the Minto solar wheel is that its thermal efficiency is strongly dependent on the material properties of the working fluid. For a fixed value of the lower temperature limit with the increase of the upper temperature limit, the thermal efficiency of the ideal cycle of the Minto solar wheel increases first rapidly and then gradually slowly. After a certain value of the upper temperature limit, the thermal efficiency will then decrease. Among the fourteen selected working fluids, R-12, R-115, R-500, R-22 and R-13B1 achieve better thermal performance than the other fluids as shown in Fig. 4.

In general, a working fluid having a small temperature increase from state 1 to state 2 of the ideal cycle of the Minto solar wheel, has the advantage that the heat source used to operate the engine, does not require a relatively high temperature.

References

1 Walters, S., "Backyard Solar Engine," *Mechanical Engineering,* Vol. 98, No. 3, 1976, p. 47.

2 Lindsley, E. F., "Wally Minto's Wonder Wheel," *Popular Science,* Vol. 208, No. 3, 1976, p. 79.

3 Lin, S., "The Thermodynamic Cycle of the Minto Solar Wheel," submitted to *Trans. ASHRAE.*

4 *ASHRAE Handbook,* 1977 Fundamentals, Chapter 16.

Downloaded 01 Jun 2010 to 171.66.16.58. Redistribution subject to ASME license or copyright; see http://www.asme.org/terms/Terms_Use.cfm

Journal of Engineering for Power

Technical Briefs

Simulation of Whirl Interaction in Pinion-Gear Systems Supported on Oil Film Bearings

B Hamad[1] and A. Seireg[2]

The pinion gear system is modeled as a coupled two-rotor problem in this study. Each rotor is centrally supported on two hydrodynamic bearings and the inertia and load interaction between the two rotors is considered throughout their whirl orbits. Numerical results are given to illustrate the effect of transmitted load on the whirl amplitudes and stability of balanced and unbalanced gears with different gear ratios.

Introduction

The prediction of gear system whirl is a problem of considerable practical interest [1, 2]. In a previous study [3], the authors investigated this problem utilizing a phase-plane simulation of the pinion rotor dynamics [4] to investigate the effect of the gear constraint on the pinion trajectories. The system considered in the previous investigation consists of a rigid pinion supported on isoviscous fluid film meshing with a rigid gear supported by a rigid shaft and the effect of the transmitted load is assumed negligible.

The study reported here is an extension of the previous investigation where the gear rotor is also assumed to be supported on isoviscous fluid bearings and the transmitted gear load is taken into consideration. Each rotor is simulated as a two degree of freedom system with the inertial and transmitted load coupling effects between the two rotors appropriately included.

Analysis

The system under consideration is diagrammatically illustrated in Fig. 1. The whirl of each rotor is modeled as described in [3, 4] as a superposition of two simultaneous vibrations in the X and Y directions. If the resulting oscillation has a component along the line of action of the teeth in the opposite direction to the gears rotation, the inertia effect of each gear on the whirl of the other is taken into consideration.

This consideration is stated as:

$$(x_1 + x_2)\cos\phi + (y_1 + y_2)\sin\phi \geq 0 \tag{1}$$

where x_1, y_1 and x_2, y_2 are the coordinates of the center of mass of both rotors and ϕ is the pressure angle for the gear mesh.

The experimental results of [1] suggest that under such conditions the inertia effects of one gear on the whirl of the other can be accounted for by including in each gear model an additional mass at the base circle having the same moment of inertia as the gear about its rotational axis. Accordingly,

$$\left.\begin{aligned}(M_1)_{\text{effective}} &= M_1 + \frac{I_2}{(R_2)^2}\\ (M_2)_{\text{effective}} &= M_2 + \frac{I_1}{(R_1)^2}\end{aligned}\right\} \tag{2}$$

for

$$(x_1 + x_2)\cos\phi + (y_1 + y_2)\sin\phi \geq 0$$

and

$$(M_1)_{\text{effective}} = M_1$$

$$(M_2)_{\text{effective}} = M_2$$

for

$$(x_1 + x_2)\cos\phi + (y_1 + y_2)\sin\phi < 0$$

The equations of motion for each rotor measured from its steady state equilibrium position with zero transmitted load can therefore be written as:

$$(M_1)_{\text{effective}}\ddot{x} + C_{xx}\dot{x} + C_{xy}\dot{y} + K_{xx}x + K_{xy}y = F_x \tag{3}$$

$$(M_1)_{\text{effective}}\ddot{y} + C_{yx}\dot{y} + C_{yy}\dot{y} + K_{yx}x + K_{yy}y = F_y \tag{4}$$

and

$$(M_2)_{\text{effective}}\ddot{x} + C_{xx}\dot{x} + C_{xy}\dot{y} + K_{xx}x + K_{xy}y = F_x' \tag{5}$$

$$(M_2)_{\text{effective}}\ddot{y} + C_{yx}\dot{y} + C_{yy}\dot{y} + K_{yx}x + K_{yy}y = F_y' \tag{6}$$

The result is a system of coupled nonlinear second order differential equations where F_x is the x-component of the force due to tooth load

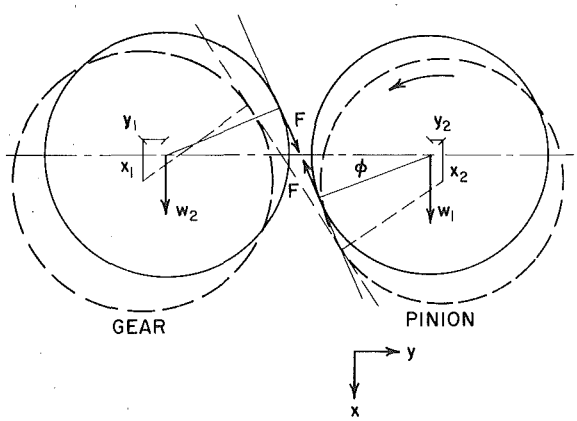


Fig. 1 Diagrammatic sketch of the geared system

[1] Mechanical Engineering Department, University of Khartoum-Sudan, Sudan

[2] Mechanical Engineering Department, University of Wisconsin at Madison, Madison, Wisc.

Contributed by the Power Transmission and Gear Committee for publication in the JOURNAL OF ENGINEERING FOR POWER. Manuscript received at ASME Headquarters December 4, 1978

Copyright © 1980 by ASME

Downloaded 01 Jun 2010 to 171.66.16.58. Redistribution subject to ASME license or copyright; see http://www.asme.org/terms/Terms_Use.cfm

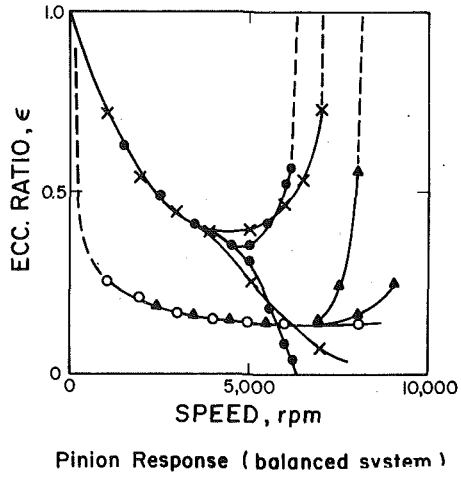


Fig. 2(*a*) Pinion response (balanced system). ●—$F/W = 0$ unconstrained by gear, ○—$F/W = 2$ unconstrained by gear, x—$F/W = 0$ with gear constraint (gear ratio = 1), ▲—$F/W = 2$ with gear constraint (gear ratio = 1)

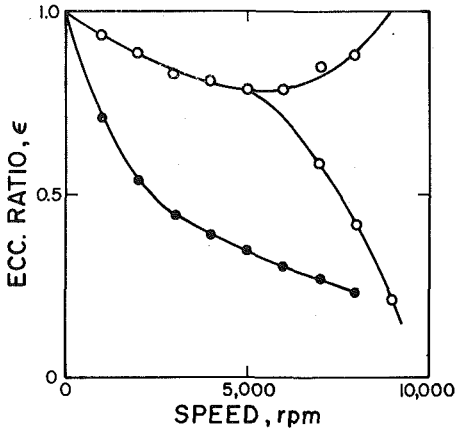


Fig. 2(*b*) Gear response with pinion constraint (balanced system). ●—$F/W = 0$ (gear ratio = 1), ○—$F/W = 2$ (gear ratio = 1)

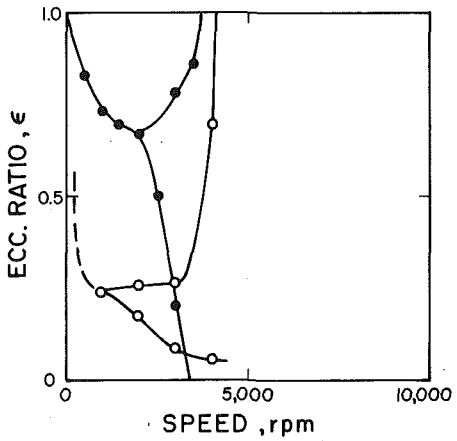


Fig. 3(*a*) Pinion response for gear ratio 1:1. (mr = 0.0007 lb s^2), (mr = 0.00032 kg s^2). ●—$F/W = 0$, ○—$F/W = 2$

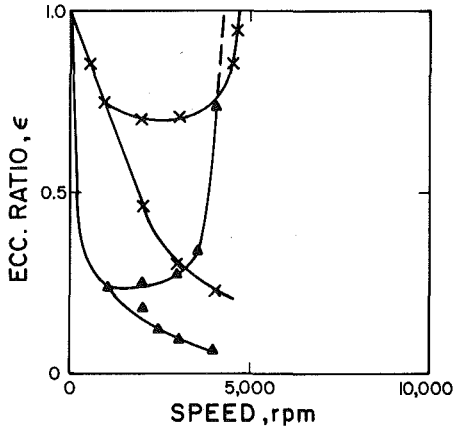


Fig. 3(*a'*) Pinion response for gear ratio 1:2. (mr = 0.0007 lb s^2), (mr = 0.00032 kg s^2). x—$F/W = 0$, ▲—$F/W = 2$

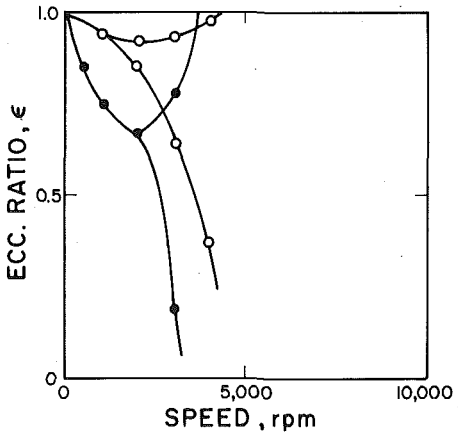


Fig. 3(*b*) Pinion response for gear ratio 1:1. (mr = 0.0007 lb s^2), (mr = 0.00032 kg s^2). ●—$F/W = 0$, ○—$F/W = 2$

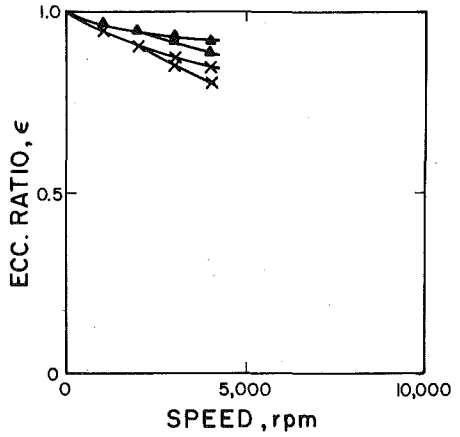


Fig. 3(*b'*) Gear response for gear ratio 1:2. (mr = 0.0007 lb s^2), (mr = 0.00032 kg s^2). x—$F/W = 0$, ▲—$F/W = 2$

and any assumed unbalance; and F_y is the y-component of the force due to tooth load and any assumed unbalance.

The stiffness and the damping coefficients of the bearing film are taken the same as in [4].

Equations (3–6) can therefore be numerically integrated by the phase-plane-δ method until a limit cycle is reached or one of the journals touches the sleeve.

Numerical Examples

The following parameters for the bearings and the geared system are used for the calculations reported in this paper: D = bearing diameter = 2.5 in. = 6.35 cm; C = radial clearance = 0.0063 in. = 0.016 cm; W = pinion weight = 100 lbs = 45.4 kg; L = length of bearing = 2.5 in. = 6.35 cm; x_0 = initial displacement of pinion from equilibrium

Downloaded 01 Jun 2010 to 171.66.16.58. Redistribution subject to ASME license or copyright; see http://www.asme.org/terms/Terms_Use.cfm

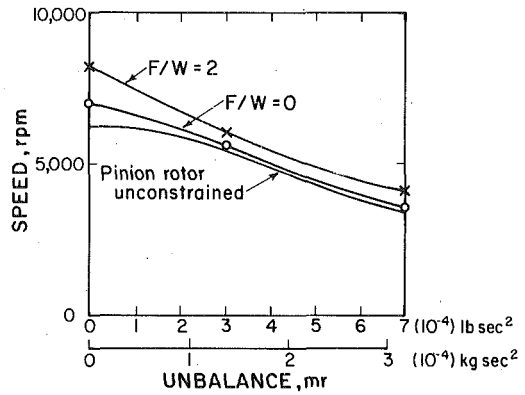


Fig. 4 Threshold of instability of gear system for gear ratio 1:1. *x*—instability occurs first in pinion rotor, O—instability occurs in both rotors at the same time

position = 0.0005 in. = 0.00127 cm. The oil used is SAE 10 at 150°F (65.5°C) average temperature (corresponding to an average viscosity of 1.76×10^{-6} Reynolds).

The numerical solution for the eceentricity ratios and its range of fluctuation at different speeds is given in Figs. 2 and 3 for gear ratios of 1 and 2, respectively. The calculated data are for transmitted gear loads F equal to zero and $2W$ where W is the pinion rotor weight.

The results for the unconstrained pinion rotor are plotted in Fig. 2(a) for comparison.

It can be seen from the figures that the transmitted gear load has, as expected, a stabilizing effect on the gear (since its effect is additive to its static weight) and a destabilizing effect on the pinion (since its effect is to reduce the static load on the bearings).

The example of identical gears and pinions with identical unbalance magnitude is believed to illustrate the transmitted load effects on the total system stability. The results for the threshold of instability are plotted in Fig. 4. As can be seen, the gear constraint with zero transmitted load causes an increase in the threshold speed. Instability in this case occurs, as expected, identically in the pinion and the gear rotors. The effect of the transmitted load can be seen to increase the threshold of instability in this case with the pinion rotor instability occurring first and therefore causing the system instability.

References

1 Seireg, A., "Whirling of Shafts in Geared Systems," ASME JOURNAL OF ENGINEERING FOR INDUSTRY, Paper No. 66-WA/MD-6, Winter Annual Meeting, New York, Nov. 27–Dec. 1, 1966.

2 Lund, J. W., "Critical Speeds, Stability and Response of Geared Train of Rotors," Trans. ASME, Paper No. 77-DET-30, *Design Engineering Technical Conference*, Chicago, IL, Sept. 26–30, 1977.

3 Hamad, B. & Seirig, A., "Whirl of Geared Systems Supported on Hydrodynamic Bearings," IFToMM 5th World Congress, July 8–13, 1979, Montreal, Canada.

4 Seireg, A. and Dandage, S., "A Phase-Plane Simulation for Investigating the Effect of Unbalance Magnitude on the Wheel of Rotor Supported on Hydrodynamic Bearings," ASME JOURNAL OF LUBRICATION TECHNOLOGY, Paper No. 75-Lub-G, 1975.

Downloaded 01 Jun 2010 to 171.66.16.58. Redistribution subject to ASME license or copyright; see http://www.asme.org/terms/Terms_Use.cfm

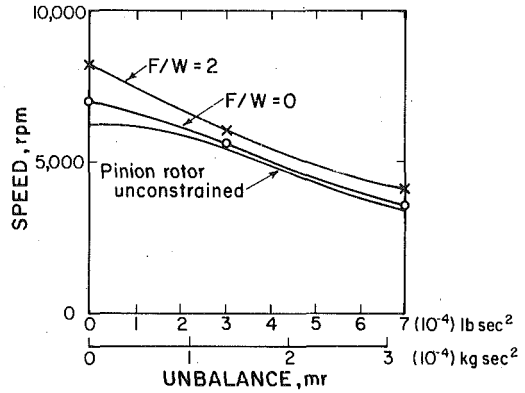


Fig. 4 Threshold of instability of gear system for gear ratio 1:1. x—instability occurs first in pinion rotor, O—instability occurs in both rotors at the same time

position = 0.0005 in. = 0.00127 cm. The oil used is SAE 10 at 150°F (65.5°C) average temperature (corresponding to an average viscosity of 1.76×10^{-6} Reynolds).

The numerical solution for the eceentricity ratios and its range of fluctuation at different speeds is given in Figs. 2 and 3 for gear ratios of 1 and 2, respectively. The calculated data are for transmitted gear loads F equal to zero and $2W$ where W is the pinion rotor weight.

The results for the unconstrained pinion rotor are plotted in Fig. 2(*a*) for comparison.

It can be seen from the figures that the transmitted gear load has, as expected, a stabilizing effect on the gear (since its effect is additive to its static weight) and a destabilizing effect on the pinion (since its effect is to reduce the static load on the bearings).

The example of identical gears and pinions with identical unbalance magnitude is believed to illustrate the transmitted load effects on the total system stability. The results for the threshold of instability are plotted in Fig. 4. As can be seen, the gear constraint with zero transmitted load causes an increase in the threshold speed. Instability in this case occurs, as expected, identically in the pinion and the gear rotors. The effect of the transmitted load can be seen to increase the threshold of instability in this case with the pinion rotor instability occurring first and therefore causing the system instability.

References

1 Seireg, A., "Whirling of Shafts in Geared Systems," ASME JOURNAL OF ENGINEERING FOR INDUSTRY, Paper No. 66-WA/MD-6, Winter Annual Meeting, New York, Nov. 27–Dec. 1, 1966.

2 Lund, J. W., "Critical Speeds, Stability and Response of Geared Train of Rotors," Trans. ASME, Paper No. 77-DET-30, *Design Engineering Technical Conference*, Chicago, IL, Sept. 26–30, 1977.

3 Hamad, B. & Seirig, A., "Whirl of Geared Systems Supported on Hydrodynamic Bearings," IFToMM 5th World Congress, July 8–13, 1979, Montreal, Canada.

4 Seireg, A. and Dandage, S., "A Phase-Plane Simulation for Investigating the Effect of Unbalance Magnitude on the Wheel of Rotor Supported on Hydrodynamic Bearings," ASME JOURNAL OF LUBRICATION TECHNOLOGY, Paper No. 75-Lub-G, 1975.

Journal of Engineering for Power

Discussion

Effects of Non-uniform Passages on Deepfold Heat Exchanger Performance[1]

A. L. London.[2] This paper deals with a difficult question: namely, how to specify manufacturing tolerances for laminar flow type heat exchanger surfaces. The discussor became aware of this problem in 1965, when he was at the General Motors Research Laboratory working with Mr. Mondt. Two papers in 12 years on this open question is possibly characteristic of the response of engineering technology to nagging, as distinct from demanding, problems. The author is to be congratulated for an excellent contribution. With like contributions, the designer will eventually have the information he needs to specify tolerances.

The task will remain a formidable one, especially until operationally convenient methods of measurement of the deviations such as fin-spacing and bulginess are developed. In this respect, the presentation in Appendix B is all too brief. It would be worthwhile to have Mr. Mondt expand on this subject in another paper.

The idea of combining a bulginess characterization with a fin-spacing characterization into a single total deviation characterization is appealing. Unfortunately, equation (10) for $\sigma_t{}^*$ does not obviously combine equation (5) for $\sigma_c{}^*$ with equation (9) for $\sigma_b{}^*$. A more direct formulation might be

$$\sigma_t{}^{**} \triangleq \sqrt{\sigma_c{}^{*2} + \sigma_b{}^{*2}} \tag{17}$$

This total deviation characterization differs from the equation (10) definition of $\sigma_t{}^*$. Numerically, however, using the Table 1 standard shapes, $\sigma_t{}^{**}$ and $\sigma_t{}^*$ agree within six percent. The test packs of Table 2 show a larger difference ranging up to 16 percent. Unfortunately, the experimental uncertainties in the test data (Figs. 10, 11) are such that one cannot tell whether $\sigma_t{}^*$ or $\sigma_t{}^{**}$ provides the better correlation with the theory curve.

A question arises in the definition of the authors $\sigma_t{}^*$, equations (10) and (11). Does this expression characterize both bulginess ($\sigma_b{}^*$) and fin nonuniform spacing ($\sigma_c{}^*$)? If $\sigma_b{}^* \to 0$, $\sigma_t{}^*$ should go to $\sigma_c{}^*$. If $\sigma_c{}^* \to 0$, $\sigma_t{}^*$ should go to $\sigma_b{}^*$. This is the case for $\sigma_b{}^* \to 0$, but not for $\sigma_c{}^* \to 0$. However, if $\sigma_b{}^*$ is redefined from the authors equation (9) to

$$\sigma_b{}^{**} = \sqrt{\frac{1}{(n-1)} \sum_1^n \left[\frac{b_i}{c_i} - 1\right]^2} \tag{18}$$

then $\sigma_t{}^*$ of equations (10) and (11) would "behave" for both limiting cases.

A research task remains which requires more precise experimentation as well as more sophisticated statistical techniques for its resolution. In the meanwhile, Mr. Mondt's paper serves as a reminder to industry that this is a nagging problem that won't go away. It needs to be resolved!

[1] By J. R. Mondt, published in the October 1977 issue of the ASME JOURNAL OF ENGINEERING FOR POWER, Vol. 99, No. 4, pp. 657–663.

[2] Professor, Department of Mechanical Engineering, Standford University, Stanford, CA.

Copyright © 1980 by ASME

Downloaded 01 Jun 2010 to 171.66.16.58. Redistribution subject to ASME license or copyright; see http://www.asme.org/terms/Terms_Use.cfm

Author's Closure

The author acknowledges with gratitude the timely discussion by Professor A. L. London. Professor London suggests a slightly different definition for bulginess, σ_b, and a different definition for combined total nonuniformity, σ_t. The proposed total combined nonuniformity, equation (17), is the root-sum-square of the bulginess and nonuniform fin spacing, σ_c, in contrast to the author's equation (10).

The author agrees that the root-sum-square approach appears more rigorous since σ_t collapses to σ_b when σ_c approaches zero. In fact, the root-sum-square approach was initially attempted by the author. However, the passage-scanning software and statistical calculations exceeded the storage capacity of the computer facility which was available to the author during the study. By using the shorter calculation procedure, outlined in the paper, a sample of 240 passages could be used for the statistical calculations. This large sample size was chosen to assure with 95 percent confidence that both the mean fin spacing and bulginess as well as the corresponding standard deviations for the passage population were estimated within ±0.5 percent by the sample measurements.

Perhaps some combinations of nonuniform geometries correlate better with equation (10), and some correlate better with equation (17). Therefore, the next logical step, if this work is extended, would be to compare nonuniformity parameters calculated by both equations using measurements from several typical nonuniform geometries.

Periodically Unsteady Flow in an Imbedded Stage of a Multistage, Axial-Flow Turbomachine[1]

G. J. Walker.[2] The authors are to be complimented on their detailed three-dimensional description of the unsteady velocity field through a compressor stage. The orderly behavior of the wake transport processes observed at different radial positions encourages the belief that allowances for wake interaction effects will ultimately be incorporated in axial turbomachinery design.

The use of helium injection to trace wake flows in an axial machine has been reported previously by Kerrebrock and Micolajczak [10]. The present paper now demonstrates that heated fluid can also be used to advantage in locating the IGV wake transport through a compressor. Further use of such passive marker techniques will undoubtedly be necessary to reveal the fine structure of the various wake interaction processes.

The 50 percent span rotor exit periodic-average axial velocity profiles described in the present paper (and shown in Fig. 6 of Schmidt and Okiishi [6]) appear quite consistent with the earlier more qualitative observations made in a similar situation by Lockhart and Walker [12], and shown in Fig. 3 of that paper. (There are, of course, some differences in appearance of the two sets of observations due to the latter measurements being offectively a plot of streamwise velocity along a streamwise traverse line, which cuts the various wake regions at a different angle). However, the Tasmanian work [12], in which observations were made at several axial stations between blade rows, suggests that some aspects of the present measurements can be interpreted in a rather different manner. For this reason some further discussion of wake-wake interaction phenomena seems warranted.

There is general agreement about the wake chopping and transport as represented in the periodic-average cascade plots of the present paper (Fig. 4 for the data under discussion). The IGV wake-rotor wake interaction is initiated by this chopping and the influence of IGV wake segments adjacent to the rotor wake. Slip flow within the IGV wake will tend to thin the rotor wake on the pressure side of the IGV wake street due to both flow convection and turbulent mixing effects; this thinning effectively restricts the slip flow towards the rotor trailing edge in the rotor wake, so that low energy rotor wake fluid accumulates against the suction side of the IGV wake street. The local rotor wake thickening thus produced is accentuated by the convective effects of slip flow within the IGV wake segments adjacent to the suction side. This process commences immediately downstream of the rotor trailing edge, and with increasing distance downstream there is a progressive thickening of the rotor wake on the suction side of the IGV wake street and a thinning on the pressure side (as indicated by the measurements in Fig. 4 of [12]). It is true that low energy IGV wake fluid must accumulate on the pressure surface during passage through the rotor, as noted by Kerrebrock and Mikolajczak [10]; but the IGV wake velocity defect is relatively small at the rotor exit, and cannot produce continued streamwise variations downstream of the rotor of the magnitude observed in [12]. According to this reasoning, the the deepest periodic-average rotor wake observed at 50 percent span for $YO_R/S_R = 0.69$ is interpreted as being mainly due to accumulation of rotor wake slip flow; the rotor wake region is in fact thicker here than on the pressure side of the IGV wake street, as shown in the profile for $YO_R/S_R = 0.17$.

The accumulation of rotor wake slip flow against the suction side of the IGV wake street immediately downstream of the rotor means that intra-stator rotor wake-stator interactions as described by Kerrebrock and Mikolajczak [10] will generally be greatly diminished for an imbedded stage. The circumferential location of the major rotor wake fluid accumulation will then be controlled mainly by the circumferential position of the next upstream stator row, and will not in general coincide with the stator pressure surface.

It is noted that Fig. 4 of [10] shows results of helium tracer tests which do indeed indicate the accumulation of rotor wake fluid on the stator pressure side in a compressor with IGV, rotor and stator rows; but the above discussion suggests that this should be regarded as a chance result in an isolated test[3], Lockhart and Walker [12] found that the region of thicker rotor wakes downstream of the stator could be moved to any desired circumferential position simply by rotating the IGV row.

The foregoing discussion suggests that it would be useful to distinguish as two quite different phenomena:

1. the rotor wake-downstream stator interaction described by Kerrebrock and Mikolajczak [10], in which accumulation of rotor wake slip flow cannot commence until the rotor wake actually enters the downstream row and the slip flow is intercepted by the stator pressure surface, and
2. the rotor wake—upstream stator wake interaction described by Lockhart and Walker [12], in which accumulation of rotor wake slip flow commences immediately downstream of the rotor trailing edge due to its restriction by interactions with the street of chopped wake segments from the upstream stator.

Similar comments apply to stator-rotor interactions.

Authors' Closure

We are appreciative of the time and effort spent by Dr. Walker in preparing his discussion of our paper.

As mentioned by Schmidt and Okiishi [6], superimposed hot-wire oscilloscope trace data observed by them were in agreement with the

---

By J. H. Wagner, T. H. Okiishi and G. J. Holbrook, published in the January 1979 issue of the JOURNAL OF ENGINERRING FOR POWER, Vol. 101, No. 1, pp. 42–51.

[2] Mechanical Engineering Department, University of Tasmania, Australia, Mem. ASME.

[3] The reservations expressed about one isolated set of results in [10] in no way invalidate the rest of that paper, which is concerned solely with single-stage machines having an isolated stage of only two blade rows. But it is suggested that the theory presented in [10] will require some modification in the case of an imbedded stage.

Downloaded 01 Jun 2010 to 171.66.16.58. Redistribution subject to ASME license or copyright; see http://www.asme.org/terms/Terms_Use.cfm

Author's Closure

The author acknowledges with gratitude the timely discussion by Professor A. L. London. Professor London suggests a slightly different definition for bulginess, σ_b, and a different definition for combined total nonuniformity, σ_t. The proposed total combined nonuniformity, equation (17), is the root-sum-square of the bulginess and nonuniform fin spacing, σ_c, in contrast to the author's equation (10).

The author agrees that the root-sum-square approach appears more rigorous since σ_t collapses to σ_b when σ_c approaches zero. In fact, the root-sum-square approach was initially attempted by the author. However, the passage-scanning software and statistical calculations exceeded the storage capacity of the computer facility which was available to the author during the study. By using the shorter calculation procedure, outlined in the paper, a sample of 240 passages could be used for the statistical calculations. This large sample size was chosen to assure with 95 percent confidence that both the mean fin spacing and bulginess as well as the corresponding standard deviations for the passage population were estimated within ±0.5 percent by the sample measurements.

Perhaps some combinations of nonuniform geometries correlate better with equation (10), and some correlate better with equation (17). Therefore, the next logical step, if this work is extended, would be to compare nonuniformity parameters calculated by both equations using measurements from several typical nonuniform geometries.

Periodically Unsteady Flow in an Imbedded Stage of a Multistage, Axial-Flow Turbomachine[1]

G. J. Walker.[2] The authors are to be complimented on their detailed three-dimensional description of the unsteady velocity field through a compressor stage. The orderly behavior of the wake transport processes observed at different radial positions encourages the belief that allowances for wake interaction effects will ultimately be incorporated in axial turbomachinery design.

The use of helium injection to trace wake flows in an axial machine has been reported previously by Kerrebrock and Micolajczak [10]. The present paper now demonstrates that heated fluid can also be used to advantage in locating the IGV wake transport through a compressor. Further use of such passive marker techniques will undoubtedly be necessary to reveal the fine structure of the various wake interaction processes.

The 50 percent span rotor exit periodic-average axial velocity profiles described in the present paper (and shown in Fig. 6 of Schmidt and Okiishi [6]) appear quite consistent with the earlier more qualitative observations made in a similar situation by Lockhart and Walker [12], and shown in Fig. 3 of that paper. (There are, of course, some differences in appearance of the two sets of observations due to the latter measurements being offectively a plot of streamwise velocity along a streamwise traverse line, which cuts the various wake regions at a different angle). However, the Tasmanian work [12], in which observations were made at several axial stations between blade rows, suggests that some aspects of the present measurements can be interpreted in a rather different manner. For this reason some further discussion of wake-wake interaction phenomena seems warranted.

There is general agreement about the wake chopping and transport as represented in the periodic-average cascade plots of the present paper (Fig. 4 for the data under discussion). The IGV wake-rotor wake interaction is initiated by this chopping and the influence of IGV wake segments adjacent to the rotor wake. Slip flow within the IGV wake will tend to thin the rotor wake on the pressure side of the IGV wake street due to both flow convection and turbulent mixing effects; this thinning effectively restricts the slip flow towards the rotor trailing edge in the rotor wake, so that low energy rotor wake fluid accumulates against the suction side of the IGV wake street. The local rotor wake thickening thus produced is accentuated by the convective effects of slip flow within the IGV wake segments adjacent to the suction side. This process commences immediately downstream of the rotor trailing edge, and with increasing distance downstream there is a progressive thickening of the rotor wake on the suction side of the IGV wake street and a thinning on the pressure side (as indicated by the measurements in Fig. 4 of [12]). It is true that low energy IGV wake fluid must accumulate on the pressure surface during passage through the rotor, as noted by Kerrebrock and Mikolajczak [10]; but the IGV wake velocity defect is relatively small at the rotor exit, and cannot produce continued streamwise variations downstream of the rotor of the magnitude observed in [12]. According to this reasoning, the the deepest periodic-average rotor wake observed at 50 percent span for $YO_R/S_R = 0.69$ is interpreted as being mainly due to accumulation of rotor wake slip flow; the rotor wake region is in fact thicker here than on the pressure side of the IGV wake street, as shown in the profile for $YO_R/S_R = 0.17$.

The accumulation of rotor wake slip flow against the suction side of the IGV wake street immediately downstream of the rotor means that intra-stator rotor wake-stator interactions as described by Kerrebrock and Mikolajczak [10] will generally be greatly diminished for an imbedded stage. The circumferential location of the major rotor wake fluid accumulation will then be controlled mainly by the circumferential position of the next upstream stator row, and will not in general coincide with the stator pressure surface.

It is noted that Fig. 4 of [10] shows results of helium tracer tests which do indeed indicate the accumulation of rotor wake fluid on the stator pressure side in a compressor with IGV, rotor and stator rows; but the above discussion suggests that this should be regarded as a chance result in an isolated test[3], Lockhart and Walker [12] found that the region of thicker rotor wakes downstream of the stator could be moved to any desired circumferential position simply by rotating the IGV row.

The foregoing discussion suggests that it would be useful to distinguish as two quite different phenomena:

1. the rotor wake-downstream stator interaction described by Kerrebrock and Mikolajczak [10], in which accumulation of rotor wake slip flow cannot commence until the rotor wake actually enters the downstream row and the slip flow is intercepted by the stator pressure surface, and
2. the rotor wake—upstream stator wake interaction described by Lockhart and Walker [12], in which accumulation of rotor wake slip flow commences immediately downstream of the rotor trailing edge due to its restriction by interactions with the street of chopped wake segments from the upstream stator.

Similar comments apply to stator-rotor interactions.

Authors' Closure

We are appreciative of the time and effort spent by Dr. Walker in preparing his discussion of our paper.

As mentioned by Schmidt and Okiishi [6], superimposed hot-wire oscilloscope trace data observed by them were in agreement with the

---

By J. H. Wagner, T. H. Okiishi and G. J. Holbrook, published in the January 1979 issue of the JOURNAL OF ENGINERRING FOR POWER, Vol. 101, No. 1, pp. 42–51.

[2] Mechanical Engineering Department, University of Tasmania, Australia, Mem. ASME.

[3] The reservations expressed about one isolated set of results in [10] in no way invalidate the rest of that paper, which is concerned solely with single-stage machines having an isolated stage of only two blade rows. But it is suggested that the theory presented in [10] will require some modification in the case of an imbedded stage.

Copyright © 1980 by ASME

Downloaded 01 Jun 2010 to 171.66.16.58. Redistribution subject to ASME license or copyright; see http://www.asme.org/terms/Terms_Use.cfm

Lockhart and Walker [12] oscilloscope data for irregular unsteadiness trends. However, periodic-average rotor wake velocity defect trends were not in agreement. Schmidt and Okiishi [6] proposed that the periodic-average rotor wake velocity defect was greater when the rotor wake was measured within the chopped inlet guide vane (IGV) wake avenue while Lockhart and Walker [12] suggested that the opposite was true.

Dr. Walker's proposed explanation of the variation of rotor wake periodic-average axial-velocity profile with rotor sampling position (see Fig. 6 of [6]) in terms of *rotor wake* "slip flow" accumulation seems plausible. Perhaps this effect and the IGV wake segment slip flow effect proposed in the present paper both contribute to the trends observed. More definitive data, especially for what is happening at different axial distances downstream from a blade row trailing edge, would help clear up the fluid mechanics involved.

The relationship between Dr. Walker's proposed IGV-rotor wake interaction model and the Kerrebrock and Mikolajczak [10] intrastator transport of rotor wake segments model should be considered further before definite conclusions are reached.

Annular Diffuser Performance for an Automotive Gas Turbine[1]

S. V. Horn.[2] I would like to express my congratulations to the authors for a very readable paper and a very clear presentation of their work.

I have the following comments on the exhaust diffuser design:

1 Is there a possibility in the automotive gas turbine to fully use the given space limitation for axial-radial bend and thus allow for an increase of the pressure recovery of the whole system?

2 Poor performance of the exhaust diffuser for elevated Mach numbers is caused by the larger longitudal velocity gradient of the core (density change) and by the earlier flow separation.

There is existing procedure for the diffuser design for given inlet Mach number (on the base of the velocity distribution derived from the low inlet Mach number diffusers) which uses the solution of inverse problem and transfer from 2-D plane to axisymmetric plane within the viscous flow model (potential core and boundary layers) [1].

Additional Reference

1 Horn, S. V., "Diffuser Design with Suitable Velocity Distribution," Dissertation (in Czech), SVÚSS Běchovice, 1975.

Authors' Closure

The authors thank Dr. Horn for his discussion of the paper and for bringing to their attention the diffuser design procedure in his dissertation.

The question he poses is interpreted to mean that space limitation of the axial-radial bend prevents diffusion down to a satisfactory regenerator inlet Mach number, say 0.05. Such a situation occurred with the last two engine designs at Chrysler. There was length available to diffuse only to about 0.15 Mach number. Dr. Horn's question then asks whether it is possible for additional diffusion by further use of available space. Presumably, this means the use of flow-spitting devices to increase recovery. These devices have been considered but not employed. One concern is whether there is enough space to make effective use of splitters and yet place them sufficiently far from the turbine exit plane to minimize their influence on the rotor performance. Perhaps experiments should be conducted to investigate the use of splitters.

---

[1] By D. Japikse and R. Pampreen, published in the July 1979 issue of the JOURNAL OF ENGINEERING FOR POWER, Vol. 101, No. 3, pp. 358–372.

[2] Ph.D., Research and Advanced Product Development, Transamerica Delaval Inc., Trenton, N.J.

Downloaded 01 Jun 2010 to 171.66.16.58. Redistribution subject to ASME license or copyright; see http://www.asme.org/terms/Terms_Use.cfm

Lockhart and Walker [12] oscilloscope data for irregular unsteadiness trends. However, periodic-average rotor wake velocity defect trends were not in agreement. Schmidt and Okiishi [6] proposed that the periodic-average rotor wake velocity defect was greater when the rotor wake was measured within the chopped inlet guide vane (IGV) wake avenue while Lockhart and Walker [12] suggested that the opposite was true.

Dr. Walker's proposed explanation of the variation of rotor wake periodic-average axial-velocity profile with rotor sampling position (see Fig. 6 of [6]) in terms of *rotor wake* "slip flow" accumulation seems plausible. Perhaps this effect and the IGV wake segment slip flow effect proposed in the present paper both contribute to the trends observed. More definitive data, especially for what is happening at different axial distances downstream from a blade row trailing edge, would help clear up the fluid mechanics involved.

The relationship between Dr. Walker's proposed IGV-rotor wake interaction model and the Kerrebrock and Mikolajczak [10] intrastator transport of rotor wake segments model should be considered further before definite conclusions are reached.

Annular Diffuser Performance for an Automotive Gas Turbine[1]

S. V. Horn.[2] I would like to express my congratulations to the authors for a very readable paper and a very clear presentation of their work.

I have the following comments on the exhaust diffuser design:

1 Is there a possibility in the automotive gas turbine to fully use the given space limitation for axial-radial bend and thus allow for an increase of the pressure recovery of the whole system?

2 Poor performance of the exhaust diffuser for elevated Mach numbers is caused by the larger longitudal velocity gradient of the core (density change) and by the earlier flow separation.

There is existing procedure for the diffuser design for given inlet Mach number (on the base of the velocity distribution derived from the low inlet Mach number diffusers) which uses the solution of inverse problem and transfer from 2-D plane to axisymmetric plane within the viscous flow model (potential core and boundary layers) [1].

Additional Reference

1 Horn, S. V., "Diffuser Design with Suitable Velocity Distribution," Dissertation (in Czech), SVÚSS Běchovice, 1975.

Authors' Closure

The authors thank Dr. Horn for his discussion of the paper and for bringing to their attention the diffuser design procedure in his dissertation.

The question he poses is interpreted to mean that space limitation of the axial-radial bend prevents diffusion down to a satisfactory regenerator inlet Mach number, say 0.05. Such a situation occurred with the last two engine designs at Chrysler. There was length available to diffuse only to about 0.15 Mach number. Dr. Horn's question then asks whether it is possible for additional diffusion by further use of available space. Presumably, this means the use of flow-spitting devices to increase recovery. These devices have been considered but not employed. One concern is whether there is enough space to make effective use of splitters and yet place them sufficiently far from the turbine exit plane to minimize their influence on the rotor performance. Perhaps experiments should be conducted to investigate the use of splitters.

---

[1] By D. Japikse and R. Pampreen, published in the July 1979 issue of the JOURNAL OF ENGINEERING FOR POWER, Vol. 101, No. 3, pp. 358–372.

[2] Ph.D., Research and Advanced Product Development, Transamerica Delaval Inc., Trenton, N.J.

Copyright © 1980 by ASME

Downloaded 01 Jun 2010 to 171.66.16.58. Redistribution subject to ASME license or copyright; see http://www.asme.org/terms/Terms_Use.cfm